



ICAROB 2018

PROCEEDINGS OF THE 2018 INTERNATIONAL CONFERENCE ON ARTIFICIAL LIFE AND ROBOTICS

February 1- 4 2018
B-Con Plaza, Beppu, Oita, JAPAN
International Meeting Series

Editor-in-Chief
Masanori Sugisaka
Editors: Yingmin Jia, Takao Ito, Ju-Jang Lee
ISBN 978-4-9908350-3-3

The 2018 International Conference on Artificial Life and Robotics (ICAROB2018), B-Con Plaza, Feb. 1- 4, Beppu, Oita, Japan, 2018

Proceedings of The 2018 International Conference on
ARTIFICIAL LIFE AND ROBOTICS
(ICAROB2018)

February 1- 4, 2018
B-Con Plaza, Beppu, Oita, JAPAN
International Meeting Series

Editor-in-Chief
Masanori Sugisaka
Editors: Yingmin Jia, Takao Ito, Ju-Jang Lee
ISBN 978-4-9908350-3-3

Contents

1	Organization, etc.	1
2	Messages	9
3	Time Table	14
4	Opening Ceremony	17
5	Technical paper index	18
6	Abstracts	
6-1	PS abstracts	41
6-2	IS abstracts	42
6-3	OS abstracts	44
6-4	GS abstracts	88
7	Authors index	106
8	Conference room	117

The 2018 International Conference on Artificial Life and Robotics (ICAROB2018), B-Con Plaza, Feb. 1- 4, Beppu, Oita, Japan, 2018

SPONSERED

ICAROB society (ALife Robotics Corporation Ltd.)



ORGANIZED BY

International Steering Committee of International Conference on Artificial Life and Robotics (ICAROB)



TECHNICAL CO-SPONSORED BY

IEEE Fukuoka Section (Japan)



CO-ORGANIZED BY

Chinese Association for Artificial Intelligence (CAAI, P. R. China)



SUPPORTRD BY

Oita Prefectural Government
Oita Prefectural Tourism association (Tourism Oita)

ADVISORY COMMITTEE CHAIR

Moshe Kam (New Jersey Institute of Technology, Former IEEE President, USA)

ADVISORY COMMITTEE

Adam Grzech (Wroclaw University of Technology, Poland)
Bruce Eisenstein (Drexel University, Former IEEE President, USA)
Guang-Ren Duan (Harbin Institute of Technology, P.R.China)
Hidenori Kimura (JST, Japan)
Jeffrey Johnson (The Open University, UK)
Jerzy Świątek (Wroclaw University of Technology, Poland)
Joshua M. Epstein (The Johns Hopkins University, USA)
Kai-Tai Song (National Chiao Tung University, Taiwan)
Masayoshi Tomizuka (University of California Berkeley, USA)
Moshe Kam (New Jersey Institute of Technology, Former IEEE President, USA)
Paul Kalata (Drexel University, USA)
Paul Oh (Drexel University, USA)
Robert Fischl (Drexel University, USA)
Steen Rasmussen (University of Southern Denmark, Denmark)

GENERAL CHAIR

Masanori Sugisaka (Alife Robotics Corporation Ltd., Japan)
(Visiting Professor, Open University, UK)

CO-GENERAL CHAIRS

Yingmin Jia (Beihang University, P. R. China)
Takao Ito (Hiroshima University, Japan)
Ju-Jang Lee (KAIST, Korea)

VICE GENERAL CHAIR

Henrik. H. Lund (Technical University of Denmark, Denmark)
John. L. Casti (International Institute for Applied Systems Analysis, Austria)
Jangmyung Lee (Pusan National University, Korea)
Luigi Pagliarini (Technical University of Denmark, Denmark)
(Academy of Fine Arts of Macerata, Italy)

PROGRAM CHAIRMAN

Makoto Sakamoto (University of Miyazaki, Japan)

CO-PROGRAM CHAIR

Marion Oswald (Technische Universität Wien, Austria)

INTERNATIONAL ORGANIZING COMMITTEE

Akira Fukuda (Kyushu University, Japan)
Andrew Gadsden (University of Guelph, Canada)
Caoli Wang (University of Shanghai for Science and Technology, P. R. China)
Chan Gook Park (Seoul National University, Korea)
Eiji Hayashi (Kyushu Institute of Technology, Japan)
Evgeni Magid (Kazan Federal University, Russia)
Fuzhong Wang (Henan Polytechnic University, P. R. China)
Hazry Desa (University of Malaysia, Perlis, Malaysia)
Hidehiko Yamamoto (Gifu University, Japan)
Hiroki Tamura (University of Miyazaki, Japan)
Hiroshi Kage ((Mitsubishi Electric Corporation, Japan)
Hiroshi Matsuno (Yamaguchi University, Japan)
Jiwu Wang (Beijing Jiaotong University, P. R. China)

Jovana Jovic (CNRS-AIST JRL, Japan, France)
Junping Du (Beijing University of Posts and Telecommunications, P. R. China)
Katsunori Shimohara (Doshisha University, Japan)
Kazuo Ishii (Kyushu Institute of Technology, Japan)
Kevin Voges (Canterbury University, New Zealand)
Kuo-Hsien Hsia (Far East University, Taiwan)
Kuo-Lan Su (National Yunlin University of Science and Technology, Taiwan)
Kyungho Park (Micro-System Programs, RDECOM, ITC-PAC, U.S. ARMY, Japan and USA)
Masao Kubo (National Defense Academy of Japan, Japan)
Masanao Obayashi (Yamaguchi University, Japan)
Maxim Sokolov (Innopolis University, Russia)
Mehta Rajiv (New Jersey Institute of Technology, USA)
Peter Sapaty (Ukrainian Academy of Science, Ukraine)
Pierre Parrend (University of Strasbourg, France)
Qiang Cai (Beijing Technology and Business University, P. R. China)
Takashi Kohno (LIMMS/CNRS-IIS, Institute of Industrial Science, The University of Tokyo, Japan)
Takashi Ogata (Iwate Prefectural University, Japan)
Teruhisa Hochin (Kyoto Prefectural University, Japan)
Tetsuro Hattori (Kagawa University, Japan)
Thi Thi Zin (University of Miyazaki, Japan)
Toru Yamamoto (Hiroshima University, Japan)
Victor Berdonosov (Komsomolsk-on-Amur State University of Technology, Russia)
Yasunari Yoshitomi (Kyoto Prefectural University, Japan)
Yi Chai (Chongqing University, P. R. China)
Yo Horikawa (Kagawa University, Japan)
Yoshifumi Morita (Nagoya Institute of Technology, Japan)
Yoshiro Imai (Kagawa University, Japan)
Zengqiang Chen (Nankai University, P. R. China)

INTERNATIONAL PROGRAM COMMITTEE

Akira Nakamura (AIST, Japan)
Ali Selamat (University of Technology of Malaysia (UTM), Malaysia)
Andre Rosendo (ShanghaiTech University, P. R. China)
Bin Zhang (Beijing University of Posts and Telecommunications, P. R. China)
Arsit Boonyaprapasorn (Chulachomkloa Royal Military Academy, Thailand)
Dongmei Ai (University of Science and Technology Beijing, P. R. China)
Endra Joelianto (Bandung Institute of Technology, Indonesia)
Fengzhi Dai (Tianjin University of Science & Technology, P. R. China)
Haisheng Li (Beijing Technology and Business University, P. R. China)
Haruna Matsushita (Kagawa University, Japan)
Hidetsugu Suto (Muroran Institute of Technology, Japan)
Hiroyuki Iizuka (Osaka University, Japan)

Huailin Zhao (Shanghai Institute of Technology, P. R. China)
Hussein Abbass (University of New South Wales and ADFA, Australia)
Istvan Harmati (Budapest Institute of Technology and Economics, Hungary)
Ivan Tanev (Doshisha University, Japan)
Jiandong Zhao (Beijing Jiaotong University, P. R. China)
Joono Cheong (Korea University, Korea)
Kathryn Elizabeth Merrick (University of New South Wales and ADFA, Australia)
Kunikazu Kobayashi (Aichi Prefectural University, Japan)
Lin Li (University of Shanghai for Science and Technology, P. R. China)
Lin Zhao (Qingdao University, P. R. China)
Manabu Yamada (Nagoya Institute of Technology, Japan)
Masahide Ito (Aichi Prefectural University, Japan)
Masayoshi Tabuse (Kyoto Prefectural University, Japan)
Masaomi Hatakeyama (University of Zurich, Switzerland)
Norrima Mokhtar (University of Malaya, Malaysia)
Noritaka Sato (Nagoya Institute of Technology, Japan)
Palakorn Tantrakool (King Mongkut's Institute of Technology Thonburi, Thailand)
Ping Wang (North China Electric Power University, P. R. China)
Qinglin Sun (Nankai University, P. R. China)
Satoshi Ikeda (The University of Miyazaki, Japan)
Sanjay S. Joshi (College of Engineering, University of California, USA)
Seong-Ik Han (Pusan National University, Korea)
Shingo Mabu (Yamaguchi University, Japan)
Shumin Fei (Southeast University, P. R. China)
Shyi-Ming Chen (National Taichung University of Education, Taiwan)
Takashi Kuremoto (Yamaguchi University, Japan)
Takayoshi Yamada (Gifu University, Japan)
Taishiro Kishimoto (Keio University, Japan)
Tetsuro Katayama (The University of Miyazaki, Japan)
Thunyaseth Sethaput (Thammasat University, Thailand)
Toshinori Nawata (Kumamoto National College of Technology, Japan)
Tsunehiro Yoshinaga (Tokuyama National College of Technology, Japan)
Weicun Zhang (University of Science and Technology Beijing, P. R. China)
Xiaoyan Fu (Capital Normal University, P. R. China)
Xuemei Ren (Beijing Institute of Technology, P. R. China)
Yunzhong Song (Henan Polytechnic University, P. R. China)

LOCAL ARRANGEMENT COMMITTEE

Makoto Sakamoto (University of Miyazaki, Japan)
Masanori Sugisaka (ALife Robotics Corporation Ltd., Japan)
(Visiting Professor, Open University, UK)
Takao Ito (Hiroshima University, Japan)

HISTORY

The International Conference on Artificial Life and Robotics (ICAROB) resulted from the AROB-symposium (International Symposium on Artificial Life and Robotics) whose first edition was held in 1996 and the eighteenth and last edition in 2013. The AROB symposium was annually organized by Oita University, Nippon Bunri University (NBU), and ALife Robotics Corporation Ltd., under the sponsorship of the Science and Technology Policy Bureau, the Ministry of Education, Science, Sports, and Culture (Monbusho), presently, the Ministry of Education, Culture, Sports, Science, and Technology (Monkasho), Japanese Government, Japan Society for the Promotion of Science (JSPS), the Commemorative Organization for the Japan World Exposition ('70), Air Force Office of Scientific Research, Asian Office of Aerospace Research and Development (AFOSR/AOARD), USA. I would like to express my sincere thanks to not only Monkasho (annually fund support from 1996 to 2013) but also JSPS, the Commemorative Organization for the Japan World Exposition ('70), and various other Japanese companies for their repeated support. The old symposium (this symposium has been held every year at B-Con Plaza, Beppu, Oita, Japan except in Oita, Japan (AROB 5th '00) and in Tokyo, Japan (AROB 6th '01).) was organized by the International Organizing Committee of AROB and was co-operated by the Santa Fe Institute (USA), RSJ, IEEJ, ICASE (Now ICROS) (Korea), CAAI (P. R. China), ISCI, IEICE, IEEE (Japan Council), JARA, and SICE. The old AROB-symposium expanded much by absorbing much new knowledge and technologies into it. This history and character of the former AROB symposiums are passed on the current ICAROB conference and to this journal, International Journal of Robotics, Networking and Artificial Life (JRNAL). From now on, ALife Robotics Corporation Ltd. is in charge of management of both the conference and the journal. The future of the ICAROB is brilliant from a point of view of yielding new technologies to human society in the 21st century. This conference invites you all.

AIMS AND SCOPE

The objective of this conference is the development of new technologies for artificial life and robotics which have been recently born in Japan and are expected to be applied in various fields. This conference presents original technical papers and authoritative state-of-the-art reviews on the development of new technologies concerning robotics, networking and artificial life and, especially computer-based simulation and hardware for the twenty-first century. This conference covers a broad multidisciplinary field, including areas such as:

- Artificial intelligence & complexity
- Artificial living
- Artificial mind research
- Artificial nervous systems for robots
- Artificial sciences
- Bipedal robot
- Brain science and computing
- Chaos
- Cognitive science

Computational Molecular biology
Computer graphics
Data mining
Disasters robotics
DNA computing
Empirical research on network and MOT
Environment navigation and localization
Evolutionary computations
Facial expression analysis, music recommendation and augmented reality
Foundation of computation and its application
Fuzzy control
Genetic algorithms
Human-welfare robotics
Image processing
Insect-like aero vehicles
Intelligence in biological systems
Intelligent control
Management of technology
Medical surgical robot
Micro-machines
Multi-agent systems
Nano-biology
Nano-robotics
Networking
Neural circuits
Neuro-computer
Neuromorphic Systems
Neuroscience
Pattern recognition
Quantum computing
Reinforcement learning system & genetic programming
Robotics
Software development support method
System cybernetics
Unmanned underwater vehicles
Unmanned Aerial Systems Technologies
Unmanned Aerial Systems designing, controls and navigation
Unmanned Aero vehicles
Virtual reality
Visualization
Hardware-oriented submissions are particularly welcome. This conference will discuss new results in the field of artificial life and robotics

COPYRIGHTS

Accepted papers will be published in the proceeding of The 2018 International Conference on Artificial Life and Robotics (ICAROB 2018) by ALife Robotics Corp. Ltd. Copyright belongs to ALife Robotics Corp. Ltd. Some of high quality papers in the proceeding will be requested to re-submit their papers for the consideration of publication in an international journal ROBOTICS, NETWORKING AND ARTIFICIAL LIFE under agreement of both Editor-in- Chief Dr. Masanori Sugisaka and 3 reviewers. All correspondence related to the conference should be addressed to ICAROB Office.

ICAROB Office

ALife Robotics Corporation Ltd.

Hig Handadai, Oita 870-1112, JAPAN

TEL/FAX : +81-97-597-7760

E-MAIL :

icarob@alife-robotics.co.jp

Home Page : <http://alife-robotics.co.jp/>

MESSAGES



Masanori Sugisaka
General Chair

**(Visiting Prof. of Open University
(UK), President of ALife Robotics
Co., Ltd. (Japan))**

Masanori Sugisaka

Masanori Sugisaka

General Chair of ICAROB

It is my great honor to invite you all to The 2018 International Conference on Artificial Life and Robotics (ICAROB 2018).

This Conference is changed as the old symposium from the first (1996) to the Eighteenth (2013) annually which were organized by Oita University, Nippon Bunri University(NBU), and ALife Robotics Corporation Ltd. under the sponsorship of the Science and Technology Policy Bureau, the Ministry of Education, Science, Sports, and Culture (Monbusho), presently, the Ministry of Education, Culture, Sports, Science, and Technology (Monkasho), Japanese Government, Japan Society for the Promotion of Science (JSPS), The Commemorative Organization for the Japan World Exposition ('70), Air Force Office of Scientific Research, Asian Office of Aerospace Research and Development (AFOSR/AOARD), USA. I would like to express my sincere thanks to not only Monkasho (annually fund support from 1996 to 2013) but also JSPS, the Commemorative Organization for the Japan World Exposition ('70), Japanese companies for their repeated support.

The old symposium was organized by International Organizing Committee of AROB and was co-operated by the Santa Fe Institute (USA), RSJ, IEEJ, ICASE (Now ICROS) (Korea), CAAI (P. R. China), ISCIE, IEICE, IEEE (Japan Council), JARA, and SICE. The old AROB symposium was growing up by absorbing many new knowledge and technologies into it.

This history and character was inherited also from ICAROB2014(The 2014 International Conference on Artificial Life and Robotics, included a series of ICAROB proceedings in [SCOPUS](#) and [CPCI](#) now. From now on, ALife Robotics Corporation Ltd. is in charge of management. This year we have The 2018 International Conference on Artificial Life and Robotics (ICAROB2018) (23rd AROB Anniversary). The future of The ICAROB is brilliant from a point of view of yielding new technologies to human society in 21st century.

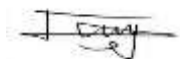
I hope that fruitful discussions and exchange of ideas between researchers during Conference (ICAROB2018) will yield new merged technologies for happiness of human beings and, hence, will facilitate the establishment of an international joint research institute on Artificial Life and Robotics in future.

Yingmin Jia

Co-General Chair of ICAROB



Yingmin Jia
Co-General Chair
(Professor, Beihang University,
R .P. China)



It is my great pleasure to invite you to The 2018 International Conference on Artificial Life and Robotics (ICAROB 2018), in B-Con Plaza, Beppu, Oita, Japan from February 1 to 4, 2018.

ICAROB develops from the AROB that was created in 1996 by Prof. Masanori Sugisaka and will celebrate her 23rd birthday in 2018. Doubtless, new mission and big challenges in the field of artificial life and robotics will promote ICAROB to start a new stage and attract wide interests among scientist, researchers, and engineers around the world.

For a successful meeting, many people have contributed their great efforts to ICAROB. Here, I would like to express my special thanks to all authors and speakers, and the meeting organizing team for their excellent works. Looking forward to meeting you at ICAROB in Beppu and wishing you enjoy your stay in Japan.



Takao Ito
Co-General Chair
(Professor Hiroshima
University, Japan)

A handwritten signature in black ink that reads "Takao Ito".

Takao Ito

Co General Chair of ICAROB

It is my great honor to invite you all to The 2018 International Conference on Artificial Life and Robotics (ICAROB 2018). This Conference is changed as the old symposium (ISAROB) from the first (1996) to the Eighteenth. I am pleased to welcome you to The 2018 International Conference on Artificial Life and Robotics in the wonderful city of Beppu, Oita city, Oita Prefecture, Japan.

The ICAROB has its long history. The former organization of the ICAROB was developed under the strong leadership of the President, famous Professor Masanori Sugisaka, the father of AROB. We gathered many researchers, faculty members, graduate students from all over the world, and published many high-quality proceedings and high-reputational journals every year.

Over the years, dramatic improvements have been made in the field of artificial life and its applications. The ICAROB has becoming the unifying the exchange of scientific information on the study of man-made systems that exhibit the behavioral characteristic of natural living systems including software, hardware and wetware. Our conference shapes the development of artificial life, extending our empirical research beyond the territory circumscribed by life-as-we-know-it and into the domain of life-as-it-could-be. It will provide us a good place to present our new research results, excellent ideas, and valuable information about artificial intelligence, complex systems theories, robotics, and management of technology.

The conference site is B-con Plaza, one of the most famous international convention centers in Kyushu island, Japan. You can find many fantastic scenic spots and splendid historical places in Beppu, Oita city. Enjoy your stay and take your time to visit Beppu, Oita city.

I am looking forward to meeting you in Beppu, Oita city, during the ICAROB 2018 and to sharing the most pleasant, interesting and fruitful conference with you.



Ju-Jang Lee
Co-General Chair
(Professor, KAIST)

A handwritten signature in cursive script, appearing to read 'J Lee'.

Ju-Jang Lee

Co-General Chair of ICAROB

The First International Conference on Artificial Life and Robotics (ICAROB) was held in Oita City, Oita, Japan from Jan. 11th to 13th, 2014. This year's Conference will be held amidst the high expectation of the increasingly important role of the new interdisciplinary paradigm of science and engineering represented by the field of artificial life and robotics that continuously attracts wide interests among scientist, researchers, and engineers around the globe.

Distinguished researchers and technologists from around the world are looking forward to attending and meeting at ICAROB. ICAROB is becoming the annual excellent forum that represents a unique opportunity for the academic and industrial communities to meet and assess the latest developments in this fast growing artificial life and robotics field. ICAROB enables them to address new challenges, share solutions, discuss research directions for the future, exchange views and ideas, view the results of applied research, present and discuss the latest development of new technologies and relevant applications.

In addition, ICAROB offers the opportunity of hearing the opinions of well-known leading experts in the field through the keynote sessions, provides the bases for regional and international collaborative research, and enables to foresee the future evolution of new scientific paradigms and theories contributed by the field of artificial life and robotics and associated research area. The twenty-first century will become the century of artificial life and intelligent machines in support of humankind and ICAROB is contributing through wide technical topics of interest that support this direction.

It is a great honor for me as a Co-General Chair of the 5th ICAROB 2018 to welcome everyone to this important event. Also, I would like to extend my special thanks to all authors and speakers for contributing their research works, the participants, and the organizing team of the 5th ICAROB.

I'm looking forward to meeting you at the 5th ICAROB in Beppu, Oita Prefecture and wishing you all the best.

GENERAL SESSION TOPICS

GS1 Robotics I (3)	GS2 Bipedal Robots & Human-Welfare Robotics (6)
GS3 Complexity (5)	GS4 Pattern recognition & image processing (4)
GS5 Neuroscience (3)	GS6 Virtual reality (5)
GS7 Intelligent Control (3)	GS8 Robotics II (5)
GS9 Poster (11)	GS10 Others (4)

ORGANIZED SESSION TOPICS

OS1 Computer Science and Information Processing (5)	OS2 Intelligent Navigation (6)
OS3 New Challenges to Adaptive & Learning Control (9)	OS4 Aspects of Natural Computing (3)
OS5 Advanced Regional Engineering (4)	OS6 Kansei Engineering and Applications (4)
OS7 Mobile Robotics (8)	OS8 Intelligence Control Systems and Applications (11)
OS9 Theory and Implementation of Neuromimetic Systems (6)	OS10 Intelligent Robotic Manufacturing (2)
OS11 Educational Application Making Control Engineering Approach (5)	OS12 Software Development Support Method (4)
OS13 Human Interface and Artificial Intelligence (5)	OS14 Advanced Technology on Sensing Technology, Devices, Application (6)
OS15 System and Control (11)	OS16 Recognition and Control (9)
OS17 Automated content generation and cognitive content generation (7)	OS18 Intelligent Control (6)
OS19 Advanced Control (5)	OS20 Advances in Marine Robotics and It's Applications (5)
OS21 Robot Competitions for Social Contribution (5)	OS22 Navigation and Control (3)

2/1(Thu.) 17:30-19:30	Welcome Party (Hotel Shiragiku)
2/1(Thu.) - 2/4(Sun.)	ICAROB Secretariat
2/4(Sun.) 15:10-15:40	Farewell Party (Conference Site: 3F, Meeting Room 32)

TIME TABLE (2/2)

2/2(Fri.)	Conference Room	Meeting Room 31	Meeting Room 32	Meeting Room 33	Meeting Room 1	Meeting Room 4
8:40-	Registration (3F)					
9:00-10:15			OS8-1 Intelligence Control Systems and Applications (5) Chair: Kuo-Hsien Hsia	OS19 Advanced Control (5) Chair: Yingmin Jia	OS5 Advanced Regional Engineering (4) Chair: Toru Hiraoka	OS4 Aspects of Natural Computing (3) Chair: Marion Oswald
10:15-10:30	Coffee break					
10:30-11:00	Opening Ceremony (Conference Room)					
11:10-12:10	Chair: Ju-jung Lee Invited session IS-1, IS-2 (Conference Room) Henrik Hautop Lund, Luigi Pagliarini					
12:10-13:10	Lunch					
13:10-14:10	Chair: Yingmin Jia Plenary Speech PS-1 (Conference Room) Jeffrey Johnson					
14:10-14:30	Coffee break					
14:30-16:00		OS21 Robot Competitions for Social Contribution (5) Chair: Kazuo ISHII	OS8-2 Intelligence Control Systems and Applications (6) Chair: Kuo-Hsien Hsia	OS3-1 New Challenges to Adaptive & Learning Control (5) Chair: Shin Wakitani	OS9 Theory and Implementation of Neuromimetic Systems (6) Chair: Takashi Kohno	GS4 Pattern recognition & image processing (4) Chair: Jiwu Wang
16:00-16:20	Coffee break					
16:20-18:20		GS8 Robotics II (5) Chair: Hazry Desa	OS7 Mobile Robotics (8) Chair: Evgeni Magid	OS3-2 New Challenges to Adaptive & Learning Control (4) Chair: Takuya Kinoshita	OS15 System and Control (10) → (3+1) OS16 Recognition and Control (9) → (2) Chair: Fengzhi Dai	GS2 Bipedal robot & Human-welfare Robotics (6) Chair: Ju-jung Lee

Meeting Room 31: Committee waiting room and Rest room

TIME TEBLE (2/3)

2/3(Sat.)	Conference Room	Meeting Room 31	Meeting Room 32	Meeting Room 33	Meeting Room 1	Meeting Room 4
8:40-	Registration					
9:00-9:45		GS9 Poster (11) Chair Evgeni Magid	GS1 Robotics I (3) Chair: Hidehiko Yamamoto	OS22 Navigation and Control (3) Chair: Chan Gook Park	OS10 Intelligent Robotic Manufacturing (2) Chair: Kensuke Harada	GS5 Neuroscience (3) Chair: Masao Kubo
9:45-10:00	Coffee break					
10:00-11:00	Chair: Takao Ito Plenary Speech PS-2 (Conference Room) Masato Nakagawa					
11:00-11:10	Coffee break					
11:10-12:10	Chair: Jangmyung Lee Invited session IS-4, IS-6 (Conference Room) Pierre Parrend, Halimahtun M. Khalid					
12:10-13:10	Lunch					
13:10-14:10	Chair: Marion Oswald Plenary Speech PS-3(Conference room) Ken-ichi Tanaka					
14:10-14:30	Coffee break					
14:30-16:00		Poster session	OS18 Intelligent Control (5) Chair: Yingmin Jia	OS2 Intelligent Navigation (6) Chair: Jangmyung Lee	OS14 Advanced Technology on Sensing Technology, Devices, Application (6) Chair: Hiroki Tamura	OS20 Advances in Marine Robotics and It's Applications (5) Chair: Kazuo ISHII
16:00-16:20	Coffee break					
16:20-17:20		Poster session	OS12 Software Development Support Method (4) Chair: Tetsuro Katayama	GS3 Complexity (5) Chair:	GS7 Intelligent Control (3) Chair: Kunikazu Kobayashi	
18:30-20:30	Banquet: Hotel Shiragiku					

Meeting Room 31: Committee waiting room and Rest roomk

TIME TABLE (2/4)

2/4(Sun.)	Meeting Room 31	Meeting Room 32	Meeting Room 33	Meeting Room 1	Meeting Room 4
8:40-	Registration				
9:00-10:15			GS6 Virtual reality (5) Chair: Andre Rosendo	OS6 Kansei Engineering and Applications (4) Chair: Tetsuo Hattori	OS11 Educational Application Making Control Engineering Approach (5) Chair: Kazuo Kawada
10:15-10:30	Coffee break				
10:30-11:10	Chair: Makoto Sakamoto Invited session IS-3 (Meeting Room 31) Takashi Yokomori				
11:10-11:30	Coffee break				
11:30-12:10	Chair: Takao Ito Invited session IS-5 (Meeting Room 31) Yuji Shinano				
12:10-13:10	Lunch				
13:10-14:55		OS17 Automated content generation and cognitive content generation (7) Chair: Hiroki Fukushima	OS13 Human Interface and Artificial Intelligence (5) Chair: Yasunari Yoshitomi	OS1 Computer Science and Information Processing (5) Chair: Makoto Sakamoto	
Farewell Party (15:10-15:40) Meeting Room 32					

Meeting Room 31: Committee waiting room and Rest room

GS10 Others (4)

no presentation, only papers

The 2018 International Conference on ARTIFICIAL LIFE AND ROBOTICS (ICAROB2018)

February 1 (Thursday)

17:30-19:30 Welcome Party (Hotel Shiragiku)

February 2 (Friday)

10:30-11:00

Opening Ceremony (Conference Room)

Chair: Marion Oswald (Technische Universität Wien, Austria)

Welcome Addresses

- | | |
|---|---|
| 1. General Chairman of ICAROB | Masanori Sugisaka (ALife Robotics Corporation, Ltd., Japan) |
| 2. Co-General Chairman of ICAROB | Yingmin Jia (Beihang University, P. R. China) |
| 3. Co-General Chairman of ICAROB | TaKao Ito (Hiroshima University, Japan) |
| 4. Co-General Chairman of ICAROB | Ju-Jang Lee (KAIST, Korea) |
| 5. Vice General Chair of ICAROB | Henrik Hautop Lund (Technical University of Denmark, Denmark) |
| 6. Vice General Chair of ICAROB | Jangmyung Lee (Pusan National University, Korea) |

February 3 (Saturday)

Banquet: Hotel Shiragiku

18:30-20:30

Chair: Takao Ito (Hiroshima University, Japan)

Welcome Addresses

- Prof. Jeffrey Johnson (The Open University, UK)
Executive Fellow, Mr. Masato Nakagawa (DENSO CORPORATION, Hiroshima University, Japan)
Executive Fellow, Mr. Ken-ichi Tanaka (Mitsubishi Electric Corporation, Japan)
Prof. Yingmin Jia (Beihang University, P.R. China)
Prof. Henrik Hautop Lund (Technical University of Denmark, Denmark)

TECHNICAL PAPER INDEX

February 2 (Friday)

8:40-Registration

Conference Room

10:30-11:00 Opening Ceremony

Chair: **Marion Oswald** (Technische Universität Wien, Austria)

11:10-12:10

Invited session IS-1, IS-2

Chair: **Ju-Jang Lee** (KAIST, Korea)

IS-1 Modular Playware and Personal Health Technology

Henrik Hautop Lund (Technical University of Denmark, Denmark)

IS-2 How new technologies might lead to a paradigm shift in psychological and neuropsychological research

Luigi Pagliarini, **Henrik Hautop Lund** (Technical University of Denmark, Denmark)

13:10-14:10

Plenary Speech PS-1

Chair: **Yingmin Jia** (Beihang University, P. R. China)

PS-1 Dynamic Structures for Evolving Tactics and Strategies in Team Robotics

Jeffrey Johnson and **Ruggero Rossi** (The Open University, UK)

Meeting Room 31

14:30-15:45 OS21 Robot Competitions for Social Contribution (5)

Chair: **Kazuo Ishii** (Kyushu Institute of Technology, Japan)

Co-Chair: **Yasunori Takemura** (Nishinippon Institute of Technology, Japan)

OS21-1 *Analysis of Team Relationship using Self-Organizing Map for University Volleyball Players*
Yasunori Takemura, **Kazuya Oda**, **Michiyoshi Ono** (Nishinippon Institute of Technology, Japan)

OS21-2 *Optimization for Line of Cars Manufacturing Plant using Constrained Genetic Algorithm*
Keiji Kamei, **Takafumi Arai** (NishiNippon Institute of Technology, Japan)

- OS21-3 *Slip model of roller driven ball*
Kenji Kimura¹, Shota Chikushi, Kazuo Ishii
(¹Nippon-Bunri University, Kyushu Institute of Technology, Japan)
- OS21-4 *Strategy Analysis of Multi-Agent Games Using Self-Organizing Map*
Moeko Tominaga, Yasunori Takemura¹, Kazuo Ishii
(Kyushu Institute of Technology, ¹NishiNippon Institute of Technology, Japan)
- OS21-5 *Analysis of Characteristics of Tomato Fruits in Infrared Images Toward Automatic Tomato Harvesting System*
Takuya Fujinaga, Shinsuke Yasukawa, Binghe Li, Kazuo Ishii
(Kyushu Institute of Technology, Japan)

16:20-17:35 GS8 RoboticsII (5)

Chair: Hazry Desa (Universiti Malaysia Perlis, Malaysia)

- GS8-1 *Design System of Cell Type Assembly Machine with Dual Arms Robot by GA*
Keita Honda, Hidehiko Yamamoto and Takayoshi Yamada (Gifu University, Japan)
- GS8-2 *Spherical Mobile Robot Driven by Biorthogonal Omnidirectional Wheels*
Liu Wei, Ma Shuanglong, Duan Lunqin, Yu Jiangtao (Beijing Jiaotong University, China)
- GS8-3 *Coordinated behaviour with a Pepper Humanoid robot to estimate the distance of other robot using Inverse Perspective Mapping*
M. Hassan Tanveer, Antonio Sgorbissa, Carmine T. Recchiuto (University of Genova, Italy)
- GS8-4 *Control Techniques of Quadrotor Uavs: A Concise Study*
¹Syed Faiz Ahmed, ¹Athat Ali, ¹M. Kamran Joyo, ¹Khusairy Abd Kader, ²Hazry Desa, ³Sheroz Khan(¹Universiti Kuala Lumpur, British Malaysian Institute, Malaysia, ²Universiti Malaysia Perlis, Malaysia, ³International Islamic University Malaysia, Malaysia)
- GS8-5 *GIS Based Hydrological Model for River Water Level Detection & Flood Prediction featuring morphological operations.*
Sarmad Zafar, H.M.SohaibAzhar, Aqeel Tahir
(Mohammad Ali Jinnah University, Pakistan)

Meeting Room 32

9:00-10:15 OS8-1 Intelligence Control Systems and Applications (5)

Chair: Kuo-Hsien Hsia (Far East University, Taiwan)

Co-Chair: Chung-Wen Hung (National Yunlin University of Science & Technology, Taiwan)

- OS8-7 *Novel Detection Scheme for Stolen Password File*
I-Hsien Liu, Chia-Hsiu Chen, Jung-Shian Li (National Cheng Kung University, Taiwan)
- OS8-8 *Honeypot System of SCADA Security Survey*
Kuan-Chu Lu, I-Hsien Liu, Jung-Shian Li (National Cheng Kung University, Taiwan)
- OS8-1 *An Automated Optical Inspection system for a tube inner circumference state identification*
Chung-Wen Hung, Jhen-Gu Jiang, Hsien-Huang P. Wu, Wei-Lung Mao
(National Yunlin University of Science & Technology, Taiwan)
- OS8-9 *An EtherCAT Battery Test System*
Chung-Wen Hung, Bo-Min Wang, Wen-Ting Hsu, Jhen-Gu Jiang
(National Yunlin University of Science & Technology, Taiwan)
- OS8-10 *Surface Defect Detection for Tube Object Based on Single Camera*
Hsien-Huang Wu, Chang-Jhu He (National Yunlin University of Science & Technology, Taiwan)

14:30-16:00 OS8-2 Intelligence Control Systems and Applications (6)

Chair: Kuo-Hsien Hsia (Far East University, Taiwan)

Co-Chair: Chung-Wen Hung (National Yunlin University of Science & Technology, Taiwan)

- OS8-2 *Implementation of the Mobile Based Robot Arm for Image Recognition*
Ji-Hua Li, Jr-Hung Guo, Kuo-Lan Su (National Yunlin University of Science & Technology, Taiwan)
- OS8-3 *Reinforced Quantum-behaved Particle Swarm Optimization Based Neural Networks for Image Inspection*
Li-Chun Lai and Chia-Nan Ko (Nan Kai University of Technology, Taiwan)
- OS8-4 *Development of IoT Module with Backup and Data-security Functions*
Jr-Hung Guo, Kuo-Hsien Hsia, Kuo-Lan Su
(National Yunlin University of Science & Technology, Taiwan)
- OS8-5 *Development of Auto-Stacking Warehouse Truck*
Kuo-Hsien Hsia, Ming-Guang Wu, Jun-Nong Lin, Hong-Jie Zhong, and Zh-Yao Zhuang
(Far East University, Taiwan)
- OS8-6 *Development of Four-axis SCARA Robotic Arm Built on Automation Control System*
Jr-Hung Guo, Kuang-Wei Chuang, Kuo-Lan Su
(National Yunlin University of Science & Technology, Taiwan)
- OS8-11 *Client Searching Privacy Protection in Encrypted Database*
I-Hsien Liu, Chuan-Gang Liu, Cheng-Jui Chang, Jung-Shian Li
(National Cheng Kung University, Taiwan)

16:20-18:20 OS7 Mobile Robotics (8)

Chair: Evgeni Magid (Kazan Federal University, Russia)

- OS7-1 *An Empirical Evaluation of Grid-based Path Planning Algorithms on Widely Used in Robotics Raspberry Pi Platform*
Anton Andreychuk, Andrey Bokovoy (Peoples' Friendship University of Russia (RUDN University) Russian Academy of Sciences, Russia)
Konstantin Yakovlev (Russian Academy of Sciences, Higher School of Economics, Russia)
- OS7-2 *Development of the insectoid walking robot with inertial navigation system*
Vitaly Egunov, Andrey Kachalov, Michail Petrosyan, Pavel Tarasov, Elena Yankina
(Volgograd State Technical University, Russia)
- OS7-3 *Enhancing semi-dense monocular vSLAM used for multi-rotor UAV navigation in indoor environment by fusing IMU data*
Andrey Bokovoy (Russian Academy of Sciences, Peoples' Friendship University of Russia (RUDN University), Russia)
Konstantin Yakovlev (Russian Academy of Sciences, Higher School of Economics, Russia)
- OS7-4 *Method of finding the android program motion for the ZMP trajectory of a certain type*
Alexander Gorobtsov, Pavel Tarasov, Andrey Skorikov, Alexey Markov, Andrey Andreev
(Volgograd State Technical University, Russia)
- OS7-5 *Path Planning for Indoor Partially Unknown Environment Exploration and Mapping*
Aufar Zakiev¹, Roman Lavrenov¹, Vadim Indelman² and Evgeni Magid¹
(¹Kazan Federal University, Russia ²Technion-Israel Institute of Technology, Israel)
- OS7-6 *Simulation of service robot swarm behavior*
Alexei Lushnikov¹, Vlada Kugurakova¹, Timur Satdarov², Arthur Nizamutdinov¹
(¹Higher School of ITIS, Kazan Federal University, ²KUKA Robotics, Russia)
- OS7-7 *Smart Spline-Based Robot Navigation on Several Homotopies: Guaranteed Avoidance of Potential Function Local Minima*
Roman Lavrenov (Kazan Federal University, Russia)
- OS7-8 *Virtual Experimental Stand for Automated Fiducial Marker Comparison in Gazebo Environment*
Ksenia Shabalina¹, Artur Sagitov¹, Hongbing Li², Edgar A. Martinez-Garcia³, Evgeni Magid¹
(¹Kazan Federal University, Russia)
(²Shanghai Jiao Tong University, China)
(³Universidad Autónoma de Ciudad Juárez, Mexico)

Meeting Room 33

9:00-10:15 OS19 Advanced Control (5)

Chair: Yingmin Jia (Beihang University (BUAA), China)

Co-Chair: Fuzhong Wang (Henan Polytechnic University, P.R.China)

- OS19-1 *Revisit Constrained Control of Chaos*
Yunzhong Song, Ziyi Fu and Fuzhong Wang (Henan Polytechnic University, P.R.China)
- OS19-2 *Research on Filtering for Random Data Packet Dropouts and Delays in Wireless Sensor Networks*
Sumin HAN, Fuzhong WANG (Henan Polytechnic University, P.R.China)
- OS19-3 *Optimal Hohmann-Type Impulsive Ellipse-to-Ellipse Coplanar Rendezvous*
Xiwen Tian, Yingmin Jia (Beihang University (BUAA), China)
- OS19-4 *Research on SVG Control Method Under Unbalanced Conditions*
Zheng Zheng, Yousong Zhou (Henan Polytechnic University, China)
- OS19-5 *Dynamics Analysis of Payload On-orbit Catapult Separation Based on ADAMS*
Yi Li, Yingmin Jia (Beihang University (BUAA), China)

14:30-15:45 OS3-1 New Challenges to Adaptive & Learning Control (5)

Chair: Shin Wakitani (Hiroshima University, Japan)

- OS3-1 *A sound-based measurement of sway angle for anti-sway control of overhead crane*
Miki Matsunaga, Masayoshi Nakamoto, and Toru Yamamoto (Hiroshima University, Japan)
- OS3-2 *Sampled-data PID control system with Sensitivity Function for a Second-order Plus Dead-time System*
Ryo Kurokawa, Takao Sato, and Yasuo Konishi (University of Hyogo, Japan)
Ramon Vilanova (Universitat Autònoma de Barcelona, Spain)
- OS3-3 *Experimental Evaluation of a Data-Driven Control System using an Electronic Thermal Regulator*
Yuka Okubo, Yoichiro Ashida, Takuya Kinoshita, and Toru Yamamoto (Hiroshima University, Japan)
- OS3-4 *Self-repairing Adaptive PID Control for Plants with Sensor Failures*
Masanori Takahashi (Tokai University, Japan)
- OS3-5 *Design and Development of a Constant Temperature Reservoir for a Database-Driven Smart Cultivation System*
Shin Wakitani, Sharma Sneha, and Toru Yamamoto (Hiroshima University, Japan)

16:20-17:20 OS3-2 New Challenges to Adaptive & Learning Control (4)

Chair: Takuya Kinoshita (Hiroshima University, Japan)

- OS3-6 *Design of a Performance-Adaptive 1-Parameter Tuning PID Controller*
Yoichiro Ashida, Shin Wakitani, and Toru Yamamoto (Hiroshima University, Japan)
- OS3-7 *Sticking Fault Detecting Method for CARIMA Model*

Toyoaki Tanikawa, and Tomohiro Henmi
(National Institute of Technology, Kagawa College, Japan)

OS3-8 *Design of a Neural Network based on E-FRIT and Its Application*
Kento Kinoshita, Shin Wakitani, and Shuichi Ohno (Hiroshima University, Japan)

OS3-9 *Parameter Optimization with Input/Output data via DE for Adaptive Control System with Neural Network*
Taro Takagi (National Institute of Technology, Maizuru College, Japan)
Ikuro Mizumoto (Kumamoto University, Japan)

Meeting Room 1

9:00-10:00 OS5 Advanced Regional Engineering (4)

Chair: Toru Hiraoka (University of Nagasaki, Japan)

Co-Chair: Minoru Kumano (University of Miyazaki, Japan)

OS5-1 *Discovering Successful Determinants of Efficiency of MICHINOEKI in Chugoku Area*
Minoru Kumano (University of Miyazaki, Japan)
Takao Ito (University of Hiroshima, Japan)
Toru Hiraoka (University of Nagasaki, Japan)
Hirofumi Nonaka (Nagaoka University of Technology, Japan)
Masaharu Hirota (Okayama University of Science, Japan)

OS5-2 *Relationship Analysis on the Number of Customers of Michinoeki in Kyushu Region*
Toru Hiraoka, Shiori Nishimura (University of Nagasaki, Japan)
Hirofumi Nonaka (Nagaoka University of Technology, Japan)
Minoru Kumano (University of Miyazaki, Japan)

OS5-3 *Emotional Contribution Analysis of Online Reviews*
Elisa Claire Alemán Carreón, Hirofumi Nonaka (Nagaoka University of Technology, Japan),
Toru Hiraoka (University of Nagasaki, Japan), Minoru Kumano (University of Miyazaki, Japan),
Takao Ito (Hiroshima University, Japan), Masaharu Hirota (Okayama University of Science, Japan)

OS5-4 *An Approach to Visualize Place of Interest and Shooting Spot Using Geo-Tagged Photographs*
Masaharu Hirota (Okayama University of Science, Japan), Masaki Endo (Polytechnic University,
Japan), Hiroshi Ishikawa (Tokyo Metropolitan University, Japan)

14:30-16:00 OS9 Theory and Implementation of Neuromimetic Systems (6)

Chair: Takashi Kohno (The University of Tokyo, Japan)

Co-Chair: Timothée Levi (The University of Tokyo, Japan, University of Bordeaux, France)

OS9-1 *Study of real-time biomimetic CPG on FPGA: behavior and evolution*

Timothée Levi^{1,2}, Kazuyuki. Aihara¹, Takashi Kohno¹
(¹The University of Tokyo, Japan, ²University of Bordeaux, France)

OS9-2 *A Metaheuristic Approach for Parameter Fitting in Digital Spiking Silicon Neuron Model*
Takuya Nanami, Takashi Kohno (The University of Tokyo, Japan)

OS9-3 *Real-time Digital Implementation of HH neural network on FPGA: cortical neuron simulation*
Farad Khoiratee¹, Sylvain Saïghi¹, Timothée Levi^{1,2}
(¹University of Bordeaux, France, ²The University of Tokyo, Japan)

OS9-4 *Finding appropriate parameter voltages for driving a low-power analog silicon neuron circuit*
Atsuya Tange, Takashi Kohno (The University of Tokyo, Japan)

OS9-5 *A low-power silicon synapse circuit with tunable reversal potential*
Ashish Gautam, Takashi Kohno (The University of Tokyo, Japan)

OS9-6 *New methodology of neural network reconstruction for "in vitro" culture on Multi Electrode Array (MEA)*
Timothée Leleu¹, Timothée Levi^{1,2}, Takashi Kohno¹, Kazuyuki Aihara¹
(¹The University of Tokyo, Japan, ²University of Bordeaux, France)

16:20-18:20 OS15 System and Control (11)

Chair: Fengzhi Dai (Tianjin University of Science & Technology, China)

OS15-1 *Analog circuit design of a novel 4D chaotic system*
Hong Niu (Tianjin University of Science & Technology, China)

OS15-2 *A method of end-to-end self-understanding of Chinese paper-dictionaries*
Zhijian Lv (Beijing Institute of Science and Technology Information (BISTI), P.R.China),
Yizhun Peng (Tianjin University of Science and Technology, P.R.China)

OS15-3 *A multi-robot rescuing system*
Huailin Zhao, Zheng Wu, Xiaoxing Wang (Shanghai Institute of Technology, China)

OS15-4 *Dynamic analysis and FPGA implementation of A novel hyper-chaotic system with one equilibrium point*
Shanfeng Wang, Hongyan Jia, Zhiqiang Guo (Tianjin University of Science and Technology, China)

OS15-5 *Analysis and circuit implementation for a new fractional-order chaotic system*
Zhiqiang Guo, Hongyan Jia, Shanfeng Wang (Tianjin University of Science and Technology, China)

OS15-6 *Application of a conservative chaotic system in image encryption*
Shilong Liu, Mei Zhang, Wei Xue (Tianjin University of Science and Technology, China)

OS15-7 *Study of plant disease detection based on near-field acoustic holography*

Jiangfan Wang, Xiuqing Wang(Tianjin University of Science & Technology, China)

- OS15-8 *Simulation of cell dielectric properties based on COMSOL*
Shudong Li, Xiaoyan Chen, Fengze Han(Tianjin University of Science & Technology, Chin)
- OS15-9 *Research on the method of electrical impedance tomography based on conjugate gradient iterative algorithm*
Yuanli Yue¹, Xiaoyan Chen², Ze Liu¹, Fengzhi Dai²
(¹ Beijing Jiaotong University, China, ² Tianjin University of Science and Technology, China)
- OS15-10 *Research on acoustic emission wireless detection system*
Xiuqing Wang¹, Yang Li², Qing Liu¹, Jiming Zhao¹
(¹ Tianjin University of Science & Technology, China;² TEXAS A and M University, U.S.A)
- OS15-11 *ORIN PAC (PC based Automation Controller)*
Toshihiro Inukai (DENSO WAVE INC., Japan)

OS16 Recognition and Control (9)

Chair: Fengzhi Dai (Tianjin University of Science & Technology, China)

- OS16-1 *Research on the synchronization and circuit realization of a four-wing chaotic system*
Yiqiao Qin, Fengzhi Dai, Yuxing Ouyang, Qijia Kang, Ce Bian, Baochang Wei, Runhua Mao, Shengbiao Chang (Tianjin University of Science & Technology, China)
- OS16-2 *Design of control system for reboiling part of distillation process*
Lingran An, Fengzhi Dai, Yujie Yan, Yuxing Ouyang, Zhongyong Ye, Xia Jin, Baochang We (Tianjin University of Science and Technology, China)
- OS16-3 *Research on intelligent control system based on machine vision*
Ce Bian¹, Fengzhi Dai¹, Yuxing Ouyang¹, Yiqiao Qin¹, Baochang Wei¹, Runhua Mao¹, Meili Li²
(¹Tianjin University of Science and Technology, ² China University of Petroleum - Beijing, China)
- OS16-4 *Development of NC power based on Buck circuit*
Yuxing Ouyang, Fengzhi Dai, Runhua Mao, Ce Bian, Baochang Wei, Yiqiao Qin, Shengbiao Chang, Qijia Kang (Tianjin University of Science and Technology, China)
- OS16-5 *Simulation of PID temperature control system based on neural network*
Yujie Yan, Fengzhi Dai, Lingran An, Yuxing Ouyang, Zhongyong Ye, Xia Jin, Ce Bian (Tianjin University of Science and Technology, China)
- OS16-6 *Design and research of real-time material management system based on production process*
Baochang Wei, Fengzhi Dai, Yuxing Ouyang, Haifang Man, Yiqiao Qin, Runhua Mao, Ce Bian (Tianjin University of Science and Technology, China)
- OS16-7 *Research on the balance control of the inverted pendulum*

The 2018 International Conference on Artificial Life and Robotics (ICAROB2018), B-Con Plaza, Feb. 1- 4, Beppu, Oita, Japan, 2018

Zhongyong Ye, Fengzhi Dai, Yuxing Ouyang, Yujie Yan, Xia Jin, Lingran An, Hongtao Zhang
(Tianjin University of Science and Technology, China)

OS16-8 *Design of intelligent saving robot based on six-legged robot*

Xinyu Zhang, Xiaokun Lin, Fengzhi Dai
(Tianjin University of Science & Technology, China)

OS16-9 *Research on multi-object recognition algorithm based on video*

Yong Hou, Runhua Mao, Yuxing Ouyang, Ce Bian, Binhu Song, Baochang Wei, Yiqiao Qin,
Shengbiao Chang, Fengzhi Dai (Tianjin University of Science and Technology, China)

Meeting Room 4

9:00-9:45 OS4 Aspects of Natural Computing (3)

Chair: Marion Oswald (Technische Universität Wien, Austria)

Co-Chair: Yasuhiro Suzuki (Nagoya University, Japan)

OS4-1 *Mathematical Expression of Minakata Kumagusu's Philosophy of Natural Science*

Yasuhiro Suzuki (Nagoya University, Japan)

OS4-2 *Toward Artificial Intelligence by Using DNA Molecules*

Yasuhiro Suzuki, Rie Taniguchi (Nagoya University, Japan)

OS4-3 *Differentiation and Integration of Sensation and its Application*

Yasuhiro Suzuki (Nagoya University, Japan)

14:30-15:30 GS4 Pattern recognition & image processing (4)

Chair: Jiwu Wang (Beijing Jiaotong University, China)

GS4-1 *Study on Detection of Nests on Pylon from Overhead View Based on Halcon*

Jiwu Wang, Haibao Luo, Pengfei Yu (Beijing Jiaotong University, China)

GS4-2 *Human gait recognition based on Caffe deep learning framework*

Jiwu Wang, Feng Chen (Beijing Jiaotong University, China)

GS4-3 *Unsupervised Image Classification Using Multi-Autoencoder and K-means++*

Shingo Mabu, Kyoichiro Kobayashi, Masanao Obayashi, Takashi Kuremoto
(Yamaguchi University, Japan)

GS4-4 *Anomaly Detection of Disaster Areas from Satellite Images Using Convolutional Autoencoder and One-class SVM*

Kohki Fujita, Shingo Mabu, Takashi Kuremoto (Yamaguchi University, Japan)

16:20-17:50 GS2 Bipedal robot & Human-welfare Robotics (6)

Chair: Ju-Jang Lee (KAIST, Korea)

- GS2-1 *Design and Evaluation of Passively Powered Knee Exoskeleton (PPKE) for Squat Lifting*
R.K.P.S. Ranaweera¹, R.A.R.C. Gopura¹, T.S.S. Jayawardena¹, G.K.I. Mann²
(¹University of Moratuwa, Sri Lanka), (²Memorial University of Newfoundland, Canada)
- GS2-2 *Behavior design of robot arm imitating the consciousness mechanism of living organisms*
Representation of facial expression in transition process of emotion
Ryohei Anshi, Eiji Hayashi (Kyushu Institute of Technology, Japan),
Wisanu Jitviriyaya (King Mongkut's University of Technology, Thailand),
Sakmongkon Chumkamon (Rajamangala University of Technology, Thailand)
- GS2-3 *Study of Robot Navigation for Forest Management*
Ayumu Tominaga, Eiji Hayashi (Kyushu Institute of Technology, Japan)
Abbe Mowshowits (The City College of New York, USA)
- GS2-4 *Development of the sense system that is combined force feedback and visual feedback*
-Deformable virtual objects simulation by using LEM-
Kaito Nagano, Eiji Hayashi (Kyushu Institute of Technology, Japan)
- GS2-5 *A four-legged robot's soft feet structural design and walking gait generated from*
Inverse kinematics
Amornphun Phunopas¹ and Eiji Hayashi²
(¹King Mongkut's University of Technology North Bangkok, Thailand,
²Kyushu Institute of Technology, Japan)
- GS2-6 *Powered Ankle Exoskeletons: Existent Designs and Control Systems*
A.H. Weerasingha, W.P.K. Withanage, A.D.K.H. Pragnathilaka, R.K.P.S. Ranaweera,
R.A.R.C. Gopura(University of Moratuwa, Sri Lanka)

February 3 (Saturday)

8:40-Registration

Conference Room

10:00-11:00

Plenary Speech PS-2

Chair: Takao Ito (Hiroshima University, Japan)

PS-2 EU-Way Development - Effective and Rational Development Way -

Masato (Max) NAKAGAWA (DENSO CORPORATION, Japan)

11:10-12:10

Invited session IS-4, IS-6

Chair: Jangmyung Lee (Pusan National University, Korea)

IS-4 Artificial Immune Ecosystems: challenges for a new generation of bio-inspired secure and resilient systems

Pierre Parrend (ECAM Strasbourg-Europe, France)

IS-6 Trust of Virtual Agent in Multi Actor Interactions

H. M. Khalid, W. S. Liew, B.S. Voong, M.G. Helander (Damai Sciences, Malaysia)

13:10-14:10

Plenary Speech PS-3

Chair: Marion Oswald (Technische Universität Wien, Austria)

PS-3 Innovation on Manufacturing Generated by Intelligent Technologies

Ken-ichi Tanaka, Haruhisa Okuda (Mitsubishi Electric Corporation, Japan)

Meeting Room 31

9:00-17:20 GS9 Poster (11)

Chair: Evgeni Magid (Kazan Federal University, Russia)

- GS9-1 *Analysis of onboard sensor-based odometry for a quadrotor UAV in outdoor environment*
Aidar Gabdullin, Grigory Shvedov, Mikhail Ivanou, Ilya Afanasyev (Innopolis University, Russia)
Konstantin Yakovlev (Russian Academy of Science, Russia)
- GS9-2 *Memristive neuron integration in digital robotic embodiment*
Max Talanov, Evgenii Zykov, Yuriy Gerasimov, Evgeni Magid, Aleksander Elizarov
(Kazan Federal University, Russia)
Victor Erokhin (Institute of Materials for Electronics and Magnetism, Italian National Council of Research, Italy)
- GS9-3 *Russian mobile robot Servosila Engineer: designing an optimal integration of an extra laser range finder for SLAM purposes*
Neil Alishev, Yuriy Gerasimov, Roman Lavrenov (Kazan Federal University, Russia)
- GS9-4 *Toward automated open wound suturing using haptic feedback: detecting wounds and planning the suture*
Artur Sagitov¹, Hongbing Li², Evgeni Magid¹
(¹Kazan Federal University, Kazan, Russia)
(²Shanghai Jiao Tong University, Shanghai, China)
- GS9-5 *Establishing Effective Teaching for Robotics: a comparison study of Bachelor students in Introduction to Robotics course*
Tatyana Tsoy, Leysan Sabirova, Mikhail Abramskiy, Evgeni Magid
(Kazan Federal University, Russia)
- GS9-6 *Development of a heterogeneous aerial swarm control framework for forest management*
Yuriy Gerasimov, Artur Sagitov, Evgeni Magid (Kazan Federal University, Russia)
- GS9-7 *Implementation of ROS package for simultaneous video streaming from several different cameras*
Ramil Safin, Roman Lavrenov (Kazan Federal University, Russia)
- GS9-8 *Consumers Preferences and Purchase Intention on New Taste of Salted Duck Eggs*
Shang-Hui Li (Far East University, Taiwan)
- GS9-9 *The Study of Green Food Image, Satisfaction and Loyalty through the Perspective of Elaboration Likelihood Model*
Shu-Fang Hsu (Far East University, Taiwan)

GS9-10 *Self-Generated Dataset for Category and Pose Estimation of Deformable Object for Manipulation by Robot*

Yew Cheong Hou, Khairul Salleh Mohamed Sahari (Universiti Tenaga Nasional, Malaysia)

GS9-11 *Design and Development of Three Arms Transmission Line Inspection Robot*

Muhammad Fairuz Abdul Jalal, Khairul Salleh Mohamed Sahari, Ho Ming Fei, Justin Chan Tuck Leong (Universiti Tenaga Nasional, Malaysia)

Meeting Room 32

9:00-9:45 GS1 Robotics I (3)

Chair: Hidehiko Yamamoto (Gifu University, Japan)

GS1-1 *Production simulation of autonomous decentralized FMS including AGVs with different personalities of mind*

Ryuichi Tsujii, Hidehiko Yamamoto and Takayoshi Yamada (Gifu University, Japan)

GS1-2 *Development of Automatic Recognition of Hazmat Marking Chart for Rescue Robot*

Wisanu Jitviriyaya, Poommitol Chaicherdkiat, Noppadol Pudchuen
(King Mongkut's University of Technology North Bangkok, Thailand)
Eiji Hayashi (Kyushu Institute of Technology, Japan)

GS1-3 *Development of Autonomous Robot for Laborsaving of the Forestry - Discrimination between trees and weeds using RGB-D -*

Shingo Yamaguchi, Eiji Hayashi, and Ayumu Tominaga (Kyushu Institute of Technology, Japan)

14:30-15:45 OS18 Intelligent Control (5)

Chair: Yingmin Jia (Beihang University (BUAA), China))

Co-Chair: Weicun Zhang (University of Science and Technology Beijing, China)

OS18-1 *Rolling Bearings Fault Diagnosis Method using EMD Decomposition and Probabilistic Neural Network*

Caixia Gao, Tong Wu, Ziyi Fu (Henan Polytechnic University, China)

OS18-2 *Detection of Dangerous Driving Behavior via Fuzzy Inference System*

Shangzheng Liu¹, Qinghui Zhu¹, Fuzhong Wang²
(¹Nanyang Institute of Technology, ²Henan Polytechnic University, P.R. China)

OS18-3 *Feature Points Designing and Matching for the Target Spacecraft in the Final Approaching Phase of Rendezvous and Docking*

Wenjing Pei, Yingmin Jia (Beihang University (BUAA), China)

OS18-4 *Construction and Visualization of Atmospheric Environment Data Map*

Dongmei Fu, Gaoyuan Wang, Chao Wu, Mengchen Cui
(University of Science and Technology Beijing, China)

OS18-5 *Multiple-Model Adaptive Estimation with New Weighting Algorithm*
Weicun Zhang (University of Science and Technology Beijing, China)

16:20-17:20 OS12 Software Development Support Method (4)

Chair: Tetsuro Katayama (University of Miyazaki, Japan)

Co-Chair: Tomohiko Takagi (Kagawa University, Japan)

OS12-1 *Negative Test Case Generation from an Extended Place/Transition Net-Based Mutants*
Tomohiko Takagi¹, Tetsuro Katayama²
(¹Kagawa University, ²University of Miyazaki, Japan)

OS12-2 *Development of a Mutant Generation Tool Using a Genetic Algorithm for Extended Place/Transition Nets*
Tomohiko Takagi, Shogo Morimoto (Kagawa University, Japan)

OS12-3 *Implementation of RETUSS to Ensure Traceability between Class Diagram in UML and Java Source Code in Real Time*
Keisuke Mori*, Tetsuro Katayama*, Yoshihiro Kita†,
Hisaaki Yamaba*, Kentaro Aburada*, and Naonobu Okazaki*
(*University of Miyazaki, †Tokyo University of Technology, Japan)

OS12-4 *Prototype of a Tool to Detect Specific Comments*
Satoshi Tanoue*, Tetsuro Katayama* Yoshihiro Kita†,
Hisaaki Yamaba*, Kentaro Aburada*, and Naonobu Okazaki*
(*University of Miyazaki, †Tokyo University of Technology, Japan)

Meeting Room 33

9:00-9:45 OS22 Navigation and Control (3)

Chair: Chan Gook Park (Seoul National University, Korea)

OS22-1 *Comparative Study of Sequential Processing TRN (Terrain Referenced Navigation)*
Hyun Cheol Jeon and Chan Gook Park (Seoul National University, Korea)

OS22-2 *Road Marking Map Matching for Road Vehicle Localization*
Kyuwon Kim and Gyu-In Jee (Konkuk University, Korea)

OS22-3 *Control System Design of Directionally Maneuvering Multicopter with Independent Heading Rate*
Byoungjin Lee, Jaehue Bae, Gwang Soo Park and Sangkyung Sung (Konkuk University, Korea)

14:30-16:00 OS2 Intelligent Navigation (6)

Chair: Jangmyung Lee (Pusan National University, Korea)

- OS2-1 *Robot Manipulator Arm Inverse Kinematics Analysis by Jacobian*
Sun Oh Park, Min Gyu Jung , Jin Gon Yoon , Min Cheol Lee (Pusan National University, Korea)
- OS2-2 *Indoor Position recognition using the pseudo-range estimation*
Jongwoo An, Hosun Kang, Jiwook Choi, Jangmyung Lee
(Pusan National University, Korea)
- OS2-3 *Distance measurement algorithm based on the object recognition*
Hosun Kang, Nahyun Lee, Jangmyung Lee (Pusan National University, Korea)
- OS2-4 *An-ion air purifier system using IoT Technology*
Heeje Kim, Dohyun Kim (Pusan University, Korea)
- OS2-5 *Solar Panel Temperature Control System using IoT*
Min-soo Kim, Hee-je Kim (Pusan National University, Korea)
- OS2-6 *Enhancement of Mobile Robots Stability and Hardware Based on Reinforcement Learning*
Ki-seo Kim, Jeong-hwan Moon, Jang-myung Lee (Pusan National University, Korea)

16:20-17:35 GS3 Complexity (5)

Chair:

- GS3-1 *Management of digital records inspired by Complex Systems with RADAR*
Anne Jeannin-Girardon¹, Alexandre Bruyant¹, Nicolas Toussaint¹, Pierre Collet¹ and
Pierre Parrend^{1,2}
(¹University of Strasbourg, ; ² ECAM Strasbourg-Europe, France)
- GS3-2 *Integrated optimization of differential evolution with grasshopper optimization algorithm*
Duangjai Jitkongchuen, Udomlux Ampant (Dhurakij Pundit University, Thailand)
- GS3-3 *Efficient collective search by agents that remember failures*
Masao Kubo, Nhuhai Phung, Hiroshi Sato (National Defense Academy of Japan, Japan)
- GS3-4 *The analysis of band structures of photonic crystals*
Wang Chenxu (Muroran Institute of Technology, Japan)
Fu Ziyi (Henan Polytechnic University, China)
- GS3-5 *A Data Estimation Technique for Incomplete Telemetry Data Based on a Genetic Algorithm with Data' Statistical Properties*
Masahiro Tokumitsu, Kaito Mikami (National Institute of Technology, Yonago College, Japan)
Fumio Asai (The Radio Amateur Satellite Corporation, USA)
Taku Takada (National Institute of Technology, Kochi College, Japan)
Makoto Wakabayashi (National Institute of Technology, Niihama College, Japan)

Meeting room 1

9:00-9:30 OS10 Intelligent Robotic Manufacturing (2)

Chair: Kensuke Harada (Osaka University, Japan)

Co-Chair: Akira Nakamura (AIST, Japan)

OS10-1 *Technique of Recovery Process and Application of AI in Error Recovery Using Task Stratification and Error Classification*

Akira Nakamura*¹, Kazuyuki Nagata*¹, Kensuke Harada*² and Natsuki Yamanobe*¹

(*¹ National Institute of Advanced Industrial Science and Technology (AIST),

*² Osaka University, Japan)

OS10-2 *Motion selection for 3D robotic snap assembly*

Peihao Shi¹, Kensuke Harada¹, Weiwei Wan¹, Ixchel G. Ramirez¹, Juan Rojas², Hiromu Onda³

(¹Osaka University, Japan, ²Guangdong University of Technology, China, ³AIST, Japan)

14:30-16:00 OS14 Advanced Technology on Sensing Technology, Devices, Application (6)

Chair: Hiroki Tamura (University of Miyazaki, Japan)

Co-Chair: Koichi Tanno(University of Miyazaki, Japan)

Co-Chair: Y.W.R.Amarasinghe (University of Moratuwa, Sri Lanka)

OS14-1 *A Study on the Lumbar Burden Evaluation of Work using One Smartphone*

Mizuki Maiguma, Hiroki Tamura, Koichi Tanno (University of Miyazaki, Japan)

OS14-2 *A Study on High Accuracy Stride Estimation on Smartphone Combining Acceleration Sensor and Gyro Sensor*

Shunta Nonaka, Hiroki Tamura, Koichi Tanno (University of Miyazaki, Japan)

OS14-3 *Development of Multi-Sensory Smart Objects Tracking Module for Mobile Robot Platforms*

B. A. D. J. C. K. Basnayake, Y. W. R. Amarasinghe (University of Moratuwa, Sri Lanka)

OS14-4 *Design and Development of a Conductive Polymer Based 3D - Printed Tactile Sensor with Square Type Spring Structure*

W.H.P. Sampath, A.H.T.E. De Silva, Y.W.R. Amarasinghe (University of Moratuwa, Sri Lanka)

OS14-5 *Design and Development of a Shape Memory Alloy Spring Actuated Gripper for Minimally Invasive Surgeries*

Roshan T.A.U, Amarasinghe Y.W.R, Dayananda N.W.N. (University of Moratuwa, Sri Lanka)

OS14-6 *Design and Development of Quantum Tunneling Composite based Tactile Sensors*

T.D.I. Udayanga, D.A.M.R. Fernando, H.L.P.L. Chaturanga, B.A.D.J.C.K. Basnayake and Y.W.R. Amarasinghe (University of Moratuwa, Sri Lanka)

16:20-17:05 GS7 Intelligent Control (3)

Chair: Kunikazu Kobayashi (Aichi Prefectural University, Japan)

- GS7-1 *Fractional Order Sliding Mode Control Applying on the HIV Infection System*
Thunyaseth Sethaput¹, Arsit Boonyaprapasorn²
(¹Thammasat University, ²Chulachomklao Royal Military Academy, Thailand)
- GS7-2 *Skill-based Job Rotation Scheduling for Occupational Noise Exposure Control*
Pavinee Rerkjirattikarn, Chatdanai Kaorapapaong, Sun Olapiriyakul
(Thammasat University, Thailand)
- GS7-3 *A Training Method for the Speech Controlled Environmental Control System Based on Candidate Word Discriminations*
Taro Shibanoki, Masaki Watanabe (Ibaraki University, Japan), Go Nakamura, Takaki Chin
(Hyogo Rehabilitation Center, Japan), Toshio Tsuji (Hiroshima University)

Meeting room 4

9:00-9:30 GS5 Neuroscience (3)

Chair:

- GS5-1 *Improving EEG-based BCI Neural Networks for Mobile Robot Control by Bayesian Optimization*
Takuya Hayakawa, Jun Kobayashi (Kyushu Institute of Technology, Japan)
- GS5-2 *Selective synchronization of the coupled bifurcating neurons for phase shift of background oscillation*
Akihiro Yamaguchi¹, Yutaka Yamaguti¹, Masao Kubo²
(¹Fukuoka Institute of Technology, ²National Defense Academy of Japan, Japan)
- GS5-3 *Review on computational techniques in solving aircraft landing problem*
Aminurafiuddin Zulkifli, Nor Azlina Ab. Aziz, Nor Hidayati Abdul Aziz
(Multimedia University, Malaysia)
Zuwairie Ibrahim (Universiti Malaysia, Malaysia)
Norrima Mokhtar (University of Malaya, Malaysia)

14:30-15:45 OS20 Advances in Marine Robotics and It's Applications (5)

Chair: Kazuo Ishii (Kyushu Institute of Technology, Japan)

Co-Chair: Keisuke Watanabe (Tokai University, Japan)

- OS20-1 *A land testbed for experimental research on autonomous ship navigation*
Keisuke Watanabe, Kazumasa Harada, Koshi Utsunomiya
(Tokai University, Japan)
- OS20-2 *Seafloor Image Color Enhancement Method based on Retinex model and Experiment Report in the undersea environment*
Jonghyun Ahn¹, Shinsuke Yasukawa², Yuya Nishida¹, Takashi Sonoda¹, Keisuke Watanabe³
Kazuo Ishii¹(¹Kyushu Institute of Technology, ²University of Tokyo, ³Tokai University, Japan)

The 2018 International Conference on Artificial Life and Robotics (ICAROB2018), B-Con Plaza, Feb. 1- 4, Beppu, Oita, Japan, 2018

- OS20-3 *Automatic recognition of benthic species using image processing*
Yuki Soejima, Yuya Nishida, Takashi Sonoda, Kazuo Ishii
(Kyushu Institute of Technology, Japan)
- OS20-4 *AUV homing using acoustic chirp signal*
Koji Masuda, Yuya Nishida, Takashi Sonoda, Kazuo Ishii
(Kyushu Institute of Technology, Japan)
- OS20-5 *Simulation of horizontal vibration suppression of a suspended structure for seabed mining*
Keisuke Watanabe (Tokai University, Japan)
Kazuo Ishii (Kyushu Institute of Technology, Japan)

February 4 (Sunday)

8:40-Registration

Meeting Room 31

10:30-11:10 Invited Session IS-3

Chair: Makoto Sakamoto (University of Miyazaki, Japan)

IS-3 Natural Computing Paradigm — A Concise Introduction

Takashi Yokomori (Waseda University, Japan)

11:30-12:10 Invited session IS-5

Chair: Takao Ito (Hiroshima University, Japan)

IS-5 Harnessing over a Million CPU Cores to Solve a Single Hard Mixed Integer Programming Problem on a Supercomputer

Yuji Shinano (Zuse Institute Berlin, Germany)

Meeting Room 32

13:10-14:55 OS17 Automated content generation and cognitive content generation (7)

Chair: Hiroki Fukushima (Kyushu Women's University, Japan)

Co-Chair: Jumpei Ono (Iwate Prefectural University, Japan)

Co-Chair: Takashi Ogata (Iwate Prefectural University, Japan)

Co-Chair: Akinori Abe (Chiba University, Japan)

OS17-1 *Reinventing the Flavor Wheel*

Hiroki Fukushima (Kyushu Women's University, Japan)

OS17-2 *Acquiring Short Scripts and Setting a Case Frame in each Acquired Script: Toward Random Story Generation*

Jumpei Ono, Takashi Ogata (Iwate Prefectural University, Japan)

OS17-3 *A Method of Naimaze of Narratives Based on Kabuki Analyses and Propp's Move Techniques for an Automated Narrative Generation System*

Takashi Ogata (Iwate Prefectural University, Japan)

OS17-4 *Narratology goes to Creativity ---Cognitive Content Generation*

Akinori Abe (Chiba University, Japan)

OS17-5 *A Framework for Haiku Generation from a Narrative*

Takuya Ito, Takashi Ogata (Iwate Prefectural University, Japan)

OS17-6 *Cognitive content generation for healthy ageing*
Yuki Hayashi (Chiba University, Japan)

OS17-7 *Museum Visitors' Behavioural Change Caused by Captions*
Kotone Tadaki (Chiba University, Japan)

Meeting Room 33

9:00-10:15 GS6 Virtual reality (5)

Chair:

GS6-1 *Interactive musical editing system to support human errors and offer personal preferences for an automatic piano -Inferring performance expression by considering change of pitch-*
Masahiro Ushio, Eiji Hayashi (Kyushu Institute of Technology, Japan)

GS6-2 *Analysis of Malaysian Facial Expressions for Designing Virtual Agents*
Halimahtun Khalid (Damai Sciences, Malaysia), Liew Wei Shiung (University of Malaya, Malaysia)

GS6-3 *Development of VR system to enhance understanding process of robot mechanisms*
Alexei Lushnikov, Vlada Kugurakova, Timur Satdarov and Artur Nizamutdinov
(Kazan Federal University, Russia)

GS6-4 *Towards the immersive VR: measuring and assessing realism of user experience*
Vlada Kugurakova, Murad Khafizov, Alexander Elizarov, Aleksei Lushnikov
and Artur Nizamutdinov (Kazan Federal University, Russia)

GS6-5 *Lessons on the Reality-Gap: Iterations between Virtual and Real Robots*
Andre Rosendo (ShanghaiTech University, China)
Charlie Houseago, Fumiya Iida (Cambridge University, UK)

13:10-14:25 Human Interface and Artificial Intelligence (5)

Chair: Yasunari Yoshitomi (Kyoto Prefectural University, Japan)

Co-Chair: Masayoshi Tabuse (Kyoto Prefectural University, Japan)

OS13-1 *A Recipe Decision Support System with Recognition Ability Recoding Function Using Knowledge Information and Agent*
Keita Saito, Taro Asada, Yasunari Yoshitomi, Ryota Kato, and Masayoshi Tabuse
(Kyoto Prefectural University, Japan)

OS13-2 *A System for Analyzing Facial Expression and Verbal Response of a Person while Answering Interview Questions by Agent*
Taro Asada¹, Daichi Kogi², Ryouichi Shimada³, Yasunari Yoshitomi¹, and Masayoshi Tabuse¹
(¹ Kyoto Prefectural University, ² S.Ten Nines Kyoto Co.,Ltd., ³ JFE Systems, Inc., Japan)

- OS13-3 *Facial Expression Analysis and its Visualization While Writing Messages*
Yasunari Yoshitomi¹, Taro Asada¹, Kenta Mori², Ryoichi Shimada³, Yuiko Yano¹
and Masayoshi Tabuse¹
(¹ Kyoto Prefectural University, ² Neyagawa City Hall, ³ JFE Systems, Inc., Japan)
- OS13-4 *Recognition of Finger Spelling from Color Images Using Deep Learning*
Yusuke Yamaguchi, Masayoshi Tabuse (Kyoto Prefectural University, Japan)
- OS13-5 *Recognition of Texting While Walking Using Convolutional Neural Networks*
Junpei Miyachi, Masayoshi Tabuse (Kyoto Prefectural University, Japan)

Meeting Room 1

9:00-10:00 OS6 Kansei Engineering and Applications (4)

Chair: Tetsuo Hattori (Kagawa University, Japan)

Co-Chairman: Yoshiro Imai (Kagawa University, Japan)

- OS6-1 *Histogram Analysis Method Based on Gaussian Distribution and Curvature Computation (I) --- Peaks and Valleys Detection ----*
Yusuke Kawakami*, Tetsuo Hattori**, Yoshiro Imai**, Kazuaki Ando**, Yo Horikawa**,
R. P. C. Janaka Rajapakse*** (*DynaxT Co., Ltd., Japan), (**Kagawa University, Japan)
(***Tainan National University of the Arts, Taiwan)
- OS6-2 *Histogram Analysis Method Based on Gaussian Distribution and Curvature Computation (II) --- - Experimentation ----*
Yusuke Kawakami*, Tetsuo Hattori**, Yoshiro Imai**, Kazuaki Ando**, Yo Horikawa**,
R. P. C. Janaka Rajapakse*** (*DynaxT Co., Ltd., Japan), (**Kagawa University, Japan)
(***Tainan National University of the Arts, Taiwan)
- OS6-3 *Experimental Evaluation of Change Detection Ability in New Sequential Probability Ratio*
Yoshihide Koyama*¹, Tetsuo Hattori*¹, Yoshiro Imai*¹, Yo Horikawa*¹,
Yusuke Kawakami*², Hiromichi Kawano*³, Takeshi Tanaka*⁴
(*¹Kagawa University, *²DynaxT Co., Ltd., *³NTT advanced technology Co., Ltd., *⁴Hiroshima
Institute of Technology, Japan)
- OS6-4 *Application Proposal of Sequential Probability Ratio to Dynamic System State Estimation*
Tetsuo Hattori*¹, Yusuke Kawakami*², Yoshihide Koyama*¹, Yoshiro Imai*¹, Yo Horikawa*¹,
Hiromichi Kawano*³, Takeshi Tanaka*⁴
(*¹Kagawa University, *²DynaxT Co., Ltd., *³NTT advanced technology Co., Ltd.,
*⁴Hiroshima Institute of Technology, Japan)

13:10-14:25 OS1 Computer Science and Information Processing (5)

Chair: Makoto Sakamoto (University of Miyazaki, Japan)

Co-Chair: Yu-an Zhang (Qinghai University, China)

- OS1-1 *k-Neighborhood Template A-Type Two-Dimensional Bounded Cellular Acceptors*
Makoto Sakamoto¹, Yu-an Zhang², Masamichi Hori¹, Haruka Tsuboi¹, Satoshi Ikeda¹,
Kenji Aoki¹, Tsutomu Ito³, Takao Ito³, Yasuo Uchida⁴, and Tsunehiro Yoshinaga⁵
(¹University of Miyazaki, Japan, ²Qinghai University, China, ³Hiroshima University, Japan,
⁴Ube National College of Technology, Japan, ⁵Tokuyama College of Technology, Japan)
- OS1-2 *An efficient structure of organization with complete individual guidance*
Mamoru Yoshimura, Tsutomu Ito¹, Makoto Sakamoto, Takao Ito¹, Yuji Shinano², Satoshi Ikeda
(University of Miyazaki, Japan) (¹Hiroshima University, Japan) (²Zuse Institute Berlin, Germany)
- OS1-3 *Consideration for the Possibility to the Tourism Support Contents by the Markerless AR
Technology*
Masamichi Hori¹, Makoto Sakamoto¹, Koshiro Mitsuhashi², Yukari Kodama², Takeshi Tanaka¹
Mihoko Fukushima¹, Chikashi Deguchi¹, Masahiro Yokomichi¹, Masayuki Mukunoki¹,
Kunihito Yamamori¹, Atsushi Iiboshi³
(¹University of Miyazaki, ²Miyazaki Multimedia Academy, ³Takachiho Muratabi Co., Ltd., Japan)
- OS1-4 *Fundamental study on tourism support using 3DCG*
Haruka Tsuboi¹, Makoto Sakamoto¹, Masamichi Hori¹, Yosuke Iriyama¹, Yuki Kai¹,
Hazuki Watanabe¹, Yu-an Zhang², Atsushi Iiboshi³, Koshiro Mitsuhashi⁴, Yukari Kodama⁴
(¹University of Miyazaki, Japan), (²Qinghai University, China), (³Muratabi, Ltd, Japan)
(⁴Miyazaki Multimedia Academy, Japan)
- OS1-5 *Clustering Analysis Based on Improved Fuzzy C - Means Algorithm*
Qiongqiong Hu¹, Yiyang Li¹, Yong Ge¹, Yu-an Zhang¹, Qinglian Ma², Makoto Sakamoto²
(¹Qinghai University, China), (² University of Miyazaki, Japan)

Meeting Room 4

9:00-10:15 OS11 Educational Application Making Control Engineering Approach (5)

Chair: Kazuo Kawada (Hiroshima University, Japan)

Co-Chair: Yoshihiro Ohnishi (Ehime University, Japan)

- OS11-1 *Control Performance Assessment Method as Assessment of Programming Learning Achievement*
Yoshihiro Ohnishi (Ehime University, Japan)
- OS11-2 *Practice of Control Education by Experiment using Robot*
Shinichi Imai, Hideto Matsui and Akira Yamada (Tokyo Gakugei University, Japan)
- OS11-3 *Development of Support Teaching Material for Nurturing Cooperativity through Playing*
Kazuo Kawada (Hiroshima University, Japan)
- OS11-4 *On Methods for Teaching in Training for Keeping Tempo Constant in Music*
Hideyuki Tanaka and Keita Ueda (Hiroshima University, Japan)

- OS11-5 *Reinforcement Learning as a Theoretical Framework for Education*
Masayasu Nagamatsu, Yuki Moriguchi (Hiroshima University, Japan)

Farewell Party

GS10 Others (4)

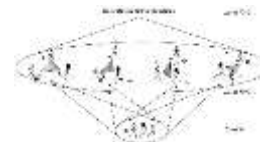
- GS10-1 *A review on fundamental advancements of black hole algorithm*
Zuwairie Ibrahim, Suad Khairi Mohammed, Norazian Subari
(Universiti Malaysia Pahang, Malaysia)
Nor Azlina Ab Aziz, Nor Hidayati Abdul Aziz (Multimedia University, Malaysia)
Tasiransurini Ab Rahman (Universiti Tun Hussein Onn Malaysia, Malaysia)
Asrul Adam, Zulkifli Md Yusof (Universiti Malaysia Pahang, Malaysia)
Mohd Ibrahim Shapiai
(Malaysia Japan International Institute of Technology, Universiti Teknologi Malaysia, Malaysia)
Norrima Mokhtar (University of Malaya, Malaysia)
- GS10-2 *A survey on applications of black hole algorithm*
Zuwairie Ibrahim, Suad Khairi Mohammed, Norazian Subari, Asrul Adam, Zulkifli Md Yusof
(Universiti Malaysia Pahang, Malaysia)
Nor Azlina Ab Aziz, Nor Hidayati Abdul Aziz (Multimedia University, Malaysia)
Tasiransurini Ab Rahman (Universiti Tun Hussein Onn Malaysia, Malaysia)
Mohd Ibrahim Shapiai
(Malaysia Japan International Institute of Technology, Universiti Teknologi Malaysia, Malaysia)
Norrima Mokhtar (University of Malaya, Malaysia)
- GS10-3 *Black hole white hole algorithm with local search*
Zuwairie Ibrahim, Suad Khairi Mohammed, Norazian Subari, Asrul Adam, Zulkifli Md Yusof
(Universiti Malaysia Pahang, Malaysia)
Nor Azlina Ab Aziz, Nor Hidayati Abdul Aziz (Multimedia University, Malaysia)
Tasiransurini Ab Rahman (Universiti Tun Hussein Onn Malaysia, Malaysia)
Norrima Mokhtar (University of Malaya, Malaysia)
- GS10-4 *Tele-Operation of a Legged Robot by a Virtual Marionette System*
- First report: *The first prototype and the usefulness of the reaching task-*
Noritaka Sato, Yasuhiko Sawai, Ryo Asami, Makoto Kitani, Yoshifumi Morita
(Nagoya Institute of Technology, Japan),
Tomofumi Fujiwara, Takahiro Endo, Fumitoshi Matsuno (Kyoto University, Japan)

PS abstracts

PS-1 Dynamic Structures for Evolving Tactics and Strategies in Team Robotics

Jeffrey Johnson, Ruggero Rossi (The Open University, UK)

The autonomous robot systems of the future will be teams of robots with complementary specialisms. At any instant robot interactions determine relational structures, and sequences of these structures describe the team dynamics as trajectories through space and time. These structures can be represented in algebraic forms that are realizable as dynamic multilevel data structures within individual robots, as the basis of emergent team data structures. Such formalisms are necessary for robots to learn new individual and collective behaviours. The theory is illustrated by the example of robot soccer where robot interactions create structures and trajectories essential to the evolution of new tactics and strategies in a changing environment.



PS-2 EU-Way Development - Effective and Rational Development Way -

Masato (Max) Nakagawa (Executive Fellow, DENSO CORPORATION, Japan)

In this Plenary Speech will cover three elements describe as follows; Firstly, “Factory-IoT” technology which is DENSO company manufacturing strategy globally. Secondly, collaboration between Germany and Japan in terms of innovation. Thirdly, EU-Way development which is effective and rational manner of development. From his working experience in Germany, United Kingdom and the Netherlands in consecutive 14 years, EU-Way development will be explained. One of the key points is that they make “Competition Field” and “Non-Competition Field” in their technical domains. In the “Non-Competition Field” which is also called a “Cooperative Field”, they cooperate together in the same industry sector to create common specification or to establish the standardization so that they can concentrate on differentiated technology as a “Competition Field” This approach is one of their driving forces for development and innovation.



Fig. Development Style Comparison between Japan and Germany

PS-3 Innovation on Manufacturing Generated by Intelligent Technologies

Ken-ichi Tanaka, Haruhisa Okuda (Mitsubishi Electric Corporation, Japan)

In order to cope with social problems such as labor population decrease, the autonomous cell production robot system had been developed to realize automation in variable variety multi production. The intelligent technologies such as random bin picking, force control, and error recovery were developed to apply the robot from simple-transport-work to assemble-task. In addition to the talk about such technologies, it will also be described that open innovation method cooperating with universities to create research results which our company would not achieve independently. The examples of the latest robot technology development using artificial intelligence will also be described.



IS abstracts

IS-1 Modular Playware and Personal Health Technology

Henrik Hautop Lund (Technical University of Denmark, Denmark)

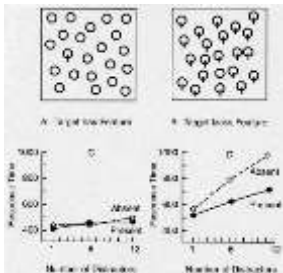
In this paper, we describe the development of personal health technology such as wearable systems monitoring health conditions. It has been advocated that such personal health technology through monitoring health status may motivate people to perform health related actions and life-style changes. Here we describe a methodology on how these personal health technologies may rather be used as a tool for designing and adapting game activities, which motivate people to perform the desired actions. Especially, we exemplify this methodology with the use of FitBit monitoring of steps and heart rate to the design of appropriate, physically demanding games for the modular interactive tiles, Moto Tiles, which are used by older adults for prevention and rehabilitation. Thereby, the motivation to perform the actions arrives from the fun play on the Moto Tiles, whereas the personal health technology is used as a tool to monitor the effect and guide the game development.



IS-2 How new technologies might lead to a paradigm shift in psychological and neuropsychological research

Luigi Pagliarini, Henrik Hautop Lund (Technical University of Denmark, Denmark)

Recently, we started to apply old psychological and neuropsychological standard tests and therapeutic exercises into a different domain of technology. Therefore, while maintaining the whole conceptual and logical structure of the traditional approach – i.e. tests mostly made by hand on paper or with the mouse and computers’ screens - intact, we moved them onto the physical interactive and playful technology, Moto Tiles. Such a translation of input/output, likewise involving dissimilar perceptions and different parts of our motor system (i.e. legs, feet and balance system), might imply a change in subjects’ mental and behavioural strategies, variations in efficacy and efficiency, as well as a redefinition of reaction times. In short, this shift, besides providing a significant extra tool to older practices, might work as a crucial test for all of the existing theoretical background, too. We describe our new method and report few of the first empirical applications.



IS-3 Natural Computing Paradigm – A Concise Introduction

Takashi Yokomori (Waseda University, Japan)

Natural computing (NC) is an emerging area of research that investigates computing techniques and models inspired by nature on one hand, and it also investigates phenomena taking place in nature in terms of computational methodologies on the other hand. Thus, research in NC congenitally has interdisciplinary flavor, which bridges between computer science and various disciplines of natural science. Because of its interdisciplinary nature, NC connects and covers a broad spectrum of fundamental research fields including biology, chemistry, physics, medical science, and so forth. In this article, we give a concise introduction to the new computing paradigm of NC. Specifically, we give an overview of selected topics of the fields from theory to experiments, where the stress is primarily put on theoretical achievements in computing paradigms called molecular computing and chemical reaction computing.

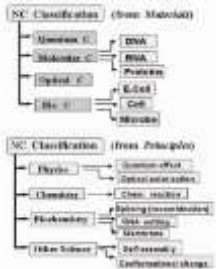
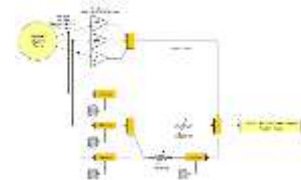


Figure1. Natural Computing Paradigms Inspired by Nature (A part)

IS-4 Artificial Immune Ecosystems: challenges for a new generation of bio-inspired secure and resilient systems

Pierre Parrend
(ECAM Strasbourg-Europe, France)

The rapid evolution of IT ecosystems significantly challenges the security models our infrastructures rely on. Beyond the old dichotomy between open and closed systems, it is now necessary to handle securely the interaction between heterogeneous devices building dynamic ecosystems. To this regard, bio-inspired approaches provide a rich set of conceptual tools, but have failed to lay the basis for robust and efficient solutions. Our research effort intends to revisit the contribution of artificial immune system research to bring immune properties: security, resilience, distribution, memory, into IT infrastructures. We introduce the concept of artificial immune ecosystems, which encompass a comprehensive immune protocol, libraries for detection and investigation of anomalies, and an underlying middleware layer, for bringing immunity to IT infrastructures, the Cloud, and IoT environment.



IS-5 Harnessing over a Million CPU Cores to Solve a Single Hard Mixed Integer Programming Problem on a Supercomputer

Yuji Shinano (Zuse Institute Berlin, Germany)

The performance of mixed integer programming (MIP) solvers has improved tremendously in the last two decades and these solvers have been used to solve many real-world problems. ParaSCIP is the most successful parallel MIP solver in terms of solving previously unsolvable instances from the well-known benchmark instance set MIPLIB by using supercomputers. ParaSCIP has been developed by using the Ubiquity Generator (UG) framework, which is a general software package to parallelize any state-of-the-art branch-and-bound based solvers. ParaSCIP is a parallelized MIP solver of a single thread solver SCIP. Since Xpress is a multi-threaded solver and ParaSCIP can run at least 80,000 processes in parallel for solving a single MIP, ParaXpress could handle over a million CPU cores. In this talk, a ground design of the UG framework and its latest extensions to harness over a million CPU cores will be presented and preliminary computational results will be provided.



IS-6 Trust of Virtual Agent in Multi Actor Interactions

H. M. Khalid, W. S. Liew, B.S. Voong, M.G. Helander (Damai Sciences, Malaysia)

Trust is crucial when integrating virtual agents in human teams. Our study investigated the combined use of subjective (general trust, psychological) and objective (physiological) measures in predicting human trust of agents undertaking social tasks. The subjective measures comprised twelve self-report trust scores on ability, benevolence and integrity (ABI). The objective measures included facial expressions, voiced speech, camera-based heart rate and gestural posture. Forty-eight subjects participated in a 2x2x2 within subject design. They interacted with two virtual agents - a male Chinese and a female Malay. Each experimental condition comprised three human subjects (a teleoperator and two clients) and one avatar. The interactive dialog involved a business set up. A neuro-fuzzy algorithm extracted rules from the psychophysiological data to predict trust at low, medium and high trust levels. The results revealed that trust can be predicted with an accuracy of 88%. However, if gestures were excluded, the accuracy increased to 90%.



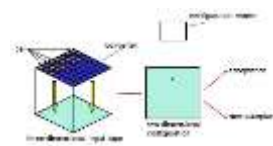
OS abstracts

OS1 Computer Science and Information Processing (5)

OS1-1 k-Neighborhood Template A-Type Two-Dimensional Bounded Cellular Acceptors

Makoto Sakamoto¹, Yu-an Zhang², Masamichi Hori¹, Haruka Tsuboi¹, Satoshi Ikeda¹, Kenji Aoki¹, Tsutomu Ito³, Takao Ito³, Yasuo Uchida⁴, and Tsunehiro Yoshinaga⁵
(¹University of Miyazaki, Japan, ² Qinghai University, China, ³Hiroshima University, Japan, ⁴Ube National College of Technology, Japan, ⁵Tokuyama College of Technology, Japan)

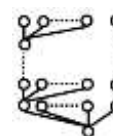
In this paper, we deal with three-dimensional computational model, k-neighborhood template A-type two-dimensional bounded cellular acceptor on three-dimensional tapes, and discuss some properties. This model consists of a pair of a converter and a configuration-reader. The former converts the given three-dimensional tape to two-dimensional configuration. The latter determines whether or not the derived two-dimensional configuration is accepted, and concludes the acceptance or non-acceptance of given three-dimensional tape. We mainly investigate some open problems about k-neighborhood template A-type two-dimensional bounded cellular acceptor on three-dimensional tapes.



OS1-2 An efficient structure of organization with complete individual guidance

Mamoru Yoshimura, Tsutomu Ito¹, Makoto Sakamoto, Takao Ito¹, Yuji Shinano², Satoshi Ikeda (University of Miyazaki, Japan) (¹Hiroshima University, Japan) (²Zuse Institute Berlin, Germany)

This research clarifies the efficient organizational structure using mathematical model. Previous studies have shown that the structure of an efficient organization is limited under given settings when there is only one criterion to evaluate. In this study, we show that an optimal organizational structure which has not been known until now occurs under the setting different from the previous research.



OS1-3 Consideration for the Possibility to the Tourism Support Contents by the Markerless AR Technology

Masamichi Hori, Makoto Sakamoto, Koshiro Mitsuhashi¹, Yukari Kodama¹, Takeshi Tanaka, Mihoko Fukushima, Chikashi Deguchi, Masahiro Yokomichi, Masayuki Mukunoki, Kunihiro Yamamori, Atsushi Iiboshi²(University of Miyazaki, ¹Miyazaki Multimedia Academy, ²Takachiho Muratabi Co., Ltd., Japan)

Currently, the tourism industry in Miyazaki prefecture has various problems, and various measures are taken. On the other hand, in 2016 virtual technology attracted much attention also on AR technology. We thought that through the AR technology experience, we could aim for an increase in tourists. Therefore, we will create new applications for smartphones using AR technology and aim for tourism support. First, prototype an application with markerless and features for smartphones etc., and conduct experiments. As a result, there was improvement and it was not completed. However, it seemed possible to become an application that realizes tourism support.



OS1-4 Fundamental study on tourism support using 3DCG

Haruka Tsuboi¹, Makoto Sakamoto¹, Masamichi Hori¹, Yosuke Iriyama¹, Yuki Kai¹,
Hazuki Watanabe¹, Yu-an Zhang², Atsushi Iboshi³, Koshiro Mitsuhashi⁴, Yukari Kodama⁴
(¹University of Miyazaki, Japan ²Qinghai University, China ³Muratabi, Ltd, Japan,
⁴Miyazaki Multimedia Academy, Japan)

The penetration rate of CG (computer graphics) in recent years has become remarkable. Currently, there are various examples of utilization such as movies and animation, various simulation and tourism projects, sales visuals and so on. Also, as the Tokyo Olympic Games are held in 2020, the demand for tourism in Japan is getting bigger. Accordingly, we believe that efforts towards tourism support are necessary even in local government units. Therefore, we considered fundamental research of this moment, considering whether we can PR such as we do not exist by using CG technology for the rich nature and sightseeing spot of Miyazaki prefecture where we live. In this research, we focused on "Takachiho-cho", which is known as a land with a connection to "Japanese mythology" among Miyazaki prefecture. As a goal, tourism support such as combining the created 3DCG model with real underwater images and aerial images, introducing rich nature as the main and historic tourist attractions.



OS1-5 Clustering Analysis Based on Improved Fuzzy C - Means Algorithm

Qiongqiong Hu, Yiyang li, Yong Ge, Yu-an Zhang, Qinglian Ma¹, Makoto Sakamoto¹
(Qinghai University, China, ¹University of Miyazaki, Japan)

Cluster analysis is one of the most important technologies in the field of data mining, and it is also a hot topic in academic research. So far, it has made great achievements in theory and method, and plays an important role in data analysis in various fields. The fuzzy C-means algorithm (FCM) maintains the simplicity of its thinking, the time complexity is close to linear, and it is efficient and scalable for large-scale data mining. Particle Swarm Optimization (PSO) is an optimization tool with global optimization ability, and the group intelligence is formed by the interaction between particles in the group, and the optimal result is found by the intelligence. However, with the deepening of algorithm research, its research prospects and application areas are increasingly bright and compelling.

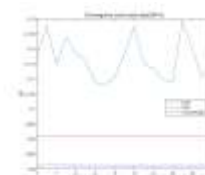


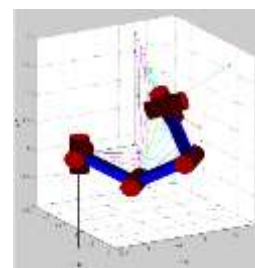
Fig. 1. Table the condition of $CM > 0$, the 10 value curve under different average of FCM represents the fuzzy C-means algorithm, PSO represents the idea of integrating the particle swarm algorithm to FCM, and the fitness function represents the fitness, clustering results (right).

OS2 Intelligent Navigation (6)

OS2-1 Robot Manipulator Arm Inverse Kinematics Analysis by Jacobian

Sun Oh Park, Min Gyu Jung, Jin Gon Yoon, Min Cheol Lee (Pusan National University, Korea)

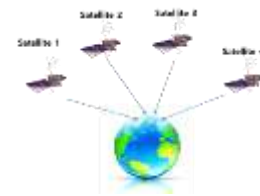
There are three methods for solving inverse kinematic that are algebraic, geometric and numerical. The advantage of algebraic and geometric method is that can analyze exactly but these two methods are not only difficult to analysis but also need to recalculate when DOF or DH-parameter are changed. That is why this paper will present how to approach numerical method by MATLAB. Otherwise previous two methods, the numerical method by using Jacobian can solve any DOF and DH-parameter easily except singular point. Therefore, we are going to explain Jacobian analysis and avoid singular point by using condition number. In the future, we will adapt this result to 7DOF dual robot arm and then compare our numerical method and real system



OS2-2 Indoor Position recognition using the pseudo-range estimation

Jongwoo An, Hosun Kang, Jiwook Choi, Jangmyung Lee (Pusan National University, Korea)

In this paper, we propose a method of position recognition in indoor environment by pseudo range estimation of each satellite. Position recognition is a core technology for operating autonomous intelligent robots such as Unmanned Aerial Vehicle System(UAV), Automated Guided Vehicle(AGV). The Position recognition technology is divided into outdoor position recognition and indoor position recognition. The outdoor position is estimated using Global Positioning System(GPS) and the indoor position is estimated using various sensors such as Beacon and Inertial Measurement Unit(IMU). Due to the development of the technology, outdoor position recognition using GPS can be precise position estimation, but indoor position recognition using various sensors has a cumulative error caused by various factors and it is difficult to operate for a long time. In this paper, to overcome this drawback, we analyze the relationship between the velocity of the moving object and pseudo-range shift each satellite, and estimate the indoor position of the moving object by estimating the pseudo-range.



OS2-3 Distance measurement algorithm based on the object recognition

Hosun Kang, Nahyun Lee, Jangmyung Lee (Pusan National University, Korea)

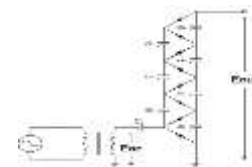
This paper implements an algorithm that recognizes an object using a vision system and measured the distance to the object. Recently, autonomous navigation systems such as UAV and AUV are attracting attention. In order to operate these systems safely, it is necessary to recognize obstacles on the moving path accurately and quickly. Generally, various sensors are used to recognize the surrounding environment. These methods are affected by disturbance caused by the surrounding environment. To overcome these drawbacks, this paper proposes an obstacle recognition algorithm using a stereo camera. For obstacle recognition, disparity is obtained by removing the remaining part of the object except the recognized object from the image in order to improve the computation speed. Finally, after calculating the distance, we confirm the algorithm by comparing with the actual distance.



OS2-4 An-ion air purifier system using IoT Technology

Heeje Kim, Dohyun Kim (Pusan National University, Korea)

We have developed the an-ion air purifier which can remove various fine dust very efficiently. It was based on the principle of high voltage corona discharge that was fabricated for air cleaning from various fine dust. That is a big issue for human society. The best switching frequency was 10kHz, and the output voltage was approximately 20kV. In order to remove the fine dust, the an-ion air purifier was controlled properly for removing the fine dust by using the Arduino and personal smart-phone app. From these experiments, we could remove various fine dust much more easily and effectively



OS2-5 Solar Panel Temperature Control System using IoT

Min-soo Kim, Hee-je Kim (Pusan National University, Korea)

Solar photovoltaic systems are renewable energy sources that are used widely around the world. On the other hand, the efficiency decreases as the temperature of the solar panels increases. To prevent this phenomenon, a cooling fan can be installed on the back side of the solar panel to increase the efficiency. The solar system efficiency also decreases due to weather conditions and unexpected situations. To overcome this problem, an IoT (Internet of Things) system was used to monitor the state of the solar system and control the cooling fan. The core microprocessor used in IoT systems was Arduino. Using Arduino, an IoT system can be implemented simply and inexpensively. The entire system was designed and tested and the efficiency increased by approximately 4.7%. Although it is a small 30W capacity photovoltaic system, its efficiency is expected to be increased by applying it to a photovoltaic system of more than 1kW in the near future.



OS2-6 Enhancement of Mobile Robots Stability and Hardware Based on Reinforcement Learning

Ki-seo Kim, Jeong-hwan Moon, Jang-myung Lee (Pusan National University, Korea)

In this paper, we apply the obstacle avoidance run reinforcement learning algorithm used in the mobile robot using the LiDAR sensor. Q-learning and Deep Learning were applied to reinforcement learning algorithms. We solve the unnatural movements in the deceleration and acceleration of the robot using feedback learning. The results of simulation are applied to actual hardware to show how to increase the safety of driving.

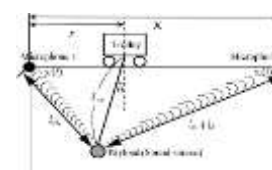


OS3 New Challenges to Adaptive & Learning Control-1(5)

OS3-1 A sound-based measurement of sway angle for anti-sway control of overhead crane

Miki Matsunaga, Masayoshi Nakamoto, Toru Yamamoto (Hiroshima University, Japan)

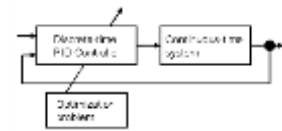
The cranes are well used in field such as transportation of load in construction field, factory and dock. For anti-swing control of overhead crane, a deflection angles must be estimated. But it is difficult to estimate deflection angles directly. Therefore, we show a new measurement method for the deflection angles by using two microphones as angle sensors. The feature of our method is to achieve contact-less sensing, high flexibility of installation, low realization cost, easy to maintenance. The method employs a time delay of arrival (TDOA) of acoustic signals which are picked up by the two microphones. Also, we show an algorithm to obtain the deflection angles from the TDOA by using the Newton's method. Finally, we show experimental results of two patterns (stationary and swaying) to demonstrate the effectiveness of the proposed method.



OS3-2 Sampled-data PID control system with Sensitivity Function for a Second-order Plus Dead-time System

Ryo Kurokawa, Takao Sato, and Yasuo Konishi (University of Hyogo, Japan)
 Ramon Vilanova (Universitat Autònoma de Barcelona, Spain)

A sampled-data proportional-integral-derivative (PID) control system is designed for a second-order plus dead-time system which includes an under-damping system, where the controlled plant and the controller are continuous-time and discrete-time systems, respectively. In order to guarantee the stability margin, the maximum value of the sensitivity function is used for designing the proposed control system. As a result, the control system is optimized subject to the user-specified stability margin. Because the relationship between the stability margin with the tracking performance is trade-off, the stability margin is selected based on the modeling accuracy. Hence, high tracking performance is selected when the modeling error is small. Furthermore, because the proposed PID control system is designed for a normalized system, the optimal PID parameters are calculated without solving the optimization problem.



OS3-3 Experimental Evaluation of a Data-Driven Control System using an Electronic Thermal Regulator

Yuka Okubo, Yoichiro Ashida, Takuya Kinoshita, Toru Yamamoto
 (Hiroshima University, Japan)

Since majority of industrial processes are of nonlinearities, a data-driven PID controller has been proposed to deal with such processes. According to that scheme, the suitable set of PID parameters are automatically computed based on a set of I/O data stored in the database. However, the data-driven technique is hardly implemented in the electronic thermal regulator due to restricted memory capacity. Therefore, the platform is required, in which the PID parameters are calculated by data-driven technique and are sent to the electronic thermal regulator shown in Fig. 1. In this study, the control results will be shown to demonstrate the effectiveness of the proposed scheme by conducting the experiment.

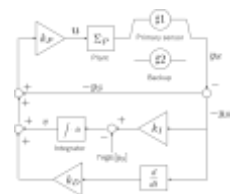


Fig. 1. Proposed platform.

OS3-4 Self-repairing Adaptive PID Control for Plants with Sensor Failures

Masanori Takahashi (Tokai University, Japan)

In our previous works, several types of self-repairing controls have been developed for plants with unknown sensor failures. The self-repairing control system (SRCS) can automatically replace the failed sensor with the healthy backup to maintain its stability if the failure occurs. However, in most existing SRCs, roughly estimated parameters of plants are required. This paper presents a new design method for a self-repairing adaptive PID control system. The control system has the adaptive adjusting mechanisms for the PID gains, and also can detect the sensor failure by self-test using the integrator (I-controller). Hence, for plants with unknown parameters, SRC can be successfully attained. Furthermore, in this paper, the control performances (stability, failure detection and recovery) are theoretically analyzed.



OS3-5 Design and Development of a Constant Temperature Reservoir for a Database-Driven Smart Cultivation System

Shin Wakitani, Sharma Sneha, and Toru Yamamoto (Hiroshima University, Japan)

Decreasing the number of agricultural working population is serious problem. Production of agricultural products in plant factories is as one of the solutions to the above problems. However, it is not easy to set optimal environment conditions for many kinds of plants in food factories. This research aims for realization of a smart plant cultivation system that uses a database as a core technique. In this work, a small size constant temperature reservoir that can control several environment conditions is developed, and a simulator of the system is designed. Moreover a database-driven nonlinear temperature control is performed.



Fig. 1 Cultivation System

OS3 New Challenges to Adaptive & Learning Control-2 (4)

OS3-6 Design of a Performance-Adaptive 1-Parameter Tuning PID Controller

Yoichiro Ashida*, Shin Wakitani*, and Toru Yamamoto (Hiroshima University, Japan)

Many self-tuning PID controllers have been proposed. In these controllers, PID gains are tuned adaptively and can maintain a good control performance to time-variant systems. However, it is difficult to employ these methods to actual systems because of low reliability of an on-line PID gain estimator. In addition, it is not preferred to tune three PID gains simultaneously in terms of the safeness of a closed loop system. In this work, a performance adaptive controller that has two stage of PID parameters tuning mechanisms is proposed. One of the tuners is a one-parameter tuner which calculates only proportional gain using the recursive least squares. The other is a PID gain tuner using ordinary least squares. When the one-parameter tuner cannot maintain a good control performance, the PID gain tuner determine new PID gains to maintain good control performance. The effectiveness of the proposed method is evaluated by a simulation example.

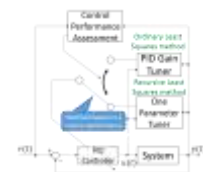
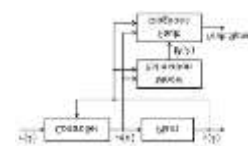


Fig. 1. Block diagram.

OS3-7 Sticking Fault Detecting Method for CARIMA Model

Toyoaki Tanikawa, Tomohiro Henmi
(National Institute of Technology, Kagawa College, Japan)

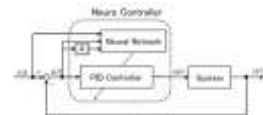
To improve the safety of control systems, it is important to detect various system faults automatically. This paper proposes a sticking fault detecting method on CARIMA model which detect the sticking fault of both the input and the feedback value. It consists of model estimation and a fault diagnosis. In the model estimation, the system parameters are estimated from the input and output data using the recursive least square method with the forgetting factor. On the other hand in the fault diagnosis, an evaluation function derived from CARIMA model is introduced. It generates a fault signal from the input and output data of the detecting period, using the estimated system parameters. Numerical simulations are performed and it is shown that this method can detect the sticking fault of the input and the feedback value.



OS3-8 Design of a Neural Network based on E-FRIT and Its Application

Kento Kinoshita, Shin Wakitani, Shuichi Ohno (Hiroshima University, Japan)

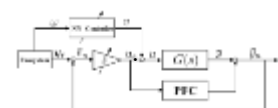
PID controllers have been widely used for process systems. However, a good control result is not always obtained with fixed PID gains when a controlled object has nonlinearity. This paper proposes a design method for a nonlinear PID controller that utilizes a neural network to overcome the problem. In the proposed controller, PID gains are tuned online by a neural network and a controlled object is manipulated by the PID controller with the tuned PID gains. The neural network is learned by an offline learning algorithm based on the extended fictitious reference iterative tuning (E-FRIT) and the backpropagation. E-FRIT is a method that tunes control parameters directly by using operating data. Simulation examples are provided to show the effectiveness of the proposed method. Moreover, the experimental result of a level control of a tank system is also given to demonstrate the performance of the proposed method.



OS3-9 Parameter Optimization with Input/Output data via DE for Adaptive Control System with Neural Network

Taro Takagi (National Institute of Technology, Maizuru College, Japan)
Ikuro Mizumoto (Kumamoto University, Japan)

During the last decades, several almost strictly positive real (ASPR) based adaptive control systems have been proposed. ASPR based adaptive control systems have a robustness with respect to uncertainty and disturbance. However, ASPR conditions are severe conditions for actual systems. Therefore, the introduction of parallel feedforward compensator (PFC), which made it possible to construct ASPR based adaptive control system, has been proposed. Also, feedforward input generated by neural network (NN), which can eliminate the tracking error caused by PFC, has been recently proposed and ASPR based adaptive control system became more practical method. Although the method became practical, it is still difficult to adopt because the parameters of adjust law for NN have to be decided by the designer and it will be decided by trial and error. In this paper, the parameter optimization of PFC and NN will be done by using one-shot experimental data via differential evolution.

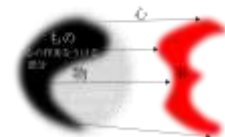


OS4 Aspects of Natural Computing (3)

OS4-1 Mathematical Expression of *Minakata Kumagusu's* Philosophy of Natural Science

Yasuhiro Suzuki (Nagoya University, Japan)

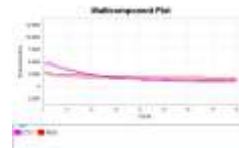
A mission of Natural Computing is understanding nature by algorithms; since an algorithm is just a sequence of computing steps, we have to extract an “algorithm” from nature which requires “viewpoints” that indicate “how to observe and consider”. Minakata Kumagusu [1867-1941], a Japanese naturalist, proposed a novel philosophy of science based on Buddhism and it affords the viewpoint. However, his philosophy of science has almost been ignored, hence we extract the principle of his philosophy from the viewpoint of Natural Computing and transform it into a mathematical form by using Category Theory.



OS4-2 Toward Artificial Intelligence by Using DNA Molecules

Yasuhiro Suzuki, Rie Taniguchi (Nagoya University, Japan)

Molecular Robotics have been realized by using bio molecules such as DNA or proteins, for example in the Molecular Robotics Research Project [2012-17, JSPS]. Such bio molecules, like DNA or proteins, are highly structured. They already have a kind of “intelligence” and adapt to environmental change. Hence, we have tried to extract their “ability” in order to induce intelligence artificially. We have used well-known DNA reactions, *Seesaw gate reaction*, and we found that DNA molecules can sense the concentration of a single strand input sequence or quasi-input (mismatch, point mutation, including sequence) and choose the one with higher concentration. This result shows that DNA molecules (short DNA sequences) can adapt to their environment.



OS4-3 Differentiation and Integration of Sensation and its Application

Yasuhiro Suzuki (Nagoya University, Japan)

Our senses can be seen as a dynamical system in a multi-dimensional sensory space, where each dimension corresponds to a type of sense such as vision, hearing, touch, and so on. Our sensory systems are composed of differentiators and we perceive sensory stimulations through differentiating sensory stimulations. In order to calculate the differentiation of sense, we have to set a measurable quantity of the sense. We can not only use quantity measures such as brightness of picture or loudness of sound, but also quality measures like the value of Semantic Differential (SD) method for measuring impressions or emotions, such as beauty, fear, happiness. We propose a method of Differentiation and Integration of sensation and we show the application of this method by transforming a painting of *Piet Mondrian's "1921"* into a music piece.

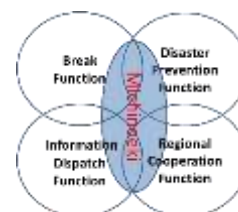


OS5 Advanced Regional Engineering (4)

OS5-1 Discovering Successful Determinants of Efficiency of MICHINOEKI in Chugoku Area

Minoru Kumano(University of Miyazaki, Japan),Takao Ito(University of Hiroshima, Japan),
Toru Hiraoka(University of Nagasaki, Japan), Hirofumi Nonaka(Nagaoka University of
Technology, Japan), Masaharu HirotaOkayama University of Science, Japan)

Many theories and analyses of Michinoeki from the viewpoints of break function, information dispatch function, and regional cooperation function have been published in the past decades. Based on our investigation, additional dimensions called disaster prevention function need to be added because a variety of activities have been developed recently. Specific to the context of Michinoeki systems, this paper develops and empirically tests a mathematical model of Michinoeki from the standpoint of how those four basic functions significantly influence its performance, thus uniquely contributing to extant knowledge. Using data drawn from Michinoeki in Chugoku area, this research attempts to shed light on the relationship between four basic functions and its performance including sales revenue and number of customers who passed through the shop cashier, to confirm the validity of the new four function model. Based on the findings, the managerial implications are discussed, the study limitations are identified and directions for further research are suggested.



OS5-2 Relationship Analysis on the Number of Customers of Michinoeki in Kyushu Region

Toru Hiraoka, Shiori Nishimura (University of Nagasaki, Japan), Hirofumi Nonaka (Nagaoka University of Technology, Japan), Minoru Kumano (University of Miyazaki, Japan)

We extract relevant factors or existence of facility / service to the number of customers of Michinoeki in Kyushu region, and estimate the number of customers from each factor or existence of facility / service. We pick up facility area (whole), facility area (sales office), number of parking units, traffic volume, number of items (sales office), overall project cost, and municipal population. By correlating these factors and the number of customers, we find factors that are related to the number of customers. And we pick up the 44 facilities / services, and analyze the correlation between the 44 facilities / services and the number of customers. In addition, we perform multiple regression analysis to estimate the number of customers from these factors or existence of facilities / services, and verify the performance of multiple regression equations for each factor or existence of facility / service.

Table Correlation analysis of the number of customers and factors

Data name	Correlation coefficient
Number of parking units	0.525
Facility area (sales office)	0.460
Traffic volume	0.428
overall project cost	0.204
number of item (sales office)	0.156
facility area (whole)	-0.122
municipal population	-0.111

OS5-3 Emotional Contribution Analysis of Online Reviews

Elisa Claire Alemán Carreón, Hirofumi Nonaka (Nagaoka University of Technology, Japan), Toru Hiraoka (University of Nagasaki, Japan), Minoru Kumano (University of Miyazaki, Japan), Takao Ito (Hiroshima University, Japan), Masaharu Hirota (Okayama University of Science, Japan)

In response to the constant increase in population and tourism worldwide, there is a need for the development of cross-language market research tools that are more cost and time effective than surveys or interviews. In order to address the issue, we extracted the most influential keywords in emotional judgement from Chinese online reviews. Using an entropy based mathematical model and SVM, we determined the words that most closely represent the demands and emotions of this customer base. Classifying these words further as grammatical or subject words, we analyzed both the tendencies in writing online reviews for this customer base and their specific topics of interest.

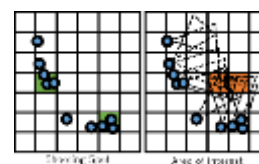
Keywords for review

The Subjects		The Reviews	
In Reply	In Progress	Answered	Unanswered
Quality	Service	Answer quickly	Don't reply
Quality	Service	Answer quickly	Don't reply
Customer service	Service quality	Answer quickly	Don't reply

OS5-4 An Approach to Visualize Place of Interest and Shooting Spot Using Geo-Tagged Photographs

Masaharu Hirota (Okayama University of Science, Japan), Masaki Endo (Polytechnic University, Japan), Hiroshi Ishikawa (Tokyo Metropolitan University, Japan)

In this paper, we extract shooting spots and area of interests using geo-tagged photographs from social media sites. Shooting spot is one of a type of hotspot in an area where many photographs have been taken. Also, area of interest is usually attractive as a tourist spot for many people (e.g., Colosseum, Statue of Liberty). These area is useful to analyze tourism industry. We demonstrate our approach by extracting areas of interest and shooting spot using photographs annotated with metadata from Flickr.



OS6 Kansei Engineering and Applications (4)

OS6-1 Histogram Analysis Method Based on Gaussian Distribution and Curvature Computation (I) ---- Peaks and Valleys Detection ----

Yusuke Kawakami*, Tetsuo Hattori**, Yoshiro Imai**, Kazuaki Ando**,
Yo Horikawa**, R. P. C. Janaka Rajapakse***
(*DynaxT Co., Ltd., Japan), (**Kagawa University, Japan)
(***Tainan National University of the Arts, Taiwan)

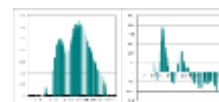
This paper presents an analysis method of image histogram using curvature computation based on Gaussian distribution. By the image histogram and curvature computing over the cumulative histogram, we can not only detect the peaks and valleys in the image histogram, but also obtain the accompanying information on the peaks and valleys such as those shapes and sizes. In this paper, we propose the information extraction method from image histogram using the curvature computation, based on the assumption that the peaks and valleys are approximated by the same number of Gauss density functions.



OS6-2 Histogram Analysis Method Based on Gaussian Distribution and Curvature Computation (II) ---- Experimentation ----

Yusuke Kawakami*, Tetsuo Hattori**, Yoshiro Imai**, Kazuaki Ando**,
Yo Horikawa**, R. P. C. Janaka Rajapakse***
(*DynaxT Co., Ltd., Japan), (**Kagawa University, Japan)
(***Tainan National University of the Arts, Taiwan)

This paper presents an analysis method of image histogram using curvature computation based on Gaussian distribution. By the image histogram and curvature computing over the cumulative histogram, we can not only detect the peaks and valleys in the image histogram, but also obtain the accompanying information on the peaks and valleys such as those shapes and sizes. In this paper, we expose the experimental results and show the effectiveness of the proposed method.



OS6-3 Experimental Evaluation of Change Detection Ability in New Sequential Probability Ratio

Yoshihide Koyama^{*1}, Tetsuo Hattori^{*1}, Yoshiro Imai^{*1}, Yo Horikawa^{*1}, Yusuke Kawakami^{*2},
Hiromichi Kawano^{*3}, Takeshi Tanaka^{*4} (^{*1}Kagawa University, ^{*2}DynaxT Co., Ltd.,
^{*3}NTT advanced technology Co., Ltd, ^{*4}Hiroshima Institute of Technology, Japan)

Previously, we have already proposed a novel method using New Sequential Probability Ratio (NSPR) for the structural change detection problem of ongoing time series data instead of using SPRT (Sequential Probability Ratio Test). And in the previous paper, we have revealed the experimental results by applying the both methods, i.e., NSPR and SPRT, to time series data that are generated by a multiple regression model. In this paper, we present the evaluation results of NSPR more concretely in two cases.

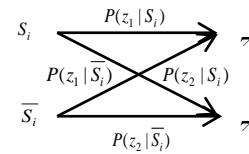


OS6-4 Application Proposal of Sequential Probability Ratio to Dynamic System

State Estimation

Tetsuo Hattori^{*1}, Yusuke Kawakami^{*2}, Yoshihide Koyama^{*1}, Yoshiro Imai^{*1}, Yo Horikawa^{*1}, Hiromichi Kawano^{*3}, Takeshi Tanaka^{*4} (*¹Kagawa University, ^{*2}DynaxT Co., Ltd., ^{*3}NTT advanced technology Co., Ltd, ^{*4}Hiroshima Institute of Technology, Japan)

Previously, we have already presented a relation between the SPRT (Sequential Probability Ratio Test) based on two hypotheses (i.e. Null hypothesis and Alternative hypothesis) and a binary channel in information theory. And we have shown that the Bayes' updating process for obtaining a posteriori probability by the received signal through binary channel is very similar to the SPRT computing. In this paper, extending the definition of SPRT to the multi hypotheses condition, we propose to apply the extended SPRT to the internal state estimation of dynamic system.

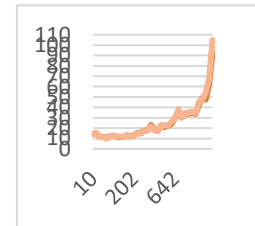


OS7 Mobile Robotics (8)

OS7-1 An Empirical Evaluation of Grid-based Path Planning Algorithms on Widely Used in Robotics Raspberry Pi Platform

Anton Andreychuk, Andrey Bokovoy (RUDN University, Russian Academy of Sciences, Russia) Konstantin Yakovlev (Russian Academy of Sciences, Higher School of Economics, Russia)

We compare three widely used grid-based path planning algorithms, A*, Jump Point Search, Theta*, in terms of runtime performance on a desktop personal computer and on the Raspberry Pi 2 embedded computer widely used in modern robotics. We also evaluate the performance of recently introduced angle-constrained path planning algorithm, LIAN, on both computers. Two principal questions are targeted. First: to what extent modern embedded computers are slower than conventional desktops when solving path finding problems on grids. The answer is – one order of magnitude. Second: how well the former scale up to larger problems. The answer is – in the same way as desktop PCs. To provide a fair comparison all the algorithms are coded from scratch using the same data structures and programming techniques.



OS7-2 Development of the insectoid walking robot with inertial navigation system

Vitaly Egunov, Andrey Kachalov, Michail Petrosyan, Pavel Tarasov, Elena Yankina (Volgograd State Technical University, Russia)

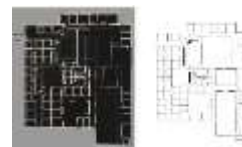
The article is devoted to the problem of managing the walking insectoid robot - hexapod. The developed robot uses an inertial navigation system based on accelerometer ADXL345 and gyroscope ITG-3200. Options for filtering data received from the inertial sensors, the methods of combining accelerometer and gyroscope data for determining the roll and pitch are considered. To visualize the position of the mobile robot the original software was designed. The program was developed for a microcomputer that transmits the calculated total variance (roll and pitch) over a wireless Wi-Fi network to the personal computer running program that processes data values. The obtained data is processed and used to display the object with the help of the OpenGL library.



OS7-3 Enhancing semi-dense monocular vSLAM used for multi-rotor UAV navigation in indoor environment by fusing IMU data

Andrey Bokovoy (Russian Academy of Sciences, RUDN University, Russia)
Konstantin Yakovlev (Russian Academy of Sciences, Higher School of Economics, Russia)

We propose the enhancement of the modern vision-based monocular simultaneous localization and mapping (vSLAM) method, e.g. LSD-SLAM, used for compact multi-rotor UAV indoor navigation, by fusing inertial measurement unit (IMU) data with camera images. We suggest removing the cost-expensive loop-closure optimization algorithm from the vSLAM pipeline and replacing it with the computationally efficient flow estimation procedure based purely on IMU data. The input IMU flow is being processed by the Extended Kalman Filter based techniques for localization purposes and used further in LSD-SLAM algorithm for UAV pose estimation. We evaluate the proposed algorithm using the modeled indoor environment originally used for RoboCup Rescue Simulation League 2013 competition and “hector_quadrotor” – commonly used in modelling simulated UAV model. Evidently, implementation of the suggested enhancement procedure results in significant drop-down of the runtime and leads to obtaining maps and trajectories of higher accuracy.



OS7-4 Method of finding the android program motion for the ZMP trajectory of a certain type

Alexander Gorobtsov, Pavel Tarasov, Andrey Skorikov, Alexey Markov, Andrey Andreev
(Volgograd State Technical University, Russia)

The problem of finding the program motion of biped robot with a given ZMP trajectory is considered. It is assumed that this provides a stable ZMP trajectory of the robot motion. The equations of the robot motion consist of the equations of the robot dynamic itself and the stability conditions equations, which include the coordinates of the ZMP trajectory. It is proposed to seek the solution of stability equations on a limited set of some concerted movements of the robot. Several types of such concerted movements are considered. The application of this method for the android with a mass of 60 kg and height of 160 cm is described. To implement the method the original multibody system dynamics modeling software (MBS software) is used. The computational aspects of the method and approaches to speed-up computations are considered.



OS7-5 Path Planning for Indoor Partially Unknown Environment Exploration and Mapping

Aufar Zakiev¹, Roman Lavrenov¹, Vadim Indelman², Evgeni Magid¹
(¹Kazan Federal University, Russia)
(²Technion-Israel Institute of Technology, Israel)

This paper addresses a problem of partially unknown environment exploration and mapping. The proposed path planning algorithm provides global and local goals search taking into account limited sensing range and visibility constraints that arise from obstacles. Looking for local goals near a global path maximizes robot utility and helps avoiding returns to regions with low potential gain. All stages were tested in ROS/Gazebo simulations and results were compared with a naive algorithm that was proposed earlier.



OS7-6 Simulation of service robot swarm behavior

Alexei Lushnikov¹, Vlada Kugurakova¹, Timur Satdarov², Arthur Nizamutdinov¹
(¹Higher School of ITIS, Kazan Federal University, Russia, ²KUKA Robotics, Russia)

In this paper, we present an implementation 3D simulation of a swarm of intelligent service robots in Unity3D. Swarm's task and purpose is clean-up of an assigned area. We compared and analyzed different possible algorithms of such swarm's behavior. Implementation includes prevention of collision between robots themselves and humans that walk through their area of effect and can be expanded to any other obstacle, moving or stationary. The implementation is suitable for serving as a basis for future real-life construction of a service robot swarm.



OS7-7 Smart Spline-Based Robot Navigation on Several Homotopies: Guaranteed Avoidance of Potential Function Local Minima

Roman Lavrenov (Kazan Federal University, Russia)

Potential function based methods provide powerful solutions in tasks of local and global path planning. They are characterized implementation simplicity, but suffer from navigation function local minima. In this paper we propose a modification of our original spline-based planning algorithm. Voronoi-based approach provides a good initial path as first iteration. A new safety criterion is integrated into path planning to guarantee path safety. The modified algorithm was implemented in Matlab environment and demonstrated significant advantages over the original algorithm.



OS7-8 Virtual Experimental Stand for Automated Fiducial Marker Comparison in Gazebo Environment

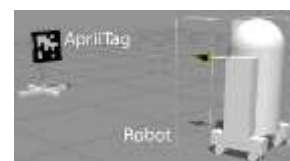
Ksenia Shabalina¹, Artur Sagitov¹, Hongbing Li², Edgar A. Martinez-Garcia³, Evgeni Magid¹

(¹Kazan Federal University, Russia)

(²Shanghai Jiao Tong University, China)

(³Universidad Autónoma de Ciudad Juárez, Mexico)

Fiducial marker systems are used by multiple visual applications, including robotics, augmented reality, industrial production, good packaging and dispensing, and all these applications require certain quality assurance for markers. In this paper, we present an experimental automated approach for fiducial marker systems comparison in virtual environment. Previously, in a set of pilot experiments, we had compared ARTag, AprilTag, CALTag marker systems under three types of conditions: systematic occlusion, arbitrary overlap with an object and marker rotation. In effort to statistically improve our previous work, we faced a necessity to conduct over a thousand of additional experiments and, as such amount of experiments is impossible to perform manually, we constructed a virtual robot in Gazebo environment that performs all necessary manipulations. This paper overviews our environment and automated comparison algorithm. Further, we will introduce Gaussian noise in order to bring our virtual experiments closer to real world conditions.



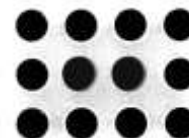
OS8 Intelligence Control Systems and Applications (11)

OS8-1 An Automated Optical Inspection system for a tube inner circumference state identification

Chung-Wen Hung, Jhen-Gu Jiang, Hsien-Huang P. Wu, Wei-Lung Mao

(National Yunlin University of Science & Technology, Taiwan)

An Automated Optical Inspection, AOI, system for a tube inner circumference state identification is proposed. In order to improve the efficiency of the traditional chopsticks industry in the process, the AOI system is developed. In the chopsticks production line, this AOI system is installed after the material feed equipment to complete the screening to reduce the unnecessary cost of expenditure. Chopsticks tube states identification base on the machine vision software –MVTec HALCON, and it will be implemented with EmguCV library. The different algorithms of image processing are used to sort the material into five groups: “Normal”, “Large”, “Small”, “deformation” and “empty”. The algorithm will be detailed in this paper, and the experimental results will also be shown in this paper to present the proposed AOI system is workable.



OS8-2 Implementation of the Mobile Based Robot Arm for Image Recognition

Ji-Hua Li, Jr-Hung Guo, Kuo-Lan Su
(National Yunlin University of Science & Technology, Taiwan)

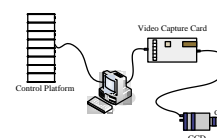
The paper develops a mobile based robot arm using KNRm system. The mobile based robot arm contains two parts : One is mobile platform: The other is a four-joint robot arm. The core of the KNRm system uses the NI Single-Board RIO 9606 module that is manufactured by National Instruments (NI) Company. The structure of the mobile based robot arm is built by Matrix element. The mobile based robot arm integrates some sensors, three DC servomotor motors, four RC servomotors, a controller, and an image processing module. Trapezoidal acceleration and deceleration algorithm and Proportional-Integral-Derivative (PID) algorithm are used to control each DC servomotor. The mobile platform embeds a robot arm with four degrees of freedom on the front side. The driver device of the robot arm is RC servomotor. In the experimental results, the mobile based robot arm can search and recognize the assigned billiard ball using image binarization method and Otsu algorithm by the image system. Finally, the robot arm moves approach to the assigned color ball, and catches the ball moving to the assigned position, and puts down the ball.



OS8-3 Reinforced Quantum-behaved Particle Swarm Optimization Based Neural Networks for Image Inspection

Li-Chun Lai, Chia-Nan Ko (Nan Kai University of Technology, Taiwan)

The paper combines the niche particle concept, quantum-behaved particle swarm optimization (QPSO) method with chaotic mutation to train neural networks for image inspection. When constructing the reinforced quantum-behaved particle swarm (RQPSO) to train neural networks (RQPSONNs) for image inspection, first, image clustering is adopted to capture feasible information. Then the database of image can be built. In this research, the use of support vector regression (SVR) method determines the initial architecture of the neural networks. After initialization, the neural network architecture can be optimized by RQPSO. Then the optimal neural networks can perform image inspection. In this paper, the program of RQPSONNs for image inspection will be built. The values of root mean square error (RMSE) and peak signal to noise ratio (PSNR) are calculated to evaluate the efficiency of the RQPSONNs. Moreover, the experiment results will verify the usability of the proposed RQPSONNs for inspecting image. This research can be used in industrial automation to improve product quality and production efficiency.



OS8-4 Development of IoT Module with Backup and Data-security Functions

Jr-Hung Guo, Kuo-Hsien Hsia, Kuo-Lan Su
(National Yunlin University of Science & Technology, Taiwan)

Internet of Things (IoT) is one of the most popular research topics. There have been many studies and products about this topic. However, there is few researches about the correctness of data and the mutual support of modules. In this paper, we developed an IoT module with multi-sensor and communication interface. It debugs and confirms the data from multiple modules and sensors using the fusion and the redundant algorithms. It can also sustain or replace a possibly fail IoT module via multiple communication interface. The dynamic identification technology is used to ensure the security of data transmission. Hence the IoT system can be more stable and more secure. In this paper, the program of RQPSONNs for image inspection will be built. The values of root mean square error (RMSE) and peak signal to noise ratio (PSNR) are calculated to evaluate the efficiency of the RQPSONNs. Moreover, the experiment results will verify the usability of the proposed RQPSONNs for inspecting image. This research can be used in industrial automation to improve product quality and production efficiency.



OS8-5 Development of Auto-Stacking Warehouse Truck

Kuo-Hsien Hsia, Ming-Guang Wu, Jun-Nong Lin, Hong-Jie Zhong, and Zh-Yao Zhuang
(Far East University, Taiwan)

Warehouse automation is a very important issue for the promotion of traditional industries. For the production of larger and stackable products, it is usually necessary to operate the stacker for the stacking and storage of the products. The general autonomous warehouse-truck does not have the ability of stacking objects. In this paper, we develop a prototype of auto-stacking warehouse-truck that can work without direct operation by a skill person. Just commanded with an RFID card, the stacker truck can move under the prior-planned route, and pick and deliver the product from the designated storage area or deliver and put the product to the designated storage area in the warehouse. It can significantly reduce the manpower requirements of the skilled-person of fork lift technician and improve the safety of the warehousing area.



OS8-6 Development of Four-axis SCARA Robotic Arm Built on Automation Control System

Jr-Hung Guo, Kuang-Wei Chuang, Kuo-Lan Su
(National Yunlin University of Science & Technology, Taiwan)

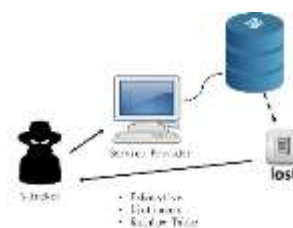
The paper presents a integral design method to integrate “DFM” (Design for Manufacturing) and “DFV” (Design for Verification), and completes the production system from simulation to actual verification using the SCARA robot arm. In the aspect of kinematics of horizontal joint, the 2D model is established by mathematical derivation and the analysis of the robot arm characteristics using “Jacobian” kinematic, and integrates into the verification design. The electromechanical integration of the proposed system is combined SCARA’s characteristics, automatic control components, sensors; electrical, pneumatic circuit design and software programming for implement. Then user can lead the robotic arm to run the coordinates and movement path with proper accuracy, efficiency and reliability. The program language of the SCARA uses “DRL” (DELTA Robot Language) that is developed by DELTA Company. This research also proposes a design method using automatic palletizing simulate layout for the SCARA robot arm, and uses the framework of “IoT” (Internet of Things) to build the near-end and remove applications via LAN and WLAN (WiFi).



OS8-7 Novel Detection Scheme for Stolen Password File

I-Hsien Liu, Chia-Hsiu Chen, Jung-Shian Li (National Cheng Kung University, Taiwan)

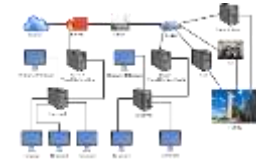
Over the past decades, with the popularity of personal computers and mobile devices, the convenience of the Internet, and the development of social networks, more and more people rely on the Internet to deal with or share things on life, such as online payment, online shopping, etc. All of the above are need to use the user authentication to achieve identity confirmation in order to use the appropriate application. The evolution of the password so far has developed a variety of forms to achieve certification. For example, fingerprints, sound waves, retina and so on. However, the traditional digital password authentication credential is still widely accepted by the public, but in the past few decades, the content of this certification mechanism hasn’t been much change. The use of traditional password is the most common and important authentication credential for today's online society. However, with the fast development of network technology and easily memorized and guessed password with low strength, password cracking events frequently occur. Consequently, the password files are leaked. The events are not easily to be detected and it results in great business losses. How to avoid password cracking and detect the event of stolen password file has become an important information security issues. Recently, Juels and Rivest published a paper about Honeyword system using one account with multiple passwords for detection of illegal intrusions. Our research explores the relevant password cracking technology and password-related policy. Accordingly, our research improves the Honeyword system proposing a new password storage mapping method. If the password file is stolen, an attacker could not know any user’s correct password. This method can reduce additional space of storing passwords with ability to detect security event for stolen password files. We apply our method to the latest version of OpenLDAP Server to prove its feasibility.



OS8-8 Honeypot System of SCADA Security Survey

Kuan-Chu Lu, I-Hsien Liu, Jung-Shian Li (National Cheng Kung University, Taiwan)

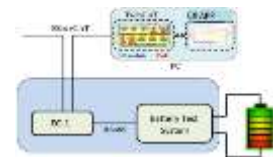
Now the essential infrastructure is used SCADA system monitoring, like nuclear plants, Water Conservancy Bureau, manufacturing, and logistics industry. With the rapid development of the internet, now the IOT (internet of things) turn every massive infrastructure from the closed network into the open way made the whole system became more convenient. by contrast, the system will face the threat never before, that is why the whole system needs to build a safe and protected mechanism through remote control for prevented the external attack, to avoid SCADA system crashed lead to international security and economy issue. For protecting the important assets, we need to understand the tools can preserve system safety to prevent the attackers invade the SCADA system. This study investigating the defense mechanism of the SCADA system and proposed an effective defensive structure to protected the safety of SCADA system.



OS8-9 An EtherCAT Battery Test System

Chung-Wen Hung , Bo-Min Wang, Wen-Ting Hsu, Jhen-Gu Jiang
(National Yunlin University of Science & Technology, Taiwan)

A battery test system is a key equipment to ensure lifetime of batteries and portable device performance. On the other hand, because of the real time requirement in industry 4.0, EtherCAT communication is considered a standard interface of industry 4.0. It is based on the Ethernet hardware, and its advantages are larger transmission bandwidth, shorter update time, and on minimum synchronization time jitter. In order to support EtherCAT communication function for battery test systems, this paper purposed an EtherCAT interface for an original battery test system. The TwinCAT environment developed by Beckhoff is adopted to be the EtherCAT interface Master, and Renesas's EC-1 evaluation board is used as the EtherCAT interface slave controller. The commands are sent to the battery test system through the RS485 interface and Modbus protocol from the EC-1 board. Finally, a C# software is proposed to provide friendly GUI interface for user.



OS8-10 Surface Defect Detection for Tube Object Based on Single Camera

Hsien-Huang Wu, Chang-Jhu He (National Yunlin University of Science & Technology, Taiwan)

Extrusion tube is a very popular product in the plastic industry produced by a extruder machine, for example, tubes used in washer machine or in reverse osmosis (RO) water purification system. To guarantee the quality of the tube produced for medical use, a surface defect detection system is needed. In this paper, we use a single camera combined with a telecentric lens and properly designed mirror set to achieve the complete coverage of the object surface for full defect detection. Based on the properly designed image acquisition equipment and image analysis techniques, the final system for extrusion tube defect detection can successfully detect defects of black spots, bumps, injury, etc., with a defect detection rate of about 95%, and the detection speed is up to 1578 mm/s, which can be deployed for the online usage.



OS8-11 Client Searching Privacy Protection in Encrypted Database

Hsien Liu, Chuan-Gang Liu, Cheng-Jui Chang, Jung-Shian Li
(National Cheng Kung University, Taiwan)

In recent years, Cloud Storage Providers (CSP) works hard to successfully achieve cheap cloud storage. To prevent losing important data in their own device, some of the people backup their data to the cloud. It becomes much more important for securing the data stored in the cloud. Although CSP claims that storage service is much more secure than before, malicious attackers invade the servers continuously. To prevent data in cloud stolen by the hackers, searchable encryption can be an useful tool. The key point of searchable encryption can relax the assumption that CSP is always truthful. Data owner can authorize users how to search and extract his files accordingly. Our proposed scheme, called SESD (Searchable Encryption Support Dynamic), provides multi-keyword based searchable encryption method for the semi-trusted cloud simulations, we observed the behaviors of the user searching in the encrypted cloud server. Secondly, the scheme employs a more dynamic way on cloud storage. By verification in the cloud data service, we found the proposed scheme effective in searchable encryption.

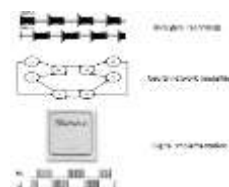


OS9 Theory and Implementation of Neuromimetic Systems

OS9-1 Study of real-time biomimetic CPG on FPGA: behavior and evolution

Timothée Levi^{1,2}, Kazuyuki. Aihara¹, Takashi Kohno¹
(¹The University of Tokyo, Japan, ²University of Bordeaux, France)

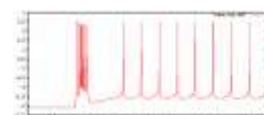
Locomotion is one of the most basic abilities in animals. Neurobiologists have established that locomotion results from the activity of half-center oscillators that provides alternation of bursts. Central Pattern Generators (CPGs) are neural networks capable of producing rhythmic patterned outputs without rhythmic sensory or central input. We propose a network of several biomimetic CPGs using biomimetic neuron model and synaptic plasticity. This network is implemented on a FPGA (Field Programmable Gate Array). The network implementation architecture operates on a single computation core and in real-time. The implementation of this CPGs network is validated by comparing it with biological data of leech heartbeat neural network. From these CPGs, we study the evolution and the behavior of chains of CPGs to understand how CPG evolves over time and how single broken CPG can be fixed.



OS9-2 A Metaheuristic Approach for Parameter Fitting in Digital Spiking Sillion Neuron Model

Takuya Nanami, Takashi Kohno (The University of Tokyo, Japan)

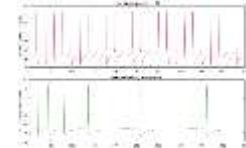
DSSN model is a qualitative neuronal model designed for efficient implementation in digital arithmetic circuit. In our previous studies, we developed automatic parameter fitting method using the differential evolution algorithm for regular and fast spiking neuron classes. In this work, we extended the method to cover low-threshold spiking and intrinsically bursting. Firstly, we optimized parameters of the fast subsystem of the DSSN model in order to reproduce that of the ionic-conductance model. Secondly, we optimized remaining slow parameters of the DSSN model that control bursting dynamics in order to reproduce that of the ionic-conductance model.



OS9-3 Real-time Digital Implementation of HH neural network on FPGA: cortical neuron simulation

Farad Khoyratee¹, Sylvain Saïghi¹, Timothée Levi^{1,2}
(¹University of Bordeaux, France, ²The University of Tokyo, Japan)

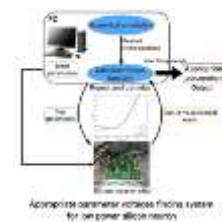
Millions of people worldwide are affected by neurological disorders. The long-term goal of replacing damaged brain areas with artificial devices also requires the development of neuronal network models. The hardware set-up that will be used to interface the biological component is a Spiking Neural Network (SNN) system. This SNN implements biologically realistic neural network models, spanning from the electrophysiological properties of one single neuron up to network plasticity rules. The most biologically relevant mathematical neuron model was proposed in 1952 by Hodgkin and Huxley (HH). Here, we propose a real-time digital implementation of hundreds biomimetic HH neurons designed by FPGA as a central processing unit and DAC (Digital to Analog Converter) as the spike generator. To validate our HH neuron, we simulate different neuron family of cortical neurons. This research will be used for neurological disease modeling and bio-hybrid experiments.



OS9-4 Finding appropriate parameter voltages for driving a low-power analog silicon neuron circuit

Atsuya Tange, Takashi Kohno (The University of Tokyo, Japan)

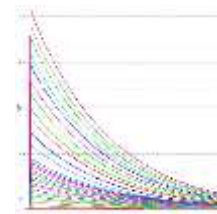
Silicon neurons are VLSI circuits that which mimic the dynamical behaviors of real neurons with electronic circuits. They are expected to be used as elements in large-scale networks of artificial biomimetic neuron circuits or bio-silico hybrid systems. We focused on a silicon neuron circuits designed by with a qualitative neuronal modeling approach for low power consumption. But tThis circuit can mimic a variety of neuronal cell classes by selecting appropriate values for its bias voltages. Its's characteristics are influenced by some factors like temperature or mismatch and secondary effects of transistors. These factors cause error between numerical simulation results in the designing stage and the characteristics of implemented circuits. Therefore we have to tune parameterthe bias voltages of individual neuron circuits to get desired dynamical behaviors after circuit implementation. We constructed the algorithm to automatically find appropriate values ofr the parameterbias voltages.



OS9-5 A low-power silicon synapse circuit with tunable reversal potential

Ashish Gautam, Takashi Kohno (The University of Tokyo, Japan)

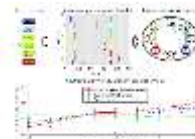
Synapses are the basic building blocks of signal processing and computation in both real and artificial simulated neuronal networks. We present the concept and simulation results of a pseudo five bit, low power silicon synapse circuit that emulates realistic postsynaptic current profiles by fitting them using the exponential current-voltage relationship of MOSFET in the sub-threshold regime of operation. Adjusting the parameters, our circuit is capable of generating both excitatory (AMPA/NMDA type) and inhibitory (GABA type) postsynaptic currents covering a wide range of time constants. Also emulating the real synapse, the post-synaptic current is proportional to the difference between the postsynaptic membrane potential and a tunable synaptic reversal potential.



OS9-6 New methodology of neural network reconstruction for "in vitro" culture on Multi Electrode Array (MEA)

Timothée Leleu¹, Timothée Levi^{1,2}, Takashi Kohno¹, Kazuyuki Aihara¹
 (1The University of Tokyo, Japan, 2University of Bordeaux, France)

The realization of neural prostheses, that could improve the quality of life for millions of people around the world affected by cognitive and/or motor disorders, requires understanding the details of the micro-connectivity between neurons in the biological tissue. Techniques for inferring the network structure are generally based on cross-correlations and result in ambiguous reconstruction. Recently, we have proposed a method for which there is one-to-one correspondence between statistical properties of packets of spikes (or avalanches) and the network structure. This method utilizes the higher order statistics of spike trains in order to reconstruct the network structure unambiguously. We show using numerical simulations of various biological neuron models that the proposed method is general, and is particularly well-fitted for the analysis of neural activity recorded from cultured neuronal networks coupled to microelectrode arrays.

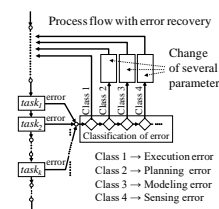


OS10 Intelligent Robotic Manufacturing (2)

OS10-1 Technique of Recovery Process and Application of AI in Error Recovery Using Task Stratification and Error Classification

Akira Nakamura^{*1}, Kazuyuki Nagata^{*1}, Kensuke Harada^{*2} and Natsuki Yamanobe^{*1}
 (*1 National Institute of Advanced Industrial Science and Technology (AIST), Japan
 *2 Osaka University, Japan)

In manipulation tasks of industrial production, plant maintenance, and housework, error recovery is an important research theme for robots. However, systematical methods of error recovery have not been appeared yet. We have proposed error recovery using the concepts of both task stratification and error classification. In the error recovery, the judgment of the error is performed in processes of the practice of the system. In this paper, the recovery process after the judgment of error is described in detail. In particular, we will explain how to change the parameters of planning, modeling and sensing when error recovery is performed. This contributes to deal with error recovery systematically. On the other hand, to experience a lot of error recoveries can accumulate the data about the recovery method. Furthermore, in this paper, we also refer to apply technique of artificial intelligence such as Deep Learning to error recovery.



OS10-2 Motion selection for 3D robotic snap assembly

Peihao Shi, Kensuke Harada, Weiwei Wan, Ixchel G. Ramirez(Osaka University, Japan)
 Juan Rojas(Guangdong University of Technology, China), Hiromu Onda(AIST, Japan)

In this paper, we aim to provide an assembly method for a snap joints assembly task. We create a 3D cellphone model and use ADAMS simulation environment to analyze the relative motion between screen and backer part. We focus on two points in this research. 1) Two kinds of relative motion between the screen and backer parts, i.e., the rotation-based and the translation-based methods, are compared, and 2) difference between assembly and disassembly is analyzed. By using the maximum elastic energy in an assembly process, we show that 1) the rotation-based assembly motion has better robustness than the translation-based assembly motion in cellphone assembly tasks when we set the same initial position error, and 2) The rotation-based assembly method is more effective for snap joint disassembly.

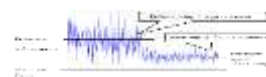


OS11 Educational Application Making Control Engineering Approach (5)

OS11-1 Control Performance Assessment Method as Assessment of Programming Learning Achievement

Yoshihiro Ohnishi (Ehime University, Japan)

It is an important problem how to estimate the learning achievement of the programming learning. However, the quantitative evaluation method according to the learning achievement is difficult. On the other hand, "work" of a control program influences the control performance of the plant by petrochemical industry, and to have an influence on the operation cost, Improvement of a program and am planning for productivity improvement are suggested by evaluating the control performance quantitatively. This research considers the using control performance assessment method for the achievement value of the programming learning.



The example of the good control result and the bad control result.

OS11-2 Practice of Control Education by Experiment using Robot

Shinichi Imai, Hideto Matsui and Akira Yamada (Tokyo Gakugei University, Japan)

For students who attend lectures in control engineering, there are not many students w1-1e many formulas. For that reason, various studies have been conducted on control education. Therefore, in this research, we propose a control education method using a robot so that interests and interests are given to students, practice lessons and verify its effectiveness.



OS11-3 Development of Support Teaching Material for Nurturing Cooperativity through Playing

Kazuo Kawada (Hiroshima University, Japan)

I have been conducted educational activities utilizing robots corresponding to each stage from kindergartens to junior high schools. In this study, I propose and verify an educational material that supports collaborative operating by experiences related to people and things. Specifically, three children have a joystick for operating the robot. The robot does not move unless you manipulate the joystick at the same time. I developed the supporting teaching material that nurture cooperativeness through play.



OS11-4 On Methods for Teaching in Training for Keeping Tempo Constant in Music

Hideyuki Tanaka and Keita Ueda (Hiroshima University, Japan)

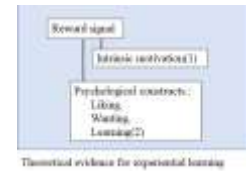
Ability of keeping rhythm is one of important factor in playing music. In this paper, the authors carry out experiments of training for keeping tempo constant in music. Experiments are carried out for experts and non-experts of music, and two methods for giving instructions are compared: The first method gives feedbacks by graphs and the other one by language. In order to ensure objectivity of the experiments, measurement data are collected by Processing, and changes of tempo etc. are analyzed by defining evaluate functions, where Scilab is used for computing the values of the evaluate functions. The experiments reveal that there are differences between experts and non-experts in giving instructions.



OS11-5 Reinforcement Learning as a Theoretical Framework for Education

Masayasu Nagamatsu, Yuki Moriguchi (Hiroshima University, Japan)

Reinforcement Learning as a computational model of human learning, has recently become the subject of intensive investigation (Barto, A.G., 2005; Vigortio, C.M., 2010). Recent findings include: neural signature of hierarchical reinforcement learning, and multiple roles of reward signals in the human brain. These findings not only provide further theoretical evidences that complementary for traditional statistical inference in educational research, but also provide framework for model based design of educational processes. Types of evidence for education, and its relation to recent findings of human reinforcement learnings are discussed.

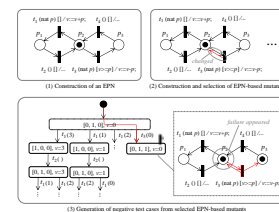


OS12 Software Development Support Method (4)

OS12-1 Negative Test Case Generation from an Extended Place/Transition Net-Based Mutants

Tomohiko Takagi¹, Tetsuro Katayama²(¹Kagawa University, ²University of Miyazaki, Japan)

EPN (Extended Place/transition Net)-based mutants are formal behavioral models of software that contain intended failures. In negative testing, well-selected EPN-based mutants are used to generate negative test cases to confirm that software does not include serious or possible failures. However, the large state space and feasibility problem on EPNs cause the difficulty of generating the negative test cases from EPN-based mutants. The aim of our research is to construct a technique in which effective negative test cases for detection of intended failures are generated from EPN-based mutants. In this technique using ant colony optimization, ants heuristically search better paths (i.e., negative test cases) to find foods (i.e., intended failures) on a field (i.e., EPN-based mutant).



OS12-2 Development of a Mutant Generation Tool Using a Genetic Algorithm for Extended Place/Transition Nets

Tomohiko Takagi, Shogo Morimoto (Kagawa University, Japan)

An EPN (Extended Place/transition Net) is used as a formal model that represents the behavior of software. When mutation testing is performed based on the EPN, failures are intentionally inserted into an original EPN (EPN that represents the expected behavior of software) in order to create mutant EPNs. A large number of higher-quality mutant EPNs are needed to expect the higher degree of accuracy for a mutation score, but the techniques to generate them have not been established. To address this problem, we construct an algorithm to generate mutant EPNs, and develop a tool to execute the algorithm. In this algorithm using a genetic algorithm, a set of mutant EPNs corresponds to a chromosome, and the fitness of each chromosome is evaluated based on an original EPN weighted by metrics.



OS12-3 Implementation of RETUSS to Ensure Traceability between Class Diagram in UML and Java Source Code in Real Time

Keisuke Mori, Tetsuro Katayama, Yoshihiro Kita†, Hisaaki Yamaba, Kentaro Aburada, Naonobu Okazaki(University of Miyazaki. †Tokyo University of Technology, Japan)

It's increasing the importance of software in society, and it's becoming more important to secure the quality of software. Ensuring the traceability of deliverables is one of effective methods to secure the quality of software. It can verify that the requirements are reflected in the programs, and close the gap between the documents and the source code. But it has two problems: taking labor and time, and causing mistakes by human handling. This paper has implemented RETUSS (Real-time Ensure Traceability between UML and Source-code System) in order to solve the above two problems. RETUSS can ensure the traceability between Class diagram in UML and Java source code in real time.



OS12-4 Prototype of a Tool to Detect Specific Comments

Satoshi Tanoue, Tetsuro Katayama Yoshihiro Kita†, Hisaaki Yamaba, Kentaro Aburada, Naonobu Okazaki(University of Miyazaki, †Tokyo University of Technology, Japan)

This paper has developed a prototype of a tool to detect specific comments. With the prototype, you can use regular expressions, describe patterns of detected strings in a configuration file, and then detect a specific comment. Even when other comments to be newly detected appears, it can flexibly be coped with by adding the pattern of the detected strings to the configuration file. The prototype was applied to projects with 5,000 LOC (Lines of Code) or more, and examined the precision and recall rate. As a result, the recall rate achieved 100% and the precision rate achieved 80%. By using the prototype, it is possible to detect comments which express tasks remaining in the source code and improper comments presented in the source code. Reducing their comments can improve understandability of the source code.



OS13 Human Interface and Artificial Intelligence (5)

OS13-1 A Recipe Decision Support System with Recognition Ability Recoding Function Using Knowledge Information and Agent

Keita Saito, Taro Asada, Yasunari Yoshitomi, Ryota Kato, and Masayoshi Tabuse (Kyoto Prefectural University, Japan)

We have developed a system for recipe recommendation with recognition ability recoding function using collaborative filtering and impression words. As a human interface, we have adopted an agent named as MMDAgent. In the proposed system, the first half recommendation process using collaborative filtering and the second half recommendation process using impression words of our previously proposed system are modified for recording the recognition ability of an elderly person as a user. The agent asks some questions to the user for finding out the initial decay on his/her recognition ability at the appropriate timings.



OS13-2 A System for Analyzing Facial Expression and Verbal Response of a Person while Answering Interview Questions by Agent

Taro Asada¹, Daichi Kogi², Ryouichi Shimada³, Yasunari Yoshitomi¹, and Masayoshi Tabuse¹
(¹ Kyoto Prefectural University, ² S.Ten Nines Kyoto Co.,Ltd., ³ JFE Systems, Inc., Japan)

We have developed a system for analyzing facial expressions of a person while answering interview questions by agent. The image signal input from web camera while answering questions is analyzed by our real-time system. Moreover, the fundamental frequencies and the time to utterance of the answerer just after an interview question is terminated are measured for estimating the mental state of the answerer. In our previously developed system for analyzing facial expression of a person while speaking with another person, facial expression intensity could be affected by (1) a conversation topic, (2) a partner and (3) the facial expression of the partner. In this research, all of (1), (2) and (3) are fixed by using an agent's interview. The experimental result suggests the usability of this system for an interview where the facial expression and the verbal response are important factors.



OS13-3 Facial Expression Analysis and its Visualization While Writing Messages

Yasunari Yoshitomi¹, Taro Asada¹, Kenta Mori², Ryoichi Shimada³, Yuiko Yano¹, and Masayoshi Tabuse¹
(¹ Kyoto Prefectural University, ² Neyagawa City Hall, ³ JFE Systems, Inc., Japan)

We have developed a real-time system for analysis of facial expressions and its visualization. The image signal input from web camera is analyzed by our real-time system using image processing software (OpenCV) and the previously proposed feature parameter (facial expression intensity). Our real-time system draws the graph expressing the facial expression intensity change using OpenCV. We applied the system for expressing emotion as a pictograph based on the facial expression intensity in writing messages. The experimental result suggests that our system can be useful for expressing emotion in writing messages.



OS13-4 Recognition of Finger Spelling from Color Images Using Deep Learning

Yusuke Yamaguchi, Masayoshi Tabuse (Kyoto Prefectural University, Japan)

We have developed a system to recognize finger spelling in Japanese sign language using deep neural networks. As deep neural networks, we adopt Faster R-CNN. By defining an output class for each finger letter and learning the object detection network, it is possible to output where the finger letter exists in the input image. This method does not require depth cameras, magnetic sensors, or other special equipment when used. Furthermore, this does not require preprocessing that extracts the hand region using human skin colored regions and color gloves used in other methods using color images. We synthesized a training data set by processing images taken with Kinect. As the test data, we input images of performing finger letters into the trained network and check the score of the output area and class.



OS13-5 Recognition of Texting While Walking Using Convolutional Neural Networks

Junpei Miyachi, Masayoshi Tabuse (Kyoto Prefectural University, Japan)

The number of people who operate a smartphone while walking increases with the spread of smartphones. Pedestrians who are texting while walking decrease attention to their surrounding environment. This is the cause of falling from station's platform or bumping into someone in public areas such as railway stations. The purpose of this study is to detect pedestrians who operate a smartphone using surveillance camera for the support of accident preventions in railways. The pedestrians have the same features of posture such as hand position and facial direction. In order to recognize the posture, we employ convolutional neural networks (CNN), which has improved results in various fields in recent years. In this paper, we propose the method of the texting while walking recognition using CNN. We show the classification results of a pedestrian who is texting while walking.



OS14 Advanced Technology on Sensing Technology, Devices, Application (6) OS14-1 A Study on the Lumbar Burden Evaluation of Work using One Smartphone

Mizuki Maiguma, Hiroki Tamura, Koichi Tanno (University of Miyazaki, Japan)

In this paper, we propose the human lumbar burden evaluation method and state estimation system using smartphone and it is application to agricultural work. The proposed system consists of two functions, 1) "State estimation" has a function of estimating posture (Stand up, Sit down, Crouch, Walk, etc.) of the subject. 2) "Lumbar burden estimation" has a function to estimate the angle of waist from the angle of the subject's upper body and calculate the lumbar burden in combination with other parameters. The aim of this paper is to get the data of the subject's work status in the agricultural field in simple manner and quasi-real time and help improve the agricultural work efficiency by constructing the agricultural work burden evaluation system using smartphone. In this paper, we show on the experimental results of two functions and the evaluation of the actual agricultural work.



OS14-2 A Study on High Accuracy Stride Estimation on Smartphone Combining Acceleration Sensor and Gyro Sensor

Shunta Nonaka, Hiroki Tamura, Koichi Tanno (University of Miyazaki, Japan)

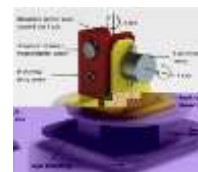
The stride is an important parameter in human motion analysis and has been extensively studied by many researchers. This paper focuses on smartphones that are popular in the world, regardless of the measurement environment. In previous research, the stride estimation using the acceleration sensor or the gyro sensor mounted on the smartphone had been studied. However, the estimation accuracy of stride has an error rate of about over 10 %. In this paper, we propose a highly accurate stride estimation method using stride correction parameter obtained from cross section movement in addition to conventional sagittal surface stride using acceleration sensor and gyro sensor mounted on smartphone. From the results, the error rate of our proposed method with the stride estimated by kinect sensor (RGB-D sensor) as the true value was about 6%, making it possible to estimate the stride with high accuracy.



OS14-3 Development of Multi-Sensory Smart Objects Tracking Module for Mobile Robot Platforms

B. A. D. J. C. K. Basnayake, Y.W.R.Amarasinghe (University of Moratuwa, Sri Lanka)

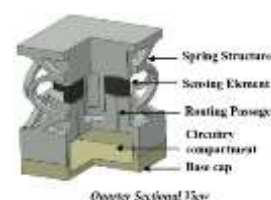
In the mobile robot systems, the ability to navigate in its environment is important. Often, the surrounding environment is dynamic and unknown. Object tracking is a sensing system employed with most of the robotics navigation systems. These sensors can provide real-time information related to the obstacles and target detections. Living object identification and positioning are difficult compared with stationary obstacles identification, because of their behaviors. But it is important for robotic platforms which operate in living premises in order to perform collision-free navigation and localization features. Therefore, we have developed infrared thermal image based smart living object tracking system which capable of detecting and positioning movable and stationary living object in a certain range. The system mainly consists of non contact thermal array sensor and sonar sensor that mounted in the 2-axes rotatable platform. These sensors capture the surface temperature, directions to the heated objects and related distance and later the captured information is analyzed by the filtering and detection algorithms. Based on the above information, the system will generate real-time point cloud related to the living objects and fix-obstacles placed in the environment. Developed system will use in navigation, human following and obstacles avoiding applications in mobile robot systems.



OS14-4 Design and Development of a Conductive Polymer Based 3D – Printed Tactile Sensor with Square Type Spring Structure

W.H.P. Sampath, A.H.T.E. De Silva, Y.W.R. Amarasinghe (University of Moratuwa, Sri Lanka)

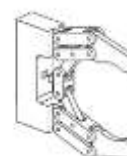
Industrial Robot Manipulators used in the industry lacks force sensory feedback relating to the force exerted on the grabbing object by the artificial manipulator. In most of the manipulators, the degree of controlling and handling only done by identifying the presence and position of objects using optical proximity sensors. However, it is possible to enhance the controlling of the artificial arm by introducing a force sensory feedback unit. In this research, design, development and testing of a force feedback system were discussed using a novel conductive polymer based 2x2 sensing element array incorporated to a novel 3D printed square type spring structure to provide the user with closed-loop controlling. Arch was featured by a combination of two – two-point splines where the gradient of starting and end points are zero. The incorporated conductive polymer is a silicone rubber based polymer which has enhancements by silica and carbon black, with Silane as the coupling agent. The spring structure stated in this paper has been designed for force scaling purpose and numerically analyzed using COMSOL Multiphysics prior to the fabrication to avoid mechanical failures. The inherent problems in conductive polymer piezo-resistive characteristics such as operation range deviation w.r.t. chemical composition could also be overcome by this design approach.



OS14-5 Design and Development of a Shape Memory Alloy Spring Actuated Gripper for Minimally Invasive Surgeries

Roshan T.A.U, Amarasinghe Y.W.R, Dayananda N.W.N. (University of Moratuwa, Sri Lanka)

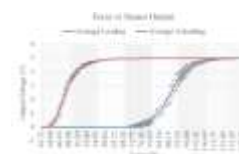
MIS is a novel and emerging surgical procedure in the medical surgery field. Miniaturization of the tools and the actuators used in MIS is important. The properties such as high energy density, excellent biocompatibility, corrosion resistance, miniaturization capability etc. highlights the selection of SMA as the actuation material. Currently there were several studies available about SMA powered grippers, but in this study, the main intension is to preserve simplicity in the design and controlling stage. A kinematic and dynamic analysis was performed in the software based environment using MATLAB and COMSOL Multiphysics respectively. In the development stage the structural components of the gripper is made by 3D printing. The SMA spring is made out of Nitinol (55% Ti and 45% Ni) wire with 0.5 mm diameter, fixed as a spring (6 mm in Dia.) and aged in a Muffle furnace at 400 C for 15 mins. For the heating of SMA material electric current was used and joule heating was enabled the actuation. This SMA spring actuator is combined with a biasing spring which is made out of normal steel in order to achieve the required opening and closing action of the gripper jaws. Among the different biasing methods, this was the suitable design as this gripper operates on the opening mode which is the best way to avoid SMA overheating. Temperature measurement and a Gripper jaw displacement measurement was taken in order to discuss the factors influencing gripper performance. As well the tests were conducted to match the best compromise between influence of cooling method, SMA activation current, and operation frequency. The controlling was done by Pulse Width Modulation (PWM) method as it significantly reduces the energy consumption and robust to the external disturbances.



OS14-6 Design and Development of Quantum Tunneling Composite based Tactile Sensors

T.D.I. Udayanga, D.A.M.R. Fernando, H.L.P.L. Chaturanga, B.A.D.J.C.K. Basnayake, Y.W.R. Amarasinghe (University of Moratuwa, Sri Lanka)

Tactile Sensing is measuring tactile parameters with the aid of physical touch. Currently, specifically regarding the robotics and biomedical fields, research were limited by having lack of tactile feedback systems. Hence, tactile sensing has come to the spotlight of research and has developed so considerably when comparing with the past decades. Also application areas of tactile sensing has been expanded as new fields of applications has emerged recently regarding tactile sensing. In this study, a miniaturized novel enclosed tactile sensor was designed and developed using Quantum Tunneling Composite (QTC™), which is a conductive polymer composite, as the sensing element. An enclosed novel structure was proposed so that the sensing element and spring will be omitted from the environmental effects. Proposed sensor structure was analysed and manufactured. Experiments were carried out and results shows that the sensitivity of this developed tactile sensor to be 0.02 V/N and repeatability of ± 3 N.

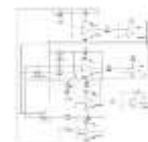


OS15 System and Control (11)

OS15-1 Analog circuit design of a novel 4D chaotic system

Hong Niu (Tianjin University of Science & Technology, China)

In this paper, a novel four-dimensional (4D) autonomous chaotic system is reviewed, and its corresponding new analog circuit is presented based on the modified module-based approach to chaotic circuit design. The chaotic phase portraits of the new circuit are given to illustrate the good qualitative agreement between the numerical simulation and the experimental realization.



OS15-2 A method of end-to-end self-understanding of Chinese paper-dictionaries

Zhijian Lyu(Beijing Institute of Science and Technology Information (BISTI), P.R.China),

Yizhun Peng (Tianjin University of Science and Technology, P.R.China)

This paper introduces a method of end-to-end self-understanding of Chinese paper-dictionaries. In this method, a page of Chinese paper-dictionaries is scanned into an electronic image. And then the electronic image is preprocessed, including un-distortion, side scrapping, binarization, and so on. Finally, using an end-to end deep learning method, the pre-processed electronic image is intelligently segmented, text recognized, and context understood. Our method has been applied to self-understand a serial of Chinese paper-dictionaries, which have more than 13000 pages and 2.1 millions of phrases. And its correct rate of self-understanding of Chinese phrases is more than 99.5%. Its performance has proved it's availability.



OS15-3 A multi-robot rescuing system

Huailin Zhao, Zheng Wu, Xiaoxing Wang (Shanghai Institute of Technology, China)

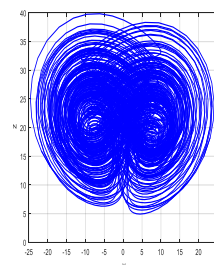
The study subject is a multi-agent system consisting of a few mobile robots. In the system, each robot collaborates with the other ones, and they all work together to complete the disaster rescuing tasks such as the fire fighting. The multi-agent system control theory is applied in the system, where each mobile robot is an independent intelligent individual. The robots communicate wirelessly among them. Even though there is trouble with the individual robots, the others will collaborate among them in time and adjust their control policy to ensure the system itself working normally and complete the disaster rescuing task. In the system, an upper computer is designed for supervising, human-machine interfacing and being the transferring station of the data exchange. The experiment shows that the multi-robot distributed control system based on WIFI, GPS and INS information is able to achieve the consistent action such as rescue gathering.



OS15-4 Dynamic analysis and FPGA implementation of A novel hyper-chaotic system with one equilibrium point

Shanfeng Wang, Hongyan Jia, Zhiqiang Guo
(Tianjin University of Science and Technology, China)

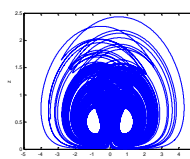
In recent decades, the study on the chaotic system and hyper-chaotic system attracts more and more interest with developing of non-linear subjects. This paper firstly presents dynamic numerical analysis of a novel hyper-chaotic system with one equilibrium, which includes the stability analysis of equilibrium point, bifurcation diagram, Lyapunov exponent and so on. Then, based on the method of converting continuous-time differential equation to discrete-time differential equation, FPGA(Field Programmable Gate Array) implementation for the novel hyper-chaotic system is finished, and the results from FPGA implementation are consistent with those from numerical analysis. The work in this paper may provide a method for the application of the hyper-chaotic system.



OS15-5 Analysis and circuit implementation for a new fractional-order chaotic system

Zhiqiang Guo, Hongyan Jia, Shanfeng Wang
(Tianjin University of Science and Technology, China)

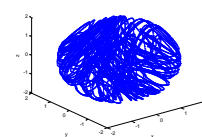
This paper firstly recommends a new fractional-order chaotic system, only including six terms and three multipliers, which is different from the Lorenz and other existing fractional-order systems. Then some numerical analyses including the phase trajectory diagrams, Lyapunov exponents diagrams and bifurcation diagrams are given to investigate the different dynamical characteristics of the chaotic system. At last, an analog circuit is designed to implement the system, further verify the effectiveness of the fractional-order chaotic system in practical application.



OS15-6 Application of a conservative chaotic system in image encryption

Shilong Liu, Mei Zhang, Wei Xue(Tianjin University of Science and Technology, China)

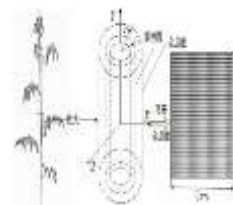
The dynamic behaviors of a new conservative system are analyzed based on its phase trajectory, Poincaré section, Lyapunov spectrum. On this basis, the conservative system is applied to digital image encryption and the security performance of the algorithm is analyzed and verified. The results show that compared with the dissipative systems, the chaotic attractor in conservative system is not apparent. The conservative system also has the characteristics of pseudo randomness and similar noise, whose safety is high, and is not easy to be cracked. Therefore, the conservative system has a quite high research value and application prospect.



OS15-7 Study of plant disease detection based on near-field acoustic holography

Jiangfan Wang, Xiuqing Wang (Tianjin University of Science & Technology, China)

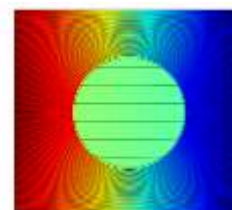
In the process of crop cultivation, pests and diseases on crop growth and development, yield and quality of the most obvious. To control pests and diseases quickly and effectively, real-time understanding of the growth of crops to the disease based on reasonable and accurate spraying of pesticides is particularly important. The key to the implementation of precision spraying is the accurate positioning of crop diseases. In this paper, the main stem of the plant was taken as the object of study. Based on the near-field acoustic holography, the sound field model of the disease was established and the three-dimensional spatial sound field was reconstructed by the algorithm to analyze the sound field of the sound source. Identify the sound source signal of the plant, locate the position of the sound source, make effective judgment on the damage status of the plant, determine the disease condition, and establish the optimal control strategy.



OS15-8 Simulation of Cell Dielectric Properties Based on COMSOL

Shudong Li, Xiaoyan Chen, Fengze Han (Tianjin University of Science & Technology, China)

The dielectric properties of single cell can be observed by injecting a low amplitude current at different frequencies (1MHz~200MHz). The simulation work is taken on the software platform named COMSOL Multiphysics. The electric field and the cell model is created with prior conductivity, the extracellular and the intracellular fluid is 1 S/m and the membrane is 1×10^{-5} S/m separately. By simulation, it's verified that at low frequencies, the region of interest (ROI) behaves the conductivity characteristic as the electrical signal cannot pass through the cell membrane due its capacitor properties. With the excitation frequency increasing, the ROI behaves more permittivity characteristic as the current flowing through the cell membrane more and the current density increases. The research of the cell dielectric property provides an auxiliary method to diagnose the status of the cell.

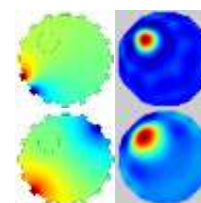


OS15-9 Research on the method of electrical impedance tomography based on conjugate gradient iterative algorithm

Yuanli Yue¹, Xiaoyan Chen², Ze Liu¹, Fengzhi Dai²

(¹ Beijing Jiaotong University, China. ² Tianjin University of Science and Technology, China)

Electrical impedance tomography is a new technology of medical imaging ,that can be used to detect the real time internal electrical impedance. This article is doing research on the method of electrical impedance tomography by using conjugate gradient iterative algorithm. Using the finite element analysis software Comsol to make a two-dimensional modeling, and make the target circular field with 16 electrodes is established. And the empty field and full field stimulation of different excitation current analysis, there are relatively adjacent to motivate and encourage .By using Matlab to make tomography reconstruction, using two different reconstruction algorithms. After the reconstruction of the graphic ,using a variety of evaluation of the graphic image reconstruction and numerical analysis, such as the use of the correlation coefficient, and the similarity relative error evaluation.

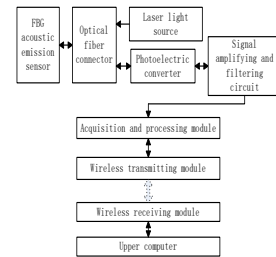


OS15-10 Research on acoustic emission wireless detection system

Xiuqing Wang¹, Yang Li², Qing Liu¹, Jiming Zhao¹

(¹ Tianjin University of Science & Technology, China;² TEXAS A and M University, U.S.A)

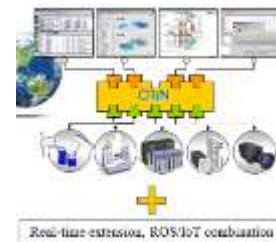
A Fiber Bragg grating (FBG) acoustic emission wireless sensing system was presented in this paper. The acoustic emission signal source was simulated by the method of breaking the automatic pencil lead core, the signals collected by the sensor were processed by photoelectric conversion, amplification, filtering and so on. The system adopted waveform feature extraction method, through wireless sensor network, characteristic values uploaded to the host computer software. A comparative experiment of piezoelectric ceramic acoustic emission sensing system and FBG acoustic emission sensing system was carried out. It can be seen from the results that the acoustic emission signal waveforms and characteristic parameters collected by the two sensing systems were different. These differences were related to the inherent structural characteristics of the sensor itself. The upper and lower surfaces of piezoelectric ceramic sensors can cause the superposition of acoustic emission signals, however, FBG acoustic emission sensor does not exist this problem. Therefore, the waveform collected by FBG sensor does not produce distortion, which is the advantage of FBG acoustic emission sensing system than piezoelectric ceramic acoustic emission sensing system in principle.



OS15-11 ORiN PAC (PC based Automation Controller)

Toshihiro Inukai (DENSO WAVE INC., Japan)

This paper introduces application examples of ORiN PAC (PC based control system utilizing ORiN as middleware). The manufacturing system is composed of huge kinds of devices, and it is necessary to make device programs for controlling these devices in cooperation. The mfg. system becomes increasingly complicated, and along with the increase in programming cost, the improvement of programing efficiency became a big issue. In this paper, we propose ORiN PAC as a solution to realize "one software architecture" applicable from small scale to large scale mfg. systems. This solution has been used in the real factories in the world (not just a demo), and it will be quite important also for realizing "Industrie 4.0" world. *ORiN: Open Resource interface for the Network*

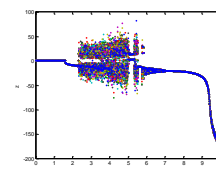


OS16 Recognition and Control (9)

OS16-1 Research on the synchronization and circuit realization of a four-wing chaotic system

Yiqiao Qin, Fengzhi Dai, Yuxing Ouyang, Qijia Kang, Ce Bian, Baochang Wei, Runhua Mao, Shengbiao Chang (Tianjin University of Science & Technology, China)

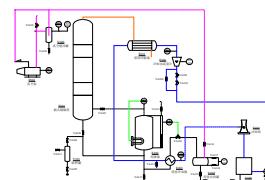
This paper introduces a three-dimensional four-wing chaotic system and the system is analyzed and circuit verified. The paper adopts two synchronous control strategies to control the three - dimensional four-wing chaotic system. One is the feedback synchronization controller based on the observer, and the other is the synchronization controller based on theory of stability. The feasibility of these two methods is proved by analyzing the numerical data and the circuit implementation. On this basis, we conducted signal encryption research. The results verify the feasibility of the synchronous design and encryption design.



OS16-2 Design of control system for reboiling part of distillation process

Lingran An, Fengzhi Dai, Yujie Yan, Yuxing Ouyang, Zhongyong Ye, Xia Jin, Baochang We
(Tianjin University of Science and Technology, China)

This paper selects the control system for re-boiling part of distillation process for major research. The control scheme is determined according to the influence of the relevant parameters on the distillation process. The hardware part uses the Siemens S7-200 series PLC as the main control machine. The lower position machine uses STEP 7-Micro / WIN programming software, and writes the control program through the ladder diagram. It combines the PID algorithm and single closed-loop control to complete the field data collection and processing and communication with the host computer. The host computer uses the configuration king named kingview6.55 monitoring system software to complete the automatic control system monitoring.



OS16-3 Research on intelligent control system based on machine vision

Ce Bian¹, Fengzhi Dai¹, Yuxing Ouyang¹, Yiqiao Qin¹, Baochang Wei¹, Runhua Mao¹, Meili Li²
(¹Tianjin University of Science and Technology, China; ² China University of Petroleum, China)

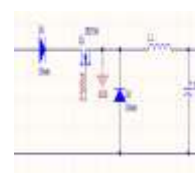
Surface Mount System is a device which function is move attachment head to make surface mount components accurately placed on the PCB pad. SMT has machine vision system and intelligent control system compose. The machine vision system through the camera to capture images of components. Then the software for image processing and camera calibration problem is one of key issue of machine vision research. Ultimately determine the component coordinate axes. The mainly function of intelligent control system is that controller drives X, Y, Z, R each axis motor to carry out the intelligent logic movement and controls the digital signal to carry on the logical response. Data exchange between Machine vision and the intelligent control part base on upper computer. On this basis, the position of the component on the PCB can be identified by the intelligent operation of machine vision.



OS16-4 Development of NC power based on Buck circuit

Yuxing Ouyang, Fengzhi Dai, Runhua Mao, Ce Bian, Baochang Wei, Yiqiao Qin, Shengbiao Chang, Qijia Kang (Tianjin University of Science and Technology, China)

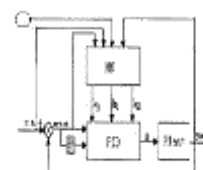
This paper develops a kind of power-supply module which uses digital control and buck circuit. The module can convert 220v alternating current into 0-30v direct current. In the aspect of circuit design, it is mainly AC- DC, DC-DC conversion circuit and SCM minimum system circuit. In the aspect of control circuit, for feedback signal of current sensor, the power-supply module can obtain average value by multiple means and remove the mutation value.



OS16-5 Simulation of PID temperature control system based on neural network

Yujie Yan, Fengzhi Dai, Lingran An, Yuxing Ouyang, Zhongyong Ye, Xia Jin, Ce Bian
(Tianjin University of Science and Technology, China)

The system designed in this paper is a combination of neural network and PID control. BP neural network has a great advantage in solving the control of nonlinear and uncertain systems. It can use the steepest descent learning method to adjust the threshold and weight values by back propagation. The ultimate goal is to adjust the PID controller adjustable parameters by the neural network learning algorithm. Using MATLAB software to simulate, the results show that the system has a strong following performance and a high anti-interference ability. Experiments show that the PID temperature control system based on neural network has some practicality.



OS16-6 Design and research of real-time material management system based on production process

Baochang Wei, Fengzhi Dai, Yuxing Ouyang, Haifang Man, Yiqiao Qin, Runhua Mao, Ce Bian
(Tianjin University of Science and Technology, China)

The paper primarily introduces the real-time material management system in the course of machinery production. This system is developed and designed using C# language and SQL2008 database, using C/S and B/S mixed mode, the C# language-related programming skill and database information together, through the C/S and B/S architecture for network communication, the database Server-related production material information sharing management system feedback to the specific user, thus enhancing the production efficiency.



OS16-7 Research on the balance control of the inverted pendulum

Zhongyong Ye, Fengzhi Dai, Yuxin Ouyang, Yujie Yan, Xia Jin, Lingran An, Hongtao Zhang
(Tianjin University of Science and Technology, China)

There are many strategies in the field of automatic control to achieve stable control of the inverted pendulum. The typical control strategy is PID control algorithm. But PID controller can only point to point control, so this paper proposes an improved strategy. This paper adopts multi-loop PID strategy to realize the stability control of inverted pendulum. Through simulation analysis, this strategy is more efficient than PID control algorithm.



OS16-8 Design of intelligent saving robot based on six-legged robot

Xinyu Zhang, Xiaokun Lin, Fengzhi Dai (Tianjin University of Science & Technology, China)

In recent years, along with the humanity to have high mobility in the complex environment, and high reliability, and easy to expand increasingly urgent demand for mobile platform, plus multi legged robot research and algorithm improvement of gait, scientists have considerable research to the application of biped multi legged robot, biped robot is in the past wheel type or track system, the motion is confined to the plane, unable to overcome many mountain disaster or rough terrain. Therefore, a rescue robot based on six legged robots came into being. This text robot can use mobile phone app to switch robot mode or remote control robot through Bluetooth or wireless mode. And the robot can switch the automatic mode and switch the automatic mode, and the robot can realize obstacle jumping through sensors to identify the types of obstacles. And the robot comes with an electronic compass, a camera and a gyroscope, which can intelligently record the path of travel and automatically return to its starting position along the source path.



OS16-9 Research on multi-object recognition algorithm based on video

Yong Hou, Runhua Mao, Yuxing Ouyang, Ce Bian, Binhu Song, Baochang Wei, Yiqiao Qin, Shengbiao Chang, Fengzhi Dai (Tianjin University of Science and Technology, China)

This paper mainly studies and improves the detection and tracking algorithm of the robot fish video and presents a background extraction method based on HSV color space. This method is more efficient than the background extraction method of RGB color space, which improves the recognition, anti-jamming ability and robustness. Through the experiment, it has a strong adaptability to external influences such as background water surface fluctuation, reflective, light change shadow.

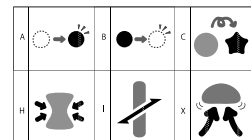


OS17 Automated content generation and cognitive content generation (7)

OS17-1 Reinventing the Flavor Wheel

Hiroki Fukushima (Kyushu Women's University, Japan)

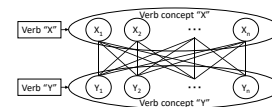
In this paper, the author proposes a new type of flavor wheels. Flavor wheel is made for the tasting professional as like sommeliers, in order to visualize the tasting words in a hierarchical way. An ordinary flavor wheel has two or three hierarchy; abstract genres (e.g. “floral”, “fruit”) are set in the inner circle, and concrete words (e.g. “jasmine”, “apple”) are set in the outer part. The hierarchical structure can be rewritten into a tree structure; hence the wheel shape needs to have its advantage in comparison to the tree structure. The author points out mainly two drawbacks of ordinal flavor wheel: 1) the whole area of the circle is evenly split by the number of the total words. And 2) the lack of the relationships among the words and genres. This paper aims to overcome these two drawbacks and propose a new type of flavor wheels.



OS17-2 Acquiring Short Scripts and Setting a Case Frame in each Acquired Script: Toward Random Story Generation

Jumpei Ono (Graduate School of Iwate Prefectural University, Japan),
Takashi Ogata (Iwate Prefectural University, Japan)

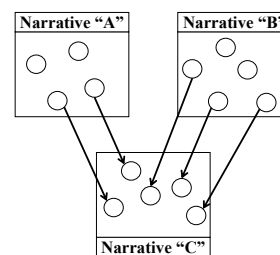
The integrated narrative generation system, that the authors have developed, generates a story to translate the story into the surface representation. In the story generation process, the INGS uses narrative knowledge that was automatically acquired from existing narrative works. This paper presents a method to acquire short scripts, which are a kind of narrative knowledge, from existing works in Aozora Bunko for the story generation. This paper presents a mechanism to generate random story-like event sequences by using 23,751,142 bi-gram scripts acquired based on the method proposed below. The authors aim to use the scripts generated by the method as a first set to be revised through the next learning process.



OS17-3 A Method of *Naimaze* of Narratives Based on Kabuki Analyses and Propp’s Move Techniques for an Automated Narrative Generation System

Takashi Ogata (Iwate Prefectural University, Japan)

Naimaze in *kabuki* has been known as a narrative creation method for combining components in existing *kabuki* works or the other genres’ narratives to make a new work. Various components, such as story, plot, character, place, are used as the components in *naimaze*. The author aims to use the *naimaze* method in an automated narrative generation system that we have been developing, namely the Integrated Narrative Generation System (INGS). In this paper, we present an approach to design the narrative techniques of *naimaze* in the INGS by applying the way for combining “move” in V. Propp’s narratological study, “morphology of folktales.” A move by Propp means a narrative macro level unit or a kind of sequence that is composed of several “functions” and he showed various ways that combine several moves to construct an entire narrative structure. This paper shows ideas of a *naimaze* techniques and the implementation of experimental programs based on various kabuki analyses and the Propp’s move method.



OS17-4 Narratology goes to Creativity ---Cognitive Content Generation

Akinori Abe (Chiba University, Japan)

In the previous studies, I discussed the creativity in IMDJ (Innovators Marketplace on Data Jacket). The Innovation Game seems a game where a new production will be obtained during the combination of various techniques, materials and previous products. Accordingly I discussed IMDJ performance from the perspective of abduction. In addition, more important matter is the effect of communication among participants which is plays a significant role in creativity. That is, for creativity, important matters are "action of a novel relational product" and "the role of interaction and collaboration with other individuals." Then I discussed the role of comfortable communication (narratology) by robots in the creative situation as well as usual situation. In this paper, I will discuss the role of narratology which is based on the cognitive content generation in the creative task.



OS17-5 A Framework for Haiku Generation from a Narrative

Takuya Ito, Takashi Ogata (Iwate Prefectural University, Japan)

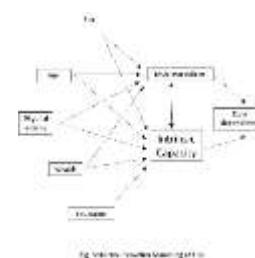
In this paper, the authors propose a framework for the mutual transformation between a narrative and haiku-like sentences. In particular, this paper shows a method for generating haiku-like sentences from a narrative fragment. The authors have been developing an integrated narrative generation system that automatically generates narratives. This paper aims to combine to this mechanism relating to haiku with the system in the future. Basic elements for generating a narrative and a haiku-like sentence are commonly the selection, arrangement, and modification of the elements. In order to generate haiku-like sentences from a narrative, the proposed method selects particular elements from a narrative and arranges them according to the form of a haiku-like sentence. Further it gives variations to the haiku-like sentence. In this paper, the authors show several forms for haiku-like sentence generation to experimentally generate haiku-like sentences from a narrative.



OS17-6 Cognitive content generation for healthy ageing

Yuki Hayashi (Chiba University, Japan)

In the previous studies, we discussed some problems in super-ageing society and how to support older people. Recently, healthy ageing has been an important concept to decrease risk of disease, care independence or any other troubles. For example, WHO has recommended healthy lifestyle to younger and middle-aged people. In addition, a concept "ME-BYO" which was originally generated in oriental medicine has been accepted around the world. Accordingly to figure out the best strategy for treating older people in Japan has been a challenging problem. However, there remains some matters, thus, how to evaluate the state of healthy and how to provide personalized approaches for healthy ageing. In this paper, we'll discuss the evaluation of healthy state and content generation for personalized approaches for healthy ageing.



OS17-7 Museum Visitors’ Behavioural Change Caused by Captions

Kotone Tadaki (Chiba University, Japan)

In museums, especially in art museum, there are several visitors only reading captions (short explanation displayed next to artwork in exhibition room) without seeing any artworks. When we regard caption as a Shikake which is aiming to make visitors see artwork, each caption already has a physical trigger. Since caption and artwork are usually displayed on the same wall so that visitors can easily see both caption and artwork in the same time. Although there are physical trigger, captions are not functioning as expected. In this paper, we try to add psychological triggers by adding some features to captions. The presence of change in how they see artwork was measured by time spent to see artworks, movement from caption to artwork, and participants’ impressions to each artworks and each captions. The result of the experiment shows museum visitor’s generation of story based on information provided by captions and artworks.

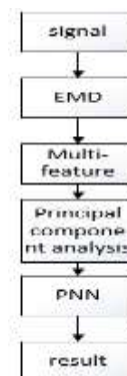


OS18 Intelligent Control (5)

OS18-1 Rolling Bearings Fault Diagnosis Method using EMD Decomposition and Probabilistic Neural Network

Caixia Gao, Tong Wu, Ziyi Fu (Henan Polytechnic University, China)

Aiming at the problem that the vibration signal of the early fault is weak, the fault information is difficult to be extracted, the accuracy of single fault feature identification is low, and the fault feature is redundant. A fault diagnosis method of rolling bearing combined with empirical mode decomposition (EMD), multi - feature parameter principal component analysis (PCA) and probabilistic neural network (PNN) is proposed. First, the EMD is used to decompose the vibration signal into the sum of several IMF components to achieve the smoothness of the non-stationary signal. Since the bearing fault information is concentrated in the high frequency band, the first five IMF vectors of high frequency are used to obtain their energy, kurtosis and skewness characteristics to form the eigenvector. Finally, the feature vector group is de-redundant by principal component analysis, and it is put into PNN for fault recognition. The simulation results are compared with the intrinsic mode energy method of EMD. It is concluded that EMD-based multi-feature parameter principal component analysis has higher accuracy. At the same time, the relationship between the number of principal components of the method and the correctness of diagnosis is analyzed.



Troubleshooting flowchart

OS18-2 Detection of Dangerous Driving Behavior via Fuzzy Inference System

Shangzheng Liu¹, Qinghui Zhu¹, Fuzhong Wang²

(¹Nanyang Institute of Technology, P.R. China, ²Henan Polytechnic University, P.R. China)

Aiming at identifying fatigue driving and drink driving, a new detection scheme for the analysis of dangerous driving behavior was proposed in this paper. First, three eye movement characteristics, average number of saccade, average fixation duration, and fixation counts. Second, membership functions and fuzzy inference system (FIS) were established. Finally, fatigue driving and drink driving were identified by the proposed FIS. In the Matlab/Simulink simulation environment, the simulation system was built. The simulation is carried out to verify the effectiveness of the proposed FIS.



OS18-3 Feature Points Designing and Matching for the Target Spacecraft in the Final Approaching Phase of Rendezvous and Docking

Wenjing Pei, Yingmin Jia (Beihang University (BUAA), China)

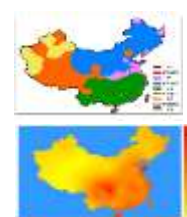
Motion information of the target spacecraft can be calculated according coordinate change of feature points based on the motion control model. In order to extract motion information including velocity, location, attitude of the target spacecraft in the final approaching phase of rendezvous and docking, feature points marking and matching for the target spacecraft is an essential step. In this paper, feature points are designed on two solar panels and the fore-end cabin in the target spacecraft by using three baselines and the feature circle methods. Thus 51 feature points can be obtained. Feature points matches are obtain by applying an improved feature points matching strategy to feature points which have been designed. Experimental results shows that running speed is improved greatly and high accuracy is maintain.



OS18-4 Construction and Visualization of Atmospheric Environment Data Map

Dongmei Fu, Gaoyuan Wang, Chao Wu, Mengchen Cui
(University of Science and Technology Beijing, China)

This paper includes two points: 1, how build the China's map of the atmospheric corrosion level, according to the ISO9223-2012 Two methods are used. One is the inverse distance weighting method, and other is the improved inverse distance weighting based on density. 2, how build the China's map of carbon steel corrosion rate, according to sparse carbon steel corrosion data. Two methods are used. One is a multi-faceted function method, and other is an improved multi-faceted function method.



OS18-5 Multiple-Model Adaptive Estimation with New Weighting Algorithm

Weicun Zhang (University of Science and Technology, China)

This paper presents a new scheme of weighted multiple-model adaptive estimation for a discrete-time stochastic dynamic system with large parameters uncertainty, in which the classical weighting algorithm is replaced by a new weighting algorithm to reduce the calculation burden and to relax the convergence conditions. Simulation results verified the effectiveness of the proposed scheme.

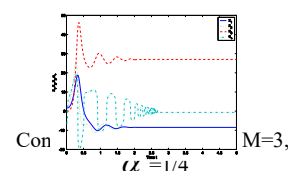


OS19 Advanced Control (5)

OS19-1 Revisit Constrained Control of Chaos

Yunzhong Song, Ziyi Fu and Fuzhong Wang (Henan Polytechnic University, P.R.China)

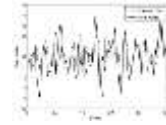
Only two conditions were considered in paper titled as constrained control of chaos in [Y.-C. Tian, M. O. Tade, and D. Levy, Physics Letters A296 (2002) 87], and thereafter a special problem was investigated and the corresponding solving strategy was provided in paper titled as some comments on constrained control of chaos appeared in [Y. Z. Song, G. Z. Zhao, and D. L. Qi, Physics Letters A359 (2006) 624], in this Letter, a soft control scheme which is chattering free dominated just by single flexible factor is suggested to improve the already existing conclusions, and simulation results indicate the validity of our project.



OS19-2 Research on Filtering for Random Data Packet Dropouts and Delays in Wireless Sensor Networks

Sumin Han, Fuzhong Wang (Henan Polytechnic University, P.R.China)

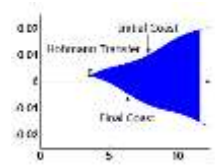
A wireless transmission data model is proposed to solve the problem of packet loss and delay in data transmission of wireless sensor network data transmission system. Based on the minimum variance estimation, the optimal fusion filter and cross covariance matrix are derived. The effectiveness of the system is verified by a simulation example.



OS19-3 Optimal Hohmann-Type Impulsive Ellipse-to-Ellipse Coplanar Rendezvous

Xiwen Tian, Yingmin Jia (Beihang University (BUAA), China)

This paper devotes to the problem of ellipse-to-ellipse coplanar rendezvous in low eccentricities, where the solution and distribution of Hohmann-type optimal impulsive rendezvous are investigated. The process of ellipse-to-ellipse coplanar rendezvous is described in the reference frame built in a circular orbit near two spacecrafts. Based on which, the analytical relation between the initial states and rendezvous time are derived for Hohmann-type, and the optimal impulse amplitudes are given thereupon. By selecting rendezvous time as the X-coordinate and special phase angle as Y-coordinate, the distribution boundary of Hohmann-type model is obtained according to the Hohmann transfer and Hohmann with coasts. Simulations are demonstrated to analyze the influences of the solution and distribution.

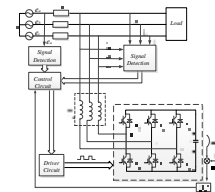


The distribution of Hohmann-type

OS19-4 Research on SVG Control Method Under Unbalanced Conditions

Zheng Zheng, Yousong Zhou (Henan Polytechnic University, China)

SVG (static var generator) is an important equipment to improve the power quality. Aiming at the complexity of the alternating current positive and negative sequence component separation method under unbalanced operating conditions, the method based on complex filter is used to reduce the control computation. Because the traditional PI control can not eliminate the steady-state error of the grid current in the nonlinear disturbance, the control method of the proportional complex integral is adopted, and the traditional proportional complex integral control based on the $\alpha \beta$ coordinate system according to the equivalent transformation relation of the phasor. The conversion to the three-phase coordinate system is based on the reduction of the amount of computation required for the traditional control to be improved by the Clark transform and the Clark inverse transform, and then gives a complete set of controller parameter tuning methods. Finally, a set of experimental platform based on DSP28335 is built. The experiment and simulation results verify the fastness and accuracy of the proposed positive and negative sequence component calculation methods and the stability and feasibility of the proportional complex integral control method.

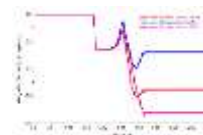


Main circuit topology of SVG

OS19-5 Dynamics Analysis of Payload On-orbit Catapult Separation Based on ADAMS

Yi Li, Yingmin Jia (Beihang University (BUAA), China)

In this paper, a catapult separation device equipped with guide mechanism is designed firstly, and the corresponding dynamic model is built through multi-body dynamics theory. Then, based on the dynamic simulation software ADAMS, the virtual prototype model of the separation device is established and the whole process of payload on-orbit catapult separation is simulated. Finally, the structure design parameters of the guide mechanism such as the number of roller group, distance between rollers or the guiding length are studied and the influences of the parameters on the separation process are analyzed. The simulation results can be applied in the design and optimization of the separation device.



1 angular velocity of payload under different distances

OS20 Advances in Marine Robotics and It's Applications (5)

OS20-1 A land testbed for experimental research on autonomous ship navigation

Keisuke Watanabe, Kazumasa Harada, Koshi Utsunomiya (Tokai University, Japan)

In the development of automated ship technology, experimental system is essential. The main navigation system is supposed to consist of GPS, AIS (Automatic Identification System), RADAR and cameras. In our land testbed, 2 ultrasound distance sensors are used as a model of GPS, which determine the coordinate of the testbed measuring the distances from 2 walls. A swinging ultrasound ranging sensor with a servo motor is used to simulate the RADAR. A xbee wireless communication module simulates the AIS. The camera is used for image processing to determine the control algorithm to avoid the collision from other moving obstacles. In this paper, we introduce our testbed's system assembly and an experiment to confirm functions of our concepts for our future experimental research on autonomous ship navigation.



OS20-2 Seafloor Image Color Enhancement Method based on Retinex model and Experiment Report in the undersea environment

Jonghyun Ahn¹, Shinsuke Yasukawa², Yuya Nishida¹, Takashi Sonoda¹, Keisuke Watanabe³
Kazuo Ishii¹ (¹Kyushu Institute of Technology, ²University of Tokyo, ³Tokai University, Japan)

Underwater robot is one of the important research tools to explore deep-sea where high pressure, darkness, radio attenuation prevent humans from direct access. Especially, Autonomous Underwater Vehicles (AUVs) attract attentions because they don't have tethered cables and can move freely. One of the important tasks of AUV is to take the seafloor images, however, the sea-floor images should be enhanced as red color attenuates rapidly and images become bluish, and the small differences of AUV altitude to the sea-floor affect the brightness of images because of light attenuation. In this paper, automatic camera parameters adjustment method is proposed to enhance seafloor images and evaluated through experiments in the Suruga-bay.



OS20-3 Automatic recognition of benthic species using image processing

Yuki Soejima, Yuya Nishida, Takashi Sonoda, Kazuo Ishii
(Kyushu Institute of Technology, Japan)

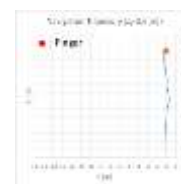
For sustainable use of fisheries resources, it is important to estimate the amount of resources such as TAC (Total Allowable Catch), TAE (Total Allowable Effort) and their investigations have been conducted by bottomed net fishing, however, the method suffers environmental damages. The survey method for wider area that does not affect the ecosystem is needed. Recently, research using an autonomous underwater robot (AUV) is introduced as a new survey method as the solution. We also introduced an AUV for the survey of fish and crabs in the Sea of Okhotsk. The number of marine lives is measured manually, and the technique of automatic measurement of the number is needed for the observation. In this research, we propose an automatic marine life recognition method from seafloor images.



OS20-4 AUV homing using acoustic chirp signal

Koji Masuda, Yuya Nishida, Takashi Sonoda, Kazuo Ishii
(Kyushu Institute of Technology, Japan)

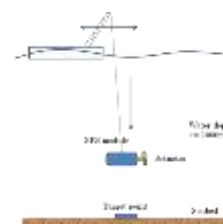
For autonomous underwater vehicle (AUV), high autonomy is required in order to accomplish mission such as inspection, observation, manipulation under extreme environments, deep-ocean. One of necessary function for AUV is acoustic navigation. In this paper, we conducted homing experiments using a small AUV and acoustic pinger with chirp signal. The chirp signal has the feature that the frequency of signal change gradually, so that the signal is suitable to calculate the correlation between the time difference between hydrophones. The homing experiments are carried out and evaluated through tank tests.



OS20-5 Simulation of horizontal vibration suppression of a suspended structure for seabed mining

Keisuke Watanabe¹, Kazuo Ishii (¹Tokai University, Kyushu Institute of Technology, Japan)

In a project of subsea mining in the near future, many work class robots such as crawlers, drilling machines, or ore collectors will be installed on the seabed. These robots are heavy but they must be landed on the seabed very softly to avoid impact damage from the seabed. So the installation method is very important and effective installation method should be investigated. In this paper, we examined vibration motion of a suspended heavy machine by a crane vessel through dynamics modeling and simulation in the horizontal plane. Descending speed of the machine affects the amplitude of the vibration, that is, if the descending speed is higher, larger amplitude will be observed. To suppress this vibration, we examined a velocity feedback control by attaching a thruster to the machine. From simulation results, we found horizontal vibration will be effectively suppressed by using simple feedback control.

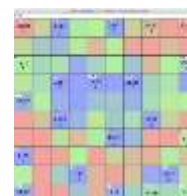


OS21 Robot Competitions for Social Contribution (5)

OS21-1 Analysis of Team Relationship using Self-Organizing Map for University Volleyball Players

Yasunori Takemura, Kazuya Oda, Michiyoshi Ono (Nishinippon Institute of Technology, Japan)

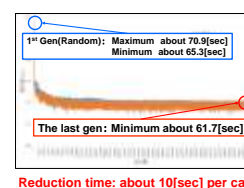
In Japan, sports efforts are actively being carried out to host the 2020 Olympic games. Especially in the field of sports science, researches on ergonomics, development of sports equipment and pattern recognition technology using artificial intelligence are actively researched. In previous research, we developed a clustering algorithm for positioning adaptation and relationships in team sports using Self-Organizing Maps in university rugby players. However, I have not yet confirmed whether the developed algorithm can be applied to other team sports. For this reason, we applied the same algorithm to an university volleyball player. Then, as an algorithm, we verify whether it can be generally used for team sports



OS21-2 Optimization for Line of Cars Manufacturing Plant using Constrained Genetic Algorithm

Keiji Kamei, Takafumi Arai (NishiNippon Institute of Technology, Japan)

Recently, improvement of production efficiency on cars manufacturers is required owing to increasing of demands in developing countries. However, that improvements under existing circumstances are depending on experience and intuition by workers. For this, we propose to objectively and efficiently improve a production line based on a GA. The production line of candidate for optimization is “Picking up assemblies” area, so that our proposal optimizes the positions of racks and boxes for assemblies by a GA. The difficulty of applying a GA is that the number of racks and boxes is defined in advance. For this, we apply constrained GA to optimization for those positions. The results of simulation for virtual production line show that our proposal succeeded in reducing about 10 seconds per car compared with random positioning.



OS21-3 Slip model of roller driven ball

Kenji Kimura¹, Chota Chikushi, Kazuo Ishii

(¹Nippon-Bunri University, Kyushu Institute of Technology, Japan)

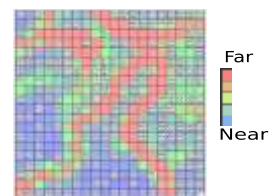
Spherical wheel motion driven by rollers attract attention due to the possibility of uneven surface. RoboCup is a platform designed to promote the research fields such as Artificial Intelligent (AI) and robotics, and one of examples is the ball dribbling mechanism of RoboCup Middle size league robot, and this mechanism controls the ball with two driving rollers. As the result of the survey at the 2017 World Cup, all teams in the world have determined the roller arrangement heuristically, and no mathematical consideration has been made. In this study, we propose a model considering slip, discuss the relationship between slip ratio and robot speed using evaluation function, and verify the model by experiment.



OS21-4 Strategy Analysis of Multi-Agent Games Using Self-Organizing Map

Moeko Tominaga, Yasunori Takemura¹, Kazuo Ishii
(Kyushu Institute of Technology, ¹NishiNippon Institute of Technology, Japan)

It is one of important subjects to know how humans and robots share the same space to realize a symbiotic society, for examples, strategies such as their positions and defense methods in multi-agent game, soccer. In the soccer games, the player's behavior changes depending on the game situation such as winning or losing, score gap, remaining time. The players act more offensive when their team is losing, or more defensive when their team is winning with minimum score difference. In this paper, we observe and analyze human soccer game, and estimate how the state vector of the player affects team behavior. The team strategy is analyzed based on parameters such as the positions of robots, the number of robots in play, scores, time and actions of robots using Self-Organizing Map (SOM).



OS21-5 Analysis of Characteristics of Tomato Fruits in Infrared Images Toward Automatic Tomato Harvesting System

Takuya Fujinaga, Shinsuke Yasukawa, Binghe Li, Kazuo Ishii
(Kyushu Institute of Technology, Japan)

Labor shortages and aging are big problems in Japanese agriculture field and farmers need systems for automation, efficiency and optimization. We focus on tomato fruits harvesting, which is one of the major fruit vegetables. Tomato harvesting needs longer working time than other fruits harvesting. We aim at the realize of a tomato automatic harvesting system, and have been researching and developing tomato harvesting robots that can harvest fruits and monitor the growth situation of tomato. It is necessary to detect the position and maturity of tomato fruit. In this paper, we analyze the plant characteristics of tomato using infrared images and propose tomato fruit recognition system. Images acquired at the tomato greenhouse of large scale facility were used. The analysis results of tomato fruits features in infrared images are reported.

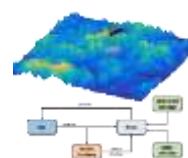


OS22 Navigation and Control (3)

OS22-1 Comparative Study of Sequential Processing TRN (Terrain Referenced Navigation)

Hyun Cheol Jeon and Chan Gook Park (Seoul National University, Korea)

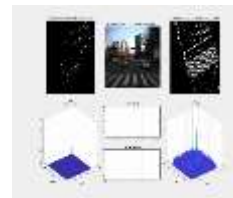
This study performs comparative analysis on the performance of sequential processing terrain referenced navigation (TRN) by applying various filtering techniques. The TRN is a navigation system that prevents divergence of inertial navigation system using terrain information. In this paper, we consider extended Kalman filter (EKF) and point mass filter (PMF) which are widely used in the TRN. The EKF estimates state variables by linearizing a nonlinear models but it has risk of divergence due to linearization errors. On the other hands, the PMF estimates the state variables robustly but it has a disadvantage of high computational load. Through this study, the advantages and disadvantages of the TRN when applying the EKF and PMF are compared and analyzed.



OS22-2 Road Marking Map Matching for Road Vehicle Localization

Kyuwon Kim and Gyu-In Jee (Konkuk University, Korea)

In this paper, we propose map matching algorithm using road marking intensity map made of 3D LIDAR. The road marking is very useful in terms of availability because it is existed anywhere on the vehicle. The map matching algorithm is used phase correlation using FFT to enable very fast matching. In addition, the road marking map is generated by binarizing the intensity. As a result, a large-scale global map can be stored with a small capacity. In addition, LIDAR scan data was accumulated for generating a high precise density local map. Accumulated local map can be supported sufficient information, especially longitudinal information. Therefore, it can be more robust and precise vehicle localization.



OS22-3 Control System Design of Directionally Maneuvering Multicopter with Independent Heading Rate

Byoungjin Lee, Jaehue Bae, Gwang Soo Park and Sangkyung Sung (Konkuk University, Korea)

In this paper, we present a comprehensive control system design of directionally maneuvering multicopter platform with independent heading rate. A directionally maneuvering multicopter system is capable of generating an arbitrary vehicle flight trajectory while it maintains an independent rotation with constant heading rate. For this, a quaternion based attitude controller is adopted in the control algorithm construction. Torque difference between clockwise and counterclockwise rotors is basically derived for yaw moment generation, while their thrust difference is harmonically configured for the desired waypoint flight via guidance logic.



GS abstracts

GS1 RoboticsI (3)

GS1-1 Production simulation of autonomous decentralized FMS including AGVs with different personalities of mind

Ryuichi Tsujii, Hidehiko Yamamoto and Takayoshi Yamada (Gifu University, Japan)

This study researches Automated Guided Vehicles (AGVs) moving control by using the model of a mind in order to avoid AGVs' interferences in autonomous decentralized Flexible Manufacturing Systems (FMS). The model of a mind can avoid the interference by repeating the two types of mind changes, the arrogant mind and the modest mind. Further, we give some personalities to the mind. The personalities have different time to change from the arrogant mind and the modest mind. By carrying out the production simulations using the AGV group with the different personalities, we acquire the production outputs. As a result, the outputs are improved compared with the traditional AGV group with a single personality. It is ascertained that the models of minds expressing different personalities are useful.



GS1-2 Development of Automatic Recognition of Hazmat Marking Chart for Rescue Robot

Wisanu Jitviriyaya¹, Poommitol Chaicherdkiat, Noppadol Pudchuen
(King Mongkut's University of Technology North Bangkok, Thailand)
Eiji Hayashi (Kyushu Institute of Technology, Japan)

A long history in the 1st place awards of World RoboCup Rescue Robot competitions are Invigorating Robot Activity Project (iRAP) such as iRAP_PRO, iRAP_FURIOUS, iRAP_JUNIOR and iRAP_ROBOT teams. In this paper, we would like to introduce and explain an autonomous system of our rescue robot for detection and recognition of Hazardous Material (Hazmat) marking chart. All Hazmat tags are considered and computed by using Speeded-Up Robust Feature (SURF) combined with Fast Library for Approximate Nearest Neighbors (FLANN) in order to match with the templates. Finally, the paper presents experimental results based on real situations in order to confirm an effectiveness of the pattern recognition of robotics system.



GS1-3 Development of Autonomous Robot for Laborsaving of the Forestry - Discrimination between trees and weeds using RGB-D -

Shingo Yamaguchi, Eiji Hayashi, Ayumu Tominaga (Kyushu Institute of Technology, Japan)

In traditional forestry, the weeding task places a large burden on workers. Therefore, it has been expected that such the problem will be solved by a robot. We have been developing an autonomous robot that eliminates the weed plants without damaging trees (these are resources). The robot should recognize trees exists in the environment. In this research, we have been focused on distinguishing between trees and other them. The system computes the RGB histogram of pixels corresponding point-cloud data of the ground extracted by plane detection. The threshold values are determined to discriminate between trees and weeds by this histogram automatically. We show the effectiveness of the developed system.



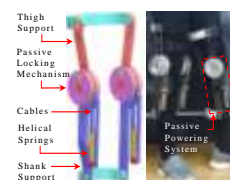
GS2 Bipedal robot & Human-welfare robotics (6)

GS2-1 Design and Evaluation of Passively Powered Knee Exoskeleton (PPKE) for Squat Lifting

R.K.P.S. Ranaweera¹, R.A.R.C. Gopura¹, T.S.S. Jayawardena¹, G.K.I. Mann²

(¹University of Moratuwa, Sri Lanka), (²Memorial University of Newfoundland, Canada)

This paper proposes a passively-powered knee exoskeleton (PPKE) to provide power assistance during squat lifting of objects from the ground. The passive powering mechanism is designed to capture 20% of the waste mechanical energy available at the biological knee joint during decent phase and to release the stored energy in ascending phase in a complete squatting cycle. The novel passive locking mechanism enables the wearer to ambulate freely posing minimum restrictions in-between squat lifting tasks. The anthropomorphic exoskeleton structure was fabricated using acrylic glass and powering system include elastic helical springs, where the entire working model only weighs at 900 g per unit. The effectiveness of proposed system was verified by experiments using surface electromyography (sEMG) signals under different test conditions. The exoskeleton is capable of reducing peak RMS averages of sEMG signals of knee extensor muscles by 15%. As such, preliminary results proved PPKE's potential to reduce human effort.



GS2-2 Behavior design of robot arm imitating the consciousness mechanism of living organisms Representation of facial expression in transition process of emotion

Ryohei Anshi, Eiji Hayashi (Kyushu Institute of Technology, Japan)

Wisanu Jitviriya (King Mongkut's University of Technology, Thailand)

Sakmongkon Chumkamon (Rajamangala University of Technology, Thailand)

Although various service robots are being developed, social robots are required to have "user affinity", which gives the user a sense of affinity, in particular. In this research, we aim to realize user affinity by paying attention to living organisms that embrace healing and affinity, giving the robot consciousness, behavior, and emotion of living organisms. In the transmission of emotions, the eyes are important parts that express various psychological states due to changes in pupil size, eyelid opening / closing degree, shape, and the like. Therefore, we give two degrees of freedom to the eyeball and the eyelid, we can also change the pupil diameter and blink cycle, and constructed the system so that the expression also changes finely according to the change of the ratio of the eight emotions using the expression.

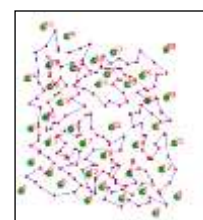


GS2-3 Study of Robot Navigation for Forest Management

Ayumu Tominaga, Eiji Hayashi (Kyushu Institute of Technology, Japan)

Abbe Mowshowits (The City College of New York, USA)

We have been developing a robotic system for labor-saving of forestry that moves between trees and cut weeds plants without damaging the trees. The trajectory computation of the forest is carried out based on a weighted graph with trees as vertices. The line graph $L(G)$ calculated from first graph represents a graph connecting the midpoints of each tree pairs that the robot can safely pass through, and the Hamiltonian circuit calculated therefrom is give a path plan for the robot to pass through all the tree pairs and return to its starting position. In order to follow the trajectory path, we combined the obstacle avoidance behavior and the vision system which has actuator for pan angle rotate.



GS2-4 Development of the sense system that is combined force feedback and visual feedback -Deformable virtual objects simulation by using LEM-

Kaito Nagano, Eiji Hayashi (Kyushu Institute of Technology, Japan)

In the medical treatment and bio-technology field, doctors and researchers need technologies that can accurately perform minute work. Such minute work is improved by using micromanipulators, but their operation is difficult because the operator has no sense of force. As a result, a person who has the skill to do minute work is needed for all minute works. The purpose of this research is to develop a combined sense system that uses both force feedback and visual feedback on a deformable virtual objects simulation. Especially, focus on a way to produce a force that is calculated in simulation of deformation using a haptic device. As the first stage, our simulation of deformation was improved by using LEM (Long Element Method) and evaluated accuracy of a virtual object’s deformation.



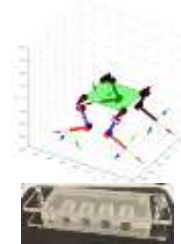
GS2-5 A four-legged robot's soft feet structural design and walking gait generated from inverse kinematics

Amornphun Phunopas¹, Eiji Hayashi²

(¹King Mongkut’s University of Technology North Bangkok, Thailand,

²Kyushu Institute of Technology, Japan)

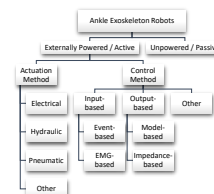
The conventional wheel is famous in the industrial mobile robot because it is simple to build and easy to control and to maneuver. On the other hand, the legged robot is complicated to control but has a high performance in locomotion like highly evolved legged-creatures. This research describes the four-legged robot design platform with the soft feet, which are made by silicone-material forming. The robot’s feet are implanted by the strain gauge sensor. The robot can percept the external force sensitively when its feet touch something. The research demonstrates the forward kinematics and inverse kinematics of a four-legged robot with three joints for each. The result has validated the kinematic equations by implementing them on the real dog-like pet robot. The robot walked with a pure walking gait and showed a sensing signal from the soft foot and ground contact.



GS2-6 Powered Ankle Exoskeletons: Existent Designs and Control Systems

A.H. Weerasingha, W.P.K. Withanage, A.D.K.H. Pragnathilaka, R.K.P.S. Ranaweera, R.A.R.C. Gopura(University of Moratuwa, Sri Lanka)

Powered ankle exoskeleton is a wearable device fitted to the ankle joint for purposes such as rehabilitation, power augmentation and locomotion assistance. Although variety of technologies were developed, commercial application was found to be minimal owing to various limitations with respect to both function and performance. Notably, conservation of metabolic energy, anatomical conformance, agility during operation, etc. are lacking factors in contemporary exoskeletons robots. In order to realize rational solutions, an improved understanding of the existent designs and control systems is paramount. In that context, this paper performs a comprehensive review on active ankle exoskeletons powered by external means. Initially, anatomy of the ankle joint complex is highlighted. Next, associated research challenges and design difficulties are recognized for the development of robotic hardware systems. Then, mechanisms, actuation methods, and control methods are systematically presented. Here, exoskeletons designs from 2005 to 2017 were studied to recognize the latest paradigm shifts. As such, this paper provides a classification, a comparison and an overview of related technologies. Finally, design recommendations are made on observed trends and patterns for the development of powered ankle exoskeletons.



GS3 Complexity (5)

GS3-1 Management of digital records inspired by Complex Systems with RADAR

Anne Jeannin-Girardon, Alexandre Bruyant, Nicolas Toussaint, Pierre Collet, Pierre Parrend (University of Strasbourg, ECAM Strasbourg-Europe, France)

(Big)Data storage poses two major challenges: security (data can be very sensitive, e.g. medical or financial records) and robustness (IT infrastructure may not be reliable due to faulty hardware, bad internet access or even power outage, especially in developing countries). Centralization in data-centres can therefore lead to bottlenecks and significant losses, in case of failure or intermittent connexions. Sensitive data must also be reliably backed-up. However, manual or automatic backups are prone to errors or failures. Consequently, we propose to apply the principles of Complex Systems (sets of autonomous interacting entities exhibiting emergent behaviour) to the problematics of storing and backing-up sensitive data in a platform called RADAR (Robust Anonymous DATA Records). Storage is no longer centralized: RADAR instances automatically fragment, replicate and distribute the data randomly over a cooperative network for anonymized and encrypted robust and secure backups and storage even over non-reliable IT infrastructure.



GS3-2 Integrated optimization of differential evolution with grasshopper optimization algorithm

Duangjai Jitkongchuen, Udomlux Ampant (Dhurakij Pundit University, Thailand)

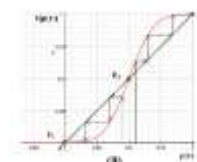
This paper proposes a scheme to improve the differential evolution algorithm (DE) performance with integrated the grasshopper optimization algorithm (GOA). The grasshopper optimization algorithm which mimics the behavior of grasshopper. The characteristic of grasshoppers is slow movement in the larval stage but sudden movement in the adulthood which seem as exploration and exploitation. The grasshopper optimization algorithm concept is added to DE to guide the search process for potential solutions. The efficiency of the DE/GOA is validated by testing on unimodal and multimodal benchmarks optimization problems. The results prove that the DE/GOA algorithm is competitive compared to the other meta-heuristic algorithms.



GS3-3 Efficient collective search by agents that remember failures

Masao Kubo, Nhuhai Phung, Hiroshi Sato (National Defense Academy of Japan, Japan)

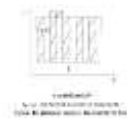
The BRT is an algorithm that the agents can find appropriate collective actions by changing their agreement in a trial-and-error manner. When the solution is the only one, computer simulations shows the number of times to find the solution is proportional to the square of the number of their collective choices on average. In this paper we propose an agent that remember failures behaviors to improve the searching time. Since the agent does not propose wrong behavior, it is trivial that the whole search time will be shortened. In this research, we exchanged the BRT agent and this "never suggest again" agent and investigated the search time and its ratio. As a result, we found that even a small number of the proposed agents can improve search time.



GS3-4 The analysis of band structures of photonic crystals

Wang Chenxu (Muroran Institute of Technology, Japan),
Fu Ziyi (Henan Polytechnic University, China)

In this paper, a finite element is developed to calculate the band structures of one-dimensional photonic crystals. The Maxwell equation governing the propagation of electromagnetic waves, which combine with Bloch theory, the FEM transforms the complex band diagram problems into a simple eigenvalue problem by solving the eigenvalue with respect to wave vector K by frequency



GS3-5 A Data Estimation Technique for Incomplete Telemetry Data Based on a Genetic Algorithm with Data' Statistical Properties

Masahiro Tokumitsu, Kaito Mikami (National Institute of Technology, Yonago College, Japan)
Fumio Asai (The Radio Amateur Satellite Corporation, USA)
Taku Takada (National Institute of Technology, Kochi College, Japan)
Makoto Wakabayashi (National Institute of Technology, Niihama College, Japan)

Satellites transmit telemetry data to ground stations in order to provide the data on their missions. The telemetry data contain a sort of data such as observations, experiments, and satellites' health status. However, the telemetry data received by the ground stations may contain errors by effects through the transmissions. This paper proposes a data estimation technique for incomplete telemetry data to attain a high availability of the received telemetry data. The proposed technique is based on a genetic algorithm with data' statistical properties. This paper demonstrates the proposed technique with simple examples. In simulations, this paper examines the proposed technique for applying the actual telemetry data obtained by the particular satellite.



GS4 Pattern recognition & Image processing (5)

GS4-1 Study on Detection of Nests on Pylon from Overhead View Based on Halcon

Jiwu Wang, Haibao Luo, Pengfei Yu (Beijing Jiaotong University, China)

There are many difficulties when researchers want to detect the nests on pylons in the electricity transmission network with image processing methods. One major difficulty is to position the pylon precisely in the image because of the variance of shooting angle and shooting distance. Plus the unobvious features of nest's edge, color and shape in the background of the image make the single-feature-based detection methods fail to realize precise positioning. Thus, this paper addresses an effective method based on Halcon, which could detect the nest in the images from unmanned aerial vehicles (UAVs). This method eliminates most of the background interference by recognizing the pylon area in the image using the Blob algorithm. Within this area, the fusion of texture and gray-scale features of nest are employed to realize the detection. An experiment result is presented to validate that this method can actually realize the precise detection of nests on pylons with images shot by the UAVs.



GS4-2 Human gait recognition based on Caffe deep learning framework

Jiwu Wang, Feng Chen (Beijing Jiaotong University, China)

Human gait recognition as an emerging biometrics technology has important theoretical significance and practical value. At present, the research on human gait recognition is still in the stage of theoretical exploration, and most of the methods to recognize the targets are realized by the traditional pattern recognition methods, which have no many advantages in detection accuracy and speed of detection. With the development of deep learning theory and technology, this paper will achieve human gait recognition of specific targets based on Caffe deep learning framework through the faster-rcnn algorithm. The main contents of the paper include the samples processing, model training and result testing.



GS4-3 Unsupervised Image Classification Using Multi-Autoencoder and K-means++

Shingo Mabu, Kyoichiro Kobayashi, Masanao Obayashi, Takashi Kuremoto (Yamaguchi University, Japan)

Image classification using machine learning has been actively studied. However, machine learning, especially deep learning, needs a large number of training data. It is tough and impractical task for users to give correct class labels to the data. Therefore, an unsupervised image classification system is proposed in this paper. The proposed method consists of multi-autoencoder and K-means++. Since it is difficult to realize unsupervised classification system due to the lack of class information, the proposed method applies some image processing techniques to the images, and the feature values are extracted from the original images and the processed images using multi-autoencoder. The images with the extracted features are clustered by K-means++ algorithm, which can make groups of similar images.

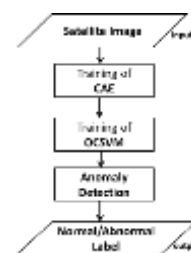


Ground piano cluster

GS4-4 Anomaly Detection of Disaster Areas from Satellite Images Using Convolutional Autoencoder and One-class SVM

Kohki Fujita, Shingo Mabu, Takashi Kuremoto (Yamaguchi University, Japan)

In recent years, research on detecting disaster areas from satellite images have been conducted. When machine learning is used for disaster area detection, a large number of training data is required, however, we cannot obtain so much training data with correct class labels. Therefore, in this research, we propose an anomaly detection system that finds abnormal areas that deviate from normal ones. The proposed method uses a convolutional autoencoder (CAE) and One-class SVM (OCSVM). First, CAE executes feature extraction from satellite images. Second, OCSVM is trained using images of normal areas only. Finally, anomaly detection for the testing images is carried out by the trained OCSVM. In the performance evaluation, the proposed method shows better performance than the method with OCSVM only.

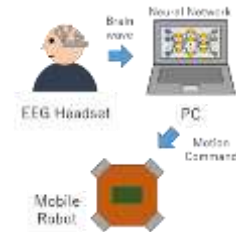


GS5 Neuroscience (3)

GS5-1 Improving EEG-based BCI Neural Networks for Mobile Robot Control by Bayesian Optimization

Takuya Hayakawa, Jun Kobayashi (Kyushu Institute of Technology, Japan)

The aim of this study is to improve classification performance of neural networks as an EEG-based BCI for mobile robot control by means of Bayesian Optimization of learning parameters and hyperparameters in training the neural networks. The parameters were intuitively decided in our preceding study. However, the performance will be improved if the parameters are determined in an appropriate way. There are several methods for parameter optimization. Grid Search draws a grid on a parameter search space, examining all intersection representing a combination of the parameters. The method can find the best parameters with a high probability, but it takes a huge amount of time. The authors have used Bayesian Optimization to optimize the parameters in a shorter time and achieved the better performance.



GS5-2 Selective synchronization of the coupled bifurcating neurons for phase shift of background oscillation

Akihiro Yamaguchi¹, Yutaka Yamaguti¹, Masao Kubo² (¹ Fukuoka Institute of Technology, ² National Defense Academy of Japan, Japan)

Synchronization in the coupled bifurcating neurons was studied in the view point of the selective formation of cell assembly. The bifurcating neuron is a simple chaotic neuron that exhibits chaotic inter-spike interval dynamic by adding the sinusoidal background oscillation. In this research, we introduce the phase shift of the background oscillation and the several types of phase response to the input spike sequence. The coupled 16 bifurcating neurons with complete bidirectional coupling were numerically simulated and their synchronized behaviors were observed, where each 4 neurons have the same phase shift value that is different with the other neurons. Fig. 1 shows the synchronization ratio of each pair of neurons. This result indicates the formation of chaotically synchronized cell assembly for the same phase shift value.

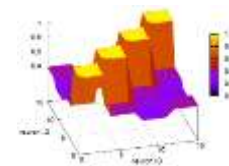


Fig. 1 Synchronization ratio of neurons

GS5-3 Review on computational techniques in solving aircraft landing problem

Aminurafiuddin Zulkifli, Nor Azlina Ab. Aziz, Nor Hidayati Abdul Aziz
(Multimedia University, Malaysia)
Zuwairie Ibrahim (Universiti Malaysia, Malaysia)
Norrima Mokhtar (University of Malaya, Malaysia)

The problem of sequencing and scheduling arriving aircraft landing is commonly known as aircraft landing problem (ALP). This problem, due to various constraints such as the number of arriving aircrafts, the number of runways, the mode of runway operation, the type of arriving aircrafts, the minimum separation between each arriving aircraft, and the weather condition, is considered to be a NP-hard problem. Therefore, it is almost impossible to compute every possible solution and computational intelligence methods had been adopted to solve ALP. In this paper, we review the computational intelligence techniques used in ALP. The main techniques include the evolutionary algorithms namely; genetic algorithm, genetic programming, scatter search and bionomic algorithm, the swarm intelligence algorithms like particle swarm optimization and ant colony optimization and also other methods such as the constrained position shifting and dynamic programming.



Figure 1. Cost variation in time window during flight

GS6 Virtual reality (5)

GS6-1 Interactive musical editing system to support human errors and offer personal preferences for an automatic piano -Inferring performance expression by considering change of pitch-

Masahiro Ushio, Eiji Hayashi (Kyushu Institute of Technology, Japan)

Electronic musical instruments' sound quality and ambience are inferior to real musical instruments. Therefore, we developed automatic piano by using grand piano. Pre-edit is needed to play music in the manner of a live pianist. In the case of piano music, there are often 1000 or more notes in the score of even a short piece of music, requiring that an editor spend a huge amount of time to accurately simulate the emotionally expressive performance of a highly skilled pianist. Therefore, we have developed an interactive musical editing system that utilizes a database to edit music more efficiently. This paper, we made a hypothesis that the pianist's performance is characterized by the pitch change, and we introduced the pianist features which considered the pitch change to further improve the efficiency.



GS6-2 Analysis of Malaysian Facial Expressions for Designing Virtual Agents

Halimahtun Khalid (Damai Sciences, Malaysia), Liew Wei Shiung (University of Malaya, Malaysia)

The perception of emotion based on facial expressions is culturally mediated. East Asians tend to focus on the central region around the nose and eyes, while Western Caucasians observe the eyebrows and mouth regions. Therefore, designing a virtual avatar with realistic facial expressions to convey emotions should consider the demographics of the users who would be interacting with the avatar. We conducted an online study to determine the facial measurements for specific emotions as perceived by Malaysians. Twenty-four facial expressions were shown to 37 subjects and they were instructed to select which emotion label matched each expression. The expressions were then decomposed into facial action unit measurements using OpenFace. Regression analysis was used to determine the combination of measurements corresponding to each emotion label. The facial expressions were then used to design the virtual agents in an experiment on human-avatar interaction where 48 subjects evaluated the virtual agents on trust.



GS6-3 Development of VR system to enhance understanding process of robot mechanisms

Alexei Lushnikov, Vlada Kugurakova, Timur Satdarov, Artur Nizamutdinov (Kazan Federal University, Russia)

For engineers and technicians in training honing one's skills in working with machines are essential. Very unfortunately, access to facilities required for this is pretty much may not always be provided: such facilities might be in short supply, or the time one is allowed to use them might be restricted, or they might be simply not present in the vicinity. The solution to this problem that we propose is the use of VR simulation of tasks that would be normally carried out at the specialized facilities, such as assembling-disassembling, maintenance, and use. To provide the most realistic and immersive experience, the simulation would be fitted with haptic feedback. This study describes the ongoing project on design and implementation of such VR system.



GS6-4 Towards the immersive VR: measuring and assessing realism of user experience

Vlada Kugurakova, Murad Khafizov, Alexander Elizarov, Aleksei Lushnikov,
Artur Nizamutdinov (Kazan Federal University, Russia)

The range of uses for Virtual Reality Continuum grows more diverse, with potential fields of application spanning from research and education to leisure and work, which increases demand for a method which can allow to precisely and reliably measure VR effectiveness. How can we determine the quality of VR? How do different people respond to its varying implementations? And could it be true that different social groups interact with VR differently? In this paper, we propose a new approach to this emerging problem, which involves applying user interface (UI) metrics to VR experience. We review existing ways to increase VR immersion and outline a series of possible experiments to study and, hopefully, find a correlation between immersiveness and VR user interface effectiveness.



GS6-5 Lessons on the Reality-Gap: Iterations between Virtual and Real Robots

Andre Rosendo (ShanghaiTech University, China),
Charlie Houseago, Fumiya Iida (Cambridge University, UK)

Due to abstractions and approximations between the virtual and real world, the transfer of knowledge from virtual (simulations) to real (robots) world is problematic. As physical conditions are prone to unknown and stochastic noise sources, the predictability reduces. In here we use data experiments from 100 real robots to tune the parameters of a simulation, and later used this tuned simulator to improve the design of the previous robots and find the optimum robot. We compare the simulated and real world behavior of this robot, and discuss our results. In this paper we address the Reality Gap by tuning a Bullet physics simulator with results extracted from real experiments with robots. Parameters defining the interaction between the robot and the floor (friction and restitution) are tuned to minimize the error between the simulated and actual behavior, and the simulated trajectories of 100 agents are compared to the trajectories of the real-world counterpart. With the newly found set of physical parameters, the simulation is then used to predict, through a Random Search approach, a robot capable of outperforming the previous ones. This new robot is built and we observe that although differences exist between the simulated and actual behavior, the final robot's trajectory strongly resembles the one predicted by the simulation. Next steps should consider stochastic differences between experiments to improve the predictability of the system.

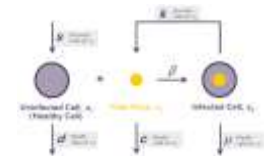


GS7 Intelligent control (3)

GS7-1 Fractional Order Sliding Mode Control Applying on the HIV Infection System

Thunyaseth Sethaput¹, Arsit Boonyaprapasorn²
 (1Thammasat University, 2Chulachomklao Royal Military Academy, Thailand)

The mathematical model of HIV dynamical system explains the interaction between immune system and virus. It represents the relationship among population size of uninfected CD4+ cells, infected CD4+ cell, and virus. The aim of the treatment is to drive the amount of uninfected CD4+ cells to the desired level and the amount of both infected CD4+ cells and virus particles approach to zero as time increased. The main objective of this study is to apply the fractional order sliding mode control (FOSMC) method to regulate HIV infection. The performance of the control method was investigated via simulation. According to the simulation of the controlled HIV system, the state variables approach to the desired values. Thus, it is feasible to apply the FOSMC method to define the treatment of the HIV infection system.



GS7-2 Skill-based Job Rotation Scheduling for Occupational Noise Exposure Control

Pavinee Rerkjirattikarn, Chatdanai Kaorapapaong, Sun Olapiriyakul
 (Thammasat University, Thailand)

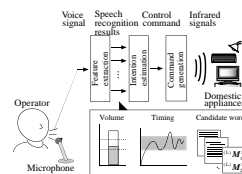
Job rotation is an inexpensive and flexible administrative control measure, used to prevent workers from being exposed to harmful levels of occupational hazards. Despite its advantages, job rotation can affect process continuity and workers' control over the timing of their work hours, resulting in reduced productivity and job satisfaction. This paper proposes a job rotation methodology for manufacturing systems with independent workstations. An integer-programming model is formulated, to determine workforce schedules capable of meeting customer demands and skill requirements for tasks, while simultaneously minimizing operational cost and reducing noise exposure levels of workers to a safe level. The overtime assignment is considered to ensure the fairness and appropriateness of the work schedules. The cost effectiveness of workforce schedules is evaluated under different overtime policies and production capacity levels. The results of this study will help decision makers to select the best workforce schedule, based on the desired production levels and overtime policies.



GS7-3 A Training Method for the Speech Controlled Environmental Control System Based on Candidate Word Discriminations

Taro Shibanoki, Masaki Watanabe (Ibaraki University, Japan), Go Nakamura, Takaki Chin (Hyogo Rehabilitation Center, Japan), Toshio Tsuji (Hiroshima University)

This paper proposes a concept of a training system for the speech controlled environmental control system: Bio-Remote based on candidate word discriminations. The proposed system can provide three-types of voice signal training: (1) volume, (2) timing and (3) candidate word which are important for accurate speech recognition based on false recognition results. During the training, such three kinds of features are extracted from measured voice signals and visually and auditory fed back to the user in real time. This allows the user to train speech abilities even if false recognition results are extracted because of slurred speech. The efficacy of the proposed system is demonstrated through training experiments for slurred speech conducted with healthy participants. The results show that the proposed training system is capable for train the speech abilities.

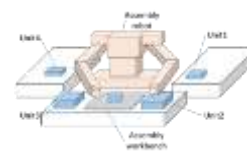


GS8 RoboticsII (5)

GS8-1 Design System of Cell Type Assembly Machine with Dual Arms Robot by GA

Keita Honda, Hidehiko Yamamoto and Takayoshi Yamada (Gifu University, Japan)

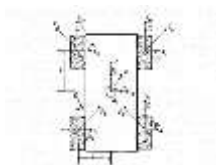
The purpose of this research is to develop a system named DELUGA which automatically decides to place a lot of assembled parts, jigs and robot hands of a cell type Assembly Machine by genetic algorithm (GA). The robot of our research adopts a dual arms robot. DELUGA consists of two modules, the conditions module and GA module. The conditions module reads work data for robot, and sets various parameters required for GA. GA module decides the efficient arrangement place of parts, for example jigs and robot hands, by GA, and outputs the acquired arrangement image. Because the left and right robot arms simultaneously carry out assembly works, DELUGA adopts the concept of waiting time of each robot arm to prevent arms interference. We applied DELUGA to assembly machine of an in-wheel motor for electric vehicles. The application resulted that the production efficiency increased. It is ascertained that DELUGA is useful.



GS8-2 Spherical Mobile Robot Driven by Biorthogonal Omnidirectional Wheels

Liu Wei, Ma Shuanglong, Duan Lunqin, Yu Jiangtao (Beijing Jiaotong University, China)

This paper presents a new spherical mobile robot driven by omnidirectional wheels. The structure is that there are two independent driving omnidirectional wheels located at the ends of the inside vertical diameter of the sphere shell, and the two wheel axes are in orthogonal position. Its principle is, that the omnidirectional wheels can roll on the inner surface of the spherical shell by the friction force, then drive the spherical shell rolling. The lower end omnidirectional wheel is responsible for walking drive, and the upper end one for steering drive.



GS8-3 Coordinated behaviour with a Pepper Humanoid robot to estimate the distance of other robot using Inverse Perspective Mapping

M. Hassan Tanveer, Antonio Sgorbissa, Carmine T. Recchiuto
(University of Genova, Italy)

This article discusses a strategy for real time distance determination applied to a humanoid robot (Pepper, Softbank Robotics) that is requested to collaborate with other robots. However, using the monocular camera embedded on the robot head, it is difficult to determine distance to objects in front of the robot with any degree of certainty. The reason is non linear relationship between the height allocation of camera and its distance to an object in a camera frame. So, the proposed method is based on the extraction of accurate bird's-eye view images, by applying Surface Substraction and Inverse Perspective Mapping (IPM) to the images captured with the Pepper head camera. The algorithm is implemented in the Python language using the OpenCV libraries



Fig. 1: Pepper FOV

GS8-4 Control Techniques of Quadrotor Uavs: A Concise Study

¹Syed Faiz Ahmed, ¹Athat Ali, ¹M. Kamran Joyo, ¹Khusairy Abd Kader, ²Hazry Desa, ³Sheroz Khan(¹Universiti Kuala Lumpur, British Malaysian Institute, Malaysia, ²Universiti Malaysia Perlis, Malaysia, ³International Islamic University Malaysia, Malaysia)

Quadrotors, the four wing UAV has drawn prominent attention amongst the researchers. The simple nonlinear structure design requires a robust control to ensure the stability during the flight. The noisy and environment with unexpected disturbances may cause issues such as drift in position. In order to tackle the severe conditions a robust control is required. This paper provides an overview of the available quadrotor models and the control techniques with their application in quadrotor control issues.



GS8-5 GIS Based Hydrological Model for River Water Level Detection & Flood Prediction featuring morphological operations.

Sarmad Zafar, H.M.SohaibAzhar, Aqeel Tahir
(Mohammad Ali Jinnah University, Pakistan)

Mostly river water level and flood forecasting methods are based on gauging stations measurements at discrete locations, which limits their capability to provide accurate and timely data over large extent, also limited or no data available on remote locations. So here we present an idea to use high resolution satellite images for real time mapping of river water level. In this project, we developed a Web based GIS system for mapping river water level, early warning and mapping for flood disasters. To improve flood forecasting/warning, we developed a decision support system (DSS) for flood monitoring and prediction that integrates GIS, satellite image processing and hydrological modeling. We present the methodology for data integration, floodplain delineation, and online map interfaces. Our Web based GIS system can dynamically display observed and predicted water levels for decision makers and the general public. The users can access a Web-based GIS system which models current flood events and displays satellite imagery and 3D visualization integrated with the flood plain area. The output from the hydrological modeling will be used for flooding prediction for the next 1 day to 2 days (24 and 48 hours) along the lower Indus River. In this stage river water level analysis has been achieved, work on the hydrological modeling is in progress to acquire river water stage & flood level and the prediction.



GS9 Poster (11)

GS9-1 Analysis of onboard sensor-based odometry for a quadrotor UAV in outdoor environment

Aidar Gabdullin, Grigory Shvedov, Mikhail Ivanou, Ilya Afanasyev
(Innopolis University, Russia)
Konstantin Yakovlev (Russian Academy of Science, Russia)

This article introduces a comparative analysis of a quadrotor UAV trajectories evaluated by onboard sensors (camera, IMU and GPS) and ROS-based monocular visual odometry. Parrot Bebop drone was launched outdoor in autonomous mode according to teleoperated closed-loop trajectory along an a-priori known perimeter of a square work area (measured by a tape measure as a ground truth) and recorded sensors telemetry data for offline processing. To verify UAV odometry trajectory, we used Bebop's firmware with integrated visual-inertial velocity estimation, the ground truth and an external observer.



GS9-2 Memristive neuron integration in digital robotic embodiment

Max Talanov, Evgenii Zykov, Yuriy Gerasimov, Evgeni Magid, Aleksander Elizarov
(Kazan Federal University, Russia)

Victor Erokhin

(Italian National Council of Research, Parma, Italy)

In the current paper, we introduce a high-level approach for an integration of a neuromorphic memristive neuron in a real-time operating robotic system. The memristive neuron schematic, which we had presented in our earlier works, is capable of inhibitory and excitatory learning (eSTDP, iSTDP) as well as modulation via dopamine input. We discuss a possibility of integration of the analog memristive neuron into a digital robotic embodiment and present block diagram of an adapter that includes pseudo-neuronal encoder and decoder.



GS9-3 Russian mobile robot Servosila Engineer: designing an optimal integration of an extra laser range finder for SLAM purposes

Neil Alishev, Yuriy Gerasimov, Roman Lavrenov (Kazan Federal University, Russia)

In our current research we determine an optimal design for integration of Hokuyo UTM-30LX-EW LRF into control system of Russian mobile robot Servosila Engineer. We designed and constructed a special static stand with an option to select an inclination of a scanning beam toward the surface of an environment. RBPF SLAM algorithm was tested to perform localization and mapping. Experiments were conducted in order to determine the best configuration of the LRF position and RBPF SLAM algorithm parameters.



GS9-4 Toward automated open wound suturing using haptic feedback: detecting wounds and planning the suture

Artur Sagitov¹, Hongbing Li², Evgeni Magid¹

(¹Kazan Federal University, Russia)

(²Shanghai Jiao Tong University, China)

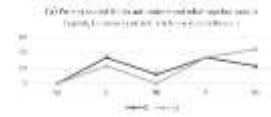
One of the key disadvantages of robotic surgery as of today is the lack of haptic feedback. While in traditional surgery surgeons using their haptic senses in all tasks most medical robot lack this ability. Using robots with haptic feedback have the potential of reducing the time spend by surgeon on such tedious subtasks as suturing helps reducing surgeon fatigue. Also decreasing the manual input of the surgeon enables remote surgery even using long communication links with big latency. In this paper we present a framework of wound detection and suture planning. We plan to implement and test our algorithms using KUKA iiwa manipulator.



GS9-5 Establishing Effective Teaching for Robotics: a comparison study of Bachelor students in Introduction to Robotics course

Tatyana Tsoy, Leysan Sabirova, Mikhail Abramskiy, Evgeni Magid
(Kazan Federal University, Russia)

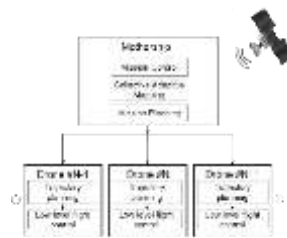
Global demand in robotics specialists arose necessity of establishing educational programs in robotics, which sets new challenges for modern educational system. In 2017 Kazan Federal University launched master's program in Intelligent Robotics to produce specialists considering core engineering competences and such important skills as self-motivation, critical thinking etc. This paper presents results of continuous survey among undergraduate students of Introduction to Robotics course that helps understanding dynamics of student's motivation to study robotics, attitude toward education methods to improve teaching strategies



GS9-6 Development of a heterogeneous aerial swarm control framework for forest management

Yuriy Gerasimov, Artur Sagitov, Evgeni Magid (Kazan Federal University, Russia)

As the prevalence of UAVs is increasing, they are becoming more accessible for wider applications. Our interest is in application of UAVs for forest management challenges including health and safety monitoring and commercial exploitation in a sustainable manner. We propose a swarm control framework for managing a group of UAVs for aforementioned tasks, including survey of tree health with infrared cameras and chemical sensors, detecting potential risky situations of illegal logging, smoke and fires, and estimating potential volume measurements. The proposed framework manages planning flight trajectories, sensor fusion and collaborative mapping. On the next stage, we plan to simulate the framework in ROS/Gazebo environment, and further to implement a pilot project with a group of DJI Phantom quadrotors and a large-size fixed-wing UAV.



GS9-7 Implementation of ROS package for simultaneous video streaming from several different cameras

Ramil Safin, Roman Lavrenov (Kazan Federal University, Russia)

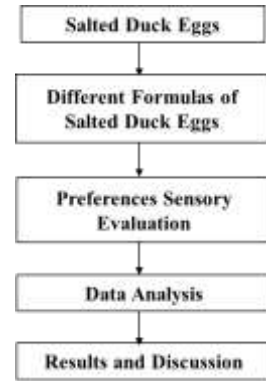
Real time video stream capturing and processing is important for a variety of tasks in robotics. We created ROS package that captures concurrent video stream from 4 different cameras of Russian mobile robot "Servosila" Engineer. V4L2 API was used to configure video devices and to retrieve raw data from cameras. Memory mapping approach of mapping device buffers increased overall performance by eliminating redundant memory copies. We demonstrate the comparison of our new package and OpenCV based package.



GS9-8 Consumers Preferences and Purchase Intention on New Taste of Salted Duck Eggs

Shang-Hui Li (Far East University, Taiwan)

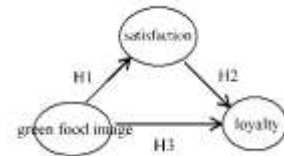
Egg is an indispensable food in people's daily life. Egg is rich in protein, easily digested by human body and metabolism. In addition to direct consumption, people created many different processed egg products by the characteristics of eggs. The traditional method of making salted duck eggs is to place the eggs in salt water or coated in laterite without any additional chemical composition. Except the eggs, this study joined other natural ingredients To produce eight different flavors of salted duck eggs. In the formal test, 70 convenience sampling were taken from Tainan area for sensory evaluation, 63 valid questionnaires, SPSS18.0 was used as the statistical analysis. Sensory evaluation included the color, oil, smell, salty and taste of egg yolk and the salty, taste of protein. Moreover, with the overall acceptance, purchase intention and willingness to buy again etc. The study results showed that cinnamon red salted duck eggs and four-herb salted duck eggs are the highest acceptance to consumers, followed by the salted citronella duck eggs. However, four-herb salted duck eggs dipped by the salted water are not favored by consumers.



GS9-9 The Study of Green Food Image, Satisfaction and Loyalty through the Perspective of Elaboration Likelihood Model

Shu-Fang Hsu (Far East University, Taiwan)

This study aims to explore the relevance of consumer satisfaction and loyalty to green food image through the perspective of Elaboration Likelihood Model. The results show that the positive impact of green food image; and will indirectly affect the satisfaction of re-purchase intention; satisfaction positive impact loyalty. We hope that the results of this study can provide relevant business management strategies and suggestions, the green food consumption theory and practice can be dedicated.



GS9-10 Self-Generated Dataset for Category and Pose Estimation of Deformable Object for Manipulation by Robot

Yew Cheong Hou, Khairul Salleh Mohamed Sahari (Universiti Tenaga Nasional, Malaysia)

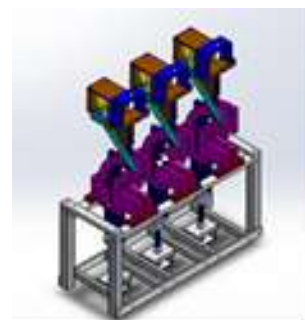
This work considers the problem of garment handling by a general household robot that focuses on the task of classification and pose estimation of a hanging garment in unfolding procedure. Classification and pose estimation of deformable objects such as garment are considered a challenging problem in autonomous robotic manipulation because these objects are in different sizes and can be deformed into different poses when manipulating them. Hence, we propose a self-generated synthetic dataset for classifying the category and estimating the pose of garment using a single manipulator. We present an approach to this problem by first constructing a garment mesh model into a piece of garment that crudely spread-out on the flat platform using particle based modeling and then the parameters such as landmarks and robotic grasping points can be estimated from the garment mesh model. Later, the spread-out garment is picked up by a single robotic manipulator and the 2D garment mesh model is simulated in 3D virtual environment. A dataset of hanging garment can be generated by capturing the depth images of real garment at the robotic platform and also the images of garment mesh model from offline simulation respectively. The synthetic dataset collected from simulation shown the approach performed well and applicable on a different of similar garment. Thus, the category and pose recognition of the garment can be further developed.



GS9-11 Design and Development of Three Arms Transmission Line Inspection Robot

Muhammad Fairuz Abdul Jalal, Khairul Salleh Mohamed Sahari, Ho Ming Fei, Justin Chan Tuck Leong (Universiti Tenaga Nasional, Malaysia)

The high-voltage transmission line had been used primarily for power distribution from power plant or power station to the end users. However, the transmission line is highly prone to damage due to exposure to various thermal - mechanical loading and material degradation. Therefore, periodical inspection on transmission line after prolonged service is needed to prevent any failure before it happens. In this paper, we present a new design of three arms inspection robot for transmission lines. The robot is able to transverse along the line and bypass the in-line obstacles namely the anti-vibration hammers, spacer, strain clamps and others. The design of the inspection robot in term of the robot design and configuration with slotted cam at each arm is presented. The detailed analysis via simulation with respect to the robot stability; kinematic and movement analysis; and power consumption during operation is executed to make sure the proposed design able to do the inspection without any unexpected difficulties. Later, the lab testing on the developed prototype is done for feasibility study and validation.



GS10 Others (4)

GS10-1 A review on fundamental advancements of black hole algorithm

Zuwairie Ibrahim, Suad Khairi Mohammed, Norazian Subari
(Universiti Malaysia Pahang, Malaysia)

Nor Azlina Ab Aziz, Nor Hidayati Abdul Aziz(Multimedia University, Malaysia)

Tasiransurini Ab Rahman(Universiti Tun Hussein Onn Malaysia, Malaysia)

Asrul Adam, Zulkifli Md Yusof(Universiti Malaysia Pahang, Malaysia)

Mohd Ibrahim Shapiai

(Malaysia Japan International Institute of Technology, Universiti Teknologi Malaysia, Malaysia)

Norrima Mokhtar(University of Malaya, Malaysia)

In recent years, there is a growing interest in the design and development of nature-inspired optimization algorithms. One of the algorithms is black hole algorithm (BHA), which is inspired by the black hole in general relativity and cosmology. This paper reports a review of the BHA. This review emphasizes on the fundamental advancements of BHA. A brief research gap is presented at the end of this paper.

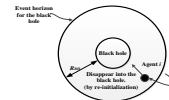


Fig. 1. Illustration of a black hole with its event horizon.

GS10-2 A survey on applications of black hole algorithm

Zuwairie Ibrahim, Suad Khairi Mohammed, Norazian Subari, Asrul Adam, Zulkifli Md Yusof
(Universiti Malaysia Pahang, Malaysia)

Nor Azlina Ab Aziz, Nor Hidayati Abdul Aziz(Multimedia University, Malaysia)

Tasiransurini Ab Rahman(Universiti Tun Hussein Onn Malaysia, Malaysia)

Mohd Ibrahim Shapiai

(Malaysia Japan International Institute of Technology, Universiti Teknologi Malaysia, Malaysia)

Norrima Mokhtar(University of Malaya, Malaysia)

In recent years, there is a growing interest in the design and development of nature-inspired optimization algorithms. One of the algorithms is black hole algorithm (BHA), which is inspired by the black hole in general relativity and cosmology. This paper reports a review of the black hole algorithm (BHA). This survey emphasizes on the applications of BHA.

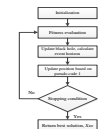


Fig. 1. Flowchart of BHA.

GS10-3 Black hole white hole algorithm with local search

Zuwairie Ibrahim, Suad Khairi Mohammed, Norazian Subari, Asrul Adam, Zulkifli Md Yusof
(Universiti Malaysia Pahang, Malaysia)

Nor Azlina Ab Aziz, Nor Hidayati Abdul Aziz(Multimedia University, Malaysia)

Tasiransurini Ab Rahman(Universiti Tun Hussein Onn Malaysia, Malaysia)

Norrima Mokhtar(University of Malaya, Malaysia)

Black hole algorithm (BHA) is an optimization algorithm inspired by the black hole discovery in relativity theory. Recently, white hole operator, which is based on the opposite of black hole, has been introduced in BHA. In this paper, a local is added in the BHA with white hole operator.

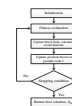


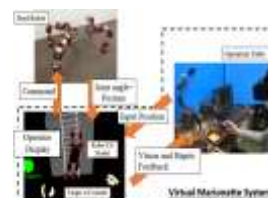
Fig. 1. Flowchart of BHA.

GS10-4 Tele-Operation of a Legged Robot by a Virtual Marionette System - First report: The first prototype and the usefulness of the reaching task-

Noritaka Sato, Yasuhiko Sawai, Ryo Asami, Makoto Kitani, Yoshifumi Morita
(Nagoya Institute of Technology, Japan),

Tomofumi Fujiwara, Takahiro Endo, Fumitoshi Matsuno (Kyoto University, Japan)

In general, a gamepad and images from a camera mounted on a robot are used for the teleoperation of a rescue robot. However, teleoperation is difficult for inexperienced users because the relationship between the user input and robot motion is not always intuitive. Therefore, we have developed an interface in which the operator operates a robot as if touching it directly in a virtual 3D space. In our previous research, we developed a virtual direct teleoperation system for a tracked rescue robot. In this study, we adapt our system to inputting target positions of a hand or a foot of a legged rescue robot. We verify the effectiveness of the proposed system by comparison with the conventional method which is used by the team participating in the DARPA Robotics Challenge.



AUTHORS INDEX

Notation of session name

PS: Plenary Session IS: Invited Session, OS: Organized Session, GS: General Session,

Note: 33/90 = (page no. in Technical Paper Index) / (page no. in Abstracts)

[A]				Alishev	Neil	GS9-3	29/100
Ab. Aziz	Nor Azlina	GS5-3	34/94	Amarasinghe		OS14-3	33/70
		GS10-1	40/104			OS14-4	33/70
		GS10-2	40/104			OS14-5	33/71
		GS10-3	40/104			OS14-6	33/71
Ab Rahman	Tasiransurini	GS10-1	40/104	Ampant	Udomlux	GS3-2	32/91
		GS10-2	40/104	An	Jongwoo	OS2-2	32/46
		GS10-3	40/104	An	Lingran	OS16-2	25/76
Abd Kader	Khusairy	GS8-4	19/99			OS16-5	25/76
Abdul Aziz	Nor Hidayati	GS5-3	34/94			OS16-7	26/77
		GS10-1	40/104	Ando	Kazuaki	OS6-1	38/53
		GS10-2	40/104			OS6-2	38/53
		GS10-3	40/104	Andreev	Andrey	OS7-4	21/55
Abdul Jalal	Muhammad	GS9-11	30/103	Andreychuk	Anton	OS7-1	21/54
	Fairuz			Anshi	Ryohei	GS2-2	27/89
Abe	Akinori	OS17-4	36/79	Aoki	Kenji	OS1-1	39/44
Abramskiy	Mikhail	GS9-5	29/101	Arai	Takafumi	OS21-2	18/85
Aburada	Kentaro	OS12-3	31/67	Asada	Taro	OS13-1	37/67
		OS12-4	31/67			OS13-2	37/68
Adam	Asrul	GS10-1	40/104			OS13-3	38/68
		GS10-2	40/104	Asai	Fumio	GS3-5	32/92
		GS10-3	40/104	Asami	Ryo	GS10-4	40/105
Afanasyev	Ilya	GS9-1	29/99	Ashida	Yoichiro	OS3-3	22/48
Ahn Ahmed	Syed Faiz	GS8-4	19/99			OS3-6	22/49
Ahn	Jonghyun	OS20-2	34/83	Azhar	H.M.Sohaib	GS8-5	19/99
Aihara	Kazuyuki	OS9-1	24/62				
		OS9-6	24/64	[B]			
Alemán Carreón	Elisa Claire	OS5-3	23/52	Bae	Jaehue	OS22-3	31/87
Ali	Athat	GS8-4	19/99	Basnayake		OS14-3	33/70

		OS14-6	33/71			OS16-1	25/75
Bian	Ce	OS16-1	25/75			OS16-2	25/76
Bian	Ce	OS16-3	25/76			OS16-3	25/76
		OS16-4	25/76			OS16-4	25/76
		OS16-5	25/76			OS16-5	25/76
		OS16-6	25/77			OS16-6	25/77
		OS16-9	26/77			OS16-7	26/77
Bokovoy	Andrey	OS7-1	21/54			OS16-8	26/77
		OS7-3	21/55			OS16-9	26/77
Boonyaprapasorn	Arsit	GS7-1	34/97	Dayananda		OS14-5	33/71
Bruyant	Alexandre	GS3-1	32/91	Deguchi	Chikashi	OS1-3	39/44
				Desa	Hazry	GS8-4	19/99
				De Silva		OS14-4	33/70
[C]				Duan	Lunqin	GS8-2	19/98
Chaicherdkiat	Poommitol	GS1-2	30/88				
Chan	Tuck Leong,	GS9-11	30/103				
	Justin			[E]			
Chang	Cheng-Jui	OS8-11	20/62	Egunov	Vitaly	OS7-2	21/54
Chang	Shengbiao	OS16-1	25/75	Elizarov	Alexander	GS6-4	37/96
		OS16-4	25/76			GS9-2	29/100
		OS16-9	26/77	Endo	Masaki	OS5-4	23/52
Chaturanga		OS14-6	33/71	Endo	Takahiro	GS10-4	40/105
Chen	Chia-Hsiu	OS8-7	20/60	Erokhin	Victor	GS9-2	29/100
Chen	Feng	GS4-2	26/93				
Chen	Xiaoyan	OS15-8	25/74	[F]			
		OS15-9	25/74	Fei	Ho Ming	GS9-11	30/103
Chikushi	Shota	OS21-3	19/85	Fernando		OS14-6	33/71
Chin	Takaki	GS7-3	34/97	Fu	Dongmei	OS18-4	30/81
Choi	Jiwook	OS2-2	32/46	Fu	Ziyi	OS18-1	30/80
Chuang	Kuang-Wei	OS8-6	20/60			OS19-1	22/81
Chumkamon	Sakmongkon	GS2-2	27/89			GS3-4	32/92
Collet	Pierre	GS3-1	32/91	Fujinaga	Takuya	OS21-5	19/86
Cui	Mengchen	OS18-4	30/81	Fujita	Kohki	GS4-4	26/93
				Fujiwara	Tomofumi	GS10-4	40/105
				Fukushima	Hiroki	OS17-1	36/78
[D]				Fukushima	Mihoko	OS1-3	39/44
Dai	Fengzhi	OS15-9	25/74				

						GS2-4	27/90
						GS2-5	27/90
						GS6-1	37/95
[G]							
G. Helander	M.	IS-6	28/43	Hayashi	Yuki	OS17-6	37/79
Gabdullin	Aidar	GS9-1	29/99	He	Chang-Jhu	OS8-10	20/61
Gao	Caixia	OS18-1	30/80	Henmi	Tomohiro	OS3-7	23/49
Gautam	Ashish	OS9-5	24/63	Hiraoka	Toru	OS5-1	23/51
Ge	Yong	OS1-5	39/45			OS5-2	23/52
Gerasimov	Yuriy	GS9-2	29/100			OS5-3	23/52
		GS9-3	29/100	Hirota	Masaharu	OS5-1	23/51
		GS9-6	29/101			OS5-3	23/52
Gopura		GS2-1	27/89			OS5-4	23/52
		GS2-6	27/90	Honda	Keita	GS8-1	19/98
Gorobtsov	Alexander	OS7-4	21/55	Hori	Masamichi	OS1-1	39/44
Guo	Jr Hung	OS8-2	20/58			OS1-3	39/44
		OS8-4	20/59			OS1-4	39/45
		OS8-6	20/60	Horikawa	Yo	OS6-1	38/53
Guo	Zhiqiang	OS15-4	24/73			OS6-2	38/53
		OS15-5	24/73			OS6-3	38/53
						OS6-4	38/54
				Hou	Yew Cheong	GS9-10	30/103
[H]							
Han	Fengze	OS15-8	25/74	Hou	Yong	OS16-9	26/77
Han	Sumin	OS19-2	22/82	Houseago	Charlie	GS6-5	37/96
Harada	Kazumasa	OS20-1	34/83	Hsia	Kuo-Hsien	OS8-4	20/59
Harada	Kensuke	OS10-1	33/64			OS8-5	20/59
		OS10-2	33/64	Hsu	Shu-Fang	GS9-9	29/102
Hattori	Tetsuo	OS6-1	38/53	Hsu	Wen-Ting	OS8-9	20/61
		OS6-2	38/53	Hu	Qiongqiong	OS1-5	39/45
		OS6-3	38/53	Hung	Chung-Wen	OS8-1	20/57
		OS6-4	38/54			OS8-9	20/61
Hayakawa	Takuya	GS5-1	34/94				
Hayashi	Eiji	GS1-2	30/88	[I]			
		GS1-3	30/88	Ibrahim	Zuwaitie	GS5-3	34/94
		GS2-2	27/89			GS10-1	40/104
		GS2-3	27/89			GS10-2	40/104

		GS10-3	40/104	Jeon	Hyun Cheol	OS22-1	31/86
Iida	Fumiya	GS6-5	37/96	Jia	Hongyan	OS15-4	24/73
Ikeda	Satoshi	OS1-1	39/44			OS15-5	24/73
		OS1-2	39/44	Jia	Yingmin	OS18-3	30/81
Iiboshi	Atsushi	OS1-3	39/44			OS19-3	22/82
		OS1-4	39/45			OS19-5	22/83
Imai	Shinichi	OS11-2	39/65	Jiang	Jhen-Gu	OS8-1	20/57
Imai	Yoshiro	OS6-1	38/53			OS8-9	20/61
		OS6-2	38/53	Jin	Xia	OS16-2	25/76
		OS6-3	38/53			OS16-5	25/76
		OS6-4	38/54			OS16-7	26/77
Indelman	Vadim	OS7-5	21/56	Jitkongchuen	Duangjai	GS3-2	32/91
Inukai	Toshihiro	OS15-11	25/75	Jitviriyaya	Wisana	GS1-2	30/88
Iriyama	Yosuke	OS1-4	39/45			GS2-2	27/89
Ishii	Kazuo	OS20-2	34/83	Johnson	Jeffrey	PS-1	18/41
		OS20-3	35/84	Joyo	M. Kamran	GS8-4	19/99
		OS20-4	35/84	Jung	Min Gyu	OS2-1	32/45
		OS20-5	35/84				
		OS21-3	19/85				
				[K]			
		OS21-4	19/86	Kachalov	Andrey	OS7-2	21/54
		OS21-5	19/86	Kai	Yuki	OS1-4	39/45
Ishikawa	Hiroshi	OS5-4	23/52	Kamei	Keiji	OS21-2	18/85
Ito	Takao	OS1-1	39/44	Kang	Hosun	OS2-2	32/46
		OS1-2	39/44			OS2-3	32/46
		OS5-1	23/51	Kang	Qijia	OS16-1	25/75
		OS5-3	23/52			OS16-4	25/76
Ito	Takuya	OS17-5	36/79	Kaorapapaong	Chatdanai	GS7-2	34/97
Ito	Tsutomu	OS1-1	39/44	Katayama	Tetsuro	OS12-1	31/66
		OS1-2	39/44			OS12-3	31/67
Ivanou	Mikhail	GS9-1	29/99			OS12-4	31/67
				Kato	Ryota	OS13-1	37/67
				Kawada	Kazuo	OS11-3	39/65
				Kawakami	Yusuke	OS6-1	38/53
Jayawardena		GS2-1	27/89			OS6-2	38/53
Jeannin-Girardon	Anne	GS3-1	32/91			OS6-3	38/53
Jee	Gyu-in	OS22-2	31/87				

		OS6-4	38/54			GS5-2	34/94
Kawano	Hiomichi	OS6-3	38/53	Kugurakova	Vlada	OS7-6	21/56
		OS6-4	38/54			GS6-3	37/95
Khafizov	Murad	GS6-4	37/96			GS6-4	37/96
Khalid	Halimahtun	IS-6	28/43	Kumano	Minoru	OS5-1	23/51
		GS6-2	37/95			OS5-2	23/52
Khan	Sheroz	GS8-4	19/99			OS5-3	23/52
Khoyratee	Farad	OS9-3	24/63				
Kim	Ki-seo	OS2-6	32/47	Kuremoto	Takashi	GS4-3	26/93
Kim	Dohyun	OS2-4	32/46			GS4-4	26/93
Kim	Heeje	OS2-4	32/46	Kurokawa	Ryo	OS3-2	22/48
		OS2-5	32/47				
Kim	Kyuwon	OS22-2	31/87	[L]			
Kim	Min-soo	OS2-5	32/47	Lai	Li-Chun	OS8-3	20/58
Kimura	Kenji	OS21-3	19/85	Lavrenov	Roman	OS7-5	21/56
Kinoshita	Kento	OS3-8	23/50			OS7-7	21/56
Kinoshita	Takuya	OS3-3	22/48			GS9-3	29/100
Kita	Yoshihiro	OS12-3	31/67			GS9-7	29/101
		OS12-4	31/67	Lee	Byoungjin	OS22-3	31/87
Kitani	Makoto	GS10-4	40/105	Lee	Jangmyung	OS2-2	32/46
Ko	Chia-Nan	OS8-3	20/58			OS2-3	32/46
Kobayashi	Jun	GS5-1	34/94			OS2-6	32/47
Kobayashi	Kyoichiro	GS4-3	26/93	Lee	Min Cheol	OS2-1	32/45
Kodama	Yukari	OS1-3	39/44	Lee	Nahyun	OS2-3	32/46
		OS1-4	39/45	Leleu	Timothée	OS9-6	24/64
Kogi	Daichi	OS13-2	37/68	Levi	Timothée	OS9-1	24/62
Kohno	Takashi	OS9-1	24/62			OS9-3	24/63
		OS9-2	24/62			OS9-6	24/64
		OS9-4	24/63	Li	Binghe	OS21-5	19/86
		OS9-5	24/63	Li	Hongbing	OS7-8	21/57
		OS9-6	24/64			GS9-4	29/100
Konishi	Yasuo	OS3-2	22/48	Li	Ji-Hua	OS8-2	20/58
Koyama	Yoshihide	OS6-3	38/53	Li	Jung-Shian	OS8-7	20/60
		OS6-4	38/54			OS8-8	20/61
Kubo	Masao	GS3-3	32/91			OS8-11	20/62

Li	Meili	OS16-3	25/76	Magid	Evgeni	OS7-5	21/56
Li	Shang-Hui	GS9-8	29/102			OS7-8	21/57
Li	Shudong	OS15-8	25/74			GS9-2	29/100
Li	Yang	OS15-10	25/75			GS9-4	29/100
Li	Yi	OS19-5	22/83			GS9-5	29/101
Li	Yiyang	OS1-5	39/45			GS9-6	29/101
Lin	Jun-Nong	OS8-5	20/59	Maiguma	Mizuki	OS14-1	33/69
Lin	Xiaokun	OS16-8	26/77	Mao	Runhua	OS16-1	25/75
Liu	Chuan-Gang	OS8-11	20/62			OS16-3	25/76
Liu	Shangzheng	OS18-2	30/80			OS16-4	25/76
Liu	Shilong	OS15-6	24/73			OS16-6	25/77
Liu	I-Hsien	OS8-7	20/60			OS16-9	26/77
		OS8-8	20/61	Mao	Wei-Lung	OS8-1	20/57
		OS8-11	20/62	Man	Haifang	OS16-6	25/77
Liu	Qing	OS15-10	25/75	Mann		GS2-1	27/89
Liu	Wei	GS8-2	19/98	Markov	Alexey	OS7-4	21/55
Liu	Ze	OS15-9	25/74	Martinez-Garcia	Edgar A.	OS7-8	21/57
Lu	Kuan-Chu	OS8-8	20/61	Masuda	Koji	OS20-4	35/84
Lund	Henrik	IS-1	18/42	Matsui	Hideto	OS11-2	39/65
	Hautop			Matsunaga	Miki	OS3-1	22/47
		IS-2	18/42	Matsuno	Fumitoshi	GS10-4	40/105
Luo	Haibao	GS4-1	26/92	Mikami	Kaito	GS3-5	32/92
Lushnikov	Alexei	OS7-6	21/56	Mitsuhashi	Koshiro	OS1-3	39/44
		GS6-3	37/95			OS1-4	39/45
		GS6-4	37/96	Miyachi	Junpei	OS13-5	38/69
Lv	Zhijian	OS15-2	24/72	Mizumoto	Ikuro	OS3-9	23/50
				Mohammed	Suad Khairi	GS10-1	40/104
	[M]					GS10-2	40/104
Ma	Qinglian	OS1-5	39/45			GS10-3	40/104
Ma	Shuanglong	GS8-2	19/98	Mohamed Sahari	Khairul	GS9-10	30/103
Mabu	Shingo	GS4-3	26/93		Salleh		
		GS4-4	26/93			GS9-11	30/103
Md Yusof	Zulkifli	GS10-1	40/104	Mokhtar	Norrima	GS5-3	34/94
		GS10-2	40/104			GS10-1	40/104
		GS10-3	40/104			GS10-2	40/104

		GS10-3	40/104	Ogata	Takashi	OS17-2	36/78
Moon	Jeong-hwan	OS2-6	32/47			OS17-3	36/78
Mori	Keisuke	OS12-3	31/67			OS17-5	36/79
Mori	Kenta	OS13-3	38/68	Ohnishi	Yoshihiro	OS11-1	39/65
Moriguchi	Yuki	OS11-5	40/66	Ohno	Shuichi	OS3-8	23/50
Morimoto	Shogo	OS12-2	31/66	Okazaki	Naonobu	OS12-3	31/67
Morita	Yoshifumi	GS10-4	40/105			OS12-4	31/67
Mowshowits	Abbe	GS2-3	27/89	Okubo	Yuka	OS3-3	22/48
Mukunoki	Masayuki	OS1-3	39/44	Okuda	Haruhisa	PS-3	28/41
				Olapiriyakul	Sun	GS7-2	34/97
				Onda	Hiromu	OS10-2	33/64
				Ono	Jumpei	OS17-2	36/78
Nagamatsu	Masayasu	OS11-5	40/66	Ono	Michiyoshi	OS21-1	18/85
Nagano	Kaito	GS2-4	27/90	Ouyang	Yuxing	OS16-1	25/75
Nagata	Kazuyuki	OS10-1	33/64			OS16-2	25/76
Nakagawa	Masato	PS-2	28/41			OS16-3	25/76
Nakamoto	Masayoshi	OS3-1	22/47			OS16-4	25/76
Nakamura	Akira	OS10-1	33/64			OS16-5	25/76
Nakamura,	Go	GS7-3	34/97			OS16-6	25/77
Nanami	Takuya	OS9-2	24/62			OS16-7	26/77
Nishida	Yuya	OS20-2	34/83			OS16-9	26/77
		OS20-3	35/84				
		OS20-4	35/84				
Nishimura	Shiori	OS5-2	23/52				
				[P]			
Niu	Hong	OS15-1	24/72	Pagliarini	Luigi	IS-2	18/42
Nizamutdinov	Artur	OS7-6	21/56	Park	Chan Gook	OS22-1	31/86
		GS6-3	37/95	Park	Gwang Soo	OS22-3	31/87
		GS6-4	37/95	Park	Sun Oh	OS2-1	32/45
Nonaka	Hirofumi	OS5-1	23/51	Parrend	Pierre	IS-4	28/43
		OS5-2	23/52			GS3-1	32/91
		OS5-3	23/52	Pei	Wenjing	OS18-3	30/81
Nonaka	Shunta	OS14-2	33/69	Peng	Yizhun	OS15-2	24/72
				Petrosyan	Michail	OS7-2	21/54
				Phung	Nhuhai	GS3-3	32/91
				[O]			
Obayashi	Masanao	GS4-3	26/93	Phunopas	Amornphun	GS2-5	27/90
Oda	Kazuya	OS21-1	18/85	Pragnathilaka		GS2-6	27/90

Pudchuen	Noppadol	GS1-2	30/88			OS1-3	39/44
						OS1-4	39/45
	[Q]					OS1-5	39/45
Qin	Yiqiao	OS16-1	25/75	Sampath		OS14-4	33/70
		OS16-3	25/76	Satdarov	Timur	OS7-6	21/56
		OS16-4	25/76			GS6-3	37/95
		OS16-6	25/77	Sato	Hiroshi	GS3-3	32/91
		OS16-9	26/77	Sato	Noritaka	GS10-4	40/105
				Sato	Takao	OS3-2	22/48
	[R]			Sawai	Yasuhiko	GS10-4	40/105
Rajapakse	R. P. C.	OS6-1	38/53	Sethaput	Thunyaseth	GS7-1	34/97
	Janaka			Sgorbissa	Antonio	GS8-3	19/98
		OS6-2	38/53	Shabalina	Ksenia	OS7-8	21/57
Ramirez	Ixchel G.	OS10-2	33/64	Shapiai	Mohd	GS10-1	40/104
Ranaweera		GS2-1	27/89		Ibrahim		
		GS2-6	27/90			GS10-2	40/104
Recchiuto	Carmine T.	GS8-3	19/98	Shi	Peihao	OS10-2	33/64
Rerkjirattikarn	Pavinee	GS7-2	34/97	Shibanoki	Taro	GS7-3	34/97
Rojas	Juan	OS10-2	33/64	Shimada	Ryouichi	OS13-2	37/68
Rosendo	Andre	GS6-5	37/96			OS13-3	38/68
Roshan		OS14-5	33/71	Shinano	Yuji	IS-5	36/43
Rossi	Ruggero	PS-1	18/41			OS1-2	39/44
				Shiung	Liew Wei	GS6-2	37/95
	[S]			Shvedov	Grigory	GS9-1	29/99
S. Liew	W.	IS-6	28/43	Skorikov	Andrey	OS7-4	21/55
S. Voong	B.	IS-6	28/43	Sneha	Sharma	OS3-5	22/49
Sabirova	Leysan	GS9-5	29/101	Soejima	Yuki	OS20-3	35/84
Safin	Ramil	GS9-7	29/101	Song	Binhu	OS16-9	26/77
Sagitov	Artur	OS7-8	21/57	Song	Yunzhong	OS19-1	22/81
		GS9-4	29/100	Sonoda	Takashi	OS20-2	34/83
		GS9-6	29/101			OS20-3	35/84
Saighi	Sylvain	OS9-3	24/63			OS20-4	35/84
Saito	Keita	OS13-1	37/67	Su	Kuo-Lan	OS8-2	20/58
Sakamoto	Makoto	OS1-1	39/44			OS8-4	20/59
		OS1-2	39/44			OS8-6	20/60

Subari	Norazian	GS10-1	40/104			OS14-2	33/69
		GS10-2	40/104	Tanoue	Satoshi	OS12-4	31/67
		GS10-3	40/104	Tanveer	M. Hassan	GS8-3	19/98
Sung	Sangkyung	OS22-3	31/87	Tarasov	Pavel	OS7-2	21/54
Suzuki	Yasuhiro	OS4-1	26/50			OS7-4	21/55
		OS4-2	26/51	Tian	Xiwen	OS19-3	22/82
		OS4-3	26/51	Tokumitsu	Masahiro	GS3-5	32/92
				Tominaga	Ayumu	GS1-3	30/88
						GS2-3	27/89
[T]							
Tabuse	Masayoshi	OS13-1	37/67	Tominaga	Moeko	OS21-4	19/86
		OS13-2	37/68	Toussaint	Nicolas	GS3-1	32/91
		OS13-3	38/68	Tsoy	Tatyana	GS9-5	29/101
		OS13-4	38/68	Tsuboi	Haruka	OS1-1	39/44
		OS13-5	38/69			OS1-4	39/45
Tadaki	Kotone	OS17-7	37/80	Tsuji	Toshio	GS7-3	34/97
Tahir	Aqeel	GS8-5	24/99	Tsujii	Ryuichi	GS1-1	30/88
Takada	Taku	GS3-5	32/92				
Takagi	Taro	OS3-9	23/50	[U]			
Takagi	Tomohiko	OS12-1	31/66	Uchida	Yasuo	OS1-1	39/44
		OS12-2	31/66	Udayanga		OS14-6	33/71
Takahashi	Masanori	OS3-4	22/48	Ueda	Keita	OS11-4	39/65
Takemura	Yasunori	OS21-1	18/85	Ushio	Masahiro	GS6-1	37/95
		OS21-4	19/86	Utsunomiya	Koshi	OS20-1	34/83
Talanov	Max	GS9-2	29/100				
Tamura	Hiroki	OS14-1	33/69	[V]			
		OS14-2	33/69	Vilanova	Ramon	OS3-2	22/48
Tanaka	Hideyuki	OS11-4	39/65				
Tanaka	Takeshi	OS1-3	39/44	[W]			
Tanaka	Takeshi	OS6-3	38/53	Wakabayashi	Makoto	GS3-5	32/92
		OS6-4	38/54	Wakitani	Shin	OS3-5	22/49
Tanaka	Ken-ichi	PS-3	28/41			OS3-6	22/49
Tange	Atsuya	OS9-4	24/63			OS3-8	23/50
Taniguchi	Rie	OS4-2	26/51	Wan	Weiwei	OS10-2	33/64
Tanikawa	Toyoaki	OS3-7	23/49	Wang	Bo-Min	OS8-9	20/61
Tanno	Koichi	OS14-1	33/69	Wang	Chenxu	GS3-4	32/92

Wang	Fuzhong	OS18-2	30/80	[Y]			
		OS19-1	22/81	Yakovlev	Konstantin	OS7-1	21/54
		OS19-2	22/82			OS7-3	21/55
Wang	Gaoyuan	OS18-4	30/81			GS9-1	29/99
Wang	Jiangfan	OS15-7	25/74	Yamaba	Hisasaki	OS12-3	31/67
Wang	Jiwu	GS4-1	26/92			OS12-4	31/67
		GS4-2	26/93	Yamada	Akira	OS11-2	39/65
Wang	Shanfeng	OS15-4	24/73	Yamada	Takayoshi	GS1-1	30/88
		OS15-5	24/73			GS8-1	19/98
Wang	Xiaoxing	OS15-3	24/72	Yamaguchi	Akihiro	GS5-2	34/94
Wang	Xiuqing	OS15-7	25/74	Yamaguchi	Shingo	GS1-3	30/88
		OS15-10	25/75	Yamaguchi	Yusuke	OS13-4	38/68
Watanabe	Hazuki	OS1-4	39/45	Yamaguti	Yutaka	GS5-2	34/94
Watanabe	Keisuke	OS20-1	34/83	Yamamori	Kunihito	OS1-3	39/44
		OS20-2	34/83	Yamamoto	Hidehiko	GS1-1	30/88
		OS20-5	35/84			GS8-1	19/98
Watanabe	Masaki	GS7-3	34/97	Yamamoto	Toru	OS3-1	22/47
Weerasingha		GS2-6	27/90			OS3-3	22/48
Wei	Baochang	OS16-1	25/75			OS3-5	22/49
		OS16-2	25/76			OS3-6	22/49
		OS16-3	25/76	Yamanobe	Natsuki	OS10-1	33/64
		OS16-4	25/76	Yankina	Elena	OS7-2	21/54
		OS16-6	25/77	Yan	Yujie	OS16-2	25/76
		OS16-9	26/77			OS16-5	25/76
Withanage		GS2-6	27/90			OS16-7	26/77
Wu	Chao	OS18-4	30/81	Yano	Yuiko	OS13-3	38/68
Wu	Hsien-Huang	OS8-1	20/57	Yasukawa	Shinsuke	OS20-2	34/83
		OS8-10	20/61			OS21-5	19/86
Wu	Ming-Guang	OS8-5	20/59	Ye	Zhongyong	OS16-2	25/76
Wu	Tong	OS18-1	30/80			OS16-5	25/76
Wu	Zheng	OS15-3	24/72			OS16-7	26/77
				Yokomichi	Masahiro	OS1-3	39/44
[X]				Yokomori	Takashi	IS-3	36/42
Xue	Wei	OS15-6	24/73	Yoon	Jin Gon	OS2-1	32/45
				Yoshimura	Mamoru	OS1-2	39/44

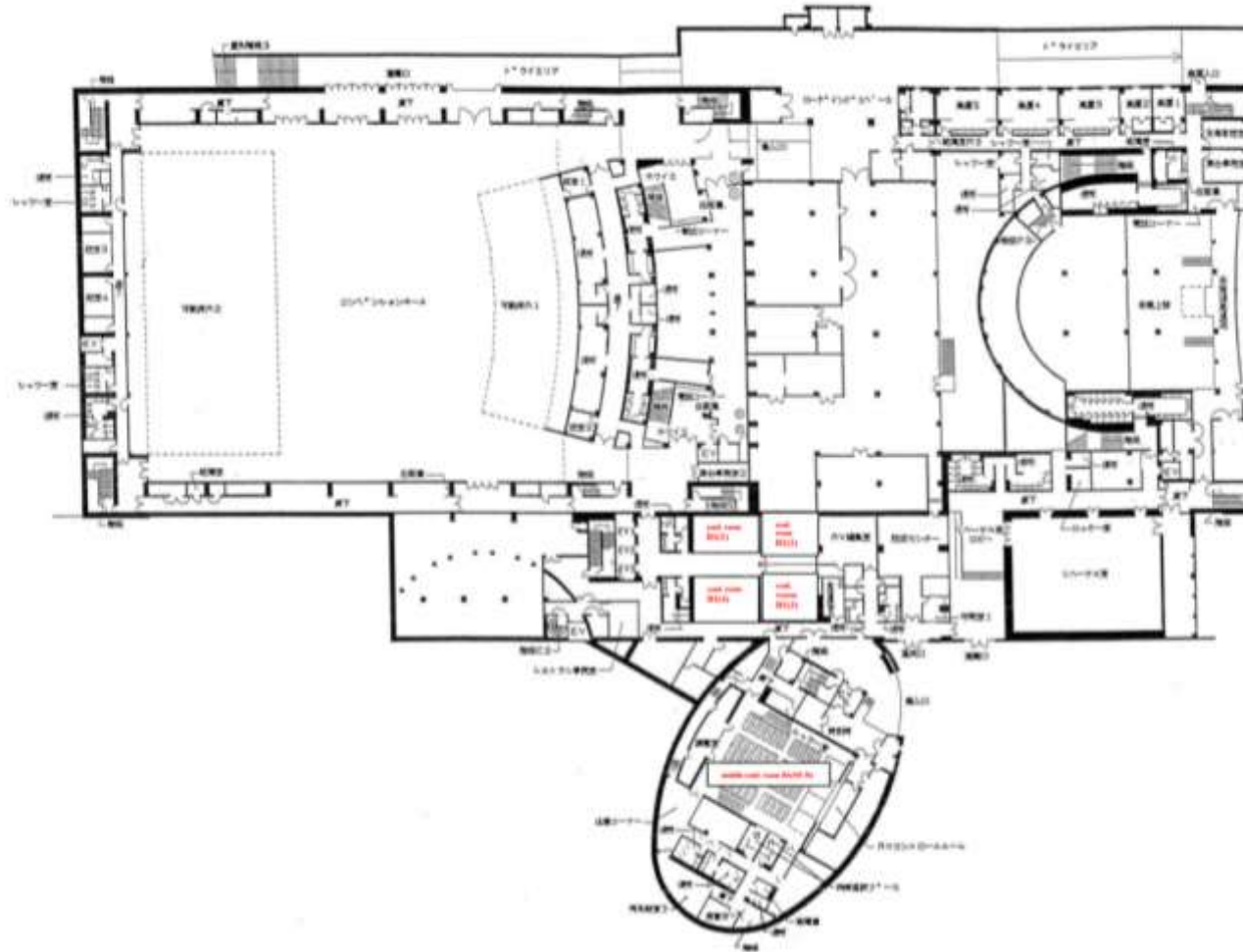
Yoshinaga	Tsunehiro	OS1-1	39/44	Zheng	Zheng	OS19-4	22/82
Yoshitomi	Yasunari	OS13-1	37/67	Zhong	Hong-Jie	OS8-5	20/59
		OS13-2	37/68	Zhou	Yousong	OS19-4	22/82
		OS13-3	38/68	Zhu	Qinghui	OS18-2	30/80
Yu	Jiangtao	GS8-2	19/98	Zhuang	Zh-Yao	OS8-5	20/59
Yu	Pengfei	GS4-1	26/92	Zulkifli		GS5-3	34/94
Yue	Yuanli	OS15-9	25/74	Zykov	Evgenii	GS9-2	29/100

[Z]

Zafar	Sarmad	GS8-5	19/99				
Zakiev	Aufar	OS7-5	21/56				
Zhang	Hongtao	OS16-7	26/77				
Zhang	Mei	OS15-6	24/73				
Zhang	Weicun	OS18-5	31/81				
Zhang	Xinyu	OS16-8	26/77				
Zhang	Yu-an	OS1-1	39/44				
		OS1-4	39/45				
		OS1-5	39/45				
Zhao	Huailin	OS15-3	24/72				
Zhao	Jiming	OS15-10	25/75				

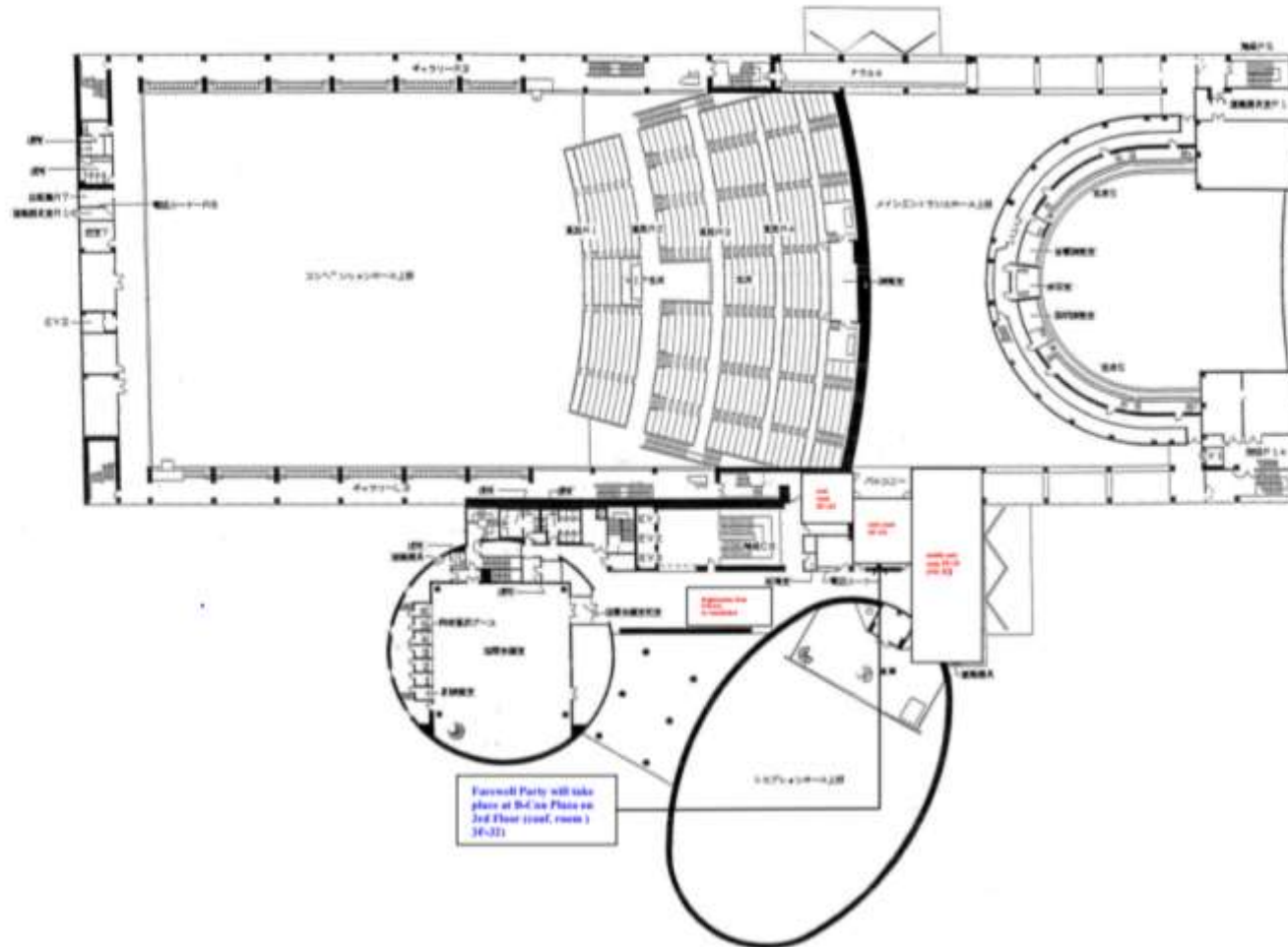
B 1 F

2F

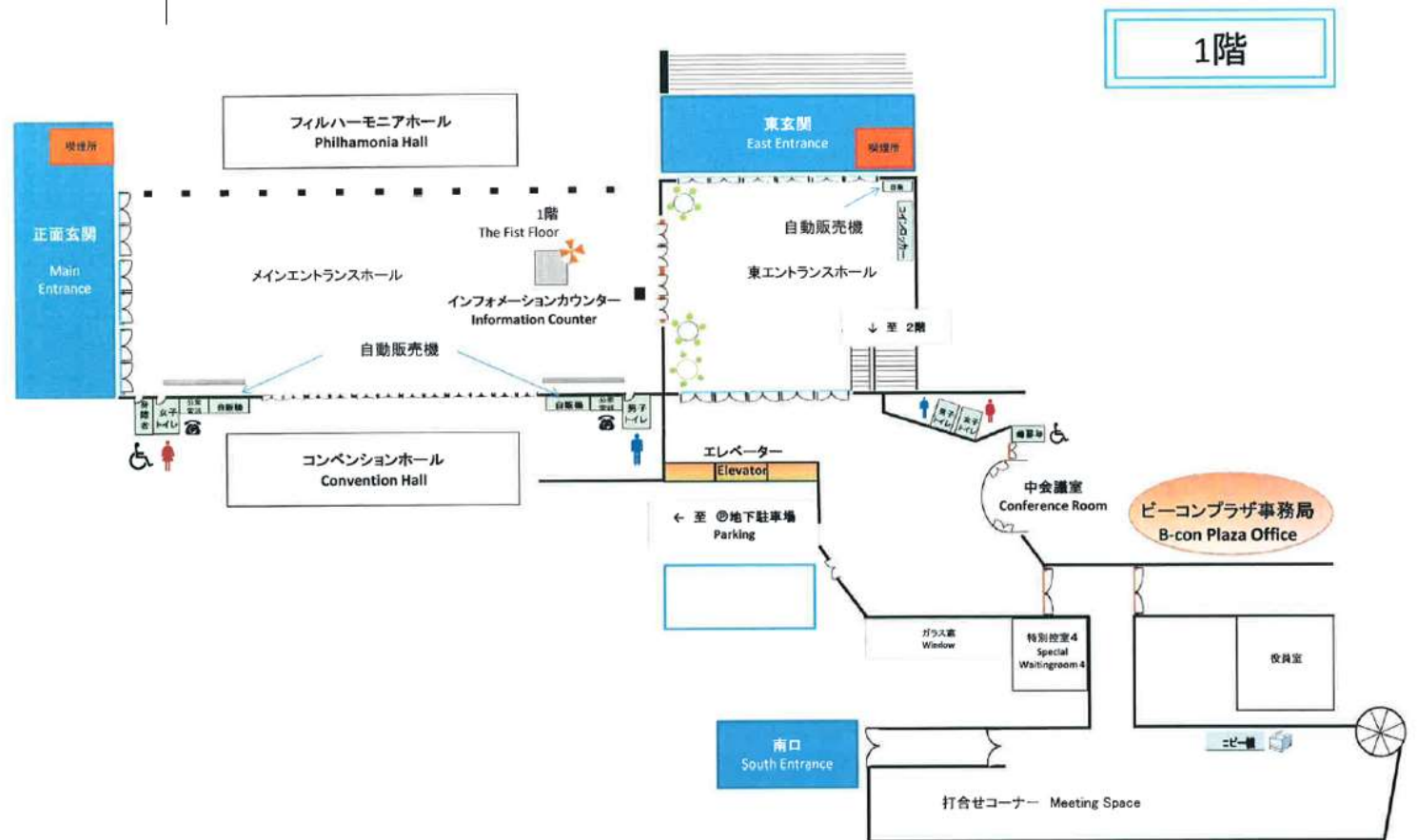


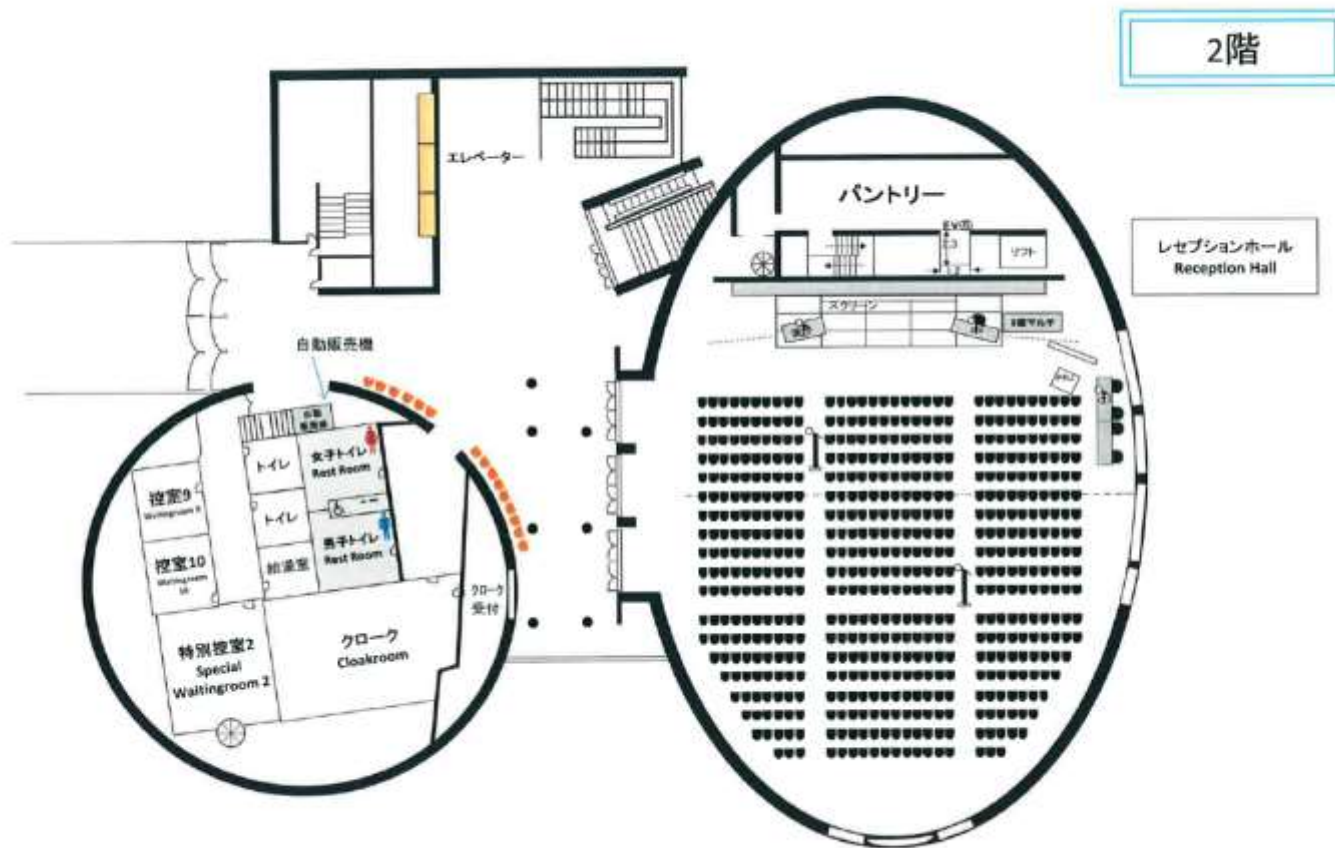
The 2018 International Conference on Artificial Life and Robotics (ICAROB2018), B-Con Plaza, Feb. 1- 4, Beppu, Oita, Japan, 2018

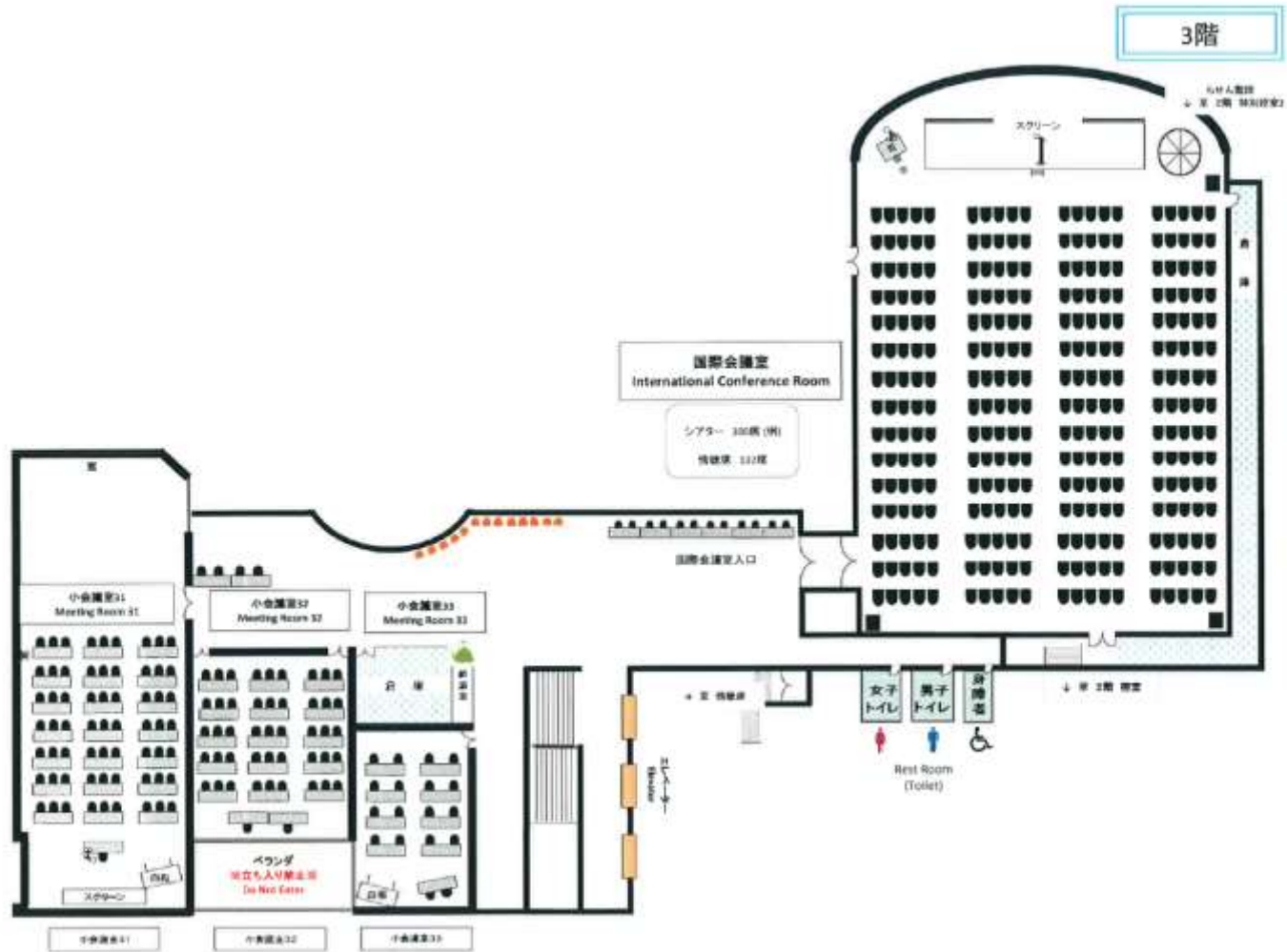
3F



The 2018 International Conference on Artificial Life and Robotics (ICAROB2018), B-Con Plaza, Feb. 1- 4, Beppu, Oita, Japan, 2018







Dynamic Structures for Evolving Tactics and Strategies in Team Robotics

Jeffrey Johnson

*The Open University, Faculty of Science, Technology, Engineering and Mathematics
Milton Keynes, Buckinghamshire, MK7 6AA, UK.*

Ruggero Rossi

*The Open University, Faculty of Science, Technology, Engineering and Mathematics
Milton Keynes, Buckinghamshire, MK7 6AA, UK.*

jeff.johnson@open.ac.uk, ruggero.rossi@open.ac.uk

www.complexityanddesign.org

Abstract

The autonomous robot systems of the future will be teams of robots with complementary specialisms. At any instant robot interactions determine relational structures, and sequences of these structures describe the team dynamics as trajectories through space and time. These structures can be represented in algebraic forms that are realizable as dynamic multilevel data structures within individual robots, as the basis of emergent team data structures. Such formalisms are necessary for robots to learn new individual and collective behaviours. The theory is illustrated by the example of robot soccer where robot interactions create structures and trajectories essential to the evolution of new tactics and strategies in a changing environment.

Keywords: multi-robot systems, robot soccer, hypernetworks, multilevel systems, multilevel dynamics

1. Introduction

We use team robotics as a model for the planning, design, management and control of multilevel complex socio-technical systems including organisations such as hospitals, airlines, and banks, and socio-economic policy at national and international levels. We choose robot soccer as the example for team robotics because it has well-established rules, there are many games to study, and it provides a platform for experimentation and communication.

The great advantage of studying team robotics as an exemplar of complex systems is being able to focus on team interactions without being distracted by the greater complexities of human agents. For example, unless such behaviour is programmed into them, robots will not pick up the ball and run with as William Webb-Ellis is said to have done in 1823, thereby inventing the game of

rugby. Thus team robotics provides a class of complex socio-technical systems that is more complex than many physical systems, but less complex than most social systems. The methodological framework developed here for team robots is intended to be extended and applied to social systems.

The challenge of robot soccer goes back more than twenty years (Kitano et al 1997)¹, and can be simply stated as “By the middle of the 21st century, a team of fully autonomous humanoid robot soccer players shall win a soccer game, complying with the official rules of FIFA, against the winner of the most recent World Cup.” Of many varieties of robot soccer we choose to study the RoboCup simulation league. This enables us to focus on the spatio-temporal structures of the team interactions without being distracted by the considerable engineering challenges of building physical robots.

2. Multidimensional Structure in Robot Soccer

In the 1970s Atkin proposed analysing the relational structure of chess with his methodology of Q-analysis². Atkin studied the relations between the pieces and the squares of the board. *E.g.*, in Fig. 1(a) the black rook, black king and white knight form a structure called a *knight fork* while in Fig. 1(b) they do not. However the configuration in Fig. 1(b) is a *precursor* to the knight fork, and this plays a part on the evolving structure of the game. Although not a knight fork itself, unless black moves to prevent it, the white knight can move to form the knight fork configuration of Fig. 1(a).



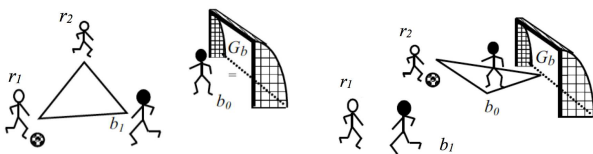
(a) a knight fork in chess (b) a knight fork precursor

Fig. 1. Structure in the game of chess

In 1979 Gould and Gatrell⁴ suggested that Atkin’s method could be applied to soccer analysing the 1977 Football Association Cup Final in the UK. In 1999 Johnson suggested applying the method to robot soccer⁵ and it was further developed by Johnson and Iravani⁶ using Johnson’s theory of hypernetworks⁷. Recently Ramos *et al* showed how the hypernetwork approach can be applied in sports science⁸.

At the heart of the hypernetwork methodology is the fact that in most complex systems the relationships of interest are not just between two elements but can be between $n > 2$ elements. This is illustrated in Fig. 2.

The ‘defender’s dilemma’ (Fig. 2(a)) involves *three* players – two red team players and a blue team player. This can be written as $\langle r_1, r_2, b_1 \rangle$ which generalises the notation of network edge. In fact this structure could be written as three binary relations $\langle r_1, r_2 \rangle + \langle r_1, b_1 \rangle + \langle r_2, b_1 \rangle$ but this would be a poor representation because the dilemma involves all the players at once, not just a combination of binary relations.



(a) The defender’s dilemma (b) The goalkeeper’s dilemma

Fig. 2. n -ary relation structures in soccer (from ⁶)

Fig 2(b) shows the *goalkeeper’s dilemma* as a 4-ary relation $\langle r_2, b_0, G_b, ball \rangle$ which, again, is not just a combination of 2-ary relations (G_b is the blue goal). Apart from the need to generalise networks to higher dimensional edges (which are called *simplices*) another essential generalisation of network theory is to include the relation symbol in the notation. Thus the defenders dilemma can be better represented by the notation

$$\langle r_1, r_2, b_1, ball ; R_{defenders_dilemma} \rangle$$

which allows the relational structure to be discriminated from other 4-ary relations on these elements – of which there may be many in a soccer match. A set of n elements with and n -ary relation between them is called a *hypersimplex*. A set of hypersimplices is called a *hypernetwork*⁶.

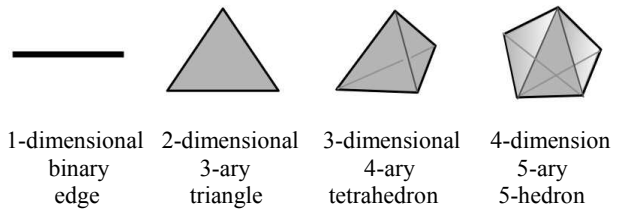
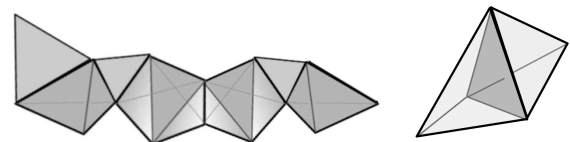


Fig. 3. Hypersimplices as multidimensional polyhedra

Fig. 3(a). shows how the binary (2-ary) relations of networks can be generalised. A 3-ary relation between three players can be represented by a triangle with three vertices; a 4-ary relation between four players can be represented by a tetrahedron with four vertices; a 5-ary relation between five players can be represented by a multidimensional polyhedron with five vertices, and so.

Fig. 4 shows that hypersimplices can have higher dimensional connectivities, *e.g.* in Fig 4(a) the tetrahedra and triangles share edges, or 1-dimensional connections. Figure 4(b) shows how two tetrahedra can be connected through a 2-dimensional triangular face. In general simplices can be connected through multi-dimensional faces, generalising network connectivity through single vertices. This provides new kind of connectivity structure with potential for exploitation in robot soccer.



(a) (b)

Fig. 4 Multidimensional connectivity between hypersimplices

In soccer three kinds of *neighbourhood structures* can be identified:

- (i) a player *has possession* of the ball
- (ii) a player *dribbles* the ball
- (iii) a player *tackles* an opponent

The first of these is characterised by a relation between the player and the ball, $\langle \text{player, ball; } R_{\text{possession; } z, t} \rangle$.

The symbol t denotes time. In the simulation version of robot soccer in this paper the game lasts for 6,000 ticks of the clock, notionally 10 minutes at 10 ticks per second. Let $\langle \text{player, ball; } R_{\text{possession; } z, t} \rangle$ be called a *possession point*. The symbol z represents the *position* of the possession point. At its simplest we could write $z = (x_{\text{player}}, y_{\text{player}}, x_{\text{ball}}, y_{\text{ball}})$. Thus the symbols z and t represent the space-time structure of the robot soccer dynamics.

The second structure, dribbling the ball, can be denoted as a sequence of possession points involving just one player $\langle \langle \text{player, ball; } R_{\text{possession; } z, t} \rangle, \langle \text{player, ball; } R_{\text{possession; } z, t'} \rangle; \langle \text{player, ball; } R_{\text{possession; } z, t''} \rangle; \dots; R_{\text{dribble}} \rangle$.

The third structure is a relation between members of opposite teams, r in the ‘red’ team and b in the ‘blue’ team, denoted $\langle \langle r, \text{ball; } R_{\text{possession; } z, t} \rangle, \langle b, \text{ball; } R_{\text{possession; } z, t'} \rangle; R_{\text{tackle}} \rangle$.

Another fundamental structure in robot soccer is

- (iv) a player passes the ball to a team-mate

This structure can be characterised as $\langle \langle \text{player, ball; } R_{\text{possession; } z, t} \rangle, \langle \text{player}', \text{ball; } R_{\text{possession; } z, t'} \rangle; R_{\text{pass}} \rangle$. Let this be called a *pass structure*.

3. Multilevel Systems

This structures (iii) and (iv) in the previous section are interesting because they are built on relations between two possession points, *i.e.* they are structures formed from more elementary structures. If the players and ball are said to be elements at *Level N*, a structure such as a possession point exists at *Level N+1*, and a pass or a tackle exists at *Level N+2*. A multilevel representation is essential for soccer because, as will be illustrated, the game is one of players trying to create ‘good’ multilevel structures and trying to destroy ‘bad’ multilevel structures.

The RoboCup simulation league soccer games that will be used for illustration last for 6,000 ticks of the clock (10 minutes if ten ticks represent one second). Although it would be possible to provide information about the whole game, *e.g.* the percentage time each team has possession, chunks of time naturally occur over intervals as short as a hundred ticks. Fig. 5 illustrates how the 6,000 ticks of a soccer game can be structured by possession between the red Gliders’ team and the blue CYRUS team.

The red rectangles represent periods when the red players are closest to the ball. For example, the period 0 – 170 is controlled by the red team at the kick-off and the period 1204 – 1346 is controlled by the blue team. The pink (cyan) line at the beginning indicates that the ball is not moving, *i.e.* the red (blue) team is taking a long time to initiate play. The solid red (blue) rectangles are periods when red (blue) is in direct possession. The white gaps at the bottom are periods when neither red nor blue players are close enough to the ball to be in possession but, in this case, the red (blue) team controls the ball. The black lines show that the ball is out of play.

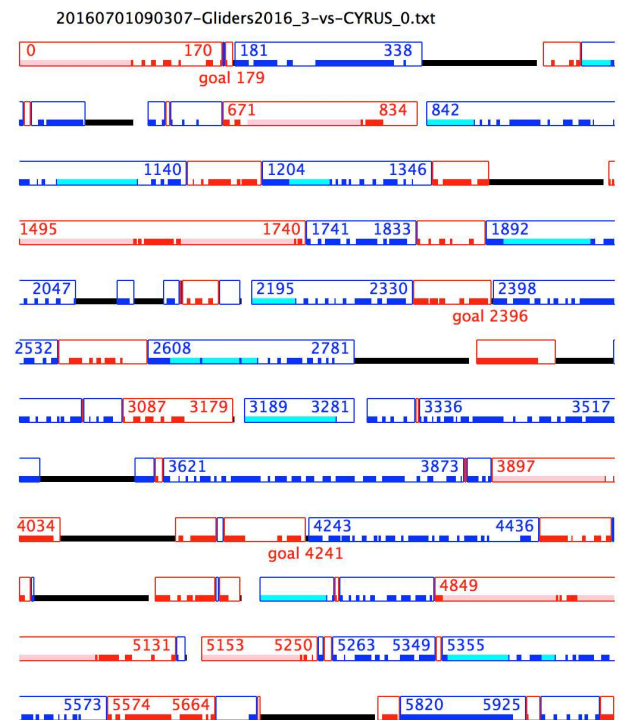


Fig. 5. The temporal possession structure in robot soccer

4. An illustrative Example

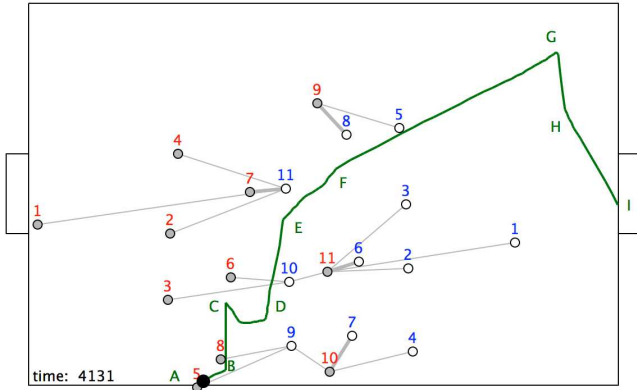


Fig. 6. A soccer ball trajectory beginning at time 4131,

Fig. 6 shows a green-coloured trajectory for the ball between a throw-in at A and a goal being scored at I. The red team has players denoted r_1, r_2, r_3, \dots , and attacks the goal on the right. The blue team has players denoted b_1, b_2, b_3, \dots , and attacks the goal on the left. The trajectory has discernable parts beginning with AB where r_5 takes the throw-in to r_8 .

Let R_{pass} be the *passing relation* where $\langle r_5, r_8; R_{pass} \rangle$ means that r_5 passes to r_8 , and $\langle r_5, r_8; z; t = 4131; R_p \rangle$ means that r_5 passes to r_8 at time $t = 4132$.

The *closest opponent* relation, $R_{closest}$, between the players at time 4131 is shown by thin grey lines. A thick grey line between players shows that they are *mutually closest* to each other under the relation $R_{mutually_closest}$. The closest opponent relation here results in four connected components:

R_c components at time $t = 4132$

- C1 $\langle r_1, r_2, r_4, r_7, b_{11}; z; t; R_{closest} \rangle$
- C2 $\langle r_3, r_6, r_{11}, b_1, b_2, b_3, b_6, b_{10}; z; t; R_{closest} \rangle$
- C3 $\langle r_5, r_8, r_{10}, b_4, b_7, b_9; z; t; R_{closest} \rangle$
- C4 $\langle r_9, b_5, b_8; R_{closest} \rangle$

The fundamental hypothesis is that structures such as these may be predisposed to good or bad outcomes for one or other team. In soccer the ultimate objective is to score goals, but usually goals only emerge at the end of a sequence of ‘good’ discrete structures such as that illustrated by the ball trajectory in Figure 6. The challenge is to be able to recognise structures as being ‘good’ or ‘bad’ and to move so that ‘good’ structures emerge.

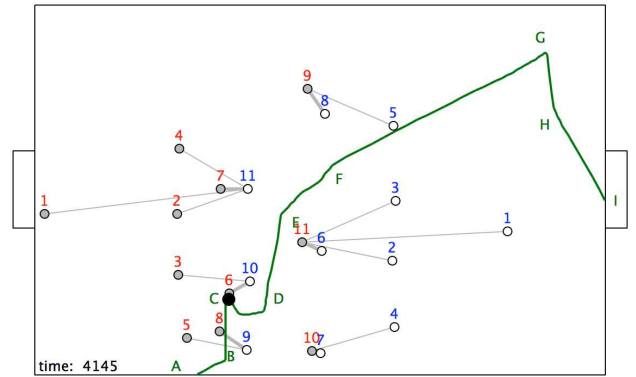


Fig. 7. The ball position at time 4145.

From Figures 6 and 7 it can be seen that the structural change between $t = 4131$ and $t = 4145$ can be summarised as follows.

Time $t = 4145$ components

- C1 $\rightarrow \langle r_1, r_2, r_4, r_7, b_{11}; R_c \rangle$
- C2 $\rightarrow \langle r_3, r_6, b_{10}; R_c \rangle + \langle r_{11}, b_1, b_2, b_3, b_6; R_c \rangle$
- C3 $\rightarrow \langle r_5, r_8, b_9; R_c \rangle + \langle r_{10}, b_4, b_7; R_c \rangle$
- C4 $\rightarrow \langle r_9, b_8; R_{mc} \rangle$

As can be seen two of the components, C1 and C4, remain unchanged while the two closest to the ball, C2 and C3, break into substructures.

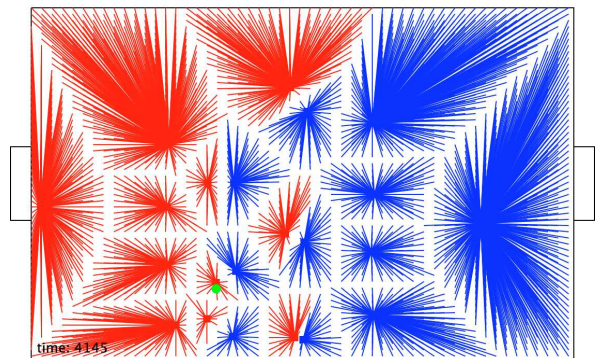


Fig. 8. The pitch possession structure at $t = 4145$

Figure 8 shows the ‘closest to’ relation between the players and small areas of the pitch. At first sight this structure suggests that the red and blue teams have comparable domination of the pitch with the blue team controlling more of it.

However, as Fig. 9 shows player r_6 has enabled new structures to emerge by dribbling the ball from C to D. During this time the configuration $\langle r_1, r_2, r_4, r_7, b_{11}; R_c \rangle$ has changed, with b_{11} moving to the left and r_7 moving to the right. This structural change is bad for blue since r_7 now controls more space (Fig. 10), enabling r_6 to pass the ball to it at E.

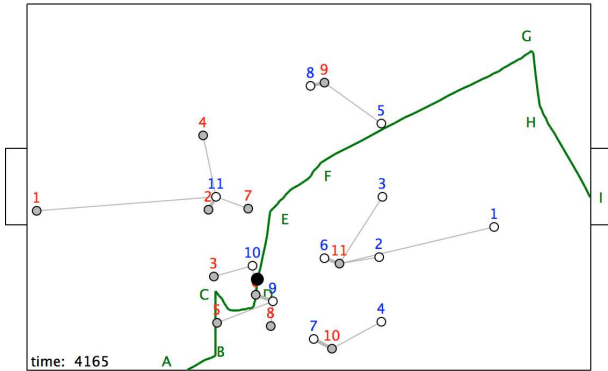


Fig. 9. The position at $t = 4165$

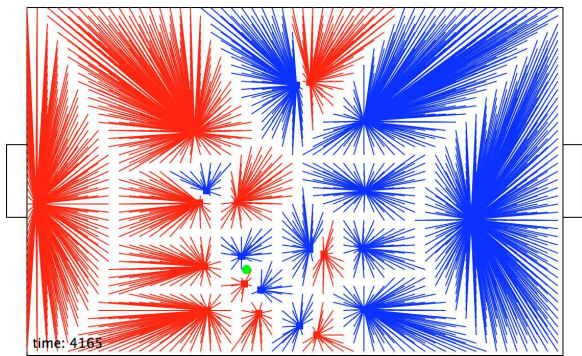


Fig. 10. The pitch possession structure at $t = 4165$

Following this pass, r_7 dribbles the ball to F (Fig. 11). During this time the structure $\langle r_9, b_5, b_8; R_c \rangle$ has changed with r_9 becoming closest to its target goal and b_5 moving upwards – a very bad structure for blue!

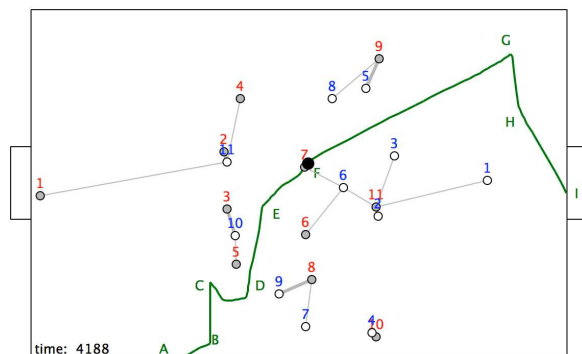


Fig. 11. The position at $t = 4188$

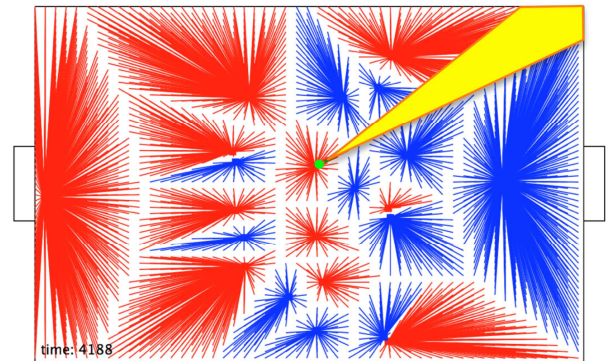


Fig. 12. The pitch-possession structure at $t = 4188$

By moving in this way the blue team has allowed a 'corridor' to emerge, shown as a yellow triangle in Fig. 12. This provides a space for the ball to be passed into an area controlled by r_9 . As shown in Fig. 13, r_7 takes this opportunity and passes the ball to r_9 at G.

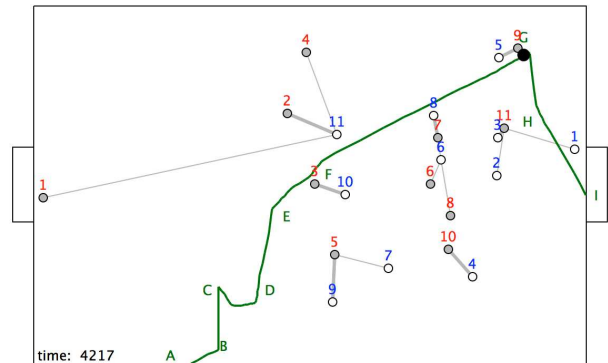


Fig. 13. The position at $t = 4217$

This involves r_9 moving a considerable distance, but note too that r_{11} has broken free from its component at the centre of the pitch and has created space in front of the goal, connected to the space occupied by r_9 and the ball.

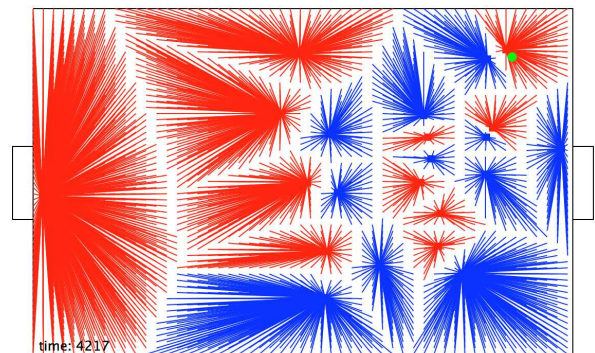


Fig. 14. The pitch possession structure at $t = 4217$

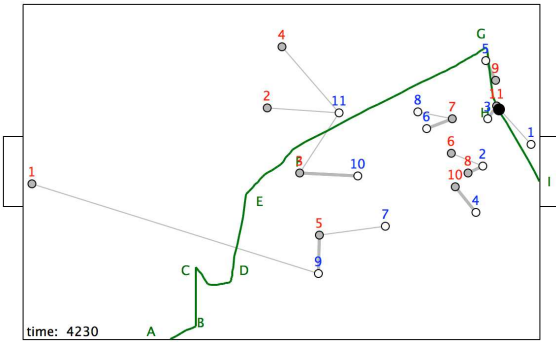


Fig. 15. The position at $t = 4230$

The ball then passed from r_9 to r_{11} , who scores the goal, as shown in Fig. 15.

5. Multidimensional hypersimplices

Although the discussion in the previous section was based on the binary relations ‘ r is closest to b ’ and ‘ b is closest to r ’, the small networks induce n -ary relations on the players. Of course, n -ary relation can be defined that cannot be resolved into binary relations, as illustrated in Figure 16.

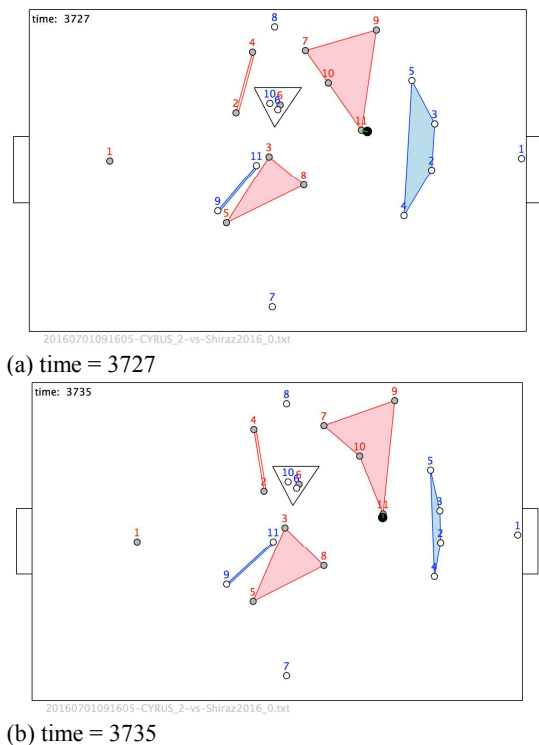


Fig 16. Configurations as multidimensional hypersimplices

In this case a set of n players is said to be R -related if they form a polygon containing no opponents. For example, $\langle r_7, r_9, r_{10}, r_{11}; R \rangle$ is shown as a pink polygon at time = 3727. These structures are remarkably enduring in time, sometimes lasting many ticks of the clock. However, inevitably the relations change and new structure emerge. Structures of particular importance are the ‘tight’ configurations of opponent players, as illustrated by the triangle $\langle r_6, b_6, b_{10}; R \rangle$. Such configurations occur frequently in the goal area and are often precursors to scoring goals.

6. Conclusions

It has been shown that configurations of soccer players in the context of areas of the pitch and its goals have a multidimensional representation as hypersimplices. This leads to three major research questions:

Research Question 1: Are some hypersimplices particularly disposed to scoring goals?

Research Question 2: Can the relevant n -ary relations of robot soccer be learned from historical games, or must they be formulated by humans?

Research Question 3: how can the multidimensional connectivity of hypersimplices be exploited to plan and control the evolutionary dynamics of robot soccer?

References

1. Kitano H, Asada M, Kuniyoshi Y, Noda I, Osawa E (1997) Robocup: The robot world cup initiative. In: Johnson L (ed) *Proceedings of the first international conference on autonomous agents* (Agents-97). ACM Press, New York, pp 340–347
2. Atkin, R. H., *Mathematical Structures in Human Affairs*, Heinemann (London), 1974.
3. Gould, P., Gatrell, A., ‘A structural analysis of a game: The Liverpool v Manchester united cup final of 1977’, *Social Networks*, 2(3), 253-273, 1979-1980.
4. Johnson, J., ‘Robot football, artificial life & complexity’, *Artificial Life and Robotics*, 3, 230-235, 1999.
5. Johnson, J., Irvani, P., ‘The multilevel hypernetwork dynamics of complex systems of robot soccer agents’. *ACM Transactions on Autonomous and Adaptive Systems*, 2007
6. Johnson, J., *Hypernetworks in the Science of Complex Systems*, Imperial College Press, (London), 2014
7. Ramos, J., Lopes, R. J., Marques, P., Araújo, D., ‘Hypernetworks Reveal Compound Variables That Capture Cooperative and Competitive Interactions in a Soccer Match’, *Frontiers in Psychology*, 28 Aug 2017

EU-Way vs JP-Way Development – Efficient & Effective Development Approach -

Masato (Max) Nakagawa

DENSO CORPORATION, Global Technical Affairs

Tokyo Office, 2-7-1 Nihonbash, Chuo-ku, Tokyo, 103-6015, Japan*

Hiroshima University, Guest Professor

1-3-2 Kagamiyama, Higashi-Hiroshima 739-8511, Japan

Abstract

This Plenary Speech will cover three elements described as follows; Firstly, “Factory-IoT” technology which is DENSO’s globally strategy manufacturing. Secondly, collaboration between Germany and Japan in terms of innovation. Thirdly, “EU-Way” development which is an efficient and effective manner of development. From 14 consecutive years experiences working in Germany, The United Kingdom and the Netherlands, “EU-Way” development will be explained. One of the key points is that in EU they differentiate between “Competition Field” and “Non-Competition Field” in each technical domains. In the “Non-Competition Field”, also called a “Cooperative Field”, Europeans cooperate together in the same industry sector to create common specifications or to establish standardization so that they can concentrate on differentiated technology in the “Competition Field”. This approach is one of the driving forces for development and innovation within EU.

1. DENSO’s “Factory-IoT”

1.1 Roadmap of Production System

DENSO is a manufacturing company mainly for automotive components and systems. DENSO started using the single automated manufacturing process like a spot machine in the 1950’s. After that DENSO expanded automation to the production line unit and then further expanded to factory unit and now to global unit like a global network.

One of the features of DENSO manufacturing is the in-house development and fabrication of the robot machines since the early 1970’s. Figure-1 represents the roadmap of the DENSO production system. DENSO pursuits “DANTOTSU” factory.

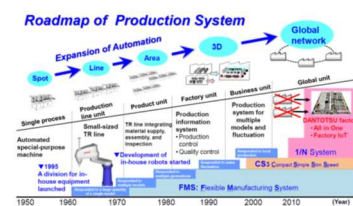


Fig.-1 Roadmap of Production System

1.2 DANTOTSU Factory

“DANTOTSU” originates from DANZEN + TOP in Japanese, meaning Outstanding. DENSO’s target of manufacturing is the status of “DANTOTSU factory”. By pursuit of “DANTOTSU factory”, DENSO respects human development which is a company legacy and in the company DNA.

In addition, DENSO pursues Concurrent Engineering as a foundation of their manufacturing concept.

With respect to Automation and Robotics, DENSO uses automation technology, mainly in Assembly and, Visual inspection processes and for in-plant logistics by using in-house machines and robots. There is however still human-based manufacturing process left for these three fields. DENSO has been working on these fields by using the intelligent technology of robots. One of the features of this technology is “collaborative robots” which means that two-robots collaborate and co-operate each other. It contributes to working efficiency and quality in the manufacturing plant.

1.3 Principle of “Factory-IoT”

It is said that IoT technology is a tool for keeping maintenance of stable production in the field of manufacturing. DENSO’s unique point of IoT is that humans are involved in this process. By utilizing human skill and knowledge, sustainable growth and continuous evolution can be achieved. This means that both human and machine can provide the optimal solutions thanks to co-creation by human and machine. DENSO pursues the “Factory-IoT” technology for all of plants globally by connecting each plant.

2. Collaboration between Japan and Germany

2.1 Example of collaborations

There are several examples of collaboration between Japan and Germany in terms of innovation. One example is that a Germany engineer invented the Facsimile machine in 1929. However it was not popular in the market at that time due to the large size of the machine and high price. TELEX was a tool for communication device until the early 1990’s. In Japan, the Japanese language characteristics are so complicated such as Kanji, Hiragana and Katakana with many different characters. Therefore, TELEX is not a suitable tool for the Japanese market and society. This is the driving force for Japanese engineers to further develop the Facsimile machine to make it compact with reasonable price. Another example is the Rotary Engine for use in automobiles. The Rotary Engine was invented by a German engineer, however it was not mass production.

Japanese car manufacture MAZDA developed the Rotary Engine and put into the market.

2.2 Example of Diesel Engine collaboration

The Diesel Engine was developed by Dr. Rudolf Diesel in 1892. His motivation was to develop an Internal Combustion Engine with better fuel consumption compared to the Gasoline Engine. From this viewpoint, his achievement was a big contribution to our society. Especially, in Europe, Diesel Engines account for approximately 50% of Internal Combustion Engines for passenger vehicles. On the other hand, heavy-duty and bus/truck applications are almost 100% powered by Diesel Engines.

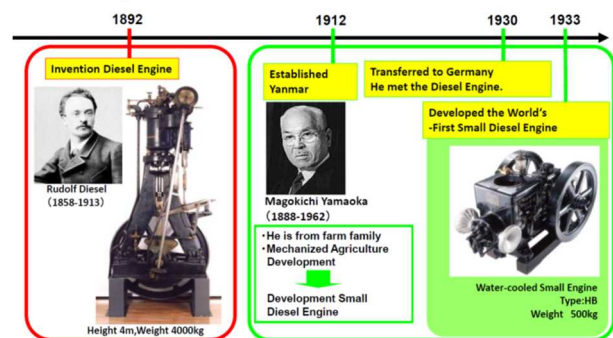


Fig.-2 Diesel Engine Development History

When Dr. Rudolf Diesel invented the diesel engine, the engine size was too big and heavy for small vehicle applications. Mr. Magokichi Yamaoka who is a founder of Yanmar wanted to utilize a diesel power unit for agriculture applications.

1858 Born in Paris (Parents are German)
1870 Transferred to Augsburg-city where his relatives lived in
1880 Graduated from Technical University München with the best performance
1893 Received the Patent for Diesel Engine
1897 World-first serial production Diesel Engine by MAN
1913 Passed away during his business trip to UK (55 years old)

Diesel Engine Patent by German Agent

Fig.-3 Dr. Rudolf Diesel Profile

He was born into a farming family in Japan. At that time, machines were not available for agriculture works. All of the jobs were done by human power. He saw very heavy load and work every time and he wanted reduce the human work load by machine. He decided to go to Germany to study the diesel engine to make it more compact and light weight for agriculture applications like

small tractors and combine machines. He developed the world-first small diesel engine for mass-production applications based on Dr. Rudolf Diesel's engine technology. Both engineers contributed to the Internal Combustion Engine for us. Mr. Magokichi Yamaoka received the Diesel Gold Prize by the Germany Patent Agency thanks to his contribution. He donated the Japanese garden in the "Rudolf Diesel Anniversary Park" in the city of Augsburg where Dr. Rudolf Diesel spent most of his life.

- 1888 Born in Japan as the 4th child in the farmer
- 1912 Formar Yanmar Company established
- 1930 Start developing the "Small Diesel Engine" when he was transferred to Munich
- 1933 Developed the World-First Small Diesel Engine
- 1955 Received the Diesel Gold Prize by Germany Patent Agent
- 1957 Donated the "Rudolf Diesel Anniversary Park" in Augsburg-city
- 1959 Engaged the friendship town between Augsburg and Nagahama / Amagasaki-city
 - Received the most oldest Diesel Engine by MAN
 - Received the "Commander's Cross" by Germany Government
- 1962 Passed away (73 years old)



Japanese Garden in Augsburg-city

Fig.-4 Mr. Mogokichi Yamaoka Profile

Later, the city of Augsburg decided to name streets in the city from Mr. Magokichi Yamaoka's home town in Japan. Nagahama-Allee and Amagasaki-Allee. This is one of the successful and beautiful collaboration stories between Japan and Germany. We should recognize the former engineer innovation spirit.

Nagahama-Allee, Amagasaki-Allee have been named in Augsburg-city



Fig.-5 Nagahama-Allee & Amagasaki-Allee in Augsburg

3. EU-Way vs JP Way Development

3.1 Comparison between EU-Way and JP-Way

Figure 6 represents the comparison between EU and JP development ways.

This chart summarizes the main features development ways, working styles and business models based on the Automotive sector of Japan and Europe. In this chart, for

EU, the German development way is used as a typical example. There are significant and remarkable differences in the EU development way compared to that of Japan-Way. In Germany, there is a clearly two fields of development style. One is "Competition Field" and the other is "Non-competition Field" for development. They co-operation and collaborate among the same industry domains in the base technology field. They establish the common technology field like standardization and/or regulations. Thanks to this system, they can concentrate on their resources on development within the unique technology field. Then, they could create the differentiated technology. On the other hand, in Japan, OEMs develop almost all technologies by themselves. In this approach, they could create unique technology, however, recently there are many new technologies to be developed like Electrification, AI and IoT connect to automobile.

Therefore, there are concerns regarding the lack of resources for the development of their unique technologies.

	Japan	Europe
Business Model	JP unique → Global	EU optimize → Global
Features	Homogeneity / Uniformly	Multinational / Diversity
Work Style	Teamwork / Harmony	Rational / Individualism
Development Style	<p style="text-align: center;">Independent (unique technology by each OEM)</p>	<p style="text-align: center;">Cooperation & Competition</p>

Fig.-6 Comparison of Europe and Japanese Characteristics

3.2 Collaboration Concept between Germany & Japan

There are good points to be learnt from German-Way development. For example, efficient and rational development by using industry standard tool-chains, model base development, cutting-edge simulation automated calibration etc. In addition Germany OEMs cooperate with R&D Engineering companies for their vehicle and engine development in not only the research phase but also for application engineering. There are remarkable R&D Engineering companies in Europe who have sophisticated development tools, testing facilities and high-talented engineering resources. In Japan also, there are good points for their development way like teamwork and harmonized development approach with dignity.



Fig.-7 Collaboration Concept between Europe and Japan

The key point is to respect each other of their development ways, then reflect and accept the good points into their development ways. Figure 7 represents the concept of collaboration between Europe and Japan. The important point is that both good points to be well-arranged like a fusion. In this case, a new development way which is a fusion between Europe and Japan could become a global competitive engineering approach. Both parties should respect their development ways and inspire each other in research and development fields.

References

1. M. Nakagawa, *26th International AVL Conference Engine 2020: Sparks versus compression ignition in a new environment* (Graz, Austria, September 2014)
2. M. Nakagawa, Dr.-Ing. O. E. Hermann and Dipl.Ing. Sebastian Visser, *Diesel Powertrain Energy Management via Thermal Management and Electrification* (Detroit *SAE* April 2017)
3. M. Nakagawa, *DENSO's Contribution for Future Predictive Powertrain Control including Electrification* (Korea, *FISITA* 2016)

Innovation on Manufacturing Generated by Intelligent Technologies

Ken-ichi Tanaka

Corporate Research and Development Group, Mitsubishi Electric Corporation,
8-1-1, Tsukaguchi-Honmachi, Amagasaki City, Hyogo 661-8661, Japan

Haruhisa Okuda

Autonomous Control System Development Project Group, Advanced Technology R&D Center,
8-1-1, Tsukaguchi-Honmachi, Amagasaki City, Hyogo 661-8661, Japan
E-mail: Tanaka.Kenichi@ah.MitsubishiElectric.co.jp, Okuda.Haruhisa@ct.MitsubishiElectric.co.jp
<http://www.mitsubishielectric.com>

Abstract

In order to cope with social problems such as labor population decrease, the autonomous cell production robot system had been developed to realize automation in variable variety multi production. The intelligent technologies such as random bin picking, force control, and error recovery were developed to apply the robot from simple-transport-work to assemble-task. In addition to the talk about such technologies, it will also be described that open innovation method cooperating with universities to create research results which our company would not achieve independently. The examples of the latest robot technology development using artificial intelligence will also be described.

Keywords: cell production robot, intelligent technologies, open innovation, artificial intelligence

1. Main Slides

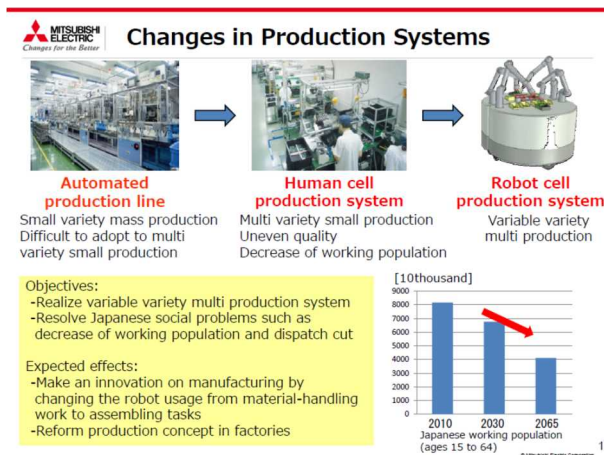


Fig. 1. Changes in Production Systems

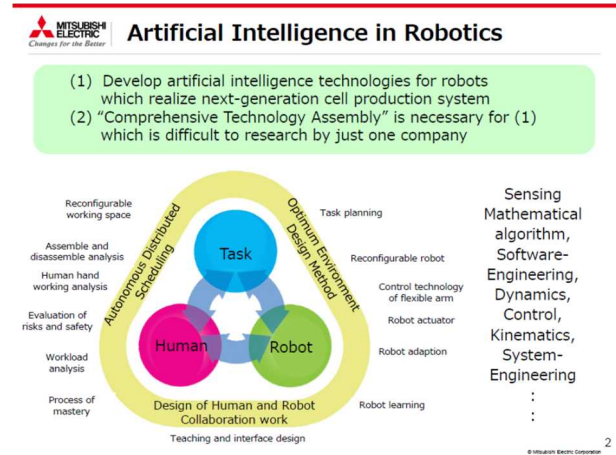


Fig. 2. Artificial Intelligence in Robotics

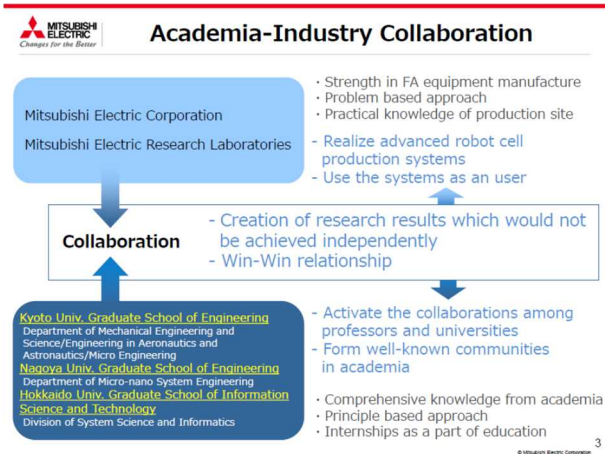


Fig. 3. Academia-Industry Collaboration

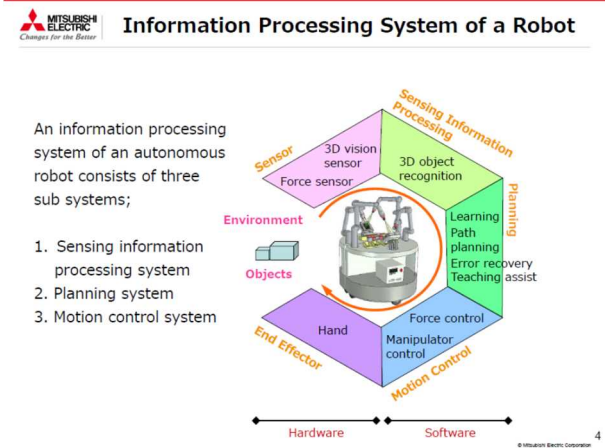


Fig. 4. Information Processing System of a Robot

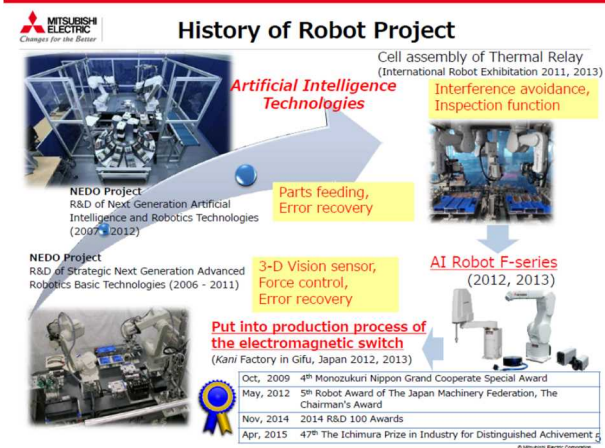


Fig. 5. History of Robot Project

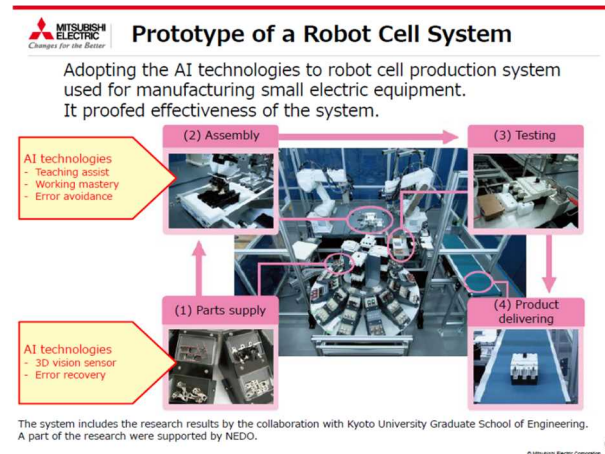


Fig. 6. Prototype of a Robot Cell System

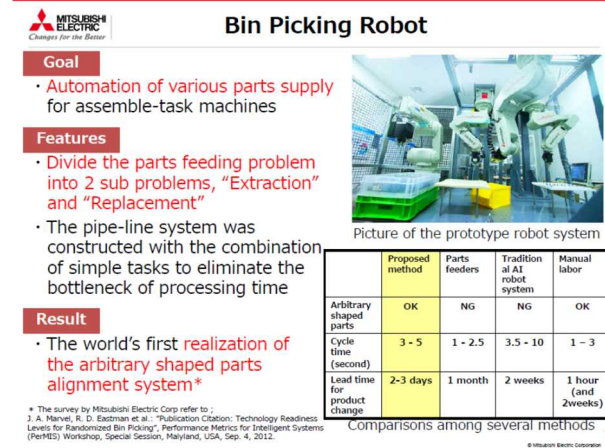


Fig. 7. Bin Picking Robot

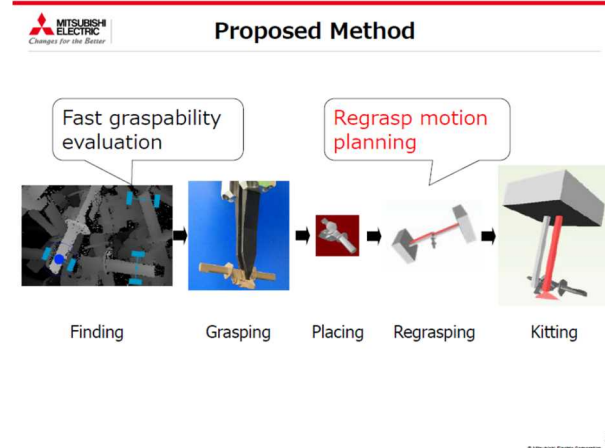


Fig. 8. Proposed Method

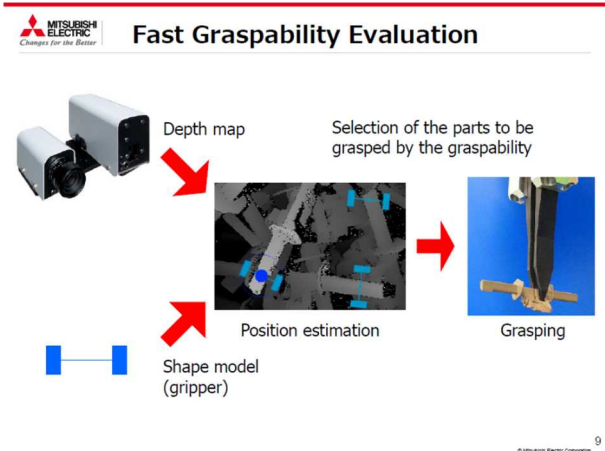


Fig. 9. Fast Graspability Evaluation

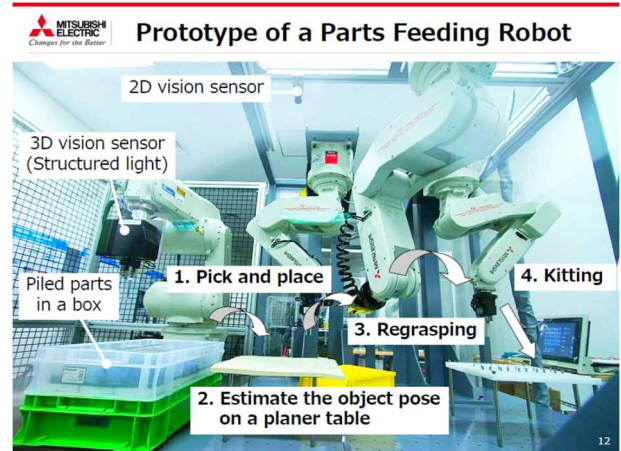


Fig. 12. Prototype of a Parts Feeding Robot

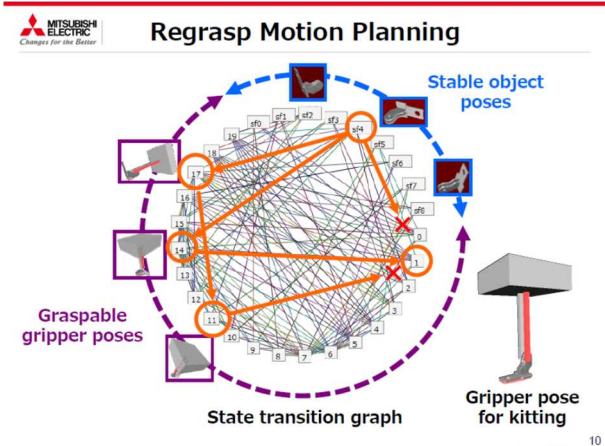


Fig. 10. Regrasp Motion Planning

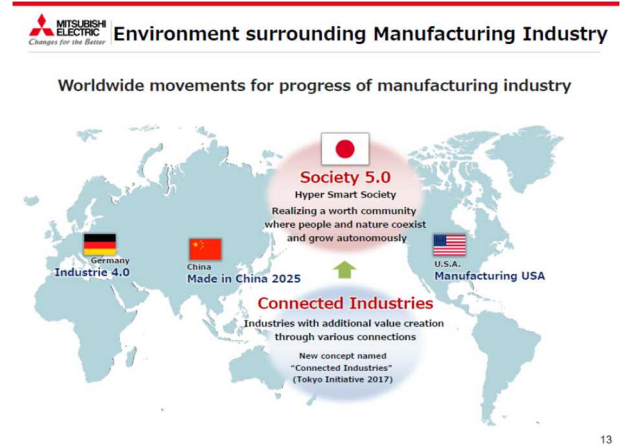


Fig.13. Environment surrounding Manufacturing Industry



Fig. 11. Examples of Adoptable Parts Shapes

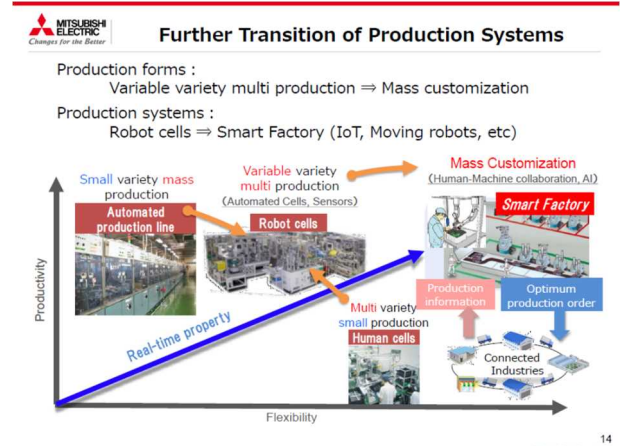


Fig. 14. Further Transition of Production Systems

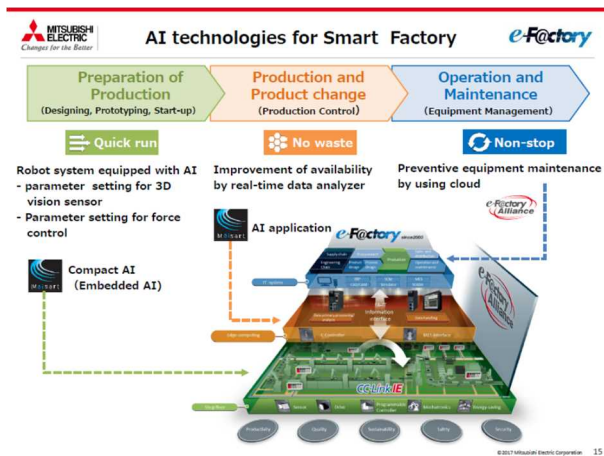


Fig. 15. AI technologies for Smart Factory

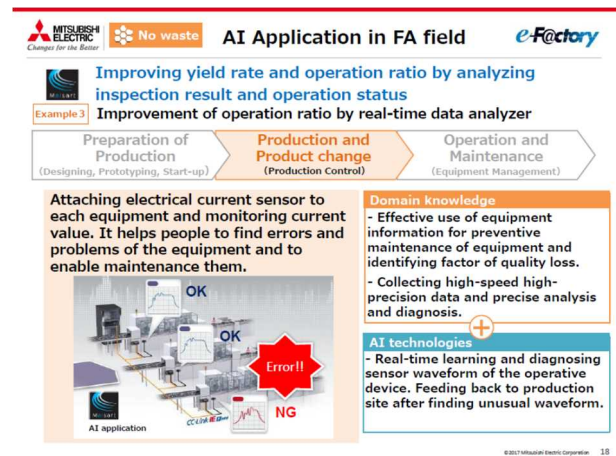


Fig. 18. AI Application in FA field -3

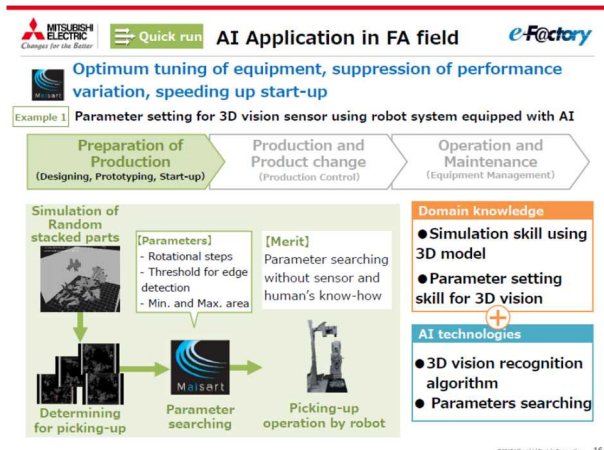


Fig. 16. AI Application in FA field -1

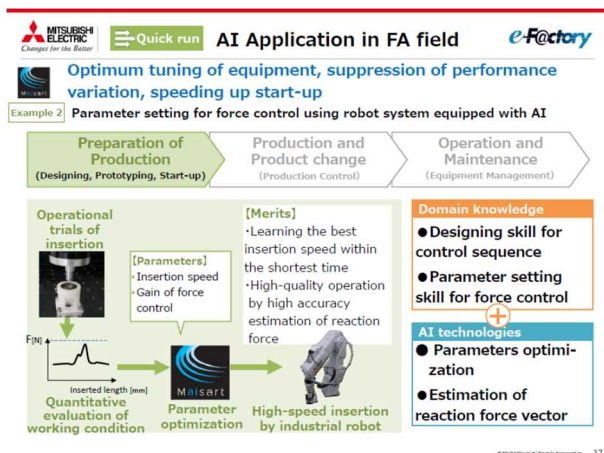


Fig. 17. AI Application in FA field -2

References

1. K. Tanaka, T. Sawaragi, Prospect of intelligent technologies realizing robotic cell production, *SICE SI2010*, 1J2-2, pp.657-659, (2010). (in Japanese)
2. A. Noda, K.Tanaka, H. Okuda, T. Nagatani, Y. Kitaaki and Y. Domae, Intelligent Robot Technologies for Cell Production System, *ISFA 2010 (2010 International Symposium on Flexible Automation)*, JPS-2562, (2010).
3. H. Okuda, R. Haraguchi, Y. Domae and K. Shiratsuchi, Novel Intelligent Technologies for Industrial Robot in Manufacturing Architectures and Applications, *2016 International Symposium on Robotics (ISR2016)*, pp. P3.8, (2016).
4. Y. Domae, H. Okuda, Y. Taguchi, K. Sumi and T. Hirai, Fast Graspability Evaluation on Single Depth Maps, *2014 IEEE International Conference on Robotics and Automation (ICRA)*, pp. 1997-2004, (2014).
5. R. Haraguchi, Y. Domae, K. Shiratsuchi, Y. Kitaaki, H. Okuda, A. Noda, K. Sumi, T. Matsuno, S. Kaneko and T. Fukuda, Development of Production Robot System that can Assemble Products with Cable and Connector, *Journal of Robotics and Mechatronics*, Vol.23 No.6, pp.939-950, (2011).
6. S. Ryu, K. Shiratsuchi, R. Haraguchi and H. Okuda, Development of industrial robot controller with force control functions, *SICE SI2011(The 12th SICE System Integration division annual conference)*, 1E2-4, (2011). (in Japanese)

Modular Playware and Personal Health Technology

Henrik Hautop Lund

Center for Playware, Technical University of Denmark, Building 326, 2800 Kgs. Lyngby, Denmark

E-mail: hhl@playware.dtu.dk

www.playware.elektro.dtu.dk

Abstract

In this paper, we describe the development of personal health technology such as wearable systems monitoring health conditions. It has been advocated that such personal health technology through monitoring health status may motivate people to perform health related actions and life-style changes. Here we describe a methodology on how these personal health technologies may rather be used as a tool for designing and adapting game activities, which motivate people to perform the desired actions. Especially, we exemplify this methodology with the use of FitBit monitoring of steps and heart rate to the design of appropriate, physically demanding games for the modular interactive tiles, Moto Tiles, which are used by older adults for prevention and rehabilitation. Thereby, the motivation to perform the actions arrives from the fun play on the Moto Tiles, whereas the personal health technology is used as a tool to monitor the effect and guide the game development.

Keywords: Playful technology, Playware, Personal Health Technology, FitBit, Adaptive Games.

1. Introduction

Personal health technology such as different wearable systems monitoring health conditions have been developed over the last decade and finds its way to the general public. These personal health technology devices are often described as a means to engage and motivate the public to perform health related actions, and e.g. change behavior to become healthier. A typical example is that wearing a step counter is believed to engage and motivate people to perform more steps (walk more, run more, bike more, etc.) due to goal setting (e.g. 10,000 steps per day) and insight into their own performance (how many steps did I take today?). As such, the personal health technology is viewed as a *persuasive technology* [1]. Persuasive technology is technology designed to change people's beliefs and behaviors, e.g. creating certain health habits amongst the users of the technology product.

With this view of personal health technology as a persuasive technology, researchers and practitioners have investigated *nudging* through the new opportunities arising with the technology. It is well-known that information, priming, peer pressure, etc. may guide people to certain behavioral actions (e.g. choosing a certain behavior) – this has nowadays been termed nudging. Nudging with personal health technology includes the simple nudge that an arm wrist wearable acts as a physical reminder to be active, and the interface on the physical device or the app acts as a positive or negative reinforcement by presenting e.g. statistics, target amount, and time since last action.

There are numerous health nudging apps and devices for hydrating, moving, sleeping, etc. It appears that the main idea of nudging in these kind of personal health persuasive technologies is based on presenting a numerical indicator, a graph and a numerical goal, which translates to nudging/persuading the user by providing

© The 2018 International Conference on Artificial Life and Robotics (ICAROB 2018), Feb. 2-4, B-Con Plaza, Beppu, Japan

the user with an insight into the personal health status. Such an insight is believed to be a strong enough motivation for people to perform more of the desired healthy behavior.

In this context, the connotation of nudging is that such an insight into personal health measurements is such a strong motivation that people will perform more of the desired healthy behavior. Accordingly, the numerical insight into one's own personal health should act as a strong *extrinsic motivation*.

However, it is questionable if everybody will respond well to such a nudging based on numerical insight into one's own personal health acting as a strong extrinsic motivation. Will everybody act equally well to such information? For instance, it is known from message tailoring that adapting persuasive messages to recipients' characteristics is more effective than providing the same message to all recipients, since recipients with different characteristics will respond more or less to the same message. For instance, Hirsch et al. [2] demonstrated effective message tailoring using a comprehensive model of recipients' personality traits. "Respondents judged an advertisement emphasizing a particular motivational concern as more effective when that concern was congruent with their own personality characteristics. Message-person congruence effects were thus observed by manipulating the framing of an appeal to target a broad variety of motives, including desires for excitement and social rewards (extraversion), connection with family and community (agreeableness), efficiency and goal pursuit (conscientiousness), safety and security (neuroticism), and creativity and intellectual stimulation (openness/intellect)." [2]. These are termed the Big Five personality dimensions:

- Openness to experience: (inventive/curious vs. consistent/cautious).
- Conscientiousness: (efficient/organized vs. easy-going/careless).
- Extraversion: (outgoing/energetic vs. solitary/reserved).
- Agreeableness: (friendly/compassionate vs. challenging/detached).
- Neuroticism: (sensitive/nervous vs. secure/confident).

Indeed, it is important to distinguish between *extrinsic* and *intrinsic* motivation [3], as the Big Five personality model may predict motivation in e.g. education, sports, and exercise, where the Big Five traits are associated with different levels of self-determined motivation. Hence, people may be motivated to different degrees and not all are given to respond positively to extrinsic motivation such as the nudging suggested by the personal health technologies. For instance, Hart et al. [4] found that "Conscientiousness, openness, and extraversion were positively associated with intrinsic achievement motivation, whereas extraversion, conscientiousness, and neuroticism were positively related to extrinsic achievement motivation. Agreeableness was also found to be negatively associated with extrinsic achievement motivation. Conscientiousness was anomalous in that it was positively related to both intrinsic and extrinsic motivation."

To investigate the effect of intrinsic motivation in personal health technology, we suggest to put focus on play. Play is often defined as a free and voluntary activity that you do with no other purpose than play itself and for the enjoyment that it brings [5]. There is no product or outcome as such of play, but people play for their own enjoyment and fulfillment, i.e. there seems to be an intrinsic motivation to play, when people are in a play dynamics. Hence, it becomes interesting to understand how people enter into such a play dynamics, in which they fully engage in play and seem to forget about time and place. It has been suggested that there exists play forces, which drive people into a play dynamics, and that playware can act as such a play force [6]. The hardware and software augmentation of objects to become playware [7, 8] may for instance draw people into moving, touching, turning, etc. due to emission of sound, light, odor, etc. and immediate explicit feedback from the playware drive people into further actions, acting as a play force pushing people into a play dynamics of continuous actions and feedback.

Even if there is no product or outcome of such play based on the intrinsic motivation for own enjoyment, there may be *collateral effects of play* [9]. For instance, the collateral effects of play can be motor skill enhancement, cognitive and physical rehabilitation, etc. These

collateral effects of play, e.g. on the health, can be significant and important [10].

Therefore, in the present work, we put focus on the creation of playful experiences and intrinsic motivation. So instead of viewing the personal health technology as a motivational tool with the health status as the primary effect, our methodology involves the personal health technology as a tool for designing and adapting game activities, which are the ones to intrinsically motivate people and with which the health status is a collateral effect.

2. Method

We exemplify the methodology with the use of FitBit monitoring of steps and heart rate to the design of appropriate, physically demanding games for the modular interactive tiles, Moto Tiles [11], which are used by older adults for prevention and rehabilitation. Thereby, the motivation to perform the actions arrives from the fun play on the Moto Tiles, whereas the personal health technology is used as a tool to monitor the effect and guide the game development.

There is an important distinction to be made between the general *long-term effect* and the *short-term effect*. It is possible to measure both the short-term effect and the long-term effect, and it is clearly interesting to obtain knowledge of the potential relationship between the short-term effect and the long-term effect.

The general effect of an intervention can typically be measured in pretest and posttest in a randomized controlled trial (RCT) with comparison between the intervention group and the control group. In our case here, we view this as a long-term effect compared to the short-term effect (or we can even call this the run-time effect), which is typically provided with the personal health technology such as the FitBit. The short-term effect or run-time effect may be measured as physical activity level (e.g. steps, heart-rate, etc.) or mental activity level (e.g. blood flow in prefrontal cortex to indicate concentration).

Here we propose that the short-term effect measurements can be used for designing for increasing the long-term effect (the collateral effect of play).

This demands that there is a relationship between the short-term (run-time) effect measurement and the long-term effect, and that we can find such relationship(s). This clearly depends on the selection of which short- and long-term health parameters we are looking at, i.e. which physiological states are measured and with which measuring tools at short-term and at long-term. It will be a whole field in itself (e.g. within AI and Big Data) to find this coupling and relationship for the range of measuring tools, measurements and intervention areas. Here, we are therefore limited to provide only a first idea. Nevertheless, to exemplify this approach, in this study, we use a personal health technology, Fitbit, to measure run-time effects and their correlations with scores from playing on the Moto tiles

Fitbit is an activity tracker, which is wireless-enabled wearable technology that measure number of steps walked, heart rate, sleep pattern, and steps climbed. It is worn as a wristband, and connects to a mobile app synched via Bluetooth. In this study, we use the Fitbit to measure heart rate and steps.

Moto tiles are modular interactive tiles used for playful prevention and rehabilitation by allowing users to play different games on the tiles that light up in different colours [11]. The Moto tiles can be put together like puzzle pieces in different patterns, and different games can be selected from a tablet to be played on the Moto tiles. In a game, the user typically will have to move around to hit different tiles according to the game pattern. In the present study, we use three games called Color Race, Final Countdown, and Reach (see videos of the games [12]).

3. Experiments and Results

In the first experiment, we used the Fitbit and Moto tiles data collection to investigate potential relationships between physiological measurements and game score in different games. The hypothesis was that there exist such relationships, and that these may guide future game

design to create games, which may result in collateral health effects of play.

A university student would wear the Fitbit while playing each game in different tiles configurations each 10 times. The first configuration were 2*3 tiles connected together in a rectangle with the games Color Race, Final Countdown and Reach. The second configuration was 2, 2, and 2 tiles put in a triangle with 1.5m in between each of the 2 tiles islands with the games Color Race and Final Countdown. The third configuration was 2, 2, and 2 tiles put in a triangle with 2.5m in between each of the 2 tiles islands, and with the games Color Race and Final Countdown.

Table I shows the Pearson correlation coefficients between the Moto game score of each game and the different activity data collected from the Fitbit (the end heart rate, the maximum heart rate during a game, the rise in heart rate during a game, and the number of steps measured during a game).

Table I. Pearson correlation coefficients between different activity data and game score (α=0.05).

Game	End HR	Max HR	Percentage HR rise	Step
Color race (2*3)	0.5996	0.6030	0.3438	0.9392
Final countdown (2*3)	0.6927	0.6827	0.5268	0.8520
Reach (2*3)	0.8029	0.7908	0.6823	0.8842
Color race (triangle, 1.5m)	0.7522	0.8146	-0.2557	0.9143
Final countdown (triangle, 1.5m)	-0.3909	-0.3021	-0.3836	0.8333
Color race (triangle, 2.5m)	0.6645	0.8093	-0.2770	0.7664
Final countdown (triangle, 2.5m)	0.5793	0.5262	0.5127	0.4868

It can be seen that both the end HR data and max HR data are able to show positive correlation in 6 out of the 7 cases, which is apparently more reliable than percentage change in HR. The average correlation coefficients of the 6 successful cases of end HR and max HR are 0.6819 and 0.7044 respectively, which implies that max HR can be a better indicator of the game intensity. In addition, the result of steps shows fairly strong correlation with Moto game score in all games.

The general indication of this small pilot study is therefore, for these six cases, a higher Moto game score signifies that the user has taken more steps and have reached a higher heart rate. It is therefore indicated, in this case, that the run-time effect is predictable from the Moto game score.

In order to investigate the relationship between the run-time effect and the long-term effect, we conducted another pilot study. In this case, 11 older adults performed Moto tiles training twice a week for 10 weeks in a senior activity center in Lyngby municipality, Denmark, as part of the EU project REACH. The older adults were pre- and posttested with standard tests such as timed-up-and-go, chair-to-stand, 6 minutes walking test, and Berg Balance Scale. Here we will look only at the data from the Berg Balance Scale, which was completely performed by 7 out of the 11 participants.

We compared the maximum score on games played on the Moto tiles of each individual with the score of the posttest (Berg Balance Scale).

Figure 1 shows the game score (each column accumulated maximum game score of the three games) and the score of the Berg Balance posttest on the x-axis.

Even if the data here is very small from such an initial pilot study, it is interesting to speculate whether there can be a correlation between the game score and the health score (such as represented with e.g. Berg Balance test score). For instance, the cut-point for low risk of falling and medium risk of falling in Berg Balance test is 40, and cut-off point 45 has been suggested for multiple fall risk and assistive need, so with a much larger data set it would be interesting to see if some game score could correlate to a Berg score above or below such cut-points.

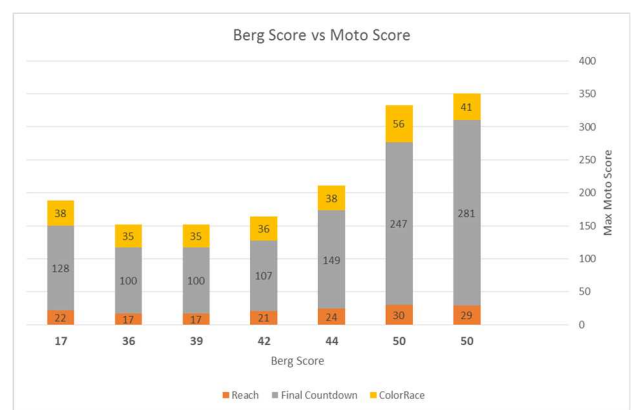


Fig 1. Relationship between Berg score (posttest) and maximum Moto game score for 7 older adults.

4. Discussion and Conclusion

It is important to notice that there may be habituation to the games, so one has to be careful in using game score as a predictor for the general health status (though one has to distinguish between habituation to the tool (i.e. Moto tiles) and habituation to the activity (i.e. game) that may change), and much more work is needed. Nevertheless, it is interesting with the small indicators of relationship between game score and measurements from the personal health technology (heart rate and steps) representing the short-term effect, and the standard balancing test representing the long-term effect. This pilot study should therefore open up for much more thorough studies on such potential relationships, their nature and their relevance.

The relationship shown between game design and set-up, heart rate and steps suggest that such physiological measurements can be used in the design process to design physical interactive games with different qualities. Some designs may be more effective than others, and they may be qualified, tested and verified for their effect as has been indicated in the work presented here.

Previously, it has also been shown that children's heart rate can be captured on a prototype playware playground, and that children's notion of entertainment correlates highly with their average heart rate during the game [13].

Importantly, the interaction was mediated by the Moto tiles acting as a playware, which motivated the participants to play for their own enjoyment. In this study, the personal health technology in the form of Fitbit acted as a measuring tool, and it was the playware (Moto tiles), which acted as the persuasive technology.

Acknowledgement

The experiments with Fitbit measurements of Moto tiles games were performed by Yancy Liu. The pilot study with older adults in Lyngby municipality was performed as part of the EU project REACH: Responsive Engagement of the Elderly Promoting Activity and Customized Healthcare (thanks to J. Jessen, DTU Management (Prof. Andersen), Lyngby Municipality, and project partners).

References

1. B. J. Fogg "Persuasive technology: using computers to change what we think and do." *Ubiquity* 2002. December (2002): 5.
2. J. B. Hirsh, S. K. Kang, & G. V. Bodenhausen "Personalized persuasion: Tailoring persuasive appeals to recipients' personality traits." *Psychological science*, 23(6), 578-581, 2012.
3. R. M. Ryan & E. L. Deci. Intrinsic and extrinsic motivations: Classic definitions and new directions. *Contemporary educational psychology*, 25(1), 54-67, 2000.
4. J. Hart, M. Stasson, J. M. Mahoney, and P. Story. The big five and achievement motivation: Exploring the relationship between personality and a two-factor model of motivation. *Individual Differences Research*. 5. 267-274, 2007
5. J. Huizinga. *Homo Ludens* IIs 86 (Vol. 3). Routledge. 2014
6. C. Jessen, & H. H. Lund, H. H. On play forces, play dynamics and playware. Unpublished manuscript, 2009.
7. H. H. Lund, and C. Jessen, "Playware - Intelligent technology for children's play," Technical Report TR-2005-1, June, Maersk Institute, University of Southern Denmark, 2005.
8. H.H. Lund, T. Klitbo, and C. Jessen, "Playware Technology for Physically Activating Play", *Artificial Life and Robotics Journal*, 9:4, 165-174, 2005
9. H. H. Lund, "Play for the Elderly - Effect Studies of Playful Technology," in *Human Aspects of IT for the Aged Population. Design for Everyday Life*. (LNCS Vol. 9194, pp 500-511, Springer-Verlag, 2015)
10. H. H. Lund, and J. D. Jessen, "Effects of short-term training of community-dwelling elderly with modular interactive tiles," *GAMES FOR HEALTH: Research, Development, and Clinical Applications*, 3(5), 277-283, 2014.
11. <http://www.moto-tiles.com> (checked: 28/11/2017)
12. <http://www.moto-tiles.com/video.php?L=en&s=games> (checked 28/11/2017)
13. G.N. Yannakakis, J. Hallam, H.H. Lund "Capturing entertainment through heart-rate dynamics in the playware playground" *Proceedings of the 5th International Conference on Entertainment Computing Lecture Notes in Computer Science*, vol. 4161, Springer, Cambridge, UK, pp. 314-317, 2006.

How the new technologies might lead to a paradigm shift in psychological and neuropsychological research.

Luigi Pagliarini ^{1,2} Henrik Hautop Lund ¹

¹ Centre for Playware, Technical University of Denmark, 2800 Kgs. Lyngby, Denmark

² Academy of Fine Arts of Macerata, Via Berardi, 6, 405111 Macerata, Italy

luigipagliarini@gmail.com

Abstract

Recently, we started to apply old psychological and neuropsychological standard tests and therapeutic exercises into a different domain of technology. Therefore, while maintaining the whole conceptual and logical structure of the traditional approach – i.e. tests mostly made by hand on paper or with the mouse and computers' screens - intact, we moved them onto the physical interactive and playful technology, Moto Tiles. Such a translation of input/output, likewise involving dissimilar perceptions and different parts of our motor system (i.e. legs, feet and balance system), might imply a change in subjects' mental and behavioural strategies, variations in efficacy and efficiency, as well as a redefinition of reaction times. In short, this shift, besides providing a significant extra tool to older practices, might work as a crucial test for all of the existing theoretical background, too. We describe our new method and report few of the first empirical applications.

Keywords: Playful robotics, Psychology, Neuropsychology, Therapy, Clinical Tests, New Paradigm.

1. Introduction

In both psychology and neuropsychology there are several tests and exercises that enable professionals to evaluate a large set of humans psychological responses to specific stimuli and try to measure or improve their abilities. This is true for both normal and clinical patients. These psychological tests have the great advantage of being properly validated and, as a consequence, they produce "an objective and standardized measure of a *sample of behaviour*" [1] with results that are very solid and steady. There is a large set of tests with different options and methods that differs between each other for at least three characteristics:

- a) Trials used to measure abilities;
- b) Trials used to improve abilities;
- c) Domain of application.

Of course, a single test might cover up both (a) and (b) simultaneously while quite rarely a single tool can range from one domain to another (c).

In this pilot study we will only be considering psychological tests that focus on basic cognitive features and abilities domain, so excluding those that try to reflect or measure psychological entities such as aptitudes, emotions, personality, interests, IQ, etc.

Moving from this valuable tradition, we considered to transfer such consistent set of data and long lasting

expertise that were originally implemented and validated with traditional tools (i.e. paper-and-pencil, mouse and computers' screen, and etc.) to a new and possibly common input/output flow, the Moto Tiles technology [2]. We look at this "translation" as a great opportunity for providing:

- A significant extra tool to older practices;
- A crucial test for all of the existing practice and theoretical background.
- A common platform (and consequently set of data) to all of the tests;

Sure enough, our transfer of input/output is to be verified and weighted, since besides requiring different perceptions, it implies the participation of different motor planning/acting systems (i.e. legs, feet and balance system). Therefore, this change in behavioural demand might imply a change in the subjects' mental and behavioural strategies, variations in efficacy and efficiency, as well as a redefinition of reaction times and some of the behavioural parameters.

Anyway, our effort should be rewarded by the advantage of moving on a common digital platform that can collect data from different experiments in a much more standardized way.

In this paper, we present a couple attempts to transfer old and consolidated tests from the psychological literature

regarding the *attentional system* in order to examine the feasibility of the above described methodology.

2. Inspiring Psychological Tests

The first set of psychological tests we moved from are two traditional tools used in clinical environments to evaluate subjects' attentional system efficiency. They are

- Line Bisection tests
- Visual Search tests

2a. Line Bisection tests

The Line Bisection [3] is used in neuropsychology to quickly assess both the type and the severity of Unilateral Spatial Neglect (USN). Probably it is the most-used and quickest test for such a diagnosis; therefore it is popular, solid and efficient. It consists of a set of paper-and-pencil tests where a line (or more) a few centimetres long is drawn and the patient is then asked to dissect the line at the midpoint (see Fig. 1). Patients exhibiting, for example, left-sided neglect will respond with a rightward deviation of the line's true midpoint. The same test can also be used for normal adults [4, 5], so it might be seen as a more generic valuation of spatial attention efficiency in any subject.

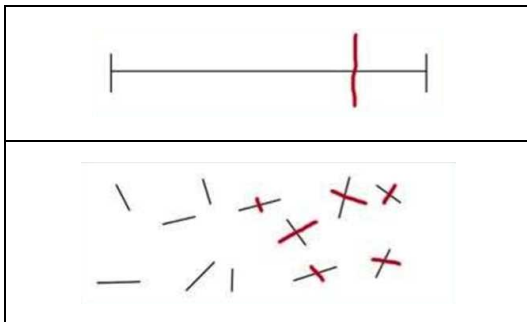


Fig. 1. Line Bisection tests. Up a single line test example. Down a multiple line test example.

2b. Visual Search tests.

The well-known visual search paradigm, designed to assess the function of visual attention, has had an enormous impact on many aspects of science. The vast majority of visual search studies performance is assessed with response times. Typically, the task is to determine whether a target is present or absent [6]. Search slopes that measure how response times change as more distractors are added to the display are presumed to assess the speed of the search and whether attention is involved or, clinically speaking, the efficiency level of a given subject attentional mechanisms.

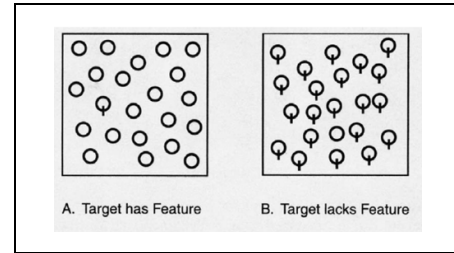


Fig. 2. Visual search tests.

This simple test is very predictive of subjects' efficiency on visual attention tasks, and, originally, it was a tool used by Treisman in defining is Feature Integration Theory (FIT) on *Selective Spatial Attention* [7].

3. Implementation of the tests on Moto Tiles

The two psychological tests described above were used as starting point and inspiration material for implementing respectively two new Moto Tiles games/exercises. Despite of the fact that, changing physical platform implies a crucial change on tests significance, we tried to keep as much faithful as possible to the original tests conception.

3a. Neglect.

The Neglect game/exercise is an attempt to transfer the psychological Line Bisection tests knowledge to the Moto Tiles environment. Neglect can be a single player task or a challenge between two players. The game indirectly measures the users' RTs (Reaction Times) and the general state of vigilance, and therefore might also be used as a therapeutic exercise for elderly and, in particular, for all of those patients with inattentive problems subsequent to a stroke, an ictus or degenerative neurological syndromes.

Tiles Configuration.

One tile is positioned in the (virtual) centre of the room and four in each side of it (left and right).



Fig. 3. Testing the *Neglect* game/exercise on Moto Tiles.

Lateral tiles can be positioned both in a squared shape (2*2) and in a linear shape (4*1, as shown in Fig. 3), accordingly to the kind data we want to collect or the game/exercise dynamic we want to impress.

Game Options.

The game options are to be selected on the tablet's software interface, and they are:

1. Number of players, one (for therapeutic reasons) or two (gaming);
2. Colour for each player;
3. Number of reiteration of the exercise/game;
4. Timing parameters (will influence the game difficulty);
5. Game start.

Game Dynamics.

Once the game is started from the tablet, the central tile is lit up with one of the two colours (in both one or two players sessions). To start the real section the player identified with that very colour has to smash it to start the real sub-section. At that point, one of the 8 lateral tiles (pseudo-randomly chosen) will be lit up for a short time (to be defined accordingly to gaming and therapeutic sections) and the goal of each individual (either in a single player or in a one-to-one section) is to squeeze it as fast as possible (using one of its feet). Timing is calculated and a threshold applied so that after a given number of milliseconds the lit tile, if not squeezed, is turned off and at that point, whatever case occurs, another tile is lit up. Such an operation is reiterated for 8 to 16 times (also accordingly with section's purposes). After that, in the case of one-2-one competition, the central tile is lit up again, with the other colour, and waits for the new sub-section to be started. At the end of the second section the tablet calculates the shortest timing and provides a visual feedback that underlines the winner. In the single player case the game/exercise simply comes to an end.

The one-2-one game/exercise is pretty dynamic, very easy to understand and quite funny. It is to be highlighted that, in both cases, the level of difficulty can also be tuned by shaping the morphology of the playground (lateral tiles are positioned far).

3a. Special Pattern or Special One.

The *Special Pattern* game/exercise is an attempt to transfer the psychological knowledge on visual search tests in our Moto Tiles environment. In short, *Special Pattern* can be used as a single player task or a challenge between two players. In the one player version four tiles are positioned in a linear (4*1 tiles) or squared shape (2*2 tiles), while in the one-2-one version everything is doubled.

Gam

e Options.

The game options are to be selected on the tablet's software interface, and they are:

1. Number of players, one (for therapeutic reasons) or two (gaming);
2. Colour for each player;
3. Number of reiteration of the exercise/game;
4. Timing parameters (will influence the game difficulty);
5. Pattern discrepancy (level of difficulty in terms of physical/visual distance between different patterns);
6. Target Feature. The target tile lacks or has a special feature (will influence the game difficulty and target analysis);
7. Game start.

The patterns correspond to different configuration of the activation of the LEDs within one tile (see Fig. 4 for some examples).

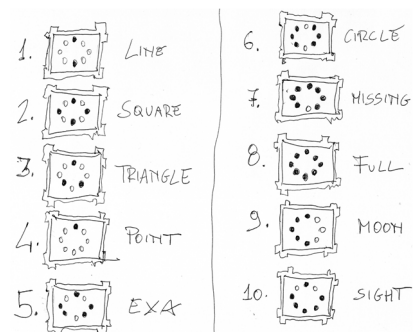


Fig. 4. Designing the *Special Pattern* game/exercise.

Game Dynamics.

When the game is started all the tiles are lit up. But three out of four tile will show the same pattern, while the fourth one will show a different pattern. The user(s) have to react as fast as possible to try to crush on the "different" tile's pattern amongst the four (neglecting the three which show the very same patterns). The game/exercise keeps on rolling like that up to the last stimuli set. At the end it provides a visual feedback that shows the winner of the one-2-one competition or, for the single player option, provides a visual feedback about the performance.

Both versions of the game/exercise, also accordingly to the options tuning made at the start when the play is configured, result in a quite effort-demanding increase of attention and/or visual search. The one-2-one version, in particular, when timing gets crucial, has been reported and turns out to be mentally speaking deeply challenging.

4. Knowledge transfer

We tried to move a couple of tests regarding Spatial Attention and Visual Search from the old paper-and-pencil school, normally used in psychological

experiments, to a new realm of technologies. Since these new technologies (i.e. the Moto Tiles) are made of digital and electronic devices and as input/output demand for a pretty different set of perceptions and action, our biggest effort is to try being as faithful and coherent as possible with the former experience and knowledge. It is too early to think of a significant outcome, though we believe we are going in the right direction. This is because the Moto Tiles technology has shown to be very adaptive to different tasks' specifications and demonstrated to be practically very close, as behavioural practice, to the original methods used.

In particular, we believe the *Neglect* task we have built, while not superimposable to the *Line Bisection* task, it should require a similar amount of spatial attention, specially if compared to *Multiple Line Bisection*, and a comparable in terms of precision/effort of action in physical space.

The *Special Pattern* task seems to be even closer to the corresponding Treisman's figure integration test, since it seems to require both a similar demand of selective spatial attention and the same precision/effort of action in physical space.

Of course, the two games/exercises might need to be perfected, integrated with additional features or fine tuned, and that's why at the very moment we are in the process of building a number validation tests in which we will compare data from traditional tests with those from Moto Tiles in a group of human subjects

5. Discussion

In this paper we depicted one method to move old psychological and neuropsychological knowledge in to a new technological tool. This is not a fully new experience since in the past the old pencil-and-paper psychological tests have been brought into software-based environments, see [8] for an example. Therefore, our attempt is just one more step towards digitally based tests, but with a little stronger stress on the standardization of the tests data and physical representation of the test tool. Our main goal is to bring old findings regarding brain oriented clinical diagnosis and therapy to a new domain of technology, the Moto Tiles, which would allow us to collect data, as well as run trials and therapy exercises, in an environment that is basically standardizable, highly stimulating and playful, as we know from our former experiences [2, 8]. In doing this we are limiting our experience to a specific subset of possibilities, visuo-attentional tests in the cognitive domain of Psychology.

This is because we believe that the Moto Tiles game/exercise can be, in general, very predictive of the general state of sensory and motor alertness of anybody [2] and, in the particular case of neurological patients, might measure the state of the attentional system quite efficiently.

The actual state of the art is that we have built two games inspired to two corresponding traditional psychological tests, whose methodology has been shown here, and we are in the process of validating them with an empirical case study.

Of course, if such a pilot experiments will result positive, we intend to move on to a larger panorama on cognition (e.g. perception, memory, sound, and etc.) and, further, on different psychological domains (e.g. aptitudes, emotions, personality, interests, IQ, etc.).

References

1. Urbina, S. Anastasi, A. *Psychological testing* (7th ed.). Upper Saddle River, NJ: Prentice Hall. p. 4. 1997.
2. H. H. Lund, "Play for the Elderly - Effect Studies of Playful Technology," in Human Aspects of IT for the Aged Population. *Design for Everyday Life*. (LNCS Vol. 9194, pp 500-511, Springer-Verlag, 2015)
3. S. Chokronab, P. Bartolomeo, M.T. Perenine, G. Helfff, M. Imbertg. Scanning direction and line bisection: a study of normal subjects and unilateral neglect patients with opposite reading habits. *Cognitive Brain Research*. Volume 7, Issue 2, October 1998, Pages 173-178
4. A. Varnava, M. McCarthy, J.G. Beaumont. Line bisection in normal adults: direction of attentional bias for near and far space. *Neuropsychologia*. Volume 40, Issue 8, 2002, Pages 1372-1378
5. A.D. Milner, M. Brechmann, L. Pagliarini. To halve and to halve not: an analysis of line bisection judgements in normal subjects. *Neuropsychologia*. 1992 Jun; 30(6):515-26.
6. Neisser, U. (1963) Decision-time without reaction-time: Experiments in visual scanning. *American Journal of Psychology* 76: 376-385.
7. A. M., Treisman & G. Gelade, (1980). A feature-integration theory of attention. *Cognitive Psychology*, 12(1), 97-136.
8. H. H. Lund, and J. D. Jessen, "Effects of short-term training of community-dwelling elderly with modular interactive tiles," *GAMES FOR HEALTH: Research, Development, and Clinical Applications*, 3(5), 277-283, 2014.
9. BrainBaseLine. <https://www.brainbaseline.com/>

Natural Computing Paradigm — A Concise Introduction

Takashi Yokomori

Department of Mathematics, Faculty of Education and Integrated Arts and Sciences,
Waseda University, Tokyo 169-8050, Japan
E-mail: yokomori@waseda.jp

Abstract

Natural computing (NC) is an emerging area of research that investigates computing techniques and models inspired by nature on one hand, and it also investigates phenomena taking place in nature in terms of computational methodologies on the other hand. Thus, research in NC congenitally has interdisciplinary flavor, which bridges between computer science and various disciplines of natural science. Because of its interdisciplinary nature, NC connects and covers a broad spectrum of fundamental research fields including biology, chemistry, physics, medical science, and so forth. In this article, we give a concise introduction to the new computing paradigm of NC. Specifically, we give an overview of selected topics of the fields from theory to experiments, where the stress is primarily put on theoretical achievements in computing paradigms called molecular computing and chemical reaction computing.

Keywords: Natural computing, molecular computing, self-assembly, chemical reaction computing.

1. Introduction

Natural computing (NC) is a novel computing paradigm inspired by nature in which NC concerns a variety of computational aspects and potential features found in natural phenomena. Also, NC has close relations to computational process inspired by those phenomena.

The goal of NC includes the following research themes.

(i) *From nature to information processing* which means investigating computational mechanism and its implementation based on lessons from nature, and

(ii) *From information processing to nature* which means computational analysis of nature in terms of designing new computing models and computer experiments (simulations). Further, NC also intends to exploit new applications in the fields of various disciplines involved. It is rather surprising that the conceptual source of the idea of NC has already appeared in an article of *Biofizika* in 1973 where an idea of cell molecular computers was discussed. Since 1974 Conrad has been conducting consistent research on the information processing capability using macro-molecules (such as proteins), and

has edited a special issue in a journal entitled *Molecular Computing Paradigms*. His initial efforts in the early days of molecular computing have been succeeded by Head's original work on *Splicing Systems and Languages* whose theoretical results on splicing phenomena should be highly appreciated, in that it was the first achievement

by means of mathematical analysis on bio-chemical operations of DNA recombination. It is possible to discuss about new computing paradigms inspired by nature with a general schema of "Computing with X ", where X ranges from various sorts of materials to those

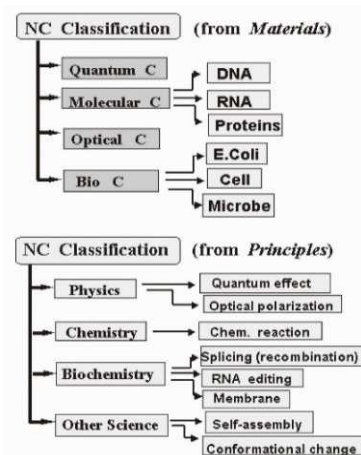


Figure 1. Natural Computing Paradigms Inspired by Nature (A part)

of principles. Figure 1 illustrates a part of natural computing paradigms proposed so far within the “Computing with X ” schema.

In this short article, among various computing paradigms we take up two computing paradigms “Molecular computing” (from *materials*), and “Chemical reaction computing” (from *principles*), and give an outline of fundamental results on computing capability of these new challenging ingenuity.

2. Molecular Computing Paradigm

In the early days, the goal of molecular computing seemed to replace silicon-based hardware with bio-molecular one. Unlike this intention of the early schema, however, by now *it is commonly recognized that molecular computers should explore challenging applications unsuitable for existing computers.*

In the theory of molecular computing, a variety of computation models have been proposed and investigated. Among others the models of computation based on *self-assembly* are well recognized to be of great importance in that they can provide one of the most basic frameworks for molecular computing paradigms. In fact, Adleman's groundbreaking wet lab experiment [1] (solving a small instance of the Hamiltonian Path Problem) is a typical example of molecular computation based on the self-assembly principle.

When we make a brief revisit to the Adleman's original work in 1994, it turns out that his algorithm may be formulated into the schema where component structures are sophisticatedly *encoded* into *linear* molecules. From these observations, a general schema of “one pot” self-assembly computation model is outlined as follows:

1. design a finite set of basic units for assembly computation (one may take this finite set as a *molecular program*),
2. put all those basic units with sufficiently high concentration into one pot, to create a *random pool* of a single pot (that is, leave the pot for a certain time period, resulting in producing all possible assembly of basic units),
3. (if necessary) perform *screening operations* to extract only necessary (or unnecessary) assembly of basic units,
4. detect whether or not there is an assembly with desired constraints, then answer *yes* if there is, and *no* otherwise.

Figure 2 illustrates the overview of computation schema based on self-assembly.

In this section, we will briefly review one of the typical models based on self-assembly computation, called *YAC model*. Based on a unique normal form grammar G (proposed by Geffert) that can generate any recursively enumerable language, a computing model YAC has been proposed, in which an input string and every rule in G

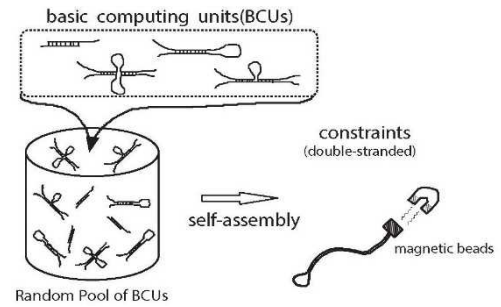


Figure 2. Computation Schema based on Self-assembly

are translated(encoded) into specific forms of two-dimensional structural molecules. These basic blocks (units) of structural molecules with sticky ends are designed so that they may form a DNA complex linearly growing by self-assembly property. This means that YAC performs a simulation of computation (generation) by G , where the input string is accepted by YAC if and only if the final DNA complex forms a completely hybridized double-stranded (that is a desired constraint to be checked by screening mechanism).

It is shown that any recursively enumerable language can be recognized by YAC model. Thus, the following holds.

Proposition 1. ([2]) *There effectively exists a computing model based on self-assembly principle whose computational power is Turing universal.*

Other molecular computing models using high-dimensional structures have been proposed to solve NP-complete problems such as the satisfiability (SAT) problem by Jonoska et al., where 3-dimensional graph structures are used and the algorithm for SAT runs in time proportional to the number variables involved in a given formula. On the other hand, Yokomori investigated a self-assembly computing model in an abstract level, called Computing by Conformational Change (CCC), and proposes the following general schema that

(Computation)=(Self-Assembly)+(Screening Mechanism), where “self-assembly” is due to hybridization of either uncoded or coded molecular components, while “screening mechanism” is regulated by either natural or artificial constraint ([2]).

3. Chemical Reaction Paradigm

Inspired by the work of reaction systems (initiated by [3]), the notion of reaction automata has been introduced in [4] by extending sets in each reaction (of a reaction system) to multisets. We start this section by reviewing basic notions concerning reaction automata.

For a finite set S , a *reaction* in S is a 3-tuple $\mathbf{a} = (R_{\mathbf{a}}, I_{\mathbf{a}}, P_{\mathbf{a}})$ of finite multisets, such that $R_{\mathbf{a}}, P_{\mathbf{a}} \in S^{\#}$, $I_{\mathbf{a}} \subseteq S$ and $R_{\mathbf{a}} \cap I_{\mathbf{a}} = \emptyset$, where $S^{\#}$ denotes the set of all finite multisets over S . The multisets $R_{\mathbf{a}}$ and $P_{\mathbf{a}}$ are called the *reactant* of \mathbf{a} and the *product* of \mathbf{a} , respectively, while the

set I_a is called the *inhibitor* of \mathbf{a} . These notations are extended to a multiset of *reactions*. A reaction $\mathbf{a} = (R_a, I_a, P_a)$ is *applicable* to a multiset D if $R_a \subseteq D$ and $I_a \cap D = \emptyset$. As a result, $D' (= (D - R_a) \cup P_a)$ is derived.

With a simple example, we introduce the notion of reaction automata. Let us consider a *reaction automaton* (RA) $\mathcal{A} = (S, \Sigma, A, D_0, f)$ defined as follows:

- $S = \{p_0, p_1, a, b, a', f\}$ (symbols of objects),
- $\Sigma = \{a, b\}$ (input symbols),
- $A = \{\mathbf{a}_0, \mathbf{a}_1, \mathbf{a}_2, \mathbf{a}_3, \mathbf{a}_4\}$ (reactions), where
- $\mathbf{a}_0 = (p_0, aba', f)$, $\mathbf{a}_1 = (p_0a, b, p_0a')$, $\mathbf{a}_2 = (p_0a'b, \emptyset, p_1)$,
- $\mathbf{a}_3 = (p_1, a'b, a, p_1)$, $\mathbf{a}_4 = (p_1, aba', f)$,
- $D_0 = p_0$ (an initial multiset), and f is the final symbol.

Let $w = aabb$ be a given input string. Since \mathcal{A} has the initial multiset $D_0 (= p_0)$, there is no reaction in A applicable to D_0 . When receiving the 1st a of w , the multiset D_0 of \mathcal{A} becomes p_0a to which only \mathbf{a}_1 is applicable and, as a result, $D_1 (= p_0a')$ is derived. On receiving the 2nd a , the multiset of \mathcal{A} becomes $p_0a'a$ from which $D_2 (= p_0a'a)$ is derived by applying \mathbf{a}_1 . Then, receiving b and applying \mathbf{a}_2 lead D_2 to $D_3 (= p_1a')$, and on receiving the final b , \mathcal{A} makes D_3 into $D_4 (= p_1)$ by \mathbf{a}_3 . After applying \mathbf{a}_4 , D_4 eventually leads to the final multiset f . Thus, an input string $aabb$ is *accepted* by \mathcal{A} . This example shows a successful reaction process of \mathcal{A} performed in *sequential manner* and the set of strings thus accepted by \mathcal{A} is denoted by $L_{sq}(\mathcal{A})$.

Figure 3 illustrates an overall view of possible reaction processes in \mathcal{A} with inputs $a^n b^n$ for $n \geq 0$, and we see that $L_{sq}(\mathcal{A}) = \{a^n b^n \mid n \geq 0\}$ which is a context-free language. We remark that this interactive process can be also performed by \mathcal{A} in *maximally parallel manner*, i.e. in the manner that every applicable reactions are performed exhaustively. That is, it holds that $L_{mp}(\mathcal{A}) = L_{sq}(\mathcal{A})$.

Besides both manners of applications in RAs, we often consider an extension of the sequential manner where RA allows a reaction without receiving any input symbol at each step, which is called *sequential manner with λ -input mode*.

We investigated the accepting powers of reaction automata with these manners of applying reactions, and obtained the following.

Proposition 2. ([4,5]) *The computing power of reaction automata in maximally parallel manner coincides with that of reaction automata in sequential manner with λ -input mode. Further, both of those computing powers are Turing universal.*

On the other hand, the equivalence may not hold for reaction automata in sequential manner with ordinary input mode (i.e., without the use of λ -input mode).

Proposition 3. ([5]) *There exists a recursively enumerable language which cannot be accepted by any reaction automaton in sequential manner.*

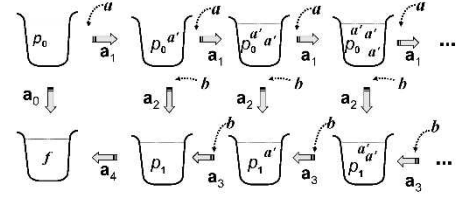


Figure 3. A graphic illustration of interactive processes for accepting strings in $L = \{a^n b^n \mid n \geq 0\}$.

In order to study the role of inhibitors of reactions in the computing power of RAs, we introduced and studied a restricted RA called *Chemical Reaction Automaton* (CRA) in which no inhibitor is allowed ([6]).

Further, the space complexity issues of reaction automata (RAs) have been considered. By restricting the volume (i.e., the state of an RA) used in reaction process for a successful computation, some subclasses of RAs were introduced and investigated on relations between classes of languages accepted by those subclasses of RAs and language classes in the Chomsky hierarchy.

Let $f(x)$ be a function defined on the set of natural numbers and X in $\{\text{sq}, \text{mp}\}$. The *workspace* of \mathcal{A} for w is intuitively defined as the mini-max size of multisets (appearing in all reaction sequences) necessary for accepting w . Then, an RA \mathcal{A} is said to be $f(n)$ -bounded if for any w in $L_X(\mathcal{A})$ with $n = |w|$, the workspace of \mathcal{A} for w is bounded by $f(n)$. Then, four classes of RA languages have been investigated.

Suppose that an RA \mathcal{A} is $f(n)$ -bounded. If a function $f(n)$ is a constant k (linear, exponential), then \mathcal{A} is termed constant- (resp. linear-, exponential-) bounded. The class of languages accepted by constant-bounded RAs (linear-bounded RAs, exponential-bounded RAs, RAs, CRAs) in X manner is denoted by $CoRA_X$ (resp., $LRAX$, $ERAX$, RA_X , CRA_X). The class of languages accepted by constant-bounded RAs (linear-bounded RAs, exponential-bounded RAs, RAs, CRAs) in X manner with λ -input mode is denoted by $CoRA_X^\lambda$ (resp., $LRAX^\lambda$, $ERAX^\lambda$, RA_X^λ , CRA_X^λ).

The results on whole view of language class relations are summarized in Figure 4, where $REG(\mathcal{CF}, \mathcal{CS}, \mathcal{RE})$ denotes the class of regular (resp. context-free, context-sensitive, recursively enumerable) languages in Chomsky hierarchy. Further, \mathcal{PN} denotes the class of languages generated by Petri net systems. Thus, except for the class \mathcal{CF} , each class in Chomsky hierarchy is exactly characterized by a subclass of RA languages. Further, the following result has been obtained.

Proposition 4. ([6,7]) *A language L is in \mathcal{RE} ($= \mathcal{RA}_{mp} = \mathcal{RA}_{sq}^\lambda = \mathcal{CRA}_{mp}^\lambda$) if and only if L is a homomorphic image of some language in $LRAX_{mp}$.*

4. Broader Perspective

Natural computing, (NC) comprises a very broad range of computational principles that varies from well-established classical research areas to newly emerging dynamical research areas with great potentiality of many promising applications to interdisciplinary fields.

The former family may include *Cellular computation*, one of the oldest computing models studied since late 1940s. In *Neural computation*, artificial neural networks are proposed as computing systems inspired by the biological neural networks mimicking brain functions. *Evolutionary computation* provides a bunch of algorithms for global optimization strategy inspired by biological evolution. Further, *Artificial life* is a long-lasting research theme from which artificial immune algorithms have been lately developed. As for the latter family of research areas in NC, there are quite a few topics to be mentioned, while due to the space limit we can regretfully name only a part of those emergence of fascinating thoughts here: *Membrane computation*, *Reaction-diffusion computation*, *Optical computation*, *Quantum computation*, *Swarm intelligence*, etc.

Further, their applications to practical problems in the real world such as drug discovery in “nano-level engineering” and “medical/life science” are highly recommended to be tackled. For one example, one may refer to a medical application, lately reported, of the use of *C.elegans* for detecting cancer patients.

Finally, the reader interested in more details about topics discussed here and other many subjects in NC is cordially advised to consult reference papers or appropriate bibliographic sources (such as [8,9,10]).

References

1. L. Adleman, Molecular Computation of Solutions to Combinatorial Problems, *Science*, vol.266, pp.1021-1024, 1994.
2. T. Yokomori, Computation = Self-assembly + Conformational Change: Toward New Computing Paradigms, *Proc. of 4th International Conference on Developments in Language Theory DLT'99*, Aachen, July, pp.21-30, 1999.
3. A. Ehrenfeucht and G. Rozenberg, Reaction systems, *Fundamenta Informaticae* vol.75, pp.263-280, 2007.
4. F. Okubo, S. Kobayashi and T. Yokomori, Reaction Automata, *Theore. Comput. Sci.*, 429, pp.247-257, 2012.
5. F. Okubo, On the Computational Power of Reaction Automata Working in Sequential Manner, 4th Workshop on Non-Classical Models for Automata and Applications, book@ocg.at series 290, pp.149-164, Osterreichische Computer Gesellschaft, 2012.
6. F. Okubo and T. Yokomori, The Computational Capability of Chemical Reaction Automata, *Natural Computing*, 15, pp.215-224, 2016.
7. F. Okubo, S. Kobayashi and T. Yokomori, On the Properties of Language Classes Defined by Bounded Reaction Automata, *Theore. Comput. Sci.*, 454, pp.206-221, 2012.
8. Gh. Păun, G. Rozenberg, A. Salomaa (Eds.), *Handbook of Membrane Computing*, Oxford Univ. Press, 2010.
9. G. Rozenberg, T. Bäck and J.N. Kok (eds.), *Handbook of Natural Computing*, 4 Volumes, Springer, 2012.
10. 萩谷昌己, 横森貴 (編), ナチュラルコンピューティング・シリーズ第0巻～第7巻: 近代科学社, 2011年.

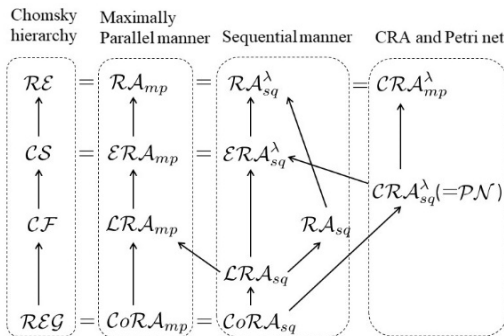


Figure 4. The diagram of the relations among RA language classes and Chomsky hierarchy. (A solid arrow denotes a proper inclusion.)

Acknowledgements

The work partly supported by Partly supported by JSPS KAKENHI, Grant-in-Aid for Scientific Research (C) 17K00021 of The Ministry of Education, Culture, Sports, Science, and Technology, Japan, and by Waseda University grant for Special Research Project: 2017K-121.

Artificial Immune Ecosystems: the role of expert-based learning in artificial cognition

Pierre Parrend*

ICube laboratory, University of Strasbourg, UMR CNRS 7357, Strasbourg, France, ECAM Strasbourg-Europe, Schiltigheim France

Fabio Guigou, Julio Navarro, Aline Deruyver, Pierre Collet

ICube laboratory, University of Strasbourg, UMR CNRS 7357, Strasbourg, France

Abstract

The rapid evolution of IT ecosystems significantly challenges the security models our infrastructures rely on. Beyond the old dichotomy between open and closed systems, it is now necessary to handle securely the interaction between heterogeneous devices building dynamic ecosystems. To this regard, bio-inspired approaches provide a rich set of conceptual tools, but they have failed to lay the basis for robust and efficient solutions. Our research effort intends to revisit the contribution of artificial immune system research to bring immune properties: security, resilience, distribution, memory, into IT infrastructures. Artificial immune ecosystems support a comprehensive model for anomaly detection and characterization, but their cognitive capacity are limited by the state of the art in machine learning and the rapid evolution of cybersecurity threats so far. We therefore propose to enrich the cognitive process with expert-based learning for reinforcement, classification and investigation. Application to system supervision using system logs and supervision time series confirms the relevance and performance of this model.

Keywords: Artificial Immune Systems, Cybersecurity, Immunity, Computational Ecosystem, Anomaly detection

1. Introduction

Old closed IT infrastructures increasingly turn into open interconnected ecosystems of heterogeneous devices: this shift is put to light in particular by the numerous challenges posed by IoT Security [1]. In this context, the detection of anomalies caused by cyberattacks becomes an ever more tedious task to identify known anomalies, new ‘zero-day’ anomalies or signs of system instability following these anomalies. Bio-inspired architectures and algorithms provide to this regard a promising set of concepts and solutions for multi-scale dynamic ecosystems. However, no robust and efficient solution exists to solve the issue of generic anomaly detection so far. We therefore work on a new generation Artificial Immune Systems (AIS) called Artificial Immune Ecosystem (AIE): it encompasses not only the analysis layer as classical AIS do, but also a basis layer for robust and resilient data management, an immune communication protocol [2] as well as a supervision and

knowledge management layer [3]. The AIE shall embed the properties of natural immune systems: security, resilience, distribution, memory. To this aim, their cognition capacity for anomaly identification and characterization in a context of dynamic systems and rapidly evolving threats is a key requirement. We are convinced that cognition, *i.e.* the support of search, adaptability, memory and learning [4] in such heterogeneous environments will not be achieved in a short time span through fully automated solution, and that the contribution of human creativity in the analysis process is a major enabler for adaptation and learning. We therefore propose in this paper to extend the AIE with expert-based learning for reinforcement, classification and investigation. We apply this model to system supervision using system logs and supervision time series to confirm its relevance and performance.

Section 2 introduces related works. Section 3 defines the role of cognition in the Artificial Immune Ecosystem (AIE). Section 4 formalizes the expert-aided learning in

*E-mail: pierre.parrend@unistra.fr, <http://ecam-strasbourg.eu/>, <https://www.unistra.fr/>

© The 2018 International Conference on Artificial Life and Robotics (ICAROB2018), Feb. 1-4, B-Con Plaza, Beppu, Oita, Japan

the AIE. Section 5 presents the experiments and the evaluation of this model. Section 6 concludes this work.

2. Related Work

2.1. Mechanisms of natural immunity

It is possible to summarize natural immunity as the perception of three types of signals by the immune system [5]:

1-signal: the affinity between antigens and antibodies enable these latter to identify known pathogens. This process typically occurs through B-cells and T-cells in acquired immunity.

2-signals: the affinity between immune receptors and PAMPs (Pathogen-Associated Molecular Patterns, such as endotoxin from certain bacteria) triggers infectious inflammation and multiplies the immune reaction. This process typically occurs through Pattern Recognition Receptors (PRR) in innate immunity.

3-signals: the affinity between immune receptors and DAMPs (Danger Associated Molecular Patterns, such as signs of necrosis or intracellular proteins like DNA when released in the intercellular milieu) triggers non-infectious inflammation. This process typically occurs through TLR (Toll-Like Receptors, a specific kind of PRR) in innate immunity.

2.2. Cognition and immunity

Natural immunity is a reference model of learning and cognition where a fully decentralized and autonomous system supports a comprehensive loop of information input, processing and subsequent reaction [6]. This loop is known since Varela as the enactment principle [7]. The cognitive domain covers the range of search, adaptability, memory and learning [4] capabilities. Search is the capability of processing input information for partially hidden signals. Adaptability is the capability of letting information processing evolve over time to cope with environment evolution. Memory enables to retain raw or processed information about passed events. Learning occurs when memory content trigger the adaptation of search capability. It can concern both facts and behaviours.

Bourguin and Steward propose a more global definition of cognition: “A system is cognitive if and only if sensory inputs serve to trigger actions in a specific way, so as to

satisfy a viability constraint” [8], *i.e.* if it is capable of reaction in a context where its viability is at risk.

Although these properties have been devised in a theoretical context, they prove to be key to the construction of an efficient Artificial Immune Ecosystem for multi-scale IT infrastructures.

3. Cognition and the Artificial Immune Ecosystem

3.1. The artificial immune process

A major difference exists between natural immunity and artificial immune processes: In natural systems, the perception of the three (3) signal types occurs through the various immune cell types in parallel. In artificial systems, detection mechanisms are best defined as a process involving several analysis approaches so far, as defined in the artificial immune detection process in Figure 1. 1) The first step for anomaly detection is deterministic memory-based recognition of pathogens. It typically uses explicit rules with a tightly define scope, such as in antiviruses. 2) The second step consists in stochastic immune detection: 2.1) detection based on known antigens, for instance using fuzzy detectors, similar to the 1-signal model of natural immunity, 2.2) recognition of a generic model similar to the 2-signals model and 2.3) detection of danger signal similar to the 3-signals models. 3) The third step consists in the characterization of the anomaly. It can be automated or assisted by the expert as specified in Section 4. 4) Next, the system memory is updated to leverage the knowledge gained through the characterization step. 5) A reaction is performed – which is beyond the scope of this contribution. One should note the difference between step 1) which is deterministic and well understood and step 2.1) which leverages stochastic technologies and is an active research field.

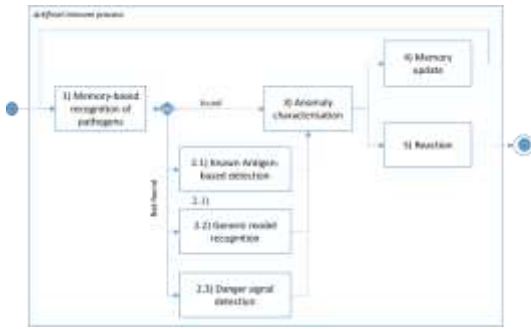


Figure 1 : The artificial immune detection process

On can note several radical differences between the natural immune system (IS) and the artificial immune system process:

- 1) Artificial immunity greatly benefits of integrating deterministic detectors since such technologies are already available and mature, whereas natural systems rely on probabilistic affinities only.
- 2) In natural IS, no notion of process flow exists, immune mechanisms occur in parallel, whereas an artificial process embeds expert knowledge in its own design.

3.2. Anomaly characterization

The step 2.2) of anomaly characterization entails an automated step and a manual-driven step, as shown in Figure 2. We share the vision of D. Engelbart that in highly evolutive environments, interactive systems which “increas[e] the capability of a man to approach a complex problem situation, to gain comprehension to suit his particular needs, and to derive solutions to problems” [9] are a necessity to overcome the intrinsic limitations of bottom-up fully automated systems. Step 3.1) consists in automated detection, typically using statistical or machine learning approaches. If the analysis process provides a satisfactory output here, anomaly characterization is completed. Otherwise, the output of this automated step is presented to the expert for further analysis. If analysis requires a manual confirmation of automated classification for reinforcement, the expert validates or invalidates the system proposal (step 3.2.1). If the analysis requires a manual classification, the expert allocates the anomaly to a category (1 dimension), potentially creating a new one (step 3.2.2). If the characterization is more complex (2 or more dimensions), the expert performs a deeper investigation (step 3.2.3).

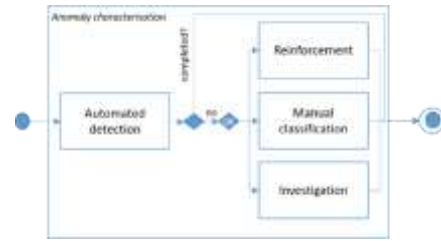


Figure 2 : Anomaly characterisation

The output of steps 3.1, 3.2.1 and 3.2.2 enables the continuous adaptation of the learning artificial immune process. Step 3.2.3 requires that the process can embed complex knowledge in latter analyses such as new detectors, new algorithms or new algorithm parameters.

4. The role of the Expert in the Artificial Immune Ecosystem

The expert intervenes in anomaly characterization for reinforcement, classification of investigation.

4.1. Expert-based reinforcement (step 3.2.1)

In expert-based reinforcement, the expert approves or invalidates the classification into a given category.

$$prop = \{S_U \xrightarrow{I} C_i\} \quad (1)$$

$$prop \stackrel{E}{=} true \vdash S_U \xrightarrow{E} C_i \vdash S_U \in C_i \quad (2)$$

$$prop \stackrel{E}{=} false \vdash S_U \notin C_i \quad (3)$$

As stated in Equation 1, a classification proposal $prop$ that a signal S_U pertains to a given category C_i is made by the system. If the expert labels this classification as correct, the membership of S_U to C_i is confirmed, as given in Equation 2. If the expert labels this classification as incorrect, the membership of S_U to C_i is invalidated, as given in Equation 3.

4.2. Expert-aided classification (step 3.2.2)

In expert-aided classification, the expert provides the category of unknown items, when the system does not manage to find a satisfactory category itself.

$$K = \{C_i\} \quad (5)$$

$$C_i \in \{A_0, \dots, A_n, AAP_0, \dots, AAP_m, D_0, \dots, D_o\} \quad (6)$$

$$S_U \xrightarrow{E} C_i \vdash S_U \in C_i \quad (7)$$

$$S_U \xrightarrow{E} C_u \in \{A_u, AAP_u, D_u\} \vdash S_U \in C_u \wedge K = \{K \cup C_u\} \quad (8)$$

Equation 5 states that system knowledge K is compound of a set of known anomaly categories $\{C_i\}$. Equation 6 states that this set of known anomaly categories entails a set of n traces of Anomalies $\{A_i\}$ [2], a set of m traces of

Anomaly Accompanying Pattern $\{AAP_i\}$ [3], a set of o traces of danger $\{D_i\}$ [2]. Equation 7 states that when this signal S_U is affected by the expert (\rightarrow) to an existing anomaly category C_i which can be either a known anomalous event A_i , a known pattern AAP_i or a known danger signal D_i symptom of abnormal system use, this existing category C_i is extended with anomaly U . This process occurs when C_i does not contain U yet. Equation 8 states that when this signal S_U is affected by the expert to a new category C_n , which is either an anomalous event A , a pattern AAP or a danger signal D , the set C of anomaly categories is extended with C_n , that entails a single anomaly U at this point.

4.3. Expert investigation (step 3.2.3)

In expert investigation, the experts performs the characterization of the properties of an unknown item. This characterization can typically lead to the definition of new detectors.

$$S_U \xrightarrow{EI} S_k = \{p_i\} \tag{9}$$

$$S_k \xrightarrow{ED} D_K \tag{10}$$

$$K = \{K \cup S_k\} \wedge D = \{D \cup D_K\} \tag{11}$$

As stated in Equation 9, expert investigation EI leads to the analysis of an unknown signal S_U as a set of anomaly properties $\{p_i\}$, which then becomes a known signal S_k .

As stated in Equation 10, the intervention of expert design process ED can lead to the creation of a detector D_K for the signal S_k . As stated in Equation 11, the knowledge base K is then extended with signal S_k , and the detector base D with detector D_K . Note that in the case of investigation, the knowledge is compound of the subproperties $S_k = \{p_i\}$ of each anomaly, rather than out of anomaly categories as in the previous cases of classification. Expert-aided classification is thus a special case of the investigation where $|S_k| = 1$ and $S_k \subseteq \{C_i\}$, i.e. the properties can be assigned to an explicit, well-known category.

5. Evaluation

5.1. A cognitive Artificial Immune Ecosystem

In the frame of Bersini’s definition of cognition domains [4], the proposed artificial immune process is actually a cognitive process: it supports search, adaptability, memory and learning, and does so for ensuring the viability of the system. Steps 1) deterministic memory-

based recognition of pathogens and 2) stochastic recognition of pathogens embed the search facility. Step 3) Anomaly characterization embeds adaptability. Step 4) Memory update ensures the memory property together with its exploitation in steps 1), 2), 3). The combination of search, adaptability and memory ensures the capability of learning facts; step 3.2.3) investigation ensures the capability of learning behaviours. In our current model, the human expert supports the reaction process, the viability constraints of IT systems equipped with an AIE and does most of the adaptability capability and behavior learning. The expert-augmented AIE is thus a cognitive system in the sense of Bourguine’s definition [8], but immense research questions are open before the community can transform the proposed process into a fully autonomous one.

5.2. Expert-based reinforcement

We studied the efficiency of expert-based reinforcement with the Morwilog tool [10], which exploits expert feedback to validate the identification of sequences of system logs as occurrences of multi-step attacks. Although these results are theoretical, they provide highly promising insights *wrt.* the capability of handling rapidly evolving complex signals in the context of cybersecurity.

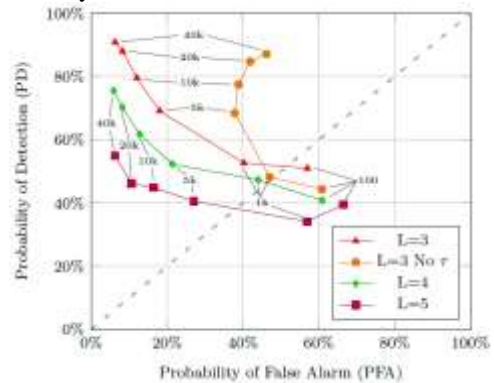


Figure 3 : Evaluation of expert-based reinforcement in Morwilog

5.3. Expert-aided classification

We studied the efficiency of expert-aided classification in the application of the Artificial Immune Ecosystem to network supervision [10], in the particular case of the analysis of time series information. Again, the theoretical results show that the involvement of an expert in the

learning process, here for classification, greatly quickens the analysis capability. On a dataset of 10.000 entries, 30 requests on expert feedback, *i.e.* 0,3%, enables to achieve 89,7% of precision as given by classification F-score. 500 expert feedbacks, *i.e.* 5%, provides 99% precision.

Maximum expert feedback	20	30	50	100	500	Unlimited
F-score	.36	.70	.72	.72	.78	.78

Table 1: Impact of expert-based classification

5.4. Expert investigation

We studied the efficiency of expert investigation in the context of Morwilog tool: before the reinforcement phase can start, the AIE provides suspicious traces as input to the expert to enable him to characterize prototypical multi-step attacks. Based on a list of suspicious traces, the expert thus identifies the actual threat and confirms that a given event sequence builds a single attack.

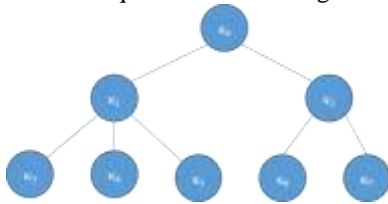


Figure 4 : Attack steps identified through Morwilog investigation

6. Conclusions and perspectives

In this contribution, we propose a process for enforcing artificial immunity, *i.e.* a bio-inspired model supporting the search for three immune signals: pathogens, pathogen-associated patterns and danger. The artificial immune process entails rich detection capabilities, as well as anomaly characterization, which is key to ensure adaptability and memory, and thus learning. In the context of a rapidly evolving environment, we show that involving the expert in this process for reinforcement, classification or investigation provides significant improvements in the learning process, which can then be considered a cognitive one.

Acknowledgements

We express our thanks to the colleagues who have contributed to projects in which we developed the Artificial Immune Ecosystem: Véronique Thomas-

Vaslin, Véronique Legrand. This work was founded by ICube Laboratory (SENSAI project), French Banque Publique d'Investissement (BPI) under AAP-19 HuMa project, Agence Nationale de la Recherche Technologique (ANRT) and the enterprise IPLine.

References

1. S. M. Hashemi and J. He. La-based approach for iot security. *Journal of Robotics Networking and Artificial Life*, 3(4):240–248, 2017.
2. P. Parrend, P. David, F. Guigou, C. Pupka, and P. Collet. The AWA artificial emergent awareness architecture model for artificial immune ecosystems. In *IEEE Congress on Evolutionary Computation 2017*, Special Session on Artificial Immune Systems: Algorithms, Simulation, Modelling & Theory, June 2017.
3. F. Guigou, P. Parrend, and P. Collet. An artificial immune ecosystem model for hybrid cloud supervision. In *Complex System Digital Campus '15*, Sep 2015.
4. H. Bersini and F. J. Varela. Hints for adaptive problem solving gleaned from immune networks. In *International Conference on Parallel Problem Solving from Nature*, pages 343–354. Springer, 1990.
5. J. Greensmith, U. Aickelin, and S. Cayzer. Detecting danger: The dendritic cell algorithm. In *Robust Intelligent Systems*, pages 89–112. Springer, 2008.
6. J. E. Hunt and D. E. Cooke. Learning using an artificial immune system. *Journal of network and computer applications*, 19(2):189–212, 1996.
7. F. Varela. Invitation aux sciences cognitives, 1988.
8. P. Bourguine and J. Stewart. Autopoiesis and cognition. *Artificial life*, 10(3):327–345, 2004.
9. D. C. Engelbart. Augmenting human intellect: A conceptual framework. Summary report afosr-3223 under contract af 49 (638)-1024, SRI project 3578 for air force office of scientific research. Stanford Research Institute. Retrieved March, 1:2007, 1962.
10. J. Navarro Lara, A. Deruyver, and P. Parrend. Morwilog: an ACO-based system for outlining multi-step attacks. In *IEEE Symposium Series on Computational Intelligence (IEEE SSCI 2016)*. IEE, Dec 2016.
11. F. Guigou, P. Collet, and P. Parrend. The artificial immune ecosystem: a bioinspired meta-algorithm for boosting time serie anomaly detection with expert input. In *EvoApplications, 20th European Conference on the Applications of Evolutionary Computation*, Apr 2017.

Harnessing over a Million CPU Cores to Solve a Single Hard Mixed Integer Programming Problem on a Supercomputer

Yuji Shinano

Mathematical Optimization and Scientific Information, Zuse Institute Berlin,
Takustrasse 7, 14195 Berlin, Germany
E-mail: shinano@zib.de

Abstract

The performance of mixed integer programming (MIP) solvers has improved tremendously in the last two decades and these solvers have been used to solve many real-world problems. ParaSCIP is the most successful parallel MIP solver in terms of solving previously unsolvable instances from the well-known benchmark instance set MIPLIB by using supercomputers. ParaSCIP has been developed by using the Ubiquity Generator (UG) framework, which is a general software package to parallelize any state-of-the-art branch-and-bound based solvers. ParaSCIP is a parallelized MIP solver of a single thread solver SCIP. Since Xpress is a multi-threaded solver and ParaSCIP can run at least 80,000 processes in parallel for solving a single MIP, ParaXpress could handle over a million CPU cores. In this talk, a ground design of the UG framework and its latest extensions to harness over a million CPU cores will be presented and preliminary computational results will be provided.

Keywords: mixed integer programming problem, massively parallel computing, SCIP, ParaSCIP, ParaXpress, UG

Slides



Harnessing over a Million CPU Cores to Solve a Single Hard Mixed Integer Programming Problem on a Supercomputer


Yuji Shinano
Zuse Institute Berlin

ug[SCIP,*]: joint work with Tobias Achterberg, Timo Berthold, Gerald Gamrath, Stefan Heinz, Thorsten Koch, Stephen J. Maher, Daniel Rehfeldt, Stefan Vigerske, Michael Winkler
ug[Xpress,*]: joint work with Timo Berthold, Stefan Heinz
ug[PIPS-SBB,MPI]: joint work with Lluís Miquel Munguia, Geoffrey Oxberry, Deepak Rajan
UGS: joint work with Lluís Miquel Munguia



04/02/2018 The 2018 International Conference on Artificial Life and Robotics 1

Outline

- 
- Background and Purpose
 - ◆ State-of-the-art Mixed Integer Programming (MIP) solvers
 - ◆ Parallelization of MIP solvers
 - Ubiquity Generator (UG) framework and ParaSCIP
 - Computational results for solving previously unsolved MIP instances on supercomputers
 - How to harness over a million CPU cores
 - Concluding remarks

Background and Purpose



MIP (Mixed Integer Linear Programming)

- **minimizes** or maximizes a linear function
- is subject to linear constraints
- has integer and continuous variables

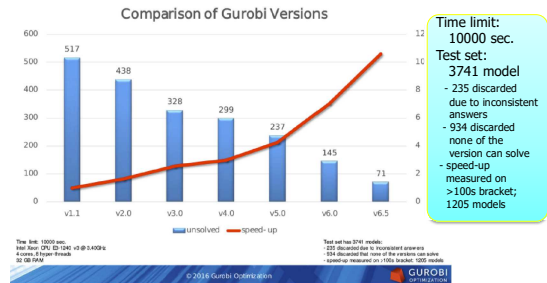


The most general form of combinatorial optimization problems
Many applications

Progress in a state-of-the-art MIP solver



Gurobi Keeps Getting Better



Customer Applications

(2012 Gurobi Sales – 200+ new customers)

- Accounting
- Advertising
- Agriculture
- Airlines
- ATM provisioning
- Compilers
- Defense
- Electrical power
- Energy
- Finance
- Food service
- Forestry
- Gas distribution
- Government
- Internet applications
- Logistics/supply chain
- Medical
- Mining
- National research labs
- Online dating
- Portfolio management
- Railways
- Recycling
- Revenue management
- Semiconductor
- Shipping
- Social networking
- Sourcing
- Sports betting
- Sports scheduling
- Statistics
- Steel Manufacturing
- Telecommunications
- Transportation
- Utilities
- Workforce Management



Background and Purpose



MIP (Mixed Integer Linear Programming)

- **minimizes** or maximizes a linear function
- is subject to linear constraints
- has integer and continuous variables



The most general form of combinatorial optimization problems
 Many applications
 MIP solvability has been improving

Development of a massively parallel MIP solver
 - can solve instances that cannot be solved by state-of-the-art MIP solvers
 - keeps catching up performance improvements of state-of-the-art MIP solvers

Background and Purpose



MIP (Mixed Integer Linear Programming)

- **minimizes** or maximizes a linear function
- is subject to linear constraints
- has integer and continuous variables



The most general form of combinatorial optimization problems
 Many applications

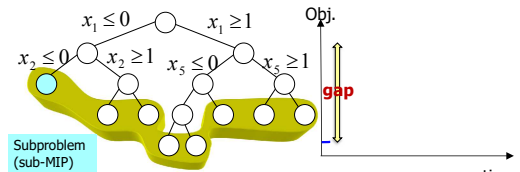
MIP solvability has been improving

Parallelization of MIP solvers



Branch-and-bound looks suitable for parallelization

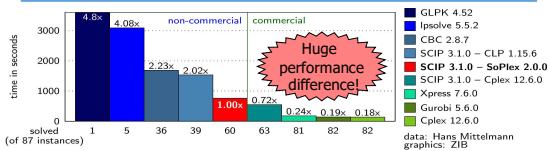
- MIP solvers: LP based Branch-and-cut algorithm



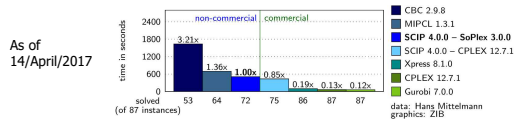
Subproblems (sub-MIPs) can be processed independently

- ➔ Utilize the large number of processors for solving extremely hard MIP instances (previously unsolved problem instances from MIPLIB)

Performance of state-of-the-art MIP Solvers



MIP solver benchmark (1 thread): Shifted geometric mean of results taken from the homepage of Hans Mittelmann (23/Mar/2014). Unsolved or failed instances are accounted for with the time limit of 1 hour.



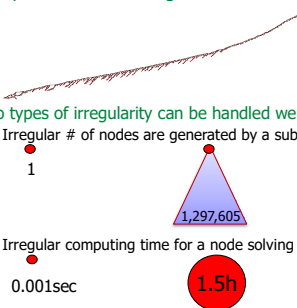
The 2018 International Conference on Artificial Life and Robotics

Dynamic load balancing is needed

Highly unbalanced tree is generated

Two types of irregularity can be handled well

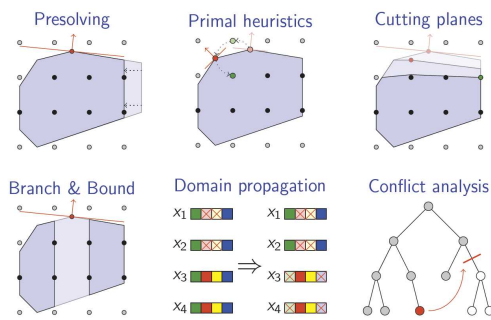
- Irregular # of nodes are generated by a sub-MIP
- Irregular computing time for a node solving



Real observation for solving ds in parallel with 4095 solvers

The 2018 International Conference on Artificial Life and Robotics

Solving techniques involved in SCIP



The 2018 International Conference on Artificial Life and Robotics

GAMS and Condor: M.R.Bussieck and M.C.Ferris (2006)



Problems with a-priori Partitioning

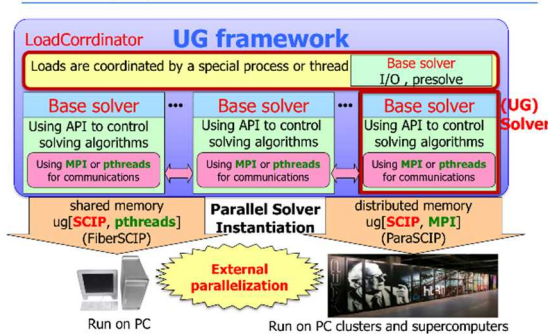
- How can we find n sub-problems with similar (but reduced) level of difficulty?
 - B&C Code keeps a list of *open/unexplored* nodes
 - Problem-bounds of these open nodes represent partitioning of the original problem

Node	Left	Objective	Inf Integer	Best Node	Cuts/	ItCnt	Gap
0	0	29.6862	64	29.6862	165		
100	37	17.0000	14	25.0000	2230		
200	70	21.8429	22	24.0000	4022		

- GAMS/CPLEX Option `dumtree n` creates n bound files

The 2018 International Conference on Artificial Life and Robotics

UG Ubiquity Generator Framework

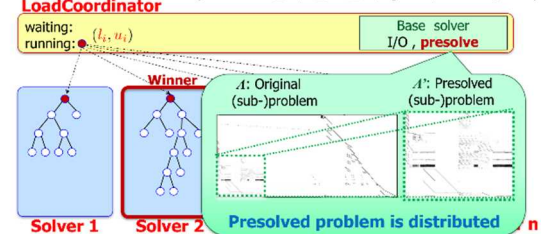


The 2018 International Conference on Artificial Life and Robotics

How UG do parallel tree search

[Ramp-up(Racing)]

$$\min \{c^T x : Ax \leq b, l \leq x \leq u, x_j \in \mathbb{Z}, \text{ for all } j \in I'\}$$



All Solvers start solving immediately, trying to generate different search trees

The 2018 International Conference on Artificial Life and Robotics

How UG do parallel tree search

ZUSE INSTITUTE BERLIN

[Ramp-up(Racing)]
 $\min\{c^T x : Ax \leq b, l \leq x \leq u, x_j \in \mathbb{Z}, \text{ for all } j \in I\}$

LoadCoordinator
 waiting: ○○○○○○
 running: ●●●●●●

Base solver
I/O, presolve

Solver 1 Solver 2 **Winner** Solver 3 Solver 4 ... Solver n

Winner is selected by taking into account dual bound, # nodes, etc.

The 2018 International Conference on Artificial Life and Robotics 15

Why can it handle large scale?

ZUSE INSTITUTE BERLIN

LoadCoordinator
 Open nodes: ○

Solver 1 Solver 2 Solver 3 Solver 4 Solver 5 ... Solver n

Collecting mode Solver
 - The # of solvers at a time is restricted
 - Starts from 1
 - Dynamically switching
 - The number is increased by at most 250 even if run with 80,000 Solvers

Objective Function Value

Computing Time (sec.)

Solver which has best dual bound node

The 2018 International Conference on Artificial Life and Robotics 18

Dynamic load balancing

ZUSE INSTITUTE BERLIN

LoadCoordinator
 Open nodes: ○

Solver 1 Solver 2 Solver 3 Solver 4 Solver 5 ... Solver n

Try to keep p open nodes in LoadCoordinator

Notification message: best dual bound, # nodes remain, # nodes solved
 - Send periodically and asynchronously
 - Interval is specified by a parameter

LoadCoordinator makes selected Solvers in collecting mode

Expected to have heavy nodes: large subtree underneath

Global view of tree search

The 2018 International Conference on Artificial Life and Robotics 16

Layered presolving

ZUSE INSTITUTE BERLIN

$\min\{c^E x : Ax \in E^b, l^E x \in E^u, x_j \in \mathbb{Z}, \text{ for all } j \in I^E\}$

A: Original (sub-)problem
 A': Presolved (sub-)problem

A: Original (sub-)problem
 A': Presolved (sub-)problem

Global view of tree search

The 2018 International Conference on Artificial Life and Robotics 19

Dynamic load balancing

ZUSE INSTITUTE BERLIN

LoadCoordinator
 Open nodes: ○○○○○○

Solver 1 Solver 2 Solver 3 Solver 4 Solver 5 ... Solver n

Collecting mode Solver
 - Changes search strategy to best dual bound first
 - Sends requested number of nodes

Objective Function Value

Computing Time (sec.)

Solver which has best dual bound node

The 2018 International Conference on Artificial Life and Robotics 17

Check pointing of UG

ZUSE INSTITUTE BERLIN

LoadCoordinator
 Open nodes: ○○○○○○

Solver 1 Solver 2 Solver 3 Solver 4 ... Solver n

Base solver
I/O, presolve

Objective Function Value

Computing Time (sec.)

Only essential root nodes of subproblems are saved
 If a sub-tree has been solved, checkpoint file contains comp. statistics

The 2018 International Conference on Artificial Life and Robotics 20

Check pointing

Only the essential nodes are saved depending on run-time situation

The 2018 International Conference on Artificial Life and Robotics 21

The biggest and the longest computation

Solving rmine10: 48 restarted runs with 6,144 to 80,000 cores

Titian with 80,000 cores
The others: HLRN III

It took about 75 days and 6,405 years of CPU core hours!

UG can handle up to 80,000 MPI process

How open nodes and active solvers evolved

The 2018 International Conference on Artificial Life and Robotics 24

Restarting

Only the essential nodes are saved depending on run-time situation

Huge trees might be thrown away, but the saved nodes' dual bound values are calculated more precisely.

The 2018 International Conference on Artificial Life and Robotics 22

Combining with internal parallelization

ug[Xpress,MPI] : ParaXpress

- A powerful massively parallel MIP solver
- Can handle, hopefully efficiently, up to 80,000 (MPI processes) x 24 (threads) = 1,920,000 (cores)

Connection network

Processing Element or Compute node

Processing Element or Compute node

■ : CPU core

The 2018 International Conference on Artificial Life and Robotics 25

Main results for MIP solving by ParaSCIP

Date	Name	Rows	Cols	Int	Bin	Con	SCIP	Cplex	Computer	Runs	Cores	Time(h.)	Optimal value	
March 2011	rnmatz200-p20	29406	29605			200	29405	2.0.1	12.2	Alibaba	1	160	2	837
March 2011													3313.18	
March 2011													16.7342	
March 2011													1.2281657	
Jun 2011													2300867	
July 2011													7903.6501	
August 2011													473840	
March 2011													6609253	
January 2011													43049708	
January 2011													72721458	

Keep solving open instances!

Novemt
Decemt

TI
ISM: FUJITSU MIKUMIKOY KAZUUSO
HLRN II: SGI Altix ICE 8200EX (Xeon QC E5472 3.0 GHz/X5570 2.93 GHz)
HLRN III: Cray XC30 (Intel Xeon E5-2695v2 12C 2.400GHz, Aries interconnect)

The 2018 International Conference on Artificial Life and Robotics 23

Solving open instances of MIPLIB2010

Number of open instances solved

Year

■ Not UG (commercial solvers and SCIP) ■ UG

75 open instances left

ParaXpress started

New ParaXpress

MIPLIB2010 was published

News <http://miplib.zib.de>
(a complete and more detailed changelog can be found here)

- Sep 2017 `gms1-75-80` and `gms1-77-40` moved from open to hard.
- Jul 2017 `german1` and `net100818` moved from hard to easy.
- Feb 2017 version 1.1.3 of the script released: fixed issue in Xpress script.
- Dec 2016 `pigeon-19` solved, moved from open to easy; `pigeon-12`, `pigeon-13`, an
- Nov 2016 `sc22` and `usAbby-8-25_70` solved, moved from open to hard; `ns1089`
- Dec 2015 `rmine10` and `tripTime2` solved, moved from open to hard.

The 2018 International Conference on Artificial Life and Robotics 26

Combining with distributed MIP solver ZUSE INSTITUTE BERLIN

ug[PIPS-SBB,MPI]

- PIPS-SBB: a specialized solver for two-stage Stochastic MIPs that uses Branch & Bound to achieve finite convergence to optimality
 - Use PIPS-S: Backbone LP solver: PIPS-S (M. Lubin, et al. *Parallel distribute-d-memory simplex for large-scale stochastic LP problems*, Computational Optimization and Applications, 2013.)
 - One branch node is processed in parallel with distributed data structure
- 80,000 (MPI processes) x 100 (PIPS-SBB MPI processes) = 8,000,000 (cores)

The 2018 International Conference on Artificial Life and Robotics 27

Run different solvers with different configurations in parallel ZUSE INSTITUTE BERLIN

UGS: UG synthesizer

- Runs many different solvers in parallel as MPMD(Multiple Program, Multiple Data) model MPI program

The 2018 International Conference on Artificial Life and Robotics 28

Conclusions

UG is a general framework to parallelize any kind of state-of-the art branch-and-bound based solver.

ug[SCIP,*] is tool to develop parallel general branch-and-cut solvers. Customized SCIP solver can be parallelized with least effort.

ug[SCIP-Jack,*] is solver for Steiner Tree Problems and its variants, namely only the solver which can run on a distributed memory computing environment (solved three open benchmark instances.

ug[Xpress, MPI](=ParaXpress) and ug[PIPS-SBB, MPI] is ready to run on over a million CPU cores.

UGS is another general framework to configure a parallel solver that can realize any combination of algorithm portfolio and racing.

References

1. Y.Shinano: *The Ubiquity Generator Framework: 7 Years of Progress in Parallelizing Branch-and-Bound*, ZIB-Report (17-60), 2017.
2. Y.Shinano, S.Heinz, S.Vigerske,M.Winker: FiberSCIP - A shared memory parallelization of SCIP, *INFORMS Journal on Computing*, 30(1):11–30, 2018
- 3.Y.Shinano, T.Achterberg, T.Berthold, S.Heinz, T.Koch, M.Winker: Solving Hard MIPLIB2003 Problems with ParaSCIP on Supercomputers: An Update, *Parallel & Distributed Processing Symposium Workshops (IPDPSW), 2014 IEEE International*, pp.1552 – 1561, 2014
4. Y.Shinano, T.Achterberg, T.Berthold, S.Heinz, T.Koch, M.Winker: Solving Open MIP Instances with ParaSCIP on Supercomputers using up to 80,000 Cores, *Proc. of 30th IEEE International Parallel & Distributed Processing Symposium*, pp.770-779, 2016
5. Y.Shinano, T.Berthold, S.Heinz, A First Implementation of ParaXpress: Combining Internal and External Parallelization to Solve MIPs on Supercomputers, to appear *ICMS 2016 proceedings*.
6. Lluís-Miquel Munguia, Geoffrey Oxberry, Deepak Rajan, Yuji Shinano: *Parallel PIPS-SBB: Multi-Level Parallelism For Stochastic Mixed-Integer Programs*, ZIB-Report (17-58), 2017.
7. Gerald Gamrath, Thorsten Koch, Stephen Maher, Daniel Rehfeldt, Yuji Shinano: SCIP-Jack – A solver for STP and variants with parallelization extensions, *Mathematical Programming Computation*, 9(2), pp. 231-296, 2017

Trust of Virtual Agent in Multi Actor Interactions

Halimahtun M. Khalid

*Damai Sciences, A-31-3 Suasana Sentral, Jalan Stesen Sentral 5,
504700 Kuala Lumpur, Malaysia**

Liew Wei Shiung

*Faculty of Computer Science and Information Technology, University of Malaya,
50603 Kuala Lumpur, Malaysia*

Voong Bin Sheng

*Damai Sciences, Suite R26-11 Dua Sentral, No. 8 Jalan Tun Sambanthan,
50470 Kuala Lumpur, Malaysia*

Martin G. Helander

*Damai Sciences, A-31-3 Suasana Sentral, Jalan Stesen Sentral 5,
50470 Kuala Lumpur, Malaysia*

E-mail: mahtunkhalid@gmail.com, liew.wei.shiung@gmail.com, sh3ng527@gmail.com, mahelander@gmail.com

Abstract

Trust is crucial when integrating virtual agents in human teams. Our study investigated the combined use of psychological and physiological measures in predicting human trust of agents undertaking social tasks. The psychological measures comprised trust scores on ability, benevolence and integrity. The physiological measures included facial expressions, voice, heart rate and gestural postures. Subjects interacted with two avatars. A neuro-fuzzy algorithm extracted rules from the psychophysiological data to predict trust. Results revealed that trust can be predicted with 88% accuracy.

Keywords: Trust, virtual agent, measurement, human-agent interaction.

1. Introduction

Trust is a key element in the development of effective human-agent-human relationships, as trust affects system effectiveness of safety, performance, and usability. With the development and integration of virtual agents in human teams, the issue of predicting trust has become a focal concern¹. One of the gaps in research is the lack of a reliable measure of human-robotic trust. Past studies have emphasized subjective measurements only². We present a method where subjective (general trust, psychological) measures and objective (physiological)

measures were mapped to predict human trust of humanoid agents in performing social tasks in a multi-actor and bilingual contexts. In this instance, the role of the humanoid agent or avatar was to mediate between a teleoperator and clients using communication dialog in either English or Bahasa Melayu (Malay language). Therefore, the main objective of our study was to estimate human trust of the avatar in a business mediation context. We hypothesized that trustor's (evaluator) trust of the trustee (agent) is influenced by factors of gender, ethnicity and trust components.

2. Method

In this section, we describe the study as follow.

2.1. Subjects and location

Forty-eight subjects (25 males and 23 females) aged between 21 to 46 years (mean age 26 ±5 years) participated in the study. Twenty-two of the subjects were Malays and 26 were Chinese. To achieve ecological validity the experiment was conducted in an office setting of a R&D studio.

2.2. Avatars and equipment

Two avatars were designed for the experiment. One represented a male Chinese and the other a female Malay using humanoid characteristics derived from an earlier study. Figure 1 illustrates the avatars.



Fig. 1 Male and female avatars

Microsoft Kinect V2 technology was used to record the audiovisual data, and a computerized scale was used to record subjective measures. Data was logged directly into a server via a gigabit router and Ethernet cables, which connected the server to the laptops used by the subjects. Headset microphones were used to record voices.

B. The experimenters and the server for recording data were positioned in an observation room.

2.3. Measures and ROS integration

We measured trust subjectively using criteria of: (a) General Trust and (b) Psychological Trust. General Trust is made up of three factors: Ability, Benevolence and Integrity (ABI)³. For each factor there were four attributes presented as semantic differential word pairs. Altogether there were 12 attributes in the General Trust scale as summarized in Table 1. These attributes were replicated from previous studies^{4,5}

Table 1. General Trust as defined by three main categories, each consisting of four polar attributes

Trust Category	Positive	Negative
ABILITY	Competent	Incompetent
	Knowledgeable	Not Knowledgeable
	Qualified	Unqualified
	Skilled	Unskilled
BENEVOLENCE	Cheerful	Not Cheerful
	Friendly	Unfriendly
	Kind	Unkind
	Pleasant	Unpleasant
INTEGRITY	Dependable	Undependable
	Ethical	Unethical
	Honest	Dishonest
	Reliable	Unreliable

The above attributes in Table 1 were embedded in the interactive dialog.

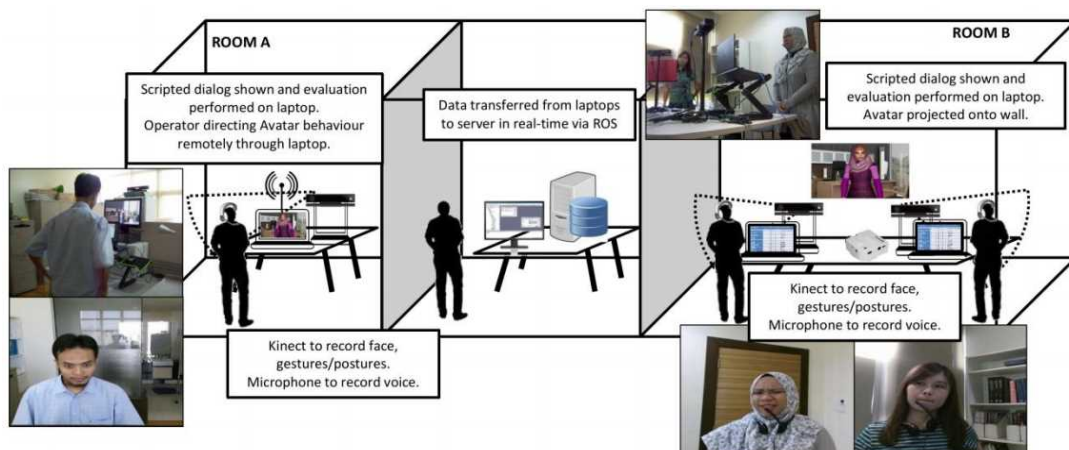


Fig. 2. Arrangement of experimental session

Figure 2 shows the layout of the experimental session, which comprised of 3 rooms. Trustor A (Teleoperator) was in Room A and Trustors B and C (Clients) in Room

Data collection and analysis were made possible via the Robot Operating System (ROS) framework, which integrated the agents, Graphical User Interface (GUI),

© The 2018 International Conference on Artificial Life and Robotics (ICAROB2018), Feb. 1-4, B-Con Plaza, Beppu, Oita, Japan

and hardware. The audiovisual and evaluation data were recorded on the server computer acting as ROS master. The avatar was controlled by a trigger signal sent by subjects through the GUI.

2.4. Experimental design and dialog

The experimental design was a within-subjects design with manipulations of gender, ethnicity, language and compliance to instructions by teleoperator, clients and avatar.

The dialog comprised a communication script of a Business scenario that concerns establishing a factory. This scenario was selected, as it was proven from the results of previous studies to be the most effective than a Disaster or Healthcare scenarios^{1,2}.

2.5. Procedure

First, subjects were briefed on the experiment and their tasks. Second, they signed an informed consent form and completed a subject profile sheet. Third, they were trained on the GUI to familiarize them with the online scoring method and dialog box.

Testing was done in a group of three subjects. The subjects were randomly assigned to the role of Operator or Clients based on a draw lot technique. Typically, the teleoperator in Room A initiated the interaction, followed by the robot confirming its task, and interacting with Trustor B and Trustor C in Room B, who then responded to the avatar, which in turn communicated back to the teleoperator. Subjects were instructed to act out the script in their respective roles. To test for systems operability and usability, a pilot study with two groups of subjects was carried out prior to the actual experiment.

Experimenters were positioned in a separate observation room and monitored the experiment via a screen and a headset. The computer server was placed in the observation room to record data in real time from the Kinects, headsets, and subject evaluation forms.

After completing each application scenario, subjects were given a 10-minutes break to complete a post-hoc questionnaire, which assessed their opinions and preferences regarding the avatar and its features.

2.6. Data analysis

We performed factor analysis, MANOVA and Pearson Correlations on the subjective data to test the hypotheses.

The objective data, which was obtained from the Kinect and headsets, were analyzed separately. The video, audio, and evaluation recordings for each subject were segmented based on the ROS timestamps corresponding to the time when subjects evaluated each trust attribute. The segments were then processed as follow: Voice recordings were processed using PRAAT⁶ and Audio Analysis Library⁷. Facial expressions were processed using OpenFace⁸. Heart rate signals were estimated from the subjects' faces using independent component analysis⁹. Gestural postures were estimated from Kinect's joint coordinates. All extracted objective features were then appended with contextual and subjective information such as the trust evaluation score, dialog condition, and the avatar type.

2.7. Trust classification

To predict trust, we mapped the objective features from the facial expressions, heart rate variability, voice, and gestures¹⁰ of subjects to their subjective scores, to create a dataset. A neurofuzzy classifier ensemble method was then used to learn and predict subjects' trust of the virtual agents.

3. Results and Discussion

The results from MANOVA and correlation analyses revealed the following.

3.1. Gender and ethnicity

The gender and ethnicity of the trustee (virtual agent) had no significant effect on trust. But the interaction effects of gender and ethnicity of the trustors (human subjects) influenced their evaluations of the trustees, with $F(1, 2304) = 18.02$, $p < .001$. Gender-wise, female subjects were more trusting, giving higher trust scores than male subjects, $F(1, 2304) = 24.69$, $p < .001$. This finding confirmed our hypothesis on the influence of gender and ethnicity in trust evaluations.

However, ethnicity alone had no significant effect. Its interaction with trust components produced a significant effect, $F(2, 2304) = 5.01$, $p = .007$. On average, Chinese subjects scored the agents highly on 'Ability' and 'Integrity' attributes, while Malay subjects scored the agents highly on the 'Ability' attributes only.

In addition, there were significant effects of intra-ethnicity on trust, with $F(2, 2304) = 4.17$, $p = .016$. When

the groups consisted of just Chinese subjects, the evaluation of trust was higher than when the groups consisted of Malays only, or when it represented a mixed-ethnic composition. However, the gender composition of the group had no significant effect on trust evaluations. This finding suggests the importance of cultural and ethnic composition of teams in trust-related tasks.

3.2. Subject preferences

An analysis of the post-experiment questionnaire revealed that subjects' trust evaluation scores correlated significantly with their explicit Trust, $r=0.09$, $p<.001$, and Liking preferences for the agents, $r=0.06$, $p=.006$. Subjects who trusted one or more agents explicitly scored higher than subjects who explicitly trusted neither agent, $F(3,2304)=7.81$, $p<.001$.

In addition, subjects who explicitly liked the avatars scored highest; subjects who explicitly disliked the avatars scored second highest, and subjects who were undecided scored lowest, $F(2,2304)=3.681$, $p=.025$.

3.3. Trust prediction

Using the neurofuzzy classifier ensemble method¹⁰, we were able to predict subject's trust in humanoid agents, with an accuracy of $88.3\% \pm 0.2\%$ (F1-score 0.8401), when all physiological data was used. Greater accuracy at 90% was achieved when gestural posture data was excluded, whether for Low, Medium, or High Trust. Details of the analysis are described elsewhere¹⁰.

4. Conclusion

This study has shown that virtual agents can be trusted to perform social tasks using communication dialogs in a multi-actor and bilingual contexts. The trust by humans varies with the gender and ethnicity of the evaluator. Also, trust can be easily evaluated for attributes of 'Ability' and 'Integrity' using dialogs than for 'Benevolence'. This implies that our design and modeling of the humanoid agents requires further anthropomorphism to appeal to humans, persona-wise.

Integration of the various data via ROS allows for real-time annotation of the data recordings. This enables segmentation of the relevant objective data to each trust score evaluation. As such, the accuracy of the neurofuzzy classifier was enhanced to predict trust.

Acknowledgment

We gratefully acknowledge the financial support by the US Aerospace Research and Development office (AOARD), Japan and the US Air Force Office of Scientific Research (AFOSR), Washington D.C. under Grant No. FA2386-14-1-0016.

References

1. P. Robinette, A. M. Howard, and A. R. Wagner, Effect of robot performance on human-robot trust in time-critical situations, in *IEEE Trans. Hum. Mach. Syst.* **47**(4) (2017) 425–436.
2. A. Steinfeld, T. Fong, D. Kaber, M. Lewis, J. Scholtz, A. Schultz, and M. Goodrich, Common metrics for human-robot interaction, in *Proc 1st ACM SIGCHI/SIGART Conf. Hum Rob Interact* (Salt Lake City, Utah, USA, 2006), pp. 33–40.
3. R. C. Mayer, J. H. Davis, and F. D. Schoorman, An integrative model of organizational trust, in *Acad. Manage. Rev.* **20**(3) (1995) 709–734.
4. H. M. Khalid, W. S. Liew, P. Nooralishahi, Z. Rasool, C. K. Loo, and M. G. Helander, Predicting trust in social communication: Implications for human-robot interaction, in *Proc. HFES 2016 Int. Annu. Meeting* (Washington, USA, 2016), pp. 19–23.
5. H. M. Khalid, W. S. Liew, P. Nooralishahi, M. G. Helander, and Z. Rasool, Toward a theory of psychological trust for human-robot-human interaction: Effects of scenarios, gender, and ethnicity, in *Proc. SEANES Int. Conference* (Bandung, Indonesia, 2016), pp. 321–330.
6. P. Boersma, Praat: doing phonetics by computer, in <http://www.praat.org> (2006).
7. T. Giannakopoulos and A. Pirkakis, Introduction to Audio Analysis: A MATLAB Approach, in *Academic Press* (2014).
8. T. Baltrušaitis, P. Robinson and L. P. Morency, Openface: an open source facial behavior analysis toolkit, in *2016 IEEE Winter Conf Appl Comput Vis* (Lake Placid, New York, USA, 2016), pp. 1–10.
9. M. Lewandowska, J. Rumiński, T. Kocejko, and J. Nowak, Measuring pulse rate with a webcam—a non-contact method for evaluating cardiac activity, in *2011 Federated Conference on Computer Science and Information Systems* (Szczecin, Poland, 2011) pp. 405–410.
10. H. M. Khalid, W. S. Liew, B. S. Voong, M. G. Helander and C. K. Loo, Technology for estimating trust in human-robot interaction, in *4th Asian Conf. Def. Tech.* (Tokyo, Japan, 2017).

Production simulation of autonomous decentralized FMS including AGVs with different personalities of mind

Ryuichi Tsujii

*Department of Human Information Systems, Gifu University, Yanagido 1-1,
Gifu, Gifu 501-1194, JAPAN*

Hidehiko Yamamoto

*Department of Mechanical Engineering, Gifu University, Yanagido 1-1
Gifu, Gifu 501-1194, JAPAN*

Takayoshi Yamada

*Department of Mechanical Engineering, Gifu University, Yanagido 1-1
Gifu, Gifu 501-1194, JAPAN*

E-mail: v3128018@edu.gifu-u.ac.jp, yam-h@gifu-u.ac.jp, yamat@gifu-u.ac.jp

Abstract

This study controls Automated Guided Vehicle (AGV) moving by using mind model in order to avoid AGVs' interference. The mind model can avoid the interference by repeating the two types of mind changes, the arrogant mind and the modest mind. In this study, further, provide multiple personality in the mind of the model. By the mind of the model of this multiple personality, we improve the increase of the production out-puts.

Keywords: Autonomous decentralized FMS, AGV with a mind, Different personality

1. Introduction

We've developed the computer control systems to realize a decentralized autonomous flexible manufacturing system (FMS). To do this, it is necessary to avoid the path interference of automated guided vehicles (AGVs) in a decentralized autonomous FMS. We controlled AGV's behavior by using if-then rules. However, as the number of AGVs increases, it is difficult to use the rules for avoiding route interferences in advance. Therefore, we install the model of mind to AGVs and research the behavior control of AGVs. In this research, we give different personalities to this model of mind, and perform production simulation using AGV group of different personalities, and investigate the influence on different personalities of mind to production efficiency.

2. Structure of Autonomous Decentralized FMS

2.1. Outline of Autonomous Decentralized FMS

An example of an autonomous decentralized FMS factory is shown in Fig.1. The factory floor is divided into a grid pattern where AGV moves on the line. The system of automated factory performs the production by carrying the parts to the warehouse or machining centers (MCs). The decentralized autonomous FMS does not have a management mechanism that controls the whole system. The agents (MCs, AGVs and Warehouses) which are the components of the FMSs exchange knowledge and determine the behavior of each agent.

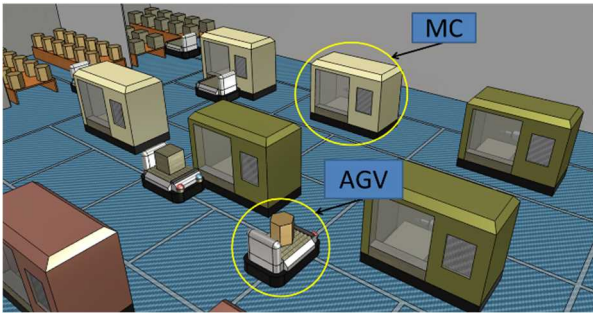


Fig. 1. Example of autonomous decentralized FMS

2.2. Model of Mind and Behavior of AGV

In the autonomous decentralized FMS, AGVs autonomously determine the behavior. In order to avoid path interferences between AGVs, the conventional research used the if-then rules. However, it was not possible flexibly to cope in the case of increasing the number of AGVs and changing the layouts of the factory. Therefore, in this research, in order to solve this, we introduce a model of mind to AGV and realize autonomous movement without AGVs' interferences.

The mind of AGV expresses two kinds of an arrogant mind and a modest mind as shown in Fig.2. Specifically, AGVs with an arrogant mind takes actions forcibly to approach the destinations and AGV with a modest mind takes action to give way to other AGVs.

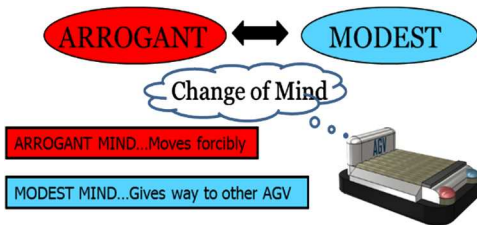


Fig. 2. Example of changing mind

By switching minds between these two kinds of mind, so-called, changing mind, AGVs perform three actions as follows.

- When the AGV with an arrogant mind and the AGV with a modest mind enters the same intersection, the AGV with a modest mind gives way and the AGV with an arrogant mind is given the priority to enter the intersection.

- When AGVs with an arrogant mind enter the same intersection, one of the AGVs changes its mind to a modest heart and gives way.
- When AGVs with a modest mind enter the same intersection, one of the AGVs changes its mind to an arrogant mind and the other AGV gives way.

In order to express the mind, we use the model of mind shown in Fig.3, Mini-mum Unit of Mind (MUM)

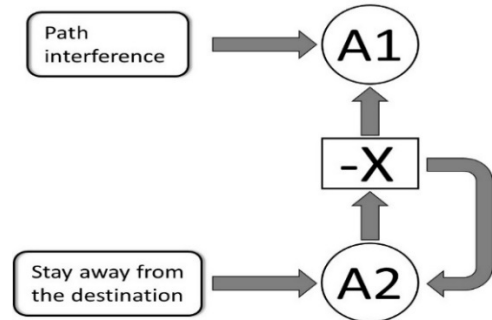


Fig. 3. MUM

[1]. A1 and A2 called as unit, X is load, and an arrow is a stimulation vector. The threshold is determined by the unit. If the internal value reaches the threshold, we call it "excited". And if it does not reach the threshold, we call it "normal". When a signal is sent to the unit, it sends a signal to the direction of the arrow if it is excited, and it is not sent if it is normal. Load has the function to change the internal value of the unit. When the signal is sent to the load, the value of the unit is increased by the value of X. Stimulation vector is a line connecting the load and the unit, and it gives a signal to the load or unit if the signal comes. When A1 is kept excited, we call it "modest mind", and when normal, we call it "an arrogant mind".

By the amount of the signal input to the unit, MUM changes the mind to arrogant or modest frequently. Next, we describe the internal functions of MUM. When the arrogant AGV has path interference, A1 is increased by 1. Keeping the situation of the interference and being increased by 1, the A1 value becomes the threshold, and the AGV is changed to a modest one. When AGVs with a modest mind keep giving a way, the value of A2 is increased by 1. When the situation is repeated at optional times, A2 becomes excited and a signal is sent to a load. The received load decreases the values of units A1 and A2 by optional values. Owing to this, A1 and A2 are returned to normal and a modest mind is

changed to an arrogant mind. In this way, AGV avoids the path interference by the change of heart.

3. Personalities of AGVs

In this study, Personalities of AGVs are defined by the difference of the time from a modest mind to an arrogant one or from an arrogant mind to a modest one. In actual human society, there are people with various personality and they are doing cooperative actions. By giving a big difference of personalities to AGVs like human beings, we try to improve the efficiency of production. This is like bringing the behavior of AGVs closer to human society.

In order to achieve this, by assigning a large or small difference to the threshold of the MUM unit, we make the difference of personality, that is the changing time becomes different. For example, as the value of the unit threshold increases, the number of path interference increases. As a result, the time to start changing time becomes long. In the contrary, as the value of the unit threshold decreases, the number of path interference decreases. As a result, the time to start changing time becomes short.

The followings are five personalities with a standard personality and big different personalities. The previous personality corresponding to the small, changing mind time is also described.

A: Standard personality

B: Personality easy to change mind

C: Personality hard to change mind

D: Personality easy to maintain an arrogant mind

E: Personality easy to maintain honest mind

Table 1 shows the values of thresholds for unit A1 and unit A2 of five personalities.

Table.1. Threshold values of MUM personality

	Unit A1	Unit A2
A	10~14	30~34
B	5~9	15~19
C	20~24	60~64
D	20~24	15~19
E	5~9	60~64

A: Standard personality is the personality used in the previous research. B: Personality easy to change mind is given a smaller value of both unit A1 and unit A2 than

that of A. Therefore, it frequently changes mind. C: Personality hard to change mind is given a large of both unit A1 and unit A2. This personality does not change the mind much. D: Personality easy to maintain an arrogant mind is given the conditions unit A1 is large and unit A2 is small. This makes it easy to maintain an arrogant mind. E: Personality easy to maintain honest mind is given the conditions unit A1 is small and unit is A2 large. This makes it easy to maintain honest mind.

4. Simulations and results

The simulation of FMS operation is carried out by AGV group of single personality adopting only one personality of A-E and AGV group of different personalities combining personality of A-E. Then, we examine the influence on production efficiency by comparing the case of AGV group with single personality and different personalities.

4.1. Simulation conditions

Apply personality to model of mind of 9 AGVs in FMS and run 8 hours simulations' 10 times. The following combination of personality is applied to nine AGVs.

●AGV group of single personality

- Combination ① A×9 units
- Combination ② B×9 units
- Combination ③ C×9 units
- Combination ④ D×9 units
- Combination ⑤ E×9 units

● AGV group of different personalities

- Combination ⑥ A×3 units, B×3 units, C×3 units
- Combination ⑦ A×5 units, B×2 units, C×2 units
- Combination ⑧ A×2 units, B×5 units, C×2 units
- Combination ⑨ A×2 units, B×2 units, C×5 units
- Combination ⑩ A×3 units, D×3 units, E×3 units
- Combination ⑪ A×5 units, D×2 units, E×2 units
- Combination ⑫ A×2 units, D×5 units, E×2 units
- Combination ⑬ A×2 units, D×2 units, E×5 units

4.2. Simulation results

As a result of the production simulation, Table 2 compares the production numbers and Table 3 shows the comparison of the average occupancy rates of the MCs. Compared with the combination ① which is the standard, the number of production decreased in the single personality AGV group. In the AGV group of different personality, the combination of A, B and C increased the

number of production outputs, the combination of A, D, E greatly decreased.

Table.2. Simulation results of production outputs

	Combination of AGV group	Production outputs	Rate of increase
combination1	A9	274.5	1.000
combination2	B9	273.9	0.998
combination3	C9	271	0.987
combination4	D9	90	0.328
combination5	E9	268.9	0.980
combination6	A3B3C3	280.2	1.021
combination7	A5B2C2	280.7	1.023
combination8	A2B5C2	278.9	1.016
combination9	A2B2C5	279.1	1.017
combination10	A3D3E3	193.9	0.706
combination11	A5D2E2	249.4	0.909
combination12	A2D5E2	94.1	0.343
combination13	A2D2E5	260.5	0.949

Table.3. Simulation results of MC efficiency

	Combination of AGV group	MC efficiency	Rate of increase
combination1	A9	0.367	1.000
combination2	B9	0.365	0.994
combination3	C9	0.361	0.984
combination4	D9	0.126	0.344
combination5	E9	0.358	0.976
combination6	A3B3C3	0.371	1.011
combination7	A5B2C2	0.370	1.007
combination8	A2B5C2	0.370	1.007
combination9	A2B2C5	0.367	0.999
combination10	A3D3E3	0.264	0.718
combination11	A5D2E2	0.334	0.909
combination12	A2D5E2	0.132	0.361
combination13	A2D2E5	0.348	0.947

5. Considerations

Compared combination②-⑤ with combination① (single personality AGV group using standard personality), the production number declined in any other single personality AGV group. Especially, in combination ④ (Personality easy to maintain an arrogant mind), the number of production dropped sharply. As this personality tends to maintain an arrogant mind, it is thought that AGVs did not give way to the route so much, the route interference could not be resolved, and the

production efficiency declined. In the AGV group (combination ⑥ - ⑨) which combined the standard personality, personality easy to change mind and personality hard to change mind, the number of production slightly increased. In the case of combination ⑦, the production number was the highest, and the number of production increased by an average of 5.7 compared with the combination ① which is the standard. This is because by combining AGVs with different threshold. It is thought that the timing of change of mind shifted in each AGVs and it was possible to effectively eliminate the path interference. However, in the AGV group (combination ⑩ ~ ⑬) which combined standard personality, personality easy to maintain an arrogant mind, and personality easy to maintain honest mind, the number of production dropped sharply. As the number of AGVs with personality easy to maintain an arrogant mind increased, the number of production declined further. Just like the combination ④, this personality does not give way to the concession of the route, so it seems that the route interference could not be resolved

6. Conclusions

In autonomous decentralized FMS which adopted AGVs with different personalities, production number slightly increased. This is because the AGV group with different personalities performed cooperative action more efficiently than the AGV group with single personality. From this result, it was found that it is effective to use models of minds of different personalities in autonomous decentralized FMS. In this research, we performed simulations with limited combinations of personalities, but there are infinite number of other combinations. How to obtain the optimum combination of personalities is our future task.

References

1. Hidehiko YAMAMOTO, Takayoshi YAMADA and Shinsuke KATO, AGV Mind Model and its Usage for Decentralized Autonomous FMS by Change of Mind, *Proceeding of Third KES International Symposium, KES-AMSTA 2009, Agent and Multi- Agent Systems : Technologies and Applications, Lecture Notes in Artificial Intelligence*, Edited by Anne Hakansson, Ngoc Thanh Nguyen etc. , ISSN 0302-9743, Uppsala, Sweden, pp.744-753, June(2009), Springer.

Development of Automatic Recognition of Hazmat Marking Chart for Rescue Robot

Wisanu Jitviriyā, Poommitol Chaicherdkiat, and Noppadol Pudchuen

Faculty of Engineering, King Mongkut's University of Technology North Bangkok.

1518 Pracharat 1, Wongsawang Rd., Bangsue, Bangkok, Thailand 10800

wisanu.j@eng.kmutnb.ac.th, poommitol.c@gmail.com, and noppadol.pudchuen@gmail.com

Eiji Hayashi

Mechanical Information Science and Technology, Kyushu Institute of Technology.

680-4, Kawazu, Izuka, Fukuoka, 820-8502, Japan.

haya@mse.kyutech.ac.jp

Abstract

A long history of first place awards in World RoboCup Rescue Robot competitions is Invigorating Robot Activity Project (iRAP) such as iRAP_PRO, iRAP_FURIOUS, iRAP_JUNIOR and iRAP_ROBOT. In this paper, we would like to introduce and explain an autonomous system of our rescue robots for detection and recognition of hazardous material (hazmat) marking charts. All hazmat tags are considered and computed by using Speeded-Up Robust Feature (SURF) combined with Fast Library for Approximate Nearest Neighbors (FLANN) to match with the templates. Finally, the paper presents experimental results based on real situations to confirm an effect of the pattern recognition of robotics.

Keywords: Hazmat marking chart, SURF, FLANN and Rescue robot.

1. Introduction

Invigorating Robot Activity Project (iRAP) is the robotics club of students from King Mongkut's University of Technology North Bangkok, Thailand. Every year, we participate in the World RoboCup Rescue Robot competitions, and our teams have won first place many times in the competitions [1]. Our rescue robot can be divided into three major parts such as the mechanical robot part, the electrical system part and the software system part. The unique point of the iRAP robot is the human-robot interface (the operator console), which can show and present extensive sensor values and visual data (CO₂ sensor, visual temperature sensor, laser-scanner, IMU sensor and four cameras) in real time as shown in Fig.1. Moreover, our rescue robot is designed based on proficiency by the agility and performance tests.

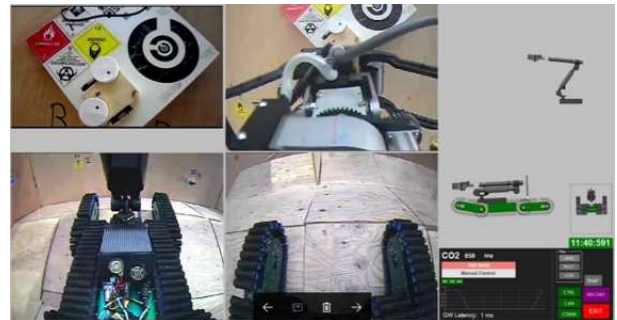


Fig.1 Operator console of iRAP ROBOT

Therefore, the robots can move over rough terrain by using a caterpillar module combined with four flipper modules. The advantage point of flipper parts is that they can help the robot to balance and go through all kinds of

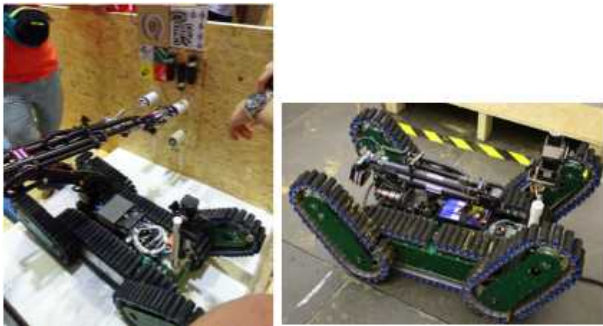


Fig.2. iRAP Rescue Robot

obstacles. In this paper, we would like to develop and improve the software system by adding an automatic recognition of Hazmat tags. The recognition model is produced and computed with Speeded-Up Robust Feature (SURF) [2], [3] combined with Fast Library for Approximate Nearest Neighbors (FLANN) [4], [5]. The results of detection and recognition will be presented and verified in a real situation.

2. Structure of iRAP Robot

The structure of the iRAP rescue robot is an original platform for the rescue robot which has two pairs of flippers (in the front and in the rear) as shown in Fig. 2. In addition, the 6-DOF robotic arm (1 prismatic joint and 5 revolute joints) is set up on a body of the robot, to search and observe the victim and situation in the surrounding area. The multi-sensors are installed in the end-effector of robotic arm, and also, the camera on the robotic arm is used for recognizing the Hazmat chart autonomously.

3. Automatic Recognition of Hazmat Chart

The proposed paper that presents the SURF method for extraction the information from the image and then using the FLANN model, which is used to match the input image with Hazmat chart templates. The overview system can be divided in two phases: the initialization phase (Fig.3) and real-time processing phase.

3.1. Initialization Phase

- Load all template images

The first part of initialization phase is to input the all the Hazmat chart templates. There are twelve templates for training the proposed methods as displayed in Fig. 4.

© The 2018 International Conference on Artificial Life and Robotics (ICAROB2018), Feb. 1-4, B-Con Plaza, Beppu, Oita, Japan

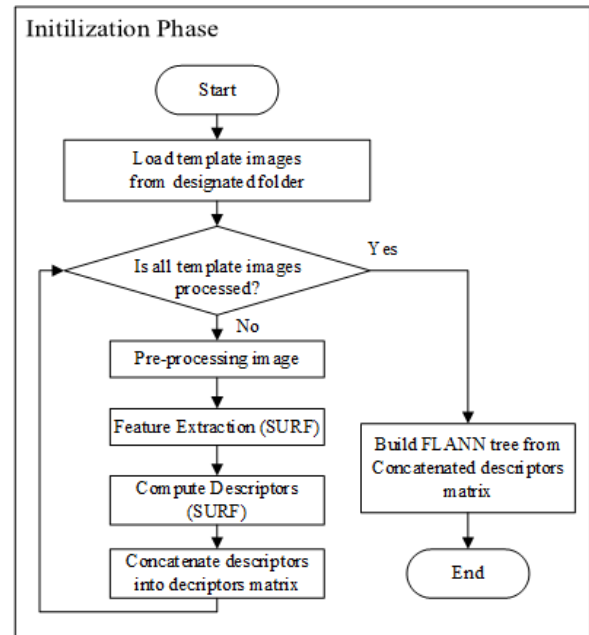


Fig.3. Initialization phase of the proposed method



Fig.4. Hazmat chart templates

- Pre-processing image

In the pre-processing image, there is common task to improve or adjust the feature of image (scale, color, edge, area etc.).

- Feature extraction

The SURF algorithm is applied to the feature extraction. It consists of detector (Hessian matrix), as expressed and descriptor schemes (Haar wavelet). The determinant of a hessian matrix in Equation (1) shows the expression of the local change around the area, where

$H(x, \sigma)$ is the hessian matrix, as illustrated in Equation (2), and $D_{xx}(x, \sigma), D_{yy}(x, \sigma)$ in Equations (3) and (4) are the convolution of the integral image and the second derivative of the Gaussian function.

$$\det(H_{approx}) = D_{xx}D_{yy} - (wD_{xy})^2 d \quad (1)$$

$$H(x, \sigma) = \begin{bmatrix} D_{xx}(x, \sigma) & D_{xy}(x, \sigma) \\ D_{xy}(x, \sigma) & D_{yy}(x, \sigma) \end{bmatrix} \quad (2)$$

$$D_{xx}(x, \sigma) = I(x) * \frac{\partial^2}{\partial x^2} g(\sigma) \quad (3)$$

$$D_{yy}(x, \sigma) = I(x) * \frac{\partial^2}{\partial y^2} g(\sigma) \quad (4)$$

After having create the response map, the next step is to consider a non-maximum suppression based on the determents of the hessian matrix that is the objective of the SURF detection.

- Compute descriptors

At each interest point, we have to indicate the unique description of a feature that do not depend on the size and rotation. The SURF descriptor is based on the Haar wavelet model that can be calculated efficiently with integral images. The wavelets response in the x and y direction is defined as dx and dy respectively as shown in Fig. 5. For each sub-area of a vector, descriptors are calculated based the Equation (5)

$$v_{sub} = \left[\sum dx, \sum dy, \sum |dx|, \sum |dy| \right] \quad (5)$$

- Concatenate descriptors

In this sub-process, it is created by the new platform of descriptors to the sample feature. Then, we have 12 sample feature descriptors to match with the input image.

- Build FLANN method from concatenate descriptors

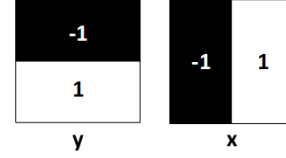


Fig.5. The wavelets response. Black and white areas show the weight -1 and 1 for the Haar kernels.

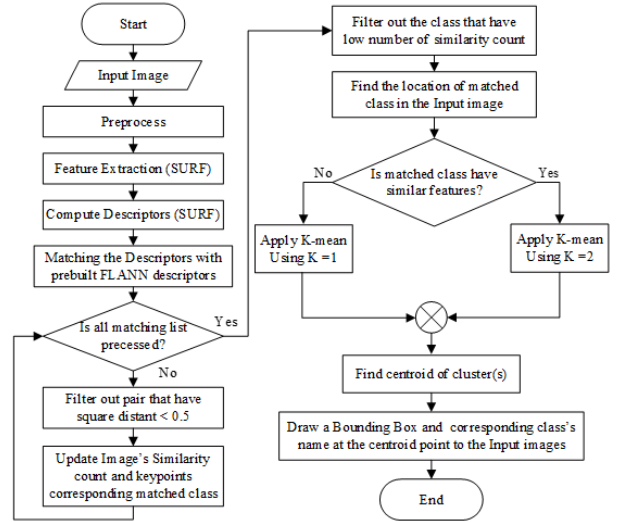


Fig.6. Real-time processing phase

In matching process, FLANN is used to classify the input image by comparing it with 12 sample feature images. FLANN is open source of a library model for performing fast approximate nearest neighbors. It is now one of the most popular model for nearest neighbor matching.

3.2. Real-time Processing Phase

The real-time processing phase (Fig.6) is similar to an initialization phase. First, the acquired image is input into the main process. The SURF method is used to extract the interest points and compute the descriptors. And then, the descriptors of the input image are compared with all sample images. The similarity score of the keypoint is calculated in each class, Finally, the input image is specified in the winner class, which is the maximum similarity score. Then, the position of the hazmat image is in the frame that will be considered to calculate the centroid of an interest area.

4. Experimental results

The experimental results were verified with the Visual Studio C# program and an open source library such as Emgu CV library. In case there is only one hazmat image in the frame, the results of the proposed method could recognition and detection autonomously, it did not depend on the size of input image and rotation as shown in Fig.7. In addition, we had more testing of the proposed method by adding 4 hazmat charts in the input image as displayed in Fig.8. The results that confirm the proposed method can classify and identify the hazmat chart accurately and correctly.

5. Conclusion

This paper presents the development of the automatic recognition of a hazmat marking chart for rescue robots. The results that affirm the proposed method can be used in detection and recognition in the real situation. In the future work, we will improve not only the speed of the recognition system but also the accuracy of method.

6. References

1. A. Phunopas, A. Blattler and N. Pudchuen, "iRAP Robot: World RoboCup Rescue Championship 2016 and Best in Class Mobility Award," the Lecture Notes on Artificial Intelligence, Springer book on RoboCup 2016, volume 9776.
2. S. U. R. F. (SURF), "Herbet bay, andreas ess, tinne tuytelaars, luc van gool," Elsevier preprint, 2008.
3. Wikipedia, "Blob detection — Wikipedia, the free encyclopedia," 2011, [Online; accessed 14-July-2010]. [Online], Available: https://secure.wikimedia.org/wikipedia/en/wiki/Blob_detection
4. Marius Muja and David G. Lowe: "Fast Matching of Binary Features," Conference on Computer and Robot Vision (CRV) 2012.
5. Marius Muja and David G. Lowe, "Fast Approximate Nearest Neighbors with Automatic Algorithm Configuration", in International Conference on Computer Vision Theory and Applications (VISAPP'09), 2009.

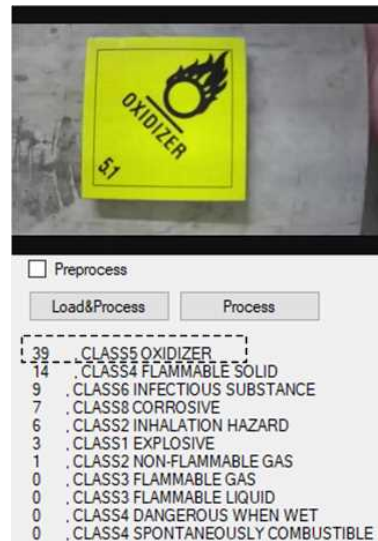


Fig.7. One hazmat chart matching

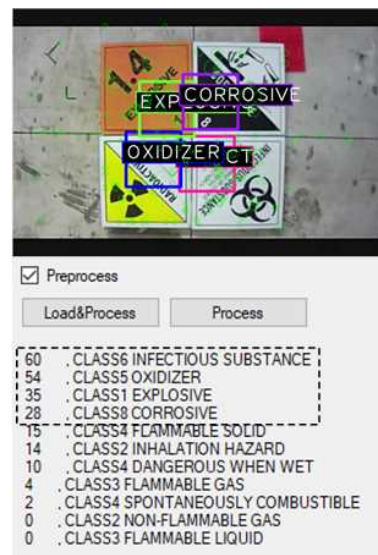


Fig.8. Four hazmat charts matching

Development of Autonomous Robot for Laborsaving of the Forestry Discrimination between trees and weeds using RGB-D

Shingo Yamaguchi

*Department of Mechanical Information Science and Technology, Kyushu Institute of Technology
680-4, Kawazu, Iizuka-City, Fukuoka, 820-8502, Japan
Email: yamaguchi@mmcs.mse.kyutech.ac.jp*

Eiji Hayashi

*Department of Mechanical Information Science and Technology, Kyushu Institute of Technology
680-4, Kawazu, Iizuka-City, Fukuoka, 820-8502, Japan
Email: haya@mse.kyutech.ac.jp*

Ayumu Tominaga

*Department of Mechanical Information Science and Technology, Kyushu Institute of Technology
680-4, Kawazu, Iizuka-City, Fukuoka, 820-8502, Japan
Email: tominaga@mmcs.mse.kyutech.ac.jp*

Abstract

In traditional forestry, the weeding task places a large burden on workers. Therefore, it has been expected that such the problem will be solved by a robot. We have been developing an autonomous robot that eliminates the weed plants without damaging trees (these are resources). The robot should recognize trees exists in the environment. In this research, we have been focused on distinguishing between trees and other them. The system computes the RGB histogram of pixels corresponding point-cloud data of the ground extracted by plane detection. The threshold values are determined to discriminate between trees and weeds by this histogram automatically.

Keywords: Autonomous Self-Moving, Depth Sensor, Forest, Image processing

1. Introduction

In primary industries such as agriculture, forestry, and fishery, labor shortages caused by the aging worker population and the declining employment rate has been a problem. To solve this issue, interest in and expectations for field robots working in the natural environment has been increasing, and it is expected that robotics will be introduced to the agricultural industry in the future. Although many investigations and experiments in real fields have already been accomplished for robots in agriculture, the mechanization and modernization of the forestry industry has been stagnant. This is especially

true for Japanese forestry, which has a remarkable delay in mechanization compared to other countries. In the Nordic region, which includes countries with a very developed forestry industry, harvesting using heavy machinery has improved not only the production efficiency but also worker safety. However, in Japan's forestry, most deployed areas are mountainous forest areas that are steep with a rough terrain. In addition, the planting density can be as high as 3000 per hectare (the world standard is 0), and the standard planting interval between two trees must be 2.5 m. For this reason, it is difficult for large-scale heavy machinery introduced in other countries, such as harvesters, to enter the forest

© The 2018 International Conference on Artificial Life and Robotics (ICAROB2018), Feb. 1-4, B-Con Plaza, Beppu, Oita, Japan

backland; thus, most of the work must be performed manually by workers.

In this research, we focus on the introduction of field robots to the forestry industry.

The robot we have developed is a compact and autonomous robot that can enter the forest hinterland. The main task of this robot is weeding with autonomous motion. In traditional forestry, weeds are primarily eliminated by workers, and the workers must move around all areas of a vast plantation. Grass weeding is an essential task for promoting the growth of trees, which are essential resources, and for improving underfoot visibility. Ideally, weeding must be done more than twice in a summer term, but it is a severe task that is performed under the blazing sun. Thus, automating weeding is an urgent task for improving safety and productivity in forestry.

Our research has focused on developing a robot platform, weeding mechanism, and autonomous moving system. The system is based on an all-terrain vehicle (ATV), and obstacle avoidance in the forest is realized by detecting the external environment with a depth sensor.

In this study, we describe the way of discriminating between trees and weeds in a real environment. Discrimination between trees and weeds is an important factor for an autonomous mobile robot to eliminate weeds without damaging trees. Therefore, we have developed the system that discriminates between trees and weeds using RGB-D data.

2. The robot platform

Fig.1 shows the robot developed in this study. The actual mountain hillside where we will operate the robot is a steep slope, and the road is rough. Therefore, the robot is based on an ATV (Kawasaki, Inc.) to handle the rough terrain. The robot measures an area that is 1400-mm long, 900-mm wide, and 1200-mm high. In the Japanese forest industry, the planting interval is approximately 2.5 m, which is narrow compared to forestry regulations in other countries. As shown in Fig.1, the size of our developed robot is sufficiently small compared to the planting interval that it can travel into the hinterland of the mountain forest. The robot has four wheels, of which the front two are turning wheels and the rear two are driving wheels. The external environment is recognized by a depth sensor and a charge-coupled device camera equipped on the ATV. The depth sensor can acquire an object's position as three-dimensional (3D) point-cloud data via an infrared laser measurement. The maximum measurable depth direction of the sensor

is 15 m. In addition, the robot has an inertial measurement unit (IMU) for pose detection and RTKGPS for global localization. The power source is a gasoline engine. The brake lever, accelerator lever, and steering are all controlled by DC motors. A weeding task is performed by a weeding mechanism that comprises a multi blade structure attached to the front of the ATV.

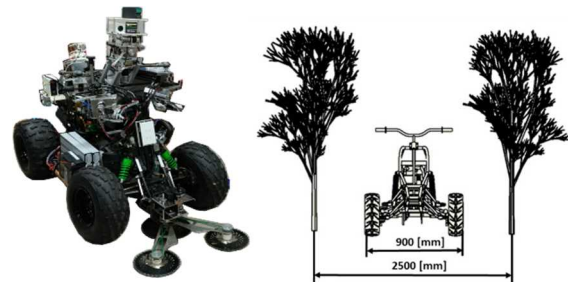


Fig.1. Robot appearance

3. Autonomous moving system

One of the required functions for the robot is to avoid collisions with the trees (especially young trees, which are the objects to be raised) while eliminating weeds. Collision avoidance is realized by the 3D point cloud obtained from the depth sensor. The process flow for the tree-avoidance behavior is shown in Fig.2. Here, the depth image is a gray-scale image expressing the depth information as shades of color, and the top-view image represents the result of projecting the 3D point-cloud data on a two-dimensional (2D) plane. The location information of objects is obtained by processing labels of the top-view image, after which the spacing between two objects that the robot can pass through is computed. Object avoidance is realized by ensuring that the robot constantly aims at the middle point of this space between objects.

Once the robot reaches the target point between the objects, the process returns to the observation process using the depth sensor. The judgment of when the target point is reached is performed using the traveling distance measured by a rotary encoder attached to the rear-wheel drive shaft.

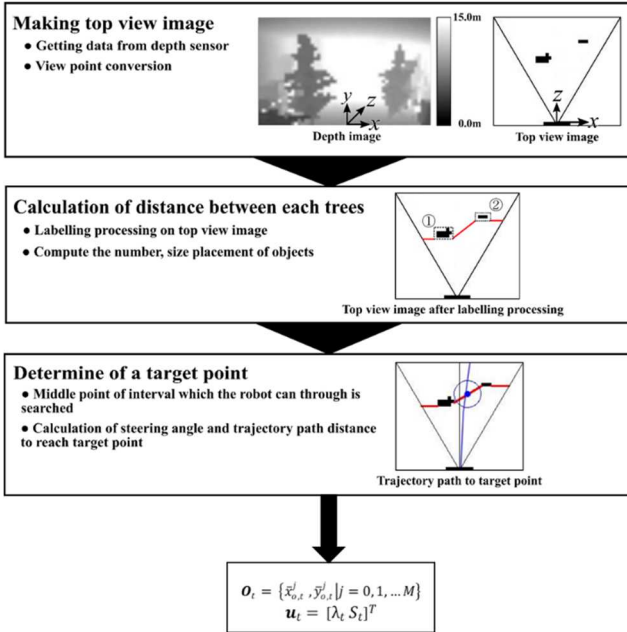


Fig.2. Flow-chart of autonomous moving system

When the target position is determined, the list of the centroid coordinates of the observed objects, expressed as shown in eq.1, and the control input for the robot, denoted by eq.2, are recorded for the localization system. Here, λ_t represents the steering angle and S_t is the distance that the robot should travel to reach the target position at each discrete time t . The steering angle is not changed until the traveling distance measured by the rotary encoder satisfies.

$$\mathbf{o}_t = \{\bar{x}_{o,t}^j, \bar{y}_{o,t}^j | j = 0, 1, \dots, M\} \quad (1)$$

$$\mathbf{u}_t = [\lambda_t S_t]^T \quad (2)$$

4. Discrimination between trees and weeds

The method for discrimination between trees and weeds is necessary so that the robot will not damage the trees while perform a weeding task. Therefore, we propose method using RGB-D data to differentiate trees from weeds. The process flow for the discrimination is shown in Fig.3.

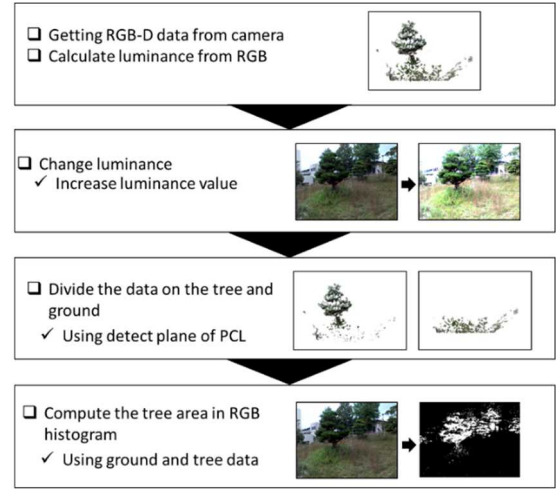


Fig.3. Flow-chart of discrimination system

A. Change luminance

In many case, both weeds and trees are green. Therefore, the values of Red, Green, and Blue are similar, which makes it difficult to discriminate. Therefore, we defined the luminance rate as P which is calculated from acquired data. We solve the problem by using this value. The luminance level P is calculated by using luminance value Y that is expressed eq.3 and expressed eq.4.

$$Y = 0.30R + 0.59G + 0.11B \quad (3)$$

$$P = \frac{\text{pixels that } Y \text{ value is more than } 200}{\text{all pixel that get from camera}} * 100 \quad (4)$$

B. Divide the data of the tree from ground

Many weeds are present on the ground. Therefore, in this system, we first divide the data into the ground and the other. we divide the acquired data into the ground and other parts by using plane detection with Point Cloud Library, and we acquire the ground and other RGB data.

C. Compute the tree region in RGB histogram

In this system, we compute the tree region in each histogram of Red, Green and Blue by using data that is bisected by plane detection. It is only necessary for the robot to discriminate whether the object in front of robot is trees or not. Therefore, we use Otsu's discriminant analysis method for computing the tree region. That method computes threshold value for bisecting the histogram[1]. Fig.4 is an example using this method. In Fig.4, shown the histogram of red, green and blue from left to right. The black line in the figure is the threshold values that is computed. In each histogram, it is defined that density value is from 0 to threshold value is class A and larger than threshold is class B. As in the Fig.4, using only this method, we do not know which of class A or

class B is the tree region in each histograms. Therefore, we use the relation between Red, Green and Blue and the relation between Green and luminance to solve this problem.

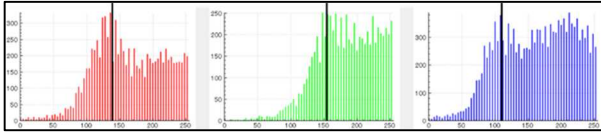


Fig.4. Discriminant analysis method applied example

C.1. selection of class in Green histogram

As can be seen from eq.1, green is the brightest color among red, blue and green. For this reason, it can be seen that there is a positive correlation between green value and luminance. Therefore, we compare the luminance levels of the planes and the other to calculate the tree region in the green histogram. Specifically, class A is regarded as the tree region in the green histogram in case of the luminance level of other than ground is 80% or more of the luminance level of the ground, but in other cases class B is regarded as the tree region.

C.2. selection of class in Red histogram

From the relation between Red, Green and Blue, the color is brownish when the density value of R is large. When the weeds die, they become brownish colored. Therefore, in the Red histogram, class A is always regarded as the tree color region so that we can also discriminate dead weeds and trees.

C.3. selection of class in Blue histogram

As in the case of red, from the relation of each color, when the density value of blue is larger than that of green, the color is bluish. Therefore, in tree color, green density value is considered to be lower than blue density value. For this reason, class A is regarded as tree region in the blue histogram in case of that the tree region is class A in the green histogram, but in other cases both class A and class B are regarded as the tree region.

5. Result

Fig.5, Fig.6 and Fig.7 show the result of experiment using this method. Fig.5 shows the case1 that luminance level of ground is larger than that of the other. Fig.6 shows the case2 that luminance level of ground is lower than that of the other. Fig.7 shows the case3 of that there is sunshine and shade. In each figure, the image named A is original image and image B is the result using this method.



Fig.5. case1 result



Fig.6. case2 result



Fig.7. case3 result

Conclusion & Future work

We can said that it is possible to compute the tree region in Red, Green and Blue histograms by using this method except the case shown Fig7. However, using only this method, it is impossible to discriminate between trees and weeds completely when some weeds is in tree color region shown Fig.6.

In future work, we will perform shape learning on the result image in order to discriminate between trees and weeds. In addition, improve a system to consider sunshine and shade.

References

- [1] Nobuyuki, Otsu (1980) "An Automatic Threshold Selection Method Based on Discriminant and Least Squares Criteria," *IEICE*, Vol.J63-D(4), pp.349-356

Design and Evaluation of Passively Powered Knee Exoskeleton (PPKE) for Squat Lifting

R.K.P.S. Ranaweera¹, R.A.R.C. Gopura¹, T.S.S. Jayawardena²

*Bionics Laboratory, Department of Mechanical Engineering¹, Department of Textile and Clothing Technology²,
University of Moratuwa, Katubedda, Moratuwa 10400, Sri Lanka*

G.K.I. Mann

*Faculty of Engineering and Applied Science, Memorial University of Newfoundland,
230 Elizabeth Ave, St. John's, NL A1B 3X9, Canada
E-mail: pubudur@uom.lk, gopurar@uom.lk, jaya@uom.lk, gmann@mun.ca
www.mrt.ac.lk*

Abstract

This paper proposes a passively-powered knee exoskeleton (PPKE) to provide power assistance during squat lifting of objects from the ground. The passive powering mechanism is designed to capture 20% of the waste mechanical energy available at the biological knee joint during decent phase and to release the stored energy in ascending phase in a complete squatting cycle. The effectiveness of proposed system was verified by experiments using surface electromyography (sEMG) signals under different test conditions. PPKE reduced the peak root-mean-square averages of sEMG signals of knee extensor muscles by 15% during squatting.

Keywords: knee exoskeleton, energy harvesting, passive mechanisms, squatting.

1. Introduction

Exoskeletons systems are mainly developed focusing on two different user groups, namely physically incapacitated population and able-bodied population.¹ According to literature, limited number of full lower-extremity exoskeletons or joint-level exoskeletons have been developed to carry out work related tasks by providing power-assistance.¹ The application areas are mostly limited to either locomotion assistance, tool holding or lift assistance.¹ Although functionality of autonomous externally powered robotic exoskeletons are satisfactory, wearer's performance is notably compromised.² In particular, such devices struggle to reduce the human effort. The main cause is the inability of the system to match the complex kinematic and kinetic requirements demanded by human biological joints. Here, limitations of the complementing technologies such as gear drives, actuators, sensors, and power sources

resulted in formulation of bulky and heavy electromechanical systems that is slow in operation.²

Alternatively, recent research studies indicate that passive-dynamic powering systems are effective at metabolic cost reduction and enhancing overall human performance.³ The body-powered exoskeletons are energetically autonomous and soft lightweight transmissions provide superior biomechanical compliance.³ However, performance and endurance augmentation through biomechanical energy harvesting still remains an open challenge. A wearable energy harnessing and releasing system that is capable of recycling the waste mechanical energy dissipated in the human body can help reduce metabolic energy consumption during activities of daily living.³ Complementing limb muscles energetically will augment the joint strength and moreover enhances endurance limits of muscle fatigue. As a result, exoskeleton wearer's productivity will improve over a period of time.

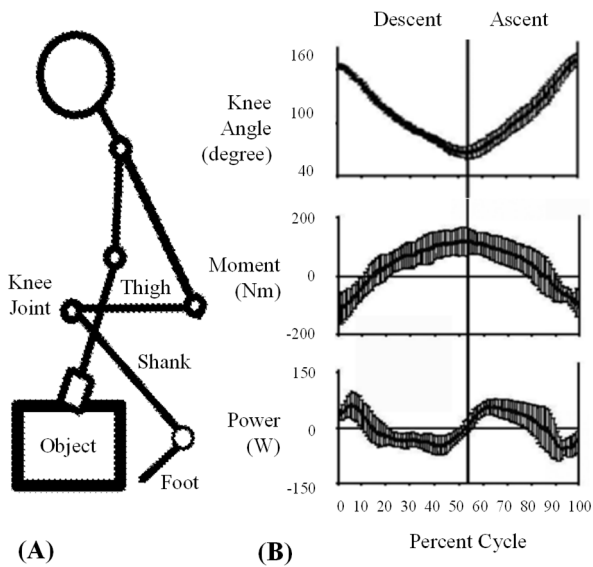


Fig. 1. Technique (A) and biomechanical data (B) of squatting adapted from Ref. 4 and 5.

In this context, a design of a passively powered knee exoskeleton is proposed to provide power assistance during squat lifting of objects from the ground (see Fig. 1(A)). The bio-inspired powering system is designed to recycle the mechanical energy at the knee joint during descending and ascending phases in sequence to help lift wearer’s own mass during a squatting cycle. The knee exoskeleton shall not pose any restrictions for walking and passively controlled locking mechanism only engages during a lifting task to capture and release mechanical energy. The design considerations for the knee exoskeleton targeting squat lifting and walking are described in section 2. The design details of the exoskeleton and the working principle of the passive powering mechanism is presented in section 3. The device was evaluated using surface muscle signals while performing semi-squats under different test conditions and results are compared in section 4.

2. Design Considerations

Load lifting is a typical industrial activity that is energy intensive.⁴ It involves moving an object from one position to another while traversing in vertical and/or horizontal directions. Considering the requirements for squatting as well as for walking, design considerations in relation to the knee joint were identified under functional and biomechanical points of view.

2.1. Functional

Among different lifting techniques the most commonly used approaches are squat lifting and stoop lifting.⁵ The knee exoskeleton is envisioned to assist wearer’s knee joint to lift moderately heavy loads. Hence squat or semi-squat lifting is selected as the technique in focus for developing the proposed device, as it also promotes use of biomechanically more favorable approach.⁵

The device should essentially allow the wearer to ambulate freely in-between lifting tasks and pose no restriction for knee flexion during swing phase of human gait. The knee joint’s limits of ranges of motion over the sagittal plane is measured to be -10° of hyper-extension and 140° of flexion.⁴ According to gait data,⁶ maximum flexion of knee joint during swing phase is 60° .

2.2. Biomechanical

Muscle activity of thigh muscles are of interest when performing a squatting cycle.⁷ Notably, the quadriceps show greater muscle activity than the hamstrings during the complete ascent phase.⁴ The focus is to relieve muscle groups of the burden of having to concentrically and eccentrically work to control motion.

Biomechanical data during squatting (see Fig. 1(B)) were analyzed to identify the role of lower limb joints to generate the mechanical power for lifting.⁴ The notion is to recover the potential energy dissipated as a result of lowering the center of gravity of human body which henceforth referred to as passive energy. Here, hip and knee joint dissipate energy through eccentric contraction of the major muscle groups on lower extremity during entire decent phase (2 seconds period).⁴ Similarly, during the entire ascending phase (2 seconds period), energy is generated while undergoing concentric contraction.⁴ In contrast, during initial stages (0-15% cycle) of the decent phase, the knee flexor muscles act concentrically followed by extensor muscles acting eccentrically for the remainder of the descent (15-53% cycle).⁴ The positive power is assumed to unlock the knee to initialize the descent. Throughout the start of the ascending phase (53-85% cycle) power is generated by knee extensor muscles by acting concentrically.⁴ However, towards end of the phase (85-100%) knee flexor muscles started to dissipate energy gathered using knee flexors acting eccentrically.⁴ Negative power is assumed to help prevent undesirable levels of hyperextension of knee joint.

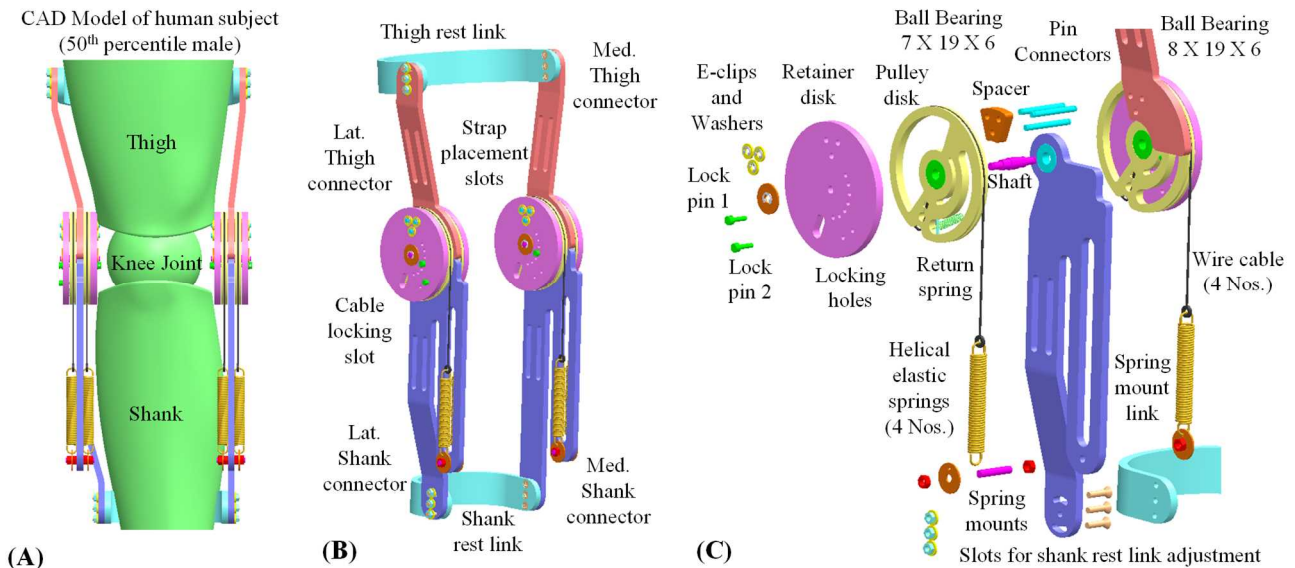


Fig. 2. PPKE on human model (A), PPKE with passive-powering mechanism (B), and exploded-view of PPKE (C).

3. Design of Passively Powered Knee Exoskeleton

Design objectives were to develop a simple, lightweight and affordable knee exoskeleton with ergonomic conformance and provide power assistance during squat lifting while posing least resistance for walking. Design specifications were derived for 50th per. male population.

3.1. Material Selection

Acrylic glass is considered as material of choice for developing the PPKE. Acrylic glass sheets can be easily cut in to various contours using computer numerically controlled laser cutting machines and formed in to complex shapes using thermoforming methods at an affordable cost. Acrylic is also considered to be non-toxic to human skin and environmental friendly. Thus making it a suitable option that has not been previously explored in exoskeleton development. In order to counter the lower tensile strength of acrylic material (approx. 70 MPa), the design of the exoskeleton should be satisfactory. The flow of forces through the acrylic structure should be entirely compressive in nature. Bending or shear forces have been eliminated by effectively utilizing the symmetry of the design.

3.2. Structural System

A computer-aided design model of a human subject was prepared using scanned data. The sizing and shaping of the structural system was then performed over the frontal

and sagittal planes (see Fig. 2(A)). In order to avoid collision of thigh rest and shank rest at full squat position, shank connectors were designed with longer legs (see Fig. 2(B)). Thigh connectors were shorter in length to minimize interference at the medial side. The structure is held firmly on the limb segments using four Velcro straps placed through the linear slots on the connectors. Resting links can be easily replaced to accommodate varying limb cross-sections, if needed. The curved slots at the hinged end of the rest links provide the ability to adjust relative angular position of rests with the connectors. The slender acrylic structure assume the body shape over the frontal plane if contact forces are significantly high. The compliant structure hence reduce the possibility of internal joint injuries due to misalignments.

3.3. Passive Powering Mechanism

It is assumed that industrial workers are more likely to assume a semi-squat position during lifting tasks. Hence, the design has been planned for parallel-squat operation, where the knee bends approx. 70^o to 100^o. In addition, wearer need to have freedom to ambulate at normal walking speed⁶ (1.3 m/s). Consequently, the knee flexion should be left unconstrained up to 60^o. The springs should engage to capture the negative energy when the knee flexes beyond this limit. Assuming the maximum knee angle happens up to 90^o in a regular squat lifting task, the effective angular displacement of 30^o can be utilized to energize a collection of linear elastic elements.

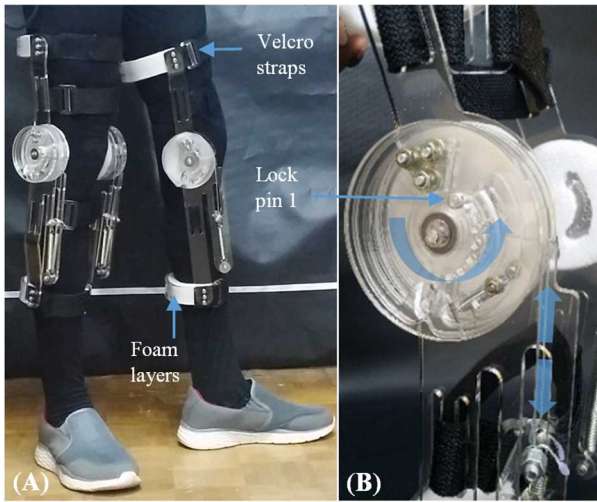


Fig. 3. Working model of PPKE on male subject (A) and close-up view of passive powering mechanism (B).

The proposed mechanism to achieve this function is comprised of energy capturing springs held parallel to shank, wire cables, pulley disks, smaller return springs and pins (see Fig. 2(C)). The pulley disks are fitted on bearings and are free to rotate about the axis of the shaft. However, by form the mechanical limits are in place to prevent rotation of the pulley in opposite or counter-clockwise direction. The clockwise rotation will be prevented by the smaller return springs that is held between the retainer disk and the pulley disk using set of pins. The lock pin 1 can be inserted in to a pulley disk locking hole that are spaced 20° apart over a range of 0° to 120° . If the lock pin is removed the knee joint can be easily flexed without notable restriction from the exoskeleton. Here the stiffer springs act as a rigid body causing the flexible return springs to extend. As a result the pulley disk will rotate in a clockwise sense to maintain wire cable length unchanged. When the knee traverse back to the rest position, the return spring gives way and the pulley disk returns to its initial position. By placing the lock pin 1 in position number-one (0°) the pulley disk gets immediately locked with retainer disk. Consequently, when the knee gets flexed the stiffer springs starts to load gradually capturing energy of decent. If the lock pin is inserted in to position number-two (20°), the knee is free to flex up to the same limit and the pulley disk will come to a stop as the lock pin 1 traverse and reach the mechanical limit over the curved slot. If PPKE is supposed to allow free flexion during walking, the lock pin 1 should be inserted in position

number-four (60°). As a result, during rest of the decent phase up to 90° , available passive energy is harnessed.

The spring selection should be done to maximize the energy retention. Considering the limited tensile strength of acrylic glass and the overall size of the device, the maximum force applied on a single spring is limited to 150 N. The limits were determined by analyzing the stress distribution over the critically loaded acrylic components of the exoskeleton. In particular, the shank connectors and pulley disks were subjected to compression loadings and torsional loadings respectively. Finite element simulation provided an insight on the safety limits for the same. To accommodate manufacturing and material defects, the factor of safety were maintained at 1.5 and above for all acrylic parts. The structure and powering mechanisms are capable of withstanding such heavy loads as a consequence of symmetrical positioning of passive actuators.

The energetic response of the proposed passive energy recycling system can be mathematically modeled as follows. If a bilateral system with elastic helical springs having 5875 N/m stiffness coefficient is used, the total strain energy stored in the system over a 30° knee angle can be determined using,

$$E = \frac{1}{2} k x^2 \quad (1)$$

Where, k – stiffness coefficient (N/m), x – spring extension (m) and E – accumulated energy (J or Nm).

The total energy dissipated and generated at the knee joint during decent and ascent phases from biomechanical studies were found to be 45 J and 50 J respectively. The selected springs thus have the capacity to collectively (eight springs on two PPKE units) capture and return approximately over 20% of total mechanical energy required considering loses due friction. Here, the maximum spring force is evaluated to be approx. 133 N.

4. Evaluation of PPKE

Overall mass of PPKE (see Fig. 3) is approx. 900 g inclusive of helical springs made of spring steel. In order to evaluate the effectiveness of the proposed system, a preliminary study was set up and conducted with a healthy average male subject (Age: 37 years, Weight: 72 kg, Height: 177.8 cm). Test protocols were developed to measure relative changes of muscle activity for squatting

- without the exoskeleton (WO),
- with exoskeleton minus passive powering (UPO),
- with exoskeleton having passive powering (PO).

4.1. Experimental Set-Up

Squatting exercises were performed to monitor possible benefits of using the passive energy recycling system to enhance strength and improve endurance limits of thigh muscles. Each of the tests were conducted for a period of 100 seconds with an ascent-descent cycle of four seconds that ranged over 0° to 100° knee angle. Wired surface electromyography (sEMG) electrodes connected to Bagnoli Desktop EMG system were placed on muscle bellies of rectus femoris (RF) and bicep femoris (BF) muscles on both limbs to measure the electrical signals.

4.2. Results and Discussion

The root mean square (RMS) average of the electrical potential of RF and BF muscles were post-processed using raw sEMG signals. When considering the first ten squatting cycles (see Fig. 4(A)), the RF muscles show a decrease in peak RMS values when wearing exoskeleton with the passive powering system by 15%. Alternatively, during the last ten cycles (see Fig. 5(A)), the peak RMS values are greater when wearing the exoskeleton with or without the powering system. Interestingly, BF muscles respond in an opposite manner as the cycles elapsed. During the first ten cycles of squatting (see Fig. 4(B)), exoskeleton tend to increase the peak RMS values than the norm, which is especially evident when it is worn without the assistance of the powering system. However, towards the latter end, in particular during last ten squatting cycles, the peak RMS values when wearing the exoskeleton remain consistent while for the case of no exoskeleton a notable increase in noted (see Fig. 5(B)). Therefore, the preliminary study has revealed that PPKE has both positive and negative impact. Considering the relative significance of quadriceps muscles to perform squat lifting, device has successfully satisfied its purpose.

5. Conclusion

PPKE is energetically autonomous, adaptable and nimble thus making it ideal for industrial use. Working model served as a proof of concept, but clinical testing with metabolic cost estimation over wide range of participants is essential to assess the design for further improvements.

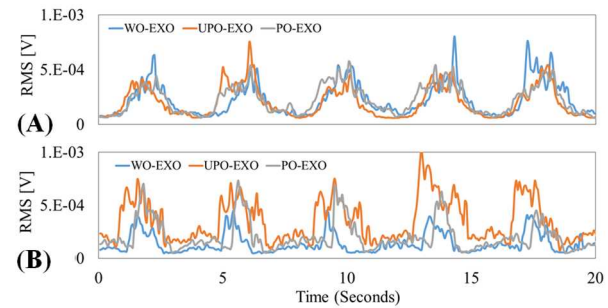


Fig. 4. RMS values of (A) RF and (B) BF muscles on right lower limb during first five squatting cycles.

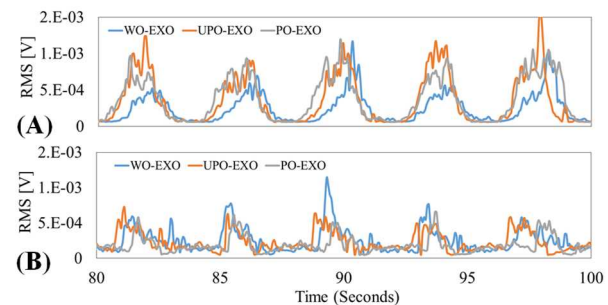


Fig. 5. RMS values of (A) RF and (B) BF muscles on right lower limb during last five squatting cycles.

Acknowledgements

Authors acknowledge Senate Research Council of University of Moratuwa (Grant No. SRC/CAP/2014/08).

References

1. B. Chen et al., "Recent developments and challenges of lower extremity exoskeletons," *J. Orthop. Transl.*, vol. 5, pp. 26–37, 2016.
2. A. J. Young and D. P. Ferris, "State of the art and future directions for lower limb robotic exoskeletons," *Trans. Neur. Syst. Rehab. Eng.*, vol. 25, no. 2, pp. 171–182, 2017.
3. S. H. Collins et al., "Reducing the energy cost of human walking using an unpowered exoskeleton," *Nature*, vol. 522, no. 7555, pp. 212–215, 2015.
4. D. G. E. Robertson et al., "Lower extremity muscle functions during full squats," *J. Appl. Biomech.*, vol. 24, no. 4, pp. 333–339, 2008.
5. S. Hwang et al., "Lower extremity joint kinetics and lumbar curvature during squat and stoop lifting," *BMC Musculoskelet. Disord.*, vol. 10, no. 1, p. 15, 2009.
6. B. R. Umberger and P. E. Martin, "Mechanical power and efficiency of level walking with different stride rates," *J. Exp. Biol.*, vol. 210, no. 18, pp. 3255–3265, 2007.
7. J. P. Pollard et al., "Forces and moments on the knee during kneeling and squatting," *J. Appl. Biomech.*, vol. 27, no. 3, pp. 233–241, 2011.

Behavior design of robot arm imitating the consciousness mechanism of living organisms Representation of facial expression in transition process of emotion

Ryohei Anashi

*Mechanical Information Science and Technology, Kyushu Institute of Technology.
680-4, Kawazu, Iizuka, Fukuoka, 820-8502, Japan.
anshi@mmcs.mse.kyutech.ac.jp*

Wisanu Jitviriya

*Faculty of Engineering, King Mongkut's University of Technology North Bangkok.
1518 Pracharat 1, Wongsawang Rd., Bangsue, Bangkok, Thailand 108000
wisanu.j@eng.kmutnb.ac.th*

Sakmongkon Chumkamon

*Faculty of Engineering, Rajamangala University of Technology Thanyaburi.
39 Moo 1 Rangsit-Nakhonnayok Rd Thanyaburi Pathum Thani 12110, Thailand.
s.chumkamon.jp@ieee.org*

Eiji Hayashi

*Mechanical Information Science and Technology, Kyushu Institute of Technology.
680-4, Kawazu, Iizuka, Fukuoka, 820-8502, Japan.
haya@mse.kyutech.ac.jp*

Abstract

In this paper, we present a system that facial expression expressions in the case of embracing multiple emotions occurring in the transition of emotions of robots having eight basic emotions. In addition to changes in eyeballs and eyelids, changes in pupil diameter and changes in blink cycle were incorporated. The facial expression is made in real time by changing these according to the always changing emotion ratio. As a result of verification experiments comparing the conventional system and this system, it was confirmed that facial expressions of the emotional transition process, which could not be expressed in the conventional system, could be expressed.

Keywords: facial expression, pupil diameter, blink cycle, emotion ratio.

1. Introduction

Various service robots such as home and nursing care are being developed. In particular, social robots are required to have "user affinity" that gives the user a sense of affinity as well as functions such as intellectual

behavior and communication ability. In this research, we aim to realize user affinity by paying attention to living organisms that embrace healing and affinity, giving the robot consciousness, behavior, and emotion of living organisms. In this fiscal year, we developed a system such as change in pupil diameter and blink cycle

so that smooth and detailed facial expressions can be made with emotional change.

2. System configuration

Fig.1 shows the robot developed in this study. Represent the robot's consciousness, behavior and emotion by arm's behavior and face expression. The arm has 7 degrees of freedom and a small camera inside the hand. Face has a CCD camera and a small display on its neck with 2 degrees of freedom, and this small display projects the created eyeball.

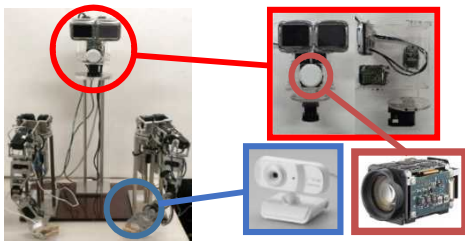


Fig.1 Overview of the Arm Robot

3. System flow

The robot recognizes the external situation by the camera. Motivation is calculated as an internal factor from the recognition result of the object. Also recognize the facial expression of the user and classify emotions. Then, based on the motivation and the emotion classification result of the user, the behavior and facial expression of the robot is selected. The flow of this system is shown in Fig. 2.

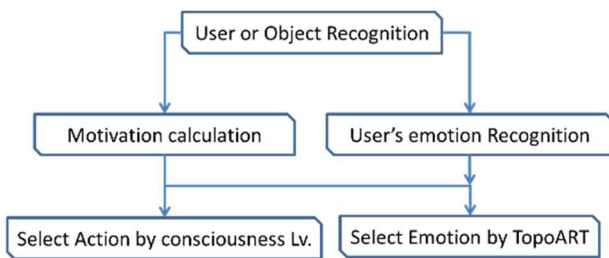


Fig.2 Flowchart for Autonomous Emotion-Behavior

3.1. External situation recognition by camera

Images acquired from the small camera are simplified into five colors of green, blue, red, skin color, and other, and labeling processing is performed. Of these, we set green / red objects as favorite objects and blue objects as dislikes. The recognition result of what the robot likes or dislikes is reflected in the calculation of motivation. Also, recognize the facial expression of the user shot by the CCD camera. We acquire the feature points of each part of the face learned beforehand, and create the shape model. Identify the region of the face in the captured image from the image around the feature point and classify the emotion from the user's facial expression based on the difference in shape vector.

3.2. Calculation of motivation according to situation and condition

As motivation to cause behavior of living things, there is the occurrence of intracerebral neurotransmitter dopamine. In this system, positive dopamine is recognized when a favorite red or green object is recognized, and negative dopamine is generated when a dislike blue object is recognized. The generation of this dopamine was expressed using a control model. Then we defined the second order lag response with the sum total of positive and negative dopamine as input motivation which is the motivation of the robot's behavior. The robot determines the behavior according to this motivation. The occurrence of dopamine and motivation is shown in Fig.3.

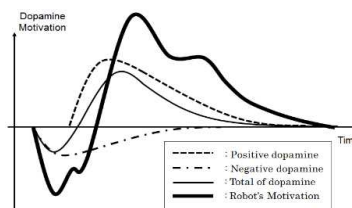


Fig.3 Relation between dopamine and motivation

3.3. TopoART(Topological Adaptive Resonance Theory)

ART (Adaptive Resonance Theory) is a theory developed based on the relationship between the living organism's brain and consciousness. As a flow of the learning algorithm, category data having information on

the center position, class, and radius in the output layer, and alert parameters for narrowing the search range of the input are defined in advance. A category with a center in the input warning parameter is set as a search target, and a vision test is performed. If category and input class match, expand the category to include the input and output the result. In case of inconsistency, decrease the warning parameter and re-search the category.

Two ARTs are prepared, each of which has roles of short-term memory and long-term memory, and layered to constitute a TopoART system. Fig.4 shows TopoART algorithm.

In this system, motivation of the robot and information of the user's emotion are input, and the ratio of each emotion is output. As a result, one facial expression including multiple emotions is selected.

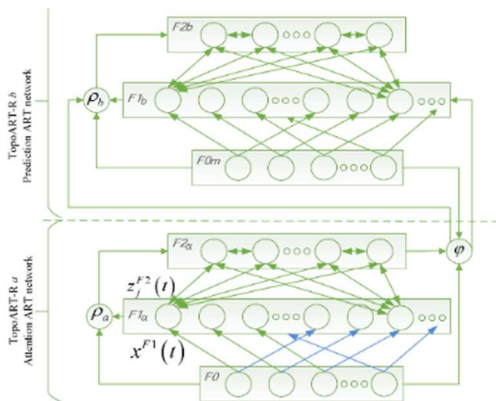


Fig.4 TopoART algorithm

4. Representation of expression in transition process of emotion

It is said that neutral, hope, happiness, surprise, fear, sadness, disgust, anger are the basic feelings. In this system, expressions for expressing basic emotions were created. It is shown in Fig.5.

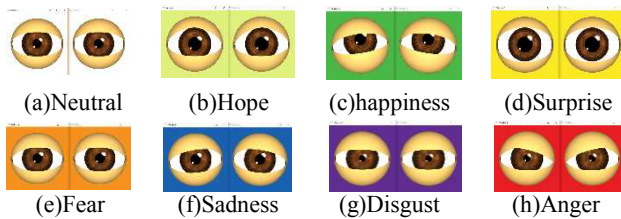


Fig.5 Facial Expression

© The 2018 International Conference on Artificial Life and Robotics (ICAROB2018), Feb. 1-4, B-Con Plaza, Beppu, Oita, Japan

4.1. Creating facial expressions by changing rotation angle

As shown in Fig. 6, the eyelids and the eyeball are given 2 degrees of freedom so that expression can be expressed. The angle of these two degrees of freedom is set for each of the facial expressions of the eight basic emotions. By updating these angles using the output of TopoART, continuous facial expression creation was made possible.

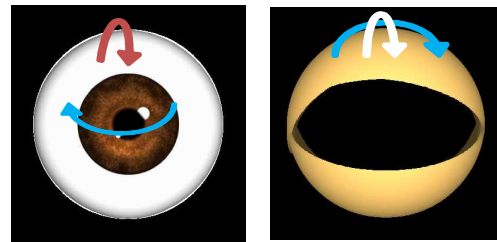


Fig.6 Axis of rotation

4.2. Change in pupil diameter

The pupil diameter is scaled down due to external factors and internal factors. We focused on internal factors in this study. Pupils are scattered for visual stimuli that are of interest and are reduced for stimuli that evoke discomfort. Based on this feature, the pupil diameter in each basic emotion is set, and the pupil diameter is determined by Equation (1) using the emotion ratio [%] which is the output of TopoART. The emotion ratio satisfies equation (2). R is the pupil diameter [mm], and ρ is the emotion ratio.

$$R = \rho_{sur} \times 100.0 + \rho_{happy} \times 78.9 + \rho_{hope} \times 89.5 + \rho_{neutral} \times 68.4 + \rho_{fear} \times 73.7 + \rho_{sad} \times 73.7 + \rho_{disgust} \times 42.1 + \rho_{anger} \times 47.4 \quad (1)$$

$$\rho_{sur} + \rho_{happy} + \rho_{hope} + \rho_{neutral} + \rho_{fear} + \rho_{sad} + \rho_{disgust} + \rho_{anger} = 1 \quad (2)$$

4.3. Change in blink period

Types of blinks are reflective blinks, voluntary blinks, and spontaneous blinks. In this study, we focused on voluntary blink and spontaneous blink. voluntary blinking is a blink of consciousness. Spontaneous blinking is a blink of eye under unconsciousness, and

the blink cycle of adults is 3000 to 3750 [ms]. The blink cycle becomes longer at rest and concentration, and becomes shorter when there is no tension, excitement or interest. Based on these features, we set the blink period in each basic emotion, and calculate the blink period by equation (3) according to emotion ratio.

$$T = \rho_{sur} \times 4300 + \rho_{happy} \times 6000 + \rho_{hope} \times 1500 + \rho_{neutral} \times 3300 + \rho_{fear} \times 2150 + \rho_{sad} \times 3500 + \rho_{disgust} \times 2700 + \rho_{anger} \times 5000 \quad (3)$$

5. Inspection result

We verified experimentally whether the expression of robot's expression changes more smoothly and finely by the developed system. The target of comparison is the system until the last year. The results are shown in Fig.7.

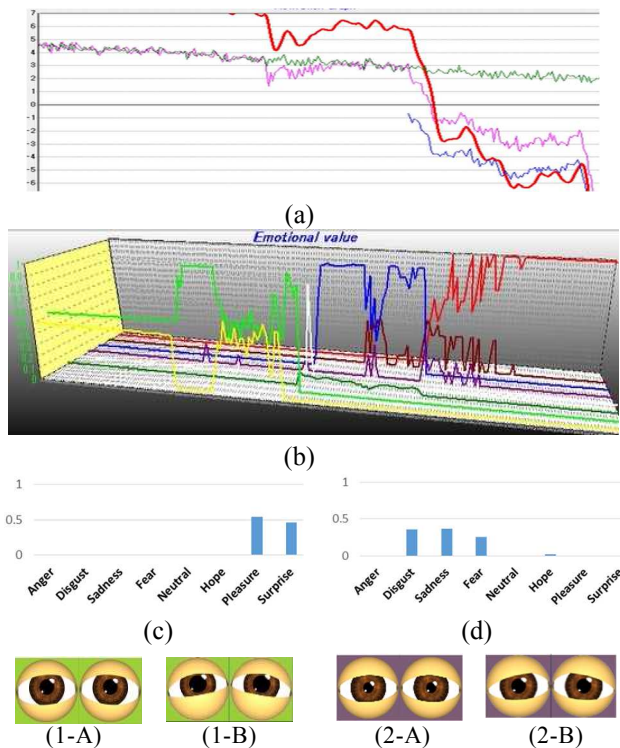


Fig.7 Result

(a) shows the trend of motivation, and (b) shows the transition of emotion ratio. 1 recognizes a favorite green object and when motivation rises, 2 recognizes a dislike blue object and is when motivation falls. The emotion ratio of each state is shown in (c) (d), the facial expression expressed by this system is (A), and the

expression expressed by the previous system is (B). In case of 1, the emotion ratio is outputting joy and surprise. (1 - A) expresses the expression in which the two emotions are compounded, but in (1 - B) the expression reflecting strongly the pleasure of the emotion ratio is expressed. In case of 2, the emotion ratio is sadness, hatred, fear and extremely few expectations are outputted. (2 - A) expresses the expression in which each emotion is compounded, but in (2 - B) the expression of sadness of basic emotion and the difference are not seen and other emotions are not reflected.

Based on the experimental results, in the conventional system, the expression reflecting strongly the emotion with the greatest emotion ratio was expressed in both cases 1 and 2, and other emotions were not reflected. On the other hand, in this system, expressions reflecting multiple emotions were both expressed. Also, in the conventional system, the facial expression transition is an intermittent change and a problem that it is an unnatural expression was seen. However, since this system creates facial expressions according to the output of TopoART, facial expression transitions become continuous, smooth facial expressions become possible, and unnatural emotional expressions until last year have been solved.

6. Conclusion

We introduced expression of pupil diameter and blink cycle corresponding to change of rotation angle change and transition of emotional ratio, and it became possible to express more diversified facial expressions. Currently the behavior of the robot is determined only by motivation. Therefore, as a future task, we aim to construct actions accompanied by smooth facial expressions including detailed changes of emotions made possible this time.

References

1. S. Chumkamon, "Study on Emotion and Behavior Generating System based on Facial Expression Recognition", Kyushu Institute of Technology, 2017, Ph.D. thesis.

Study of Robot Navigation for Forest Management

Ayumu Tominaga

*Graduate School of Computer Science and System Engineering, Kyushu Institute of Technology,
680-4 Iizuka, Fukuoka, Japan*

** E-mail: tominaga@mmcs.mse.kyutech.ac.jp*

Eiji Hayashi

*Graduate School of Computer Science and System Engineering, Kyushu Institute of Technology
680-4 Iizuka, Fukuoka, Japan*

E-mail: haya@mse.kyutech.ac.jp

Abbe Mowshowits

*Department of Computer Schience, The City College of New York,
Convent Avenue at 138th Street, NY 10031, U.S.A*

E-mail: abbe@cs.ccny.cuny.edu

Abstract

We have constructed a robotic system enabling an autonomous robot to move between the trees without damaging them and to cut the weeds as it traverses the forest. Computation of a trajectory in a forest is facilitated by treating the trees as vertices in a graph. This paper proposes how recognition the unreached area in the field to navigate in order to make the robot move whole of the forest. Finally, the proposed method was experimented in the experimental forest

Keywords: Autonomous Robot, Navigation, Forest Management, Graph theory

1. Introduction

The application of robotics in forestry is well established [1]. These applications have been introduced to increase productivity, to enhance safety, and to compensate for the workforce which trends toward a decrease. Particularly, by improvement Simultaneous Localization and Mapping (SLAM) techniques, the monitoring and management of a forest resource could be automatically [2, 3]. Such systems and related techniques allow for utilizing the autonomous robot for support of forestry industry by identifying individual tree location. In this research, we have been focused a navigation assuming using of them for an autonomous moving robot.

We have been developing the robot achieved by automatically elimination weed plants in the forest. As mention above, the trees in the environment can be used as a landmark for navigating of the robot in the forest. When patrolling in the forest, it is necessary for the robot to traverse whole areas of the forest as possible as. Because, the weeding work is important for promoting the growth of the trees, and ideally all weed plants should be rejected from the forest. In this paper proposes a method based on graph theory to realize it. First, the graph structure which has Hamiltonian cycle is constructed trees as vertices. Then the destination location will be determined to traverse of its. When the robot moves to the destination, the obstacle avoidance

behavior is performed without using precision control system. The Hamiltonian cycle will be separated to two cycles least, that can be represented by the unreached area for the robot.

This paper reports the proposed system in the experimental forest.

2. Forestry Robotic System “SOMA”

2.1. System description

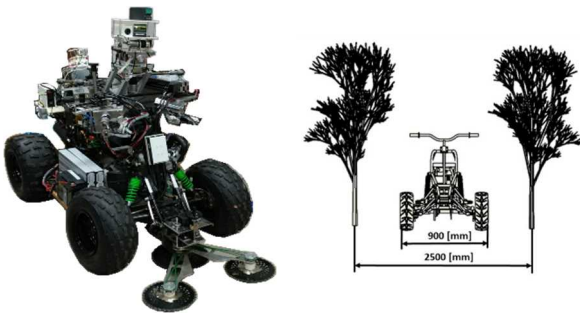


Fig. 1. Appearance of forestry robot “SOMA”

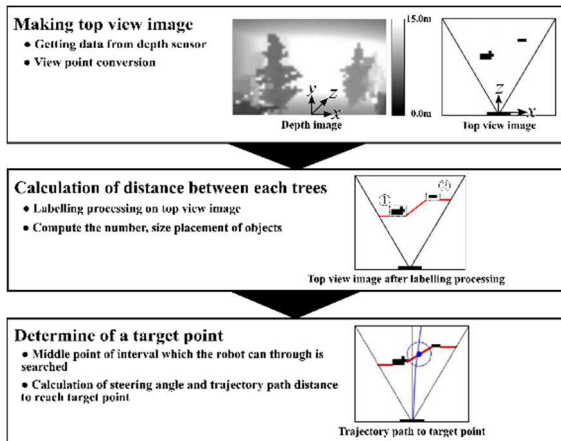


Fig.2. Flow of obstacle avoidance behavior

The autonomous robot “SOMA” shown in Fig. 1 is built on the platform of an All-Terrain Vehicle (ATV). An ATV was chosen for its robust design for outdoor use in rough terrain. The power source is a gasoline engine, and the throttle, brake lever, and steering are controlled by DC motors. Weeding operation is facilitated by a specialized device attached to the front of the ATV. Also important is the ATVs ability to climb steep hills, up to an incline of 26 degrees.

SOMA is equipped with a Real Time Kinematic GPS (RTK-GPS) for determining position. The angle θ of the

robot’s heading is obtained from the Inertial Measurement Unit (IMU). In this research, external situation recognition is achieved mainly with the aid of a depth sensor. This sensor can provide 3-dimensional point cloud data obtained by scanning with an infrared laser.

2.2. Obstacle Avoidance

Obstacle avoidance is an essential function for an autonomous mobile robot. The trees in a forestry application can be viewed as obstacles to be avoided by a robot so as not to damage them. Until recently, such systems were designed for the use of image processing with color information obtained from monocular cameras [4,5]. Improvements in the technology of measurement using infrared lasers, such systems were possible to construct using 3-dimensional point cloud data that can obtain in real time in outdoor. The depth sensor (R200, Intel Inc.) used on SOMA.

Fig.2 shows a flowchart of the obstacle avoidance procedure. After getting point cloud data from the depth sensor, a top view 2-dimensional image is produced. Next, labeling processing is carried out on the top view image to enable recognition of the boundary point and the location of the objects in the robot’s field of vision. Then, the length of line segment between the boundary points of each object is computed, and longest line segment is determined. The midpoint of the longest line segment is defined as the robot’s target point. By performing the procedure recursively, the robot can avoid the tree and move forward between two trees at the next location in front of the robot.

2.3. Following a destination position methods

This subsection describes the method of following of destination position. This is accomplished by means of the pan rotate actuator on the vision system that can rotate up to 30 degrees on one side. The program works as follows.

- (i) The current position of the robot is represented P_k . P_{dest} is a destination position that given to the robot.
- (ii) Calculate the angle ϕ_k , direction angle from P_k to P_{dest} . The robot heading θ_k is obtained from IMU.
- (iii) Turn the pan rotate actuator to angle $\phi_k - \theta_k$. Following its obstacle avoidance procedure the robot approaches P_{dest} .

- (iv) When the robot reaches the circle of radius 1.0 meters centered on P_{dest} , the program returns to (i) with update a new destination point.

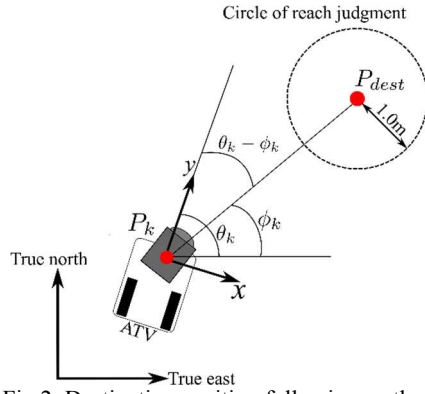


Fig.2. Destination position following method

3. Navigation Method in the Forest

Fig. 4 shows the relative positions of the trees determined by measurements of RTK-GPS in an experimental forest. The positive directions of the y-axis and x-axis are oriented true north and true east respectively. The size of the field was defined 35 meter square.

In this research, the navigation system for the robot is carried out using two types set of coordinate points. One is a set of the coordinate point of individual trees, other one is a set of midpoint of every pair of tree. These tree's pairs in order to compute midpoints was decided under the condition that each tree of the pair exists on light-of-sight with direct distance less than 10 meters. In addition, these sets can be represented a graph $G = (V, E)$ by associating each coordinate points as a vertex.

First, generate a Hamiltonian graph H to define the initial enclosed space. The Hamiltonian cycle represents an enclosed space in 2-dimensional space (shown in Fig.5). Then, determine the destination point in order to make the robot traverses such enclosed space. When the H was traversed accompany intersected any 2 edges by the autonomous robot, it can be separated 2 enclosed space. These enclosed spaces will be considered suggesting unreached spaces in environmental map. How determine the destination point is performed by follows.

- (i) From the set of midpoint coordinates, a set of interior points within the constructed enclosed space is extracted.
- (ii) Generate a minimum spanning tree using these interior points as vertices after the complete graph was constructed using these.

- (iii) Computing the vertex within the spanning tree that is farthest from the current position. This vertex is determined as the destination point P_{dest} for the robot (shown in Fig.6).

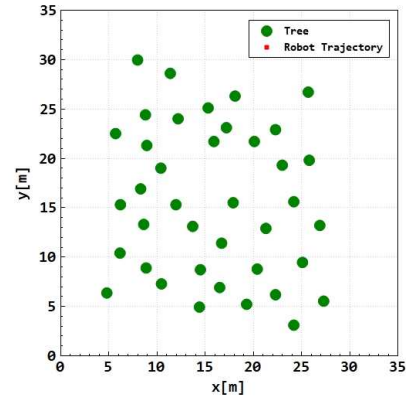


Fig. 4. Position of trees in experimental forest

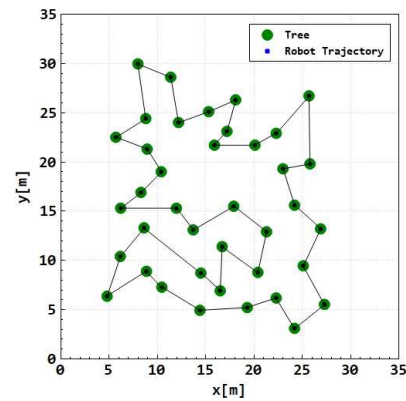


Fig. 5. Initial Hamilton cycle (enclosed space) in the experimental forest

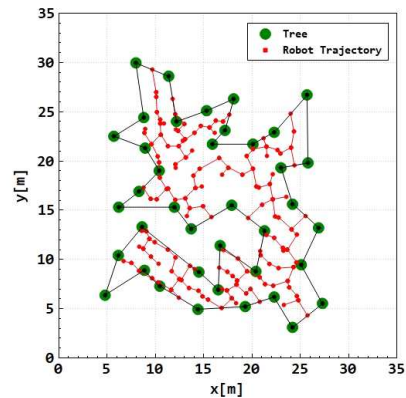


Fig.6. Minimum spanning tree using midpoint coordinates that interior points within initial enclosed space

The robot performs obstacle avoidance mentioned above until the robot reached P_{dest} . When the robot traversed 2 edges that constructing the closed space, then the Hamiltonian cycle is updated. Let the edges which intersected by the robot be $e_1 = \{s_1, t_1\}$ $e_2 = \{s_2, t_2\}$, update of Hamiltonian cycle will be completed by simply swapping the vertices such that $e_1 = \{s_1, t_2\}$ $e_2 = \{s_2, t_1\}$ (see Fig.7).

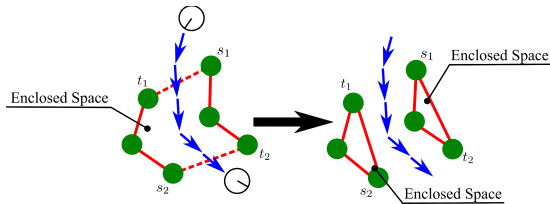


Fig.7 Separation of the enclosed space

4. Experimental Result

The experimental forest on the campus of the Kyushu Institute of Technology consists of 39 trees. There are no object, other than the trees, in this area that might impede the movement of a robot. This trees is small enough to allow for determining the positions of the trees and measuring.

The Hamiltonian cycle and the minimum spanning tree used the experiment was shown in Fig.5 described in the preceding section. Fig.8(a) is shown the initial position of the robot P_0 and the destination point P_{dest} , Fig.8(b) is the trajectory history that the robot performed autonomous moving. As the result in this experiment, the robot could traverse the enclosed space, the Hamiltonian cycle could be separated two cycle. These enclosed spaces are recognized as the unreachable area for the robot.

5. Conclusion

In this paper, we proposed a navigation method of autonomous forestry support robot. We are aiming to guide in order to make the robot traverses all area of a forest, using the coordinate of trees which unchanged in the long term. In order to achieve an patrol of the whole forest, the system decides a destination point based on a minimum spanning tree constructed by the midpoints of tree pairs within enclosed space expressed by Hamiltonian cycles. In the experiment, the robot could separate the spaces and succeeded in breaking the Hamiltonian cycle into two. In the future works, we will experiment the robot operate of autonomous moving for long time to verification for effectiveness of the system proposed.

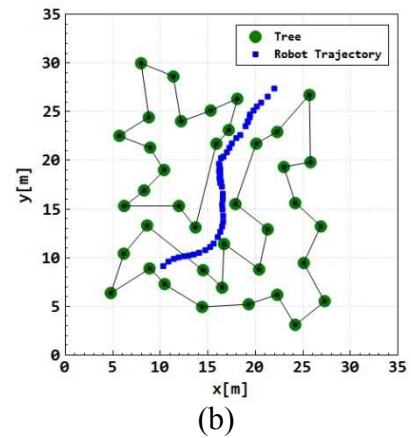
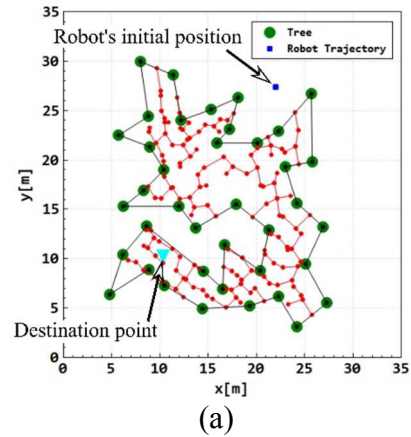


Fig.8. Experimental result

References

1. R. Parker, K. Bayne, and P.W. Clinton, "Robotics in forestry," *New Zealand Journal of Forestry*, 60, 2016, pp. 8-14.
2. G. Brolly, and G. Király,. "Algorithms for stem mapping by means of terrestrial laser scanning," *Acta Silv. Lign. Hung.* 5, 2009, pp. 119-130.
3. T. Ritter, M. Schwarz, A. Tockner, F. Leisch, and A. Nothdurft, "Automatic mapping of forest stands based on three-dimensional point clouds derived from terrestrial laser-scanning," *Forests*, 8(8), 2017, pp. 1-19.
4. K.H. Chen and W.H. Tsai, "Vision-based obstacle detection and avoidance for autonomous land vehicle navigation in outdoor roads," *Automation in Construction*, 10(1), pp.1-25, 2000.
5. A. Ohya, A. Kosaka, and A. Kak, "Vision-based navigation of mobile robot with obstacle avoidance using single-camera vision and ultrasonic sensing," *Proceedings of the 1997 IEEE/RSJ International Conference on Intelligent Robot and Systems. Innovative Robotics for Real-World Applications. IROS '97*, 2, 1997, pp. 704-711.

Development of the sense system that is combined force feedback and visual feedback -Deformable virtual objects simulation by using LEM-

Kaito Nagano

*Graduate School of Computer Scienc and System Engineering
Kyushu Institute of Technology, 680-4, Iizuka City, Fukuoka, Japan, 820-8502
nagano@mmcs.mse.kyutech.ac.jp*

Eiji Hayashi

*Department of Mechanical Information Science and Technology
Kyushu Institute of Technology, 680-4, Iizuka City, Fukuoka, Japan, 820-8502
haya@mmcs.mse.kyutech.ac.jp*

Abstract

The purpose of this research is to develop a combined senses system that uses both force feedback and visual feedback on a deformation simulation. Especially, focus on a way to produce a force that is calculated in simulation of deformation using a haptic device. As the first stage, our simulation of deformation was improved by using LEM (Long Element Method) and evaluated accuracy of a virtual object's deformation.

Keywords: force feedback, haptic interface, simulation, LEM

1. Introduction

In the medical treatment and bio-technology field, doctors and researchers need technologies that can accurately perform minute work. Such minute work is improved by using micromanipulators, but their operation is difficult because the operator has no sense of force. The operator relies only on sight through a microscope. As a result, a person who has the skill to do minute work is needed for all minute work. The efficiency of minute work would be improved if the operator is able to feel a sense of force while using a manipulator.

Here we describe the development of a more efficient system for minute operations. Our aim is to develop the combined system that that uses both force feedback from the manipulator and visual feedback on a deformation simulation. By reproducing force sense and visual sense of a sample, an operator can feel these sense of a virtual

object. For this research, focus on a way to produce a force calculated in simulation of deformation using a haptic device. As the first stage, our simulation of deformation was improved by using LEM (Long Element Method) and evaluated accuracy of a virtual object's deformation.

2. System Structure

The system structure is shown in Fig. 1. This system consists of a force feedback part and a visual feedback part. At a force feedback part, this system is equipped with the haptic device and a microcomputer for controlling the haptic device. At a visual feedback part,

© The 2018 International Conference on Artificial Life and Robotics (ICAROB2018), Feb. 1-4, B-Con Plaza, Beppu, Oita, Japan

It is equipped with a simulation video in a main computer. The main computer also sends parameters to the haptic device. The parameters are obtained by measuring dynamic characteristics of a sample using microscope.

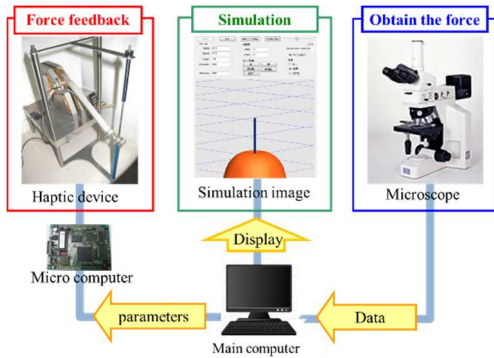


Fig.1. The system structure.

3. Haptic device

Fig. 2 provides a diagram of the haptic device. It consists primarily of a rotor, a laser, and a position-sensitive detector (PSD). The angle of the rotor can be measured by the laser and the PSD. The haptic device has a coil on the rotor with a polarity magnet. When current flows through the coil, the coil experiences a force (Lorentz force) perpendicular both external magnetic field and to the direction of the current flow. The rotor is moved depend on an input waveform that has the frequency less than 36Hz. An operator holds a moving part like a pen and receives the thrust which is generated in the rotor. Hereinafter, the moving part is called a pen slide.

Fig. 3 shows the connection between the haptic device and a microcomputer. The haptic device is controlled by command signals from the microcomputer process.

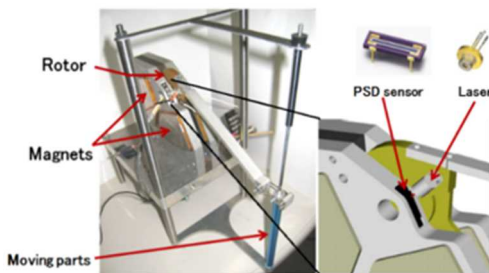


Fig.2. The structure of the haptic device.

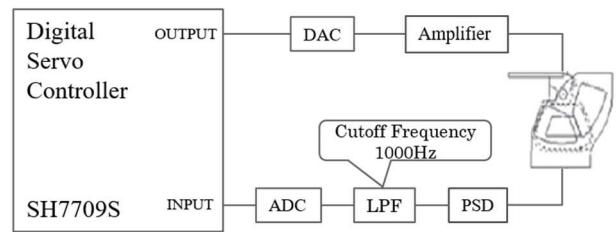


Fig.3. The connection between the haptic device and a microcomputer.

4. Simulation interface

In this study, the working system using a microscope, a haptic device and a simulation is built. A fundamental element was simulating the deformation of a minute object. Fig. 4 shows the graphical user interface (GUI) of the simulator. A graphic tool was created using OpenGL to draw the object.

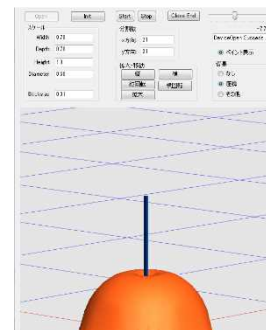


Fig.4. Simulator

5. Modeling of an object using by LEM

In the previous deformable virtual objects simulation, model of an object and reproduction of the deformation were performed by the spring · mass · damper model. However, It is difficult to model an object with complicated shape and measure spring-damper coefficient between mass points. Therefore, the modeling of an object is performed by LEM. The deformation of the object is also reproduced using LEM.

$$(i = 1 \text{ to } N; i \neq \alpha)$$

LEM (Long Element Method) is suitable for the deformation reproduction of living tissue like surgical simulation. As a feature of LEM, The pressure, density and volume required for displacement calculation can be measured relatively easily. Moreover, It is said that the accuracy of deformation reproduction using LEM is higher than that of spring mass point model. Fig. 5 shows a method of reproducing the deformation. The deformed object is divided into LE(Long Element), and the surface shape is reproduced by the set of deformation of each LE.

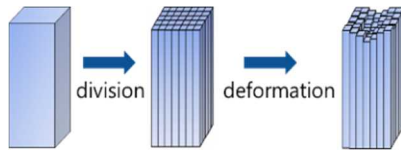


Fig.5. LEM model.

6. Implementation of LEM

In modeling by LEM, mainly three equations are treated. The first equation is given by equation (1) that describes preservation of volume. Here, A is the cross-sectional area, ΔL is the amount of displacement of LE, and N is the number of LE.

$$\sum_{i=1}^N A_i \Delta L_i = 0 \quad (1)$$

The second equation is given by equation (2) which explains LE in contact with the pen slide. Here, α represents the LE in contact with the pen slide, and y represents the displacement amount of the pen slide.

$$\Delta L_\alpha = y \quad (2)$$

The third equation is given by equation (3) about the LE not touching pen slide. Where E is the Young's modulus, k is the surface tension, ΔP is the pressure difference inside and outside the object, d is the density, g is the gravitational acceleration, h is the distance from the surface Nbr indicates the i -th adjacent LE .

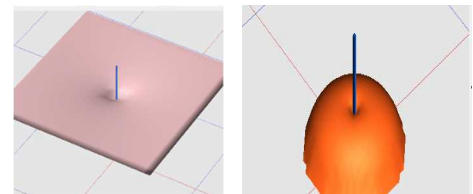
$$\frac{E}{L_i} \Delta L_i + \frac{k}{A_i} \sum_{j \in Nbr_i} (\Delta L_i - \Delta L_j) - \Delta P = dgh_i \quad (3)$$

In this study, the deformation of a part of the deformed object, not the whole, is reproduced. For this reason, the displacement (ΔL) of each LE was obtained from the equations (2) and (3) without using equation (1).

7. Deformation simulation

In the modeling using the mounted LEM, a part of silicone gel(α GEL, Taica) and salmon roe was modeled by LEM. Fig. 6 shows states of deformation simulation. Fig. 7 shows a state of the deformable virtual objects simulation combined with the haptic device.

A part of silicone gel spreading infinitely is modeled for the silicone gel. Hemisphere of the salmon roe is modeled for the salmon roe. As reference values for modeling the silicone gel, the size is 20 mm \times 20 mm \times 10 mm and the Young's modulus is 28.9 kPa. As reference values for modeling the salmon roe, the diameter is 6.2 mm and the Young's modulus is 5.58 MPa. The cross-sectional area and the surface tension depend on the number of partitions.



(a) silicone gel (b) salmon roe

Fig.6. The simulation of deformation.

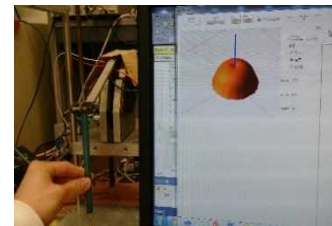


Fig.7. The simulation system combined with the haptic device.

8. Conclusion

In this study, modeling an object and reproducing the deformation of a sample is performed using by LEM. For reproducing objects, the deformation of a part of silicone gel and salmon roe is reproduced. By using LEM, the reproducibility is improved as compared with the conventional simulation.

Future research should focus on calculating force from equations of LEM and generating calculated force with the haptic device. Such a system would make it possible to test smaller samples easily.

9. Acknowledgement

This research was partially supported by the Ministry of Education, Science, Sports and Culture, Grant-in-Aid for Scientific Research, 2012.

10. References

1. T.OKADA(2017) Re-creation of a membrane puncture's sense of an object constituted of liquid and an outer membrane by a haptic device and a deformation simulation of the virtual objects. *International conference on artificial life and robotics (ICAROB2017)*, Jan 19-22, Miyazaki, Japan, 2017
2. Costa IF, Balaniuk R: LEM - An approach for real time physically based soft tissue simulation. *Proc of IEEE ICRA 2001*, Korea, 2001, pp. 2337-2343.

A four-legged robot's soft feet structural design and walking gait generated from inverse kinematics

Amornphun Phunopas

Department of Production Engineering, King Mongkut's University of Technology North Bangkok, 1518 Pracharat 1 Road Bangsue, Bangkok, 10800, Thailand

Eiji Hayashi

Computer Science and Systems Engineering, Kyushu Institute of Technology, 680-4 Kawazu, Iizuka Fukuoka, 820-0067, Japan

*E-mail: amornphun.p@eng.kmutnb.ac.th, haya@mse.kyutech.ac.th
www.kmutnb.ac.th*

Abstract

The conventional wheel is famous in the industrial mobile robot because it is simple to build and easy to control and to maneuver. On the other hand, the legged robot is complicated to control but has a high performance in locomotion like highly evolved legged-creatures. This research describes the four-legged robot design platform with the soft feet, which are made by silicone-material forming. The robot's feet are implanted by the strain gauge sensor. The robot can percept the external force sensitively when its feet touch something. The research demonstrates the forward kinematics and inverse kinematics of a four-legged robot with three joints for each. The result has validated the kinematic equations by implementing them on the real dog-like pet robot. The robot walked with a pure walking gait and showed a sensing signal from the soft foot and ground contact.

Keywords: Soft material robot, Robot's foot sensing, statics balance condition

1. Introduction

The legged robot consumes energy more than wheel type robot. The equation of motion of the legged robot is also complicated. However, the legged robot has a good maneuver and mobility like the revolute vertebrate animal, which has legs. The robot can perform mimicking from animal's movement using a mathematical model or a trained behavior. The smooth floor is a primary test that the robot can repetitive its movement pattern when it walks with stable balance control condition. Moreover, the robot has to adapt its movement simultaneously on the stepping terrain or multi-levels. In the high-level cognition in fast movement, the human has the experiences to plan its motion before moving for example in a hurdle race. Elsewhere, the human can sometimes focus on the smartphone while he

is walking without paying attention to everyday walking path. However, it is possible to make an accident. For those views basically, the robot has to be able to sense when the feet contact the ground in every direction. For the animal, the body is covered by skin which has a nerve cell to sense the impact force. The reviewed works use various methods regarding the sensors of the robot's perception. The humanoid robot foot has an effective contact area (ECA) of perception. Thus, the sensor is a flexible force sensor array (FFSA) with the spatial rectangle in Ref. 1. The robot transfers weight to its foot while it is walking under a dynamic equilibrium criterion or Zero Moment Point (ZMP). Next, a curvature sensor module can be embedded into the soft-bodied robots in Ref. 2. The sensor type is an electro-mechanical sensor that is fabricated and merged into a soft robot. For an

© The 2018 International Conference on Artificial Life and Robotics (ICAROB2018), Feb. 1-4, B-Con Plaza, Beppu, Oita, Japan

application, a soft robotic glove has a soft fiber-reinforced actuator to sense the human hand movement as a human interface device in Ref. 3. Another sensor is a strain gauge, which is a skin-like, ultra-thin sensor. It can be bent and used for prosthetic devices in Ref. 4. There is research about soft robotic fingertips that is a similar idea to its use as a robot foot soft tip. The soft robotic fingertip has a metal bar as a bone, a body, and a skin layer. The receptors are strain gauges and PVDF films. The body is made of liquid silicone rubber in Ref. 5. The soft robot is a series elastic actuator (SEA) that interfaces with an environment. To control the soft robot is designed with impedance-controlled compliant actuators in Ref. 6. For previous work of this research in Ref. 7, the robot has a plastics material for robot foot. This paper presents to test the robot walking pattern with a defined static balanced condition and the sensing signals from the robot foot.

2. The robot structures

The robot has four legs that have the same module for each leg. It has three joints for shoulder, wing and, knee. It has 12 joints. The robot size is approximately a small pet in 1 cubic-foot volume. The robot weight is about two kilogram including mini pc and battery. The robot body frame is made from ABS plastic as in Fig. 1.

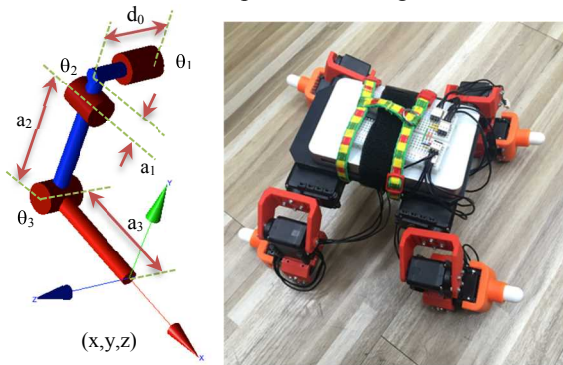


Fig. 1. (Left) A robot leg configuration. (Right) The robot structure with four legs.

2.1. Robot's soft foot design

The robot feet are made from soft material which is implanted a strain gauge sensor inside to sense the impact force as in Fig. 2. From the sensor placement, it can sense on the vertical axial load because of its weight pressing and distribute in various directions along the axial load.

However, it does not sense the torsional and bending load. A strain gauge sensor has an amplifier circuit which sends the analog signal to the analog to digital converter.

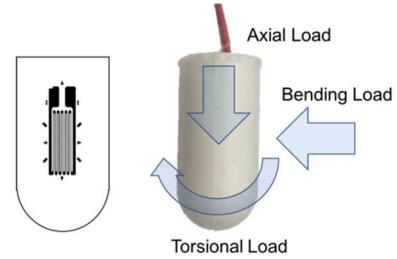


Fig. 2. The robot foot material is the end-effector of the robot leg or the soft tip.

3. Kinematics

The summary of forward and inverse kinematics is used to control the robot posture. The equation is individually applied to each leg. First is the forward kinematics in Eq. (1-3)

$$x = -a_3 \cos \theta_1 \cos \theta_2 \cos \theta_3 + a_3 \sin \theta_1 \sin \theta_3 - a_2 \cos \theta_1 \cos \theta_2 - a_1 \cos \theta_1 \quad (1)$$

$$y = a_3 \sin \theta_2 \cos \theta_3 + a_2 \sin \theta_2 + d_0 \quad (2)$$

$$z = -a_3 \sin \theta_1 \cos \theta_2 \cos \theta_3 - a_3 \cos \theta_1 \sin \theta_3 - a_2 \sin \theta_1 \cos \theta_2 - a_1 \sin \theta_1 \quad (3)$$

Where a_1, a_2, a_3 and d_0 are link's length parameters.

Second is inverse kinematics in Eq. (4-6) that is the solved equations from the Eq. (1-3) using the Harmonic Addition Theorem. The singularity condition is that θ_2 equals to zero degrees in case of dividing by zero in Eq. (6).

$$\theta_1 = \arccos \left(\frac{x+y}{\text{sign}(A+B) \sqrt{(A+B)^2 + (A-B)^2}} \right) - \alpha \quad (4)$$

$$\theta_2 = \arccos \left(\frac{-2a_1 a_2 + \sqrt{4a_1^2 a_2^2 - 4(a_1^2 + c^2)(a_2^2 - c^2)}}{2(a_1^2 + c^2)} \right) \quad (5)$$

$$\theta_3 = \arccos \left(\frac{z - a_2 \sin(\theta_2) - d_0}{a_3 \sin(\theta_2)} \right) \quad (6)$$

Where $A, B,$ and C are derived coefficient.

The sequence of the robot walking gait and static balance configuration is generated in the walking gait pattern.

4. Walking gait pattern

The walking gait possibly has many patterns under the condition of a smooth floor with the Zero Momentum Point (ZMP) area as a stability criterion. Commonly, ZMP is used for dynamical walking, but in this case, it is to initiate some conditions to make the robot walk continuously with no falling head over heels or stumbling as in Fig. 3. The robot configurations are posed by kinematic equations to keep all feet's tip or the end-effector of the robot's legs on the same planar floor. The center of gravity is approximately in the ZMP area on the floor plane. The robot's body plane orientates itself around the XYZ axes, as shown in Fig. 4.

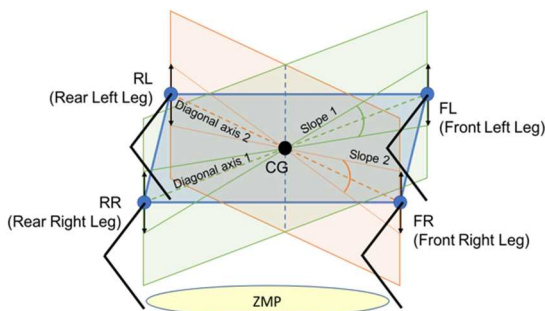


Fig. 3. The robot's body plane can change its planar slope when changing each leg's height on the smooth floor.

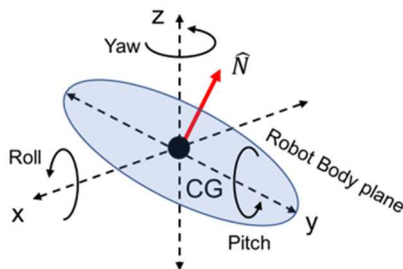


Fig. 4. The defined normal vector of the robot's body plane has three orientations: roll, pitch, and yaw.

The normal vector is created to define the robot's body plane in Eq. (7-8). In Eq. (9), there are three rotations, roll, pitch, and yaw, for the X, Y, and Z axes respectively.

$$\hat{N} = a\hat{i} + b\hat{j} + c\hat{k} \quad (7)$$

$$|\hat{N}| = \sqrt{a^2 + b^2 + c^2} \quad (8)$$

$$R(\text{roll}, \text{pitch}, \text{yaw}) = R_x(\text{roll})R_y(\text{pitch})R_z(\text{yaw}) \quad (9)$$

Where a is the position of the normal vector on the X-axis, b is the position of the normal vector on the Y-axis, and c is the position of the normal vector on the Z-axis.

The normal vector is perpendicular to the robot's body plane. The point of the normal vector represents the tilt plane and the transfer CG position. The robot walks by lifting its legs one by one. Therefore, when the other three legs are on the floor, the CG will transfer the ZMP area to the floor area contacted by the three feet. The normal vector will move along the diagonal axis 1 from point P2 to point P4 and along diagonal axis 2 from point P1 to point P3, as shown in Fig. 5.

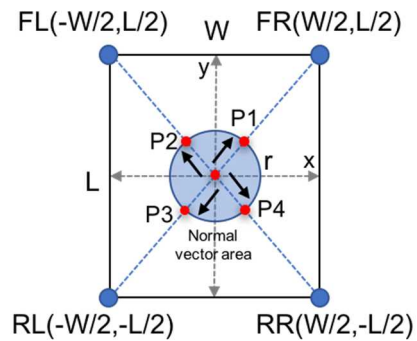
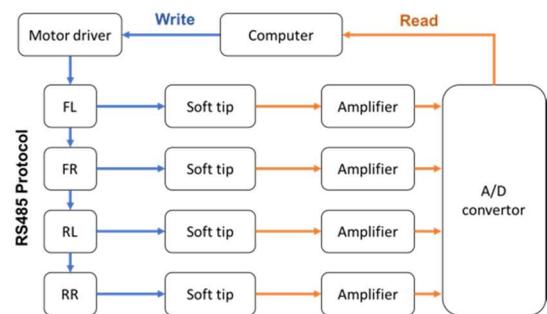


Fig. 5. From the top view, the point of the normal vector moves in the unit circle of the normal vector area.

4.1. Control system

Respectively to the walking-gait pattern, the robot walks in a sequence, sensing the floor contact simultaneously. Fig. 6 shows the hardware and the software that support the robot system. The computer sends a command to the robot by writing the motor's trajectory. The strain gauge sensor amplifier is the differential bridge operational amplifier circuit with gain adjustment. The output analog



voltage is 0-3.5 volts, which is compatible to the analog input of the general microcontroller.

Fig. 6. The soft tip foot of each leg can sense the floor contact signal. Moreover, the computer reads the signals of the floor-contact detection.

5. Result

The first experiment showed the signal from a robot foot in Fig. 7 when it contacted the floor in the axial load. Similarly, the four legs have the same result because it has the same structure.

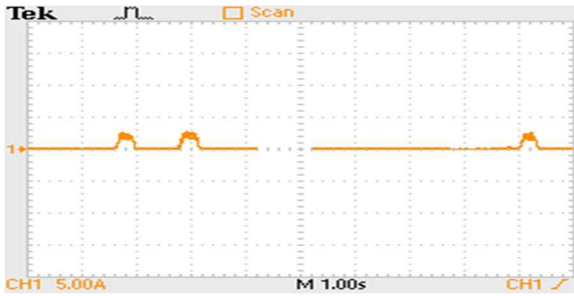


Fig. 7. A soft robot foot contacted the floor. The analog voltage signal is measured by oscilloscope.

In the second experiment, the robot walks applying the designed walking gait. The walking gait is generated from kinematic equations. For every walking step, one leg paces and the remaining three legs are on the floor, as in Table 1 and Table 2.

Table 1. One pace of the front left leg and the relative joint angles (degree) of all legs.

t	Front Left Leg			Rear Right Leg			Front Right Leg			Rear Left Leg		
	θ_1	θ_2	θ_3	θ_1	θ_2	θ_3	θ_1	θ_2	θ_3	θ_1	θ_2	θ_3
0	20	-5	55	-20	-5	-55	-20	5	-55	20	5	55
1	20	-5	55	-19	-5	-64	-20	5	-55	20	5	55
2	18	-5	70	-19	-5	-64	-20	5	-55	20	5	55
3	18	-6	79	-20	-5	-55	-20	5	-55	20	5	55

Table 2. One pace of the front left leg and the relative foot tip XZ-positions (mm) of all legs.

t	Front Left Leg		Rear Right Leg		Front Right Leg		Rear Left Leg	
	x	z	x	z	x	z	x	z
0	-103.57	-103.07	-103.57	-103.07	-103.57	-103.07	-103.57	-103.07
1	-103.57	-103.07	-103.57	-93.07	-103.57	-103.07	-103.57	-103.07
2	-87.86	-102.65	-103.57	-93.07	-103.57	-103.07	-103.57	-103.07
3	-76.01	-103.07	-103.57	-103.07	-103.57	-103.07	-103.57	-103.07

6. Discussion

The soft material is made of silicone. A hardness level is a maximum number, but it is still too soft to take the robot weight. Consequently, the soft robot foot is

immoderately deformed its shape. The strain gauge sensor is very fragile and easy to be broken. Due to the robot moves dynamically, CG, inertia and external force affect the system. The walking stability constraint is very complicated to maintain its balance when the robot walks.

7. Conclusion

The robot can walk and sense the floor contact from the soft foot using the implanted strain gauge sensor. The foot tip position and trajectory can independently be designed depending on the solved kinematic equations coherently. However, the walking gait in the fixed pattern is very difficult to define the stability state. It had better apply the control law or soft computation for robot control.

Acknowledgements

King Mongkut’s University of Technology North Bangkok and Kyushu Institute of Technology have supported this research.

References

- Wu, B., Wang, Z., Luo, J., & Wu, Z. (2013). Perception of effective contact area distribution for humanoid robot foot. *Measurement*, 46(7), 2093-2098.
- Ozel, S., Keskin, N. A., Khea, D., & Onal, C. D. (2015). A precise embedded curvature sensor module for soft-bodied robots. *Sensors and Actuators A: Physical*, 236, 349-356.
- Polygerinos, P., Wang, Z., Galloway, K. C., Wood, R. J., & Walsh, C. J. (2015). Soft robotic glove for combined assistance and at-home rehabilitation. *Robotics and Autonomous Systems*, 73, 135-143.
- Sencadas, V., Mutlu, R., & Alici, G. (2017). Large area and ultra-thin compliant strain sensors for prosthetic devices. *Sensors and Actuators A: Physical*, 266, 56-64.
- Hosoda, K., Tada, Y., & Asada, M. (2006). Anthropomorphic robotic soft fingertip with randomly distributed receptors. *Robotics and Autonomous Systems*, 54(2), 104-109.
- Calanca, A., & Fiorini, P. (2017). Impedance control of series elastic actuators based on well-defined force dynamics. *Robotics and Autonomous Systems*, 96, 81-92.
- Phunopas, A., Suwichien, N. (2017). Kinematic analysis and trajectory of a dog-like robot. *The 8th TSME International Conference on Mechanical Engineering*, 8, 101.

Powered Ankle Exoskeletons: Existent Designs and Control Systems

A.H. Weerasingha, W.P.K. Withanage, A.D.K.H. Pragnathilaka, R.K.P.S. Ranaweera, R.A.R.C. Gopura

*Bionics Laboratory, Department of Mechanical Engineering,
University of Moratuwa, Katubedda, Moratuwa 10400, Sri Lanka*

*E-mail: amashiweerasingha@gmail.com, kesarawithanage5@gmail.com, kasun.adkh@gmail.com,
pubudur@uom.lk, gopurar@uom.lk
www.mrt.ac.lk*

Abstract

This paper performs a comprehensive review on active ankle exoskeletons powered by external means. Initially, anatomy of the ankle joint complex is highlighted. Next, associated research challenges and design difficulties are recognized for the development of robotic hardware systems. Then, mechanisms, actuation methods, and control methods are systematically presented. Here, exoskeletons designs from 2005 to 2017 were studied to recognize the latest paradigm shifts. As such, this paper provides a classification, a comparison and an overview of related technologies. Finally, design recommendations are made for the development of powered ankle exoskeletons.

Keywords: powered ankle exoskeleton, mechanisms, actuation methods, control methods.

1. Introduction

Robotic exoskeletons are classified as upper-extremity, lower-extremity, and other systems.¹ Lower extremity exoskeletons (LEE) are predominantly used for gait rehabilitation, power augmentation and motion assistance.² According to statistics around the globe, elderly population exceeds 10% of the total population. Conversely, people suffering with neurological or muscular disorders are on the rise.³ As such, medical industry has shown a growing interest to use LEE for restoring patients' mobility and to alleviate health care issues arising from locomotion difficulties.³

LEE is designed to support anatomical functions of the six different human joints of the lower extremity. In general, hip, knee and ankle have seven degrees of freedom (DOF) per limb. Here, the ankle joint complex, having tri-planar motions, plays a major role in performing locomotion. Over the years, powered ankle exoskeletons have been rapidly advancing with the introduction of novel materials, actuators, and sensors. Contemporary ankle exoskeletons have been designed to

achieve proper functionality while ensuring safety of the wearer. However, their performance in terms of metabolic energy saving, ergonomic conformity, agility, etc. need further improvements. In order to eliminate such limitations, an improved understanding of their features and characteristics is paramount. In that context, this paper focus on reviewing both mechanical and control systems of recently developed ankle exoskeletons at research-level. In order to limit the scope of the study and to provide a broad understanding of the knowledge base, powered ankle exoskeletons using different state-of-the-art technologies are selected for this review. In particular, exoskeletons designs from 2005 to 2017 is studied to recognize the latest paradigm shifts. In summary, section 2 summarizes the design difficulties arising from anatomical and/or biomechanical complexity of ankle joint. Under section 3 and 4, existent powered ankle exoskeletons which support locomotion are reviewed based on actuation and control methods respectively. The discussion in section 5 explains latest trends, patterns and possible future directions for developing assistive powered ankle exoskeletons.

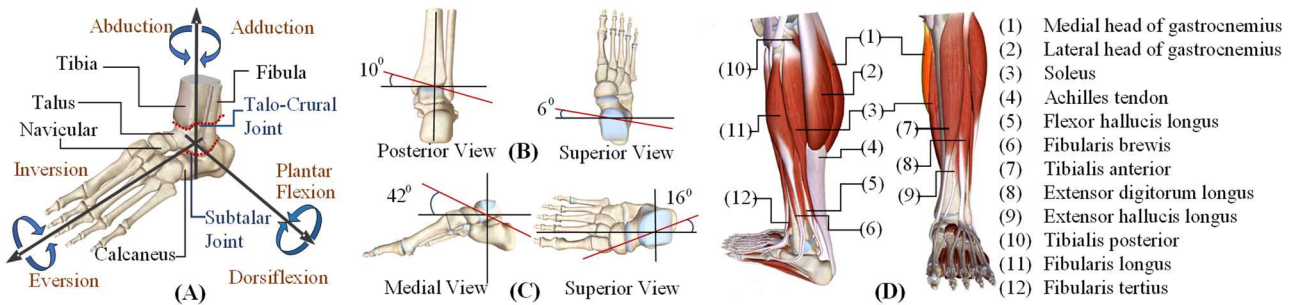


Fig. 1 Anatomy of ankle joint complex: (A) bone structure and DOF, (B) oblique axis of talocrural joint⁷, (C) oblique axis of subtalar joint⁷, (D) muscles responsible for triplanar ankle motions⁴.

2. Design Considerations for Ankle Exoskeletons

Anatomy of ankle joint complex and design difficulties of ankle exoskeletons is summarized in this section.

2.1. Anatomy of Ankle Joint Complex

The three significant DOF of ankle joint complex are plantarflexion-dorsiflexion, eversion-inversion and abduction-adduction (see Fig. 1(A)). Plantarflexion during stance phase supplies majority of the energy required for propulsion while walking.⁴ Range of motions (ROM) for each DOF are plantarflexion 50° - dorsiflexion 20°, inversion 35° - eversion 25°, and abduction 20° - adduction 25°.⁵ However, studies shown that ROM may vary with age and gender.⁶

Ankle movements mainly happens about talocrural and subtalar joints (see Fig. 1(A)). Talocrural joint is formed by talus, tibia and fibula bones.⁴ Top of the talus fits inside the socket formed by tibia and fibula. This joint is mechanically similar to a mortise and tenon joint providing plantarflexion-dorsiflexion. Bottom of the talus locates on the calcaneus forming subtalar joint that allows eversion-inversion and abduction-adduction of ankle.⁷ Thus joint complex supports triplanar motions.

Collection of muscles are responsible for generating the motions of foot segment during ambulation (see Fig. 1(D)). The tibialis anterior, extensor digitorum longus, extensor hallucis longus and fibularis tertius muscles with tendons dorsiflexes the foot. The gastrocnemius, soleus, plantaris, fibularis longus, fibularis brevis, tibialis posterior, flexor digitorum longus and flexor hallucis longus muscles with tendons plantarflexes the foot. Fibularis longus, Fibularis brevis, Fibularis tertius muscles and their tendons performs the eversion. Tibialis anterior and tibialis posterior muscles along with related tendons performs the inversion of ankle.⁴

2.2. Design Difficulties of Ankle Exoskeletons

According to biomechanics studies, synovial hinge joints at ankle plays a crucial role in supporting motions of human lower extremity⁸. The fitting of the exoskeleton at the ankle is more difficult than hip and knee, due to strict requirements of smaller space as well as anatomical complexity introduced by talocrural and subtalar joints.⁷ The anatomical axes (see Fig. 1(B and C)) of talocrural and subtalar joints are placed in an oblique sense that cause foot to move across all three planes allowing pronation and supination to occur during walking.⁷ Hence, constraining motions to a single plane can lead to abnormal joint movements, poor muscle recruitment and increasing overall energetic cost.⁸

Ground irregularities, body weight and walking speed directly affect the mechanical stiffness assumed by ankle and foot.⁹ Hence, the exoskeleton should adjust the system resistance to account for the variable stiffness of the biological counterpart during walking, running, etc. If stiffness not properly adjusted, it may even lead to loss of stability or even injury of the joint.¹⁰

If a person weighing 75 kg walks at an average speed of 1.3 m/s, maximum torque and power generated at the ankle joint according to kinetic analysis is 150 Nm and 200 W respectively.⁸ This is considerably greater than the calculated values at hip and knee joints. A powerful electromechanical, pneumatic or hydraulic actuation system can be introduced to satisfy this requirement,¹¹ however such a system will ultimately increase size and weight of the exoskeleton. Here, bulky designs tend to disrupt the normative motions of the lower extremity and added inertia may burden the actuators energetically.¹² Although, tethered systems are acceptable for rehabilitation applications, portability is an indispensable trait for power-assist ankle exoskeletons.¹³

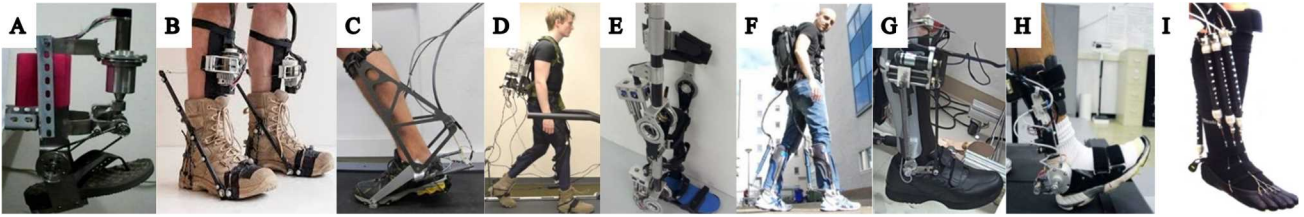


Fig. 2. Ankle exoskeletons: (A) PAFO¹⁴ by Beijing Institute of Technology 2015, (B) autonomous exoskeleton¹⁵ by MIT 2014, (C) ankle exoskeleton¹⁶ by Carnegie Mellon University 2014, (D) soft exosuit¹⁷ by Harvard University 2013, (E) knee-ankle-foot robot¹⁸ by NUS 2013, (F) achilles ankle exoskeleton¹⁹ by Delft University of Technology 2015 (G) AFO²⁰ by Case Western Res. University 2012, (H) PPAFO²¹ by University of Illinois 2011, (I) soft orthotic device²² by Harvard University 2011.

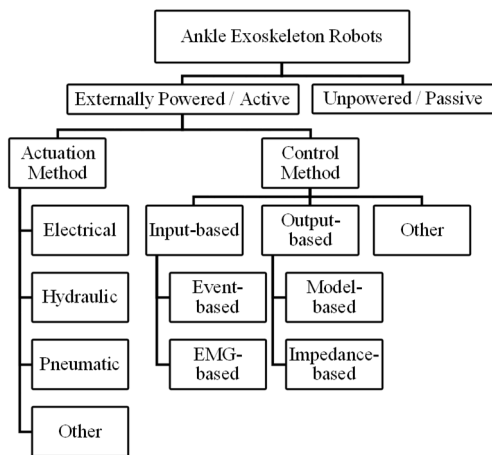


Fig. 3. Classification of powered ankle exoskeletons

3. Mechanisms and Actuation Methods

In this paper both actuation methods and mechanisms are classified as in Fig. 3. Details are then presented under electric, pneumatic, hydraulic, and other categories.

3.1. Electric Actuators

Beijing Institute of Technology in 2015 developed a portable powered ankle foot orthosis (PAFO), which employs electric motor drive to provide plantarflexion and dorsiflexion assistance (see Fig. 2(A)) for treatment of ankle injuries.¹⁴ The powertrain is composed of an electric actuator, which is the elementary unit to provide energy for ankle movement, and a transmission system, that deliver power to the ankle joint at desirable speeds. The transmission is composed of a harmonic drive, a bevel gear drive, and a synchronous belt drive. Although the device is capable of delivering higher torques, the system is bulky and heavy to warrant everyday use.

An autonomous battery powered exoskeleton¹⁵ was developed by MIT to reduce metabolic cost of human

walking during load carriage in 2014 (See Fig. 2(B)). A device is a self-contained and has all necessary components on board such as power supply, actuator and controllers. The bilateral exoskeleton was comprised of three main sub-assemblies such as a pair of fiberglass struts attached to each foot, unidirectional actuators mounted on the anterior of shank segments, and control package including battery worn on the waist. Power is transmitted to the ankle joint by pulling on the struts during propulsion phase. Features such as autonomous operation, lightweight architecture and ergonomic conformity have contributed to its successful implementation.¹⁵

An exoskeleton that provide greater peak torque, peak velocity and range of motion, was developed by Carnegie Mellon University in 2014. It was actuated by a powerful off-board motor and real-time controller with mechanical power transmission through a flexible and tethered Bowden cable.¹⁶ The exoskeleton frame includes rotational joints on either side of the ankle with axes of rotation approximately co-linear with the human joint. Each of the frames are attached to the foot and shank segments (See Fig.2(C)). The foot mount has a lever arm posterior to the ankle that wraps around the heel. A Bowden cable tethered to the lever transmit the required joint power to assist propulsion. Proposed system mainly served as a universal platform to test influence of powered assistance.

The Soft Exosuit developed by Harvard University in 2013 is a battery-powered portable device actuated by a cable-driven system.¹⁷ It is essentially worn like a garment with a backpack unit (See Fig. 2(D)). Hence, the effective dynamic stiffness of the flexible suit and its interaction with the lower extremity are important design considerations. The sheath of the Bowden cable is strapped to the suit, where one terminal is located at the

backside of the calf muscle and other connected to the motor drive unit carried on the back. A moment is generated directly about the biological ankle joint by means of pulling the heel upward using Bowden cable. The cable acts in a similar way to the biological muscle that stretches pre-stressed tendons. The Exosuit is designed to support power absorption through passively extending as well as assisting the muscle contractions.

Series elastic actuator (SEA) is a type of electrically powered actuation method with elastic spring elements connected in series. National University of Singapore in 2013 developed a portable knee-ankle-foot orthosis using modified SEA which eliminate conventional limitations of earlier SEA models.¹⁸ It (See Fig. 2(E)) consists of a DC motor, a ball screw, a pair of spur gears and a pair of spring assemblies.

Similarly, Achilles Ankle Exoskeleton developed by Delft University in 2015 uses a SEA to provide push-off assistance for healthy subjects during walking.¹⁹ Achilles exoskeleton is comprised of three units. The two boot units include SEAs, sensors and mechanisms to transmit power to the human leg and, and a backpack unit, to carry batteries and power management system (See Fig. 2(F)). It is the most commonly used actuation method in recent powered ankle exoskeletons. The active power submitted to the ankle joint by the electric motor is supplemented by the passive energy stored in the springs. Hence, an increase of the overall energetic input to the joint results in better performance of the actuator.

An Ankle Foot Orthosis (AFO) was developed by Case Western Reserve University in 2012 to assist plantar-dorsiflexion.²⁰ It is comprised of a series elastic actuator, a four-bar linkage and a crank-slider mechanism (See Fig. 2(G)). Actuation force is derived from a pre-tensioned spring and torque is delivered to the ankle via four-bar linkage. The drive link which the actuator acts on is attached to the slider mechanism that support the insertion point of the four-bar linkage mechanism. Thereby the moment arm of the spring is dynamically adjusted. Yet, low speed of operation of this powered device is a notable drawback.

3.2. Pneumatic Actuators

A Portable Powered Ankle-Foot Orthosis (PPAFO) was designed by University of Illinois in 2012.²¹ Pneumatics was used to supply plantarflexion and dorsiflexion torque

through rotary pneumatic actuator mounted at the ankle (See Fig. 2(H)). The recycling scheme is used to capture the exhaust gas from plantarflexion cycle and to drive the following dorsiflexion cycle. The normal circuit consists of two solenoid valves which can be used to control rotary actuator in both directions. An additional solenoid valve and custom accumulator were added into the pneumatic system, to implement the recycling scheme.

Bio inspired active soft orthotic device, developed by Harvard University in 2011, has multiple pneumatic artificial muscles (PAM) that imitate morphology and functionality of the actual biological muscles to control plantarflexion-dorsiflexion and inversion-eversion movements.²² Flexible reinforced closed membrane, the core element of PAM is attached between limb segments to transmit mechanical power (See Fig. 2(I)). The behavior of PAM closely represents the biological muscles in generating forces and motions in addition to absorbing shock loads. Bulkiness of the pneumatic circuit limit its use for stationary rehabilitation robots and laboratory experimentations.

3.3. Hydraulic Actuators

Ankle exoskeleton powered by hydraulic actuators are most rare for locomotion assistance. BLEEX developed by University of California in 2005 include an ankle joint having three DOF.²³ BLEEX uses double acting linear hydraulic actuators, which have two opposite facing pistons to achieve force control in both directions. Although hydraulic actuators have the highest power-to-weight ratio, the complexities in attaching a hydraulic circuit on body is notably high.

3.4. Other Actuators

AFO developed by Osaka University in 2007 has been actuated using a computer controlled Magneto-rheological (MR) type damper, which uses viscous damping to achieve resistive plantar-flexor torque during selected phases of gait.²⁴ Passive AFO was developed by University of Toledo in 2014, which consists of a hinged brace and series of SMA wires.²⁵ The super-elastic wires can store mechanical energy during plantarflexion and release it during dorsiflexion to compensate the inability. These types of actuators are compact and lightweight than conventional ones and behaves similarly to the natural change in stiffness of ankle joint in normal gait.

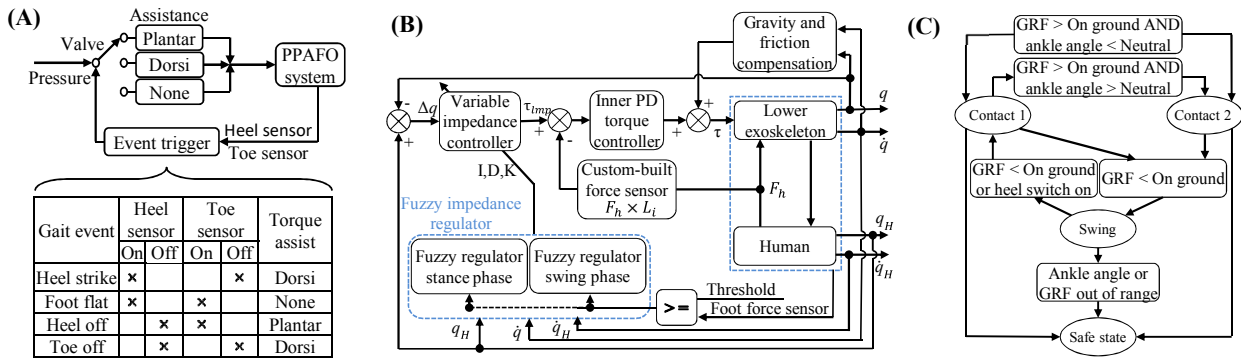


Fig. 4. Control algorithms in powered ankle exoskeletons: (A) event-based control method²¹ 2011, (B) impedance control method²⁹ 2015, (C) finite-state control algorithm³¹ 2004.

4. Control Methods

In this paper, control methods of ankle exoskeletons are classified (see Fig. 3) and presented under input-based, output-based and other control methods.

4.1. Input-Based Control Methods

4.1.1. Event-based Controlling Method

In event-based control method, current gait phase is detected by means of monitoring sensor inputs. Accordingly, assistive torque is provided while speed and position control is achieved using controller modules. PPAFO developed by University of Illinois in 2012 used an event-based control algorithm (see Fig. 4(A)). It describes the gait phase detection and torque assisting algorithm according to the force sensing input. Events were detected when sensor magnitudes exceeded the tuned user-specific thresholds for the heel and metatarsal sensors.²¹ Similarly, Achilles ankle exoskeleton in 2015 was controlled with force and encoder feedback using an event-based control scheme. A feed-forward signal was taken as a function of gait phase by using a non-linear filter that fits a number of primitives such as Gaussian functions to the signal to be extracted.¹⁹

4.1.2. EMG-based Controlling Method

In this controlling method electromyography (EMG) signals are taken from limb muscles to determine motion intention of the wearer. EMG sensors produces a signal which varies in amplitude proportional to the magnitude of muscle recruitment. The AFO, developed by University of Michigan in 2010, was controlled using EMG-based control system.²⁶ It consists of two input

linguistic variables, the EMG signal and the acceleration angle with one output linguistic variable, the motor status. EMG signals contain important details useful to determining motion intention. However, raw EMG signals are random in shape and readings can be different from user to user. Strength of EMG signal can be affected by different thicknesses of muscle tissues and noisy electrical environments. Further it cannot be used for patients who have lost their muscle control.

4.2. Output-Based Control Methods

4.2.1. Model-based Controlling Method

In a model-based control structure, a desired robotic action is computed based on a human–exoskeleton model, relying on the accuracy of the model which requires series of sensors to recognize kinematics and dynamics variables. Generally, this control method can be divided into two types, based on the model used: the dynamic model and the muscle model.²⁷ The dynamic model can be achieved by modeling the human body as rigid links joined together, using mathematical method. And the muscle model predicts the muscle forces by taking EMG signal inputs and gives an output of force estimation. A Neuromuscular model (NMM) based controlled ankle exoskeleton by NINRA in 2017 used a reflex-based force feedback controller, to explore the adaptability to variable speeds of the wearer.²⁸

4.2.2. Impedance Controlling Method

The notion of impedance control method in rehabilitation robots is to regulate the dynamic relation between the assistive device and the wearer by relating the position error (joint angles) to interaction force/torque via

mechanical impedance (output impedance of the exoskeleton, which is usually modelled as a mass-damper spring system). High output impedance will increase the assistance from the exoskeleton to guide the patient's limb onto the reference trajectory. If the patient shows greater control in the training, the desired output impedance of the exoskeleton will similarly be low to allow the patient to deviate more from reference trajectory. An AAFO (see Fig. 4(B)) designed by Natural Science Foundation of China (NSFC) in 2015, was controlled using a fuzzy based impedance control architecture.²⁹

4.3. Other Control Methods

Adaptive control method is a special type of nonlinear control system which can alter its parameters to adapt to a changing environment. This can cover a set of techniques which provide a systematic approach for automatic adjustment of controllers, to achieve or to maintain a desired level of control system performance, when the parameters of the plant dynamic model are unknown and/or change in time. An AEO has been proposed in 2016, which the human muscle activity is feedback to adapt the assistive joint torque behavior.³⁰ The triggers or transitional parameters for the finite state algorithm are based on gait events (see Fig. 4(C)). The MIT AAFO has been designed to assist ankle movements of patients having drop-foot gait.³¹ Ground reaction force (GRF) sensors are used to determine the gait phase and ankle angle sensor is used to determine the angle between the shank and the foot. In a Contact-1 state (from heel strike to mid-stance), the objective of the controller was to prevent foot slap. During a Contact-2 state, (from mid-stance to toe-off) the controller minimized the impedance of the brace so as not to impede plantarflexion movements. Finally, during swing state, the user's foot was lifted to prevent toe drag. Safe state is created to shut down the device if any unexpected situation occurs.

5. Discussion and Future Directions

Powered ankle exoskeletons are commonly designed to perform selected task(s) of the biological ankle joint. However, mechanisms, powering systems and controlling methods employed in modern robotic devices are diverse. In that context, several research-level powered ankle exoskeletons representing various technological domains have been presented throughout

this paper. As such, Table 1 include a comparison of the technical characteristics of contemporary ankle exoskeletons based on method of actuation. The most common and recent actuation method used for powered ankle exoskeleton is electrical actuators with different types of transmission systems such as belt drives, Bowden cable drives, harmonic drives and others transmission methods. Even though SEA has a limited bandwidth and performance issues, there is a notable trend of their usage in powered ankle exoskeletons since its inception. SEA is capable of storing passive energy in the spring element and has low output impedance which makes it a suitable actuation method for ankle exoskeletons. However, to overcome performance drawbacks and sensor integration issues, continuous improvements to SEA technology is required from a futuristic point-of-view. On the other hand, pneumatic actuators have a notable advantage over electric actuators as they are more comparable to biological muscles. The artificial pneumatic muscles can remarkably mimic human kinematics and dynamic behavior by closely reproducing joint stiffness properties of the lower limbs. A better actuation system with efficient power transmission method can be developed by combining different technologies reviewed in this paper. Even though there is a trend of combining different actuation methods in modern LEEs or prostheses, it has not yet been realized with ankle exoskeletons. In general, powered ankle exoskeletons designed for locomotion assistance only focus on actively supporting one DOF: namely plantarflexion and dorsiflexion, as evident from Table 1. Instead, a hybrid actuation method can be introduced to support multi DOF to overcome the key design difficulties described under section 2.2. On the other hand, a modern ankle exoskeleton design should necessarily focus in achieving ergonomic conformity, metabolic energy saving and improving agility.

In order to support the complex kinematic and dynamic behavior of human motion, a combination of control methods can be implemented. However, no existent exoskeletons have attempted to integrate control strategies as a whole. An exoskeleton controller has to meet several requirements. One of the key requirements can be identified as controllability as per the user's intention. This requirement can be implemented using EMG-based control method. But EMG signal generation is inconsistent among user population.

Table 1 Technical characteristics of modern ankle exoskeletons

Actuation Method	Name / Institute / Year	Powering Method	Control Method	Sensory Information	Advantages	Limitations	Wt (kg)
Electric Actuators	PAFO ¹⁴ / Beijing Inst. / 2015	Harmonic, bevel and belt drive, Brushless DC motor	Event-based control with PID	Encoders, Ground reaction force sensors	Portable, High power and torque	Bulky, heavy	N/A
	Auto. Exo. ¹⁵ / MIT / 2014	Belt drive, Brushless DC motor	Event-based control	Incremental optical encoders	Low metabolic cost	Limited range of control	4.0
	Ankle Exo. ¹⁶ / Carnegie Mel. Uni. / 2014	Bowden cable drive, Off-board AC servomotor	Adaptive control with iterative learn.	Optical encoders, Foot contact switches, Torque sensors	High peak torque and bandwidth, Lightweight	Tethered, Bulky	0.87
	Exosuit ¹⁷ / Harvard Uni. / 2013	Bowden cable drive, Brushless DC motor	Event-based control	Foot switches, Force sensors	No rigid external structure, Flexible	Heavy backpack and suit	12.15
	Achilles AE ¹⁹ / Delft Uni. / 2016	SEA, Brushless DC motor	Event-based control	Incremental and absolute encoders, Pressure sensors	Low metabolic cost	Limited speed of operation	N/A
	PKAFO ¹⁸ / NUS / 2013	SEA, Brushless DC motor	EMG-based control with PD	sEMG sensors, Liner potentiometers, Rotary encoders, IMUs	Modular design, High bandwidth	Sensor integration and control	0.85 (Ac.)
Pneumatic Actuators	Soft Orth. Dev. ²² / Harvard Uni. / 2011	PAM	Event- and Model-based hybrid control	Strain sensors, Pressure sensors, IMUs	Lightweight, Greater flexibility, Higher Stability	Need compressed air supply	0.95
	PPAFO ²¹ / Uni. of Illinois / 2011	Pneumatic rotary actuator	Event-based control	Potentiometers, Force sensors	High system efficiency, Low fuel cons.	Limited duration of operation	N/A
Hydraulic Actuators	BLEEX ²³ / Uni. of California / 2005	Hydraulic pistons	Event-based control	Encoders, Linear Accelerometers, Force sensors	Active control of multiple DOF	Bulky, Need hydraulic supply	N/A

N/A - Not Available

A patient with muscular disorder will fail to use an EMG controlled devices effectively. To overcome this situation, a separate (pressure/ force) sensor based control strategy can be implemented concurrently with EMG. Importantly, with the EMG controller the user can instruct the device in rapid succession using electrical signals of the muscles. However, it may be difficult to find a stable correlation between the EMG signals and the output of the actuators.

Ability to assist user movements according to varying conditions is also another consideration when developing a robust controller for ankle exoskeletons. Here, the adaptive controller architecture have been successful in achieving this goal. When multiple DOF are controlled, the centralized single controller won't be much effective, as the single controller will be overburdened to control multiple DOF. Thus, modular controllers would be suitable choice to assist the multiple DOF separately for increasing system performance. Stability is the next issue in designing a control system, which occurs due to high-

frequency and high-amplitude external perturbation induced by robot-human interaction. This can cause vibrations which may reduce the exoskeleton performance.

In summary, the functional performance of the robot device can be further enhanced with improvements to both actuation method and control system. It is suggested to perform experiments on hybrid powered ankle exoskeleton which consist of combined actuation methods, efficient power transmissions and modular control systems to achieve multi DOF motions while offering greater degree of agility and support to the wearer.

References

1. M. Cenciarini and A. M. Dollar, "Biomechanical considerations in the design of lower limb exoskeletons," in *IEEE Int. Conf. Rehab. Robot. (ICORR)*, 2011, pp. 1–6.
2. B. Chen *et al.*, "Recent developments and challenges of lower extremity exoskeletons," *J. Orthop. Transl.*, vol. 5, pp. 26–37, 2016.

3. N. Li, L. Yan, H. Qian, H. Wu, J. Wu, and S. Men, "Review on Lower Extremity Exoskeleton Robot," *Open Autom. Control Syst. J.*, vol. 7, pp. 441–453, 2015.
4. J.E. Muscholino, L. Whitney, *Kinesiology – The skeletal system and muscle function*, 2nd edition, Mosby, 2011, pp. 124–316.
5. T. R. D. J. Hamill and K. M. Knutzen, *Biomechanical basis of human movement*, 4th edition, Philadelphia : Wolters Kluwer Health, 2015.
6. B. M. Nigg, V. Fisher, T. L. Allinger, J. R. Ronsky, and J. R. Engsborg, "Range of motion of the foot as a function of age," *Foot Ankle*, vol. 13, no. 6, pp. 336–343, 1992.
7. D. A. Neumann, "Ankle and Foot," *Kinesiology of the musculoskeletal system*, 2nd edition, Mosby, 2010, pp. 1–8.
8. Y. Fan and Y. Yin, "Mechanism design and motion control of a parallel ankle joint for rehabilitation robotic exoskeleton," in *IEEE Int. Conf. on Robot. Biomim. (ROBIO)*, 2009, pp. 2527–2532.
9. J. L. McKay and L. H. Ting, "Optimization of muscle activity for task-level goals predicts complex changes in limb forces across biomechanical contexts," *PLoS Comput. Biol.*, vol. 8, no. 4, pp. 1–17, 2012.
10. M. Cestari, D. Sanz-Merodio, J. C. Arevalo, and E. Garcia, "An adjustable compliant joint for lower-limb exoskeletons," in *IEEE/ASME Trans. Mechatronics*, vol. 20, no. 2, pp. 889–898, 2015.
11. M. Alam, I. A. Choudhury, and A. Bin Mamat, "Mechanism and Design Analysis of Articulated Ankle Foot Orthoses for Drop-Foot," *Sci. World J.*, vol. 2014, pp. 1–14, 2014.
12. S. Superiore, S. Anna, N. Vitiello, S. Superiore, and S. Anna, "Robotics and Autonomous Systems Review of assistive strategies in powered lower-limb orthoses and exoskeletons," *J. Rob. Aut. Syst.*, vol. 64, pp. 120–136, 2015.
13. K. Z. Takahashi, M. D. Lewek, and G. S. Sawicki, "A neuromechanics-based powered ankle exoskeleton to assist walking post-stroke: a feasibility study," *J. Neuroeng. Rehabil.*, vol. 12, no. 1, pp. 12–23, 2015.
14. Y. Bai, X. Gao, J. Zhao, F. Jin, F. Dai, and Y. Lv, "A Portable Ankle-Foot Rehabilitation Orthosis Powered by Electric Motor," *Open Mech. Eng. J.*, vol. 9, no. 1, pp. 982–991, 2015.
15. L. M. Mooney, E. J. Rouse, and H. M. Herr, "Autonomous exoskeleton reduces metabolic cost of human walking," *J. Neuroeng. Rehabil.*, vol. 11, no. 1, pp. 1–5, 2014.
16. K. A. Witte, J. Zhang, R. W. Jackson, and S. H. Collins, "Design of two lightweight, high-bandwidth torque-controlled ankle exoskeletons," in *IEEE Int. Conf. Robot. Autom.*, pp. 1223–1228, 2015.
17. A. T. Asbeck, S. M. M. De Rossi, K. G. Holt, and C. J. Walsh, "A biologically inspired soft exosuit for walking assistance," *Int. J. Rob. Res.*, vol. 34, no. 6, pp. 744–762, 2015.
18. H. Yu *et al.*, "Mechanical design of a portable knee-ankle-foot robot," in *IEEE Int. Conf. Robot. Autom.*, pp. 2183–2188, 2013.
19. W. Van Dijk, C. Meijneke, and H. Van Der Kooij, "Evaluation of the achilles ankle exoskeleton," *IEEE Trans. Neural Syst. Rehabil. Eng.*, vol. 25, no. 2, pp. 151–160, 2017.
20. A. Polinkovsky, R. J. Bachmann, N. I. Kern, and R. D. Quinn, "An Ankle Foot Orthosis with Insertion Point Eccentricity Control," in *IEEE/RSJ Int. Conf. Int. Robot. and Syst.*, 2011, pp. 1603–1608.
21. K. A. Shorter, G. F. Kogler, E. Loth, W. K. Duffee, and E. T. Hsiao-Wecksler, "A portable powered ankle-foot orthosis for rehabilitation," *J. Rehabil. Res. Dev.*, vol. 48, no. 4, 2011, pp. 4594–472.
22. Y. L. Park *et al.*, "Bio-inspired active soft orthotic device for ankle foot pathologies," in *IEEE Int. Conf. Intell. Robot. Syst.*, pp. 4488–4495, 2011.
23. A. B. Zoss, H. Kazerooni, and A. Chu, "Biomechanical design of the Berkeley lower extremity exoskeleton (BLEEX)," *IEEE/ASME Trans. Mechatronics*, vol. 11, no. 2, pp. 128–138, 2006.
24. K. I. J. Furusho *et al.*, "Development of Shear Type Compact MR Brake for the Intelligent Ankle-Foot Orthosis and Its Control," in *IEEE Int. Conf. Rehab. Robot. (ICORR)*, 2007, pp. 89–94.
25. L. Deberg and M. T. Andani, "An SMA Passive Ankle Foot Orthosis: Design, Modeling, and Experimental Evaluation," *Smart Mater. Res.*, vol. 2014, 2014.
26. P. C. Kao, C. L. Lewis, and D. P. Ferris, "Invariant ankle moment patterns when walking with and without a robotic ankle exoskeleton," *J. Biomech.*, vol. 43, no. 2, pp. 203–209, 2010.
27. H. S. Lo and S. Q. Xie, "Medical Engineering & Physics Exoskeleton robots for upper-limb rehabilitation : State of the art and future prospects," *Med. Eng. Phys.*, vol. 34, no. 3, pp. 261–268, 2012.
28. S. M. T. Reza, N. Ahmad, I. A. Choudhury, and R. A. R. Ghazilla, "A fuzzy controller for lower limb exoskeletons during sit-to-stand and stand-to-sit movement using wearable sensors," *Sensors (Basel)*, vol. 14, no. 3, pp. 4342–4363, 2014.
29. J. V. McCall, S. A. Philius, R. W. Nuckols, and G. S. Sawicki, *Performance of a powered ankle exoskeleton using neuromuscular model-based control over a range of walking speeds* [Online]. Available: http://hpl.bme.unc.edu/McCall_ASB_2017.pdf.
30. L. Peternel, T. Noda, T. Petri, A. Ude, J. Morimoto, and J. Babić, "Adaptive control of exoskeleton robots for periodic assistive behaviours based on EMG feedback minimisation," *PLoS One*, vol. 11, no. 2, 2016.
31. J. A. Blaya and H. Herr, "Adaptive Control of a Variable-Impedance Ankle-Foot Orthosis to Assist Drop-Foot Gait," *IEEE trans. Neur. sys. Rehab. Eng.*, vol. 12, no. 1, pp. 24–31, 2004.

Management of digital records inspired by Complex Systems with RADAR

Anne Jeannin-Girardon, Alexandre Bruyant

ICube laboratory, University of Strasbourg, UMR CNRS 7357, Strasbourg, France

Nicolas Toussaint, Ismaila Diouf

Complex System Digital Campus UNESCO Unitwin

Pierre Collet

ICube laboratory, University of Strasbourg, UMR CNRS 7357, Strasbourg, France

Pierre Parrend

ICube laboratory, University of Strasbourg, UMR CNRS 7357, Strasbourg, France, ECAM Strasbourg-Europe, Schiltigheim France

Abstract

Storing sensitive data in a centralized way can lead to significant loss, should the central node or networks links be defective as is the case in numerous countries, especially developing countries. Consequently, we propose a platform called RADAR (Robust Anonymous DATA Records) that automatically fragments, replicates and distributes data all over the network for anonymized, robust, encrypted storage and backup. RADAR gets nodes of a network cooperate for storage and backups of sensitive data, even in case of non-reliable IT infrastructure.

Keywords: Epidemic replication, distributed storage, complex systems, anonymity

1. Introduction

In some of the most important countries around the world such as India, China but also in Africa, Internet access is still precarious and therefore not reliable. This means that it is difficult for such nations to setup and use digital platforms that would help them to bridge the gap with highly connected countries which, on their side, are plagued with the opposite problem: having a very reliable network infrastructure makes them want to develop deterministic and perfect data management systems that can simply not be implemented in practice. The RADAR system presented in this paper proposes a more pragmatic approach, that can overcome the problems inherent to an unreliable network while at the same time, providing a reliable enough Quality Of Service that may satisfy the demands of high-tech countries.

2. Related work

Distributed databases all use data replication to improve robustness.

Most approaches focus on improving access time, bandwidth consumption while guaranteeing that absolutely no piece of data can be lost. This is very costly and very difficult to achieve. Paper [1] proposes a hierarchical approach to ensure replicas are consistent over the network. The cluster of databases used to implement this approach stores newest data at the topmost level, while the lowest levels propagate replicas from one level to the next in an epidemic way. This allows them to define a range of Quality of Service that is related to the consistency level that is required by the client application. Epidemic replication protocol is widely used to replicate data consistently in distributed databases. This approach is evaluated in [2]: in practice, it is very difficult to propose an analytic methodology to evaluate the variables associated with epidemic replication (such as bandwidth consumption, replicas consistency, ...) so the authors propose a simulator allowing one to optimize the parameters of their replication algorithms that scale with their network configuration. Across large scale networks, such as data grids, hybrid approaches are used, such as in [3]. In

order to ensure efficient access to the distributed data of the grid, a scalable replica management system (using both hierarchical and flat topologies) and a dynamic data distribution algorithm are used jointly. The hierarchical topology contains nodes propagating replicas to direct ancestors/children while the flat topology propagates replicas using a Peer-to-Peer protocol. Such protocols are also widely used in distributed databases systems. Data in Peer-to-Peer systems are often assumed to be static and not subject to many updates. But, for many applications, data are frequently added, deleted or updated. In paper [4], the authors propose an epidemic replication method dedicated to Peer-to-Peer systems. One main characteristic of Peer-to-Peer systems is that no assumptions can be made on whether the machines of the network are online or not. Using rumor spreading algorithms [5] and push/pull methods so that peers can request updates or send updates to peers that sent a request update, the authors ensure some level of consistency for the data and achieve low latencies.

In this paper, we propose the RADAR model : it relies on Complex Systems principles and does not need to define complicated hierarchical architectures or algorithms in order to ensure data consistency. We do not make assumptions about the level of reliability of the network on which RADAR is deployed, allowing unreliable infrastructures to use RADAR for distributed data storage. Moreover, our model ensures security and can thus be used for sensitive data storage such as medical records.

3. Proposed RADAR model

Complex Systems

A *Complex System* can be defined as a set of autonomous entities in interaction exhibiting multi-level emergent behaviour where - as Aristotle said some 2300 years ago - the whole is more than the sum of the parts. The typical example is turbulence. The local behaviour of particles results at a higher scale in the apparition of swirls and vortices that can be described using Navier-Stokes equations. However these equations do not appear at all at the particle level.

RADAR implements storage entities that have no global picture of the network, but that as a whole, behave like a reliable and secure data storage system: machines rely on each other to automatically backup their data.

Modus operandi

The whole RADAR system is composed of many (ideally more than 50) loosely interconnected machines. Because the network is deemed unreliable, machines never “expect” anything from other machines unless they need to recover from a complete data loss. Therefore, under normal operation mode, machines:

- backup their own data by sending it to n other machines they know about (using a non-connected protocol such as UDP),
- accept data from other machines for backup.

Whenever a machine needs to store a new local piece of data, it is timestamped, encrypted using the local cryptographic key of the machine, replicated and depending on the required level of reliability, sent to n other machines randomly chosen in the network (the more required reliability, the greater n) for backup.

If the piece of data is of a sensitive nature (such as medical records) it is furthermore fragmented into several pieces before each piece is sent to n other machines. For instance, medical records are fragmented into:

1. patient personal data (name, address, telephone number, e-mail address, ...),
2. medical textual data (sex, date of birth, weight, blood pressure, a.s.o. along with symptoms, diagnostics, medication, ...),
3. digital data (medical imaging, audiogram, electrocardiogram, ...),
4. private data not related to medical condition (death of brother, ...) for a personal follow-up of the patient.

For each patient, each fragment is encrypted and sent separately to n machines chosen at random among the known machines. This means that if data is stolen on a given machine, patient data is not compromised because for a particular patient, each machine will keep only one of the 4 (encrypted) fragments. For instance, if medical data are stolen, the attacker has no information about the personal data of the patient such as his/her name.

Security

- If a hacker gets hold of the cryptographic key of one machine and gets access to this machine, only the local data is compromised. All other data stored as a backup for other machines remains protected because it is

encrypted with the cryptographic keys of the other machines.

- If a hacker gets hold of all the cryptographic keys of all the machines in the network, and physically gets access to one machine, the data of the machine is compromised (as above) and the hacker will be able to read all the fragments stored by the machine as a backup for other machines. However, because data is fragmented, the hacker will either get the personal data of a patient, but not his medical data or digital data or private data because when data are backed up on the network of machines, they are fragmented and all the fragments are sent to different machines of the network chosen at random.

To sum up, with RADAR, the only way to have access to a particular patient's record that is not locally stored on one machine is to have full access (with passwords) to enough machines in the network to hope to gain access to all the fragments belonging to a particular patient, which in practice is not feasible if the network is made of hundreds of machines situated in different places (hospitals, medical centers spread across the country).

Hybrid encryption

RADAR uses the RSA [6] asymmetric encryption algorithm with 2048 bits keys: it is an asymmetric algorithm that uses a public key to encrypt the data, and a private key for decryption. Unfortunately, this algorithm is computationally intensive and cannot natively encrypt data that are longer than its key (2KB in our case). In order to circumvent these limitations, we use RSA in conjunction with AES [7], a much faster but symmetric algorithm (the same key must be used for encryption and decryption).

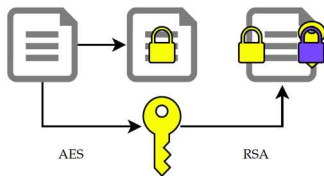


Fig. 1. Hybrid encryption used by RADAR

The data are encrypted thanks to AES using a randomly generated key, that is itself encrypted with RSA (cf. Fig. 1).

This makes it possible to verify the origin and the integrity of the data. A hash code is generated using the data to be signed. The code is encrypted thanks to the private key of the sender. The receiver can verify the authenticity of the signature by deciphering the hash code and by comparing it with a new code generated on the data.

Each node receives an RFC 5280 signed certificate delivered by the administrator of the network, that guarantees that the node is indeed part of the network.

Data loss and recovery

RADAR comes in when a local database is completely lost and not recoverable. What happens next is that the person in charge with the database that has disappeared contacts the administrator of the network, asking for a database rebuild. When the new machine is ready, it is added to the network again, but in recovery mode. The rebuild starts with one machine of the network passing over the message to the other machines it knows (epidemic message transmission) that all files that have been received in the past from the failed machine must be sent back to it. The machine in recovery mode then starts to receive from the whole network all the data it previously sent. It uses the timestamps of the data to reconstruct its database in a consistent way. During the recovery, the machine keeps an account on the number of replicas it has received for all its data. After recovery, the machine sends again the missing number of replicas of a given data to random machines, so that it sums back to n .

Data loss probability

It is very difficult to estimate the probability that when a machine has lost all its data, all n copies of a given patient record are also lost at the same time. Computing this probability is so complex that most similar data replication systems use network simulation tools such as Chive [2] and Network Simulator (NS) [8] to run empirical tests to evaluate the robustness of their approach. Using the same methods shows that for most realistic RADAR configuration and failure probabilities, it is very difficult to effectively lose data.

Expected disk consumption

Depending on n , the number of replications that is chosen, for the reliability of a particular network, expected disk consumption is in average $n+1$ times the

disk consumption of a single machine. Indeed, if one machine sends n copies of its data to other machines in the network, this means that it will receive data from (in average) n other machines in the network. Scaled to the medical information system of Senegal, (for which RADAR was initially designed) the system could use around 1000 medical centers (with at least one machine per center) to deal with a population of 15M inhabitants. With a uniform distribution of patients per center (which is of course not the case), each machine would store the medical records of 15k local patients. With $n=3$, this means that each machine would need to store the equivalent of 45k medical records, which is a reasonable amount by 2018 disk storage space. This is to be compared with the cost needed to create, maintain and operate a data center capable of dealing with all 15 million medical records of the country in a reliable and secure way over an unreliable internet network.

4. Conclusion

Where most other systems focus on perfect consistency and reliability resulting in over-complex time consuming algorithms which, eventually, are not 100% bullet-proof, RADAR accepts that data may be lost, but focusses on reducing such occurrence to very low probability. It offers a system that is simple, while robust enough to work over an unreliable network. RADAR is currently tested on a huge patient cohort of more than 300 000 patients over 60 nodes in India. Following work will concentrate on reliability thanks to large scale testing using network simulation tools.

Acknowledgements

The authors thank the N'Light foundation that funds this project, as well as the JIVA Ayurveda Indian company, on which RADAR is currently tested.

References

1. I. Arrieta-Salinas, J. E. Armendáriz-Iñigo and J. Navarro, "Classic Replication Techniques on the Cloud," *2012 Seventh International Conference on Availability, Reliability and Security*, Prague, 2012, pp. 268-273.
2. A. Jiménez-Yáñez, J. Navarro, F. D. Muñoz-Escóí, I. Arrieta-Salinas and J. E. Armendáriz-Iñigo, "Chive: A simulation tool for epidemic data replication protocols benchmarking," *2014 9th International Conference on Software Engineering and Applications (ICSOFT-EA)*, Vienna, Austria, 2014, pp. 428-436.
3. H. Lamahemedi, B. Szymanski, Z. Shentu and E. Deelman, "Data replication strategies in grid environments," *Fifth International Conference on Algorithms and Architectures for Parallel Processing, 2002. Proceedings.*, Beijing, China, 2002, pp. 378-383.
4. A. Datta, M. Hauswirth and K. Aberer, "Updates in highly unreliable, replicated peer-to-peer systems," *23rd International Conference on Distributed Computing Systems, 2003. Proceedings.*, 2003, pp. 76-85.
5. Laijun Zhao, Hongxin Cui, Xiaoyan Qiu, Xiaoli Wang, Jiajia Wang, SIR rumor spreading model in the new media age, In *Physica A: Statistical Mechanics and its Applications*, Volume 392, Issue 4, 2013, Pages 995-1003
6. Xin Zhou and Xiaofei Tang, "Research and implementation of RSA algorithm for encryption and decryption," *Proceedings of 2011 6th International Forum on Strategic Technology*, Harbin, Heilongjiang, 2011, pp. 1118-1121.
7. D. M. Alghazzawi, S. H. Hasan and M. S. Trigui, "Advanced Encryption Standard - Cryptanalysis research," *2014 International Conference on Computing for Sustainable Global Development (INDIACom)*, New Delhi, 2014, pp. 660-667.
8. C. Leng, M. Lehn, R. Rehner, and A. Buchmann, "Designing a testbed for large-scale distributed systems," in *Proceedings of the ACM SIGCOMM 2011 conference on SIGCOMM*, New York, NY, USA, 2011, pp. 400-401.

Integrated Optimization of Differential Evolution with Grasshopper Optimization Algorithm

Duangjai Jitkongchuen

*College of Innovative Technology and Engineering
Dhurakij Pundit University, Thailand*

Udomlux Ampant

*College of Innovative Technology and Engineering
Dhurakij Pundit University, Thailand
E-mail: duangjai.jit@dpu.ac.th, udomlux.amp@dpu.ac.th
<http://cite.dpu.ac.th>*

Abstract

This paper proposes a scheme to improve the differential evolution algorithm (DE) performance with integrated the grasshopper optimization algorithm (GOA). The grasshopper optimization algorithm mimics the behavior of grasshopper. The characteristic of grasshoppers is slow movement in the larval stage but sudden movement in the adulthood which seem as exploration and exploitation. The grasshopper optimization algorithm concept is added to DE to guide the search process for potential solutions. The efficiency of the DE/GOA is validated by testing on unimodal and multimodal benchmarks optimization problems. The results prove that the DE/GOA algorithm is competitive compared to the other meta-heuristic algorithms.

Keywords: Meta-heuristic, Differential Evolution Algorithm, Grasshopper Optimization Algorithm, Optimization

1. Introduction

Meta-heuristic algorithm techniques constitute range from simple local search procedures to complex learning processes. The basic concepts of meta-heuristics permit an abstract level description. Nature-inspired meta-heuristic can be grouped in four main classes: evolution-based, physics-based and swarm-based.

Evolution-based algorithms are inspired by the concepts of nature evolution. The population in search process are randomly generated which are developed over subsequent generation. The next generation is created by combination of the individuals in the previous generation. These provide the population to be optimized over the course of generations. The most popular evolution-based algorithm is Genetic Algorithms (GA) [1]. Other popular

algorithms are Differential Evolution Algorithms (DE) [2], and Biogeography-Based Optimizer (BBO) [3].

The second class of meta-heuristic is physics-based algorithms that imitate the physical rules. The most popular algorithms are Gravitational Search Algorithm (GSA) [4], Galaxy-based Search Algorithm (GbSA) [5], and Curved Space Optimization (CSO) [6].

The third class of meta-heuristic is swarm-based algorithms that imitate the social behavior of swarms, herds, flocks, or schools of animals. The most popular algorithms are Particle Swarm Optimization (PSO) [7]. Other popular swarm-based algorithms are Bat Algorithms (BA) [8], and Firefly Algorithm (FA) [9].

The new meta-heuristic has been focused on this paper is differential evolution algorithm (DE) and to improve performance of it, grasshopper optimization algorithm is added to DE to improve performance in crossover operation.

The rest of the paper is structured as follows. Section 2 describes some backgrounds of the differential evolution algorithm. In Section 3, the proposed algorithm is presented. Section 4 shows the experimental results and the conclusions will be discussed in Section 5.

2. The Differential Evolution Algorithm

The differential evolution algorithm (DE) optimizes a problem by sustaining a population of candidate solutions and creating new candidate solutions by combining existing ones according to its simple procedure, and then keeping whichever candidate solution has the best score or fitness on the optimization problem at hand.

The procedure of differential evolution algorithm starts to initialize target vectors $X_i^G = (x_{1,i}, x_{2,i}, \dots, x_{j,i}, \dots, x_{N,i})$ where $i = 1, 2, \dots, NP$. NP is the population size. N is the dimension of the population. The superscript G identifies the Gth generation.

The target vectors are used to generate the mutant vectors $V_i^G = (v_{1,i}, v_{2,i}, \dots, v_{j,i}, \dots, v_{N,i})$ in next steps. The DE/current-to-best/1 mutation scheme is showed in Eq. (1).

$$V_i^G = X_i^G + F(X_{best}^G - X_i^G) + F(X_{r_1}^G - X_{r_2}^G) \quad (1)$$

where r_1 and r_2 are integer number chosen from the set $\{1, 2, \dots, NP\}$ and must be different from index i . X_{best}^G is the best solution in the generation G. F is used to control amplification of the differential evolution. The value of F is set in the range $[0, 2]$. The target vectors and mutant vectors are used to generate the trial vectors $U_i^G = (u_{1,i}, u_{2,i}, \dots, u_{j,i}, \dots, u_{N,i})$ in crossover operation to increase the diversity of population.

$$u_{j,i} = \begin{cases} v_{j,i} & ,if (rand \leq CR) or (j = j_{rand}) \\ x_{j,i} & ,otherwise \end{cases} \quad (2)$$

where $j = 1, 2, \dots, N$. rand is a uniform random number chosen in the range $[0,1]$. $CR \in [0, 1]$ is the crossover parameter. j_{rand} is an index randomly chosen in the range $[0, N]$.

The last step is the selection operation to chosen a better vector for next generation. The new generations are selected by comparing the fitness value between the target vector and the trial vector.

$$X_i^{G+1} = \begin{cases} U_i^G & ,if (f(U_i^G) < f(X_i^G)) \\ X_i^G & ,otherwise \end{cases} \quad (3)$$

The whole process is repeated until the termination criteria are satisfied or a predefined number of iterations are reached.

3. The Proposed Algorithm

The schema of DE/current-to-best/1 in mutation operation is updated by splitting F mutation parameter to λ and F. The new mutation schema is showed in Eq. (4).

$$V_i^G = X_i^G + \lambda(X_{best}^G - X_i^G) + F(X_{r_1}^G - X_{r_2}^G) \quad (4)$$

where λ is used to balance the difference vectors between the best vectors and the target vectors. The value of λ is decreased in each generation.

$$\lambda^{G+1} = \lambda^G - (\lambda^G \times c_1) \quad (5)$$

While the mutation parameter F is used to perform the amplification of the difference between two random population members. When the procedure is trapped in the local optimum, the value of F is increased.

$$F^{G+1} = F^G + (F^G \times c_2) \quad (6)$$

The parameters c_1 and c_2 are uniform random numbers. $c_1 \in [0, 0.1]$ is a random value and $c_2 \in [0, 1]$ is a random value. And the crossover parameter (CR) is regenerated at the end of each generation to find an optimized parameter. The new crossover parameter is generated by Eq. (7).

$$CR^{G+1} = CR^G + (mean_A(S_{CR}) \times c_3) \quad (7)$$

where $mean_a$ is the usual arithmetic mean. S_{CR} is the set of crossover parameter values. $C_3 \in [0, 1]$ is a uniform random number.

And the crossover operation is rearranged that starts with the vectors that created from the target vectors and the mutant vector is called new name is the prime vectors (U_i'). The prime vectors is used to generate the trial vectors by comparing the fitness value between the prime vectors and the mutant vectors, otherwise the trial vectors is generated by grasshopper optimization algorithm.

The grasshopper optimization algorithm was proposed in [10] mimics the behavior of grasshopper. The characteristic of the swarm in the larval stage is slow movement and small steps but is long range and suddenly movement in adulthood. These two characters seem as exploration and exploitation. The search agents are encouraged to move suddenly in exploration and conduce to move locally during exploitation. These two functions as well as target seeking are performed by grasshopper naturally.

The proposed algorithm takes the feature of movement of the grasshopper to generate a new value for the trial vectors is showed in Eq. (8).

$$U_i^d = c \left(\sum_{\substack{j=1 \\ j \neq i}}^{NP} c \frac{ub_d - lb_d}{2} s(|x_j^d - x_i^d|) \frac{x_j - x_i}{d_{i,j}} \right) + \hat{T}_d \quad (8)$$

where ub_d and lb_d is the upper bound and the lower bound in the D^{th} dimension. $s(r) = fe^{-r/l} - e^{-r}$. $d_{i,j}$ is the distance between the i^{th} and the j^{th} grasshopper. \hat{T}_d is the value of the D^{th} dimension in the target. The parameter c is decreased equivalent to the number of iteration to balancing exploration and exploitation is calculated as Eq. (9).

$$c = c_{max} - l \frac{c_{max} - c_{min}}{L} \quad (9)$$

where c_{max} and c_{min} is the maximum value and the minimum value, respectively. l is the current iteration and L is the maximum number of iterations.

4. The Experimental Results

The proposed algorithm has been evaluated performance with thirteen benchmark functions [11]. The test functions are unimodal ($f_1 - f_7$) and multimodal ($f_8 - f_{13}$). The details of benchmark functions are shown in Table 1. The proposed algorithm was run 30 times on each benchmark functions. The mutation parameters set λ , $F = 0.5$, the crossover parameter set $CR = 0.9$ and population size set $NP = 100$. Table 2 reported the statistical. The performance of the proposed algorithm is compared with two EAs: DE and Fast Evolutionary Programming (FEP) and compared with swarm-based algorithm: PSO. The results of DE, FEP and PSO were taken from the results reported in [12].

According to the results of Table 2, DE/GOA is able to provide very competitive results. This algorithm outperforms all others in f_1, f_2, f_3 and f_7 . Both DE/GOA and DE were successful to find the optimal solution in f_4 and f_6 . In the function f_5 , only DE could solve the optimum. Therefore, these results show the performance of DE/GOA in terms of exploiting the optimum.

The multimodal functions have many local optima with the number increasing exponentially with dimension. This makes them suitable for benchmarking the exploration ability of an algorithm. The experimental showed that DE/GOA is able to provide very competitive results on the multimodal benchmark functions as well.

5. Conclusions

This work proposed to improve the differential evolution algorithm (DE) performance with integrated the grasshopper optimization algorithm (GOA). Thirteen benchmark functions were employed the performance in terms of exploitation and exploration. The results showed that DE/GOA was able to provide competitive results compared to well known heuristics such as DE, FEP and PSO.

Table 1. The Benchmark Functions

Functions	Range
$f_1(x) = \sum_{i=1}^N x_i^2$	[-100, 100]
$f_2(x) = \sum_{i=1}^N x_i + \prod_{i=1}^N x_i $	[-100, 100]
$f_3(x) = \sum_{i=1}^N (\sum_{j=1}^i x_j)^2$	[-10, 10]
$f_4(x) = \max_i \{ x_i , 1 \leq i \leq N\}$	[-100, 100]
$f_5(x) = \sum_{i=1}^{N-1} [100(x_{i+1} - x_i^2)^2 + (x_i - 1)^2]$	[-100, 100]
$f_6(x) = \sum_{i=1}^N (x_i + 0.5)^2$	[-30, 30]
$f_7(x) = \sum_{i=1}^N ix_i^4 + \text{random}[0, 1)$	[-100, 100]
$f_8(x) = \sum_{i=1}^N -x_i \sin(\sqrt{ x_i })$	[-1.28, 1.28]
$f_9(x) = \sum_{i=1}^N [x_i^2 - 10 \cos(2\pi x_i) + 10]$	[-500, 500]
$f_{10}(x) = -20 \exp\left(-0.2 \sqrt{\frac{1}{N} \sum_{i=1}^N x_i^2}\right) - \exp\left(\frac{1}{N} \sum_{i=1}^N \cos 2\pi x_i\right) + 20 + e$	[-5.12, 5.12]
$f_{11}(x) = \frac{1}{4000} \sum_{i=1}^N x_i^2 - \prod_{i=1}^N \cos\left(\frac{x_i}{\sqrt{i}}\right) + 1$	[-32, 32]
$f_{12}(x) = \frac{\pi}{n} \left\{ 10 \sin(\pi y_1) + \sum_{i=1}^{n-1} (y_i - 1)^2 [1 + 10 \sin^2(\pi y_{i+1})] + (y_n - 1)^2 \right\} + \sum_{i=1}^n u(x_i, 10, 100, 4)$	[-600, 600]
$u(x_i, a, k, m) = \begin{cases} k(x_i - a)^m, & x_i > a \\ 0, & -a < x_i < a \\ k(-x_i - a)^m, & x_i < -a \end{cases} \quad y_i = 1 + \frac{x_i + 1}{4}$	[-50, 50]
$f_{13}(x) = 0.1 \left\{ \sin^2(3\pi x_1) + \sum_{i=1}^n (x_i - 1)^2 [1 + \sin^2(3\pi x_i + 1)] + (x_n - 1)^2 [1 + \sin^2(2\pi x_n)] \right\} + \sum_{i=1}^n u(x_i, 5, 100, 4)$	[-50, 50]

Table 2. The Experimental Results

Functions	DE/GOA	DE	FEP	PSO
f_1	2.35E-220	8.20E-14	5.70E-04	1.36E-04
f_2	4.28E-11	1.50E-09	8.10E-03	4.21E-02
f_3	3.50E-226	6.80E-11	1.60E-02	70.12562
f_4	0.00E+00	0	3.00E-01	1.086481
f_5	28.98017	0	5.06	96.71832
f_6	0	0	0	1.02E-04
f_7	2.11E-05	4.63E-03	1.42E-01	1.23E-01
f_8	-8831.53	-11080.1	-12554.5	-4841.29
f_9	6.76E-10	69.20	4.60E-02	46.70423
f_{10}	4.44E-16	9.70E-08	1.80E-02	2.76E-02
f_{11}	0	0	1.60E-02	9.22E-03
f_{12}	2.87E-09	7.90E-15	9.20E-06	6.92E-03
f_{13}	3.01E-08	5.10E-14	1.60E-04	6.68E-03

References

- JH. Holland, Genetic algorithms, *Scientific American* (1992), pp. 66–72.
- R. Storn and K. Price, Differential evolution – a simple and efficient heuristic for global optimization over continuous spaces, *Journal of Global Optimization* (1997), pp. 341–359.
- D. Simon, Biogeography-based optimization, *IEEE Transactions on Evolutionary Computation* (2008), pp. 702–713.

- E. Rashedi, H. Nezamabadi-Pour and S. Saryazdi, GSA: a gravitational search algorithm, *Information Science* (2009), pp. 2232–2248.
- H. Shah-Hosseini, Principal components analysis by the galaxy-based search algorithm: a novel metaheuristic for continuous optimization, *Int. J. Computer Science and Engineering* (2011), pp. 132–140.
- FF. Moghaddam, RF. Moghaddam and M. Cheriet, Curved space optimization: a random search based on general relativity theory, (2012), arXiv:1208.2214.
- J. Kennedy and R. Eberhart, Particle swarm optimization, in *Proc. IEEE Int. Conf. Neural Networks* (1995), pp. 1942–1948.
- XS. Yang, A new metaheuristic bat-inspired algorithm, *Springer Berlin* (2010), pp. 65–74.
- I. Fister, I. Fister Jr., XS. Yang and J. Brest, A comprehensive review of firefly algorithms, *Information Science* (2013), pp. 34–46.
- S. Saremi, S. Mirjalili and A. Lewis, Grasshopper optimization algorithm: theory and application, *Advances in Engineering Software* (2017), pp. 30–47.
- X. Yao, Y. Liu and L. Gao, Evolutionary programming made faster, *IEEE Transactions on Evolutionary Computation* (1999), pp. 82–102.
- S. Saremi, SM. Mirjalili and A. Lewis, Grey wolf optimizer, *Advances in Engineering Software* (2014), pp. 46–61.

Efficient collective search by agents that remember failures

Masao Kubo, Nhuhai Phung, Hiroshi Sato

Department of Computer Science, National Defense Academy of Japan,
1-10-20 Hashirimizu, Yokosuka, Kanagawa, 239-8686, Japan
E-mail: {masaok, ed17006, hsato}@nda.ac.jp

Abstract

The BRT agent is an algorithm that can find appropriate collective behaviors by changing the agreement contents in a trial and error manner. Computer experiments show that it is necessary to change the agreement contents the number of times that is proportional to the square of the number of choices on average. In this paper, we attempted to shorten this search time by introducing an agent that memorizes behaviors that were not able to achieve the expected effect of what we executed. As a result, we found that search time can be improved by just mixing a few this taboo list agents.

Keywords: swarm intelligence, machine learning, complex systems

1. Introduction

Roughly speaking, if a set of required roles (for example, collecting foods and resting) and the relationship between these elements are embedded in individual behavior beforehand, for example they can keep energy of them constant.

On the other hand, it is anticipated that it will not be able to lead to some reasonable macro states of the swarm by the above division of labor methods such as when a new environment is encountered. They need methods how to emerge the swarm in a better macro state against such a situation.

To solve this issue we have to discuss individual's learning but also learning capability as swarm and no general models as to whether to discover, memorize, and learn new micro interactions leading have not been proposed. It has become a bottleneck in the construction of a more advanced self-organizing swarm system⁴.

To this problem, a voting model (BRT model, Bias and Rising Threshold model) has been proposed that emerges a trial and error process at the macro level by momentary change of agreement of an agent group⁶. Every agent chooses one action from among the actions

and notifies all of them. The agent changes its action in view of the number of supporters of each action. They keep voting until actions of the all members are same. This is a model that expands the 2-option consensus building model against the agreement of Namatame³ and others so that it can be used even in the case of multiple options and incorporates the passage of time. By appropriately designing the bias value θ which expresses the degree of preference of the behavior selected by itself, this algorithm has the feature of reaching consensus in almost constant time regardless of the number of agents in the group. A series of computer experiments shows that it is possible to find suitable consensus actions in a time proportional to approximately M^2 for the number of actions M . This is inefficient in cases other than dynamic environments where the environment and tasks frequently change.

Here, we introduce a derivation agent of BRT that memorizes a set of behavior that were once executed but not appropriate, and removes them from their own action selection. In the following, this function is called UEM (unsuitable experience memory), and an agent having this function is called an UEM agent. The memory used here is a short term, and it forgets

© The 2018 International Conference on Artificial Life and Robotics (ICAROB2018), Feb. 1-4, B-Con Plaza, Beppu, Oita, Japan

probabilistically. As will be described later, if all agents have UEM they can expect to discover a good macroscopic behavior in proportion to M .

This paper is organized as follows. First, we will explain the BRT and its characteristics. Next we propose an UEM agent and estimate its characteristics. Finally, we verify the characteristics of the proposed method by computer experiment. As a result, we found that it is possible to reduce the time required for solution search even if all agents do not have UEM function.

2. Related works

2.1. BRT model

Now, we assumed that there are n agents P_1, \dots, P_n . $A = \{a_1, \dots, a_j, \dots, a_M\}$ is the set of agent's behavior candidates with $M \geq 2$. $A_j(t) \in A$ is the behavior of agent P_i at time t . The agent P_i has a bias θ_i ($0 < \theta_i < 1$). $n(a_j)$ is number of agents selecting behavior a_j .

As a result of everyone performing the same action, a macro state of the group occurs, and if this is suitable for the environment and tasks, this agreement behavior is assumed to be "suitable". a_{goal} is set of desirable behavior candidates ($a_{goal} \subset A$). In advance, the agent does not know a_{goal} , only when all have agreed, it is understood that a_{goal} includes that agreed behavior.

At this time, the agent P_i decides the behavior $A_j(t+1)$ at the time t as follows. If

$$n(A_j(t))/N \geq \theta_i + \tau \cdot (t - t_{i,last}) \tag{1}$$

is satisfied, $A_j(t+1) = A_j(t)$. Otherwise, behavior other than $A_j(t)$ is stochastically chosen and becomes $A_j(t+1) \in A \setminus A_j$. Here, τ is a constant representing the increment of proponents number. $t_{i,last}$ is the clock time at which the agent P_i last changed its behavior, and $(t - t_{i,last})$ is the time, which the same action continues to be selected.

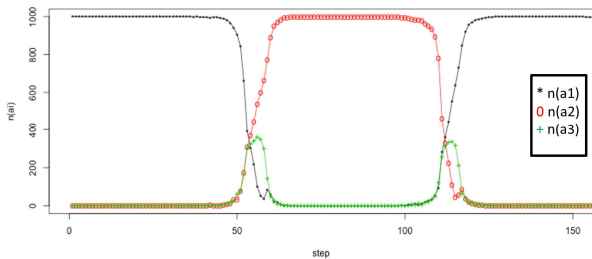


Fig.1 Transition example (Starting from agreed state)

2.2. Behavior example of BRT model and its search time characteristics

Here we illustrate the behavior of the BRT model. We will introduce its characteristics.

The fig.1 is rendition of what was described in our past work⁵. This figure shows the transition process from an agreed state. In the initial state, all of agents have agreed to a_0 , but everyone agreed to another action (a_1) in about 65 steps. Again, 1000 agents agreed to a_0 action again in 125 steps. From the above it can be seen that agreed behavior can be switched from either state.

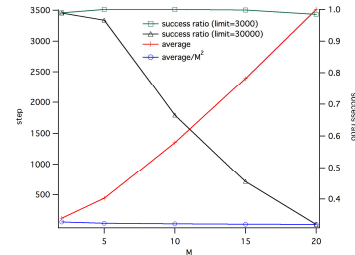


Fig.2 Characteristics of search time cost by BRT

Here, we show that it is possible to agree with the desired behavior by computer experiment. The experimental results are shown in Fig.2. The + mark is the average time required for discovery, and the o mark is the value obtained by dividing it by M^2 . Since the o mark is almost parallel to the x axis, it is mentioned that the average of the time required to discover the solution is proportional to M^2 .

3. The proposed Agent(UEM agent)

The BRT agent remembers the last action that was agreed but did not suit, and select other behaviors. Namely this short-term memory is limited to the most recent behavior. Then they repeatedly agree on behaviors that were not suitable a while ago. If the environment has not changed since the last execution, this is not an efficient search. Therefore, we will introduce an agent that memorizes behavior that agreed but did not suit for a long time, and tried to make solution searching more efficient.

The agent has a list $L_i(t)$ that remembers actions that were agreed but not suitable, and adds it to this list with the probability p_{in} at the time when it is determined that it is inappropriate while agreeing.

$$L_i(t+1) = \begin{cases} L_i(t) \cup A_i(t) & \text{probability } p_{in} \\ L_i(t) & \text{otherwise} \end{cases} \quad (2)$$

$$\text{where } A_i(t) = \{ \forall j, A_i(t) = A_j(t), A_j(t) \neq a_{goal} \} \quad (3)$$

When selecting a new action, select actions that are not included in $L_i(t)$ stochastically. Namely,

$$A_i(t+1) \subset A \setminus L_i(t) \quad (4)$$

The agent stores it with Eq.4 and select a candidate with Eq.2. This BRT agent will be referred to as an UEM (unstable experience memory) agent below.

Table 2. Probability to support one unselected action

# trial	BRT agent	UEM agent
1st	$\frac{1}{M}$	$\frac{1}{M}$
2nd	$\frac{1}{M-1}$	$\frac{1}{M-1}$
3rd	$\frac{1}{M-1}$	$\frac{1}{M-2}$
x-th	$\frac{1}{M-1}$	$\frac{1}{M-(x-1)}$

3.1. Approximate characteristics of the proposed method

Consider the ratio of UEM agents. The table 1 indicates the number of attempts to agree and the probability of selecting an arbitrary unselected action. When trying an agreement for the first time, the probability of selecting one action is $1/M$ with BRT, UEM agent. Both agents know that one action was inappropriate at the second time, so both are $1/(M-1)$. However, in the third and subsequent times, the behavior selection probabilities of both agents will differ. The BRT agent remains $1/(M-1)$, but the UEM agent does not select actions that are already selected as inappropriate, so candidates are reduced and $x (\leq M)$. The selection probability of x trial is $1/(M-(x-1))$. In order to shorten the search time it is necessary to reduce the number of times you agree with the action you tried already. This corresponds to the vote of UEM agent.

$$\frac{u}{M-(x-1)} \quad (5)$$

where $u (< n)$ is the number of UEM agents. This equation shows that if the population of UEM agents is large, it is less likely to choose actions that have already been tried. Also, as the denominator decreases as the

number of attempts to reach an agreement progresses, it indicates that less agreement on already selected actions will be reduced. Therefore, even if the population of the UEM agent is small, the effect of shortening the search time can be expected.

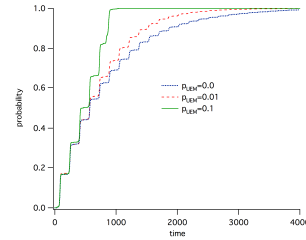


Fig.3 When changing the ratio of UEM agent

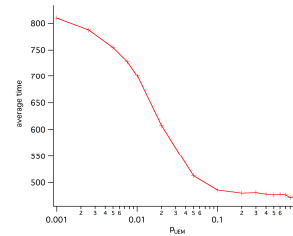


Fig.4 Relation between ratio of UEM agent and search time

4. The experimental result

This chapter shows the behavior of the UEM agent and confirms that it has the expected characteristics. The figure 3 represents the search time as a cumulative probability density distribution, and the horizontal axis is the time required. The vertical axis represents the probability of finding a solution by this time. The solid line represents the case of $p_{UEM} = 0.1$. The search time has been found by 99% trial by 1000 steps. As estimated by the formula 5, even a small number of UEM agents can greatly improve search time.

The relationship between the ratio of UEM agent and the average search time is shown in Figure 4. The horizontal axis shows the ratio of the UEM agent, and the vertical axis shows the average search time. $p_{UEM} = 0.0$ requires an average of 834 steps, and $p_{UEM} = 1.0$ took an average of 462 steps. With $p_{UEM} = 0.001$, it is 810 steps, and search time can be improved just by mixing minute UEM agents. As we increased the proportion of UEM agents, dramatic improvements were seen up to $p_{UEM} = 0.1$ (meaning that $p_{UEM} = 0.1$ required an average of 486 steps).

From these two experiments, we found that the proposed UEM agent can improve the search time of BRT agent.

5. Conclusion

In this paper, in order to improve the efficiency of the trial and error search behavior that the BRT agent group emerges, we proposed a derived type of BRT agent from the candidates by recording the failed experience called UEM agent. If all flocks are composed of UEM agents, we can expect that the search time increases linearly with M . However, even in the case of mixing with the BRT agent, we estimate that even a small number of UEM agents are effective, and verified the trend in computer experiments. As a result, it turned out to show the behavior as expected.

References

1. Eric Bonabeau, Guy Theraulaz and Jean-Louis Deneubourg, “Fixed Response Thresholds and the Regulation of Division of Labor in Insect Societies”, *Bulletin of Mathematical Biology*, Vol. 60, pp. 753–807, 1998.
2. E. Castello, T. Yamamoto, F.D. Libera, W. Liu, F. Alan, T. Winfeld, Y. Nakamura, H. Ishiguro, “Adaptive Foraging for Simulated and Real Robotic Swarms: The dynamical response threshold approach”, *Swarm Intelligence DOI*, Vol. 10, pp. 1–31, 2016.
3. Akira Namatame (In Japanese), “*Strategic Decision Making*”, Asakura Publisher, pp. 119–149, 2001.
4. Masao Kubo, Nhu Hai Phung, Hiroshi Sato, Akira Namatame, “Direction switch behavior to enclose a pack of targets based on phase transition”, *Swarm2015*, 2015.
5. Nhu Hai Phung, Masao Kubo, Hiroshi Sato, Saori Iwanaga, Akira Namatame, “Agreement algorithm with trial and error method at macro level”, *Swarm2017*, 2017.
6. Nhu Hai Phung (In Japanese), “A Study on Extension of Enclosing Algorithm for Multiple Mobile Agents”, Master’s thesis at National Defense Academy, 2017.
7. Wenguo Liu, Alan Winfield, Jin Sa, Jie Chen, and Li-hua Dou, “A Strategies for Energy Optimization in a Swarm of Foraging Robots”, *Swarm Robotics*, pp.14–26, 2006.

The Analysis of Band Structure of Photonic Crystals

Wang Chenxu

*The school of Electrical Engineering and Automation, Henan Polytechnic University,
Jiaozuo, 454000/Henan, China **

Fu Ziyi

*Jiaozuo, 454000/Henan, China
next219@outlook.com, Fuzy@hpu.edu.cn
www.hpu.edu.cn*

Abstract

In this paper, a finite element is developed to calculate the band structures of one dimensional photonic crystals. The Maxwell's equation governing the propagation of electromagnetic waves, which combine with Bloch theory, the FEM transform the complex band diagram problems into a simple eigenvalue by solving the eigenvalue with respective to wave vector K by frequency. And then using the COMSOL for simulation.

Keywords: band structure, finite element method, Maxwell equation, eigenvalue, COMSOL.

1. Introduction

Photonic crystals^[1] are a kind of artificial microstructure material formed by periodic arrangement of the medium. According to the periodic structural features in different directions of space, photonic crystals are divided into one-dimensional, two-dimensional and three-dimensional photonic crystals. When electromagnetic waves propagate in photonic crystal, due to the periodic arrangement of materials, Bragg diffraction^[2] occurs and the electromagnetic wave is modulated to form an energy band structure. This energy band structure is called a photonic band structure. If the ratio of the dielectric constants of the constituent materials is large enough, a bandgap may exist in the photonic band structure, which is called Photonic Band Gap^[3]. Ellipsoid, Brillouin, and Bloch state in solid state physics can all be used to describe photonic crystals.

As a starting point for the study of photonic crystal theory, band structure is the object of all calculations. It is one of the research focuses in the field of photonic crystals to study the band structure of photonic crystals.

There are many ways to calculate the energy band structure, commonly used are the plane wave expansion method, the finite difference time domain method, the transfer matrix method, etc., but these methods have their own drawbacks and limitations. For example, the use of plane wave expansion method can only be limited to simple geometry. Time-domain finite-difference methods may not be useful for some practical engineering problems in some cases. It is therefore important to develop a solver that is fast and accurate in calculating the band structure.

In this paper, starting from Maxwell's equation^[4], to derive the scalar equation of wave equation, and using the finite element method to get the eigenvalue matrix equation, finally, using the COMSOL^[6] for simulation, COMSOL specify the scalar function and translate the scalar equation into weak form.

2. Numerical derivation of band structure of photonic crystals

The propagation of an electromagnetic wave through a periodic medium (such as the photonic crystals) is described by Maxwell's equations.

$$\nabla \times H = J + \frac{\partial \epsilon E}{\partial t} \quad (1)$$

$$\nabla \times E = -\frac{\partial H}{\mu_0 \partial t} \quad (2)$$

$$\nabla \cdot \epsilon E = \rho \quad (3)$$

$$\nabla \cdot H = 0 \quad (4)$$

where E and H are the electric and magnetic fields, ϵ is relative permittivity, J and ρ are the free charge and current densities. With this type of medium in mind, we can set $\rho=0$ and $J=0$.

For mathematical convenience, this allows us to write a harmonic mode as a spatial pattern times a complex exponential:

$$H(r, t) = H(r)e^{-i\omega t} \quad (5)$$

$$E(r, t) = E(r)e^{-i\omega t} \quad (6)$$

put (5) and (6) insert into Maxwell's equation, the wave equation can be expressed by the form of electric field:

$$\frac{1}{\epsilon(r)} [\nabla \times \nabla \times E(r)] = \left(\frac{\omega}{c}\right)^2 E(r) \quad (7)$$

In TE case, there is no electric field component in the propagation. In this paper, assuming that Electromagnetic waves propagate along the z axis, as shown in Figure 1.

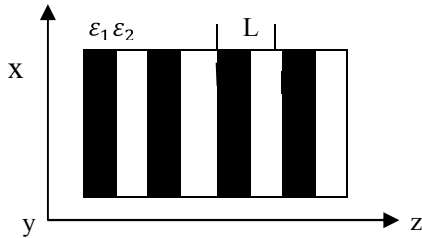


Fig.1. The Multilayer film, 1D photonic crystals. Where ϵ_1, ϵ_2 are different dielectric constants, L is spatial period.

In the TE case, $E(\vec{r})=(0, E, 0)$, (7) can be derived:

$$-\frac{1}{\epsilon(r)} \nabla^2 E(\vec{r}) = \left(\frac{\omega}{c}\right)^2 E(\vec{r}) \quad (8)$$

According to the Bloch State:

$$E(\vec{r}) = \hat{y} E_o(z) e^{-i\vec{K} \cdot \vec{r}} \quad (9)$$

$$\vec{K} \cdot \vec{r} = K_z \hat{z} \cdot \vec{r} = K_z z$$

$$E(\vec{r}) = \hat{y} E_o(z) e^{-iK_z z} \quad (10)$$

Setting Φ replace $E_o(z)$, $\Phi = E_o(z)$, and put (10) insert into (2), we can get the scalar function:

$$\frac{1}{\epsilon(z)} \frac{\partial^2 \Phi}{\partial z^2} - 2 \frac{1}{\epsilon(z)} iK_z \frac{\partial \Phi}{\partial z} - \frac{1}{\epsilon(z)} K_z^2 \Phi = \left(\frac{\omega}{c}\right)^2 \Phi \quad (11)$$

3. FEM solution

The finite element method is a numerical analysis method that is very important for solving the photonic crystals problem. In FEM, it is first step to get the Weak form:

$$\int V_i \left[\frac{1}{\epsilon(z)} \frac{\partial^2 \Phi}{\partial z^2} - 2 \frac{1}{\epsilon(z)} iK_z \frac{\partial \Phi}{\partial z} - \frac{1}{\epsilon(z)} K_z^2 \Phi - \left(\frac{\omega}{c}\right)^2 \Phi \right] dz = 0 \quad (12)$$

V_i : test function

division points:

$$\int \left\{ \frac{1}{\epsilon(z)} \frac{dV_i}{dz} \frac{d\Phi}{dz} - 2 \frac{1}{\epsilon(z)} iK_z V_i \frac{d\Phi}{dz} - \left[\frac{1}{\epsilon(z)} K_z^2 \Phi + \left(\frac{\omega}{c}\right)^2 \Phi \right] \right\} dz = 0 \quad (13)$$

3.1. Discrete the area and constructs interpolation function

In this part, we will choose the second order element. This can achieve higher accuracy without increasing the number of nodes. Every node has three nodes, in every element, unknown function can be approximated as second order function:

$$\Phi^e(x) = a^e + b^e x + c^e x^2 \quad (14)$$

$$\begin{cases} \Phi_1^e = a^e + b^e x_1^e + c^e (x_1^e)^2 \\ \Phi_2^e = a^e + b^e x_2^e + c^e (x_2^e)^2 \\ \Phi_3^e = a^e + b^e x_3^e + c^e (x_3^e)^2 \end{cases}$$

solve the a^e, b^e, c^e , put them insert into (14), we can get:

$$\Rightarrow \Phi^e(x) = \sum_{j=1}^3 N_j^e(x) \Phi_j^e \quad (15)$$

e: element i, j: local node

e: 1,2,3,4...m

i, j: 1,2,3

The interpolation function is given by:

$$N_1^e = \frac{(x - x_2^e)(x - x_3^e)}{(x_1^e - x_2^e)(x_1^e - x_3^e)}$$

$$N_2^e = \frac{(x - x_1^e)(x - x_3^e)}{(x_2^e - x_1^e)(x_2^e - x_3^e)}$$

$$N_3^e = \frac{(x - x_1^e)(x - x_2^e)}{(x_3^e - x_1^e)(x_3^e - x_2^e)}$$

put (15) insert into (13):

$$\sum_{j=1}^3 \phi_j^e \int_{z_1^e}^{z_3^e} \left\{ \frac{1}{\varepsilon(z)} \frac{dV_i^e}{dz} \frac{dN_j^e}{dz} - 2iK_z \frac{1}{\varepsilon(z)} \frac{dN_j^e}{dz} V_i^e - \left[\frac{1}{\varepsilon(z)} K_z^2 + \left(\frac{w}{c}\right)^2 \right] N_j^e V_i^e \right\} dz = 0 \tag{16}$$

sort out above equation, we can get eigenvalue matrix

equation

$$\sum_{j=1}^3 \phi_j^e \left(\frac{w}{c}\right)^2 \int_{z_1^e}^{z_3^e} N_j^e V_i^e dz = \sum_{j=1}^3 \phi_j^e \int_{z_1^e}^{z_3^e} \left[\frac{1}{\varepsilon(z)} \frac{dV_i^e}{dz} \frac{dN_j^e}{dz} - 2iK_z \frac{1}{\varepsilon(z)} \frac{dN_j^e}{dz} V_i^e \right] dz \tag{17}$$

4. Simulation by COMSOL

COMSOL is a finite element solution software for solving multiphysics. It can be used to numerically solve the complex physical problems that are mutually coupled by incorporating a variety of physics equations and corresponding solvers. It is very important tool in physics research. Itself is a finite element solver that can be set to solve the equations needed for the weak form, and then solved. However, not all problems can be solved by the built-in weak form module. At this time, it is helpful to know the weak form equation and its finite element algorithm to solve practical physical problems. By setting the material factor, selected Floquet periodic condition, using study to compute the frequency of any wave vector k.

Dielectric materials are alternately arranged, dielectric constant $\varepsilon_1=13$, dielectric constant $\varepsilon_2 = 1$.

When solving eigenvalues, we give the dependent variable as frequency. Within the frequency range of interest, the eigenvector K, and the value of wave vector K is limited to the simplest Brillouin zone. using weak form of COMSOL, we can carry out the band calculation

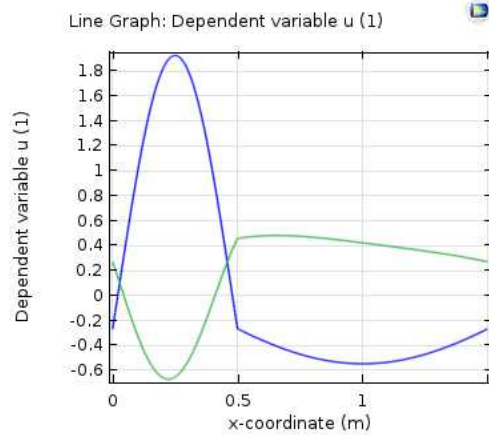


Fig. 2. The band structure of a multilayer film for E-field for mode.

for complex photonic crystals. weak form equations are the usual approaches to general finite element calculations

5. Conclusion

Discussed the basic characteristics of photonic crystals, and introduced weak form and eigenvalue matrix equation of one-dimensional photonic crystals from Maxwell's equations. Using COMSOL Multiphysics to compute band structure of 1D photonic crystals.

References

1. Sajeev John. Strong localization of photons in certain disordered dielectric superlattices[J]. *Physical Review Letters*, 1987,58(23): 2486-2489.
2. Eli Yablonovitch. Inhibited Spontaneous Emission in Solid-State Physics and Electronics[J]. *Physical Review Letters*, 1987, 58(20): 2059-2062.
3. J. D. Joannopoulos, R. D. Meade, and J. N. Winn. *Photonic Crystals: Molding the Flow of Light* (Princeton University Press, Princeton, 2008).
4. Hiroshi Isakari, Toru Takahashi, Toshiro Matsumoto. periodic band structure calculation by the Sakurai-Sugiura method with a fast direct solver for the boundary element method with the fast multipole representation[J]. *Engineering Analysis with Boundary Elements* 68(2016) 42-53.
5. Gagandeep Kaur, Amandeep Singh, Sappal Harjinder Singh, "Band Gap Computation of 1-Dimensional Silicon Photonic Crystal for High Contrast Grating Application", *International Journal of Computer Applications* (0975-8887) Volume 94-No.7, May 2014.

6. J. Zhao, X. Li, L. Zhong, G. Chen, "Calculation of photonic band-gap of one dimensional photonic crystal. Journal of Physics: Conference Series (Dielectrics 2009: Measurement Analysis and Applications, 40th Anniversary Meeting)", 183 012–018. 2009.
7. Gagandeep Kaur, Amandeep Singh, Sappal Harjinder Singh, "Band Gap Computation of 1-Dimensional Silicon Photonic Crystal for High Contrast Grating Application", *International Journal of Computer Applications* (0975-8887) Volume 94-No.7, May 2014.
8. Y. Zhang, S. Bai, P. Chen, and S. Qu, "A novel second-order DFP-based Volterra filter and its applications to chaotic time series prediction," *Proc. 31st Chinese Control Conf.*, pp.1036-1039,2012.
9. Ayyub O B, Ibrahim M B, Briber R M, Kofinas P. Self-Assembled Block Copolymer Photonic Crystal for Selective Fructose Detection[J]. *Biosensors and Bioelectronics*, 2013, 46: 124-129.

A Data Estimation Technique for Incomplete Telemetry Data based on a Genetic Algorithm with Data' Statistical Properties

Masahiro Tokumitsu and Kaito Mikami

*Department of Control Engineering, National Institute of Technology, Yonago College, 4448, Hikonacho
Yonago, Tottori 683-0854, Japan*

Fumio Asai

*Mmeber, The Radio Amateur Satellite Corporation, 10605 Concord St, #304
Kensington, MD 20895-2526 USA*

Taku Takada

*Department of Social Design, National Institute of Technology, Kochi, 200-1, Monobe Otsu
Nankoku, Kochi, 783-0093, Japan*

Wakabayashi Makoto

*Department of Electrical and Computer Engineering, National Institute of Technology, Niihama College,
7-1, Yakumocho, Niihama, Ehime, 792-8580, Japan*

Yoshiteru Ishida

*Department of Computer Science and Engineering, Toyohashi University of Technology, 1-1, Hibarigaoka
Toyohashi, Aichi 441-8580, Japan
E-mail: tokumitsu@yonago-k.ac.jp
www.yonago-k.ac.jp*

Abstract

Satellite in the space transmits their own mission data (so-called “telemetry data”) to ground stations. The telemetry data contain a sort of data such as observations, experiments, and satellites’ health status. However, the data received by the ground stations may contain errors by effects through the transmissions. This paper proposes a data estimation technique for incomplete telemetry data to attain a high availability of the received telemetry data. The proposed technique is based on a genetic algorithm with data’ statistical properties. This paper firstly demonstrates the proposed technique with simple examples, and then it simulates our technique with actual telemetry data obtained by the satellite.

Keywords: social diversity, intelligent information processing, telemetry data, data estimation, genetic algorithm.

1. Introduction

Universities and Technical Colleges have developed small satellites called “CubeSat” all over the world. They develop the CubeSats to provide an opportunity for satellite development. They also provide to achieve their

scientific or technological missions. The CubeSats usually communicate with ground stations in amateur radio bands to transmit their data with a weak signal. The satellites in the space transmit their own mission data (so-called “telemetry data”) to the ground stations. The telemetry data contain a sort of data such as observations,

experiments, and satellites' health status. However, the data received by the ground stations may contain errors by effects through the transmissions. The telemetry data, containing the errors, would reduce an availability of the data. The major technical issues are as follows: (1) A Doppler shift between a satellite and a ground station, (2) jamming by unlicensed radio stations, and (3) a signal attenuation by an atmospheric attenuation.

In operations of the CubeSats, the transmitted data usually contain additional redundant information to detect or to correct the corrupted parts. The implementations of the error correction depend on the policies of the satellite development projects. The error correction is not implemented if the projects determine to use only error detection.

The errors contained in the telemetry data is an unavoidable issue in satellite communications. Some organizations run interesting projects to support satellite operational teams by gathering the telemetry data from the Internet. Volunteers submit the received telemetry data to the servers to support operations of the satellite projects. The telemetry data are published on the websites of the projects. Further, SatNOGS¹ project provides information on the ground stations and the positions of the satellites in maps.

The DESPATCH² project by Tama Art University showed an impact of aggregated support by the volunteers. The DESPATCH project designed a sculpture as the satellite, and then it launched it into deep space. The sculpture equipped with the communication devices. In this project, the volunteers supported the mission by contributing the telemetry data. Finally, the communications with 4.7 million km between the sculpture and the ground station were successful. The communication of this immense distance was established by collecting the telemetry data provided by the volunteers.

The SatNOGS and the Online Telemetry Forwarder³ of the present active projects mainly focus collecting and publishing the gather data on their website. The error detection and correction would be feasible by intelligent information processing with huge collected data. The authors develop and operate "social diversity⁴". The main purpose of the project is to support satellite operational teams by providing the processed data with intelligent information processing. This paper proposes an intelligent information processing technique for data

estimation to recovery the incomplete data received by the ground stations. The proposed technique is based on a genetic algorithm⁵, and then the technique estimates the data with statistical properties of the data. This paper evaluates the performance how many the proposed technique estimate the original data. The remainder of this paper as follows. In Section 2, this paper describes the proposed technique in detail and demonstrates two illustrative examples. In Section 3, the simple experiment is presented. In Section 4, this paper discusses the issues in the proposed technique and future work. In Section 5, this paper summarizes this work.

2. Proposed Technique

This section describes the proposed technique in detail for incomplete telemetry data. The telemetry data is expressed as multiple binary bits. The entire telemetry data usually consists of multiple parts such as a header information, satellites' health status, and observation data. The length of the telemetry data depends on the format of each data. Further, the telemetry data usually contains redundant information for error detection or correction. Some CubeSats implement only error detection to transmit the telemetry data. This paper assumes that the telemetry data consists of the message body and a frame check sequence (FCS) (Fig. 1).

This paper estimates the incomplete telemetry data by extending technique of the genetic algorithms. The telemetry data in a packet level consists of multiple binary bits. The genetic algorithm handles multiple symbols to present individuals. The genetic algorithm is suitable for our purpose to present the digital data as the individuals.

The proposed technique searches the best telemetry data that matches the FCS if the FCS of the received data is incorrect. However, a lot of the solutions can be considered as the candidate solutions in the estimation process. The proposed technique uses the mean values as the statistical property for searching the best solution. Obviously, other knowledge and information of the telemetry data are would be options for searching the original telemetry data.

Fig. 1 shows an overview of the proposed technique. The telemetry data consists of three data fields and the FCS. The value of each data field is expressed 16 bits. The estimated data is obtained if the proposed technique finds the data that matches the FCS. The error parts in the

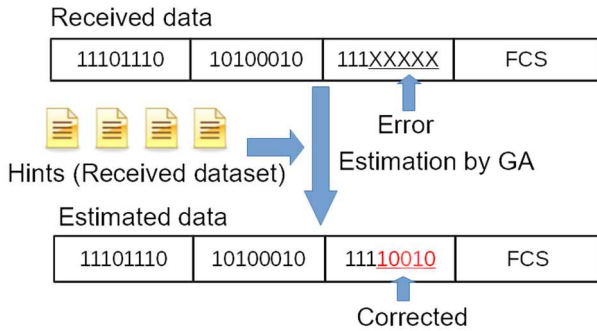


Fig. 1 Overview of the proposed technique by the genetic algorithm with data’s statistical properties.

obtained telemetry data are corrected by the proposed technique. The FCS with a short length detects the error of the received data incorrectly. For the data estimation, the probability of incorrect detection can be low by choosing the FCS with the long length such as 32 bits.

The related technique for our data estimation is a rainbow table attack⁶ that reverses input from a given hash and a precomputed table. This attack is proposed for cracking a password. The proposed technique relates to the rainbow table attack because our technique uses the predefined mean values and the FCS.

This paper demonstrates simple two examples to examine a significance of the proposed technique. Both examples use CRC-16 (CRC-CCITT) as the FCS. The CRC-16 is one of the major FCSs and used in a sort of applications. The digits of the data are arranged in a big-endian style in the both cases. The number of individuals in a population is 30. The two-point method is used for a crossover in the proposed technique. The fitness function is defined to minimize an error between the values presented by the individuals and it’s the mean value. The individuals of the next generation are chosen by a generation model. This paper implements a program for the proposed method with Go language and a gago⁷. The gago is an integrated library for implementing genetic algorithms with supporting parallel processing and a variety of functions.

In the first example, the single data with 16 bits is estimated by the proposed technique. The single data presents an unsigned integer with 16 bits. The mean value of the received data is only given to the proposed technique. The mean value is 1000 and it is given to the proposed technique as an input. The FCS is $(347A)_{16}$. The expected output is $(1000)_{10}$. In this example, the expected value corresponds to the mean value of the best

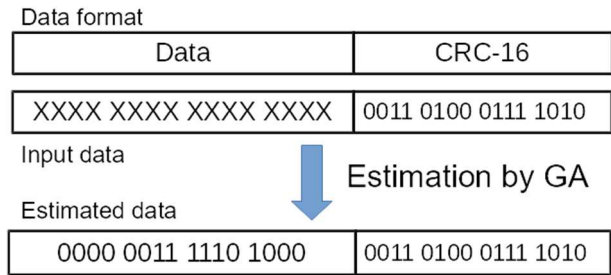


Fig. 2 Test input data and its estimation result for the illustrative example 1. The symbol X in the frame indicates unknown.

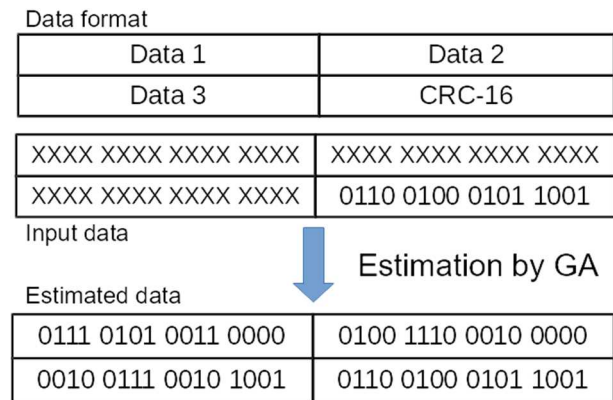


Fig. 3 Test input data and its estimation result for the illustrative example 2. The symbol X in the frame indicates unknown.

solution. In other words, the proposed technique optimizes the solution to minimize the error between the candidate solutions and the given mean value. This paper carried out this example with the proposed technique with the above parameters. Eventually, the proposed technique was successful for estimating the expected solution. Fig. 2 shows the estimation sequence for the first example.

In the second example, the triple data with 16 bits are estimated by the proposed method. Each data also presents an unsigned integer with 16 bits. The mean values of the received data are also given only to the proposed technique. The mean values of Data 1, Data 2, and Data 3 are respectively $(30022)_{10}$, $(19857)_{10}$, and $(10050)_{10}$.

The FCS of the received data is $(6459)_{16}$. The expected output values $(Data 1, Data 2, Data 3)_{10} = (30000, 20000, 100025)_{10}$. In this example, the expected value does not correspond to the mean values of the best solution. This paper carried out this example

Table 1. Numbers and names of the data fields

No.	Name of data name
1	Black Chassis deg. C
2	Silver Chassis deg. C
3	Black Panel deg. C
4	Silver Panel deg. C
5	Solar Panel +X deg. C
6	Solar Panel -X deg. C

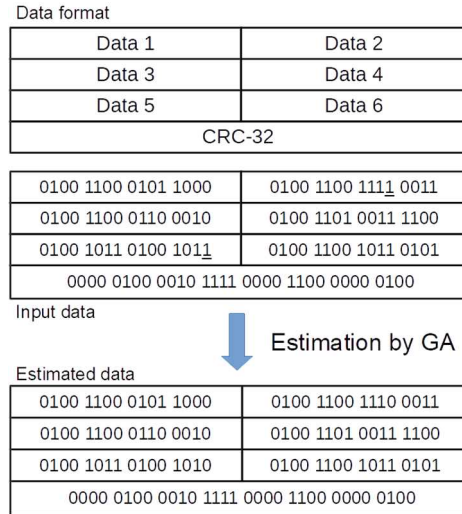


Fig. 4 The example of test input and estimated data by the proposed technique. The underlines of the digits indicate errors.

Table 2. Estimated results by the proposed technique.

Item\ Number of data fields	3	4	5	6
Used data No.	1, 2, 3	1, 2, 3, 4	1, 2, 3, 4, 5	1, 2, 3, 4, 5, 6
Total length of frame	48	64	80	96
Number of total test input	500	500	500	500
Number of successful detection	346	283	237	202
Estimated success rate	0.692	0.556	0.474	0.404

with the proposed technique with the above parameters. The proposed technique was successful for estimating the best solution. Fig. 3 shows the estimation sequence for the second example.

3. Simulations

This section demonstrates the significance of the proposed technique for the actual data transmitted by the CubeSat. However, the telemetry data as the packet data is not provided. The project only provides the numerical data that present the satellite’s health status. This paper manually makes the telemetry data from the published data.

The simulation uses the dataset of FUNcube-1⁸ (AO-73) operated by AMSAT-UK. The dataset is provided by the FUNcube-1 operational team in a website⁹. The project website publishes weekly the telemetry data that is recorded at every minute. The telemetry data of FUNcube-1 contains its working status such as a solar panel voltage, a battery voltage, and the battery

temperature. This paper chooses some kinds of the data field from the telemetry data format. Table 1 shows the data fields used in the simulation. Although the project provides sixteen kinds of the data in total, this paper chooses six kinds of the data fields. In the test dataset, all the data fields represent half-precision floating-point numbers that are presented by IEEE 754-2008 format with 16 bits.

This paper evaluates the proposed technique by changing the total length of the test telemetry data from three to six. The mean values of the data fields are calculated by the data for 21 days (About three months). The total number of the telemetry dataset is 24501. This paper randomly chooses the test data from 10% of the dataset. The total number of the test dataset is 2451. The test data contains randomized errors with two bits. The FCS of each test data is calculated from the original data. This section uses CRC-32 as the FCS instead of CRC-16 used in the previous examples because the authors revealed that the proposed technique with CRC-16

incorrectly estimated the original data. The proposed technique with CRC-16 finds the incorrect solution that matches the given FCS where some parts of the incorrect solution differ from the original data.

Table 2 shows the estimated results by the proposed technique. This paper prepares 500 test inputs and examines them by the proposed technique. The estimated success rate decreases as the total length of the data increases. The short length of the frame is easier to find the best solutions than using the longer-length frames because the combinatorial patterns with the short-length frames are small. The proposed technique obtained the estimated success rate 0.404 for the longest frame in the simulation.

4. Discussion

The proposed technique is difficult to find the best solution where the values of the data fields deviate their mean values. Because the fitness function in the proposed technique optimizes the errors between the values presented by individuals and their mean values. The mutation models and crossover models produce more variety of individuals than the present model. The mutation models and crossover models would improve the probability of finding the best solution.

The maximum length of the data estimation is 96 bits. This length is not enough to apply to actual data such as the telemetry data of the FUNcube. The length of the FUNcube's telemetry data is 2048 bits. The proposed method needs to extend the limits of the maximum data length. The long frame data would guild the problem more difficult to find the best solution that matches the given FCS. However, the genetic algorithm by using multiprocessing, GPGPU, and supercomputers would relax this limitation.

5. Conclusion

Satellite in the space transmits their own telemetry data to ground stations. The telemetry data may contain some errors by the effects through the transmissions. The telemetry data generally have not only the message body but also the redundant information to error the detection or correction. This paper focused on the redundant data for the error correction to estimate the original telemetry data by the genetic algorithms. The proposed technique is based on a genetic algorithm with data's statistical

properties. This paper firstly demonstrated the proposed technique with simple two examples. This paper also demonstrated that the proposed technique estimated the original data successfully.

Acknowledgements

The authors acknowledge useful comments and continuous encouragement in a collaborative education forum for a design of networked satellites by the collaborative project between Toyohashi University of Technology and Colleges of Technology in 2017. This paper was supported by Grants-in-Aid for Scientific Research in 2016 by the Telecommunications Advancement Foundation. This paper also was supported by Grants-in-Aid Program in 2017 by National Institute of Technology, Yonago College. The KOSEN space technology education project was supported by the Human Resource Development program of the MEXT, Japan, in 2017.

References

1. Libre Space Foundation, SatNOGS Network, <https://network-dev.satnogs.org/> (2017). (Accessed on 20/12/2017)
2. ARTSAT, DESPATCH (FO-81) – ARTSAT, <http://artsat.jp/en/project/despatch>, (2014). (Accessed on 20/12/2017)
3. M. Rupprecht (DK3WN), Online Telemetry Forwarder, <http://www.dk3wn.info/p/?p=69954>, (2016). (Accessed on 20/12/2017)
4. Social diversity project, Social diversity: a global and integrated telemetry receiving system with volunteers and an intelligent information processing, <https://social-diversity-devel.appspot.com/>, (2017). (Accessed on 20/12/2017)
5. J. H. Holland, *Adaptation in Natural and Artificial Systems*, (1975, MIT Press).
6. P. Oechslin, Making a Faster Cryptanalytical Time-Memory Trade-Off, in *Advances in Cryptology - CRYPTO 2003. CRYPTO 2003, Lecture Notes in Computer Science 2729* (Springer, Berlin, Heidelberg, 2003).
7. M. Halford, GitHub - MaxHalford/gago: Golang genetic algorithm library, <https://github.com/MaxHalford/gago>, (2017). (Accessed on 20/12/2017)
8. The FUNCube project, Welcome to the FUNCube Web Site, <https://funcube.org.uk/>. (Accessed on 20/12/2017)
9. D. Johnson, G4DPZ, The Data Warehouse, <http://warehouse.funcube.org.uk/realtime.html?satelliteId=2>, (2013). (Accessed on 20/12/2017)

Study on Detection of Nests on Pylon from Overhead View Based on Halcon

Jiwu Wang¹

School of Mechanical, Electronic and Control Engineering, Beijing Jiaotong University, China

Haibao Luo¹

School of Mechanical, Electronic and Control Engineering, Beijing Jiaotong University, China

Pengfei Yu¹

School of Mechanical, Electronic and Control Engineering, Beijing Jiaotong University, China

E-Mail: jwwang@bjtu.edu.cn, 16121251@bjtu.edu.cn, 16121256@bjtu.edu.cn

Abstract

Aiming at the disadvantages of low accuracy and efficiency of the existing methods of nest detection, this paper proposes an effective method based on Halcon, which could detect the nest in the images from unmanned aerial vehicles(UAVs). This method eliminates most of the background interference by Extracting XLD contour algorithm to identify the pylon area in the image. Within this area, the fusion of texture and gray-scale features of nest are employed to realize the detection. An experiment result is presented to validate that this method can actually realize the precise detection of nests on pylon with images shoot by the UAVs.

Keywords: XLD contour, pylon, nest detection, fusion of texture and gray-scale features

1. Introduction

In recent years, according to the statistics of the State Grid[1], the occurrence of transmission line tripping caused by bird activities frequently. Therefore, the detection of the bird's nest on the pylon has become a hot spot of current research. in the existing detection algorithm for power transmission system is mainly aimed at detecting an object with special shapes and colors that are obviously different from the background. However, it's difficult to accurately detect and locate the nests with the small size and no specific shape and color features. In recent years, some scholars have made a preliminary study on the detection of the bird's nest on pylon. In recent years, some scholars have made a preliminary study on the detection of the bird's nest on pylon. Sun F J et al[2] proposed a new kind of recognition scheme basing on digital image processing. this method can only achieve good results if the image background is very simple. Wu Xiao et al[3] proposed an image-based railway contact net bird-nest abnormal condition

detection method. This method is only better for the bird's nest on the railway network Xu Jing et al[4] proposed a bird's nest detection method based on the combination of color and texture features. This method not only complicates the calculation process when extracting the pylon area, but also obtains the pylon area is still large and does not eliminate complex background interference, which also poses great difficulties for the final nest identification. Zhang Yilian et al[5] proposed a nest detection method based on Coarse-to-fine detection on pylon. The method of positioning the bird's nest is not accurate enough because of the surrounding background of flowers and trees, mountains and mud whose color are very similar to nest, which will result in a large degree of false positives happen. Therefore, how to accurately detect the pylon in a complicated background and further search for the nest's candidate position is the key to detecting the nest. Considering the shortcomings of existing methods, this paper proposes an

effective method based on Halcon, which could detect the nest in the images from unmanned aerial vehicles(UAVs). This method eliminates most of the background interference by Extracting XLD contour algorithm to identify the pylon area in the image. Within this area, the fusion of texture and gray-scale features of nest are employed to realize the detection. Thereby narrowing the detection range and improving the detection efficiency and accuracy.

2. Pylon detection algorithm

In order to make the area of pylon in the captured image appear to be compact, this paper adopts the UAV to take a picture from overhead view and then extracts and filters the pylon sub-pixel edge XLD contour algorithm to detect and extract the pylon area, that can greatly reduce the detected range, effectively eliminate a large number of complex background interference. Finally, based on this, a nest detection method based on texture and gray value fusion is proposed. Algorithm of the overall process shown in Figure 1:

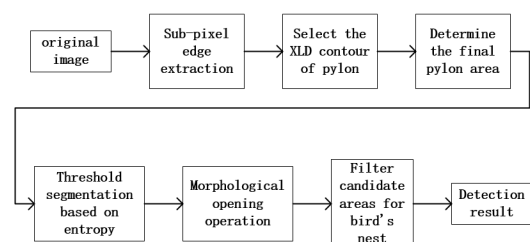


Fig. 1. The overall process of the nest detection

Considering that the backgrounds in different images are different, and it is difficult to separate the pylon area from the complex background by using the traditional threshold algorithm. Therefore, this paper proposes a direct method for obtaining the sub-pixel edge XLD contour from the whole image. The effect is shown in Figure 2 (b):

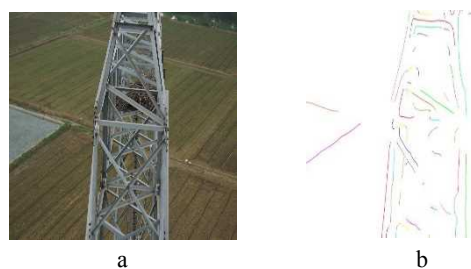


Fig. 2. (a) is original image, (b) is XLD contour

When sub-pixel edge extraction is performed on the contour of the pylon in the original image, the contour

of the object with obvious edge features such as wires in the background of the image is also extracted. In this paper, all the edge XLDs are screened by taking advantage of the two important conditions of the outer edge contour of the pylon within a certain length and angular interval, and ultimately exclude the influence of the image background object on the contour extraction of the pylon. Converted to image format as shown in Figure 3:

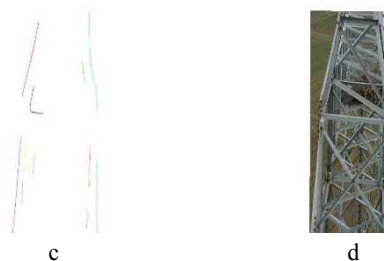


Fig. 3. (c) is screening result image, (d) is final result image

3. Nest detection algorithm

Due to the material of the nest area itself and the influence of different illumination factors, the gray value of each pixel in the nest area is greatly different. Therefore, it is very difficult to separate the nest area by the traditional threshold algorithm. The entropy of the image is the judgment of how much the image contains the information. It is of great benefit to calculate the entropy of the image to judge the effect of the image. The image with higher entropy has many details and changes in brightness, which characterizes the clustering characteristics of the grayscale distribution of the image. Therefore, this paper uses the entropy threshold segmentation technique to separate nest area from the image background. the separated effect shown in Figure 4 (b):

By observing the result of threshold, it is found that some background pixels which the gray value is similar to the nest area will not be eliminate. In this paper, Morphological opening operation is used to perform the pre-screening of nesting candidate regions. As shown in Figure 4 (c), By using the area of the bird's nest in a certain range, thus the other areas which are out of the range can all be deleted. The effect after the screening is shown in Figure 4 (d).

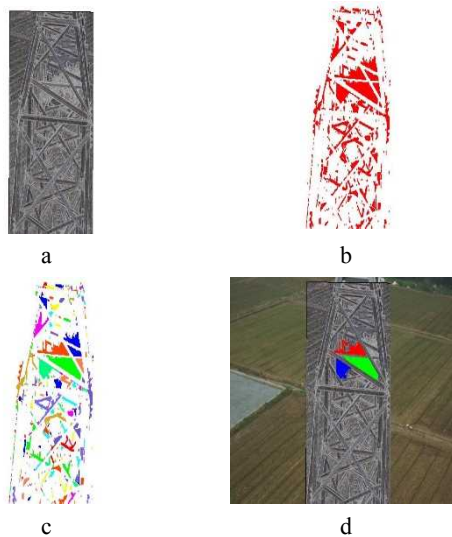


Fig. 4. (a) is entropy image, (b) is entropy threshold image, (c) is opening operator image, (d) is preliminarily detected result of the nest

After dividing the bird's nest area by the above-mentioned method, although the large number of background areas is removed, the final nest candidate area may still contain non-nest areas. Thus, this paper uses the fusion of the bird's nest texture and gray-scale features to achieve accurate detection of the nest.

Considering the high roughness of the nest area, resulting in a greater variance in the gray value of the bird's nest area, so it is possible to eliminate the candidate area of the nest whose gray value is not much different.

The Grayscale Co-occurrence Matrix (GLCM) is a commonly used method for describing textures by studying the spatial correlation of grayscale. So in the paper, by selecting the area of the experimental test image that contains the bird's nest and the typical background area, and calculate the texture feature respectively to obtain the comparison curve of the texture features in Figure 5. Through multiple experiments, we found that the entropy of the bird's nest area is generally higher than that of the non-nest area, Entropy characteristics of the bird's nest area as the final judge nest area conditions, to achieve the detection of the nest on pylon.

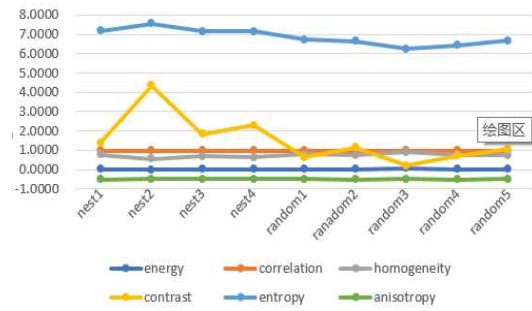


Fig. 5. The curves of texture characteristics of the nest and non-nest areas

4. Experiments

Using the images actually collected by UAV as a data source, and it is a high-resolution color image of 6000 pixels multiply 4000 pixels.

As shown in Fig. 6, we can use the algorithm proposed in this paper to test the images of the bird's nest under two different background conditions randomly, all of which can achieve accurate detection.



Fig. 6. The detection results of the bird's nest on the pylon under different backgrounds

5. Summary

According to the method proposed by the previous researchers, the area of the pylon detected is too large, which can't well remove the interference of the large number of complex backgrounds to the final detection of the bird's nest. By using the method of this paper, most of the background interference can be eliminated, thereby reducing the detection range and improving the detection efficiency and accuracy of the bird's nest on pylon.

References

1. Wang S H, Ye Z Q. Analysis of bird damage accidents on overhead transmission lines and prevention techniques[J]. *High Voltage Apparatus*, 2011, 47(2):61-67.

2. Sun F J, Wang Z, Fan J Q. The Recognition Research of Birds' Nest on Transmission Line Towers[J]. *Advanced Materials Research*, 2013, 651:820-824.
3. Wu Xiao, Yuan Ping, Peng Qiang, et al. Image-based railway contact net bird-nest abnormal condition detection method:, CN 103745224 A[P]. 2014.
4. XU Jing, HAN Jun, TONG Zhigang, et al. Method for detecting bird's nest on tower based on UAV image. *Computer Engineering and Applications*, 2017, 53 (6):231-235.
5. Zhang Yilian, Chen Yong et al. Coarse-to-fine detection for nests on pylon[J]. based on information technology, 2017 (3): 104-109.

Human gait recognition based on Caffe deep learning framework

Jiwu Wang¹

School of Mechanical Electronic and Control Engineering of Beijing Jiaotong University of China

Feng Chen¹

School of Mechanical Electronic and Control Engineering of Beijing Jiaotong University of China

E-Mail: jwwang@bjtu.edu.cn, 16125922@bjtu.edu.cn

www.bjtu.edu.cn

Abstract

Human gait recognition as an emerging biometrics technology has important theoretical significance and practical value. At present, the research on human gait recognition is still in the stage of theoretical exploration. With the development of deep learning theory and technology, this paper will achieve human gait recognition of specific targets based on Caffe deep learning framework through the faster-rcnn algorithm. The main contents of the paper include the samples processing, model training and result testing.

Keywords: deep learning; faster rcnn; gait recognition; contour recognition; feature extraction.

1. Introduction

The gait recognition is one of the main methods of biometrics, which verifies targets' identity mainly through their contours and behavior characteristics. Compared with other biometrics methods, the gait recognition has many advantages, just like long-distance recognition, low-pixel recognition and non-contact recognition. At present, there are more and more methods of the gait recognition as the research develop constantly. Among these methods, Bae et al. analyze and research the stage of movement by Hidden Markov Model¹. Begg detects changes of the gait automatically by machine learning method², which is limited to small sample to recognize. Heng Zhang describes the contour features of the human body by wavelet descriptor to achieve real-time recognition³, however, the accuracy is

not well. Puspitasari proposes a method for gait recognition based on Hough Transform⁴, he converts the human body information into the line information and gets the angle between the legs for further calculation. Because of the occlusion and filming angle, the robustness of the method is poor.

In order to fulfil the accuracy and real-time requirements of the recognition, and reduce the interference that caused by some factors, such as the different apparels and accessories, background complexity and so on. As for the shortcomings of existing methods, this paper proposes a faster-rcnn algorithm based on deep learning. We can use the convolution neural network to extract and fit the features of the body contour and the gait features from the prepared samples. Comparing the similarity with the features of the experimental pictures. If the similarity

exceeds the set threshold, the experimental pictures can be regarded as the target.

2. Sample Selection and Processing

The samples of this experiment is taken from the gait database B⁵ that collected by the CASIA (Institute of Automation, Chinese Academy of Science). Among these samples, we choose 1503 pieces of pictures that taked under 90° viewpoints include 1 to 4 characters, and calibrate the target’s truth candidate region for the selected sample, as shown in fig.1 below:

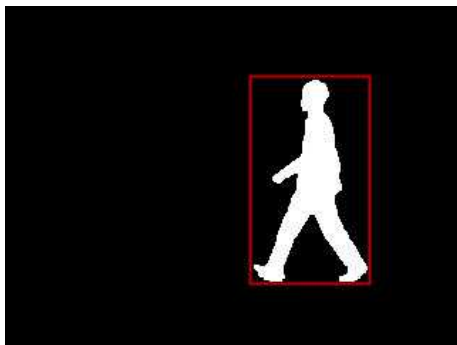


Fig.1. Annotation example diagram

At the same time generate the corresponding file to describe the picture. In practical samples preparation and target detection, there are some methods like background subtraction based on Gaussian of Mixture Models can help process samples and experimental pictures.

3. Feature Extraction and Recognition

The gait recognition of the target person mainly completes the feature extraction of the body contour and gait information of the target person. Completing the person recognition main by comparing the features. Each sample with the scale of 320x240x2 will be input to the neural network layer to train. First, convoluting and rectifying the samples twice and conducting max pooling operation to get the initial characteristic data. Next, putting the part of the feature data into the next layer of neural network to continue feature extraction, so repeat 5 times until getting the final feature map. The final feature map as the fig.2 follows:

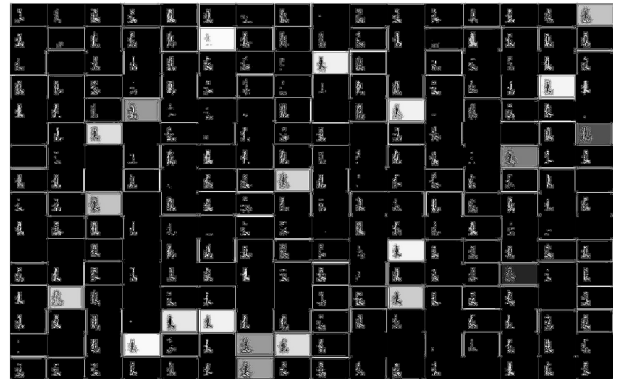


Fig.2.The final feature map

Next, sending the feature map to the RPN (Region Proposal Network) network. The network will put the proposals map on the final feature map, and generate a fixed-size feature map for each Rol through the Rol pooling layer. The proposal feature maps as the fig.3 follows:

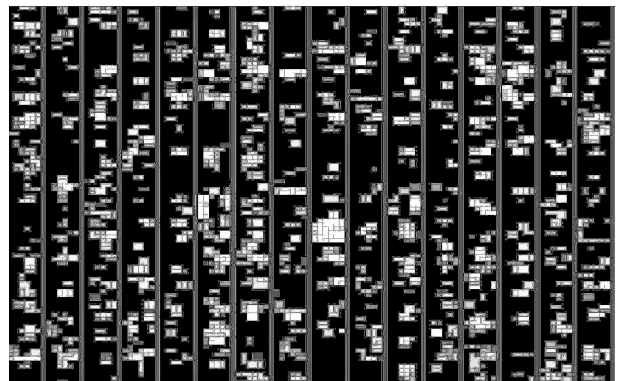


Fig.3. Roi_pool_conv5

Then, the combined training of classification probability and bounding box regression is trained by Softmax Loss and Smooth L1 Loss. At last, drawing the loss and accuracy curves of the training process and giving backpropagation data to make the proposals and the target frame position correct more precisely, which can make the target feature extraction and description more accurate. The recognition will be better.

The experiment’s process is carried out on the basis of deep training. The experimental pictures are completed feature extraction, feature comparison, classification and marking sequentially. The result of the recognition is displayed through the experimental pictures and the terminal.

4. Experiment

For the above deep learning method, we take some pictures that are not trained in the train process as the samples of the experiment. Part of the pictures to be modified accordingly in order to verify the effectiveness of the recognition.

In this experiment we select a total of 100 pieces of pictures, include 70 pieces of normal pictures and 30 pieces of abnormal pictures. About the abnormal pictures, there are 10 pieces of pictures that part of body of the target is blocked by accessories and other things, there are 10 pieces of pictures that the person is similar to the target but not the target, other pictures with the complicated background. The threshold of similarity is setted as: 0.85.

One of the experiment's results as the fig.5 follows:



Fig.5. Sample annotation example diagram

The precision: 95%.

The spend time: 0.050s/piece of pictures.

5. Summary

There is the great advantage on the accuracy and time of recognition through the faster-rcnn algorithm based on deep learning. Meanwhile, the method has the higher requirements about the computer configuration, especially the GPU. The samples selected and the number of the samples also have the significant effect on the recognition. As the amounts of samples is less in the experiment, next experiment will be improved in the sample selection, amounts and other parameters, so as to better enhance the recognition. In addition, we will have more try on changing the layers of the

convolutional neural network and adjusting the parameters.

References

1. Bae J, Tomizuka M. Gait phase analysis based on a Hidden Markov Model [J]. *Mechatronics*, 2011, 21(6):961-970.
2. Begg R, Kamruzzaman J. A machine learning approach for automated recognition of movement patterns using basic, kinetic and kinematic gait data [J]. *Journal of Biomechanics*, 2005, 38(3):401-408.
3. Heng Zhang. *Gait Recognition based on the contour* [D]. Nanjing University of Information Science & Technology, 2011.
4. Puspitasari C. IMPLEMENTASI HOUGH TRANSFORM DALAM EKSTRAKSI FITUR GAIT MANUSIA. [J]. Fti/ia/skripsi/00398, 2011.
5. CASIA Gait Database [EB/OL]. <http://www.cbsr.ia.ac.cn/english/Gait%20Database.asp>

Unsupervised Image Classification Using Multi-Autoencoder and K-means++

Shingo Mabu

*Graduate School of Sciences and Technology for Innovation, Yamaguchi University, Tokiwadai2-16-1
Ube, Yamaguchi 755-8611, Japan*

Kyoichiro Kobayashi

*Department of Information Science and Engineering, Faculty of Engineering, Yamaguchi University, Tokiwadai2-16-1
Ube, Yamaguchi 755-8611, Japan*

Masanao Obayashi

*Graduate School of Sciences and Technology for Innovation, Yamaguchi University, Tokiwadai2-16-1
Ube, Yamaguchi 755-8611, Japan*

Takashi Kuremoto

*Graduate School of Sciences and Technology for Innovation, Yamaguchi University, Tokiwadai2-16-1
Ube, Yamaguchi 755-8611, Japan*

E-mail: mabu@yamaguchi-u.ac.jp, m.obayas@yamaguchi-u.ac.jp, wu@yamaguchi-u.ac.jp

Abstract

Supervised learning algorithms such as deep neural networks have been actively applied to various problems. However, in image classification problem, for example, supervised learning needs a large number of data with correct labels. In fact, the cost of giving correct labels to the training data is large; therefore, this paper proposes an unsupervised image classification system with Multi-Autoencoder and K-means++ and evaluates its performance using benchmark image datasets.

Keywords: neural network, deep autoencoder, K-means++, clustering

1. Introduction

Recently, deep learning¹ has been actively applied to various problems and shown distinguished performance. Especially, in image classification problems, since deep neural networks can automatically extract features contained in each image², it becomes easier to apply deep neural networks to image classification comparing to the conventional methods that extract features using manually created feature extraction method.

However, classification systems using deep learning are generally based on supervised learning. Thus, a large

number of training data with correct labels are necessary for the learning. Since it is a tough task to give correct labels to many (hundreds ~thousands) images, this paper proposes an unsupervised image classification (clustering) algorithm that does not use data with correct labels to reduce the cost of preparing training data. However, when we do not use correct labels, the classifier cannot know the explicit information on the classes. Therefore, sufficient information to distinguish the differences between the images is necessary for accurate classification. To obtain sufficient information, we apply some image processing techniques to increase

the variation of the images. Then, the increased images are inputted to Multi-autoencoder to extract feature information. In summary, the proposed method has two features; 1) increasing the variation of original images using some image processing techniques, and 2) extracting features using Multi-autoencoder that uses the original and generated images. Autoencoder-based data clustering has been already proposed³. However, the aim of the conventional method is to enhance Single-autoencoder, while the aim of the proposed method is to evaluate the effectiveness of Multi-autoencoder.

The rest of this paper is organized as follows. In section 2, the proposed unsupervised image classification algorithm is explained. In section 3, a benchmark image dataset (caltech101) and experimental settings are explained, then experimental results are shown. Section 4 is devoted to conclusions.

2. Unsupervised image classification algorithm

The flow of the proposed method is shown in Fig. 1. First, some image processing techniques (gray-scale transformation and edge detection by Sobel filter⁴) are applied to the original images to generate variations. Second, several independent autoencoders (Multi-autoencoder) are prepared (the number of autoencoders is three corresponding to the number of datasets, i.e., the original dataset and two generated datasets). Then, feature values are obtained by the Multi-autoencoder. Finally, the image clustering is carried out by K-means++ algorithm.

2.1. Feature extraction using Image processing and Multi-autoencoder

The image dataset used in this paper is caltech101⁵ that is a set of color natural images (32×32 pixel) such as watch, motorbike, airplane, grand piano, etc. We apply gray-scale transformation and Sobel filter independently to the original dataset, and two new datasets are generated (Fig. 2). Then, the original and generated images are encoded by Multi-autoencoder. Fig. 3 shows 9-layered autoencoder used for the feature extraction. The original or generated images inputted to the autoencoder are encoded by second–fifth layers, decoded by sixth–ninth layers and finally reconstructed images can be obtained. The autoencoder is trained so that the mean squared error between the input and output values is minimized. After finishing the training, the feature values of the input image are obtained by the fourth layer.

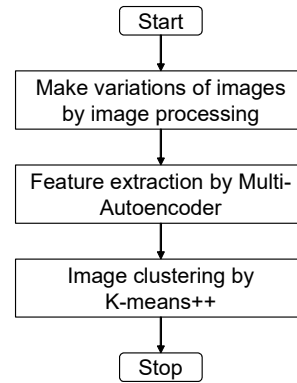


Fig. 1. Flowchart of the proposed method

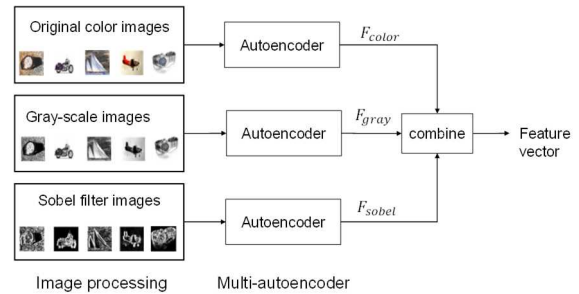


Fig. 2. Feature extraction using image processing and Multi-autoencoder

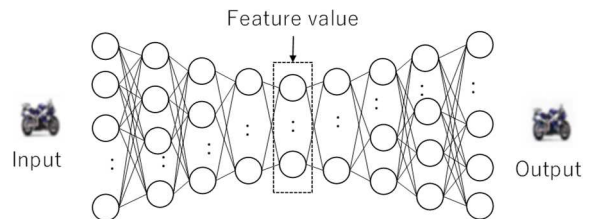


Fig. 3. Structure of autoencoder

Here, let the original image data number be d , the feature values of data d extracted by the autoencoder for the color image be $F_{color}(d)$, those for the gray-scale image be $F_{gray}(d)$, and those for the Sobel filter image be $F_{sobel}(d)$. Then, a feature vector combining $\{F_{color}(d), F_{gray}(d), F_{sobel}(d)\}$, $\{F_{color}(d), F_{gray}(d)\}$, $\{F_{color}(d), F_{sobel}(d)\}$ or $\{F_{sobel}(d), F_{gray}(d)\}$ is defined by $F(d)$ which is used in the next K-means++ clustering⁶.

2.2. Clustering by K-means++

K-means⁷ is a clustering algorithm that makes groups (clusters) of data where each data belongs to one of the groups whose centroid is the nearest. K-means++ is an extension of K-means that improves the initialization of cluster centroids. The centroid initialization method of K-means++ is summarized as follows.

1. Randomly select one data d out of N data as a cluster centroid. Here, let m be 1.
2. Repeat the following until $m=K$ (K is the total number of clusters).
 - i. Calculate $D(d)$ which is the Euclidian distance between data d and the nearest centroid.
 - ii. Select one data $d(d = 1, 2, \dots, N - m)$ with probability $\phi(d)$ as a new centroid.

$$\phi(d) = \frac{D(d)^2}{\sum_{d=1}^{N-m} D(d)^2}$$

- iii. $m \leftarrow m + 1$

By applying K-means++ to all the feature vectors $F(d)$, similar images are put into the same cluster.

3. Experiment

The image data set is caltech101 which contains pictures of objects belonging to 101 classes. In this paper, images of 10 classes are selected and used for the experiment. The 10 classes are airplanes, bonsai, faces_easy, hawksbill, ketch, leopards, motorbikes, watch, grand_piano, chandelier, and each class contains 90 images (totally 900 images). The clustering performance of the proposed method is evaluated by F-measure comparing to the conventional methods. The conventional methods include 1) clustering for the features extracted by single-autoencoder, 2) clustering

Table 1. Parameters of Multi-autoencoder

# of nodes (1 st layer–5 th layer)	3072 or 4096, 2048, 1024, 512, 256 or 171
Activation function	Sigmoid
Pre-training epoch	300
Fine-tuning epoch	200
Learning algorithm	Adam

for the original images without feature extraction, 3) clustering for the Histogram of oriented gradients (HOG) features⁸ of the original images. The parameters of Multi-autoencoder are shown in Table 1. The number of layers is nine, and the number of input nodes is determined according to the sizes of input images. The size of the original color images is 3072 (32 pixel \times 32 pixel \times 3 channels) and that of gray-scale images and Sobel filter images is 4096 (64 pixel \times 64 pixel \times 1 channel). Since gray-scale and Sobel filter images have one channel, the size is enlarged to increase the number of pixel information. The number of nodes in the 5th layer is 256 or 171 depending on the combination of $\{F_{color}(d), F_{gray}(d), F_{sobel}(d)\}$. When two kinds of feature values are combined to make $F(d)$, 256 nodes are used and obtain $F(d)$ with 512 ($= 2 \times 256$) values. When all the three kinds of feature values are combined, 171 nodes are used to obtain $F(d)$ with 513 ($= 3 \times 171$) values. This is for making the dimensional size of feature vectors be almost the same between the different settings. Multi-autoencoder is learned by stochastic gradient descent method with Adam (adaptive moment estimation)⁹ which is an online estimation method of appropriate learning rate.

Table 2 shows the clustering performance of the proposed method and some conventional methods averaged over 10 independent trials. The proposed

Table 2. Clustering performance

Method	Image set	Precision [%]	Recall [%]	F-measure [%]
Proposed method with Multi-autoencoder	Color+Sobel	73.6	69.1	71.3
	Color+Gray	66.6	62.4	64.4
	Gray+Sobel	69.6	67.7	68.6
	Color+Gray+Sobel	68.2	65.4	66.7
Conventional method with Single-autoencoder	Color	69.4	64.9	67.1
	Gray	62.9	61.8	62.6
	Sobel	68.5	65.6	67.0
Conventional method without autoencoder	Color	60.8	57.6	59.1
	HOG feature	69.8	62.7	66.0

Table 3. Results of t-test

Methods	p-value
Color+Sobel vs. Color	1.23×10^{-4}
Color+Sobel vs. Sobel	7.62×10^{-4}

Color+Sobel: Proposed method with color and Sobel filter images
 Color: Conventional method (Single-autoencoder) with color images
 Sobel: Conventional method (Single-autoencoder) with Sobel filter images

method with color and Sobel filter images shows the best F-measure of 71.3%. The proposed method with gray and Sobel filter images shows the second best F-measure of 68.6%. From these results, we can see that the Sobel filter images can give additional useful information for the clustering. The proposed method with all the three kinds of images does not show the best result because too much (redundant) information would even cause bad effect on the learning efficiency. Among the three settings of Single-autoencoder, the method with color images shows the best F-measure; thus, we can say that the color original image contains the useful information comparing to gray and Sobel filter images. However, the difference of F-measure between color and Sobel filter is small; thus, we can see the Sobel filter still contains useful information. As for the method without autoencoder, HOG feature shows better F-measure than the method using raw color images.

Table 3 shows the results of t-test for F-measure between the proposed method with color and Sobel filter images and the conventional methods with color or Sobel filter images. We selected the methods for the t-test that show better F-measure among all the settings of the proposed method or conventional methods. From Table 3, we can see that there are significant differences between the proposed method and conventional methods.

Fig. 4 shows an example of the generated cluster. This cluster mainly contains grand_piano images; however, some other classes of images whose features are very similar are also contained. The squares in Fig. 4 show the images that are not grand_piano. The proposed method is based completely on unsupervised learning, thus it is difficult to realize perfect clustering due to the lack of class information. Nevertheless, the proposed method can generally grasp the essential features for selecting similar images.

4. Conclusions

This paper proposed an unsupervised image classification algorithm using Multi-autoencoder and K-means++, which can increase the useful information by applying some image processing and automatically

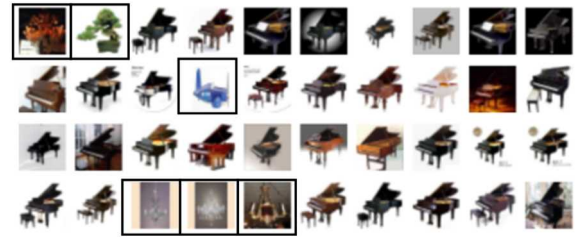


Fig. 4. Example of the generated cluster

extract features by Multi-autoencoders. From the experimental results, it was clarified that the proposed method showed better clustering accuracy than the conventional methods with significant differences. In the future, we will make an application of the proposed method, for example, medical image analysis where the number of data with correct labels is limited.

References

1. Y. LeCun, Y. Bengio and G. Hinton, Deep learning, *Nature*, **521** (2015) 436–444.
2. P. Vincent, H. Larochelle, I. Lajoie, Y. Bengio and P. A. Manzagol, Stacked Denoising Autoencoders: Learning Useful Representations in a Deep Network with a Local Denoising Criterion, *Journal of Machine Learning Research*, **11** (2010) 3371–3408.
3. C. Song, F. Liu, Y. Huang, L. Wang and T. Tan, Autoencoder Based Data Clustering, *CIARP2013, Part I, LNCS 8258* (2013) pp. 117–124.
4. N. Kanopoulos, N. Vasanthavada and R. L. Baker, Design of an image edge detection filter using the Sobel operator. *IEEE Journal of solid-state circuits*, **23**(2) (1988) 358–367.
5. L. Fei-Fei, R. Fergus and P. Perona, One-shot learning of object categories. *IEEE transactions on pattern analysis and machine intelligence*, **28**(4) (2006) 594–611.
6. D. Arthur and Dergei Vassilvitskii, k-means++: The Advantages of Careful Seeding, *Proc. of the 18th annual ACM-SIAM symposium on Discrete algorithm* (2007), pp. 1027–1035
7. J. MacQueen, Some methods for classification and analysis of multivariate observations, *Proc. of the Fifth Berkeley Symposium on Mathematical Statistics and Probability, Volume 1: Statistics*, (1967), pp. 281–297.
8. N. Dalal and B. Triggs, Histograms of oriented gradients for human detection, In *IEEE Computer Society Conference on Computer Vision and Pattern Recognition, 2005*, **1** (2005) pp. 886–893.
9. D. Kingma and J. Ba, Adam: A method for stochastic optimization, *arXiv preprint arXiv:1412.6980* (2014)

Anomaly Detection of Disaster Areas from Satellite Images Using Convolutional Autoencoder and One-class SVM

Kohki Fujita

Graduate School of Sciences and Technology for Innovation, Yamaguchi University, Tokiwadai 2-16-1, Ube, Yamaguchi 755-8611, JAPAN

Shingo Mabu

Graduate School of Sciences and Technology for Innovation, Yamaguchi University, Tokiwadai 2-16-1, Ube, Yamaguchi 755-8611, JAPAN

Takashi Kuremoto

Graduate School of Sciences and Technology for Innovation, Yamaguchi University, Tokiwadai 2-16-1, Ube, Yamaguchi 755-8611, JAPAN

E-mail: {w084vg, mabu, wu}@yamaguchi-u.ac.jp

Abstract

In recent years, research on detecting disaster areas from satellite images has been conducted. When machine learning is used for disaster area detection, a large number of training data are required; however, we cannot obtain so much training data with correct class labels. Therefore, in this research, we propose an anomaly detection system that finds abnormal areas that deviate from normal ones. The proposed method uses a convolutional autoencoder (CAE) and One-class SVM (OCSVM).

1. Introduction

Japan is a country with many natural disasters such as sediment-related disasters, earthquakes, volcanic eruptions, typhoon, etc. compared to foreign countries. In order to make provisions against such natural disasters, it is important to quickly find abnormalities. Therefore, there is a demand for a system to find the anomaly as soon as possible. In recent years, research on detecting disaster areas from satellite images has been conducted^{1,2}. In addition, since machine learning, especially, deep learning³ has shown distinguished abilities in image classification problems, it is expected to apply machine learning to disaster detection problems. When machine learning is used for disaster area detection, a large number of training data is required, however, we cannot obtain so much training data with correct class labels, and especially, it is quite difficult to obtain a large number of

disaster images. Therefore, in this research, we propose an anomaly detection system that finds abnormal areas that deviate from normal ones. The proposed method does not use abnormal (disaster) images for the training, but only uses normal images. The proposed method consists of a convolutional autoencoder (CAE) and One-class Support Vector Machine (OCSVM)⁴. First, CAE executes feature extraction from satellite images with unsupervised learning method. Second, OCSVM is trained using the extracted features of normal areas only. Finally, anomaly detection for the testing images is carried out by the trained OCSVM. The proposed method does not need training data with correct labels of abnormal areas, thus the cost of collecting training data can be reduced.

This paper is organized as follows. Section 2 describes the proposed method including CAE and OC SVM. Section 3 introduces a satellite image data and the

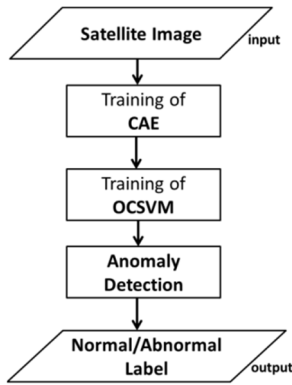


Fig. 1. Flowchart of the proposed method

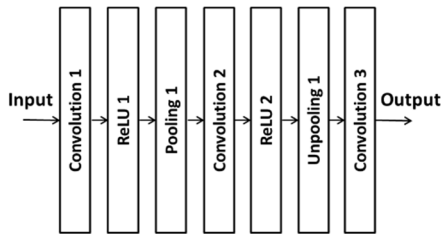


Fig. 2. Convolutional autoencoder (CAE)

simulation conditions and shows the simulation results. Finally, Section 4 is devoted to conclusions.

2. Proposed method

A flowchart of the proposed method is shown in Fig. 1. First, a satellite image is given as an input, convolutional autoencoder (CAE) is trained and feature values are extracted from the input image. Then, One-class SVM (OCSVM) is trained using the feature values of normal areas. Finally, normal and abnormal areas of the testing (unknown) images are detected by the trained OCSVM.

2.1. Convolutional Autoencoder (CAE)

Autoencoder⁵ trains a neural network so that the input and output become the same. In the same way as the general neural network, the weights of the network are learned by stochastic gradient descent. Autoencoders have been used in dimensional reduction and expression learning. Convolutional neural network (CNN)³ is known to have higher performance than the conventional neural networks such as multilayer perceptron (MLP), especially in image and speech recognition. For example,

© The 2018 International Conference on Artificial Life and Robotics (ICAROB2018), Feb. 1-4, B-Con Plaza, Beppu, Oita, Japan

when applying CNN to the recognition of printed characters, CNN can automatically extract important shapes contained in the images such as vertical, horizontal and diagonal lines, etc. in the convolutional layers. By stacking the convolution layers, it becomes possible to identify features in complex pictures and photographs and classify each image. Convolutional autoencoder (CAE) (Fig. 2) is a kind of CNN that is based on unsupervised learning and executes feature extraction from input images. Fig. 2 shows a CAE structure used in this paper that consists of convolution, pooling and unpooling layers. The aim of the learning is the same as autoencoder, that is, the input images are reconstructed in the output layer. In fact, CAE can encode the input images using the layers of Convolution 1 and Pooling 1, and then decode using the layers of Convolution 2, Unpooling 1 and Convolution 3. Therefore, the values obtained at the layer of Pooling 1 can be used as feature values of the input images. The activation function is Rectified Linear Unit (ReLU)⁶.

2.2. One-class SVM (OCSVM)

SVM is originally a classification algorithm for two classes using supervised learning. OCSVM (Fig. 3) is an unsupervised learning algorithm that applies SVM to region discrimination problems to estimate high-density region of data. In other words, OCSVM is an unsupervised outlier detection method. OCSVM is trained using images of normal areas only. Anomaly detection for the testing images is carried out by the trained OCSVM and abnormal images can be detected when they are out of the normal area. OCSVM has a parameter ν that determines the proportion of normal and abnormal areas. For example, when ν is set at a large value as shown in Fig. 4, the normal area becomes small. In this case, only the data that is very near to the center of the normal area is regarded as normal. Conversely, when ν is small, the normal area becomes large and it is easier for the data to belong to the normal area as shown in Fig. 5. Because there is a trade-off between the false positive (abnormal) and false negative (normal), the value of ν should be determined carefully.

3. Simulations

3.1. Simulation conditions

In this paper, a satellite image data of Yagi-Midorii area in Hiroshima, Japan (Fig. 6) are used for the evaluation

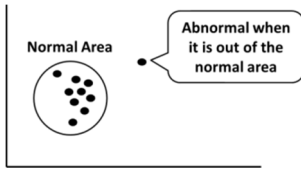


Fig. 3. One-class SVM (OCSVM)

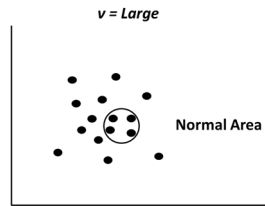


Fig. 4. OCSVM ($v = Large$)

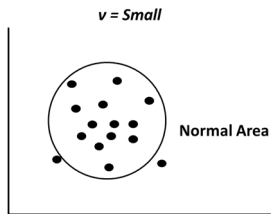
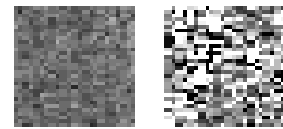


Fig. 5. OCSVM ($v = Small$)

of anomaly detection. In 2014, large-scale landslides occurred in this area due to the torrential rain. The satellite image was taken by Advanced Land Observing Satellite-2 (ALOS-2) that can observe the surface of the earth anytime without being influenced by day/night and weather due to its Synthetic Aperture Rader (SAR)⁷. Fig. 6 shows the preprocessed satellite image (1327×900) and the lines in Fig. 6 are manually traced landslide areas. The upper left shading area is excluded from the image for the simulations because that area is located on the other side of the mountain ridge from ALOS-2 and the obtained signal is weak. This image is divided into 32×32 pixel patch images as shown in Fig. 7 and each patch is regarded as a region of interest (ROI) that is classified by the proposed method. Then, the patch images are divided into training data (Training), testing data 1 (Test 1) and testing data 2 (Test 2). As shown in Fig. 8 and Table 1, "Training" contains 589 images of normal areas, "Test 1" contains 70 images of normal areas (that are not overlapped with Training), and "Test 2" contains 70 images of abnormal (landslide) areas. In the next subsection, the detection ability of the proposed method is evaluated and compared with the method using OCSVM only.



Fig. 6. Satellite image and the area of landslide (Shading area is excluded from the original image)



(a) Normal (b) Abnormal

Fig. 7. Examples of patch images (32×32 pixel)

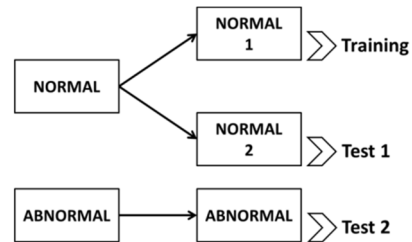


Fig. 8. Division of data for making training and testing data

Table 1. Number of patch images

Training	589
Test1	70
Test2	70

3.2. Simulation results

Table 2 shows the precision of the detection obtained by the proposed method (CAE + OCSVM) where v is set at various values in the range between 0.2 and 0.7. Table 3 shows the precision obtained by OCSVM with the same settings of v . From these tables, we can see that the precision of the proposed method for Test 2 is better than OCSVM only for all the settings of v . When we pay attention to the precision of Test 1 and Test 2 in Table 2, the precision of Test 1 is better when v is smaller, while that of Test 2 is better when v is larger. If more than 80%

Table 2. Precision of CAE + OCSVM (proposed method)

		v					
		0.2	0.3	0.4	0.5	0.6	0.7
Precision [%]	Training (normal)	80.1	70.1	59.9	50.0	40.1	30.0
	Test1 (normal)	78.7	69.7	60.3	45.4	39.6	31.7
	Test2 (abnormal)	65.9	80.3	85.3	89.4	91.4	93.0

Table 3. Precision of OCSVM

		v					
		0.2	0.3	0.4	0.5	0.6	0.7
Precision [%]	Training (normal)	80.0	70.0	60.0	50.0	39.9	30.0
	Test1 (normal)	77.7	70.3	60.4	50.6	35.6	30.3
	Test2 (abnormal)	2.9	11.4	15.7	21.6	38.0	56.0

detection rate of abnormal areas is required, v should be set at 0.3 or more, and if more than 90% is required, v should be set at 0.6 or more. However, the larger v causes larger false positives (over detection); thus, the value of v has to be determined considering the balance between the false positive and false negative rates. Generally, the false negatives should be minimized not to miss the disaster areas; in this sense, larger v is desired.

4. Conclusions

In this study, an anomaly detection algorithm using CAE and OCSVM for satellite images was proposed. CAE automatically extracts features from image data, and OCSVM detects abnormal areas. From the simulation results, the proposed method showed better detection ability of the abnormal areas comparing to the method with OCSVM only. Therefore, the effectiveness of the feature extraction by CAE was clarified. As future work, we will apply trained neural networks using ImageNet⁸ such as VGG and GoogleNet for enhancing the feature extraction ability.

References

1. A. Bormudo and M. Nagai, A remote-sensing-based vegetative technique for flood hazard mitigation of Jadhah basin, India, *Natural Hazards*, **83**(1) (2016) pp. 411–423.
2. N. Tamkuan and M. Nagai, Fusion of Multi-Temporal Interferometric Coherence and Optical Image Data for the 2016 Kumamoto Earthquake Damage Assessment, *ISPRS International Journal of Geo-Information* 2017, **6**(7), 188 (2017).
3. Y. LeCun, Y. Bengio and G. Hinton, Deep learning, *Nature*, **521** (2015) pp. 436–444.
4. L. M. Manevitz and M. Yousef, One-Class SVMs for Document Classification, *Journal of Machine Learning Research*, **2** (2001), pp. 139–154.
5. P. Vincent, H. Larochelle, I. Lajoie, Y. Bengio and P. A. Manzagol, Stacked Denoising Autoencoders: Learning Useful representations in a Deep Network with a Local Denoising Criterion, *Journal of Machine Learning Research*, **11** (2010) pp. 3371–3408.
6. V. Nair and G. E. Hinton, Rectified linear units improve restricted boltzmann machines, *Proc. of the 27th international conference on machine learning*, (2010) pp. 807–814.
7. K. Ouchi, *Principles of Synthetic Aperture Rader for Remote Sensing*, 2nd edn. (Tokyo Denki University Press, 2009).
8. O. Russakovsky, J. Deng, H. Su, J. Krause, S. Satheesh, S. Ma, Z. Huang, A. Karpathy, A. Khosla, M. Bernstein, A. C. Berg and L. Fei-Fei, ImageNet Large Scale Visual Recognition Challenge, *International Journal of Computer Vision*, **115**(3) (2015) pp. 211–252.

Improving EEG-based BCI Neural Networks for Mobile Robot Control by Bayesian Optimization

Takuya Hayakawa and Jun Kobayashi

Department of Systems Design and Informatics, Kyushu Institute of Technology,
Kawazu 680-4, Iizuka, 820-8502, Japan

E-mail: jkoba@ces.kyutech.ac.jp
lab.jkoba.net

Abstract

The aim of this study is to improve classification performance of neural networks as an EEG-based BCI for mobile robot control by means of hyperparameter optimization in training the neural networks. The hyperparameters were intuitively decided in our preceding study. It is expected that the classification performance will improve if you determine the hyperparameters in a more appropriate way. Therefore, the authors have applied Bayesian optimization to training the EEG-based BCI neural networks and achieved the performance improvement.

Keywords: brain computer interface, electroencephalography, neural network, hyperparameters, Bayesian optimization, mobile robot control

1. Introduction

Brain Computer Interface (BCI) is a promising technology that provides means of direct communication through your brain. Since brain activities bring about perception, recognition, and sensory-motor functions in human beings, BCI based on a state of your brain has potential to be applicable to support many kinds of human activities. A lot of studies on BCI have used non-invasive brain activity measurement methods, especially Electroencephalography (EEG) because of its superior time resolution and ease of use. Furthermore, portable and low-cost EEG measurement devices have become readily accessible lately.

EEG-based BCI have already applied for assisting handicapped people and augmenting human capability^{1,2}. R. Single et al. developed a SSVEP-based BCI for controlling a wheelchair using multi-class SVM^{3,4}. J. Meng et al. experimentally investigated a noninvasive BCI for reach and grasp task of robotic arm⁵. In these

studies, the subjects did not directly imagine desired behavior of a controlled object.

As an EEG-based BCI for mobile robot control, the authors are developing a neural network (NN) for EEG signal classification. In our earlier studies⁶⁻⁸, we instructed a subject to imagine an arrow representing a desired behavior of a controlled object with closed eyes for removing visual stimuli unrelated to experiments. In addition to the experiments with the subjects closed their eyes, we conducted an experiment to confirm open eyes influence on constructing an EEG-based BCI NN⁹. Considering practical use of BCI, actually imagining a desired motion of a controlled object with open eyes would be a more appropriate way for controlling a mobile robot. However, none of the constructed NNs achieved practical performance.

The authors conjectured that one of the reasons for the insufficient results was due to hyperparameter settings in training the NNs. The hyperparameters were intuitively set in the preceding studies. It is expected that the classification performance will improve if you

determine the hyperparameters in a more appropriate way. Therefore, the study described in this paper aims at improving the performance of the EEG-based BCI NNs for mobile robot control by hyperparameter optimization. For optimization, the authors adopted Bayesian approach that optimizes hyperparameters for NN training by determining the hyperparameters to be next verified on the basis of results already checked. In consequence, the method can find the optimal hyperparameters efficiently.

In this paper, the authors present experiments introducing Bayesian optimization using the EEG signals recorded in our previous study. The experimental results demonstrated that Bayesian optimization of hyperparameters improved the classification rate of the EEG-based BCI NNs for mobile robot control.

2. EEG Signal Classification Using Stacked Autoencoder

This section describes the structure of the multilayered NNs used in the preceding study⁹. Stacked Autoencoder (SAE) was employed as an EEG-based BCI NN for mobile robot control in the study. SAE is a multilayered NN initialized by stacking encoder layers of pretrained Autoencoder (AE), which is a three layered NN shown in Fig. 1.

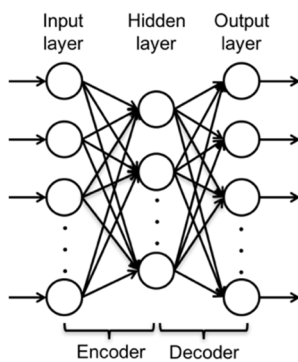


Fig. 1. Autoencoder (AE)

A typical AE has equal-sized input and output layers, and a less-sized hidden layer. The whole of AE is trained in order that it can yield an output signal equal to an input one. Since the hidden layer has less nodes than the input layer, significant information is extracted from the input signal through the encoder part, which is between the input and hidden layers, for restoring the signal through the hidden and output layers; namely AE is a NN for

dimensionality reduction. G. E. Hinton and R. R. Salakhutdinov revealed that AE surpasses Principal Component Analysis (PCA) for dimensionality reduction¹⁰.

SAE is a way to construct a multilayered NN avoiding vanishing gradient in backpropagation. As stated above, an initial multilayered NN is prepared by stacking encoders of pretrained AEs in cascade, and the whole NN is trained again using the same input signals and target ones. The last training is called finetuning.

3. Bayesian Optimization of Hyperparameters

Ahead of training a NN, you must determine some parameters, such as number of layers, number of nodes, learning rate, and so on, which are called hyperparameter. The preceding study has not achieved practical performance of the SAEs for EEG-based BCI probably because the hyperparameters were intuitively determined. Optimization of hyperparameters is an essential process to improve performance of NNs.

One of the methods for hyperparameter optimization is grid search, in which combinations of hyperparameters are uniformly arranged in the form of a grid in a hyperparameter space, all of the parameter combinations are verified. Therefore, the optimal hyperparameters are found with a high probability if the grid arrangement in the hyperparameter space is sufficiently dense. In the case of high dimensional hyperparameter space, however, it becomes difficult to conduct verification in the dense grid within a realistic time due to huge number of hyperparameter combinations. In addition, if some of the hyperparameters have little influence on the performance of the NN, calculation time for grid search is wasted on searching in worthless regions of the hyperparameter space.

J. Bergstra and Y. Bengio have shown empirically and theoretically that random search can find optimal hyperparameters more efficiently than grid search¹¹. Furthermore, J. Snoek et al. have demonstrated that Bayesian optimization for hyperparameter selection of machine learning algorithms found optimal hyperparameters faster, and outperformed hyperparameter selection by a human expert¹². The Bayesian approach determines the hyperparameters to be next examined on the basis of results already verified.

First, Bayesian optimization randomly selects hyperparameters and verifies them. Following that, a

region where the optimal hyperparameters are likely to exist are estimated from the previous results and preferentially verified hyperparameter in the region. The estimation of the region to be examined is made by maximizing an acquisition function that includes probability and expected values under the assumption that a function to be optimized follows Gaussian process. In this research, the authors attempted to optimize the hyperparameter of the SAEs for EEG-based BCI for mobile robot control using GPyOpt¹³, which is a Python library for Bayesian optimization.

4. Results and Discussion

The authors empirically confirmed effects of Bayesian optimization for tuning hyperparameters on improving the classification performance of the SAEs for EEG-based BCI mobile robot control using the EEG signal dataset obtained in the preceding study. Fig. 2 is a schematic diagram of the apparatus for EEG measurement experiments conducted in the preceding study⁹. In the EEG measurement experiments, two different imagining tasks, named "CLOSED-EYES" and "OPEN-EYES", were given to three subjects as follows.

- CLOSED-EYES: close your eyes and imagine a specified arrow
- OPEN-EYES: watching the mobile robot moving to a certain direction, imagine the robot's motion

Refer to Ref. 9 for the other experimental conditions of the EEG measurement, such as experimental procedure, information of the subjects, and so on.

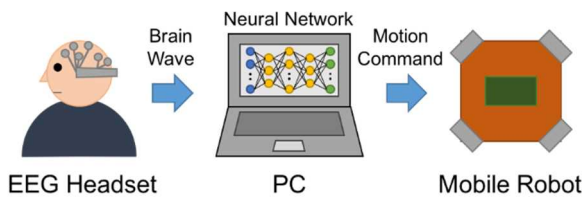


Fig. 2. Experimental apparatus

Chainer¹⁴ (ver. 1.18.0) for implementing the SAEs and GPyOpt¹³ (ver. 1.2.0) for Bayesian Optimization were used in the confirmation experiments. Table 1 shows the computation environment for development and execution of the SAEs. Table 2 describes the hyperparameters optimized in the experiments and their

options; the settings enclosed in parentheses are the options chosen in the preceding study⁹. GPyOpt optimized the hyperparameters so that false recognition rate is minimized. The false recognition rate of each SAE was calculated using 5-fold cross validation.

Table 1. Specifications of computation environment for development and execution of stacked autoencoders

CPU	Intel® Core™ i7-6800K CPU @ 3.40GHz
Memory	16GB (DDR4-2133 4GBx4)
Storage	SSD 240GB + HDD 1TB
GPU	NVIDIA GeForce GTX1060 6GB GDDR5
OS	Ubuntu 16.04 LTS

Table 2. Hyperparameters and options

Hyperparameter	Options (setting value in Ref. 9)
Number of hidden layers	1 ~ 3 (3)
Number of nodes in 1st hidden layer	250 or 300 (250)
Number of nodes in 2nd hidden layer	150 or 200 (150)
Number of nodes in 3rd hidden layer	50 or 100 (100)
Iteration of pretraining each AE (epoch)	1000 or 2000 (1000)
Iteration of finetuning (epoch)	5000 or 10000 (10000)
Dropout 50% in pretraining AEs	OFF or ON (ON)
Dropout 50% in finetuning	OFF or ON (ON)

Table 3 and Table 4 show the results obtained in the preceding study⁹. Table 5 and Table 6 report the classification rate percentages of the SAEs calculated in this study with Bayesian optimization. Compared the updated results with the previous ones, it is indicated that we could improve the performance of the SAEs trained with the hyperparameters optimized by Bayesian approach. However, the options of the hyperparameters given to the optimization algorithm were very restricted. Therefore, we would consider further improvement to be possible by revising the hyperparameter options more carefully.

5. Conclusion

This paper presented the performance improvement of the EEG-based BCI neural networks for mobile robot control proposed in the preceding study. The authors

introduced Bayesian optimization in order to find the better hyperparameters for training the neural networks and then experimentally confirmed the expected effect of the method. The authors will design the appropriate options of hyperparameters that considerably ameliorate the classification performance of the EEG-based BCI neural networks for mobile robot control.

Table 3. Classification rate percentages of SAEs trained using 120 samples recorded in CLOSED_EYES without Bayesian optimization⁹

Subject	1 st day	2 nd day	3 rd day	4 th day	5 th day	Ave.
A	50.00	54.17	58.33	73.33	85.83	64.33
B	47.50	60.83	61.67	55.83	48.33	54.83
C	31.67	40.00	45.00	66.67	31.67	43.00

Table 4. Classification rate percentages of SAEs trained using 120 samples recorded in OPEN_EYES without Bayesian optimization⁹

Subject	1 st day	2 nd day	3 rd day	4 th day	5 th day	Ave.
A	95.00	45.00	52.50	31.67	67.50	58.33
B	60.00	49.17	53.33	25.83	43.33	46.33
C	54.17	30.00	38.33	59.17	25.00	41.33

Table 5. Classification rate percentages of SAEs trained using 120 samples recorded in CLOSED_EYES with Bayesian optimization

Subject	1 st day	2 nd day	3 rd day	4 th day	5 th day	Ave.
A	55.00	57.50	66.67	79.17	92.50	70.17
B	50.00	70.00	53.33	66.67	54.17	58.83
C	44.17	49.17	51.77	76.67	33.33	51.02

Table 6. Classification rate percentages of SAEs trained using 120 samples recorded in OPEN_EYES with Bayesian optimization

Subject	1 st day	2 nd day	3 rd day	4 th day	5 th day	Ave.
A	95.83	48.33	45.83	41.67	75.00	61.33
B	66.67	57.50	60.83	33.33	43.33	52.33
C	60.00	40.00	49.17	76.67	38.33	52.83

References

1. A. Kübler et al., Patients with ALS can use sensorimotor rhythms to operate a brain-computer interface, *Neurology* **64**(10) (2005) 1775–1777.
2. T. P. Luu et al., Gait adaptation to visual kinematic perturbations using a real-time closed-loop brain-computer interface to a virtual reality avatar, *J. Neural Engineering* **13**(3) (2016).
3. R. Singla et al., Influence of stimuli color on steady-state visual evoked potentials based BCI wheelchair control, *J. Biomedical Science and Engineering* **6**(11) (2013) 1050–1055.
4. R. Singla et al., Influence of stimuli color in SSVEP-based BCI wheelchair control using support vector machines, *J. Medical Engineering & Technology* **38**(3) (2014) 125–134.
5. J. Meng et al., Noninvasive Electroencephalogram Based Control of a Robotic Arm for Reach and Grasp Tasks, *Scientific Reports* **6**(38565) (2016).
6. K. Tomonaga et al., Experiments on classification of electroencephalography (EEG) signals in imagination of direction using a wireless portable EEG headset, in *Proc. of Int. Conf. on Control, Automation and Systems* (Busan, South Korea, 2015), pp. 1805–1810.
7. S. Wakamizu et al., Experiments on Neural Networks with Different Configurations for Electroencephalography (EEG) Signal Pattern Classifications in Imagination of Direction, in *Proc. of IEEE Int. Conf. on Control System, Computing and Engineering* (Penang, Malaysia, 2015), pp. 477–481.
8. K. Tomonaga et al., Experiments on Classification of Electroencephalography (EEG) Signals in Imagination of Direction using Stacked Autoencoder, *J. Robotics, Networking and Artificial Life* **4**(2) (2017) 124–128.
9. T. Hayakawa and J. Kobayashi, Open Eyes Influence on Electroencephalography Signals for Constructing Neural Network Classifiers as Mobile Robot Control Brain-Computer Interface, in *Proc. of Int. Conf. on Advanced Mechatronic Systems* (Xiamen, China, 2017), ThuM01-03.
10. G. E. Hinton and R. R. Salakhutdinov, Reducing the Dimensionality of Data with Neural Networks, *Science* **313** (2006), pp. 504–507.
11. J. Bergstra and Y. Bengio, Random Search for Hyper-Parameter Optimization, *J. Machine Learning Research* **13** (2012) 281–305.
12. J. Snoek et al., Practical Bayesian Optimization of Machine Learning Algorithms, in *Proc. of Int. Conf. on Neural Information Processing Systems* (Lake Tahoe, Nevada, 2012), pp. 2951–2959.
13. GPyOpt: A Bayesian Optimization framework in Python, <http://github.com/SheffieldML/GPyOpt>, 2016.
14. Chainer: A Powerful, Flexible, and Intuitive Framework for Neural Networks, <https://chainer.org/>.

Selective synchronization of the coupled bifurcating neurons for phase shift of background oscillation

Akihiro Yamaguchi*, Yutaka Yamaguti

Department of Information and Systems Engineering, Fukuoka Institute of Technology,
3-30-1 Wajiro-higashi, Higashi-ku, Fukuoka, 811-0116, JAPAN

Masao Kubo

Department of Computer Science, National Defense Academy of Japan,
1-10-20 Hashirimizu, Yokosuka, Kanagawa, 239-8686, JAPAN
E-mail: *aki@fit.ac.jp

Abstract

Synchronization in the coupled bifurcating neurons was studied in the view point of the selective formation of cell assembly. The bifurcating neuron is a simple chaotic neuron that exhibits chaotic inter-spike interval dynamic by adding the sinusoidal background oscillation. In this research, we introduce the phase shift of the background oscillation and the several types of phase response to the input spike sequence. The coupled 16 bifurcating neurons with complete bidirectional coupling was numerically simulated and their synchronized behaviors were analyzed. As a result, the formation of chaotically synchronized cell assemblies for the phase shift value were observed.

Keywords: chaotic synchronization, neural coding, bifurcating neuron, binding information

1. Introduction

The synchronized neural activity is regarded to have an important role in the neural information coding and the brain information processing¹. For The correlated firing among neurons was observed in the visual information processing in the brain^{2,3}. In the view point of neural coding, authors have studied the chaotic synchronization of neural spike response and its application to the segmentation of input image⁴, the feature linking of visual image of moving objects⁵, and the decomposition of superimposed chaotic spike sequences⁶. In order to represent multiple information by the chaotic synchronized cell assemblies, coexistence of such synchronized assemblies is necessary.

In this study, we construct the network of the bifurcating neuron⁷ with complete bidirectional coupling and design the coupling model to achieve selective chaotic synchronization based on the phase response. In

Sec. 2 and 3, we explain the network of the bifurcating neuron and the coupling model. In Sec. 4, the numerical simulation is performed to examine the selective synchronization for the phase shift of the background oscillation. We summarize results in Sec. 5.

2. Network model of the bifurcating neuron

The bifurcating neuron was introduced by Lee and Farhat⁷. In our previous research⁶, we defined the bifurcating neuron as a form of the spike response model⁸ to extend the coupling term based on the phase response.

In the following sections, we explain the extended bifurcating neuron model and its network. Let the network of bifurcating neurons consist of N neurons, and $n^{(i)}$ be the i -th neuron. The dynamics of the i -th bifurcating neuron is defined as follows:

$$u^{(i)}(t) = u_{rest} + \eta^{(i)}(t) + \xi_+^{(i)}(t) + \xi_-^{(i)}(t) + \nu^{(i)}, \quad (1)$$

where $u^{(i)}$, u_{rest} , $\eta^{(i)}$, $\xi_+^{(i)}$, $\xi_-^{(i)}$, and $v^{(i)}$ denotes the internal potential of $n^{(i)}$, the resting potential, the kernel function of internal dynamics, the positive coupling term, the negative coupling term, and the external noise, respectively. The coupling terms are described in the next section.

The kernel function $\eta^{(i)}$ is defined as

$$\eta^{(i)}(t) = \alpha (t - t_{last}^{(i)}) + \eta_0(t_{last}^{(i)}, \phi^{(i)}); \quad (2)$$

$$\eta_0(t, \phi) = A_\eta \sin(2\pi\omega t + \phi), \quad (3)$$

where α is the time constant of the kernel $\eta^{(i)}$, and $t_{last}^{(i)}$ is the last firing time of $n^{(i)}$. The internal potential $u^{(i)}$ is linearly increasing by the kernel $\eta^{(i)}$. The neuron $n^{(i)}$ is firing when $u^{(i)}$ exceeds the threshold θ , and then $u^{(i)}$ is reset to the initial potential given by the back ground oscillation $\eta_0(t, \phi)$. The constants A_η , ω , and $\phi^{(i)}$ is the amplitude, the frequency, and the phase shift value of background oscillation, respectively. The dynamics of the single neuron without coupling term is the same with the original bifurcating neuron. The single neuron

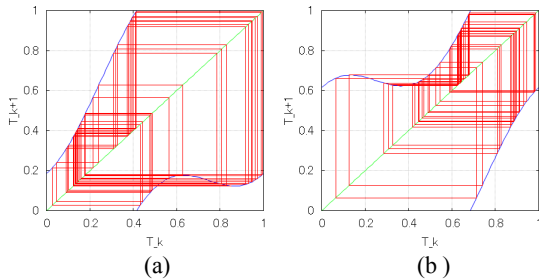


Fig. 1. Examples of the chaotic one dimensional map of the phase of the single bifurcating neuron with the phase shift (a) $\phi = \pi/2$ and (b) $\phi = 3\pi/2$.

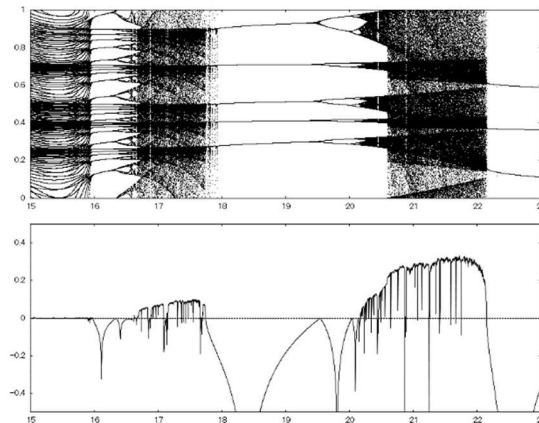


Fig. 2. The bifurcation diagram and the Lyapunov exponents of the single bifurcating neuron without coupling.

without coupling exhibits various chaotic dynamics of the inter-spike interval and the phase of the next firing time is determined by the chaotic one dimensional map of the phase of the last firing time^{6,7}. The shape of this chaotic map is determined by the phase shift value $\phi^{(i)}$. Examples of this chaotic map is shown in Fig. 1. Furthermore, the bifurcation diagram and the Lyapunov exponents of this map are also shown in Fig. 2.

3. Coupling model with phase response

Let the set $S^{(k)} = \{t_0^{(k)}, t_1^{(k)}, t_2^{(k)}, \dots\}$ be a set of firing time of the neuron $n^{(k)}$, where $t_j^{(k)}$ is the firing time of j -th spike of $n^{(k)}$. The set of firing time of the input spikes to $n^{(i)}$ is denoted as $\Gamma^{(i)}$. For the bidirectional complete coupling, $\Gamma^{(i)}$ is defined as

$$\Gamma^{(i)} = \bigcup_{0 \leq k \neq i < N} S^{(k)}. \quad (4)$$

The coupling term $\xi_+^{(i)}$ and $\xi_-^{(i)}$ in Eq. (1) are the summation of the positive phase response $\varepsilon_+^{(i)}$ and the negative $\varepsilon_-^{(i)}$ such that

$$\xi_{\pm}^{(i)}(t) = \sum_{s \in \Gamma^{(i)}, t_{last}^{(i)} \leq s < t} \varepsilon_{\pm}^{(i)}(s). \quad (5)$$

Simple phase response is constant value such that

$$\varepsilon_{\pm}^{(i)}(s) = \pm\beta_{\pm}, \quad (6)$$

where β_+ and β_- are non-negative coupling constant. The next firing time is hastened by the positive response and delayed by the negative response. We call the coupling with these simple responses the constant positive coupling and the constant negative coupling, respectively.

We designed the phase response in order to strengthen the chaotic synchronization between coupled neurons with the same phase shift value⁶. The positive phase response based on the predicted next firing time is defined as

$$\varepsilon_+^{(i)}(s) = \begin{cases} 0 & s < \hat{t}_{next}^{(i)} - \Delta_\varepsilon \\ +\beta_+ & \hat{t}_{next}^{(i)} - \Delta_\varepsilon \leq s < \hat{t}_{next}^{(i)} \\ 0 & \hat{t}_{next}^{(i)} \leq s \end{cases} \quad (7)$$

where $\hat{t}_{next}^{(i)}$ is the predicted next firing time of $n^{(i)}$ such that

$$\hat{t}_{next}^{(i)} = t + \frac{\theta - u(t)}{\alpha}. \quad (8)$$

We call the coupling with this response the adaptive positive coupling. The negative phase response based on the last firing time is defined as

$$\varepsilon_{\pm}^{(i)}(s) = \begin{cases} 0 & s \leq t_{last}^{(i)} \\ -\beta_{\pm} \frac{s - t_{last}^{(i)}}{\Delta_{\varepsilon}} & t_{last}^{(i)} < s \leq t_{last}^{(i)} + \Delta_{\varepsilon} \\ 0 & t_{last}^{(i)} + \Delta_{\varepsilon} < s \end{cases} \quad (9)$$

We call the coupling with this response the adaptive negative coupling.

If the time s is within the range Δ_{ε} from the predicted next firing time $\hat{t}_{next}^{(i)}$, then the phase response is positive to hasten the next firing time. Otherwise, if the time s is within the range Δ_{ε} from the last firing time $t_{last}^{(i)}$, then the phase response is negative to delay the next firing time. By using these phase response (Eq. (7) and Eq. (9)), the decomposition of the superimposed chaotic spike sequences with the different phase shift values is possible⁶.

4. Numerical experiments

4.1. Experimental setting

In this article, we numerically simulate the network of the 16 bifurcating neurons to analyze the selective synchronization to the same phase shift value for complete bidirectional coupling. The different 4 phase shift values are assigned as follows:

$$\phi^{(i)} = \Delta_{\phi} \lfloor i/4 \rfloor \quad (i = 0, \dots, 15), \quad (10)$$

where $0 < \Delta_{\phi} \leq \frac{\pi}{2}$ is the difference of the assigned phase shift value. In this setting, each 4 neurons have the same phase shift value. We examine the selective synchronization among each 4 neurons with the same phase shift value. Numerical simulation is performed with the following setting: $\alpha = 100$, $\theta = -30$, $u_{rest} = -70$, $A_{\eta} = 21.5$, $\omega = 1$, $\beta_{-} = \beta_{+} = 2.1$, $\Delta_{\varepsilon} = 0.05$, and $\Delta_{\phi} = \pi/2$.

4.2. Characteristics of synchronization

As an index of the synchronization between two spike sequences, the synchronization ratio is defined as

$$SR(S^{(i)}; S^{(k)}) = \frac{\#\{t^i \mid |t^i - t^k| \leq \Delta_s, t^i \in S^{(i)}, t^k \in S^{(k)}\}}{\#S^{(k)}}, \quad (11)$$

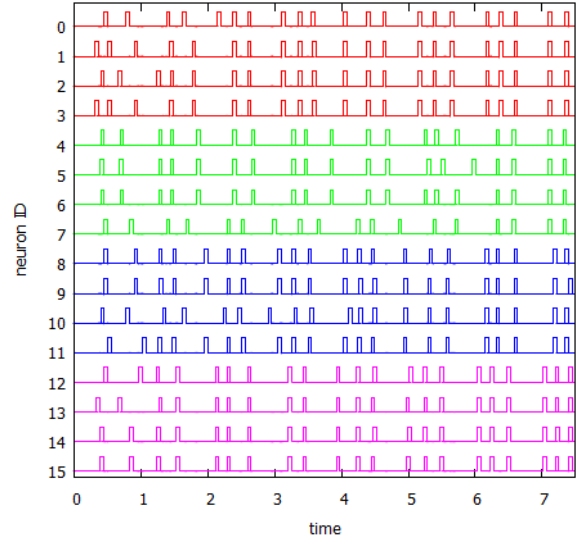


Fig. 3. An example of the generated spike sequences for the network with the adaptive positive and negative coupling.

where $\#(\cdot)$ denotes the number of elements and Δ_s is the time resolution of the firing time. Furthermore, in order to characterize the assembly formation of the synchronized cluster of neurons, we define the average synchronization ratio for the neurons with the same phase shift value such as

$$ASR_{\phi^{(i)}=\phi^{(k)}} = \sum_{\substack{0 \leq i \neq k \leq 15, \\ \phi^{(i)}=\phi^{(k)}}} SR(S^{(i)}; S^{(k)})/48, \quad (12)$$

and the average synchronization ratio for the neurons with the different phase shift value such as

$$ASR_{\phi^{(i)} \neq \phi^{(k)}} = \sum_{\substack{0 \leq i \neq k \leq 15, \\ \phi^{(i)} \neq \phi^{(k)}}} SR(S^{(i)}; S^{(k)})/192. \quad (13)$$

4.3. Experimental results

As a result of the numerical simulation, an example of the generated spike sequences are shown in Fig. 3, where the phase response coupling is the adaptive positive and negative one. The generated spikes were synchronized for each 4 neurons with the same phase shift value, and the selective synchronization for the same phase shift value was observed. In order to analyze the effect of coupling, we numerically simulated the network and evaluated the synchronization ratio and the averaged one for the 5 types of the coupling defined in Sec.3. Results are shown in Fig. 4 and Table 1. These results indicate

that the selective synchronization was observed for the coupling types (c) and (e), and the synchronization ratio is higher than 90% for the neurons with the same phase shift value and lower for different ones.

5. Conclusion

The network of the bifurcating neuron was constructed and the formation of the chaotically synchronized cell assemblies was examined for the several types of coupling model. As a result, the chaotically synchronized cell assemblies was observed for the adaptive positive coupling of the phase response, where the neurons which have the same phase shift value were selectively synchronized. This result might be indicate the possibility of binding information based on the phase shift value of the background oscillation. To realize such information coding is one of our future works.

References

1. Fuji, H., Ito, H., Aihara, K., Ichinose, N., and Tsukada, M., Dynamical cell assembly hypothesis - Theoretical possibility of spatio-temporal coding in the cortex, *Neural Networks*, Vol.9, No.8, pp.1303-1350, 1996.
2. Gray, C.M., Koenig, P., Engel, A. K., and Singer, W., Oscillatory responses in cat visual cortex exhibit inter-columnar synchronization which reflects global stimulus properties, *Nature*, 338, pp.334-337, 1989.
3. Eckhorn, R., Reitboeck, H.J., Arndt, M., Dicke, P., Feature linking via stimulus-evoked oscillations: experimental results from cat visual cortex and functional implications from a network model, *International Joint Conference on Neural Networks*, pp. 723-730, 1989.
4. M. Fujiwara, A. Yamaguchi, and M. Kubo, Synchronized Response to Grayscale Image Inputs in Chaotic Cellular Neural Network, *J. Robotics, Networking and Artificial Life*, Vol.2, No.1, pp. 26-29, 2016.
5. A. Yamaguchi, S. Arakane, and M. Kubo, Feature Linking using Synchronized Responses in Chaotic Cellar Neural Networks for Visual Stimulus of Moving Objects, *J. Robotics, Networking and Artificial Life*, Vol.2, No.4, pp. 230-233, 2016.
6. A. Yamaguchi, Y. Yamaguti, and M. Kubo, Decomposition of superimposed chaotic spike sequences by using the bifurcating neuron, to appear in *Advances in cognitive neurodynamics (VI)*, Springer, 2018.
7. Lee G., and Farhat, N.H., The Bifurcating Neuron Network 1, *Neural Networks*, Vol. 14, pp. 115-131, 2001.
8. Gerstner, W., and Kistler, W., *Spiking Neuron Models: Single Neurons Populations Plasticity*, Cambridge University Press, 2002.

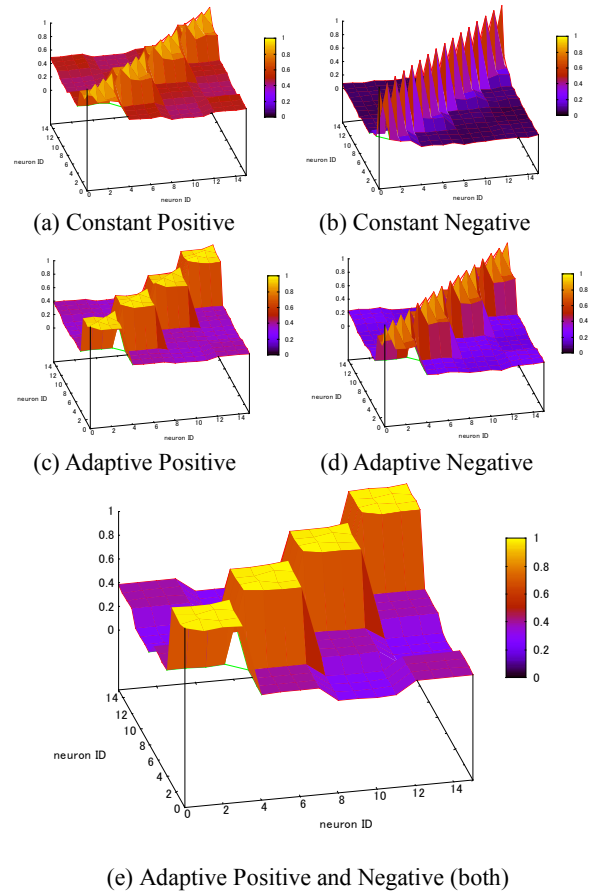


Fig. 4. The synchronization ratio between two neurons for the coupling type (a) constant positive, (b) constant negative, (c) adaptive positive, (d) adaptive negative, and (e) both of adaptive positive and negative, respectively.

Table 1. Average Synchronization Ratio

Coupling type	$ASR_{\phi^{(i)}=\phi^{(k)}}$	$ASR_{\phi^{(i)}\neq\phi^{(k)}}$
(a) Constant Positive	0.7861	0.4766
(b) Constant Negative	0.1819	0.0638
(c) Adaptive Positive	0.9414	0.3694
(d) Adaptive Negative	0.6520	0.2057
(e) Adaptive Positive and Negative	0.9723	0.3519

Review on computational techniques in solving aircraft landing problem

Aminurafiuiddin Zulkifli, Nor Azlina Ab. Aziz, Nor Hidayati Abdul Aziz
Faculty of Engineering and Technology, Multimedia University, 75450 Melaka, Malaysia

Zuwairie Ibrahim
Faculty of Electrical and Electronics Engineering, Universiti Malaysia Pahang, Pekan, 26600 Pahang, Malaysia

Norrima Mokhtar
Faculty of Engineering, University of Malaya, 50603 Kuala Lumpur, Malaysia

Email: aminurafiuiddin@gmail.com, azlina.aziz@mmu.edu.my, hidayati.aziz@mmu.edu.my, zuwairie@ump.edu.my, norrimamokhtar@um.edu.my

Abstract

The problem of sequencing and scheduling arriving aircraft landing is commonly known as aircraft landing problem (ALP). This problem, due to various constraints such as the number of arriving aircrafts, the number of runways, the mode of runway operation, the type of arriving aircrafts, the minimum separation between each arriving aircraft, and the weather condition, is considered to be a NP-hard problem. Therefore, it is almost impossible to compute every possible solution and computational intelligence methods had been adopted to solve ALP. In this paper, we review the computational intelligence techniques used in ALP. The main techniques include the evolutionary algorithms namely; genetic algorithm, genetic programming, scatter search and bionomic algorithm, the swarm intelligence algorithms like particle swarm optimization and ant colony optimization and also other methods such as the constrained position shifting and dynamic programming.

Keywords— aircraft landing problem; computational intelligence; evolutionary algorithms; swarm intelligence; scheduling; runway operation

1. Introduction

Over the years, many studies had been conducted in the field of air traffic control. Since the aviation industry is expanding, a need for closer attention to this field has arisen. The complexity of air traffic operation is motivated by the increase in air traffic volume every year. In Europe and US, increase in air traffic demand is expected to double in the next 15 years [1]. In Malaysia, according to Malaysian Ministry of Transport an increase of 2.7% was reported in term of total commercial aircraft movements handled by Malaysian airport in 2015 compared to 2014 [2].

One of the important task in air traffic control is managing the air traffic operations for aircraft take-off and landing. This task is handled by air traffic controllers. The controllers determine which aircraft is taking off from, or landing on, available runway at airports, subject to operational constraints. To handle the landing and taking-off of an aircraft, is a very challenging process. It is highly related to safety, efficiency, robustness, and competitiveness issues. The common practice is to tackle the task using first come first serve (FCFS) basis. This method may not be efficient but it is certainly the simplest way to manage the operation.

However, with rapid development in computing, researchers have been developing multiple ways to aid the process of scheduling and sequencing aircrafts. This include the adaptation of computational intelligence. In this paper, we focus on the application of computational intelligence in solving the problem of sequencing and scheduling landing aircrafts, which is commonly known as aircraft landing problem (ALP).

The remainder of this paper is organized as follows. Basic concept of aircraft landing problem is briefly explained in section II. Section III describes the computational techniques used in order to optimize ALP. Section IV concludes this work.

2. Aircraft Landing Problem

ALP can be defined as a process of sequencing and scheduling the arriving aircrafts. Nowadays with airports operating with more than one runways, ALP can be viewed as two objectives problem, which are sequencing the optimal landing order of the arriving flights and scheduling a runway for each arriving aircraft [3]. In [1], the objectives are listed as; a) maximizing runway throughput, b) minimizing the approach time of aircraft before landing, c) minimizing the

arrival delay, d) minimizing air traffic controller's workload. Thus, one of the challenges for the researchers in this field is to develop a solution capable of dealing with a variety of objectives. This raises the issue of which objective function to adopt. By far ALP's objective function causes the most discussion among researchers. Arguments can convincingly be made for many different objective functions. Different users will, for perfectly legitimate reasons, use different objective functions [4].

ALP is a dynamic problem as the controller needs to operate in real-time. The controller must generate an updated schedule for the set of arriving aircraft to be sequenced and scheduled both periodically and in response to aperiodic events, while the length of the periodic cycle is related to the basic radar update time interval, which is 4–12 seconds long [5].

In most studies, the common structure of ALP (static case) has n number of landing aircrafts, which the aircrafts denoted as $i = 1, 2, \dots, n$, and the estimated earliest landing time is E , and the latest landing time is L . Therefore, the time window for an aircraft can be bounded within $[E(i), L(i)]$. Controller will assign a target landing time for every landing aircraft, T , and it must be in between E and L , hence, $E(i) \leq T(i) \leq L(i)$. The controller must also obey the minimum separation time constraint between leading aircraft and trailing aircraft. This is a mandatory safety measure to avoid complications like the wake turbulence and aircraft collision.

2.1 Problem modelling

Psarafitis [6] models ALP into a simple version. He sums up the landing times of the arriving aircraft as cost/delay, which is described as Total Passenger Delay (TPD) while the throughput is measured based on the landing time of the last aircraft in the sequence, described as Last Landing Time (LLT). The objective is to minimize both TPD and LLT. Psarafitis also stated that aircraft sequencing problem is the same, as the NP-hard Travelling Salesman Problem (TSP), where, the cost of the graph represents the landing cost and the route represents the aircraft landing sequence. However, Psarafitis did not consider the aircraft latest landing, L , which allows the aircraft to land at any given time.

On the other hand, Bayen et al. [7] focuses on formulating holding time using two approaches. The scheduling process is optimized when the holding time is minimized and, therefore, minimize the sum of arrival time. They formulated ALP as a single machine job scheduling problem. However, they consider that all arriving flights in one large class. Thus, the required separation between landings is independent of the aircraft type.

Cheng et al. [8] emphasize on runway assignment for ALP. They discuss sequencing and scheduling a number of arrivals to a number of runways. The paper focuses on static case of ALP. The data set used contains the estimated time of arrivals (ETA). The aircraft performances and the flight pattern are also taken into consideration. The main objective is to minimize the delay, which is the difference between the scheduled time of arrival (STA) and the earliest ETA in all the runways for an aircraft. Hansen [9] improves the implementation made by Cheng with an experiment on larger set of aircrafts made up to

the possible realistic level. The same formulation is also adopted in various work [10],[11],[12],[13].

Another study regarding to the static case of ALP was carried by Krishnamoorthy et al. [14] and then improved by Beasley et al. [4]. The study comprises both single-runway and multiple-runway cases. The objective is to minimize the total cost, where the cost is linearly related to deviation from target landing time for landing planes. Figure 1 shows how the cost of aircraft landing is introduced in the paper. Although the cost function shown is nonlinear, it can be linearized by decomposing the two linear portions and formulate the problem with a linear objective function. The paper includes various mathematical constraints to manifest every possible condition of ALP. This study has been cited by many ALP researchers as it presented a general description of the model, goals, and mathematical formulation of the landing planning for one or more runways [15], [16], [17], [18],[19],[20].

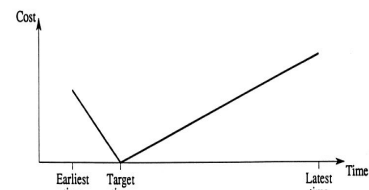


Figure 1. Cost variation in time window during flight

3. Computational Intelligence on ALP

This section reviews the literature related to ALP. The subsections are organized according to the computational intelligence method used.

3.1 Evolutionary algorithms

Genetic algorithm (GA) is a famous evolutionary algorithm. It has been used in various problems including ALP. In previous work of Cheng et al. [8] the runway assignment is carried using genetic search algorithm. Four schemes of genetic search were used to solve a simple scenario involving 12 flights in 3 runways. The result shows application of genetic search gives an impressive result. The method is later improved by Hansen [9] with a larger data set, which is nearer to the realistic case. Hansen proposed the improved version of genetic algorithm called Genetic Programming (GP). GP shows a better performance than GA when dealing with larger set of arriving aircrafts. Liu [11] compared GA with newly developed Genetic Local Search (GLS), which is an extension of GA in solving ALP. Liu uses Hansen's case as well to experiment with GLS and it is proven to be more efficient in terms of both optimality and time cost than GA.

Wang et al [3] adopted GA to solve ALP on parallel runways, which include independent approach and relevant approach. It is tested on 40 arriving flights.

Abela et al. [14] discussed two different solutions for ALP which are using GA and branch-and-bound. Both approaches are tested with a data set and GA is proven to be effective in small problems. Hu and Di Paolo [13] have integrated GA with receding horizon (RH) strategy to tackle ALP. The chromosomes in GA are constructed using the arriving order and/or arriving time of each aircraft.

Pinol and Beasley [15] introduce a hybrid method using another evolutionary algorithms, scatter search and bionomic algorithm for ALP. Both methods are combined and used for problem instances up to 500 aircrafts and 5 runways. In linear ALP cases, scatter search performs better than bionomic algorithm while in non-linear cases, bionomic algorithm performs better than scatter search. These methods, are flexible to be adapted and able to change objective between linear and non-linear ALP cases.

3.2 Swarm Intelligences

Other than evolutionary algorithms, swarm intelligence algorithms are also used in solving ALP. Among the Swarm intelligence algorithms used are particle swarm optimization (PSO), ant colony optimization (ACO) and gravitational search algorithm (GSA).

A PSO hybridized with local search (LS) on rolling horizon (RH) is proposed by Girish [21] to minimize the deviation cost of aircraft landings by using Beasley's formulations [4]. It is then compared with another two PSO variants. The RH framework with hybrid PSO-LS is proven to be more efficient and has shorter computational time.

Benceikh [19] uses ACO to solve ALP and the Beasley's formulation is improved by incorporating dynamic cases, for example, flight cancellation and runway closing. They also improved ACO with more robust heuristic named Improved ACO (IACO) to reduce the penalty cost.

Kazem et al [10] introduce GSA in their paper for the purpose of solving ALP. GSA is a swarm intelligence algorithm which was inspired by Newton's law of gravity [22]. Firstly, random sequence of aircrafts with their allocated runway are generated as initial solutions and each solution's fitness is computed. Using the Newton's law of gravity, each solution is improved on the next iteration. The study uses Hansen's data set and compared with genetic search algorithm, GA, scatter search and bionomic algorithm, and GSA is found to provide better solution in shorter amount of time.

3.3 Other techniques

Dear [23] describes ALP as a dynamic problem and introduced the constrained position shifting (CPS) method. CPS works as the sequencing mechanism where the order of landing aircraft is only shifted by limited k positions from its FCFS position. Psaraftis [6] further improved Dear's study using backward dynamic programming algorithms that use the number of aircraft from each classes that has not yet been scheduled to land and the class of the last aircraft to land as the state variables. His method is also adaptable using CPS without increasing the time complexity. However, Psaraftis method assumes there is no landing restriction which means, the aircraft can land at any time. Balakrishnan et al [24] develop the work of Psaraftis's CPS by simultaneously handling precedence constraints, landing restriction and CPS operational constraints, which reduces the computational time and make it easy to be adopted in real-time for both static and dynamic cases. The updated work on CPS by Rodriguez-Diaz et al [25] show how CPS is adapted on single mixed-mode runway operation. They use simulated annealing (SA) to

experiment with CPS on a very large data set. The data considered is up to 200 flights and 2000 instances. The study emphasizes on how the focus of research should include mixed-mode operation in their problem modelling.

Beasley et al. [4] on the other hand approach the problem from a different perspective using mixed-integer zero-one formulation which is adopted using a basic tree search strengthen with linear programming (LP) relaxation. A scenario of 50 aircraft and four runways is tested and the result showed the LP-based tree search are able to work with various constraints that commonly encountered in practice. However, since the problem is NP-hard, it is likely for the computation time to grow exponentially with the number of flights.

Bayen et al. [7] use dynamic programming (DP) and linear programming relaxation (LP) with rounding approach. DP approaches have the performance ratio of 5 for the sum of arrival times of all aircraft and LP relaxation with rounding has the performance ratio of 3 for the landing time of the last aircraft.

Lieder et al. [26] introduce DP in solving ALP with different aircraft classes on multiple runways with positive target landing times and limited time windows. A new dominance criterion is developed order to improve the performance of DP approach. The criterion based on the formulation by Briskorn et al [27].

Table 1 comprises all the techniques discussed on this section. The techniques are tabulated according to the methodology, the formulation and the instances used in their respective studies.

4. Conclusions

This paper provides an overview on how computational intelligence is used in ALP. From the review, it can be seen that computational intelligence techniques are popular in solving ALP. The problem modelling of ALP is also observed not to be uniform across the literature. For example, in some literatures, ALP is viewed as static case while other view it as dynamic case. For our future work, we will investigate on how to solve ALP using computational intelligence approach that are more robust and dynamic similar to the real problems faced by air traffic controllers.

Acknowledgement

This research is funded by the Fundamental Research Grant Scheme (FRGS/1/2015/ICT02/MMU/03/1), which is awarded by Ministry of Higher Education Malaysia to Multimedia University.

References

- [1] J. A. Bennell, M. Mesgarpour, and C. N. Potts, "Airport runway scheduling," *Ann. Oper. Res.*, vol. 204, no. 1, pp. 249–270, 2013.
- [2] M. of Transport, "Transport Statistics Malaysia 2015," 2015.
- [3] L. L. Wang and Q. L. Gu, "Optimization model for sequencing arrival flights on parallel runways," *Proc. - 2014 Int. Conf. Inf. Sci. Electron. Electr. Eng. ISEEE 2014*, vol. 1, no. 61179042, pp. 489–492, 2014.
- [4] J. E. Beasley, M. Krishnamoorthy, Y. M. Sharaiha, and D. Abramson, "Scheduling Aircraft Landings — The Static Case,"

Transp. Sci., vol. 34, no. 2, pp. 180–197, 2000.

[5] H. Erzberger and E. Itoh, “Design Principles and Algorithms for Air Traffic Arrival Scheduling,” no. May, pp. NASA/TM—2014–218302 Design, 2014.

[6] H. N. Psaraftis, “A Dynamic Programming Approach to The Aircraft Sequencing Problem,” 1978.

[7] A. M. Bayen and C. J. Tomlin, “An Approximation Algorithm for Scheduling Aircraft with Holding Time †,” pp. 2760–2767, 2004.

[8] V. H. L. Cheng, L. S. Crawford, and P. K. Menon, “Air traffic control using genetic search techniques,” *Proc. 1999 IEEE Int. Conf. Control Appl. (Cat. No.99CH36328)*, vol. 1, pp. 249–254, 1999.

[9] J. V. Hansen, “Genetic search methods in air traffic control,” *Comput. Oper. Res.*, vol. 31, no. 3, pp. 445–459, 2004.

[10] K. Dastgerdi, N. Mehrshad, and M. Farshad, “A new intelligent approach for air traffic control using gravitational search algorithm,” *Sadhana*, vol. 41, no. 2, pp. 183–191, 2016.

[11] Y. H. Liu, “A genetic local search algorithm with a threshold accepting mechanism for solving the runway dependent aircraft landing problem,” *Optim. Lett.*, vol. 5, no. 2, pp. 229–245, 2011.

[12] A. Salehipour, L. M. Naeni, and H. Kazemipour, “Scheduling aircraft landings by applying a variable neighborhood descent algorithm: Runway-dependent landing time case,” *J. Appl. Oper. Res.*, vol. 1, pp. 39–49, 2009.

[13] X. B. Hu and E. Di Paolo, “An efficient genetic algorithm with uniform crossover for air traffic control,” *Comput. Oper. Res.*, vol. 36, no. 1, pp. 245–259, 2009.

[14] G. M. M. Krishnamoorthy, J. Abela, D. Abramson, A. De Silva, “Computing Optimal Schedules for Landing Aircraft,” in *The 12th National Conference of the Australian Society for Operations Research*, 1993, pp. 1–15.

[15] H. Pinol and J. E. Beasley, “Scatter Search and Bionomic Algorithms for the aircraft landing problem,” *Eur. J. Oper. Res.*, vol. 171, no. 2, pp. 439–462, 2006.

[16] J. E. Beasley, M. Krishnamoorthy, Y. M. Sharaiha, and D. Abramson, “Displacement problem and dynamically scheduling aircraft landings,” pp. 54–64, 2004.

[17] F. Farhadi, A. Ghoniem, and M. Al-Salem, “Runway capacity management - An empirical study with application to Doha International Airport,” *Transp. Res. Part E Logist. Transp. Rev.*, vol. 68, pp. 53–63, 2014.

[18] K. Dastgerdi, N. Mehrshad, and M. Farshad, “Journal of Soft Computing and Decision Support Systems A New Intelligent Approach to Aircrafts Take-off/ Landing Planning at Congested Single Runway Airports,” vol. 2, no. 2, pp. 17–25, 2015.

[19] G. Bencheikh, J. Boukachour, and A. Alaoui, “Improved Ant Colony Algorithm to solve the aircraft landing problem,” *Int. J. Comput. Theory Eng.*, vol. 3, no. 2, pp. 224–233, 2011.

[20] I. Moser and T. Hendtlass, “Solving dynamic single-runway aircraft landing problems with extremal optimisation,” *Proc. 2007 IEEE Symp. Comput. Intell. Sched. CI-Sched 2007*, pp. 206–211, 2007.

[21] G. B.S., “An efficient hybrid particle swarm optimization algorithm in a rolling horizon framework for the aircraft landing problem,” *Appl. Soft Comput.*, vol. 44, pp. 200–221, 2016.

[22] E. Rashedi, H. Nezamabadi-pour, and S. Saryazdi, “GSA: A Gravitational Search Algorithm,” *Inf. Sci. (Ny)*, vol. 179, pp. 2232–2248, Jun. 2009.

[23] Roger G. Dear, “The dynamic scheduling of aircrafting in the near terminal area,” pp. 1–325, 1976.

[24] H. Balakrishnan and B. G. Chandran, “Algorithms for Scheduling Runway Operations Under Constrained Position Shifting,” *Oper. Res.*, vol. 58, no. 6, pp. 1650–1665, 2010.

[25] A. Rodriguez-Diaz, B. Adenso-Diaz, and P. L. Gonzalez-Torre, “Minimizing deviation from scheduled times in a single mixed-operation runway,” *Comput. Oper. Res.*, vol. 78, pp. 193–202, 2017.

[26] A. Lieder and R. Stolletz, “Scheduling aircraft take-offs and landings on interdependent and heterogeneous runways,” *Transp. Res. Part E Logist. Transp. Rev.*, vol. 88, pp. 167–188, 2016.

[27] A. Lieder, D. Briskorn, and R. Stolletz, “A dynamic programming approach for the aircraft landing problem with aircraft classes,” *Eur. J. Oper. Res.*, vol. 243, no. 1, pp. 61–69, 2015.

Table 1. Overview of related literatures

Source	Methodology	Type of case	Objective	Problem instances
Dear (1978)	Constrained Position Shifting	Static/dynamic	Max throughput Min Σ total delay	Random generated instances
Psaraftis (1978)	Constrained Position Shifting	Static	Min Σ costs/min makespan	Random generated instances
Balakrishnan et al. (2006)	Constrained Position Shifting	Static	Min Σ costs/min makespan	Denver airport real data
Rodriguez-Diaz (2017)	Constrained Position Shifting	Static	Min Σ delay	Random generated instances, Beasley (2000) and Gatwick airport
Beasley et al (2000)	Linear programming	Static	Min Σ penalty cost	Beasley (1990)
Bayen (2004)	Linear programming and dynamic programming	Static	Min Σ arrival time Min last aircraft landing time	No instances (theoretical analysis)
Cheng et al (1999)	Genetic algorithm	Static	Min Σ delay	Sampling data
Hansen (2004)	Genetic Algorithm, Genetic programming	Static	Min Σ delay	Cheng et al (1999)
Wang (2014)	Genetic Algorithm	Static	Min Σ delay	Sampling data
Liu (2011)	Genetic local search	Static	Min Σ penalty cost	Beasley (2000)
Abela et al (1993)	Genetic algorithm, Branch and bound	Static	Min Σ deviation cost	Randomly generated test data
Hu and Di Paolo (2009)	Genetic algorithm	Static	Min Σ delay Max arrival queues	Hansen (2004)
Pinol and Beasley (2006)	Scatter search and Bionomic algorithm	Static	Min Σ penalty cost	Beasley (2000)
Girish (2016)	Particle swarm optimization with local search	Static	Min Σ penalty cost	Beasley (2000)
Benceikh et al (2011)	Ant Colony Optimization	Dynamic	Min Σ penalty cost and displacement function	Beasley (2000)
Kazem et al (2016)	Gravitational search algorithm	Static	Min Σ total delay	Hansen (2004)

Interactive musical editing system to support human errors and offer personal preferences for an automatic piano -Inferring performance expression by considering change of pitch-

Masahiro Ushio

*Department of Mechanical Information Science and Technology, Kyushu Institute of Technology
680-4, Kawazu, Iizuka-City, Fukuoka, 820-8502, Japan
Email: ushio@mmcs.mse.kyutech.ac.jp*

Eiji Hayashi

*Department of Mechanical Information Science and Technology, Kyushu Institute of Technology
680-4, Kawazu, Iizuka-City, Fukuoka, 820-8502, Japan
E-mail: haya@mmcs.mse.kyutech.ac.jp*

Abstract

We have developed a system that allows a piano to perform automatically. In order to play music in the manner of a live pianist, we must add expression to the piano's performance. In the case of music, there are often 1,000 or more notes in the score, requiring that an editor spend a huge amount of time to edit. Therefore, we have developed an interactive musical editing system that utilizes a database to edit music more efficiently.

Keywords: Automatic Piano, Knowledge Database, Computer Music, Music Interface

1. Introduction

We have developed a system that allows a piano to perform automatically. In this system, 90 actuators have been installed on the keys and pedals of a grand piano. These actuators execute key strokes and pedal movements to govern the piano's performance. (See Fig.1)

In order to develop an automatic piano that plays music in the manner of a live pianist, we have to add expression to the piano's performance. Essentially, variations in tempo, dynamics, and so on are needed in order to arrange the respective tones in a desired way. Moreover, in the case of piano music, there will often be 1000 or more notes in the score of even a short piece of music, and the editor must spend a huge amount of time to accurately simulate an actual emotionally expressive performance that a highly skilled pianist could give.

Moreover, a highly skilled pianist is able to play an unfamiliar piece of music by sight, even if the performance is not completely in accord with an intended specific musical interpretation. Current computing systems cannot perform a new piece of music by sight,

and thus they cannot simulate a human pianist's musical expression. Therefore, we have developed an interactive musical editing system that utilizes a database in order to edit music more efficiently¹.

In a current research, MIDI data regarding the performances of highly skilled pianists has been analyzed in order to observe the stylistic tendencies of their performances. The results showed that phrases having similar patterns in the same composition were performed in the similar style.

We developed a system that searches for similar phrases throughout a musical score and infers the style of the performance. Here, we proposed a method using Dynamic Programming (DP) matching as a way to search for similar phrases. In our interactive musical editing system, we have created the Score Database which contains information regarding a musical score. This database contains a field called "Note Value," in which data indicates the type of note--e.g., a quarter note, a triplet, and so on. This system converts notes into character strings using the "Note Value" data. (Fig.3)

In addition, the system computes DP matching using the character strings and calculates the degree of

disagreement between these strings. It uses an index to judge the resemblance between the strings. For its method of inferring performance expression, it uses the best alignment for DP matching, which enables it to express the best correspondence between notes. In order to edit music more efficiently, we must consider dynamic marking, beat and so on and we created database contains them. We developed an inferring process with regards to similar phrases using the best alignment and database.

In this paper, we describe the results of searching for similar phrases using DP matching and inferring for them using DP matching and database. By the research until last year, an editing system for notes with performance symbols has been constructed. However, there is little inference about notes without performance symbols, and there is a problem that inference cannot be performed sufficiently. In this fiscal year, we focused on the change in pitch to improve the accuracy of the phrase without the performance symbol. We aimed at developing a system that can get closer to actual performance by finding characteristics of performance due to change in pitch and editing it based on its characteristics.

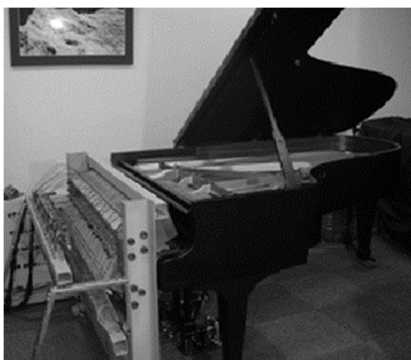


Fig. 1. The automatic piano.

2. Editing support system

2.1. Performance information

The automatic piano that we have developed uses a music data structure that is similar to MIDI. We defined performance information, dividing it into two categories: the notes and the pedals. The note information is comprised of the six parameters involved in producing a tone: “Key” (note), “Velo” (velocity), “Gate”, “Step”, “Bar” and “Time”. “Velo” is the dynamics, given by the

value of 1-127. “Gate” is the duration of the note in milliseconds. “Step” is the interval of time between notes, and it also exhibits tempo. “Bar” is the vertical line placed on the staff to divide the music into measures.

The pedal information is comprised of four parameters: “Key” (indicating the kind of pedal: “Damper” or “Shifting”), “Velo” (the pedaling quantity), “Time” (the duration for which the pedal is applied), and “Bar”.

2.2. System Architecture

As shown in Fig.2, the editing support system includes a database and a user interface. The database is divided into one storing the characteristics and one storing the music information of the music, and refer to each other with the user interface.

In addition to a system that manually edits music data, the user interface incorporates a system that can infer the performance expression desired by the user based on the information of the database storing the characteristics. Also, it consists of a search system and inference system. Search system searches or phrases (similar phrases) similar in sequence of phrases and notes input by the user. Inference system edits the similar phrases using the database.

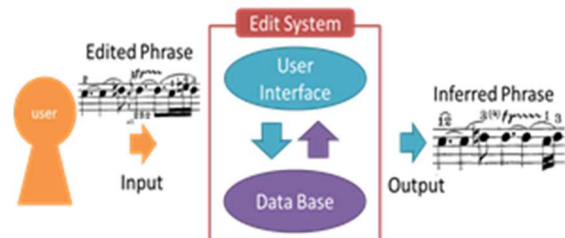


Fig.2 The structure of the edit system

2.3. Search system

As a result of the analysis, it was found that phrases of the same pattern existing in the same tune are performed in a similar expression. This time, we used DP matching to search for similar phrases.

DP matching is a technique used widely in the field of speech recognition, bioinformatics and so on. It has a feature that can calculate the similarity between two words that are different in a number of characters from each other.

In Fig.4, the route of minimum cost in each point is taken, and the route with the lowest cost is assumed finally to be the optimal path. The cost at that time is defined as the distance between patterns. In this system,

this distance is handled as a threshold to judge whether the phrases are similar to each other.

For example, if the cost moves up or to the right, then it is increased by 1. If it moves to the upper right, then it does not increase. Also, if the characters do not correspond in each point, then the cost is increased by 5.

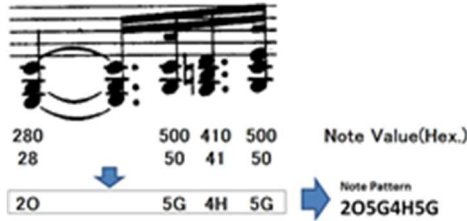


Fig.3 patterning of notes

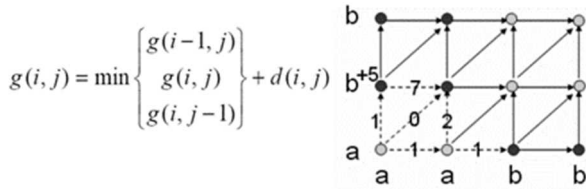


Fig.4 DP Matching

2.4. Performance information

2.4.1. System overview

Inference of similar phrases is performed based on correspondence by DP matching. Inference is done using the value stored in the database, and the user determines whether or not to use items such as dynamics marks and rendition style symbols and expresses similar phrases. This year we added inference based on change in pitch to this inference system. Hereinafter, this inference system is called a new inference system.

2.4.2. Inference by pitch change

In order to understand the characteristics of the performance expressions due to the change in pitch, the trend was investigated from the performance data of the pianist. The studied songs are the first movement of "Appassionata", performed by Gerhard Opitz.

As a result of the survey, it turned out that there are the following two features.

- (i) In the main melody, Velo also increases as the pitch increases
- (ii) Gate / Step decreases in case of repetitive keystrokes of the same key

The obtained results are shown in Table.1. The relationship between the pitch and Velo was obtained by

averaging the slope values of the first order approximate expression obtained from the pitch of each dynamics marks and the distribution of Velo. Fig.5 shows the distribution of Fortissimo's strength of sound. The "Gate / Step" of the sound of repetition and non-repetition of the same key was obtained by classifying all the sounds in the song and averaging them.

Table.1 Search result of varying pitch

Performance trend	Gate/Step	Velo/Key
Repetition of the same Key	0.2950	—
Not repetition of the same Key	0.8092	—
Slope between Velo and Key	—	0.2346

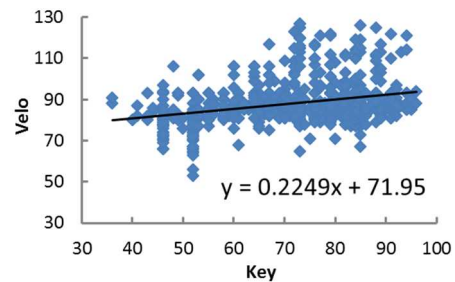


Fig.5 Fortissimo's strength distribution in the main melody

Inference was made using the values in Table.1. Velo's inference method was based on the approximate linear equation shown in Fig.5. Gate inference was made based on the average value obtained in the survey.

The inference formula of Velo is shown in Expression (1), and the inference formula of Gate from non-repetitive key (or repetitive keystroke) to repetitive keystroke (or non-repetitive keystroke) is shown in Expression (2). Inference is made for each note, NewVelo and NewGate indicate the values after inference, respectively, and Velo and Gate indicate values before inference, respectively. Key 1 is Key of search phrase, Key 2 is Key of similar phrase.

$$\text{NewVelo} = \text{Velo} + (\text{Key1} - \text{Key2}) \times 0.2346 \quad (1)$$

$$\text{NewGate} = \text{Gate} \times \frac{0.2950(\text{or}0.8092)}{0.8092(\text{or}0.2950)} \quad (2)$$

3. Inference experiment

3.1. Experiment procedure

We conducted experiments comparing the new inference system and the existing inference system. The target song is the first movement of "Appassionata".

First, similar phrases were inferred by a new inference system and an existing inference system. Next, in order

to obtain the similarity with actual performance for each inference result, DP matching was used. Specifically, in DP matching, VeloRate and Gate / Step are patterned to obtain the distance. Finally, comparing each distance, we made judgment of improvement / deterioration.

In this experiment, the phrase in Fig.6 was set as a search phrase. We searched from the search phrase in Fig.6 and inferred all similar phrases found. The inference result was compared with the existing inference result.

3.2. Result

Table.2 shows the results of inference experiment for all similar phrases found by the search system between the new inference system and the existing inference system.

From Table.2, we found that the number of phrases from the new inference is higher than the existing one. From this fact, it was possible to confirm the effectiveness of the inference system which added the pitch change in consideration.



Fig.6 Search phrase

Table.2 Comparison result with existing system

	Quantity
Similar phrase	2264
Improved result	449
Deterioration result	51
Unchanged result	1764

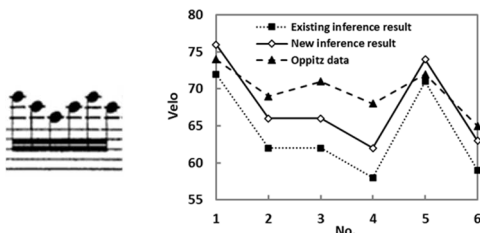


Fig.7 Phrases with improved Velo

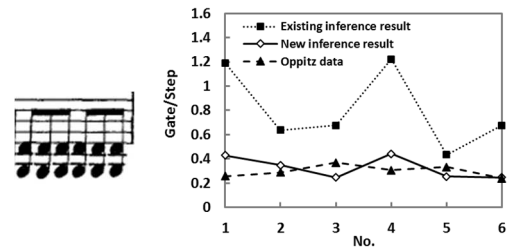


Fig.8 Phrases with improved Gate

3.3. Consideration

From Velo's improved phrase and Fig.7, it was confirmed that the sound size (Velo) approached to the real performance. This is because Velo is made larger considering that the pitch of similar phrases is generally higher than the search phrase.

From Gate's improved phrase and Fig.8, it was confirmed that the value of Gate / Step became smaller and it became close to real performance. This is because Gate was reduced in consideration of the similar phrase being repetitive keystrokes.

4. Conclusion

We investigated the tendency of the pianist's performance due to pitch change. The sound was inferred by adding two features to the system that are "sound magnitude" and "sound length" that occur due to pitch of change. By inference experiments, it was confirmed that the accuracy was improved from the existing inference's result.

However, there remain problems that there are a large number of phrases that could not be inferred and phrases that did not change. In order to improve the accuracy, improvement of the inference method corresponding to those phrases is required. Future prospects include inference methods considering fingering that focuses on the movement of fingers.

References

1. E. Hayashi et al, Behavior of piano-action in a grand piano. I, *Journal of acoustical Society of America*, Vol.105, pp.3534-3544, 1999.

Analysis of Malaysian Facial Expressions for Designing Virtual Agents

Halimahtun Mohd Khalid

*Damai Sciences, A-31-3 Suasana Sentral, Jalan Stesen Sentral 5,
50470 Kuala Lumpur, Malaysia
E-mail: mahtunkhalid@gmail.com*

Wei Shiung Liew

*Faculty of Computer Science and Information Technology, University of Malaya
50603 Kuala Lumpur, Malaysia*

Abstract

The perception of emotion from facial expressions is culturally mediated. Designing facial expressions of avatars should consider the demographics of users who would be interacting with them. An online survey was conducted to determine the facial measurements for emotions. Sixteen facial expressions of Malaysians were presented to subjects. They were instructed to select an emotion label that matched each expression. The expressions were decomposed into action units using OpenFace. Regression analysis determined the combination of facial measurements for each emotion.

Keywords: facial expressions; emotion; facial action units; avatar design.

1. Introduction

The universality hypothesis states that certain facial expressions represent six basic emotions: anger, disgust, fear, happiness, sadness, and surprise; and they are easily recognizable by people regardless of culture, language or ethnicity. Several studies have supported and/or refuted the universality hypothesis. Ekman et al.¹ showed consistent agreement across cultures in their interpretation of emotions in facial expressions. Arguments against the hypothesis typically cited several factors such as the use of forced choice method, whereby participants were given only a small list of possible emotion labels to match with the facial expressions², and the use of posed as opposed to spontaneous facial expressions³. A meta-analysis of emotion recognition⁴ indicated that emotions were recognized more accurately when expressed by members of the same national, ethnic or regional group. More recent studies displayed

differences between Western and Eastern cultures⁵ particularly for negative facial expressions⁶.

When designing realistic artificial faces for virtual avatars or humanoid robots, appearance matters as users prefer robots that appear friendly and polite, thereby encouraging emotional connection⁷. The robot's ability to perceive and express emotions via facial expressions gives an illusion of empathy, which positively influences human-robot interactions⁸. Cross-cultural variances in facial expressions would mean that the robots' expressions would have to be tailored specifically for the demography of persons who would be interacting with the robot.

In this study, we present our methodology and findings for surveying and constructing a facial expression emotion model for an East Asian demographic, represented by two Malaysian ethnic groups: Chinese and Malays. The objective of the study was to determine

how they express and perceive specific emotions based on facial expressions, measured in terms of facial action units. Emotion definitions can then be used in designing realistic facial expressions of virtual avatars that mimic Chinese and Malay faces.

Figure 1 presents the Arousal-Valence circumplex⁹ model for analysis of facial expressions. The Arousal axis (vertical arrow) represents the strength of the emotion, with emotions such as anger and joy having high arousal, while sad and passive have low arousal. The Valence axis (horizontal arrow) is an indicator of the intrinsic attractiveness/averseness of the emotion label. For example, fear and disgust have negative valence, while happiness and relaxed have positive valence. Figure 1 also shows an arrangement of the test form, comprising of a test facial image, instructions, response format and emotion wheel.

2. Method for Facial Expression Survey

2.1. Study design, material and sample

The study was conducted using an online survey. The material comprised video recordings of eight test subjects; two subjects each represented a Malaysian Male Malay, Male Chinese, Female Malay, and Female Chinese. Sixteen facial expressions were selected from each subject corresponding to the emotion labels presented in the Arousal-Valence circumplex model.

The sample comprised thirty-seven subjects. They were recruited from the same four demographics and were shown the selected facial expressions along with the corresponding emotion label. Subjects were instructed to confirm whether the facial expressions match the label. If not, they were asked to select the most appropriate emotion label from a given emotion wheel.

Table I shows sixteen emotion labels selected for the study.

Table I. Sixteen emotion labels divided into four quadrants by Arousal-Valence axes

Quadrants	Emotion labels
Low-Arousal, Negative Valence	Anxious, Bored, Miserable, Passive

Low-Arousal, Positive Valence	Comfortable, Happy, Relaxed, Satisfied
High-Arousal, Negative Valence	Angry, Disgusted, Fearful, Sad
High-Arousal, Positive Valence	Aroused, Excited, Pleased, Surprised

The facial expressions were then processed using

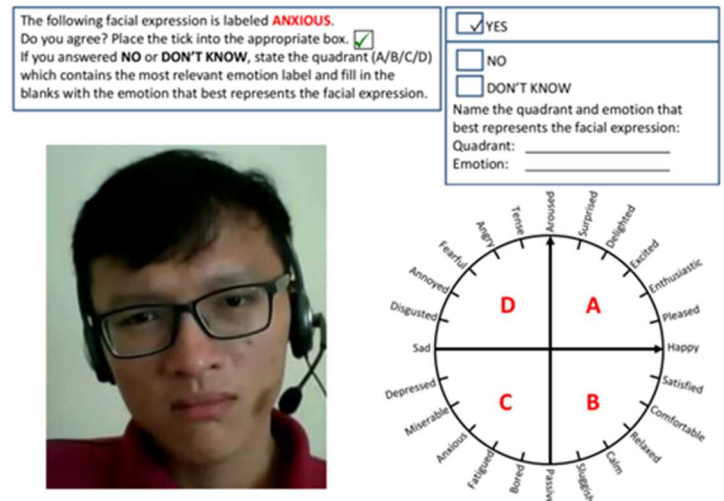


Fig. 1. Online survey form for one facial expression

OpenFace¹⁰ to extract action unit (AU) measurements according to the Facial Action Coding System.

2.2. Data analysis and results

The AU measurements for each facial expression were combined with the emotion labels selected by the subjects and compiled into a dataset. Each entry in the dataset represented a single facial expression evaluation by one subject. The dataset was then pruned to exclude emotion labels that were selected infrequently compared to other emotion labels, namely: Delighted (1.7% of all emotion labels), Depressed (2.2%), Enthusiastic (1.0%), Fatigued (0.5%), and Sluggish (1.7%). The dataset was then processed using PART classifier¹¹, which achieved an accuracy of 51% in selecting the correct emotion label given the AU measurements.

2.2.1. Arousal-Valence classification

Classification of the dataset was repeated but the emotion labels were replaced with the Arousal-Valence quadrant, where the emotion labels were located. For example,

Angry, Fearful, and Delighted were replaced by High-Arousal Negatives. Classification using PART achieved 72% accuracy in selecting the correct quadrant given the AU measurements. Table III is a partial list of the 62 rules derived from the PART decision list, and Table IV shows the partial list of rules generated for each emotion quadrant.

Table III. Action unit rules for each Arousal-Valence quadrant

Action unit rules	Quadrant	Support
Lip corner depressed, lip corner pulled, upper eyelid raised, mouth opened	High-Arousal Positive	3.98% (21/527)
Lip corner depressed, lips parted, upper eyelid raised, lip corner not pulled, lips not stretched, nose not wrinkled, upper lip slightly raised	Low-Arousal Positive	2.27% (12/527)
Lip corner not pulled, lips not stretched, nose not wrinkled, lip corner depressed, upper eyelid raised, lips parted, inner brow slightly raised,	High-Arousal Negative	2.27% (12/527)
Lip corner not pulled, lips not stretched, nose not wrinkled, upper eyelid raised, lip corner depressed, lips slightly parted, brows lowered, upper lip slightly raised	Low-Arousal Negative	4.93% (26/527)

Table IV. Action unit rules for individual emotion labels

Action unit rules	Quadrant/Emotion	Support
Mouth opened, cheek raised, upper lip raised, lips slightly stretched	High-Arousal Positive: Happy	21.48% (29/135)
Upper lip not raised, jaw dropped	High-Arousal Positive: Surprised	16.29% (22/135)
Lips slightly parted, brow slightly lowered, slight dimple, lip corner not pulled, nose not wrinkled	Low-Arousal Positive: Relaxed	14.38% (20/139)
Lip corner pulled, cheeks slightly raised, outer brow not raised	Low-Arousal Positive: Happy	13.66% (19/139)

Jaw dropped, inner brow slightly raised, outer brow not raised, lips slightly tightened, cheeks raised, upper lip raised, lips parted	Low-Arousal Negative: Bored	31.65% (44/139)
Upper lip raised, lips slightly parted, eyelids not tightened, lips not tightened	High-Arousal Negative: Fearful	7.46% (10/134)

In Table IV, the dataset was segmented into four data subsets, each containing only the emotion labels from one quadrant. Classification of emotion labels was then performed individually for each quadrant. The PART classifier achieved 72% accuracy in selecting the correct emotion label for facial expressions within the High-Arousal Positive emotion labels, 64% accuracy for the Low-Arousal Positive emotions, 63% for the Low-Arousal Negative emotions, and 35% accuracy for the High-Arousal Negative emotions.

3. Designing Virtual Agents

Using facial expressions attributes from Table III, we modeled faces of virtual avatars with iClone software. Facial features of the avatars were manipulated following the action unit rules. The avatars were then used in a human-agent interaction experiment¹² to emote various facial expressions during dialog interactions with humans. Figure 2 illustrates two avatars designed using these rules.





Fig. 2. Male and female avatars exhibiting anger (top), sad (middle), and happy (bottom).

4. Conclusion

Clearly, the perception of emotion from facial expressions is culturally mediated. Design of avatars' facial expressions should consider the demographics of users who would be interacting with them.

Acknowledgements

This material is based on work partially supported by the US Aerospace Research and Development office (AOARD), Japan and the US Air Force Office of Scientific Research (AFOSR), Washington D.C. under Grant No. FA2386-14-1-0016.

References

1. P. Ekman and W. V. Friesen, Constants across cultures in the face and emotion, in *J. Pers. Soc. Psychol.* **17**(2) (1971) 124–129.
2. M. G. Frank and J. Stennett, The forced-choice paradigm and the perception of facial expressions of emotion, *J. Pers. Soc. Psychol.* **80**(1) (2001) 75–85.
3. P. J. Naab and J. A. Russell, Judgments of emotion from spontaneous facial expressions of New Guineans, in *Emotion* **7**(4) (2007) 736–744.
4. H. A. Elfenbein and N. Ambady, On the universality and cultural specificity of emotion recognition: a meta-analysis, in *Psychol Bull*, **128**(2) (2002) 203–235.
5. R. E. Jack, O. G. Garrod, H. Yu, R. Caldara, R. and P. G. Schyns, Facial expressions of emotion are not culturally universal, in *Proc Natl Acad Sci* **109**(19) (2012) 7241–7244.
6. R. E. Jack, C. Blais, C. Scheepers, P. G. Schyns, P.G. and R. Caldara, Cultural confusions show that facial expressions are not universal, in *Curr Biol* **19**(18) (2009) 1543–1548.
7. R. Parasuraman and C. A. Miller, Trust and etiquette in high-criticality automated systems, in *Commun ACM*, **47**(4) (2004) 51–55.
8. B. Gonsior, S. Sosnowski, C. Mayer, J. Blume, B. Radig, D. Wollherr, D. and K. Kühnlenz, Improving aspects of empathy and subjective performance for HRI through mirroring facial expressions, in *RO-MAN 2011*, eds. M. Scheutz and H. I. Christensen (Atlanta, Georgia, USA, 2011), pp. 350–356.
9. J. A. Russell, A circumplex model of affect, in *J. Pers. Soc. Psychol.* **39**(6) (1980) 1161–1178.
10. T. Baltrušaitis, P. Robinson and L. P. Morency, Openface: an open source facial behavior analysis toolkit, in *2016 IEEE Winter Conf Appl Comput Vis* (Lake Placid, New York, USA, 2016), pp. 1–10.
11. E. Frank, E. and I. H. Witten, Generating accurate rule sets without global optimization, in *Proc Int Conf Mach Learn*, ed. J. W. Shavlik (Madison, Wisconsin, USA, 1998), pp. 144–151.
12. H. M. Khalid, W. S. Liew, B. S. Voong and M. G. Helander, Trust of virtual agent in multi-actor interactions, in *Proc 2018 Int. Conf. on Artificial Life and robotics* (Oita, Japan, 2018), in press.

© The 2018 International Conference on Artificial Life and Robotics (ICAROB2018), Feb. 1-4, Beppu International Convention Center, Oita, Japan

Development of VR system to enhance understanding process of robot mechanisms

Alexei Lushnikov

*Higher School of ITIS, Kazan Federal University, Kremlyevskaya str., 18,
Kazan, Russia*

Vlada Kugurakova

*Higher School of ITIS, Kazan Federal University, Kremlyevskaya str., 18,
Kazan, Russia*

Arthur Nizamutdinov

*Higher School of ITIS, Kazan Federal University, Kremlyevskaya str., 18,
Kazan, Russia*

Timur Satdarov

KUKA Robotics

*E-mail: alexkenny@gmail.com, vlada.kugurakova@gmail.com,
yalopata@gmail.com, Timur.Satdarov@kuka.com
www.kpfu.ru*

Abstract

Training for assembly, disassembly, and maintenance skills for engineers or technicians is very important for various industries. However, preparing these users for the effective use of new skills remains a challenge. Virtual Reality (VR) system integrated with haptic feedback as device interaction is seen as a powerful tool for development and implementation of a more natural and intuitive user interface. Such user interface can greatly improve the training experience required for successful execution of the mentioned tasks for complex machinery and at production facilities. This study describes the ongoing project on the development of a VR training system for an assembly process of robots or other machinery. A natural interface is proposed that increases the immersiveness of the virtual learning environment. The combination of VR-enhanced training should be a great help for users in mastering the assembly procedure and maximize their skill performance as well.

Keywords: virtual reality, VR, immersive, training method, virtual training system, device interaction, NUI, natural user interface.

1. Introduction

Training and learning are crucial processes for developing skills and knowledge for new users in order

to perform certain tasks or works. Currently, various industries and education sectors are looking for alternative training method in order to support their

© The 2018 International Conference on Artificial Life and Robotics (ICAROB 2018), Feb. 1-4, Beppu, Oita, Japan

demand in producing new technicians with high skill performance. However, the process of learning, training and acquiring new skills for assembly or disassembly for these new users is quite challenging. There is a need to find an alternative method to help these sectors in producing effective user and employee with high skill performance and able to perform the required tasks as soon as the training is completed. Surely Virtual Reality (VR) system is a powerful tool in developing and implementing a more natural and intuitive interface as training systems that have been developed in the assembly or disassembly training context. VR environment offers an intuitive and immersive human-computer interface, which can be an effective tool for assembly or maintenance training because users can experience and familiarise with virtual parts or 3D models in real-time simulation in a virtual environment system. Additional special equipment integrated with VR environments such as haptic feedback technologies which allow for interaction between humans and virtual parts will be beneficial and effective for the learning and training of assembly sequences [1].

Since 1990, the industry has seen the interest of VR. By creating interactive and versatile environments and mock-ups, VR allows, inter alia, to evaluate the accessibility, feasibility, and ergonomics problematic of assembly and maintenance tasks, in early stages of the design process. It could have a very positive impact, in terms of cost and time, by reducing the need for physical mock-ups and validating (or not) early designs. In the context of fusion plants, the integration constraints, maintenance, and safety requirement are key parameters for the design. VR technologies are very efficient to optimize such integration, integration within parallel designing processes while taking into account assembly, maintenance and safety issues.

2. Related Work

Researchers are talking about learning with using VR, but are not used to it yet. Nevertheless, the article [2] offers a simple assessment of the specific method of instruction and the method of training for two experiments with subsequent analysis of the results. Article [3] describes the logical use of device haptic devices to increase the immersion of such VR systems. Actually, this approach is still brand new.

The researches that we've met describe a natural user interface (NUI) as the main approach to successful learning in VR.

Natural user interfaces (NUIs) [6] aim to read and perceive user inputs without using a fixed position or limited input devices such as a keyboard. As a rule, NUI uses computer visualization to identify and track movements of the whole body, hands or fingers. These devices are widely being used in gaming applications now. Devices, such as GloveOne™, Avatar™, or in case of AR it can be limited by using Microsoft Kinect™, Leap Motion™, allow to capture complicated body gestures with high accuracy. Integration of NUI with virtual reality (VR) [7] is a natural progression. Thus, users have no need to rely on usual input methods for interacting, instead they can interact directly with objects in VR.

An interesting example is represented in [9] as the union of Remote Access Laboratories (RAL), AR и NUI, allowing users to interact with virtual objects in their physical work area leading to the creation of interactive engineering and scientific experiments.

Natural user interfaces (NUI) rely on specialized devices for obtaining information about the physical position of a user [10, 11]. Usually this is a real-time data stream in the form of an array containing the Cartesian coordinates of the X, Y, Z parts of user's body, joints and bone segments.. NUIs are usually oriented on "gesture" control. A gesture is a fixed set of known movements, representing the specific transition, orientation and

position of users. NUI system identifies the set of gestures, that are recognized by an appropriate devices. A video output is identified on the basis of these gestures. Recently, physical engines have been included in NUI applications [12]. It helps to avoid the need for the gestures based solely on parts of the user's body. These physical engines can allow the direct interaction between virtual object, representing a user's body in virtual three-dimensional space, and each interaction between them and experimental objects..

The researchers in [14] investigate the effectiveness and efficiency of the first prototype of the virtual training system developed within Virtual Simulation and Training of Assembly and Service Processes in Digital Factories, and results demonstrate, that virtual training effectively reduces an error probability during the completing the task in comparison with traditional training.

3. Our idea

It is necessary to be able to know each time how components of each three-dimensional model of real mechanistic devices are attached and connected.

Our idea is to combine several positions: (1) a hierarchical description of the model elements; (2) a formation of a list of connection types (hinges in different degrees of freedom, rail, swivel lock, complex composite compounds, for example, grenade, etc.); (3) a formation of a list of fastener types characteristic of mechanical objects (bolt, clip, latch, clamp, yoke, pin, etc.); (4) type of object from the list; (5) inclusion in a name of the parameters describing it; (6) a meaningful name for the used materials.

Our idea is to create models with the developed convention of individual model elements (key nodes) using hierarchical nesting and name, which allows in-situ to disassemble such model automatically in VR, no matter what it is - car, robot or another mechanism. Hierarchy is necessary to understand what details are

© The 2018 International Conference on Artificial Life and Robotics (ICAROB 2018), Feb. 1-4, Beppu, Oita, Japan

located in what level, the degree of their nesting and order of disassembly. The convention in naming is necessary to understand the ways of fastening elements, which are finite.

Also the name contains parameters of connection or fastening, for example, for a hinge – degrees of freedom of links, axes and degrees, which allow control the hinge; for a rail type of fastening – the axis on which can be moved, the percentage or a specific value, on which the node can be moved.

Using the correctly constructed hierarchy of model, describing the mechanism it can be implemented in-situ restriction to get an opportunity of automatic movement of individual parts, but it is not developed by us as an incidental possibility of a hierarchical convention of the name. A full description of convention requires serious consideration.

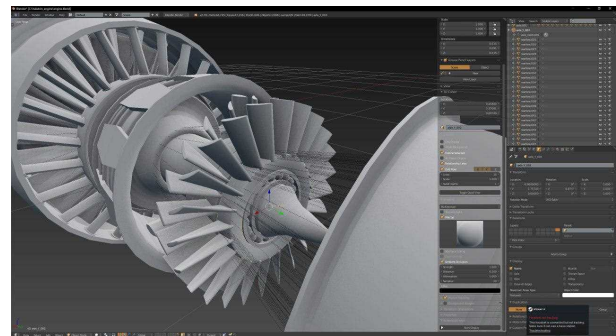


Fig.1. Hierarchical nesting of sub-elements by the example of a turbine impeller

Moreover, in order to use NUI it is necessary to take in hands (in VR) or to exchange a type of controller on a necessary tool (spanner, hexahedron, torx, other different types of screwdrivers (cruciform, slotted, etc.), pliers, etc.) to disassemble an appropriate connection. This appropriateness must be specified in a list of connection types.

4. Our method

Our development is based on Unity. The parser, created for realtime upload of models, using structure and model name, adds necessary components to the prefab of the object on the stage.

Such system allows to process each model, in which the names of objects follow the chosen convention. All uploaded models after the processing by the program are structured so they can be assembled and disassembled in correct order. For example, an object with a name obj[3.3] can be disassembled only after an object with a name obj[2.3] is disassembled and so on. The essential feature is independence of the program on a specific implementation, i.e. on a specific model. A universal constructor of virtual environment is developed.

5. Concrete realization

The format of the training complex proposed by us allows create product placement for each firm, that specializes in unique technique that needs not only for using by individual purchasers, but for training, for example, for training employees of repair services.

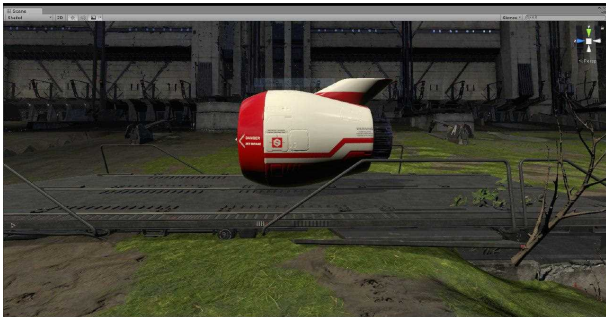


Fig.2. Assembled jet engine model

A model of an abstract jet engine is taken for realization (Fig.2 – Assembled jet engine model; Fig.3 – procedurally disassembled).

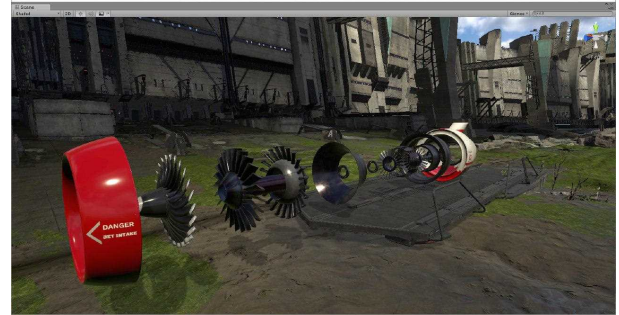


Fig.3. Disassembled jet engine model

A similar solution has been developed for the popular Ubot robot (Fig.4) by KUKA Robotics corporation to demonstrate our ideas of using combination of the special convention for creating 3d models, natural user interface to learn the structure of mechanisms, using disassembly based on a approach of a changeable toolkit (Fig.5).

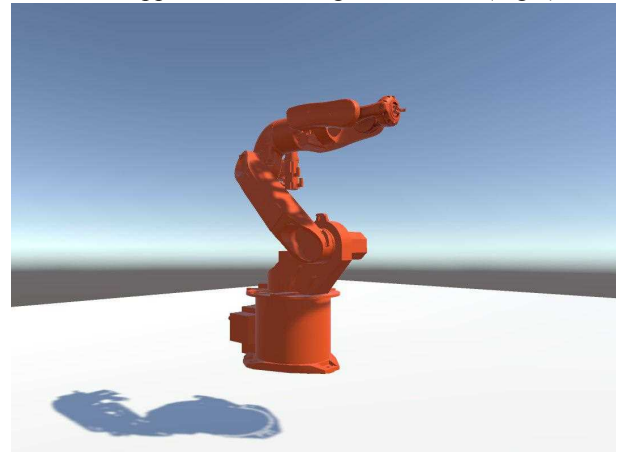


Fig.4. Assembled KUKA Ubot robot model

6. Conclusion

These systems are great alternatives and are also effective in learning and training in order to prevent the excessive cost of using the real machine or components which could cause damages; or create disruptions to the actual working process.

This VR-solution helps to explore quickly the device of unfamiliar technology, "in the field", to understand the structure of mechanisms and their components, to study the necessary tools for those or other connections.

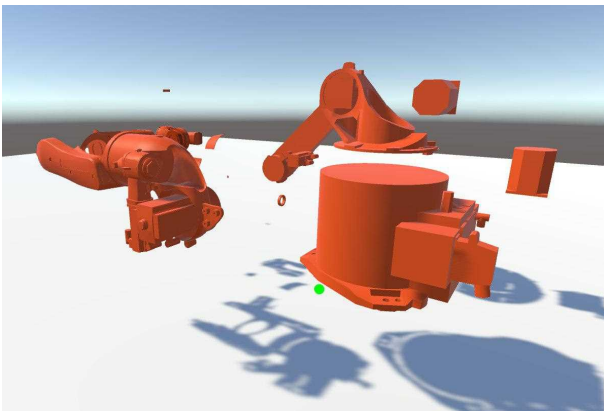


Fig.5. Disassembled KUKA Ubot robot model

Main application of our idea is an educational system of each mechanisms as a product placement for big corporations. Also this method can be applied to other applications, for example, to study the composition of chemical substances or for virtual prototyping of nanostructures.

Acknowledgements

This work was funded by the subsidy allocated to the Kazan Federal University for the state assignment in the sphere of scientific activities.

References

1. T. Gutiérrez, J. Rodríguez, Y. Vélaz, S.C.A. Suescun, and E.J. Sánchez, IMA-VR: A Multimodal Virtual Training System for Skills Transfer in Industrial Maintenance and Assembly Tasks (*Journal of Mechanical Engineering*, Vol. ME 40, No.1, 2009), pp.68-71.
2. M.W. Rohidatun, A.A. Faieza, M.Y. Rosnah, S. Nor Hayati and I. Rahinah, Development of Virtual Reality (VR) System with Haptic Controller and Augmented Reality (AR) System to Enhance Learning and Training Experience, *International Journal of Applied Engineering Research*, vol.11, no.6, 2016), pp.8806-8809.
3. F.A. Aziz and M. Mousavi, "A Review of Haptic Feedback in Virtual Reality for Manufacturing Industry", in *J. Mech. Eng.*, vol.40, no.1 (2009), pp.68-71.
4. V. Abramov, V. Kugurakova, A. Rizvanov, Abramskiy, M., N. Manakhov, M. Evstafiev, M. and D. Ivanov, Virtual Biotechnological Lab Development (*BioNanoScience*, vol.7, no 2, 2017), pp.363-365.
5. V. Kugurakova, M. Khafizov, R. Akhmetsharipov, A. Lushnikov, D. Galimova, V. Abramov and O. Correa Madrigal, Virtual surgery system with realistic visual effects and haptic interaction (*ICAROB 2017: Proceedings of the 2017 International Conference on Artificial Life and Robotics, 2017*), pp.P86-P89.
6. W. Liu, Natural user interface-next mainstream product user interface (Computer-Aided Industrial Design & Conceptual Design – CAIDCD), *2010 IEEE 11th International Conference on*, vol. 1, pp. 203-205, 2010.
7. D. Müller, A. Chilliischi, S. Langer, Integrating immersive 3D worlds and real lab equipment for teaching mechatronics (*Remote Engineering and Virtual Instrumentation – REV*) *2012 9th International Conference on 2012*), pp. 1-6.
8. Y. Ohta, H. Tamura, *Mixed reality: merging real and virtual worlds* (Incorporated: Springer Publishing Company, 2014).
9. Maiti, A., Maxwell, A.D. and Kist, A.A., Using marker based augmented reality and natural user interface for interactive remote experiments (*Proceedings of 2017 4th Experiment at International Conference: Online Experimentation*, exp.at 2017), pp. 159.
10. L. Garber, Gestural Technology: Moving Interfaces in a New Direction [Technology News], *Computer*, vol. 46, pp. 22-25, 2013.
11. M. N. Kamel Boulos, B. J. Blanchard, C. Walker, J. Montero, A. Tripathy, R. Gutierrez-Osuna, Web GIS in practice X: a Microsoft Kinect natural user interface for

Alexei Lushnikov, Vlada Kugurakova, Arthur Nizamutdinov, Timur Satdarov

Google Earth navigation (*International Journal of Health Geographics*, 2011), vol. 10, pp. 45.

12. C. Donalek, S. G. Djorgovski, A. Cioc, A. Wang, J. Zhang, E. Lawler et al., Immersive and collaborative data visualization using virtual reality platforms (*2014 IEEE International Conference on Big Data*), pp. 609-614.
13. H.G. Hoffmann, Physically touching virtual objects using tactile augmentation enhances the realism of virtual environments (*Virtual Real. Annu. Int. Symp. 1998, Proc. IEEE, IEEE, 1998*), pp. 59-63
14. Langley, A., Lawson, G., Hermawati, S., D'Cruz, M., Apold, J., Arlt, F. & Mura, K., Establishing the Usability of a Virtual Training System for Assembly Operations within the Automotive Industry (*Human Factors and Ergonomics in Manufacturing*, 2016), vol. 26, no. 6, pp. 667-679.

Towards the immersive VR: measuring and assessing realism of user experience

Vlada Kugurakova

*Higher School of ITIS, Kazan Federal University, Kremlyevskaya str. 18,
Kazan, Russia*

Alexander Elizarov

*Higher School of ITIS, Kazan Federal University, Kremlyevskaya str. 18,
Kazan, Russia*

Murad Khafizov

*Higher School of ITIS, Kazan Federal University, Kremlyevskaya str. 18,
Kazan, Russia*

Alexei Lushnikov

Higher School of ITIS, Kazan Federal University, Kremlyevskaya str. 18,

Arthur Nizamutdinov

*Higher School of ITIS, Kazan Federal University, Kremlyevskaya str. 18,
Kazan, Russia*

*E-mail: vlada.kugurakova@gmail.com, amelizarov@gmail.com,
murkorp@gmail.com, alexkenny@gmail.com, yalopata@gmail.com
www.kpfu.ru*

Abstract

The use of Virtual Reality Continuum grows more diverse with possible applications varying from research and education to leisure and work, so the demand rises to for a method for a precise and reliable way of measuring Virtual Reality (VR) effectiveness. How can we tell apart "badly made" VR from the "good" one? How do different people respond to different implementation and aspects of it? And could it possibly be true that different social groups handle VR in a different way? In this paper, we propose a new approach to this emerging problem, which involves applying user interface (UI) metrics to VR experience. We review existing ways to increase VR immersion and outline a series of possible experiments to study and hopefully find a correlation between immersiveness and VR user interface effectiveness.

Keywords: Virtual Reality, Virtual environments, immersion, user interface, natural user interface.

1. Introduction

“Virtual reality is a high-end user-computer interface that involves realtime simulation and interactions through multiple sensorial channels. These sensorial modalities are visual, auditory, tactile, smell and taste” [1].

Well, now, when VR is emerging from the zone of pure science-fiction to become a ubiquitous technology, new problems arise. The fundamental research is necessary for the first place to find solutions to basic challenges encountered in all application areas.

Virtual Reality (VR) allows people to experience immersive virtual worlds in a way that makes them feel as if they are in them. During such an experience, multiple channels of the user’s perceptual system such as the visual, auditory and haptic channel are stimulated by the virtual world. These stimuli are triggered by computer systems simulating the Virtual Environment (VE).

Immersiveness is a degree of user involvement in VE. It characterizes, how a user feels in it and how quickly he can learn to manage it.

Thus, immersion is a user property to perceive virtual space as an existing reality. By definition, the higher value of immersion, the more comfortable and productive a user interacts with VR.

As the problem of seeing and hearing the virtual world is solved by modern VR goggles, the next modality to be included in VR systems is touch. As passive observation will not be enough in the long term, solutions that let the user interact with the virtual world in a natural way become crucial. One possible way to make VR tangible is to use real-world physical props, also called proxies, that are coupled to virtual objects. The user can then interact with virtual objects by interacting with the corresponding representative prop.

To develop predictable systems it is necessary to know about the influence of this mismatch on the user’s behavior in the VR and his perception of the virtual object.

To measure the immersiveness it is enough to measure the effectiveness of interaction with VR. However, there are other approaches to measure immersion.

2. Related Work

The term immersion is frequently mentioned in the same breath with the term presence in VR literature. In fact, depending on which definition of immersion or presence is considered, the difference between immersion and presence can be so small that both terms are frequently used as synonyms. However, subtle differences exist as immersion is a more "technology-related" term while

presence is considered the "psychological, perceptual and cognitive consequence of immersion" [2]. The origin of two different names describing almost the same or similar phenomena is due to the areas those terms are commonly used in or come from. While presence is a term originating from the area of teleoperation, immersion is commonly used in areas like games or movies [3].

There exist various conceptions of what immersion is, but an exact definition is hard to formulate. Among the most recognized definitions of immersion is the one by Murray: Murray describes immersion as "the experience of being transported to an elaborately simulated place". He details that immersion is "the sensation of being surrounded by a completely other reality, [...] that takes over all of our attention, our whole perceptual apparatus" [4]. Lombard and Ditton analyzed several definitions and concepts of presence and they identified a "central idea" shared by all conceptualizations that are very close to Murray’s definition of immersion: Presence means "the perceptual illusion of nonmediation" [4]. In other words, when immersed, the user behaves as if the perceived world would not be mediated by human-made technology but instead as if he would really be inside the virtual environment. The user "fails to perceive or acknowledge the existence of a medium in his/her communication environment and responds as he/she would if the medium were not there" [5]. In the context of VR systems, this can be interpreted as a mental and physical state in which the user is not directly aware of the VR system. Instead, the VE has taken over most (if not all) of his attention. As a consequence, the user unconsciously behaves as if he would really be present in the computer generated world and not as if he would control a computer [6]. When being immersed, there is no longer a border between the user and the virtual world with its virtual objects because the technology behind the illusion becomes perceptually invisible [5].

As immersion is a perceptual phenomenon, immersion is not a property of the system but instead a property of the user. It is something individual and dynamic that is different across users and also time-varying for each individual user [5]. A user’s degree of immersion changes as he interacts with the VR system. In some moments in time he may be more immersed than in others. Research on immersion in games showed that once a certain degree of immersion is established, it can make the user fail to notice usability issues and behavioral discrepancies [7].

2.1 Influential Factors and Layers of Immersion

As immersion originates from the interaction of the user with the VR system, the VR system is not solely

responsible for the experienced immersion. It is rather a property of the user. But some aspects of the VR system can facilitate immersion while others can be obstructive. VR systems aim to be media that foster long-lasting and strong immersion. Concerning the audiovisual dimension in VR systems, the usage of e.g. VR-HMDs and headphones blends out the stimuli of reality and substitutes it with stimuli of the VE. By this, some factors that may inhibit immersion are effectively removed which, in principle, opens the way to greater degrees of immersion. But it is important to note, that this is not a necessity for immersion to ensue. Immersion occurs also during desktop gameplay at a PC with a normal sized computer monitor that does not completely blend out the surrounding [6]. The audiovisual implementation is presumably an important factor influencing immersion but certainly not the only one nor the most important. While quality improvements in all three modalities (visual, auditory and haptic) of multimodal VRs does influence immersion, structural aspects concerning the virtual world seem to be at least as crucial [3, 6]. McMahan states that for an immersive VR experience,

- the conventions of the VE should match the expectations of the user,
- the user should be able to do non-trivial and meaningful actions that influence the VE and
- the virtual world must be consistent.

These structural factors promote interactivity which is encouraged by challenges and tasks. There even exists evidence, that the difficulty of the challenges in the virtual world can affect immersion [6]. This again emphasizes the importance of taking the step from pure passive VR applications to interactive applications as interactivity unlocks the potential of greater immersivity. Ermi and Mäyrä developed a gameplay experience model that describes three kinds of immersion that occur during gameplay [6]. These levels of immersion exist in VR and non-VR gameplay. The first level is sensory immersion, which describes the immersion coming purely from the sensation of audio/visual and haptic stimuli. The virtuality-based sensations overpower those from reality and thus immerse the player on a sensory level. The second level is challenge-based immersion which is the immersion coming from balanced challenges in the world. The user's tasks are demanding but match his abilities and through interaction he enjoys to fulfill and master them. The third level of immersion is the imaginative immersion that accrues when the user is absorbed in the stories of the game, uses his imagination and starts to feel for or identify with a game character.

Brown and Cairns introduced another model of immersion which is divided into three levels representing increased immersion [8]. According to the authors, the

prerequisite for each of those levels is that the barriers to them (on user-side and system-side) are removed and that all previous levels are already established. Fulfillment of this prerequisite does not, however, guarantee the next highest level of immersion to ensue but rather allows for it. The lowest level in this model is *engagement*, followed by an increased immersion in the level *engrossment*. The ultimate level of immersion is called *total immersion* and refers to the extreme case as defined above by Lombard and Murray. Concerning interaction, Brown and Cairns mention that "*an invisibility of controls*" is a fundamental prerequisite for total immersion to accrue [8].

2.2 Virtual reality and natural user interfaces

A user interface is an interlayer, providing the sharing information between a machine and a person. VR technology allows a person to interact with a machine with new, previously unused methods. Therefore, VR has a variety of user interface, or its possible characteristic, or a range of technologies, which can be used in the interface.

It is necessary to define a new type of user interfaces: natural user interface (NUI).

Currently, we are moving into the era of the NUI, which uses a user's natural gestures and voice, through the era of the most widely - used GUI. Examples of NUIs include a user interface based on gestures using fiber, magnetic sensors, and a data glove [17]. A UI using physical devices will accurately recognize a user's gestures, but the specific physical device must be attached to the user. Another example is a UI based on voice, which is the most universal and easiest method of communication between humans.

Characteristics of NUI are following:

- Using for communication and interaction with a machine the same resources as for communication and interaction with people and real world.
- Intuitiveness, that is not easy to evaluate objectively, due to its abstractness. In order to evaluate the intuitiveness of the proposed system, in [18] not provide subjects with instructions on the proposed hand-mouse interface, but measured the time taken to learn how to use it. Most of the subjects learned how to use the hand-mouse interface within 1 min.

The previous examples of using NUI: Anthropomorphic Artificial Social Agent with Simulated Emotions for free communication [13], Virtual Biotechnological Lab [14], Virtual surgery system with realistic visual effects and haptic interaction [15], VR system to enhance understanding process of robot mechanisms.

With the development of new haptic devices NUI application spheres are increased. The aim behind the natural paradigm is to remove barriers and offer a style of interaction more similar to the utilized in the real world; conveniently, the use of gestures can provide an attractive and natural alternative [19]. To our opinion, to measure the effectiveness of immersion it is sufficient to measure the effectiveness of NUI.

Haptic feedback can increase the realism when interacting with virtual objects in a virtual environment. User test [20] shows that users can perceive the simulated surface texture with at least 70% of correct rate.

2.3 Immersiveness measurement

Different methodologies exist to measure immersion or presence. One can try to capture the degree of immersion by observing the user's behavior or by monitoring physiological signs [9, 10]. Moreover, a huge body of literature exists on presence measurement questionnaires that try to deduce the degree of immersion from answers and ratings of the user [11].

A common questionnaire used in the related literature is the so called SUS-Presence-Questionnaire, named after the authors Slater, Usoh and Steed [9-12]. It aims to map the user's degree of immersion to a number between 0 (not immersed at all) and 6 (totally immersed). It consists of six questions rated on a scale from 1 to 7 and the final score is the amount of high ratings (6 or 7) per person.

The SUS questionnaire primarily considers the "sense of being there", the "extent to which the VE becomes more 'real or present' than reality" and the "extent to which the VE is thought of as a place visited" [11].

Interesting results are represented in the article [16], where is defined the concept of Dynamic Passive Haptic Feedback (DPHF) for VR by introducing the weight-shifting physical DPHF proxy object Shifty, combines actuators known from active haptics and physical proxies known from passive haptics to construct proxies that automatically adapt their passive haptic feedback.

The results show that such object enhances the perception of weight and thus the perceived realism by adapting its kinesthetic feedback to the picked-up virtual object. Такие подходы shown to increase the user's fun and perceived realism significantly, compared to an equivalent passive haptic proxy. Adaptations in all dimensions of proxy properties like for example shape, size, temperature, texture, absolute weight, and combinations thereof, can be imagined.



Fig.1. View of the virtual environment, representing the biotechnology laboratory

3. Technical implementation

Our aim is to develop an algorithm with different ways of increasing of the immersion, which could be typical for VR and frequently used.

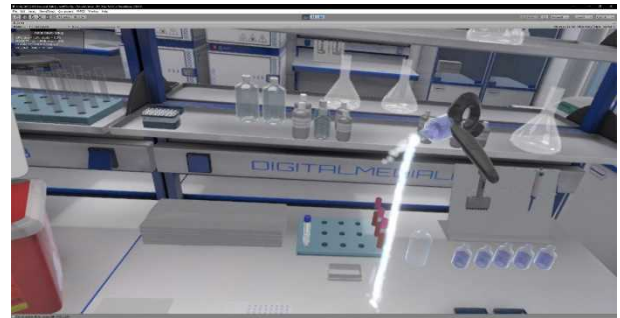


Fig.2. Pouring liquid is accompanied with visual effects and the sound of falling water from a certain height

We chose (Fig.1) the development of virtual biotechnology laboratory as the implementation [13]. This project was implemented in VR using Unity and accompanied by additional visual effects such as pouring liquid (Fig.2), bouncing back of virtual objects from virtual surfaces, sound effects of broken glass, opened doors (Fig.3), working engines and other effects.



Fig.3. Mechanisms are accompanied with sounds, fading with user's moving away; Opening doors are accompanied with sounds, that vary depending on door's weight

4. Results

Within the full synchronization of movement with according visual and audible feedback a user's perception of the virtual environment changes. Moreover, we claim, that users perceive a virtual object as heavier, more solid or softer depending on visual and audible feedback with an increasing number of according effects (sound of fall, amplitude of rebound, etc.) in a real laboratory. On the contrary, being decreased a virtual object is perceived as, for example, more fragile or lightweight.

Realism, perceived by a user can be improved by greatly synchronizing properties of virtual and real objects. These statements were reflected in some our experimental estimates.

5. Future work

Future work could integrate weight-shifting feedback into vibrotactile VR controllers. it would be interesting to investigate all types of object changes that can be enhanced by weight shifts. Considering new haptic devices as an input device for native user interfaces in VR, we can investigate how it changing interactions of a user with a virtual environment. we can be imagined a variation of adaptations in all dimensions of proxy properties like for example shape, size, temperature, texture, absolute weight, and combinations thereof.

References

1. G. C. Burdea and P. Coiffet, *Virtual Reality Technology*. 2 (New York, NY, USA: John Wiley & Sons, Inc., 2003).
2. D. Mestre, P. Fuchs, A. Berthoz and J. L. Vercher, *Immersion et présence. In: Le traité de la réalité virtuelle*. (Paris: Ecole des Mines de Paris, 2006), pp. 309–38.
3. A. Mcmanhan, *Immersion, engagement and presence* (The video game theory reader 67, 2003), pp. 86.
4. J. H. Murray, *Hamlet on the Holodeck: The Future of Narrative in Cyberspace* (Free Press, 1997).
5. M. Lombard and T. Ditton, *At the Heart of It All: The Concept of Presence* (Journal of Computer-Mediated Communication 3, 1997), N. 2.
6. L. Eemi and F. Mäyrä, *Fundamental components of the gameplay experience: Analysing immersion* (Worlds in play: International perspectives on digital games research 37, 2005).
7. K. Cheng and P. A. Cairns, *Behaviour, Realism and Immersion in Games* (CHI '05 Extended Abstracts on Human Factors in Computing Systems. New York, NY, USA: ACM, 2005). – ISBN 1–59593–002–7, pp. 1272–1275.
8. E. Brown and P. A. Cairns, *A Grounded Investigation of Game Immersion* (CHI '04 Extended Abstracts on Human Factors in Computing Systems. New York, NY, USA : ACM, 2004). – ISBN 1–58113–703–6, pp. 1297–1300.
9. B. E. Insko, *Passive haptics significantly enhances virtual environments* (University of North Carolina at Chapel Hill, Diss., 2001).
10. M. Usoh, K. Arthur, M. C. Whitton, R. Bastos, A. Steed, M. Slater, Jr F. P. Brooks, *Walking> walking-in-place> flying, in virtual environments* (Proceedings of the 26th annual conference on Computer graphics and interactive techniques ACM Press/Addison- Wesley Publishing Co., 1999), pp. 359–364.
11. J. Van Baren and W. Ijsselsteijn, *Measuring presence: A guide to current measurement approaches* (Deliverable of the OmniPres project IST-2001-39237, 2004).
12. M. Slater, M. Usoh and A. Steed, *Depth of presence in virtual environments* (Presence 3, 1994), Nr. 2, pp. 130–144.
13. V. Abramov, V. Kugurakova, A. Rizvanov, Abramskiy, M., N. Manakhov, M. Evstafiev, M. and D. Ivanov, *Virtual Biotechnological Lab Development*, in *BioNanoScience*, vol. 7, no. 2 (2017), pp. 363–365.
14. V. Kugurakova, M. Talanov, N. Manakhov, N. and D. Ivanov, *Anthropomorphic Artificial Social Agent with Simulated Emotions and its Implementation*, in *Procedia Computer Science* (2015), pp. 112.
15. V. Kugurakova, M. Khafizov, R. Akhmetsharipov, A. Lushnikov, D. Galimova, V. Abramov and O. Correa Madrigal, *Virtual surgery system with realistic visual effects and haptic interaction*, in *Icarob 2017: Proceedings of the 2017 International Conference on Artificial Life and Robotics* (2017), pp. P86-P89.
16. A. Zenner and A. Kruger, *Shifty: A Weight-Shifting Dynamic Passive Haptic Proxy to Enhance Object Perception in Virtual Reality* (IEEE Transactions on Visualization and Computer Graphics 23 (4), 2007), pp. 1312–1321.

17. D. J. Sturman and D. Zeltzer, "A survey of glove-based input," *IEEE Comput. Graph. Appl.*, vol. 14, no. 1, pp. 30–39, Jan. 1994.
18. S. Kim, S. Yeom, O. Kwon, D. Shin, *Hand-Mouse Interface using Virtual Monitor Concept for Natural Interaction* (IEEE, Access, doi:10.1109/ACCESS.2017.2768405, 2017).
19. D. M. Kaushik and R. Jain, *Gesture based interaction NUI: an overview* (*Int. J. Eng. Trends Technol.* 9(12), 2014), pp. 633–636.
20. Z. Lin and S. Smith, *A natural user interface for realistic tactile perception of object surface texture* (*Proceedings - 9th International Conference on Intelligent Human-Machine Systems and Cybernetics, IHMSC 2017*), pp. 370.

Lessons on the Reality-Gap: Iterations between Virtual and Real Robots

Andre Rosendo

*Living Machine Laboratory, ShanghaiTech University
Shanghai, 201210, China*

Charlie Houseago, Fumiya Iida

*Bio-inspired Robotics Laboratory, University of Cambridge
Cambridge, CB21PZ, United Kingdom*

*E-mail: arosendo@shanghaitech.edu.cn, charliehouseago@gmail.com, fi224@cam.ac.uk
www.shanghaitech.edu.cn*

Abstract

Due to approximations between the virtual and real world, the knowledge transfer from simulations to robots is problematic. As physical conditions are prone to unknown and stochastic noise sources, the predictability reduces. We use data experiments from 100 real robots to tune the parameters of a simulation, and later used this tuned simulator to improve the design of the previous robots and find the optimum robot. We compare the simulated and observed behavior of this robot, and discuss our results.

Keywords: Reality gap, evolutionary robotics, virtual robots, design optimization, body-mind co-optimization.

1. Introduction

The major obstacle of researchers creating a bridge between computer simulations of robots and the behavior seen in the real world is termed the ‘reality-gap’ problem [1]. Although simulations can be helpful to predict behaviors, a few researchers in robotic simulation community have repeatedly warned of the dangers of using over-simplified tools to simulate the behavior of real-world robotic agents [2]. A simulation by its very nature involves a number of levels of abstraction from true physical behavior, and thus fundamentally differ from the real robots they are attempting to emulate.

One common way of overcoming the reality gap for design of controllers is to use the notion of transferability, whereby it is hypothesized that different controllers will correspond better across the reality gap than others. The work of Jakobi [3] stressed the use of minimal simulations, which targeted areas of reality that would

insure robust, transferable behavior, but is therefore limiting in terms of broad applicability.

One successful approach to handling the reality-gap problem for control policy evolution is the transferability function, most notably employed in [4]. Under this framework, an additional measure aside from the objective function is employed which assigns a transferability to each potential control policy based on a small number of experiments in reality. They were able to demonstrate success in producing a transferability function using only 10 evaluations from the hardware in reality. Alternatively, rather than attempting to bridge the reality-gap for co-evolution of structure and control policy, the work conducted in [5] evolved 200 robots in the real world using an automated assembly and evaluation process. This consisted of a UR5 robotic arm, and a number of cubic modules, which were attached together using hot-melt adhesive. This experiment demonstrated the success of a real-world evolutionary

process which co-evolved both the physical structure and the control policy of a population of robotic agents.

In here we use the training data of experiments performed in the aforementioned experimental setting [6] to tune the parameters governing physical interaction in simulation. In this data-driven approach, we design our simulation environment to create a stronger correlation with the real-world and eventually achieve better correlation between reality and simulation. In addition, we wish to demonstrate that the relationship between simulation and reality is dependent both on the morphology and the control, and thus there is no universal transferability function that is independent of the morphology.

2. Methods

In the first stage of work, a simulation environment is designed to conduct virtual experiments similar to the ones performed at [6], and the output of which can be changed with different floor parameters which describe the response of the environment. Then we perform a Principal Component Analysis (PCA) of the results from reality with those of simulation to evaluate how close the behaviors are. A training process is then applied to choose the next set of parameters, and the process repeated. The output of the process is the choice of parameters which gives the smallest reality-gap, i.e. those for which the results from reality and from simulation are closest together.

2.1. Simulator and virtual model

A plentitude of physics simulators exists, and for this work we oriented our choices with the references [7], and we eventually chose Bullet to recreate virtually experiments that we performed a few years ago [6]. Bullet handles rigid collisions with greater accuracy, and we avoid the main limitation of the environment – poor damping behavior - due to the simplistic nature of the agents involved in this experiment.

The process was performed in a similar way to the aforementioned model-free morphology experiment. The genome structure comprises of 10 numeric values per cube (control and morphology), with one additional parameter per robot which defines the total number of cubes. Specifics of these parameters can be found at [6]. The comparison between the baseline real-world

experiments and the simulated structure can be seen in Fig.1.

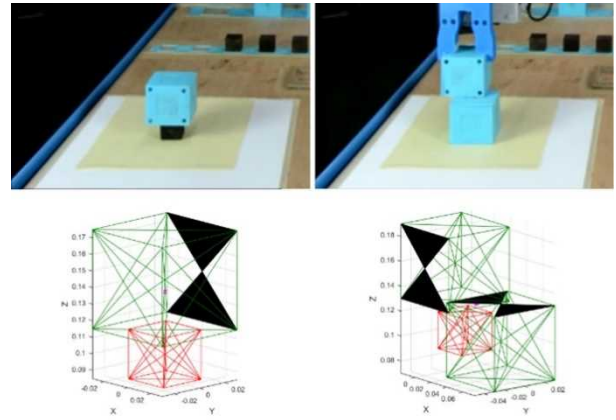


Fig. 1. Comparison of the real-world construction (above) and the simulation created from these constructions (below).

2.2. PCA of simulator with reality

In addition to comparing agents between reality and simulation based on fitness, we can use a more advanced method of matching agents based on the entire trajectory travelled. A number of different methods of performing 2D trajectory comparison exist, and there is an existing body of research into their applications in video motion tracking. As an example, in [8], the Hausdorff distance is used to express the spatial similarity between two trajectories.

In here, we employ an approach developed in [9], based on representing a trajectory as a cluster of data points using it's PCA coefficients. Given the relatively short length of trajectories in our experiment, and the large number of evaluations, we will work on the entire trajectory as one data cluster. The procedure while applying to a simulated trajectory consists of:

1. Subsample simulated trajectory to 182 data points
2. Translate both trajectories to start at the origin
3. Rotate trajectories such that their vector is aligned
4. Compute principal components and compare

As it can be seen in Fig. 2 and 3, the main trajectory of the real-world experiment depicted in Fig. 2 is compared with nine simulated trajectories from Fig. 3. The simulated behaviors from Fig. 3 have different floor parameters, simulating different friction and restitution coefficients. The number above each of these nine trajectories indicate the PCA discrepancy to the real-world result. The simulations from the middle row of

Fig.3 better approximate the real-world behavior, as not only the first principal component (fitness) is closer, but the shape of the trajectory curve is closer (better match with second and subsequent components).

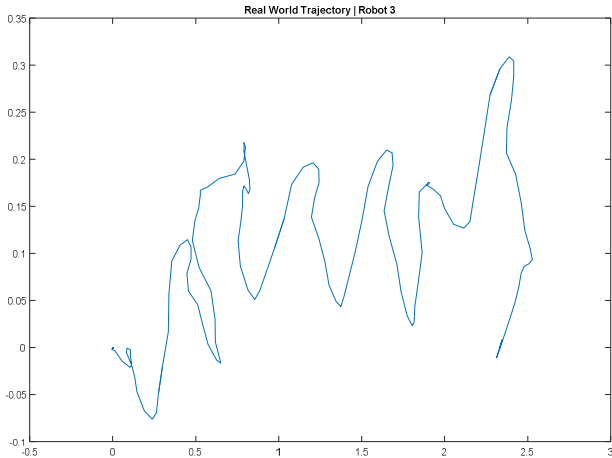


Fig. 2. Trajectory observed at the real-world experiment. The initial position is at (0,0), and distances are in centimeters.

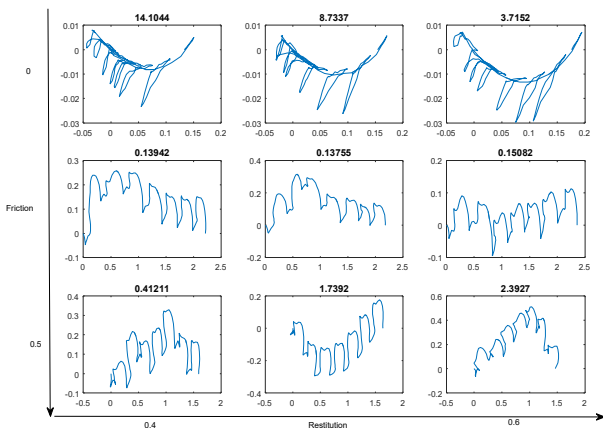


Fig. 3. Simulated trajectories with different friction and restitution coefficients. The number above each of these nine graphs stands for the difference between this particular case and the real-world behavior.

2.3. Optimizing parameters

The interaction between the agent and the ground is very complicated, and increasing the friction not only increases the impulse given to the agent by collisions of the rotating face with the terrain, but also increases the drag on the body as the agent moves itself along the ground. Changes in the restitution impact the time that an

agents body spends in contact with the terrain, and thus directly impact the response due to friction.

In Fig. 4 we show a heat map of the friction/restitution difference between the simulated fitness and the real world fitness for the robot morphology used to create the trajectory from Fig. 2. This data was collected at 441 evenly spaced points across the specified parameter ranges. The plot displays much steeper gradients in regions of high friction and restitution, as the response to changing either of the parameters becomes more severe. The shape of this plot is dependent on the robot morphology, in this case, the adopted robot moves with three active faces in contact with the ground surface. Depending on the physical values, different servos can be in contact with the ground at different parts of the motion cycle.

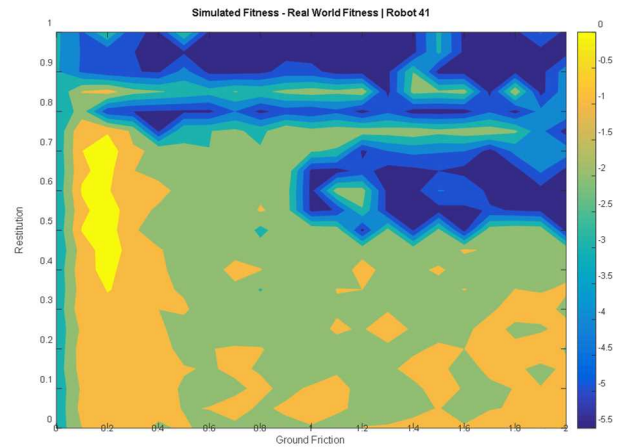


Fig. 4. Heat map of the difference between Simulated and Real behavior for changes in friction and restitution. The yellow area shows a promising region, where those parametric choices translate into a faithful reproduction in reality of the simulated trajectory.

3. Results and Discussion

With an optimized simulator in our hands we decided to conduct a Grid Search through the possible morphological and control combinations to create the best performing robot. The robot depicted in Fig. 5

showed the best behavior, and it was build and tested in the real world.



Fig. 5. Picture of the best predicted morphology, to which the behavior is finally compared with the simulated behavior.

In Fig. 6 we present the final outcome of this work. The comparison between the simulated trajectory and the real-world trajectory can be seen. Although both trajectories present a strong resemblance in trajectory shape, the simulated behavior was apparently a scaled down version of the real world output. One additional, and extremely important caveat: This resemblance in trajectory shape was only possible in 15% of the trials, as the robot followed different trajectories in other 60% of the cases, and in the last 25% didn't translate at the testing platform (solely rotation).

The previous result brings in question the deterministic approach to the Reality Gap: if the stochastic influence is such that a predicted behavior is rarely occurring, probabilistic approaches, with means and standard deviations of fitness values, might be a

better solution for this problem. Although a strong methodology was adopted, in this work we failed to predict the behavior of our proposed robot, and we believe that this work will guide others in search of a similar answer.

4. References

1. N. Jakobi, P. Husbands and Harvey I, "Noise and the Reality Gap: The use of simulation in Evolutionary Robotics," in *Advances in Artificial Life: Proceedings of the 3rd European Conference on Artificial Life*, 1995.
2. R. A. Brooks, "Artificial Life and Real Robots," in *Toward a Practice of Autonomous Systems: Proceedings of the First European Conference on Artificial Life*, 1992.
3. N. Jakobi, "Half-Baked, Ad-hoc and Noisy: Minimal Simulations for Evolutionary Robotics," in *Fourth European Conference on Artificial Life*, 1997.
4. S. Koos, J. B. Mouret and S. Doncieux, "The Transferability Approach: Crossing the Reality Gap in Evolutionary Robotics," *IEEE Transactions on Evolutionary Computation.*, vol. 17, pp. 122-145, 2013.
5. V. Vujovic, A. Rosendo, L. Brodbeck, F. Iida, "Evolutionary developmental robotics: Improving locomotion of physical robots." *Artificial Life* 23, 2 (2017).
6. L. Brodbeck, S. Hauser and F. Iida, "Morphological Evolution of Physical Robots through Model-Free Phenotype Development," *PLOS One*, 2015.
7. A. Boeing and T. Braunl, "Evaluation of real-time physics simulation systems," *Graphite '07*, pp. 281-288, 2007.
8. I. Junejo, O. Javed and M. Shah, "Multi-Feature Path Modelling for Video Surveillance," *Proceedings 17th international Conference on Pattern Recognition*, 2004.
9. F. I. Bashir, A. A. Khokhar and D. Schonfeld, "Segmented trajectory based indexing and retrieval of video data," *Proceedings International conference on Image Processing*, 2003.

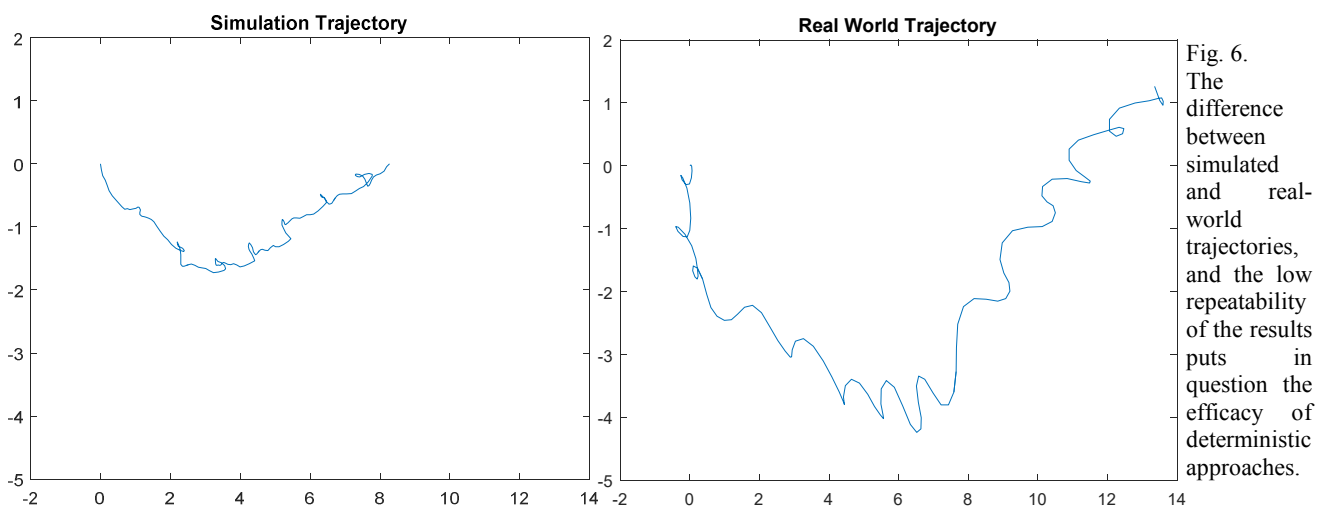


Fig. 6. The difference between simulated and real-world trajectories, and the low repeatability of the results puts in question the efficacy of deterministic approaches.

Fractional Order Sliding Mode Control Applying on the HIV Infection System

Thunyaseth Sethaput

Dept. of Mechanical Engineering, Sirindhorn International Institute of Technology, Thammasat University,
Pathum Thani, Thailand

Arsit Boonyaprapasorn

Dept. of Mechanical Engineering, Chulachomklao Royal Military Academy,
Nakhon-Nayok, Thailand

E-mail: thunyaseth@siit.tu.ac.th urarl.urarl9@gmail.com,
www.siit.tu.ac.th

Abstract

The mathematical model of HIV dynamical system explains the interaction between the immune system and virus. It represents the relationship among population size of uninfected CD4+ cells, infected CD4+ cell, and virus. The aim of the treatment is to drive the amount of uninfected CD4+ cells to the desired level and the amount of both infected CD4+ cells and virus particles approach to zero as time increased. The main objective of this study is to apply the fractional order sliding mode control (FOSMC) method to regulate HIV infection. The performance of the control method was investigated via simulation. According to the simulation of the controlled HIV system, the state variables approach to the desired values. Thus, it is feasible to apply the FOSMC method to define the treatment of the HIV infection system.

Keywords: Fractional order sliding mode control, Nonlinear control, Mathematical model, HIV.

1. Introduction

HIV infection damages the body's immune system by destroying CD4+ helper cells which are the defense cell. The amount number of circulating CD4+ helper cells is commonly used as an indicator of immune competence [1]. In other words, the HIV infection system describes the dynamic between virus infection and the immune system. To understand and analyze the dynamical HIV infection system, many mathematical models of HIV infection system have been developed [2, 3]. Based on the basic HIV mathematical model, the previous studies proposed both linear and nonlinear control method to assign the optimal treatment strategy or drug dosage [4-8].

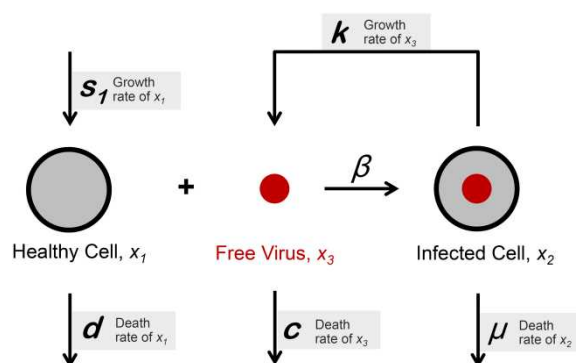


Fig. 1. Schematic illustration of the basic HIV infection model (modified from [2]). The healthy CD4+ cells grow at a rate s_1 and die at a rate d . The free viruses penetrate into the cells at a rate β and die at a rate c . The infected CD4+ cells produce free viruses at a rate k and die at a rate μ .

In any previous studies, to the best of our knowledge, the fractional order sliding mode control (FOSMC) method has not been developed for the HIV infection model. In this study, we proposed the feasibility of the fractional order sliding mode control method to regulate HIV infection and provide the treatment strategy.

2. Mathematical Model of HIV Infection System

The basic HIV mathematical model or the relationship between virus infection and the immune system through the number of CD4+ cells was proposed by Wodarz and Nowak [2]. As illustrated in Fig. 1, the model is composed of the interaction of three state variables: the healthy CD4+ cells (x_1), the infected CD4+ cells (x_2), and the free viruses (x_3).

$$\left. \begin{aligned} \dot{x}_1 &= s_1 - dx_1 - \beta x_1 x_3 (1 - u) \\ \dot{x}_2 &= \beta x_1 x_3 - \mu x_2 - \beta x_1 x_3 u \\ \dot{x}_3 &= kx_2 - cx_3 \end{aligned} \right\} \quad (1)$$

Generally, to boost the immune system, a treatment of HIV infection is to minimize the growth of new free virus particles (x_3) or to drive virus particles approach to zero. As presented in (1), the control input (u) is introduced as treatment effectiveness or drug dosage. The range of control input is between $u = 0$ (non-effective treatment) and $u = 1$ (most effective treatment). s_1 represents the production rate of healthy CD4+ cells. d, μ and c represent the death rate of healthy CD4+ cells, infected CD4+ cells and the free viruses respectively. k represents the production rate of free virus particles which depends on the population size of infected CD4+ cells. β represents the intensity of HIV infection process.

3. Design of Fractional Order Sliding Mode Controller

A definition of the fractional order derivative was proposed by Caputo [9-11] as

$$\frac{d^\alpha}{dt^\alpha} \sigma(t) = D^\alpha \sigma(t) = \frac{1}{\Gamma(1-\alpha)} \int_0^t \frac{D\sigma(\tau)}{(t-\tau)^\alpha} d\tau \quad (2)$$

where $0 < \alpha < 1$ and α is the order of the differentiation. Controller design procedure for the considered HIV model in (1) can be summarized as follows:

1) The sliding surface is selected in term of a linear combination of state variable (x_1, x_2, x_3) and

corresponding to desired values (x_{1r}, x_{2r}, x_{3r}) as in (3) [9]

$$s = c_1(x_1 - x_{1r}) + c_2(x_2 - x_{2r}) + c_3(x_3 - x_{3r}) \quad (3)$$

The differentiation of s can be obtained as in (4)

$$\begin{aligned} \dot{s} &= c_1 \dot{x}_1 + c_2 \dot{x}_2 + c_3 \dot{x}_3 \\ \dot{s} &= c_1[s_1 - dx_1 - \beta x_1 x_3 (1 - u)] \\ &\quad + c_2[\beta x_1 x_3 - \mu x_2 - \beta x_1 x_3 u] + c_3[kx_2 - cx_3] \end{aligned} \quad (4)$$

2) According to the fractional exponential approach as in (5) [9]

$$s^\alpha = k_1 \text{sign}(s) - k_2(s) \quad (5)$$

The first derivative can be determined as in (6)

$$\dot{s} = -D^{1-\alpha}[k_1 \text{sign}(s) + k_2(s)] \quad (6)$$

3) The control input can be solved from (7) given by equating (4) and (6) as follows

$$\begin{aligned} -D^{1-\alpha}[k_1 \text{sign}(s) + k_2(s)] &= c_1[s_1 - dx_1 - \beta x_1 x_3 (1 - u)] \\ &\quad + c_2[\beta x_1 x_3 - \mu x_2 - \beta x_1 x_3 u] + c_3[kx_2 - cx_3] \end{aligned} \quad (7)$$

Then,

$$\begin{aligned} u(t) &= \{-D^{1-\alpha}[k_1 \text{sign}(s) + k_2(s)] - c_1[s_1 - dx_1 - \beta x_1 x_3] \\ &\quad - c_2[\beta x_1 x_3 - \mu x_2] - c_3[kx_2 - cx_3]\} / \\ &\quad (-c_1 \beta x_1 x_3 - c_2 \beta x_1 x_3) \end{aligned} \quad (8)$$

See [9] for the proof of stability of the control system.

4. Simulation

To examine the ability of fractional order sliding mode controller on HIV model, the simulations of the control system are performed in MATLAB. The numerical integration method is the Runge-Kutta method with sampling time of 0.01 days from 129 to 1000 days.

4.1. Simulation Example

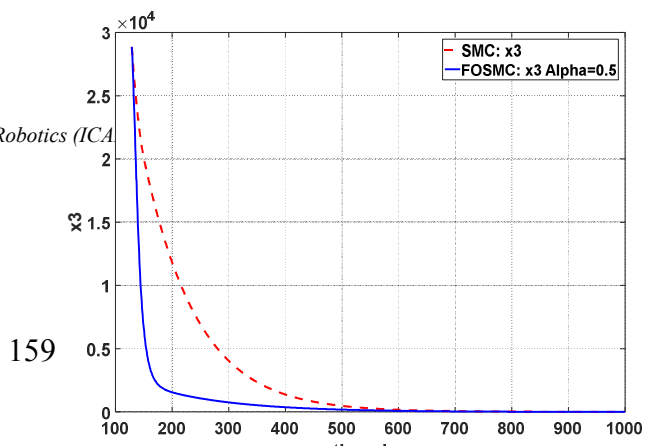
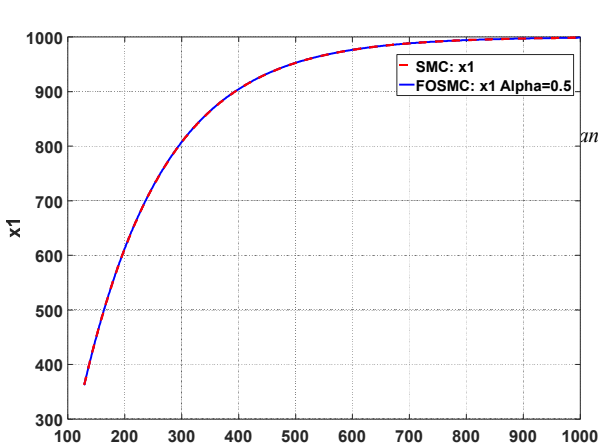
The parameter values and the initial conditions are obtained from [5, 6, 12] as follows: $s_1 = 7, d = 0.007, \mu = 0.0999, c = 0.2, k = 90.67, \beta = 00000042163$ and the initial condition at $t = 129$ days is $x(129) = [363, 57, 28860]^T$. For the highest HIV treatment effectiveness, the system requires the drive the

population size of healthy CD4+ cells, infected CD4+ cells and the free viruses to reach an equilibrium level at $[x_1, x_2, x_3]^T = [s_1/d, 0, 0]^T$.

The design control parameters are selected as follows: $c_1=800, c_2=160, c_3=200, k_1=0.1$ and $k_2=0.01$.

4.2. Simulation Results and Discussions

The simulation results show the ability of fractional order sliding mode controller (FOSMC) and sliding mode controller (SMC) on HIV model. As presented in Fig. 2, after treatment, the population size of healthy CD4+ cells increases as time increase and reach the assigned equilibrium level. Both control methods provide almost identical results. However, when the difference (error) between the amount of healthy CD4+ cells and the desired level is thoroughly observed, the FOSMC provides a faster rate of convergence compared to SMC as shown in Fig. 3. Fig. 4 shows the amount of infected CD4+ cells after treatment. The amount of infected CD4+ cells responses abruptly to effective therapy by decreasing rapidly and approaching zero. Obviously, FOSMC is able to drive the amount of infected CD4+ cells to desired level at a faster rate compared to SMC. Similarly, as shown in Fig. 5, the population of free virus particles drastically converges to equilibrium level at zero after effective therapy. The reasonable strategy of treatment provided by FOSMC is shown in Fig. 6. To prevent the production of new infected CD4+ cells and free viruses, the system requires the highest treatment effectiveness at early infection stage (loading dose). Then, the treatment effectiveness drops down and converges to maintenance dose to ensure that all of state variables (the amount of healthy CD4+ cells, infected CD4+ cells and free viruses) maintain at desired level.



5. Conclusion

In this paper, the mathematical model of HIV infection system with the fractional order sliding mode control method has been proposed. The numerical simulation results show the ability of fractional order sliding mode controller to regulate the amount of healthy CD4+ cells, infected CD4+ cells and free viruses. The results also provide reasonable treatment strategy or drug dosage. Based on the mathematical model, hence, the fractional order sliding mode controller is feasible to control HIV infection and direct the optimal guidelines for HIV treatment.

References

1. H. Masur, F. P. Ognibene, R. Yarchoan, J. H. Shelhamer, B. F. Baird, W. Travis, A. F. Suffredini, L. Deyton, J. A. Kovacs, J. Falloon, CD4 counts as predictors of opportunistic pneumonias in human immunodeficiency virus (HIV) infection, *Ann Intern Med.* 111(3) (1989) 223-31.
2. D. Wodarz and M. A. Nowak, Mathematical models of HIV pathogenesis and treatment, *BioEssays* 24(12) (2002) 1178-1187.
3. A. S. Perelson and P. W. Nelson, Mathematical analysis of HIV-1 dynamics in vivo, *SIAM Review* 41(1) (1999) 3-44.
4. I. K. Craig and X. Xia, Can HIV/AIDS be controlled? Applying control engineering concepts outside traditional fields, *IEEE Control Systems* 25(1) (2005) 80-83.
5. M. J. Mhaweji, C. H. Moog, F. Biafore, and C. B. François, Control of the HIV infection and drug dosage, *Biomedical Signal Processing and Control* 5(1) (2010) 45-52.
6. M. Shirazian and M. Farahi, Optimal control strategy for a fully determined HIV model, *Intelligent Control and Automation*, 1 (1) (2010) 15-19.
7. M. R. Zarrabi, M. H. Farahi, S. Effati, and A. J. Koshkouei, Using sliding mode control in stability treatment of HIV disease *Advanced Modeling and Optimization*, 14(1) (2012) 165-173.
8. A. Boonyaprapasorn, P. SaNgiamsunthorn, and T. Sethaput, Synergetic control for HIV infection system of CD4+T cells, *In Proceedings of the 2016 16th International Conference on Control, Automation and Systems (ICCAS)* (2016) 484-488.
9. M. O. Efe, Fractional order sliding mode control with reaching law approach, *Turk J. Electr. Eng. Comput. Sci.* 18(5) (2010) 731-747.
10. C. A. Monje, Y. Q. Chen, B. M. Vinagre, D. Xue and V. Feliu-Battle, *Fractional-order Systems and Controls*, 1st edn. (Springer-Verlag London, 2010)
11. I. Petras, *Fractional-Order Nonlinear Systems*, 1st edn. (Springer-Verlag Berlin Heidelberg, 2011)
12. X. Xia, Estimation of HIV/AIDS parameters, *Automatica* 39(11) (2003) 1983-1988.
1. H. Masur, F. P. Ognibene, R. Yarchoan, J. H. Shelhamer, B. F. Baird, W. Travis, A. F. Suffredini, L. Deyton, J. A. Kovacs, J. Falloon, CD4 counts as predictors of opportunistic pneumonias in human immunodeficiency

Skill-based Job Rotation Scheduling for Occupational Noise Exposure Control

Pavinee Rerkjirattikarn, Chatdanai Kaorapapaong, Sun Olapiriyakul*

*School of Manufacturing Systems and Mechanical Engineering, Thammasat University,
Pathum Thani, 12121, Thailand*

pavinee.rerk@gmail.com, chatdanaik@gmail.com, suno@siit.tu.ac.th
https://www.siit.tu.ac.th/*

Abstract

This paper proposes a job rotation methodology for noise exposure control in manufacturing systems, with task skill requirements. A situation where management needs workers to work overtime to meet demand is considered. An integer programming is formulated, to simultaneously minimize the labor cost and to reduce the noise exposure levels of workers to a safe level. The use of the model is illustrated by applying the model to prepare job rotation plan over a 10-day period. The labor cost associated with different overtime policies is investigated.

Keywords: noise exposure, hearing loss, job rotation, scheduling, optimization, overtime

1. Introduction

In most cases, a complete protection of workers against excessive occupational noise exposure can be quite challenging for complex and large manufacturing systems. Noise mitigation strategies involving parts or equipment modification, usually require an extended period of time for implementation. Job rotation is shown to be an effective temporary noise exposure control measure. As demonstrated in previous research, job rotation can be used to control the noise exposure duration, and the maximum daily noise exposure level of workers¹. Job rotation can also be used to limit the number of workers exposed to excessive noise levels². Recently, research on noise-safe job rotation has contributed to an understanding of the effects of job rotation on productivity. For systems with extended process setup time, job rotation can cause significant productivity loss, due to the excessive setup time required for workers to adjust to new working conditions³. For systems comprising tasks with high skill requirements, it is difficult to assign workers to the full extent of their capacity. In noise-safe job rotation models developed by Nanthavanij et al. (2010), productivity is measured in terms of competency-based scores and defined as an optimization objective, ensuring that the highest possible level of competency in performing tasks of the workforce is achieved⁴. Skill-based job rotation

models for noise exposure control are developed, to cope with the assignment of workers with varying levels of skill, experience, and limitations⁵⁻⁹. These previous studies help improve the practical application of noise-safe job rotation measures. Nonetheless, crucial research gaps remain in this field: 1) insufficient evaluation of the ability of the workforce to fulfill demand requirements; 2) lack of quantitative assessment of productivity loss, due to the inability of workers to fulfill skill requirements of tasks; 3) insufficient understanding of the effects of job rotation on job satisfaction of workers. This study aims to design a skill-based job rotation model, under a 10-day planning horizon, with demand fulfillment requirements. The objective is to simultaneously minimize the labor cost and reduce noise exposure levels of workers to a safe level. The effects of job rotation on the productivity of the workforce are considered. This paper also shows that job rotation plans, with an appropriate workforce size and overtime usage, can be used to meet demands, while maintaining the fairness of overtime assignments.

2. Mathematical Model

An integer programming model is formulated to find an optimal job rotation plan, to minimize labor cost and to reduce the noise exposure levels of workers to a safe level. The daily noise exposure limitations and demand requirements of all independent workstations are

formulated as constraints. In this study, the workforce comprises skilled- and unskilled-workers. Skilled workers perform tasks with higher productivity levels. The assignment of unskilled workers is restricted to unskilled tasks only. In a workday, there are two regular 4-hour shifts, and a 4-hour overtime shift. Workers can be rotated between tasks at the end of shifts. Other important working conditions are summarized as follows.

- When performing tasks at the same workstations for more than one shift consecutively, workers perform tasks at higher levels of productivity, specified as an extra production rate.
- The number of workers assigned to tasks varies, according to the production capacities needed to meet demands over the planning horizon.
- Labor cost can be classified into direct and indirect costs. The direct cost includes regular- and overtime-shift wage costs, whereas the indirect cost is overhead cost per worker.
- All costs related to skilled workers are higher than that of unskilled-workers.
- Overtime costs 1.5 times the regular shift wage.
- A worker can perform only one task at a time.

2.1 Mathematical model formulation

2.1.1 Indices

i	Number of workstations ($i = 1, \dots, I$)
j	Number of shifts ($j=1, \dots, J$; morning, afternoon, and overtime shifts are denoted as MO, AFT, and OT, respectively)
s	Skill levels of workers ($s = 1, \dots, S$)
n	Number of workers ($n = 1, \dots, N$)
t	Number of workdays ($t = 1, \dots, T$)

2.1.2 Parameters

D_i	Noise dose of workstation i
W_i	Demand requirement of workstation i
$P_{i,s}$	Production rate of workers with skill level s , at workstation i
$E_{i,s}$	Extra productivity gained by skill level s workers for performing task at the workstation i over consecutive shifts.
LR_s	Regular-shift wage of worker skill s
LO_s	Overtime wage of worker skill s
OH_s	Overhead cost of worker skill s
$Max\ dose$	Maximum allowable noise exposure level
$Max\ OT$	Maximum allowable overtime shifts

2.1.3 Decision Variables

$X_{i,j,s,n,t}$	= 1 if worker n , skill s , works at workstation i , shift j , on day t ; 0 otherwise.
$Y_{i,s,n,t}$	= 1 if worker n , skill s , works at workstation i of both morning and afternoon shift; 0 otherwise.
$Z_{i,s,n,t}$	= 1 if worker n , skill s , works at station i of both afternoon and overtime shift; 0 otherwise.
$A_{s,n,t}$	= 1 if worker n , skill, s is scheduled to work on day t ; 0 otherwise.
$C_{s,n}$	= 1 if worker n , skill s , is selected under the job rotation plan; 0 otherwise.

2.1.4 Mathematical Model

Minimize

$$\sum_{t=1}^T \sum_{n=1}^N \sum_{s=1}^S LR_s \cdot A_{s,n,t} + \sum_{t=1}^T \sum_{n=1}^N \sum_{s=1}^S \sum_{i=1}^I LO_s \cdot X_{i,j=OT,s,n,t} + \sum_{n=1}^N \sum_{s=1}^S OH_s \cdot C_{s,n} \quad (1)$$

Subject to

$$\sum_{i=1}^I X_{i,j,s,n,t} \leq 1 \quad \forall j, s, n, t \quad (2)$$

$$\sum_{i=1}^I \sum_{j=1}^J X_{i,j,s,n,t} \leq 3 \cdot A_{s,n,t} \quad \forall s, n, t \quad (3)$$

$$\sum_{i=1}^I \sum_{j=1}^J D_i \cdot X_{i,j,s,n,t} \leq Max\ dose \quad \forall s, n, t \quad (4)$$

$$2 \cdot \sum_{i=1}^I X_{i,j=OT,s,n,t} - \sum_{i=1}^I X_{i,j=MO,s,n,t} + X_{i,j=AFT,s,n,t} = 0 \quad \forall s, n, t \quad (5)$$

$$\sum_{t=1}^T \sum_{n=1}^N \sum_{s=1}^S \sum_{j=1}^J P_{i,s} \cdot X_{i,j,s,n,t} + \sum_{t=1}^T \sum_{n=1}^N \sum_{s=1}^S Y_{i,s,n,t} \cdot P_{i,s} \cdot E_{i,s} + \sum_{t=1}^T \sum_{n=1}^N \sum_{s=1}^S Z_{i,s,n,t} \cdot P_{i,s} \cdot E_{i,s} \geq W_i \quad \forall i \quad (6)$$

$$Y_{i,s,n,t} \leq \frac{X_{i,j=MO,s,n,t} + X_{i,j=AFT,s,n,t}}{2} \quad \forall i, s, n, t \quad (7)$$

$$Y_{i,s,n,t} \geq (X_{i,j=MO,s,n,t} + X_{i,j=AFT,s,n,t}) \cdot M - (2M - 1) \quad \forall i, s, n, t \quad (8)$$

$$Z_{i,s,n,t} \leq \frac{X_{i,j=AFT,s,n,t} + X_{i,j=OT,s,n,t}}{2} \quad \forall i, s, n, t \quad (9)$$

$$Z_{i,s,n,t} \geq (X_{i,j=AFT,s,n,t} + X_{i,j=OT,s,n,t}) \cdot M - (2M - 1) \quad \forall i, s, n, t \quad (10)$$

$$\sum_{t=1}^T A_{s,n,t} \leq M \cdot C_{s,n} \quad \forall s, n \quad (11)$$

$$\sum_{t=1}^T \sum_{i=1}^I X_{i,j=OT,s,n,t} \leq Max\ OT \quad \forall s, n \quad (12)$$

The objective function (1) minimizes the total labor cost. Constraint (2) ensures that each worker can perform only one task at a time. Constraint (3) records the working days of workers. Constraint (4) ensures that the maximum allowable noise exposure limit is maintained for all workers. In a working day, constraint (5) specifies that a worker, who works for both morning and afternoon

shifts, is eligible to work overtime. Constraint (6) ensures that the demand requirements of all workstations are fulfilled. Constraints (7) and (8) record the continuity of morning and afternoon shift assignments. Constraints (9) and (10) record the continuity of afternoon and overtime shifts. Constraint (11) counts the number of workers to be included in a job rotation plan. Constraint (12) ensures that the number of overtime shifts, assigned to workers over the planning horizon, does not exceed the maximum allowable number of overtime shifts.

3. Numerical Example

A manufacturing system with 5 independent workstations is considered. The workforce consists of 5 skilled workers and 5 unskilled workers. Demand requirements and noise levels of workstations are shown in Table 1. The noise levels are recorded in decibel A units (dBA), which are the relative loudness perceived by human ears. As recommended by OSHA, the safe limit of Daily Noise Dose (DND) is 1, which is equivalent to 90 dBA.

Table 1. Demand requirements and noise levels of workstations.

Workstation	Demand Requirement (Units)	Noise Level (dBA)	Noise dose per shift
W1	3,450	90	0.50
W2	1,265	93	0.76
W3	1,495	70	0.03
W4	2,300	85	0.25
W5	2,530	80	0.13

The regular and extra production rates of skilled and unskilled workers are shown in Table 2. The tasks at workstation W2 and W3 are complex, and can only be performed by skilled workers. For these workstations, the production rate of unskilled workers is specified as zero. The wages of regular and overtime shifts, as well as the overhead cost per worker, are shown in Table 3.

Table 2. Regular and extra production rate.

Workstation	Regular Production Rate (Units)		Extra Production Rate (Percentage)	
	Skilled	Unskilled	Skilled	Unskilled
W1	100	70	40%	25%
W2	80	0	25%	0
W3	60	0	35%	0
W4	60	35	20%	15%
W5	80	50	15%	35%

Table 3. Direct and indirect labor costs.

Labor Cost	Skilled Workers	Unskilled Workers
Regular (THB per shift)	300	150
Overtime (THB per shift)	450	225
Overhead (THB per worker)	5000	3000

The use of overtime in job rotation, to meet demand, is considered. There are 3 overtime policies considered: 1) no overtime allowed; 2) unlimited overtime; 3) limited overtime (at most 5 times per worker).

4. Result and Discussion

Opensolver version 2.8.6 is used as a problem solving tool. Under the cost minimization objective, the labor costs of the optimal rotation plans associated with different OT policies are shown in Table 4.

Table 4. Total labor cost of each overtime policy.

	No overtime	Unlimited overtime	Limited overtime
Total Cost (THB)	70,700	62,635	67,875
No. of Workers	9	7	8
Average noise dose	0.549	0.783	0.661

In this paper, the use of overtime to meet demand appears to be cost-effective, by avoiding the cost of hiring additional workers. The unlimited overtime plan has the lowest labor cost. However, this plan requires some workers to work more than 9 overtime shifts during the 10-day period. This may lead to adverse effects, related to safety, health, and job satisfaction. The limited overtime plan, as shown in Table 5, enables a more balanced distribution of regular and overtime shifts, among each group of workers. When there is no overtime, a larger number of workers is required to meet demands, resulting in higher labor cost. However, the use of a large workforce size results in a reduced average noise dose level.

Table 5. Job rotation plan under the limited overtime policy

Workforce		Daily noise dose										Number of Shifts		Work-Days
		Day 1	Day 2	Day 3	Day 4	Day 5	Day 6	Day 7	Day 8	Day 9	Day 10	Regular	Overtime	
		Skilled worker	1	0.758	0.313	0.500	0.531	0.789	0.031	0.789	0.820	0.820	0.820	
2	0.789		0.758	0.750	0.820	0.820	0.750	0.758	0.820	0.031	0.063	17	5	10
3	0.000		0.000	0.000	0.000	0.000	0.000	0.000	0.000	0.000	0.000	0	0	0
4	0.000		0.000	0.000	0.000	0.000	0.000	0.000	0.000	0.000	0.000	0	0	0
5	0.758		0.000	0.000	0.000	0.789	0.000	0.758	0.000	0.758	1.000	7	1	8
Unskilled worker	1	0.375	0.750	0.750	1.000	1.000	0.750	1.000	1.000	1.000	0.375	20	5	10
	2	1.000	1.000	1.000	0.375	0.375	0.750	0.375	0.750	1.000	0.375	20	5	10
	3	0.125	1.000	0.750	1.000	0.625	0.375	1.000	0.750	1.000	1.000	19	5	10
	4	0.375	0.375	1.000	0.750	1.000	0.500	1.000	0.750	1.000	0.375	20	5	10
	5	1.000	0.375	0.750	0.750	0.375	1.000	0.375	1.000	1.000	0.125	19	5	10
Cost (THB)												27,300	10,575	30,000*

*overhead cost

5. Conclusion

This study proposes a noise-safe job rotation methodology that can be used in manufacturing systems with skill and demand requirements. In the proposed model, job rotation is used at the cost of losing productivity by performing the same tasks repetitively. The validity of the proposed model is investigated, using a numerical example where workers are assigned to work overtime to meet demands. The ability of the workforce to meet demand, usually neglected from previous job rotation studies, is included as one of the essential components of our job rotation model. The development of noise-safe job rotation plans with overtime shifts is also introduced. The result shows a case where the total labor cost is minimized by employing a small-sized workforce and assigning workers to work overtime. It is shown that, the limited overtime results in a more even allocation of overtime shifts among each group of workers. Our future study aims to focus more on the effects of job rotation on job satisfaction. The fairness of workload distribution and injury risk perception of workers are important elements to be further explored in the context of job rotation.

References

1. W. Thammaphornphilas, B. Green, B. J. Carnahan, B. A. Norman, Applying mathematical modeling to create job rotation schedules for minimizing occupational noise exposure, *J. American Industrial Hygiene Association*. **64**(3) (2010) 401-405.
2. S. Yaoyuenyong and S. Nanthavanij, Hybrid procedure to determine optimal workforce without noise hazard exposure, *Computers & Industrial Engineering*. **51** (2006) 743-764.

3. P. Rerkjirattikarn, S. Satitanekchai, S. Olapiriyakul, Designing safe job rotation schedules with minimum productivity loss, *J. Supply Chain and Operations Management*. **14**(2) (2016) 48-60.
4. S. Nanthavanij, S. Yaoyuenyong, C. Jeenanunta, Heuristic approach to workforce scheduling with combined safety and productivity objective, *IJIE*. **17**(4) (2010) 319-333.
5. B. A. Norman, W. Thammaphornphilas, K. L. Needy, B. Bidanda, R. C. Warner, Worker assignment in cellular manufacturing considering technical and human skill, *Int. J. Production Research*. **40**(6) (2002) 1479-1492.
6. V. Delijoo, S.M.J. Mirzapour Al-e-hashem, H. Malekly, A. Bozorgi-Amiri, M.B. Aryanejad, Applying multi objective modeling to create safe job rotation schedules based upon workers' skills and idleness, *Int. Conf. Computers and Industrial Engineering*, (Troyes, France, 2009), pp. 262-267.
7. T. Wongwien and S. Nanthavanij, Ergonomic workforce scheduling under complex worker limitation and task requirements: mathematical model and approximation procedure, *SJST*. **34**(5) (2012) 541-549.
8. F. Niakan, A. Baboli, T. Moyaux, V. Botta-Genoulaz, A bi-objective model in sustainable dynamic cell formation problem with skill-based worker assignment, *J. Manufacturing Systems*. **38** (2016) 46-62.
9. T. Wongwien and S. Nanthavanij, Priority-based ergonomic workforce scheduling for industrial workers performing hazardous jobs, *J. Industrial and Production Engineering*. **34**(1) (2017) 52-60.

A Training Method for the Speech Controlled Environmental Control System Based on Candidate Word Discriminations*

Taro Shibanoki[†], Masaki Watanabe[†], Go Nakamura[‡], Takaaki Chin,[‡] and Toshio Tsuji[§]
[†]Ibaraki University, [‡]Hyogo Rehabilitation Center, [§]Hiroshima University

Abstract

This paper proposes a concept of a training system for the speech controlled environmental control system: Bio-Remote based on candidate word discriminations. The proposed system can provide three-types of voice signal training: (1) volume, (2) tempo/timing and (3) candidate word which are important for accurate speech recognition based on false recognition results. During the training, such three kinds of features are extracted from measured voice signals and visually and auditory fed back to the user in real time. This allows the user to train speech abilities even if false recognition results are extracted because of slurred speech.

The efficacy of the proposed system was demonstrated through training experiments for slurred speech conducted with healthy participants. The results showed that the proposed system was capable for train the speech abilities.

Keywords: speech training, environment control system (ECS), speech recognition, candidate word, learning-type look-up table.

1. Introduction

The number of disabled people in Japan continues to increase annually and stands at 1.76 million. The population of severely disabled people in particular was around 760,000, and such patients associated with a speech disability reached 81,000 [1].

Against such a background, many speech-controlled environmental control systems (ECSs) have been developed [2], [3]. However, it is difficult for patients with dysarthria to use such systems, since the models used in these systems considers standard adults' speech. Although some studies have investigated the use of speaker-dependent models to support the learning of individual users' voices [4], and the authors' research group also proposed the voice signal-based manipulation method for ECS based on candidate word discrimination [5], fluctuating speech makes discrimination difficult.

The speech training system can support the recovery of as much of a user's speech as possible, and it has been widely discussed as motivation and long-term experiences for users [6], [7]. However, it can be difficult to fully recover verbal functioning because of individual differences and degrees of disability.

This paper proposed a training system for a speech-controlled environmental control system based on candidate word discrimination that can acquire the skill of fixed speech. After the training, the user's intention can be accurately discriminated, even if the user cannot fully recover his/her verbal functioning.

2. Speech Training System Based on Candidate Word Discrimination

Figure 1 shows the structure of the proposed speech training system based on candidate word discrimination.

* This work was partially supported by JSPS/MEXT KAKENHI Grant Numbers 17K12723 and 26330226.

[†]4-12-1, Nakanarusawacho, Hitachi, 316-8511 JAPAN (e-mail: taro.shibanoki.ts@vc.ibaraki.ac.jp, 14t4070a@vc.ibaraki.ac.jp)
<http://bs.cis.ibaraki.ac.jp>

[‡]1070 Akebonocho, Nishi-Ku, Kobe, 651-2181 JAPAN (e-mail: g_nakamura@assistech.hwc.or.jp, chin@assistech.hwc.or.jp)

[§]1-4-1, Kagamiyama, Higashi-Hiroshima, 739-8527 JAPAN (e-mail: tsuji@bsys.hiroshima-u.ac.jp)

© The 2018 International Conference on Artificial Life and Robotics (ICAROB2018), Feb. 1-4, B-Con Plaza, Beppu, Oita, Japan

The proposed system provides training for patients with dysarthria to speak the same way every time, even with slurred speech. This training can be applied to control the training of a voice-controlled environmental control system [5] with slurred speech.

The proposed speech training system consists of a PC with a feedback display, audio processor, and microphone. During the speech training, the display provides the extracted features of voice signals and current status of the users' abilities to improve their speech skills. The details of the system are described in the following subsections.

2.1. Voice signal processing

The structure of the voice signal processing is shown in Fig. 1. First, the amplitude and timing information of voice signals are extracted, and discrimination results are then obtained using the candidate words/phenomes W_h/M_h and the log-likelihoods $T(W_h)$ with the candidate word discrimination method [5].

2.1.1. Extraction of voice signal features

Voice signals were recorded using a microphone and sampled at 16 [kHz]. The amplitude information $v(t)$ of the measured voice signals with full-wave rectification and low-pass filtering (cut-off frequency: 1 [Hz]) is obtained based on the gains of the amplifier and microphone input levels.

Feature vector X used for speech recognition is then defined as the low-frequency components of Mel-frequency cepstrum coefficients (MFCCs) for each frame, and the output probabilities $P(X|W)$ of a feature vector X from word $W = \{w_1, w_2, \dots, w_K\}$ (w_k : word, K : number of words) are calculated using an N-gram model and phoneme-hidden Markov model (phoneme HMM) dividing the words W into phonemes $m = \{m_1, m_2, \dots, m_J\}$ (m_j : phoneme, J : number of phonemes) and matching phoneme HMM to X . Subsequently, the top H words W_h ($h = 1, 2, \dots, H$) with the maximum log-likelihood, their phonemes M_h , and log-likelihoods $T(W_h)$ are extracted using Julius [8].

2.1.2. Intention estimation using candidate word discrimination

The user's intention is discriminated using the learning-type look-up table (LUT) [5]. The user is instructed to

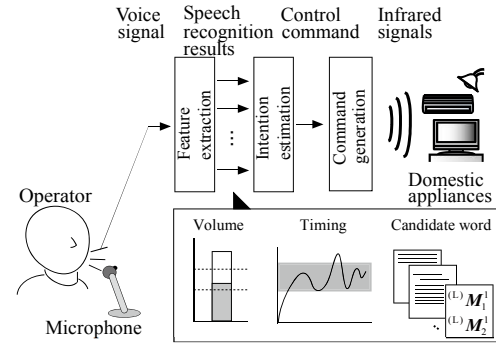


Fig. 1. Structure of the proposed training system

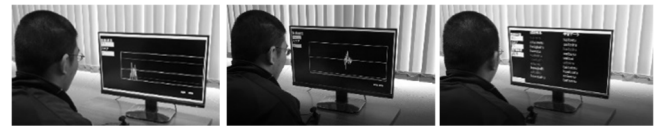


Fig. 2. Scenes from the training

utter C words (corresponding to the control commands of domestic appliances) multiple times, and top V words W^c_v with their maximum log-likelihood and their phonemes M^c_v and log-likelihood $T(W^c_v)$ in H extracted words are corresponded to each discrimination class ($c = 1, 2, \dots, C$; $v = 1, 2, \dots, V$; $V < H$) in the learning stage. In the discrimination stage, a new set of H words are extracted, and the phonemes ${}^{(D)}M_u$ ($u = 1, 2, \dots, U$; $U < H$) of top U words with their maximum log-likelihood are compared to phoneme ${}^{(L)}M_i$ ($i = 1, 2, \dots, I_c$; I_c : number of learning data for class c) of each discrimination class memorized in the learning-type LUT. The coincidence $s_{u,i}^c$ between ${}^{(D)}M_u$ and ${}^{(L)}M_i$ is then calculated, and a class with a maximum value of r^c representing the average of all $s_{u,i}^c$ values (the number of coincident phonemes) is then taken as the discrimination result. To disambiguate discrimination, the difference between log-likelihoods $T({}^{(D)}W_u)$ and $T({}^{(L)}W^c_i)$ is used to determine the result when the same values for some classes are obtained.

2.2. Speech training for candidate word discrimination method

For speech therapy, the treatment of articulation, prosody and pitch range, speech rate, vocal volume, or resonance is important [6]. The proposed speech training is therefore composed of three stages (see Fig. 2), as explained in the following subsections.

Before the training, to make the learning data sets used in each training, the trainee is instructed to utter C words

T times, and the maximum/minimum and average volumes of each word are determined. The durations of $C \times T$ words [$^{\text{start}}D^c_i, ^{\text{end}}D^c_i$] used in the timing/tempo control training are also determined using Julius [8].

2.2.1. Volume control training

In this training, the trainee practices controlling the vocal volume level. During the training, the amplitude information extracted from a measured voice signal is presented on the display with the desired values (predetermined maximum/minimum and average). The trainee controls his/her voice signal so the extracted amplitude information follows the average value and falls within the min./max. range. The training result is evaluated using the following equation.

$$S_t = \begin{cases} 100 - (V_{\text{ave}} - v(t)) & (V_{\text{min}} \leq v(t) \leq V_{\text{max}}) \\ 0 & (V_{\text{min}} > v(t), v(t) > V_{\text{max}}) \end{cases} \quad (1)$$

The closer the amplitude information is to the average, the higher the score, and if it exceeds the min./max. values, the score becomes zero. The average of the S_t value of speech duration is output at the end of each trial.

2.2.2. Tempo/timing control training

For accurate discrimination using the candidate word discrimination method, it is also important to control the timing and time from the start to the end of speech. In this training, the trainee controls the tempo/timing of his/her speech. During the training, the stored voice signals of each word are randomly shown in the display. The trainee is instructed to regulate his/her speech duration and timing according to the pre-specified timing shown in waveforms. The system evaluates the ratio of extracted speech duration to pre-specified duration in this training.

2.2.3. Candidate word speech training

Candidate word speech training is conducted so the trainee speaks approximately the same way every time. The candidate phonemes for each discrimination word and extracted trainee's phonemes are shown in the display during this training. The trainee practices to control his/her speech so similar candidate phonemes are extracted. The score of this training is defined as a ratio of the number of complete/ambiguous coincidence in candidate and extracted phonemes:

$$S_h = \begin{cases} (100 - S_{\text{th}})/D_{\text{cmp}} & (L^{(L)}M_i^c, M_h) = 0 \\ (100 - S_{\text{th}})/D_{\text{amb}} & (0 < L^{(L)}M_i^c, M_h) \leq L_{\text{th}} \\ 0 & (L_{\text{th}} < L^{(L)}M_i^c, M_h) \end{cases} \quad (2)$$

where $L(\cdot)$ represents Levenshtein distance.

3. Training Experiments

3.1. Method

To verify the efficacy of the proposed training system, training experiments were performed with three healthy males (subjects A–C, 22.3 ± 1.15 [year]). In the experiments, participants were instructed to speak with their tongue touching the maxillary central to simulate slurred speech. The parameters used in the experiments were set as $C = 7, T = 10, H = 10, V = 10, U = 5, D = 10, L_{\text{th}} = 1, D_{\text{cmp}} = 10, D_{\text{amb}} = 500$, and $S_{\text{th}} = 50$. The other parameters, K, J , and I_c , were adjusted based on the input voice signal durations and learning procedure results. Ten sessions of each training stage were performed in the training experiments, and discrimination experiments were also performed before and after training to verify the effectiveness of the proposed training method. In the discrimination experiments, participants were asked to utter each word three times without feedback.

3.2. Results and discussion

Figure 3 shows examples of experimental results. From this figure, the training scores were stable as the number of sessions increased, and the average discrimination rates before and after training have relatively high accuracy. Although participants simulated slurred speech, they can utter each word the same way from the beginning of the training.

Therefore, other training experiments were performed so the participants could mimic other participants' speech. In the experiments performed, Sub. A trained using Subs. B and C's learning data sets. These experimental results are shown in Fig. 4, and it is confirmed that Sub. A cannot follow other participants' speech during 10 training sessions. An additional 10 training sessions were therefore performed with words, the score of which was below 40. In the latter 10 sessions, each score was gradually increased as the number of training sessions increased. The average discrimination rates before and after 20 training sessions were 61.90 ± 48.56 [%] and 80.95 ± 39.27 [%], respectively, and the significant

difference before and after training was confirmed at a level of 1 [%]. These outcomes indicated that the proposed training system was capable of speech training.

4. Conclusion

This paper proposed a speech training system for the voice signal controlled ECS based on candidate word discriminations. The proposed training system provides three types of speech training that are important to speak in the same way every time. In the training experiments, it could be confirmed that the trainees' speech skills were gradually improved through training using the proposed system.

In future work, the authors plan to perform training experiments for patients with dysarthria and establish an online tuning method of training levels for each stage.

References

1. Ministry of Health, Labour and Welfare, "Ministry of Health, Labour and Welfare Fact-Finding Investigation of Fistically Disabled," http://www8.cao.go.jp/shougai/whitepaper/h25hakusho/zenbun/furoku_08.html (accessed December 2017).
2. Glamo Inc., iRemocon Wi-Fi, <http://i-remocon.com/aboutiremoconwifi/> (accessed December 2017). Nature Inc., Nature Remo, <http://nature.global/> (accessed December 2017).
3. M. S. Hawley, P. Enderby, P. Green, S. Cunningham, S. Brownsell, J. Carmichael, M. Parker, A. Hatzis, P. O. Neill and R. Palmer, A Speech-controlled Environmental Control System for People with Severe Dysarthria, *Medical Engineering & Physics*, **29** (5) (2007) 586-593.
4. T. Shibanoki, G. Nakamura, K. Shima, T. Chin and T. Tsuji, Operation Assistance for the Bio-Remote Environmental Control System Using a Bayesian Network-based Prediction Model, *Proceedings of 37th Annual International Conference of the IEEE Engineering in Medicine and Biology Society* (Milan, Italy, 2015), pp. 1160-1163.
5. J. Mühlhaus, H. Frieg, K. Bilda, and U. Ritterfeld, Game-Based Speech Rehabilitation for People with Parkinson's Disease, *UAHCI 2017, Part III, LNCS10279* (M. Antona and C. Stephanidis Eds) (2017) 76-85.
6. J. Tamplin, A Pilot Study into the Effect of Vocal Exercises and Singing on Dysarthric Speech, *Neurorehabilitation*, **23** (2008) 207-216.
7. Large vocabulary Continuous Speech Recognition Engine, Julius, <http://julius.sourceforge.jp/index.php> (accessed December 2017).

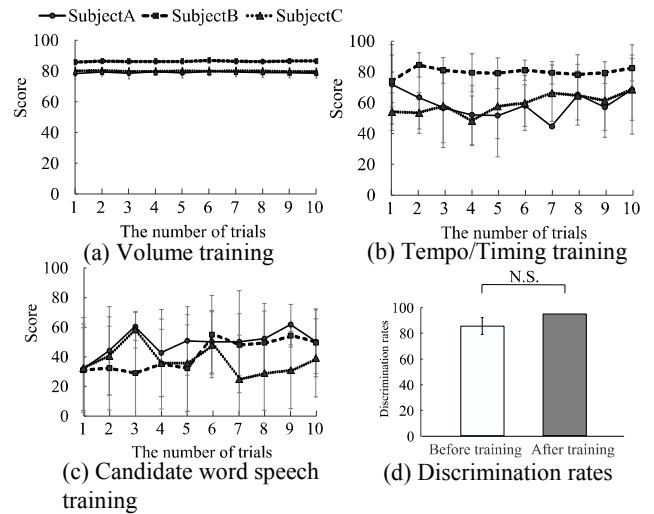


Fig. 4. Experimental results

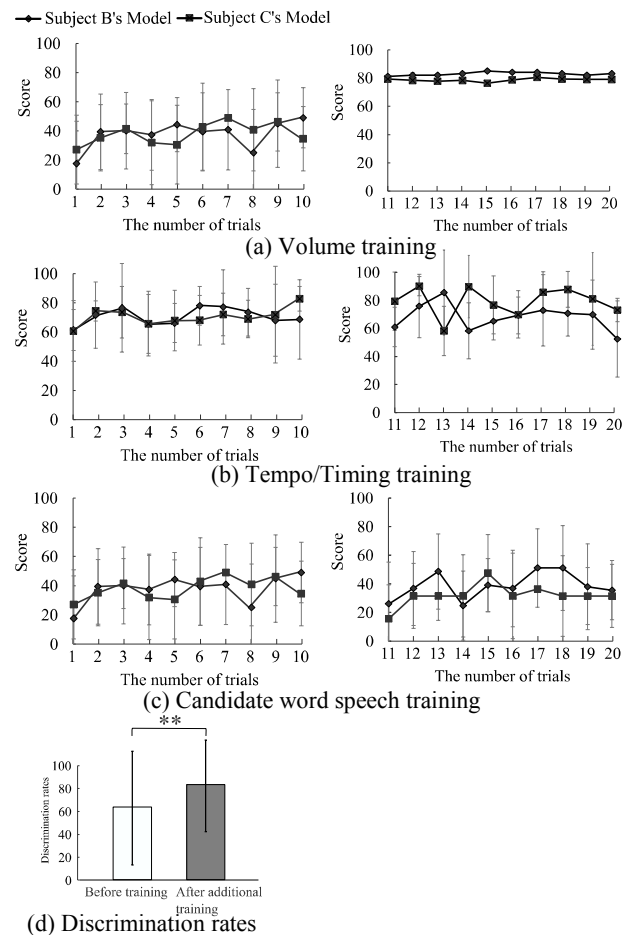


Fig. 5. Experimental results using the other subjects' learning data sets (Sub. A).

Design System of Cell Type Assembly Machine with Dual Arms Robot by GA

Keita Honda

*Department of Human Information Systems, Gifu University, Yanagido 1-1,
Gifu, Gifu 501-1194, JAPAN*

Hidehiko Yamamoto

*Department of Mechanical Engineering, Gifu University, Yanagido 1-1
Gifu, Gifu 501-1194, JAPAN*

Takayoshi Yamada

*Department of Mechanical Engineering, Gifu University, Yanagido 1-1
Gifu, Gifu 501-1194, JAPAN*

E-mail: v3128027@edu.gifu-u.ac.jp, yam-h@gifu-u.ac.jp, yamat@gifu-u.ac.jp

Abstract

The purpose of this research is to develop a system named DELUGA which automatically decides by genetic algorithm (GA) where to place a lot of assembled parts, jigs and robot hands in the workstation when designing a cell type assembly machine with a dual arms robot. In DELUGA, since the left and right robot arms simultaneously perform assembly work, adopt the concept of waiting time to prevent interference between the left and right arms. The cycle time from assembly to completion is used as fitness, GA operation is performed, and better arrangement is decided.

Keywords: genetic algorithm, Unit arrangement decision, Dual arm robot, Assembly machine

1. Introduction

In this research, we develop the system called DEciding Locations of Units by Genetic Algorithm (DELUGA) for determining the units arrangement of cell type assembly machines with a dual arms robot by Genetic algorithm (GA). The unit means dual arm robot's hands, parts trays and jigs. Generally, the units arrangement which is one of the components of the workstation was decided by the production engineer. We aim to improve the design and production efficiency by automating the units arrangement determination.

2. Cell type assembly machine

As shown in Fig. 1, the cell type assembly machine of this research consists of an assembly dual arms robot which is located in the center of the assembly machine, an assembly

workbench in front of the robot and the units located around the robot.

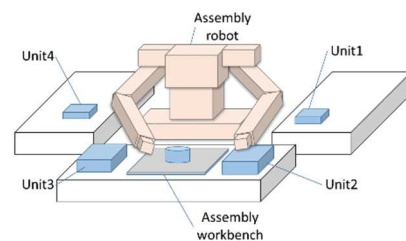


Fig. 1. Cell type assembly machine

2.1. Assembly process

The assembly machine of this study uses a dual arm robot, that is, each arm chucks a unit necessary for an assembly work, carries it to the assembly workbench and assembles parts. In this research, we define three positions existing on the movement path of the robot arm, approach 1,

approach 2 and chuck position. Each definitions is as follows.

Chuck position: position to put or grasp the unit

Approach 1: position upward away from the chuck position

Approach 2: position further upward than Approach 1

The arm passes from approach 2 through approach 1 and arrives at the chuck position. When the arm leaves the unit, it performs the reverse operation (see Fig. 2). With this definition, the assembly time calculations can be formulated.

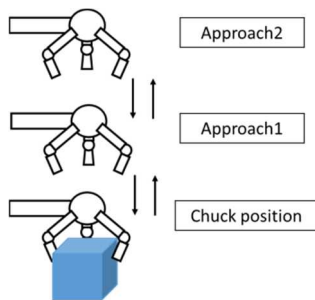
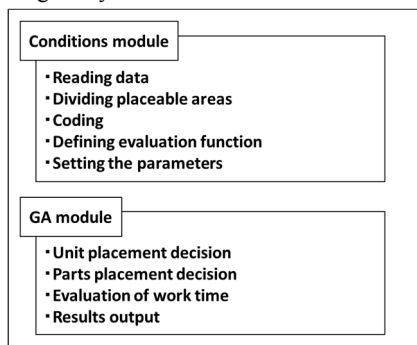


Fig. 2. Movement of arm

3. DELUGA

DELUGA is the system that determines the arrangement of each unit with a high efficiency by using GA when a cell type part assembly machine is designing. DELUGA consists of two modules, the conditions module and GA module (Fig. 3). The conditions module reads the placement possible area of the unit and work data, divides the placement possible area, and sets various parameters required for GA. GA module decides the arrangement place of the unit by GA, determines the arrangement of parts in the parts tray which is one of the units by a full search method, evaluates the total working time, and shows the coordinates of the arrangement place of each unit and the output of the acquired arrangement image.

Fig. 3. System construction of DELUGA



3.1. Condition creation module

The conditions module is as follows.

Step 1: Read work data of parts assembly, placement possible area, parts arrangement data and create their database

Step 2: Divide placement possible area into a lattice shape to create placement possible place

Step 3: Carry out genes coding

Step 4: Define the fitness function

Step 5: Determine various parameters

3.2. GA module

The process flowchart of the GA module is shown in Fig. 4.

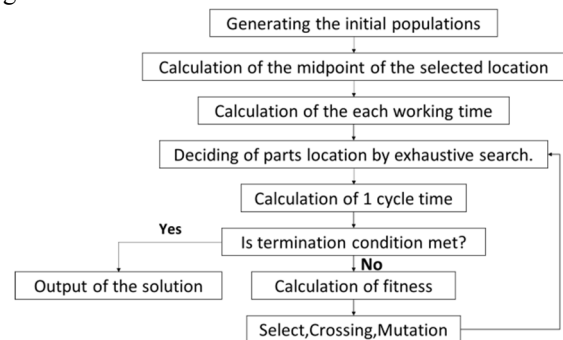


Fig. 4. Flowchart of GA module

This detailed process is described below.

Step 1: Generate an initial population

Step 2: Calculate the arrangement coordinates of each unit

Step 3: Determine part placement inside a parts tray by full search method

Step 4: Calculate the time taken for each work

Step 5: Calculate the cycle time of each individual in order not to collide with both arms

Step 6: Calculate fitness

Step 7: Give selection, crossover and mutation

Step 8: Judge whether the termination condition is satisfied or not. If it is satisfied, go to Step 10

Step 9: Give Step 4 to new individuals

Step 10: The unit arrangement of individuals with the smallest cycle time is adopted as the optimal arrangement and output as a solution

4. Application example of DELUGA

The example cell type assembly machine with dual arm robot consists of the units, the left parts tray, the right parts tray, the left parallel hand, the left three nail hand, the right parallel hand, the right four nail hand, the jig A, the jig B. The goal of DELUGA is to decide the better layout of the units. The layout image of the machine is shown in Fig. 5.

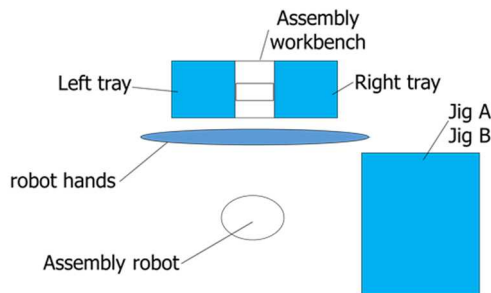


Fig. 5. Units layout

4.1. System comparison

We compared DELUGA with the following two systems.

- System that determines unit arrangement only by reinforcement learning
- System that determines unit arrangement only by GA

The above two systems cannot find the parts layout in the tray. On the contrary, DELUGA can determine the arrangement of parts in the tray.

Fig. 6 is the left and right parts tray. Each number means each part. DELUGA decides the part arrangement in the tray by full search as follows.

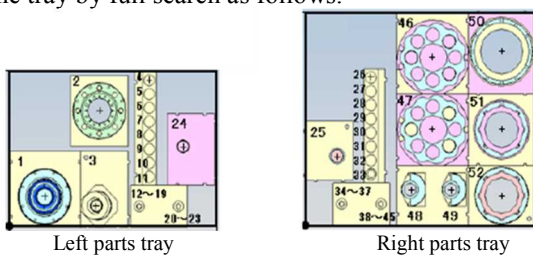


Fig. 6. Parts trays

As shown in Fig. 7, we divide the parts in left and right trays into two groups and three groups. Left tray has Group A and Group B, and right tray has Group C, Group D and Group E. Group A has 6 arrangement patterns. Group B to E also have arrangement patterns. Also, we consider arrangements in which Group A and Group B are rearranged, and Group C, Group D and Group E are rearranged. The number of each pattern is shown in Table 3.

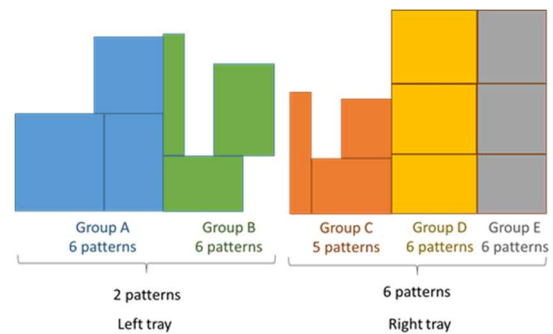


Fig. 7. Arrangement pattern of parts

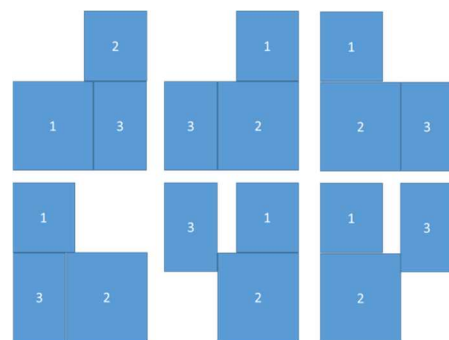


Fig. 8. Arrangement of group A

Table 1. Number of patterns

Group A	6
Group B	6
Sorting A and B	2
Group C	5
Group D	6
Group E	6
Sorting C, D and E	6
All patterns	77,760

Table 1 shows $6 \times 6 \times 2 = 72$ patterns in the left tray and $5 \times 6 \times 6 \times 6 = 1080$ patterns in the right tray. That means $72 \times 1,080 = 77,760$ patterns exist.

4.2. Arrangement determination method

DELUGA calculated 77,760 pattern cycle times of parts arrangement in the tray for each individual during GA operations and the parts arrangement in the tray with the smallest cycle time among them is adopted.

4.3. Details of placement possible area

Table 2 shows the detailed data for the possible placement areas of each unit.

Table 2. Placement area of each unit

Unit	x1	y1	z1	x2	y2	z2
Left tray	1,811.5	1,760	740	1,918.5	1,804.5	740
Right tray	2,522	1,806.5	740	2,628	1,807.5	740
Left parallel hand	1,280	1,480	629	2,320	1,480	629
Left three claw hand	1,280	1,480	629	2,320	1,480	629
Right parallel hand	2,100	1,480	629	3,140	1,480	629
Right four claw hand	2,100	1,480	629	3,140	1,480	629
Jig A	3,034	83	740	3,656	1,117	740
Jig B	3,034	83	740	3,656	1,117	740

Table 3. Coordinates of dual arm robot

	x	y	z
Dual arm Robot	2,210	915	740

Table 3 shows the coordinates of the dual arm robot. All units of the label values are mm.

5. Simulation results

We acquired the simulation results as follows.

- Minimum working time: Smallest working time in each simulation
- Average working time: average of 100 hours simulation work time
- Plane drawing of unit arrangement: plan view of arrangement of each unit whose working time is the smallest

The minimum cycle time and the average cycle time of 100 simulations are summarized in Table 4. Acquired unit layouts are shown in Fig. 9, Fig. 10 and Fig. 11. From the Table 4, DELUGA has the shortest cycle time compared with other two systems.

Table 4 Simulation results comparison (seconds)

	Reinforcement learning	GA	DELUGA
Minimum time	237.41	237.25	234.38
Average time	237.68	237.26	234.89

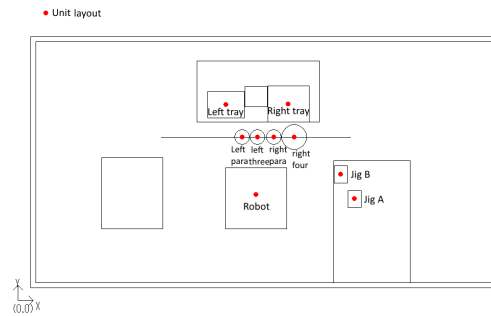


Fig. 9. Layout of DELUGA

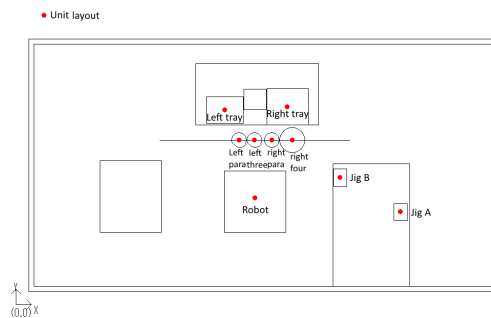


Fig. 10. Layout of GA

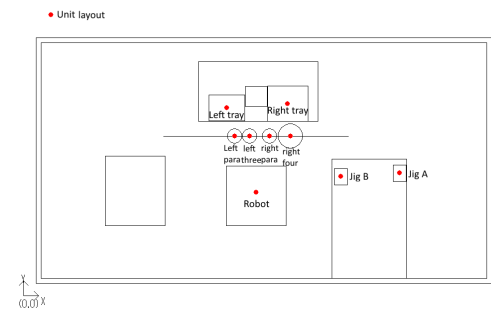


Fig. 11. Layout of Reinforcement learning

6. Conclusions

DELUGA is the system that aims the improvement of design and production efficiency by automating the unit arrangement determinations of cell type assembly machine by GA. Compared DELUGA with a dual arm robot system with using reinforcement learning and the system using only GA, we were able to obtain the unit arrangement more efficient than the two systems. It is ascertained that DELUGA is effective for unit arrangement determinations in cell type assembly machine.

Spherical Mobile Robot Driven by Biorthogonal Omnidirectional Wheels

Liu Wei, Ma Shuanglong, Duan Lunqin, Yu Jiangtao

Mechanical Engineering Department, School of Mechanical, Electronic and Control Engineering,
Beijing Jiaotong University, Beijing, 100044, P.R.China

E-mail: liuw@bjtu.edu.cn

www.bjtu.edu.cn

Abstract

This paper presents a new spherical mobile robot with two independent driving omnidirectional wheels locating at the ends of the inside vertical diameter of the sphere shell, and the two wheel axes being in orthogonal position. The omnidirectional wheels can roll along the inner surface of the spherical shell, and then drive the spherical shell rolling. The lower omnidirectional wheel is responsible for walking drive, and the upper one for steering drive. The prototype shows the spherical robot moving well.

Keywords: Spherical mobile robot, Omnidirectional wheel, Biorthogonal position, Eccentric gravitational moment.

1. Introduction

The spheroid has simple shape, the smallest surface area, the largest volume, and it can roll in all directions. It is an excellent rolling body. Tumbleweed is a typical example in the nature. The typical characteristics of the spheroid is: when the mass centroid is far away from the sphere center, the overturning spheroid has a strong tendency to stabilize itself, otherwise, it is easy to lose stability. The characteristics of spheroid inspire the enthusiasm of scholars to create the spherical robots. The first appearance of spherical robot concept was considered a new technology not only to lead the industrial revolution in the implementation in planet-moon exploration, military purposes, but also raise the demand in the toy entertainment industry.¹

Based on the literature and patents of representative spherical robots, the existing spherical robots with omnidirectional motion performance could be divided into two categories according to their physical driving principles: 1) **Inertia moment driving type**² relies on the rotating inertia moment to drive the omnidirectional rolling of a spherical robot. 2) **Eccentric torque drive type** relies on the motion of eccentric mass centroid to produce the eccentric torque on the fulcrum, and the

eccentric torque drives the spherical robot rolling, as shown in Fig.1, $M=mg \cdot r \cdot \sin(\theta)$. Here the influence of rolling resistance is ignored, and only the torque M is driving or steering the robot rolling. θ is the attitude angle. r is the distance from the sphere center to the mass centroid m directly determines the quantity of the driving moment M . There are lots of inventions using the eccentric moment mechanism to drive the spherical robots.^{3, 7, 8} One of the earliest and simplest spherical robots was invented by Halme etc.(1996).³ Its driving mechanism is made up of a driving wheel, a steering shaft and a balance wheel.

This paper proposes a new and simple spherical robot mechanism, which uses the omnidirectional wheel to realize the driving principle of eccentric torque. The omnidirectional wheel is arranged by a series of small rollers around the circumference. The rollers' axes are perpendicular to the wheel's turning direction. The mechanism is shown in Fig. 2. The effect is that the wheel can be driven with full force, but will also slide laterally on the wheel periphery. The lateral rolling of small rollers does not interfere its circumferential driving function. The new spherical robot driven by the biorthogonal omnidirectional wheels will be analyzed in following

aspects, including mechanism composition, motion and dynamics analysis etc.

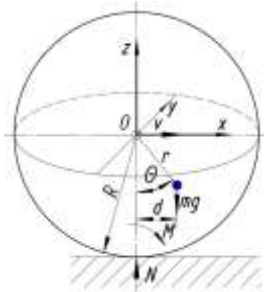


Fig. 1. Eccentric gravitational moment drive



Fig. 2. Omnidirectional wheel

2. Mechanic Structure

The physical principle of biorthogonal omnidirectional wheel drive is that the two omnidirectional wheels whose axes are perpendicular to each other are arranged on the upper and lower ends of the vertical diameter (frame) in the spherical shell, as shown in Fig. 3. The omnidirectional wheel at lower end is for driving, and it

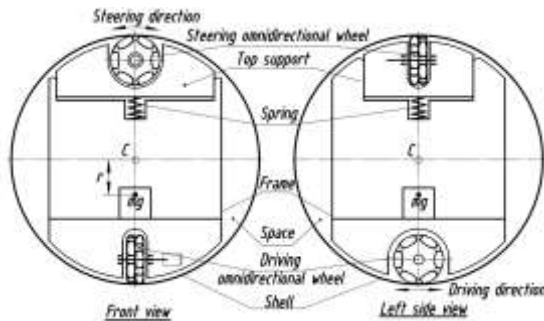


Fig. 3. The spherical robot mechanism with biorthogonal omnidirectional wheels

produces friction at the inner surface of the spherical shell under the co-function of two forces of gravity and spring pre-pressure. The omnidirectional wheel at upper end is for steering, and it produces friction at the inner surface of the spherical shell with the function of the spring pre-pressure. The centroid within the sphere shell deviates from the center of the sphere (distance r). When driving the omnidirectional wheel, the generated friction is transmitted to the frame, which causes the frame swing forwards or backwards. At this moment the steering omnidirectional wheel rolls sideways (left or right

direction) freely, and it does not hinder the driving function, so that the generated eccentric torque drives the spherical shell to roll backwards or forwards. Similarly, when steering the upper omnidirectional wheel, the generated friction is transmitted to the frame, causing the frame to swing towards left or right. At this time, the driving omnidirectional wheel rolls sideways without hindering the steering drive, thereby an eccentric moment is generated to steer the sphere shell move leftwards or rightwards.

3. Mechanics Analysis

Before carrying out the mechanism mechanics analysis, we assume that: 1) the rolling contact of the whole system is pure rolling (i.e. temporarily excluding the influence of sliding); 2) all the components are rigid bodies, including omnidirectional wheels. In this way, a series of simplified kinematic and dynamic analysis can be carried out.

3.1. Kinematics analysis

The coordinate system $G-XYZ$ is established on the ground, and the inertial coordinate system $O-xyz$ is established on the spherical center. As shown in Fig.4, since the spherical shell always rotates with respect to the frame, the $O-xyz$ coordinate system is fixed to the middle point of the frame. To facilitate the description of the spherical robot position-orientation, Euler angle coordinate system $O-x^e y^e z^e$ is fixed to the center of the frame. In order to facilitate the kinematic analysis, the parameters are set as following: m is the mass of all the parts inside the spherical shell, r is the distance between this mass centroid and the spherical center, m_s is the mass of the spherical shell, t is the wall thickness of the spherical shell, v is the velocity of the sphere center, ω is the angular velocity of the sphere rolling, r_o is the radius of omnidirectional wheel. ω_w is the angular velocity of the driving omnidirectional wheel, and v_A is the instantaneous velocity at point A outside the shell.

To demonstrate the theoretical and mechanical characteristics of this spherical robot, we decompose the motion into several phases: start-up, uniform motion, obstacle crossing, taking off and ground landing etc.

At the phases of start-up and uniform motion, the velocity and acceleration at point A can be analyzed. As shown in Fig. 4, the absolute velocity of point A can be obtained from $G-XYZ$:

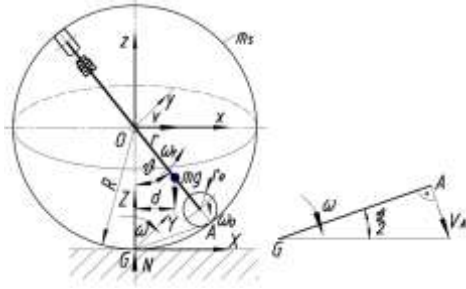


Fig. 4. Start-up and uniform motion

$$v_A = 2v \cdot \sin \frac{\theta}{2} \quad (1)$$

In addition, the absolute velocity at point A can be obtained by setting up a convected coordinate based on the sphere center:

$$\vec{v}_A = \vec{v} + \vec{R} \times \vec{\omega}_f - \overline{(r_o + t)} \times \vec{\omega}_o \quad (2)$$

where ω_f is the convected angular velocity of the frame, $\vec{v} + \vec{R} \times \vec{\omega}_f$ is the instantaneous convected velocity at point A, $\overline{(r_o + t)} \times \vec{\omega}_o$ is the relative velocity at point A. When $\omega_f = 0$, the robot is in a state of uniform movement.

Put the Eq. (2) into Eq. (1), the relationship between the angular velocity of the omnidirectional wheel ω and the velocity of the spherical center v can be acquired.

The acceleration of point A is as follows:

$$\vec{a}_A = \vec{a} + \vec{R} \times \vec{\alpha}_f + \vec{\omega}_f \times \vec{\omega}_f R + \overline{(r_o + t)} \times \vec{\alpha}_w \quad (3)$$

where $\vec{a} + \vec{R} \times \vec{\alpha}_f$ is the instantaneous convected acceleration of the frame at point A, α_f is the relative acceleration of the frame; $\vec{\omega}_f \times \vec{\omega}_f R$ is the centripetal acceleration of the frame; $\overline{(r_o + t)} \times \vec{\alpha}_w$ is the relative acceleration at point A, α_w is the angular acceleration of the omnidirectional wheel, and the Coriolis acceleration in Eq. (3) is 0. In addition, the acceleration at point A can be obtained from G - XYZ :

$$\vec{a}_A = \vec{a}_t + \vec{a}_n \quad (4)$$

Where $a_t = 2a \sin \frac{\theta}{2}$, $a_n = 2R\omega^2 \sin \frac{\theta}{2}$.

The relationship between the angular acceleration at the spherical center and its acceleration is:

$$\alpha_o = a/R \quad (5)$$

3.2. Kinetic analysis

In order to facilitate kinetic analysis, the parameters are set as follows, as shown in Fig. 5 and Fig. 6: M_f is the

resistance couple of spherical shell rolling friction, F_{ar} is air resistance, M_{wl} is the rolling friction resistance couple of the walking omnidirectional wheel, M_{wu} is the rolling friction resistance couple of the steering omnidirectional wheel, F_s is the spring force on the frame, F_w is the friction force of the walking omnidirectional wheel, F_{wu} is the friction force of the steering wheel, N_A is the pressure to the omnidirectional wheel inside the spherical shell, and M_{wd} is the driving torque of the omnidirectional wheel.

The rolling of the spherical shell is due to the principle moment of the mass eccentricity. Here $J_{SG}\omega$ is the momentum moment of the spherical shell to the G - Y axis.

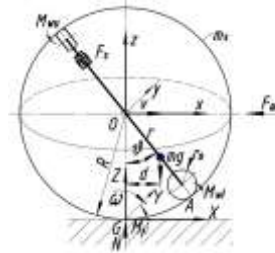


Fig. 5. The eccentric moment of couple

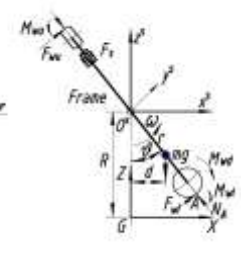


Fig. 6. The forces of the frame system

According to the angular momentum moment, there is:

$$\frac{d}{dt} (J_{SG}\omega + J_{fG}\omega) = mg \cdot r \cdot \sin \theta - M_f - F_{ar} \cdot R \quad (6)$$

where, the moment of inertia of the spherical shell is $J_{SG} = J_{SO} + m_s R^2 = \frac{2m_s}{5} \left(\frac{R^5 - (R-t)^5}{R^3 - (R-t)^3} \right) + m_s R^2$, the moment of inertia of the frame is $J_{fG} = J_f + m((R - r \cos \theta)^2 + (r \sin \theta)^2)$, the resistance couple of spherical shell rolling friction is $M_f = \delta(m + m_s)g$. The Eq. (6) can determine the angular acceleration of the spherical center as $\alpha = \frac{d}{dt}(\omega)$.

In the spherical shell coordinate system $O^s-x^s y^s z^s$, when the frame is in the attitude angle θ , the moment of couple reaches balance:

$$M_{wd} - M_{wu} - M_{wl} - mg \cdot r \cdot \sin \theta = 0 \quad (7)$$

The equation can deduce the position angle θ .

When considering the effect of the rolling friction resistance couple, the start-up phase can be divided into the following sub-phases: 1) When the driving torque of the omnidirectional wheel $M_{wd} > M_{wu} + M_{wl}$, the omnidirectional wheel starts rolling inside the shell, i.e. the attitude angle $\theta > 0$; 2) When the eccentric moment accumulates to $mg \cdot r \cdot \sin \theta > M_f$, the robot shell starts rolling on the ground.

4. Prototype and Experiment

First, the mechanism of the omnidirectional wheel spherical robot was simulated by using the 3D solid modeling and multi-body dynamics software. Second, a prototype was made after simulating and analyzing the robot's detailed properties and its feasibility, as shown in Fig. 7. The experimental prototype uses two motors to drive the upper and lower omnidirectional wheels respectively. In order to lower the height of centroid, the control system, the power supply and the drive motor of the upper omnidirectional wheel are all arranged away



Fig. 7. Physical prototype

from and below the center of the sphere. In order to ensure that the upper and lower omnidirectional wheels are always on the vertical diameter, an important task - static balance needs to be completed before the frame components are installed into the spherical shell. The walking and steering of the prototype have achieved the expected effect.

5. Conclusion

The spherical robot's driving scheme makes use of the characteristics of the omnidirectional wheel to simplify the driving mechanic structure, and it is better to increase the distance from the mass centroid to sphere center so as to generate a maximized eccentric driving torque. This orthogonal arrangement makes the walking omnidirectional wheel and the steering one independent at force directions, so its motion directions are independent too. This can facilitate the motion towards any direction successfully, and is very conducive to the control system. However, as the contact area of the sphere with the ground is small, the stability of the sphere position-orientation is poor. It is necessary to use control method to improve the motion stability. In addition, further research is needed in the following aspects: 1) to determine the proper pre pressure of the spring so that it

not only can obtain the necessary non-sliding friction required by the omnidirectional wheel, but also reduces the rolling friction resistance couple of the omnidirectional wheels. 2) to explore kinematic and dynamic characteristics of this spherical robot, such as the behaviors of obstacle crossing, and taking off, etc.

Acknowledgements

This research was funded by China National High Technology Research and Development Plan (863 Plan) 2013AA041302.

References

1. Rhodri H A, Julian F v., Rolling in nature and robotics: a Review, *Journal of Bionic Engineering*, **3**(4) (2006) 195-208.
2. Li Tuanjie, Zhu Chao, Design and Analysis of a spherical omnidirectional rolling robot with a stable platform, *Journal of Xidian University*, **33**(1) (2006) 53-56.
3. Halme A, Schonberg T, Wang Y., Motion control of a spherical mobile robot, *4th IEEE International Workshop on Advanced Motion Control*, (Mie, Japan, Jan,1996) 259-264.
4. Bhattacharya S, Agrawa S K, Spherical rolling robot: a design and motion planning studies, *Proceedings of the IEEE International conference on Robotics and Automation*, (San Francisco, CA, April, 2000) pp.835-839
5. Joshi V A, Banavar R N, Hippalgaonkar R, Design and analysis of a spherical mobile robot, *Mechanism and Machine Theory*, **45**(2) (2010) 130-136.
6. Zhao Kailiang, Sun Hanxu, Jia Qingxuan, Liu Daliang, Shi Chengkun, Analysis on Acceleration Characteristics of Spherical Robot Based on ADAMS, *Journal of Machine Design*, **27**(6) (2009) 24-27.
7. Javadi A H A, Mojabi P., Introducing august: A novel strategy for an omnidirectional spherical rolling robot, *IEEE International Conference on Robotics and Automation*, Washington, (DC, USA, 2002) 3527-3533.
8. Sun Hanxu, Zhao Wei, Zhang Yanheng, Mechanical analysis about a new kind of variable structure spherical mobile robot, *Journal of Mechanical Engineering*, **49**(19) (2013) 40-46.

Coordinated behavior with a Pepper Humanoid robot to estimate the distance of other robot using Inverse Perspective Mapping

M. Hassan Tanveer, Antonio Sgorbissa, Carmine T. Recchiuto
Department of Bio-Robotics and Intelligent systems (DIBRIS)
University of Genova 16145 Genova, Italy

Email: muhammadhassan.tanveer@dibris.unige.it, antonio.sgorbissa@unige.it, carmine.recchiuto@dibris.unige.it

Abstract

This article discusses a strategy for real time distance determination applied to a humanoid robot (Pepper, Softbank Robotics) that is requested to collaborate with other robots. However, using the monocular camera embedded on the robot head, it is difficult to determine distance to objects in front of the robot with any degree of certainty. The reason is non linear relationship between the height allocation of camera and its distance to an object in a camera frame. So, the proposed method is based on the extraction of accurate bird's-eye view images, by applying Surface Subtraction and Inverse Perspective Mapping (IPM) to the images captured with the Pepper head camera. The algorithm is implemented in the Python language using the OpenCV libraries.

Keywords: Pepper Humanoid Robot, Monocular Camera, Inverse Perspective Mapping, OpenCV.

1. Introduction

One of the major aspects of research in robotic is to implement social robots algorithms that help robots to anticipate the desired task which results the ease for humans. During 20th century, many steps forward have been taken for the realization of fully autonomous humanoid Ref. 1. In robots, the problem of position estimation and distance determination has been one of the concerned domain due to destruction in robots collision Ref. 2. Collision detection systems can provide robots with a warning prior to a potential collision allowing them to take preventative action Ref. 3. They can also be incorporated into safety systems, as seen in Ref. 4 which immediately stops the robot processes if an imminent object is detected.

Distance determination in robots could allow us to provide feedback and alerts to the user Ref. 5. This can promote the commands to take preventative action, or prepare the safety systems for an imminent collision [6]. Most of the research work for distance determination has been conducted by using active systems such as RADAR

or LIDAR. They are active systems, potentially leading to higher power requirements and interference issues, in comparison with optical camera sensors Ref. 7. It works on relatively simple concept: signals transmitted from an antenna reflect back to the transmitter from the target object. The distance can be calculated based on the length of time taken for the signal to travel from the target.

A robot should detect the relative position of another robot, while the other robot is in the floor. A large amount of research has been done for distance determination to an object using forward facing cameras Ref. 8, SONAR, LASER Scanner that could not be specifically used if the height of other robot is too low. A multi-camera setup as employed by Ref. 9, provides depth information by establishing feature correspondence and performing triangulation. However, it also carries severe processing and configuration overheads, which are undesirable in the cost and power sensitive robots.

In this article, two robots has been adopted Pepper Humanoid robot and iRobot Roomba. The Pepper robot has capabilities for vision which include facial and shape

recognition (in-built cameras). Secondly, the iRobot Roomba is a unicycle mobile robot that performs a wide range of task from autonomous cleaning and surveillance, to transportation and assistance to the elderly. By combining both of these robots, a solution that consists in the composition of a IPM view (bird’s eye view) of Pepper head camera has been proposed. This view will serve as a virtual map for the iRobot Roomba in the Pepper Frame of view (FOV) to help the user to adequately specify the commands to be sent to the other Roomba under its control, as in Fig. 1 that is referred to Pepper Frame of view. The proposed system consists of a single forward facing Pepper camera, capturing video images at 30 frames per second (fps).

Section II of this paper discusses distance the Methodology for distance determination that includes Inverse Perspective Mapping which allows the image perspective to be linearized, the surface subtraction requirement for object detection and the calibration issues. The technological platform with discussion of results are described in section III. Future work concludes the paper in section IV.

2. Methodology

2.1. IPM Model

A transformation of coordinates system can be done mathematically by using Inverse Perspective Mapping (IPM). It converts the coordinates of image from one perspective to another Ref. 10. The final homogeneously distribution of a remapped two dimensional acquired image (input data image) form in pixels are first transformed by using IPM technique in order to remove the perspective effect.

Obviously, the application of the IPM transform requires the knowledge of the specific acquisition conditions (camera position, orientation, optics, etc.) Ref. 11 some assumption on the scene represented in the image (here defined as a priori knowledge). Thus, the IPM transform can be of use in structured environments, where, for example, the camera is mounted in a fixed position or in situations where the calibration of the system and the surrounding environment can be sensed via other kind of sensor Refs. 12.

In this case we use IPM to attain a top-down view from Pepper robot camera. The transformation in this manner removes the non linearity of distances between world frame and object.



Fig. 1. Pepper FOV.

Using IPM, the aim is to map pixel points (u, v) to world coordinate points (X_w, Y_w, Z_w) , as in Eq. 1. The requirement of a rotation about q , a translation along the cameras optical axis, and a scaling by the camera parameter matrix Ref. 13, can be expressed as:

$$(u, v, 1)^T = KTR (x, y, z, 1)^T \quad (1)$$

$$R = \begin{pmatrix} 1 & 0 & 0 & 0 \\ 0 & \cos \theta & -\sin \theta & 0 \\ 0 & \sin \theta & \cos \theta & 0 \\ 0 & 0 & 0 & 1 \end{pmatrix} \quad (2)$$

$$T = \begin{pmatrix} 1 & 0 & 0 & 0 \\ 0 & 1 & 0 & 0 \\ 0 & 0 & 1 & -\frac{h}{\sin \theta} \\ 0 & 0 & 0 & 1 \end{pmatrix} \quad (3)$$

The intrinsic parameters of the camera are represented by the following matrix:

$$K = \begin{pmatrix} f * ku & s & u_0 & 0 \\ 0 & f * kv & v_0 & 0 \\ 0 & 0 & 1 & 0 \end{pmatrix} \quad (4)$$

where h is the height of camera, f correspond to the focal length measured in horizontal and vertical pixel units ku and kv respectively. The positions u_0, v_0 are the principal points where the optical axis fixes the image plane. The camera performs a perspective projection of a 3D world point onto an image point located on a retinal plane. By using homogenous coordinate, the projective relation between 3D world point and its image points can be rewritten as in [5], It relates world points to image points according to the camera location with respect to the reference frame, represented by a camera matrix K Eq. 4, rotation matrix R Eq. 2 and a translation vector T Eq. 3.

$$(v_i) = \begin{pmatrix} M_{11} & M_{12} & M_{13} & M_{14} \\ M_{21} & M_{22} & M_{23} & M_{24} \\ 1 & M_{31} & M_{32} & M_{34} \end{pmatrix} \begin{pmatrix} X_W \\ Y_W \\ Z_W \\ 1 \end{pmatrix} \quad (5)$$

The 3×4 matrix $M(i,j)$ is the transformation matrix in Eq. 5. When the structure under observation is a plane, a simpler formulation becomes available. Since the world coordinates system can be set anywhere, it can be conveniently positioned on the plane, such that this latter has zero Z coordinate. This choice reduces the projection matrix to:

$$(v_i) = \begin{pmatrix} M_{11} & M_{12} & M_{13} & X_W \\ M_{21} & M_{22} & M_{23} & Y_W \\ 1 & M_{31} & M_{32} & 1 \end{pmatrix} \quad (6)$$

The updated transformation that maps a world plane to an image points as per the given source image can be rewritten as:

$$dst(u, v) = src \left(\begin{array}{l} \frac{M_{11}X_W + M_{12}Y_W + M_{13}}{M_{31}X_W + M_{32}Y_W + M_{33}} \\ \frac{M_{21}X_W + M_{22}Y_W + M_{23}}{M_{31}X_W + M_{32}Y_W + M_{33}} \end{array} \right) \quad (7)$$

The sampling rate in X direction at this point is simply the number of source image pixels between $(X, Y, l)T$ and the point $(X+(dX), Y, l)T$ divided by the distance between these two points.

Fig. 3 is the frame captured by static camera and its IPM view. The picture transformation can be seen in Fig. 4, as the src coordinates in image changes as per perspective

2.2. Detection Phase

Normally, the available conventional techniques which requires the prior knowledge of the object for detecting it with a camera Ref. 14. In spite of it, a more efficient method of doing this is used by adopting a surface subtraction (SS) algorithm. The wheeled robot Roomba to be detected has a small green object on top, and thus the surface subtraction algorithm starts from the detection of green object. Considering the scene in Figs. 8 and 11, the object we must detect is deemed to be the nearest part of the image that is not surface directly in. From the above steps, the adaptation becomes easy in different light and surface conditions. By using morphology tool in OpenCV, we get the green object detected in different light conditions as the range of BGR channels can be manually fed. So, in conditions of light impact the result will remains same in detection of green color because of the defined constraints of upper and lower limit of BGR morphological tool. It do helps to

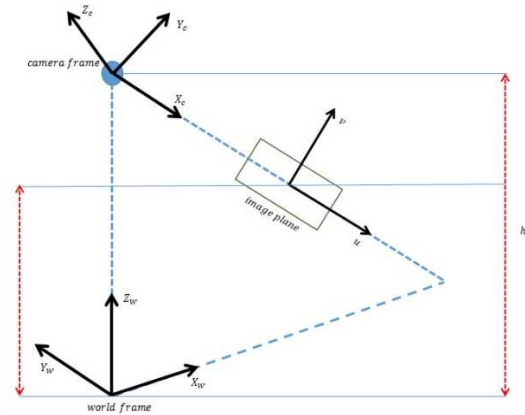


Fig. 2. Image coordinate system in relation to world coordinate system

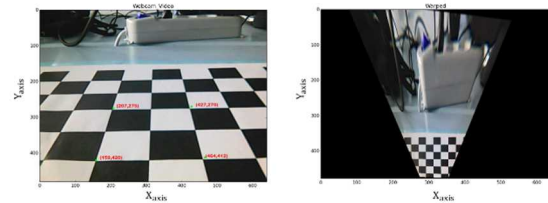


Fig. 3. Static camera Image and its IPM view

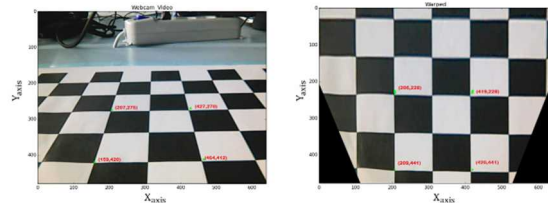


Fig. 4. Static camera IPM view with src and dst points

view. The transformation depends upon the Eq. 6 and can be warped to its dst coordinates as mentioned in Eq. 7 front of the Pepper. Therefore the easiest way to from the image, leaving

only the required object, as mentioned in steps:

- Green channel is separated to its constituent in the BGR image.
- Taking Green channel into account, the algorithm calculates the average pixel values in x and y axes in the captured Pepper image.
- The algorithm loops though every rows and columns in the image, creating a new binary image where 0 signifies a plane pixel, and a 1 is a green color pixel.
- The algorithm repeats steps 2 and 3.

detect the potential object by detecting its color of different ranges as well, so there is no distortions in different light conditions.

Before we can calculate the distance of the Roomba from the Pepper, we need to calculate the height of the object in pixels from the bottom of the image as shown in Fig. 8. Beginning at the bottom of the binary image in each RGB color space, we calculate the average pixel intensity for each row of pixels in the image. From this we can ascertain how high in the image the nearest object lies. Only the area directly in front of the Pepper is analyzed. This was to minimize the rate of false positive object detections caused by other objects in Pepper captured frame.

With the previous steps, the pixel points of potential object measured in image is known but to calculate it as per world frame requires a calibration tool in terms to convert the available pixel value in understandable measuring unit (i.e.: meters). There are several method of calibration as in Ref. 15. The methods like chessboard calibration and marking points calibration discussed in Ref. 16 can be used as well but in this case, the proposed system would be implemented with a Pepper camera in a fixed position. The placement of a green color box with known distance (i.e.: known x and y axes distance) in the FOV of the camera, along a flat surface, would allow for the measurement of the number of pixels equivalent to distance. Using this value, the number of pixels in the image could be converted to a real world value in meters.

3. Results and Discussion

The algorithm presented here was first investigated with a static camera and then implemented to Pepper in real time. For this purpose, the Python language, complemented by the OpenCV library of functions was chosen for implementation that allows the rapid development of image processing algorithms without the need to develop complex algorithms by using its open source library of functions Ref. 17.

With Pepper robot, a database of video samples was captured at 30 frames per second (fps), at a resolution of 320 X 240 pixels. Considering that the change in distance of potential objects is relatively slow compared to the full frame rate of the system, a slower frame rate was considered for the purposes of calculating distance and computing position. Using a sampling rate of every 10 frames produced smooth and reliable results. A rate of 10 frames per second was chosen as it provides a good trade-

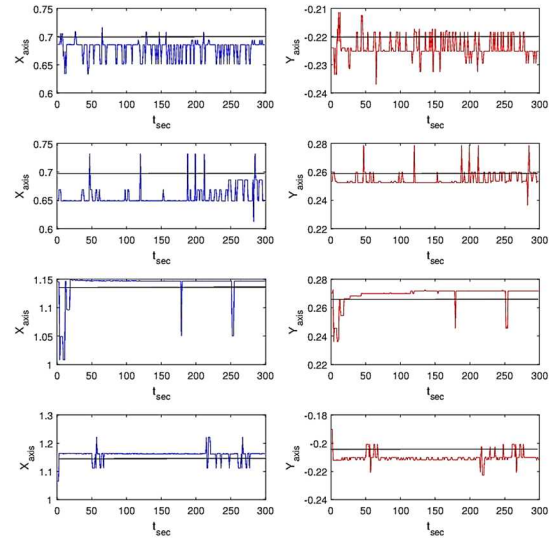


Fig. 5. Pepper RedBall API response at static points.

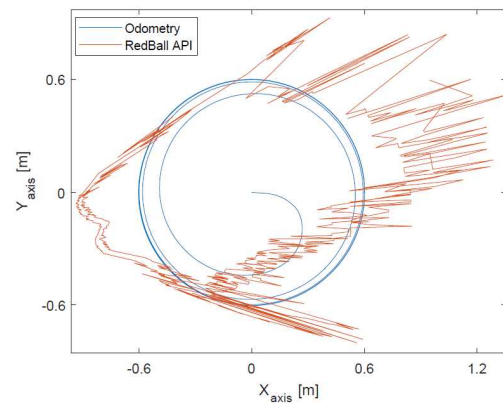


Fig. 6. Pepper Red ball API response while tracking a circular response.

off between computation time and number of calculations per second.

A comparative analysis has been shown in this section. The first experiment is being conducted with Pepper Red Ball API. The Red ball API works by considering the size in pixels of the red ball, and comparing it to the known size of the red ball to be detected. Obviously this works well only if the red ball is directly in front of the camera. A Red ball is being placed at a static point in the FOV of

Pepper Head camera. First, it is placed at 0.7m on X-axis and 0.22m on Y-axis, then the data have been recorded for 300 samples. The same acquisition has been performed in other three different points, as shown in Fig. 5.

It can be seen, how due to a continuous transient a second test has been conducted: in this case the red ball has been placed on board the wheeled robot, while it is performing a circular path as done in Ref. 18, shown in Fig. 6. The average error in this case is $av|e| = 0.43m$. It is clear with the analysis that the API are not enough to determine the distance of objects in Pepper camera view. However, in order to determine the distance between the Pepper and Roomba in its FOV (as shown in Fig. 1), the first step is to determine where the Roomba lies in the plane with respect to Pepper IPM view. So, Fig. 7 shows the Pepper camera view and IPM view respectively. It can be seen from the green arrow in rectified bird's-view image, Fig. 7, that the relationship between the potential object and its distance from the camera is linear in nature. However, the change in the length of the green arrow will proportionally reflect this difference in distance. In order to determine the position of potential object in bird eye view, the calibration with different distance on pixels is considered and sum up in a formula as in Eq. 8. It goes something like: we first calibrate the world points in Bird eye view frame with a known distance of object. Then the object is being placed at some distance from Pepper camera and by measuring at the same time the pixel (in bird's-view) corresponding to the object detection. The apparent pixels is measured corresponding to the detected object.

$$i_{n+1} = o + p_n + i_n + noise \quad (8)$$

where i is frame point, o is the offset, p is the pixel. The calibration result captured in Pepper FOV at different distances is shown in Fig. 8. The static point comparison between Pepper Red ball API and IPM view is shown in Fig. 9.

Fig. 10, shows the Pepper camera and IPM view to clarify the robot is moving in a circular path, the Roomba position is being calculated depending upon the potential object tracked. So, it implies that the smaller the value of pixel the farther the distance. The odometry of Roomba while following a circular path and Pepper IPM view response is presented in Fig. 10 to determine the distance and position, with an average error

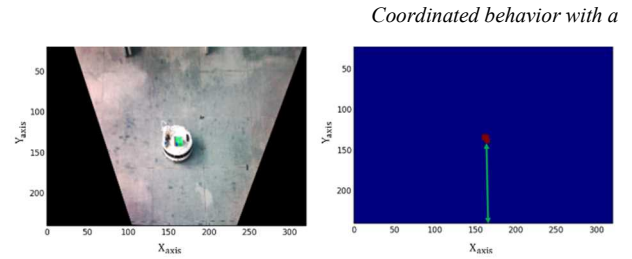


Fig. 7: Distant object as shown by Pepper Top-Down view, Top Down view, distance in this image may be measurable

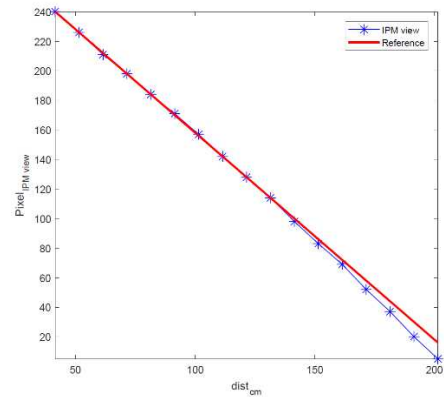


Fig. 8: IPM view pixel values in different distances.

The same test have been performed, in this case a green box has been placed on top of the wheeled robot Roomba as a potential object. The green box has the same size as Red ball used in Red Ball API experiment. As per discussed in methodology section, the use of a Pepper Head camera does not directly provide depth information in a scene so surface subtraction and IPM for getting a bird's-view image has been applied Fig.7.

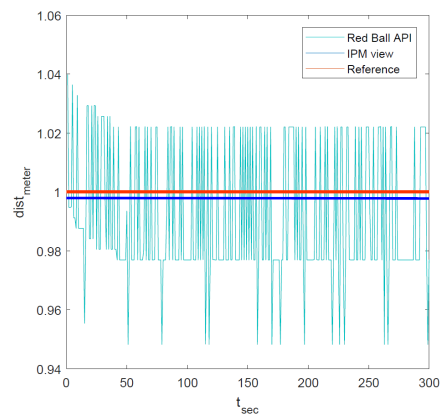


Fig. 9: comparison of IPM view and Redball API at static point

$av|e|=0:086m$. It validates the IPM method (for static camera and moving objects on the floor). Successful comparison between Red Ball and IPM view is shown and obtained from a video samples of Pepper camera in real time operation. The experiments performed confirms that the implementation of an IPM approach with surface subtraction gives better results in comparison with the usage of standard Red Ball API.

4. Conclusion

This paper presented a IPM approach with surface subtraction, implemented with a humanoid robot (Pepper, Softbank Robotics) in charge of detecting the position of a wheeled robot (Roomba, iRobot) by using the head-mounted camera. The proposed approach has been tested in different configurations, by keeping the wheeled robot in static position, or by letting it move in circular path. The comparison of the method with the API for distance detection embedded in the humanoid robot shows that using IPM reduces the average error in distance estimation. The limitation of the current approach is that the IPM transform can be of use in structured environments, where, for example, the camera is mounted in a fixed position. Future works will be aimed at overcoming the current limitation, by including Yaw/Pitch parameters with an adaptive IPM model.

References

1. B. Siciliano and O. Khatib, Springer handbook of robotics. Springer, 2016.
2. S. Lemaignan, M. Warnier, E. A. Sisbot, A. Clodic, and R. Alami, "Artificial cognition for social human-robot interaction: An implementation," *Artificial Intelligence*, vol. 247, pp. 45–69, 2017.
3. G. Stein, E. Dagan, O. Mano, and A. Shashua, "Collision warning system," May 23 2017, uS Patent 9,656,607.
4. D. E. Maurino, J. Reason, N. Johnston, and R. B. Lee, Beyond aviation human factors: Safety in high technology systems. Routledge, 2017.
5. M. Rubenstein, A. Cornejo, and R. Nagpal, "Programmable selfassembly in a thousand-robot swarm," *Science*, vol. 345, no. 6198, pp. 795–799, 2014.
6. A. Mukhtar, L. Xia, and T. B. Tang, "Vehicle detection techniques for collision avoidance systems: A review," *IEEE Transactions on Intelligent Transportation Systems*, vol. 16, no. 5, pp. 2318–2338, 2015.
7. S. A. Hiremath, G. W. Van Der Heijden, F. K. Van Evert, A. Stein, and C. J. Ter Braak, "Laser range finder model for autonomous navigation of a robot in a maize field using a particle filter," *Computers and Electronics in Agriculture*, vol. 100, pp. 41–50, 2014.

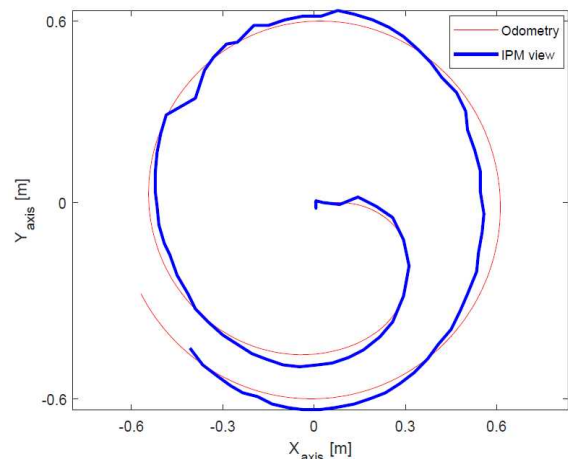


Fig. 10. Response of IPM view in a circular path.

8. S. Tuohy, D. O’cualain, E. Jones, and M. Glavin, "Distance determination for an automobile environment using inverse perspective mapping in opencv," 2010.
9. L. Ma, X. Yang, and D. Tao, "Person re-identification over camera networks using multi-task distance metric learning," *IEEE Transactions on Image Processing*, vol. 23, no. 8, pp. 3656–3670, 2014.
10. J. Jeong and A. Kim, "Adaptive inverse perspective mapping for lane map generation with slam," in *Ubiquitous Robots and Ambient Intelligence (URAI), 2016 13th International Conference on. IEEE*, 2016, pp. 38–41.
11. R. Laganriere, "Compositing a bird’s eye view mosaic," *image*, vol. 10, p. 3, 2000.
12. J. Civera, A. J. Davison, and J. M. Montiel, "Inverse depth parametrization for monocular slam," *IEEE transactions on robotics*, vol. 24, no. 5, pp. 932–945, 2008.
13. M. Oliveira, V. Santos, and A. D. Sappa, "Multimodal inverse perspective mapping," *Information Fusion*, vol. 24, pp. 108–121, 2015.
14. X. Wang, "Intelligent multi-camera video surveillance: A review," *Pattern recognition letters*, vol. 34, no. 1, pp. 3–19, 2013.
15. D. P. Boyle, H. V. Gupta, and S. Sorooshian, "Toward improved calibration of hydrologic models: Combining the strengths of manual and automatic methods," *Water Resources Research*, vol. 36, no. 12, pp. 3663–3674, 2000.
16. P. Miraldo and H. Araujo, "Calibration of smooth camera models," *IEEE transactions on pattern analysis and machine intelligence*, vol. 35, no. 9, pp. 2091–2103, 2013.
17. A. Morro, A. Sgorbissa, and R. Zaccaria, "Path following for unicycle robots with an arbitrary path curvature," *IEEE Transactions on Robotics*, vol. 27, no. 5, pp. 1016–1023, 2011.

Control Techniques of Quadrotor UAVs: a Concise Analysis

¹Syed Faiz Ahmed, ¹Athar Ali, ¹M. Kamran Joyo, ¹Khusairy Abd Kader, ¹Izhar A. Bakar, ²Hazry Desa, ³Sheroz Khan

¹Universiti Kuala Lumpur, British Malaysian Institute, Malaysia

²Universiti Malaysia Perlis, Malaysia

³International Islamic University Malaysia, Malaysia

E-mail: syedfaiz@unikl.edu.my, athar.ali@s.unikl.edu.my, m.kamran@s.unikl.edu.my, hazry@unmap.edu.my

Abstract

UAVs have become popular in the recent years. Quadrotors, the four wing UAV has drawn prominent attention amongst the researchers. The simple nonlinear structure design requires a robust control to ensure the stability during the flight. The noisy and environment with unexpected disturbances may cause issues such as drift in position. In order to tackle the severe conditions a robust control is required. This paper provides an overview of the available quadrotor models and the control techniques with their application in quadrotor control issues.

Keywords: Quadrotor UAVs; Control algorithm; flight stability.

1. Introduction

Due to rapid advancement in technology and demand the unmanned aerial vehicles have become the focus of study among the researcher. ¹⁻² UAVs are remote controlled flight vehicles that works without any direct human intervention.

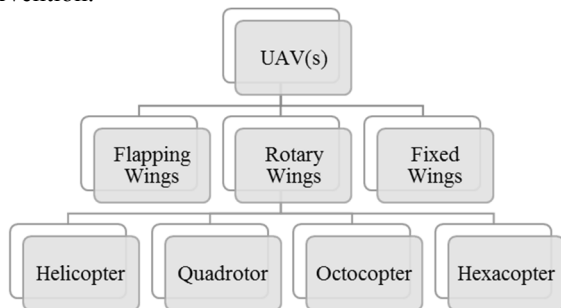


Fig.1. Classification of UAVs.³

Several applications such as search and rescue missions, wild life surveillance and monitoring, inspection of power plants and nuclear reactors, agricultural mapping and photographing, marine operations, battle damage assessment and law enforcement use such type of devices.

These devices are useful in several kinds of hazardous environments where reach of humans is not possible.*

The above-mentioned applications influence the requirement of such systems which have ability to operate in severe conditions and perform complex and difficult missions. In the unmanned aviation industry, helicopters and rotorcrafts have proved to be one of the finest solutions due to their capabilities of hovering, accurate positioning, vertically takeoff and landing. ⁴

There exist numerous types of UAVs shown in Fig.1, one of them is a quadrotor UAV consisting of four rotors mounted at the four ends of the cross frame ⁵⁻⁶ which is prominent among the researchers. The cause of its prominence is due to its light weight, simple mechanical structure that makes its assembly trouble-free.

In this paper, various quadrotor models are reviewed, and a comparative analysis of these quadrotors is presented in TABLE 1. The comparison is based on the parameters of control technique used for the position, altitude or attitude stabilization and DOF. Furthermore, paper provides the survey of different available control algorithms. The perception of this research work is to analyze the best available configuration and control technique of the quadrotor UAV.

Table 1: Comparative Analysis of The Developed Quadrotor UAVs

Sr.No	Developer	Year	Description	DOF	Control Technique
1	Sujit Rajappa. ⁸	2016	Super Twisting controller was developed and implemented for the UAV, using the adaptive laws for tracking the position of the UAV in the presence of uncertainties and external disturbances.	6	Adaptive Super Twisting Controller
2	M. Zaki Mustapa ⁹	2015	Model was derived using Newton-Euler equations for attitude control of the UAV. PID controller was developed for altitude control of quadrotor. The model is implemented on a real-time system in MATLAB Simulink.	6	PID control
3	Emran ¹⁰	2014	A model reference adaptive control method was used for an under-actuated quadrotor assumed to be suffering from parametric uncertainty and noise signals. A robust controller was developed to overcome the effect of noise on the quadrotor.	6	Composite adaptive controller (Sliding mode and Adaptive control)
4	M. Hassan Tanveer. ¹¹	2014	A model was derived using PID control for stabilizing the attitude of quadrotor under external disturbances. The system was derived using Newton Euler equations.	3	PID control
5	M. Hassan Tanveer. ¹²	2014	A system was designed with NMPC-PID controller for the attitude and altitude stabilization of UAV. The problems of noise and external disturbances were solved. The robustness of the developed system was proved by the simulation.	4	NMPC-PID control
6	Vijaykumar ¹³	2014	Quadrotor UAV model was developed, simulated and implemented using Fuzzy logic control. Quadrotor was developed using '+' configuration. Six FLC's were designed to control all the six states of the quadrotor.	6	Intelligent Fuzzy Control
7	Wei Wang. ¹⁴	2013	This model was developed for the attitude and altitude control of the UAV quadrotor. For attitude control Model Reference Sliding Mode control technique was used and for altitude control Linear Quadratic Gaussian control technique was applied. The MRSMC technique provides robustness to the model.	4	1. Model Reference Sliding Mode Control 2. Linear Quadratic Gaussian controller
8	Shayegan Omidshafiej ¹⁵	2013	A linear quadrotor model was developed, providing waypoint- based trajectory control.	6	Reinforcement Learning
9	Ankit Patel ¹⁶	2012	A model for fully actuated and stable quadrotor was developed. Control techniques are used to obtain the desirable altitude and yaw angle.	2	Sliding Mode control and PD control
10	Elruby. ¹⁷	2012	CAD model was developed using Solid Edge ST to determine the parameters for simulation. PID controller was used to provide attitude control and Euler theory is used to obtain the desired position of the UAV.	6	PID control
11	Konrad Rudin ¹⁸	2011	The UAV model was developed with the attitude stability and a robust control design that can overcome the uncertainties and external disturbances. The controller was designed using Lyapunov Methodology.	3	Non-linear hierarchical controller
12	Z. Fang ¹⁹	2011	Adaptive controller was designed for the UAV for compensating the system uncertainties. The system was divided into two loops: Outer loop for horizontal position controller and the inner loop for the attitude controller.	6	Adaptive integral backstepping
13	Alpen ²⁰	2009	A non-linear dynamic model of quadrotor was developed with attitude control. The model was suitable for higher velocities.	4	PD control
14	Holger Voos ²¹	2009	The developed UAV model resolves the problems of accurate stabilization and attitude control using feedback linearization method. Eight parameters were defined for the model. The model comprises of two loops: The underlying loop was meant for attitude control to stabilize the quadrotor and the outer loop was for velocity control to determine the desired trajectory.	3	Feedback Linearization
15	Patrick Adigbli ²²	2007	A simple UAV model was developed with the attitude and position controllers.	5	1. Sliding Mode 2. Backstepping

Table 2. (Continued)

16	B. Erginer ²³	2007	The UAV model with gyroscopic effects was derived. PD control technique was used to control the altitude, pitch and roll angles and independently the yaw angle of the quadrotor.	4	PD control
17	Bouabdallah et al. ²⁴	2006	The model was to rectify the control parameters used in the control technique and test obstacle avoidance techniques. The attitude and altitude controllers for this UAV were developed.	6	1. PID & LQR 2. Backstepping
18	Bouabdallah ²⁵	2006	Fully autonomous UAV was developed using VTOL methodology and consists of the avionics and energy devices necessary for the flight. A dynamic simulation model was derived.	6	PD control
19	Bouabdallah ²⁶	2005	The model was developed using the latest sensors, actuators and energy storage devices. Simulations were performed in open and closed loops for stabilization and formation and validation of control laws.	6	1. Backstepping 2. Sliding mode
20	Bouabdallah ²⁷	2004	Development of this UAV was initiated at the Autonomous System Laboratory and is focused on the autonomous VTOL in indoor environment. It's equipped with the sensors that could measure position, altitude and orientation.	6	PID and LQ

2. Survey of Former Designed Quadrotor UAV(s)

Since last few decades, UAVs are gaining attention and are continuously developing at a phenomenal rate. At present, there are more than 1000 UAVs developed by more than 50 countries as a major contribution for the military and civil assistance.¹⁷ Table 1 presents the comparative analysis of the developed quadrotor UAVs so far, based on the control algorithm used in developing the model and the DOF.

Different control techniques have been applied to the quadrotor. The available control techniques are mainly divided into linear or non-linear in nature. Here in the comparative analysis of few control techniques that have been implemented in recent years.

3. Discussion and Analysis

PID is widely utilized to control the industrial applications.^{28,57} PID control technique can also be applied in the quadrotors to address the issues related to vertical takeoff and landing, position and angular orientation. With the appropriate values of control variables minimum overshoot and steady error minimized to zero were achieved.²⁹ TABLE 2 describes the effects of PID parameters on the system.

Table 2: Effects of PID Parameters

Controller	Rise Time	Overshoot	Settling Time	Steady state error
K_p	Decrease	Increase	Small Change	Decrease
K_i	Decrease	Increase	Increase	Eliminate

The transfer function of PID controller is shown in equation 1:

$$K_P + \frac{K_i}{s} + K_d s \quad (1)$$

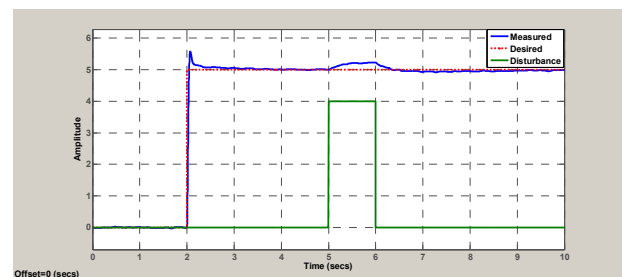


Fig.2. PID response along X-axis under air turbulence and sensor noisy conditions.³⁵

A research was carried out on quad-rotor position control. The analysis of the model was done on MATLAB. PID control was implemented and compiled better results.³⁵ Fig. 2 shows that PID control is able to overcome disturbance while stability is highly effected due to sensor noises.

PID control may be applied to resolve above mentioned issues of position and orientation of quadrotors. The response of the PID control shows the stability with almost zero steady state error.³⁰

A control technique used to achieve desired performance optimally at minimal cost. LQR control technique may also be used for quadrotor position, altitude and attitude controlling. Results shown in Fig. 3 represent that LQR performs well under noisy conditions but doesn't perform well under disturbance conditions. LQR response under heavy disturbance and noisy conditions shown in Fig.3.³⁶ In 2009, another researcher used LQR for position controlling of a quadrotor. The results were satisfactory but in his research work author did not consider the effect of disturbance on a quadrotor system.¹⁴

SMC is a non-linear control whose control output moves in a prescribed path. The control is applied to stabilize the system effectively. Sometimes SMC is referred to as gain scheduling

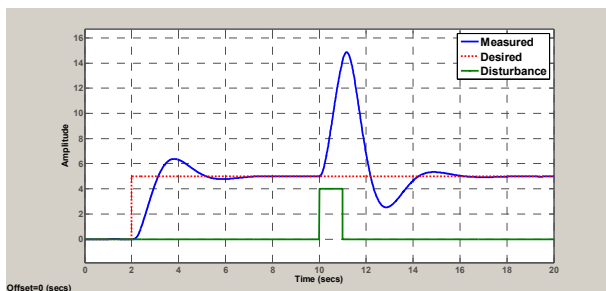


Fig.3. LQR response under heavy disturbance and noisy conditions [35].

control as its gain is actively changing from positive to negative directions.

A researcher used an impulse function as a disturbance to the quadrotor system while using SMC to overcome the applied disturbance.³³ In 2007, another researcher used sliding mode to observe the disturbances. In the simulation tests step function were applied on the vehicle as a wind gust and external disturbance.³⁴

Quadrotors are highly nonlinear and under actuated systems and that what makes them a great platform for control system research. Back stepping control (BSC) is modular in nature and a recursive control algorithm which divides system into subsystems to achieve stability. Quadrotor motion can be divided into two subsystems; a translational subsystem (altitude, x and y motion) and a rotational subsystem (attitude and heading).

In,³⁵ The nonlinear dynamic model of the quadcopter is formulated using the Newton-Euler method and backstepping control technique was applied for stabilizing the quadrotor by using the Lyapunov stability analysis.

Adaptive control algorithms adapt the changing parameters like uncertainties or change in time that occurred in the system. In 2011 a technique called Adaptive Integral Backstepping was developed for position control of quad-rotor. Initially it was observed that only integral backstepping was not enough so adaptive technique was introduced to gain better robustness [19]. The performance of controller was better but it did not provide any solution to noisy measurement issues.

To control the altitude of quadrotor adaptive sliding backstepping control is an important field of research. Adaptive elements in the sliding mode control formulation the proposed control law avoids a priori knowledge of the upper bounds on the uncertainty.

In 2011, a researcher developed robust adaptive control for a quadrotor helicopter. The researcher applied a step function as disturbance to its system. The developed controller could regain the equilibrium state.

To track a reference trajectory in the presence of disturbances and uncertainties a robust quadrotor controller known as Super Twisting controller is introduced in 2016. A Super Twisting controller is implemented using the gain adaptation law, which has the advantage of not requiring the knowledge of the upper bound of the lumped uncertainties. The design of the controller is developed without separation in two nested control loops for altitude and position and design is on regular form of quadrotor dynamics.⁸

In 2013, for controlling quadcopters reinforcement learning based control technique was developed which was applied to black box quadcopter system along with the learning control. This technique treats system as a black box and stores the results in a transition matrix, hence preferred for nonlinear systems.¹⁵

A common network can be trained to directly map state to actuator command with reinforcement learning, making any predefined control structure obsolete for training. The application of a learning algorithms that allows the training of suitable control actions relaxes the difficult task of nonlinear control design. Reinforcement learning is applied as one form of unsupervised learning.

Besides these control algorithms other control algorithms are also developed and implemented like: Robust Control Algorithms with deals with the all types of uncertainties and disturbances in the system and ensures performances within acceptable ranges, Optimal

Control Algorithms which includes LQR, L1, H_∞ and Kalman filter, Feedback Linearization which converts the non-linear system into its equivalent linear system and hybrid control algorithms which involves more than one control techniques for controlling the quadrotors.^{31,32,36}

4. Conclusion

Several quadrotor models and their control algorithms have been introduced in the recent years. This purpose of this document is to provide the review of available quadrotors models and the control schemes applied for stabilizing the control of attitude, altitude and position to provide a generic reference about existing solutions and assist the development of improved devices.

5. References

- [1] Muhammad Hassan, T., Hazry, D., Faiz, S., Muhammad Kamran, J., Faizan, A. W., Zuradzman, M. R., ... & Abadal-Salam, T. H. (2014). PID based controller design for attitude stabilization of Quad-rotor.
- [2] Joyo, M.K. et al., 2013. Altitude and horizontal motion control of quadrotor UAV in the presence of air turbulence. *Proceedings - 2013 IEEE Conference on Systems, Process and Control, ICSPC 2013*, (December 2013), pp.16–20.
- [3] Máthé, K. & Buşoni, L., 2015. Vision and Control for UAVs: A survey of general methods and of inexpensive platforms for infrastructure inspection. *Sensors* (Basel, Switzerland), 15(7), pp.14887–916.
- [4] Norouzi Ghazbi, S. et al., 2016. Quadrotors unmanned aerial vehicles: A review. *International Journal on Smart Sensing and Intelligent Systems*, 9(1), pp.309–333.
- [5] Zulu, A. & John, S., 2014. A review of control algorithms for autonomous quadrotors. *Open Journal of Applied Sciences*, 4(December), pp.547–556.
- [6] Huo, X., Huo, M. and Karimi, H.R. (2014) Attitude stabilization control of a quadrotor uav by using backstepping approach. *Mathematical Problems in Engineering*, 2014, 1-9.
- [7] Cai, Guowei, Jorge Dias, and Lakmal Seneviratne. "A survey of small-scale unmanned aerial vehicles: Recent advances and future development trends." *Unmanned Systems* 2.02 (2014): 175-199.
- [8] Rajappa, S. et al., 2016. Adaptive Super Twisting Controller for a Quadrotor UAV. , (1), pp.2971–2977.
- [9] Mustapa, M.Z., 2015. Altitude controller design for quadcopter UAV. *Jurnal Teknologi*, 74(1), pp.187–194.
- [10] Emran, B.J. & Yesildirek, A., 2014. Robust Nonlinear Composite Adaptive Control of Quadrotor. *International Journal of Digital Information and Wireless Communications*, 4(2), pp.213–225.
- [11] Hassan Tanveer, M. et al., 2013. Stabilized controller design for attitude and altitude controlling of quad-rotor under disturbance and noisy conditions. *American Journal of Applied Sciences*, 10(8), pp.819–831.
- [12] Tanveer, H. & Hazry, D., 2014. Model Predictive Control based reference point tracking of quad-rotor UAV in prevalence of disturbance 1. , 8(4), pp.428–431.
- [13] Vijaykumar Sureshkumar, K.C., 2014. Intelligent Fuzzy Flight Control of an Autonomous. *AIAA SciTech*, (January), pp.1–10.
- [14] Singh, A.M., Lee, D.J. & Chong, K.T., 2013. Attitude and altitude controllers for quadrotor. *대한전자공학회 학술대회*, 2013, pp.1436–1437. Available at: <http://www.dbpia.co.kr/Article/NODE02275371>.
- [15] Omidshafiei, S., 2013. Reinforcement Learning-based Quadcopter Control. , (1).
- [16] Patel, A.R., Patel, M. a & Vyas, D.R., 2012. Modeling and analysis of quadrotor using sliding mode control. *Proceedings of the 2012 44th Southeastern Symposium on System Theory (SSST)*, pp.111–114.
- [17] Elruby, a Y., El-khatib, M.M. & Hashad, N.H.E.-A. a I., 2012. Dynamics Modeling and Control of Quadrotor Vehicle. *Amme*, pp.280–286.
- [18] Rudin, K. et al., 2011. A robust attitude controller and its application to quadrotor helicopters. *IFAC Proceedings Volumes (IFAC-PapersOnline)*, 18(PART 1), pp.10379–10384.
- [19] Fang, Z. & Gao, W., 2011. Adaptive integral backstepping control of a Micro-Quadrotor. *Proceedings of the 2nd International Conference on Intelligent Control and Information Processing, ICICIP 2011*, (PART 2), pp.910–915.
- [20] Alpen, M., Frick, K. & Horn, J., 2009. Nonlinear modeling and position control of an industrial quadrotor with on-board attitude control. *2009 IEEE International Conference on Control and Automation, ICCA 2009*, pp.2329–2334.
- [21] Voos, H., 2009. Nonlinear Control of a Quadrotor Micro-UAV using. , (April), pp.4–9.
- [22] Adigbli, P. et al., 2007. Nonlinear Attitude and Position Control of a Micro Quadrotor using Sliding Mode and Backstepping Techniques. *European Micro Air Vehicle Conference and Flight Competition*, (September), pp.17–21.
- [23] Erginer, B. & Altug, E., 2007. Modeling and PD Control of a Quadrotor VTOL Vehicle. *2007 IEEE Intelligent Vehicles Symposium*, pp.894–899.
- [24] Bouabdallah, S., Becker, M. & Siegwart, R., 2007. Autonomous miniature flying robots: Coming soon! - Research, development, and results. *IEEE Robotics and Automation Magazine*, 14(3), pp.88–98.
- [25] Bouabdallah, S. & Siegwart, R., 2006, Towards Intelligent Miniature Flying Robots. , pp.1–12.
- [26] Bouabdallah, S. & Siegwart, R., 2005. Backstepping and sliding-mode techniques applied to an indoor micro Quadrotor. *Proceedings - IEEE International Conference on Robotics and Automation*, 2005(April), pp.2247–2252.
- [27] Bouabdallah, S. et al., 2004. PID vs LQ Control Techniques Applied to an Indoor Micro Quadrotor. *IEEE/RSJ International Conference on Intelligent Robots and Systems*, 3, pp.2451–2456.
- [28] John, S. (2013) Artificial Intelligent-Based Feedforward Optimized PID Wheel Slip Controller. *AFRICON*, 12 September 2013, Pointe-Aux-Piments, 1-6.
- [29] Li, J., & Li, Y. (2011). Dynamic analysis and PID control for a quadrotor. Paper presented at the Mechatronics and Automation (ICMA), 2011 International Conference.
- [30] Salih, A. L., Moghavvemi, M., Mohamed, H. A., & Gaed, K. S. (2010). Flight PID controller design for a UAV

- quadrotor. *Scientific Research and Essays*, 5(23), 3660-3667.
- [31] Yibo, L. (2012, 18-20 Oct. 2012). A survey of control algorithms for Quadrotor Unmanned Helicopter. Paper presented at the Advanced Computational Intelligence (ICACI), *2012 IEEE Fifth International Conference*.
- [32] Rinaldi, F., Chiesa, S., & Quagliotti, F. (2013). Linear quadratic control for quadrotors UAVs dynamics and formation flight. *Journal of Intelligent & Robotic Systems*, 70(1-4), 203-220.
- [33] Benallegue, A., Mokhtari, A., & Fridman, L. (2006). Feedback linearization and high order sliding mode observer for a quadrotor UAV. Paper presented at the *Variable Structure Systems*, 2006. VSS'06.
- [34] Besnard, L., Shtessel, Y. B., & Landrum, B. (2007, 9-13 July 2007). Control of a Quadrotor Vehicle Using Sliding Mode Disturbance Observer. Paper presented at the *American Control Conference*, 2007. ACC '07.
- [35] Kamran Joyo M., Ahmed S.F., Bakar M.I.A., Ali A. (2018) Horizontal Motion Control of Underactuated Quadrotor Under Disturbed and Noisy Circumstances. In: Mishra D., Azar A., Joshi A. (eds) *Information and Communication Technology. Advances in Intelligent Systems and Computing*, vol 625. Springer, Singapore.
- [36] S. Faiz Ahmed, Kushsairy Kadir and M. Kamran Joyo, 2016. LQR based controller design for altitude and longitudinal movement of quad-rotor. *J. Applied Sci.*, 16: 588-593.

A GIS Based Hydrological Model for River Water Level Detection & Flood Prediction featuring morphological operations.

Sarmad Zafar

*Mohammad Ali Jinnah University, Pakistan
Sarmadzafar10@gmail.com*

H.M.Sohaib Azhar

*Mohammad Ali Jinnah University, Pakistan
Engr.sohaib.azhar@hotmail.com*

Aqeel Tahir

*Mohammad Ali Jinnah University, Pakistan
Engr.aqtahir84@hotmail.com*

Abstract

Mostly river water level and flood forecasting methods are based on gauging stations measurements at discrete locations, which limits their capability to provide accurate and timely data over large extent, also limited or no data available on remote locations. So here we present an idea to use high resolution satellite images for real time mapping of river water level. In this project, we developed a Web based GIS system for mapping river water level, early warning and mapping for flood disasters. To improve flood forecasting/warning, we developed a decision support system (DSS) for flood monitoring and prediction that integrates GIS, satellite image processing and hydrological modelling. We present the methodology for data integration, floodplain delineation, and online map interfaces. Our Web based GIS system can dynamically display observed and predicted water levels for decision makers and the general public. The users can access a Web-based GIS system which models current flood events and displays satellite imagery and 3D visualization integrated with the flood plain area. The output from the hydrological modeling will be used for flooding prediction for the next 1 day to 2 days (24 and 48 hours) along the lower Indus River. In this stage river water level analysis has been achieved, work on the hydrological modelling is in progress to acquire river water stage & flood level and the prediction.

Keywords: Hydrological modelling, GIS based system, morphology, satellite imagery, 3D visualization.

1. Introduction

Droughts and floods are both water-related natural disasters which have a widespread effect on environmental factors and activities like human life, agriculture, vegetation, local economies and wild life. These both are natural disasters which are thought to be beyond human control, but drought is the one of the most important weather-related natural disaster which is often aggravated by human action. Drought affects a very large area for months and even for years. So it has a severe impact on regional food production, life expectancy of the entire populations and overall economic performance

of large regions or countries. If we observe the recent data large-scale severe droughts have been observed in different areas of the world encompassing all continents leading to economic and natural resources loss, this destruction lead to food shortages and starvation of masses. On the other hand floods are the most devastating natural hazards in the world. Floods were most baleful than any other natural disaster both in claiming more lives and causing more property damage.

For effective management of disaster users like top level policy makers at the national and international organizations, middle level policy makers at local levels consultants, researchers, relief agencies and local

© The 2018 International Conference on Artificial Life and Robotics (ICAROB2018), Feb. 1-4, B-Con Plaza, Beppu, Oita, Japan

producers which includes farmers, water managers suppliers and traders are interested in reliable, accurate and timely information of drought and flood. The disaster management activities can be grouped into three major phases: The Preparedness phase in which prediction and risk zone are identified, identification is done long before the actual disaster event occur; in Prevention phase different activities are carried out like, monitoring, early warning & Forecasting, and preparation of contingency plans that should be taken up just before or during the event; and the Response/Mitigation phase includes the activities which are done damage assessment and relief management.

Though flood cannot be stop but their effect can be minimized if we have proper data, so in this project our objective is to map the river flow data on geographical information system. As rivers cover a large geographical area so we can obtain data using remote sensing techniques and distribute information to control stations rapidly over large areas by means of satellites or transponders mounted on drones or aircraft. A satellite orbits the Earth, can explore the whole surface in a few days and repeat its survey of the same area at regular intervals. For these satellite images we will use publically available high resolution images like NASA MODIS, SPOT etc.

2. Methodology

The proposed project models a particular area on the GIS and collect relevant data like satellite images of high resolution at different time period. The backend processing application will take these images as input; image will go through multiple stages of processing and output of this will be quantifiable data along will the geo location. The front end GIS based web or mobile application will take date from the data base and model it on the geographical information system.

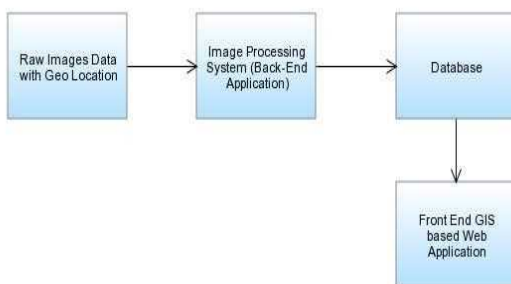


Fig. 1. GIS based Prediction system block diagram

2.1. Satellite Image Processing Research

Satellite image processing techniques will be used for effective management of water bodies on land and used for decision making for disaster management. An extensive research has been done for identifying and designing the best suited algorithm for analyzing and processing the high resolution satellite images. The process of identifying the stage of a river using satellite images is a difficult process, because the images captured from satellite are remotely sensed at a very long distance. We utilize the Support Vector Machine algorithm for this purpose. The work is divided into three phases the training phase, analysis phase and the testing phase. In the training phase, water region is extracted from the image and the stage of river is identified both by training two different ANNs. In the testing process, the input raw river image was passed through different process first image filtration to de-noised and morphological operation was carried out on the de-noised image. After that the river image was segmented into water regions with the aid of the ANN. Finally in the analysis phase, the stage of the river water was categorized on scale of three whether river is in Normal, drought or flood condition.

2.2. Satellite Image Data Gathering

One of the most important thing in our project is the high-resolution satellite image data, which is publically available on different platforms some are:

- NASA MODIS Imagery
- SPOT Imagery
- JAXA's Global ALOS 3D World
- NOAA Data Access Viewer – Discover Authoritative Datasets
- Global Land Cover Facility – Derived Satellite Data.

2.3. Layout Designing

Low fidelity prototypes have been designed, some basic prototypes are shown below:

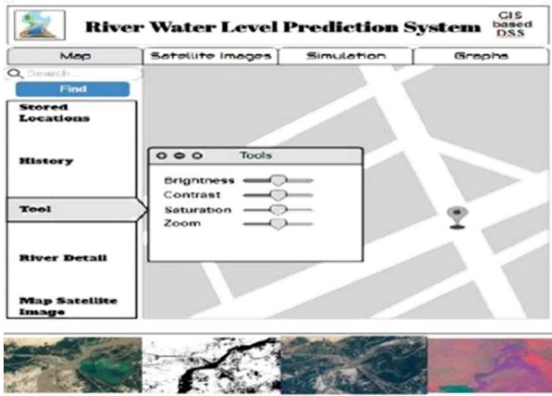


Fig. 2. River Geographical Map View

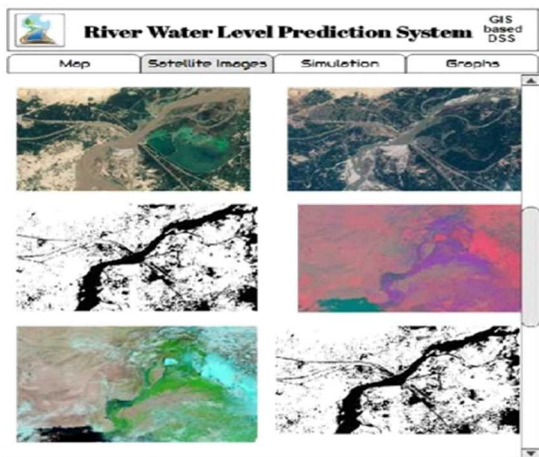


Fig. 3. High resolution Satellite Image

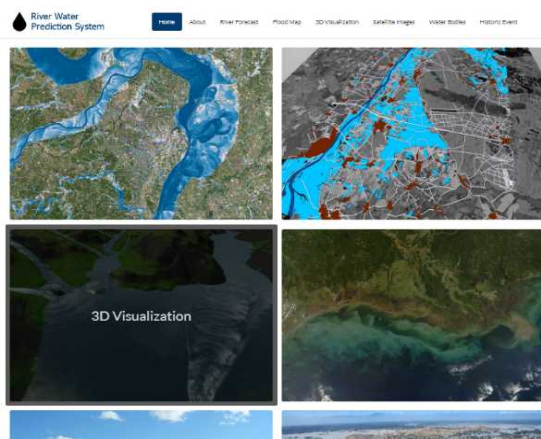


Fig. 4. GIS Application Mockup

2.4. Image Processing

The developed algorithm is able to identify the water bodies in the high resolution satellite images. In order to understand the flood dynamics and hydrological exchange between river and related floodplains, it relies on the data gathered of water levels at discrete locations on main channel. But due to vast expansion of the river basins limited gauging stations and river passes through locations selected where it's difficult to have these stations, so some other techniques must be implied in order to improve the spatial sampling, like radar remote sensing using interferometric phase measurements this can improve the spatial sampling, but the phase is temporally incoherent over open water so this technique is used to determine water levels. Satellite images are processed and passed through these different stages to extract the river stage.

Complete flow is shown with Image Processing steps in Fig. 5:

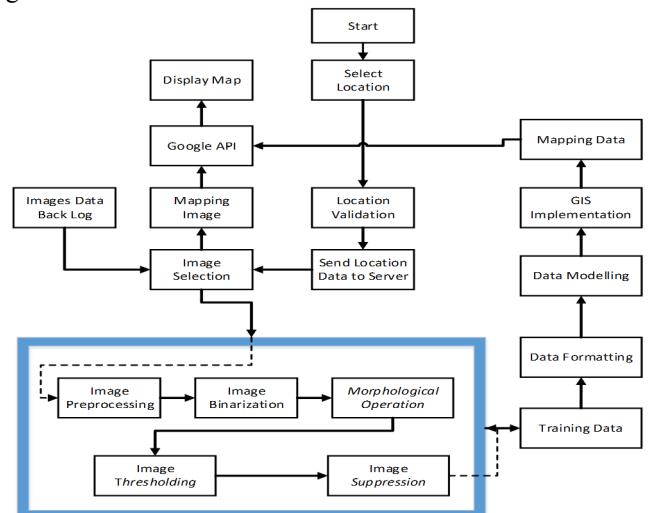


Fig. 5. Steps involve in the process

2.4.1. Image Acquisition

Acquired an image from open access NASA database

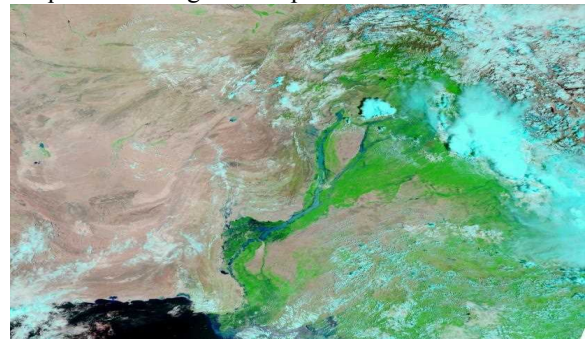


Fig. 6. This is a moderate resolution satellite image

The image is passed through different steps to extract the river stage.

2.4.2. Image Filtration:

Filtering is used to modify and enhance the image by removing the unwanted pixel values in the image. For example, you can filter out an image to emphasize certain features or remove other features. Image processing operations implemented with filtering include smoothing, sharpening, and edge enhancement.

In image processing filtering is a neighborhood operation, in which the value of each pixel in the output image is calculated by applying some algorithm to the values of the pixels in the neighborhood of the corresponding input pixel. A pixel's neighborhood is the surrounding pixels, defined by their locations relative to that pixel.

2.4.3. Lab color space Conversion

The Lab color space mathematically describes all perceivable colors in the 3 dimensional space. L used for lightness, 'a' and 'b' for the color components, green-red and blue-yellow. The Lab color space has more enhanced than the RGB and CMYK color models. For the conversion of RGB image to the Lab color format below given equations are used.

$$\begin{bmatrix} X \\ Y \\ Z \end{bmatrix} = \begin{bmatrix} 0.412453 & 0.357580 & 0.180423 \\ 0.212671 & 0.715160 & 0.072167 \\ 0.019334 & 0.119193 & 0.950227 \end{bmatrix} * \begin{bmatrix} r \\ g \\ b \end{bmatrix}$$

$$L^* = \begin{cases} 116 * (Y/Y_n)^{1/3} - 16, & \text{for } Y/Y_n > 0.008856 \\ 903.3 * Y/Y_n, & \text{otherwise} \end{cases}$$

$$a^* = 500 * (f(X/X_n) - f(Y - Y_n))$$

$$b^* = 200 * (f(Y/Y_n) - f(Z - Z_n))$$

After conversion to CIE Lab color image look like:

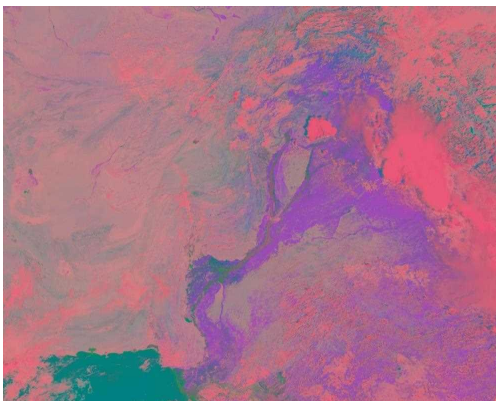


Fig. 7. CIE color converted Image.

© The 2018 International Conference on Artificial Life and Robotics (ICAROB2018), Feb. 1-4, B-Con Plaza, Beppu, Oita, Japan

2.4.4. Anisotropic diffusion segmentation:

In image processing and computer vision: anisotropic diffusion, is a technique used to reduce the noise level without affecting substantial image contents parts. The contents, usually edges, lines or other details that are significant for the analysis of the image. In Anisotropic diffusion a scale space has created, in which an image generates a parameterized family of consecutively more and more blurred images based on the result of diffusion process. Each of the resulting image in this family are given as a convolution between the image and a 2D isotropic. The following equation details the segmentation process.

$$\frac{\partial \text{Im}}{\partial t} = \text{div}(c(x, y, t) \nabla \text{Im}) = \nabla c \cdot \nabla \text{Im} + c(x, y, t) \Delta \text{Im}$$

Equation 2. Delta Function applied to Image.

Where div is the representation for the divergence operator, Δ stands for the Laplacian, ∇ for the gradient and $c(x, y, t)$ is the diffusion coefficient. $c(x, y, t)$ is used to control the rate of diffusion and it is selected as a function of the image gradient in order to conserve edges in the image.

2.4.5. Image Binarization

The segmented image is transformed into binary image which is then used for further processing. Binarization is a process of converting an image by extracting lightness (brightness & density) intensities as a feature amount from the image. In this process pixel image is converted into binary image. When a pixel area is picked of an image, sensitivity value is added to or subtracted, concerning the Y values of the selected pixel to describe a threshold range value. Further, when another pixel is chosen, the same process is applied to set new threshold value. The pixel with the value concerning the Y value of any pixel in the image within the threshold value range is extracted as the same brightness as the selected pixel and the extraction result is displayed. The output image after binarization contain only black and white image.

2.4.6. Morphological operation:

The morphological operation is applied in order to achieve the smoothness, so that intended information be extracted. The impact of the morphological operation depends on the application for example in machine learning & computer vision, object detection in which we may apply it to classify the structure of an image. Morphological operation is useful to differentiate boundaries of objects or to identify objects present in an

image. In this, we apply the “**imclose**” function as morphological operation closes the image. The following equation details the process.

$$Im_{bin} \circ st = (Im_{bin} \oplus st) \ominus st$$

Equation. 3. Image segmentation expression Here **st** is structuring element which is required by which the morphological operation is applied.

Image after morphological operation looks like:

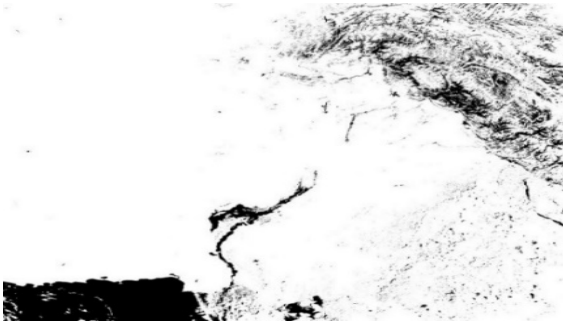


Fig. 8. Morphological Image

2.5. Training Data

So as to identify the stage of Support Vector Machine (SVM) technique is employed, SVM is trained by a set of water identifies images. Support Vector Machine is a machine learning method that classifies binary classes by finding and using a class boundary the hyper plane maximizing the margin in the given training data. The training data samples along the hyper planes close to the class boundary are called support vectors, and the margin is the distance between the class boundary, support vectors and hyper-planes. The SVM work on the basis of the decision boundaries defined by the decision planes. A decision plane separates between assets of objects having different class memberships. SVM is a one of the very useful technique for data classification. For classification task training and testing date is utilized which consists of some data instances. Each instance in the training set contains one “target value” (class labels) and several “attributes” (features).



Fig. 9. River water levels

3. Conclusion

This paper presents the idea for the integration of satellite imagery, hydrological modeling and geographical information system to come up with a decision support system which will be used for continuously monitoring the river water level. By processing the satellite imagery we can extract the river stage over the entire spatial range from where the river passes.

The system for flood events prediction and monitoring integrated with the web map interface will facilitates in monitoring, prediction and decision making of the flooding events. It works as an early warning and mapping of flood disasters.

4. References

1. Laurence C. Smith, "Satellite Remote Sensing of River Inundation Area, Stage, And Discharge: A Review", *Hydrological Processes*, Vol. 11, pp.1427-1439, 1997
2. Flood Forecasting GIS Water-Flow Visualization Enhancement (WaVE): A Case Study Timothy R. Petty¹, Nawajish Noman², Deng Ding², John B. Gongwer³
3. DROUGHTS & FLOODS ASSESSMENT AND MONITORING USING REMOTE SENSING AND GIS by A.T. Jeyaseelan
4. Nipuni Hettiarachchi “Water Level Forecasting and Flood Warning System A Neuro-Fuzzy Approach”, *International Conference in Video Image and Signal Processing*, At India
5. Michael T. Coe, "Calculation of river discharge and prediction of lake height from satellite radar altimetry: Example for the Lake Chad basin", *Water Resources Research*, Vol. 40, 2004
6. D. Mioc “EARLY WARNING AND MAPPING FOR FLOOD DISASTERS”, The International Archives of the Photogrammetry, *Remote Sensing and Spatial Information Sciences*. Vol. XXXVII. Part B4. Beijing 2008
7. HJ Barneveld “APPLICATION OF SATELLITE DATA FOR IMPROVED FLOOD FORECASTING AND MAPPING”, *4th International Symposium on Flood Defence: Managing Flood Risk, Reliability and Vulnerability* Toronto, Ontario, Canada, May 6-8, 2008
8. R. Loren and D. B. Benson (eds.), *Introduction to String Field Theory*, 2nd edn. (Springer-Verlag, New York, 1999).
9. R. M. Karp, Reducibility among combinatorial problems, in *Complexity of Computer Computations* (Plenum, New York, 1972), pp. 85–104.

Analysis of onboard sensor-based odometry for a quadrotor UAV in outdoor environment

Aidar Gabdullin, Grigory Shvedov, Mikhail Ivanou, Ilya Afanasyev

Robotics Institute, Innopolis University

1 Universitetskaya street, 420500 Innopolis, Russia

E-mail: {a.gabdullin, g.shvedov, m.ivanov, i.afanasyev}@innopolis.ru

<http://university.innopolis.ru>

Abstract

This article introduces a comparative analysis of a quadrotor UAV trajectories evaluated by processing onboard sensors (camera and IMU) with ROS-based monocular visual odometry software. Parrot Bebop drone was launched outdoor within teleoperated closed-loop trajectory along a known perimeter of a square work area, recording sensor's telemetry data for offline processing. We compared UAV monocular SLAM trajectories with Bebop visual-inertial odometry and verified them with the ground truth estimated by an external observer (a hovering quadcopter DJI Mavic, flying at the height of 40m with a camera pointing downwards and tracking near-surface Bebop's flight).

Keywords: monocular visual odometry, GPS-denied environment, quadrotor UAV, SLAM, ROS

1. Introduction

At present, the tasks of autonomous quadrotor UAV localization, mapping and navigation in GPS-denied environment are solved mainly by vision-based sensing and inertial navigation systems (INS), combining visual feature data from a monocular camera with inertial sensor measurements [1-4]. During the last years many studies of GPS-denied indoor navigation have focused on the monocular visual localization applications [5-8] and comparative analysis of different vision-based algorithms [9-11], since visual localization is frequently a natural substitution of a GPS approach. However, there is still a lack of investigations dealt with efficiency and robustness of monocular visual odometry methods for UAV quadrotors in GPS-denied outdoor environment.

When hovering outdoors, especially in a windy condition, a conventional quadrotor UAV with uncalibrated fixed camera actively changes pitch and roll angles, recording a video with a poor quality due to

shakes and high-frequency vibrations from motors and propellers. To solve this issue, it is used a camera with a good image quality and robust digital stabilization. In our research, we employ a Parrot Bebop drone outdoor in teleoperated mode, making a closed-loop trajectory along a known perimeter of a work area at a height of 1.5-2m, acquiring sensors telemetry data for offline processing with Robot Operating System (ROS) packages.

The rest of this paper is organized as follows. Section 2 describes system setup. Section 3 presents ROS-based computations of visual odometry trajectories and their verification by an external observer. Section 4 provides outdoor experiment results with comparative accuracy analysis. Section 5 concludes this paper.

2. System setup

In our outdoor experiments we used Parrot Bebop drone (Fig. 1), as a robust quadrotor UAV, which has a digitally stabilized camera and special flight modes with drone

landing in case of collisions^a. Bebop controls stability and maneuverability of its flight by automatic processing sensors data from 3D inertial measurement unit (IMU), an ultrasound sensor of an 8m range, a pressure sensor and a vertical camera (to track the speed). Bebop quadrotor can record video in a 180° panoramic view by the 14mpx "fisheye" camera with digital image stabilization, taking stable aerial footage independently on UAV maneuvers. Parrot Bebop drone has a firmware with integrated visual-inertial velocity estimation (without GPS), and an open source ROS wrapper^b to get and process telemetry data.

For a top-view Bebop's trajectory validation (as the ground truth) we used a hovering DJI Mavic quadcopter^c as an external observer. It was also teleoperated to hold a position at the height of 40m with a camera pointing downwards and tracking near-surface Bebop's flight. Its camera is actively gyro-stabilized with a brushless gimbal, recording a video with the resolution of 1920*1080 at 60 fps. For observer sensor's data processing we utilized OpenCV 3.0^d and ROS Kinetic^e.

3. Bebop drone odometry and its verification

3.1. Bebop visual-inertial odometry

Parrot Bebop drone has a default option of odometry calculation by a bebop_autonomy driver^f, which allows reading from UAV camera, odometry, GPS and drone states (i.e. on-board data also known as Navdata). The odometry integrates visual-inertial velocity over time (dead reckoning), using video stream from Bebop's front camera with a bebop_driver and Bebop's position & velocity in an ENU aligned odometry (which is based on REP-103 specifies an ENU (East, North, Up) coordinate frame for outdoor navigation^g). Since odometry is calculated from Bebop States (Navdata), the update rate is limited to 5 Hz that can be a reason for growth of trajectory deviation error during Bebop flight (see loop closure displacements in trajectories in Fig. 2a during three cycles of UAV flight along the same work area perimeter in Fig. 1). Visual-inertial odometry seems to

provide relevant results in steady-weather conditions, but in strong wind and rapid changes in accelerations, we observed a displacement at ~10m per cycle at a wind of 6m/s (Fig. 2) Therefore, we employed DJI Mavic drone as an external observer for a ground truth.

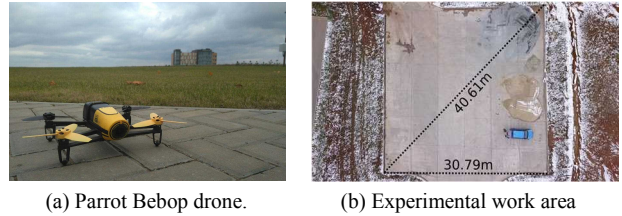


Fig. 1. Outdoor experiments with Parrot Bebop drone

3.2. Odometry verification by external observer

As a ground truth (reference trajectory) we used an external observer data taken from a hovering DJI Mavic quadcopter, flying at an altitude of 40m with a camera pointed down and tracking near-surface Bebop's flight. We processed the image footages offline, tracking Bebop with following steps: (1) Computing a dense optical flow with color coding for each video frame [12]; (2) Converting images to grayscale and thresholding; (3) Detection of Bebop contour and its center position (x,y). As additional DJI Mavic camera calibration the landmark size in work area were measured in advance, thus we transformed image pixels to geocoordinates in meters.

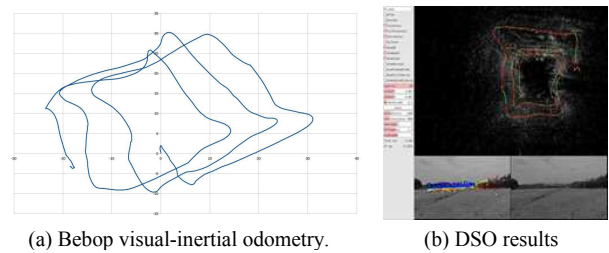


Fig. 2. Difficulties with UAV odometry estimations: (a) Three loop closure displacements in Bebop visual-inertial odometry trajectories (in meters) for UAV flight under the same work area in windy conditions; (b) Divergence of UAV trajectory received with Direct Sparse Odometry (DSO).

^a Parrot Bebop Drone description: <http://global.parrot.com/>
^b ROS driver for Parrot Bebop drone, based on Parrot's official ARDroneSDK3: http://wiki.ros.org/bebop_autonomy
^c DJI Mavic drone: <https://www.dji.com/mavic>
^d OpenCV 3.0 library: <https://opencv.org/opencv-3-0.html>

^e ROS Kinetic Kame middleware : <http://wiki.ros.org/kinetic>
^f ROS Driver for Parrot Bebop Drone (quadcopter) 1.0 & 2.0: <http://bebop-autonomy.readthedocs.io/en/latest/index.html>
^g REP-103 provides a reference for the units and coordinate conventions used within ROS: <http://www.ros.org/rep/rep-0103.html>

3.3. ROS-based Visual SLAM

ORB-SLAM: Oriented FAST and Rotated BRIEF^h [13] in most cases is one of the most accurate and robust SLAM solution that has ROS-based package with bundle adjustment, monocular feature-based observations and camera trajectory estimation. Thus, ORB SLAM includes features from different images in 3D space and visual odometry tracks for unmapped regions (Fig. 3). Finally, we built the UAV trajectory, but while testing we detected some ORB-SLAM difficulties with: (1) random character of initialization (mostly, due to lack of features); (2) adding new points to a map (since ORB-SLAM needs some time for new keyframes); (3) camera rotations (then SLAM tracking tends to get lost features and trajectory); (4) dependence trajectory deviation accuracy on camera calibration and scaling to metric scale. To overcome some problems in our experiment we teleoperated Bebop drone along closed-loop trajectory with slow rotations in the work area corners.

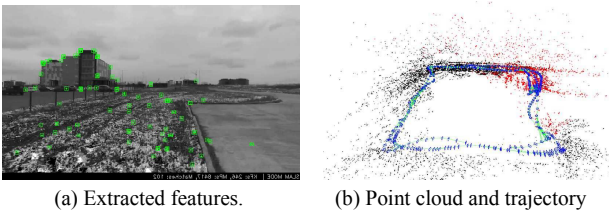
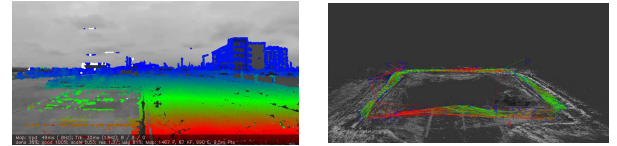


Fig. 3. ORB SLAM point clouds and trajectory visualization

LSD-SLAM: Large-Scale Direct Monocular SLAMⁱ [14] performs image-to-image alignment with simultaneous tracking, depth map estimation and optimization (Fig. 4). However, this method is highly demanding of computing resources and sensitive to camera calibration. Despite map optimization, which includes loop closure detection, the resulting trajectory has lower precision than ORB-SLAM one (although LSD-SLAM point cloud is much denser than for ORB-SLAM). In our case, Bebop’s camera has a rolling shutter, thus the results were not so accurate as they could be with global shutter camera. Nevertheless, LSD-SLAM demonstrates stable work, excepting the cases of fast camera rotation, and has no problems with initialization.

^h ORB-SLAM2 package, github.com/raulmur/ORB_SLAM2

ⁱ LSD-SLAM package, https://github.com/tum-vision/lsd_slam



(a) Depth map with features. (b) Point cloud and trajectory

Fig. 4. LSD-SLAM featured depth map and UAV trajectory.

DSO: Direct Sparse Odometry^j [15] combines sparse and direct visual odometry methods, minimizing a photometric error evaluated directly from images. DSO is sensitive to camera calibration and suffers from Bebop camera distortions, therefore in our case instead of loop closure we got divergence of UAV trajectories (Fig. 2b).

4. Outdoor Experiment and Results

Experimental dataset was recorded in bag-file during Parrot Bebop drone flight and sensor’s telemetry data was processed offline with visual SLAM algorithms. Fig. 5 illustrates the comparison of all UAV odometry trajectories evaluated with ROS-based monocular visual SLAM methods, Bebop visual-inertial odometry and the reference trajectory (ground truth) from the external observer (DJI Mavic drone). For monocular SLAM methods (ORB and LSD) the computed trajectories were properly scaled. For error estimation we computed maximum and average deviations with the formulae:

$$\max \text{ dev.} = \max \left(\sqrt{(x_i^{\text{traj}} - x_i^{\text{gt}})^2 + (y_i^{\text{traj}} - y_i^{\text{gt}})^2} \right), \quad (1)$$

$$\text{avg. dev.} = \frac{1}{N} \sum_{i=1}^N \sqrt{(x_i^{\text{traj}} - x_i^{\text{gt}})^2 + (y_i^{\text{traj}} - y_i^{\text{gt}})^2}. \quad (2)$$

where x, y are coordinates of odometry estimation and ground truth correspondingly, and N is a number of samples (points) in path. Table 1 illustrates the error estimations (deviations) for UAV odometry trajectories.

Table 1. Estimated max and mean errors of UAV trajectory deviations for UAV sensor-based odometry

Method	Average deviation, m	Maximum deviation, m
Bebop visual-inertial odometry	2.53	9.85
ORB-SLAM	2.56	8.52
LSD-SLAM	4.45	14.91

^j DSO package, <https://github.com/JakobEngel/dso>

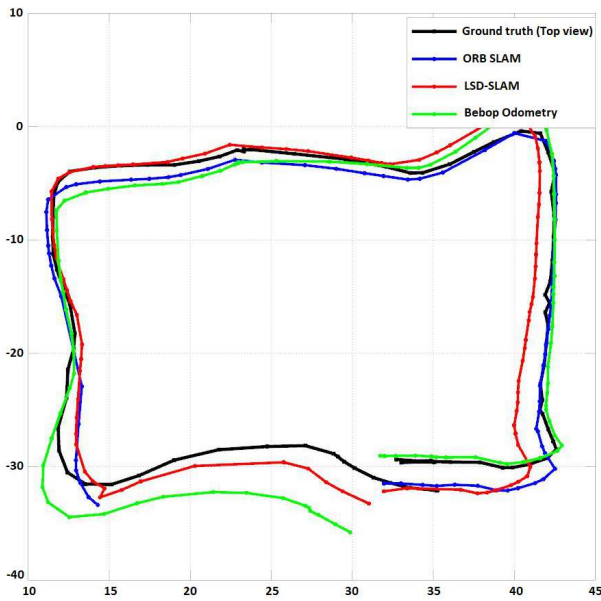


Fig. 5. Comparison of Bebop drone trajectories computed by monocular ORB-SLAM (blue curve), monocular LSD-SLAM (red curve), Bebop Visual-Inertial Odometry (Green curve). Black curve is the ground truth (top view from the external observer). The units for the XY axes are meters.

5. Conclusions

In this paper we studied the experimental results for application of some monocular visual odometry methods to Parrot Bebop drone outdoor closed-loop flight and analyzed UAV trajectories evaluated by offline processing of onboard sensors (camera and IMU) with ROS-based software. We compared UAV monocular SLAM trajectories with Bebop visual-inertial odometry and verified them with the ground truth estimated by an external observer (a hovering quadcopter DJI Mavic, flying at the height of 40m with a camera pointed down and tracking near-surface Bebop’s flight).

The main conclusions from our experiment are: (1) There are difficulties with Parrot Bebop drone trajectory recovering for all considered monocular SLAM algorithms (due to possible tracking failure in case UAV rotations, and SLAM sensitivity to Bebop camera geometric distortions and calibration). (2) All monocular SLAM methods need rescaling to metric scale for proper UAV trajectory evaluation (that requires a reliable ground truth). (3) In our experiments, visual odometry based on ORB-SLAM is more accurate and robust to

outdoor environment than Bebop visual-inertial odometry and LSD-SLAM, although sometimes it has difficulties with initialization and camera rotations.

Acknowledgements

The research was partially supported by Russian Foundation for Basic Research (RFBR), project ID 15-07-07483, Russian Ministry of Education and Science within the Federal Target Program (research grant ID RFMEFI60917X0100) together with KAMAZ company as the industrial partner, and Innopolis University.

References

1. M.J. Milford et al, Aerial SLAM with a single camera using visual expectation, in *IEEE ICRA* (2011), 2506-2512
2. D. Scaramuzza et al., Vision-controlled micro flying robots, *Robotics & Automation Magazine* 21 (2014)
3. P. Li, M. Garratt, A. Lambert, Monocular Snapshot-based Sensing and Control of Hover, Takeoff, and Landing for a Low-cost Quadrotor, *Field Robotics*, 32 (2015), 984-1003
4. M. Faessler et al., Autonomous, Vision-based Flight and Live Dense 3D Mapping with a Quadrotor Micro Aerial Vehicle. *Journal of Field Robotics* 33.4 (2016), 431-450
5. A. Buyval, M. Gavrilencov, Vision-based pose estimation for indoor navigation of unmanned micro aerial vehicle based on the 3D model of environment, in *MEACS* (2015)
6. K. Yakovlev et al., Distributed control and navigation system for quadrotor UAVs in GPS-denied environments. In *Intelligent Systems*, Springer (2015), 49-56
7. A. Buyval, M. Gavrilencov, E. Magid, A multithreaded algorithm of UAV visual localization based on a 3D model of environment, in *ICAROB* (2017)
8. A. Bokovoy, K. Yakovlev, Original Loop-closure Detection Algorithm for Monocular vSLAM, *ArXiv preprint arXiv:1707.04771* (2017)
9. A. Buyval, I. Afanasyev, E. Magid, Comparative analysis of ROS-based Monocular SLAM methods for indoor navigation, in *Machine Vision*, SPIE (2017), 103411K
10. M. Sokolov, et al., Analysis of ROS-based Visual and Lidar Odometry for a Teleoperated Crawler-type Robot in Indoor Environment, in *ICINCO* (2017)
11. I. Ibragimov, I. Afanasyev, Comparison of ROS-based Visual SLAM methods in homogeneous indoor environment, in *IEEE WPNC* (2017)
12. G. Farneback, Two-frame motion estimation based on polynomial expansion, in *Image analysis* (2003), 363-370
13. R. Mur-Artal, and J.D. Tardós, ORB-SLAM2: an Open-Source SLAM System for Monocular, Stereo and RGB-D Cameras, *ArXiv preprint arXiv:1610.06475* (2016)
14. J. Engel, T. Schöps, and D. Cremers, LSD-SLAM: Large-scale direct monocular SLAM. In *European Conference on Computer Vision*. Springer, Cham (2014), 834-849
15. J. Engel, V. Koltun, and Daniel Cremers, Direct sparse odometry, *IEEE Trans. PAMI* (2017)

Memristive neuron integration in digital robotic embodiment

Max Talanov, Evgenii Zykov, Yuriy Gerasimov, Evgeni Magid, Aleksander Elizarov
Kazan Federal University, Kazan, Russia
E-mail: max.talanov@gmail.com

Victor Erokhin
Institute of Materials for Electronics and Magnetism,
Italian National Council of Research, Parma, Italy
E-mail: victor.erokhin@fis.unipr.it

Abstract

In the current paper, we introduce a high-level approach for an integration of a neuromorphic memristive neuron in a real-time operating robotic system. The memristive neuron schematic, which we had presented in our earlier works, is capable of inhibitory and excitatory learning (eSTDP, iSTDP) as well as modulation via dopamine input. We discuss a possibility of integration of the analog memristive neuron into a digital robotic embodiment and present block diagram of an adapter that includes pseudo-neuronal encoder and decoder.

Keywords: artificial intelligence, robotics, spiking neural network, memristors.

1. Introduction

Previously we have demonstrated successive attempts to implement in bio-plausible manner four of eight basic emotions or affects in a computational system^{1,2}. These emotional drives could be useful for the self-learning autonomous robotic systems to be used as reward-and-punishment systems. This development of our research put us in a position to answer the question of a robotic embodiment therefore we have started the project “Robot dream”¹.

The idea of proposed project is to discriminate two phases of real-time (a so-called “wake”) phase and not real-time bio-inspired calculations (“dream”) phase. The “wake” phase is performed via a robotic system that is synchronized periodically with the “dream” phase, which is implemented at a cluster or a supercomputer due to their high performance impact. NeuCogAr project² describes in details the bio-plausible neuromodulating cognitive architecture. For the purpose of implementation of the real-time operating robotic

embodiment system we have selected a memristive approach that was introduced during several decades in various optional implementations including organic polyaniline^{3,4} and silicon memristive devices⁵ etc. One of promising features of memristive devices is spike timing dependent plasticity (STDP) characteristic of learning or self-learning of a memristive devices^{5,6}. Using this feature we have implemented excitatory and inhibitory STDP and dopamine modulation of a memristive artificial neuron⁷.

2. Problem

The idea to use memristive device as synapse is not new but still we have failed to find a successful implementation of bio-plausible neural network capable of neuromodulation, excitatory (eSTDP) and inhibitory (iSTDP) STDP. The listed above basic neurobiological mechanisms are crucial for mammalian emotional regulation, decision-making and behavioral strategies generation and implementation^{8,9,10,11}. Even if we could create a bio-inspired memristive brain there is still a

fundamental problem of its embodiment. We believe that the most promising approach for the embodiment problem solution is through a use of a robotic body. How do we integrate a spiking neural network with a digital robotic environment?

This position paper describes a high level architecture for memristive neuromorphic devices integration with a realtime or semi-realtime robotic embodiment system and is based on our previous papers on memristive neuromorphic computing solution for neuromodulating neuron with eSTDP and iSTDP¹¹.

3. Proposed Solution

3.1. Memristive neuron

Previously we have proposed an overall block diagram and the implementation of memristive neuromodulatory neuron¹¹. We have demonstrated the bio-inspired learning via STDP and modulation of learning functions via dopamine input. The proposed schematic has three types of input: excitatory, inhibitory and modulatory. Excitatory and inhibitory inputs have their memristive devices that implement the learning functions of eSTDP and iSTDP. The modulating input alters the eSTDP functions increasing and decreasing its amplitude in bio-inspired manner¹². Currently we carry on with making the schematic more bio-plausible to get easier integration option into biological environment. We have successfully demonstrated the simulation results of the Hebbian learning via levels of memristive device conductivity that was determined by series of learning impulses $\Delta w = 1/\Delta t$ where Δt is the time lag between pre-synaptic spike and post-synaptic spike or inbound and outbound impulses of the memristive neuron, and their modulation by the dopamine level. The dopamine level is identified via the setup of dopamine potentiometer that influences the learning impulses amplitude and in its turn influences the memristive device conductivity.

The simulation results are presented in Figure 1. The top graph depicts the dopamine (DA) level and identifies the level of modulation of learning impulses that is visible as the increment of green graph amplitude (the bottom graph), that in its turn influences the memristive device conductivity, described below. In

Figure 1 (in the middle) the lilac graph represents the result of the memristive device learning the overall conductivity. It is set by modulated learning impulses that are formed as Hebbian learning. For the simplification of the simulation purposes we used two different generators with phase shift to simulate different Δt . This way we could depict the entire Hebbian learning in one graph. Simulation methods were used to calculate required nominal values of the electronic components and to validate the quality of the

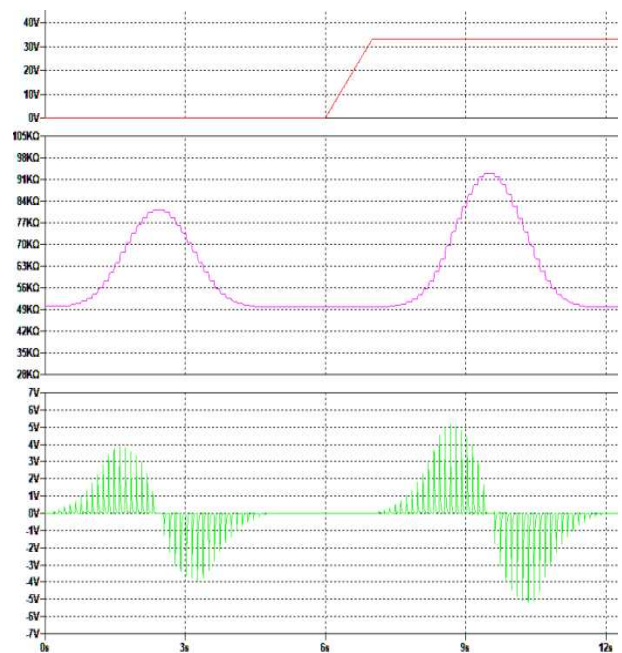


Fig. 1. The simulation results of learning STDP: (top) level of DA influence or setup of DA potentiometer, (middle) graph of memristive device conductivity, (bottom) learning impulses

proposed model. We used integrated schematic editor and mixed analog/digital simulator LTspice. Figure 2 represents the wiring schematic, where excitatory and inhibitory learning impulses are transmitted to memristive elements. Two different sources generate signals with different phase to gain the effect of viable Δw . Temporal and amplitude characteristics of impulses have been simulated. Impulses have been investigated in the time range from 1 to 800 milliseconds. The excitatory and inhibitory impulses replicate the Hebbian and "sombbrero" learning functions according to the theoretically predicated forms.

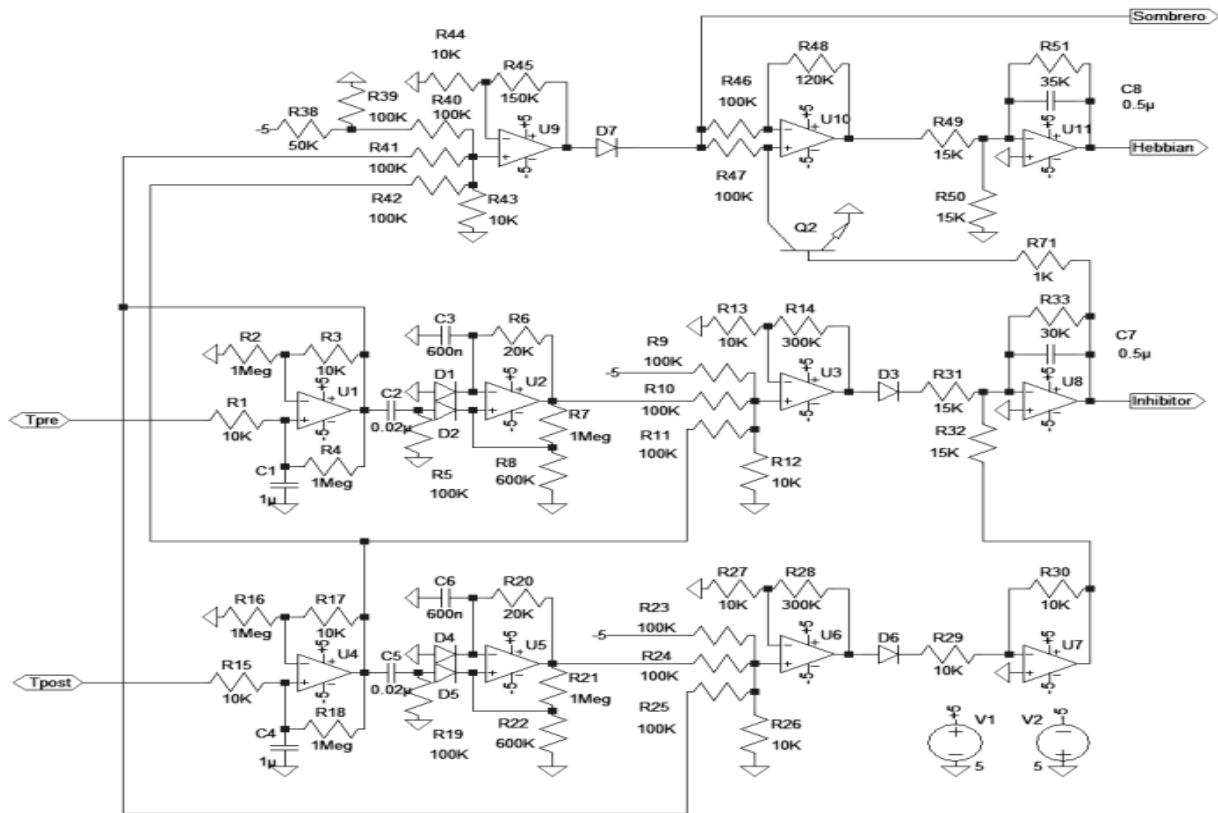


Fig. 2. Wiring schematic of modulatory, excitatory and inhibitory memristive neuron device.

3.2. Integration

The other interesting goal is the integration into digital robotic embodiment system, which could be the anthropomorphic¹³ or non-anthropomorphic¹² system. The presented in the Figure 3 high-level architecture includes: memristive neuron presented above. The neuron has three types of inputs: sensory, inhibitory and modulatory.

Sensory is usually excitatory and is the input from different sensors that are connected via controllers and digital-to-neuronal converters (DNC) or encoders that translate the digital input in form of pseudo-neuronal activity via, for example inverse rate encoding. The pseudo-neuronal activity is similar to neuronal but is generated by artificial for example memristive neuronal devices. The inhibitory input is usually the input that comes from different neurons; for example, for reciprocally inhibition, this is frequent pattern in spinal cord. This could be considered as a blocking system for unwanted behavior.

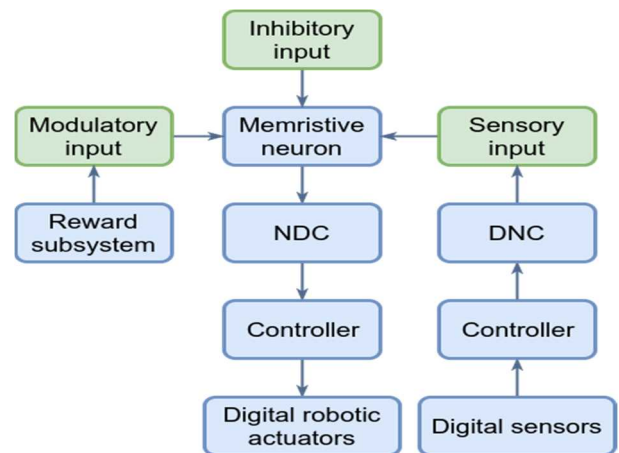


Fig. 3. The basic integration high-level architecture to integrate spiking memristive neuron with digital environment.

The modulatory input balances the neuron towards spiking or generating output impulses. It could represent a reward subsystem of a robotic system embodiment. This way we could “naturally implement the rewarding associations with, e.g., power supply.

The output of the memristive neuron schematic is processed via NDC (neuronal activity to digital converter) that converts pseudo neuronal activity into digital output activating more intensively robot actuators with higher firing rate of memristive artificial neuron. This way in the boundaries of one neuron and several sensors, we could associate modulating reward with power supply and then train a robotic embodiment system to look for the energy supply autonomously.

4. Discussion

In this position paper we proposed the overall architecture for the integration of memristive neuromodulating neuron introduced earlier.

To the best of our knowledge, there is no existing memristive schematic that successfully implements neuromodulation, though it plays important role in emotional regulation of mammals. Therefore, it seems fruitful to implement these mechanisms in a robotic environment in order to solve the integration problem.

We have proposed the overall integration approach of memristive analog devices with digital robotic environment. This approach could be used to implement "natural" reward system. The reward system could use the dopamine modulating input of proposed earlier memristive modulating device. Hopefully using pain/pleasure stimulus we could train proper associations in a real-time robotic embodiment similar to mammalian training.

Acknowledgements

Part of the work was performed according to the Russian Government Program of Competitive Growth of Kazan Federal University.

References

1. A. Tchitchigin, M. Talanov, L. Safina and M. Mazzara, Robot Dream, *Smart Innovation, Systems and Technologies* (2016), V.58, pp. 291–298.

2. M. Talanov, J. Vallverdú, B. Hu, P. Moore, A. Toshev, D. Shatunova and A. Leukhin, Emotional simulations and depression diagnostics. *Biologically Inspired Cognitive Architectures* (2016).
3. A. V. Emelyanov, D. A. Lapkin, V. A. Demin, V. V. Erokhin, S. Battistoni, G. Baldi, A. Dimonte, A. N. Korovin, S. Iannotta, P. K. Kashkarov and M. V. Kovalchuk, First steps towards the realization of a double layer perceptron based on organic memristive devices. *AIP Advances* (2016), 6 (11), 111301.
4. V. A. Demin, V. V. Erokhin, A. V. Emelyanov, S. Battistoni, G. Baldi, S. Iannotta, P.K. Kashkarov and M. V. Kovalchuk, Hardware elementary perceptron based on polyaniline memristive devices, *Organic Electronics* (2015), 25, pp. 16–20.
5. A. Serb, J. Bill, A. Khat, R. Berdan, R. Legenstein, and T. Prodromakis, Unsupervised learning in probabilistic neural networks with multi-state metal-oxide memristive synapses, *Nature Communications* (2016), 7, 12611.
6. M. Prezioso, F. Merrih Bayat, B. Hoskins, K. Likharev, and D. Strukov, Self-Adaptive Spike-Time-Dependent Plasticity of Metal-Oxide Memristors, *Scientific Reports* (2016), 6 (1).
7. M. Talanov, E. Zikov, V. Erokhin, E. Magid, S. Distefano, Y. Gerasimov and J. Vallverdú, Modeling inhibitory and excitatory synapse learning in the memristive neuron model, *Proc. 14th Int. Conf. on Informatics in Control, Automation and Robotics* (2017), V.2, pp. 514-521.
8. R. W. Picard, Affective computing, *Cambridge* (The MIT Press 1997).
9. R. W. Picard, What does it mean for a computer to “have” emotions, *Emotions in Humans and Artifacts, MIT press* (2002), pp. 213–235.
10. M. A. Arbib and J.-M. Fellous, Emotions: from brain to robot, *Trends in Cognitive Sciences* (2004), 8(12), pp. 554–561.
11. K. N. Gurney, M. D. Humphries and P. Redgrave, A New Framework for Cortico-Striatal Plasticity: Behavioural Theory Meets In Vitro Data at the Reinforcement-Action Interface, *PLoS Biology* (2015), 13(1), e1002034.
12. E. Magid, T. Tsubouchi, E. Koyanagi, and T. Yoshida, Building a search tree for a pilot system of a rescue search robot in a discretized random step environment, *J. of Robotics and Mechatronics* (2011), 23(4), p. 567.
13. E. Magid, and A. Sagitov, Towards Robot Fall Detection and Management for Russian Humanoid AR-601, *KES Int. Symposium on Agent and Multi-Agent Systems: Technologies and Applications* (Springer, Cham, 2017), pp. 200-209.

Russian mobile robot Servosila Engineer: designing an optimal integration of an extra laser range finder for SLAM purposes

Neil Alishev, Roman Lavrenov, Yuriy Gerasimov

*Intelligent Robotic Systems Laboratory, Higher Institute for Information Technology and Information Systems,
Kazan Federal University, 35 Kremlyovskaya street,
Kazan, 420008, Russian Federation*

*E-mail: alishev.neil@gmail.com. lavrenov@it.kfu.ru, yurger2009@gmail.com
<http://kpfu.ru/robolab.html>*

Abstract

In our current research we determine an optimal design for integration of Hokuyo UTM-30LX-EW LRF into control system of Russian mobile robot Servosila Engineer. We designed and constructed a special static stand with an option to select an inclination of a scanning beam toward the surface of an environment. RBPF SLAM algorithm was tested to perform localization and mapping. Experiments were conducted in order to determine the best configuration of the LRF position and RBPF SLAM algorithm parameters.

Keywords: Robotics, algorithm, ground mobile robot, SLAM, LRF, ROS, RViz, experiments.

1. Introduction

Sensory information is crucial for operation of any mobile robot. In mobile robotics, sensors are typically used for such tasks as localization, mapping, obstacle avoiding and more. In this research, we tackle the challenge of simultaneous localization and mapping (SLAM) of a Russian crawler-type mobile robot Servosila Engineer¹. SLAM could be performed for UGVs² and UAVs³ in many ways using different sensors:

- Using single or multiple cameras (visual based SLAM). This type of SLAM algorithm uses monocular or stereo camera as a main source of information about environment.
- Using laser range finder (LRF-based SLAM). LRF SLAM algorithms use reflected laser beam to get the information about environment.
- Using sonar. These SLAM algorithms use reflected sound to get information about environment.

Different SLAM approaches have their own benefits and limitations. Visual-based SLAM does not require

special expensive equipment and can be performed using standard monocular or stereo cameras but sometimes lack accuracy, especially in indoor environments with low number of distinctive features². Laser-based SLAM on the other hand is known for its' accuracy and stability but requires special equipment. Sonar-based SLAM can be beneficial in some situations where both previous SLAM approaches fail (e.g. detecting doors and walls made of glass).

In this research LRF-SLAM approach was selected for building a map of the environment and localizing robot within this map. As Russian crawler-type mobile robot Servosila Engineer is not equipped with LRF in its original configuration, we added a special platform on the top of the robot head with Hokuyo UTM-30LX-EW LRF, integrated this LRF into robot control system and verified its performance within LRF-SLAM.

The rest of this paper is structured as follows: Section 2 describes system setup. Section 3 describes the process of laser integration and SLAM. Section 4 summarizes everything and hints on a future work.

2. Robot system setup

Servosila Engineer⁴ (Fig. 1) is a Russian crawler-type mobile robot designed for various areas of use including search and rescue operations⁵, operations within dangerous or inaccessible for a human environment and many other areas. The robot in its original configuration

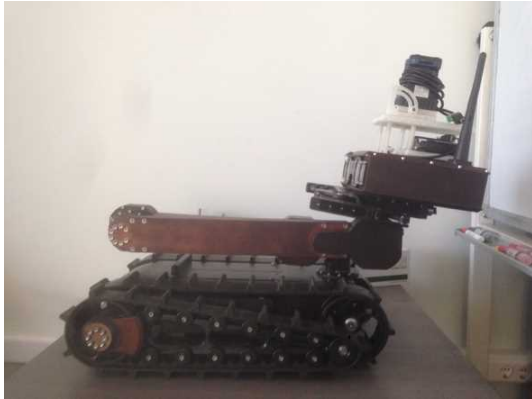


Fig. 1. Servosila Engineer crawler-type robot with a Hokuyo UTM-30LX-EW LRF mounted on its top.

is equipped with an optical zoom camera and a pair of stereo vision cameras. The robot is operated with the original interface in a teleoperation mode only and an operator controls speeds of the servos and positions of the robot's parts.

For SLAM purposes, Hokuyo UTM-30LX-EW range finder was used. We designed and constructed with a 3D printer a special static stand for the LRF with an option to select an inclination of a scanning beam toward the surface of an environment. Due to mounting with adjustable angle it is possible to use the LIDAR in overcoming obstacles and solving the problem of robot balance while moving through 3D debris⁶. The stand was attached to the top of the robot head (Fig. 2).

In addition to the original server and software, which were provided by the maker, we installed Robot Operating System (ROS) Indigo in order to run ROS nodes, which are required for the laser range finder output data streaming and LRF SLAM algorithms. Even though modern versions of ROS, e.g., Kinetic Kame, are already available, we were restricted to use ROS Indigo version because Servosila Engineer comes with a special version of Ubuntu 14.04, which is tailored to the robot's internals so we can't install another version of Linux

Ubuntu to the robot. Being restricted with the OS version, we decided that the best option of ROS would be Indigo.

3. Laser range finder integration and LRF-based SLAM

First step in establishing SLAM for the robot was to get data stream from the laser range finder. For these



Fig. 2. Hokuyo laser on a stand. Laser is strictly parallel to the surface of the floor.

purposes `urg_node` ROS package was used. This package allows to run ROS-node, which reads data from the laser range finder and publishes LaserScan messages to the `/scan` topic⁷. Next, `laser_scan_matcher` ROS package was used to get odometry from the laser scans⁸. This package compares consecutive LaserScan messages to estimate position of the LRF in space. Laser-based odometry turned out to be quite accurate but in Section 4 we describe our future plans in establishing odometry from the crawler encoders in order to further improve odometry accuracy through the use of multiple data sources and combining this information together. After getting odometry, we aimed to perform mapping and localization for our robot.

Prior to that, experiments were conducted in a simulation in order to identify the most suitable for our purposes LRF-SLAM algorithm. We had tested `gmapping`^{8,9}, `Google Cartographer`¹⁰ and `Hector SLAM`¹¹

algorithms on prerecorded rosbag files with laser range data and concluded that gmapping together with laser_scan_matcher significantly outperformed other SLAM algorithms. Thus, we opted for gmapping as the package for SLAM⁸.

Gmapping SLAM package is implemented using Rao-Blackwellized particle filter. Each particle in this

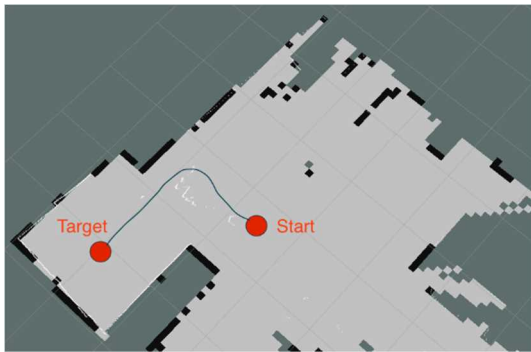


Fig. 3. RBPF-SLAM with default parameters results: virtual experiment in RViz.

algorithm is a separate Dynamic Bayesian Network that stores its own version of a map. Rao-Blackwellized particle filter is applied to these particles in order to pick out the most plausible information about the environment¹². Also, the process called marginalization is used to reduce the number of particles. This process solves the main challenge when using the particle filter. It groups similar particles into one particle in some area

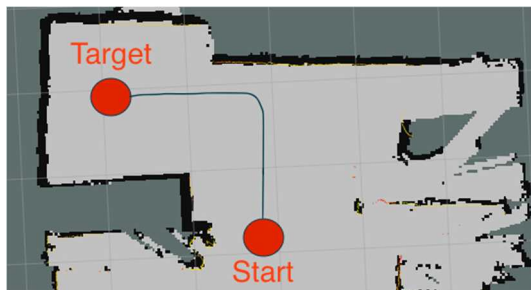


Fig. 4. The same experiment with the new RBPF-SLAM parameters: virtual experiment in RViz.

R. This reduces the number of particles and allows faster execution of the algorithm and lower memory costs¹³. After establishing gmapping for our robot with default parameters, real-world experiments were conducted in order to determine the quality of mapping and

localization. During the experiment, the robot was teleoperated from the start point to the target point while performing LRF-SLAM and the generated map was stored. Figure 3 demonstrates that the obtained map is not detailed enough. Thus, further experiments were conducted in order to improve mapping results.

Figure 4 demonstrates the results of the same experiment, but this time the map, which provides significantly more details about the environment, was obtained by manipulating the RBPF-SLAM configuration parameters. For example, linear and angular update parameters were both set to 0.1. These parameters depend on laser frequency and range, odometry information source and level of sensor shaking when the robot moves. Therefore, these parameters must be finely tuned for each particular case in order to obtain the best mapping and localization quality.

After fine-tuning of RBPF-SLAM parameters further

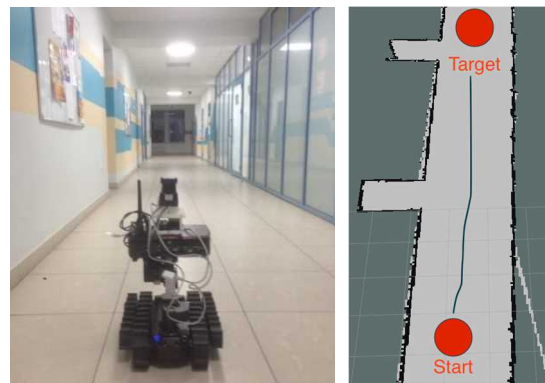


Fig. 5. RBPF-SLAM experiment in the corridor (left) and virtual experiment in RViz (right).

experiments were conducted in another location. A long corridor was selected as the next experiment location because such locations are the most challenging ones when the odometry is coming from the laser range finder. In the experiment, the robot was teleoperated along the corridor from the start point to the target point, and the generated map was stored. Figure 5 (on the right) demonstrates that although the corridor itself does not contain a large number of feature points, laser_scan_matcher algorithm succeeded to provide quite accurate odometry information, which in turn provided the map without any significant errors.

4. Conclusions and future work

Accurate mapping and localization is important for the majority of tasks in the mobile robotics. In our research we used laser range finder to perform simultaneous localization and mapping. We used laser range finder both for SLAM and for getting odometry information. We demonstrated that this configuration is sufficient for getting quite accurate mapping and localization results. Fine tuning is required and it strongly depends on a particular laser range finder and mobile base characteristics. Unfortunately, under certain circumstances (e.g., in feature-poor environments) laser_scan_matcher may fail and start to accumulate odometry error. Therefore, as a part of our future work we plan to obtain odometry information from crawler encoders of the robot and to perform sensor fusion of laser range finder odometry and encoders odometry. This should result in better odometry accuracy, which is crucial for mapping and localization of a robot.

After completing SLAM part, we plan to apply it to the problem of robot autonomous return to the starting point. This means that on the outward way the robot will record its' position and the map of the environment, and next, on the return way, it will autonomously navigate itself to the starting point similarly to^{14,15}.

Acknowledgements

This work was partially supported by the Russian Foundation for Basic Research (RFBR) and Ministry of Science Technology & Space State of Israel (joint project ID 15-57-06010). Part of the work was performed according to the Russian Government Program of Competitive Growth of Kazan Federal University.

References

1. I. Afanasyev, A. Sagitov and E. Magid, ROS-based SLAM for a Gazebo-simulated mobile robot in image-based 3D model of indoor environment, *Int. Conf. on Advanced Concepts for Intelligent Vision Systems*. Springer, Cham (2015), pp. 273-283.
2. A. Buyval, I. Afanasyev and E. Magid, Comparative analysis of ROS-based Monocular SLAM methods for indoor navigation, *9th Int. Conf. on Machine Vision. – International Society for Optics and Photonics* (2017), pp. 103411K-103411K-6.
3. V. Khithov, A. Petrov, I. Tishchenko and K. Yakovlev, Toward autonomous UAV landing based on infrared beacons and particle filtering, *Proc. 4th Int. Conf. on Robot Intelligence Technology and Applications*, (Springer International Publishing 2016), pp. 529-537.
4. M. Sokolov, R. Lavrenov, A. Gabdullin, I. Afanasyev and E. Magid, 3D modelling and simulation of a crawler robot in ROS/Gazebo, *4th Int. Conf. on Control, Mechatronics and Automation* (2016), pp. 61-65.
5. E. Magid and T. Tsubouchi, Static Balance for Rescue Robot Navigation-Translation Motion Discretization Issue within Random Step Environment, *Proc. Int. Conf. on Informatics in Control, Automation and Robotics* (2010), pp. 415-422.
6. E. Magid and T. Tsubouchi, Static balance for rescue robot navigation: Discretizing rotational motion within random step environment, *Int. Conf. on Simulation, Modeling, and Programming for Autonomous Robots* (Springer, Berlin, Heidelberg, 2010), pp. 423-435.
7. Laser scan matcher, ROS package: http://wiki.ros.org/laser_scan_matcher
8. Gmapping, ROS package: <http://wiki.ros.org/gmapping>
9. M. Quigley, D. Stavens, A. Coates and S. Thrun. Sub-meter indoor localization in unmodified environments with inexpensive sensors, *IEEE/RSJ Int. Conf. on Intelligent Robots and Systems*, (2010), pp. 2039-2046.
10. Google Cartographer, repository: <https://github.com/googlecartographer>
11. Hector SLAM, ROS package: http://wiki.ros.org/hector_slam
12. M. He, E. Takeuchi, Y. Ninomiya and S. Kat, Precise and efficient model-based vehicle tracking method using Rao-Blackwellized and scaling series particle filters, *IEEE/RSJ Int. Conf. on Intelligent Robots and Systems* (2016), pp.117-124.
13. A. Doucet, N. De Freitas, K. Murphy and S. Russell, Rao-Blackwellised particle filtering for dynamic Bayesian networks, *Proc. 16th Conf. on Uncertainty in artificial intelligence* (Morgan Kaufmann Publishers Inc. 2000, June), pp. 176-183.
14. N. Tsuda, S. Harimoto, T. Saitoh and R. Konishi, Mobile robot with following and returning mode, *18th IEEE Int. Symposium on Robot and Human Interactive Communication* (2009), pp. 933-938.
15. M. Awai, T. Shimizu, T. Kaneko, A. Yamashita and H. Asama, HOG-based person following and autonomous returning using generated map by mobile robot equipped with camera and laser range finder, *Intelligent Autonomous Systems 12* (2013), pp. 51-60.

Toward automated open wound suturing using haptic feedback: detecting wounds and planning the suture

Artur Sagitov¹, Hongbing Li², Evgeni Magid¹

¹*Intelligent Robotics Department, Higher School of Information Technology and Information Systems, Kazan Federal University, Kremlyovskaya str. 35, Kazan, Russian Federation*

²*Department of Instrument Science and Engineering, Shanghai Jiao Tong University, Shanghai, China*
E-mail: sagitov@it.kfu.ru, lihongbing@sjtu.edu.cn, dr.e.magid@ieee.org
<http://kpfu.ru/robolab.html>

Abstract

One of the key disadvantages of robotic surgery as of today is the lack of haptic feedback. While in traditional surgery surgeons using their haptic senses in all tasks most medical robot lack this ability. Using robots with haptic feedback have the potential of reducing the time spend by surgeon on such tedious subtasks as suturing helps reducing surgeon fatigue. Also decreasing the manual input of the surgeon enables remote surgery even using long communication links with big latency. In this paper we present a framework of wound detection and suture planning. We plan to implement and test our algorithms using KUKA iiwa manipulator.

Keywords: Robotics, robot assisted surgery, medical robotics, manipulator, algorithm, modelling, trajectory.

1. Introduction

Injury to tissues of a body, which are generally caused by physical means with tissue continuity destruction, is defined as a wound. In cases when a tissue has been damaged severely up to the level that it cannot be healed without intervention (i.e., without complications), a complicated treatment procedure is applied. During the procedure dead tissue (and possibly foreign objects) should be removed, infection should be treated, and the tissue should be maintained in apposition until the healing processes provides the wound with sufficient strength to withstand mechanical stress without additional support (i.e. sutures, staples, strips, or topical adhesives). Intervention allowing the wound to go through a repair is referred as wound suturing. Suturing is a challenging and time-consuming task. Existing manual suture techniques could be used for automatic robot-assisted surgical suture, with all steps of suture

being planned and executed under surgeon expert supervision.

We target to implement procedures of automatic robot-assisted surgical suture using KUKA iiwa robot, which includes haptic feedback sensors that could provide significant contribution to interactions with soft tissue. We plan a line of sutures that holds a wound edges in approximation during a healing procedure, consisting of a continuous strand of material or a series of interrupted suture strands. The goal of this paper is to establish a procedure for automatic wound detection and intervention planning that is a first step toward the suture automation.

The rest of our position paper is organized as follows. We overview several existing techniques in Section 2. Section 3 presents suture factors and Section 4 describes suture models. Suturing procedure and parameters are discussed in Section 5. Wound detection and constructing

suture exit/entry points algorithm is described in Section 6. Section 7 briefly explains suture plan supervision and finally we conclude in Section 8.

2. Related Work

Autonomous suturing using various surgical robots is a thriving research field. Previous studies examined different separate parts of suture, e.g., such as knot tying^{1,2,3}, thread tracking^{4,5} and others, or described an entire suturing procedure. R. C. Jackson and M. C. Çavuşoğlu⁶ described development of an autonomous needle path planning during a simple interrupted suture. Using kinematic model of needle-tissue interaction and surgeon specified entry/exit points, S. A. Pedram et.al. developed an algorithm for optimal selection of a needle diameter, shape, and path⁷. Using a mechanical needle guide S. Sen et.al. developed a framework for optimizing a needle size, trajectory, and control parameters⁴. All related work required surgeon input in selecting a suture path with a wound width and depth. T. Osa et.al. proposed an online trajectory planning and a force control system for surgery task automation⁵ that could be applicable in real time suturing.

3. Suturing factors

Our research focus is on skin wounds. Skin is composed of an epithelium and an underlying dermis, which require sharp needle for every stitch in order to minimize tissue trauma. Sutures need only to be strong enough for natural skin tension withstand while holding wound edges in apposition. A suturing technique for skin closure may be either continuous or interrupted, but the interrupted technique is usually preferred⁸. Each individual suture strand is passed through the skin only once, thus reducing a chance of a cross-contamination across the entire suture line. We emphasize several factors that affect successful suturing intervention:

Closing tension. Tension in the suture must be sufficient to approximate tissue and eliminate dead space. At the same time, the tension should be loose enough to prevent patient discomfort, tissue ischemia and necrosis. Thus, there should be a proper control for closing tension.

Needle. During a placement of sutures in tissue procedure, surgical needle is attached to the suture strand in order to permit repeated passes through the tissue. As there are

multiple types of needles, the algorithm should integrate needle parameters into a preplanning procedure.

Suture. The suture is a strand of material being used to approximate tissue. There are several parameters for sutures, such as a suture size, a tensile strength, and a number of strands. The suture size is stated numerically; as a number of zeros in the suture size increases, the diameter of the strand decreases. With the size decrease suture the tensile strength decreases. Sutures are classified according to a number of strands of which they consist. Monofilament sutures are made of a single strand of material; they encounter less resistance as they pass through tissue than multifilament suture material. Multifilament sutures consist of several strands, twisted or braided together to increase tensile strength, pliability, and flexibility.

Knot tying. Each knot that is placed for approximation of tissues or ligation of vessels should be tied with a high precision and each should hold with a proper tension. A particular knot type to be applied largely depends upon the used suture, the depth, and the amount of stress that will be placed postoperatively. When the knot has been securely tied, the ends must be cut in a way that they are left relatively long, approximately 6mm from the knot.

4. Sutures model

There are several types of suture techniques. With regard to continuity we distinguish continuous and interrupted sutures.

Continuous sutures are made with one strand that is connected to itself at each end, or with both ends being connected together. The mechanical strength comes from the tension distributed over all strand length. Thus, we should produce enough tension, while avoiding excess leading to tissue strangulation. Excessive tension can also lead to full suture failure.

Interrupted sutures combine multiple strands to close a wound with each stitch being tied separately after the procedure completion. This provides a more secure closure, as while individual stitch breaks, the rest of the stitches would hold the wound edges close to each other. Other types of primary sutures, such as deep sutures, buried sutures, purse-string sutures, and subcuticular sutures, are used for specific purposes.

Deep sutures are placed completely under an epidermal skin layer. They may be placed as continuous or interrupted sutures and are not further removed postoperatively.

Buried sutures are sutures that are placed with a knot protruding to the inside, under a layer, which is to be closed.

Purse-string sutures are continuous sutures placed around a lumen and tightened like a drawstring to invert the opening.

The described above continuous and interrupted sutures are in the focus of our long term research work and modelling.

5. Suturing procedure and parameters

Outline of suturing procedure is shown in Figure 1. After capturing an image from a robot camera, we estimate wound dimensional parameters. A supervising surgeon then specifies a suture technique and material to be applied. The robot proceeds with the generation of initial plan of an intervention, which consists of an exit/entry and a knot point locations. After the surgeon finalizes the plan, the robot proceeds with individual point planning and procedure execution under the surgeon supervision. Full sensor data of the process is recorded for further post

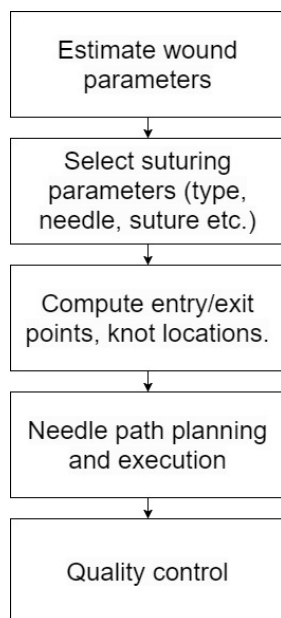


Fig. 1. Automatic suture procedure

intervention analysis. After completion of the plan suture undergoes quality control by the surgeon.

6. Wound detection and constructing suture exit/entry points

General recommendation for most areas of the body, except a human face, is that sutures should be placed in skin 3–4 mm from a wound edge and 5–10 mm apart⁹.

As the wound is an irregularity of the skin, clustering will allow us to detect possible wound locations. We use following successive image transformation to generate wound borders and placing exit/entry points (Fig.2):

1. Apply low-pass filtering;
2. Extract cluster components using mean shift clustering method;
3. From a wound cluster image extract points using a skeleton transform;
4. Construct a wound centerline approximation spline;
5. Construct the upper and the lower wound suture splines by placing points tangentially to local vicinity by stitch width;
6. Place exit/entry points on border splines;
7. Assign point order according to selected suturing techniques;

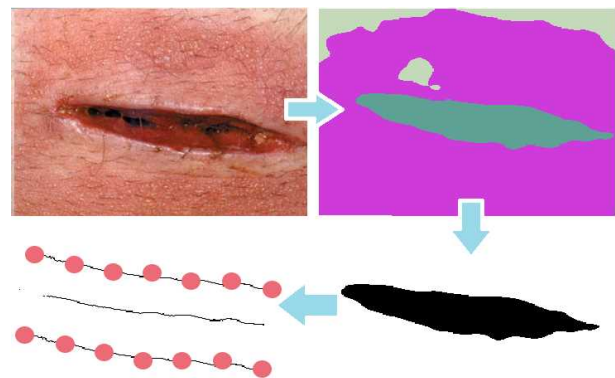


Fig. 2. Wound borders and exit/entry point evaluated step by step for continuous suture

7. Suture plan supervision

After determining the entry/exit points we add knotting points at the ends of each continuous stitch. The combination of ordered list of entry/exit points and knots comprise our initial suture plan.

The initial suture plan that is generated by our algorithm is presented to a supervising surgeon. The surgeon then can modify the plan by moving/adding/deleting points/knots and changing the order of stitching. It is possible to use such corrections to progressively learn suturing procedure of a robot under direct supervision. Thus, using artificial machine intelligence, we can improve outcomes of surgical procedures and significantly reduce surgeon fatigue.

After a surgeon approval the assisting robot can proceed to plan and execute individual point operations. The supervising surgeon continuously observes a current action and a plan of next actions of the robot as well as suture tension. Moreover, the surgeon is authorized to interrupt and/or correct the robot at any moment. All actions of the assisting robot and sensory data are carefully recorded for future analysis.

8. Conclusions and Future Work

This position paper presented initial stages of autonomous supervised suturing including a wound border detection and exit/entry points generation, that are followed by knot points allocation, being specific to particular selected technique and parameters. Our future work is to adopt the existing methods in needle path planning and integrate them into our framework to evaluate performance on KUKA iiwa robot using haptic feedback. Suture thread tension management using haptic feedback and tracking a position or a deformation of the suture thread are also under consideration.

We plan to use ZED camera stereo vision to reconstruct a wound profile and to extend the planning into a 3D space of tissue.

Acknowledgements

Part of the work was performed according to the Russian Government Program of Competitive Growth of Kazan Federal University.

References

1. A. Knoll, H. Mayer, C. Staub, and R. Bauernschmitt, Selective automation and skill transfer in medical robotics: a demonstration on surgical knot-tying, *The Int. J. of Medical Robotics and Computer Assisted Surgery* (2012), vol. 8, no. 4, pp. 384–397.
2. J. Van Den Berg, S. Miller, D. Duckworth, H. Hu, A. Wan, X.-Y. Fu, K. Goldberg, and P. Abbeel. Superhuman performance of surgical tasks by robots using iterative learning from human-guided demonstrations, *Proc. of IEEE Int. Conf. on Robotics and Automation* (2010), pp. 2074–2081.
3. H. Kang and J. T. Wen, Autonomous suturing using minimally invasive surgical robots, *Proc. of the International Conference on Control Applications* (2000), pp. 742–747.
4. S. Sen, A. Garg, D. V. Gealy, S. McKinley, Y. Jen and K. Goldberg, Automating multi-throw multilateral surgical suturing with a mechanical needle guide and sequential convex optimization, *IEEE Int. Conf. on Robotics and Automation* (2016), pp. 4178-4185.
5. T. Osa, N. Sugita and M. Mitsuishi, Online Trajectory Planning and Force Control for Automation of Surgical Tasks, *IEEE Transactions on Automation Science and Engineering* (2017), vol. PP, no. 99, pp. 1-17.
6. R. C. Jackson and M. C. Çavuşoğlu. Needle path planning for autonomous robotic surgical suturing, in *IEEE Int. Conf. on Robotics and Automation* (2013), pp. 1669-1675.
7. S. A. Pedram, P. Ferguson, J. Ma, E. Dutson and J. Rosen, Autonomous suturing via surgical robot: An algorithm for optimal selection of needle diameter, shape, and path, in *IEEE Int. Conf. on Robotics and Automation* (2017), pp. 2391-2398.
8. Ethicon Wound Closing Manual, Somerville, N.J., Ethicon, Inc. (1994).
9. N. B. Semer. Practical plastic surgery for nonsurgeons, *iUniverse* (2007), ISBN 0595461891.

Establishing Effective Teaching for Robotics: a comparison study of Bachelor students participated in Introduction to Robotics course

Tatyana Tsoy, Leysan Sabirova, Mikhail Abramsky, Evgeni Magid

Higher Institute of Information Technology and Information Systems, Kazan Federal University,

35 Kremlyovskaya str., Kazan, Russia, 420008,

E-mail: {tt, sabirova, ma, magid}@it.kfu.ru

<http://kpfu.ru/eng/itis>

Abstract

Global demand in robotics specialists arose necessity of establishing educational programs in robotics, which sets new challenges for modern educational system. In 2017 Kazan Federal University launched master's program in Intelligent Robotics to produce specialists considering core engineering competences and such important skills as self-motivation, critical thinking etc. This paper presents results of continuous survey among undergraduate students of Introduction to Robotics course that helps understanding dynamics of student's motivation to study robotics, attitude toward education methods to improve teaching strategies.

Keywords: Robotics, education, engineering education, master program, motivation.

1. Introduction

Global demand in robotics specialists increases every year as robotics flourishes and integrates into more and more fields of modern economy. Currently higher educational institutions of Russia are facing problems in robotics education: shortage of experts with special education in robotics field, shortage of up-to-date educational materials in Russian, shortage of highly priced equipment etc.^{1,2,3} According to study carried out by the HSE Institute for Statistical Studies and Economics of Knowledge (ISSEK), over 60% of Russian employers' organizations in the field of robotics note that they are experiencing a lack of specialists, particularly highly qualified researchers and engineers⁴. Those contradictions between employers' requirements and employees' expertise raise new challenges to prepare effective and highly motivated engineers^{5,6,7}.

Considering the fact that robotics is an interdisciplinary field^{8,9} it is our task to develop a multifaceted educational program that would allow students to diversify their educational activity and determine their area of interest. In our previous work we

highlighted history and current teaching environment in robotics field in Russia to understand major problems after considering which we developed robotics master's program at Higher Institute of Information Technology and Information Systems (ITIS) of Kazan Federal University (KFU)¹. In September 2017 our team of Intelligent Robotics Department (IRD) launched a new track in Intelligent Robotics within Software Engineering master's degree program. All robotics courses are taught in English, and the first semester includes such courses as Introduction to Robotics, Introduction to Robotics Operational System and Computer Vision.

In spring 2017, before opening the program, we had conducted several surveys among bachelor students who took Introduction to Robotics course in English to capture drawbacks and receive feedback from students in order to improve teaching methods and course modules¹. This paper presents results of our continuing research and the rest of it is structured as follows: Section 2 describes research method, Section 3 is focused on analysis and in Section 4 we observe conclusions and future work.

2. Research Method

We implemented the same research methodology that we had used in our previous work¹ and provided students with statements and questions on English language comprehension, self-efficiency, active learning strategies, significance of studying robotics, stimulation of learning environment. Each item had 5-point scale with optional answers - (1) SD, Strongly Disagree; (2) D, Disagree; (3) NO, No opinion; (4) A, Agree; (5) SA, Strongly Agree – which appear along X-axis in Fig.1-4. Y-axis of Fig.1-4 indicate percentage of respondents that selected the corresponding options. Two surveys were conducted within the same semester: one after the first class (B1) and another after the end of the course (B2). Both surveys were conducted in Russian language to guarantee that all respondents understand the questions. Responses that were received in first survey depict students' attitude towards robotics and expectations from themselves and the course. Results obtained after the course was finished represent the student experience gained during the course. Total number of respondents in the first survey was 37 and in second was 15. To follow the dynamics we selected responds of 9 students, which participated in both surveys, and analyzed the results.

3. Analysis

The comparative analysis covers two check-points during the same semester: after the first class (B1) and after the course was finished (B2). We compared results of survey B1 with results of survey B2.

3.1. Student English language comprehension

Considering that Introduction to Robotics class was the first course taught in English for bachelors of ITIS and the fact that 44,4% of students never took robotics related courses in the past, there was positive dynamics in material comprehension in English language in the class. During the course Prof. Magid lectured in English language, however students were allowed to talk, answer questions and ask the lecturer to explain unclear terms and material in Russian. Additionally, no strict English grammar requirements were applied for students when talking or making presentations. Such concessions targeted to minimize limitations for students in course participation, ease material understanding and at the

same time provide them with robotics terms and definitions in English.

The results demonstrate positive dynamics in students' comprehension (Fig.1a) of the material, though we could observe subtle negative dynamics in confidence when students talked in English. There were insignificant fluctuations on the item "I do not want to participate in class because it is conducted in English" (Fig.1b), which demonstrates that for some students in the class English was still a barrier to learn robotics through foreign language. However, studying robotics increased students' motivation to improve their English skills by the end of the course (Fig.1c)

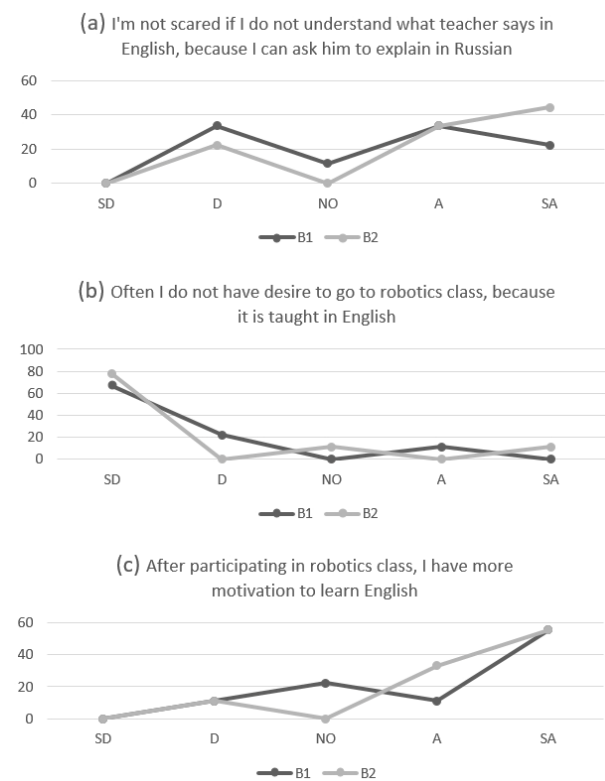


Fig.1 English language comprehension

3.2. Self-efficiency in studying robotics

By the end of the course there was no negative change in self-estimation on confidence of studying robotics, yet a number of respondents thought that they could not understand difficult robotics definitions during the class increased (Fig.2a). These results reinforce another graph (Fig.2b), which demonstrates that less students agreed on

the statement that even though a home assignment was difficult, they did not do it; moreover, when home assignments were too difficult for them, they did only easy ones (Fig.2c). The survey showed that by the end of the course the students' applied more efforts in implementing home assignments and in-class tasks.

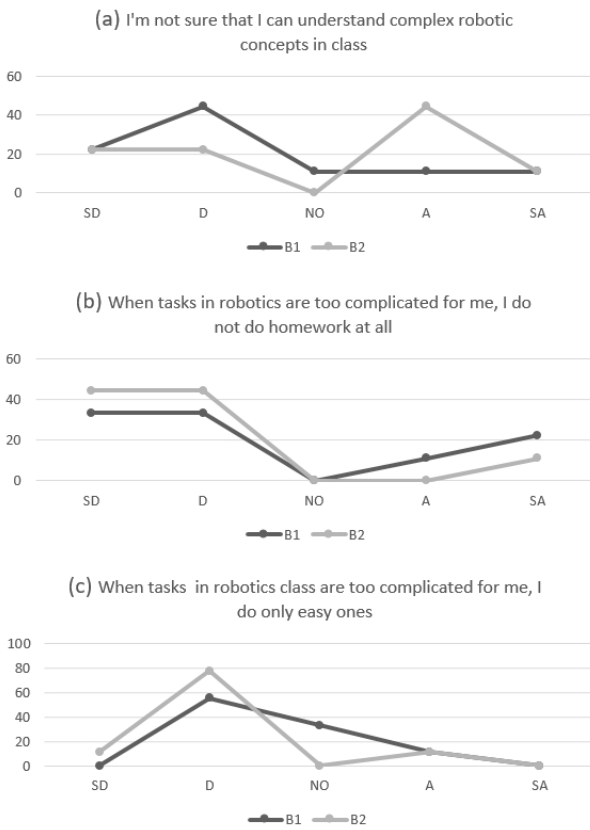


Fig. 2 Student self-efficiency

3.3. Active learning strategies in studying robotics

There was more motivation among students to learn material and think on mistakes they had made in home assignments or in-class tasks (Fig.3a), and there was a significant increase in studying complicated concepts when students searched sources by themselves to obtain additional explanations (Fig.3b).

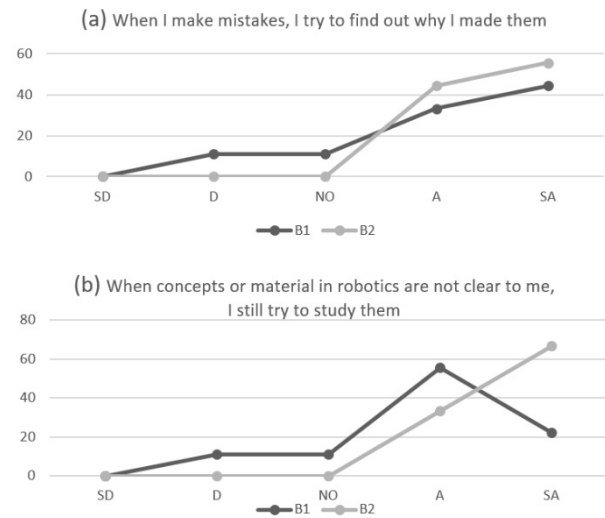


Fig. 3 Active learning strategies

3.4. Significance of studying robotics

Unfortunately, there was negative dynamics in thinking on significance of robotics in context of their future occupation (Fig.4a). Additionally, an equal number of students thought that they could and couldn't independently program or model a robot, while by the end of the course the number of those who thought they couldn't - increased by 11,1%. This demonstrate that the students realized the complexity of robotics, which was a positive result of gaining knowledge, and more students confirmed that robotics stimulated their thinking (Fig.4b). Also there was slight positive shift in students thinking that robotics is a team work item "4 - Agree" of 5-point scale increased by 11,1%, and more students by the end of the course started considering robotics to be a multidisciplinary field.

4. Conclusions and future work

The results of comparative analysis showed that by giving students freedom to express their opinion either in English or in Russian, we observed positive dynamics in class content comprehension provided in English by the teacher, although students still felt less confident while speaking English. For a small number of students the class content understanding in English was still a barrier to actively participate in the class. However, for other students the class activities increased motivation (by the

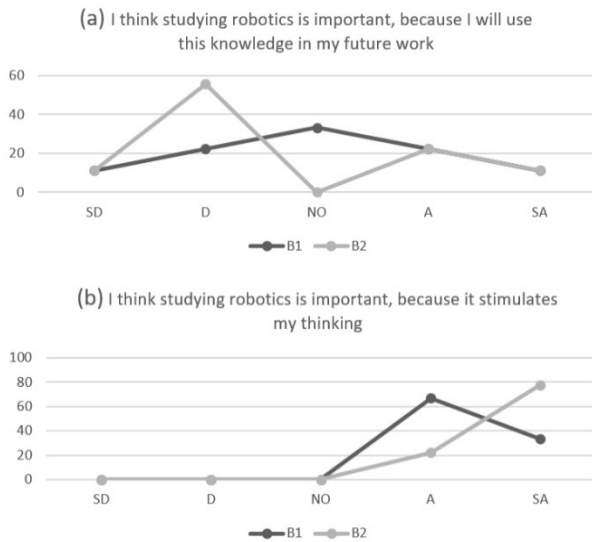


Fig.4 Significance of studying robotics

end of the course) to learn English language further. Considering this, we included English language test for master program entrance examinations.

Further self-efficiency in studying robotics overall depicted no major change at the end of the course; however, few issues were discovered that could be related to difficult content of the classes for students. Nonetheless, respondents used more active learning strategies in studying robotics and spent extra time to find additional information that could assist understanding the material. In cooperation with teaching methods and teaching environment (e.g., project work and problem-based learning) robotics stimulated students to apply more efforts in implementing home assignments and in-class tasks during the after-the-class time. As robotics industry is yet not massively developed in Russia comparatively to IT-leading countries and robotics field is not widely highlighted among other engineering fields, most of software engineering bachelor students are still uncertain about robotics bright future and thus did not link their future employment with robotics.

In our future work we plan to pursue our continuous research and observations of student needs to improve teaching methods in order to make it easier for them to understand robotics. Our emphasis is to motivate students in attaining skills required for robotics specialists in

global market. In addition, we have conducted a preliminary research among robotics related companies in Russia on required skills for a young roboticist. Next, to research this topic in depth we plan to develop and launch a large survey among industry and academia representatives in order to analyze and meet labor market requirements by our robotics master program graduates, both in Russia and abroad.

Acknowledgements

Part of the work was performed according to the Russian Government Program of Competitive Growth of Kazan Federal University.

References

1. T. Tsoy, L. Sabirova and E. Magid, Towards Effective Interactive Teaching and Learning Strategies in Robotics Education, *IEEE 10th Int. Conf. on Developments in eSystems Engineering* (2017), in press.
2. M. B. Dias, G.A. Mills-Tettey and T. Nanayakkara, Robotics, education, and sustainable development, *IEEE Int. Conf. on Robotics and Automation* (2005), pp. 4248-4253.
3. Z. Shiller, A bottom-up approach to teaching robotics and mechatronics to mechanical engineers, *IEEE Transactions on Education* (2013), 56(1), pp. 103-109.
4. N.A. Shmatko and G.L. Volkova, Robotics: the need for organizations in scientific personnel and competencies, Science, Technology and Innovations series, *Institute for Statistical Studies and Economics of Knowledge, National Research University – Higher School of Economics* (2017), URL: https://issek.hse.ru/data/2017/05/29/1172143877/NTI_N_53_19052017.pdf
5. Kh.G. Tkhangapsoyev and M.M. Yakhutlov, To the problems of engineering education in modern Russia, *Quality Management, IEEE Conf. on Transport and Information Security, Information Technologies* (2016), pp. 224-227.
6. L. M. Ogorodova, V. M. Kress and Y. P. Pokholkov, Engineering education and engineering in Russia: problems and solutions, *Engineering education* (2012), (11), pp. 18-23.
7. I. A. Gurban and Jr, A. A. Tarasyev, Global trends in education: Russia case study, *IFAC-PapersOnLine* (2016), vol. 49(6), pp. 186-193.
8. B. A. Maxwell and L. A. Meeden, Integrating robotics research with undergraduate education, *IEEE Intelligent systems and their applications* (2000), 15(6), pp. 22-27.
9. J. Han & R. Gao, Motivation and training program on robotics education, *Int. Conf. on Computational Intelligence and Software Engineering* (2009), pp. 1-4.

Development of a heterogeneous aerial swarm control framework for forest management

Yuriy Gerasimov, Artur Sagitov, Evgeni Magid

*Intelligent Robotic Systems Laboratory, Higher Institute for Information Technology and Information Systems (ITIS),
Kazan Federal University, 35 Kremlyovskaya street, Kazan, 420008, Russian Federation*

E-mail: yurger2009@gmail.com, sagitov@it.kfu.ru, dr.e.magid@ieee.org

http://kpfu.ru/robolab.html

Abstract

As the prevalence of UAVs is increasing, they are becoming more accessible for wider applications. Our interest is in application of UAVs for forest management challenges including monitoring health and safety and commercial exploitation in a sustainable manner. We propose a swarm control framework for managing a group of UAVs for aforementioned tasks, including survey of tree health with infrared cameras and chemical sensors, detecting potential risky situations of illegal logging, smoke and fires, and estimating potential volume measurements. The proposed framework manages planning flight trajectories, sensor fusion and collaborative mapping. On the next stage, we plan to simulate the framework in ROS/Gazebo environment, and further to implement a pilot project with a group of DJI Phantom quadrotors and a large-size fixed-wing UAV.

Keywords: robotics, algorithms, swarm control, robotic framework, unmanned aerial vehicle (UAV)

1. Introduction

Over the last decade unmanned aerial vehicles (UAVs) becoming increasingly used all over the world to collect data for various applications including urban search and rescue¹ and forest monitoring², as a result of miniaturization and cost reduction of GPS receivers, inertial navigation system, computers, motors, batteries and sensors for remote sensing.

UAVs are competing with aircrafts and satellites, bringing the advantages, such as low material and operational costs and flexibility in different sensors loadout, i.e. choosing sensors according to the mission objectives³. Moreover, data acquired with UAVs usually have higher spatial resolution, which is essential for assess local-scale variation in forest stand and species measures². Disadvantages are limited flight time (current systems typically have limited operation maximum of 1-2 hours) and payload capacity, limiting simultaneous acquisition of the entire area of interest.

In the literature, rotary-wing and fixed-wing UAVs are both equally distributed among various case studies. In the vast majority, off-the-shelf solutions are preferred over self-designed and self-constructed UAVs. Different types of sensors are used in experiments: visible-red, green, and blue, multispectral invisible and near-infrared, middle-infrared, thermal infrared imagery, and LRF⁴. Forest applications span over different types of missions, including available resources estimation, species classification, spread of diseases mapping, fire and its effects monitoring, spatial gaps quantification etc.

As UAVs applications continue to spread across different domains, there is increasing need for control framework that incorporates forestry specific mission planning, sensor fusion and control framework. Using heterogeneous aerial robotic swarm that could successfully combine long endurance, range, and processing capabilities of mothership vehicle with low cost, flexibility and maneuverability of UAVs swarms was shown to be applicable for cooperative search,

© The 2018 International Conference on Artificial Life and Robotics (ICAROB2018), Feb. 1-4, B-Con Plaza, Beppu, Oita, Japan

acquisition, and tracking missions in urban environment⁵. Therefore we recognize significant potential advantages of such architecture in forestry applications, which could reduce mission time and increase operational coverage.

The rest of this position paper is organized as follows. We review common missions that influenced our framework composition in Section 2. Section 3 outlines applicable hardware architecture and in Section 4 we focus on framework's individual components, e.g. assignment and tracking task status for individual UAVs.

2. Typical UAV-assisted forest management missions

Information about vegetation conditions of a forest is important both for monitoring protected areas and for estimating potential economic value of the forest. Sensors being used in majority of case studies are near-infrared spectrometers and hyperspectral cameras^{6,7}.

Estimation of dendrometric parameters missions involve acquiring imagery from UAVs in order to estimate Lorey's mean height, dominant height, stem number, basal area, and stem volume estimation of stands using various statistical models. This mission type is used to estimate available resources, identify potential areas of logging, and provide information on plant growth dynamics and biomass allocation. In addition, it makes possible to identify and quantify spatial gaps in forests that could indicate illegal logging activities.

Species classification goal is to differentiate forest species and provide species distribution maps. Knowledge of such distributions is an important information, as it plays important role in sustainable forest management, as some tree species provide higher market value timber, influencing both economic value and potential illegal logging. This information also allows identification of invasion species, allowing earlier interventions.

Post-fire recovery monitoring involves analyzing burned areas and capturing ongoing processes of post-fire recovery: agamic regeneration, deadwood dynamics, and logging activities with or without log extraction⁸.

Forest fire measuring during an ongoing forest fire UAVs could measure location and shape of the fire front, its rate of spread, and the fire flame height using visual and infrared cameras⁴ and provide information that is

necessary to predict fire spread direction and help plan firefighting processes.

Forest health monitoring goal is to produce distribution maps of dead trees and infestation levels to support intervention by authorities.

3. Heterogeneous swarm structure

We investigate robot swarm that is composed of one main vehicle (mothership) and multiple simple UAVs (drones) being connected through wireless network. The motherships act as data storage, recharging and sensor fusion stations, assist negotiation between agents, and supervise a mission while drone control is achieved using cooperative mapping. Each set of drones is assigned to a particular mothership. In the role of the mothership an aircraft, a ship or a ground vehicle could be used.

Drones are small light UAVs used for the data collection and equipped with communication devices to coordinate their operations locally. Commercial off-the-shelf UAVs are usually not intended for group operation, and thus require hardware upgrades. We also assume that an individual UAV is equipped with a low-level control system that provides stability and altitude-hold capability. The choice of deployed sensory loadout on UAVs depends on specific mission planned and on required spatial and temporal scales of the analysis.

The framework is designed in a way that each drone could operate autonomously and recognize other neighboring drones within the limited operational area in order to form cooperative groups.

4. Framework structure

One common task for all above mentioned forestry missions is mapping. Using collective sensory data, it is possible to overcome the individual drone limitations and address the issue with environmental conditions variability. SAGE experiment addresses this issue, demonstrating the usage of a small UAVs group to collectively monitor an agricultural field with weed mapping^{10,11}. Network composition is based upon heterogeneous aerial robot network architecture for search and tracking developed by Elston and Frew¹².

Figure 1 depicts a schematic representation of a heterogeneous swarm control architecture. The highest level is mothership-drone coordination level that is used to allocate specific tasks through negotiation between

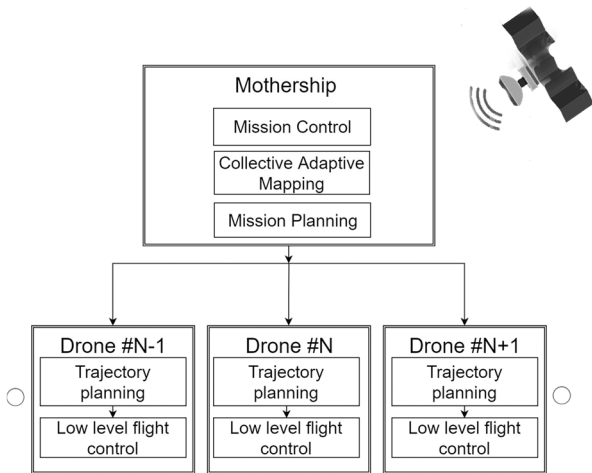


Figure 1. Framework structure

mothership and individual drones. When the mission type and parameters are specified mothership is issuing subtasks that are derived from the planning layer on the mothership vehicle to the trajectory generation layer on each drone. Here, each task is converted into a trajectory, which is passed to the lowest Flight Control Layer that performs low-level drone control. This decomposition is minimizing the computations performed by drones. The mothership has a GPS-receiver and can plan its activities on the global scale, including cooperation with other motherships of a large fleet.

While payload capabilities of UAVs fundamentally limit amount of sensory information, communication, and processing that can be acquired and carried out, a size of the mothership vehicles allows them to carry much complex systems that can perform communications over larger distances, store and process more information than individual drones. Consequently, swarm architecture utilizes technical advantages of a mothership to minimize the amount of communication, planning, and coordination performed by drones.

4.1. Mission control

A mothership keeps tracking drones health (flight hours, battery status, etc.). When amount of data acquired by a drone is reaching drone memory capacity limit, the drone returns to the mothership to perform fast data transfer for storage and processing. Drone is landed on the mothership using methods of autonomous landing with

infrared beacons, e.g.^{13,14}. Localization during landing could be assisted using a variation of the method by Yakovlev et.al.¹⁵. The same landing procedure is triggered by a low level of drone battery charge.

We also use data preprocessing that keeps tracking drone's data quality rating. As each data chunk contains drone signature, if during data preprocessing we identifying problem data (e.g., corrupted data or contradictory data about a same particular map cell that comes from two different drones) we consequently mark a map cell as unexplored and add it to a task list with lowering drone data quality rating.

4.2. Mission planning

Mapping is achieved using task assignment based on a decomposed coverage map. The map is decomposed into cells, which are defined by its boundary coordinates and data acquisition parameters (e.g., velocity, flying altitude etc.). The division of the mission area into cells simplifies motion planning of each agent, and it insures that no two agents inspect the same cell at the same time.

Mothership uses a network to assign drones with responsibilities for free cells by transmitting cell information. We treat drones that inspect cells as a simple collision-free model in C-space while agents are treated as points simplifying collision prevention strategy.

Covering mission area effectively with our drones involves two stages - area decomposition into cells and path planning inside the cells. Our framework is being developed with modularity in mind so it supports different methods of decomposition and path planning in individual cells.

4.3. Collective Adaptive Mapping

Some of mission objectives require a precise mapping only for particular affected areas, so a uniform coverage of the environment becomes ineffective. Therefore we add adaptive strategies to increase efficiency of a swarm by allocating more drones to such areas, while other areas could be only monitored superficially or even entirely skipped. At first mission, the exploration area is divided into multiple cells and each cell is coarsely inspected with a fast flyby by a drone, with interesting areas being added to the map and communicated to the mothership and other drones. The mothership issues special orders to

inspect all interesting areas with more precision by splitting interesting area into smaller cells. Drones that are not performing high precision data acquisition could be assigned to search the rest of the environment in order to mark new potentially interesting areas.

5. Conclusions

The designed framework of coordinated control for a mothership and drones in heterogeneous swarm architecture fully utilizes individual advantages of each robot type improving mission performance. This is a position paper that overviews our framework, while implementation of modules is an ongoing work. Our goal in developing this framework is to demonstrate applicability of aerial swarm robotics approach to forestry using heterogeneous robots, as forestry missions are complex problems with large economic impact. We intend to implement aforementioned missions in ROS Gazebo simulator¹⁶ and use the simulated experiments results to evaluate economic advantages and drawbacks of a heterogeneous swarm robotics approach within the forestry industry.

Acknowledgements

This work was partially supported by the Russian Foundation for Basic Research (project ID 18-58-50008). Part of the work was performed according to the Russian Government Program of Competitive Growth of Kazan Federal University.

References

1. E. Magid, T.Tsubouchi, E. Koyanagi and T. Yoshida, Static balance for rescue robot navigation: Losing balance on purpose within random step environment, *IEEE Int. Conf. on Intelligent Robots and Systems* (2010), pp. 349-356.
2. J. Zhang, J. Hu, J. Lian, Z. Fan, X. Ouyang and W. Ye, Seeing the forest from drones: Testing the potential of lightweight drones as a tool for long-term forest monitoring, *Biological Conservation*, 198 (2016) 60-69.
3. L.Tang, and G. Shao, Drone Remote Sensing for Forestry Research and Practices, *J. of Forestry Research* **26**(4) (2015) 791–797.
4. Y. Ban, S. Marullo and L. Eklundh, European Remote Sensing: progress, challenges, and opportunities, *Int. J. of Remote Sensing* **38**(7) (2017).
5. D. Gross, S. Rasmussen, P. Chandler, and G. Feitshans, Cooperative operations in urban terrain (counter), *Defense Transformation and Network-Centric Systems* 6249 (Proc. SPIE, 2006).
6. J. R. K. Lehmann, F. Nieberding, T. Prinz, and C. Knoth, Analysis of Unmanned Aerial System-Based CIR Images in Forestry - A New Perspective to Monitor Pest Infestation Levels, *Forests* **6**(3) (2015) 594–612.
7. R. Näsi, E. Honkavaara, P. Lyytikäinen-Saarenmaa, M. Blomqvist, P. Litkey, T. Hakala, N. Viljanen, T. Kantola, T. Tanhuanpää and M. Holopainen, Using UAV-Based Photogrammetry and Hyperspectral Imaging for Mapping Bark Beetle Damage at Tree-Level, *Remote Sensing* **7**(11) (2015) 15467–15493.
8. I. Aicardi, M. Garbarino, A. Lingua, E. Lingua, R. Marzano, and M. Piras, Monitoring Post-Fire Forest Recovery Using Multitemporal Digital Surface Models Generated from Different Platforms, *Earsel Eproceedings* **15**(1) (2016) 1–8.
9. J.R. Martinez-de Dios, L. Merino, F. Caballero and A. Ollero, Automatic Forest-Fire Measuring Using Ground Stations and Unmanned Aerial Systems, *Sensors (Basel)* **11** (2011) 6328-6353.
10. D. Albani, D. Nardi and V. Trianni, Field Coverage and Weed Mapping by UAV Swarms, *IEEE/RSJ Int. Conf. on Intelligent Robots and Systems* (2017), pp. 1–7.
11. D. Albani, J. IJsselmuiden, R. Haken and V. Trianni, Monitoring and Mapping with Robot Swarms for Agricultural Applications, *Intelligent Technologies for Environmental Monitoring Workshop, IEEE AVSS Conference* (2017), pp. 1–6.
12. J. Elston and E. W. Frew, Hierarchical distributed control for search and tracking by heterogeneous aerial robot networks, *IEEE Int. Conf. on Robotics and Automation* (2008), 170 - 175.
13. V. Khithov, A. Petrov, I. Tishchenko and K. Yakovlev, Toward autonomous UAV landing based on infrared beacons and particle filtering, *Proc. 4th Int. Conf. on Robot Intelligence Technology and Applications* (Springer International Publishing 2016), pp. 529-537.
14. W. Kong, D. Zhang, X. Wang, Z. Xian and J. Zhang, Autonomous landing of an UAV with a ground-based actuated infrared stereo vision system, *IEEE/RSJ Int. Conf. on Intelligent Robots and Systems* (2013), pp. 2963-2970.
15. K. Yakovlev, V. Khithov, M. Loginov and A. Petrov, Distributed Control and Navigation System for Quadrotor UAVs in GPS-Denied Environments, *Proc. 7th IEEE Int. Conf. on Intelligent Systems*, (Springer International Publishing 2015), pp. 49-56.
16. M. Sokolov, R. Lavrenov, A. Gabdullin, I. Afanasyev and E. Magid, 3D modelling and simulation of a crawler robot in ROS/Gazebo, *Proc. 4th Int. Conf. on Control, Mechatronics and Automation* (2016), pp. 61-65.

Implementation of ROS package for simultaneous video streaming from several different cameras

Ramil Safin, Roman Lavrenov

*Intelligent Robotic Systems Laboratory, Higher Institute for Information Technology and Information Systems (ITIS),
Kazan Federal University, 35 Kremlyovskaya street
Kazan, 420008, Russian Federation
E-mail: safin.ramil@it.kfu.ru, lavrenov@it.kfu.ru
<http://kpfu.ru/robofab.html>*

Abstract

Real time video stream capturing and processing is important for a variety of tasks in robotics. We created ROS package that captures concurrent video stream from 4 different cameras of Russian mobile robot “Servosila” Engineer. V4L2 API was used to configure video devices and to retrieve raw data from cameras. Memory mapping approach of mapping device buffers increased overall performance by eliminating redundant memory copies. We demonstrate the comparison of our new package and OpenCV based package.

Keywords: Video Streaming, V4L2, ROS, C++11, OpenCV, mobile ground robot, experiments.

1. Introduction

Capturing video stream from a robot is an important task for multiple purposes, e.g., visual simultaneous localization and mapping (SLAM)¹ in path planning², human-robot interaction³, teleoperation in urban search and rescue⁴, etc. In some cases, it is necessary to retrieve and process video data in a real-time mode. Moreover, while single cameras are used for monocular SLAM algorithms⁵ for UAVs and simple robots, for more sophisticated robots multiple cameras could be used, for example, as a stereo pair in order to implement SLAM. Thus, as these algorithms may request large computing powers a mobile robot may require transferring sensory data to a more powerful computing device for information processing and analysis.

In our ROS package development process, we used Russian crawler robot Servosila Engineer⁶. It has four cameras and client-server application programming interface (API). Even though it is possible to switch between the cameras using original GUI of the robot, it

cannot stream video data from all cameras at one time. Therefore, we created robot operating system (ROS) package that enables streaming video from the four cameras simultaneously. Our next goal is to stream real time video data via a wireless connection and to develop a server based on a real-time transport protocol (RTP) that will enable clients to receive video data from the robot and improve teleoperation process as an operator can receive more information about environment.

2. Vision-related features of the robot

A crawler-type mobile robot Engineer (Fig.1) is equipped with four cameras that provide good situation awareness. Three of the four cameras in the robot head are located on the front side and one is a rear view camera:

- frontal optical zoom camera
- frontal wide-angle cameras pair (stereo vision)
- wide-angle rear view camera

The installed operating system (OS) is Ubuntu 14.04 LTS (Trusty Tahr). The CPU is Intel® Core™ i7-3517UE (1.70GHz) with 2 physical cores.



Fig. 1. Servosila Engineer crawler-type UGV

3. Video streaming ROS package

3.1. Streaming with V4L2 API

To capture video from the cameras, we use the second version of Video4Linux API (V4L2 API), which is pre-installed within the OS by the maker. Programming a V4L2 video device consists of the following steps⁷:

- Opening the device
- Changing device properties
- Selecting a video standard
- Negotiating a data format
- Negotiating an input/output method
- The actual input/output loop
- Closing the device

Video device parameters are adjusted by input/output control (ioctl) requests. It is a system call for manipulating underlying device parameters (i.e. video format, frames per second, etc.).

The workflow of typical V4L2 application (Fig. 2) may vary depending on use case. For example, our implementation does not render captured frames. The initial step is to open the device as it is needed in order to be able to adjust device for streaming. In order to invoke ioctl requests, device’s file descriptor should be opened for reading and writing operations.

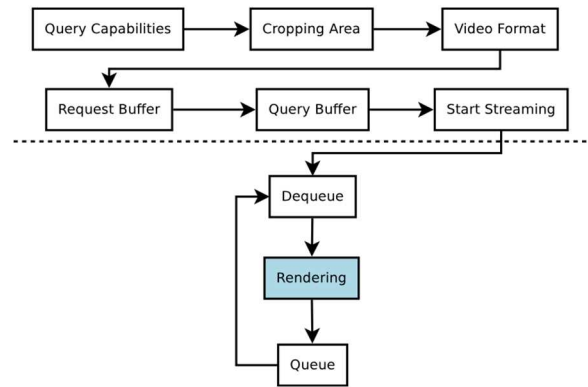


Fig. 2. Common V4L2 video capturing application workflow

Secondly, device capabilities are queried. The purpose of this step is to ensure whether device is able to stream and capture video. It is necessary to negotiate exchanged data (image) format in order to avoid ambiguity. In our case, Engineer’s three cameras (stereo pair and rare view) support only Bayer pattern format⁸ as a raw data from the device’s driver. The optical zoom camera’s raw data presents an image encoded in YUV color space.

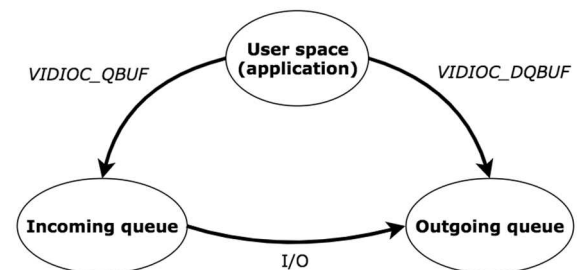


Fig. 3. The process of retrieving frames from V4L2 device using special V4L2 API calls (placing buffer in the incoming queue and getting raw data from outgoing queue)

After negotiating video streaming data format, device buffers are allocated. A buffer contains raw image data exchanged by the application and device’s driver using streaming input/output (I/O) methods. In order to handle captured video data, memory mapping (mmap) I/O approach is used. It increases performance by eliminating redundant memory copies from user to kernel space. The application and the driver exchange pointers to buffers. Hence, we can access captured video data directly in application memory.

Then, we need to query buffers in order to obtain information about allocated buffers, such as memory location (pointers) and buffer length (size).

The process of getting recent frames consists of the queuing and dequeuing parts (Fig. 3). Special API calls are invoked (VIDIOC_QBUF and VIDIOC_DQBUF). Queue operation puts the buffer in the driver’s incoming queue. The buffer will be waiting for the driver to fill it with data. Dequeue operation is used to retrieve processed buffer (with video data) from the outgoing queue⁹.

3.2. ROS package implementation

Originally, no ROS distribution was installed on the robot’s OS. Therefore, we installed Ubuntu 14.04 compatible ROS Indigo distribution. The architecture of the package consists of the following main parts (Fig. 4):

- ROS publisher node. Each camera independently publishes its raw image data.
- V4L2 API layer. All low-level interactions with video devices are handled by V4L2 API.

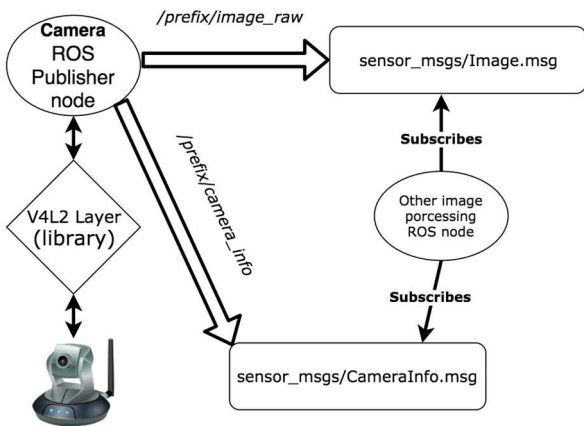


Fig. 4. Our ROS video streaming package architecture (ROS publisher node, V4L2 API layer, raw image and camera information topics)

The ROS publisher node streams video data from a selected camera to the assigned topic. A subscribed node could be a server or some image processing node. Also, the following node’s streaming parameters are used:

- Frames per second (fps). Video frames publishing rate.
- Image resolution.

- ROS image format (i.e. “bayer_grbg8”).
- Device path (i.e. “/dev/video0”).

```
robot@robot-computer:~$ pidstat 10 -p 9402
Linux 4.4.0-83-generic (robot-computer)      02.11.2017      _x86_64_      (4 CPU)
11:12:07      UID      PID      %usr  %system  %guest  %CPU      CPU      Command
11:12:17      1000     9402     0,00   0,40   0,00   0,40      0      video_stream
11:12:27      1000     9402     0,00   0,40   0,00   0,40      1      video_stream
11:12:37      1000     9402     0,00   0,30   0,00   0,30      2      video_stream
11:12:47      1000     9402     0,00   0,40   0,00   0,40      0      video_stream
11:12:57      1000     9402     0,00   0,40   0,00   0,40      0      video_stream
11:13:07      1000     9402     0,00   0,40   0,00   0,40      2      video_stream
11:13:17      1000     9402     0,00   0,50   0,00   0,50      1      video_stream
robot@robot-computer:~$ pidstat 10 -p 9402
Linux 4.4.0-83-generic (robot-computer)      02.11.2017      _x86_64_      (4 CPU)
11:18:29      UID      PID      %usr  %system  %guest  %CPU      CPU      Command
11:18:39      1000     9402     0,00   3,90   0,00   3,90      1      video_stream
11:18:49      1000     9402     0,00   4,70   0,00   4,70      3      video_stream
11:18:59      1000     9402     0,00   4,20   0,00   4,20      3      video_stream
11:19:09      1000     9402     0,00   4,40   0,00   4,40      0      video_stream
11:19:19      1000     9402     0,00   4,40   0,00   4,40      1      video_stream
```

Fig. 5. Our ROS video streaming package’s CPU usage statistics (measured by the pidstat utility in the idle and non-idle modes)

Captured image is distorted, therefore, camera calibration is an essential part of our future work plans.

At the development stage, several issues were faced. The most important one consisted in the inability to determine video frame’s captured time, which are important for stereo SLAM algorithms implementation. V4L2 API gives the ability to determine frame’s captured time by means of captured buffer structure’s parameter. Originally, this parameter had an invalid state, and a proper solution was obtained from the OpenCV GitHub repository¹⁰. The timestamp data of the buffer structure should be extracted after dequeuing and before the next queuing stage.

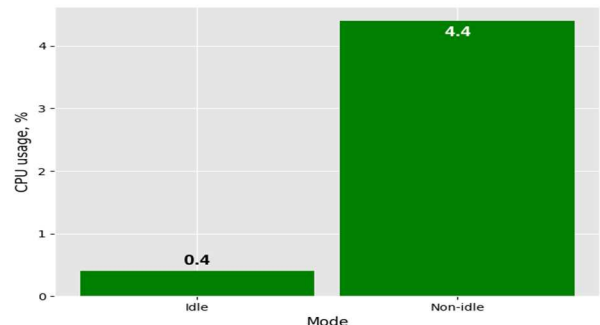


Fig. 6. Average CPU usage of our ROS video streaming package (in the idle and non-idle modes)

All further experiments conducted on Servosila Engineer’s OS.

The created ROS video streaming package shows encouraging results (Fig. 5, 6). Note, that if there are no subscribers to the video stream package’s topic CPU usage tends to zero. Otherwise, if there is at least one

subscriber, then our package consumes approximately 4% of CPU resources. It should be mentioned that no image data conversion is performed, and video data is published as a raw data by means of creating ROS image message. Hence, we can decrease precious CPU usage on a robot's system, not wasting resource on image conversion. Our package does not depend on the OpenCV.

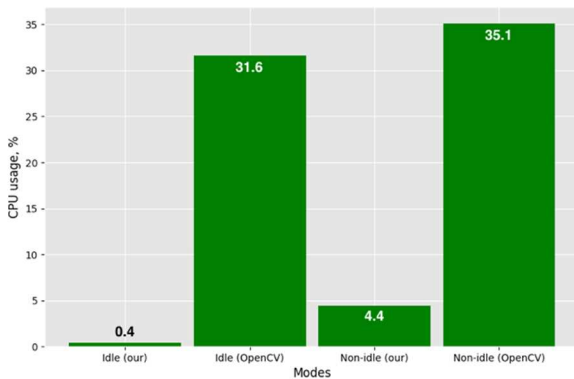


Fig. 7. Average CPU usage of OpenCV based ROS package in comparison with our implementation (in the idle and non-idle modes) (using *pidstat* utility)

We reviewed other ROS video streaming packages. The most interesting one seemed to be an OpenCV based package¹¹. Comparing CPU usage of this package to our implementation we concluded that OpenCV based one uses considerably more computational resources (Fig. 7). If we stream from more cameras, then CPU usage will increase and computational power will not be enough for other applications. Also, it is important to note that in idle mode, when there are no subscribers to the streaming node, OpenCV based package continues to consume a lot of CPU resources.

4. Conclusions and future plans

Streaming video from multiple cameras is an important task. The key point is not only to get frames from camera but also to decrease the usage of system resources. In this paper, we introduced video streaming ROS package implementation. This package demonstrated relatively low consumption of system resources in either idle or non-idle modes. As our long-term goal, we plan to develop an RTP server, which will enable to stream video data from several cameras in a real-time mode via

wireless connection. Our source code is available for public access on the GitHub version control system¹².

Acknowledgements

This work was partially supported by the Russian Foundation for Basic Research (RFBR) and Ministry of Science Technology & Space State of Israel (joint project ID 15-57-06010). Part of the work was performed according to the Russian Government Program of Competitive Growth of Kazan Federal University.

References

1. J. Fuentes-Pacheco, J. Ruiz-Ascencio and J. M. Rendón-Mancha, Visual simultaneous localization and mapping: a survey, *Artificial Intelligence Review* (2015), v 43(1), pp. 55-81.
2. E. Magid, R. Lavrenov and A. Khasianov, Modified spline-based path planning for autonomous ground vehicle, *Int. Conf. on Informatics in Control, Automation and Robotics* (2017), pp.132-141.
3. A. Karpov, S. Carhini, A. Ronzhin and J. Viallet, Two similar different speech and gestures multimodal interfaces, *Multimodal User Interfaces* (2008), pp. 155-184.
4. E. Magid and T. Tsubouchi, Static balance for rescue robot navigation: Discretizing rotational motion within random step environment, *Int. Conf. on Simulation, Modeling, and Programming for Autonomous Robots* (Springer, Berlin, Heidelberg, 2010), pp. 423-435.
5. A. Buyval, I. Afanasyev and E. Magid, Comparative analysis of ROS-based Monocular SLAM methods for indoor navigation, *9th Int. Conf. on Machine Vision* (2017), pp. 103411K-103411K-6.
6. M. Sokolov, R. Lavrenov, A. Gabdullin, I. Afanasyev and E. Magid, 3D modelling and simulation of a crawler robot in ROS/Gazebo, *4th Int. Conf. on Control, Mechatronics and Automation* (2016), pp. 61-65.
7. L. Yinli, Y. Hongli, and Zh. Pengpeng. The implementation of embedded image acquisition based on V4L2, *IEEE Int. Conf. on Electronics, Communications and Control* (2011), pp. 549-552.
8. A. Lukin and D. Kubasov, High-quality algorithm for Bayer pattern interpolation. *Programming and Computer Software* 30.6 (2004), pp. 347-358.
9. V4L2 manual; <https://linuxtv.org/downloads/v4l-dvb-apis/uapi/v4l/v4l2.html>
10. OpenCV GitHub Issues, timestamp issue; <https://github.com/opencv/opencv/issues/8763>
11. GitHub video_stream_opencv ROS package; https://github.com/ros-drivers/video_stream_opencv
12. LIRS video streaming ROS package; https://github.com/chupakabra1996/lirs_ros_video_streaming

Consumers Preferences and Purchase Intention on New Taste of Salted Duck Eggs

Shang-Hui Li

Department of Food and Beverage Management,
Far East University, Taiwan, R.O.C.
E-mail: a0956358700@gmail.com

Abstract

Egg is an indispensable food in people's daily life. Egg is rich in protein, easily digested by human body and metabolism. In addition to direct consumption, people created many different processed egg products by the characteristics of eggs. The traditional method of making salted duck eggs is to place the eggs in salt water or coated in laterite without any additional chemical composition. Except the eggs, this study joined other natural ingredients To produce eight different flavors of salted duck eggs. In the formal test, 70 convenience sampling were taken from Tainan area for sensory evaluation, 63 valid questionnaires, SPSS18.0 was used as the statistical analysis. Sensory evaluation included the color, oil, smell, salty and taste of egg yolk and the salty, taste of protein. Moreover, with the overall acceptance, purchase intention and willingness to buy again etc. The study results showed that cinnamon red salted duck eggs and four-herb salted duck eggs are the highest acceptance to consumers, followed by the salted citronella duck eggs. However, four-herb salted duck eggs dipped by the salted water are not favored by consumers.

Keywords: Duck Eggs, Laterite, Purchase Intention, Sensory Evaluation

1. Introduction

Duck eggs are not less nutritious than eggs. Both are filled with high-density cholesterol, which easily digested by our body and metabolism. There are many processing methods about duck eggs in China, the most common style was being produced as the salted duck eggs. The traditional salted duck eggs are being coated with laterite and rice bran. The research team used the laterite of Tainan General Hill to make the different formula of salted duck eggs. There are two purposes for this study, one is to understand the consumer preferences for the new taste of salted duck eggs through sensory evaluation, then to explore the consumers' purchase intension if they buy the new taste of salted duck eggs.

In this study, duck eggs were added to the different formulations, either being immersed by salt water or being coated with laterite for 20 days before the consumer sensory evaluation. The research flowchart is shown as in Chart 1.

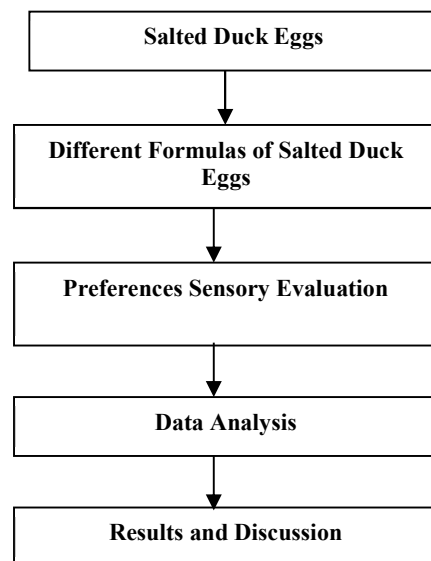


Chart 1. Salted Duck Eggs Test

2. Literature Review

2.1 Duck Eggs

Usually, colored eggs (cyan or brown) have better price and competitive advantages than white shell eggs in the egg market. In Taiwan, most of eggs laid by the brown duck were the major resource of the salted duck eggs rather than as the fresh eggs. Many duck eggs processing businessmen expressed that it would have a high rate of production if century eggs, preserved duck egg, made by cyan eggs, so they have a high preference on cyan shell eggs [1].

2.2 Laterite

Laterite is generally applicable to many construction projects due to it is sticky and tightly hold water, fertilizer, good ventilation and will form a group easily. Clay mine was composed of rocks and minerals in nature after long-term weathering formed by the relatively fine particles. It can be called aluminum clay ore if the aluminum content is higher, and called magnesia clay ore when high in magnesium. It was laterite while in high iron manganese [2].

2.3 Seasoning

Kanehira, Taiwan endemic species, belongs to lauraceae. Due to kanehira's root flavor is similar with both Ceylon and China cinnamon, it was often used as a substitute for cinnamon in Taiwan folk. Its roots, bark, and leaves have a special cinnamon and essential oil ingredients. It is one of the most edible and medicinal species in Taiwan's native plants [3].

Lemongrass, *Cymbopogon nardus* rendlel, is a perennial evergreen herb. Lemongrass was extensively cultivated in mass tropical and subtropical regions. The whole grass of lemongrass can be used, which has a rich lemon flavor, including fresh grass, dried leaves, and stems plant. Lemongrass is applied widely as seasoning on soup and meat in India, Vietnam, Thailand and other Asia countries [4].

As for the ingredients of Chinese four-herbs, or "Siwu" includes prepared rehmannia root, *ligusticum wallichii*, debark peony root, and *angelica sinensis*. "Siwu" was first recorded in the official medical book, "Taiping Huimin Heji Fang" in Song Dynasty, China. For modern clinical, "Siwu" often used to deal with blood deficiency, women's irregular menstruation and dysmenorrhea and other issues etc. At present, "Siwu" is used as the basic

medicine of traditional Chinese prescription, it is also widely used in the modulation of folk food or drinks [5].

2.4 Sensory Evaluation

Please According to the definition of Institute of Food Technologists, IFT, the so-called sensory evaluation is to use of scientific and objective methods by human eyes, nose, mouth, hands and ears to measure and analysis of food. In other words, sensory evaluation means to combine five sensory systems, including sight, smell, taste, touch, and feel, with psychology, physiology, physics, chemistry and statistics and other disciplines to measure and analysis of food in order to understand the human feelings or likes of these products and test the quality of the product itself [6]. For human, food is no longer just for survival, it is a more important consideration to meet the human satisfaction [7]. Basically, sensory evaluation methods could be divided into two major categories [8]. The first category is a type of consumer-oriented evaluation either for the preference or for acceptance. The second category is for the experimental analysis including the sensitivity test and analysis of the differences and description. Hedonic test refers to the consumer sensory evaluation is sensual, it depends upon the consumer's feeling to determine if he/she likes it or not. Scoring method, simple comparison method, ranking method, multiple comparative methods are the common methods to evaluate whether the product is liked by consumers [9]. In this study, preference tests were used for sensory evaluation.

2.5 Purchase Intension

Purchase intension means that consumers are willing to consider the possibility of buying products. The consumer have the higher perceived value to the product, the more intention to purchase the product [10]. The intention to purchase is the most accurate predictor of predictive buying behavior [11]. If consumers who hold a positive purchase intention will form a positive purchase promise [12]. [13] pointed out that willingness to buy was the judgment to buy the agreed product again for the current or possible demand. [14] proposed the use of perceived value to measure the purchase intention measured by questions such as might purchase, want to buy, consider buying. This study referred to the "purchase intention" of a total of 3 questions, the scale was largely modified from the questionnaire by [15] to

test consumer intention to buy a new taste of salted duck eggs. Based on personal self-perception, questions were evaluated on a scale of Likert five-point scale.

3. Research Method

The test is divided into preliminary tests and formal tests, 2 preparatory tests were immersed for both 16 days and 20 days in different taste of salted duck eggs. There were 24 kinds of samples for each preliminary test which are conducted with 20 persons who had evaluation experience before. However, the formal test was based on the Tainan participants, Taiwan, conducted the sensory evaluation by sampling distributed 70 questionnaires, and 63 valid questionnaires were collected. The results of the evaluation were analyzed by SPSS18.0 statistical software. And the most 8 appropriate products from the two preliminary test results were conducted as the formal test sample. The evaluation items were divided into appearance, color, egg yolk oil, smell, protein salty taste, egg yolk salty taste, protein taste degree, protein tenderness, egg yolk softness, egg yolk softness, egg yolk flavor, egg yolk flavor, the overall acceptance, and purchase intention as well. Likert 5-point scale was used for questionnaire scoring. 5 for the most salty, most concentrated or most favorite, 1 was the least salty, the lightest or the least like. Demographic variables subjected to gender, age, occupation, education level.

4. Data Analysis

Data sample structure included 31 males (48.4%) and 32 females (50%). In terms of age, most participants were under age of 20, a total of 32 (50%), followed by 41 to 50 years old, a total of 13 people (20.3%). As for occupation, to the largest number of students, a total of 32 people (50%), followed by the service industry, a total of 11 people (17.2%). 29 participants graduated from college (45.3%), followed by high school, a total of 19 people (29.7%). The overall preferences of the differences on innovative taste of salted duck eggs were shown in Table 1. In the overall acceptance of the difference analysis, the participants considered the lemongrass salted duck eggs (#514, mean 2.44) had the very significant differences with the original salted duck egg (#348, mean 3.21), cinnamon salted duck eggs (#872, mean 3.24), the original cyan salted duck egg (#122, mean 3.32), and cinnamon cyan salted duck (#423, mean 3.32). Compared with the five, the lemongrass salted

duck eggs (#514) was in the lowest level of overall acceptance.

Table 1: Overall Preferences of the Difference Analysis

Item	Sample	Number	Average	Standard deviation	F-test	Distinctiveness
Overall Acceptance	348	63	3.21±1.180 ^c		4.243	0.000***
	514	63	2.44±1.202 ^a			
	872	63	3.24±1.254 ^c			
	165	63	2.70±1.265 ^{ab}			
	122	63	3.32±1.229 ^c			
	951	63	2.92±1.182 ^{bc}			
	423	63	3.21±1.109 ^c			
	946	63	3.11±1.166 ^{bc}			

1)*P<0.05, significant, **P<0.01, very significant, ***P<0.001 unusual significant

2) 348(original salted duck egg), 514(lemongrass salted duck eggs), 872(cinnamon salted duck eggs), 165(Siwu salted duck egg), 122(original cyan salted duck egg), 951(lemongrass cyan salted duck eggs), 423(cinnamon cyan salted duck).

5. Conclusion and Suggestion

References In this study, sensory evaluation preference test was conducted to develop a new taste salted duck egg. The conclusions are as follows:

1. Consumers' evaluation on the siwu salted duck (#165) was the lowest rating which showed that consumers did not like siwu style. However, the siwu cyan salted duck (#946) on the average number are more than 3, it maybe the cooked siwu's juice inserted into the duck eggs to stimulate the different flavor. Perhaps, the amount of siwu could be increased in the future or replace other Chinese medicine, such as the "four gods" salted duck eggs, Angelica salted duck eggs.
2. Consumers are less favored on lemongrass salted duck, average number was less than 3 (#514), it probably because of the lack of lemongrass flavor,
3. Suggest that it may increase the proportion of lemongrass into the salted duck in the future or replaced by other herbs such as vanilla grass.
4. The acceptance of cinnamon cyan salted duck (#423) was also higher. it maybe the cooked cinnamon's aroma inserted into the duck eggs to stimulate the different flavor.
5. Although the production process of laterite-coated salted duck egg was more complicated than without laterite-coated. But, it is worthy to promote because it did enhance the flavor of salted duck eggs.

References

1. Lin, R. X., Du, S. H., Huang, Z. F., Liu, X. Z., Hu, Y. H. & Chen, T. F. (2007). Study on consumers' cognition and purchase tendency of general duck eggs and green-shell duck eggs. *Livestock Research*, 39(3), 149-163.
2. Huang, J. Y. (2005). Clay mine and life. *Land Resources Guide*, 2, 58-59.
3. Yang, Z. C. (2010). Study on germination and storage of Kanehira seeds. *Agricultural policy and agricultural situation*. 220, 2017/6/15 from <https://www.coa.gov.tw/ws.php?id=22227>.
4. Zhang, L. R. (2011). Gramineous herb plant-Lemongrass. *Taichung District Agricultural News*, 73, 13-16.
5. Qiu, X. L. (2010). Chinese medicine school-Siwu Tang introduction. *Pharmacist Weekly*, 1665, 2017/6/30 from <http://tcpa.taiwan-pharma.org.tw/node/5168>.
6. Jellinek, G. (1985). *Sensory evaluation of food*. VCH Publishers. Florida. U.S.A.
7. Yao, N. Z. (2002). Sensory evaluation introduction, application and future development. *Taiwan Food News*, 192, 44.
8. Ou, A. S. M. (2003). *Sensory Evaluation and Practice*. Wagner Publishing. Taipei.
9. Lin Q. S. & Ye R. Y. (2004). *Application and practice of sensory evaluation*. Ruiyu Publishing. Pingtung.
10. Dodds, W. B., Monroe K. B. & D. Grewal. (1991). The effects of price, brand and store information on buyer's product evaluations. *Journal of Marketing Research*, 28(3), 307-319.
11. Morwitz, V. G. & Schmittlein, D. (1992). Using segmentation to improve sales forecasts based on purchase intent: Which "intenders" actually buy? *Journal of Marketing Research*. 29(4). 391-405.
12. Moorman, C., Zaltman, G. & Deshpande, R. (1992). Relationships between providers and users of market research: The dynamics of trust within and between organizations. *Journal of Marketing Research*. 29(3). 314-328.
13. Hellier, P. K., Geursen, G. M., Carr, R. A. & Rickard, J. A. (2003). Customer Repurchase Intention: A General Structural Equation Model. *European Journal of Marketing*, 37(11/12), 1762-1800.
14. Zeithaml, V. A. (1998). Consumer Perceptions of price, quality, and value: A meansend model and synthesize of evidence. *Journal of Marketing*, 52, 2-22.
15. Grewal, D., Krishnan, R., Baker, J. & Borin, N. (1998). The effects of store name, brand name and price discounts on consumers' evaluations and purchase intentions. *Journal of Retailing*, 74(3), 331-352. doi: 10.1016/S0022-4359(99)80099-2.

The Study of Green Food Image, Satisfaction and Loyalty through the Perspective of Elaboration Likelihood Model

Shu-Fang Hsu

Department of Food and Beverage Management,
Far East University, Taiwan, R.O.C.
E-mail:h99582004@gmail.com

Abstract

This study aims to explore the relevance of consumer satisfaction and loyalty to green food image through the perspective of Elaboration Likelihood Model. The results show that the positive impact of green food image; and will indirectly affect the satisfaction of re-purchase intention; satisfaction positive impact loyalty. We hope that the results of this study can provide relevant business management strategies and suggestions, the green food consumption theory and practice can be dedicated.

Keywords: Green Food, Satisfaction, Loyalty, Elaboration Likelihood Model

1. Introduction

Many companies actively developed and manufactured of green-related foods and delivered green food messages to consumers via products, service packaging or advertising. [1] studied food quality considered the intention of customer behavior was caused by customer interaction. The purchase behavior of consumers was, therefore, gradually generated through many reactions. [2] studied the concept of green practices arguing that green affected customer attitudes and consuming attitudes toward restaurants. And Elaboration Likelihood Model (ELM) of [3] was used as the theoretical basis for the study. ELM refers to the think way in our human brain which can be divided into the central path and the surrounding path. Central path emphasizes the relevant information processing, peripheral path refers to any factors that can convince the central path. Satisfaction and loyalty are the two most important variables of consumer behavior. As a result, many businesses are thinking about how to enhance consumer satisfaction and thereby increase their loyalty.

[4] pointed out that image refers to the internal beliefs and impressions formed on the basis of individual message processing. Image is an indirect experience, however, satisfaction is a direct experience. And green food was produced on the base of environmental protection. This study defined the green food as

consumers considered that it is harmless, pollution-free, fresh, safe and nutritious in the food production, manufacturing and sales process, and minimizes the damage to the planet. Therefore, this study explored the relevance of consumer perceptions of green food to satisfaction and loyalty under the perspective of Elaboration Likelihood Model, meanwhile, explored the mediating effect of satisfaction on green food image and loyalty.

2. Literature Review

2.1 Elaboration Likelihood Model

[5] put forward an "Elaboration Likelihood Model" for consideration to know more about the formation of consumption patterns, they tried to understand how to deal with the communicate of information and to convince the effect of the consumers. Depend on the "Elaboration Likelihood Model", when consumers received the various kinds of information and messages from the outside world. The consumers would process and evaluate this information in the form of central route and peripheral route, then to make the final attitude or opinion about a product or service. The degree which consumers think about the message will influence how they choose which message to evaluate. When consumers think hard, it means that consumers invest a higher

© The 2018 International Conference on Artificial Life and Robotics (ICAROB2018), Feb. 1-4, B-Con Plaza, Beppu, Oita, Japan

cognitive mind. Consumers will carefully evaluate from the information related to the message, thus forming a product attitude or view. The "Elaboration Likelihood Model" has been widely used to apply the effects of communication [6]; [7], such as the formation of wishes and attitudes [8]; [9] and other issues.

2.2 Satisfaction

The task of business is to create the satisfied customers. Peter Drucker was the first to put forward the concept of customer satisfaction. Satisfaction refers to the overall assessment of the comprehensiveness of a service or product generated by a customer after using the product or service.

[10] pointed out that consumer satisfaction came from the expectations before the product was purchased and the actual perceived to the product features and characteristics after purchase and the happiness or disappointment was formed after comparing the two. The consumers felt dissatisfied if the result was not as good as the expectations and consumers felt satisfied if the result exceeded expectations. [11] studied the causal relationship among destination image, attribute satisfaction, overall satisfaction and loyalty. The results showed that destination image was divided into positive impact on overall satisfaction and attribute satisfaction, attribute satisfaction positively affected overall satisfaction and loyalty, and overall satisfaction positively affected loyalty.

2.3 Loyalty

Loyalty is the preferred attitude and behavior of consumers to purchased items. Consumers will collect and evaluate a variety of related product information and advantages and disadvantages of product, then give the final decision to buy the product. How to form a purchase intension, therefore, will be an important key. [12] found that loyalty was the customer purchased repeatedly, promised to introduce a friend to the company's products or services, and is willing to persuade others to use the company's products or services, or voluntarily recommend the company's products or are willing to help improve their services [13].

3. Research Method

The study explored the relationship between consumer satisfaction and the loyalty of the image of green food

according to the literature review, and in accordance with the point of view of "Elaboration Likelihood Model". The research framework was shown in Figure 1.

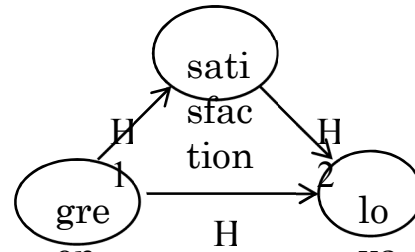


Figure 1. Research Framework

This study, therefore, proposed the following research hypotheses:

- H1: Green food image positively affected satisfaction.
- H2: Green food satisfaction positively affected loyalty.
- H3: Green food image positively affected loyalty.

This study mainly explored consumer's issue of green food image. Therefore, the consumers who had purchased green food would be considered as the major participants. Questionnaire was issued through internet and distributed at the green food store. A total of 258 internet questionnaires were collected and 222 were useful after excluding the invalid ones. As for the field survey, a total of 242 questionnaires were collected and 210 were the effective ones excluding the blank, chicken writing and incompletely answers. In total, 432 valid questionnaires were collected and the effective recovery rate was 86.4%.

4. Data Analysis

The obtained information was analyzed and stated on statistical data after the formal questionnaires were issued, then to test the structural equation model according to research hypothesis and discuss the influence coefficient and the adaptability of the overall mode among each variable. After the model analysis, the parameters of the overall model of this study can be learned from Table 1. The standardized coefficients of the potential variables of the overall model range was from 0.74 to 0.87. None of them was greater or nearly 1 and standard errors were all between 0.010 and 0.027, there were no negatives and all were significant. Obviously, the study model did not produce an offending estimate.

Table 1: Standardized Parameter Estimates of Potential Variables to Observed Variables

Potential Variables	Observed Variables	Standardized Parameter Estimates	T Values	Error Variation Number	T Values	Standard Error
Green Food Image	Fresh & Nutritious	0.83*	16.49	0.67*	5.46	0.027
	Environmental Safety	0.87*	17.12	0.75*	4.20	0.025
Satisfaction	Meets Requirements	0.76*	17.56	0.58*	12.26	0.017
	Wise Choice	0.85*	20.16	0.72*	10.29	0.013
	Feel Good	0.85*	20.30	0.73*	10.13	0.013
	Feel Happy	0.81*	18.96	0.65*	11.34	0.020
Loyalty	Repurchase Intention	0.84*	18.42	0.70*	10.85	0.010
	Price Tolerance	0.84*	18.10	0.71*	10.76	0.018
	Initiative to Recommend	0.84*	17.89	0.71*	10.80	0.013
	Cross Purchase	0.74*	16.46	0.60*	12.34	0.015

* indicated the significant level at $p = 0.05$.

In this study, green food image was as an independent variable, loyalty as a variable, the satisfaction was the intermediary variables of green food image and loyalty. Based on this, this study used the structural equation model to verify the path assumptions, to verify the causality of satisfaction between green food image and loyalty. Satisfaction coefficient of green food was 0.41, t value was 6.809, a significant level. Obviously, the green food image had a positive and significant impact on the

satisfaction. Namely, if the consumer's awareness of green food was higher, the degree of satisfaction was stronger. Therefore, H1 was established. The influence coefficient of satisfaction on loyalty was 0.57 and t was 10.326, which also reached to a significant level. It was clear that satisfaction was positive and significantly affected loyalty. Namely, consumers were more satisfied with green food image, and their loyalty is stronger. Therefore, H2 was established. The coefficient of loyalty for green food was 0.51 and t value was 8.709, reached a significant level. Obviously, green food had a positive and significant impact on loyalty. That was, the higher consumers perceived the green food image, the stronger their loyalty. Therefore, H3 was established. The direct effects, indirect results, and hypothesis test of research variables results were shown in Table 2.

Table 2: The Direct Effects, Indirect Effects, and Hypothesis Test of Research Variables

Path	Direct Effects	Indirect Effects	Test Results
Green Food Image → Satisfaction	0.41***		H1 Established
Satisfaction → Loyalty	0.57***	-	H2 Established
Green Food Image → Loyalty	0.51***	-	H3 Established

5. Conclusion and Suggestion

The results showed that green food image positively affects satisfaction and will indirectly affect the repurchase intention through satisfaction. Satisfaction positively affected loyalty. As about the impact of satisfaction on loyalty under the "Elaboration Likelihood Model" showed that if the price of green food was higher and the efficacy of the product could not be immediately effective, then the consumers will perceive a higher risk. Under such condition, the consumers will pay attention to the product information or seek advice from others in attempt to reduce the purchase risk. At this point, consumers mainly relied on central clues to evaluate information, to think about the content of the product information in a rational way. If consumers perceived the received content as fair and persuasive, they would have more positive thoughts about the product, and change your attitude towards the product in the direction described by product information. When consumers were more satisfied with the green food image, their loyalty is

higher. Green food industries should commit to the pursuit of a higher level of satisfaction in order to enhance consumers' positive consumption of green food. Since satisfaction could affect loyalty for both directly and indirectly. For the industry, therefore, the measurement and promotion of satisfaction are important. As [14] argued that the quality of the environment, food, and service are important determinants of restaurant imagery. Food safety in Taiwan should promote "clean green" instead of changing the public's response to the environment, food safety and quality. Hence, [15] suggested that industries should understand their market segmentation with the right strategy and direction. Finally, the industries need to define effectively the image of green product in the minds of consumers.

References

1. Cheng, F. C., Cheng, F.Y. & Fan, W. S. (2013). Factors Affecting Customer Behavior Intentions Toward Taiwan Restaurant Industry Using Response Hierarchy Model-Discussion on Brand Image as Moderating Variable. *Journal of Sport, Leisure and Hospitality Research*, 8(4), 49-76.
2. Jeong, E., Jang, S. C., Day, J., & Ha, S. (2014). The impact of eco-friendly practices on green image and customer attitudes: An investigation in a café setting. *International Journal of Hospitality Management*, 41, 10-20.
3. Petty, R. E., & Cacioppo, J. T. (1981). *Attitudes and Persuasion: Classic and Contemporary Approaches*. Dubuque, IA: William C. Brown.
4. Suh, J. C., & Yi, Y. (2006). When brand attitudes affect the customer satisfaction-loyalty relation: The moderating role of product involvement. *Journal of Consumer Psychology*, 16(2), 145-155.
5. Petty, R. E., & Cacioppo, J. T. (1996). *Attitudes and Persuasion: Classic and Contemporary Approaches*. Boulder, CO: Westview Press.
6. Rucker, D. D., & Petty, R. E. (2006), Increasing the effectiveness of communications to consumers: Recommendations based on elaboration likelihood and attitude certainty perspectives. *Journal of Public Policy & Marketing*, 25 (1), 39-52.
7. Tormala, Z. L., & Petty, R. E. (2004). Source Credibility and Attitude Certainty: A Metacognitive Analysis of Resistance to Persuasion. *Journal of Consumer Psychology*, 14(4), 427-442.
8. Bhattacharjee, A., & Sanford, C. (2006). Influence Processes for Information Technology Acceptance: An Elaboration Likelihood Model. *MIS Quarterly*, 30(4), 805-825.
9. Agarwala, R., Angsb, C. M., & Magni, M. (2009). The performance effects of coaching: a multilevel analysis using hierarchical linear modeling. *The International Journal of Human Resource Management*, 20(10), 2110-2134.
10. Kotler, P. (2000). *Marketing Management: The Millennium Edition*. (10th ed.). NJ:Prentice Hall.
11. Chi, C. G. Q., & Qu, H. (2008). Examining the structural relationships of destination image, tourist satisfaction and destination loyalty: An integrated approach. *Tourism Management*, 29(4), 624-636.
12. Lai, F., Griffin, M., & Babin, B. J. (2009). How quality, value, image, & satisfaction create loyalty at a Chinese telecom. *Journal of Business Research*, 62, 980-986.
13. Heskett, J. L. (2002). Beyond Customer Loyalty. *Managing Service Quality*, 12(6), 355-357.
14. Ryu, K., Lee, H. R., & Kim, W. G. (2012). The influence of the quality of the physical environment, food, and service on restaurant image, customer perceived value, customer satisfaction, and behavioral intentions. *International Journal of Contemporary Hospitality Management*, 24(2), 200-223.
15. Noor, M. N. M., Masuod, M. S., Said, A. A., Kamaruzaman, I. F. & Mustafa, M. A. (2016). Understanding Consumers and Green Product Purchase Decision in Malaysia: A Structural Equation Modeling - Partial Least Square (SEM-PLS) Approach. *Asian Social Science*, 12(9), 51-64.

Self-Generated Dataset for Category and Pose Estimation of Deformable Object

Yew Cheong Hou, Khairul Salleh Mohamed Sahari*

Department of Mechanical Engineering, Universiti Tenaga Nasional
Selangor, Malaysia

E-mail: ychou_my@hotmail.com, *khairuls@uniten.edu.my

Abstract

This work considers the problem of garment handling by a general household robot that focuses on the task of classification and pose estimation of a hanging garment in unfolding procedure. Classification and pose estimation of deformable objects such as garment are considered a challenging problem in autonomous robotic manipulation because these objects are in different sizes and can be deformed into different poses when manipulating them. Hence, we propose a self-generated synthetic dataset for classifying the category and estimating the pose of garment using a single manipulator. We present an approach to this problem by first constructing a garment mesh model into a piece of garment that crudely spread-out on the flat platform using particle based modeling and then the parameters such as landmarks and robotic grasping points can be estimated from the garment mesh model. Later, the spread-out garment is picked up by a single robotic manipulator and the 2D garment mesh model is simulated in 3D virtual environment. A dataset of hanging garment can be generated by capturing the depth images of real garment at the robotic platform and also the images of garment mesh model from offline simulation respectively. The synthetic dataset collected from simulation shown the approach performed well and applicable on a different of similar garment. Thus, the category and pose recognition of the garment can be further developed.

Keywords: Deformable object, robotic manipulation, computer vision, particle based model.

1. Introduction

Handling deformable object by robot is a challenging problem in robotic research. To teach a general household robot to handle these deformable objects is difficult compared with rigid object due to the variety of sizes, textures and poses for these objects. Figure 1 shows a pipeline for the autonomous garment handling by a robot. In order to manipulate it from initial state to final desired state successfully, the category and pose of the garment should be recognized by the robotic system. The computer vision technique integrated with the robust machine learning algorithm through garment perception should be acquired by a robot to manipulate these objects dexterously by recognized their deformed configuration. In this research, we are focusing the task of classify the

category and recognizing the pose of hanging garment grasped by single robotic manipulator. The main idea of this work is to generate a dataset of hanging garment that combine the real and synthetic images from the real garment and deformable model respectively. The deformation poses of the garment can be reduced by hanging the garment under gravity. A dataset of hanging real garment by robotic manipulator can be obtained by capturing the depth images. For deformable object modeling, the particle based model is constructed to the garment in an image and then used into the simulation to acquire the synthetic dataset. This work is extended to include the 2D garment mesh model that able to represent the real garment that not found in the database. The dataset will take advantages of this algorithm to generate large number of data for learning purposes without using

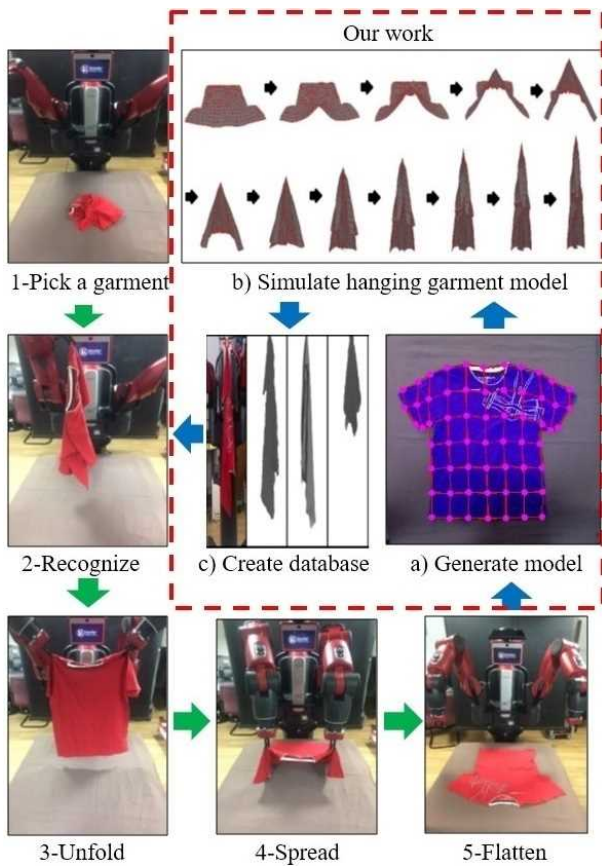


Fig. 1. The pipeline for garment handling in autonomous robotic manipulation.

professional graphic software. The main contribution in these works are:

- The simple 2D garment mesh model is extracted from the real garment that crudely spread-out on the flat platform. The multiple poses of hanging garment model under gravity are simulated, and different viewpoints of the model are captured as an image.
- Different types and sizes of garment are simulated and the dataset is generated from the synthetic data of hanging garment mesh model integrated with the real data.

2. Related Work

Modeling and simulation are commonly used to compute the deformation of the deformable objects and becomes essential in future autonomous robotic manipulation since the result produced from simulation is seeming real and applicable. In robotic manipulation, the research on autonomous laundry service for general household robot

has gained attention and increase significantly. The end-to-end task of garment folding had been decomposed into several sub-tasks, the existing approaches had been proposed from different aspects to solve the particular problem in order to achieve its accuracy and robustness. Generally, majority contributions in the literature of garment handling mainly focus on the grasping skills, recognition, and motion planning strategy of unfolding and folding.

There has been previous work on the recognition and manipulation of deformable objects. Doumanoglou et al. proposed a dual-arm industrial robot to unfold different garments such as sweater and trouser¹. They focused on classification and pose recognition of hanging garment and then proceeded to unfold it into desired configuration. Mariolis et al. proposed an approach of recognize the pose for garment using convolutional neural network. Their model is trained by the combination of real and synthetic dataset in 2D garment model². Li et al. presented a series of laundry works in recognition and manipulation of garment. Initially, the model-driven approach based on precomputed deformable model of hung garments has been proposed. A set of deformable models had been trained using the method of Support Vector Machine (SVM) to recognize the category and pose of garment³. They improve their recognition approach using Kinect Fusion technique to reconstruct a deformable 3D model⁴.

3. Particle Based Polygonal Model

We suppose a piece of garment that is crudely spread-out and uniformly placed on a flat platform. We perform a computer vision analysis to a single color image that captured from the top view from the garment. By applying the dynamic programming algorithm, the real garment is matched by the particle based polygonal model and its parameters are extracted. The flowchart for the model generation is described as shown in Figure 2.

3.1. Simulate the Hanging Garment

The particle based modeling is applied into the dynamic programming and used to simulate the movement and deformation of the garment mesh model. The approach in the previous work is adopted and the mass-spring model is utilized in this work⁵. The hanging process of garment mesh model generated from a real garment is

simulated as shown in Figure 1, where a piece of crudely spread-out garment mesh model is placed flat on the simulated environment. For each step, a specified particle from the garment mesh model will be picked up by the robot as a grasping point and then moved to the hanging position following the simulated trajectory.

3.2 Generate Synthetic Dataset

One of the hardest problems need to be solved in deep learning is to collect the large scale data into the desired format. Collecting the data for different categories of real garment are very time consuming particularly encompassing the different types, sizes and material properties with its deformation. Hence, a training set that gather relevant information of garment which can be used in visual recognition purposes is required. The features such as colors and textures of the garments are less significant in this work. The dynamic programming modeling is applied to the garment mesh model, the

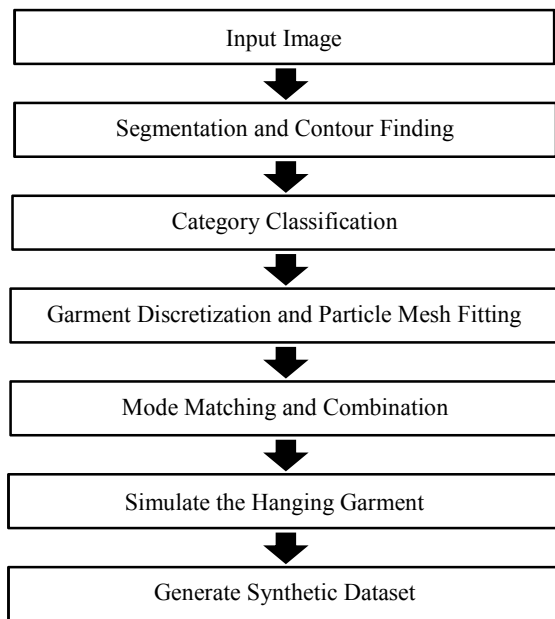


Fig. 2. Flowchart for the particle based polygonal model generation for synthetic dataset.

deformation poses of the model hanging by robotic manipulator is simulated. By applying different physical properties of the garment mesh model, the model look visually similar with depth images can be produced from the virtual simulation. An amount of images that simulate the deformation of real garment can be acquired. A series

of images are captured for each pose of garment, the model is rotated vertically with 360 degrees and the virtual camera captures the image of the rotated garment by increasing one rotating degree until full rotation is achieved.

4. Preliminary Results

4.1 Robotic Manipulation Setup

Robotic manipulations have been conducted using a Baxter robot with two Kinect depth sensor. The depth images of the hanging garments have been acquired by a Kinect depth sensor placed in front of the Baxter robot at a fixed height. The second Kinect sensor is placed at the head of Baxter robot which used to capture the images for a piece of crudely spread out garment on the flat platform.

4.2 Real and Synthetic Dataset

To collect the real garment dataset, a piece of the garment placed on the flat platform is hung by a Baxter robot and a Kinect depth sensor located in front of the Baxter robot. The hanging garment is then rotated 360 degree vertically and the color and depth images are captured. As shown in Figure 3, the threshold of the depth images are determined in order to distinguish the garment from the background.

The 200×340 pixels depth images that only consists of a piece of hanging garment are extracted from 640×480 original images. For category classification, three categories which are towels, shirts and trousers are selected in this current work. A total of 9 different real garments have been used as the samples, 3 real garments for each category. Each garment have been hung 2 or 3 times and about 360 depth images have been acquired for each grasping point. For pose recognition, 21 poses for shirts, 15 pose for trousers and 9 poses for towels are selected by defined by the markers. Total around 48600 depth images including towels, shirts and trousers are collected, the procedure of image acquisition is considered slow and time consuming.

For synthetic dataset, a large dataset of synthetic depth images are constructed by using computer graphic software and dynamic programming algorithm respectively. Using Blender software, the total 9 garment models which 3 models of towels, 3 models of trousers and 3 models shirts are constructed with different in size

and shape. To simplify task in designing the model in simulation, the garment models are constructed in 2D by assuming the front and back sides of shirt and trouser are not separated during grasped by robotic arm. In addition, the 2D garment model also can be generated by using the proposed dynamic programming algorithm. The particle based polygonal model can be generated from a crudely spread out garment placed on the flat platform.

The towel models consists of 81 particles, the trouser models consists of 121 particles and the shirt model consists of 209 particles are constructed. Due to the symmetry axes of the garment and reduce the dense of the particles in the model, only selected particles in the garment model that matching with the markers in the real garment are simulated. The hanging garment models can be simulated by each of their particles. Different views of the hanging garment model can be acquired by rotating the model 360 degree in front of virtual camera that placed at fixed height as similar as possible with the setup of Kinect sensor for image acquisition in robotic platform. The approximately 97200 virtual depth images have been generated. For synthetic dataset, the condition in the virtual environment is set as close as possible to the depth images in real dataset. Hence, the images acquired from the virtual simulation are comparable with real depth images, then allow to use as training dataset in the learning model.

5. Conclusion

In this work, an approach to generate the dataset of hanging garment using both real and synthetic images is proposed. The garment mesh model is extracted from the crudely spread-out garment using particle based

polygonal model, then the different poses of hanging garment can be simulated in the virtual environment. Experiment results demonstrate the proposed approach is applicable in dataset collection that need a large volume of data to train the learning model. By using this proposed approach, different types and sizes of garment mesh model can be extracted and simulated rather than design them in the graphics software.

Acknowledgements

This work is supported by the Ministry of Higher Education, Malaysia through research grant: 20140127FRGS.

References

1. A. Doumanoglou, A. Kargakos, T.-K. Kim, and S. Malassiotis, Autonomous active recognition and unfolding of clothes using random decision forests and probabilistic planning, in *Proc. ICRA*, pp. 987–993, 2014.
2. I. Mariolis, G. Peleka, A. Kargakos, and S. Malassiotis, Pose and category recognition of highly deformable objects using deep learning, in *International Conference Advanced Robotics (ICAR)*, pp. 655–662, IEEE, 2015.
3. Y. Li, C-F Chen, and P.K. Allen, Recognition of deformable object category and pose, In *Proc. ICRA*, 2014
4. Y. Li, C-F. Chen, and P.K. Allen, Real-time pose estimation of deformable objects using a volumetric approach. In *Proc. IROS*, 2014.
5. K.S.M Sahari, and Y.C. Hou. "3D Elastic Deformable Object Model for Robot Manipulation Purposes." *Journal of Advanced Computational Intelligence and Intelligent Informatics*, vol. 18, no.3, pp. 375-382, 2014.

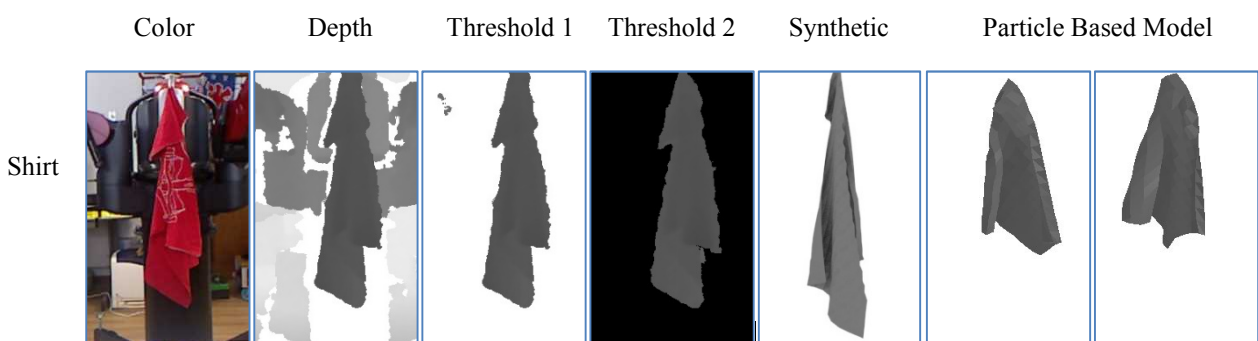


Fig. 3. Example images of color, depth, threshold 1 (white), threshold 2 (black), synthetic and particle based model of hanging garment grasped by specified point.

Design and Development of Three Arms Transmission Line Inspection Robot

Muhammad Fairuz bin Abdul Jalal*, Khairul Salleh Mohamed Sahari, Ho Ming Fei, Justin Chan Tuck Leong
Department of Mechanical Engineering, College of Engineering, Universiti Tenaga Nasionaly, Jalan IKRAM-UNITEN,
Kajang, Selangor 43000, Malaysia

E-mail: mfairuz@uniten.edu.my, khairuls@uniten.edu.my
www.uniten.edu.my

Abstract

The high-voltage transmission line had been used primarily for power distribution from power plant or power station to the end users. However, the transmission line is highly prone to damage due to exposure to various thermal - mechanical loadings and material degradation. Therefore, periodical inspection on transmission line after prolonged service is needed to prevent any failure before it happens. In this paper, we present a new design of three arms inspection robot for transmission lines. The robot is able to transverse along the line and bypass the in-line obstacles namely the anti-vibration hammers, spacer, strain clamps and others. The design of the inspection robot in term of the robot design and configuration with slotted cam at each arm is presented. The detailed analysis via simulation with respect to the robot stability; kinematic and movement analysis; and power consumption during operation is executed to make sure the proposed design able to do the inspection without any unexpected difficulties. Later, the lab testing on the developed prototype is done for feasibility study and validation.

Keywords: inspection robot, transmission line, power line, obstacle avoidance, robot design, mobile robot

Introduction

High-voltage transmission lines is one of the main elements in power distribution from the power plant or power station to the customer. However, the transmissions is exposed the harsh environment conditions that leads to damages by various circumstances namely effect of mechanical tension, material degradation and flashover. The transmissions lines undergoing such circumstances eventually lead to many problems such electrical breakdown or even major accident if transmissions lines were not being inspect, fixed and replaced in appropriate time¹.

The process of inspections of transmission line involved activities such as changing the ceramic insulators and switching on or off the circuit in between poles². However, the manual inspection process of transmission line exposed the workers to various unfavorable circumstance of dangerous working environment that is taxing with long duration³. Therefore, it is crucial demand to develop a mobile inspection robot to replace manual transmission line inspection job. The development of the mobile inspection robot will not only create a safer work environment in the transmission line inspection job, but also improve the efficiency of the inspection process³. A two arms transmission line robot is developed by Wang et al.⁴ utilize a line walking

mechanism that based on biped structure either having both feet placed on the line or each feet is placed alternatively on and off the line. Another dual arm robot self-balancing was developed by Songyi et al. The two arm of the robot hold onto the transmission line and move with the wheel installed on the arm. The robot is integrated with counter weight to improve the robot stability while travelling on the transmission line⁵.

Xu et al.⁶ developed a 3-arms transmission line robot that features 2 supporting arms and 1 assistant arm placed in between both supporting arms. This robot was designed to overcome obstacles by evading them with the lifting mechanism on each arm. Rui et al.⁷ developed 3-arm transmission line inspection robot. The robot arms consist of rubber wheel and the both outer arm installed with gripper to hold onto the line. The rubber wheel enables the robot to pass over minor obstacles like the splicer and damper without avoiding them.

Our research group already took initiatives to propose various conceptual design and selection based on requirement set by Tenaga Nasional Berhad (TNB), the main utility supplier to peninsular Malaysia⁸.

Transmission Line inspection Robot Design

General Design Requirement

There are many components, which are installed on the transmission line for various purposes namely tension insulator chain, suspension clamp, damper, tension clamp, jumper, splicing sleeve and others depending on type of transmission line as shown in Fig. 1. It is deemed necessary for robot to bypass these in-line components so that the inspection process can be executed effectively⁹.

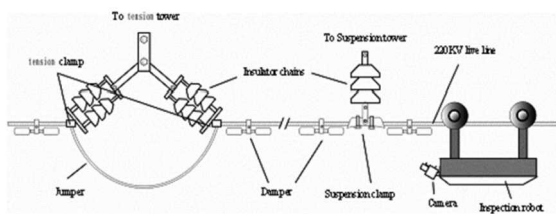


Fig. 1. Transmission line environment⁹.

Transmission Line Inspection Robot

The robot travel on the transmission line with the help of rollers that installed in each arm and cross obstacles by moving its arm up by rotating the power screw installed in each arm. The robot is installed with six motors; three motors run the roller at each arm for traversing on the transmission line and the others three motors attached to the power screw for obstacles crossing process. The conceptual design and the prototype are shown in Fig. 2.

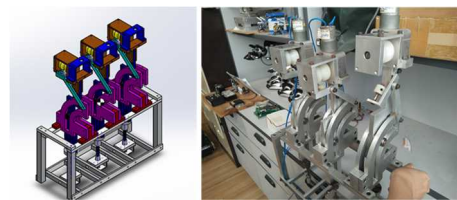


Fig. 2. The conceptual design (left) and prototype of the three arms transmission line inspection robot (right).

The three arms robot is hanged to the transmission line by means of roller and lower jaw as a gripping element. The movement is propelled by the roller at each arm. Each roller is powered by a motor as shown in Fig. 3.

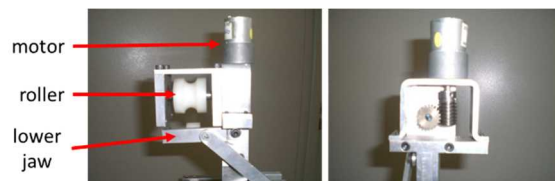


Fig. 3. The front view (left) and side view (right) of the gripper.

The mechanism to bypass obstacle is illustrated in Fig. 4.

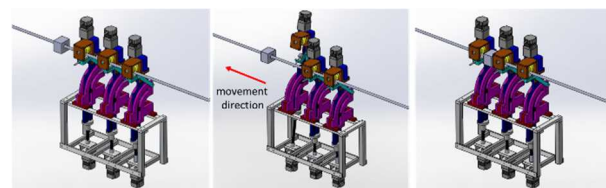


Fig. 4. Mechanism to bypass inline obstacles.

The gripping position and bypassing obstacle movement are realized by the rotational direction of the motor linked to power screw. To bypass the in-line obstacle, the motor is then actuated. The power screw pushes the arm upwards. As the arm moves up, it follows the curve of the

slotted profile. The bottom of the arm will have a pin joint with a support to enable it to rotate as the arm follows the curve of the slot. The arm will move back to its original position by reversing the motor direction and the wheel on arm attached back to the line. The same step applied to the following next two arm. The mechanism to bypass the obstacles is shown in Fig. 5.

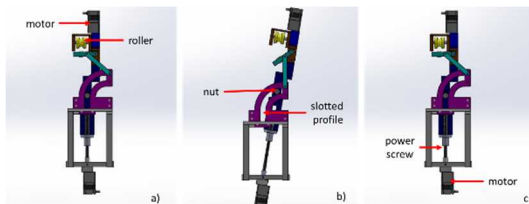


Fig. 5. The arm movement to bypass obstacles.

The stability of the transmission line inspection robot is an important aspect to be considered as it influences the overall quality of the image taken during the inspection process.

Result and Discussion

Capability to bypass obstacles

The robot must be able to avoid obstacles along the transmission line or else the design will be deemed as a failure. Fig. 6 shows that the roller and lower jaw do not interfere with the line as the arm gripper loosening and tightening its grip.

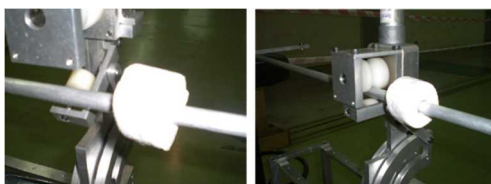


Fig. 6. The arm gripper during loosening (left) and tightening (right) its grip to the line.

The clearance between the arm and the obstacles is ranged from 90mm to 130mm with the maximum angle of arm rotation 21.6° as shown in Fig. 7.

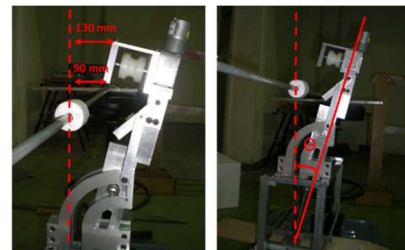


Fig. 7. The arm gripper during loosening (left) and tightening (right) its grip to the line.

Stability analysis

The significant changes of robot center of mass during the process to bypass the obstacle provide instability and tendency for the robot to swing. The analysis of the design center of gravity is done by means of center of mass analysis of the following arm configurations:

- Configuration 1: original configuration; all the arms rest on the transmission line
- Configuration 2: the first arm move up to avoid obstacles while the other two arm rest on the line
- Configuration 3: the second arm move up to avoid obstacles while the other two arm rest on the line
- Configuration 4: the third arm move up to avoid obstacles while the other two arm rest on the line

The robot xyz axis and value of center of mass for each configuration is extracted from the CAD software as is shown in Fig. 8. The coordinate center of mass of the different arm configuration is tabulated in the Table 1.

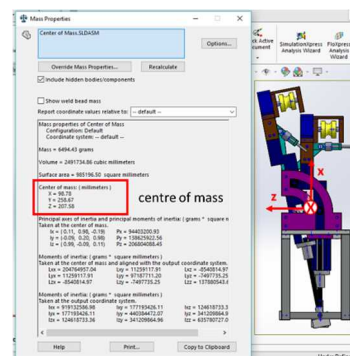


Fig. 8. The arm gripper during loosening (left) and tightening (right) its grip to the line.

Table 1. The coordinate of the center of mass by various arm configuration.

Arm Configuration

Coordinate	1	2	3	4
x	88.45	98.78	98.80	98.80
y	250.65	258.67	258.83	258.83
z	207.58	207.58	207.58	207.58

There is a small change of the coordinate of the center of mass in the x-axis and y-axis as the robot change it configurations from the original configuration while the z-axis remained constant throughout the operation. The average change of x-axis is 10.33 mm and y-axis is 8.07 mm. The average distance between center of mass in various arm configuration is 13.1 mm. The results are plotted in in x-y plane as shown in Fig. 9.

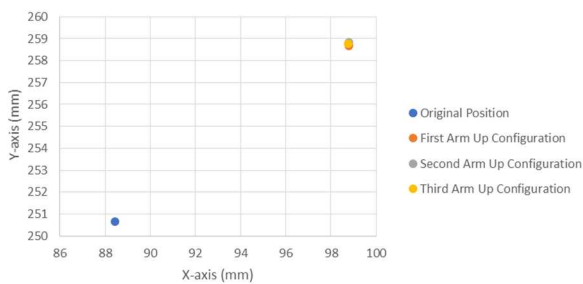


Fig. 9. The coordinate of robot center of mass in x-y plane for different arm configuration

Motor Torque and Power Consumption

The value of the motor torque required to rotate the power screw to move the arm up for bypassing the obstacle is analyzed in Solidworks Motion. The motor speed is set to reach 225 RPM based on the motor specification. The time needed for the arm to move up to bypass the obstacle is 20 seconds. The average motor torque and power consumption are 13Nmm and 0.254W. The graph of the motor torque and power consumption against time is shown in Fig 10.

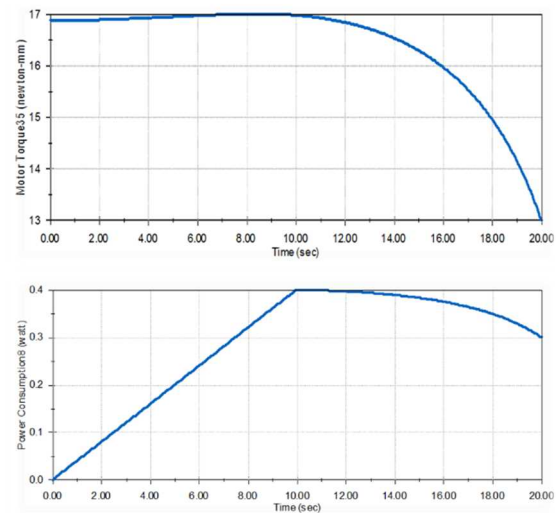


Fig. 10. Graph of motor torque (top) and power consumption (bottom) against time.

Conclusion

In this paper, the three arms transmission line inspection robot is presented. The mechanism to bypass the obstacles is achieved by using power screw and slotted profile. The robot is considered stable during operation due to minimal changes of its centre of mass. The testing and analysis in term of robot capability to bypass the obstacles as well as analysis of motor torque and power consumption.

Acknowledgements

This work was supported by Universiti Tenaga National BOLD Research Grant 10289176/B/9/2017/63. Authors would like to thank TNB for the access of information and data for formulating the robot design specification.

References

Y.C. Zhang, Z.Z. Liang and M. Tan, Mobile Robot for Overhead Powerline Inspection-a Review, in *Robot* 9(5) (2009), pp. 467-473.
 L.E. Parker and J.V. Draper (1998). *Robotics applications in maintenance and repair*, in Handbook of Industrial Robotics (1998) pp. 1023-1036.
 F.Y. Zhou, J.D. Wang, Y.B. Li, and H.R. Xiao, Control of an inspection robot for 110KV power transmission lines based on expert system design methods, in *Proc. 2005 IEEE Conf. on Control Applications* (2005), pp. 1563-1568.

- L. Wang, F. Liu, Z. Wang, S. Xu, S. Cheng and J. Zhang, Development of a practical power transmission line inspection robot based on a novel line walking mechanism, in *IEEE/RSJ Int. Conf. on Intelligent Robots and Systems* (2010), pp. 222-227.
- D. Songyi, W. Xuefeng, D. Hang, and W. Tao, Development of a self-balance dual-arm robot for inspection of high-voltage power transmission lines, in *IEEE Int. Conf. on Mechatronics and Automation* (2012), pp. 2482-2487.
- B. Xu, X. Wang, Y. Zhu and H. Chen, Design of obstacle crossing mechanism of high-voltage transmission line inspection robot, in *IEEE Int. Conf. on Robotics and Biomimetics* (2015), pp. 2539-2544.
- G. Rui, Z. Feng, C. Lei and Y. Jun, A mobile robot for inspection of overhead transmission lines, in *Proc. of the 3rd Int. Conf. on Applied Robotics for the Power Industry* (2014), pp. 1-3.
- M.F. Abdul Jalal, K.S. Mohamed Sahari, A. Anuar, A.D. Mohd Arshad, M.S. Idris, Conceptual design for transmission line inspection robot, in *IOP Conf. Ser.: Earth and Environmental Science*, (2013).
- G. Wu, T. Zheng, H. Xiao and C. Li, Navigation, location and non-collision obstacles overcoming for high-voltage power transmission-line inspection robot, in *Int. Conf. on Mechatronics and Automation* (2009), pp. 2014-2020.

A review on fundamental advancements of black hole algorithm

Zuwairie Ibrahim, Suad Khairi Mohammed, Norazian Subari

Faculty of Electrical and Electronics Engineering, Universiti Malaysia Pahang, Pahang, Malaysia

Nor Azlina Ab Aziz, Nor Hidayati Abdul Aziz

Faculty of Engineering and Technology, Multimedia University, Melaka, Malaysia

Tasiransurini Ab Rahman

Faculty of Electrical and Electronic Engineering, Universiti Tun Hussein Onn Malaysia, Johor, Malaysia

Asrul Adam, Zulkifli Md Yusof

Faculty of Manufacturing, Universiti Malaysia Pahang, Pahang, Malaysia

Mohd Ibrahim Shapiai

Malaysia Japan International Institute of Technology, Universiti Teknologi Malaysia, Malaysia

Norrma Mokhtar

Faculty of Engineering, University of Malaya, Kuala Lumpur, Malaysia

Email: zuwairie@ump.edu.my, suad.khairim@gmail.com, aziansubari@ump.edu.my,

azlina.aziz@mmu.edu.my, hidayati.aziz@mmu.edu.my, surini@uthm.edu.my,

asrul@ump.edu.my, zmdyusof@ump.edu.my, md_ibrahim83@utm.my, norrimamokhtar@um.edu.my

Abstract

In recent years, there is a growing interest in the design and development of nature-inspired optimization algorithms. One of the algorithms is black hole algorithm (BHA), which is inspired by the black hole in general relativity and cosmology. This paper reports a review of the BHA. This review emphasizes on the fundamental advancements of BHA. A brief research gap is presented at the end of this paper.

Keywords— black hole algorithm, fundamental, optimization

1. Introduction

A black hole is a region of space packed with so much matter that its own gravity prevents anything from escaping – even a ray of light. Black holes can form when massive stars run out of fuel and collapse under their own weight, creating strong gravity. The idea of the black hole is shown in Figure 1. The R_{BH} determines the event horizon for the black hole. If a star appears near the black hole (within the event horizon), the star is pulled towards the black hole due to the massive gravity of the black hole.

The BH algorithm (BHA) [1] is a population-based meta-heuristic algorithm inspired by the physical phenomenon of black hole. In BHA, the agent with the best solution mimics the black hole. The event horizon is calculated and any agent within the event horizon vanishes and re-initialized in the search space.

The BHA is shown in Figure 2. Since BHA is a population-based algorithm, N number of agents are needed. Let d as the number of dimension for an optimization problem, a solution, X , in a search space is kept by an agent i at iteration t as follows:

$$X_i(t) = (X_i^1(t), X_i^2(t), \dots, X_i^d(t)) \quad (1)$$

The BHA begins with initialization where a randomly generated population of candidate solutions are placed in the search space. For each agent i , the initial solution can be represented as:

$$X_i(0) = (X_i^1(0), X_i^2(0), \dots, X_i^d(0)) \quad (2)$$

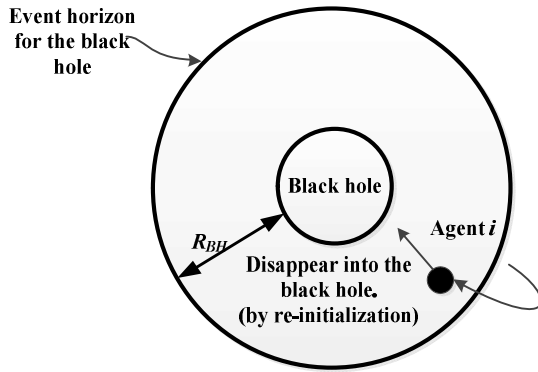


Fig. 1. Illustration of a black hole with its event horizon.

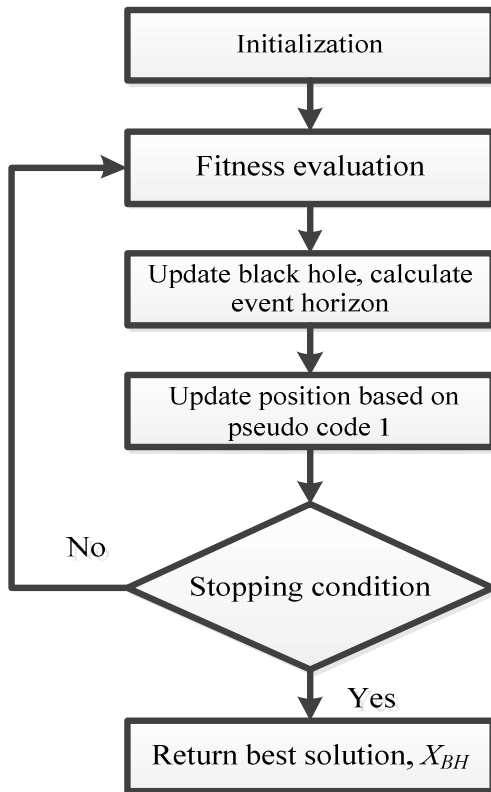


Fig. 2. The black hole algorithm.

After the initialization, the fitness values of the population are evaluated. The best agent, which has the best fitness value, is chosen as the black hole while other agents are selected as normal agents. For the case of function minimization problems, during initialization, the black hole agent is determined as follows:

$$BH = \underset{i \in \{1, \dots, N\}}{\text{min}} fit_i(t) |_{t=0} \quad (3)$$

In this study, the black hole agent keeps the best-so-far solution, X_{BH} . The best-so-far solution is different than the best solution. The best solution is defined as the best solution obtained at specific iteration, t . On the other hand, the best-so-

far solution is the best solution found from the initial iteration, $t = 0$, until current iteration, t . Hence, for $t \neq 0$, an agent i is selected as the black hole agent if the fitness value of that agent, f_i , is better than the fitness value of the black hole agent, f_{BH} . Specifically, for the case of function minimization, $f_i < f_{BH}$.

Once the black hole agent and normal agents are identified, the radius of the event horizon, R_{BH} , is formulated as follows:

$$R_{BH} = \frac{f_{BH}}{\sum_{i=1}^N f_i} \quad (4)$$

where f_{BH} is the fitness value of the black hole agent, N is the number of agents, and f_i is the fitness value of the i^{th} star.

The next step is solution update, which is applied to all agents except the black hole agent. Other than black hole agent, the agents can be categorized into two groups. The first group of agents is the agents located within the event horizon. This agent will be swallowed by the black hole agent. Then, a new agent following the swallowed one is generated and distributed randomly in the search space. This generation is to keep the number of agent constant. The second group of agents are agents located far from the black hole agent. In other words, these agents are not within the event horizon. These agents move towards the black hole agent and the updated solution can be computed as follows:

$$X_i(t+1) = X_i(t) + rand \times (X_{BH} - X_i(t)) \quad (5)$$

where $X_i(t+1)$ and $X_i(t)$ are the locations of the i^{th} agent at iterations $t+1$ and t , respectively. The $rand$ is a random number belonging to $[0,1]$ and X_{BH} is the location of the black hole agent. This solution update can be summarized in the Pseudocode 1.

PSEUDOCODE 1: Solution update in BHA

```

if agent  $i^{\text{th}}$  position is within the event horizon
then
do re-initialization
if agent  $i^{\text{th}}$  position is not within the event horizon
then
update the position based on Eq. (5)
else
end
    
```

After all the agents have updated their position, the next iteration begins if the termination criteria is not met. Otherwise, the best-so-far, X_{BH} , solution is reported.

2. Fundamental advancements of black hole algorithm

As shown in Figure 3, the fundamental advancement of BHA can be grouped into five categories: (1) accelerate the computation in software and hardware, (2) implementation in membrane system, (3) extension of BHA for combination optimization, (4) hybridization with others meta-heuristics, and (5) diversity improvement for premature convergence avoidance.

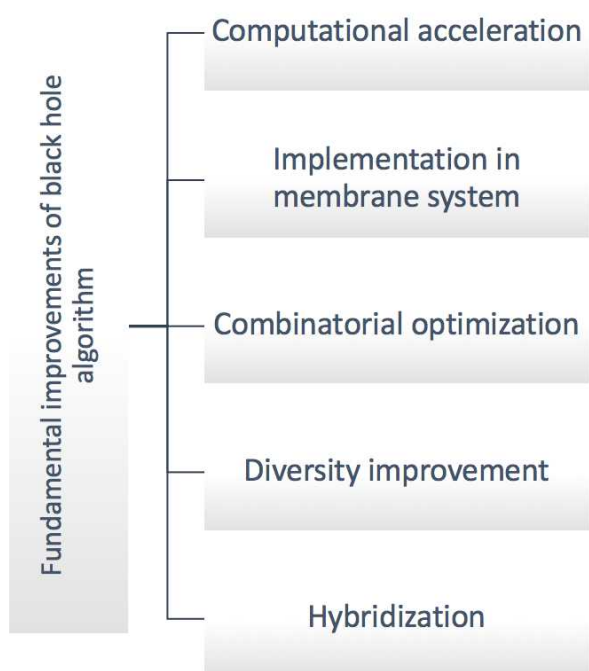


Fig. 3. Classification of fundamental improvement of black hole algorithm.

In 2015, Tsai has introduced the BHA to accelerate the clustering speed by both software and hardware [2]. The authors introduced a solution for the input data which exceeds the size of storage or memory of such a system. To ease this problem, an efficient clustering algorithm, called MapReduce Black Hole (MRBH), is presented to leverage the strength of the black hole algorithm and the MapReduce programming model. By using MapReduce, MRBH will then divide a large dataset into several small data sets and cluster these smaller data sets in parallel.

The BHA can be implemented based on membrane system [3]. In this study, the authors inserted the black hole clustering algorithm in the membrane structure, provide the three parts of the membrane system to perform black hole clustering algorithm, which are the membrane structure based on membrane computing, the objects in elementary membrane and the evolution rules in the elementary membrane, and analyse the performance of the black hole clustering algorithm based on membrane computing.

The original BHA need to be extended for solving combinatorial optimization problems. One of the extension of BH algorithm is called Binary Black Holes (BBH) and it is used to solve multiple instances of known benchmarks obtained from the OR-library [4]. Another binary version of BHA called BBHA was introduced by Pashaei, which is used to solve feature selection problem in biological data [5].

The BHA has been actively hybridized with other algorithms. For example, the BHA is combined with the stars gravities information and applied to unmanned combat aerial vehicle (UCAV) planning [6]. The BHA is also used as an

operator and hybridized with GSA in order to prevent facing the premature convergence and to improve the abilities of GSA in exploration and exploitation [7-8]. In other study, the BHA is hybridized with a heuristic search algorithm to overcome the problem of BHA. The BHA is used to produce an initial solution to the clustering problem and then a heuristic search algorithm is applied to improve the quality of this solution [9]. In addition, a bisecting k-means algorithm is hybridized with BHA [10] to improve the performance of bisecting k-means algorithm. Moreover, Black Hole Artificial Bee Colony (BHABC) algorithm has been introduced in 2016 [11]. In this new algorithm, the BHA gives a high exploration ability while maintaining the original exploitation ability of the ABC algorithm.

To improve the diversity of BHA, genetic algorithm operators have been used [12]. Other study has shown that the chaotic characteristic also can be used to enhance the performance of BHA. This algorithm is called Chaotic Inertia Weight Black Hole (CIWBH) algorithm [13].

Recently, a white hole operator has been introduced in BHA to avoid premature convergence in BHA [14]. In general relativity, theoretically, if black holes exist, then it should be possible to reverse the equations governing them to get the opposite of black hole, which is the white hole [15]. As oppose to black hole agent in the BH algorithm, the white hole was assigned to the worst agent in the population.

3. Concluding remark

All the meta-heuristic algorithms perform differently when they are used to solve different optimization problems. One algorithm may perform better than the other in solving one problem and it may perform unsatisfactorily in other set of problems. Based on the review in this paper, BHA did not performed well in solving numerical optimization problems. In most studies, the BHA is weak to perform global search completely especially in the big problem spaces, due to its limited exploration and exploitation capability.

Using the progress of other optimization algorithms as reference, the premature convergence of the BHA could be avoided by applying local and global neighbourhood, or by introducing more randomness in the search process using chaotic methods, for example. Also, hybridization with another optimization algorithms could be investigated, such as with differential evolution [16], biogeography-based optimization [17], simulated annealing [18], harmony search [19], and simulated Kalman filter optimization [20-21]. Since all the publications on BHA deal with single-objective optimization problem, multi-objective optimization algorithm based on BHA could also be established.

It is also worth to mention a paper published in Information Sciences journal which explained that the BHA is in fact a simplified version of particle swarm optimization (PSO) with inertia weights. Hence, the novelty of BH algorithm is questionable [22]. Based on the popular CEC2005 benchmark set [23], they proved that the BHA is inferior to the performance of PSO with inertia weights for most of the test functions. This finding could motivate the researchers in this

field to search for a novel approach to establish a new version of BHA that is different than the other optimization algorithms.

Nevertheless, modifications to the original BHA are still needed to be done in order to continuously improve the performance of this algorithm. Although some studies have been done on improving the BHA, the algorithm still has a lot of possible improvements.

Acknowledgement

This research is funded by the Universiti Malaysia Pahang (Research Grant RDU1703224).

References

- [1] A. Hatamlou, "Black hole: A new heuristic optimization approach for data clustering", *Information Sciences*, 222, 175-184, 2012.
- [2] C.W. Tsai, C. H. Hsieh, and M.C. Chiang, "Parallel Black Hole Clustering Based on MapReduce", *IEEE International Conference on Systems, Man, and Cybernetics (SMC)*, 2015.
- [3] Q. Li and Z. Pei, "The Black Hole Clustering Algorithm Based on Membrane Computing", 2015.
- [4] A. G. Rubio, B. Crawford, R. Soto, A. Jaramillo, S. M. Villablanca, J. Salas, and E. Olguin, "A Binary Black Hole Algorithm to Solve Set Covering Problem", *International Conference on Industrial, Engineering and Other Applications of Applied Intelligent Systems*, 2016.
- [5] E. Pashaei and N. Alydin, "Binary black hole algorithm for feature selection and classification on biological data", *Applied Soft Computing*, 56, 94-106, 2017.
- [6] A. Heidari and R. Abbaspour, "A gravitational black hole algorithm for autonomous UCAV mission planning in 3D realistic environments", *International Journal of Computer Applications*, 95(9), 2014
- [7] M. Doraghinejad and H. Nezamabadi-pour, "Black hole: A new operator for gravitational search algorithm", *International Journal of Computational Intelligence Systems*, 7(5), 809-826, 2014.
- [8] S.K. Mohammed, Z. Ibrahim, H. Daniyal, and N.A. Ab. Aziz, "A New Hybrid Gravitational Search - Black Hole Algorithm", *The National Conference for Postgraduate Research*, 834-842, 2016.
- [9] P. Chandrasekar and M. Krishnamoorthi, "BHOHS: A two stage novel algorithm for data clustering", *International Conference on Intelligent Computing Applications (ICICA)*, 2014.
- [10] M. Eskandarzadehalamdary, B. Masoumi, and O. Sojodishijani, "A new hybrid algorithm based on black hole optimization and bisecting k-means for cluster analysis", *22nd Iranian Conference on Electrical Engineering (ICEE)*, 2014.
- [11] J. C. Bansal, "Black Hole Artificial Bee Colony Algorithm", *6th International Conference Swarm, Evolutionary, and Memetic Computing (SEMCCO 2015)*, 2015.
- [12] S. Yaghoobi and H. Mojallali, "Modified Black Hole Algorithm with Genetic Operators", *International Journal of Computational Intelligence Systems*, 9(4), 652-665, 2015.
- [13] H. Aslani, M. Yaghoobi, and M. R. Akbarzadeh-T, "Chaotic inertia weight in black hole algorithm for function optimization", *International Congress on Technology, Communication and Knowledge (ICTCK)*, 2015.
- [14] S.K. Mohammed, Z. Ibrahim, H. Daniyal, and N. A. Ab. Aziz, "White Hole-Black Hole Algorithm", *The National Conference for Postgraduate Research*, 824-833, 2016.
- [15] S. Mirjalili, S.M. Mirjalili, and A Hatamlou, "Multi-verse optimizer: a nature-inspired algorithm for global optimization", *Neural Computing and Applications*, 27(2), 495-513, 2016.
- [16] R. Storn and K.V. Price, "Differential evolution – a simple and efficient heuristic for global optimization over continuous spaces", *J. Global Optim.*, 11(4), 341-359, 1997.
- [17] D. Simon, "Biogeography-based optimization", *IEEE Trans. Evol. Comput.*, 12(6), 702-713, 2008.
- [18] S. Kirkpatrick, C.D. Gelatt, and M.P. Vecchi, "Optimization by simulated annealing", *Science*, 220, 671-680, 1983.
- [19] Z.W. Geem, J.H. Kim, and G.V. Loganathan, "A new heuristic optimization algorithm: harmony search", *Simulation*, 76(2), 60-68, 2001.
- [20] Z. Ibrahim, N.H. Abdul Aziz, N.A. Ab. Aziz, S. Razali, and M.S. Mohamad, "Simulated Kalman Filter: a novel estimation-based metaheuristic optimization algorithm", *Advanced Science Letters*, 22, 2941-2946, 2016.
- [21] Z. Ibrahim, N.H. Abdul Aziz, N.A. Ab. Aziz, S. Razali, M.I. Shapiai, S.W. Nawawi, and M.S. Mohamad, "A Kalman filter approach for solving unimodal optimization problems", *ICIC Express Letters*, 9(12), 3415-3422, 2015.
- [22] A.P. Piotrowski, J.J. Napiorkowski, and P.M. Rowinski, "How novel is the "novel" black hole optimization approach?", *Information Sciences*, 267, 191–200, 2014.
- [23] P.N. Suganthan, N. Hansen, J.J. Liang, K. Deb, Y.P. Chen, A. Auger, and S. Tiwari, "Problem Definitions and Evaluation Criteria for the CEC 2005 Special Session on Real-Parameter Optimization", *Nanyang Technol. Univ., Singapore, Tech. Rep. KanGAL #2005005*, IIT Kanpur, India, 2005.

A survey on applications of black hole algorithm

Zuwairie Ibrahim, Suad Khairi Mohammed, Norazian Subari, Asrul Adam, Zulkifli Md Yusof
Universiti Malaysia Pahang, Pahang, Malaysia

Nor Azlina Ab Aziz, Nor Hidayati Abdul Aziz
Faculty of Engineering and Technology, Multimedia University, Melaka, Malaysia

Tasiransurini Ab Rahman
Faculty of Electrical and Electronic Engineering, Universiti Tun Hussein Onn Malaysia, Johor, Malaysia

Mohd Ibrahim Shapiai
Malaysia Japan International Institute of Technology, Universiti Teknologi Malaysia, Malaysia

Norrma Mokhtar
Faculty of Engineering, University of Malaya, Kuala Lumpur, Malaysia

Email: zuwairie@ump.edu.my, suad.khairim@gmail.com, aziansubari@ump.edu.my, asrul@ump.edu.my, zmdyusof@ump.edu.my, azlina.aziz@mmu.edu.my, hidayati.aziz@mmu.edu.my, surini@uthm.edu.my, md_ibrahim83@utm.my, norrimamokhtar@um.edu.my

Abstract

In recent years, there is a growing interest in the design and development of nature-inspired optimization algorithms. One of the algorithms is black hole algorithm (BHA), which is inspired by the black hole in general relativity and cosmology. This paper reports a review of the black hole algorithm (BHA). This survey emphasizes on the applications of BHA.

Keywords— application, black hole algorithm, optimization

1. Introduction

A black hole is a region of space packed with so much matter that its own gravity prevents anything from escaping – even a ray of light. Black holes can form when massive stars run out of fuel and collapse under their own weight, creating strong gravity.

The black hole algorithm (BHA) [1] is a population-based meta-heuristic algorithm inspired by the physical phenomenon of black hole. In BHA, the agent with the best solution mimics the black hole. The event horizon is calculated and any agent within the event horizon vanishes and re-initialized in the search space.

The BHA is shown in Figure 1. Since BHA is a population-based algorithm, N number of agents are needed. Let d as the number of dimension for an optimization problem, a solution, X_i in a search space is kept by an agent i at iteration t as follows:

$$X_i(t) = (X_i^1(t), X_i^2(t), \dots, X_i^d(t)) \quad (1)$$

The BHA begins with initialization where a randomly generated population of candidate solutions are placed in the search space. For each agent i , the initial solution can be represented as:

$$X_i(0) = (X_i^1(0), X_i^2(0), \dots, X_i^d(0)) \quad (2)$$

After the initialization, the fitness values of the population are evaluated. The best agent, which has the best fitness value, is chosen as the black hole while other agents are selected as normal agents. For the case of function minimization problems, during initialization, the black hole agent is determined as follows:

$$BH = \underset{i \in \{1, \dots, N\}}{\min} fit_i(t) |_{t=0} \quad (3)$$

In this study, the black hole agent keeps the best-so-far solution, X_{BH} . The best-so-far solution is different than the best solution. The best solution is defined as the best solution obtained at specific iteration, t . On the other hand, the best-so-

far solution is the best solution found from the initial iteration, $t = 0$, until current iteration, t . Hence, for $t \neq 0$, an agent i is selected as the black hole agent if the fitness value of that agent, f_i , is better than the fitness value of the black hole agent, f_{BH} . Specifically, for the case of function minimization, $f_i < f_{BH}$.

Once the black hole agent and normal agents are identified, the radius of the event horizon, R_{BH} , is formulated as follows:

$$R_{BH} = \frac{f_{BH}}{\sum_{i=1}^N f_i} \quad (4)$$

where f_{BH} is the fitness value of the black hole agent, N is the number of agents, and f_i is the fitness value of the i^{th} star.

The next step is solution update, which is applied to all agents except the black hole agent. Other than black hole agent, the agents can be categorized into two groups. The first group of agents is the agents located within the event horizon. This agent will be swallowed by the black hole agent. Then, a new agent following the swallowed one is generated and distributed randomly in the search space. This generation is to keep the number of agent constant. The second group of agents are agents located far from the black hole agent. In other words, these agents are not within the event horizon. These agents move towards the black hole agent and the updated solution can be computed as follows:

$$X_i(t+1) = X_i(t) + rand \times (X_{BH} - X_i(t)) \quad (5)$$

where $X_i(t+1)$ and $X_i(t)$ are the locations of the i^{th} agent at iterations $t+1$ and t , respectively. The $rand$ is a random number belonging to $[0,1]$ and X_{BH} is the location of the black hole agent. This solution update can be summarized in the Pseudocode 1.

PSEUDOCODE 1: Solution update in BHA

```

if agent  $i^{\text{th}}$  position is within the event horizon
then
do re-initialization
if agent  $i^{\text{th}}$  position is not within the event horizon
then
update the position based on Eq. (5)
else
end

```

After all the agents have updated their position, the next iteration begins if the termination criteria is not met. Otherwise, the best-so-far, X_{BH} , solution is reported.

2. Applications of black hole algorithm

The BHA has been used to solve many problems and applied in many fields. The BHA has been used to train a neural network, which is used as workload prediction model [2]. The BHA has been also used with higher order neural network for solving nonlinear classification problems of data mining [3].

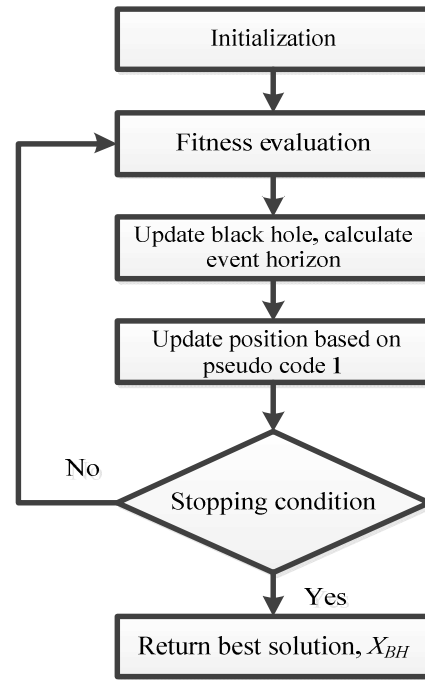


Fig. 1. Flowchart of BHA.

The BHA is used in engineering design of electromagnetic devices [4]. The new optimization technique based on the black hole phenomenon is called the black-hole-based optimization technique. To show the effectiveness of the proposed technique, it has been demonstrated on a magnetizer by optimizing its pole face to obtain a desired magnetic flux density distribution.

In the field of software engineering, Jeet and Dhir combined a nature-inspired black-hole algorithm and a genetic algorithm to propose a search-based technique for software clustering [5]. This technique is used to manage a software system by partitioning it into smaller subsystems containing highly related modules. Search-based software clustering techniques are found to be beneficial in effective partitioning of software systems.

Moreover, the BHA has been used to solve the manufacturing cell design problem, in which different machines are grouped into sets or cells with the objective to minimize the movement of materials. In order to increase the efficiency and productivity, machines that create products with similar requirements must be close to each other. This machine- grouping, known as cell, allow the production to be dedicated and organized [6].

In civil engineering, the BHA has been introduced in the generalized constitutive law. The problem of model identification is transformed to a problem of parameter back analysis, which is a typical and complicated optimization. To improve the efficiency of the traditional optimization method, a black hole algorithm is applied in this study, by combining the generalized constitutive law for an elastic-plastic constitutive model and black hole algorithm. A new back

analysis method for model identification of rocks surrounding underground roadways in coal mine is proposed to solve a parameter back analysis for elastic-plastic constitutive model [7]. While the slope instability of embankment is very complex, which may develop locally, near the facing, within the embankment, or through the foundation soil as local, surficial, general, or deep-seated failure. The BHA is used to analyze the stability of one high embankment slope for one airport in the plateau loess area [8].

In the field of operations research, the BHA has been employed by Soto *et al.*, in which, they presented two new systems for online control of enumeration strategies based on bat algorithm and BHA [9]. The BHA is used to improve performance in the exploration of search tree and updating the enumeration strategy online [10].

The BHA has been actively applied in the field of power system. The BHA has been combined with GSA to solve day-ahead reactive power optimization problem in distribution network [11]. Also, BHA has been used in non-technical losses characterization [12] and optimal reactive power dispatch problem [13]. The BHA has been combined with BBO algorithm [14] and DE algorithm [15] to solve the economic dispatch problem incorporating the wind energy (EDIW) [16]. Boucekara also used BHA to solve the optimal power flow problem in a power system [17]. Finally, in the field of power system, a gradient-based modified teaching-learning-based optimization combined with BHA to seek the optimum operational cost [18].

Image enhancement is considered as an optimization problem and a meta-heuristic optimization algorithm is used to solve this problem. Image enhancement is a nonlinear optimization problem with its constraints and the enhancement process will be done by intensifying each pixel's content. BHA is employed to find the image's optimum parameters of the transfer function in order to get the best results [19].

In the medical field, the BHA has been integrated with decision tree [20] in medical data classification. In addition, Binary Black Hole Algorithm (BBHA) and Random Forest Ranking (RFR) have been used for gene selection and classification of microarray data [21]. While in the same field, Pashaei and Aydin presented a binary version of BHA called BBHA for solving feature selection problem in biological data [22].

The original BHA was proposed for clustering problem. Many variants of BHA have been introduced in clustering. As an example, BHA has been used to accelerate the clustering speed by both software and hardware [23]. Also, for clustering, the BHA has been combined with bisecting k-means algorithm, this algorithm is called BH-BKmeans algorithm [24]. Jeet and Dhir proposed to use the hybrid of BHA, auxiliary archive, and GA to optimize multiple objectives for clustering of android mobile applications [25].

The BHA has been used as multi-objective scheduling method for workflow application [26]. Also in scheduling, the multi-objective BHA has been used to optimize scheduling of jobs on two machines taking into consideration the fuzziness in the environment involved [27].

In the field of industries and induction motors, the design, performance evaluation and control of induction motors are based on circuit parameters. Though conventional techniques produce good results for accurate measurement of electrical parameters, like resistance (or reactance), the swarm intelligence-motivated techniques still better results for real-world optimization problems. The disrupted Black Hole Artificial Bee Colony (DBHABC) algorithm is proposed and applied for optimizing induction motor parameter estimation [28].

The set covering problem (SCP) is one of the most representative optimization problems. The BHA is used to solve multiple instances of the problem with known benchmarks obtained from the OR-library [29]. Set covering problems were also solved in 2016 by employing a recent nature-inspired metaheuristic based on the black hole phenomena [30]. A multi-dynamic binary black hole algorithm for resolving the set covering problem has been introduced [31]. The same problems were also solved by cuckoo search and BHA [32].

Finally, an application of BHA in mission planning has also been reported. Unmanned combat aerial vehicle (UCAV) mission planning in realistic test fields is a well-known optimization problem, so many algorithms have been designed to solve this multi-constrained problem. The BHA is one of these swarm intelligence approaches which applied to the UCAV mission planning scheme [33].

3. Concluding remark

This paper reports a survey on the applications of BHA. At the moment, the BHA has been applied in artificial intelligence, engineering design, software engineering, manufacturing, civil engineering, operations research, image processing, wireless sensor network, scheduling, parameter estimation, power system, medical analysis, clustering, set covering problem, and mission planning. Due to the popularity of BHA, we expect the BHA will be applied in another area of applications such as routing in VLSI [34], DNA sequence design [35], and adaptive beamforming for antenna engineering [36].

Acknowledgement

This research is funded by the Universiti Malaysia Pahang (RDU1703224).

References

- [1] A. Hatamlou, "Black hole: A new heuristic optimization approach for data clustering", *Information Sciences*, 222, 175-184, 2012.
- [2] J. Kumar and A.K. Singh, "Dynamic resource scaling in cloud using neural network and black hole algorithm," *Fifth International Conference on the Eco-friendly Computing and Communication Systems (ICECCS)*, 2016.
- [3] J. Nayak, B. Naik, and H.S. Behera, "Solving nonlinear classification problems with black hole optimisation and higher order Jordan Pi-sigma neural network: a novel approach," *International Journal of Computational Systems Engineering*, 2(4), 236-251, 2016.
- [4] H.R. Boucekara, "Optimal design of electromagnetic devices

- using a black-hole-based optimization technique," *IEEE Transactions on Magnetics*, 49(12), 5709-5714, 2013.
- [5] K. Jeet and R. Dhir, "Software architecture recovery using genetic black hole algorithm," *ACM SIGSOFT Software Engineering Notes*, 40(1), 1-5, 2015.
- [6] R. Soto, B. Crawford, N. Fernandez, V. Reyes, S. Niklander, and I. Araya, "Solving Manufacturing Cell Design Problems Using the Black Hole Algorithm," *The Mexican International Conference on Artificial Intelligence*, 2016.
- [7] W. Gao, M. Ge, D. Chen, and X. Wang, "Back analysis for rock model surrounding underground roadways in coal mine based on black hole algorithm," *Engineering with computers*, 32(4), 675-689, 2016.
- [8] W. Gao, X. Wang, S. Dai, and D. Chen, "Study on stability of high embankment slope based on black hole algorithm," *Environmental Earth Sciences*, 75(20), 1381, 2016.
- [9] R. Soto, B. Crawford, R. Olivares, S. Niklander, F. Johnson, F. Paredes, and E. Olguín, "Online control of enumeration strategies via bat algorithm and black hole optimization," *Natural Computing*, 16(2), 241-257, 2017.
- [10] R. Olivares, R. Soto, B. Crawford, M. Barria, and S. Niklander, "Evaluation of choice functions to self-adaptive on constraint programming via the black hole algorithm," *The Computing Conference (CLEI)*, Latin American, 2016.
- [11] H. Pei, Y. Li, and K. Liu, "A multi-object black hole gravitational search algorithm for day-ahead reactive optimization in distribution network," *The Guidance, Navigation and Control Conference (CGNCC)*, Chinese, 2016.
- [12] D. Rodrigues, C.C.O. Ramos, and J.P. Papa, "Black hole algorithm for non-technical losses characterization," *6th Latin American Symposium on the Circuits & Systems (LASCAS)*, 1-4, 2015.
- [13] K. Lenin, B.R. Reddy, and M.S. Kalavathi, "Black hole algorithm for solving optimal reactive power dispatch problem," *International Journal of Research in Management, Science & Technology*, 2(1), 2321-3264, 2014.
- [14] D. Simon, "Biogeography-based optimization," *IEEE transactions on Evolutionary Computation*, 12(6), 702-713, 2008.
- [15] R. Storn, and K. Price, "Differential evolution—a simple and efficient heuristic for global optimization over continuous spaces," *Journal of global optimization*, 11(4), 341-359, 1997.
- [16] Z. Hasan and M. El-Hawary, "Economic dispatch incorporating wind energy by BH, BBO and DE," *IEEE Canadian Conference on the Electrical and Computer Engineering (CCECE)*, 2016.
- [17] H. Boucekara, "Optimal power flow using black-hole-based optimization approach," *Applied Soft Computing*, 24, 879-888, 2014.
- [18] R. Azizpanah-Abarghoee, T. Niknam, F. Bavafa, and M. Zare, "Short-term scheduling of thermal power systems using hybrid gradient based modified teaching-learning optimizer with black hole algorithm," *Electric Power Systems Research*, 108, 16-34, 2014.
- [19] S. Yaghoobi, S. Hemayat, and H. Mojallali, "Image gray-level enhancement using Black Hole algorithm," *2nd International Conference on the Pattern Recognition and Image Analysis (IPRIA)*, 2015.
- [20] E. Pashaei, M. Ozen, and N. Aydin, "An application of black hole algorithm and decision tree for medical problem," *IEEE 15th International Conference on the Bioinformatics and Bioengineering (BIBE)*, 2015.
- [21] E. Pashaei, M. Ozen, and N. Aydin, "Gene selection and classification approach for microarray data based on Random Forest Ranking and BBHA," *IEEE-EMBS International Conference on the Biomedical and Health Informatics (BHI)*, 2016.
- [22] E. Pashaei and N. Aydin, "Binary black hole algorithm for feature selection and classification on biological data," *Applied Soft Computing*, 56, 94-106, 2017.
- [23] C.-W. Tsai, C.-H. Hsieh, and M.-C. Chiang, "Parallel black hole clustering based on MapReduce," *IEEE International Conference on the Systems, Man, and Cybernetics (SMC)*, 2015.
- [24] M. Eskandarzadehalamdary, B. Masoumi, and O. Sojodishijani, "A new hybrid algorithm based on black hole optimization and bisecting k-means for cluster analysis," *22nd Iranian Conference on the Electrical Engineering (ICEE)*, 2014.
- [25] K. Jeet and R. Dhir, "Software clustering using hybrid multi-objective black hole algorithm," *Paper presented at the SEKE*, 2016.
- [26] F. Ebadifard and S.M. Babamir, "Optimizing multi objective based workflow scheduling in cloud computing using black hole algorithm," *3th International Conference on the Web Research (ICWR)*, 2017.
- [27] K. Jeet, S. Sharma and K.K. Nailwal, "Two-Machine Fuzzy Flow Shop Scheduling Using Black Hole Algorithm," *Global Journal of Pure and Applied Mathematics*, 13(6), 1935-1946, 2017.
- [28] F.B. Sharma and S.R. Kapoor, "Induction motor parameter estimation using disrupted black hole artificial bee colony algorithm," *International Journal of Metaheuristics*, 6(12), 85-106, 2017.
- [29] Á.G. Rubio, B. Crawford, R. Soto, A. Jaramillo, S.M. Villablanca, J. Salas, and Olguín, E., "A binary black hole algorithm to solve set covering problem," *The International Conference on Industrial, Engineering and Other Applications of Applied Intelligent Systems*, 2016.
- [30] R. Soto, B. Crawford, I. Figueroa, S. Niklander and E. Olguín, "A black hole algorithm for solving the set covering problem," *The International Conference on Industrial, Engineering and Other Applications of Applied Intelligent Systems*, 2016.
- [31] J. García, B. Crawford, R. Soto and P. García, "A multi dynamic binary black hole algorithm applied to set covering problem," *The International Conference on Harmony Search Algorithm*, 2017.
- [32] R. Soto, B. Crawford, R. Olivares, J. Barraza, I. Figueroa, F. Johnson, and E. Olguín, "Solving the non-unicost set covering problem by using cuckoo search and black hole optimization," *Natural Computing*, 16(2), 213-229, 2017.
- [33] A. Heidari and R. Abbaspour, "A gravitational black hole algorithm for autonomous UCAV mission planning in 3D realistic environments," *International Journal of Computer Applications*, 95(9), 2014.
- [34] M.N. Ayob, Z. Md Yusof, A. Adam, A.F. Zainal Abidin, I. Ibrahim, Z. Ibrahim, S. Sudin, N. Shaikh-Husin, M.K. Hani, "A particle swarm optimization approach for routing in VLSI," *2010 Second International Conference on Computational Intelligence, Communication Systems and Networks (CICSyN)*, 49-53, 2010.
- [35] S.M. Mustaza, A.F.Z. Abidin, Z. Ibrahim, M.A. Shamsudin, A.R. Husain and J.A.A. Mukred, "A Modified Computational Model of Ant Colony System in DNA Sequence Design," *IEEE Student Conf. on Research and Development (SCOREd)*, 169-173, 2011.
- [36] K. Lazarus, N.H. Noordin, Z. Ibrahim, M.F. Mat Jusof, A.A. Mohd Faudzi, N. Subari, and K.Z. Mohd Azmi, "An Opposition-based Simulated Kalman Filter algorithm for adaptive beamforming," *International Conference on Applied System Innovation (ICASI)*, 91-94, 2017.

Black hole white hole algorithm with local search

Zuwairie Ibrahim, Suad Khairi Mohammed, Norazian Subari, Asrul Adam, Zulkifli Md Yusof
Universiti Malaysia Pahang, Pahang, Malaysia

Nor Azlina Ab Aziz, Nor Hidayati Abdul Aziz
Faculty of Engineering and Technology, Multimedia University, Melaka, Malaysia

Tasiransurini Ab Rahman
Faculty of Electrical and Electronic Engineering, Universiti Tun Hussein Onn Malaysia, Johor, Malaysia

Norrima Mokhtar
Faculty of Engineering, University of Malaya, Kuala Lumpur, Malaysia

Email: zuwairie@ump.edu.my, suad.khairim@gmail.com, aziansubari@ump.edu.my, asrul@ump.edu.my,
zmdyusof@ump.edu.my, azlina.abaziz@mmu.edu.my, hidayati.abaziz@mmu.edu.my, surini@uthm.edu.my,
norrimamokhtar@um.edu.my

Abstract

Black hole algorithm (BHA) is an optimization algorithm inspired by the black hole discovery in relativity theory. Recently, white hole operator, which is based on the opposite of black hole, has been introduced in BHA. In this paper, a local is added in the BHA with white hole operator.

Keywords— black hole algorithm, fundamental, optimization

1. Introduction

A black hole is a region of space packed with so much matter that its own gravity prevents anything from escaping – even a ray of light. Black holes can form when massive stars run out of fuel and collapse under their own weight, creating strong gravity.

The BHA algorithm (BHA) [1] is a population-based meta-heuristic algorithm inspired by the physical phenomenon of black hole. In BHA, the agent with the best solution mimics the black hole. The event horizon is calculated and any agent within the event horizon vanishes and re-initialized in the search space.

The BHA is shown in Figure 1. Let N is the number of agents and d is the number of dimension for an optimization problem, a solution, X , in a search space is kept by an agent i at iteration t as follows:

$$X_i(t) = (X_i^1(t), X_i^2(t), \dots, X_i^d(t)) \quad (1)$$

The BHA begins with initialization where a randomly generated population of candidate solutions are placed in the search space. For each agent i , the initial solution can be represented as:

$$X_i(0) = (X_i^1(0), X_i^2(0), \dots, X_i^d(0)) \quad (2)$$

After the initialization, the fitness values of the population are evaluated. The best agent, which has the best fitness value, is chosen as the black hole while other agents are selected as normal agents. For the case of function minimization problems, during initialization, the black hole agent is determined as follows:

$$BH = \min_{i \in \{1, \dots, N\}} fit_i(t) |_{t=0} \quad (3)$$

In this study, the black hole agent keeps the best-so-far solution, X_{BH} . The best-so-far solution is different than the best solution. The best solution is defined as the best solution obtained at specific iteration, t . On the other hand, the best-so-far solution is the best solution found from the initial iteration, $t = 0$, until current iteration, t . Hence, for $t \neq 0$, an agent i is selected as the black hole agent if the fitness value of that agent, f_i , is better than the fitness value of the black hole agent, f_{BH} . Specifically, for the case of function minimization, $f_i < f_{BH}$.

Once the black hole agent and normal agents are identified, the radius of the event horizon, R_{BH} , is formulated as follows:

$$R_{BH} = \frac{f_{BH}}{\sum_{i=1}^N f_i} \quad (4)$$

where f_{BH} is the fitness value of the black hole agent, N is the number of agents, and f_i is the fitness value of the i^{th} star.

The next step is solution update, which is applied to all agents except the black hole agent. Other than black hole agent, the agents can be categorized into two groups. The first group of agents is the agents located within the event horizon. This agent will be swallowed by the black hole agent. Then, a new agent following the swallowed one is generated and distributed randomly in the search space. This generation is to keep the number of agent constant. The second group of agents are agents located far from the black hole agent. In other words, these agents are not within the event horizon. These agents move towards the black hole agent and the updated solution can be computed as follows:

$$X_i(t+1) = X_i(t) + rand \times (X_{BH} - X_i(t)) \quad (5)$$

where $X_i(t+1)$ and $X_i(t)$ are the locations of the i^{th} agent at iterations $t+1$ and t , respectively. The $rand$ is a random number belonging to $[0,1]$ and X_{BH} is the location of the black hole agent. This solution update can be summarized in the Pseudocode 1.

PSEUDOCODE 1: Solution update in BHA

```

if agent  $i^{\text{th}}$  position is within the event horizon
then
do re-initialization
if agent  $i^{\text{th}}$  position is not within the event horizon
then
update the position based on Eq. (5)
else
end
    
```

After all the agents have updated their position, the next iteration begins if the termination criteria is not met. Otherwise, the best-so-far, X_{BH} , solution is reported.

2. The black hole white hole (BHW) algorithm

As oppose to black hole agent in the BHA, the white hole can be assigned to the worst agent in the population. Hence, the white hole is updated as follows:

$$WH = \max_{i \in \{1, \dots, N\}} fit_i(t) \quad (6)$$

Also, similar to the black hole, the white hole has its own event horizon and the radius of the event horizon, R_{WH} , can be calculated based on the following equation:

$$R_{WH} = \frac{fit_{WH}}{\sum_{i=1}^N fit_i} \quad (7)$$

where fit_{WH} is the fitness value of the white hole, N is the number of agents, and fit_i is the fitness value of the i^{th} star.

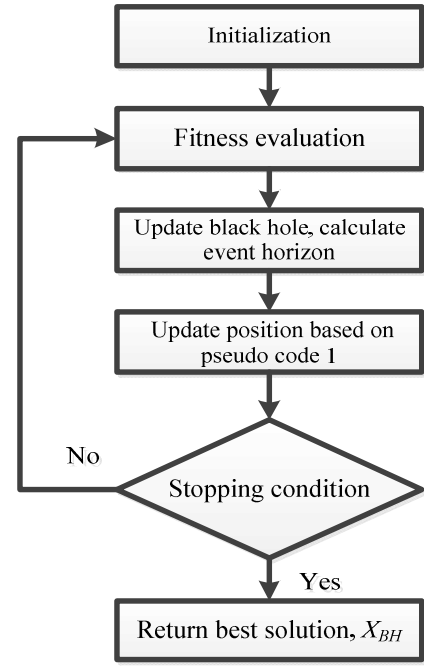


Fig. 1. Flowchart of BHA.

An arbitrary agent i could be updated to a position in the search space within the event horizon of the white hole. In this case, the agent is pushed by the white hole. Due to this, the position of the agent i is updated as follows:

$$X_i(t+1) = X_i(t) + rand \times (X_{WH} - X_i(t)) \quad (8)$$

where $X_i(t+1)$ and $X_i(t)$ are the locations of the arbitrary agent i at iterations $t+1$ and t , respectively. The $rand$ is a random number belonging to $[0,1]$ and X_{WH} is the location of the white hole agent.

Figure 2 shows the flowchart of the black hole algorithm with white hole operator, which is also termed as BHW algorithm [2]. The difference between the proposed BHW algorithm with the BHA shown in Figure 1 is the inclusion of a white hole agent as the worst solution. Note that there are two kind of event horizons. These are the event horizon for black hole and white hole agents and should be calculated at every iteration. Also, due to the inclusion of white hole agent which pushes any nearby agent, the position update in BHW algorithm can be explained in Pseudocode 2.

3. The proposed BHW algorithm with local search

The basic idea of the local search is to find neighbourhood solution around the best solution. In this study, not all the agents are subjected to local search. The white hole agent that keep the worst solution at the iteration, t , is selected and the local search is applied to the white hole agent.

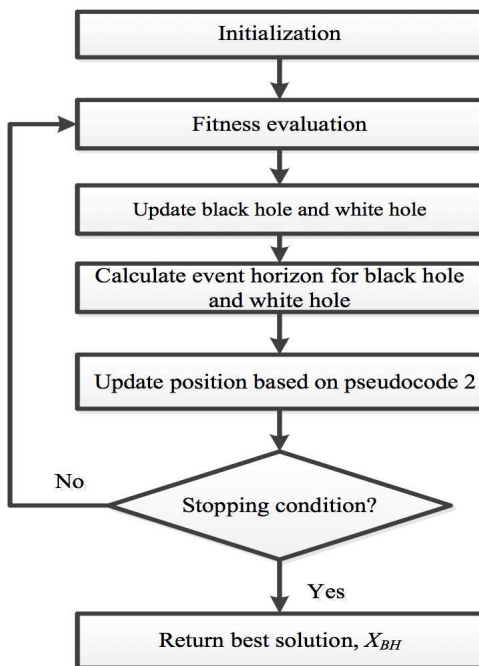


Fig. 2. Flowchart of BHWHL algorithm.

Table 1. Experimental setting parameter

Iteration	10000
Runs	51
Agents	100
Dimension	50
Search Space	[-100 100]

PSEUDOCODE 2: Solution update in BHWHL algorithm

```

if agent  $ith$  is black hole agent then
  position not updated
if agent  $ith$  position is within the event horizon of black hole then
  do re-initialization
if agent  $ith$  position is within the event horizon of white hole then
  update the position based on Equation (8)
else
  update the position based on Equation (5)
end
  
```

Let $X_i^d = X_{worst}^d = X_{WH}^d$, the local search is applied to every dimension, d , based on Equation (9).

$$X_i^d(t+1) = X_{BH}^d(t) + rand_d \times e^{-5t/T_{max}} \quad (9)$$

where $X_i^d(t+1)$ is the solution after the local search is applied, X_{BH} is the location of the black hole agent, t is the iteration number, T_{max} is the maximum number of iteration, and $rand_d \in [0,1]$ is a random number, which is generated at every dimension.

The local search is applied to the worst agent in the population. It is possible to select any worst solution at iteration t during an implementation of an optimization algorithm and apply Equation (9) to the worst agent. In this study, the local search is incorporated in the BHWHL algorithms. As a result, a variant of BH algorithm can be developed, which is called black hole white hole (BHWHL) algorithm with local search (BHWHLs). The flowchart of BHWHLs algorithm is similar to the flowchart of BHWHL algorithm in Figure 2. However, considering the local search, the solution for BHWHLs algorithm is updated according to Pseudocode 3, which replaces the Pseudocode 2.

PSEUDOCODE 3: Solution update in BHWHLs algorithm

```

if agent  $ith$  is black hole agent then
  position not updated
if agent  $ith$  position is within the event horizon of black hole then
  do re-initialization
if agent  $ith$  is the white hole then
  apply local search based on Equation (9)
if agent  $ith$  position is within the event horizon of white hole then
  update the position based on Equation (8)
else
  update the position based on Equation (5)
end
  
```

4. Experiment, result, and discussion

The experiments in this study were implemented based on the parameter setting tabulated in Table 1. The performance of the BHWHLs algorithm and the original BHA were studied by solving CEC2014 benchmark functions [3]. The results are tabulated in Table 2. The values in bold indicate the smaller or better result. Table 2 shows that the BHWHLs algorithm outperforms BHA for all the unimodal functions, while for simple multimodal functions, the accuracy of BHWHLs algorithm is very good, except for Function 14. For hybrid functions, the BHWHLs algorithm reaches to optimum solution for all functions except for Function 18 and Function 19. Finally, even though the BHWHLs algorithm performs BHA in most of the composition functions, the accuracy are quite unsatisfactorily for the case of Function 24 and Function 25. An example of convergence curve is shown in Figure 3.

Acknowledgement

This research is funded by the Universiti Malaysia Pahang (RDU1703224).

References

- [1] A. Hatamlou, "Black hole: A new heuristic optimization approach for data clustering", *Information Sciences*, 222, 175-184, 2012.
- [2] S.K. Mohammed, Z. Ibrahim, H. Daniyal, and N.A. Ab. Aziz, "White Hole-Black Hole Algorithm", *The National Conference for Postgraduate Research*, 824-833, 2016.

Table 2. Performance comparison between the BHA and BHWHLs

Type of Function	Function ID	The ideal value	BHA (Mean value)	BHWHLs (Mean value)
Unimodal	F1	100	5611014.427	2395827.785
	F2	200	4997329.195	8365.062195
	F3	300	14041.12327	6624.351763
Simple multimodal	F4	400	609.8508916	549.1541895
	F5	500	520.0161923	520.0000065
	F6	600	658.7739009	657.1073197
	F7	700	701.1662029	700.0187492
	F8	800	953.499765	928.9684462
	F9	900	1249.316564	1221.594196
	F10	1000	3816.305871	3214.544468
	F11	1100	8308.348714	7890.732838
	F12	1200	1200.797984	1200.757164
	F13	1300	1300.56279	1300.492432
	F14	1400	1400.261316	1400.308738
	F15	1500	1810.089933	1722.79273
	F16	1600	1621.682464	1621.5487
Hybrid	F17	1700	639170.063	235277.876
	F18	1800	2476.577727	3470.864961
	F19	1900	1960.011302	1965.653521
	F20	2000	9023.306146	4135.276728
	F21	2100	429192.2267	187917.412
	F22	2200	3786.065395	3758.516987
Composition	F23	2300	2652.810511	2645.194641
	F24	2400	2665.506218	2668.43428
	F25	2500	2749.939581	2753.661216
	F26	2600	2796.226359	2702.390476
	F27	2700	4729.276014	4655.848694
	F28	2800	11732.29457	10898.23985
	F29	2900	10839.35982	8746.81227
	F30	3000	69850.72279	37593.04308

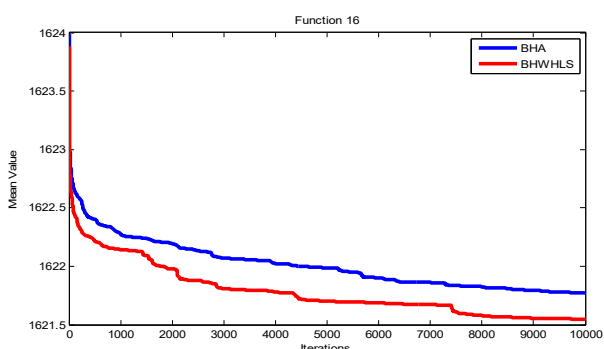


Fig. 3. Example of convergence curve (Function 16).

- [3] J. J. Liang, B-Y. Qu, and P. N. Suganthan, "Problem Definitions and Evaluation Criteria for the CEC 2014 Special Session and Competition on Single Objective Real-Parameter Numerical Optimization", *Technical Report 201311, Computational Intelligence Laboratory, Zhengzhou University, Zhengzhou, China and Technical Report, Nanyang Technological University, Singapore, December 2013.*

Tele-Operation of a Legged Robot by a Virtual Marionette System - First report: The first prototype and the usefulness of the reaching task-

Noritaka Sato, Yasuhiko Sawai, Ryo Asami, Makoto Kitani, Yoshifumi Morita

Department of Electrical and Mechanical Engineering, Nagoya Institute of Technology, Gokiso-cho, Syowa-ku,
Nagoya, Aichi 466-8555, Japan

Tomofumi Fujiwara, Takahiro Endo, Fumitoshi Matsuno

Department of Mechanical Engineering and Science, Kyoto University, Katsura Campus, Nishikyo-ku,
Kyoto, Kyoto 615-8530, Japan

E-mail: sato.noritaka@nitech.ac.jp

www.nitech.ac.jp/

Abstract

Generally, the target position of a hand or a foot is input into a virtual space by using a mouse as a user interface of a legged robot. However, its operation time is too long. Further it is difficult for the operators to recognize the spatial relationship between a robot and its environment. To solve these problems, we have proposed an interface that mixes and presents both visual and haptic senses. In this study, we have adapted the system to the operation of a legged robot.

Keywords: Rescue robot, User interface, Virtual Reality, Tele-operation

1. Introduction

Many rescue robots have been developed to gather information instead of humans at disaster sites, such as the sites of the Great East Japan Earthquake, the terrorist attacks against the US on September 11, and other disasters [1][2]. Generally, these robots have been crawler-type because they can move on the rough terrains by using their tracks. However, a crawler-type rescue robot cannot move up and down a ladder and is weak at moving on circular stairs. Therefore, legged robots have recently received a lot of attention. Currently, it is difficult for an operator to tele-operate a legged robot, because a legged robot has many degrees of freedom.

The Defense Advanced Research Projects Agency (DARPA) Robotics Challenge (DRC), which is an international competition for legged robots staged by DARPA, was participated in December 2013. Figure 1 shows the user interface of DRC-HUBO for tele-

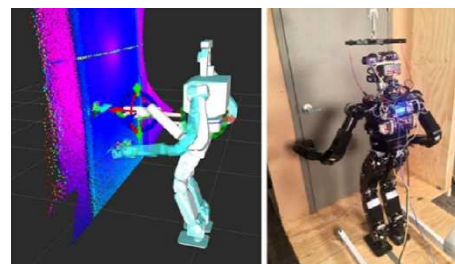


Fig. 1 Interface of DRC-HUBO [3]

operation of the robot [3]. This is a typical user interface which was found in the DRC. The operator inputs a target position for the hand or the foot of the robot in a 3D virtual space. The environment around the robot was reconstructed in this virtual space. However, because the team used a plane display to display the virtual space, it is difficult for the operator to recognize the positional relationship between the robot and its environment.

Moreover, the team used a normal mouse to input the target position, and it took a relatively long time to input.

On the other hand, Arai et al. have developed the Marionette System [4], which allows the operator to input the posture of the robot directly by using a small robot which has the same configuration as the controlled robot. However, we think that it took time and money to apply their system to various robots, and the usability may not be good because the environment cannot be displayed near the small robot.

We have developed a system which can display visual and haptic senses simultaneously to the operator so that the operator can tele-operate a crawler-type rescue robot intuitively and to reduce the operational load [5]. Figure 2 shows our developed system. The system shows the images shown in Fig. 3 to the operator by using a stereoscopic head mounted display (HMD). The HMD shows computer-generated (CG) images of a model of the robot, the environment around the robot, and the hand of the operator. Moreover, a haptic device is used to provide a reaction force against the motion of pinching, at the thumb and the index finger of the operator, when a part of the CG model of the robot is located between the CG model of the thumb and the first finger in the virtual space.

In this paper, our developed system will be applied to the tele-operation of a legged robot.

As mentioned previously, we believe that the previous user interfaces, [3] and [4], have the following issues:

- It took a long time to input the target position in the 3D virtual space.
- It is difficult to recognize the positional relationship between the robot and its environment.
- It is necessary to develop a real small “Marionette” robot when the controlled robot is changed.

Therefore, in this study, a new user interface for the tele-operation of a legged robot, which overcomes the above problems, was developed based on our proposed system [5] for a crawler-type rescue robot.

We called this new user interface the “Virtual Marionette System (VMS)”. The purpose of this study was to verify the effectiveness of the VMS by carrying out experiments, in which the operator changed the posture (configuration) of the robot by inputting a target position for its hand.



Fig. 2 Robot operation device with haptic device [4]

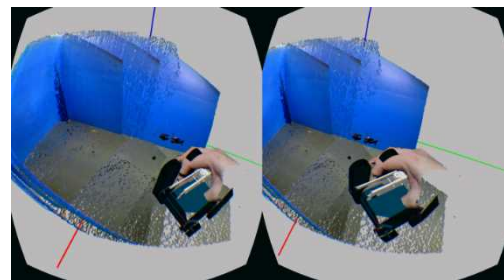


Fig. 3 Image showed by HMD[4]

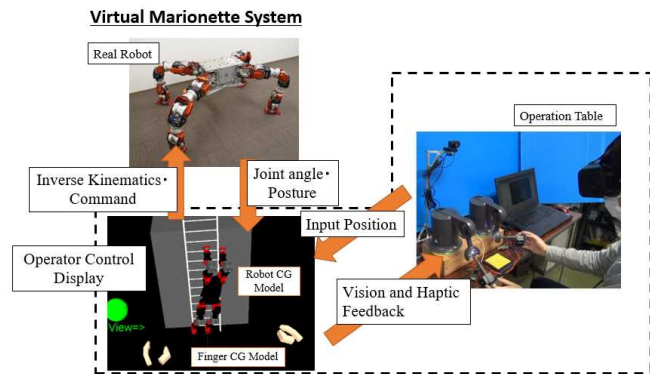


Fig. 4 Overview of the system in this research

2. Proposed system

2.1. Overview of the proposed system

Figure 4 shows an overview of the system. The left-upper image is the controlled robot. The left-bottom image is a view which the operator sees through the HMD. In this image, CG image consists of a model of the robot, the environment around the robot, and the operator’s fingers. The right image of Fig. 4 shows the situation of the operator. When the operator moves his/her fingers or hand, the CG models of the fingers in the virtual space are moved to the positions corresponding to the real fingers. The operator can control the robot in the virtual space by using the CG models of the fingers. When the

operator pinches the CG models of the hand or the foot of the robot he/she feels the reaction force from the haptic device. Therefore, the operator feels that he/she directly pinches the hand or foot of the real robot in the remote site.

The operator can change the posture of the robot while he/she pinches the CG model of the hand or foot of the robot as he/she wishes. After he/she releases the CG model, the system calculates the joint angles of the robot to achieve the target position of the hand or foot and sends a command to the robot. In this study, we used the simulator named “Gazebo” instead of a real robot for the experiment.

2.2. System configuration

Figure 5 shows a system configuration of the proposed system. To measure the position and posture (x, y, z, roll, pitch, and yaw) of the thumb and the index finger of the operator, a Touch 3D stylus, developed by 3D Systems, Inc., was used. Note that the function of generation of the reaction force by the Touch 3D stylus was not used in this system.

To apply a reaction force to the thumb and index finger of the operator when a CG model exists between the CG models of the thumb and index finger, a servo motor (Dynamixel AX-18 developed by ROBOTIS, Inc.) was used. The servo motor was installed at the tip of the pen of the Touch 3D stylus, and parts similar to the handle of a pair of scissors were made by using a 3D printer and were attached to the joint of the servo motor. Because the servo motor can measure the angle of the joint, the system could calculate the distance between the thumb and index finger. The system could then represent this in the virtual space with the CG model of the fingers. An Oculus Rift DK2 was used for the HMD of our proposed system. As mentioned previously, the screen of the HMD shows CG images of a model of the robot, the environment around the robot, and the fingers of the operator in a 3D virtual space.

2.3. Operation procedure

Figure 6 shows a flow chart of the tele-operation of a legged robot with our proposed system. Our system was designed to be used when the operator wants to move manually, such as in an emergency situation. We assumed that the robot moves automatically in a normal

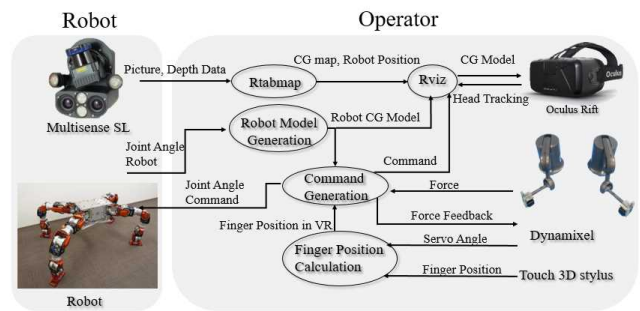


Fig. 5 System configuration

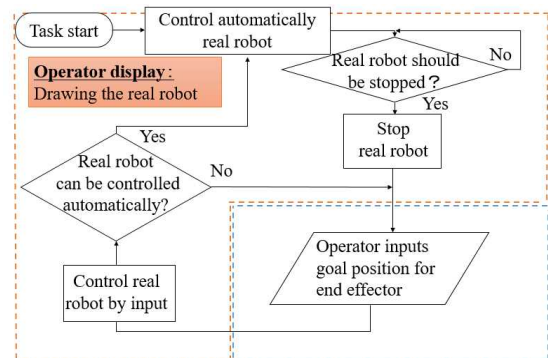


Fig. 6 The flowchart of operation process

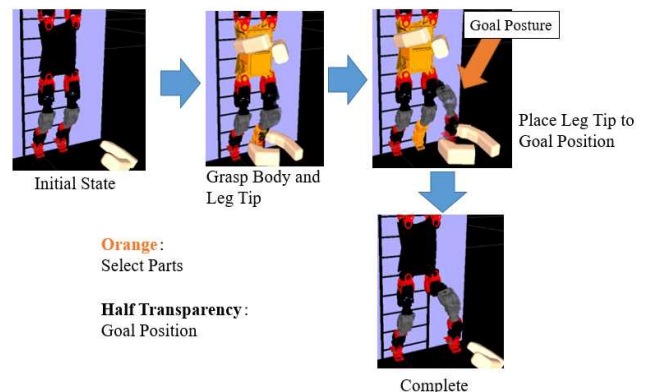


Fig. 7 Operation process

situation. When the operator wants to move the robot manually, he/she would stop the automatic control of the robot, and then he/she would tele-operate the robot. After tele-operation, he/she could change the control mode of the robot from tele-operation to automatic control.

In the case of the tele-operation mode, the operator can move the CG model of the hand, the foot, or the body of the robot by using the CG models of the fingers of the operator, which are synchronized with the operator’s actual fingers, in the virtual space.

Figure 7 shows the operation process for the foot of the robot. First, the operator grasps the body with his/her right or left hand and the foot (Leg Tip) with his/her other hand by using the CG models of the fingers. This is a similar interaction to the changing of the configuration of a doll. The color of the CG models of the fingers is a flesh color and the color of the CG model of the grasped parts of the robot is orange. After grasping, the operator could move the foot of the robot, and the target joint angles of the leg of the CG model of the robot were calculated by the inverse kinematics, which are explained in the next section. The joint would then automatically move to achieve the target foot position. When the operator grasped and moved the CG model, the target posture of the leg was displayed as a translucent CG model. After the operator moved the foot to the target position and released the CG model of the foot, the leg of the real robot was controlled to achieve the posture of the translucent CG model. By this procedure, the operator could control the robot as if he/she were grasping a miniature of the robot on the diorama existing in front of him/her or as if he/she were becoming a giant and grasping the robot with his/her hands.

2.4. Inverse kinematics

In our proposed system, IKFast, which is open source software, was used for calculation of the inverse kinematics. IKFast is a module for inverse kinematics in OpenRAVE and by using IKFast the calculation could be performed quickly. To use IKFast, the developer sets up a model file of a controlled robot. When a single target position of the end effector is input, IKFast outputs the joint angles to move the end effector on a linear trajectory from the current position to the target position with constant velocity.

When multiple target positions are input, the final one is set as the final target position and the others are set as way points.

When multiple solutions were obtained by inverse kinematics, the solution which satisfies the following conditions was used in this study:

- The minimum sum of the differences between the target joint angles obtained by the inverse kinematics and the current joint angles.
- Each joint angle obtained by the inverse kinematics is near the center of the range of the movement

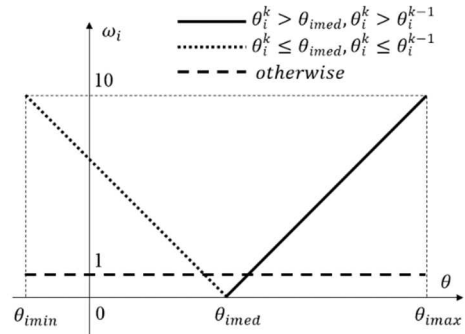


Fig.8 The weigh value of the leg angle

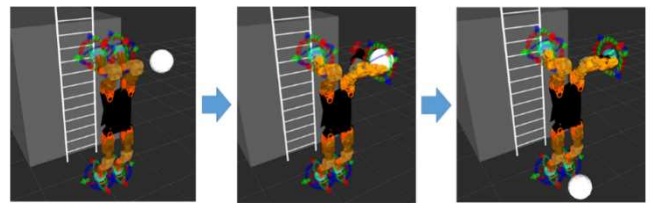


Fig.9 Experiment task

Therefore, the solutions obtained by inverse kinematics were evaluated by

$$\phi = \sum_{i=1}^n \omega_i |\theta_i^k - \theta_i^{k-1}|, \tag{1}$$

where

$$\omega_i \begin{cases} = 10 - 10 * \frac{\theta_{imax} - \theta_i^k}{\theta_{imax} - \theta_{imed}} & (\theta_i^k > \theta_{imed}, \theta_i^k > \theta_i^{k-1}) \\ = 10 - 10 * \frac{\theta_{imed} - \theta_i^k}{\theta_{imed} - \theta_{imin}} & (\theta_i^k \leq \theta_{imed}, \theta_i^k \leq \theta_i^{k-1}) \\ = 1 & (\text{otherwise}) \end{cases} \tag{2}$$

In Eq. (2), θ_{imax} , θ_{imin} , and θ_{imed} are maximum, minimum and center angle of the range of the movement of i-th joint, respectively. In Eq. (1) and Eq. (2), θ_i^k is the angle of the i-th joint of the k-th solution obtained by inverse kinematics. Figure 8 shows a graph of the weight coefficient ω_i . The solution which can minimize the evaluation function ϕ , was used to control the robot.

3. Experiment

The purpose of the experiment in this study was to verify the effectiveness of the proposed system compared with the conventional tele-operation system [2].

Table 1 Questionnaires

Number	Question
Q1	Were you able to recognize depth of the displayed environment?
Q2	Is it easy for you to decide the leg position in three dimensions?
Q3	Were you able to control the robot as you think?

3.1. Experimental method

Figure 9 shows the task of the robot in this experiment. The robot is the WAREC-1 developed by Takanishi and Hashimoto et al. [6]. We used a simulator built in Gazebo for this experiment. One white ball was displayed near the robot in the 3D virtual space. The operator grasped and moved the CG model of the hand or foot of the robot, by using the proposed system or the conventional system, to the ball. After touching the ball, a new ball was displayed at a different position. The operator repeated this reaching task 10 times. The position and the order of the balls were the same during all the trials (One trial consisted of 10 ball-reaching tasks.)

The total time was recorded for comparison. The number of the subjects was 10. Five subjects used the proposed system first and the other five used the conventional system first. After the experiment, the subjects answered a questionnaire about the usability of the tele-operation system. The score 5 meant "I think so very much," 4 meant "I think so," 3 meant "I cannot agree with," 2 meant "I don't think so," and 1 meant "I don't think so very much."

3.2. Experimental results

Figure 10 shows the average of the total time of the trial with each tele-operation system. A paired t-test shows that the total time was significantly shorter using the proposed system than using the conventional system ($p < 0.05$). Figure 11 shows the average score of the questionnaires. The answers of Q1 and Q2 are significantly better when using the proposed system compared to using the conventional system ($p < 0.05$).

3.3. Discussion

The total time was shorter when using the proposed system. The reason for this seems to be that the operator can more easily feel the depth distance because a stereoscopic HMD was used and the three dimensional

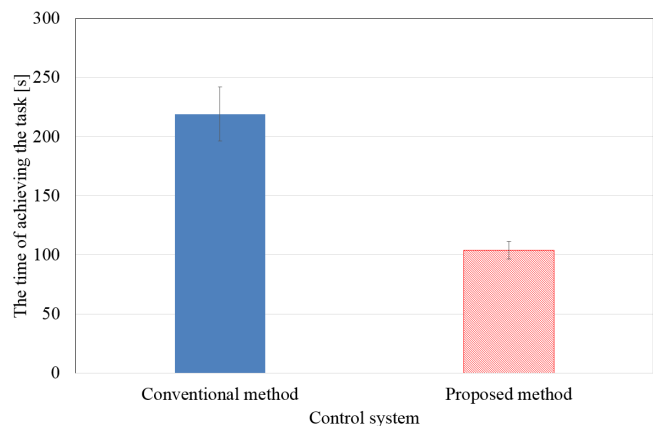


Fig.10 The time of achieving the task

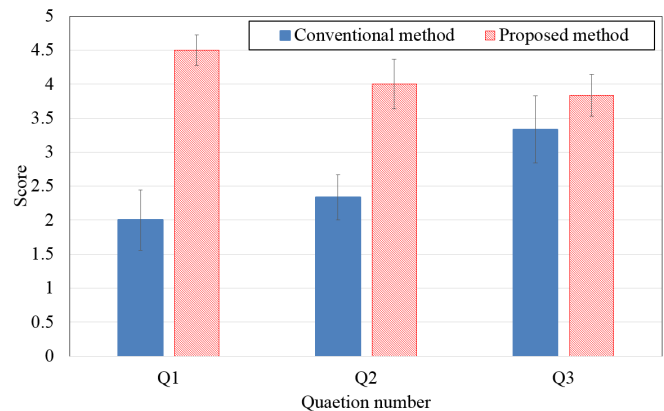


Fig.11 The questionnaire answer

position was input directly into the virtual space with the proposed system.

The answers to Q1 show that the operator recognized the depth of the environment more easily with the proposed system. Moreover, the answers to Q2 show that the operator could input the target position of the hand or foot of the robot more easily with the proposed system.

We confirmed that inputting the target position and recognition of the environment was easier when using the proposed system compared to the conventional system.

4. Conclusion

In this study, a novel tele-operation system for a legged robot was developed to solve the issues of existing systems. We carried out an experiment in which the operator moved the hand or the foot of a legged robot by tele-operation. As a result, we confirmed that inputting the target position and recognition of the environment

was easier when using the proposed system compared to the conventional system.

In the future, we will carry out the experiment with a real robot and will apply the proposed system to the teleoperation of a legged robot in other tasks, such as stair climbing, ladder climbing and the motions of recovering from falling down.

Acknowledgements

This research was funded by ImPACT Program of Council for Science, Technology and Innovation (Cabinet Office, Government of Japan).

References

1. J. Casper, R. Murphy, Human-Robot Interactions during the Robot-Assisted Urban Search and Rescue Response at the World Trade Center, *IEEE Transactions on Systems, man, and cybernetics society*, vol. 33, No.3, pp. 367-385, 2003.
2. R. R. Murphy, S. Tadokoro, D. Nardi, A. Jacoff, P. Fiorini, H. Choset, A.M. Erkmen, *Search and Rescue Robotics*, Springer Handbook of Robotics, pp. 1151-1173, 2008.
3. M. Zucker, S. Joo, M. X. Grey, C. Rasmussen, E. Huang, M. Stilman and A. Bobick, A general-purpose system for teleoperation of the DRC-HUBO humanoid robot, *Journal of Field Robotics*, Vol. 32, Issue 3, pp.336-351, 2015.
4. T. Takubo, K. Nishii, K. Inoue, T. Arai, Wholebody Teleoperation for Humanoid Robot by Marionette System, *Journal of Robotics Society of Japan*, Vol. 25, No. 3, pp.457-465, 2007. (In Japanese)
5. K. Kato, N. Sato, Y. Morita, Development of Direct Operation System for Mobile Robot by Using 3D CG Diorama, *Proc. 12th International Conference on Control, Automation and Systems*, pp. 1486-1490, 2012.
6. T. Matsuzawa, K. Hashimoto, X. Sun, K. Uryu, A. Koizumi, S. Hamamoto, T. Teramachi, A. Takanishi, Development of Disaster Response Robot with Commonly Structured Limbs and Experiment in Climbing Vertical Ladder, *Proc. International Conference on Advanced Mechanics*, pp.142-143, 2015.

***k*-Neighborhood Template *A*-Type Two-Dimensional Bounded Cellular Acceptors**

Makoto Sakamoto, Yu-an Zhang, Masamichi Hori, Haruka Tsuboi, Satoshi Ikeda, Kenji Aoki
Faculty of Engineering, University of Miyazaki, 1-1 Gakuen Kibanadai Nishi
Miyazaki, Miyazaki 889-2192, Japan
E-mail: sakamoto@cs.miyazaki-u.ac.jp

Tsutomu Ito, Takao Ito
Institute of Engineering, Hiroshima University, 4-1, Kagamiyama 1-chome
Higashi-Hiroshima, Hiroshima 739-8527, Japan
E-mail: itotakao@hiroshima-u.ac.jp

Yasuo Uchida
Department of Business Administration, Ube National College of Technology, Tokiwadai
Ube, Yamaguchi 755-8555, Japan
E-mail: uchida@ube-k.ac.jp

Tsunehiro Yoshinaga
Department of Computer Science & Electronic Engineering,
National Institute of Technology, Tokuyama College, Gakuendai
Shunan, Yamaguchi 745-8585, Japan
E-mail: yosimaga@tokuyama.ac.jp

Abstract

In this paper, we deal with three-dimensional computational model, k -neighborhood template A -type two-dimensional bounded cellular acceptor on three-dimensional tapes, and discuss some basic properties. This model consists of a pair of a converter and a configuration-reader. The former converts the given three-dimensional tape to two-dimensional configuration. The latter determines whether or not the derived two-dimensional configuration is accepted, and concludes the acceptance or non-acceptance of given three-dimensional tape. We mainly investigate some open problems about k -neighborhood template A -type two-dimensional bounded cellular acceptor on three-dimensional tapes whose configuration-readers are $L(m)$ space-bounded deterministic (nondeterministic) two-dimensional Turing machines.

Keywords: acceptor, configuration-reader, converter, neighbor, space-bounded, three-dimension, Turing machine.

1. Introduction

Due to the advances in many application areas such as computed tomography, robotics, and so on, the study of three-dimensional pattern processing has been of crucial importance. Thus, the study of three-dimensional

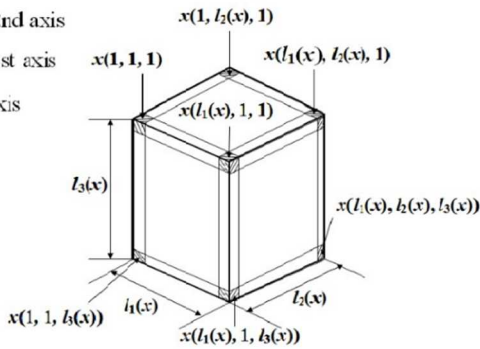
automata as the computational models of three-dimensional pattern processing has been meaningful. From this point of view, we proposed several three-dimensional automata as computational models of three-dimensional pattern processing, and investigated their

© The 2018 International Conference on Artificial Life and Robotics (ICAROB2018), Feb. 1-4, B-Con Plaza, Beppu, Oita, Japan

several accepting powers [2]. By the way, in the multi-dimensional pattern processing, designers often use a strategy whereby features are extracted by projecting high-dimensional space on low-dimensional space. So, from this viewpoint, a new computational model, *k-neighborhood template A-type two-dimensional bounded cellular acceptor* (abbreviated as *A-2BCA(k)* ($k \in \{1,5,9\}$)) on three-dimensional tapes was introduced, and discussed some basic properties[3]. An *A-2BCA(k)* is a three-dimensional automaton which consists of a pair of a *converter* and a *configuration-reader*. The former converts the given three-dimensional tape to the two-dimensional configuration and the latter determines the acceptance or non-acceptance of given three-dimensional tape whether or not the derived two-dimensional configuration is accepted. This paper mainly investigates some open problems about accepting powers of *A-2BCA(k)*'s whose configuration-readers are $L(m)$ space-bounded deterministic (nondeterministic) two-dimensional Turing machines [1]. We first show that a relationship between the accepting powers of deterministic *A-2BCA(1)* and nondeterministic *A-2BCA(1)*. We then show that there exists a language accepted by any deterministic *A-2BCA(9)*.

2. Preliminaries

Definition 2.1. Let Σ be a finite set of symbols. A *three-dimensional tape* over Σ is a three-dimensional rectangular array of elements of Σ . The set of all three-dimensional tapes over Σ is denoted by $\Sigma^{(3)}$. Given a tape $x \in \Sigma^{(3)}$, for each integer $j(1 \leq j \leq 3)$, we let $m_j(x)$ be the length of x along the j th axis. The set of all $x \in \Sigma^{(3)}$ with $l_1(x)=m_1$, $l_2(x)=m_2$, and $l_3(x)=m_3$ is denoted by $\Sigma^{(m_1, m_2, m_3)}$. If $1 \leq i_j \leq l_j(x)$ for each $j(1 \leq j \leq 3)$, let $x(i_1, i_2, i_3)$ denote the symbol in x with coordinates (i_1, i_2, i_3) , as shown in Fig.1.



© The 2018 International Conference on Artificial Life and Robotics (ICAROB2018), Feb. 1-4, B-Con Plaza, Beppu, Oita, Japan

Fig.1. Three-dimensional tape.

Furthermore, we define

$$x[(i_1, i_2, i_3), (i'_1, i'_2, i'_3)],$$

when $1 \leq i_j \leq l_j(x)$ for each integer $j(1 \leq j \leq 3)$, as the three-dimensional tape y satisfying the following (i) and (ii):

- (i) for each $j(1 \leq j \leq 3)$, $l_j(y) = i'_j - i_j + 1$;
- (ii) for each $r_1, r_2, r_3(1 \leq r_1 \leq l_1(y), 1 \leq r_2 \leq l_2(y), 1 \leq r_3 \leq l_3(y))$, $y(r_1, r_2, r_3) = x(r_1 + i_1 - 1, r_2 + i_2 - 1, r_3 + i_3 - 1)$. (We call $x[(i_1, i_2, i_3), (i'_1, i'_2, i'_3)]$ the $x[(i_1, i_2, i_3), (i'_1, i'_2, i'_3)]$ -segment of x .)

We now introduce a *k-neighborhood template A-type two-dimensional bounded cellular acceptor* (*A-2BCA(k)*), which is a main object of discussion in this paper.

Definition 2.2. Let A be the class of an automaton moving on a two-dimensional configuration. Then, an *A-2BCA(k)* M is defined by the 2-tuple $M=(R, B)$. R and B are said to be a *converter* and a *configuration-reader* in view of its property, respectively.

(1) R is a two-dimensional infinite array consists of the same finite state machines and is defined by the 6-tuple

$$M = (\mathbf{Z}^2, \mathcal{N}^2, K, \Sigma, \sigma, q_0),$$

① \mathbf{Z} is the set of all integer, and the finite state machines are assigned to each point of $\mathbf{Z}^2 (= \mathbf{Z} \times \mathbf{Z})$. The finite state machine situated at coordinates $(i, j) \in \mathbf{Z}^2$ is called the (i, j) -th *cell* and denoted by $A(i, j)$,

② $\mathcal{N}^2 (\subseteq \mathbf{Z}^2)$ represents the *neighborhood template* of each cell and $\mathcal{N}^2 = \{(i, j) \mid -1 \leq i, j \leq 1\}$,

③ K is a finite set of states of each cell and contains $q_{\#}$ (the boundary state) and q_0 (the initial state),

④ Σ is a finite set of input symbols ($\#\notin \Sigma$ is the boundary symbol),

⑤ $\sigma: K^9 \times (\Sigma \cup \{\#\}) \rightarrow 2^K$ is the *cell state transition function*. Let $q_{i,j}(t)$ be the state of the $A(i, j)$ at time t . Then $q_{i,j}(t+1) \in \sigma(q_{i-1, j-1}(t), q_{i-1, j}(t), q_{i-1, j+1}(t), q_{i, j-1}(t), q_{i, j}(t), q_{i, j+1}(t), q_{i+1, j-1}(t), q_{i+1, j}(t), q_{i+1, j+1}(t), a)$, where a is the symbol on the $A(i, j)$ at time t . If $q_{i,j}(t) = q_{\#}$, however, $q_{i,j}(t+1) = \{q_{\#}\}$ for each $(i, j) \in \mathbf{Z}^2$ and each $t \geq 0$.

(2) A set of input symbols of B is $K - \{q_{\#}\}$ (where $B \in A$). Intuitively, $M=(R, B)$ moves as follows, given a three-dimensional input tape $x \in \Sigma^{(m_1, m_2, m_3)}$ ($m_1, m_2, m_3 \geq 1$) (x is surrounded by the boundary symbol $\#$).

First, each cell $A(i, j)$ of $R(1 \leq i \leq m_1, 1 \leq j \leq m_2)$, reads each symbol on the first plane $x(i, j, 1)$ in the initial state q_0 , and all of the other cells read the boundary symbols $\#$'s in the boundary state $q_{\#}$'s at time $t=0$. Starting from this

condition, *R* keeps reading *x* according to the cell state transition function, and moving down the cell array by one plane, every time *R* reads one plane all.

Next, *B* starts to move regarding a two-dimensional configuration of *R* just after *R* finished reading *x* as a two-dimensional input tape and determines whether or not can accept the configuration. If *B* accepts it, *x* is said to be accepted by *M*. Let $T(M)$ be the set of all accepted three-dimensional tape by *M* (see Fig.2).

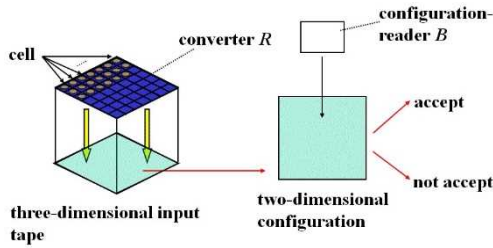
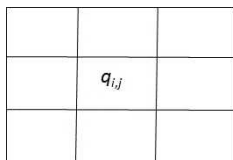


Fig.2. *A-2BCA(k)*.

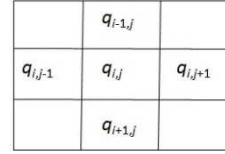
Definition 2.3. An *A-2BCA* in Definition 2.2 is called a *k*-neighborhood template *A-2BCA*. If ② and ⑤ of (1) in Definition 2.2 in replaced with ②' and ⑤' in Table 1, each *A-2BCA* is called a 1-neighborhood template *A-2BCA* and a 5-neighborhood template *A-2BCA*, respectively. From now on, we denote *k*-neighborhood template *A-2BCA* by *A-2BCA(k)* ($k \in \{1,5,9\}$) (see Fig.3).

	1-neighbor	5-neighbor
②'	$N^2 = \{(0,0)\}$	$N^2 = \{(i,j) \mid i + j \leq 1\}$
⑤'	<ul style="list-style-type: none"> • $\sigma: k \times \Sigma \rightarrow 2^k$ • $q_{i,j}(t+1)$ $\in \sigma(q_{i,j}(t), a)$ 	<ul style="list-style-type: none"> • $\sigma: k^5 \times \Sigma \rightarrow 2^k$ • $q_{i,j}(t+1)$ $\in \sigma(q_{i-1,j}(t), q_{i,j-1}(t),$ $q_{i,j}(t), q_{i,j+1}(t),$ $q_{i+1,j}(t), a)$

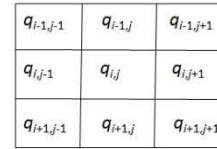
Table 1. 1- or 5-neighborhood template *A-2BCA*.



(a) 1-neighbor.



(b) 5-neighbor.



(c) 9-neighbor

Fig.3. Illustration of neighborhood templates.

Definition 2.4. If the image generated by σ in Definitions 2.2 and 2.3 is a singleton, the converter is said to be deterministic, and if not, it is said to be nondeterministic. An *A-2BCA(k)* ($k \in \{1,5,9\}$), which converter is deterministic (nondeterministic), is said to be a deterministic (nondeterministic) *A-2BCA(k)* and denoted by *A-2DBC A(k)* (*A-2NBC A(k)*).

We now consider the class of two-dimensional automata described by the following abbreviations as the class of the configuration-reader of *A-2BCA(k)* *A*.

In this paper, we assume that the reader is familiar with the definition of these automata. If necessary, see [1].

- $2\text{-DTM}^S(L(m))$... The class of $L(m)$ space-bounded deterministic two-dimensional Turing machine
- $2\text{-NTM}^S(L(m))$... The class of $L(m)$ space-bounded nondeterministic two-dimensional Turing machine
- DO^S ... The class of deterministic two-dimensional on-line tessellation acceptor
- DB^S ... The class of deterministic one-dimensional bounded cellular acceptor

For example $2\text{-DTM}^S(L(m))\text{-}2\text{DBC A}(9)$ represents such the class as its converter is deterministic and 9-neighborhood, and its configuration-reader is an $L(m)$ space-bounded deterministic two-dimensional Turing machine. Moreover, for any $A \in \{2\text{-DTM}^S(L(m)), 2\text{NTM}^S(L(m))\}$, for any $X \in \{D, N\}$ and for any $k \in \{1,5,9\}$, the class of set of all three-dimensional tapes accepted by *A-2XBCA(k)* is denoted by $L[A\text{-}2\text{XBC A}(k)]$. Especially, the class of all three-dimensional tapes accepted by *A-2XBCA(k)* whose input tapes are restricted to cubic ones is denoted by $L^C[A\text{-}2\text{XBC A}(k)]$, and the class of set of all square tapes accepted by *A* is denoted

by $L^S[A]$. In this paper, we discuss regarding the three-dimensional input tapes as cubic ones all.

3. Main Results

In this section, we discuss some properties of A - $2BCA(k)$'s whose configuration-readers are $L(m)$ space-bounded deterministic (nondeterministic) two-dimensional Turing machines. First, we show that a relationship between determinism and nondeterminism.

Theorem 3.1. For any $X \in \{D, N\}$, $L^C[2\text{-XTM}^S(m^2)\text{-}2DBCA(1)] = L^C[2\text{-XTM}^S(m^2)\text{-}2NBCA(1)]$.

Proof: From above definition, it is obvious that $L^C[2\text{-XTM}^S(m^2)\text{-}2DBCA(1)] \subseteq L^C[2\text{-XTM}^S(m^2)\text{-}2NBCA(1)]$. We below show that $L^C[2\text{-XTM}^S(m^2)\text{-}2NBCA(1)] \subseteq L^C[2\text{-XTM}^S(m^2)\text{-}2DBCA(1)]$. We now show only that $L^C[2\text{-DTM}^S(m^2)\text{-}2NBCA(1)] \subseteq L^C[2\text{-DTM}^S(m^2)\text{-}2DBCA(1)]$ (We can prove another case (i.e., $X=N$) in the same way). Now, let $M=(R, B)$ ($R=(Z^2, N^2, K, \Sigma, \sigma, q_0)$, $B=(K, Q, \Sigma, \Gamma, \delta, p_0, F)$) be some $2\text{-DTM}^S(m^2)\text{-}2NBCA(1)$ (see [1-5,8], if you would like to know about the 7-tuple constructs B). Then, we consider an $M'=(R', B')$ ($R'=(Z^2, N^2, K', \Sigma, \sigma', q_0')$, $B'=(K', Q, \Sigma, \Gamma, \delta', p_0', F')$) constructed as follows.

(1) Construction of R'

① $K' = 2^{(K \cdot \{q_\#\})} \cup \{q_\#\}$, $q_0' = \{q_0\}$.

② For any $a \in \Sigma$ and any $K'' \in K' - \{q_\#\}$,

$$\sigma'(K'', a) = \cup_{q \in K'} \sigma(q, a).$$

(2) Construction of B'

For any $p \in Q$ and any $K'' \in K' - \{q_\#\}$,

$$\delta'(p, K'') = \cup_{r \in K'} \delta(p, r).$$

Intuitively, we explain the movement of $M'=(R', B')$ constructed in this way. Let us suppose that a three-dimensional tape $x \in \Sigma^{(3)+}$ is given to M' . R' is one-neighborhood, so we can consider each cell of R' as usual one-dimensional finite automata. Then, each cell of R' moves to store all states that each corresponding cell of R can enter in each state at each time by using the well-known subset construction method (see (1)).

B' nondeterministically chooses only one state from each state of each cell of R' , and simulates the movement of B regarding the selected states as the input symbol. If B' can not accept the input, B' selects the next input and simulates the movement of B . From the way such as the above manner, B' checks the all input patterns, and if B' can accept one input, B' can accept the configuration of R' (see (2)).

It is clear that $T(M')=T(M)$ for $M'=(R', B')$ constructed in this manner. \square

Next, we show that there exists a language accepted by a $2\text{-DTM}^S(0)\text{-}2NBCA(1)$, but not accepted by any $2\text{-NTM}^S(L(m))\text{-}2DBCA(9)$ for any $L(m) = o(\log m)$.

Theorem 3.2. For any function $L(m) = o(\log m)$, $L^C[2\text{DTM}^S(0)\text{-}2NBCA(1)]$

$$-L^C[2\text{-NTM}^S(L(m))\text{-}2DBCA(9)] \neq \varphi.$$

Proof: Let $C = \{w_0 w_1 w_2 \cdots w_k \mid k \geq 1 \ \& \ \forall i (0 \leq i \leq k) [w_i \in \{0, 1\}^+ \ \& \ \exists j (0 \leq j \leq k) [w_0 = w_j^r]]\}$ (where, for any one-dimensional tape w , w^r denotes the reversal of w), and $T_1 = \{x \in \{0, 1, 2\}^{(3)+} \mid \exists m \geq 3 [l_1(x) = l_2(x) = l_3(x) = m \ \& \ x[(1, 1, m), (1, m, m)] \in C]\}$. Then, by using a technique similar to that in the proof of Lemma 2(1) in [3], we show that T_1 is accepted by $2\text{DTM}^S(0)\text{-}2NBCA(1)$, but not accepted by any $2\text{-NTM}^S(L(m))\text{-}2DBCA(9)$ for any $L(m) = o(\log m)$. \square

From Theorem 3.2, we get the following.

Corollary 3.1. For any $L(m) = o(\log m)$ and any $X \in \{D, N\}$, $L^C[2\text{-XTM}^S(L(m))\text{-}2DBCA(1)] \subsetneq L^C[2\text{-XTM}^S(L(m))\text{-}2NBCA(1)]$.

Remark 3.1. In Theorem 3 in [3], it has already shown that for any function $L(m)$ and any $k \in \{5, 9\}$, $L^C[2\text{-XTM}^S(L(m))\text{-}2DBCA(k)] \subsetneq L^C[2\text{-XTM}^S(L(m))\text{-}2NBCA(k)]$.

Finally, by using the well-known technique, we can show that there exists a language accepted by a $DO^S\text{-}2NBCA(1)$ and a $DB^S\text{-}2NBCA(1)$, but not accepted by any $2\text{-DTM}^S(L(m))\text{-}2DBCA(9)$ for any function $L(m) = o(\log m)$.

Theorem 3.3. For any function $L(m) = o(\log m)$, $(L^C[DO^S\text{-}2NBCA(1)] \cap L^C[DB^S\text{-}2NBCA(1)]) - L^C[2\text{-DTM}^S(L(m))\text{-}2DBCA(9)] \neq \varphi$.

4. Conclusion

In this paper, we showed some properties of A - $2BCA(k)$'s. We conclude this paper by giving the following problem. For any $X \in \{D, N\}$ and any $L(m)$ ($\log m \leq L(m)$ and $L(m) = o(m^2)$), $L^C[XTM^S(L(m))\text{-}2DBCA(1)] \subsetneq L^C[XTM^S(L(m))\text{-}2NBCA(1)]$?

References

1. K. Inoue and I. Takanami, A Survey of Two-Dimensional Automata Theory, *Information Sciences*, 55 (Elsevier Inc.,

- Amsterdam, Netherlands, 1991), pp.99-121.
2. M. Sakamoto, Three-Dimensional Alternating Turing Machines, *Ph.D. Thesis* (Yamaguchi University, Yamaguchi, Japan, 1999).
 3. H. Taniguchi, K.Inoue, and I.Takanami, *k-Neighborhood Template A-Type 2-Dimensional Bounded Cellular Acceptor*, *IECE of Japan Transactions D*, 69(3) (IECE, Tokyo, Japan, 1986), pp.291-301.

An efficient structure of organization with complete individual guidance

Mamoru Yoshimura*

Graduate School of Engineering, University of Miyazaki
E-mail: hm13056@student.miyazaki-u.ac.jp

Tsutomu Ito†

Graduate School of Engineering, Hiroshima University
E-mail: 0va71-2538f211n@ezweb.ne.jp

Makoto Sakamoto*

Department of Computer Science and System Engineering, Miyazaki University
E-mail: sakamoto@cs.miyazaki-u.ac.jp

Takao Ito†

Graduate School of Engineering, Hiroshima University
E-mail: itotakao@hiroshima-u.ac.jp

Yuji Shinano‡

Zuse Institute Berlin
E-mail: shinano@zib.de

Satoshi Ikeda*

Department of Computer Science and System Engineering, Miyazaki University
E-mail: bisu@cs.miyazaki-u.ac.jp

Abstract

In the previous paper, we reported on the efficient organizational shape under a setting called complete group guidance. In this paper, we investigate the shape of an efficient organization in the case of organizational communication in general, and report the existence of shapes that have not seen so far.

Keywords: Combinatorial Optimization, Efficient structure of organization, Weight policy, Complete guidance

1. Introduction

Recently, a mathematical model that can quantitatively evaluate the structure of the organization was proposed [1, 2, 3]. The basic idea of this model is as follows.

- 1) Represent a hierarchical organization as a rooted tree with its members as their nodes.
- 2) The effort of each member of the organization is represented as input / output working in the direction of the leaf node.

- 3) The output of each member is classified as internal contribution which is the effort to maintain the organization and external contribution which is the effort spent on achieving the purpose of the organization.
- 4) The evaluation value of the organization structure is the sum of external contributions of each member in the organizational structure.

In the paper [1,2], if the organization has only one evaluation measure, the hierarchical organization structure that maximizes the evaluation value is classified

* 1-1 Gakuen Kibanadai, Miyazaki, 889-2192, Japan

† 1-4-1 kagamiyama, Higashi-Hiroshima, 739-8527, Japan

‡ Takustraße 7 14195 Berlin-Dahlem, Germany

© The 2018 International Conference on Artificial Life and Robotics (ICAROB2018), Feb. 1-4, B-Con Plaza, Beppu, Oita, Japan

into the three types in Fig. 1 according to the capacity value of the member.

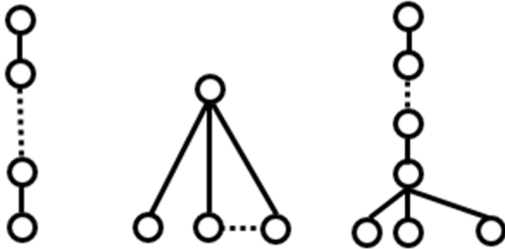


Fig. 1. 3 types of efficient tree

Any of these three have an undifferentiated organizational structure. This result means that the reason why modern organization are divided into multiple divisions is that each division shares a task consisting of different values.

Then in the paper [3], we modified the mathematical model of the paper [1, 2]. Major improvements are follows.

- 1) Generalization of organization's communication style.
- 2) Categorize the contribution of each member to internal and external.

The setting of the paper [1, 2] corresponds to the case where the form of communication is a complete group guidance and the external contribution other than the leaf node is set to 0.

In this paper, we report on the most efficient organizational shape of generalized communication style (external contribution is 0).

2. Mathematical Model

Suppose that $G = (V(G), E(G))$ is a graph. Throughout this paper, a graph is a finite undirected simple graph with order $n = |V(G)| (n > 2)$ and size as $m = |E(G)|$. For $u \in V(G)$, by $N(u) = \{v | \{u, v\} \in E(G)\}$, we denote the set of vertices adjacent to u , and call $\text{deg}(u) = |N(u)|$ the degree of $u \in V(G)$. For an arbitrary fixed rooted tree T with its root r and leaves $L(T)$, we denote

$$\text{deg}^*(s) = \begin{cases} \text{deg}(s) & \text{if } s \in \{r\} \cup L(T_r), \\ \text{deg}(s) - 1 & \text{otherwise.} \end{cases}$$

When $x_0 x_1 \dots x_n$ is the path on the tree graph T , we denote

$$T(x_0, x_n) \equiv x_0 x_1 \dots x_n.$$

Writing $x < y$ for $x \in T_r(r, y)$, we then define a partial ordering on $V(T_r)$, the tree-order associated with T_r .

Suppose that S and $\mathcal{A} (|\mathcal{A}| \geq 1)$ are finite sets. Throughout this paper, S is interpreted as the set of members of a given organization, which consists of s_0, s_1, \dots, s_n . And \mathcal{A} is the set of the evaluation measures.

We denote the set of rooted tree graphs with S as vertex set as $\mathcal{T}(S)$, and let each tree graph in $\mathcal{T}(S)$ correspond as an organization tree.

For a given S , we call $(S, \{\phi_i\}_{i \in \mathcal{A}})$ an evaluation system if

$$\phi_i: S \rightarrow \mathbb{R}^+ \equiv \{x \in \mathbb{R} | x > 0\} \text{ for } i \in \mathcal{A}.$$

We call $\phi_i(s)$ the personal ability of $s \in S$ with respect to an evaluation measure $i \in \mathcal{A}$.

In order for an organization to achieve its purpose to aim at, it is also necessary that appropriate instructions are transmitted to subordinates from superiors. Thus, for a fixed organization tree T_r with $V(T_r) = S$, we considered that the output of s is determined as the interaction of "ability value of subordinate $\phi(s)$ " and "accuracy of instruction from superior".

For the subordinate $s \in S$ who received instructions from his superior, it is necessary to transmit appropriate instructions to his own subordinates as superior, while s as subordinate carries out the instructions. For a given organizational structure tree T_r , we assume that the value of the input for subordinate $x > s$ with $x \in N(s)$ is obtained by multiplying its weight w_{sx}^i to appropriate instructions to his/her own subordinates as superior.

Weight range is

$$0 \leq w_{sx}^i \leq 1, \\ 1 \leq \sum_{x>s, x \in N(s)} w_{sx}^i \leq \text{deg}^*(s).$$

Let us set

$$\sum_{x>s, x \in N(s)} w_{sx}^i = 1.$$

This case corresponds to the organization model which $s \in S$ as superior instruct his/her subordinates individually. The style of communication at this time is called complete individual guidance.

Also,

$$\sum_{x>s, x \in N(s)} w_{sx}^i = \text{deg}^*(s) \Leftrightarrow w_{sx}^i = 1.$$

This case corresponds to the organization model which $s \in S$ as superior complete his/her indication to all subordinates with only one instruction.

Throughout this paper, we assume that $\{w_{sx}\}_{x>s, x \in N(s)}$ for $s \in S \setminus L(T_r)$ is a sequence depends only on $\text{deg}^*(s)$ and $i \in \mathcal{A}$. the selection that we can do is which weight to assign whom. We call the way of determination of a weights' policy. For any weights'

policy, we assume that if $\text{deg}^*(s) \geq \text{deg}^*(s')$ for $s, s' \in S$,

$$w_{sx_1} \geq w_{sx_2} \geq \dots \geq w_{sx_{\text{deg}^*(s)}}$$

and

$$w_{s'x'_1} \geq w_{s'x'_2} \geq \dots \geq w_{s'x'_{\text{deg}^*(s)'}}$$

then $\{w_{sx}\}_{x>s, x \in N(s)}$ and $\{w_{s'x'}\}_{x'>s', x' \in N(s')}$ satisfy

$$w_{sx_j} \leq w_{s'x'_j} (j = 1, 2, \dots, \text{deg}^*(s')).$$

We will evaluate the rooted tree T_r as organization model by

$$\Phi(T_r) = \sum_{i \in \mathcal{A}} \sum_{l \in L(T_r)} \sum_{s \in T_r(r, l)} w_{p(s)s}^i \phi_i(s).$$

Here, $p(s)$ represents the parent node of $s \in S$, and for convenience, $w_{p(r)r}^i = 1$. We call $\Phi(T_r)$ the ability value of T_r with respect to $(S, \{\phi_i\}_{i \in \mathcal{A}})$ for $\{w_{sx}\}_{s, x}$.

3. Results

Let us set $S = \{1, 2, 3, 4, 5, 6, 7\}$, and the interpretation of the members' ability values is shown in Table 1.

Table 1. Interpretation of the members' ability value

ability value	Interpretation.
Higher than 2	High
1 or more and 2 or less	Middle
Low than 1	Low

We considered three different settings of Setting 1 and Setting 2 and Setting 3.

3.1. Setting 1

The setting is

$$\begin{aligned} |\mathcal{A}| &= 1, \\ w_{sx} &= \frac{1}{\text{deg}^*(s)}, \\ \phi(1) = \phi(2) = \phi(3) &= 2.0, \\ \phi(4) = \phi(5) &= 1.2, \\ \phi(6) = \phi(7) &= 0.1. \end{aligned}$$

This case is a complete individual guidance. A superior instruct his/her subordinates individually. An efficient tree is Fig.2. Evaluation value is 6.42. Fig.2 is efficient shapes not found in Fig. 1.

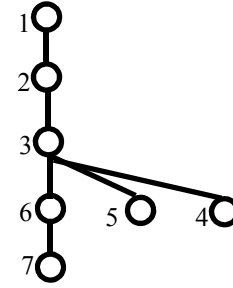


Fig. 2. One of the efficient tree in complete individual guidance in $|\mathcal{A}| = 1$.

3.2. Setting 2

The setting is

$$\begin{aligned} |\mathcal{A}| &= 1, \\ \{w_{sx}\}_{x>s, x \in N(s)} &= \{1.0, 1.0/2.0, \dots, 1.0/\text{deg}^*(s)\}, \\ \phi(1) = \phi(2) &= 2.0, \\ \phi(3) = \phi(4) = \phi(5) &= 1.2, \\ \phi(6) = \phi(7) &= 0.1. \end{aligned}$$

This case is a general weight policy setting. If $\text{deg}^*(s) = 4$, $\{w_{sx}\}_{x>s, x \in N(s)}$ is $\{1.0, 1.0/2.0, 1.0/3.0, 1.0/4.0\}$. An efficient tree is Fig.3.

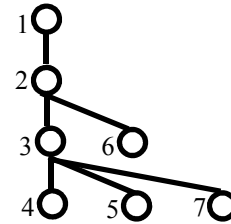


Fig. 3. One of the efficient tree in general communication style in $|\mathcal{A}| = 1$.

Evaluation value is 9.36, the weight is

$$\begin{aligned} w_{12} = 1.0, w_{23} = 1.0, w_{26} &= 0.5, \\ w_{34} = 1.0, w_{35} = 0.5, w_{37} &= 0.33. \end{aligned}$$

Fig.3. is efficient shapes not found in Fig. 1.

3.3. Setting 3

The setting is

$$\begin{aligned} \mathcal{A} &= \{a, b, c\}, \\ \{w_{sx}\}_{x>s, x \in N(s)} &= \{1.0, 1.0/2.0, \dots, 1.0/\text{deg}^*(s)\}, \\ \phi_a(1) = 2.0, \phi_b(1) = 2.0, \phi_c(1) &= 2.0, \\ \phi_a(2) = 2.0, \phi_b(2) = 0.2, \phi_c(2) &= 1.2, \\ \phi_a(3) = 1.2, \phi_b(3) = 2.0, \phi_c(3) &= 0.2, \\ \phi_a(4) = 1.2, \phi_b(4) = 2.0, \phi_c(4) &= 0.2, \\ \phi_a(5) = 1.2, \phi_b(5) = 2.0, \phi_c(5) &= 0.2, \\ \phi_a(6) = 0.2, \phi_b(6) = 0.2, \phi_c(6) &= 2.0, \end{aligned}$$

$$\phi_a(7) = 0.2, \phi_b(7) = 0.2, \phi_c(7) = 2.0.$$

This case is a general weight policy setting in the same Setting 2. An efficient tree is Fig. 4.

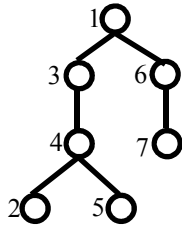


Fig. 4. One of the efficient tree in general communication style in $|\mathcal{A}| = 3$.

Evaluation value is 27.28, the weight is

$$w_{13} = 1.0, w_{216} = 0.5, w_{34} = 1.0, \\ w_{42} = 0.5, w_{45} = 1.0, w_{67} = 1.0.$$

Fig. 4. has a differentiated organizational structure which is two divisions.

4. Conclusion

Based on section 3, we found that the general shape of the efficient organization tree when the evaluation measure is only one is Fig. 5.

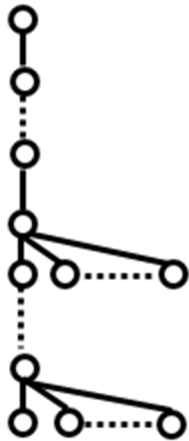


Figure 5. General shape of an efficient tree.

This means that it is generally shown that there is an efficient organization tree different from the efficient organization tree shown in the paper [1, 2].

Furthermore, from this result, it is inferred that the general efficient tree shape in the evaluation system with

multiple evaluation criteria will be as shown in Fig. 6.

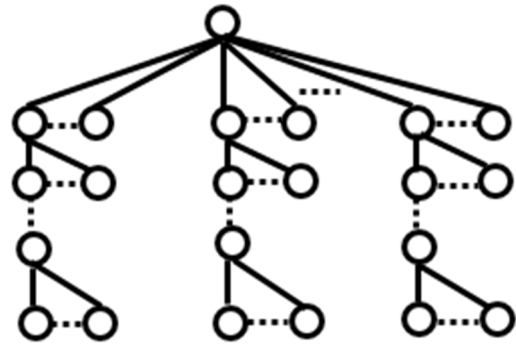


Figure 6. General form of an efficient tree in the evaluation system with multiple evaluation criteria.

References

1. S.Ikeda, T.Ito and M.Sakamoto, "Discovering the efficient organization structure: horizontal versus vertical", *Artificial Life and Robotics*, vol.15, 4, pp.478-481, 2011.
2. S.Ikeda, "An Efficient Structure of Organization", *International Interdisciplinary Workshop on Robotics, Ecosystem, and Management*, pp.72-78, 2010.
3. S.Ikeda, T.Ito, M.Sakamoto, T.Ito, "An Evaluation Model of Internal and External Contributions in Hierarchical Organizations", *International Journal of Mathematical Model and Methods in Applied Sciences*, Vol.9, pp.636-645, 2015.
4. Reinhard Diestel, "Graph Theory(Third Edition)", Springer, 2000.
5. Alvesson Mats, "A Flat Pyramid: ASymbolic Processing of Organizational Structure ", *International Studies of Management and Organization*, 19-4,5-23,1989/1990.

Consideration for the Possibility to the Tourism Support Contents by the Markerless AR Technology

Masamichi Hori¹

¹ Graduate School of Engineering, University of Miyazaki,
1-1 Gakuenkibanadai-nishi Miyazaki-shi, Miyazaki, 889-2192, Japan

Makoto Sakamoto^{2*}, Haruka Tsuboi², Koshiro Mitsuhashi³, Yukari Kodama³,
Takeshi Tanaka⁴, Mihoko Fukushima⁴, Chikashi Deguchi⁴, Masahiro Yokomichi²,
Masayuki Mukunoki², Kunihito Yamamori², Atsushi Iiboshi⁵

² Faculty of Engineering, University of Miyazaki,
1-1 Gakuenkibanadai-nishi Miyazaki-shi, Miyazaki, 889-2192, Japan

³ Miyazaki Multimedia Academy, 2-4-37 takachihodori Miyazaki-shi, Miyazaki, 880-0812, Japan

⁴ Faculty of Regional Innovation, University of Miyazaki,
1-1 Gakuenkibanadai-nishi Miyazaki-shi, Miyazaki, Miyazaki, 889-2192, Japan

⁵ Takachiho Muratabi Co., Ltd., 6604 ohazamukouyama takachiho-cho nishiusuki-gun,
Miyazaki, 882-1103, Japan

¹hm13061@student.miyazaki-u.ac.jp, ²sakamoto@cs.miyazaki-u.ac.jp, ³koshiro@multi-m.jp, ⁴deguchi@cc.miyazaki-u.ac.jp,
⁵muratabi@bz04.plala.or.jp (* Corresponding author)

Abstract

Currently, the tourism industry in Miyazaki prefecture has various problems, and various measures are taken. On the other hand, in 2016 virtual technology attracted much attention also on AR technology. We thought that through the AR technology experience, we could aim for an increase in tourists. Therefore, we will create new applications for smartphones using AR technology and aim for tourism support. First, prototype an application with markerless type and features for smartphones etc., and conduct experiments. As a result, there was improvement and it was not completed. However, it seemed possible to become an application that realizes tourism support.

Keywords: Promotion, Augmented reality, Sightseeing, Traditional culture.

1. Introduction

Due to the popularization of mobile terminals and the emergence of interactive technology, the tourism industry is changing drastically. In order to be a tourist destination that is attractive and win the competition, it is essential to improve unique experiences and value-added services. Miyazaki Prefecture · Takachiho Town is one of the most famous sightseeing places in Japan, but it has

various problems and countermeasures have been taken [1]. Especially, it is urgent to introduce new technology. In 2016 and 2017, the virtual technology called AR, VR, MR showed great excitement and it was the year when it became commonly recognized. Among them, AR is premised on the real world and expands it. It can be seen in a wide range of fields such as advertisement, tourism, education, entertainment [2].

© The 2018 International Conference on Artificial Life and Robotics (ICAROB2018), Feb. 1-4, B-Con Plaza, Beppu, Oita, Japan

In this study, we will link AR with the tourism industry and aim to solve problems related to sightseeing of Takachiho Town. Specifically, we aim to produce sightseeing applications that have map functions, AR functions linked with places, and so on. We urge the creation and re-visit of tourists by giving consumers who visit sightseeing spots an AR technology experience and offering "Omochikaeri (it means takeaways)" of tourist spots that reproduce and share their experiences in any environment. For that purpose, we will prototype contents for sightseeing support by using markerless type AR technology as a fundamental study, and evaluate and consider it.

2. Background

The tourist site that is the target of this study is Takachiho Town, Miyazaki Prefecture. Takachiho Town is located at the northernmost tip of Miyazaki Prefecture and the center of Kyushu. It has a beautiful natural treasure Takachiho Gorge, a great change due to the four seasons, and it is blessed with wonderful nature. Takachiho Gorge and Akimoto shrine are shown in Figure 1. The history of the town is old and there are reports that there were villages since about 4000 BC [3].

It is a place where God descended in Japanese mythology and is regarded as a land with considerably deep connection with the birth of Japan.

There are Kagura, born from the Amanoiwato legend of Japanese mythology, and land that is related to myths. In recent years as a power spot attracts attention from a wide range of age groups.

Especially the Akimoto area called Okutakachiho focuses on people living in the village. And they are doing have tourists experience village-specific experiences activities. Tourists can eat cuisine using regional ingredients, and can visit shrines and sacred trees standing in majestic nature. In 2016, it was selected as a good example of the "treasure of Discover rural mountain fishing village" designated by the Ministry of Agriculture, Forestry and Fisheries, and it is thought that tourists will further increase in the future [4].

However, as a change in the environment surrounding tourism, Miyazaki prefecture states that the population declines, the declining birthrate and aging, intensified competition, and the development of information and communication technology are left behind.

The number of sightseeing tourists is at a lower level [5] than at peak hours. Creating attractive sightseeing sites that you want to visit many times, and sending out information using media, ICT, and SNS are issues.



Fig.1 : Takachiho Gorge(left) and Akimoto shrine(right).

3. Literature review

According to Kangdon Lee's study [6], education and training is one of the areas where AR is mainly used. The breakdown is a wide range of area such as astronomy, chemistry, biology, mathematics and geometry. Another is business. Also application examples are wide, tourism, museums, games, industries, etc. What we can see from this is that the characteristics and maximum benefits of AR are to extend the information based on reality. It is useful to be able to visualize what is difficult to recognize by 3DCG and to approach it as a new cognitive method. AR is often combined with situation training." A Situational Training System for Developmentally Disabled People Based on Augmented Reality" [7] and "Augmented Reality Integrated Simulation Education in Health Care" [8] is a situation training system build up a reality-based level scenario and can repeat. The reality of the AR is linked with simulation education, and significant results are obtained by improving the cognitive ability.

"ToARist: An Augmented Reality Tourism App created through User-Centred Design" [9] is an AR application design with an emphasis on discussion with users. This study was revealed what visitors really wanted in the AR display, and how the AR navigation should be displayed.

"Augmented Reality and Gamification in Heritage museums " [10] conducted a definition and analysis of AR communication model and noise at the museum, and approached better experience. Furthermore, adding the game elements revealed that the depth of the AR system will increase.

As a study of the meta-viewpoint of introducing AR, there is " How can Tourist Attractions profit from Augmented Reality?" [11]. This study revealed the AR profit model through collaboration with stakeholders in the field and showed the possibility to introduce AR with minimal risk.

The impact on sightseeing in the AR application "Pokémon GO" which became one of the keywords in 2016 is great. According to the official report, the

collaboration event with Miyagi Prefecture in November 2016 mobilized about 100,000 people in 11 days, tourism consumption amount of 2 billion yen [12], the collaboration event with Tottori Prefecture in November 2017 mobilized about 89,000 people in 3 days, tourism consumption amount of 1.3 billion yen and PR effect 500 million yen [13]. Players visit sightseeing spots triggered by content capabilities, leading to attraction discovery and economic activities. It is a characteristic result of AR based on reality.

4. Fundamental study

In this study is fundamental one, a markerless type AR application is prototyped and compared with the marker type AR application, characteristics and behavior are compared. After that, we examine which one is actually suitable for applying to tourist spots. Through consideration, we show the definition of 'Omochikaeri' function which is unique point of application.

5. Methods

I will explain the method used to create the application.

5.1. 3DCG modeling

About 3DCG model production cooperate with vocational schools in Miyazaki prefecture. The 3DCG model to be produced is shown in Figure 2. The left is one of the gods in Japanese myths appearing in Amanoiwato legend. In addition, the 3DCG model of Miyazaki University's mascot character of the 3DCG model used this time is shown on the right side of figure.



Fig.2 : Bird's eye view of Tadarao(left) and Miyadaimoukun(right).

5.2. Unity3D

We chose Unity 3d as a software that can produce applications for mobile from the viewpoint of future development and application creation that is not bound by OS. Unity 3 d is an integrated game development

environment compatible with many platforms, and a variety of plug-ins accompanying it are also present.

5.3. Marker type AR and markerless type AR

The marker type is a technique for specifying the presentation position of the 3D CG model with a fixed pattern as an input. The markerless one is inputting a natural image (an image having a use other than a marker). An example is shown in figure 3. We'd like to run it as an application alone, and implement it on a mobile terminal, especially on a smartphone.



Fig3 : AR marker(left) and Natural image as a logomark(right).

6. Experiment and Result

We look at the characteristics and operation of marker type AR application that was used in previous study and markerless type AR application and compare them.

6.1. Development environment

We created the entire application using Unity 3 d and the Blender in 3D CG model. The mobile terminal used is an Android smartphone.

6.2. Comparative experiment

Figure 4 shows the operation results. When we read the target with both marker type and markerless type, applications presented the 3DCG model. When the natural image of the target is placed in the markerless camera, it keeps track of the model at high speed even if the terminal is moved intensely up and down, left and right, and continues to display the model.



Fig.4 : markerless type(left) and marker type(right).

7. Conclusion

In this study, we tried to make an application using Unity 3d. We confirmed the operation which is excellent in initial recognition and high follow-up performance in the markerless type. Since natural images are input, we think that it can fit in the landscape without incongruity by inputting pamphlets etc. in the tourist spots. Also, the cost of preparing markers by sightseeing spots is not required, so I think that it is suitable for introduction. In addition, through case studies of previous study and experiments, I felt the lack of many functions until actually applied to tourist spots.

8. Future plans

We plan to develop an integrated Takachiho tourism support application centering on markerless type AR technology. We plan about the 3DCD model display function of the attraction by loading the map and the function that can take virtual character and commemorative shooting when reading buildings and signboards. We also plan basic map functions and shop profit information that are considered convenient for visitors.

We plan "Omochikaeri" as one of the unique functions. This is a function that will become possible when visiting tourist resources, shrines and spots, it is an idea to unlock special AR content functions as benefits. One of them reproduces Kagura on hand. The aim is to have the opportunity to visit by telling Kagura that tourists actually saw in a user-friendly way of understanding easily.

However, in implementing these functions, it is important to closely discuss with stakeholders of tourist spots and questionnaire to visitors. Because AR technology extends the reality.

Acknowledgements

Miyazaki multimedia vocational school people are very busy, thank you hearty thank you for your cooperation in 3DCG modeling and advice etc. Also, the Miyazaki Tourism Convention Association, Inc., abc Corporation, Inc., Phoenix Seagaia Resort Co., Ltd., people in the Akimoto district who took care of me in the interview, other prefectures within the prefecture I would like to express my gratitude to all concerned parties in each municipality.

References

1. Heisei27 July Miyazaki Prefecture Tourism Promotion Plan ~ Toward revival of tourism miyazaki ~. [Online] Official website of Miyazaki Prefecture http://www.pref.miyazaki.lg.jp/kanko-suishin/kanko/miryoku/documents/21689_20160301163637-1.pdf (accessed 2017/12/1).
2. Takashi Kurida, Kiyoshi Kiyokawa, Takashi Okuma, "Fundamentals, Development and Practice of AR Technology", *Science Information Publishing*, 2015, pp 377-385.
3. Overview of Takachiho | Introduction / History of the town | administrative information | Takachiho cho [Online] Takachiho cho information official website. <http://www.town-takachiho.jp/administration/history/outline.html> (accessed 2017/12/1).
4. Takachiho Mura Council "Treasure of Discover Rural Farm Village (Mura)" was selected. | What's New | Takachiho-cho Tourist Association [Online] Takachiho cho information official website. <http://takachiho-kanko.info/news/detail.php?log=1479688433> (accessed 2017/12/1).
5. Miyazaki Prefecture tourist statistics survey result in Heisei27. [Online] Official website of Miyazaki Prefecture https://www.pref.miyazaki.lg.jp/kanko-suishin/kanko/miryoku/documents/26823_20161226163703-1.pdf (accessed 2017/12/1).
6. Kangdon Lee, "Augmented Reality in Education and Training", *Tech Trends* Vol56, No. 2, pp 13-21, 2012.
7. Tae-Young KIM, A Situational Training System for Developmentally Disabled People Based on Augmented Reality", *IEICE Transactions on Information and Systems* Vol.E96.D, No. 7, pp 1561-1564, 2013.
8. Kasey J. Carlson RN, MSN, MEd, David J. Gagnon MS. Kangdon Lee, "Augmented Reality Integrated Simulation Education in Health Care", *Clinical Simulation in Nursing*, Vol.12, No.4, pp 123-127, 2016.
9. Williams, M, Yao, KKK and Nurse, JRC et al., "ToARist: An augmented reality tourism app created through user-centred design.", *31st British Human Computer Interaction Conference*, 2017.
10. Ramy Hammady, Minhua Ma, Nicholas Temple, "Augmented Reality and Gamification in Heritage Museums.", *Serious Games*, Vol. 9894, pp 181-187, Springer, Cham, 2017.
11. Eleanor E Cranmer, M. Claudia tom Dieck, Timothy Jung, "How can Tourist Attractions profit from Augmented Reality?", *Augmented Reality and Virtual Reality - Empowering Human, Place and Business*, pp 21-32, Springer, Forthcoming, 2017.
12. About the number of tourists etc. of Pokèmon GO related events - Official website of Miyagi Prefecture. [Online] Miyagi Prefecture official website. <https://www.pref.miyagi.jp/release/ho20161219-6.html> (accessed 2017/12/1).
13. Number of participants in "Pokèmon GO Safari Zone in Tottori Sand Dunes" and Economic Effect. [Online] Tottori prefecture official website. <http://www.pref.tottori.lg.jp/271365.htm> (accessed 2017/12/1).

Fundamental Study on Tourism Support Using 3DCG

Haruka Tsuboi, Makoto Sakamoto*, Masamichi Hori, Yosuke Iriyama, Yuki Kai, Hazuki Watanabe

Faculty of Engineering, University of Miyazaki, 1-1 Gakuen Kibanadai Hishi

Miyazaki, Miyazaki 889-2192, Japan

E-mail: sakamoto@cs.miyazaki-u.ac.jp

Yu-an Zhang

Department of Computer Technology and Applications,

Qinghai University 810016 China

E-mail: zhangyuan198101092000@yahoo.co.jp

Atsushi Iboshi

Takachiho Muratabi Co., Ltd.,

6604 ohazamukouyama takachiho-cho nishiusuki-gun,

Miyazaki, 882-1103, Japan

E-mail: muratabi@bz04.plala.or.jp

Koshiro Mitsuhashi, Yukari Kodama

Miyazaki Multimedia Academy,

2-4-37 takachihodori Miyazaki-shi, Miyazaki, 880-0812, Japan

E-mail: koshiro@multi-m.jp

*(*Corresponding author, E-mail: sakamoto@cs.miyazaki-u.ac.jp)*

Abstract

Three-dimensional computer graphics (3DCG) is a technique of generating an image having a stereoscopic effect by converting an object in a virtual three-dimensional space into two-dimensional information. It is also possible to generate images that can not be distinguished from genuine objects using 3DCG. 3DCG is expected to be applied to visual expression very much. Currently it is expected to be applied in tourism. While being a photorealistic, we are aiming to make people interested by images from viewpoints that we can not normally see. In this thesis we will use 3DCG for sightseeing

Keywords: 3DCG, Blender, Unity

1. Introduction

The penetration rate of CG (computer graphics) in recent years has become remarkable. Currently, there are various examples of utilization such as movies and animation, various simulation and tourism projects, sales visuals and so on.

Also, as the Tokyo Olympic Games are held in 2020, the demand for tourism in Japan is getting bigger.

Accordingly, we believe that efforts towards tourism support are necessary even in local government units.

Therefore, we considered fundamental research of this moment, considering whether we can PR such as we do not exist by using CG technology for the rich nature and sightseeing spot of Miyazaki prefecture where we live.

In this research, we focused on "Takachiho-cho", which is known as a land with a connection to "Japanese mythology" among Miyazaki prefecture (Fig 1, 2).

As a goal, tourism support such as combining the created 3DCG model with real underwater images and aerial images, introducing rich nature as the main and historic tourist attractions.

© The 2018 International Conference on Artificial Life and Robotics (ICAROB 2018), Feb. 1-4, B-Con Plaza, Beppu, Oita, Japan

Takachiho-cho, however, has a problem of population decline due to the declining birthrate and aging population.

This line chart is the future population estimate of Takachiho-cho by the survey of the National Institute of Population and Social Security Research(Fig.3).

As you can see, the population tends to decline to the right every year.

Due to this population decline, it is presumed that there is great influence on the succession of traditional culture and tourism resources.

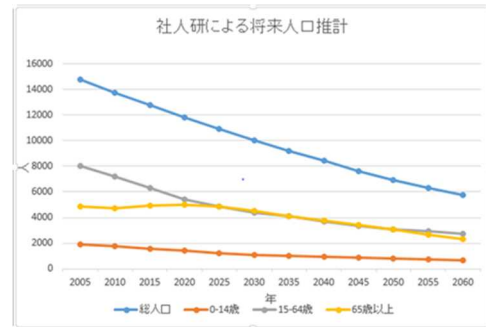


Fig.3: Population estimate



Fig.1: Amanoyasukawara



Fig.2: Takachihokyo

2. Principle

In recent years, CG has become more popular as a tool for revitalizing tourism projects. It has been making it possible to provide visitors with the experience gained by using CG, such as the power and atmosphere that can only be experienced locally, and the reproduction of environment and buildings lost in the past.

In this research, I am considering attracting nature as the main among them. From a person's point of view only the scenery lower than the mountain can be seen, but birds and insects can look down Takachiho from the viewpoint higher than that. Likewise the same thing can be said for aquatic creatures. Things that can not be seen from the usual point of view can be noticed by the good point that we have not noticed by looking from a different point of view. By thinking as a hawk's point of view, we could imagine what kind of living things are usually living, and thinking that Takachiho could be promoted from a different viewpoint than before, we tried out.[1][2]

3. Creation

This time I used Blender and Unity.

Blender creates animation models and animations.

Unity synthesized with the actual image using the model and animation created.

Both are software that can be operated sensuously, so we adopted it because it can be used easily and has high quality.

3.1. Modeling

First I will create a model of Hawk and a river fish at Blender. Figures 4 and 5 are created.

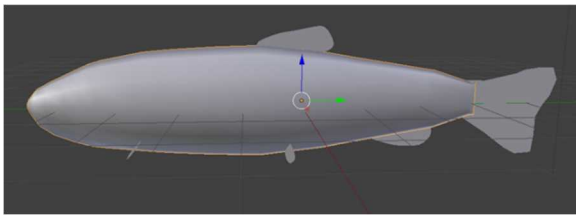


Fig.4: River fish model

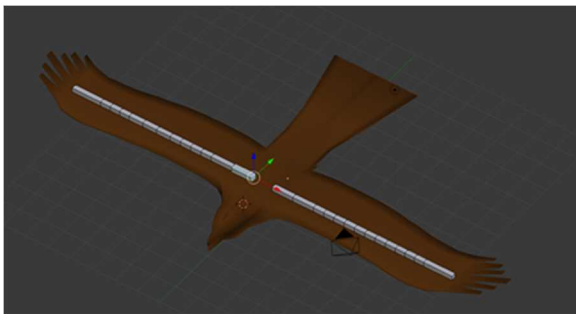


Fig.5: Hawk's model

3.2. Material setting

The material setting is done by mapping. This time UV mapping is executed. UV mapping is a part of texture mapping and texturing is stretched to a stereoscopically wrapped part without being stretched by applying a texture to the two-dimensional expanded view of the surface of the object. The result is shown in Figure 6.

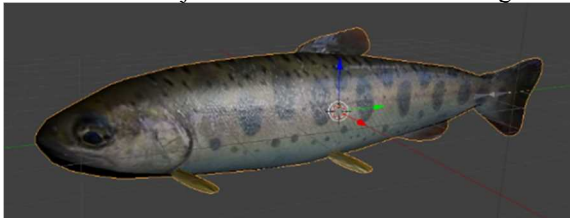


Fig.6: Fabrication of map by UV development

4. Result

The function implemented this time can move 3DCG (3 dimensional CG) model by user's keyboard operation. Although it is a function unsuitable for compositing with the picture taken beforehand, I thought that it would be interesting to have game properties instead of just flowing video, and I implemented it.

A part of the finally formed model and action is shown below (Fig. 7, 7).



Fig.7: Hawk combined with video

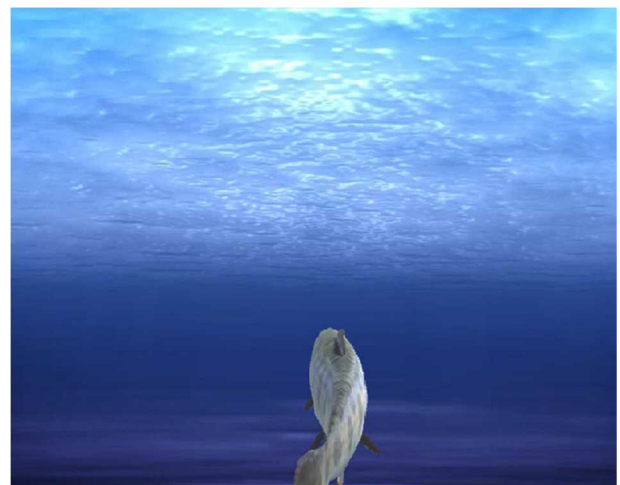


Fig.8: Fish combined with video

5. Discussion

In this research, we made a blogger and Unity based on the intention of composing CG of the falcon dancing in the sky of Takachiho in the sky photographed in drone, and creating a CG animation to PR for Takachiho .

Although river fish could not prepare actual underwater video for synthesis, I think that we could expand the range of video production with the function that we can actually move on ourselves.

Ultimately, since the video shot in advance is used for the composition of the video, it is necessary to incorporate the movement according to the video to the right place in the right place. Also, delicate light

adjustment must be considered. In addition, it is necessary to actually underwater and aerial photographs diversely, and investigate what type of photographing will be effective images.

6. Conclusion

In this research, from the viewpoint which is slightly different from the past, we have created images introducing the rich nature of Takachiho Town, historic sightseeing spots and people living there, and are investigating to link tourism support. In future, I think that it is possible to add "fun" to this tourism support by using Unity and incorporating game elements as one of the contents.

References

- [1] Kai Yuki, *Fundamental study on the description of river fish using CG*, graduation thesis of Information Systems Engineering, Faculty of Engineering, Miyazaki University, 2017
- [2] Yosuke Iriyama, *Approach on Tourism Support by Aerial Photography Using CG*, graduation thesis of Information Systems Engineering, Faculty of Engineering, Miyazaki University, 2017

Clustering Analysis Based on Improved Fuzzy C - Means Algorithm

Qiongqiong Hu,

*Department of Computer Technology and Applications,
Qinghai University 810016 China*

Yiyang Li,

*Department of Computer Technology and Applications,
Qinghai University, Xining 810016 China*

Yong Ge,

*School of Mechanical Engineering,
Qinghai University, Xining 810016 China*

Yu-an Zhang*,

*Department of Computer Technology and Applications,
Qinghai University 810016 China*

Qinglian Ma,

*Interdisciplinary Graduate School of Agriculture and Engineering,
University of Miyazaki, Miyazaki City 889-2192 Japan*

Makoto Sakamoto,

*Faculty of Engineering,
University of Miyazaki, Miyazaki City 810016 Japan*

Abstract

Cluster analysis is one of the most important technologies in the field of data mining, and it is also a hot topic in academic research. So far, it has made great achievements in theory and method, and plays an important role in data analysis in various fields. The fuzzy C-means algorithm (FCM) maintains the simplicity of its thinking, the time complexity is close to linear, and it is efficient and scalable for large-scale data mining. Particle Swarm Optimization (PSO) is an optimization tool with global optimization ability, and the group intelligence is formed by the interaction between particles in the group, and the optimal result is found by the intelligence. However, with the deepening of algorithm research, its research prospects and application areas are increasingly bright and compelling.

Keywords—particle swarm optimization algorithm, clustering analysis, fuzzy C - means algorithm.

I. INTRODUCTION

Clustering analysis is one of the most important technologies in the field of data mining and plays an important role in data analysis in all fields [1]. Clustering is an unsupervised and efficient learning method, and its data is similar and unique to each molecule, so it can be classified according to its different characteristics. At present, clustering analysis has been widely used in many aspects, and with the development of science technology has been more and more attention. In essence, clustering belongs to the local search algorithm, which uses an iterative climbing technique to find the optimal solution [5]. Therefore, the traditional clustering algorithm has two fatal problems: First, with large-scale data processing, the original algorithm fails or takes a lot of time, the second is easy to fall into the local minimum.

Among them, the fuzzy C-means algorithm (FCM) keeps its thinking simple and easy. The time complexity is close to linear, and it has high efficiency and scalability for large-scale data mining [2]. After years of development of particle swarm optimization algorithm [3], its optimization speed, quality and algorithmic robustness has been greatly improved. However, most of the current research focused on the realization, improvement and application of algorithms [6]. At present, there are still many unsolved problems in the study of particle swarm algorithm: (1) stochastic convergence analysis; (2) determination of algorithm parameters; (3) discrete / binary particle swarm optimization; (4) the use of different problems to design a corresponding effective algorithm; (5) Should be committed to complement and extend the algorithm with other algorithms or techniques to solve the problem of PSO easy to fall into the local optimum [4].

*Corresponding author: Yu-an Zhang, e-mail:2011990029@qhu.edu.cn

II. THE PSO ALGORITHM

The basic idea of the particle swarm algorithm is that the first step is to initialize a group of random solutions to obtain the particles in the particle swarm. The second step is to find the optimal value in the algorithm by repeating the result of repeated feedback. At each repetition the two optimal values of *pbest* and *gbest* are obtained according to Equation 1 and Equation 2 in the feedback. Fig.1 shows the PSO algorithm flow chart.

$$V_i = v_i * w + rand(1) * c_1 * (rand(1) * c_2 * (gbest[i] + pbest[i] - present[i])) \quad (1)$$

$$Present[i] = present[i] + v[i] \quad (2)$$

V_i is the velocity value of particle *i*, *present [i]* is the position of the current particle *i*, *w* is the inertia weight, c_1 , c_2 is the learning factor, *rand (1)* is between (0,1) random number.

The execution flow of the PSO can be described as follows:

1. Determine the population size of the particle N, determine the maximum number of iterations, randomize the velocity and position of the particles;
2. Calculate the fitness value of each particle according to the fitness function;
3. The current fitness value of each particle is taken as the initial optimal value of the particle, and the whole optimal value is obtained by comparing all the initial optimal values.
4. Update the particle's position and speed according to the update formula;
5. Calculate the fitness value of the particles in the new population;
6. Compare the new fitness value of each particle with the previous optimal fitness value of the particle. If it is good, update the individual optimal value of the particle, otherwise it will not be updated.
7. The new fitness value of each particle and the overall fitness value of the comparison, if the good, then update the overall fitness value, or not updated;
8. Repeat steps 5 through 7 until a certain number of iterations is satisfied.

gbest and *pbest*, that is, the individual optimal value and the population optimal value, in each iteration process, the two optimal values will be repeated according to the *Formula 1* and *Formula 2*. The advantage of PSO is that the concept is relatively simple, relatively easy to achieve, while the need to adjust the parameters less, and the convergence rate. The basic features of the PSO algorithm can be summarized as follows: Intelligent search; progressive optimization; black box structure; implicit parallelism; flexibility; global optimization; robustness; self-organization.

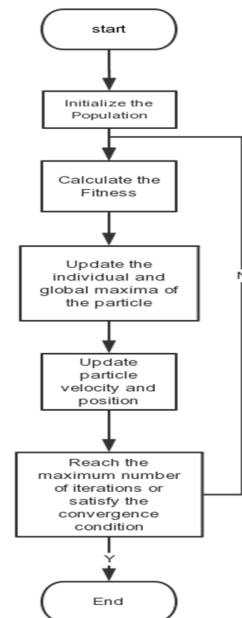


Fig. 1. PSO optimization flow chart

III. CLUSTER ANALYSIS

A. The basic concept of cluster analysis

Clustering is a process of sorting according to data characteristics. If a class as a group, you can cluster as a data compression form. Clustering can be more specific image is defined as follows: Data space in the data set D in the number of data points is n, each data points have d attributes, then each data point can be expressed as $X_i = (x_{i1}, x_{i2}, \dots, x_{id})$, the entire data set can be seen as a matrix of ND dimensions. By clustering the data set, we can get k different clusters C_i ($i = 1, 2, \dots, k$). In the process of clustering, it is possible that some data points do not belong to any clusters. These data points are called outliers or noise points.

B. FCM (Fuzzy C-means Algorithm) clustering algorithm

The fuzzy C-means algorithm (FCM) is an improvement of the general C-means algorithm. The ordinary C-means algorithm is hard for the data partitioning, and FCM is a flexible fuzzy partition.

First, the concept of membership function is described. The membership function is a function that represents the degree of an object x belonging to the set A, usually denoted by $\mu_A(x)$, whose range of arguments is all the objects that may belong to the set A (ie, all the points in the space in which the set A is located) The value range is $[0,1]$, that is, $0 \leq \mu_A(x) \leq 1$. $\mu_A(x) = 1$ means that x is completely subordinate to set A, which is equivalent to $x \in A$ on the traditional set concept. A membership function defined on space $X = \{x\}$ defines a fuzzy set A, or a fuzzy subset defined on the universe $X = \{x\}$. For the finite objects $X_1, X_2, X_3, \dots, X_n$, the fuzzy set can be expressed as:

$$A = \{\mu_A(x_i), x_i | x_i \in X\} \tag{3}$$

Through the concept of fuzzy set, in the problem of cluster analysis, we can treat clusters clustered by clustering as a fuzzy set, and all membership points belong to the group $[0, 1]$. In the fuzzy C-means clustering algorithm, it divides n data into c data sets and finds the center on the basis of this, so that the value function of the non-similarity index is minimized. However, for each data set membership, its sum is equal to 1:

$$\sum_{i=1}^c \mu_{ij} = 1, \quad \forall j = 1, \dots, n \tag{4}$$

then, at this time FCM value function (or objective function) is:

$$J(U, c_1, \dots, c_c) = \sum_{i=1}^c J_i = \sum_{i=1}^c \sum_j^n \mu_{ij}^m d_{ij}^2 \tag{5}$$

Where μ_{ij} is between 0 and 1; c_i is the clustering center of fuzzy group I, $d_{ij} = \|c_i - x_j\|$ is the Euclidean distance between the i_{th} cluster center and the j_{th} data point; Is a weighted index. By constructing the Formula 6, we obtain the necessary conditions for the Formula 5 to reach the minimum value:

$$\begin{aligned} \bar{J}(U, c_1, \dots, c_c, \lambda_1, \dots, \lambda_n) &= J(U, c_1, \dots, c_c) + \sum_{j=1}^n \lambda_j (\sum_{i=1}^c \mu_{ij} - 1) \tag{6} \\ &= \sum_{i=1}^c \sum_j^n \mu_{ij}^m d_{ij}^2 + \sum_{j=1}^n \lambda_j (\sum_{i=1}^c \mu_{ij} - 1) \end{aligned}$$

here, $\lambda_j, j = 1$ to n , is the Formula 4 of the n constraints of the Lagrangian multiplier. Generate guidance for all input parameters. It can be seen that the necessary condition for the Formula 5 to be minimized is:

$$c_i = \frac{\sum_{j=1}^n \mu_{ij}^n x_j}{\sum_{j=1}^n \mu_{ij}^m} \tag{7}$$

$$\mu_{ij} = \frac{1}{\sum_{k=1}^c (\frac{d_{ij}}{d_{kj}})^{2/(m-1)}} \tag{8}$$

that the fuzzy C-means clustering algorithm is essentially a repetitive feedback process. When running in a batch mode, the FCM algorithm uses the following steps to determine the clustering center c_i and the membership matrix $U[I]$:

Step 1: Initialize the membership matrix U This value requires a random number in the range 0 to 1 to satisfy the constraint in Equation 4.

Step 2: Calculate c clustering centers $c_i, i = 1, \dots, c$ using Formula 7

Step 3: Calculate the value function according to *Formula 5*. According to the value of the function to determine whether the algorithm to stop.

Step 4: Use the *Formula 8* to compute the new *U* matrix. Return to step 2. The algorithm can also initialize the cluster center and then repeat it.

1) The Achievement of FCM Algorithm

Where *x* is the 400 points from 0 to 1, that is, 400 sets of data, using the *Rand ()* function in excel. By running the algorithm, the data of the four types of data and the five types of data are realized, and the value function (objective function) *J_b* of the corresponding non-similarity index is obtained. The following related images are generated using MATLAB 7.0, and the different shapes in the picture represent different clusters. Each population center has a triangle that is used to represent the cluster center. In *Fig.2*, the four small circles It is shown that the number of groups is 4 clusters, and the five small circles in *Fig.3* show that the number of groups is 5 clusters, and the *J_b* values are compared to prove the enhancement of the improved algorithm.

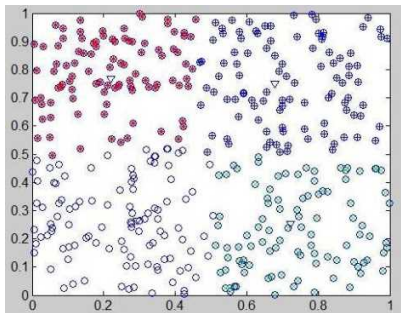


Fig. 2. When *cn* = 4, *J_b* = 3.3191 (result of a random experiment)

C. Apply the particle swarm algorithm to fuzzy C-means clustering

Through the above we can see that the FCM clustering in the processing of 400 sets of data, the implementation process is in the gradient method of decline, very rigid, step by step the

© The 2018 International Conference on Artificial Life and Robotics (ICAROB 2018), Feb. 1-4, B-Con Plaza, Beppu, Oita, Japan

implementation process will not record each of the optimal solution steps will be achieved on the line Error stops, and outputs the objective function. Based on the limitations of FCM algorithm, it is easy to fall into the local optimal solution. Therefore, it is considered that PSO will replace the gradient descent method in FCM and change it to iterative calculation. This advantage is that the whole algorithm is advancing in the optimal solution, which is more conducive to finding the optimal solution. Although a large number of calculations are added, the similarity in the group is improved, the non-similarity is reduced, and the *jb* value is optimized.

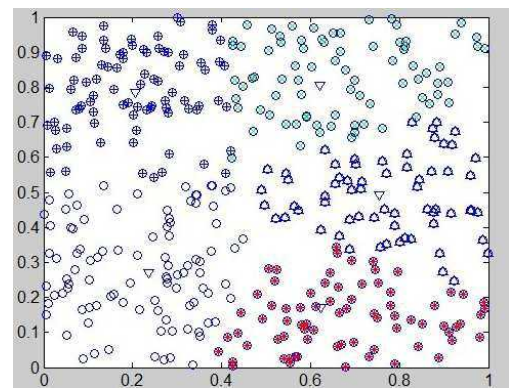


Fig. 3. When *cn* = 5, *J_b* = 2.0944 (a random result)

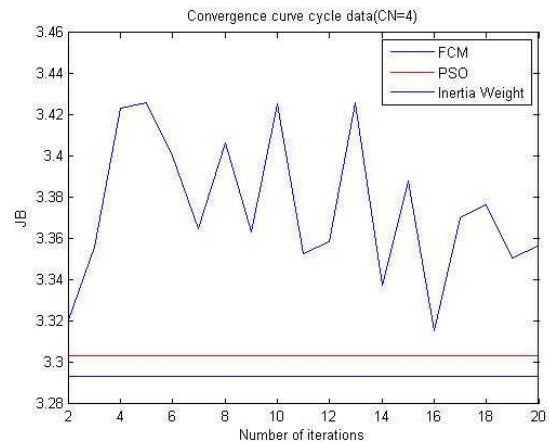


Fig. 4. Under the condition of *CN* = 4, the *J_b* value curve under different strategies ((FCB represents the fuzzy C-means algorithm,

PSO represents the idea of integrating the particle swarm algorithm in FCM, and the Inertia Weight represents the linearly decreasing inertia weight))

D. Apply linear inertia weighting strategy

Taking into account the optimization in this hope that the early have a higher global search capabilities, and later have a higher open capacity to speed up the convergence rate, so the value of inertia weight should be diminishing, and therefore on the basis of the initial improvement plus the decreasing linear weight, the inertia weight value is no longer used with a fixed value of 1, and it is set to a weight drop between 0.9 and 0.4.

Note: In order to describe the convenience in the form, the improvement refers to: only the use of FCM, the initial improvement refers to: FCM in the integration of the idea of particle swarm algorithm; re-improvement refers to: the initial improvement on the basis of the use of Linearly decreasing inertia weight values. The following description has the same meaning.

The above two graphs show that the improved J_b value is stable and the value is small, which converges to 3.2934 and 2.0811, respectively, when the program is run for 2 to 20 times and the average of the J_b values is obtained.

TABLE I
CONVERGENCE CURVE CYCLE DATA(CN=4)

Cycle-index	Before improvement	First improvement	Secondary improvement
2	3.319930289	3.30345825	3.293458078
3	3.355932514	3.303458248	3.293458177
4	3.42322518	3.303458172	3.293458117
5	3.426067281	3.303458416	3.293458145
6	3.400340325	3.303458182	3.293459015
7	3.364774648	3.303458318	3.293459013
8	3.406441959	3.30345819	3.293458177
9	3.363434596	3.303458244	3.293458196
10	3.425287692	3.303458303	3.293458745
11	3.352790831	3.303458203	3.293458676
12	3.358763164	3.303458242	3.29345866
13	3.426013215	3.303458326	3.29345836
14	3.33766005	3.303458286	3.293458688
15	3.388138626	3.303458241	3.293458702
16	3.315347435	3.303458217	3.293458521
17	3.370346834	3.30345827	3.293458323
18	3.376711892	3.303458259	3.293458509
19	3.350576588	3.303458256	3.293458746
20	3.3567382	3.303458276	3.293458488

TABLE II
CONVERGENCE CURVE CYCLE DATA(CN=5)

© The 2018 International Conference on Artificial Life and Robotics (ICAROB 2018), Feb. 1-4, B-Con Plaza, Beppu, Oita, Japan

Cycle-index	Before improvement	First improvement	Secondary improvement
2	2.116946479	2.091145987	2.081188193
3	2.127751484	2.091163385	2.081261095
4	2.114908503	2.091140444	2.081247198
5	2.123793236	2.091163526	2.081226471
6	2.118510332	2.091142244	2.0812091
7	2.116134805	2.091163586	2.081188193
8	2.108827784	2.091180206	2.081193212
9	2.107951404	2.091192388	2.081185936
10	2.110614058	2.091165532	2.081183326
11	2.11809571	2.091161191	2.081178895
12	2.127541954	2.091169919	2.081189653
13	2.115151641	2.091148045	2.08119233
14	2.113399393	2.091161057	2.081160813
15	2.109794086	2.09116062	2.081184913
16	2.109062738	2.09116664	2.081197084
17	2.129499201	2.091152719	2.081190877
18	2.120138722	2.091167363	2.081191144
19	2.110598647	2.091155037	2.081188943
20	2.115272508	2.091170088	2.081193307

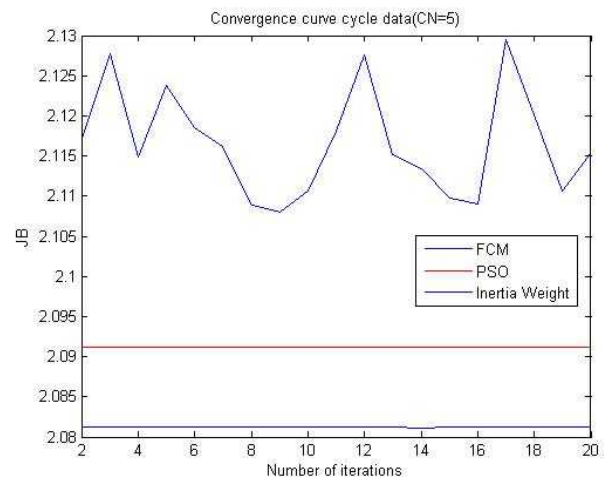


Fig. 5. Under the condition of CN = 5, the J_b value curve under different strategies ((FCB represents the fuzzy C-means algorithm, PSO represents the idea of integrating the particle swarm algorithm in FCM, and the Inertia Weight represents the linearly decreasing inertia weight))

IV. CONCLUSION AND PROSPECT

In this paper, the main goal is to achieve the combination of particle swarm optimization and clustering analysis, so as to optimize the clustering analysis algorithm and optimize it by introducing PSO algorithm. Finally, the improved algorithm is proved on the convergence curve is superior to the original algorithm. With the advent of large data age, large data

analysis in the future will be more and more people's attention. The intelligent, diversity, good self-service checkability and adaptability of the group intelligence theory will bring great prospects for the common development of particle swarm optimization and clustering algorithm.

Acknowledgements

This work is supported by Natural Science Foundation of China(No.61640206); Chunhui Research Program from Ministry of Education (Z2016082,Z2015050) ; China Scholarship Council (CSC:201608635010); Youth Foundation of Qinghai University(No.2014-QGY-30).

1. Lect. Shital P. Bora. Data Mining and Ware Housing[C]//3rd International Conference on Electronics Computer Technology(ICECT), Kanyakumari, 2011, 1:15.
2. M. Kholghi, H. Hassanzadeh, M. R. Keyvanpour, Classification and Evaluation of Data Mining Techniques for Data Stream Requirements[C]//International Symposium on Computer Communication Control and Automation (3CA), Tainan, 2010, Vol.1: 474-478.
3. Song Z, Chen J, Zheng B. A Multi-Objective Optimization Evolutionary Algorithm with Multiple Indicators Enhanced[J]. *Journal of South-Central University for Nationalities* (Natural Science Edition), 2011, 30:89-93.
4. Jianguo Chen, Zhongshan Song, Bojin Zhenget al. A Multi-objective Optimization Evolutionary Algorithm With Better Performances on Multiple Indicators *International Symposium on Intelligent Computation and Application ISICA 2010* 2010:47-56.
5. Vanden Bergh F. An analysis of particle swarm optimizer[C]. *Proceedings of the 1998 conference of Evolutionary computation* Piscataway IEEE Press 1998:67-63.
6. Luo Huilan, WEI Hui. Clustering Algorithm for Mixed Data Based on Clustering Ensemble Technique[J]. *Computer Science*, 2010(11):234-238.

References

© The 2018 International Conference on Artificial Life and Robotics (ICAROB 2018), Feb. 1-4, B-Con Plaza, Beppu, Oita, Japan

Robot Manipulator Arm Inverse Kinematics Analysis by Jacobian *

Sun Oh Park, †

Department of Mechanical Engineering, Pusan National University 2, Busandaehak-ro 63beon-gil, Geumjeong-gu, Busan, 46241, Rep. of KOREA

Jin Gon Yoon

Department of Mechanical Engineering, Pusan National University 2, Busandaehak-ro 63beon-gil, Geumjeong-gu, Busan, 46241, Rep. of KOREA

Min Gyu Jung

Department of Mechanical Engineering, Pusan National University 2, Busandaehak-ro 63beon-gil, Geumjeong-gu, Busan, 46241, Rep. of KOREA

Min Cheol Lee‡

Department of Mechanical Engineering, Pusan National University 2, Busandaehak-ro 63beon-gil, Geumjeong-gu, Busan, 46241, Rep. of KOREA

E-mail: sunoh425@pusan.ac.kr, y1k1000@pusan.ac.kr, aha0075@naver.com, mcllee@pusan.ac.kr

Abstract

There are three methods for solving inverse kinematic that are algebraic, geometric and numerical. The advantage of algebraic and geometric method is that can analyze exactly but these two methods are not only difficult to analysis but also need to recalculate when DOFs of a robot arm or DH-parameters are changed and increased. That is why this paper will present how to approach numerical method by Jacobian in place of previous two methods. The Jacobian based numerical method can easily solve any DOF and DH-parameter except singular point problem. Therefore, Jacobian based solution for solving inverse kinematics of 7-DOFs robot arm is introduced. A method to avoid singular point by using condition number is introduced. In the future, we will adapt this result to 7DOF dual robot arm and then compare our numerical method and real system

Keywords: Inverse Kinematics, Jacobian, Singular Point, 7-DOF Robot.

1. Introduction

For controlling robot manipulator, each joint angle at a desired position and orientation of the end-effector should be obtained when the manipulator moves to follow a desired trajectory, which is inverse kinematics problem. The inverse kinematics can be solved analytically and numerically. Analytical methods include

geometric method and algebraic method[1][2]. A numerical method is iterative method. Otherwise, if Jacobian based on differential motion is obtained, inverse kinematics can be solved by using differential motion relation between robot frame and hand one. The advantage of analytical methods quickly finds a correct solution, but it is difficult to find a solution according to increasing of DOF. On the other hands, the Jacobian

based solution inverse needs time for calculating, but this method is adapted not only high degree of freedom(DOF) but also DH-parameter change. In this research, the robot manipulator has redundancy with 7-DOFs that is why Jacobian based inverse kinematic solution is introduced.

2. Concept of using Jacobian

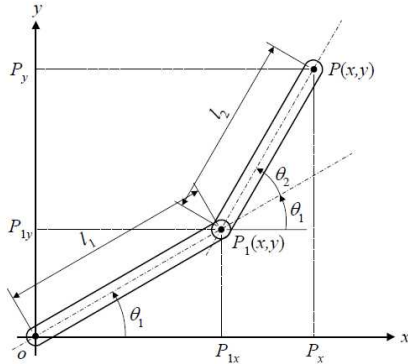


Fig. 1. This is 2-DOFs model to approach concept of Jacobian

$$P = \begin{bmatrix} x \\ y \end{bmatrix} = \begin{bmatrix} l_1 C_1 & l_2 C_{12} \\ l_1 S_1 & l_2 S_{12} \end{bmatrix} \quad (1)$$

$$dP = \begin{bmatrix} dx \\ dy \end{bmatrix} = J d\theta \quad (2)$$

$$= \begin{bmatrix} -l_1 S_1 - l_2 S_{12} & -l_2 S_{12} \\ l_1 C_1 - l_2 C_{12} & l_2 C_{12} \end{bmatrix} \begin{bmatrix} d\theta_1 \\ d\theta_2 \end{bmatrix} \quad (2)$$

$$P(i + 1) = P(i) + dP = P(i) + Jd\theta \quad (3)$$

$$d\theta = \frac{\theta_{obj} - \theta_{ini}}{n} \quad (4)$$

Where n is divided number and i is each step from 1 to n.

The Jacobian[3] matrix is the matrix of all first order partial derivatives. If each angle θ is decided, the object angles can be reached to goal position P by using Jacobian method. Like this method, each angle is calculated when initial position and object position are decided.

$$d\theta = \begin{bmatrix} d\theta_1 \\ d\theta_2 \end{bmatrix} = J^{-1} dP \quad (5)$$

$$= \frac{1}{\det(J)} \begin{bmatrix} l_2 C_{12} & l_2 S_{12} \\ -l_2 C_{12} + l_1 C_1 & -l_2 S_{12} - l_1 S_1 \end{bmatrix} \begin{bmatrix} dx \\ dy \end{bmatrix} \quad (5)$$

$$dP = \frac{P_{obj} - P_{ini}}{n} \quad (6)$$

$$\theta(i + 1) = \theta(i) + d\theta = \theta(i) + J^{-1} dP \quad (7)$$

So, each angle θ can be computed when desired position is decided.

3. Robot model and D-H parameter

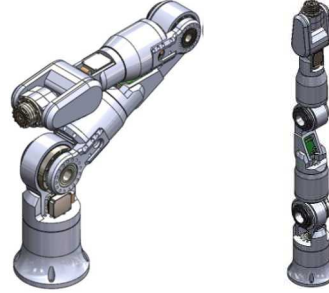


Fig. 2. Robot model

Table 1. The D-H parameter table

Joint	θ (°)	d (mm)	a (mm)	α (°)
1	θ_1^*	278	0	90
2	θ_2^*	0	0	-90
3	θ_3^*	425	0	90
4	θ_4^*	0	0	-90
5	θ_5^*	326	0	90
6	θ_6^*	0	0	-90
7	θ_7^*	171	0	0

*: variable rotation angle

θ is rotation of z-axis, d is distance of z-axis, a is distance of x-axis and α is rotation of x-axis. The following equation can be derived using DH parameter.

4. Numerical approach about 7-DOFs model

Now, considering the 7-DOFs case. When a coordinate system is defined, coordinator can be represented by 3 positions and 3 rotation angles(orientation).

$$\begin{bmatrix} dx \\ dy \\ dz \\ d\theta_x \\ d\theta_y \\ d\theta_z \end{bmatrix} = [J] \begin{bmatrix} d\theta_1 \\ d\theta_2 \\ d\theta_3 \\ d\theta_4 \\ d\theta_5 \\ d\theta_6 \\ d\theta_7 \end{bmatrix} \quad (8)$$

The 6-coordinator representation are composed Jacobian J and finite difference angle $d\theta$. So, considering 7-DOFs case, Jacobian has 6×7 matrix. Angles are desired to get solution θ to reach object

position and orientation. Therefore, the equation is writing on the below it.

$$\begin{bmatrix} d\theta_1 \\ d\theta_2 \\ d\theta_3 \\ d\theta_4 \\ d\theta_5 \\ d\theta_6 \\ d\theta_7 \end{bmatrix} = [J_{7 \times 6}^{-1}] \begin{bmatrix} dx \\ dy \\ dz \\ d\theta_x \\ d\theta_y \\ d\theta_z \end{bmatrix} \quad (9)$$

Before calculating this equation, J^{-1} is must calculated from J , but J is not square matrix so it is not possible to compute inverse matrix operation. Therefore, Pseudo concept is needed to solve inverse Jacobian matrix

$$(JJ^T)(JJ^T)^{-1} = I \quad (20)$$

$$J_{6 \times 7} [J_{7 \times 6}^T (J_{6 \times 7} J_{7 \times 6}^T)^{-1}] = JJ_{7 \times 6}^* = I \quad (31)$$

Where $J_{7 \times 6}^*$ is new inverse matrix.

$J_{7 \times 6}^*$ is obtained from Pseudo concept. The concept of Pseudo is to compute the inverse of a square matrix using transpose matrices.

Of course, Jacobian matrix is necessary when calculate $J_{7 \times 6}^*$ matrix, so that the Jacobian is considered how to make correct form. The Jacobian matrix can be made next concept.[4][5][6]

$$P_0^n = P_0^{i-1} + R_0^{i-1} P_{i-1}^n \quad (12)$$

$$O_n - O_{i-1} = R_0^{i-1} P_{i-1}^n \quad (13)$$

$$\dot{P}_0^n = R_0^{i-1} \frac{d}{dt} P_{i-1}^n \quad (14)$$

$$\dot{P}_{i-1}^n = \dot{q}_i k \times P_{i-1}^n \quad (15)$$

$$\dot{P}_0^n = \dot{q}_i z_{i-1} \times (O_n - O_{i-1}) \quad (16)$$

$$\frac{\partial P}{\partial q_i} = z_{i-1} \times (O_n - O_{i-1}) \quad (17)$$

$$J = \begin{bmatrix} z_0 \times (o_7 - o_0) & z_1 \times (o_7 - o_1) & \dots & z_6 \times (o_7 - o_6) \\ z_0 & z_1 & \dots & z_6 \end{bmatrix} \quad (18)$$

$$z_0 = \begin{bmatrix} 0 \\ 0 \\ 1 \end{bmatrix}, z_1 = R_0^1 z_0, \dots, z_6 = R_5^6 z_5 = R_0^1 \dots R_5^6 z_0 \quad (19)$$

Where P_0^n is the coordinates of n in 0, O_n is distance between origin and point n.

If each joint are independent, end-effect position can usually be written Eq.(12), Eq.(12) also can rewrite

Eq.(13). Eq.(14) is derived from Eq.(12) when only i -th joint is operating. q_i is rotated about z_{i-1} axis so Eq.(15) can be expressed. Therefore, use Eq.(15), Eq.(14) and Eq.(13) Eq.(16) and Eq.(17) are defined. About angular Jacobian, it is assumed that 1st joint only depend z-axis that is why 1st angular Jacobian component is $z_0 = [0 \ 0 \ 1]^T$, and 2nd Jacobian component is depend on first joint and second joint and each joint only rotate on relative coordinate z-axis, so we can obtain $z_1 = R_1 z_0$. From Eq.(17) and angular velocity, Jacobian matrix write Eq.(19).

Now, all of parameter are defined so that next step is to approach the sequence of Jacobian method.

For using numerical method, first, sequence of solving must be decided initial position and orientation.

The initial condition is considered like below

$$T_1 = \begin{bmatrix} 0 & -1 & 0 & 326 \\ 1 & 0 & 0 & -425 \\ 0 & 0 & 1 & 449 \\ 0 & 0 & 0 & 1 \end{bmatrix} \rightarrow \begin{bmatrix} 326 \\ -425 \\ 449 \\ 0^\circ \\ 0^\circ \\ 90^\circ \end{bmatrix}$$

And final positions are

$$[300 \ 200 \ 100 \ 80^\circ \ 80^\circ \ 80^\circ]^T$$

But rotation must be keep rotate order, so rotation will be rotated in order Roll-Pitch-Yaw.

$$\begin{bmatrix} 326 \\ -425 \\ 449 \\ 0^\circ \\ 0^\circ \\ 90^\circ \end{bmatrix} \xrightarrow{(Roll)} \begin{bmatrix} 300 \\ 200 \\ 100 \\ 0^\circ \\ 0^\circ \\ 80^\circ \end{bmatrix} \xrightarrow{(Pitch)} \begin{bmatrix} 300 \\ 200 \\ 100 \\ 0^\circ \\ 80^\circ \\ 80^\circ \end{bmatrix} \xrightarrow{(Yaw)} \begin{bmatrix} 300 \\ 200 \\ 100 \\ 80^\circ \\ 80^\circ \\ 80^\circ \end{bmatrix}$$

The result of rotating between the z -axis by 90° and then rotating the x-axis by 90° and the result of rotating the 90° on the x-axis by 90° on the z -axis are totally different result. That is why the rotations are separately rotate to desire position.

Ex) $n = 10$, $P(1) =$ initial position $[326 \ -425 \ 449]^T$

Object $P =$ final position $[300 \ 200 \ 100]^T$

$$dP = \frac{[300 \ 200 \ 100]^T - [326 \ -425 \ 449]^T}{10} = \frac{[-26 \ 625 \ -349]^T}{10}$$

$$P(2) = P(1) + dP, \dots, P(n+1) = P(1) + n dP,$$

Of course, when calculating dP , the angle must be calculated in radian despite of that it is shown in 60-degree-form.

In summary, the Jacobian process is as follows, initial and object condition decided so that it can obtain dP , n and $\theta(1) \rightarrow J(1) \rightarrow J^{-1}(1)$

$$d\theta(1) = J^{-1}(1)dP$$

$$\theta(2) = \theta(1) + d\theta(1)$$

$$\theta(2) \rightarrow J(2) \rightarrow J^{-1}(2) \rightarrow \theta(3) \rightarrow \dots \rightarrow \theta(n+1)$$

eventually We can get final angle $\theta(n+1)$.

5. Simulation Result [7][8]

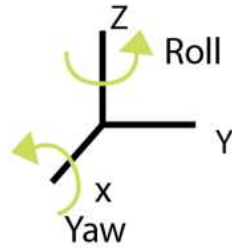
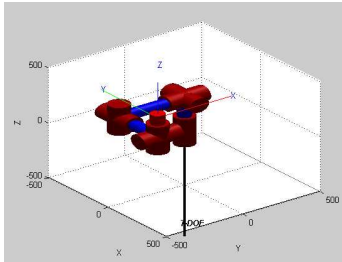


Fig. 3. 7-DOF initial position

Fig. 4. Define rotation

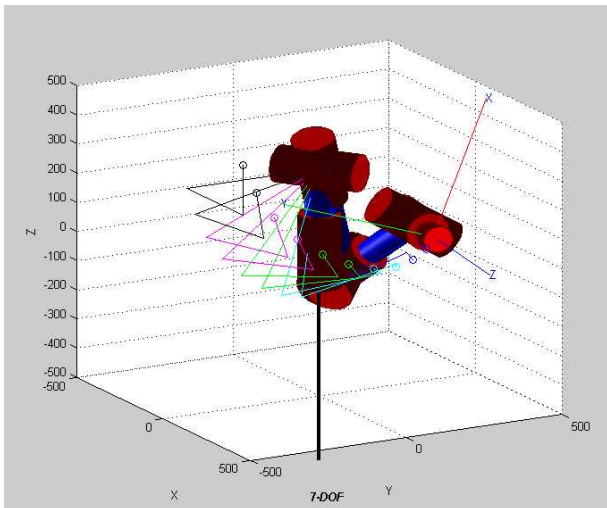


Fig. 5. Object point result image

$$\begin{bmatrix} \theta_1 \\ \theta_2 \\ \theta_3 \\ \theta_4 \\ \theta_5 \\ \theta_6 \\ \theta_7 \end{bmatrix} = \begin{bmatrix} 126.49^\circ \\ 201.32^\circ \\ 82.41^\circ \\ 131.45^\circ \\ 103.25^\circ \\ 50.25^\circ \\ 14.90^\circ \end{bmatrix} \rightarrow \begin{bmatrix} 0.0295 & -0.1717 & 0.9847 & 300 \\ 0.3353 & -0.9264 & -0.1716 & 200 \\ 0.9417 & 0.3352 & 0.0303 & 100 \\ 0 & 0 & 0 & 1 \end{bmatrix} \rightarrow \begin{bmatrix} 300 \\ 200 \\ 100 \\ 80^\circ \\ 80^\circ \\ 80^\circ \end{bmatrix}$$

The initial line is black and the circle over the line is end-effect-point. The line color indicates the sequence of the robot movement from the initial value. The robot arm moves in order of black, purple, green and finally blue. After moving, we got final angle θ for reaching target position $[326 \ -425 \ 449]^T$ and target angle $[80^\circ \ 80^\circ \ 80^\circ]^T$. Robot shape are displayed that red

cylinders are each joint and blue cylinder are connector. End-effect-coordinator is marked over 7-th joint.

6. Conclusion

Jacobian based inverse kinematics solution was applied to 7-DOFs robot arm. The result of the Jacobian approaching is well matched to the desired position and orientation of end-effector. Therefore, it was confirmed that the Jacobian approach method can adapt to easily solve inverse kinematics problem of 7-DOFs system.

In the future work, the method to avoid a pose out of workspace due to rotation limitation of joint motor will be studied.

Acknowledgements

The Technology Innovation Program(10073147, Development of Robot Manipulation Technology by Using Artificial Intelligence) funded By the Ministry of Trade, Industry & Energy(MOTIE, Korea).

References

1. K.S. Fu, R.C Gonzalez, C.S.G.Lee, *ROBOTICS : Control, Sensing, Vision, and Intelligence*, McGraw-Hill, 1987
2. Saeed B Niku, *Introduction to Robotics Analysis, Systems, Application*, PrenticeHall, 2001
3. Mark W. Spong, Seth Hutchinson, and M. Vidyasagar (2004), *Robot Dynamics and Control* pp 33-130.
4. Jeong-Seul, *Robotics Application of Matlab & Simulink(2015)* pp1 130-150
5. William A. Wolvich, *“ROBOTICS: Basic Analysis and Design”*, CBS College Publishing, 1987
6. K. S. FU, R. R. C. Gonzales, C.S.G.Lee, *“ROBOTICS”*, McGraw-Hill, 1987
7. John J. Craig, *“Introduction to Robotics”*, Addison-Wesley Publishing, 1989
8. Peter Corke, *“Robotics, vision and Control”*, pp 137-160, Springer Publishing, 2011

Indoor Position recognition using the pseudo-range estimation

Jongwoo An, Hosun Kang, Jiwook Choi, Jangmyung Lee

Dep. of Electronic Eng., Pusan National University, Jangjeon-dong, Geumjeong-gu, Busan, 609-735, Korea Republic

E-mail: jongwoo7379@pusan.ac.kr, hosun7379@pusan.ac.kr, jiwook7379@pusan.ac.kr,

jmlee@pusan.ac.kr

www.pusan.ac.kr

Abstract

In this paper, we propose a method of position recognition in indoor environment by pseudo range estimation of each satellite. Position recognition is a core technology for operating autonomous intelligent robots such as Unmanned Aerial Vehicle System(UAV), Automated Guided Vehicle(AGV). The Position recognition technology is divided into outdoor position recognition and indoor position recognition. The outdoor position is estimated using Global Positioning System(GPS) and the indoor position is estimated using various sensors such as Beacon and Inertial Measurement Unit(IMU). Due to the development of the technology, outdoor position recognition using GPS can be precise position estimation, but indoor position recognition using various sensors has a cumulative error caused by various factors and it is difficult to operate for a long time. In this paper, to overcome this drawback, we analyze the relationship between the velocity of the moving object and pseudo-range shift each satellite, and estimate the indoor position of the moving object by estimating the pseudo-range

Keywords: GPS, Pseudo-range, Navigation, Satellites

1. Introduction

Position estimation is a core technology for airplanes, ships, and Automated Ground Vehicles(AGV). The Position recognition technology is divided into outdoor position recognition and indoor position recognition. The outdoor position is estimated using Global Positioning System(GPS) and the indoor position is estimated using various sensors such as Beacon and Inertial Measurement Unit(IMU)[1,2].

In the case of outdoor location recognition, it is possible to estimate the position with an error of cm unit due to the development of GPS, but indoor location recognition is not.

Since the satellite signals are blocked by the buildings in the indoor area, it is difficult to use the GPS, and the location is estimated by using various sensors.

Beacon and IMU are used for indoor location estimation.

In the case of Beacon, a relatively precise position estimation is possible by installing a separate device in a specific area.

However, it can be used only in the space where the device is installed, and maintenance is required separately. In the case of indoor location recognition using the IMU sensor, there is no spatial limitation because the acceleration, gyro, and compass information measured by the sensor are fused with various filters, but it is disadvantageous in that it is difficult to use for a long time due to accumulated error.

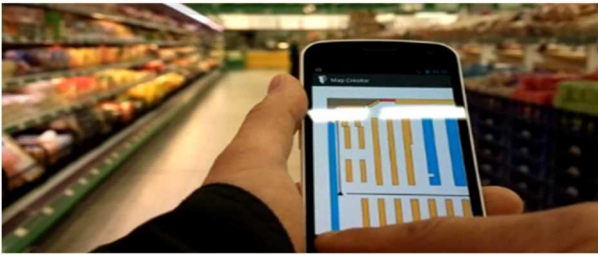


Fig. 1. Navigation System.

To overcome these drawbacks, in this paper, we proposed a method of indoor position estimation without additional system through pseudo range estimation with GPS satellites. The composition of the paper is as follows. In the chapter 2, introduces the Global Positioning System, chapter 3 Proposed Algorithm, In the chapter 4, Experiments & result and finally conclusion with the chapter 5.

2. Global Positioning System

GPS satellites are configured to determine the three-dimensional location of the receiver, expressed as latitude, longitude, and height. This point-by-point receiver positioning method is called stand-alone positioning. The stand - alone positioning determines the position of the receiver using the measured distance for each satellite based on the receiver present on the ground.

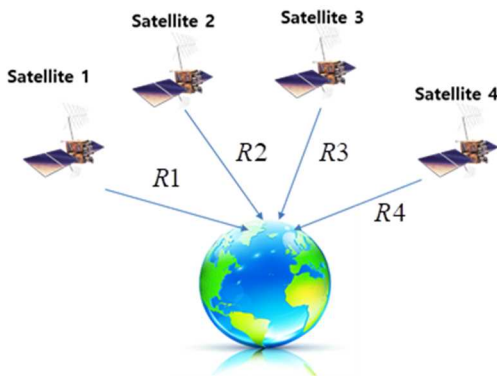


Fig. 2. Global Positioning System

© The 2018 International Conference on Artificial Life and Robotics (ICAROB2018), Feb. 1-4, B-Con Plaza, Beppu, Oita, Japan

In this paper, proposed a method of independent positioning using code pseudo-range. The code pseudo-range at time t is defined as follows.

$$R_i^j(t) = \rho_i^j(t) + c\Delta\delta_i^j(t) \quad (1)$$

In the above Eq. (1), $R_i^j(t)$ is the pseudo-range measured between the observation point i and the satellite j , $\rho_i^j(t)$ is the geometric distance between the receiver and the phase, and c is the speed of light. $\Delta\delta_i^j(t)$ is the amount of time bias and is the combination of the receiver and the satellite clock deviation with respect to the GPS reference time. In this way, pseudo-ranges can be represented by a single sphere centered on the coordinates of each satellite, and the intersection of the spheres becomes the position of the receiver. In this way, it is possible to use only three satellites for the latitude, longitude and altitude determination of the receiver's three-dimensional coordinates, but only when there is no time error because the receiver's clock and satellite clock have the same performance. Generally, a clock used in a receiver has a pseudo-range error due to a clock error when a low-cost crystal having a low precision is used. In order to compensate for this error, four unknowns, including the positional components of the receiver and the clock bias, are required, and pseudo-ranges measured from four or more satellites are required to obtain these four unknowns[6,7].

3. Proposed Algorithm

Since the GPS signal is blocked by the building when entering the building, there is a blank space in the pseudo-range information as shown in the figure below.

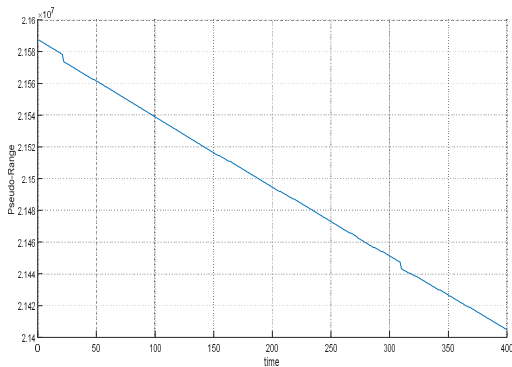


Fig. 3. Pseudo-range(outdoor)

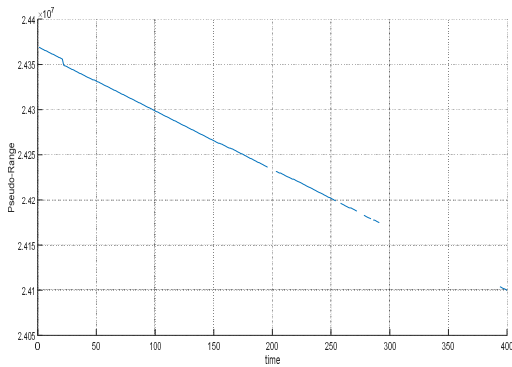


Fig. 4. Pseudo-range(indoor)

As shown in Fig. 4, it is difficult to estimated the position of the receiver because the satellite signal is blocked by the buildings. In this paper, proposed a position estimation method of GPS receiver by Pseudo-range estimation while satellite signal is blocked. The following figure is show the proposed algorithm.

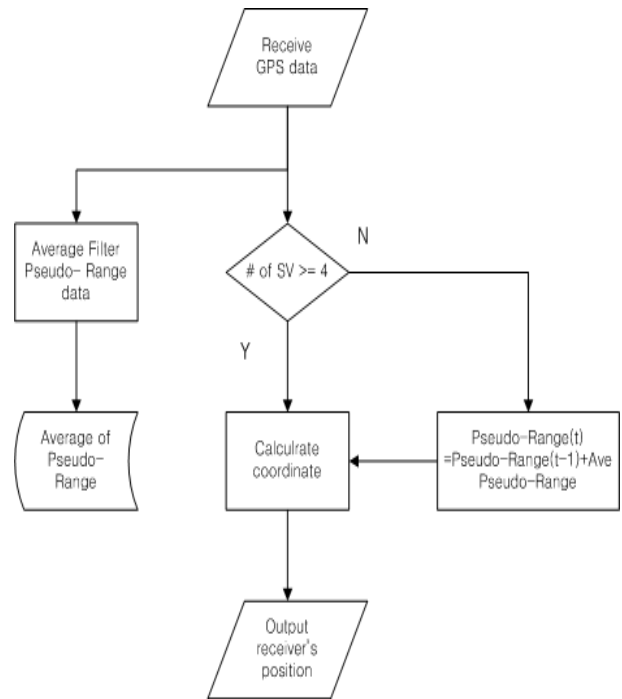


Fig. 5. Proposed Algorithm

When the signal is blocked, a method of estimating the pseudo-range with the satellite uses a characteristic that the pseudo-range changes linearly as shown in Fig. 3 at constant speed of object. Using this characteristic, the pseudo distance is estimated by adding the average value to the previous information when entering the room by using the average of the measured data for a certain period of time.

4. Experiment & Result

Fig. 6 shows the experimental environment. The experiment was conducted at Pusan National University. As shown in the figure below, the experiment was conducted through the inside of the building while moving in a straight line.

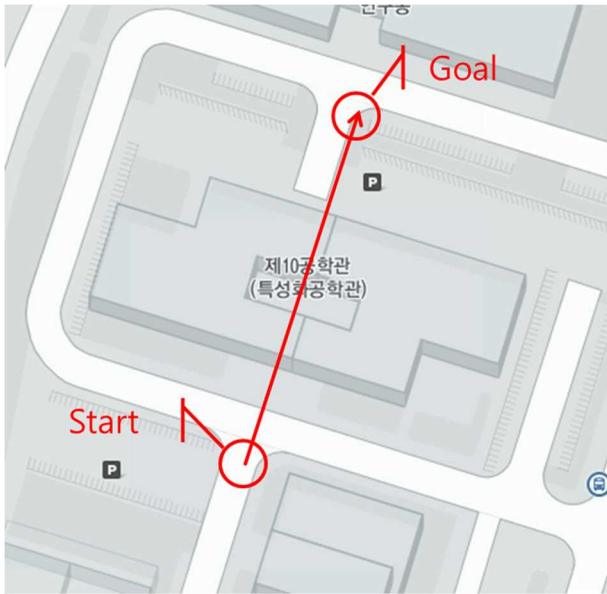


Fig. 6. Experiment environment

Figure 7 shows the experimental results.

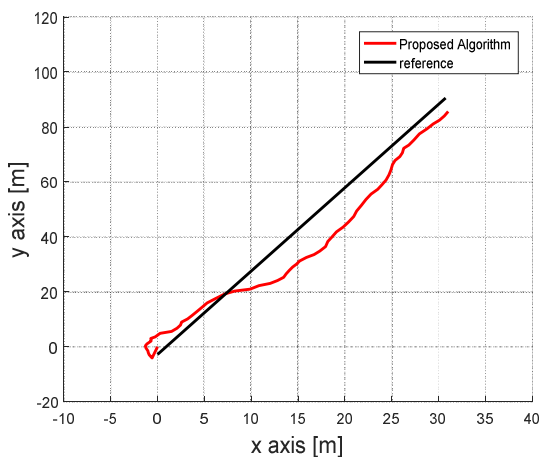


Fig. 7. Experiment result

Experimental results show that although the position of the moving object can be estimated through the pseudo range estimation in the room, the error of about 10m occurs

5. Conclusion

In this paper, we proposed a method to estimate the position in the building by Pseudo-Range estimation. The position of the user is estimated by taking into account various parameters such as clock bias error and

atmospheric error. In this paper, we have experimented with the assumption that these errors are the same as those measured outdoors, and confirmed that it is possible to estimate the position without additional system through pseudo range estimation. In the future, we intend to improve the accuracy of position estimation by considering various parameters.

Acknowledgements

This research was supported by the MOTIE (Ministry of Trade, Industry & Energy), Korea, under the Industry Convergence Liaison Robotics Creative Graduates Education Program supervised by the KIAT (N0001126).

References

References are to be listed in the order cited in the text. Use the style shown in the following examples. For journal names, use the standard abbreviations. Typeset references in 9 pt Times Roman.

1. Y. Yuan, X. Huo, J. Ou, K. Zhang, and Y. Chai, Refining the Klobuchar ionospheric coefficients based on GPS observations, *Aerospace and Electronic Systems, IEEE Transactions on*, vol. 44, no. 4, pp. 1498-1510, Feb. 2008.
2. Q. Zhu, Z. Zhao, and L. Lin, Real time estimation of slant path tropospheric delay at very low elevation based on singular ground-based global positioning system station, *Institution of Engineering and Technology(IET) Radar, Sonar & Navigation*, vol. 7, no. 7, pp. 808-814, Aug. 2013.
3. B. W. Parkinson and J. J. Spilker. Jr, *Global Positioning System: Theory and Applications*, Volume I, (American Institute of Aeronautics and Astronautics, Washington, DC, 1996).
4. S. Y. Kim, C. H. Kang, and C. G. Park, Station based detection algorithm using an adaptive fading Kalman filter for ramp type GNSS spoofing, *Journal of Institute of Control, Robotics and Systems (in Korean)*, vol. 21, no. 3, pp. 283-289, Mar. 2015.

Distance measurement algorithm based on the object recognition

Ho-sun Kang*

*Dep. of Electronic Eng., Pusan National University, 2, Busandaehak-ro 63beon-gil Geumjeong-gu
Busan, 46241, Republic of Korea[†]*

Na-hyun Lee[‡]

*Dep. of Electronic Eng., Pusan National University, 2, Busandaehak-ro 63beon-gil Geumjeong-gu
Busan, 46241, Republic of Korea[§]*

Jang-myung Lee

*Dep. of Electronic Eng., Intelligent Robot Laboratory, 2, Busandaehak-ro 63beon-gil Geumjeong-gu
Busan, 46241, Republic of Korea*

*E-mail: hosun7379@pusan.ac.kr, nahyun7379@pusan.ac.kr, jmlee@pusan.ac.kr
www.pusan.ac.kr*

Abstract

This paper implements an algorithm that recognized an object using a vision system and measured the distance to the object. Autonomous navigation systems such as UAV (Unmanned Aerial Vehicle) and AUV (Autonomous Underwater Vehicle) have been a world-wide trend in recent year. To operate these systems safely, it is necessary to recognize obstacles on the moving path accurately and quickly. Generally, various sensors are used to recognize the surrounding environment. These methods are affected by disturbance caused by the surrounding environment. To overcome these drawbacks, this paper proposes an obstacle recognition algorithm using a stereo camera. For obstacle recognition, disparity is obtained by removing the remaining part of the object except the recognized object from the image to improve the computation speed. Finally, after calculating the distance, we confirm the algorithm by comparing with the actual distance.

Keywords: Autonomous navigation system, key-point matching algorithm.

1. Introduction

Recently, the development of various sensors and the development of technology are rapidly expanding the market for autonomous navigation systems such as UAV and AUV. The most important consideration in studying the autonomous navigation system is the recognition of

obstacles on the moving route and the securing of safety through avoidance. In general, SLAM (Simultaneous Localization and Mapping) is performed using various sensors such as an infrared sensor and a laser sensor to recognize the surrounding environment. However, these methods are disturbed by the surrounding environment, and the amount of information is enormous. Therefore,

in recent years, the vision system is mainly used to overcome these shortcomings. A stereo camera can acquire distance information that is difficult to obtain with a single camera through its role as a human eye. Therefore, this paper also proposes an obstacle recognition algorithm using a stereo camera [1].

2. Used algorithm

2.1. ASIFT algorithm

The ASIFT (Affine Scale-Invariant Feature Transform) is an algorithm that performs key-point matching using SIFT key-point extraction algorithm and then matches the images using affine transformation as shown in the following fig.1 below. The SIFT algorithm is robust against image size change and has excellent performance. However, it has a drawback that it takes a long time to extract feature points because of a large amount of computation [2][3].

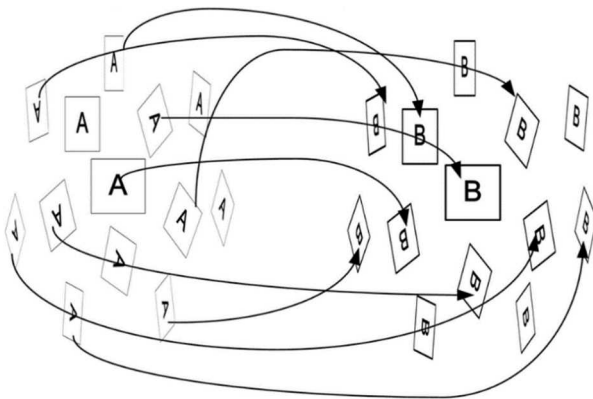


Fig. 1. ASIFT algorithm overview

2.2. Distance measurement

With a stereo camera, you can get two images for the same object. As shown in Fig.2 below, the two images are separated by a base line. As a result, even if the two images correspond to each other, a difference in coordinate value of the image occurs. This is called disparity. In addition, disparity must be grasped to obtain distance information about an object. In Fig.2, the disparity is shown as the difference between x and x' , which decreases as the distance between the object and the camera increases. The formula for calculating the disparity is shown in Eq. (1) below. Where B is the distance between two cameras in the stereo camera, f is

the focal length, and z is the distance from the object to the origin. When the equation Eq. (1) is transformed, the distance can be obtained through disparity, baseline, and focal length as shown in the following Eq. (2) [4].

$$disparity = x - x' = \frac{B \times f}{z} \tag{1}$$

$$distance = z = \frac{B \times f}{x - x'} \tag{2}$$

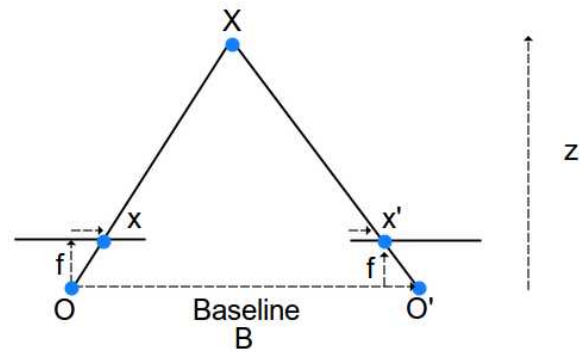


Fig. 2. Relationship between disparity and distance

3. Implementation

3.1. Basic environment

The basic environment for implementation is Visual Studio 2017 and OpenCV3.2 version. And the stereo camera was modeled by ZED. The ZED stereo camera has a baseline of 120mm and a focal length of 350pixels. Also, the image size is 640x480 pixels as shown fig.3 below.



Fig. 3. Stereo camera images

3.2. Key-point matching

Using ASIFT key-point matching algorithm, two images of a given object image and stereo camera are displayed

as rectangles as shown in Fig.4 and Fig.5 below. This is called the Region of Interest(ROI).



Fig. 4. Key-point matching result(Left)



Fig. 5. Key-point matching result(Right)

3.3. Distance measurement

To obtain the distance from the camera to the object, the disparity for the object should be calculated. If all the pixels within the region of interest are calculated, the

© The 2018 International Conference on Artificial Life and Robotics (ICAROB2018), Feb. 1-4, B-Con Plaza, Beppu, Oita, Japan

computation speed will be reduced by a large amount of data. Therefore, in this paper, we use only the coordinates of the four corners of the ROI drawn by the key-point matching as shown in Fig.6 below. The disparity is obtained by using the coordinate value from 1 to 4 coordinates, and the disparity is averaged by assuming that the object is one-pixel point [5].

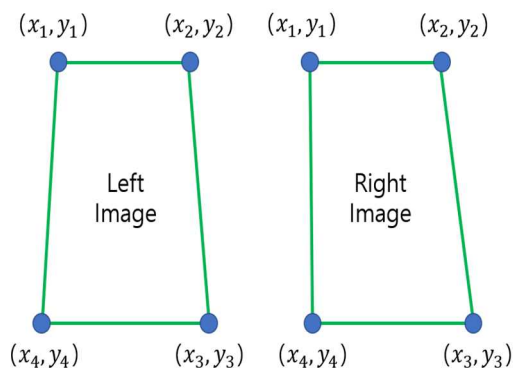


Fig. 6. Region of Interest

The result of applying it to the image taken at 50cm is shown in the following fig.7. In this figure, the horizontal lines of green, emerald, white, and yellow are the lines connecting each vertex. The more perfect horizontal line is, the more accurate disparity can be obtained.

The disparity calculated by the above method is

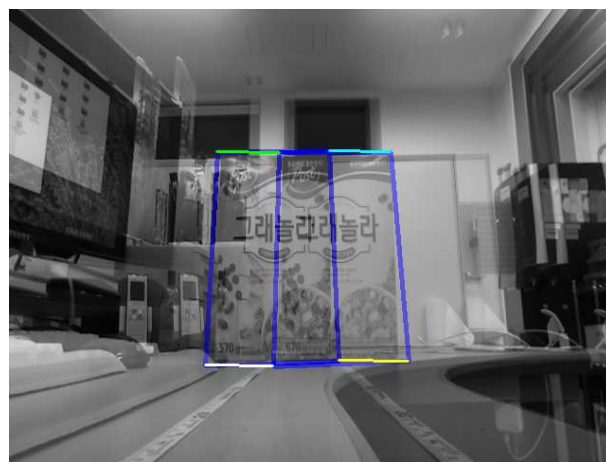


Fig. 7. Disparity

substituted into the Eq.2, and the distance from the actual distance of 400mm to the 1200mm is estimated from the following Table.1.

Table.1. Result of distance measurement

Real distance	Measured distance	Error rate
400	413.696	-3.424
450	465.5048	-3.44551
500	511.998	-2.3996
550	565.576	-2.832
600	615.997	-2.66617
650	664.248	-2.192
700	709.612	-1.37314
750	759.599	-1.27987
800	811.2512	-1.4064
850	871.8664	-2.57252
900	904.3482	-0.48313
950	964.214	-1.49621
1000	979.3174	2.06826
1050	1061.65	-1.10952
1100	1145.604	-4.14582
1150	384.594	66.55704
1200	562.9423	53.08814

Expect for cases where the actual distance is larger than 1100mm, very accurate calculation results can be obtained from the maximum error rate of -4.14582 to the minimum error rate of 0.48313. Also, when the actual distance is larger than 1100mm, as shown in Fig.8, the key-point matching using the ASIFT algorithm is not performed properly, resulting in a large error.



Fig. 8. Result of key-point matching(case : 1150mm)

4. Conclusion

In this paper, we use ASIFT key-point matching algorithm to recognize objects by using stereo vision camera. To improve the computation speed, distance is calculated by solving only the disparity of the four corners rather than the disparity of the whole recognized

object. As a result, it was confirmed that the maximum error rate of the distance was calculated to be a very accurate value of about -4.14582. However, when the distance between the camera and the object is larger than 1100mm, the region extraction using the ASIFT key-point matching is not performed properly. So, Result has very inaccurate distance values. Therefore, in future research, we will study algorithms for correcting the key-point matching when the distance between the camera and the object is getting longer to solve this problem. In addition, although the ASIFT algorithm has different calculation speeds depending on computer performance, it takes a very long time to obtain the results. Therefore, it is necessary to develop a key-point matching algorithm that increases the computation speed while maintaining the performance of ASIFT.

Acknowledgements

This research was supported by the MOTIE (Ministry of Trade, Industry & Energy), Korea, under the Industry Convergence Liaison Robotics Creative Graduates Education Program supervised by the KIAT (N0001126).

References

1. Jawon Seo, Changik Kim “Stereo camera image processing technology and motion”, Vol.38 No.2, 2011.2, 31-36 (6 pages).
2. GUOSHEN YU, AND JEAN-MICHEL MOREL, ASIFT: An Algorithm for Fully Affine Invariant Comparison, *Image Processing On Line*,1 (2011), pp. 11–38.
3. Donggeun Kim, C++API OpenCV Programming, Game publisher, 2016.
4. Yoonhee Lee, Dongsuk Kim, Hogi Jung, Falju Yoon, “Stereo Vision based front obstacle distance monitoring system”, *Korea Automotive Engineers Conferenc*, pp1181~1187.
5. Robert ragani, *Computer vision programming using OpenCV from basic image processing to advanced computer vision*, PACKT, 2015.

An-ion air purifier system using IoT Technology

Heeje Kim

Department of Electrical Engineering, Pusan University, Busan, Republic of Korea

Dohyun Kim

Department of Electrical Engineering, Pusan University, Busan, Republic of Korea

E-mail: heeje@pusan.ac.kr, kdh8486@naver.com,

Abstract

We have developed the an-ion air purifier which can remove various fine dust very efficiently. It was based on the principle of high voltage corona discharge that was fabricated for air cleaning from various fine dust. That is a big issue for human society. The best switching frequency was 10kHz, and the output voltage was approximately 20kV. In order to remove the fine dust, the an-ion air purifier was controlled properly for removing the fine dust by using the Arduino and personal smart-phone app. From these experiments, we could remove various fine dust much more easily and effectively.

Keywords: High voltage corona discharge, Fine dust, Arduino, Smart-phone app

1. Introduction

Recently, environmental pollution has increased the amount of fine dust, and air cleaning technology for removing fine dust is increasing day by day.

Fine dust refers to particles less than 10 micrometers in diameter and larger than 2.5 micrometers, and it is difficult to remove because it is impossible to identify with the naked eye. Therefore, filter method was mainly used to remove fine dust. However, such methods has a certain disadvantages for example it is not economically efficient because it generates noises and the filter must be periodically exchanged. If the filter is not replaced, bacteria will multiply in the filter, and the bacteria will be discharged from the air cleaner during use, which will adversely affect the human body.

In this paper, we used the high voltage corona method differentiated from the conventional method and applied the IoT(Internet of things) technology to design an efficient method to simultaneously perform fine dust measurement and removal. The combination of IoT technology makes it possible to control fine dust and air cleaning system at the same time, and it can solve economical and environmental part at same time.

2. Design of air cleaner

Table 1. Design Considerations

Design Considerations	
Frequency	10khz
Duty Ratio	50%
Input Voltage(DC)	30~70V
Output Voltage(DC)	20~25kv
Transformer ratio	5 : 380 (primary side : secondary side)

The air purifier system designed in this paper is an electric dust collection system using corona discharge. Basically, it is necessary to generate a high voltage of 20kV or more in order to discharge the corona. Designed air cleaners consist of half bridge inverters, step-up transformers, and Cockcroft Walton circuits.

When DC is input, the DC voltage is converted to AC voltage through the half bridge inverter and then the AC

voltage is boosted to AC high voltage first by using the step-up transformer. The second boosted AC voltage is converted to a DC high voltage through a Cockcroft Walton circuit to cause a corona discharge.

2.1. The half bridge inverter

Half bridge inverters divide the input voltage in half and connect alternately to the load via two switches. Therefore, the half bridge inverter uses two P-MOSFETs (IRF250). To divide the input voltage in half, two capacitors of the same capacity are used, and the input voltage is half the time. The switches S1 and S2 of the single-phase half-bridge inverters are turned on alternately and the output voltage is determined by the switch state. When S1 is ON, the output voltage is $-V_{dc} / 2$. When S2 is ON, the output voltage is $V_{dc} / 2$.

If the switches S1 and S2 are all ON, the input power is shorted by the switches S1 and S2, so the switches S1 and S2 should not be all ON. Therefore, since the switches S1 and S2 are alternately turned on, the output voltage alternates between $V_{dc} / 2$ and $-V_{dc} / 2$. [1]

In this paper, PWM signal applied to S1 and S2 is controlled by DSP chip F28335.

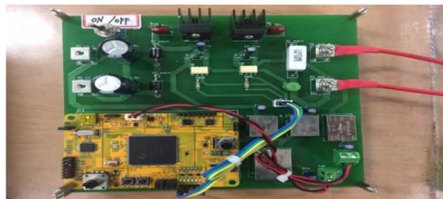


Fig. 1. The half bridge inverter

2.2. Step-up transformers

The transformer in this paper uses EI core. Ferrites are used as high permeability materials in the frequency range from low frequency to hundreds of MHZ.

Therefore, it is most suitable for economical part and efficiency in the step-up transformers design.

Table 2. Transformers design

Transformers design	
Core	Ferrite
Turns Ratio	76
Primary Voltage	15~35V
Secondary Voltage	1140~2660V
Frequency	10~20kHz

2.3 Cockcroft Walton circuit

The Cockcroft Walton circuit, when stacking n number of rectifiers and capacitors (Fig. 3 N=8), If no load is applied, a dc voltage of n times the secondary voltage peak value of the transformer can be generated.

Using this principle, DC high voltage such as 20 ~ 25kV can be obtained. Corona discharge occurs by using DC high voltage. The generated corona discharge can remove various fine dust quickly. [2]

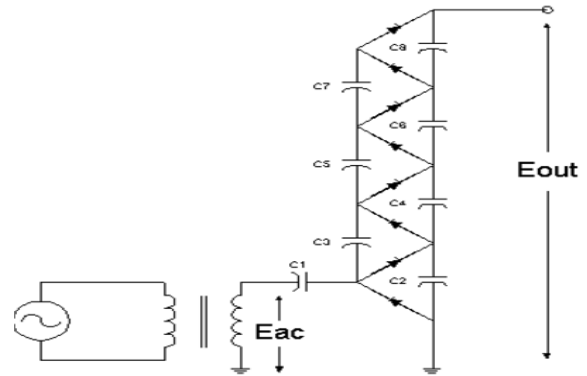


Fig. 2. Cockcroft Walton circuit

2.4 Transformers &Cockcroft Walton circuit molding

The design of the air cleaner proposed in this paper is based on high voltage corona discharge. Therefore, the circuit and the step-up transformer generate a considerable high voltage and the dielectric breakdown easily occurs.

If isolation is not done properly, the transformer or Cockcroft Walton circuit will be easily damaged due to insulation breakdown. The insulation design is essential. In this paper, dielectric breakdown is solved by molding epoxy into transformers and Cockcroft Walton circuit.



Fig. 3. Transformers & Cockcroft Walton circuit molding

3. IoT Technology

IoT technology refers to intelligent technologies and services that connect all things based on the Internet and communicate information between people, between smart devices plus inter device communications. Recently, due to the development of internet and smart phone, the utilization of IoT technology has been diversified and much research has been done.

IoT technology is remotely controllable. Data can be received and transmitted remotely. In addition, the desired data can be used in real time and the management is very easy.

In this paper, IoT technology is combined with air purifying technology using corona discharge. [3]

3.1 Arduino & Wi-Fi Shield

Arduino is an open source computing platform and software development environment based on simple microcontroller boards. Arduino can be used as smart receiver as well, it can deal with real time data transmitter such as sensors, switches

However, Arduino is not advance enough yet to implement IoT technology. Get access on data from internet cloud is still not approachable by Arduino

In this paper, IoT technology is implemented using Arduino and Wi-Fi Shield. The combination of Arduino and Wi-Fi Shield makes it possible to transmit and receive information over the internet cloud. [4]



Fig. 4. Arduino & Wi-Fi Shield

3.2. Fine dust sensor

Sharp optical dust sensors have internal infrared diodes and diagonally arranged phototransistors. Light emitting diode projects and phototransistors detect dark areas due to the passage of fine particles. In addition to this function, it is possible to check whether there is smoke or dust by the output pulse pattern. Fine dust sensors can measure up to 2.5 μm particles.

3.3 The Air cleaner App

There are many smartphone users in modern society in recent years. And the utilization of smartphone is significant. IoT technology is also growing rapidly in conjunction with smartphone apps.

In this paper, we developed and implemented a smartphone app based on App Inventor 2. The main function of the fine dust app is the fine dust measurement function and ON / OFF control of the air cleaning system. Application is used to check the current fine dust condition and the user controls the air purifier



Fig. 5. Fine dust App

4. Experiment

The experiment was conducted by combining IoT technology with the air cleaner using the designed high voltage corona discharge.

- 1) Acrylic box dimensions[50cmx50cmx50cm], fine dust is generated into the box by using a mosquito net.
- 2) Fine dust application is used to measure the fine dust concentration in the acrylic box.
- 3) Run the air purifier using the App to remove the third fine dust.
- 4) Confirm the reduction of fine dust visually and through App, and finish.





Fig. 6. Before and After (air cleaner & App)

5. CONCLUSION

In this paper, we have developed a high voltage air cleaning system. It is operated by smart phone application, with the help of Transformers & Cockcroft Walton circuit Corona discharge is generated, and smoke free acrylic box confirmed the fine dust removal. All the data are supported by laboratory experiments. And this proposed method can be used to keep the environment clean by removing the dust from air.

Future experiments will improve the removal level and removable range of fine dust in the air cleaner.

References

1. **Won Chungyeon** "Power of Electronics" pp.268-273,
2. **LEE Deokchul** "High-Voltage Plasma Engineering" pp.152-154.
3. **W. Y. Lee, H.M. Ko, J. H. Yu, and K. B. Sim**, "An Implementation of Smart Dormitory System Based on Internet of Things," *Journal of Korean institute of Intelligent System*, vol.26,no.4,pp.295-300,Aug.2016
4. **S. H. Seo, and S. W. Jang**, "Design and Implementation of a smart shoes module based on Arduino," *Journal of the Korea Institute of Information and Communication Engineering*, vol.19, no. 11, pp. 2697-2702, Nov. 2015.

Solar panel temperature control system using IoT

Min-soo Kim

Department of Electrical Engineering, Pusan University, Busan, Republic of Korea

Hee-je Kim

Department of Electrical Engineering, Pusan University, Busan, Republic of Korea

E-mail: rlaalstn5122@naver.com, heeje@pusan.ac.kr

www.pusan.ac.kr

Abstract

Solar photovoltaic systems are renewable energy sources that are used widely around the world. On the other hand, the efficiency decreases as the temperature of the solar panels increases. To prevent this phenomenon, a cooling fan can be installed on the back side of the solar panel to increase the efficiency. The solar system efficiency also decreases due to weather conditions and unexpected situations. To overcome this problem, an IoT (Internet of Things) system was used to monitor the state of the solar system and control the cooling fan. The core microprocessor used in IoT systems was Arduino. Using Arduino, an IoT system can be implemented simply and inexpensively. The entire system was designed and tested and the efficiency increased by approximately 4.7%. Although it is a small 30W capacity photovoltaic system, its efficiency is expected to be increased by applying it to a photovoltaic system of more than 1kW in the near future.

Keywords: Arduino, Cooling fan, IoT, Smart phone, Solar panel, Wi-Fi

1 Introduction

Nowadays, IoT (Internet of Things) is getting popular in home and industry [1]. IoT is a future network technology that can share information and control things between people, things, things and things [2]. This allows remote control and monitoring from a distance. Based on this IoT, it can be applied to solar power systems currently used worldwide.

Solar power generation system uses solar energy to produce electricity, so if the temperature of the solar panel rises, the power generation efficiency becomes low [3]. In particular, at noon time, the surface temperature of the solar panel reaches from 60 to 70 degrees. There are several ways to prevent such degradation of efficiency. First, cooling water is sprayed on the solar panel surface to lower the temperature. Second, lower the temperature by attaching a heat sink. Third, use a cooling fan to lower the temperature. Experimental results show that the last of these three methods is optimal for lowering the temperature of the solar panel.

However, this cooling fan must be activated when the temperature of the solar panel rises, and turned off when the temperature is low. Although the temperature can be controlled automatically, it is impossible to control the entire system when the temperature sensor fails or is not ideal. For this reason, the system is manually controlled through monitoring.

The microcontroller used in this paper is Arduino. Arduino is popular among engineers because it is easy to use and inexpensive [4]. However, Arduino alone can't

communicate over distance. So it controls the cooling fan through Wi-Fi communication between Smartphone and Arduino. Arduino is combined with a Wi-Fi shield, and there is a server in the Wi-Fi shield. Through this server, various sensor signals and switch signals can be sent to smart phone and Arduino. This makes it possible to turn on and off the switch directly after checking the solar panel temperature.

After making the actual model, we confirmed the normal operation between Arduino and smart phone using Wi-Fi communication and also confirmed that the temperature of solar panel is lowered. Through the monitoring and control as above, the solar power generation system can make more efficient electricity generation.

2 Major System Components

The system consists of several important parts. Arduino which acts as a brain, Wi-Fi shield for Wi-Fi communication, infrared temperature sensor for receiving infrared signals, and relays that activate the cooling fan are important components. Sub-components include voltage, current sensor, ambient temperature sensor, and LCD. The temperature of the solar panel can be appropriately maintained by the organic operation of these parts.

2.1 Arduino

Fig. 1 shows the Arduino Mega used in this system. The main chip is atmega2560, which has 54 digital input / output pins, 16 analog input pins, 256kb flash memory and 8KB SRAM.

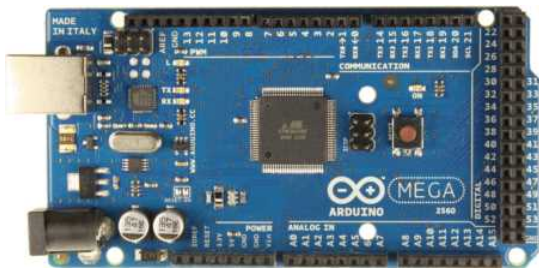


Fig. 1. Arduino MEGA 2560

And Arduino is programmed in assembly language like C language and Java.

2.2 Wi-Fi shield

The Wi-Fi shield is used in conjunction with Arduino to communicate with Arduino and the smart phone. The jsn270 model was used and the specifications are shown in Table 1 below.

Table 1. JSN270 Specification

Wireless Standard	IEEE 802.11 b/g/n
Frequency Range	2.412~2.477 GHz
Data Rates	Max 72Mbps
Modulation Type	OFDM, DSSS
Wi-Fi Security	WEP 64/128bit, WPA/WPA2 personal

2.3 Infrared sensor

The infrared sensor is a device that measures the temperature by detecting the infrared rays coming from the object. Remote measurement is possible and failure does not occur. In this system, non-contact infrared sensor (MLX90614) is used and can be measured from -70.01°C to +382.19°C. It has resolution of 0.01°C and communication method is I2C. It is shown in Fig. 2.



Fig. 2. MLX90614

2.4 Relay

Relay receives signal from Arduino and turns cooling fan on and off. The maximum input voltage is 250V for AC and 30V for DC.

2.5 Other sensors and devices

There are other sensors except for the main components. For example, voltage and current sensor, ambient temperature sensor, cooling fan, LCD. Other devices include AC-DC converter, 30W solar panel, cradle, and electric box.

3 Fabrication

3.1. Design

The total system was designed using the parts described above. Various sensors and relays are attached to the center of Arduino, and finally one system is completed. In addition, a smart phone application for operating the Arduino is also designed. The app was designed with easy-to-use App Inventor 2 interface. Fig. 3 and Fig. 4 show the system schematic and App Inventor 2 interface.

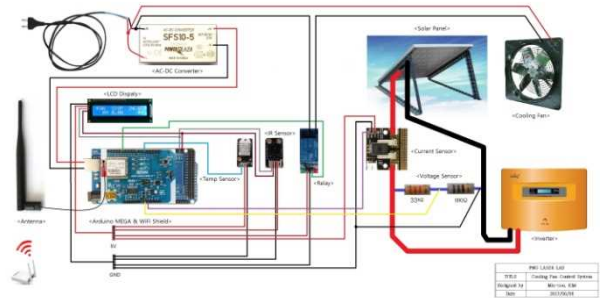


Fig. 3. The Schematic of the System

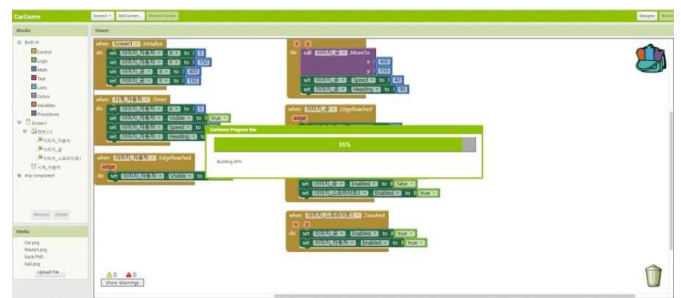


Fig. 4. App Inventor 2 interface

3.2 Program Code

Finally, Arduino requires source code for device operation. The source code is divided into four parts: Wi-Fi connection, LCD display, temperature and voltage and current sensors, and switch operation. The code below shows only some important parts. The first is a header part where you set the header file to use in your code. The second part

is for Wi-Fi connection, where you can set the SSID, Password and encryption method.

```

/* Wi-Fi connect part */
#define SSID      "air"
// your wifi network SSID
#define KEY       ""
// your wifi network password
#define AUTH      "NONE"
// your wifi network security (NONE,
// WEP, WPA, WPA2)

/*Server part*/
// HTTP headers always start with a
// response code (e.g. HTTP/1.1 200 OK)
// and a content-type so the client
// knows what's coming, then a blank
// line:
JSN270.println("HTTP/1.1 200 OK");
JSN270.println("Content-
type :text/html");
JSN270.println("Refresh: 30");
JSN270.println();

```

3.3 Final model

A final model was created as shown in Fig. 5. Six cooling fans were attached to the solar panel and a converter was added to change the input voltage to 12V. An LCD was attached to the main box to verify the data directly. Finally, the completed application is shown in Fig. 6. There is a cooling fan switch button and added function to check various data in real time.



Fig. 5. Final model



Fig. 6. Smart phone application

4 System Test

We confirmed that the manufactured system works normally. The On / Off of the cooling fan was controlled by a smart phone and Heater was used to simulate sunlight. And heat the solar panel using a heater as shown in Fig.7.



Fig. 7. Testing set-up

The temperature of the solar panel was maintained at over 57°C and the ambient temperature was maintained at 28°C.

After running the cooling fan through the smart phone, the temperature dropped by 40°C. At this time, it takes about 20 minutes. The temperature change of the solar panel is shown in Fig. 8. The temperature of the solar panel is generally lowered.

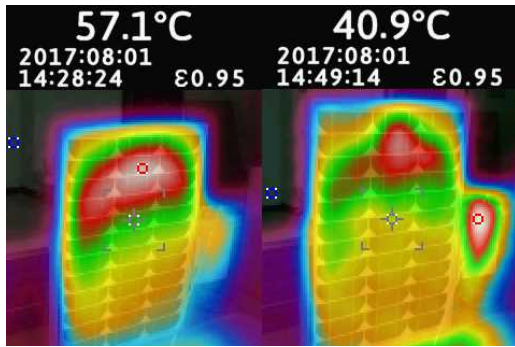


Fig. 8. Temperature change after cooling fan operation

5 Conclusion

In this paper, we designed and manufactured a solar panel temperature control system. With Arduino and Wi-Fi shield, it is now possible to control the temperature of the solar panel at anywhere and anytime. By lowering the temperature of the solar panel, the power generation efficiency can be increased. In addition, this system control via smart phone is very simple. In the near future, we need to research more about technologies that can significantly lower the temperature of solar panels while reducing costs. It's possible to maximize power generation efficiency by applying this system to general household and large-scale photovoltaic system.

References

- [1] K. J. Park (2017), "Arduino makes your imagination a reality," Edu-I, pp.198
- [2] O. Vermesan et al., "Internet of things strategic research roadmap," *Internet of Things-Global Technological and Societal Trends*, vol. 1, pp.9-52, 2011.
- [3] S. Dubey, J. N. Sarvaiya, B. Seshadri, "Temperature Dependent Photovoltaic(PV) Efficiency and Its Effect on PV Production in the World – A Review," *Energy Procedia*, vol. 33, 2013, pp.311- 321.
- [4] Adriansyah A, Dani, A.w., "Design of Small Smart Home system based on Arduino," in *Electrical Power, Electronics, Communications, Controls and Informatics Seminar (EECCIS)*, 2014, pp.121-125, 27-28 Aug. 2014

Enhancement of Mobile Robot Stability and Hardware Based on Reinforcement Learning

Ki-Seo Kim*

Electrical and Computer Engineering, Pusan University, Pusan, 46241, Republic of Korea[†]

Jeong-Hwan Moon[‡]

Electrical and Computer Engineering, Pusan University, Pusan, 46241, Republic of Korea

Jang-Myung Lee[§]

Electric Engineering, Pusan University, Pusan, 46241, Republic of Korea

Abstract

In this paper, we apply the obstacle avoidance run reinforcement learning algorithm used in the mobile robot using the LiDAR sensor. Q-learning and Deep Learning were applied to reinforcement learning algorithms. We solve the unnatural movements in the deceleration and acceleration of the robot using feedback learning. The results of simulation are applied to actual hardware to show how to increase the safety of driving.

Keywords: List four to six keywords which characterize the article.

1. Introduction

Past robots have evolved in the field of industrial and aerospace industries. Past robots, however, have done nothing but act solely on programmed behavior and behavior and have not acted on their own. But the hardware evolution and AI research changed the old robot industry. Examples include Google's AlphaGo, the world champion of the world's champion, and IBM's Watson, who is currently active in the medical industry. However, these robots are not yet completed, but they are becoming more and more evolvable. You know, you know, rather than just repeating the changing behavior, you know, you know, you know, you know, you know, you know, you know, you know, we're going to have to learn a better thing. It also led to the development of new, emerging LiDAR sensors and simulators as well as autonomous driving of automobiles and mobile robots. In reality, while driving is accelerating and slowing down when driving obstacles, the past studies the drag and deceleration of the runway, avoiding obstacles, without

considering the acceleration of the runway.

In this paper, we studied the algorithms to study natural driving without solving the current state of the robot, as well as solving these acceleration and deceleration problems, as well as learning the current behaviors of the robot.

2. System Configuration

Robots that perform self-driving learning robots are modeled on two-wheeled robotic drives. The ambient environment and obstacles surrounding the surroundings were sensed by RPLIDAR-2 sensors. The two-wheel drive can be rotated, and the sensor used is recognized as 360 degrees and the resolution is 1 degree. The sensor is mounted on the center of the robot, which can measure the distance of the robot. Maximum detection distance is 6 m.

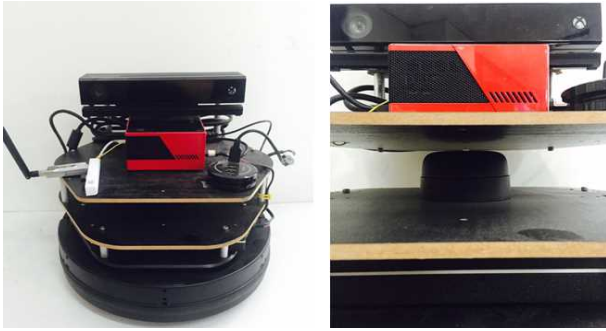


Fig. 1. Mobile Robot

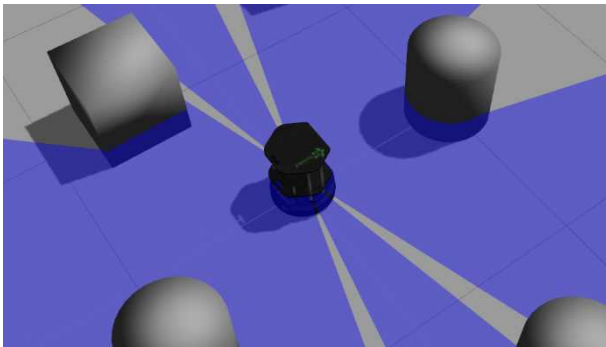


Fig. 2. LIDAR Sensor and Mobile Robot Simulation Environment

3. Training Algorithm

Google's deep-minded team has trained Atari games in reinforcement learning, bringing AI's capabilities closer to humans. In this paper, neural network is applied to action-value estimation by applying idea of Deep Learning algorithm to existing reinforcement learning, and the learning performance is greatly improved as a result. In this paper, Deep Q Network, which is a fusion of Q-learning and Deep learning, is applied.

3.1. Q-Learning

For an agent learning, defining a state is a very important task. This is because the state provides the criterion information for the agent to select the action that the agent will take by the policy. LiDAR sensor data is input to the state used in the experiment, and the state angles used for the learning input of the q function are 11, and the forward direction is 15 degrees and the forward direction is 180 degrees [105, 120, 135, 150, 165, 180, 195, 210, 225, 240 and 255].

Q-learning is one of the popular reinforcement learning methods and the learning of Q value is the most important.

This gives a Q table for each state and updates the Q value given the current states, the behavior to be taken, the corresponding compensation r , and the next state $s [s, a, r, s']$.

$$Q^*(s, a) \leftarrow Q(s, a) + \alpha(\gamma \max_{a'} Q(s', a') - Q(s, a)) \quad (1)$$

In the above equation, γ is the discount rate and a' represents the action to be taken by the next robot (input 1 to 5 in this system).

The action and reward applied to this learning are shown in the following table

TABLE 1 POLICY VALUE

Training Policy			
	<i>ACTION</i>	<i>velocity</i>	<i>reward</i>
0	Go Straight	x : 0.8 m/s z : 0 r/s	5
1	Turn left in place	x : 0 m/s z : 1.5 r/s	-5
2	Turn right in place	x : 0 m/s z : 1.5 r/s	-5
3	Go straight and turn left	x : 0.5 m/s z : 0.7 r/s	-1
4	Go straight and turn right	x : 0.5 m/s z : 0.7 r/s	-1
	Collision	-	-100

If the episode is repeated in the above procedure, the Q value gradually converges to the optimal Q value (Q^*).

3.2. Deep Q Network

After each learning of each episode in the general Q-learning table is completed, the Q value for each state is stored in the register. However, as the complexity of the problem becomes more and more confusing to the storage space, the application of Deep learning, which is a field of active research recently, is used to approximate the optimal Q (Q^*) Thereby enabling efficient learning as well as complex problems. Network is that The Q function is learned by using the loss function as the following equation

$$L_t(\theta_i) = E_{(s,a,r,s') \sim U(D)} [(r + \gamma \max_{a'} Q(s', a'; \theta_i^-) - Q(s, a; \theta_i))^2] \quad (2)$$

3.3. Experience Replay

In the existing DQN (Deep Q Network), similar data are continuously entered and learned during reinforcement learning, which causes unbalanced learning that is biased toward one side. This is called data correlation, and

Google's deep-mindedness has found an experience replay approach to solve this problem. This trick is applied to the autonomous driving learning method as follows. First, the state, action, reward, and next state $[s, a, r, s']$ obtained during obstacle avoidance driving learning are all stored in the external memory. Next, instead of learning the most recently obtained transition at the start of learning as a Q-value, we randomly select as many minibatch samples as possible from the stored transition memory and input them into the network. This is because it uses the transition obtained from various situations as a sample and thus obtains a Q-value that does not deviate to a specific situation due to this method. This plays a role similar to network generalization and helps to keep the network from falling to the local minimum.

3.4. Target Q network and Q network

The target Q method is a method of learning the Q network with the target value obtained by obtaining the target network separately from the target network and the Q network when obtaining the target. Then, update target network to Q network for every certain time step. In the existing DQN method, the value of the target constantly changes during a certain episode is fixed, and then the rate of change of the target is applied to reduce the correlation between the action value and the target, thereby contributing to the improvement of the learning success rate.

3.5. Action-Memory

In the conventional learning method, a simple laser distance value is inputted into the network (eg. 0, 0, 4, 4, 1) as a state to obtain the action value of the motor output, and the robot is moved. The speed of the robot is determined by the action value determined for each frame. Due to the rapid change in the action value due to the surrounding environment, the speed change rate also changes sharply. As a result, the mobile robot can't smoothly travel.

In order to solve the abrupt speed change problem, PID controller was used for speed control. In order to prevent the action which causes rapid change in speed during acceleration and deceleration, enter it with state.

Therefore, the total neural network is as shown in the following figure.

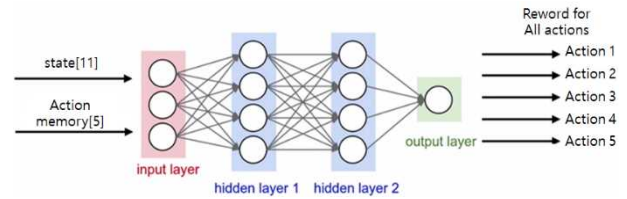


Fig. 3. DQN Model

3.6. Training Network

The neural network has two hidden layers, and the ReLU activator is set up for the neural network excluding the output layer. The learning was optimized using the Adam optimizer and initialized before learning according to Xavier initializer. The parameters used in the learning are as follows.

The reinforcement learning of the proposed DQN consists of the following steps.

1. Random environmental exploration and learning with random action according to E-greedy law
2. robot will get minus score when robot hit an obstacle or rotate in place and immediately reset the learning environment
3. Save the previous action records of the robot in the buffer $[s, a, r, s', m]$
4. Adding action-memory and learning to replay buffer
5. Target Q update and weight value optimization according to defined target-Q update cycle

4. Experiment

Experiments were carried out with ROS and GAZEBO simulator, and reinforcement learning experiments were conducted. The robot scored according to the determined policy, and the robot was free to run without any special destination and ends the episode when it hit the obstacle. The study was considered to be successful if it exceeded score 1000 for the last 30 averages.

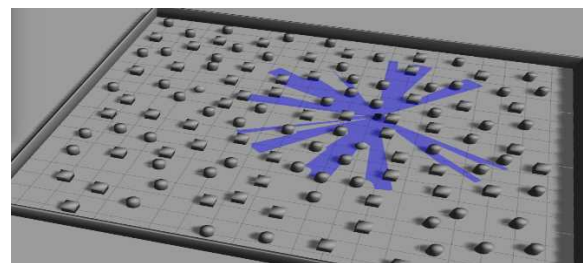


Fig. 4. Simulation Environment

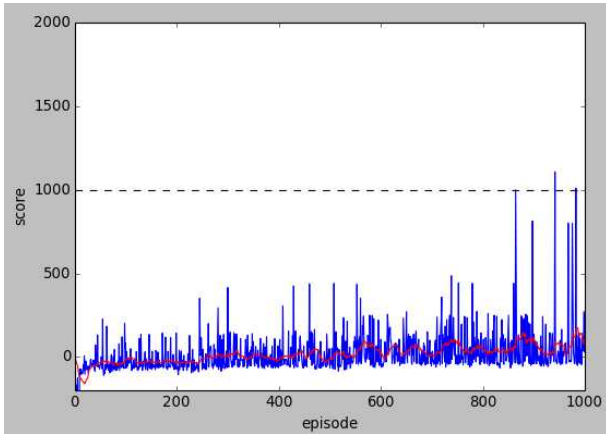


Fig. 5. Learning result when Action-Memory Buffer is not applied

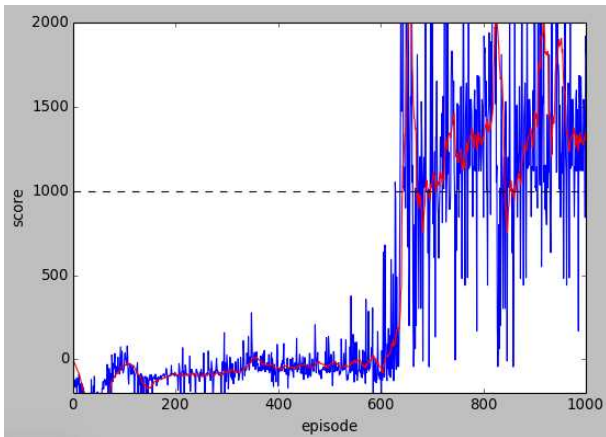


Fig. 6. Learning result when Action-Memory Buffer is applied

In the graph above, the blue line represents the acquisition score of each episode and the red line represents the average score of the last 30 episodes. As shown in the graph above, when the agent accelerates and decelerates smoothly, the agent frequently hits the obstacle due to sudden action change. On the other hand, when the action-memory is learned together with the input, the agent learns the state change itself. It can be confirmed that it has gotten high score by avoiding it well.

5. Conclusion

This study applied obstacle avoidance driving experiment to a mobile robot by applying reinforcement learning, which is popular among many kinds of deep learning algorithms applied in many fields in recent years. In order to prevent the unnaturalness caused by the

sudden action change of the agent, not only the application of the existing DQN research but also the information of the current speed, attitude, etc. of the robot in this paper. We propose an algorithm to determine the next behavior by feedback. This proved its validity through simulation and actual experiments. Furthermore, it is expected that the system will have natural acceleration / deceleration without any input and modeling of additional sensors, which will be effective for reinforcement learning application of relatively small scale system.

6. Acknowledgment

This research was supported by Basic Science Research Program through the National Research Foundation of Korea(NRF) funded by the Ministry of Education(NRF-2010-0024129)

This research was supported by the MOTIE (Ministry of Trade, Industry & Energy), Korea, under the Industry Convergence Liaison Robotics Creative Graduates Education Program supervised by the KIAT (N0001126)

7. Reference

- [1] Yann LeCun, Yoshua Bengio & Geoffrey Hinton “Deep learning” *Nature* 521, 436-444, 28 May 2015
- [2] David Silver, Aja Huang, Chris J et al “Mastering the game of Go with deep neural networks and tree search” *Nature* 529, 484-489 28 January 2016
- [3] Iker Zamora, Nestor Gonzalez Lopez et al “Extending the OpenAI Gym for robotics: a toolkit for reinforcement learning using ROS and Gazebo” arXiv:1608.05742v2 [cs.RO] 7 Feb 2017
- [4] Jesse Levinson, Jake Askeland et al “Towards Fully Autonomous Driving: Systems and Algorithms” *2011 IEEE Intelligent Vehicles Symposium (IV)* Baden-Baden, Germany, June 5-9, 2011
- [5] Volodymyr Mnih, Koray Kavukcuoglu et al “Playing Atari with Deep Reinforcement Learning” *NIPS Deep Learning Workshop* 2013, USA, December 2013
- [6] Diederik P. Kingma, Jimmy Ba “Adam: A Method for Stochastic Optimization” *3rd International Conference for Learning epresentations*, San Diego, 2015

A sound-based measurement of sway angle for anti-sway control of overhead crane

Miki Matsunaga

*Graduate School of Engineering, Hiroshima University, 1-4-1, Kagamiyama,
Higashi-Hiroshima city, Hiroshima, Japan*

Masayoshi Nakamoto

*Graduate School of Engineering, Hiroshima University, 1-4-1, Kagamiyama,
Higashi-Hiroshima city, Hiroshima, Japan*

Toru Yamamoto

*Graduate School of Engineering, Hiroshima University, 1-4-1, Kagamiyama,
Higashi-Hiroshima city, Hiroshima, Japan*

*E-mail: matsunaga-miki@hiroshima-u.ac.jp, msy@hiroshima-u.ac.jp,
yama@hiroshima-u.ac.jp*

Abstract

For anti-swing control of overhead crane, a deflection angle must be estimated. However, it is difficult to estimate deflection angles with a contact sensor such as rotary encoder. Therefore, we show a non-contact measurement method for the deflection angles by using two microphones. The method employs a time delay of arrival (TDOA) of acoustic signals which are picked up by the two microphones. Also, we show an algorithm to obtain the angle from the TDOA by using the Newton's method. Finally, we show experimental results to demonstrate the effectiveness of the proposed method.

Keywords: Overhead crane, microphones, correlation function, Newton's method

1. Introduction

Overhead cranes are well-used for transportation of load in factory and dock. For safety and efficiency transportation with the overhead cranes, the anti-sway control¹⁻⁵ has been received remarkable attention.

Since the dynamics of the sway angle of the crane can be described by the state-space equations, the sway can be controlled. However, the sway angle should be obtained for anti-sway control. It is known that the measurement of the sway angle is very difficult with contact sensor due to the hardware constraint.

From the background above, we focus on the sound signal⁶ for the anti-sway control of overhead cranes. Our measurement scheme is to obtain the sway angle without

attached angle sensor. Here, we assume the payload includes a sound source such as friction sound, squeak noise or active noise. With two microphones, we detect the sound (acoustic) signal generated in the payload. That is, we use the microphones for contact-less sensing of the angle. Next, we estimate the time delay of arrival (TDOA) between the acoustic signals obtained from the two microphones where the TDOA can be computed from the correlation function. Also, we transform the TDOA to the sway angle by using the Newton's method.

In the experiment, we treat the case when the payload is swaying and the position of trolley is changed. From experimental results, we show the proposed method can follow the sway angle even when the payload is moving.

© The 2018 International Conference on Artificial Life and Robotics (ICAROB2018), Feb. 1-4, B-Con Plaza, Beppu, Oita, Japan

2. Anti-sway Control of Overhead Crane

In the crane, a road is moved by motor driven trolley. Table I shows the parameters of the overhead crane.

Let l_w be the distance from fulcrum of the trolley to the payload (sound source). x ($0 \leq x \leq X$) is the position of the trolley where $x=0$ is the left end and $x=X$ is the right end. That is, the distance between the Microphone 1 and the trolley is x (variable). Also, θ is the angle of the line (sway angle). Assume T is kinetic energy and U is potential energy. Then, we have

$$T = \frac{1}{2} M \dot{x}^2 + \frac{1}{2} m v^2$$

$$U = mg l_w (1 - \cos \theta)$$

Also, define $L=T-U$ is the Lagrangian. Now, let the state vector be

$$x(t) = [x - x_d \quad \theta \quad \dot{x} \quad \dot{\theta}]^T,$$

where x_d is the desired position, and its time derivation be

$$\dot{x}(t) = [\dot{x} \quad \dot{\theta} \quad \ddot{x} \quad \ddot{\theta}]^T$$

Based on the Euler-Lagrange equation, the dynamics of the crane can be written in a state space from:

$$\dot{x}(t) = \begin{bmatrix} 0 & 0 & 1 & 0 \\ 0 & 0 & 0 & 1 \\ 0 & \frac{mg}{M} & 0 & 0 \\ 0 & -\frac{(M+m)g}{M l_w} & 0 & 0 \end{bmatrix} x(t) + \begin{bmatrix} 0 \\ 0 \\ \frac{1}{M} \\ -\frac{1}{m l_w} \end{bmatrix} u(t)$$

$$y(t) = \begin{bmatrix} 1 & 0 & 0 & 0 \\ 0 & 1 & 0 & 0 \end{bmatrix} x(t)$$

where $u(t)$ is an input signal, $y(t)$ is an output signal. Based on the state-space model above, x and θ can be controlled using a state feedback. To achieve the control, the angle θ must be estimated.

Table 1. Parameters of the overhead crane

weight of trolley	M
weight of payload	m
velocity of payload	v
external force	f
acceleration of gravity	g

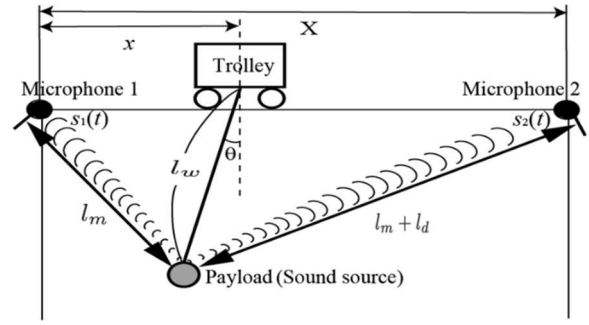


Fig. 1. Overhead crane with two microphones (Microphone 1 and Microphone 2) and sound source

3. Sound-based Measurement of the Sway Angle

3.1. Estimate of the TDOA

Fig. 1 shows the overhead crane system with two microphones (Microphone 1 and Microphone 2). With two microphones, we observe the sound signal originated from the sound source in the payload. Since the microphones have a directivity, the sensitivity of microphone is very low to the sound signal which is coming behind the microphones. Now, let $s_1(t)$ and $s_2(t)$ be the sound signal observed in the Microphone 1 and the Microphone 2, respectively. The distance between the two microphones is X since the microphone is located on the end of trolley rail. Further, let the distance between the Microphone 1 and the sound source be $l_m + l_d$ and the distance between the Microphone 2 and the sound source be l_m . Thus, l_d is the difference of the distances. Assume that x, X, l_w , are known. Now, the purpose is to estimate l_d based on the TDOA.

Using the two acoustic signals, we compute a correlation coefficients of $s_1(t + \tau)s_2(t)$ as follows.

$$\Phi(\tau) = \sum_{t=0}^{T_0} s_1(t + \tau) \cdot s_2(t) \tag{1}$$

where T_0 the number of sampled point.

Let τ' be the sampled point which maximizes (1). Now, the TDOA between the Microphone 1 and the Microphone 2 is $\tau' T_s$ where T_s is the sampling period. It follows that

$$l_d = \tau' T_s v_a \quad (2)$$

where v_a is the velocity of sound.

3.2. Conversion to angle θ

We introduce how to obtain θ with l_d . Using the law of cosines in Fig. 1, we have simultaneous equations as:

$$l_m = \sqrt{x^2 + l_w^2 - 2xl_w \cos\left(\frac{\pi}{2} - \theta\right)} \quad (3)$$

$$l_m + l_d = \sqrt{(X-x)^2 + l_w^2 - 2(X-x)l_w \cos\left(\frac{\pi}{2} + \theta\right)} \quad (4)$$

Now, eliminating l_m in (3) and (4), we have a function below.

$$f(\theta, l_d) = \left\{ x^2 + l_w^2 - 2xl_w \cos\left(\frac{\pi}{2} - \theta\right) \right\}^{\frac{1}{2}} + l_d - \left\{ (X-x)^2 + l_w^2 - 2(X-x)l_w \cos\left(\frac{\pi}{2} + \theta\right) \right\}^{\frac{1}{2}} \quad (5)$$

Hence, we can obtain θ corresponds l_d by computing the solution which satisfies

$$f(\theta, l_d) = 0, \theta \in \left(-\frac{\pi}{2}, \frac{\pi}{2}\right). \quad (6)$$

It should be noted that since l_m can also be obtained from (3) or (4), sensor delay can also be estimated by the velocity of sound v_a .

Here, let us show how to compute the solution of (6). Now, we employ the Newton's method to solve the solution of (6). The Newton's method uses the iterative equation as

$$\theta_{n+1} = \theta_n - \frac{f(\theta_n, l_d)}{\left\{ \frac{\partial f(\theta_n, l_d)}{\partial \theta} \right\}} \quad (7)$$

where θ_n is the angle at n -th iteration.

4. Experiment

Fig. 2 shows the experimental equipment. We use a Gaussian random signal with 0~1000 [Hz] as the sound source. The signal is generated by an electronic device. The sampling frequency is 14700 [Hz]. The correlation is calculated with data of samples corresponding to the position x . We consider the case when the payload is swaying (i.e. the sway angle is moving). Fig. 3 shows the result with $x=20$ where the vertical axis is the sway angle [deg.]. From Fig. 3, we can see that the payload is swaying around 0 [deg.]. In the same way, we show the results the position x is changed as $x=30$, $x=40$, and $x=50$. Similarly, Figs. 4-6 show the result with $x=30$, $x=40$, and $x=50$, respectively.

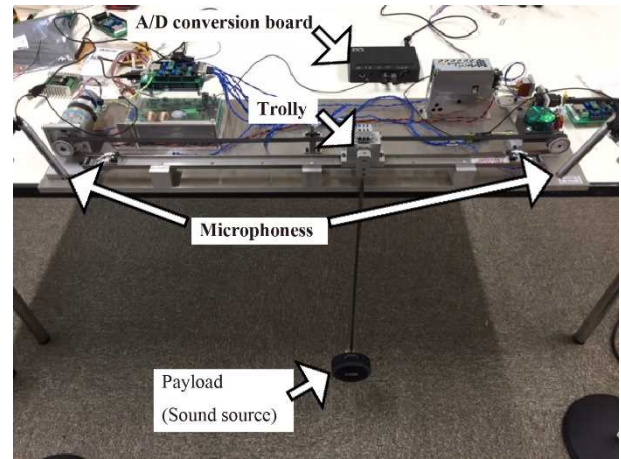


Fig. 2. Experimental equipment

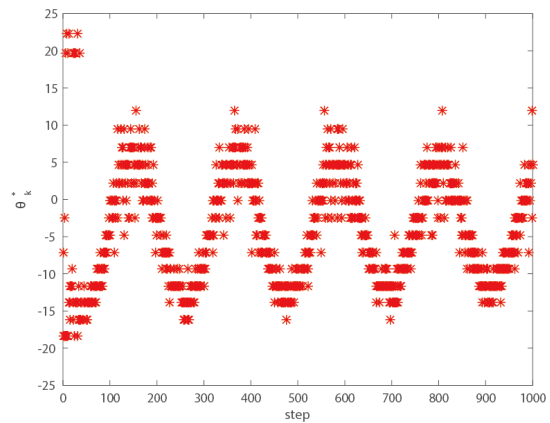


Fig. 3. Experimental result with $x = 20$

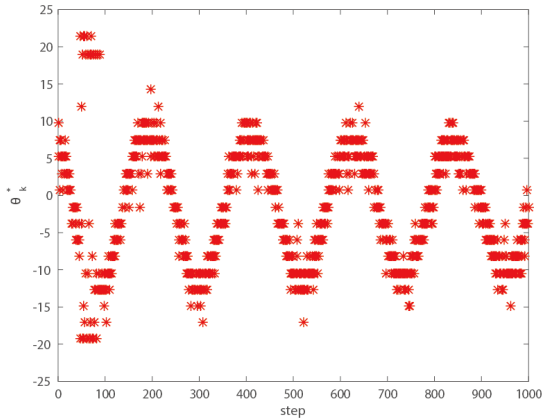


Fig. 4. Experimental result with $x = 30$

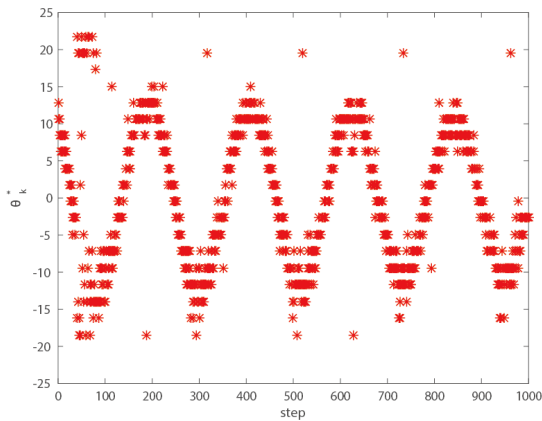


Fig. 5. Experimental result with $x = 40$

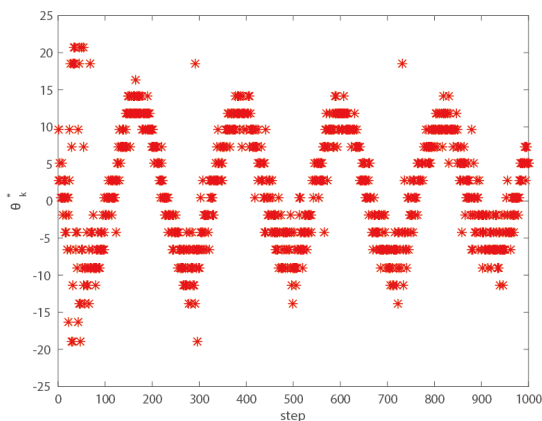


Fig. 6. Experimental result with $x = 50$

5. Conclusion

We have proposed the measurement method of sway angle for anti-sway control of overhead crane with two microphones. The method uses a time delay of arrival (TDOA) of acoustic signals measured from the microphones. Also, we have presented the algorithm to obtain the sway angle from the TDOA with the Newton's method. In experimental results, we demonstrate that our sound-based measurement method can follow the sway angle when the payload is moving.

References

1. C.-Y. Chang and H. W. Lie: Real-Time Visual Tracking and Measurement to Control Fast Dynamics of Overhead Cranes, *IEEE Trans. Ind. Electron.*, vol.59, no. 3, pp.1640-1649, March 2012.
2. N. Sun and Y. Fang: New Energy Analytical Results for the Regulation of Underactuated Overhead Cranes: An End-Effector Motion-Based Approach, *IEEE Trans. Ind. Electron.*, vol.59, no.12, pp.4723-4734, Dec. 2012
3. L.-H. Lee, C.-H. Huang, S.-C. Ku, Z.-H. Yang, C.-Y. Chang: Efficient Visual Feedback Method to Control a Three-Dimensional Overhead Crane, *IEEE Trans. Ind. Electron.*, vol.61, no.8, pp.4073-4083, Aug.2014.
4. K. Zavari, G. Pipeleers and J. Swevers: Gain-Scheduled Controller Design: Illustration on an Overhead Crane, *IEEE Trans. Ind. Electron.*, vol.61, no.7, pp.3713-3718, July 2014.
5. N. Sun, Y. Fang and H. Chen: A New Antiswing Control Method for Underactuated Cranes With Unmodeled Uncertainties: Theoretical Design and Hardware Experiments, *IEEE Trans. Ind. Electron.*, vol. 59, no.3, pp.453-465, Jan. 2015.
6. M. Matsunaga, M. Nakamoto and T. Yamamoto: An acoustic signal processing for anti-sway control of overhead crane system, *Proc. of 2017 International Workshop on Smart Info-Media Systems in Asia (SISA 2017)*, pp.124-127, Sept. 2017.

Sampled-data PID Control System with a Sensitivity Function for a Second-order Plus Dead-time System*

Ryo Kurokawa and Takao Sato

*Department of Mechanical Engineering, University of Hyogo
2167 Shosha, Himeji, Hyogo 671-2280 Japan
E-mail: tsato@eng.u-hyogo.ac.jp*

Ramon Vilanova

*Department of Telecommunications and Systems Engineering, Universitat Autònoma de Barcelona
Edifici Q-Campus de la UAB, 08193 Bellaterra, Barcelona, Spain
E-mail: ramon.vilanova@uab.cat*

Yasuo Konishi

*Department of Mechanical Engineering, University of Hyogo
2167 Shosha, Himeji, Hyogo 671-2280 Japan
E-mail: konishi@eng.u-hyogo.ac.jp*

Abstract

In this paper, we design a second-order plus dead-time (SOPDT) sampled-data Proportional-Integral-Derivative (PID) control system, where the continuous-time plant is controlled using the discrete-time controller. The proposed control system is designed so that the tracking performance is optimized subject to the stability margin constraint. In the present study, the servo and regulation optimal controllers are designed. Finally, the effectiveness of the proposed method is demonstrated through numerical examples.

Keywords: PID control, Sampled-data system, SOPDT system, Sensitivity function, Robust

1. Introduction

Proportional-Integral-Derivative (PID)^{1,2} control has been widely used in industry. Since the performance of PID control depends on the tuning parameters, additional tuning methods have been studied recently. Although the stability of a control system is critical, its tracking performance is also important. However, because of the

trade-off relationship between stability and tracking performance, they cannot be optimized simultaneously. Arrieta and Vilanova^{3,4} proposed a simple PID tuning method that optimizes the tracking performance subject to a prescribed robust stability. In this method, the optimal PID parameters are decided based on a first-order plus dead-time (FOPDT) continuous-time system. In order to design a discrete-time control system, Tajika et

al.⁵ proposed a design method for controlling a discrete-time FOPDT system. The present study discusses a design method of the PID controller for controlling a second-order plus dead-time (SOPDT) system, in which the continuous-time plant is controlled using the discrete-time controller. In the proposed method, both servo and regulation optimized control methods are designed. Finally, the effectiveness of the proposed method is demonstrated through numerical examples.

2. Description of the Control System

Consider the continuous-time controlled plant given as follows:

$$P(s) = \frac{K\omega_n^2}{s^2 + 2\zeta\omega_n s + \omega_n^2} e^{-Ls} \quad (1)$$

where K is the plant gain, ω_n is the natural angular frequency, ζ is the damping coefficient, and L is the dead-time. In the present study, we discuss the design method of the sampled-data control system using the following discrete-time PID control law:

$$\begin{aligned} u(k) &= C_e(z^{-1})e(k) + C_y(z^{-1})y(k) \quad (2) \\ C_d(z^{-1}) &= C_e(z^{-1}) + C_y(z^{-1}) \\ C_e(z^{-1}) &= K_p \left\{ 1 + \frac{T_s}{T_i(1 - z^{-1})} \right\} \\ C_y(z^{-1}) &= K_p \left\{ \frac{T_d(1 - z^{-1})}{T_s} \right\} \end{aligned}$$

where $u(k)$ is the control input, $y(k)$ is the plant output, $e(k) (= r(k) - y(k))$ is the control error, and $r(k)$ is the reference. Moreover, T_s , K_p , T_i , and T_d are the sampling time, the proportional gain, the integral time, and the differential time, respectively.

3. Definition of the Optimization Problem

As the constraint condition, the stability margin is defined using the sensitivity function, and the evaluation function for the tracking performance is also defined.

3.1. Constraint condition

The sensitivity function $S_f(z^{-1})$ is defined as follows:

$$S_f(z^{-1}) = \frac{1}{1 + C_d(z^{-1})P_d(z^{-1})} \quad (3)$$

where $P_d(z^{-1})$ is the discrete-time controlled plant. Using the sensitivity function, the constraint condition is defined as follows:

$$\begin{aligned} |M_s - M_s^d| &= 0 \quad (4) \\ M_s &= \max_{\omega} |S_f(e^{-j\omega})| \end{aligned}$$

where M_s is the maximum value of the sensitivity function, and M_s^d is the desired value selected by the designer. The recommended range of M_s^d is from 1.4 to 2.0¹. The smaller the value of M_s , the larger the stability margin. On the other hand, the larger the value of M_s , the better the tracking performance, although the stability margin becomes small.

3.2. Evaluation function

In the present study, the evaluation function J is defined as the integral absolute error:

$$J = \sum_{k=0}^{\infty} |e(k)| = \sum_{k=0}^{\infty} |r(k) - y(k)| \quad (5)$$

A trade-off relationship exists between the servo performance and the regulation performance. In the present study, the PID parameters are optimized for the servo and regulation control, respectively.

4. Controller Design

The PID parameters are optimized for a normalized system, and hence, dimensionless parameters are defined as $\tau = L\omega_n$, $h = T_s\omega_n$, $\kappa_p = K_pK$, $\tau_i = T_i\omega_n$, and $\tau_d = T_d\omega_n$. The range of these parameters are set as $0.1 \leq \tau \leq 1.0$, $0.01 \leq h \leq 0.10$, and $0.3 \leq \zeta \leq 1.2$.

In the proposed method, the constrained optimal problem is preliminarily solved for a designated finite plant, which is defined by discrete τ , h , and ζ , and the data set in which the optimal normalized PID parameters for discrete τ , h , and ζ , is obtained. In Fig. 1, the obtained normalized PID parameters are plotted by \circ , where $M_s^d = 1.4$ and $T_s = 0.01$.

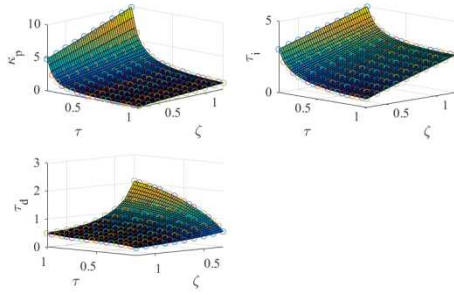


Fig. 1. Relationships among τ , ζ , and κ_p , τ_i and τ_d (servo design, $M_s^d = 1.4$ and $T_s = 0.01$)

The desired normalized PID parameters for an arbitrary plant are decided by the linear interpolation from the data set. Practically speaking, the interpolated parameters are calculated using the nearest four points, as shown in Fig. 2. From this figure, the vector equation is obtained as follows:

$$\begin{aligned} \overline{OP} &= \alpha\overline{OA} + \beta\overline{OB} + \gamma\overline{OC} \quad (6) \\ 0 &\leq \alpha \leq 1 \\ 0 &\leq \beta \leq 1 \\ 0 &\leq \gamma \leq 1 \end{aligned}$$

where point O [τ^0 , ζ^0 , h^0 , κ_p^0 , τ_i^0 , τ_d^0], A [τ^A , ζ^A , h^A , κ_p^A , τ_i^A , τ_d^A], B [τ^B , ζ^B , h^B , κ_p^B , τ_i^B , τ_d^B], and C [τ^C , ζ^C , h^C , κ_p^C , τ_i^C , τ_d^C] are the nearest points of the desired [τ^P , ζ^P , h^P]. Then, Eq. (6) is rearranged as follows:

$$\begin{aligned} \kappa_p^P &= \kappa_p^O + \alpha(\kappa_p^A - \kappa_p^O) + \beta(\kappa_p^B - \kappa_p^O) + \gamma(\kappa_p^C - \kappa_p^O) \\ \tau_i^P &= \tau_i^O + \alpha(\tau_i^A - \tau_i^O) + \beta(\tau_i^B - \tau_i^O) + \gamma(\tau_i^C - \tau_i^O) \\ \tau_d^P &= \tau_d^O + \alpha(\tau_d^A - \tau_d^O) + \beta(\tau_d^B - \tau_d^O) + \gamma(\tau_d^C - \tau_d^O) \end{aligned}$$

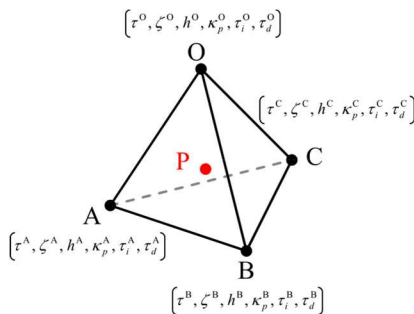


Fig. 2. Image of the linear interpolation

Solving these equations, the desired κ_p^P , τ_i^P , and τ_d^P for [τ^P , ζ^P , h^P] are obtained, where α , β , and γ are decided based on the following equations:

$$\begin{aligned} \tau^P - \tau^O &= \alpha(\tau^A - \tau^O) + \beta(\tau^B - \tau^O) + \gamma(\tau^C - \tau^O) \\ \zeta^P - \zeta^O &= \alpha(\zeta^A - \zeta^O) + \beta(\zeta^B - \zeta^O) + \gamma(\zeta^C - \zeta^O) \\ h^P - h^O &= \alpha(h^A - h^O) + \beta(h^B - h^O) + \gamma(h^C - h^O) \end{aligned}$$

In Fig. 1, the interpolated parameters are plotted over the discrete calculated optimal parameters. Furthermore, M_s is calculated for both the preliminarily solved and interpolated systems using the approximation method, and the obtained M_s values are shown in Table 1. This result reveals that the proposed decision method is sufficiently effective.

Table 1. Obtained M_s

M_s^d	Servo design			Regulation design		
	Min	Mean	Max	Min	Mean	Max
1.4	1.398	1.403	1.440	1.399	1.403	1.453
1.6	1.599	1.605	1.668	1.597	1.605	1.663
1.8	1.790	1.807	1.909	1.798	1.807	1.897
2.0	1.996	2.010	2.156	1.997	2.009	2.137

5. Numerical Simulation

In this section, the effectiveness of the proposed method is confirmed.

5.1. Control performance for various values of ζ

First, the control performance is confirmed for ζ . The controlled plant is defined as $K = 4.2$, $\omega_n = 1.13$, and $L = 0.44$ in Eq. (1), and $T_s = 0.018$. Here, we consider four pattern damping coefficients: $\zeta^1 = 0.451$, $\zeta^2 = 0.69$, $\zeta^3 = 1.0$, and $\zeta^4 = 1.199$. The control results are shown in Fig. 3. The reference value is set to 1.0, and the unit step disturbance signal is added after 20 s. Figure 3 shows that the proposed method is effective for under- and over-damping systems.

5.2. Verification of stability margin

Next, the stability margin is confirmed. Here, the controlled plant is defined as $K = 2.02$, $\omega_n = 0.91$,

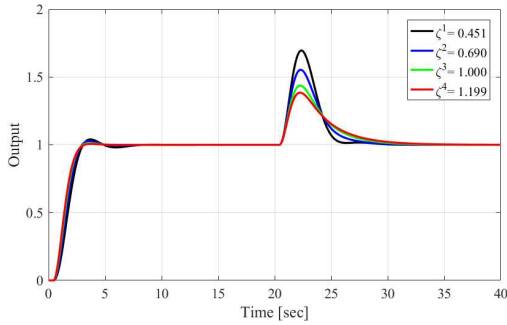


Fig. 3. Output responses for each damping coefficient ζ^i (servo design and $M_s^d = 1.4$)

$\zeta = 0.33$, and $L = 0.98$ in Eq. (1), and $T_s = 0.05$. After 40 s, the dynamics is changed to $K = 2.6$, $\omega_n = 1.3$, $\zeta = 0.43$, and $L = 0.43$ as the model variation. Furthermore, M_s^d is varied as 1.4, 1.6, 1.8, and 2.0, respectively, and the control results are compared. The obtained results are shown in Fig. 4. The reference value is 1.0, and the unit step disturbance signal is added after 20 s. The model variation is caused at 40 s. Figure 3 shows that the smaller the value of M_s^d , the larger the stability margin, and vice versa. On the other hand, the larger the value of M_s^d , the better the tracking performance, and vice versa.

Conclusion

In the present study, we proposed a new design method for controlling an SOPDT sampled-data system, where the continuous-time plant is controlled by the discrete-time PID control law. In the proposed method, the PID

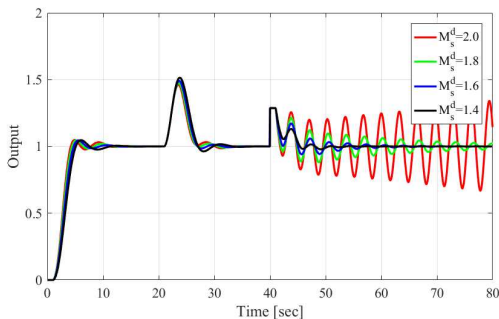


Fig. 4. Output responses for each M_s^d

parameters are designed for the normalized system, and the tracking performance is optimized subject to the assigned M_s^d . Finally, the effectiveness of the proposed method is demonstrated through numerical examples.

Acknowledgements

The present study was supported by a Grant-in-Aid for Scientific Research (C) 16K06425. The authors would like to express their sincere thanks for the support from the Japan Society for the Promotion of Science.

References

1. K. J. Åström and T. Häggglund, *Advanced PID Control*, (ISA-Instrumentation, Systems, and Automation Society, 2006).
2. R. Vilanova and A. Visioli, *PID Control in the Third Millennium* (Springer, UK, 2012)
3. O. Arrieta and R. Vilanova, Simple PID Tuning Rules with Guaranteed M_s Robustness Achievement, *IFAC Proceedings* **44**(1) (2011) 12042-12047.
4. O. Arrieta and R. Vilanova, Simple Servo/Regulation Proportional-Integral-Derivative (PID) Tuning Rules for Arbitrary M_s -Based Robustness Achievement, *Industrial & Engineering Chemistry Research* **51**(6) (2012) pp. 2666-2674.
5. H. Tajika, T. Sato, R. Vilanova and Y. Konishi, Optimal PID Control in Discrete Time Using a Sensitivity Function, *23th Mediterranean Conference on Control and Automation (MED)* (2015) pp. 249-254.

Experimental Evaluation of a Data-Driven Control System using an Electronic Thermal Regulator

Yuka Okubo

*Graduate School of Engineering, Hiroshima University,
1-4-1, Kagamiyama, Higashihiroshima city, Hiroshima, Japan*

Yoichiro Ashida

*Graduate School of Engineering, Hiroshima University,
1-4-1, Kagamiyama, Higashihiroshima city, Hiroshima, Japan*

Takuya Kinoshita

*Graduate School of Engineering, Hiroshima University,
1-4-1, Kagamiyama, Higashihiroshima city, Hiroshima, Japan*

Toru Yamamoto

*Graduate School of Engineering, Hiroshima University,
1-4-1, Kagamiyama, Higashihiroshima city, Hiroshima, Japan*

*E-mail: okubo-yuka@hiroshima-u.ac.jp, ashida-yoichiro@hiroshima-u.ac.jp, kinoshita--takuya@hiroshima-u.ac.jp,
yama@hiroshima-u.ac.jp
<http://www.hiroshima-u.ac.jp>*

Abstract

IoT (Internet of Things) attracting attention, the data of the controlled objects is expected to be utilized to control systems in industries. Therefore, the data-driven scheme is hoped to be implemented to the electronic thermal regulator. The technique is hardly to be implemented in it due to restricted memory capacity, hence, a computer calculates PID gains by the data-driven and sends the gains to the electronic thermal regulator. The effectiveness of the proposed platform is demonstrated by the experiment.

Keywords: PID controller, data-driven controller, electronic thermal regulator, FRIT

1. Introduction

In recent years, IoT has been received attentions, and the data of systems obtained through a lot of sensors is hoped to be utilized to control systems in industries¹. Such data, which is collected by communication between sensors and cloud, is stored in database.

On the other hand, the electronic thermal regulators² are employed to control systems as general controllers, in which PID controller^{3, 4} is basically applied. In the case of using PID controller, the PID gains must be tuned considering the properties of controlled objects. Most of

the practical controlled objects have nonlinearity, and it is difficult to control them suitably by using the fixed PID controller. Therefore, the data-driven technique⁵ having effectiveness for non-linear systems has been proposed. Calculating a set of PID gains based on the database depending on current operating data, the data-driven scheme can appropriately control such systems. The data-driven technique needs the large memory for database. Therefore, it is hard to implement this technique to the electronic thermal regulator due to its restricted memory capacity. If the computer is utilized for implementing the data-driven control scheme, the new interface between

the computer and controlled object must be introduced instead of the electronic thermal regulator. Hence, the data-driven scheme is hardly implemented to the industrial field.

In this paper, the construction of the data-driven control platform using the electronic thermal regulator is firstly explained, in which the database is introduced in order to realize the data-driven PID controller. According to the proposed platform, the computer calculates PID gains by the data-driven technique and sends them to the electronic thermal regulator. As a result, the aforementioned memory capacity restriction of the electronic thermal regulator can be avoided. Furthermore, the existing interfaces between electronic thermal regulator and control objects do not need to be changed for implementing the data-driven scheme.

In this paper, section 2 shows the schematic of the data-driven control platform. The design of data-driven controller is explained in section 3. In section 4, it is shown the effectiveness of the proposed platform by conducted experiment using actual equipment. The paper ends with concluding remarks in section 5.

2. Construction of data-driven control platform

The schematic of data-driven control platform is shown in Fig. 1. In this paper, the electronic thermal regulator plays a roll of a controller. The electronic thermal regulator receives control outputs, e.g. temperature, humidity or pressure through a sensor and determines the control input. In the proposed platform, the reference signal and control I/O data are sent to the computer having database from the electronic thermal regulator. The computer sends a set of PID gains calculated on data-driven scheme to the electronic thermal regulator. Since the computer sends not control input but PID gains, the electronic thermal regulator can control systems using last PID gains even if the communication is fault.

3. Design of the data-driven controller

3.1. Controlled Object

The controlled object can be described by the following nonlinear system:

$$y(t) = f(\phi(t-1)), \quad (1)$$

where $y(t)$ is system output, $f(\cdot)$ denotes the function of nonlinearity and $\phi(t-1)$ is an information vector showing the historical data of the system. $\phi(t-1)$ is defined by following equation:

$$\phi(t-1) := [y(t-1), \dots, y(t-n_y), u(t-1), \dots, u(t-n_u)], \quad (2)$$

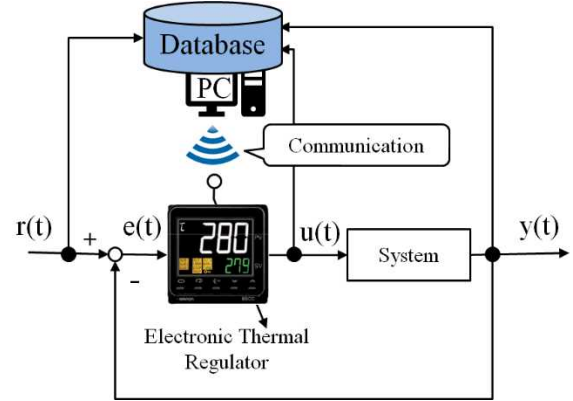


Fig. 1. The schematic of data-driven control platform.

where $u(t)$ is the control input, and n_y, n_u are the orders of the system output and the control input, respectively. In this paper, the following control law with a PID structure is introduced:

$$\Delta u(t) = \frac{k_c T_s}{T_i} e(t) - k_c \left(\Delta + \frac{T_d}{T_s} \Delta^2 \right) y(t) = K_I e(t) - K_P \Delta y(t) - K_D \Delta^2 y(t), \quad (3)$$

where $e(t)$ denotes the control error signal defined by the following equation:

$$e(t) = r(t) - y(t), \quad (4)$$

where $r(t)$ is the reference signal. The $k_c, T_i,$ and T_d in equation (3) express the proportional gain, integral time, and derivative time, respectively. K_p, K_i and K_D similarly denote the proportional gain, integral gain and derivative gain. The z^{-1} shows the backward operator. T_s and $\Delta (= 1 - z^{-1})$ are the sampling time and differencing operator.

3.2. Design of data-driven controller

[STEP1] Generate initial database: In the data-driven control, the control parameters are calculated from the historical closed-loop data stored in a database. If there are no stored information vectors in the database, the data-driven scheme cannot work. To create initial database, it is required to obtain the closed-loop data. The data stored in the form by the following equation:

$$\Phi(t) := [\bar{\phi}(t), \mathbf{K}(j)], \quad j = 1, 2, \dots, N(0) \quad (5)$$

$$\mathbf{K}(t) := [K_p(t), K_i(t), K_D(t)], \quad (6)$$

where $N(0)$ is the number of information vectors stored in the initial database. The query is defined by the following equation:

$$\bar{\phi}(t) := [r(t+1), r(t), y(t), \dots, y(t-n_y+1), u(t-1), \dots, u(t-n_u+1)], \quad (7)$$

[STEP2] Calculate distances and Select neighbors: The distances between query $\bar{\phi}(t)$ and every information vector $\bar{\phi}(i)$, where $i \neq t$, in the database are calculated by the following equation:

$$d(\bar{\phi}(t), \bar{\phi}(j)) = \sum_{l=1}^{n_u+n_y+1} \left| \frac{\bar{\phi}_l(t) - \bar{\phi}_l(j)}{\max_m \bar{\phi}_l(m) - \min_m \bar{\phi}_l(m)} \right|, \quad (8)$$

$$(j = 1, 2, \dots, N(t))$$

where $N(t)$ is the number of information vectors in the database at t . The $\max_m \bar{\phi}_l(m)$ denotes the maximum value of l_{th} elements in all information vectors. Similarly, the $\min_m \bar{\phi}_l(m)$ expresses the minimum value of l_{th} elements in all information vectors. The k -pieces vectors with the smallest d are selected from all information vectors. The selected information vectors and PID gains corresponding to the information vectors are neighbor vectors.

[STEP3] Calculate PID gains: The suitable PID gains around the query are calculated by applying the steepest decent method to selected neighbor vectors in STEP 2.

$$\mathbf{K}^{old}(t) = \sum_{i=1}^k w_i \mathbf{K}(i), \quad \sum_{i=1}^k w_i = 1, \quad (9)$$

where w_i in equation (9) is weight for $\mathbf{K}(i)$ corresponding to the i_{th} information vector $\bar{\phi}(i)$ as follows:

$$w_i = \frac{e^{-d_i}}{\sum_{i=1}^k e^{-d_i}}, \quad (10)$$

where d_i expresses the distance calculated by equation (8) between query and i_{th} information vector.

3.3. Off-line learning by FRIT

The fictitious reference iterative tuning (FRIT)⁶ is a technique calculating directly the control parameters from a pair of I/O data. The new PID gains \mathbf{K}^{new} are obtained by updating the database stored PID gains \mathbf{K}^{old} . The following steepest decent method is applied to modify the PID gains:

$$\mathbf{K}^{new} = \mathbf{K}^{old} - \boldsymbol{\eta} \frac{\partial J(t+1)}{\partial \mathbf{K}}, \quad (11)$$

$$\boldsymbol{\eta} := [\eta_p, \eta_i, \eta_d],$$

where $\boldsymbol{\eta}$ denotes the learning rates for each control parameters. The $J(t+1)$ expresses the error criterion as follows:

$$J(t+1) := \frac{1}{2} \varepsilon(t+1)^2 \quad (12)$$

$$\varepsilon(t+1) := y_0(t+1) - \tilde{y}_m(t+1). \quad (13)$$

When $J(t+1)$ is minimized, the PID gains can be calculated such that $y_0(t)$ and $\tilde{y}_m(t)$ are equal. In equation (13), the fictitious reference output $\tilde{y}_m(t)$ is

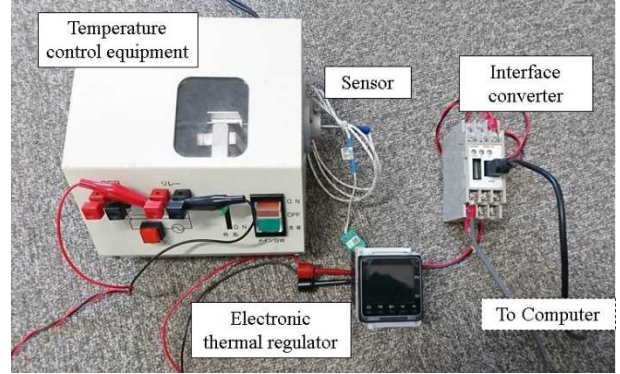


Fig. 2. Appearance of the temperature control equipment.

used so that the closed-loop system including a controller has a desired characteristic of the reference model. $\tilde{y}_m(t)$ is shown by the following equation:

$$\tilde{y}_m(t) = \frac{z^{-1}P(1)}{P(z^{-1})} \tilde{r}(t). \quad (14)$$

$P(z^{-1})$ is a user-specified polynomial included in the reference model and arbitrarily designed in advance such that the model has a desired characteristic.

$$P(z^{-1}) := 1 + p_1 z^{-1} + p_2 z^{-2}, \quad (15)$$

$$\left. \begin{aligned} p_1 &= -2 \exp\left(-\frac{\rho}{2\mu}\right) \cos\left(\frac{\sqrt{4\mu-1}}{2\mu} \rho\right) \\ p_2 &= \exp\left(-\frac{\rho}{\mu}\right) \\ \rho &:= \frac{T_s}{\sigma} \\ \mu &:= 0.25(1-\delta) + 0.51\delta \end{aligned} \right\}. \quad (16)$$

σ denotes the rise-time, and δ is a parameter relevant to dumping. It is required that σ is set to between 1/2 and 1/3 sum of time constant and dead time. δ is desired to set to between 0 and 2. When $\delta = 0$, the step response is the Binomial model response. When $\delta = 1$, the step response shows the Butterworth model response.

In equation (14), the fictitious reference input $\tilde{r}(t)$ is calculated by input-output relation of controller $C(z^{-1})$. The $C(z^{-1})$ is expressed as follows:

$$C(z^{-1}) = c_0 + c_1 z^{-1} + \dots + c_n z^{-n}, \quad (17)$$

where n is the control law order. n equals 2 in the case where PID controller is used. The input-output relation of controller is shown by the following equation:

$$u_0(t) = \frac{C(z^{-1})}{\Delta} \{\tilde{r}(t) - y_0(t)\}, \quad (18)$$

$$\tilde{r}(t) = C^{-1}(z^{-1}) \Delta u_0(t) + y_0(t). \quad (19)$$

the fictitious reference signal $\tilde{r}(t)$ is obtained by deformation of equation (18).

4. Experimental control results

In this paper, the data-driven control platform was applied to the temperature equipment shown in Fig. 2.

The electronic thermal regulator E5CC-QQ2ASM and the interface converter K3SC-10 for connection between the electronic thermal regulator and a computer was utilized, which they made by OMRON Corporation. The temperature equipment equips with a ceramic heater and an aluminum block. The control output $y(t)$ is the temperature of the aluminum and is measured with a thermocouple of K-type. The control input $u(t)$ is duty ratio which determines how much to heat through a relay. The reference signal $r(t)$ was set to $r(t) = 60$ [°C] and the sampling time T_s was set to 2 [s]. After the control output can track to the reference signal, a disturbance was applied that non-heated aluminum contacts and cools the heated one.

The PID parameters for generating initial database were denoted as follows:

$$K_p = 2.07, K_I = 0.021, K_D = 1.29. \quad (20)$$

The initial data vectors were stored database according to equation (5). User-specified parameters for the experiment are shown in Table 1.

The desired polynomial $P(z^{-1})$ was designed as

$$P(z^{-1}) = 1 - 1.91z^{-1} + 0.91z^{-2}, \quad (21)$$

where σ and δ were set to $\sigma = 90$ and $\delta = 0$. The control results of using the fixed PID gains and the proposed platform are respectively shown in Fig. 3. The upper figure shows that solid line is the control output by the proposed platform, dotted line is the desired control output, dash line is the reference signal and chain line is the control output using the fixed PID gains. The control result of using fixed PID controller cannot track to the desired control output and the disturbance let it cool 13°C approximately at $t = 700$. In comparison with two results, the rise-time of the proposed scheme is shorter than one of the fixed PID controller. Therefore, the effectiveness of data-driven control platform was verified.

5. Conclusion

In this paper, the effectiveness of data-driven control platform has been verified. In the proposed platform, it is handily permitted advance control law that a computer sends PID gains to the electronic thermal regulator using an existing interface. Even if PID gains cannot be sent to the electronic thermal regulator, a system is controlled using the last PID gains. In this paper, the PID gains are adjusted at every step. In future work, the control design method, in which PID gains are adjusted only the case where the control performance is deteriorated, will be considered.

Table 1: User-specified parameters for the experiment.

Orders of the information vector	$n_u = 1$ $n_y = 2$
Number of neighbors	$k = 6$
Learning rates	$\eta_p = 1.0 \times 10^{-3}$ $\eta_I = 1.0 \times 10^{-4}$ $\eta_D = 1.0 \times 10^{-3}$
Initial Number of data	$N(0) = 1138$

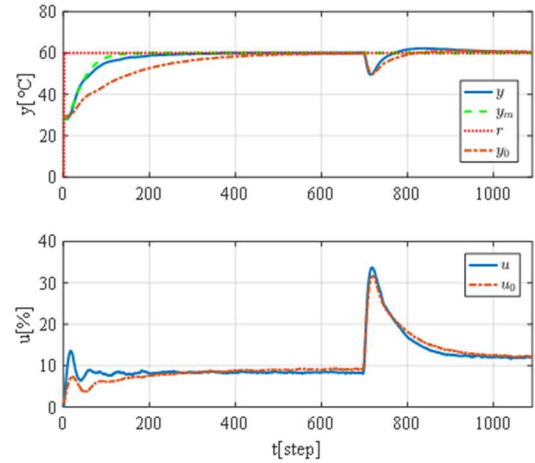


Fig. 3. The control results by the proposed platform, and by fixed PID controller.

References

1. T. Munaka, Newly Coming World by IoT-The Trend of Industrial Internet, *System, Control and Information*, Vol. 60, No. 10, (2016) pp. 425-430. (in Japanese)
2. Tateishi Electric Co., Temperature Controller Thermac X Series, *Journal of The Society of Instrument and Control Engineers*, Vol. 27, No. 12 (1988) pp. 1130-1131. (in Japanese)
3. K. J. Astrom, T. Hagglund, Advanced PID Control, *International Society of Automation*, (2005)
4. K.L. Chien, J.A. Hrones, and J.B. Reswick, On the Automatic Control of Generalized Passive Systems, *Trans. ASME*, Vol.74, (1972) pp. 175-185
5. T.Yamamoto, K.Takao, and T.Yamada, Design of a Data-Driven PID Controller, *IEEE Transaction on Control Systems Technology*, Vol.17, No.1 (2009), pp. 29-39
6. S. Soma, O. Kaneko, and T. Fujii, A New Approach to Parameter Tuning of Controllers by Using One-Shot Experimental Data: A Proposal of Fictitious Reference Iterative Tuning, *Trans. Institute of Systems Control and Information Engineers*, Vol.17, No.12, (2004) pp. 528-536

Self-repairing Adaptive PID Control for Plants with Sensor Failures

Masanori Takahashi

Department of Electrical Engineering and Computer Science, Tokai University
9-1-1 Toroku, Higashi-ku, Kumamoto, 862-8652, Japan

E-mail: masataka@ktmail.tokai-u.jp

Abstract

This paper presents a new design method for a self-repairing adaptive PID control system. The control system has the adaptive adjusting mechanisms for the PID gains, and also can detect the sensor failure by self-test using the integrator in the PID controller. Hence, for plants with unknown parameters, self-repairing control can be successfully attained. Furthermore, in this paper, the control performances are theoretically analyzed.

Keywords: PID control, Adaptive control, Fault-tolerant control, Sensor failure.

1. Introduction

Against sensor failure, several types of self-repairing control systems (SRCS) have been developed in the previous works. The SRCS can detect failure by self-testing using the internal signals, and automatically replace the failed sensor with the healthy backup to maintain its stability. They belong to active fault-tolerant control (AFTC) based on dynamic redundancy¹. The main difference (feature point) from the conventional AFTC is that the fault detector is quite simple, and its structure does not depend on the mathematical model of the plant.^{2,3,4} For example, the integrator in the PID controller can be utilized as fault detector for the SRCS⁵.

However, in most existing SRCSs, roughly estimated parameters of plants are required to construct the controller. This paper presents a new design method for a self-repairing adaptive PID control system. The control system has the adaptive adjusting mechanisms for the PID gains, and also can detect the sensor failure by self-

test using the integrator in the PID controller. Thus, no *a priori* information about the plant is needed to attain the SRC. The proposed SRCS is expected to be widely utilized as fault-tolerant PID control.

Furthermore, in this paper, the control stability, failure detection and sensor-recovery are theoretically analyzed. In addition, the numerical simulation is explored to confirm the effectiveness of the proposed adaptive SRCS.

Throughout this paper, with $x \in \mathbb{R}$, we define the “sgn” function by

$$\text{sgn}[x] = \begin{cases} 1 & (x \geq 0) \\ -1 & (x < 0) \end{cases}$$

Notice that this is slightly different from the ordinary one.

2. Problem Statement

Consider the following linear time invariant system:

$$\begin{aligned} \dot{y} &= ay + bu + \mathbf{h}^T \mathbf{z} \\ \dot{\mathbf{z}} &= \mathbf{F}\mathbf{z} + \mathbf{g}y \end{aligned} \quad (1)$$

where $y \in \mathbb{R}$ is the actual output, $u \in \mathbb{R}$ is the input, and $\mathbf{z} \in \mathbb{R}^{n-1}$ is the state of the plant. Here, assume that the plant is minimum-phase, that is, all eigenvalues of $\mathbf{F} \in \mathbb{R}^{(n-1) \times (n-1)}$ lie in \mathbb{C}^- .

For measurement of the output y , the two sensors are exploited; one is the primary sensor #1 and the other is the backup sensor #2 for occasion of failure. Then, the measured feedback signal can be represented as

$$y_S(t) = \begin{cases} y_1(t) & (t \leq t_D) \\ y_2(t) & (t > t_D) \end{cases} \quad (2)$$

where $y_i \in \mathbb{R}$, $i = 1, 2$ is the output of the sensor # i , and $t_D \in \mathbb{R}$ is the detection time whose details will be determined later. If the sensors are healthy, then the measured signals are equivalent to the actual output, that is, we have $y_i = y$. Unfortunately, the primary sensor fails in the following way.

$$y_1(t) = \varphi, \quad t \geq t_F \quad (3)$$

where $t_F \in \mathbb{R}^+$ is the unknown failure time, and $\varphi \in \mathbb{R}$ is the unknown stuck value.

The problem to be considered here, is to construct the active fault-tolerant PID control system for plant with unknown parameters and sensor failures (3), that can automatically replace the failed sensor with the backup to maintain the control stability.

3. Basin Design of the Control System

First of all, the adaptive PID controller is designed by

$$u = k_P(-y_S + v) - k_D \dot{y}_S \quad (4)$$

where $v \in \mathbb{R}$ is the output of the integrator:

$$\dot{v} = -k_I y_S - \tau \text{sgn}[y_S] \quad (5)$$

with a constant $\tau \in \mathbb{R}^+$, which is introduced for detection of failure. The fault detection using the signal v will be discussed in the next subsection.

In the above adaptive controller, the PID gains, $k_P: \mathbb{R}^+ \rightarrow \mathbb{R}^+$, $k_I: \mathbb{R}^+ \rightarrow \mathbb{R}^+$ and $k_D: \mathbb{R}^+ \rightarrow \mathbb{R}^+$ are adaptively tuned as follows.

$$\begin{aligned} \dot{k}_P &= -\sigma k_P + \gamma(-y_S + v)^2 \\ \dot{k}_I &= -\sigma k_I - \gamma y_S (y_S - 2v) \\ \dot{k}_D &= -\sigma k_D - \delta \gamma \dot{y}_S (-y_S + v) \end{aligned} \quad (6)$$

where $\sigma \in \mathbb{R}^+$ is an any small constant, and $\gamma \in \mathbb{R}^+$ is a positive constant. Also, a small constant $\delta \in \mathbb{R}^+$ is

introduced as a scaling factor. These are given by designers.

Here, we shall analyze the control stability on the time period $[0, t_F)$ where the sensor is healthy, i.e., $y_S = y$. Now, define the augmented signal $\varepsilon: \mathbb{R}^+ \rightarrow \mathbb{R}$ by

$$\varepsilon := -y_S + v \quad (7)$$

Then, the signals, ε , \mathbf{z} , v obey the following equations.

$$\begin{aligned} \dot{\varepsilon} &= \left(\frac{1}{1 + bk_D^*} \right) \{ -(bk_P^* - a - k_I^* + bk_D^* k_I^*) \varepsilon + b \Delta_P \varepsilon \\ &\quad - \Delta_I (\varepsilon - v) - (k_I^* + a - bk_D^* k_I^*) v - b \Delta_D \dot{y} \\ &\quad - \mathbf{h}^T \mathbf{z} - (1 - bk_D^*) \tau \text{sgn}[y] \} \\ \dot{\mathbf{z}} &= \mathbf{F} \mathbf{z} - \mathbf{g} \varepsilon + \mathbf{g} \\ \dot{v} &= -k_I^* v + k_I^* \varepsilon - \Delta_I (\varepsilon - v) - \tau \text{sgn}[y] \end{aligned} \quad (8)$$

where $\Delta_P := k_P^* - k_P$, $\Delta_I := k_I^* - k_I$ and $\Delta_D := k_D^* - k_D$, and $k_P^* \in \mathbb{R}^+$, $k_I^* \in \mathbb{R}^+$ and $k_D^* \in \mathbb{R}^+$ are the ideal gains for PID control.

Consider the positive definite function $S: \mathbb{R}^+ \rightarrow \mathbb{R}^+$:

$$S = \frac{1}{2} \left\{ (1 + bk_D^*) \varepsilon^2 + \mathbf{z}^T \mathbf{P} \mathbf{z} + v^2 + \frac{b}{\gamma} \Delta_P^2 + \frac{1}{\gamma} \Delta_I^2 + \frac{b}{\delta \gamma} \Delta_D^2 \right\} \quad (9)$$

where $\mathbf{P} \in \mathbb{R}^{(n-1) \times (n-1)}$ is the positive definite matrix which satisfies $\mathbf{F}^T \mathbf{P} + \mathbf{P} \mathbf{F} = -2\mathbf{Q}$ for any positive definite $\mathbf{Q} \in \mathbb{R}^{(n-1) \times (n-1)}$.

Taking the time derivative of S , gives

$$\begin{aligned} \dot{S} &= -(bk_P^* - a - k_I^* + bk_D^* k_I^*) \varepsilon^2 \\ &\quad + b \Delta_P \varepsilon^2 - \Delta_I (\varepsilon - v) \varepsilon - b \Delta_D \dot{y} \varepsilon \\ &\quad - (k_I^* + a - bk_D^* k_I^*) v \varepsilon - \mathbf{h}^T \mathbf{z} \varepsilon \\ &\quad - (1 - bk_D^*) \tau \text{sgn}[y] \varepsilon \\ &\quad - \mathbf{z}^T \mathbf{Q} \mathbf{z} - \mathbf{z}^T \mathbf{P} \mathbf{g} \varepsilon + \mathbf{z}^T \mathbf{P} \mathbf{g} v \\ &\quad - k_I^* v^2 + k_I^* \varepsilon v - \Delta_I (\varepsilon - v) v - \tau \text{sgn}[y] v \\ &\quad - \frac{b}{\gamma} \Delta_P \dot{k}_P - \frac{1}{\gamma} \Delta_I \dot{k}_I - \frac{b}{\delta \gamma} \Delta_D \dot{k}_D \end{aligned} \quad (10)$$

Furthermore, from (6), it follows that

$$\begin{aligned} \dot{S} &= -\frac{1}{2} \alpha_1 \varepsilon^2 - \frac{1}{2} \alpha_2 \|\mathbf{z}\|^2 - \frac{1}{2} \alpha_3 v^2 \\ &\quad - \frac{b\sigma}{2\gamma} \Delta_P^2 - \frac{\sigma}{2\gamma} \Delta_I^2 - \frac{b\sigma}{2\delta\gamma} \Delta_D^2 + \beta \end{aligned} \quad (11)$$

where

$$\alpha_1 = bk_p^* + bk_D^*k_i^* - 3|a| - 2k_i^* - \|\mathbf{h}\|^2 - \|\mathbf{P}\mathbf{g}\|^2$$

$$\alpha_2 = 2\lambda_{\min}[\mathbf{Q}] - 3$$

$$\alpha_3 = (1 - bk_D^*k_i^*)k_i^* - |a| - \|\mathbf{P}\mathbf{g}\|^2$$

$$\beta = \frac{\tau^2}{2} \left(\frac{1}{bk_p} + bk_D + \frac{1}{k_i} \right) + \frac{b\sigma}{2\gamma} (k_p^*)^2 + \frac{b\sigma}{2\gamma} (k_i^*)^2 + \frac{b\sigma}{2\delta\gamma} (k_D^*)^2$$

Here, choose \mathbf{Q} , k_p^* , k_i^* and k_D^* so that $\alpha_i > 0$, $i = 1, 2, 3$.

Then, we have

$$\begin{aligned} \dot{S} &\leq -\alpha S + \beta, \\ \alpha &= \min \left[\alpha_1, \alpha_2, \alpha_3, \frac{\sigma}{2\gamma}, \frac{b\sigma}{2\gamma} \right] \end{aligned} \quad (12)$$

which yields,

$$S(t) \leq S(0)\exp(-\alpha t) + \frac{\beta}{\alpha}, t \in [0, t_F] \quad (13)$$

Hence, from (9), it is verified that all the signals in the adaptive control system are bounded on $[0, t_F]$.

The block diagram of the proposed control system is illustrated in Fig. 1.

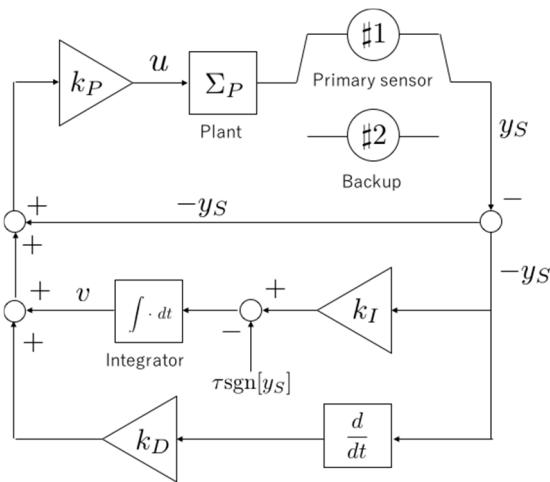


Fig. 1. Block diagram of the proposed adaptive PID control system with self-repairing function.

4. Failure Detection & Repairing

This section shows the concrete detection method utilizing the integrator (5).

© The 2018 International Conference on Artificial Life and Robotics (ICAROB2018), Feb. 1-4, B-Con Plaza, Beppu, Oita, Japan

From the above discussion, on the time period $[0, t_F)$, there exists $\Gamma \in \mathbb{R}^+$ such that

$$v(t) < \Gamma, t \in [0, t_F) \quad (14)$$

However, if the sensor fails, and $\varphi = 0$, then the output of the integrator can be represented by

$$v = v(t_F) - \int_{t_F}^t \tau dt = v(t_F) - \tau(t - t_F) \quad (15)$$

Clearly, v is unbounded with respect to t . Hence, the inequality (14) hold no longer. By using this unstable behavior, we can find failure, and define the detection time t_D by

$$t_D := \min\{t \mid |v(t)| \geq \Gamma\} \quad (16)$$

Next, we consider the faulty situation where $\varphi \neq 0$. Then, the solution (v, k_i) obeys

$$\begin{aligned} \dot{v} &= -k_i\varphi - \tau \operatorname{sgn}[\varphi] \\ \dot{k}_i &= -\sigma k_i - \gamma\varphi(\varphi - 2v) \end{aligned}$$

Hence, the equilibrium point (\bar{v}, \bar{k}_i) , is given by

$$\begin{aligned} \bar{v} &= \frac{\varphi}{2} + \frac{\sigma\tau}{2\gamma\varphi^2} \operatorname{sgn}[\varphi] \\ \bar{k}_i &= -\frac{\tau}{\varphi} \operatorname{sgn}[\varphi] \end{aligned}$$

Now, we suppose that Γ, γ, σ and τ are selected so that

$$\Gamma < \left| \frac{\varphi}{2} + \frac{\sigma\tau}{2\gamma\varphi^2} \right|$$

Then, even if v approaches to the equilibrium point, it hits the threshold Γ . Therefore, the detection time t_D defined by (16) exists when $\varphi \neq 0$. Failure detection can be successfully achieved. After detection, the failed sensor is replaced with the backup, and the control stability can be maintained.

5. Numerical Simulation

To confirm the effectiveness of the proposed method, the numerical simulation is explored.

Consider the following unstable plant:

$$\begin{aligned} \dot{y} &= y + 2u + z, \quad y(0) = 1 \\ \dot{z} &= -z + y, \quad z(0) = -0.5 \end{aligned}$$

The failure scenario is supposed that

$$t_F = 25 [s], \varphi = y(t_F) \quad (17)$$

In the simulation, they are assumed to be unknown.

For the above plant, we construct the adaptive PID controller based on (4) and (5). By trial and error, the design parameters are selected as follows.

$$\sigma = 0.01, \gamma = 1, \delta = 0.1$$

The other parameters for failure detection are given by

$$\tau = 1, \Gamma = 1$$

The simulation results are shown in Figs. 2 and 3. In Fig. 2, the measured output y_s , the actual output y (top) and the absolute value of v (bottom) are shown. Also, in Fig. 3, the three adaptive gains, k_P (top), k_I (middle) and k_D (bottom) are shown.

From these results, it is clear that the failure (17) can be found and the failed sensor is replaced at $t_D \cong 26 [s]$. Furthermore, the control system can be well stabilized, and the actual output converges to a very small ball before and after the failure.

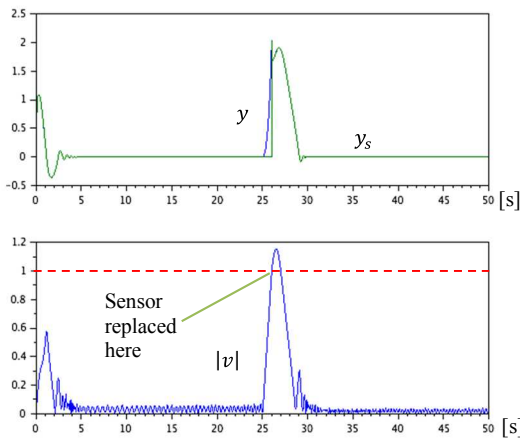


Fig. 2. Simulation results: the measured output, the actual output and the absolute value of the integrator output.

6. Conclusions

In this paper, a new adaptive PID control system has been developed that has self-repairing function against sensor failures, and the concrete failure detection is shown by using the integrator in the PID controller.

The applications to MIMO case, nonlinear systems and so on are still left in the future works.

Acknowledgment

This work is supported by JSPS KAKENHI Grant Number JP16K06429.

References

1. R. Isermann, R. Schwarz and S. Stolz: Fault-tolerant, Drive-by-wire systems, *IEEE Control Systems Magazine*, Vol. 22, No. 5, pp. 64-81 (2002).
2. Y. Zhang and J. Jiang: Biographical review on reconfigurable fault-tolerant control systems, *Annual Reviews in Control*, Vo. 32, No. 2, pp. 229-252 (2008)
3. K. Zhang, B. Jiang and V. Cocquempot: Fast adaptive fault estimation and accommodation for nonlinear time-varying delay systems, *Asian Journal of Control*, Vol. 11, No. 6, pp. 643-652 (2009).
4. Y. Wan, D. Zhou, S. J. Qin and H. Wang: Active fault-tolerant control for a class of nonlinear systems with sensor faults, *Int. J. of Control, Automation and Systems*, Vol. 6, No. 3, pp. 339-350 (2008)
5. M. Takahashi: Self-repairing PI/PID control against sensor failures, *Int. J. Innovative Computing, Information and Control*, Vol. 12, No. 1, Feb. pp. 193-202 (2016)

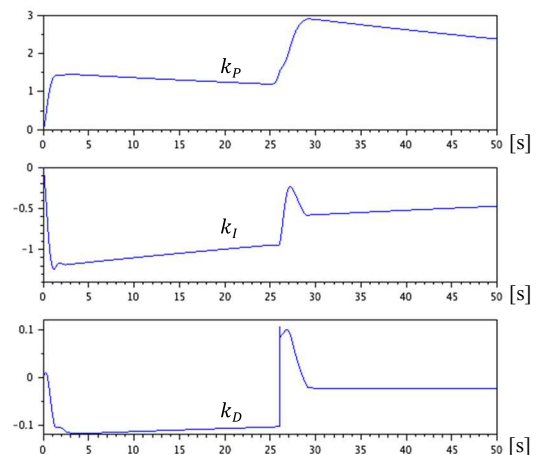


Fig. 3. Simulation results: the three adaptive PID gains.

Design and Development of a Constant Temperature Reservoir for a Database-Driven Smart Cultivation System

Shin Wakitani

Graduate School of Engineering, Hiroshima University, 1-4-1 Kagamiuyama Higahsi-hiroshima, Hiroshima 739-8527, Japan

Sharma Sneha

Graduate School of Engineering, Hiroshima University, 1-4-1 Kagamiuyama Higahsi-hiroshima, Hiroshima 739-8527, Japan

Toru Yamamoto

Graduate School of Engineering, Hiroshima University, 1-4-1 Kagamiuyama Higahsi-hiroshima, Hiroshima 739-8527, Japan

*E-mail: wakitani@hiroshima-u.ac.jp, sharma-sneha-atul@hiroshima-u.ac.jp, yama@hiroshima-u.ac.jp
<https://www.hiroshima-u.ac.jp>*

Abstract

Decreasing the number of agricultural working population is serious problem. Production of agricultural products in plant factories is as one of the solutions to the above problems. However, it is not easy to set optimal environment conditions for many kinds of plants in food factories. This research aims for realization of a smart cultivation system that uses a database-driven (DD) technique. In this work, a pilot scale constant temperature reservoir is developed, and a DD nonlinear temperature control is performed.

Keywords: Cultivation System, Temperature control, Data-driven control, Nonlinear control.

1. Introduction

Recently interests and requirements to domestic production and pesticide-free production of agricultural products have been increasing in Japan. However, it has not putting the brake on the decreasing of agricultural workforce. Because of this situation, a plant factory, that can make many production processes of agricultural products automate and is able to produce them safely and stably, has been gotten much attention. A plant factory can be said as one form of protected horticulture that can control production schedule by manipulating its environment conditions such as temperature, humidity, CO₂ concentration. Techniques for such environments controls have been actively studied in process control,

and they can be applied to the system easily. Although, actual controlled variables that should be manipulated in plant factories are growth speed, taste, nutrition etc. of plants, and the environment control system must be designed to maximize a criterion including the above variables, a uniform method that can deal with many kinds of plants has not been established.

A plant can be regarded as a controlled object which has strong nonlinearity from a point of view of control engineering. Thus, it is difficult to manipulate them by a linear controller with fixed control parameters. Moreover, it may difficult to maintain ideal environment conditions of a plant factory by the controller due to the changing environment around the factory and aged deterioration of equipment. For such systems, a database-driven (DD)

© The 2018 International Conference on Artificial Life and Robotics (ICAROB2018), Feb. 1-4, B-Con Plaza, Beppu, Oita, Japan

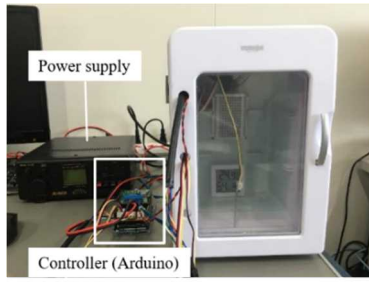


Fig. 1. Appearance of constant temperature reservoir.

control method¹, that adaptively tunes control parameters corresponding to environment conditions by utilizing a database which is stored a lot of previous operation data, is expected to achieve high control performance. Moreover, as related researches of the DD control technique, design methods of nonlinear modeling², soft-sensor, expert controller³ (that can imitate several experts' control action) based on a database have been proposed. From these circumstances, it can consider to be able to realize a smart cultivation system that utilizes DD methods as core technique.

In this research, a pilot scale constant temperature reservoir is developed as a first step. In this system, a Peltier device which is one of thermoelectric conversion devices is implemented to control temperature. In the Peltier device, by supplying current to the device, one side exhausts the heat, and the other side absorptions the heat corresponding to the amount of the current. Moreover, the exhaust and absorption face of the heat can be switched by changing the direction of the current. However, the amount of generated Joule heat follows the square of the amount of the current, thus a linear controller with fixed control parameters does not maintain a good control performance due to the nonlinearity. Therefore, in this paper, the DD temperature controller is designed and applied to the system to track the actual temperature to wide range temperature references. However, it spends much time to evaluate the effectiveness of the system due to the large time constant of the system. In order to perform debug and performance evaluation of an algorithm the DD controller rapidly, a nonlinear simulator is first constructed based on a principal of the heat balance. This paper is organized as follows. In Section 2, the pilot scale constant temperature and its nonlinear modeling is explained. In Section 3, control results of a fixed PID

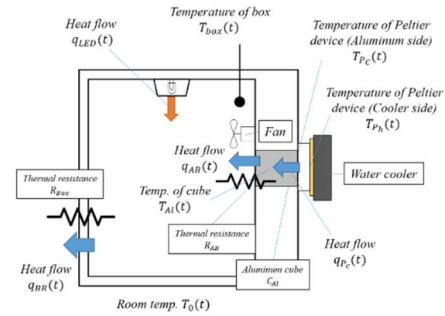


Fig. 2. Schematic of constant temperature reservoir.

Table 1. System parameters.

Variable name	Explanation	Value
R_P	Resistance of Peltier device	3.85
λ_P	Thermal conductivity of Peltier device	10.0
π_P	Peltier coefficient	1.00
α_P	Proportionality constant for T_{Ph}	5.00
R_{AB}	Thermal resistance	0.83
C_{Al}	Thermal capacity	5.00
R_{Box}	Thermal resistance	39211
C_{Box}	Thermal capacity	994.6

controller and the DD controller is shown. Finally, Section 4 summarizes the research findings.

2. Constant Temperature Reservoir Design

Appearance of the constant temperature reservoir is shown in Fig. 1. The schematic and system parameters are shown in Fig. 2 and Table 1. Specific values of system parameters are identified by the genetic algorithm.

2.1. Constant Temperature Reservoir

A Peltier device is implemented on the back of the system, and temperature sensor and humidity sensor are putted on the inside wall. Moreover, full color LEDs for growing plants is putted on the ceiling. The Arduino is utilized as a controller, and it can manipulate the amount of current from the power supply by changing a duty ratio of PWM output voltage of the controller.

2.2. Modeling

In this section, the following couple of heat balance relationships are derived:

- (1) Peltier device – Aluminum block.
- (2) Aluminum block – Space of constant temperature reservoir.

A simulator based on these heat balance models is constructed by using MATLAB/Simulink.

2.2.1. Heat balance between Peltier device and aluminum block

A derivative equation related into the time variation of $T_{Al}(t)$ is given as follows:

$$C_{Al} \frac{dT_{Al}(t)}{dt} = q_{Pc}(t) - q_{AB}(t). \quad (1)$$

Where the maximum voltage of the power supply V_{Pmax} is set to 15 V, and the range of the manipulated value $u_p(t)$ is set between $-100\% \leq u_p(t) \leq 100\%$, the amount of the current in the Peltier device can be given as follows:

$$i(t) = \frac{V_{Pmax} u_p(t)}{R_p \cdot 100}. \quad (2)$$

$q_{Pc}(t)$ that is generated by the above current in the Peltier device is described as follows:

$$q_{Pc}(t) = \pi_p i(t) + \lambda_p \Delta T_p(t) + \frac{1}{2} R_p i(t)^2, \quad (3)$$

$$\Delta T_p(t) = T_{Ph}(t) - T_{Pc}(t). \quad (4)$$

Note that the exhaust heat face of the Peltier device touches a water-cooling face, and it is assumed that the temperature of the contact face is given the following equation:

$$T_{Ph}(t) = \alpha_p i(t). \quad (5)$$

The $q_{AB}(t)$ is given as follows:

$$q_{AB}(t) = \frac{1}{R_{AB}} \{T_{Al}(t) - T_{Box}(t)\}. \quad (6)$$

2.2.2. Heat balance between aluminum block and Space of constant temperature reservoir

A derivative equation related into the time variation of $T_{Box}(t)$ is given as follows:

$$C_{Box} \frac{dT_{Box}(t)}{dt} = q_{AB}(t) - q_{BR}(t) + q_{LED}(t). \quad (7)$$

Where $q_{BR}(t)$ is given as follows:

$$q_{BR}(t) = \frac{1}{R_{BR}} \{T_{Box}(t) - T_0(t)\}. \quad (8)$$

The $q_{LED}(t)$ is the heat flow from the full color LEDs. Thus, the $q_{LED}(t)$ is given as follows by introducing the maximum heat discharge of each color LED (red, green, blue) q_{Rmax} , q_{Gmax} , q_{Bmax} and command signals to each LED u_R , u_G , u_B ($0\% \leq u_{R,G,B} \leq 100\%$):

$$q_{LED}(t) = q_{Rmax} \frac{u_R(t)}{100} + q_{Gmax} \frac{u_G(t)}{100} + q_{Bmax} \frac{u_B(t)}{100}. \quad (9)$$

The static property between $u_p(t)$ and $T_{Box}(t)$ of the obtained simulation model is shown in Fig. 3. The figure shows that the system has nonlinearity.

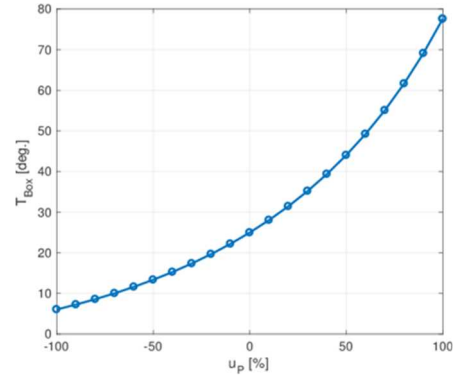


Fig. 3. Static property of simulation model.

3. Application of DD Control Technique

Temperature of the constant temperature reservoir must be controlled properly in order to produce many kinds of plants. In this work, the DD control technique is applied to control the temperature. In the DD controller design scheme, the initial database is required. Thus, in order to generate an initial database, a fixed PID controller is applied to the system, and its operation data is stored into a database.

3.1. Control result by Fixed PID controller

Initial PID parameters are obtained based on a model munching. Firstly, it is assumed that the controlled object can be approximated as the following first order system with time delay around an equilibrium point:

$$G(s) = \frac{K}{1+Ts} e^{-Ls}. \quad (9)$$

Where, T , K , and L is the time constant, the system gain, and the time-delay. By using the least squares method, the system parameters around $T_{Box} = 20$ are obtained as $T = 934$, $K = 0.282$, and $L = 60$, respectively. The following approximated model can be obtained by applying first order approximation to the time-delay:

$$G(s) \cong \frac{K}{1+Ts} \frac{1}{1+Ls}. \quad (10)$$

Secondly, the following I-PD control law is introduced:

$$u(t) = k_c \left\{ \frac{1}{T_I} e(t) - \frac{dy(t)}{dt} - T_D \frac{d^2y(t)}{dt^2} \right\}, \quad (11)$$

$$e(t) = r(t) - y(t). \quad (12)$$

Where, $u(t)$ and $y(t)$ are the controller output and the system output, respectively. In this simulation, $u(t) = u_P(t)$ and $y(t) = T_{Box}(t)$. $r(t)$ is the reference temperature. The following transfer function is introduced as a reference model:

$$G_r(s) = \frac{1}{1 + \left(\frac{\sigma}{s}\right)^2}. \quad (13)$$

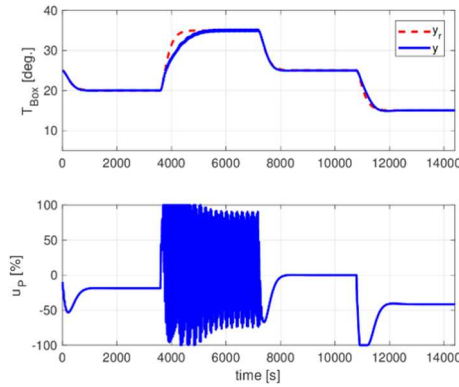


Fig. 4. Control result obtained by fixed PID controller.

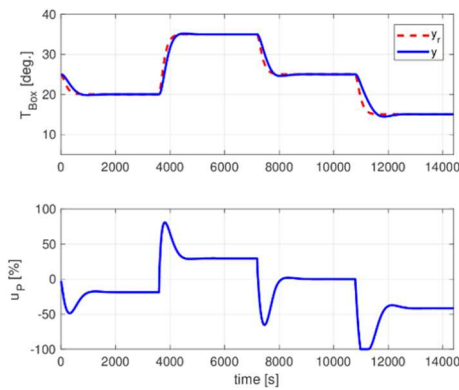


Fig. 5. Control result obtained by DD-PID controller.

σ is the required rise-time of the closed loop system, which is arbitrarily set by a user. The following relationship can be obtained by comparing the transfer function of the closed loop system, constructed by (10) and (11), and the reference model (13):

$$kc = c_1, T_I = \frac{c_1}{c_0}, T_D = \frac{c_2}{c_1} \quad (14)$$

$$c_0 = \frac{27(T+L)}{K\sigma^3}, c_1 = \frac{27(T+L)-\sigma^2}{K\sigma^2}, c_2 = \frac{9(T+L)-\sigma TL}{K\sigma} \quad (15)$$

The control result by fixed the I-PD controller is shown in Fig. 4. In this simulation, the rise time is set to $\sigma = 500$, and the discrete I-PD controller whose sampling time $T_s = 10$ is applied. Moreover, the reference temperature is given as follows:

$$r(t) = \begin{cases} 20 & (0 \leq t < 3600) \\ 35 & (3600 \leq t < 7200) \\ 25 & (7200 \leq t < 10800) \\ 15 & (10800 \leq t < 14400) \end{cases} \quad (16)$$

From Fig. 4, the controller output around $y(t) = 35$ oscillates due to the nonlinearity of the system, and the tracking property is deteriorating.

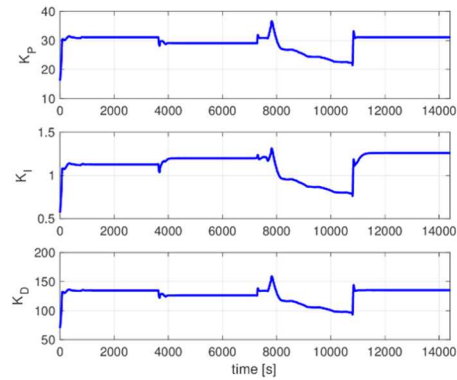


Fig. 6. Trajectories of PID gains corresponding to Fig. 5.

3.2. Control result by DD-PID controller

The control result in Fig. 4 and PID gains are stored into a database, and a DD controller is designed according to the reference¹. The control result using the DD controller is shown in Fig. 5. And trajectories of PID gains are shown in Fig. 6. In this simulation, the rise time is set to $\sigma = 210$, that is faster than the fixed I-PD controller design. These results show that a good control performance is obtained by adaptively tuning PID gains based on the DD control technique.

4. Conclusions

In this work, a constant temperature reservoir that can manipulate several environmental variables was developed to establish a smart cultivation system based on the DD technique. The mathematical model based on a principal of the heat balance was derived and a simulator is constructed by MATLAB/Simulink. The DD controller was also designed, and the effectiveness of the controller was verified by using the simulation model. The implementation of the control system to the real system and designing the structure of smart cultivation system are future works.

References

1. T.Yamamoto, K.Takao, and T.Yamada, Design of a Data-Driven PID Controller, *IEEE Trans. Control Systems Technology*, **17** (1) (2009) pp. 29-39.
2. G. Bontempi, M. Birattari, and H. Bersini, Lazy Learning for Local Modeling and Control Design, *International Journal of Control*, **72** (7-8) (1999), pp. 643-658.
3. H. Matsumori, S.Wakitani and M. Deng, Design and Application of a Data-Driven Expert Controller based on the Operating Data of a Skilled Worker, *Journal of Robotics and Mechatronics (JRM)*, **28** (5) (2016), pp. 730-738.

Design of a Performance-Adaptive 1-Parameter Tuning PID Controller

Yoichiro Ashida

*Graduate School of Engineering, Hiroshima University, 1-4-1 Kagamiyama
Higashihiroshima city, Hiroshima, Japan*

Shin Wakitani

*Graduate School of Engineering, Hiroshima University, 1-4-1 Kagamiyama
Higashihiroshima city, Hiroshima, Japan*

Toru Yamamoto

*Graduate School of Engineering, Hiroshima University, 1-4-1 Kagamiyama
Higashihiroshima city, Hiroshima, Japan*

*E-mail: ashida-yoichiro@hiroshima-u.ac.jp, wakitani@hiroshima-u.ac.jp, yama@hiroshima-u.ac.jp
www.hiroshima-u.ac.jp*

Abstract

Many self-tuning PID controllers have been proposed. However, these methods are rarely employed to actual systems because of low reliability of an on-line PID parameter estimator. In this work, a performance adaptive controller that has two stage of PID parameters tuning mechanisms is proposed. One of the tuners is a one-parameter tuner using the recursive least squares. The other tunes PID parameters using ordinary least squares. The effectiveness of the proposed method is evaluated by an experimental example.

Keywords: PID control, data-oriented, self-tuning control, performance-driven, 1-parameter tuning.

1. Introduction

Most of the controllers in industries have fixed control parameters. However, the controllers cannot obtain good control performances against time -variant systems. To tackle this problem, self-tuning controllers^{1,2} have been proposed. In these controllers, control parameters are tuned adaptively and can maintain a good control performance to time-variant systems. However, it is difficult to employ these methods to actual systems because of low reliability of an on-line estimator. In addition, it is not preferred to tune many control parameters simultaneously in terms of the safeness of a closed-loop system.

Especially in process industries, proportional-integral-derivative (PID) controllers³ have been widely

employed. The reasons why PID controllers have been widely applied include that: (1) PID controllers have simple structure, and (2) physical meanings of the control actions are clear. Therefore, some self-tuning PID control schemes² have been proposed.

In this work, a performance-adaptive controller that has two stage of PID parameters tuning mechanisms is proposed. One of the tuners is a one-parameter tuner which calculates only the proportional gain using the recursive least squares. The other is a PID parameters tuner using least squares. When the one-parameter tuner cannot maintain a good control performance, the PID parameters tuner determines new PID parameters to maintain a desired control performance. The effectiveness of the proposed method is evaluated by an experimental example.

© The 2018 International Conference on Artificial Life and Robotics (ICAROB2018), Feb. 1-4, B-Con Plaza, Beppu, Oita, Japan

2. The tuning method of PID parameters

The PID parameters tuning method is described at this section. A velocity-type PID controller in discrete time domain is given as follows:

$$\Delta u(k) = k_c \left\{ \frac{T_s}{T_i} e(k) - \Delta y(k) - \frac{T_d}{T_s} \Delta^2 y(k) \right\}, \quad (1)$$

where k_c , T_i , and T_d are the proportional gain, the integral time and the derivative time, respectively. Δ denotes the differencing operator defined by $\Delta := 1 - z^{-1}$, where z^{-1} is the shift operator which means $z^{-1}y(k) = y(k - 1)$. In addition, $u(k)$ is the input signal and $y(k)$ is the output signal. Furthermore, T_s denotes the sampling time, and $e(k)$ denotes the output error signal defined by $e(k) := r(k) - y(k)$ where $r(k)$ denotes the reference signal. (1) can be rewritten by

$$\Delta u(k) = K_p e(k) - K_p \Delta y(k) - K_D \Delta^2 y(k), \quad (2)$$

where K_p , K_I , and K_D are proportional, integral, and derivative gains, respectively. By assuming $K_I \neq 0$, (3) can be obtained by rewriting (2).

$$r(k) = \frac{1}{K_I} \Delta u(k) + \frac{K_p + K_I + K_D}{K_I} y(k) - \frac{K_p + 2K_D}{K_I} y(k - 1) + \frac{K_D}{K_I} y(k - 2). \quad (3)$$

Generalized output $\Phi(k)$ is defined as follows:

$$\Phi(k) := a_1 \Delta u(k) + a_2 \{y(k) - y(k - 2)\} + a_3 \{y(k - 1) - y(k - 2)\} + y(k - 2). \quad (4)$$

Where coefficients a_1 , a_2 , and a_3 are defined as follows:

$$\left. \begin{aligned} a_1 &:= \frac{1}{K_I} \\ a_2 &:= \frac{K_p + K_I + K_D}{K_I} \\ a_3 &:= -\frac{K_p + 2K_D}{K_I} \end{aligned} \right\}. \quad (5)$$

From (3) to (5), the following relationship can be obtained:

$$r(k) = \Phi(k). \quad (6)$$

In the proposed method, it is desired to make the system output $y(k)$ track the reference model output $y_r(k)$ which is defined by

$$y_m(k) = G_m(z^{-1})r(k), \quad (7)$$

$$G_m(z^{-1}) := \frac{z^{-(d+1)}P(1)}{P(z^{-1})}, \quad (8)$$

Where d denotes the time-delay of the controlled object, and d is assumed to be known.

$P(z^{-1})$ is given as follows:

$$P(z^{-1}) = 1 + p_1 z^{-1} + p_2 z^{-2}. \quad (9)$$

Where p_1 and p_2 are determined by following equations:

$$\left. \begin{aligned} p_1 &= -2 \exp\left(-\frac{\rho}{2\mu}\right) \cos\left(\frac{\sqrt{4\mu-1}}{2\mu}\rho\right) \\ p_2 &= \exp\left(-\frac{\rho}{\mu}\right) \\ \rho &:= \frac{T_s}{\sigma} \\ \mu &:= 0.25(1-\delta) + 0.51\delta \end{aligned} \right\}. \quad (10)$$

σ and δ denote the rise-time and the damping coefficient, respectively, and μ is adjusted by δ . When $\delta = 0$, $G_m(z^{-1})$ indicates the Binomial model, and when $\delta = 1$, $G_m(z^{-1})$ indicates the Butterworth model. In practice, the value of δ is considered to design between 0 and 2, and by using bigger δ , the response becomes oscillating. The evaluation function J is defined as follows:

$$J = \sum_{j=0}^N \varepsilon(j)^2, \quad (11)$$

where N denotes the number of data and $\varepsilon(k)$ is defined as follows:

$$\varepsilon(k) := y(k) - G_m(z^{-1})\phi(k). \quad (12)$$

By minimizing the evaluation function J , the following relationship can be obtained:

$$G_m(z^{-1})\phi(k) \rightarrow y(k). \quad (13)$$

From (4), parameters to be optimized are a_i ($i = 1, 2, 3$). When the minimization has been finished, it leads the following relationship:

$$y(k) \rightarrow G_m(z^{-1})\phi(k), \quad (14)$$

Therefore, the reference response is realized by using the optimized a_i . To apply a PID controller, PID parameters are derived from a_i as follows.

$$\left. \begin{aligned} k_c &= \frac{2a_2 + a_3 - 2}{a_1} \\ T_i &= (2a_2 + a_3 - 2)T_s \\ T_d &= \frac{1 - a_2 - a_3}{2a_2 + a_3 - 2} T_s \end{aligned} \right\}. \quad (15)$$

3. Design of a performance driven PID controller

3.1. 1-parameter tuning

Both 1-parameter tuning and retuning of all PID parameters are realized by using the PID tuning method described at the previous section. In the 1-parameter tuning, only overall gain of the PID controller k_c is tuned. From (15), k_c is rewritten as follows:

$$k_c = \frac{T_i}{a_1 T_s}. \quad (16)$$

Furthermore, T_i and T_d are constant values, and a_2 and a_3 are also constant values. Therefore, 1-parameter tuning can be realized by tuning only a_1 . In this paper, a

recursive least squares method⁴ is applied to minimize $\varepsilon(k)$. Estimated parameter vector $\hat{\theta}(k)$ and data vector $\psi(k)$ are defined as follows:

$$\hat{\theta}(k) := \hat{a}_1(k), \quad (17)$$

$$\psi(k) := G_m(z^{-1})\Delta u(k), \quad (18)$$

where $\hat{a}_1(k)$ denotes estimated value of a_1 at k steps. The recursive estimation algorithm with forgetting factor is shown as follows:

$$\hat{\theta}(k) = \hat{\theta}(k-1) + K(k)\varepsilon(k)$$

$$\begin{aligned} \varepsilon(k) &= y(k) - G_m(z^{-1})[a_2\{y(k) - y(k-2)\} \\ &\quad + a_3\{y(k-1) - y(k-2)\} + y(k-2)], \end{aligned} \quad (19)$$

$$K(k) = \frac{P(k-1)\psi(k)}{\omega(k) + \psi^T(k)P(k-1)\psi(k)}, \quad (20)$$

$$(21)$$

$$P(k) = \frac{1}{\omega(k)} [P(k-1) - K(k)\psi(k)^T P(k-1)].$$

3.2. Control performance evaluation (22)

When 1-parameter tuning cannot maintain good control performance, all PID parameters should be tuned. In this subsection, the evaluation criterion of control performance is described. A reference signal is assumed to be the step-type signal. The criterion of control performance is defined as follows:

$$\varepsilon_{G_m}(k) = \frac{1}{k - k_0 + 1} \sum_{i=k_0}^k |G_m(z^{-1})r(i) - y(i)|, \quad (23)$$

where k_0 denotes a recent step when a reference signal is changed. $\varepsilon_{G_m}(k)$ denotes an average of errors between controlled output and reference model output. All PID parameters are tuned when $\varepsilon_{G_m}(k)$ satisfies the following condition:

$$\varepsilon_{G_m}(k) > \beta|\Delta r(k_0)|, \quad (24)$$

where α is a user-specified parameter which determines a threshold. $|\Delta r(k_0)|$ is introduced because $\varepsilon_{G_m}(k)$ have proportional relationship to the $|\Delta r(k_0)|$.

3.3. A method of PID parameters tuning

In order to tune all PID parameters, the PID tuning method described at Sec. 2 are used. The optimized parameters are a_1 , a_2 , and a_3 . In addition, least squares method is employed to minimize $\varepsilon(k)$. In the ordinary least squares, the data between k_0 and k steps are used.

4. An experimental result

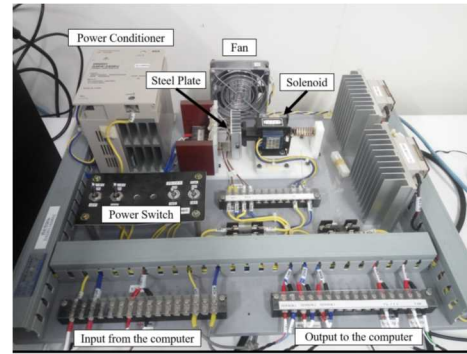


Fig. 1. Appearance of the experimental temperature control system.

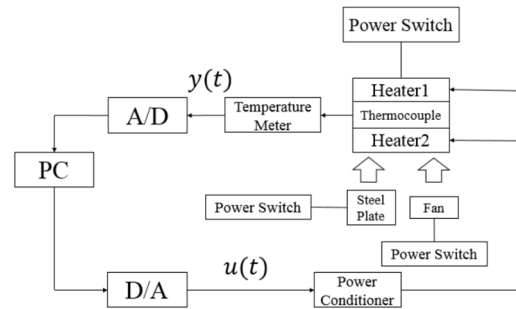


Fig. 2. Schematic figure of the experimental temperature control system.

The usefulness of the proposed self-tuning method is experimentally evaluated on a pilot-scale temperature control system. Fig. 1 shows an appearance of the controlled object, and the schematic figure is illustrated in Fig. 2. In this experimental system, two heaters are secured on a steel plate. These heaters work synchronously, corresponding to the input signal from the computer. One thermo-couple is also prepared, and the measured temperature of the steel is sent to the computer as the system output signal. The control objective is to regulate the temperature of the steel to the desired reference signal by manipulating the power of the heater. In this experimental result, the sampling time T_s is 1 second and the reference signal is changed alternately from 70 [°C] in the temperature and 100 [°C].

To simulate heater deterioration, the relationship between controlled input $u(k)$ and the voltage of the power conditioner $v(k)$ is varied as follows:

$$\left. \begin{aligned}
 v(k) &= 1 + \frac{4}{100} u(k) \quad (k \leq 200) \\
 v(k) &= 1 + \frac{4 - 3(k - 200)}{100 \cdot 600} u(k) \quad (200 < k \leq 800) \\
 v(k) &= 1 + \frac{1}{100} u(k) \quad (k < 800)
 \end{aligned} \right\} \quad (25)$$

The control result by using the proposed performance-adaptive controller is shown as Fig. 3, and the trajectories of PID parameters corresponding to Fig. 3 is shown in Fig. 4. In this result, the initial PID parameters were determined by using the PID tuning method described at Sec. 2 as follows:

$$k_c(0) = 0.70, T_i(0) = 28.9, T_d(0) = 4.67. \quad (26)$$

Parameters of the proposed method were set as follows: $\alpha = 1, \beta = 0.2, d = 8, w(k) = 0.995, \sigma = 30$, and $\delta = 0$. From (26), initial estimated parameter was determined as $\hat{\theta}(0) = 41.3$.

Fig. 3 indicates that the control performance gradually deteriorated after 200 steps. Fig. 4 shows that only k_c was tuned before 863 steps to maintain good control performance, and all PID parameters are tuned at 863 steps. As a result, good control result was obtained after 863 steps.

4.1. Conclusions

In this paper, a performance-adaptive 1-parameter tuning PID controller is proposed, and effectiveness of the proposed method is evaluated by the pilot-scale temperature control system. The proposed performance adaptive controller has two stage of PID parameters tuning mechanisms. Features of the proposed method are summarized as follows:

- The proposed method is the 1-parameter tuning method, and only k_c is tuned.
- All PID parameters are retuned only when control performance deteriorates.
- Both the 1-Parameter tuning and the retuning method of all PID parameters are based on the same PID tuning scheme.

From these characteristics, the proposed method can be easily understood. However, the effectiveness of the 1-parameter tuning in this paper does not proved analytically. This is a future work.

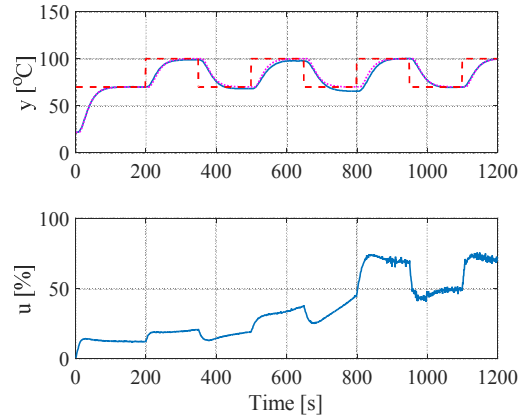


Fig. 3. Experimental control result by using the proposed control method.

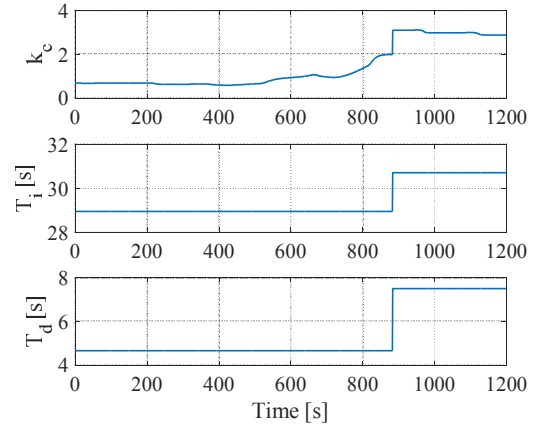


Fig. 4. Trajectories of the PID parameters corresponding to the Fig. 3.

References

1. D. W. Clarke, and P. J. Gawthrop, Self-tuning controller, *Proceedings of the Institution of Electrical Engineers* **122**(9) (1975) 929–934.
2. Y. Ashida, S. Wakitani and T. Yamamoto, Design of an implicit self-tuning pid controller based on the generalized output, *Proc. of the 20th IFAC World Congress* (2017) 14511–14516.
3. K. J. Åström and T. Hägglund, *Advanced PID Control*, (International Society of Automation, North Carolina, 2006).
4. E. B. M. Costa and G. L. O. Serra, Self-Tuning Robust Fuzzy Controller Design Based on Multi-Objective Particle Swarm Optimization Adaptation Mechanism, *Journal of Dynamic Systems, Measurement, and Control* **139**(7) (2017).
5. G. C. Goodwin and K. S. Sin, *Adaptive Filtering Prediction and Control*, (Prentice Hall, New Jersey, 1984).

Sticking Fault Detecting Method for CARIMA Model

Toyooki Tanikawa

*Advanced Course in Industrial and Systems Engineering, National Institute of Technology, Kagawa College
355 Chokushicho, Takamatsu, Kagawa, 761-8058 Japan*

Tomohiro Henmi

*Department of Electrical and Computer Engineering, National Institute of Technology, Kagawa College
355 Chokushicho, Takamatsu, Kagawa, 761-8058 Japan
E-mail: toyookipd0@gmail.com, henmi@t.kagawa-nct.ac.jp
www.kagawa-nct.ac.jp*

Abstract

This paper proposes a sticking fault detecting method for CARIMA model which detect the sticking fault of control input and feedback signal. It consists of model estimation using recursive least square method with the forgetting factor and fault detection. In the fault detection, an evaluation function is introduced, and it generates a fault signal from the input and output data. Numerical simulations are performed, and it is shown that this method can detect the sticking fault.

Keywords: fault detection, sticking fault, CARIMA model.

1. Introduction

If a system with a fault continues to be operated, it can cause a serious accident or a considerable damage. Thus, it is important to detect faults and compensate them, and many fault detection methods have been proposed.¹ The advantage of fault detection is that the safety is improved, you can cope with the fault more promptly, and sometimes the system can be controlled compensating the fault. There are two kinds in fault detection, signal-based detection and model-based one. The signal-based detection is for example a method using spectral analysis, statistical signal analysis or pattern recognition, while the model-based detection uses an observer or a parameter estimation. In model-based detection, a general method detecting additive faults is proposed in Ref. 2.

In detecting a fault where control input or feedback signal is fixed, a general detection method is not established. In this paper, we propose a model-based detection method for the sticking fault of control input and feedback signal on a system expressed as a controlled auto-regressive integrated moving average (CARIMA)

model. Then, we discuss its effectiveness performing a numerical simulation.

2. Sticking Fault Detecting Method

In this section, we discuss how to detect sticking fault of control input and feedback signal on the general linear systems.

2.1. Problem Statement

First, we assume the control object is single input and single output system and expressed as following CARIMA model:

$$\begin{aligned} A[z^{-1}]y_m(k) &= z^{-k_m}B[z^{-1}]u_m(k) + C[z^{-1}]\frac{\xi(k)}{\Delta} \\ A[z^{-1}] &= 1 + a_1z^{-1} + a_2z^{-2} + \dots + a_nz^{-n} \\ B[z^{-1}] &= b_0 + b_1z^{-1} + b_2z^{-2} + \dots + b_mz^{-m} \\ C[z^{-1}] &= 1 + c_1z^{-1} + c_2z^{-2} + \dots + c_lz^{-l} \end{aligned} \quad (1)$$

where $y_m(k)$ represents a system output, $u_m(k)$ is a control input, $\xi(k)$ is a white Gaussian noise with 0 mean and k_m is a time delay. z^{-1} is a backshift operator where $z^{-1}y_m(k) = y_m(k-1)$, and Δ is a difference operator

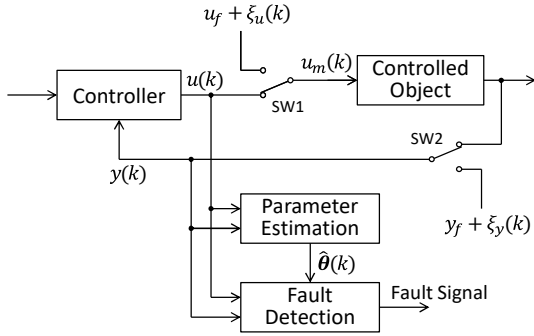


Fig. 1. Block diagram of sticking fault detection

defined as $\Delta = 1 - z^{-1}$. System parameters, a , b and c in Eq. (1) changes gradually or do not change at all. We suppose the reference value of the control system changes depending on time.

Let us define the sticking fault. When the sticking fault of control input occurs, the input to the system $u_m(k)$ becomes a white noise and expressed as follows:

$$u_m(k) = \begin{cases} u(k) & \text{(normal)} \\ u_f + \xi_u(k) & \text{(fault)} \end{cases} \quad (2)$$

where $u(k)$ is a control input calculated by the controller, u_f is a constant value and $\xi_u(k)$ is a white Gaussian noise with 0 mean. When the sticking fault of feedback signal occurs, the feedback signal to the controller $y(k)$ becomes a white noise and expressed as:

$$y(k) = \begin{cases} y_m(k) & \text{(normal)} \\ y_f + \xi_y(k) & \text{(fault)} \end{cases} \quad (3)$$

where y_f is a constant value and $\xi_y(k)$ is a white Gaussian noise with 0 mean.

Fig. 1 shows a block diagram of the fault detection for the above-mentioned faults. This method consists of two parts, model estimation and fault analysis.

2.2. Model Estimation

Least square method with the forgetting factor³ is used for the model estimation. In this method, the cost function is given by:

$$I_N(\boldsymbol{\theta}) = \sum_{k=1}^N \lambda^{N-k} [y(k) - \hat{y}(k|\boldsymbol{\theta})] \quad (4)$$

where $\boldsymbol{\theta}$ is a system parameter vector, λ is a forgetting factor where $0 < \lambda \leq 1$, $\hat{y}(k|\boldsymbol{\theta})$ is an estimated output and N is the number of the input-output data. The estimated parameter $\hat{\boldsymbol{\theta}}$ which minimizes the cost function

on CARIMA model is obtained by the following recursive algorithm:

$$\begin{aligned} \hat{\boldsymbol{\theta}}(k) &= \hat{\boldsymbol{\theta}}(k-1) + \frac{\mathbf{P}(k-1)\boldsymbol{\psi}(k)}{\lambda + \boldsymbol{\psi}^T(k)\mathbf{P}(k-1)\boldsymbol{\psi}(k)} \boldsymbol{\epsilon}(k) \\ \mathbf{P}(k) &= \frac{1}{\lambda} \left[\mathbf{P}(k-1) - \frac{\mathbf{P}(k-1)\boldsymbol{\psi}(k)\boldsymbol{\psi}^T(k)\mathbf{P}(k-1)}{\lambda + \boldsymbol{\psi}^T(k)\mathbf{P}(k-1)\boldsymbol{\psi}(k)} \right] \\ \boldsymbol{\epsilon}(k) &= \Delta y(k) - \boldsymbol{\psi}^T(k)\hat{\boldsymbol{\theta}}(k-1) \\ \boldsymbol{\eta}(k) &= \Delta y(k) - \boldsymbol{\psi}^T(k)\hat{\boldsymbol{\theta}}(k). \end{aligned} \quad (5)$$

$\boldsymbol{\epsilon}(k)$ is a priori error and $\boldsymbol{\eta}(k)$ is a posterior error. The parameter vector $\hat{\boldsymbol{\theta}}(k)$ and the data vector $\boldsymbol{\psi}(k)$ are defined as follows:

$$\begin{aligned} \hat{\boldsymbol{\theta}}(k) &= [\hat{a}_1(k), \dots, \hat{a}_n(k), \hat{b}_0(k), \dots, \hat{b}_m(k), \\ &\quad \hat{c}_1(k), \dots, \hat{c}_i(k)]^T \\ \boldsymbol{\psi}(k) &= [-\Delta y(k-1), \dots, -\Delta y(k-n), \\ &\quad \Delta u(k-k_m), \dots, \Delta u(k-k_m-m), \\ &\quad \eta(k-1), \dots, \eta(k-l)]^T \end{aligned} \quad (6)$$

where \hat{a} , \hat{b} and \hat{c} represent the estimated parameter of a , b and c in Eq. (1) respectively. The initial value of the covariance matrix $\mathbf{P}(k)$ is given by:

$$\mathbf{P}(0) = \gamma \mathbf{I} \quad (7)$$

where \mathbf{I} is an identity matrix. γ is usually set as a large value like 10^3 or 10^4 .

The weight of a past input-output data in cost function $I_N(\boldsymbol{\theta})$ becomes smaller as the time goes by due to the forgetting factor. Thus, the estimated parameter $\hat{\boldsymbol{\theta}}(k)$ is calculated using resent data mainly. Thus, this parameter estimation method is also effective for systems where its parameters change.

2.3. Fault Detection

Fig. 2 shows the outline of the fault detection. To detect sticking fault, it uses the estimated system parameters and the input-output data of past n_d steps called detecting period. The fault state is evaluated by the following function:

$$V(k) = \frac{\sum_{i=k-n_d+1}^k \{\Delta \hat{A}[z^{-1}]y(i) - z^{-k_m} \Delta \hat{B}[z^{-1}]u(i)\}^2}{\sum_{i=k-n_d+1}^k \{\Delta \hat{A}[z^{-1}]y(i)\}^2 + \beta} \quad (8)$$

where β is an infinitesimal value to avoid dividing by 0. $\hat{A}[z^{-1}]$ and $\hat{B}[z^{-1}]$ are the estimated system parameter polynomials at step $k - n_d - n_m$ which are gained from $\hat{\boldsymbol{\theta}}(k - n_d - n_m)$ calculated in Eq. (5), where n_m is order of the system defined by $n_m = \max\{m, n\} + 1$. It is

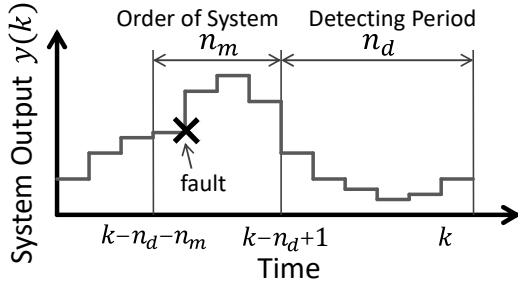


Fig. 2. Outline of fault detection

assumed that $\hat{\theta}(k - n_d - n_m)$ is a good estimation of the actual system at step k because we are focusing on systems whose parameters do not change abruptly.

We assume a situation that a fault has occurred. The estimated parameters become useless values after the fault. However, at a moment like Fig. 2, estimated parameter $\hat{\theta}(k - n_d - n_m)$ is still valid and only the input-output data after the fault are used for the evaluation value $V(k)$. Then $V(k)$ becomes bigger than 1 as being mentioned in section 3, and a fault signal is generated after satisfying the following inequality:

$$V(k) > V_{th} \quad (9)$$

where V_{th} is a threshold value set as $V_{th} > 1$. After detecting the fault, it stops updating the estimated parameters in Eq. (5).

3. Sticking Fault Evaluation Value

We discuss the size of the evaluation value $V(k)$ on the normal state and the fault one. First, let us define the error polynomials of the system parameters, $E_A[z^{-1}]$ and $E_B[z^{-1}]$ as follows:

$$\begin{aligned} E_A[z^{-1}] &= \hat{A}[z^{-1}] - A[z^{-1}] \\ E_B[z^{-1}] &= \hat{B}[z^{-1}] - B[z^{-1}]. \end{aligned} \quad (10)$$

Using Eq. (1), (2), (3) and (10) and ignoring the infinitesimal value β , evaluation function in Eq. (8) on the normal state can be deformed as follows:

$$V(k) = \frac{\sum_i \{\Delta E_A y(i) - z^{-k_m} \Delta E_B u(i) + C \xi(i)\}^2}{\sum_i \{z^{-k_m} \Delta B u(i) + \Delta E_A y(i) + C \xi(i)\}^2} \quad (11)$$

where the polynomial expression is abbreviated like B instead of $B[z^{-1}]$, and \sum_i means $\sum_{i=k-n_d+1}^k$. Assuming that the terms of error polynomials and that of white noise $\xi(i)$ are relatively small compared to the term of $u(i)$ in Eq. (11), $V(k) \approx 1$ is gained.

On the other hand, after the sticking fault of the input has occurred, the evaluation value at a moment described in fig. 2 is deformed using Eq. (2) of the fault state and Eq. (1), (3) and (10), and expressed as follows:

$$\begin{aligned} V(k) &= \frac{\sum_i \{-z^{-k_m} \Delta \hat{B}(u(i) - \xi_u(i)) + \Delta E_A y(i) + C \xi(i)\}^2}{\sum_i \{\Delta E_A y(i) + z^{-k_m} \Delta B \xi_u(i) + C \xi(i)\}^2} \end{aligned} \quad (12)$$

while the evaluation value on a sticking fault of the feedback signal is deformed using Eq. (3) of the fault state, and expressed as following equation:

$$V(k) = \frac{\sum_i \{-z^{-k_m} \Delta \hat{B} u(i) + \Delta \hat{A} \xi_y(i)\}^2}{\sum_i \{\Delta \hat{A} \xi_y(i)\}^2}. \quad (13)$$

Because the terms of error polynomials and white noises are smaller than that of $u(i)$ as assumed before, $V(k) \geq 1$ is obtained in both Eq. (12) and (13). Therefore, the evaluation value becomes greater after the sticking fault occurs, and the fault can be detected by Eq. (9). However, the threshold V_{th} has to be set based on an input-output data on an actual system or a simulation results because the evaluation value $V(k)$ is dependent on the estimation error and disturbances.

Systems usually have limitations of the control input. When designing a controller considering the limitation, higher and lower constant limits are generally used. However, Eq. (11), (12) and (13) state that $\Delta u(i)$ has to have a value, and $\Delta u(i)$ can be 0 when the input is limited by the constant value. Thus, the limitation has to be dependent on time, and is given by:

$$\begin{aligned} u(k) &= \begin{cases} u_{max}(k), & u_c(k) > u_{max}(k) \\ u_c(k), & u_{min}(k) \leq u_c(k) \leq u_{max}(k) \\ u_{min}(k), & u_c(k) < u_{min}(k) \end{cases} \\ u_{max}(k) &= A \sin(\omega k) + u_h \\ u_{min}(k) &= A \sin(\omega k) + u_l \end{aligned} \quad (14)$$

where $u_c(k)$ is the control input calculated by the controller, and A , ω , u_h and u_l are setting parameters.

4. Simulation Example

To verify the effectiveness of this fault detecting method, we apply it to a system expressed as follows:

$$\begin{aligned} A[z^{-1}] &= 1 - 1.307z^{-1} + 0.3768z^{-2} \\ B[z^{-1}] &= 0.05158 + 0.03729z^{-1} \end{aligned} \quad (15)$$

where $k_m = 1$. We set the disturbance characteristics polynomials $C[z^{-1}]$ as $C[z^{-1}] = 1$. The system parameter polynomials do not change throughout the simulation. $\xi(k)$, $\xi_u(k)$ and $\xi_y(k)$ are set as a zero mean white Gaussian noise with the variance of 0.01^2 , 0.1^2 and 0.005^2 respectively.

In the model estimation, we assume that the order of the system parameter polynomials l , m and n and the time delay k_m are known. Then, the estimated parameter vector $\hat{\theta}(k)$ is given by:

$$\hat{\theta}(k) = [\hat{a}_1(k), \hat{a}_2(k), \hat{b}_0(k), \hat{b}_1(k)]^T. \quad (16)$$

We set γ to 10^3 and λ to 0.98 . In the fault detection, $n_d = 20$, $V_{th} = 1.5$ and $\beta = 10^{-10}$ are used.

Generalized Predictive control which uses CARIMA model to predict the output is used as a controller. When designing it, Eq. (14) is used for the internal model, and $N_1 = 1$, $N_2 = 5$, $NU = 5$, $\lambda(j) = 0.01$, and time constant of the reference trajectory $\tau = 0.3$ s are taken. For the input limitation, $A = 1$, $\omega = 0.1\pi$, $u_h = 4$ and $u_l = -4$ are used.

Fig. 3 shows a simulation result where the sticking fault of control input occurs at a step 400. $r(k)$ represents reference value and the dashed line on the graph $V(k)$ is the threshold value V_{th} . The evaluate value $V(k)$ is normally smaller than 1, and it becomes greater after the fault occurs. It surpasses V_{th} at a step 406, and then the fault signal is generated. $V(k)$ takes relatively great value on the beginning due to the error of the parameter estimation.

Fig. 4 shows a result of the sticking fault of feedback signal. Like Fig. 3, $V(k)$ becomes greater after the fault, and the fault signal is generated at a step 404.

5. Conclusion

We proposed the sticking fault detecting method in which the evaluation function is introduced. It evaluates the input-output data on a detecting period, using the past estimated parameter calculated by the recursive least square method. Performing a numerical simulation, it is confirmed that the sticking fault of control input and feedback signal can be detected.

Acknowledgements

This work was supported by JSPS KANKENHI Grant Number 15K21591.

References

1. T. Hukuda, Diagnosis on Machinery(Part 1) -The Outline and an Evaluation of its Diagnostic Reliability-(in Japanese), in *Journal of Japan Society for Safety Engineering*, vol.36, no.4 (1997), pp. 247-252.
2. R. Isermann, Model-based Fault-detection and Diagnosis – Status and Applications, *IFAC Automatic Control in Aerospace, Saint-Petersburg, Russia* (2004), pp. 49-60.
3. L. Ljung and T. Söderström, *Theory and Practice of Recursive Identification* (MIT Press, Cambridge, MA, 1983).

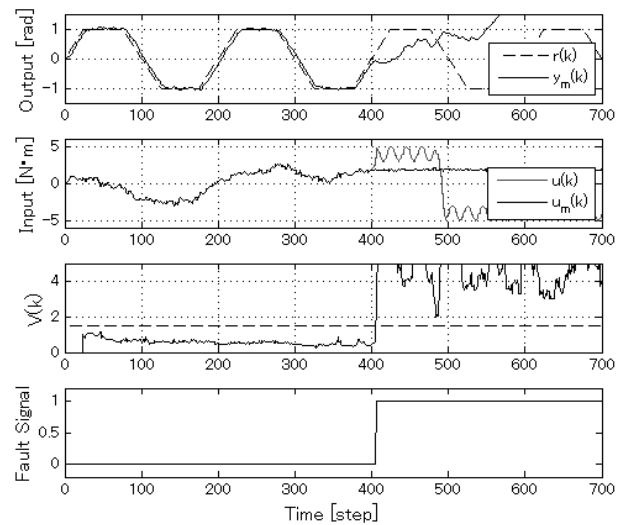


Fig. 3. Detection result on control input sticking fault

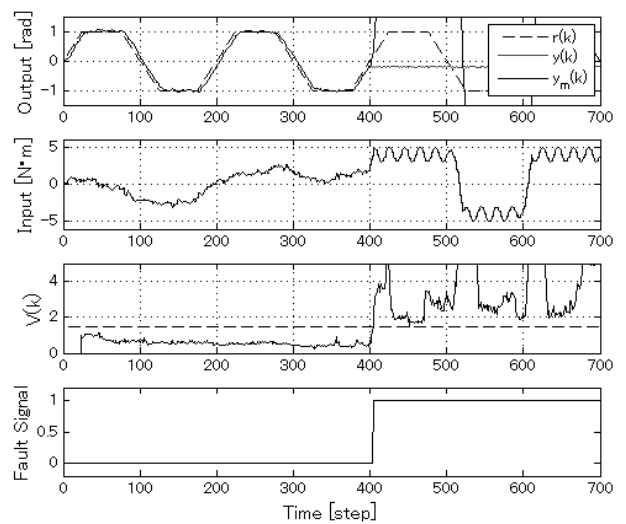


Fig. 4. Detection result on feedback sticking fault

Design of Neural Network PID Controller Based on E-FRIT and Online Learning

Kento Kinoshita*

*Graduate School of Engineering, Hiroshima University, 1-4-1 Kagamiyama
Higashihiroshima city, Hiroshima, Japan*

Shuichi Ohno

*Graduate School of Engineering, Hiroshima University, 1-4-1 Kagamiyama
Higashihiroshima city, Hiroshima, Japan*

Shin Wakitani

*Graduate School of Engineering, Hiroshima University, 1-4-1 Kagamiyama
Higashihiroshima city, Hiroshima, Japan*

*E-mail: kinoshita-kento@hiroshima-u.ac.jp, ohno@hiroshima-u.ac.jp, wakitani@hiroshima-u.ac.jp
<https://www.hiroshima-u.ac.jp/>*

Abstract

PID controllers have been widely used in industrial world. When a controlled object has a nonlinear characteristic, a good control result is not always obtained with fixed PID gains. To overcome the problem, a design method of a nonlinear PID controller using a neural network has been proposed. In this paper, an online learning method of the proposed controller to attenuate the effect of the system change of the controlled object has been presented.

Keywords: PID control, E-FRIT, neural network, data-driven, online learning.

1. Introduction

The proportional-integral-derivative (PID) control has a long history and has been a main control method in the industrial world. The fictitious reference iterative tuning (FRIT) has been presented to determine PID gains.¹ By the FRIT, PID gains are tuned directly from a set of operating data. However, when a controlled object has a nonlinear characteristic, a good control result may not be obtained with the fixed PID gains. Therefore, methods that utilize the FRIT and effective control methods for nonlinear systems, such as a data-driven (DD) control and a neural network control have been proposed.^{2,3}

The FRIT evaluates only the control response. Hence, the FRIT is insufficient for controlling an object whose stability is important.⁴ The E-FRIT (Extended Fictitious Reference Iterative Tuning) has been developed to enhance the stability of the control system.⁴ The E-FRIT considers variations of the manipulated variable in its criterion. An algorithm for learning a database used in the DD control based on the E-FRIT has been proposed.⁵ However, DD control requires a large amount of memory and high processing speed to calculate its control parameters, because DD control uses a database. This paper proposes a design method of a nonlinear PID controller which combines a neural network and the E-FRIT. In addition, we also presented an online learning method of the designed controller. The proposed

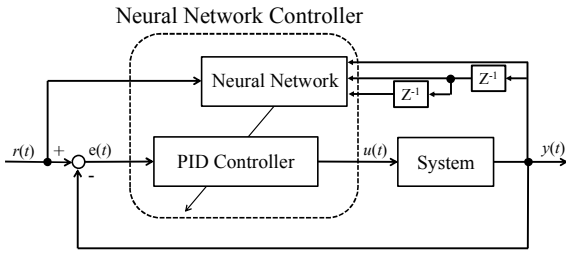


Fig. 1. Block diagram of a neural network PID control system.

controller makes the closed loop system which has desired response with low computational costs. Moreover, the controller is adequately updated by the online learning method to mitigate the effect of system change.

1. Neural Network PID Controller

Let us consider discrete-time systems. A neural network PID control system is illustrated by the block diagram in Fig. 1. The neural network in Fig. 1 has one hidden layer. At time t , the neural network calculates PID gains from $r(t)$, $y(t)$, $y(t - 1)$ and $y(t - 2)$ which are the reference and system output, respectively. The PID controller controls the system with the calculated PID gains.

Let z^{-1} be a unit-time delay operator, that is,

$$z^{-1}y(t) = y(t - 1), \quad (1)$$

and define the difference operator Δ as

$$\Delta = 1 - z^{-1}. \quad (2)$$

In this paper, the PID controller has velocity type PID control law given by

$$\Delta u(t) = K_I(t)e(t) - K_P(t)\Delta y(t) - K_D\Delta^2 y(t), \quad (3)$$

where $y(t)$ is the controlled variable at time t . Moreover, $K_P(t)$, $K_I(t)$ and $K_D(t)$ are the proportional gain, the integral gain and the derivative gain at time t , respectively.

A neural network consists of many neurons connected each other. Fig. 2 shows a schematic diagram of a neuron. A neuron has multiple inputs and one output. If the output is O and the inputs are x_1, x_2, \dots, x_m , the input-output relation is described by

$$O = f\left(\sum_{i=1}^m w_i x_i + b\right), \quad (4)$$

where the variables $w_i (1 \leq i \leq m)$ are called synaptic weights and the variable b is a bias. The function $f(\cdot)$ is the so-called activation function. We use the standard

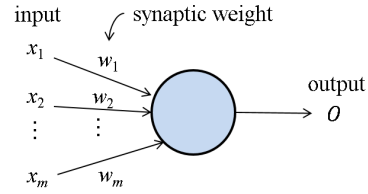


Fig. 2. Schematic diagram of a neuron.

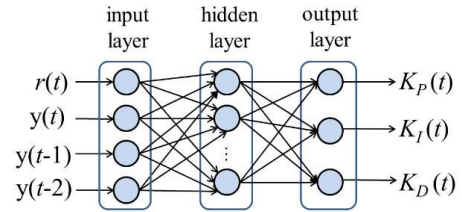


Fig. 3. Illustration of PID gain tuning.

sigmoid function as the activation function because the sigmoid function is often used in practice. The standard sigmoid function is given by

$$f(x) = \frac{1}{1 + e^{-x}}. \quad (5)$$

The calculation of PID gains by the neural network PID tuner is illustrated in Fig. 3. The outputs of neural network are in the range (0,1) because the range of Eq. (5) is (0,1). Hence, the output of neural network are scaled by constant c when desired PID gains are larger than 1.

2. Controller Design

A schematic diagram of the E-FRIT is depicted in Fig. 4. The E-FRIT is a direct control parameter tuning method by using operating data.⁴ The parameter tuning by the E-FRIT does not require any mathematical models of controlled objects. In Fig. 4, $C(\theta, z^{-1})$ is a controller consists of a control parameter vector θ . In the PID controller, θ is K_P, K_I and K_D . In addition, $y_0(t)$ and $u_0(t)$ are the output and manipulated variables of the operating data, respectively. The relation between the input to a controller and the output from the controller is denoted by

$$u_0(t) = \frac{C(\theta, z^{-1})}{\Delta} (\tilde{r}(\theta, t) - y_0(t)), \quad (6)$$

where $\tilde{r}(\theta, t)$ is a fictitious reference signal which is given by

$$\tilde{r}(\theta, t) = C^{-1}(\theta, z^{-1})\Delta u_0(t) + y_0(t). \quad (7)$$

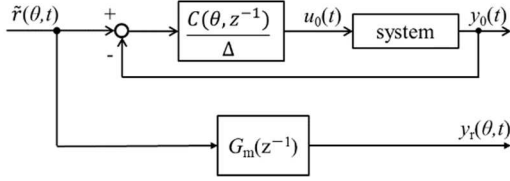


Fig. 4. Block diagram of the E-FRIT.

We set $G_m(z^{-1})$ as our desired system and obtain $y_r(\boldsymbol{\theta}, t)$ which is the output of reference model $G_m(z^{-1})$ for $\tilde{r}(\boldsymbol{\theta}, t)$. Additionally, a difference of the manipulated variable $\Delta\tilde{u}(\boldsymbol{\theta}, t)$ is given by

$$\Delta\tilde{u}(\boldsymbol{\theta}, t) = C(\boldsymbol{\theta}, z^{-1})(\tilde{r}(\boldsymbol{\theta}, t) - y_r(\boldsymbol{\theta}, t)). \quad (8)$$

Then, the parameters in $\boldsymbol{\theta}$ are given by minimizing a criterion $J_{E-FRIT}(\boldsymbol{\theta})$ which is defined as

$$J_{E-FRIT}(\boldsymbol{\theta}) = \frac{1}{N} \sum_{t=1}^N \left\{ (y_0(t+1) - y_r(\boldsymbol{\theta}, t+1))^2 + \lambda f_s(\boldsymbol{\theta}) \Delta\tilde{u}(\boldsymbol{\theta}, t)^2 \right\}, \quad (9)$$

where N is the number of sample data and $f_s(\boldsymbol{\theta})$ is a scaling parameter which is expressed as

$$f_s(\boldsymbol{\theta}) = \sqrt{\frac{\text{Var}(y_0(t) - y_r(\boldsymbol{\theta}, t))}{\text{Var}(\Delta\tilde{u}(\boldsymbol{\theta}, t))}}. \quad (10)$$

with $\text{Var}(\cdot)$ which means variance.

The design method of the neural network control system is based on the E-FRIT. In our neural network controller, parameters in $\boldsymbol{\theta}$ are PID gains which are tuned by a neural network. Therefore, $\boldsymbol{\theta}$ represents $\boldsymbol{\theta}(\mathbf{w}, t)$ when the synaptic weight of the neural network is \mathbf{w} . From the above, we define a criterion such as

$$J_{E-FRIT}(\mathbf{w}) = \frac{1}{N} \sum_{t=1}^N \left\{ (y_0(t+1) - y_r(\boldsymbol{\theta}(\mathbf{w}, t), t+1))^2 + \lambda f_s(\mathbf{w}) \Delta\tilde{u}(\boldsymbol{\theta}(\mathbf{w}, t), t)^2 \right\}, \quad (11)$$

where

$$f_s(\mathbf{w}) = f_s(\boldsymbol{\theta}(\mathbf{w}, t)). \quad (12)$$

synaptic weight \mathbf{w} is updated to decrease the criterion by backpropagation.

Our criterion of the online learning method is

$$J_{online}(\mathbf{w}, t) = \frac{1}{2} \left\{ (y_m(t) - y(\mathbf{w}, t))^2 + \bar{\lambda} \bar{f}_s(t) \Delta u(\mathbf{w}, t-1)^2 \right\}, \quad (13)$$

where

$$\bar{f}_s(t) = \sqrt{\frac{\text{Var}(y_m(t) - y(\mathbf{w}, t))}{\text{Var}(\Delta u(\mathbf{w}, t))}}. \quad (14)$$

The output $y_m(t)$ is the response of the reference model to $r(t)$. In Eq. (14), variance is calculated by all control result until time t . The synaptic weight w is updated to decrease the criterion by backpropagation. The update rule of the synaptic weights is given by Adam.⁶ Adam is a stochastic gradient descent which has high convergence speed.

3. Simulation Example

To begin, the controlled object is discussed. We consider the controlled object whose property are changed in the simulation. Two Hammerstein model are denoted by the following equations:

$$\begin{aligned} & \text{[System 1]} \\ & \left. \begin{aligned} y(t) &= 0.6y(t-1) - 0.1y(t-2) \\ &+ 1.2x(t-1) - 0.1x(t-2) + \zeta(t) \\ x(t) &= 1.5u(t) - 1.5u^2(t) + 1.5u^3(t) \end{aligned} \right\}, \quad (15) \end{aligned}$$

$$\begin{aligned} & \text{[System 2]} \\ & \left. \begin{aligned} y(t) &= 0.6y(t-1) - 0.1y(t-2) \\ &+ 1.2x(t-1) - 0.1x(t-2) + \zeta(t) \\ x(t) &= 1.6u(t) - 2.0u^2(t) + 3.0u^3(t) \end{aligned} \right\}, \quad (16) \end{aligned}$$

where $\zeta(t)$ is white Gaussian noise, whose arithmetical mean is 0 and variance is 1.0×10^{-3} . The sample time is set as 1s. Moreover, the reference is set as follows:

$$r(t) = \begin{cases} 1.0 & (0 \leq t \leq 50) \\ 2.0 & (51 < t \leq 100) \\ 2.5 & (101 < t \leq 150) \\ 1.0 & (151 \leq t \leq 200) \end{cases}. \quad (17)$$

We assume the controlled object is System1 when the learning data is obtained. We also assume the controlled object is change from System 1 to System 2 at 30 s, when the controlled object is controlled by the proposed controller. In addition, we set the reference model $G_m(z^{-1})$ to

$$G_m(z^{-1}) = \frac{0.2368z^{-1}}{1 - 1.0268z^{-1} + 0.2636z^{-2}}. \quad (18)$$

We set parameters of our neural network and the learning method are set as follows: The number of neurons in hidden layer of the neural network is set as 7. The parameter λ and $\bar{\lambda}$ in the criteria is set to 1.

The learning data is obtained by a fixed PID controller. The PID gains of the controller is set as $K_p = 0.2502$, $K_I = 0.0779$, $K_D = 0.1137$. The control result of the fixed PID method is shown in Fig. 5. The neural network PID controller is designed using the data depicted in Fig. 5. It approximates the response of the

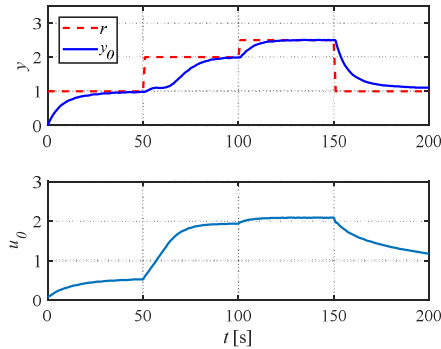


Fig. 5. Control result by the fixed PID controller (System 1).

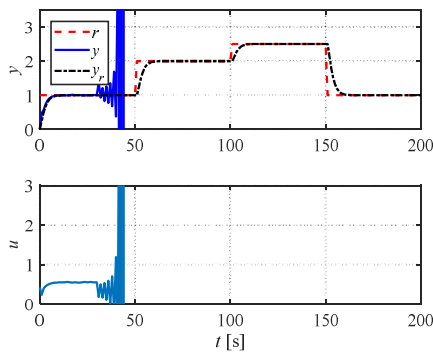


Fig. 6. Control result without the online learning (Controlled object is change from System 1 to System 2 at 30 s).

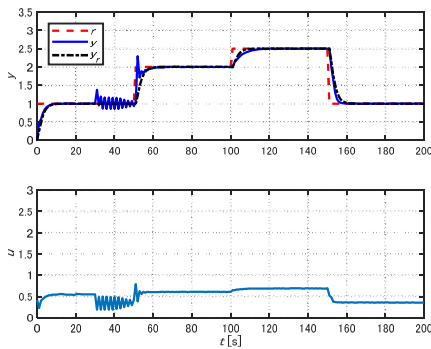


Fig. 7. Control result by the proposed method (Controlled object is change from System 1 to System 2 at 30 s).

closed loop to the response of the reference model when the controlled object is not changed from System1.

The control result by the designed controller without the online learning is shown in Fig. 6. From Fig.6, it is clear that the output diverges.

The control result by the designed controller is demonstrated in Fig. 7. The trajectories of PID gains are presented in Fig. 8. Although the control result oscillates

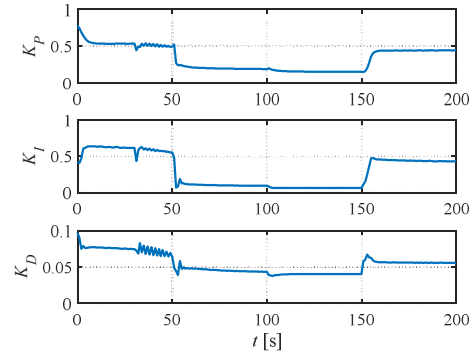


Fig. 8. Trajectories of PID gains corresponding to Fig. 7.

immediately after the system change occurs, the control result follows the desired response gradually. From the above, we conclude proposed method is effective.

5. Conclusion

This paper proposed a design method of a neural network PID controller based on the E-FRIT, whose performance is evaluated by simulations. The output of the controlled object by the proposed controller is close to the output of the desired reference model, even if the system changes. This work was partly supported by JSPS KAKENHI Grant Number JP16H02921.

References

1. S. Soma, O. Kaneko, T. Fujii, A New Approach to Parameter Tuning of Controllers by Using One-Shot Experimental Data - A Proposal of Fictitious Reference Iterative Tuning , *Transactions of the Institute of Systems, Control and Information Engineers* **17**(12) (2004) 528-536, (in Japanese).
2. K. Takao, T. Yamamoto, T. Hinamoto, A Design of Memory-Based PID Controllers, *Transactions of the Society of Instrument and Control Engineers* **40**(9) (2004) 895-905, (in Japanese).
3. Y. Ohnishi, H. Kitagawa, S. Mori, S. Wakitani, and T. Yamamoto, Design of Neural Networks Based FRIT PID Controllers and Its Applications, *11th IFAC Workshop on Adaptation and Learning in Control and Signal Processing*, (2013).
4. K. Tasaka, K. Manabu, M. Ogawa, S. Masuda, and T. Yamamoto, Direct PID Tuning from Closed-Loop Data and Its Application to Unstable Processes, *Trans. of ISCIE* **22**(4) (2009) 137-144, (in Japanese).
5. S. Wakitani, M. Deng, A New Learning Algorithm for Data-driven PID Controller Based on E-FRIT , *IEEJ Transactions on Electronics, Information and Systems*, **136**(5) (2016) 683-689, (in Japanese).
6. D. P. Kingma, J. Ba, Adam: A Method for Stochastic Optimization, *Conference paper at ICLR 2015*.

Parameter Optimization with Input/Output Data via DE for Adaptive Control System with Neural Network

Taro Takagi

*Department of Control Engineering, Natl. Inst. of Tech., Maizuru College,
234 Shiroya, Maizuru, Kyoto 625-8511, Japan*

Ikuro Mizumoto

*Graduate School of Science and Technology, Kumamoto University,
2-39-1 Kurokami Chuo-ku, Kumamoto 860-8555, Japan
E-mail: t.takagi@maizuru-ct.ac.jp, ikuro@kumamoto-u.ac.jp*

Abstract

In this paper, adaptive control system with neural network (NN) will be designed. At the beginning, parallel feedforward compensator (PFC) will be designed by using one-shot experimental data of controlled system via differential evolution (DE). From the obtained PFC and the ideal almost strictly positive real (ASPR) model, nominal model of controlled system can be obtained. Then, parameters of adjust law for NN will be optimized by using obtained nominal model via DE.

Keywords: Adaptive Control, ASPR, PFC, Neural network, Differential evolution.

1. Introduction

In spite of their simple structure, Almost strictly positive real (ASPR) based adaptive control systems have high robustness with respect to disturbances and uncertainties^{1, 2}. However, the ASPR conditions which controlled system has to satisfy are very severe conditions for actual systems. To overcome this problem, introduction of parallel feedforward compensator (PFC) has been proposed³. Several design methods of PFC which are based on mathematical model of controlled system such as relative degree have been proposed⁴. However, to obtain the mathematical model, iterative of identification experiments have to be done and it cost time and money. Therefore, a design method which is using system's input/output data has been proposed^{5, 6}. For ASPR system, an adaptive control system with feedforward input generated by neural network (NN) has been proposed⁷. This input is applied to avoid tracking error caused by PFC. In theory, PFC and NN parameters can be any value

if the conditions are satisfied. However, those parameters are directly affect to control performance. Therefore, it has to be appropriate value in actual control systems. Since there are no decision method for those parameters, designer has been decided it by trial and error of numerical simulations. Therefore, it is quite difficult to decide appropriate value.

In this paper, the parameter optimization method of PFC and NN by using input/output data via differential evolution (DE) will be proposed. DE is one of the evolutionary computation methods and it has a good convergence and uniqueness of solution⁸.

2. Adaptive Control System with Adaptive NN Feedforward Input

Consider the controlled system is described in equation state model as follows.

$$\begin{aligned}\dot{\mathbf{x}}(t) &= \mathbf{A}\mathbf{x}(t) + \mathbf{b}u(t) \\ y(t) &= \mathbf{c}^\top \mathbf{x}(t)\end{aligned}\quad (1)$$

For this system, a PFC described as follows is introduced.

$$\begin{aligned} \dot{\mathbf{x}}_f(t) &= A_f \mathbf{x}_f(t) + \mathbf{b}_f u(t) \\ y_f(t) &= \mathbf{c}_f^\top \mathbf{x}_f(t) \end{aligned} \quad (2)$$

Then, supposed that the augmented system:

$$\begin{aligned} \dot{\mathbf{x}}_a(t) &= A_a \mathbf{x}_a(t) + \mathbf{b}_a u(t) \\ y_a(t) &= \mathbf{c}_a^\top \mathbf{x}_a(t) \end{aligned} \quad (3)$$

where

$$\begin{aligned} \mathbf{x}_a(t) &= [\mathbf{x}^\top \ \mathbf{x}_f^\top]^\top, A_a = \text{diag}[A \ A_f], \\ \mathbf{b}_a &= [\mathbf{b}^\top \ \mathbf{b}_f^\top]^\top, \mathbf{c}_a^\top = [\mathbf{c}^\top \ \mathbf{c}_f^\top] \end{aligned}$$

is ASPR. Fig. 1. shows the block diagram of augmented system. Then, for this augmented system, design an adaptive output feedback control system with adaptive NN as follows.

$$\begin{aligned} u(t) &= u_e(t) + u_{nn}(t) \\ u_e(t) &= -k(t)\bar{e}_a(t) \\ u_{nn}(t) &= \hat{W}(t)^\top S(\omega) \\ \dot{k}(t) &= \gamma \bar{e}_a(t)^2 - \sigma k(t) \\ \dot{\hat{W}}(t) &= -\Gamma S(\omega)\bar{e}_a(t) - \sigma_n \hat{W}(t) \end{aligned} \quad (4)$$

where

$$\bar{e}_a(t) = \bar{y}_a(t) - y_r(t) \quad (5)$$

$$\bar{y}_a(t) = y(t) + \bar{y}_f(t) \quad (6)$$

and $\bar{y}_f(t)$ is the output of PFC obtained by

$$\begin{aligned} \dot{\bar{\mathbf{x}}}_f(t) &= A_f \bar{\mathbf{x}}_f(t) + \mathbf{b}_f u_e(t) \\ \bar{y}_f(t) &= \mathbf{c}_f^\top \bar{\mathbf{x}}_f(t) \end{aligned} \quad (7)$$

Also, $\hat{W} = [\hat{w}_1, \dots, \hat{w}_l]^\top \in \mathbf{R}^l$ is the estimated value of ideal weight vector of NN and l is the number of NN nodes. In addition, $S(\omega) = [s_1(\omega), \dots, s_l(\omega)]^\top$ is a radial basis function vector generally designed by the Gaussian functions such as

$$s_i(\omega) = \exp \left[\frac{-(\omega - \mu_i)^\top (\omega - \mu_i)}{\eta_i^2} \right] \quad (8)$$

where μ_i is the center of receptive field and η_i is the width of Gaussian function. Fig. 2. shows the block diagram of adaptive control system which is shown in this section.

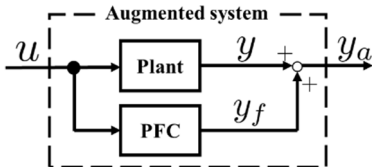


Fig. 1. Block diagram of augmented system.

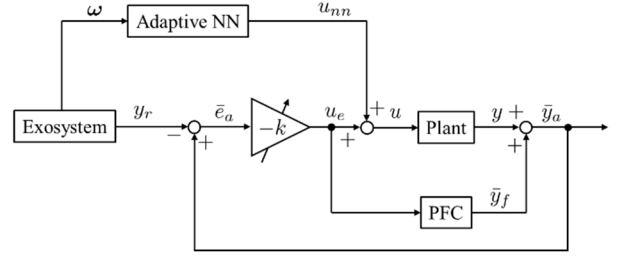


Fig. 2. Block diagram of adaptive control system with NN feedforward input.

Here, the problems are how to design the PFC and how to decide the parameters of adjusting laws.

3. Design of PFC by Input/Output Data

Define the ideal output of the ideal augmented system by using the input data as follows.

$$y_a^*(t) = G_a^*(s)[u(t)], \quad (9)$$

Then, the ideal output of PFC can be described by using the output of controlled system as follows.

$$y_f^*(t) = y_a^*(t) - y(t). \quad (10)$$

Here, suppose that the ideal PFC given by the following:

$$H^*(s) = \frac{N_H^*(s)}{D_H^*(s)} = \frac{b_1^* s^{n_f-1} + \dots + b_{n_f}^*}{s^{n_f} + a_1^* s^{n_f-1} + \dots + a_{n_f}^*} \quad (11)$$

then the ideal output of PFC also can be given as

$$y_f^*(t) = H^*(s)[u(t)]. \quad (12)$$

By introducing a stable filter:

$$F(s) = \frac{1}{s^{n_f} + f_1 s^{n_f-1} + \dots + f_{n_f}}, \quad (13)$$

Eq. (4) can be represented as

$$y_f^*(t) = \frac{D_H^*(s) - F(s)}{F(s)} y_f^*(t) + \frac{N_H^*(s)}{F(s)} [u(t)] \quad (14)$$

By defining the ideal parameters as

$$\rho^* = [z_1 \ \dots \ z_{n_f} \ b_1 \ \dots \ b_{n_f}]^\top \quad (z_i = f_i - a_i) \quad (15)$$

and the filtering signal as

$$z = \left[\frac{s^{n_f-1}}{F(s)} y_f^* \ \dots \ \frac{1}{F(s)} y_f^* \ \frac{s^{n_f-1}}{F(s)} u \ \dots \ \frac{1}{F(s)} u \right]^\top \quad (16)$$

then the ideal output of PFC can be represented as

$$y_f^*(t) = \rho^{*\top} z(t). \quad (17)$$

From eq. (9), for any parameters, the output of PFC can be given as

$$y_f(t) = \rho^\top z(t). \quad (18)$$

Finally, consider minimizing the following evaluation function.

$$J(\rho) = \int_0^T (y_f(t) - y_f^*(t))^2 dt \quad (19)$$

Although the order of PFC and parameters of filter affect to the output of PFC, there are no theoretical method to decide these parameters. Therefore, it will be optimized by DE later. Remark that the ideal output of PFC is known but parameters of ideal PFC and filter are unknown.

4. Differential Evolution

In this section, the basic algorithm of DE which is applied in this study will be shown.

(i) Creation of initial population

Randomly create an initial N sets of population as follows.

$$\mathbf{X}_i^{(1)} = [X_{i,1}^{(1)}, \dots, X_{i,D}^{(1)}], \quad i = 1, \dots, N \quad (20)$$

The superscript means a generation number of the vector, and D is the order of decision variables.

(ii) Extraction of base vector

Extract the best vector from n th generation vector $\mathbf{X}_1^{(n)} \dots \mathbf{X}_N^{(n)}$ which minimizing the evaluation function. This is, set the base vector as follows when the l th target vector minimize the evaluation function.

$$\mathbf{X}_{\text{base}}^{(n)} = \mathbf{X}_{\text{best}}^{(n)} = \mathbf{X}_l^{(n)} \quad (21)$$

(iii) Mutation

Generate a mutated vector from randomly chosen two vectors $\mathbf{X}_{r_{1,i}}^{(n)}, \mathbf{X}_{r_{2,i}}^{(n)}$ ($r_{1,i} \neq r_{2,i} \neq l$) as follows.

$$M_i^{(n)} = \mathbf{X}_{\text{base}}^{(n)} + F(\mathbf{X}_{r_{1,i}}^{(n)} - \mathbf{X}_{r_{2,i}}^{(n)}) \quad (22)$$

Here, F is a scaling factor for scaling the difference vector.

(iv) Crossover

Generate a trial vector from the target vector and the mutated vector as follows.

$$U_{i,j}^{(n)} = \begin{cases} M_{i,j}^{(n)} & (\text{rand}_{i,j} \leq C \vee j = j_r) \\ X_{i,j}^{(n)} & (\text{rand}_{i,j} > C \wedge j \neq j_r) \end{cases} \quad (23)$$

$j = 1, 2, \dots, D$

Here, C is a crossover rate, rand_{ij} is a random uniform numbers in the range $[0, 1]$ and j_r is a randomly chosen integer number in the range $[1, D]$.

(v) Selection

Select the next generation as follows.

$$\mathbf{X}_i^{(n+1)} = \begin{cases} \mathbf{U}_i^{(n)} & (f(\mathbf{U}_i^{(n)}) \leq f(\mathbf{X}_i^{(n)})) \\ \mathbf{X}_i^{(n)} & (f(\mathbf{U}_i^{(n)}) > f(\mathbf{X}_i^{(n)})) \end{cases} \quad (24)$$

The shown DE algorithm is so-called DE/best/1/bin strategy⁹.

5. Control System Design via Differential Evolution

Here, concrete designing method of control system via DE will be shown.

(i) PFC design

- (a) Obtain the input/output data set of controlled system.
- (b) Creation of initial population
Randomly create an initial N sets of population as follows

$$\mathbf{X}_i^{(1)} = [X_{i,1}^{(1)}, \dots, X_{i,2n_f}^{(1)}], \quad i = 1, \dots, N \quad (25)$$

- (c) Extraction of base vector

Extract the best vector from n th generation vector as Eq. (21) which minimizing the evaluation function Eq. (19) by using obtained input/output data.

- (d) Mutation

Generate a mutated vector from randomly chosen two vectors as Eq. (22).

- (e) Crossover

Generate a trial vector from the target vector and the mutated vector as Eq. (23).

- (f) Selection

Select the next generation as Eq. (24).

(ii) Adaptive controller design

- (a) Obtain an approximation model of controlled system

From ASPR model $G_a^*(s)$ and obtained PFC $H(s)$ in above step as

$$\tilde{G}_p(s) = G_a^*(s) - H(s) \quad (26)$$

- (b) Creation of initial population

Randomly create an initial N sets of population as follows

$$\mathbf{X}_i^{(1)} = [\gamma_i, \sigma_i, \text{diag}(\Gamma_i), \sigma_{ni}, \eta_i, \mu_i] \quad (27)$$

- (c) Extraction of base vector

Extract the best vector from n th generation vector as Eq. (21) which minimizing the evaluation function as follows.

$$J(\rho) = \int_0^T (y_r(t) - y(t))^2 dt \quad (28)$$

(d) Mutation

Generate a mutated vector from randomly chosen two vectors as Eq. (22).

(e) Crossover

Generate a trial vector from the target vector and the mutated vector as Eq. (23).

(f) Selection

Select the next generation as Eq. (24).

6. Numerical Simulation

Assume that input/output data shown in Fig. 3 are obtained. From these data, by setting the parameters $F=0.8$ and $C=0.9$ with ASPR model

$$G_a^*(s) = \frac{0.5}{s + 1},$$

third order PFC was obtained as

$$H(s) = \frac{0.7692s^2 + 6.229s + 2.292}{s^3 + 12.15s^2 + 22.8s + 7.639}.$$

Then the adaptive controller parameters were optimized.

The initial value of design parameters were

$$\gamma=50.020, \sigma=0.05, \Gamma=50.008, \sigma_n=0.05, \mu=0.7879, \eta=50.009$$

Then the optimized parameters were

$$\gamma=100, \sigma=0.052, \Gamma=32.082, \sigma_n=0.049, \mu=-31.658, \eta=100$$

Fig.4 and Fig. 5 show the control result by initial adaptive controller parameters and optimized parameters respectively. It can be seen that the control performance became better after optimizing the parameters.

7. Conclusions

In this paper, the parameter optimization method which using input/output data via DE was proposed. The numerical simulation shows the usefulness of the method.

References

1. I. Mizumoto, S. Ohdaira and Z. Iwai, Output feedback strictly passivity of discrete-time nonlinear systems and adaptive control system design with a PFC, *Automatica*, **46**(9) (2010) 1503-1509.
2. T. Takagi and I. Mizumoto, Adaptive PID control system with adaptive NN feedforward for discrete-time systems, *IEEJ Transactions on Electronics, Information and Systems*, **134**(9) (2014) 1175-1181 (in Japanese)
3. H. Kaufman, I. Barkana and K. Sobel, *Direct Adaptive Control Algorithms 2nd Ed.*, (Springer-Verlag New York, 1997)

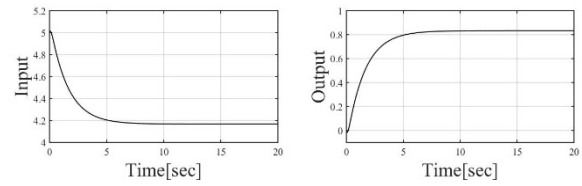


Fig. 3. Control input/output data.

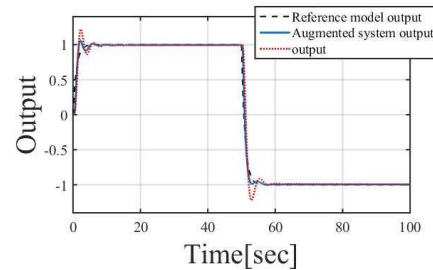


Fig. 4. Control result by initial parameters.

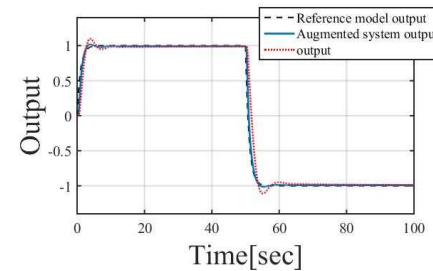


Fig. 5. Control result by optimized parameters.

4. Z. Iwai, I. Mizumoto and H. Ohtsuka, *Simple Adaptive Control SAC*, (Morikita Publishing, 2008)
5. I. Mizumoto and T. Takagi, PFC design via FRIT approach and adaptive PID control system design for discrete-time systems, *In proc. of IFAC Conference on Advances in PID control*, (2012) 64-69.
6. T. Takagi and I. Mizumoto, Adaptive output feedback control with adaptive PFC and its stability analysis, *ICIC Express Letters, Part B: Applications*, **6**(12) (2015) 3189-3195.
7. I. Mizumoto, H. Tanaka and T. Tokimatsu, Adaptive output regulation of a class of discrete-time nonlinear systems based on output feedback and NN feedforward control, *In proc. of 49th IEEE Conference on Decision and Control*, (2010) 3631-3636.
8. M. Ito and M. Tanaka, A comparative study of particle swarm optimization, differential evolution, real-coded genetic algorithm on function optimization, *Konan University Bulletin. Science and Technology, ed.*, **52**(1) (2005) 125-135. (in Japanese)
9. G. C. Onwubolu, B. V. Babu, *New Optimization Techniques in Engineering* (Springer Science & Business Media, 2004).

Mathematical Expression of *Minakata Kumagusu's* philosophy of Natural Science

Yasuhiro Suzuki

Graduate School of Informatics Nagoya, University, Furocho Chikusa
Nagoya City, 464 0814, Japan

Abstract

We interpret the mandalic epistemology of 南方熊楠 (Minakata Kumagusu) using Category theory and show that it can be interpreted by set theory. Based on this result, we give philosophical foundation of Abstract Rewriting System on Multisets, ARMS, a hybrid theoretical computational model, which synthesizes continuous and discrete computation, based on Theoretical Chemistry and Computer Science.

Keywords: Natural Computing, Natural Philosophy, Philosophy of Computation, Minakata Kumagusu

1. Introduction

南方 熊楠 (Minamata Kumagusu , 1867-1941) is a naturalist, with research themes ranging from humanities, cultural anthropology, astronomy, biology, bacteriology and others (he published 51 papers on Nature magazine only).

Kumagusu stated scientific theory and scientific philosophy in a round-trip with Horyu Togi (土宣法竜), a high priest in the Buddhist world at the time. We call his scientific theory as Kumagusu Mandala [1].

His mandalic epistemology consists of MONO, (物) corresponding to physics, KOKORO, (心) corresponding to truth, and KOTO, (事) equivalent to recognition of things by mind. His idea can be clearly shown using Category theory. Also, considering using Category theory, we can complement the ambiguous part of his thought. In this paper, we use only the basic definition of Category theory (for example [2]) so no advanced knowledge is required.

2. Elements of the Mandalic Epistemology

The text is to be typeset in 10 pt Times Roman, single spaced with interline spacing of 13 pt. Text area (excluding running title) is 6.75 inches across and 8.8 inches deep. Final pagination and insertion of running titles will be done by the publisher, so make sure that no page numbers are given in your paper and only the running titles provided in this template (authors' names and paper title) are used.

His epistemology is composed of four basic elements, 心(KOKORO), 物(MONO), 事(KOTO), 名(NA) and an extra element 印(IN).

心 is the collection of arrows and defined as $\text{Hom}(\text{物}, \text{事}) = \text{心}$, where "arrow" means operations such as map or function and $\text{Hom}(A, B)$ is a collection of all arrows from A to B; 物 can include empty element.

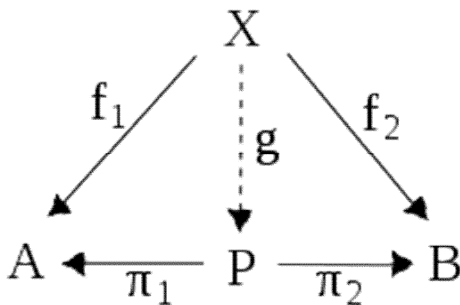
When the operation of 心(KOKORO) disappears 事(KOTO) disappears, while 物(物) does not disappear. If

© The 2018 International Conference on Artificial Life and Robotics (ICAROB 2018), Feb. 1-4, Oita, Japan

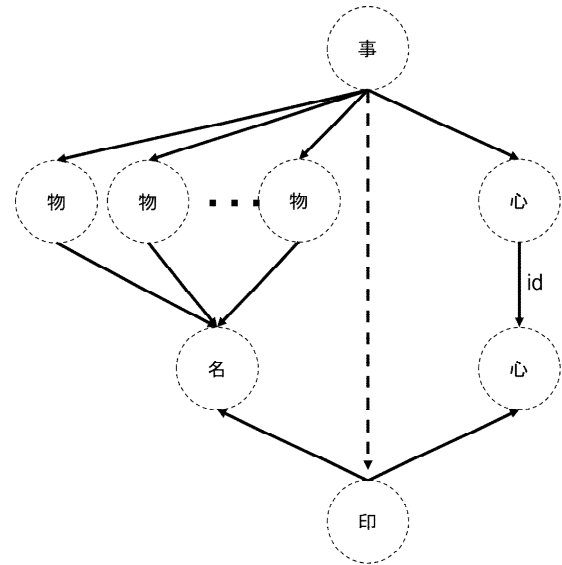
(collection of) same 事(KOTO) appear repeatedly, 名 (NA) emerges. 名 (NA) is a kind of 物(MONO) hence if a 事 (KOTO), which produces the 名 (NA) disappeared, 名 (NA) can be remain as a set of 物 (MONO). Kumagusu did not describe the mechanism of emergence of NA(名) and gave examples of NA(名) as language or religion. So we can derive it naturally from the examples of NA (名); Language or religion have “some structure” inherent; if a language is composed by completely random KOTO(事), such “language” would not be able to convey any information. Language or religion must have some structures; such structure is NA(名). KOTOS(事) that produce NA(名) are generated and extinct repeatedly, that is because the MOMOs(物) that produce the NA(名) through KOTO(事) will continue to exist. Therefore, NA(名) can be regarded as a collection of such MONOs(物)s.

Kumagusu argued that KOTO(事) and KOKORO(心) have internal interaction (it is called CHIKARA(力), it means “force” in English), we will denote CHIKARA(力) interaction as CHI(x).

We will assume that KOTO(事) and KOKORO(心) are categories. Hence the definition of Category requires that CHI must satisfy the association law in composition of CHI as $CHI_j(CHI_i(MONO(物) (or KOKORO(心)))) = CHI_l(MONO(物) (or KOKORO(心)))$. When KOTO(事) and KOKORO(心) possesses this association law in composition, we will call it is conserved. Hence, if MONO(物) and KOKORO(心) are conserved, we can define KOTO(事) as Cartesian product of MONO(物) and KOKORO(心) as follows;



,where X is KOTO(事) and A and B are respectively MONO(物) and KOKORO(心), f_1 and f_2 are called as Projections and these projections index X as the KOTO



and MONO. Because NA(名) is obtained from MONOs(物)s, we can regard the collection of MONOs as NA(名). IN(印) is obtained from projections of KOKORO(心)to NA(名), since MONO(物)is category, IN(印)also can be regarded as Cartesian product of NA(名)and KOKORO(心); then we can obtain following proposition from the definition of Category theory.

Proposition 1. *When Categories of MONO(物) and KOKORO(心) are conserved and NA(名) exist, IN(印) is uniquely obtained.* □

Kumagusu did mention about MONO(物), KOKORO(心), KOTO(事), NA(名), but did not about IN(印). Mathematically, IN(印)will be naturally obtained from other four elements and can be ignored.

3. Isomorphism of 物 and 名

When 物(MONO) and 事(KOTO) share the same 名 (NA), 物(MONO) and 名(NA) are isomorphic.

We define the equivalence of 物 (MONO) as follows: when $Hom(物, 事) = G$ and $Hom(事, 名)=H$, if when $f \circ h = g \circ h = NA(名)$, $f, g \in G, h \in H$, then $f = g$, $物_1$: from $f(物_1) = g(物_2)$, $物_1 = 物_2$, which corresponds to Mono morphism in Category.

And also we define the equivalence of KOTO(事) as follows: when $Hom(物, 事)=H$, $Hom(事, 名) = G$, if when $H \circ g = H \circ f = NA(名)$, $f, g \in G$ then $f = g$, 事₁:

from $f(\text{事}_1)=g(\text{事}_2)$, $\text{事}_1=\text{事}_2$, which corresponds to Epi morphism in Category.

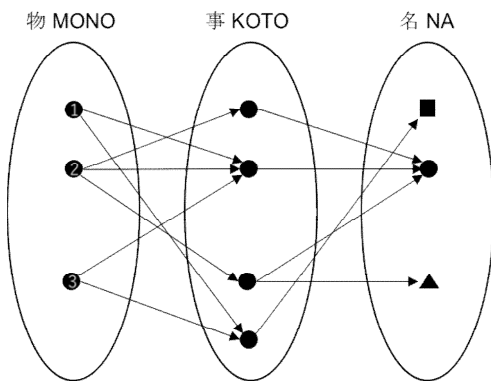
Hence, from the definition of Category theory we can have the corollary;

Corollary. *Hom(物, 名) and Hom(名, 物) are bi-morphism.* □

So, from this corollary we obtain proposition 2, which is obtained straight forwardly from the corollary, definition of isomorphism in Category;

Proposition 2. *If and only if 物 and 名 are category, Hom(物, 名) is isomorphism.* □

Mathematically, in the mandalic epistemology, 名(NA) is representative element and 物 (MONO) is element, while 心(KOKORO) and 事(KOTO) are recognitions of matters. Based on this epistemology, in order to introduce numeric concept, we will expand this framework by using multisets, which allows duplicate of the same representative elements. Hence, if we have following arrows among 物, 事 and 名,



;if we take the circle as 名, then 物 1, 2, and 3 are the same, the rectangular 物 1 and 3 are the same. It is easy to check with refereeing the definitions.

Acknowledgement

This research has supported by Grant in Aid for Scientific Research (KAKENHI) No. 15K00268, 16H03093 and 15K02105.

References

1. Minakata Kumagusu, *Toki Horyu, Round trip letters*, Yasaka Syobou, 1990.
2. Michael Barr, Charles Wells, *Category Theory for Computing Science*, Prentice Hall, 1990

Toward Artificial Intelligence by using DNA molecules

Yasuhiro Suzuki

*Graduate School of Informatics, Nagoya University, Furocho
Chikusa, Nagoya city 464-0814, Japan*

Rie Taniguchi

*Graduate School of Informatics, Nagoya University, Furocho
Chikusa, Nagoya city 464-0814, Japan
E-mail: ysuzuki@nagoya-u.jp
<http://ysuzuki.info>*

Abstract

Molecule Robotics have been realized by using bio molecules such as DNA, proteins, for example in Molecular Robotics Research Project [2012-17, JSPS]; bio molecules, such as DNA or proteins are highly structured and they already have a kind of “intelligence” and adapt environment change. Hence, we have tried to extract their “ability” and induce Intelligence artificially. We have used well-known DNA reactions, *Seesaw gate reaction* and we found that DNA molecule can senses concentration of single strand input sequence or quasi-input (mismatch, point mutation, including sequence) and chooses higher concentration one; this result shows DNA molecule (short DNA sequence) can adapt its environment.

Keywords: DNA computing, Molecular Robotics, Strand Displacement Reactions

1. Introduction

Adelman solved Hamilton Path Problem by using a computer, which was synthesized by DNA molecules. His research opens up novel era of molecular computing. DNA computing has evolved as a method of Bonino technology and realized a molecular robot.

For example, S. Nomura’s team has chemically implemented a molecular robot [1]. This robot is composed of bio molecules, which is composed of a body, an actuator, and an actuator-controlling device (clutch); whose body is composed of a lipid bilayer, the actuator consists of proteins, kinesin, and microtubules and the clutch is made of designed DNA molecules. This clutch transmits motor proteins generated force to

the membrane and the shape of body to be changed. Gears of clutch is changed by a signal molecule composed of sequence-designed DNA.

2. Molecular Artificial Intelligence

Artificial Intelligence has developed on electrical device, where every information is coded as electrical signals. On the other hand, in a molecular robot every information is coded as chemicals such as DNA or proteins. Hence, if we can realize Artificial Intelligence by using chemicals, we will be able to give intelligence to the molecular robots.

© The 2018 International Conference on Artificial Life and Robotics (ICAROB 2018), Feb. 1-4, Oita, Japan

2.1. Abstract Chemical Reactions by DNA

Several logical gates have realized by using DNA [Quian]. Various simulations of Abstract Chemical Reactions, ACR based on Chemical kinetic have been made by using the DNA logical gates [3]. For example, [3] et. al. chemically implemented the Lotka-Vorterra, LV model and showed that their reaction can realize the same behavior to analytic solution of LV modeled by differential equations.

Quian et.al., have proposed collection of DNA reactions as a “tool box” to implement ACR by using DNA; they showed that an Artificial Neural Network can be implemented by using the tool box [3].

3. Intelligence of Molecular Robot

Philosopher, prof. Kazuhisa Todayama has argued a possible development of philosophy as Concept Engineering. Concept engineering provides novel concept based on thinker’s assets. For example, in the case when we have to face with difficult problems such as create a regulation for robots in order to ready for a case when a fully autonomous intelligent robot kill a human. In such a case, philosophers can provide wide varieties of concepts in different aspects and they can support to create a novel concept through collaborating with specialists and citizens. Todayama points out that Human right is a legacy of concept engineering, which has invented by philosophers based on the asset of philosophy[2,3].

3.1. How to create intelligence in molecular robots

Todayama proposed how to create intelligence in a molecular robot from concept engineering view point; if we let the molecular robot free as possible as we can and if the robot can have own purpose, intelligence to be emerged, where any purpose is granted and no matter how it is simple or not, it is important to have its own purpose. In order to create molecular AI, we give a purpose to a robot, which is maintaining the self.

4. Methods

Chemical reactions in the toolbox are mainly modification of the toehold strand displacement reaction of DNA. Strand displacement reaction is initiated from a complementary single-stranded domains and branch

migration process exchanges a single strand DNA with double strand DNA through random-walk like; the complementary single-stranded domains is called as toeholds. In this reaction, at least one single stranded nucleic is released and this released strand can evoke downstream reactions. Since branch migration does not change the free energy during the reaction of exchanging strand pairs, it can be described by a random walk process with equal transitions probabilities of displacement in both directions at each position of the branch point [5].

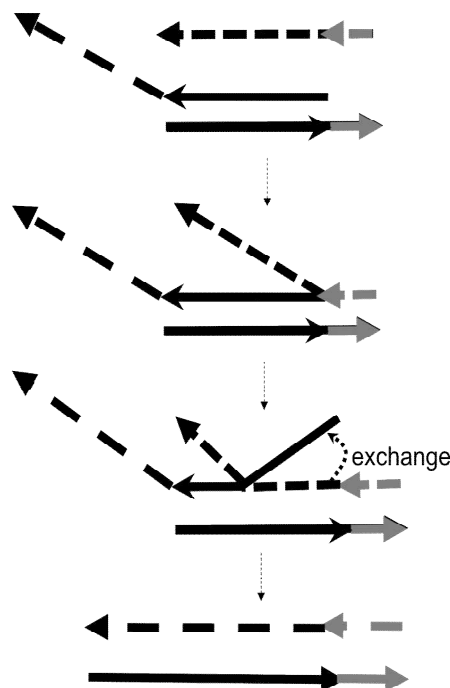


Fig.1. Strand displacement reaction; In this example, the short strand, which is denoted as an arrow binds to the toehold domains, through branch migration process across region 2, the strand is displaced and freed from the complex.

In order to implement molecular AI, we modified the Seesaw gate reaction [4]; since this reaction is self-maintaining reaction, we can give the reactions a purpose as self-maintaining. This reactions are composed of basically two strand displacement reactions; $input + gate: fuel \leftrightarrow gate: input + fuel$ (1) and $gate: input + output \leftrightarrow gate: output + input$ (2); in order to confirm the reactions circulate, we add the reaction, $fuel + gate: marker \leftrightarrow gate: fuel + marker$ (3).

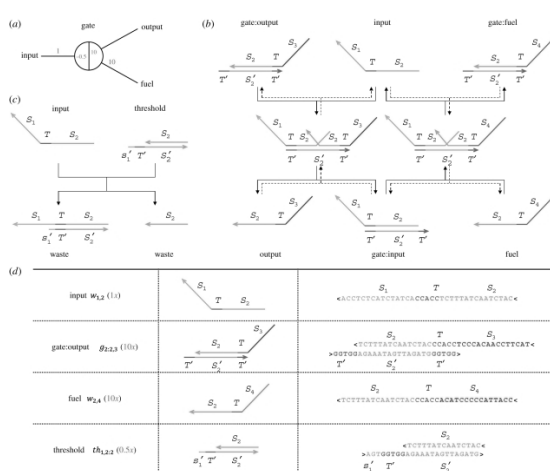
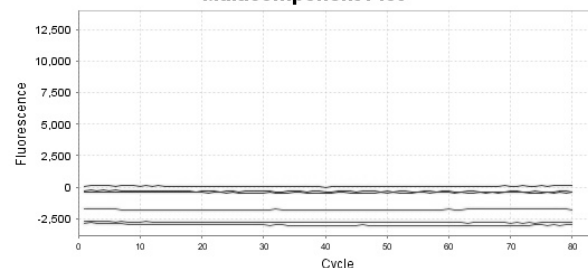


Fig. 2. Seesaw gate reaction: (a) Abstract gate diagram. Red numbers indicate initial concentrations. (b) The DNA gate motif and reaction mechanism. S1, S2, S3 and S4 are the recognition domains; T is the toehold domain; T0 is the Watson–Crick complement of T, etc. Arrowheads mark the 3' ends of strands. Signal strands are named by their domains from 30 to 50, All reactions are reversible and unbiased; solid lines indicate the dominant flows for the initial concentrations shown in (a), while the reverse reactions are dotted. (c)

5. Result

From biochemical experiments, we observed that when we added non-mutated input and mutated input, system select higher concentration one (Fig.3). And we also confirmed behaviors in the time series of concentration of normal input and mutated input sequences showed oscillations (Fig.3). And when the concentration decreases, the concentration of another input increases, hence we conjecture that the because of system select higher concentration one, selected input sequences are switched among non-mutated and mutated input sequences. These results illustrate that the system made of DNA reaction networks are able to select input sequences in higher concentration so it will able to adapt the environmental change. Therefore, from Biological and philosophical points of views, this system realizes molecular Artificial Intelligence (Fig.3).

Multicomponent Plot



Multicomponent Plot

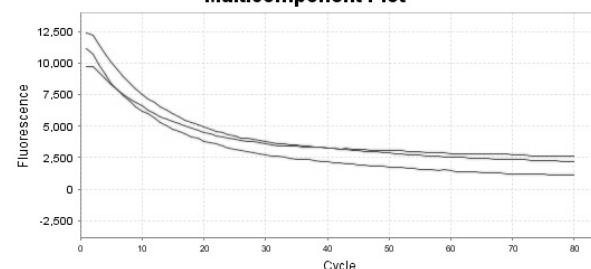


Fig. 3. Time series of concentration of Input sequences obtained by the real time PCR: top) input sequence in bulk water only, below) Input sequence without toehold and gate:fuel, the concentration of Input sequences decreased through binding to gate:fuel sequences.

Acknowledgement

I am deeply grateful to prof. Kasuhisa Todayama, Nagoya University. This research has supported by Grant in Aid for Scientific Research (KAKENHI) No. 15K00268, 16H03093 and 15K02105.

References

1. Y. Sato, et.al., Micrometer-sized molecular robot changes its shape in response to signal molecules *Science Robotics* 01 Mar 2017: Vol. 2, Issue 4, eaa13735
2. R. G. Millican, *Varieties of Meaning*, (MIT press, 2002).
3. K. Todayama, *Tetsugaku Nyumon* (in Japanese, introduction to philosophy, Chikuma shobo publishing, 2014)
4. L.Qian and E. Winfree, A simple DNA gate motif for synthesizing large-scale circuits, *J R Soc Interface*. 2011 Sep 7; 8(62): 1281–1297.
5. Luis P. Reynaldo, et.al., The Kinetics of Oligonucleotide Replacements, *J. Mol. Biol.* (2000) 297, 511±520

Differential and Integration of Sensation and its Application

Yasuhiro Suzuki

Graduate School of Informatics, Nagoya University, Furocho Chikusa
Nagoya City, 464-0841, Japan

Abstract

Our sense can be seen as a dynamical system in multi-dimensional sensory space, where each dimension corresponds to the sort of sense such as visual, audio, tactile, and so on. Our sensory systems are composed of differentiators and we perceive sensory stimulations through differentiating sensory stimulations. In order to calculate differentiation of sense, we have to set measurable quantity of the sense, we can use not only quantity measure such as brightness of picture, loudness of sound but also can use quality measure such as value of Semantic Differential (SD) method for measuring impressions or emotion such as beautiful, fear, happy. We propose a method of Differential and Integration of sensation and we show the case when transforming a drawing of *Piet Mondrian's "1921"* into a music piece by using this method.

Keywords: Computational Aesthetics, Tactile Communication, Tactile Score, Kansei Computing

1. Introduction

To see shapeless or unseen things and to hear unheard things have been challenges in Arts and Sciences. Visualizing shapeless things such as light, air, emotions, etc. or unseen things such as concepts, atmosphere, etc. have been challenges in visual Art and Science. For example, Leonard da Vinci, who is an artist, engineer, biologist and a pioneer of data science, drawn a normalized human anatomical chart based on dissecting many human dead bodies.

Tactile sense directly makes an appeal to the deep feeling without language or words [3]. Tactile sense has a language however the way of using the language is obscure. If we could have full command of the language of tactile sense, and express the feeling and tell it by using the language, cold media would be changing into intimate organic ones.

Visual media are systematized with colors and their combinational principles such as color circles, and music [1] in auditory media is systematized with combinational principles of theories of harmonics [2, 5]. On the other

hand, there is no such a combinational principle for tactile sense.

We communicate through tactile sense in the form of shaking hands to express your trust, hugging a grieving friend instead of speaking to him or her, and stroking cute dogs and cats. These communications directly make an appeal to the sensitivity and feeling, and we tactilely grasp the innermost truth of who someone is from the way of using the language and behavior.

Tactile sense has been of interest to basic science, such as psychology, psychophysics, cognitive science, and recently it has also been of interest to engineering and design. In engineering, technologies of tactile sense have been developed in virtual reality, e.g., robotics and ergonomics. One of the main issues they have addressed is "how to regenerate the tactile sense mechanically" and the necessary and desirable applications of such technologies have been explored. Reviewing the large amount of research on tactile engineering should preferably be included elsewhere, in another book. In the past, tactile engineering has mainly been applied to entertainment, such as the integration of a tactile sensing

device into a video game controller, and to communication technology, such as in mobile phones.

2. Calculus of Senses

Our sense can be seen as a dynamical system in multi-dimensional sensory space, where each dimension corresponds to the sort of sense such as visual, audio, tactile, and so on. Our sensory systems are composed of differentiators and we perceive sensory stimulations through differentiating sensory stimulations.

In order to calculate differentiation of sense, we have to set measurable quantity of the sense, we can use not only quantity measure such as brightness of picture, loudness of sound but also can use quality measure such as value of Semantic Differential, SD method for measuring impressions or emotion such as beautiful, fear, happy. Major headings should be typeset in boldface with the first letter of important words capitalized.

The most important concept of the differentiation of sense is measuring the differences in time or / and space of sense; it shares the concept of differentiation in mathematics but this is not mathematical concept and a mathematical equation of sense is not required; in calculating differentiation of sense, we use differentiable measure. Algorithm of differentiation of sense is as follows;

I. Differentiation of Sense

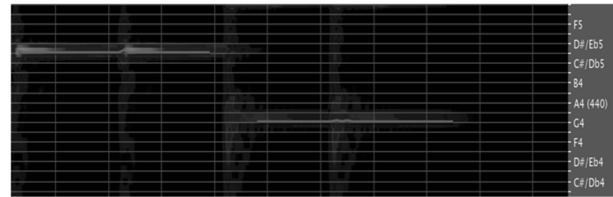
- 1 select a sense to calculate differentiation,
- 2 set the width of differentiation,
- 3 measure the differences by the time width (2.);
 - 3.1 (if it is required) measure of the differences of 3.

For example, we will differentiate a music piece;

1. a sense to calculate differentiation = the frequencies of sound,
2. the time width of differentiation = 0.5 second,
3. the differences by the time width (2.);

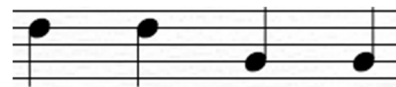
then we differentiation the sound measure and obtain the spectral pitch, which is the amount of vibration at each individual frequency and it corresponds to pitch of music note (Fig. 1).

Fig.1 Spectral pitch, the horizontal axis illustrates time and the



vertical, frequencies that correspond to pitches of music notes. D, D, G, G and duration of each note is the same as 0.5 second.

and by setting the duration of quarter note is 0.5, we obtain the music score of D, D, G, G;



, this differentiation of sound corresponds to draw the music piece in musical notation.

II. Transform Sense

1. select a differentiated sense and the sense to transform (e.g. the volume of sound into the brightness of movie)
2. transform the sense and reconcile time width each other,

Transform sensory such as audio sensory to visual has been developed well, for example, the sound-on-film recording, which is the most prevalent method of recording analog sound on a film print; in short, transform the volume of sound (audio sense) into brightness (visual sense) of a film and synchronize the sound and film. For example, by using this method we transform a picture into a music score; we differentiate a picture of Piet Mondrian, 1921 and transform into a music score.

1. the differentiated sense = the area of the same color grid square (square centimeter), space width = the area of a grid square
2. the sense to transform = musical pitches, reconcile space width;

we coarse grained the area as more than 90 square centimeters = whole note, between 90 and 45 = half note, between 45 and 22.5 = quarter note, between 22.5 and 11.25 = eighth note, between 11.25 and 5.625 = 16th note, between 5.625 and 2.8125 = 32th note and less than

2.8125 = 64th note, respectively; and we are assigned color and musical pitch as; black as C, blue, D, red E, yellow G and white, A by borrowing Major Pentatonic Scale (Table 1).

	1	2	3	4	5	6	7	8	9	10	11	12	13	14
a	1.0	2.9	3.9	2.7	7.8	2.4	6.5	0.9	3.7	2.1	8.2	1.6	1.97	1.4
b	12.4	34	24.3	30.9	89.5	28.1	75.1	10.6	42.2	24.3	93.6	18.2	22.5	16.2
c	1.3	3.6	2.6	3.3	9.6	3.1	8	1.1	4.7	2.4	10.1	1.9	2.4	1.5
d	4.3	12.0	8.6	10.9	31.6	9.9	26.5	3.7	14.7	8.5	33.1	6.4	7.9	5.7
e	9.6	26.5	18.9	24.1	69.8	21.9	58.5	8.3	32.9	18.9	73.0	14.2	17.6	12.6
f	1.1	3.2	2.3	2.9	8.5	2.6	7.1	1.0	4.0	2.3	8.9	1.7	2.1	1.5
g	6.3	17.3	12.4	15.8	45.7	14.3	38.3	5.4	21.5	12.4	47.5	9.3	11.5	8.4
h	4.1	11.3	8.1	10.3	29.8	9.3	25	3.5	14.0	8.1	31.0	6.0	7.5	5.4
i	1.4	3.9	2.8	3.6	10.5	10.5	8.8	1.2	4.1	2.8	10.9	2.1	2.6	1.9
	41.5	114.7	83.9	104.5	302.8	102.1	253.8	35.7	141.8	81.8	316.3	61.4	76.1	54.6

Table 1, Area of grid square of Mondrian 1921, in square centimeter; 8.1 is black, 24.1 and 31.0, red, 58.5 yellow, 93.6 and 47.5 are blue, 1.5 is black and all others are white

III. Integral of Sense

And also once a sense is differentiated we can calculate integral of sense as follows;

1. select the differentiated sense (time width was defined),
2. define the interval of calculating integral.
3. calculate an area of sense at each time width and calculate the sum of areas in the interval.

Then we obtained a music score of Mondrian 1921(Fig.2);

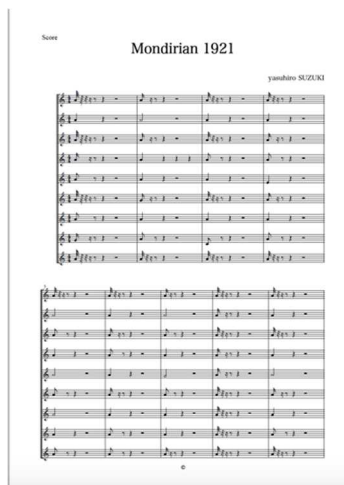


Fig 2. From the music score, which is transformed P.Mondrian's 1921;

3. Tactile Score

Massage, which is composed of various tactile senses of movements of hands on the body, is a form of haptic

© The 2015 International Conference on Artificial Life and Robotics (ICAROB 2015), Jan. 10-12, Oita, Japan

engineering that we have been developing for more than two thousand years. For this reason, we chose to investigate massage as a way to devise a method of describing the tactile sense [4]. Through our investigations, we found massage to be composed of pressure, an area of contact or touching, and the velocity of the movement of massager's hands. We modeled our tactile description on the musical score (Fig.3). In staff notation of the tactile note, we defined the third line as the basic pressure—the basic pressure with which we might hold a baby or delicate, breakable object. Hence, the basic pressure is not defined absolutely but may change from person to person or for different types of massage.

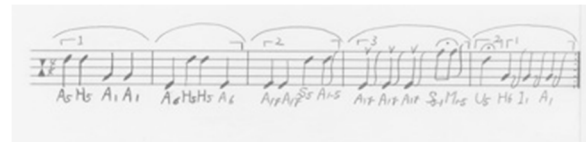


Fig.3: (Top) An example of a tactile score, with special marking above the staff notation. 1 denotes both hands moving the same; 2 indicates a small gap between hands; and 3 indicates a large gap between hands. The slur-like marks illustrate a unit component, a massage phrase; the integral-like marks illustrate releasing pressure; and the breath-like marks correspond to a short pause in massaging, much like a breath in playing music

We also defined the part of the hand used in massage and the kind of stroke used when massaging (see Fig. 4). For example, the fingertip to the first joint is 1, the second joint is 2, the third joint is 3, the upper part of the palm is 4, the center of the palm is 5, and the bottom of the palm is 6. Thus, a flowing motion from a fingertip to the third joint is denoted as “1-3.”

For massage strokes, we analyzed the method of massaging in face therapy and the stroking action of the hands' movements. For example, A₅ illustrates drawing a circle on the cheek with the center of the palm.

In the tactile score (Fig.3), at the first count in the beginning part, A₅ circles are drawn on both sides of the cheeks using the center of the palm with weaker pressure than the basic pressure; at the second count, the hands are moved to the tails of the eyes and a small circle is drawn using the center of the palm while keeping the same pressure as the first count; and, at the third and fourth counts, the hands are moved to both sides of the cheeks

and circles are drawn using the fingertips with a stronger pressure than the basic pressure.



Fig. 3: (Top) Strokes of massaging on a face. These strokes are obtained from massage experiences in beauty shops. Strokes that pass uncomfortable areas have been excluded. (Bottom) Usage of part of the hand.

3.1. Transform sounds to Tactile Score

According to the method of differentiate sense in the section 2; we select a sense to calculate differentiation is pressure (step 1), the width of differentiation is the same the range of pressures of sound (step 2) and measuring the differences by the time width is the same as the rhythm of sound (step 3).

Tactile score denotes pressure, contact area and rhythm. In this example, we will denote pressure and rhythm, where the contact area is defined as frequency of sound; we assume that lower frequency has broad contact area and higher frequency has narrow contact area so we take the reciprocals of frequencies and multiply by amplitudes. We show an example when the noise in the cabin of Japanese bullet train (Shin-kan-sen train, Fig.4).

Fig.4. Tactile score, which is transformed from the noise of cabin in Japanese bullet train (Shin-kan-sen train).

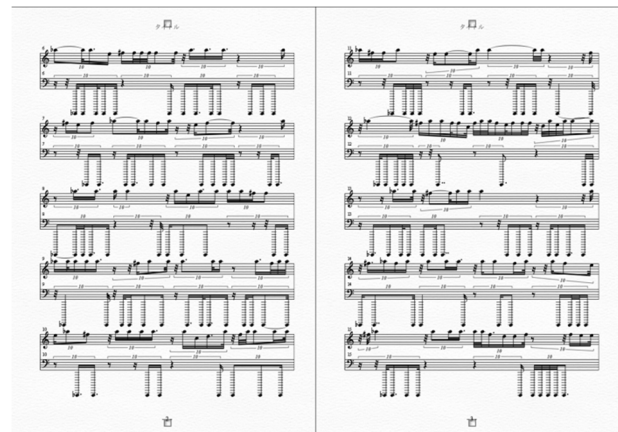


Fig. 4 Tactile score transformed from the noise in a cabin of Japanese bullet train (Shin-kan-sen train).

Acknowledgements

This research has supported by Grant in Aid for Scientific Research (KAKENHI) No. 15K00268, 16H03093 and 15K02105.

References

References are to be listed in the order cited in the text. Use the style shown in the following examples. For journal names, use the standard abbreviations. Typeset references in 9 pt Times Roman.

1. J. Huang, D. Gamble, K. Sarnlertsophon, X. Wang, S. Hsiao Feeling Music: Integration of Auditory and Tactile Inputs in Musical Meter Perception, PLOS ONE Vol.7(10), Oct 2010
2. S. Merchel, M. E. Altinsony, Designing auditory-tactile perception of music, Proceedings of ICMEM 2015, 2015
3. L. Skedung, M. Arvidsson, J. Young Chung, C. M. Stafford, B. Berglund, M. W. Rutland, Feeling Small: Exploring the Tactile Perception Limits, SCIENTIFIC REPORTS Sep 2013
4. Y. Suzuki and R. Suzuki (2013) *Tactile Score*, Springer Verlag
5. J. Ward, Acquired Auditory-Tactile Synesthesia, Annals of Neurology Vol.62, No.5, Nov, 2007

Discovering Successful Determinants of Efficiency of MICHINOEKI in Chugoku Area

Minoru Kumano

*Faculty of Regional Innovation, University of Miyazaki
1-1 Gakuendai-Nishi, Miyazaki, 889-2192 Japan
E-mail: kumano@cc.miyazaki-u.ac.jp*

Tsutomu Ito, Takao Ito

*Graduate School of Engineering, Hiroshima University
1-4-1 Kagamiyama, Higashi Hiroshima, 739-7527*

Toru Hiraoka

*Department of Information Systems, University of Nagasaki
1-1-1, Manabino Nagayo, Nishisonogi, Nagasaki, 815-2195, Japan
E-mail: hiraoka@sun.ac.jp*

Hirofumi Nonaka

*Department of Information Management System Engineering, Nagaoka University of Technology
1603-1, Kamitomioka, Nagaoka, Niigata, 940-2188, Japan
E-mail: nonaka@kjs.nagaokaut.ac.jp*

Masahara Hirota

*Department of Information Science, Faculty of Informatics, Okayama University of Science
1-1 Ridaicho, Kita-ku, Okayama-shi, Okayama, 700-0005, Japan
E-mail: hirota@mis.ous.ac.jp*

Abstract

Many theories and analyses of Michinoeki from the viewpoints of break function, information dispatch function, and regional cooperation function have been published in the past decades. Based on our investigation, additional dimensions called disaster prevention function need to be added because a variety of activities have been developed recently. Specific to the context of Michinoeki systems, this paper develops and empirically tests a mathematical model of Michinoeki from the standpoint of how those four basic functions significantly influence its performance, thus uniquely contributing to extant knowledge. Using data drawn from Michinoeki in Chugoku area, this research attempts to shed light on the relationship between four basic functions and its performance including sales revenue and number of customers who passed through the shop cashier, to confirm the validity of the new four function model. Based on the findings, the managerial implications are discussed, the study limitations are identified and directions for further research are suggested.

Keywords: four-function model, regional economy, performance, Michinoeki, efficiency

1. Introduction

Many theories and analyses of Michinoeki from the viewpoints of break function, information dispatch

function, and regional cooperation function have been published in the past decades. Based on our investigation, additional dimensions called disaster prevention function need to be added because a variety of activities have been

developed recently. Specific to the context of Michinoeki systems, this paper develops and empirically tests a mathematical model of Michinoeki from the standpoint of how those four basic functions significantly influence its performance, thus uniquely contributing to extant knowledge. Using data drawn from Michinoeki in Chugoku area, this research attempts to shed light on the relationship between four basic functions and its performance including sales revenue and number of customers who passed through the shop cashier, to confirm the validity of the new four function model.

This paper is structured as follows: Section 2 introduces the history of the Michinoeki and background literature. In section 3, the paper explicates data collection and the estimation of the regression model using specific internal and external variables. Section 4 shows the results and discusses our findings. The conclusions, directions for further research and managerial implications are proffered in the final section..

2. Background

Regional areas development plays important role in the national economy. Storper stressed that regions are the cornerstones of the global economic organization—just as firms, sectors and nations do. Thus, innovative solutions need to be developed to foster regional economic revitalization [1]. Cooke and Morgan [2] indicate that the ability of a region to cope with competitiveness challenges increasingly depends on the extent of collaboration between its firms, and the ability of regional governments in supporting such collaboration. Michinoeki roadside rest stations for those driving automobiles and/or trucks to deliver products and services is a special case of a successful model of an innovative ecosystem. These stations have been developed under the support of residents, farms, and local government. They are located along major national highways and provide free parking space, restrooms, and regional and tourist information for automobile drivers and travelers. Therefore, Michinoeki within a specific area serve the three functions of providing rest space for visitors, spreading information, and allying with regional society. Recently, disaster prevention is has also become an important consideration of Michinoeki after the 3.11

Tsunami decimated Fukushima and other towns. Therefore, the four-function model of Michinoeki could be illustrated in Fig. 1.

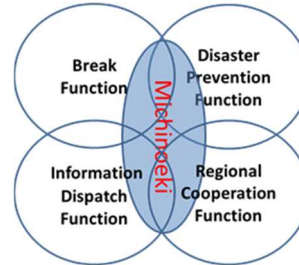


Fig. 1 Four-function model of Michinoeki

This paper is try to discover successful determinants of efficiency of Michinoeki in Chugoku area, Japan based on the four-function model.

3. Data Collection and Model Building

In this paper, we selected ten determinants as the variables to express the four functions in Michinoeki. They are square meters of land space (SMLS), weekdays' traffic near the station (WTNS), operating cost (OC), total parking number (TPN), total number of the restroom (TNR), square meters of free rest place (SMFRP), seats of the free rest space (SFRS), number of items handled (NIH), number of local products items (NLPI), and population of the city located (PCL). SMLS and OC could be considered as the determinants of variables of information dispatch function, WTNS, NIH, NLPI and PCL are designed as the indexes of regional cooperation function, TPN, TNR, SMFRP and SFRS will play important role in break function and disaster prevention function. Sales revenue and number of purchasers are selected as the performance of Michinoeki. Thus, this leads to the formation of the following regression equation:

$$y = a_1SMLS + a_2WTNS + a_3OC + a_4TPN + a_5TNR + a_6SMFRP + a_7SFRP + a_8NIH + a_9NLPI + a_{10}PCL + \varepsilon \quad (1)$$

The data were extracted from the internal databases and provided by senior administrators of Michinoeki headquarters.

Table 1. Results of the regression models of sales and number of the purchasers.

	Models			
	Sales		Number of the Purchasers	
	Standardized coefficient	Probability	Standardized coefficient	Probability
SMLS	-0.1378	0.4405	-0.1988	0.1463
WTNS	-0.0204	0.8724	0.0429	0.6739
OC	0.0624	0.6851	-0.0932	0.4713
TPN	0.2731	0.0774	0.3053	0.0198
TNR	0.0759	0.662	0.1559	0.2696
SMFRP	0.1788	0.1568	0.4364	0.0001
SFRS	-0.075	0.5776	-0.0304	0.7877
NIH	-0.1019	0.5785	-0.0846	0.5924
NLPI	0.4878	0.0083	0.39	0.0133
PCL	0.2228	0.0672	0.2294	0.0277
Intercept	0	0.7033	0	0.7636
Coefficient of determination	0.34596		0.50529	
multiple correlation coefficient	0.58818		0.71084	
Adjusted R-square	0.48678		0.65230	
Data number	71		73	

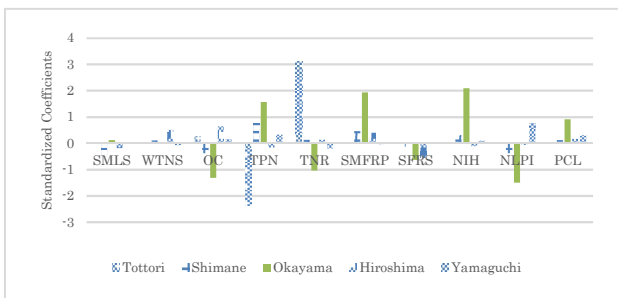


Fig. 2 Results of Sales revenue model.

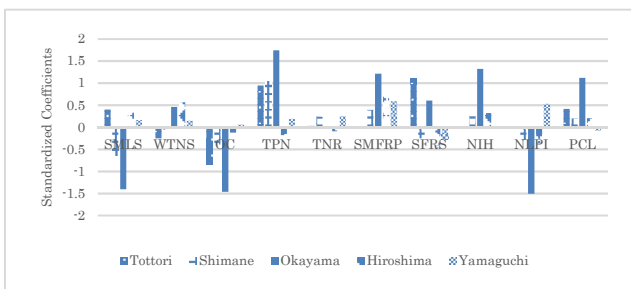


Fig. 3. Results of number of purchaser's model

4. Calculation and Discussion

We first calculated the relationship between the ten variables and sales revenue and the Number of the purchasers. The results is shown as in Table 1. Next, we calculated standardized coefficients of sales revenue and number of purchasers regression model respectively of each prefecture. They are reported in Fig. 2 and 3.

In the regression model of number of purchasers, only four parameters are significant: SMLS (Shimane), TPN (Okayama), SMFRP and NLPI (Yamaguchi). In the regression model of sales revenue, Okayama's TPN, SMFRP, and NIH, Yamaguchi's TPN, NLPI, and PCL are significant. Therefore, square meters of land space total parking number, square meters of free rest place, number of local products items, and population of the city located could be considered as the important determinants in the management of Michinoeki. Moreover, break function and regional cooperation function works in Okayama and Yamaguchi while information dispatch function plays role in Yamaguchi.

5. Conclusion

The relationship between ten variables and sales and number of purchasers are calculated and discussed. Only part of the determinants such as SMLS and TPN have impacts on the performance of Michinoeki. Only one-year Data set is sufficient. Much more data set and investigation is required.

References

1. Successful examples of regional revitalization, http://www.kantei.go.jp/jp/singi/sousei/meeting/top_seminar/h29-01-13-haifu4.pdf#search=%27%E5%9C%B0%E6%96%B9%E5%89%B5%E7%94%9F+%E4%BA%8B%E4%BE%8B%27, retried April 20, 2017.
2. Satoyama (2003), *The Traditional Rural Landscape of Japan*, Takeuchi, et al. eds., Springer.

Relationship Analysis on the Number of Customers of Michinoeki in Kyushu Region

Toru Hiraoka, Shiori Nishimura

*Department of Information Systems, University of Nagasaki,
1-1-1, Manabino Nagayo, Nishisonogi, Nagasaki, 815-2195, Japan
E-mail: hiraoka@sun.ac.jp, bs116025@sun.ac.jp*

Hirofumi Nonaka

*Department of Information and Management System Engineering, Nagaoka University of Technology,
1603-1, Kamitomioka, Nagaoka, Niigata, 940-2188, Japan
E-mail: nonaka@kjs.nagaokaut.ac.jp*

Minoru Kumano

*Faculty of Regional Innovation, University of Miyazaki,
1-1, Gakuendai-nishi, Miyazaki, 889-2194, Japan
E-mail: kumano@cc.miyazaki-u.ac.jp*

Abstract

We identify factors related to the number of customers at roadside stations (Michinoeki) in the Kyushu region, and analyze the relation. We also consider the number of customers and the availability of various facilities and services at Michinoekies, and analyze the relation. We pick up the following factors: land area of all facility, area of the retail facility, parking capacity, traffic volume, number of products sold at the retail facility, total project cost, and population of the local municipality. By correlating these factors and the number of customers, we find factors that are related to the number of customers. We also pick up 44 types of facilities and services, and analyze the correlation between the existence of these facilities and services. In addition we perform multiple regression analysis and quantification method I to estimate the number of customers from these factors or the existence of these facilities and services, respectively.

Keywords: Michinoeki, roadside station, number of customer, relationship analysis, Kyushu region

1. Introduction

Michinoekies in Japan are roadside stations that provide information, offer facilities for resting, and promote local cooperation in order to contribute to a safe and comfortable road environment and create local activities¹. Municipalities build Michinoekies and register them with the Road Bureau of the Ministry of Land, Infrastructure, Transport and Tourism (MLIT). The first 103 locations were registered in 1993, and 1,117 locations were registered as of April 21, 2017. Recently, Michinoekies have begun playing fulfilling roles, such as promoting disaster prevention² and tourism³, in addition to their

usual roles. Sales levels are high at many Michinoekies, but maintenance costs associated with age are becoming a burden for some facilities. Future maintenance and growth of Michinoekies will require tax-derived resources from MLIT and municipalities as well as increased profits and higher sales amounts at Michinoekies. To increase sales, Michinoekies must increase the number of their customers.

In this situation, the purpose of this paper is to identify factors related to the number of customers at Michinoekies and analyze the relation. The availability of various facilities and services at Michinoekies is also considered, and the relation between the number of

© The 2018 International Conference on Artificial Life and Robotics (ICAROB2018), Feb. 1-4, B-Con Plaza, Beppu, Oita, Japan

customers and the existence of facilities and services is analyzed.

This paper focuses on the following factors related to the number of customers at Michinoekies: land area of all facilities, the area of the retail facility, parking capacity, traffic volume, number of products sold at the retail facility, total project cost, and population of the local municipality. Factors that are strongly associated with the number of customers are identified through correlation analysis. In addition, multiple regression analysis is performed to estimate the number of customers based on a set of factors, and the goodness of the multiple regression equation for each set of factors is examined.

This paper considers 44 types of facilities and services provided at Michinoekies that include free rest area and tourist information booth (see Table 1). For each of these 44 types of facilities and services, the correlation with the number of customers is analyzed to identify which types of facilities and services are associated with the number of customers. Quantification method I is used to estimate the number of customers on the basis of the correlated facility and service types.

This paper identifies the factors that significantly impact the number of customers. This information will be useful in modifying the layout of existing Michinoekies and in selecting appropriate sites for new Michinoekies. This paper also examines the types of facilities and services that should be prioritized for development at Michinoekies to increase the number of customers. This analysis considers 128 Michinoekies in the Kyushu region, using the number of customers who made a payment at a cashier counter in FY 2015. Although many customers report using only a restroom

Table 1. Facilities and services of Michinoekies collected in this research.

Free rest area, Shower, Tourist information boot, Post, ATM, Baby cot, Space for selling local products, Restaurant, Cafe, Accommodation, Hot spring, Camp site, Car camping place, Marina, Park, Observatory, Plaza, Athletic field, Cultural facilities (Theater, Museum, etc.), Conference room, Local product processing plant, Experience farm, Experience workshop, Gas station, Hospital, Experience and exhibition facility of disaster prevention, Function of the government office, Nursing room, Powder room, Charging stations for electric vehicles, Highway bus, Bus, Demand transportation, Tourist bus, Tourist information staff, Services related to tourist programs such as an agricultural experience program, Delivery service to the elderly and others, information on traffic congestion, Accident information, Information on traffic regulation, Homepage, Blog, Twitter, Facebook
--

or vending machine, counting such customers is difficult. The main data used in this paper are from FY 2015 and were collected through a September 2016 questionnaire survey of municipalities that administer Michinoekies.

2. Analysis of the Relation between the Number of Customers and Various Factors

2.1. Data preparation

Data were collected for 128 Michinoekies in the Kyushu region. For each Michinoeki, data on the number of customers, land area of all facilities, area of the retail facility, parking capacity, traffic volume, the number of products sold at the retail facility, total project cost, and population of the local municipality were collected. The data on traffic volume and the municipal population were obtained from the FY 2010 National Survey of the Roads and Traffic and the FY 2010 National Census, respectively. Sales data and other data are from FY 2014 and FY 2015, respectively, collected through the September 2016 questionnaire survey of municipalities that administer Michinoekies.

For the land area of all facilities and the area of the retail facility, total floor area is used, not site area. The area of the retail facility refers to the area of the space devoted to sale of local products (agricultural products, wood products, fishery products, etc.); the number of products sold at the retail facility refers to the number of distinct products sold in the space. Parking capacity is measured in the number of vehicles that can be parked simultaneously. On a parking spot for a large, heavy vehicle (e.g., truck, bus) is treated as equivalent to two spots for ordinary vehicles. Traffic volume is measured in the number of vehicles per day. Total project cost is the initial cost of constructing Michinoekies. Complete data were obtained for 111 Michinoekies, and the following analysis is performed for these 111 locations.

2.2. Method and result of correlation analysis

Correlation analysis was performed for the number of customers at Michinoekies against a set of factors. Table 2 shows the calculated correlation coefficients. The variables in the table are listed in order of descending correlation coefficient.

Parking capacity has the strongest correlation with the number of customers; the area of the retail facility and traffic volume have weaker correlations; total project

Table 2. Correlation coefficients between the number of customers and a set of factors.

No.	Factor name	Correlation coefficients
1	Parking capacity	0.525
2	The area of the retail facility	0.460
3	Traffic volume	0.428
4	Total project cost	0.204
5	The number of products sold at the retail facility	0.156
6	Population of the local municipality	-0.122
7	Land area of all facilities	-0.111

cost, the number of products sold at the retail facility, population of the local municipality, and land area of the entire facilities have relatively little correlation. Increasing the number of vehicles that can be parked and expanding the space for selling local products, instead of simply increasing land area of all facilities, is thus expected to be effective in increasing the number of customers. Building Michinoekies on high-traffic roads, rather than on the basis of municipal population, is also seen to be effective. Since the correlation coefficient between total project cost and the number of customers is not high, Michinoeki projects may need restructuring. However, the appropriateness of such restructuring must be judged comprehensively, with consideration given to the fact that Michinoekies serve multiple purposes: they offer information, provide facilities for resting, and promote tourism, local cooperation, and disaster prevention. The relatively low correlation between the number of customers and the number of local products sold at the retail space suggests a need for proper product selection.

2.3. Method and result of multiple regression analysis

Multiple regression analysis is performed with the number of customers as the explained variable and the factors as explanatory variables. The explanatory variables are added to the regression equation one by one (see Table 1 for order of entry), starting with parking capacity which had the strongest correlation with the number of customers. Case 1 is the model with only No. 1 in Table 2 included, Case 2 also includes No. 2, and so on, through Case 7. In each case, the regression equation is estimated; the estimated number of customers is predicted for each of the 111 Michinoekies from the included the explanatory variables; and the mean of the

Table 3. Absolute residual mean and multiple correlation coefficient according to the usage factors in multiple regression analysis.

Case	Use factor (No. in Table2)	Absolute residual mean	Multiple correlation coefficient
1	1	100,432	0.525
2	1, 2	91,244	0.645
3	1, 2, 3	83,263	0.692
4	1, 2, 3, 4	84,199	0.704
5	1, 2, 3, 4, 5	82,477	0.708
6	1, 2, 3, 4, 5, 6	78,651	0.742
7	1, 2, 3, 4, 5, 6, 7	79,067	0.742

absolute values of the differences between the estimated number of customers and the observed number of customers (the absolute residual mean) is calculated. Table 3 shows the results.

The absolute residual mean is smallest in Case 6, but Cases 3-7 differ only a small amount, and so parking capacity, the area of the retail facility, and traffic volume are sufficient as explanatory variables for estimating the number of customers by multiple regression. Also, since adding total project cost or the area of the entire facilities as an explanatory variable leads to an increase in the absolute residual mean, these variables may as well be excluded in estimating the effect on the number of customers. The use of such a multiple regression equation makes it possible to estimate the effect on the number of customers of a change in parking capacity or the area of the retail facility at an existing Michinoeki. Such estimation is also possible during the process of selecting the appropriate site or designing facilities for a planned Michinoeki.

3. Analysis of the Relation between the Number of Customers and the Existence of Specific Facilities and Services

3.1. Data preparation

Data were collected for 128 Michinoekies in the Kyushu region. This paper considers the 44 types of facilities and services listed in Table 1. The data are for FY 2015 and were collected through a questionnaire survey of municipalities administering Michinoekies, which was conducted in September 2016. There are no missing observation points for the 44 variables, but the number of customers were collected for only 123 stations. This set of 123 Michinoekies was used in the following analysis.

Table 4. Correlation coefficient with the number of customers and the number of installations of facilities and services.

Name of facilities and services	The number of installations	Correlation coefficient
Information on traffic congestion	48	0.406
Charging stations for electric vehicles	69	0.277
ATM	8	0.271
Cafe	72	0.230
Services related to tourist programs such as an agricultural experience program	12	0.220

3.2. Method and result of correlation analysis

This section shows correlation analysis of the relation between the number of customers at Michinoekies and the existence of certain facilities and services at that location. Each facility and service was dummy coded, with value 1 if it exists and 0 otherwise. Table 4 shows the correlation coefficients between the number of customers and the facility and service indicator variables (Top 5 with large correlation coefficient). Missing values for two variables (marina and space for selling local products) reflected data-related irregularities: no Michinoeki has marina, and the number of customers could not be obtained for the one Michinoeki without space for selling local products.

Five variables have a relatively correlation (a correlation coefficient with 0.2 or larger): information on traffic congestion (0.406), charging stations for electric vehicles (0.277), ATM (automated teller machines) (0.271), cafe (0.230), and services related to tourist programs such as an agricultural experience program (0.220). The number (percentage) of Michinoekies offering these five facilities and services is 48 (37.5%), 69 (53.9%), 8 (6.3%), 72 (56.3%), and 12 (9.4%), respectively. This result implies that there are many Michinoekies that do not offer these facilities and services. In summary, Michinoekies should prioritize these five facilities and services when aiming to improve service for their users and increase the number of customers.

3.3. Method and result of quantification method I

Quantification method I was used to estimate the number of customers according to the existence of the correlated facilities and services. These variables are included one at a time in the estimation process in descending order of correlation coefficient. The 123 Michinoekies for which the number of customers is known are considered. Table

Table 5. Absolute residual mean and multiple correlation coefficient according to the usage facilities and services in quantification method I.

Number of facilities and services used	Absolute residual mean	Multiple correlation coefficient
1	131,284	0.052
2	126,552	0.284
3	118,420	0.409
4	114,131	0.447
5	113,273	0.457

5 shows the mean differences between the number of customers (the absolute residual mean), as well as the corresponding multiple correlation coefficient.

For cases in which five or more facility and service indicator variables are included, differences in the absolute residual mean and the multiple correlation coefficient are small. It therefore would suffice to include four indicator variables (information on traffic congestion, charging stations for electric vehicles, ATM, and cafe), when estimating the number of customers via quantification method I. That is, the use of this quantification method I makes it possible to predict the effect of introducing these facilities and services at Michioekies.

4. Conclusion

This paper identified factors related to the number of customers at Michinoekies and analyzed the relation. The availability of various facilities and services at Michinoekies was also considered, and the relation between the existence of facilities or services and the number of customers was analyzed.

We would like to express our sincere gratitude to Kyushu-Okinawa “Michinoeki” Renrakukai that gave us much cooperation in conducting questionnaire survey.

References

1. Michi-no-Eki Official Website, <https://www.michi-no-eki.jp/stations/> (2017).
2. A. Tanaka and K. Kawasaki, Current state and future issues of the development of roadside stations as disaster prevention function –A case study of roadside stations in Fukushima Prefecture-, *Reports of the City Planning Institute of Japan*, **14** (2016) 236–241.
3. Y. Yamamoto and A. Yuzawa, A Study on Actual Situation and Effect of Farmer's Market in Roadside Station from Viewpoint of Regional Promotion Function: A Case Study in Kanto Region, *Journal of the City Planning Institute of Japan*, **47**(3) (2012) 985–990.

Emotional Contribution Analysis of Online Reviews

Elisa Claire Alemán Carreón, Hirofumi Nonaka

*Department of Information and Management System Engineering, Nagaoka University of Technology,
1603-1, Kamitomioka, Nagaoka, Niigata, 940-2188, Japan
E-mail: nonaka@kjs.nagaokaut.ac.jp*

Toru Hiraoka

*Department of Information Systems, University of Nagasaki,
1-1-1, Manabino Nagayo, Nishisonogi, Nagasaki, 815-2195, Japan
E-mail: hiraoka@sun.ac.jp, bs116025@sun.ac.jp*

Minoru Kumano

*Faculty of Regional Innovation, University of Miyazaki,
1-1, Gakuendai-nishi, Miyazaki, 889-2194, Japan
E-mail: kumano@cc.miyazaki-u.ac.jp*

Masaharu Hirota

*Department of Information Science, Okayama University of Science,
1-1, Ridaicho, Kita-ku, Okayama, 700-0005, Japan
E-mail: hirota@mis.ous.ac.jp*

Takao Ito

*Graduate School of Engineering, Hiroshima University,
1-7-1, Kagamiyama, Higashi-Hiroshima, 739-8521, Japan
E-mail: itotakao@hiroshima-u.ac.jp*

Abstract

In response to the constant increase in population and tourism worldwide, there is a need for the development of cross-language market research tools that are more cost and time effective than surveys or interviews. Focusing on the Chinese tourism boom and the hotel industry in Japan, we extracted the most influential keywords in emotional judgement from Chinese online reviews of Japanese hotels in the portal site Ctrip. Using an entropy based mathematical model and a machine learning algorithm, we determined the words that most closely represent the demands and emotions of this customer base.

Keywords: Entropy, Support Vector Machine (SVM), Online Review Analysis, Sentiment Analysis

1. Introduction

Worldwide, the population of Chinese tourists has recently increased significantly over the years. This increase has led to a significant impact to several industries over the world, most directly the hotel industry, as their customer bases changed. In addition to this impact on business, there is a current increase of academic research across the world about Chinese tourist

populations¹. Now, there was a particularly notable increase in the Chinese tourist population in Japan of 107.3% from 2014 to 2015, and a total number of tourists of 6,372,948 in 2016 (Japan National Tourism Organization, 2017). However, while there are studies of Chinese tourists in several countries, for example, one researching the satisfaction levels of Chinese tourists in Vietnam² or another studying their food preferences in Australia³, these studies are done mainly outside Japan,

© The 2018 International Conference on Artificial Life and Robotics (ICAROB2018), Feb. 1-4, B-Con Plaza, Beppu, Oita, Japan

which has been largely impacted by Chinese tourism. Many if not most of these studies are performed based on the results of surveys or interviews, as are the market studies performed by companies. However, depending on the formulation of the questions, the results of questionnaire based surveys can be altered and they also present difficulties and costs of the survey by itself and in this case, the need for translations. Furthermore, the sample size of these survey studies is commonly limited to tens or hundreds of people at most. On the other hand, Data mining and text mining techniques can not only cheaply and quickly gather tens of thousands if not more samples, but the source of this extensive amount of information also can be thought to be unaltered by any part of the data extraction process. Considering this, in our study, we developed a text-mining method to analyze the demands and needs of Chinese customers of Japanese Hotels, exploring our results in the perspective of business or management decisions. In order to perform this analysis, we have extracted a large quantity of text reviews from a Chinese portal site Ctrip (<http://www.ctrip.com>), and determined the most commonly used words that would contribute the most to emotional judgement behind positive and negative opinions in a review using an entropy based mathematical extraction method. These extracted keywords related to emotional judgement not only allow us to perform a Support Vector Machine based emotional classification of the reviews, but conceptual words in these lists bring insight into which concrete topics are the Chinese tourists concerned with. After classifying the sentences in the extracted reviews as positive and negative with an optimized SVM, we have analyzed the weight value assigned to them by the SVM. For words that are not part of the support vector this is equal to 0; however, the support vector lets us observe the words that, while potentially close to the border between positive and negative sentiments, provide a strong and clear distinction in the emotional classification. These words allow us to analyze the writing tendencies of Chinese customers in either positive or negative reviews. We also observed the frequency of the terms in all of the reviews to extract the most utilized words in either kind of reviews. This is valuable information for making business management decisions from the point of view of the hotel industry companies. Because these keywords are most related to customer satisfaction, a company can

improve customer service or facilities to increase profit.

2. Introduction

2.1. Data collection and processing

In this study, we used the HTML parsing python library BeautifulSoup, and the local database management tool SQLite using the python library sqlite3 to automatize data managing processes. Different from the English language, Chinese texts lack a separation between different words, and as such, when collecting these texts, they are all a single string of characters. To be able to perform a statistical analysis of each word, the Stanford Word Segmenter⁴ program developed by the Stanford NLP Group was implemented for this task using the python nltk library. During the segmentation of all the words in our corpus, irregularities occurred where the reviews were written in other languages or where unusual punctuation marks were used. We designated a list of characters that could be recognized as noise and then cleared all the text in the corpus of these characters.

2.2. Sentiment analysis

In order to determine the words that clearly impact the user's emotional judgement we calculated the entropy value of each word in relation to each class. Shannon's Entropy, in the field of Information Theory, is defined to be the expected value of the information content in a signal⁵ or it can be thought of as the grade of impossibility of predicting an outcome. Using this value, we can observe the probability distribution of each word inside the corpus. A word that is included in many documents, it will have a high entropy value for that set of documents, since it becomes uncertain to predict in which document it will appear. Opposite to this, a word appearing in only one document will have an entropy value of zero, since it is completely predictable. We show this concept in the figure below. To apply this logic, we retrieved a sample of our corpus and with the collaboration of a group of Chinese students, tagged each sentence as the classes positive or negative depending on the emotion that the text conveyed, then calculated the entropy values for each word in relation to the set of sentences from each class. Words with higher entropy relating to the positive set than to the negative set by a factor of α were determined to be keywords influencing

positive emotional judgement in Chinese reviews of hotels. Likewise, words with higher entropy for the negative set than the positive set by a factor of α' were determined to be keywords related to the negative emotional judgement in our texts.

Support Vector Machines are supervised machine learning models usually applied to classification or regression problems⁶. We use it to classify the rest of our corpus into emotional classes in our study. An SVM is trained to classify data based on previously labeled data, generalizing features of the data by defining a separating (p-1)-dimensional hyperplane in a p-dimensional space in which each dimension is a feature of the data. The separating hyperplane, along with the support vectors, divide the multi-dimensional space and minimize the error of classification. In our study we used the linear kernel of the SVM classification process. Each training sentence is a point of data, a row in the vector x , where each column represents a feature, in our case the quantities of each of the keywords in that particular sentence. The labels of previously known classifications (1 for positive, 0 for negative) for each sentence comprise the $f(x)$ vector. The Weight Vector w is comprised of the influences each point has had in the training process to define the angle of the hyperplane and the bias coefficient b determines its position. In the field of corpus study and Natural Language Processing, each of the features of a data point is the number of times that a word is included in a document. In our study we used a number of keyword lists, defined by our entropy calculations with different comparison coefficients, as the possible features; trained the SVMs implementing the Support Vector Classifier included in the python library scikit-learn ; managed the vector mathematics with the mathematical python library numpy ; and tested for each one using the K-fold Cross Validation method, which has been proven to provide good results in small samples⁷. In each test we calculated the Precision, Recall and F1-measure⁸ for our predictions. As stated earlier in section, each point of data that is classified incorrectly causes a change in the weight vector to better locate the separating hyperplane and classify new data correctly. These changes to the weight vector are strong for features that needed to be taken account of to classify with a minimal error, those contained in the support vectors, close to the separating hyperplane. Sequentially, the weight vector can be interpreted as a numerical representation of the effect

each feature, or in our case, each of these normally ambiguous words, had for the classification process and the class it has decisive influence in. Because the weight vector assigns value to the words that comprise the support vectors, the words with higher weights are thought to be closer to the dividing hyperplane, while still clearly and decisively belonging to one of the categories the hyperplane divides the high-dimensional space in.

3. Results and Discussions

After having our training data tagged by a group of Chinese student collaborators, we experimented with different comparison coefficients for the entropy values calculated from 'positive' and 'negative' emotional classes. The mutually independent coefficients α and α' were tested from 1.5 to 3.75 in intervals of 0.25. The result was 20 lists, 10 for each emotional class.

At the beginning we experimented with different kernels for the SVM, as well as some Ensemble Learning methods, like the Boosting, Voting and Stacking. We ultimately decided to use the linear kernel for the benefits of the weight vector obtainability. We also experimented with different parameters for the SVC, finding that the best performing value for C , a constant that affects the optimization process when minimizing the error of the separating hyperplane. Low values give some freedom of error minimizes false positives, but depending on the data it can increase false negatives. Inversely, high values of C will likely result in minimal false negatives, but a possibility of false positives. We found the ideal value for this parameter was $C=0.5$ in our final classifier. We trained a different Support Vector Classifier with each of the 20 lists, and we chose the best performing lists for each emotional class, resulting in a positive emotion classifier (positive or not positive), based on the results of a k-fold cross validation process in which we calculated their accuracy and F-measure means and standard deviations. Table 1 shows the results of our system performance. After observing the misclassification behavior for the positive emotion classifier, which mostly misclassified negative sentences, we decided to combine both keyword lists into a single large list to train the positive emotion classifier.

Below Table 2 we show some of our keywords from the subject class (words that help us understand demands of the users) that have a relatively high weight value for both positive and negative extremes, and their translations in the relevant context.

Table 1. Performance of our method

Emotion	C	Acc- uracy μ	Acc- uracy σ	F1 μ	F1 σ
Positive ($\alpha=2.75$)	0.5	0.88	0.15	0.90	0.09

Analyzing the extracted subject keywords is the key to performing a market study of Chinese customers of Japanese Hotels. They can be interpreted as explicit needs and demands. Analyzing words with an influence of positive emotions, we found that the most relevant subjects Chinese customers perceive positively are cleanliness and size, very possibly of the room they had stayed in. There is also the possibility that reviewers were praising in general the cleanliness of Japan’s environment, easily accessible and their culture of respecting spaces.

Table 2. Positive Emotion Keyword

Word	English	Weight
干净	Clean	0.638
大	big, wide	0.624
交通	Traffic	0.586

4. Conclusion

In our study, with the purpose to understand emotional responses of Chinese customers of Japanese hotels, their demands and needs, we extracted keywords from their reviews from the Chinese portal site Ctrip using entropy calculations from a manually classified sample of our data; then we used these keywords in machine learning experiments. Using the keywords to train a linear kernel Support Vector Classifier, we obtained the highest performance entropy based keywords.

Using the weight vectors of our classifiers, as well as frequency of the words in our data set, we found that Chinese customers have a preference for big and clean rooms, big thermal baths or bathhouses, expect good cost-performance regardless of price, that there is a lack

of Chinese text translation and that they prefer hotels where breakfast is included.

In future works we plan to investigate further into this topic, extending our data set, researching for other factors, such as time, scoring, revenue, and others. Another subject to investigate is to determine subjects that are classifiable as general topics in tourism compared to those only applicable in hotels. As mentioned before, we would also like to study the food preferences of Chinese tourists. Additionally, it would be interesting to study further into more specific emotions than the positive and negative classification we performed in our study.

Acknowledgements

This research is supported by Japan Construction Information Center Foundation (JACIC).

References

1. Sun, Y., Wei, Y., & Zhang, L. (2017). International academic impact of Chinese tourism research: a review based on the analysis of SSCI tourism articles from 2001 to 2012. *Tourism Management*, 58, 245-252.
2. Truong, T., & King, B. (2009). An evaluation of satisfaction levels among Chinese tourists in Vietnam. *International Journal of Tourism Research*, 11(6), 521-535.
3. Chang, R., Kivela, J., & Mak, A. (2010). Food preferences of Chinese tourists. *Annals of Tourism Research*, 37(4), 989-1011.
4. Chang, P., Galley, M., & Manning, C. (2008). Optimizing Chinese Word Segmentation for Machine Translation Performance. *Statmt '08 Proceedings of The Third Workshop on Statistical Machine*, 224-232.
5. Shannon, C. (1948). A Mathematical Theory of Communication. *Bell System Technical Journal*, 27(3), 279-423.
6. Cortes, C., & Vapnik, V. (1995). Support-vector networks. *Machine Learning*, 20(3), 273-297.
7. Kohavi, R. (1995). A study of cross-validation and bootstrap for accuracy estimation and model selection. *International Joint Conference on Artificial Intelligence*, 14(2).
8. Powers, D. (2011). Evaluation: From Precision, Recall and F-Measure to ROC, Informedness, Markedness & Correlation. *Journal of Machine Learning Technologies*, 2(1), 37-63.

An approach to visualize place of interest and shooting spot using geo-tagged photographs

Masaharu Hirota

*Faculty of Informatics, Okayama University of Science
Okayama, 7000005, Japan*

Masaki Endo

*Division of Core Manufacturing, Polytechnic University
Kodaira, 1870035, Japan*

Hiroshi Ishikawa

*Faculty of System Design, Tokyo Metropolitan University
Hino, 1910065, Japan*

E-mail: hirota@mis.ous.ac.jp, endou@uitech.ac.jp, ishikawa-hiroshi@tmu.ac.jp

Abstract

Hotspots are interesting places where many people do sightseeing. Hotspots are classifiable into two types: area of interest and shooting spot. In this paper, we describe the method for visualizing the area of interest and shooting spot from social media sites. Our method classifies an area into the area of interest or shooting spot using a distribution of photographic orientation. We demonstrate our approach using photographs annotated with metadata from Flickr.

Keywords: Geographical characterization, Visualization, Photograph location, Photograph orientation

1. Introduction

Because of the increasing popularity of mobile devices such as digital cameras, numerous photographs taken by photographers have been uploaded to photo-sharing web services. Recently, those devices have included embedded global positioning system (GPS). Using them, photographers annotate photographic metadata to photographs. A photographic location, which is one type of metadata observed by GPS, shows a place at which photographer took photographs. Also, modern cameras and smartphone equipped with a digital compass can add metadata of the photographic orientation when a photograph is taken by a photographer. The photographic orientation denotes the direction from which the photograph was taken, and from the photographic

location. Photographs that include a photograph-orientation have become numerous recently.

Many photographer take photographs of subjects or landscapes that satisfy their own interests. Subsequently, some of them upload their photographs to web sites. As places from which many photographs have been taken, these locations might also be interesting places for many people to visit. The main approach to extract the interesting places uses huge photographs obtained from photo-sharing sites, because the photographs present the interest of people. As described in this paper, we define such places as hotspots.

Hotspots are classifiable into two types: place of interest (area of interest, point of interest) and shooting spot. We define a shooting spot as a type of hotspot in an area where many photographs have been taken. A

© The 2018 International Conference on Artificial Life and Robotics (ICAROB2018), Feb. 1-4, B-Con Plaza, Beppu, Oita, Japan

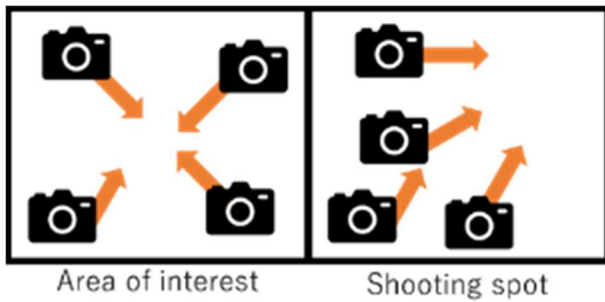


Fig.1. Examples of area of interest and shooting spot.

photographer who takes a photograph of an attractive spot such as a landmark or landscape takes the photograph at a place that is distant from the spot. As a result, photographic orientation of photographs in the shooting spot is oriented in a specific direction. Also, area of interest (point of interest or place of interest), the other type of hotspot, is usually attractive as a tourist spot for many people (e.g., Colosseum, Statue of Liberty). In such areas, many photographers take many photographs inside or near places. As a result, photographic orientation of photographs in area of interest is oriented in various directions.

In this paper, we classify an area into the area of interest or shooting spot based on the distribution of photographic orientation of photographs taken at the area. Here, we show Figure 1 of the examples of the area of interest and shooting spot. In this figure, an icon of the camera shows the photographic location of a photograph, and the orange arrow shows the photographic orientation of the photograph. The distribution of photographic orientation in an area of interest is various, because there is a landmark around a place of the area of interest. As a result, the direction of photographs is not specified like Figure 1. On the other hand, the distribution of photographic orientation in a shooting spot is unbalanced, because shooting spot is distant from a landmark. As a result, the difference of the distribution of photographic location in an area may be effective for the classification of the area of interest and shooting spot.

In this paper, we address the method for extracting shooting spot and area of interest from huge photographs annotated with metadata. Our approach to extract the shooting spot and area of interest uses machine learning algorithm based on photographic orientation.

2. Related Work

Some researchers study approaches to analyze hotspots obtained from large data annotated with photographic locations.

The method used to extract hotspots is used to find geographical characterization. Spyrou et al. proposed a method to elucidate the underlying semantics of extracted hotspots using user-generated tags [1]. Omori et al. evaluate geo-referenced photographs annotated with user-generated tags related to coastlines showing actual coastlines [2]. In addition, some methods exist to extract relations between hotspots and other hotspots such as the relations between photographic subjects and shooting spots. Shirai et al. proposed a method to extract hotspots using DBSCAN and to calculate the relations of hotspots [3]. Also, Hirota et al. proposed a method to detect and to visualize various relations of hotspots using photographic orientations and social tagging [4]. Those researches extract hotspots based on density-based approach. In this paper, we propose a method to extract two types of hotspot of area of interest and shooting spot uses the distribution of photographic orientation of huge photographs in an area.

3. Proposed method

We propose a method to visualize area of interest and shooting spot using classification algorithm based on photographic location and orientation. Our approach includes the following steps.

1. For a particular area to analyze, we obtained vast numbers of photographs with metadata of photographic orientation and location from a social media sites.
2. From photographs, we used to analyze the particular area, we create a grid space and cells with the size specified by a user.
3. We extract the cells in which many photographs were taken and create the histogram of photographic orientation in each area.
4. In each area, we apply the classification method to identify location which is area of interest or shooting spot based on the distribution of photographic orientation.

3.1. Calculation of grid

To identify location of area of interest and shooting spot from which many people have taken photographs, we create a two-dimensional grid that consists of square cells based on photographic location.

Photograph $p_i \in P = \{p_1, p_2, \dots, p_n\}$ is mapped to the coordinate as shown below.

$$y_i = \left((p_i^{\text{lat}} - \text{Lat}_{\min}) * M_{\text{height}} \right) / (\text{Lat}_{\max} - \text{Lat}_{\min})$$

$$x_i = \left((p_i^{\text{lng}} - \text{Lng}_{\min}) * M_{\text{width}} \right) / (\text{Lng}_{\max} - \text{Lng}_{\min})$$

Here, y_i and x_i shows the coordinate of photograph p_i in the grid. Lat_{\max} , Lat_{\min} , Lng_{\max} and Lng_{\min} respectively represent the maximum and minimum values of latitudes and longitudes in a dataset. Additionally, M_{height} and M_{width} respectively denote the height and width of the grid. There are found using parameter m for adjustment of how many cells we want to make in this procedure. Using the obtained grid, we extract the cells for which the number of photographs including its cell is greater than threshold minP as a hotspot.

3.2. Classification of hotspots

To identify each hotspot in the area of interest and shootings, we apply machine learning algorithm to the hotspots. The classification is based on the feature of the distribution of the photographic location of photographs in a hotspot. In this paper, we use Support Vector Machine (SVM) as classification algorithm to classify a hotspot into the area of interests or shooting spot.

To create a feature vector of a hotspot, we create a histogram of the photographic orientation. We count the number of photographs every 30 degrees, and we use the result as a histogram. Then, the histogram is normalized to the sum to 1. Also, the histogram is sorted based on the count of photographs. This reason is the approach of this classification does not consider of ordering of the photographic orientation. In other words, the feature for our classification is based only on the distribution. After the learning of classification, we classify each hotspot into the area of interest or shooting spot, and we visualize classified results on OpenStreetMap [5].

4. Experiments

In this section, we visualize the area of interests and shooting spots using our proposed method from vast photographs obtained from Flickr [6].

4.1. Experimental conditions

We describe a dataset for experiments for visualizing areas of interest and shooting spot. Photographs for experiments are obtained from the Flickr photographic search results. Those photographs have Exchangeable image file format (Exif) metadata for latitude, longitude, and orientation. We obtained 370,626 photographs taken in London. To prepare a training dataset which contains the area of interest and shooting spot, we annotate labels (area of interest or shooting spot) to areas. Table 1 presents the number of each label.

Table 1 Number of labels

	Number of label
Area of interest	45
Shooting spot	100

SVM employed for the experiments used a Gaussian kernel. Additionally, we experiment using five cross-validation, and we tune hyperparameters c and γ by grid search.

4.2. Classification

We describe the performance of our classification results. Table 2 presents our classification results. In this paper, criteria of classification performance are F1-measure, Precision and Recall.

Table 2 Results of classification

	Score
F1-measure	0.928
Precision	0.937
Recall	0.931

In Table 2, our classification is high scores in each criterion. This result shows that using the distribution of photographic orientation of photographs in an area as feature vector is effective for classification of area of interest and shooting spot. We use the classifier created in this section at the following visualization steps.

4.3. Visualization

Figure 2 and 3 present the results of the area of interest and shooting spot extracted from photographs taken in the same area of London using our proposed method. The sides of cells in figure2 and 3 is 50 and 25 meter, respectively. In those cells, red cell shows the area of interest. Black cell shows the shooting spot.

In a to c in figure 2 and 3, the point where figure 2 encloses figure 3 is classified as the area of interest in each figure. In a and b of the figures, the large area of

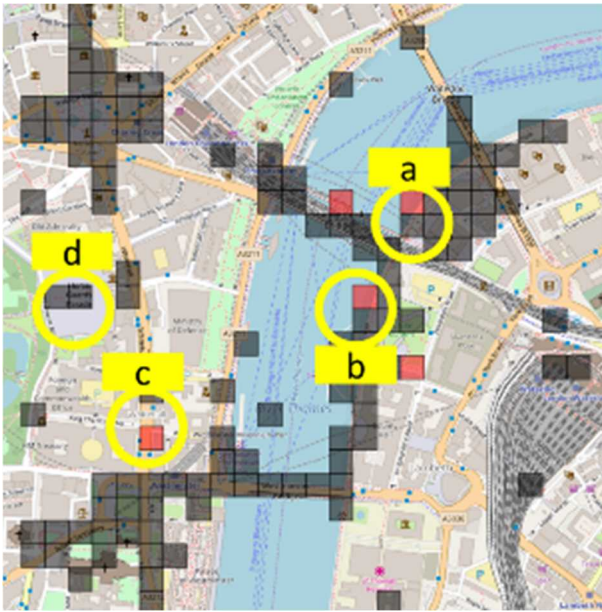


Fig.2. Visualization result (50 meter cells).

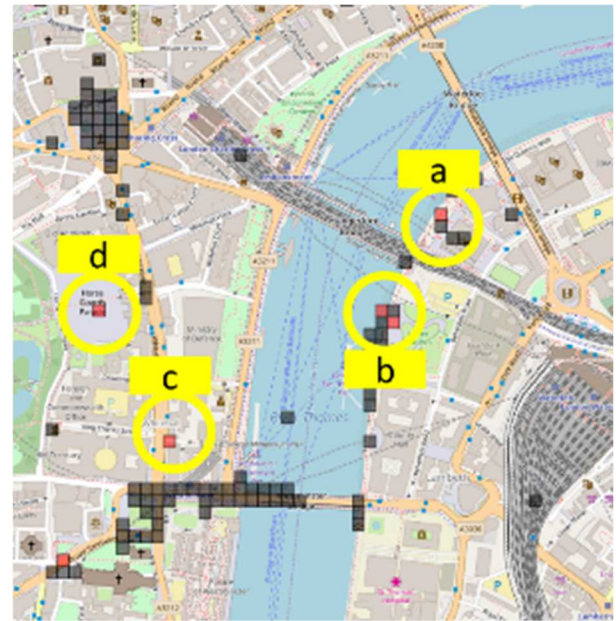


Fig.3. Visualization result (25 meter cells).

interest is divided into small area of interests and shooting spots. Also, in c of the figures, the same area is extracted as the area of interest. Therefore, the extracted area of interest in figure 3 is smaller. These result shows reducing the size of the cell, we can extract more detailed points.

Also, in the d in figure 2 and 3, the classification result changes shooting spot to the area of interest according to reducing the size of cells. This result shows even at points including the area of interest, if the cell size is not appropriate, the approach cannot extract appropriate geographical characteristics. Adjusting the cell size automatically for extracting the area of interest and shooting spot is a future work.

5. Conclusions

In this paper, we proposed a method for visualizing area of interest and shooting spots using the classification method. Our classification uses the distribution of photographic orientation in an area. After using our proposed method with photographs obtained from Flickr, we presented and discussed example of result.

As a future work, we will recommend travel routs considering this result, because such places that allow people to take photographs around famous landmarks are important for tourism.

Acknowledgements

This work was supported by JSPS KAKENHI Grant Number 16K00157, 16K16158, and Tokyo Metropolitan University Grant-in-Aid for Research on Priority Areas Research on social big data.

References

1. E. Spyrou, M. Korakakis, V. Charalampidis, A. Psallas, and P. Mylonas. A geo-clustering approach for the detection of areas-of-interest and their underlying semantics. *Algorithms*, 10(1):35, 2017.
2. M. Omori, M. Hirota, H. Ishikawa, and S. Yokoyama. Can geo-tags on flickr draw coastlines? In *Proceedings of the 22Nd ACM SIGSPATIAL International Conference on Advances in Geographic Information Systems*, pages 425–428. ACM, 2014.
3. M. Shirai, M. Hirota, H. Ishikawa, and S. Yokoyama. A method of area of interest and shooting spot detection using geo-tagged photographs. In *Proceedings of The First ACM SIGSPATIAL International Workshop on Computational Models of Place*, pages 34:34–34:41. ACM, 2013.
4. M. Hirota, M Shirai, H. Ishikawa, and S Yokoyama. Detecting relations of hotspots using geo-tagged photographs in social media sites. In *Proceedings of Workshop on Managing and Mining Enriched Geo-Spatial Data*, pages 7:1–7:6. ACM, 2014.
5. OpenStreetMap, <http://www.openstreetmap.org/>
6. Flickr, <https://www.flickr.com/>

Histogram Analysis Method Based on Gaussian Distribution and Curvature Computation (I) ---- Peaks and Valleys Detection ----

Yusuke Kawakami*

*DynaxT Co., Ltd., 2217-6 Hayashi
Takamatsu City, Kagawa 761-0301, Japan*

Tetsuo Hattori, Yoshiro Imai, Kazuaki Ando, Yo Horikawa
*Graduate School of Kagawa University, 2217-20 Hayashi
Takamatsu City, Kagawa 761-0396, Japan*

R. P. C. Janaka Rajapakse

*Tainan National University of the Arts, 66 Daci
Guantian District, Tainan 72045, Taiwan*

E-mail: riverjp2002@gmail.com, {hattori imai, ando, horikawa}@eng.kagawa-u.ac.jp, janakaraja@gmail.com

Abstract

This paper presents an analysis method of image histogram using curvature computation based on Gaussian distribution. By the image histogram and curvature computing over the cumulative histogram, we can not only detect the peaks and valleys in the image histogram, but also obtain the accompanying information on the peaks and valleys such as those shapes and sizes. In this paper, we propose the information extraction method from image histogram using the curvature computation, based on the assumption that the peaks and valleys are approximated by the same number of Gauss density functions.

Keywords: Image processing, Histogram Analysis, Cumulative histogram, Curvature computation

1. Introduction

As we have already suggested, automated image processing for the enhancement of color images has become very familiar, for example, Digital Signage, Smart Phone, etc ¹⁻³.

In our previous papers, we presented a Histogram Matching based on Gaussian Distribution (HMGD) processing for the image arrangement and ⁴⁻⁶. And we

illustrated that HMGD processing can improve feeling (or Kansei) impression of the original image. Moreover, we have proposed the method for peaks detection of the image histogram and the variance estimation of Gauss density function that is approximated at each of the peaks, based on curvature computation of the cumulative histogram.

Since we consider that the method for peaks detection can also be applied to valleys detection and that the

*1882-36, Yashima-nishi, Takamatsu City, Kagawa 761-0113 Japan

© The 2018 International Conference on Artificial Life and Robotics (ICAROB2018), Feb. 1-4, B-Con Plaza, Beppu, Oita, Japan

method can be developed for the whole histogram analysis, then in this paper, we newly propose the method based on the curvature computation over the cumulative histogram as a useful one for the whole histogram analysis. Also in this paper, repeating our previously presented methods, we suggest the capability of our proposed method to make analysis of histogram analysis.

2. Useful Principles

2.1. Peaks and Valleys Detection of Histogram

In the section, we firstly describe the principle of peak detection of original image.

Let y be a function with respect to x , the definition curvature $R(x)$ is given by Eq. (1)⁶⁻⁹.

$$R(x) = \frac{d^2y}{dx^2} \left(1 + \left(\frac{dy}{dx} \right)^2 \right)^{-\frac{3}{2}}. \quad (1)$$

Let $g(x)$ and K be a Gaussian distribution function approximated at a peak and its coefficient that are defined by the following equations.

$$g(x) = \frac{K}{\sqrt{2\pi\sigma^2}} \exp\left(-\frac{(x-a)^2}{2\sigma^2}\right) \quad (2)$$

$$\left(\frac{K}{\sqrt{2\pi\sigma^2}} \int_0^L \exp\left(-\frac{(u-a)^2}{2\sigma^2}\right) du = 1 \right)$$

Next, let $y=f(x)$ be a function representing the cumulative histogram which is represented Eq. (3). That is, dy/dx and d^2y/dx^2 be described as Eq. (4) and (5), respectively. From Eq. (4) and (5), we obtain the approximation of curvature $R(x)$ as Eq. (6).

$$f(x) = \int_0^x g(u) du = \frac{K}{\sqrt{2\pi\sigma^2}} \int_0^x \exp\left(-\frac{(u-a)^2}{2\sigma^2}\right) du. \quad (3)$$

$$\frac{dy}{dx} = g(x) = \frac{K}{\sqrt{2\pi\sigma^2}} \exp\left(-\frac{(x-a)^2}{2\sigma^2}\right). \quad (4)$$

$$\frac{d^2y}{dx^2} = \frac{dg(x)}{dx} = \frac{(a-x)}{\sigma^2} g(x) \quad (5)$$

$$R(x) = \frac{\frac{(a-x)}{\sigma^2} g(x)}{\left(1 + g(x)^2\right)^{\frac{3}{2}}} \approx \frac{(a-x)}{\sigma^2} g(x). \quad (6)$$

From Eq. (6), we understand that the curvature $R(x)$ varies the sign according to the value of x ⁹. That is, if $x < a \rightarrow R > 0$ (downward convex shape), and if $x > a \rightarrow R < 0$ (upward convex shape).

As for valley detection, we can approximate the shape of the neighbor points at the valley point as $1.0 - g(x)$. So, around the valley point, the curvature $R(x)$ is shown as follows:

$$R(x) = \frac{-\frac{(a-x)}{\sigma^2} g(x)}{\left(1 + g(x)^2\right)^{\frac{3}{2}}} \approx \frac{(x-a)}{\sigma^2} g(x). \quad (6')$$

Then, if $x < a \rightarrow R < 0$ (upward convex shape), and if $x > a \rightarrow R > 0$ (downward convex shape).

In any case, it holds that if $R > 0$, the shape of the original histogram curve is downward convex.

In this way, from the value of curvature over the cumulative histogram, we can detect peaks and valleys in the original histogram curve.

2.2. Variance Estimation

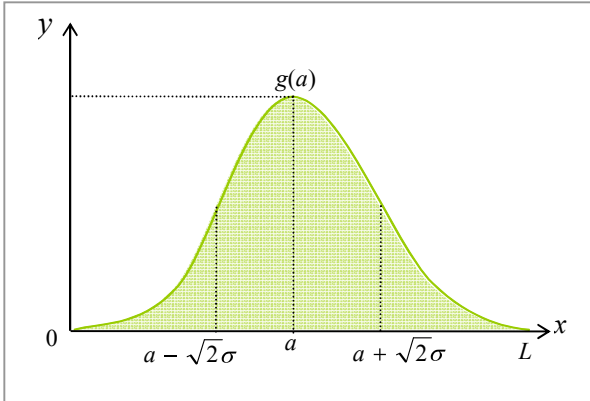
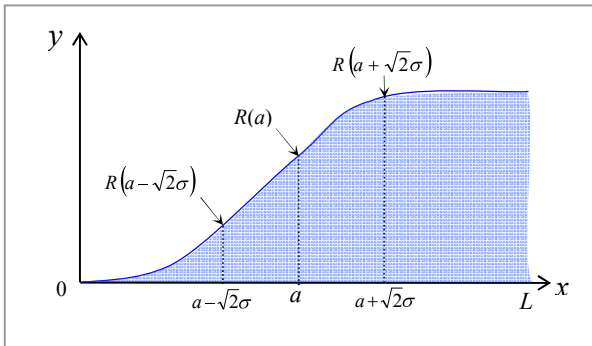
In this section, we explain two methods of variance estimation for the Gauss density function.

2.2.1. Variance Estimation Based on Symmetry

Fig. 1 shows the conceptual image of the original image histogram which is variance σ^2 and average a . And Fig. 2 shows its cumulative histogram. From Eq. (2), we have the following Eq. (7) and Eq. (8).

$$g(a) = \frac{K}{\sqrt{2\pi\sigma^2}} = \frac{K}{\sigma\sqrt{2\pi}}. \quad (7)$$

$$\begin{aligned} g(a \pm \sqrt{2}\sigma) &= \frac{K}{\sigma\sqrt{2\pi}} \exp\left(-\frac{(a \pm \sqrt{2}\sigma - a)^2}{2\sigma^2}\right) \\ &= g(a) e^{\mp 1} \end{aligned} \quad (8)$$


 Fig. 1. Conceptual image of the original image histogram^{8,9}.

 Fig. 2. Conceptual image of the original image cumulative histogram^{8,9}.

Then, the curvature value R at $a \pm \sqrt{2}\sigma$ is represented as Eq. (9).

$$R(a \pm \sqrt{2}\sigma) = \frac{(a - (a \pm \sqrt{2}\sigma))}{\sigma^2} \frac{g(a \pm \sqrt{2}\sigma)}{(1 + g(a \pm \sqrt{2}\sigma)^2)^{3/2}} \quad (9)$$

$$= \left(\mp \frac{\sqrt{2}}{\sigma} \right) \frac{g(a)e^{-1}}{(1 + (g(a)e^{-1})^2)^{3/2}}$$

Let $S = g(a)e^{-1}$, we have Eq. (10).

$$R(a \pm \sqrt{2}\sigma) = \left(\mp \frac{\sqrt{2}}{\sigma} \right) \frac{S}{(1 + S^2)^{3/2}} \equiv \left(\mp \frac{\sqrt{2}}{\sigma} \right) H. \quad (10)$$

$$H = \frac{S}{(1 + S^2)^{3/2}} = \frac{g(a)e^{-1}}{(1 + (g(a)e^{-1})^2)^{3/2}}.$$

That is, we can obtain the variance σ^2 . For example, let $v = \sqrt{2}\sigma$ be the distance from average a ,

$$R(a-v) - R(a+v) = \frac{2\sqrt{2}}{\sigma} H = \frac{4}{v} H, \quad \sigma^2 = \frac{v^2}{2}. \quad (11)$$

2.1.2. Variance Estimation by Regression Analysis

From Eq. (6), the $R(x)$ can be shown as the following Eq. (12).

$$R(x) \approx \frac{(a-x)}{\sigma^2} g(x) = \frac{1}{\sigma^2} (a-x)g(x). \quad (12)$$

And, let $C = 1/\sigma^2$ and $H(x) = (a-x)g(x)$ respectively, we can derive Eq. (13).

$$R(x) \approx CH(x) \quad (13)$$

Now, we can calculate a constant C by using least-square regression analysis¹⁰ as in the following Eq. (14).

$$R_i = CH_i + \varepsilon_i, \quad (14)$$

$$\varepsilon_i \sim N(0, \sigma^2) \quad (i = 1, \dots, n)$$

Thus, we can evaluate σ^2 as following Eq. (15).

$$C = \frac{\sum_{i=1}^n (H_i R_i)}{\sum_{i=1}^n (H_i)^2}, \quad \sigma^2 = \frac{1}{C} \quad (15)$$

Both of the variance estimation methods are equally useful for the whole histogram analysis.

3. Experimentation

Fig. 3 shows an example of the curvature computation and peak and valley points detection. Peaks are detected at $x=53$, $x=91$, $x=151$. Valleys are detected at $x=61$, $x=112$. Moreover, the variances around those points will be obtained by the aforementioned method. So, the

approximated Gauss density functions can be obtained at each of those points.

We consider that this will be very useful for histogram analysis.

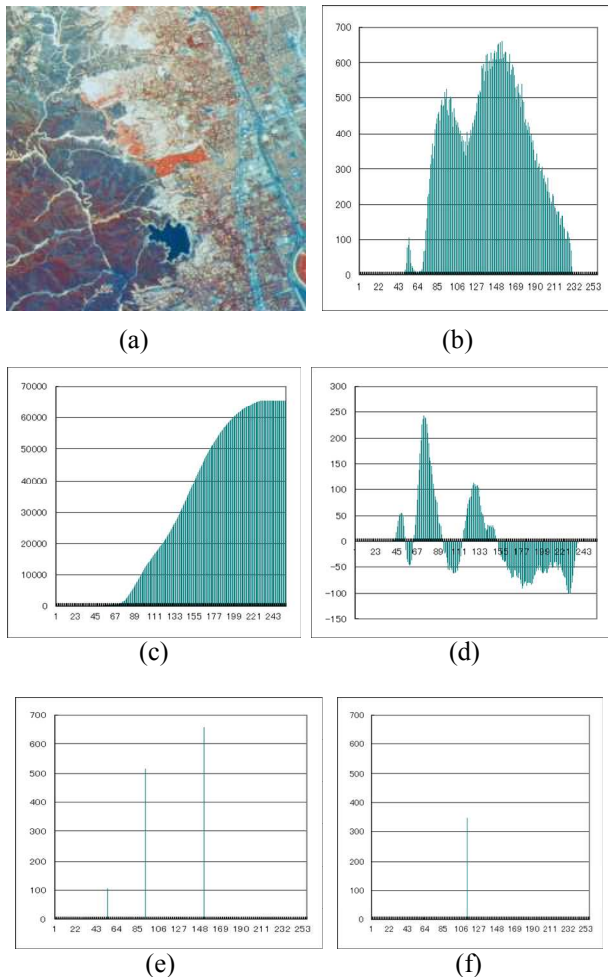


Fig.3. Example of the curvature computation. (a)Original image. (b) Histogram of the original image. (c) Cumulative histogram. (d) Curvature of the cumulative histogram. (e) Peaks are detected at $x=53$, $x=91$, $x=151$. (f) Valleys are detected at $x=61$, $x=112$.

References

1. R. C. Gonzalez and R. E. Woods, *Digital Image Processing* (Addison-Wesley Publishing Company, 1993).
2. B. Jahne, *Digital Image Processing --Concepts, Algorithms, and Scientific Applications-- 4th edition* (Springer, 1995).

3. E. S. Umbaugh, *Computer Vision and Image Processing: A Practical Approach Using CVIP tools* (Prentice Hall PTR, 1998).
4. W. Burger and J. M. Burge, *Principles of Digital Image Processing: Fundamental Techniques* (Springer 2009).
5. T. Izumi, T. Hattori, S. Sugimono, and T. Takashima, Color Image Arrangement Using Elastic Transform on Principal Component Axis (in Japanese), *Journal of Japan Society of Kansei Engineering* **8**(3) (2009) 667-674.
6. Y. Kawakami, T. Hattori, D. Kutsuna, H. Matsushita, Y. Imai, H. Kawano, R.P.C. Janaka Rajapakse, Automated Color Image Arrangement Method Based on Histogram Matching - Investigation of Kansei impression between HE and HMGD -, *International Journal of Affective Engineering* **14**(2) (2015) ISSN 2187-5413, 85-93.
7. Y. Kawakami, T. Hattori, Y. Imai, H. Matsushita, H. Kawano, R. P. C. Janaka Rajapakse, Kansei Impression and Automated Color Image Arrangement Method, *Journal of Robotics, Networking and Artificial Life* **1**(1) (2014) ISSN 2352-6386, 60-67.
8. Y. Kawakami, T. Hattori, Y. Imai, H. Matsushita, H. Kawano, and R. P. C. Janaka Rajapakse, Automated Color Image Arrangement Method Using Curvature Computation in Histogram Matching, in *Proceedings of International Conference on Artificial Life and Robotics (ICAROB 2015)* (Oita, Japan, 2015) ISBN 978-4-9902880-9-9, pp. 272-277.
9. Y. Kawakami, T. Hattori, Y. Imai, Y. Horikawa, H. Matsushita, R. P. C. Janaka Rajapakse, Automated Processing of Multiple-Brightness Peak Histogram Image Using Curvature and Variance Estimation, *Journal of Robotics, Networking and Artificial Life* **3**(1) (2016) ISSN 2352-6386, 55-60.
10. D. G. Kleinbaum, L. L. Kupper, A. Nizam, E. S. Rosenberg, *Applied Regression Analysis and Other Multivariable Methods* (Brooks/Cole Pub Co, 2013).
11. Yusuke Kawakami, Tetsuo Hattori, Yoshiro Imai, Kazuaki Ando, Yo Horikawa, R. P. C. Janaka Rajapakse, Histogram Matching Based on Gaussian Distribution Using Regression Analysis Variance Estimation”, *Proceedings of International Conference on Artificial Life and Robotics (ICAROB 2017)*, ISBN 978-4-9908350-2-6, pp.575-578, 2017.
12. Yusuke Kawakami, Tetsuo Hattori, Yoshiro Imai, Kazuaki Ando, Yo Horikawa, R. P. C. Janaka Rajapakse, Histogram Matching Based on Gaussian Distribution Using Variance Estimation --- Comparison between Curvature Computation and Regression Analysis --- *Proceedings of International Conference on Artificial Life and Robotics 2017 (ICAROB 2017)*, ISBN 978-4-9908350-2-6, pp.579-582, 2017.

Histogram Analysis Method Based on Gaussian Distribution and Curvature Computation (II) ---- Experimentation ----

Yusuke Kawakami*

*DynaxT Co., Ltd., 2217-6 Hayashi
Takamatsu City, Kagawa 761-0301, Japan*

Tetsuo Hattori, Yoshiro Imai, Kazuaki Ando, Yo Horikawa
*Graduate School of Kagawa University, 2217-20 Hayashi
Takamatsu City, Kagawa 761-0396, Japan*

R. P. C. Janaka Rajapakse

*Tainan National University of the Arts, 66 Daci
Guantian District, Tainan 72045, Taiwan*

E-mail: riverjp2002@gmail.com, {hattori imai, ando, horikawa}@eng.kagawa-u.ac.jp, janakaraja@gmail.com

Abstract

This paper presents an analysis method of image histogram using curvature computation based on Gaussian distribution. By the image histogram and curvature computing over the cumulative histogram, we can not only detect the peaks and valleys in the image histogram, but also obtain the accompanying information on the peaks and valleys such as those shapes and sizes. In this paper, we expose the experimental results and show the effectiveness of the proposed method.

Keywords: Image processing, Histogram Analysis, Cumulative histogram, Curvature computation

1. Introduction

Nowadays, automated image processing for enhancement of color images and/or image arrangement has become very familiar, for example, Digital Signage, Smart Phone, etc¹⁻³. In such automated image processing, histogram analysis of original image plays a very important role⁴⁻¹².

This paper presents an analysis method of image histogram using curvature computation based on Gaussian distribution. By computing the curvature of the cumulative histogram curve, we can not only detect the peaks and valleys in the image histogram, but also obtain the accompanying information on the peaks and valleys such as those shapes and sizes.

*1882-36, Yashima-nishi, Takamatsu City, Kagawa 761-0113 Japan

© The 2018 International Conference on Artificial Life and Robotics (ICAROB2018), Feb. 1-4, B-Con Plaza, Beppu, Oita, Japan

In this paper we also provide the experimental results for some color images and show the effectiveness.

2. Useful Principles¹³

2.1. Peaks and Valleys Detection of Histogram¹³

Let y be a function with respect to x , the definition curvature $R(x)$ is given by Eq. (1)⁶⁻⁹.

$$R(x) = \frac{d^2y}{dx^2} \left(1 + \left(\frac{dy}{dx} \right)^2 \right)^{-\frac{3}{2}}. \quad (1)$$

Let $g(x)$ and K be a Gaussian distribution function approximated at a peak and its coefficient that are defined by the following equations.

$$g(x) = \frac{K}{\sqrt{2\pi\sigma^2}} \exp\left(-\frac{(x-a)^2}{2\sigma^2}\right) \quad (2)$$

$$\frac{K}{\sqrt{2\pi\sigma^2}} \int_0^L \exp\left(-\frac{(u-a)^2}{2\sigma^2}\right) du = 1 \quad (3)$$

Next, let $y (= f(x))$ be a function representing the cumulative histogram which is represented as Eq.(4). That is, dy/dx and d^2y/dx^2 be described as Eq. (5) and (6), respectively. From Eq.(5) and (6), we obtain the approximation of curvature $R(x)$ as Eq. (7).

$$f(x) = \int_0^x g(u) du = \frac{K}{\sqrt{2\pi\sigma^2}} \int_0^x \exp\left(-\frac{(u-a)^2}{2\sigma^2}\right) du. \quad (4)$$

$$\frac{dy}{dx} = g(x) = \frac{K}{\sqrt{2\pi\sigma^2}} \exp\left(-\frac{(x-a)^2}{2\sigma^2}\right). \quad (5)$$

$$\frac{d^2y}{dx^2} = \frac{dg(x)}{dx} = \frac{(a-x)}{\sigma^2} g(x) \quad (6)$$

$$R(x) = \frac{\frac{(a-x)}{\sigma^2} g(x)}{\left(1 + g(x)^2\right)^{\frac{3}{2}}} \approx \frac{(a-x)}{\sigma^2} g(x). \quad (7)$$

From Eq.(7), we understand that the sign of the curvature $R(x)$ varies according to the value x ⁽⁹⁾. That is, if $x < a \rightarrow R > 0$ (downward convex shape), and if $x > a \rightarrow R < 0$ (upward convex shape).

Here, $R > 0$ (downward convex shape) and $R < 0$ (upward convex shape) correspond to the peak and valley in the original histogram curve, respectively.

2.2. Variance Estimation by Regression Analysis¹³

From Eq.(7), the $R(x)$ can be shown as the following Eq.(8).

$$R(x) \approx \frac{(a-x)}{\sigma^2} g(x) = \frac{1}{\sigma^2} (a-x)g(x). \quad (8)$$

And, let $C=1/\sigma^2$ and $H(x) = (a-x)g(x)$ respectively, we have Eq.(9).

$$R(x) \approx CH(x) \quad (9)$$

Now, we can calculate a constant C by using least-square regression analysis¹⁰ as in the following Eq.(10).

$$\begin{aligned} R_i &= CH_i + \varepsilon_i, \\ \varepsilon_i &\sim N(0, \sigma^2) \quad (i = 1, \dots, n) \end{aligned} \quad (10)$$

Thus, we can evaluate σ^2 as the following Eq.(11).

$$C = \frac{\sum_{i=1}^n (H_i R_i)}{\sum_{i=1}^n (H_i)^2}, \quad \sigma^2 = \frac{1}{C} \quad (11)$$

3. Experimentation

In order to how far the methods works, we have applied the aforementioned them to some images that are transformed from the original color images into grey level images.

Fig.1 and Fig.2 show the examples of the curvature computation over cumulative histogram. And they also show the peak and valley points detection. Those peaks and valleys are very well detected.

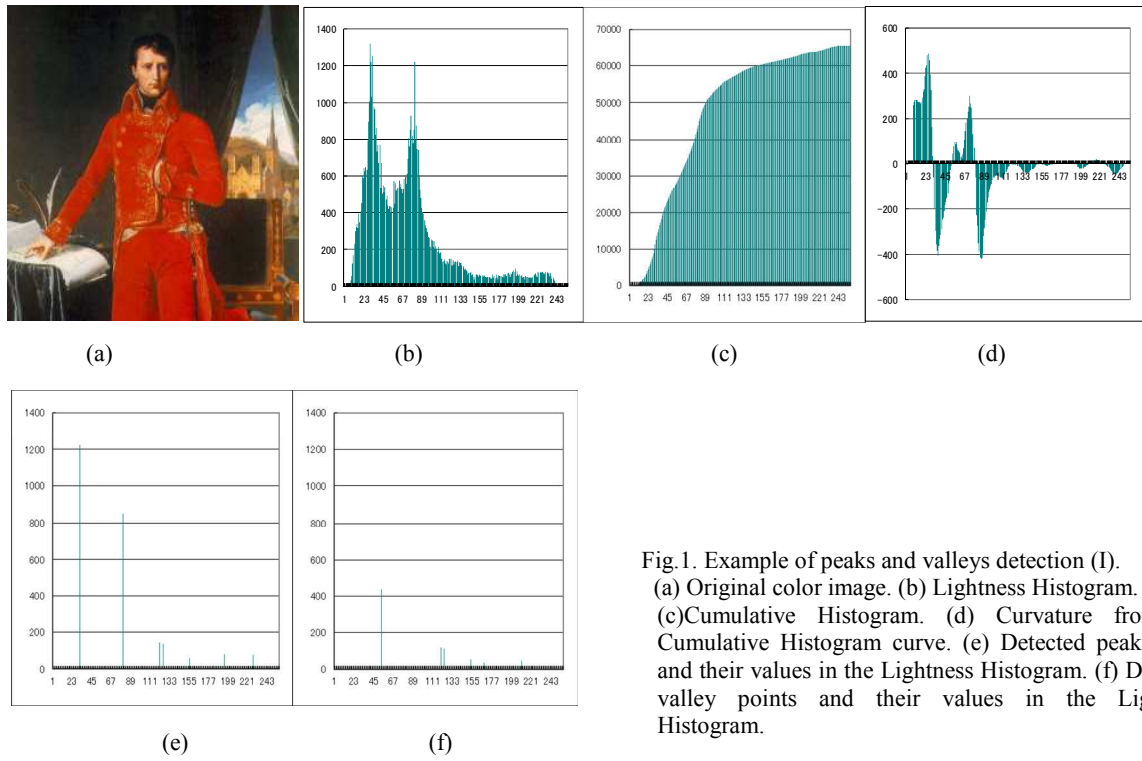


Fig. 1. Example of peaks and valleys detection (I).
 (a) Original color image. (b) Lightness Histogram.
 (c) Cumulative Histogram. (d) Curvature from the Cumulative Histogram curve. (e) Detected peak points and their values in the Lightness Histogram. (f) Detected valley points and their values in the Lightness Histogram.

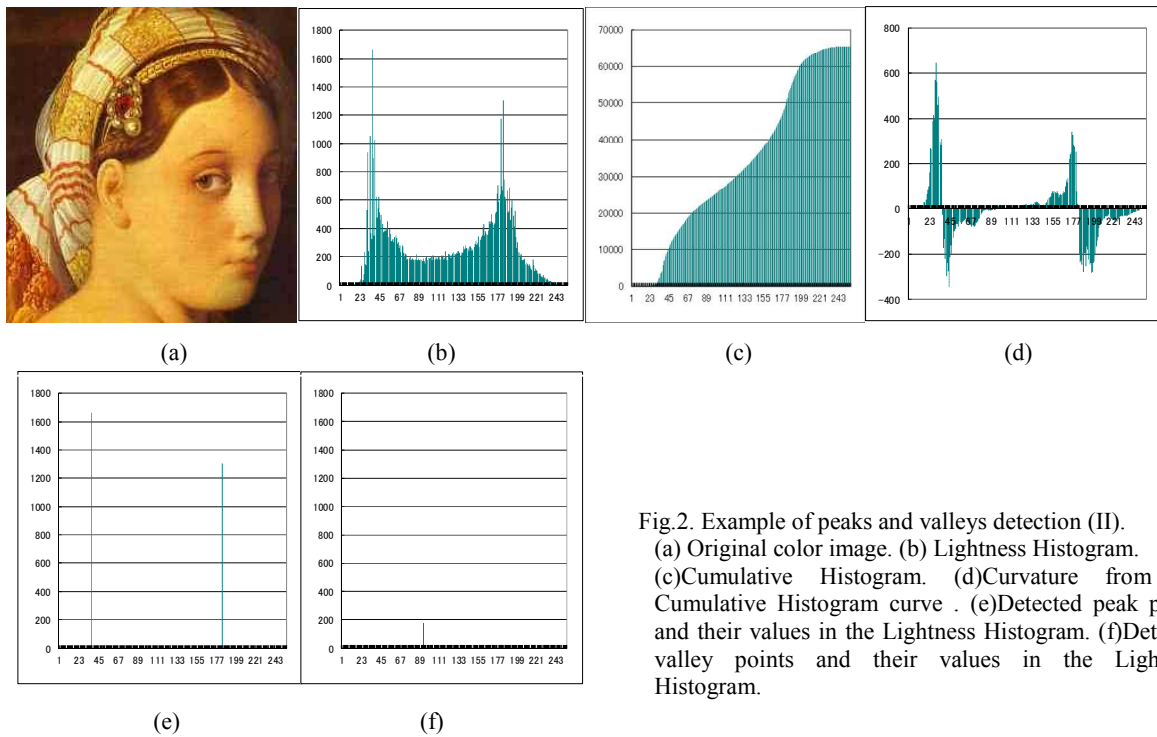


Fig. 2. Example of peaks and valleys detection (II).
 (a) Original color image. (b) Lightness Histogram.
 (c) Cumulative Histogram. (d) Curvature from the Cumulative Histogram curve. (e) Detected peak points and their values in the Lightness Histogram. (f) Detected valley points and their values in the Lightness Histogram.

Moreover, each variances of the approximated Gauss density function around those points are detected by the aforementioned method as well.

4. Conclusion

This paper has described a histogram analysis method for Lightness histogram, using curvature computation over the cumulative histogram based on the assumption that each peak in the Lightness histogram can be locally approximated to a Gaussian density function.

And by considering that the same curvature computation also gives the valley detection at the same time, we have proposed the analysis method as a very promising one.

In fact, the experimentation results for the five images have revealed that the method has correctly detected the peaks and valleys.

As for the local approximation of Gaussian density function, that is, as for the variance extraction, the regression method also has worked very well.

As a result, we consider that the proposed method is very effective and promising.

As a further study, we think to take the following two-stage strategy for the histogram analysis.

(i) First stage: Peaks and valleys detection and local approximation of Gaussian density function (its average and variance estimation) at each peaks that is equal to the proposed method in this paper.

(ii) Second stage: The shape information extraction of Mountains between neighboring two valleys and/or the perspective analysis using Scale Space Filtering.

References

1. R. C. Gonzalez and R. E. Woods, *Digital Image Processing* (Addison-Wesley Publishing Company, 1993).
2. B. Jahne, *Digital Image Processing --Concepts, Algorithms, and Scientific Applications-- 4th edition* (Springer, 1995).
3. E. S. Umbaugh, *Computer Vision and Image Processing: A Practical Approach Using CVIP tools* (Prentice Hall PTR, 1998).
4. W. Burger and J. M. Burge, *Principles of Digital Image Processing: Fundamental Techniques* (Springer 2009).
5. T. Izumi, T. Hattori, S. Sugimoto, and T. Takashima, Color Image Arrangement Using Elastic Transform on Principal Component Axis (in Japanese), *Journal of Japan Society of Kansei Engineering* **8**(3) (2009) 667-674.
6. Y. Kawakami, T. Hattori, D. Kutsuna, H. Matsushita, Y. Imai, H. Kawano, R.P.C. Janaka Rajapakse, Automated Color Image Arrangement Method Based on Histogram Matching - Investigation of Kansei impression between HE and HMGD -, *International Journal of Affective Engineering* **14**(2) (2015) ISSN 2187-5413, 85-93.
7. Y. Kawakami, T. Hattori, Y. Imai, H. Matsushita, H. Kawano, R. P. C. Janaka Rajapakse, Kansei Impression and Automated Color Image Arrangement Method, *Journal of Robotics, Networking and Artificial Life* **1**(1) (2014) ISSN 2352-6386, 60-67.
8. Y. Kawakami, T. Hattori, Y. Imai, H. Matsushita, H. Kawano, and R. P. C. Janaka Rajapakse, Automated Color Image Arrangement Method Using Curvature Computation in Histogram Matching, in *Proceedings of International Conference on Artificial Life and Robotics (ICAROB 2015)* (Oita, Japan, 2015) ISBN 978-4-9902880-9-9, pp. 272-277.
9. Y. Kawakami, T. Hattori, Y. Imai, Y. Horikawa, H. Matsushita, R. P. C. Janaka Rajapakse, Automated Processing of Multiple-Brightness Peak Histogram Image Using Curvature and Variance Estimation, *Journal of Robotics, Networking and Artificial Life* **3**(1) (2016) ISSN 2352-6386, 55-60.
10. D. G. Kleinbaum, L. L. Kupper, A. Nizam, E. S. Rosenberg, *Applied Regression Analysis and Other Multivariable Methods* (Brooks/Cole Pub Co, 2013).
11. Yusuke Kawakami, Tetsuo Hattori, Yoshiro Imai, Kazuaki Ando, Yo Horikawa, R. P. C. Janaka Rajapakse, Histogram Matching Based on Gaussian Distribution Using Regression Analysis Variance Estimation”, *Proceedings of International Conference on Artificial Life and Robotics (ICAROB 2017)*, ISBN 978-4-9908350-2-6, pp.575-578, 2017.
12. Yusuke Kawakami, Tetsuo Hattori, Yoshiro Imai, Kazuaki Ando, Yo Horikawa, R. P. C. Janaka Rajapakse, Histogram Matching Based on Gaussian Distribution Using Variance Estimation --- Comparison between Curvature Computation and Regression Analysis --- *Proceedings of International Conference on Artificial Life and Robotics 2017 (ICAROB 2017)*, ISBN 978-4-9908350-2-6, pp.579-582, 2017.
13. Yusuke Kawakami, Tetsuo Hattori, Yoshiro Imai, Kazuaki Ando, Yo Horikawa, R. P. C. Janaka Rajapakse, Histogram Analysis Method Based on Gaussian Distribution and Curvature Computation (I) ---- Peaks and Valleys Detection ----, *Proceedings of International Conference on Artificial Life and Robotics 2018 (ICAROB 2018)*, to be published.

Experimental Evaluation of Change Detection Ability in New Sequential Probability Ratio

Yoshihide Koyama ^{*1}, Tetsuo Hattori ^{*1}, Yoshiro Imai ^{*1}, Yo Horikawa ^{*1}
Graduate School of Kagawa University, 2217-20 Hayashi
Takamatsu City, Kagawa 761-0396, Japan

Yusuke Kawakami ^{*2}
DynaxT Co., Ltd., 2217-6 Hayashi
Takamatsu City, Kagawa 761-0301, Japan

Hiromichi Kawano ^{*3}
NTT Advanced Technology Corporation, 19-18, Nakamachi
Musashino, Tokyo 180-0006, Japan

Takeshi Tanaka ^{*4}
Hiroshima Institute of Technology, 2-1-1 Miyake, Saeki-ku
Hiroshima 731-5193, Japan

^{*1}{hattori, imai, horikawa}@eng.kagawa-u.ac.jp, ^{*2}riverjp2002@gmail.com, ^{*3}hiromichi.kawano@ntt-at.co.jp,
^{*4}tanaka@cc.it-hiroshima.ac.jp

Abstract

Previously, we have already proposed a novel method using New Sequential Probability Ratio (NSPR) for the structural change detection problem of ongoing time series data instead of using SPRT (Sequential Probability Ratio Test). And in the previous paper, we have revealed the experimental results by applying the both methods, i.e., NSPR and SPRT, to time series data that are generated by a multiple regression model. In this paper, we present the evaluation results of NSPR more concretely in two cases.

Keywords: Time series data, structural change detection, SPRT, New Sequential Probability Ratio (NSPR)

1. Introduction

Change point detection (CPD) problem for ongoing time series data is very important problem ¹⁻⁷. It is for identifying whether the generation structure of

monitoring data has changed or not, correctly and early as much as possible.

We consider that it is very applicable to a wide range of fields. For the structural change detection problem, we have already proposed some kinds of methods ⁶⁻¹³

^{*}2217-20 Hayashi-Cho, Takamatsu, Kagawa 761-0396 Japan

© The 2018 International Conference on Artificial Life and Robotics (ICAROB2018), Feb. 1-4, B-Con Plaza, Beppu, Oita, Japan

and have suggested that the New Sequential Probability Ratio (NSPR) method is very promising. In this paper, we compare and evaluate the two Tests that are Sequential Probability Ratio Test (SPRT) and New Sequential Probability Ratio (NSPR) by the experimental result⁶⁻¹³.

2. SPRT¹¹⁻¹⁵

The Sequential Probability Ratio Test (SPRT) is used for testing a null hypothesis H_0 (e.g. the quality is under pre-specified limit 1%) against hypothesis H_1 (e.g. the quality is over pre-specified limit 1%). And it is defined as follows:

Let Z_1, Z_2, \dots, Z_i be respectively observed time series data at each stage of successive events, the probability ratio λ_i is computed as follows.

$$\lambda_i = \frac{P(Z_1 | H_1) \cdot P(Z_2 | H_1) \cdots P(Z_i | H_1)}{P(Z_1 | H_0) \cdot P(Z_2 | H_0) \cdots P(Z_i | H_0)} \quad (1)$$

where $P(Z | H_0)$ denotes the distribution of Z if H_0 is true, and similarly, $P(Z | H_1)$ denotes the distribution of Z if H_1 is true.

Two positive constants C_1 and C_2 ($C_1 < C_2$) are chosen. If $C_1 < \lambda_i < C_2$, the experiment is continued by taking an additional observation. If $C_2 < \lambda_i$, the process is terminated with the rejection of H_0 (acceptance of H_1). If $\lambda_i < C_1$, then terminate this process with the acceptance of H_0 .

$$C_1 = \frac{\beta}{1-\alpha}, \quad C_2 = \frac{1-\beta}{\alpha} \quad (2)$$

where α means type I error (reject a true null hypothesis), and β means type II error (accept a null hypothesis as true one when it is actually false).

3. New Sequential Probability Ratio (NSPR)

3.1. Definition of NSPR¹¹⁻¹⁵

Let $C_n = a_1 a_2 \dots a_i \dots a_n$ $a_i \in \{IN, OUT\}$ be a string (or symbol sequence) obtained from the observed data.

Let θ_i and $\tilde{\theta}_i$ be the conditional probability that receives the observed data a_i in the state S_0 and S_1 ,

respectively, where S_0 and S_1 mean the state of unchanged state and changed state, respectively.

That is, it means that $\theta_i \in \{R, 1-R\}$ and $\tilde{\theta}_i \in \{R_c, 1-R_c\}$, respectively, where $R = P(OUT | S_0)$, $R_c = P(OUT | S_1)$. And let $P(C_n, H_0)$ and $P(C_n, H_1)$ be the joint probability of the symbol sequence C_n that happen with the event H_0 (the structural change is not occurred) and H_1 (the change is occurred), respectively. Then, the following equations hold.

$$P(a_1 \dots a_n, H_0) = (1-\gamma)^n \theta_1 \dots \theta_n = (1-\gamma)^n \prod_{i=1}^n \theta_i \quad (3)$$

$$\begin{aligned} P(a_1 \dots a_n, H_1) &= \gamma \prod_{i=1}^n \tilde{\theta}_i + ((1-\gamma)\theta_1)(\gamma \prod_{i=2}^n \tilde{\theta}_i) \\ &\quad + ((1-\gamma)^2 \theta_1 \theta_2)(\gamma \prod_{i=3}^n \tilde{\theta}_i) + \dots \\ &= \sum_{k=1}^n ((1-\gamma)^{k-1} \cdot \prod_{j=0}^{k-1} \theta_j)(\gamma \prod_{i=k}^n \tilde{\theta}_i) \end{aligned} \quad (4)$$

$$P(H_0 | a_1 \dots a_n) \equiv P(H_0 | C_n) = \frac{P(C_n, H_0)}{P(C_n)} \quad (5)$$

$$P(H_1 | a_1 \dots a_n) \equiv P(H_1 | C_n) = \frac{P(C_n, H_1)}{P(C_n)} \quad (6)$$

Using these above equations (Eq.(3)-(6)), the New Sequential Probability Ratio (NSPR) that we propose can be represented as follows.

$$\begin{aligned} \text{NSPR} &\equiv \frac{P(H_1 | a_1 \dots a_n)}{P(H_0 | a_1 \dots a_n)} = \frac{P(H_1 | C_n)}{P(H_0 | C_n)} = \frac{P(C_n, H_1)}{P(C_n, H_0)} \\ &= \frac{\sum_{k=1}^n ((1-\gamma)^{k-1} \cdot \prod_{j=0}^{k-1} \theta_j)(\gamma \prod_{i=k}^n \tilde{\theta}_i)}{(1-\gamma)^n \prod_{i=1}^n \theta_i} \end{aligned} \quad (7)$$

3.2. Recursive Form

When the NSPR is greater than 1.0, we can regard that the structural change has been occurred before the present time.

In the similar way as SPRT, the definition of NSPR can also be described in a recursion formula. Let

Λ_n be the value of NSPR defined by Eq.(7), we have the following recursive equation.

$$\Lambda_n = \frac{1}{1-\gamma}(\Lambda_{n-1} + \gamma)\left(\frac{\tilde{\theta}_n}{\theta_n}\right) \quad (8)$$

where $\Lambda_0 = 0, \theta_0 = 1, \tilde{\theta}_0 = 1$.

4. Experimental Evaluation

We have done the comparison experimentation by SPRT and NSPR for a time series data that is generated based on the following equations.

$$\begin{cases} y = x_1 + 20x_2 + 5 + \varepsilon & (t \leq t_c) \\ y = x_1 + 10x_2 + 5 + \varepsilon & (t_c \leq t) \end{cases} \quad (9)$$

where $\varepsilon \sim N(0, \sigma^2)$, i.e., the error ε is subject to the Normal Distribution with the average 0 and the variation σ^2 , and t_c means the change point. In addition, we have set $t_c=70$ and $\sigma=5$. The number of the time points is 100 (i.e. .

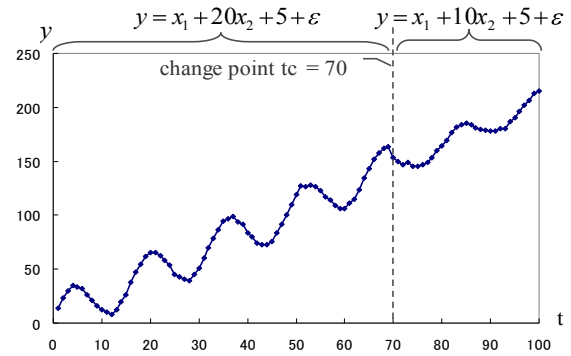
Setting the two kinds (or cases) of coefficients in Eq.(9) as shown in Eq.(10) for Case 1 and Eq.(11) for Case 2, respectively. And we have generated 200 sets of time series data for the two kinds (or cases) of time series, respectively.

$$x_1 = t, x_2 = \sin\left(\frac{1}{8}\pi t\right) \quad (10)$$

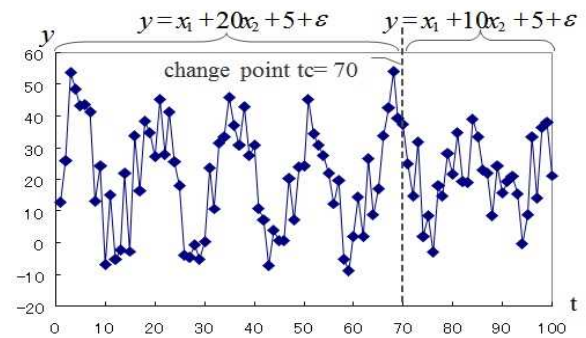
$$x_1 = random, x_2 = \sin\left(\frac{1}{8}\pi t\right) \quad (11)$$

For the two kinds of time series data (400 time series data in total), we have examined the change detection ability and the accuracy of each method (SPRT and NSPR) by setting some various evaluation criteria.

In the experimentation, the prediction model is constructed using the first 40 time points and the rest of time points from $t=41$ to $t=100$ are used for change detection.



(a) (Case 1)



(b) (Case 2)

Fig.1. Example of two kinds of time series data generated based on Eq.(9).

(a)Case1 ($x_1=t$, and $x_2 = \sin(\pi/8)$).

(b)Case2 ($x_1=random$, and $x_2 = \sin(\pi/8)$).

We define a two dimensional vector $I=(I_1, I_2)$ as follows.

$$I = (I_1, I_2) = \left(\sum_{t=41}^{t=70} f_r(t) \times |t - t_c|, \sum_{t=71}^{t=100} f_r(t) \times |t - t_c| \right) \quad (12)$$

where $t_c=70$, and $f_r(t)$ means the detection frequency at time point t in 200 time series data.

We can consider that the detection ability and the accuracy become higher as the absolute value of I_1 and I_2 approach to 0.

The all plotted data obtained by the experimentation in the case for Case1 and Case2 are shown in Fig.2.

As a result, in the sense of the abovementioned criteria, the NSPR method has revealed that it is superior to SPRT for the both cases of time series data used in the experimentation.

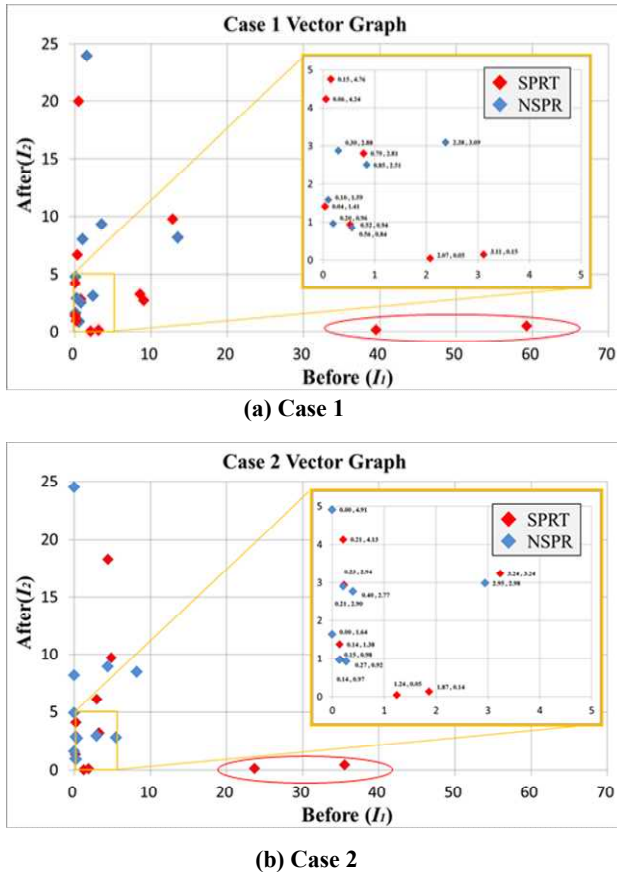


Fig.2. All plotted data : $(X,Y)=(I_1,I_2)$.

References

1. C. G. E. P. Box and G. M. Jenkins, *Time Series Analysis: Forecasting and Control* (Prentice Hall, 1976).
2. Peter J. Brockwell and Richard A. Davis, *Introduction to Time Series and Forecasting*, 2nd ed. (Springer; 2003)
3. C. Han, P. K. Willet and D. A. Abraham, Some methods to evaluate the performance of Page's test as used to detect transient signals, *IEEE Trans. Signal processing.* **47**(8) (1999) 2112-2127.
4. S. D. Blostein, Quickest detection of a time-varying change in distribution, *IEEE Trans. Information Theory.* **37**(4) (1991) 1116-1122.
5. A. Wald, *Sequential Analysis* (John Wiley & Sons, 1947).
6. H. Kawano, T. Hattori, and K. Nishimatsu, Structural Change Point Detection Method of Time Series Using Sequential Probability Ratio Test -Comparison with Chow Test in the ability of early detection- (in Japanese), *IEEJ Trans. EIS.* **128**(4) (2008) 583-592.
7. G. C. Chow, Tests of Equality Between Sets of Coefficients in Two Linear Regressions, *Econometrica.* **28**(3) (1960) 591-605.
8. K. Takeda, T. Hattori, T. Izumi and H. Kawano, Extended SPRT for Structural Change Detection of Time Series Based on Multiple Regression Mode, in *Proceedings of the 15th International Symposium on Artificial Life and Robotics*, (Feb. 2010), ISBN: 978-4-9902880-4-4, pp.755-758.
9. K. Takeda, T. Hattori, Tetsuya Izumi and H. Kawano, Extended SPRT for Structural Change Detection of Time Series Based on Multiple Regression Model, *International Journal of Artificial Life and Robotics* Springer, ISSN: 1433-5298, **15**(4), (2010) 417-420.
10. T. Hattori and H. Kawano, Change Detection Method of Time Series as an Optimal Stopping Problem -- Constructive Proof of Optimal Solution Theorem --, in *Proc. of 2011 International Conference on Biometrics and Kansei Engineering*, (2011), IEEE Computer Society, ISBN: 978-0-7695-4512-7, pp.100-105.
11. Yoshihide Koyama, Tetsuo Hattori, Hiromichi Kawano, Model Introduced SPRT for Structural Change Detection of Time Series (I), in *Proc. of The International Conference on Artificial Life and Robotics* (Jan. 2014), ISBN: 978-4-9902880-8-2, pp.252-255.
12. Yoshihide Koyama, Tetsuo Hattori, Hiromichi Kawano, Model Introduced SPRT for Structural Change Detection of Time Series (II) --- Kansei Channel and Bayes' Estimation ---, in *Proc. of The International Conference on Artificial Life and Robotics* (Jan. 2014), ISBN: 978-4-9902880-8-2, pp.256-259.
13. Yoshihide Koyama, Tetsuo Hattori, Hiromichi Kawano, "Model Introduced SPRT for Structural Change Detection of Time Series (I)", *Journal of Robotics, Networks and Artificial Life* (ISSN: 2352-6386), Vol.1, No.1, pp.55-60 (Atlantis Press, Jun. 2014)
14. Yoshihide Koyama, Tetsuo Hattori, Katsunori Takeda, Hiromichi Kawano, "Model Introduced SPRT for Structural Change Detection of Time Series (II)", *Journal of Robotics, Networks and Artificial Life* (ISSN: 2352-6386), Vol.1, No.3, pp.237-243 (Atlantis Press, Dec. 2014)
15. Yoshihide Koyama, Tetsuo Hattori, Hiromichi Kawano, Katsunori Takeda, Change Detection Experimentation for Time Series data by New Sequential Probability Ratio, *Proceedings of International Conference on Artificial Life and Robotics 2015 (ICAROB 2015)*, ISBN 978-4-9902880-9-9, pp.278-281, 2015.

Application Proposal of Sequential Probability Ratio to Dynamic System State Estimation

Tetsuo Hattori^{*1}, **Yoshihide Koyama**^{*1}, **Yoshiro Imai**^{*1}, **Yo Horikawa**^{*1}
*Graduate School of Kagawa University, 2217-20 Hayashi
Takamatsu City, Kagawa 761-0396, Japan*

Yusuke Kawakami^{*2}
*DynaxT Co., Ltd., 2217-6 Hayashi
Takamatsu City, Kagawa 761-0301, Japan*

Hiromichi Kawano^{*3}
*NTT Advanced Technology Corporation, 19-18, Nakamachi
Musashino, Tokyo 180-0006, Japan*

Takeshi Tanaka^{*4}
*Hiroshima Institute of Technology, 2-1-1 Miyake, Saeki-ku
Hiroshima 731-5193, Japan*

^{*1}{hattori, imai, horikawa}@eng.kagawa-u.ac.jp, ^{*2}riverjp2002@gmail.com, ^{*3}hiromichi.kawano@ntt-at.co.jp,
^{*4}tanaka@cc.it-hiroshima.ac.jp

Abstract

Previously, we have already presented a relation between the SPRT (Sequential Probability Ratio Test) based on two hypotheses (i.e. Null hypothesis and Alternative hypothesis) and a binary channel in information theory. And also we have shown that the Bayes' updating process for obtaining a posteriori probability from the received signals through binary channel is very similar to the SPRT computing. In this paper, extending the definition of SPRT to the multi hypotheses condition, we propose to apply the extended SPRT to the internal state estimation of dynamic system.

Keywords: Time series data, structural change detection, SPRT(Sequential Probability Ratio Test)

1. Introduction

Time series data analysis is a very important problem and it has a wide variety of application fields. For a structural change point detection problem in ongoing

time series, we have previously proposed an application of the SPRT (Sequential Probability Ratio Test) to the change point detection problem.¹⁻¹⁵ We also have shown the relation between the SPRT based on two hypotheses (i.e. Null hypothesis and

*2217-20 Hayashi-Cho, Takamatsu, Kagawa 761-0396 Japan

© The 2018 International Conference on Artificial Life and Robotics (ICAROB2018), Feb. 1-4, B-Con Plaza, Beppu, Oita, Japan

Alternative hypothesis) and a binary channel in information theory. Moreover we have shown that the Bayes' updating process for obtaining a posteriori probability from the received signals through binary channel is very similar to the SPRT computing. In this paper, extending the definition of SPRT to the multi hypotheses condition, we propose to apply the extended SPRT to the internal state estimation of dynamic system.

2. SPRT¹¹⁻¹⁵

2.1 Definition

The Sequential Probability Ratio Test (SPRT) is used for testing a null hypothesis H_0 (e.g. the quality is under pre-specified limit 1%) against hypothesis H_1 (e.g. the quality is over pre-specified limit 1%). And it is defined as follows:

Let Z_1, Z_2, \dots, Z_n be respectively observed time series data at each stage of successive events, the probability ratio λ_n is computed as follows.

$$\lambda_n = \frac{P(Z_1 | H_1) \cdot P(Z_2 | H_1) \cdots P(Z_n | H_1)}{P(Z_1 | H_0) \cdot P(Z_2 | H_0) \cdots P(Z_n | H_0)} \quad (1)$$

where $P(Z | H_0)$ denotes the distribution of Z if H_0 is true, and similarly, $P(Z | H_1)$ denotes the distribution of Z if H_1 is true.

Two positive constants C_1 and C_2 ($C_1 < C_2$) are chosen. If $C_1 < \lambda_n < C_2$, the experiment is continued by taking an additional observation. If $C_2 < \lambda_n$, the process is terminated with the rejection of H_0 (acceptance of H_1). If $\lambda_n < C_1$, then terminate this process with the acceptance of H_0 .

$$C_1 = \frac{\beta}{1-\alpha}, \quad C_2 = \frac{1-\beta}{\alpha} \quad (2)$$

where α means type I error (reject a true null hypothesis), and β means type II error (accept a null hypothesis as true one when it is actually false).

The definition of λ_n can be described in the following recursive form.

$$\lambda_n = \lambda_{n-1} \cdot \frac{P(Z_n | H_1)}{P(Z_n | H_0)} \quad (3)$$

2.2 Relation between SPRT and Bayes' Updating on Binary Channel

We regard that the observation and SPRT process for the aforementioned structural change point detection of time series data is essentially a kind of Bayes' Updating by a binary channel as shown in Fig.1, where input event $X=(x_1, x_2)$ and output event $Y=(y_1, y_2)$.

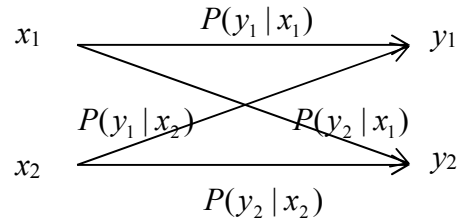


Fig.1. Binary channel.

The transition matrix (or channel matrix) P_{Binary} is represented using conditional probability as follows.

$$P_{Binary} = \begin{bmatrix} P(y_1 | x_1) & P(y_2 | x_1) \\ P(y_1 | x_2) & P(y_2 | x_2) \end{bmatrix} \quad (4)$$

Let the prior probability distribution of input event X be $\{P_0(x_1), P_0(x_2)\}$ as initial values.

Let the observed output sequence $\{y_{j_1}, y_{j_2}, \dots, y_{j_n}\}$ ($y_{j_k} = y_1$ or y_2 ($k=1, 2, \dots, n$)).

Then, by the first observation of output, the posterior probability is given by Bayes' theorem.

$$\begin{aligned} p(x_1 | y_{j_1}) &= \frac{P_0(x_1)P(y_{j_1} | x_1)}{P(y_{j_1})} \\ p(x_2 | y_{j_1}) &= \frac{P_0(x_2)P(y_{j_1} | x_2)}{P(y_{j_1})} \end{aligned} \quad (5)$$

where $P(y_{j_1}) = \sum_i P_0(x_i)P(y_{j_1} | x_i)$.

According to the Bayes' Updating rule, we have the following updated prior probability $\{P_1(x_1), P_1(x_2)\}$.

$$P_1(x_1) = p(x_1 | y_{j_1}) = \frac{P_0(x_1)p(y_{j_1} | x_1)}{P(y_{j_1})}$$

$$P_1(x_2) = p(x_2 | y_{j_1}) = \frac{P_0(x_2)p(y_{j_1} | x_2)}{P(y_{j_1})}$$
(6)

Similarly, by the second observation, we have

$$P_2(x_1) = p(x_1 | y_{j_2}) = \frac{P_1(x_1)p(y_{j_2} | x_1)}{P(y_{j_2})}$$

$$P_2(x_2) = p(x_2 | y_{j_2}) = \frac{P_1(x_2)p(y_{j_2} | x_2)}{P(y_{j_2})}$$
(7)

where, $P(y_{j_2}) = \sum_i P_1(x_i)P(y_{j_2} | x_i)$

Thus, by the n th observation of output, we have

$$P_n(x_i) = p(x_i | y_{j_n}) = \frac{P_{n-1}(x_i)P(y_{j_n} | x_i)}{P(y_{j_n})}$$

$$= \frac{P_0(x_i) \prod_{k=1}^n P(y_{j_k} | x_i)}{\prod_{k=1}^n P(y_{j_k})} \quad (i=1, 2)$$
(8)

Then the probability ratio λ_n is as follows.

$$\lambda_n = \frac{P_n(x_2)}{P_n(x_1)} = \frac{P_0(x_2) \prod_{k=1}^n P(y_{j_k} | x_2)}{P_0(x_1) \prod_{k=1}^n P(y_{j_k} | x_1)}$$
(9)

If we assume that

$$P_0(x_1) = P_0(x_2) = \frac{1}{2}$$
(10)

Then, we obtain the same ratio as that of SPRT. Therefore, we consider that the Bayes' Updating based on binary channel has a strong relation to SPRT.

3. Application to State Estimation of Dynamic System

We extend the SPRT to apply it to the internal state estimation of dynamic system.

For example, suppose that the dynamic system is given the finite state automaton (for example, as shown in Fig.2 (a)) and that the transition probability from a state to the other state is unclear. However, we assume

that the conditional probability $P(Z=z | S=S_i)$ ($i=1,2,3$) is computable.

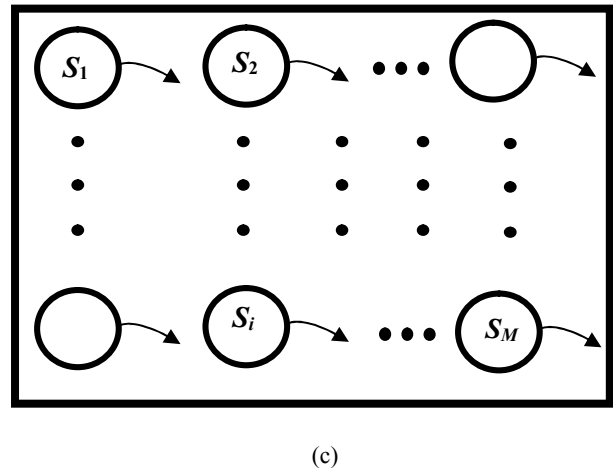
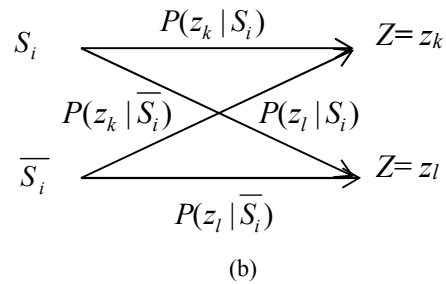
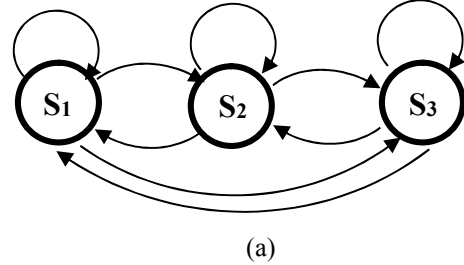


Fig.2. Conceptual images of finite state automaton as a dynamic system and the state outputs with conditional probability. (a) Three states automaton model such as phase change material. (b) Conditional probabilities $P(z_k | S_i)$ and $P(z_k | \bar{S}_i)$ where the state S_i and the other states output $Z (=z_k)$, respectively. (c) General finite state automaton model where the probability of the state transition is unclear.

Let $P(Z=z|\bar{S}_i)$ be the conditional probability that other states than the state S_i output $Z (=z)$ as shown in the following equation.

$$P(Z = z | \bar{S}_i) = \sum_{m \neq i} P(Z = z | S_m) \quad (11)$$

Then the extended SPRT for the state S_i is defined as follows

$$\lambda_n^i = \lambda_{n-1}^i \cdot \frac{P(Z_n | S_i)}{P(Z_n | \bar{S}_i)} \quad (12)$$

where λ_n^i means that the ratio of the conditional probabilities $P(Z|S_i)$ and $P(Z|\bar{S}_i)$ at the n time point. For the internal state estimation of dynamic system such as a finite state automaton, we follow the behavior from the starting state and keep tracking the state transition. Then the λ_t^i at the time point t can also be shown as the following equation by two hypotheses H_0 (the current state is unchanged) and H_1 (the state has changed into the other state).

$$\lambda_t^i = \lambda_{t-1}^i \cdot \frac{P(Z_t | H_0)}{P(Z_t | H_1)} \quad (13)$$

Accordingly, like the structural change detection problem, when λ_t^i becomes less than a threshold, we decide that the state has changed from the former state S' into the next state S_{next} . And we estimate the S_{next} should be the state that satisfies the following.

$$S_{next} = \arg \max_{S \neq S'} \left\{ \frac{P(Z_t | S)}{P(Z_t | \bar{S})} \right\} \quad (14)$$

References

1. C. G. E. P. Box and G. M. Jenkins, *Time Series Analysis: Forecasting and Control* (Prentice Hall, 1976).
2. Peter J. Brockwell and Richard A. Davis, *Introduction to Time Series and Forecasting*, 2nd ed. (Springer; 2003)
3. C. Han, P. K. Willet and D. A. Abraham, Some methods to evaluate the performance of Page's test as used to detect transient signals, *IEEE Trans. Signal processing.* **47**(8) (1999) 2112-2127.
4. S. D. Blostein, Quickest detection of a time-varying change in distribution, *IEEE Trans. Information Theory.* **37**(4) (1991) 1116-1122.
5. A. Wald, *Sequential Analysis* (John Wiley & Sons, 1947).
6. H. Kawano, T. Hattori, and K. Nishimatsu, Structural Change Point Detection Method of Time Series Using Sequential Probability Ratio Test -Comparison with Chow Test in the ability of early detection- (in Japanese), *IEEJ Trans. EIS.* **128**(4) (2008) 583-592.
7. G. C. Chow, Tests of Equality Between Sets of Coefficients in Two Linear Regressions, *Econometrica.* **28**(3) (1960) 591-605.
8. K. Takeda, T. Hattori, T. Izumi and H. Kawano, Extended SPRT for Structural Change Detection of Time Series Based on Multiple Regression Mode, in *Proceedings of the 15th International Symposium on Artificial Life and Robotics*, (Feb. 2010), ISBN: 978-4-9902880-4-4, pp.755-758.
9. K. Takeda, T. Hattori, Tetsuya Izumi and H. Kawano, Extended SPRT for Structural Change Detection of Time Series Based on Multiple Regression Model, *International Journal of Artificial Life and Robotics* Springer, ISSN: 1433-5298, **15**(4), (2010) 417-420.
10. T. Hattori and H. Kawano, Change Detection Method of Time Series as an Optimal Stopping Problem -- Constructive Proof of Optimal Solution Theorem --, in *Proc. of 2011 International Conference on Biometrics and Kansei Engineering*, (2011), IEEE Computer Society, ISBN: 978-0-7695-4512-7, pp.100-105.
11. Yoshihide Koyama, Tetsuo Hattori, Hiromichi Kawano, Model Introduced SPRT for Structural Change Detection of Time Series (I), in *Proc. of The International Conference on Artificial Life and Robotics* (Jan. 2014), ISBN: 978-4-9902880-8-2, pp.252-255.
12. Yoshihide Koyama, Tetsuo Hattori, Hiromichi Kawano, Model Introduced SPRT for Structural Change Detection of Time Series (II) --- Kansei Channel and Bayes' Estimation ---, in *Proc. of The International Conference on Artificial Life and Robotics* (Jan. 2014), ISBN: 978-4-9902880-8-2, pp.256-259.
13. Yoshihide Koyama, Tetsuo Hattori, Hiromichi Kawano, "Model Introduced SPRT for Structural Change Detection of Time Series (I)", *Journal of Robotics, Networks and Artificial Life* (ISSN: 2352-6386), Vol.1, No.1, pp.55-60 (Atlantis Press, Jun. 2014)
14. Yoshihide Koyama, Tetsuo Hattori, Katsunori Takeda, Hiromichi Kawano, "Model Introduced SPRT for Structural Change Detection of Time Series (II)", *Journal of Robotics, Networks and Artificial Life* (ISSN: 2352-6386), Vol.1, No.3, pp.237-243 (Atlantis Press, Dec. 2014)
15. Yoshihide Koyama, Tetsuo Hattori, Hiromichi Kawano, Katsunori Takeda, Change Detection Experimentation for Time Series data by New Sequential Probability Ratio, *Proceedings of International Conference on Artificial Life and Robotics 2015 (ICAROB 2015)*, ISBN 978-4-9902880-9-9, pp.278-281, 2015.

An Empirical Evaluation of Grid-based Path Planning Algorithms on Widely Used in Robotics Raspberry Pi Platform

Anton Andreychuk

*Peoples' Friendship University of Russia (RUDN University),
Moscow, Russia*

Andrey Bokovoy

*Peoples' Friendship University of Russia (RUDN University),
Federal Research Center "Computer Science and Control" of Russian Academy of Sciences,
Moscow, Russia*

Konstantin Yakovlev

*Federal Research Center "Computer Science and Control" of Russian Academy of Sciences,
Higher School of Economics,
Moscow, Russia*

E-mail: andreychuk@mail.com, bokovoy@isa.ru, yakovlev@isa.ru

Abstract

We compare three widely used path planning algorithms, A*, Jump Point Search, Theta*, in terms of runtime performance on a desktop personal computer and on the Raspberry Pi 2 embedded computer widely used in robotics. We also evaluate the performance of recently introduced path planning algorithm, LIAN, on both computers. Two principal questions are targeted: first) to what extent modern embedded computers are slower than conventional desktops when solving path finding problems (the answer is – one order of magnitude); second) how well the former scale up to larger problems (the answer is – in the same way as desktop PCs).

Keywords: path finding, path planning, grid, A*, LIAN, Raspberry Pi.

1. Introduction

Typically when a new grid-based path planning algorithm is developed robotics is mentioned as one of the main application. It's also typical that researchers presenting the new path finding algorithm evaluate it empirically (experimentally) using one of the following approaches (depending on their background). If the experimental study is conducted by someone with strong background in heuristic search it is likely that thousands of tests will be performed on a desktop computer with the use of the input data gained from the widespread benchmark collections¹. If more-into-the-

robotics researcher conducts the experiments, it is likely that limited number of runs (usually involving a small number of single-type scenarios) on a real robotic system equipped with the real robotic hardware (which can differ a lot from the desktop PC) will be performed (see Refs. 2-4). Both approaches are quite valuable as the first one helps to answer the question "how good the algorithm is in comparison to existing competitors (in large number of different scenarios)" and the second one – "how well the algorithm actually works on a real robot (in limited number of similar type scenarios)". Answering these questions is of great value to the community, especially to those researchers aiming at

creating robust and fully autonomous mobile robots capable of solving complicated navigation tasks like the ones mentioned in Refs. 5-7.

To the best of authors' knowledge no survey has been done so far on how long will it take to conduct grid-based path planning on modern robot's hardware in comparison to PC. Our work aims at filling this gap. We have run plentiful of experiments on both desktop PC and wide-spread in robotics Raspberry Pi 2 (see Refs. 8-9) computer. We have evaluated three well-known in path planning community heuristic search algorithms A*¹⁰, Jump Point Search¹¹, Theta*¹² as well as recently introduced path finding algorithm LIAN¹³, which can be of particular value to robotics community as it is capable of finding smoother paths with no sharp turns.

2. Experimental Setup

2.1. Hardware

Two computers and two operating systems were used. First was a conventional desktop PC: Intel Core i7-4790 3.6 GHz with 16 GB of RAM run by Linux Debian 8 Kernel 3.16.7. Second was the compact, widely used in robotics Raspberry Pi 2 Model B computer equipped with 900MHz quad-core ARM Cortex-A7 CPU and 1GB of RAM run by Linux Raspbian Kernel 4.1.7 PREEMPT_RT.

2.2. Map and tasks

The following map bundles from the N. Sturtevant's movingai collection¹ were used: Baldur's Gate (75 maps), Warcraft III (36 maps), Random obstacles 10%, 25%, 40% fill (30 maps), Mazes corridor width 2, 4, 8 (30 maps), Rooms size 16, 32, 64 (30 maps). We also run experiments on the City maps collection introduced by us. We have extracted 100 fragments of the real city environments from www.openstreetmaps.org sized 1 347 x 1 347 m each and discretized them to 501 x 501 grids. Cells corresponding to areas that overlap buildings were marked un-traversable. Five different start-goal locations for each map were fixed. Thus in total 1505 path planning tasks comprised the test collection.

2.3. Algorithms

A* - heuristic modification of Dijkstra algorithm⁹. Golden standard in the AI and robotics. A* path is the sequence of traversable adjacent cells and the algorithm guarantees finding the shortest path.

Jump Point Search (JPS) – modification of A* which allows the algorithm to skip large portions of the search space without reducing the quality of the solution¹. JPS finds paths much faster than A* without sacrificing the optimality.

Theta* (or Basic Theta*) – any-angle modification of A* which interleaves exploration of the search space with path smoothing¹¹. Theta* path is the sequence of pairs of traversable, but not necessarily adjacent cells, – sections.

LIAN – recently introduced angle-constrained path planning algorithm that searches for a path as a sequence of sections (like Theta*) holding the property that an angle between any two consecutive sections doesn't exceed predefined threshold¹². LIAN is of particular interest to the robotics community as it is capable of finding smooth paths without sharp turns that can be easily followed by mobile robots. Due to the larger state-space LIAN is notably slower than A*/Theta*/JPS and in some cases its runtime exceeds reasonable threshold (1-10s).

All algorithms were coded in OS independent C++. In our implementation we explicitly generate elements of the OPEN and CLOSE lists and use vector of lists and unordered map to store them.

3. Results

3.1. First series of the experiments

In the first series of the experiments JPS, A* and Theta* were executed to solve all the available 1505 path planning tasks. Here we present aggregated average figures (all times are in milliseconds).

As one can see path planning on Raspberry Pi is generally 10 times slower than on a desktop PC, but the exact value of average runtime difference varies slightly from collection to collection from algorithm to algorithm. We believe that there are two reasons for that: first) measuring timestamps for a single run is not

100% accurate, and second) operating system influences the runtime (via interruptions, for example).

Strictly speaking, this means that it is not possible in general to 100% accurately measure the algorithm’s runtime. Definitely, this question should be investigated further, but as for now, it goes beyond the scope of the paper. We would like to mention though, that we believe the figures obtained by us are relevant and comparable as we run each single experiment (= particular algorithm + particular map + particular start and goal locations) several times and use the average runtime for further analysis (see table 1).

Table 1. A*, JPS, Theta* averaged runtimes (in milliseconds).

	City/Game Maps	Mazes	Random Obstacles	Rooms
JPS (pc)	2.52	11.58	36.54	5.82
JPS (ras)	23.46	110.37	366.29	50.95
A* (pc)	42.86	164.95	66.64	164.33
A* (ras)	509.31	1844.98	739.00	1996.80
Theta* (pc)	83.29	258.32	56.55	268.48
Theta* (ras)	749.52	2544.49	582.10	2664.54

3.2. Second series of the experiments

For LIAN evaluation the angle constraint was set consecutively to 20°, 25° and 30° (these values were advised by peers involved in unmanned aerial vehicle (UAV) controllers design). LIAN’s other parameters were set as advised in Ref. 15, i.e. $\Delta=5$, $w=2$. Experiments were run on Game and City maps only. As for the Baldur’s Gate, Warcraft III and City maps collections – more than 95% of all tasks within these collections are solvable for LIAN with angle constraints equal or above 20°. As it’s known that LIAN is time-consuming algorithm we set the cut-off time for each experiment to be 10 seconds. If the algorithm was not able to find a path within allotted time, the result for this run was considered to be *failure*. Averaged results are presented in table 2 (*failures* were not taken into account when measuring runtimes).

In the table t – is time (in ms), and sr – is success rate. As one can see in up to 20% of cases (depending

on the map type and on the angle constraint) LIAN on Raspberry was not able to find a solution within 10 seconds limit. As for the desktop PC – less than 1.2% of tasks were not processed within the cap. In general, Baldur’s Gate collection is the toughest for LIAN to work on, while tasks from Warcraft III are handled by LIAN more effortlessly and City tasks even more effortlessly.

Table 2. LIAN averaged runtimes and success rate.

	W III		BG		CM	
	t	sr	t	sr	t	sr
20°						
LIAN (pc)	99.0 ^a	100%	407.0	100%	28.5	100%
LIAN (ras)	336.2	97,6%	1 131.3	89,4%	140.2	95,5%
25°						
LIAN (pc)	77.1	100%	645.2	99.7%	21.7	99.9%
LIAN (ras)	424.3	98.3%	1 486.1	82.2%	115.7	93.2%
30°						
LIAN (pc)	79.6	100%	663.9	98.9	23.6	99.6
LIAN (ras)	321.2	96.5%	1 473.6	79.3	126,1	91.8%

Please note that runtimes are directly incomparable between *pc* and *ras* as the number of solved tasks is different.

Next question we were interested in was how well does Raspberry Pi scale up to larger problems. To answer this question, the dependency between the number of steps (expansions) and the resultant runtime should be analyzed – see figure 1.

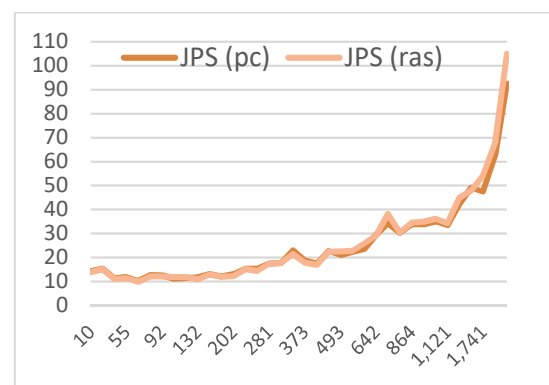


Fig. 1. Time (Y-axis, in milliseconds) needed to accomplish the exact number of steps (X-axis) of JPS algorithm. Inflated values for *pc* are used for better scaling.

Figure 1 depicts results for JPS algorithm for the Game and City maps collections as other algorithms/collections demonstrate similar tendencies and dependencies. PC runtimes are multiplied by 9,3 (the exact average difference value between PC and Raspberry runtimes on the considered collections) for better scaling.

As one can see dependency between number of steps and runtime is the same on PC and Raspberry, so one can say that Raspberry Pi 2 scales to larger path planning problems in the same way as desktop PCs. Non-monotone pattern observed on the chart can be explained in the following way. Cost (runtime) of a single algorithm's step is not the same across different path planning tasks due to the fact that the number of "insert (update) to *OPEN*" and "lookup in *CLOSE*" operations varies from one step to the other (and depends on the properties of the exact map and start-goal locations).

4. Summary

Analyzing all the obtained experimental data we can make the following conclusions. Solving path planning tasks on the wide spread in robotics community Raspberry Pi 2 computer is one order of magnitude times slower than on conventional desktop PCs. If any-angle (or angle-constrained) paths are targeted than it's likely that path planning will take more than 1-2 seconds (which can be sensible for some practical application). Raspberry scales up to larger path planning problems in the same way desktop PC does. An interesting question for further investigation is – how to correctly measure algorithm runtimes as it looks like that they are subject to certain (or uncertain?) deviations caused by the operating system's influence.

Acknowledgments

This work was supported by the Russian Foundation for Basic Research (Project No.17-07-00281).

References

1. N. Sturtevant, "Benchmarks for grid-based pathfinding". *Transactions on Computational Intelligence and AI in Games*, 4(2), 2012, pp. 144-148.
2. D. Dolgov, S. Thrun, M. Montemerlo and J. Diebel, "Path planning for autonomous vehicles in unknown semi-structured environments." *The International Journal of Robotics Research*, 29(5), 2010, pp. 485-501.
3. Y. Kuwata, S. Karaman, J. Teo, E. Frazzoli, J. P. How and G. Fiore, Real-time motion planning with applications to autonomous urban driving. *IEEE Transactions on Control Systems Technology* 17(5), 2009, pp. 1105-1118.
4. E. Magid and E. Rivlin, "CAUTIOUSBUG: A competitive algorithm for sensory-based robot navigation". *Proceedings of the 2004 IEEE/RSJ International Conference on Intelligent Robots and Systems*, Vol. 3, 2004, pp. 2757-2762.
5. A.I. Panov and K. Yakovlev, "Behavior and path planning for the coalition of cognitive robots in smart relocation tasks". In *Proceedings of The 4th International Conference on Robot Intelligence Technology and Applications (RiTA 2015)*, 2015, pp. 3-20.
6. E. Magid, R. Lavrenov, A. Khasianov. Modified spline-based path planning for autonomous ground vehicle. *International Conference on Informatics in Control, Automation and Robotics*, (Madrid, Spain, 2017), pp. 132-141.
7. V. Karpov, A. Migalev, A. Moscovsky, M. Rovbo, V. Vorobiev. Multi-robot Exploration and Mapping Based on the Subdefinite Models. In: Ronzhin A., Rigoll G., Meshcheryakov R. (eds) *Interactive Collaborative Robotics (ICR 2016). Lecture Notes in Computer Science*, vol 9812. 2016, Springer, Cham.
8. J. Betthausen, D. Benavides, J. Schornick, N. O'Hara, J. Patel, J. Cole and E. Lobaton, "WolfBot: A distributed mobile sensing platform for research and education". *Proceedings of IEEE 2014 Zone 1 Conference of the American Society for Engineering Education*, 2014, pp. 1-8.
9. J. D. Brock, R. F. Bruce and M. E. Cameron, "Changing the world with a Raspberry Pi". *Journal of Computing Sciences in Colleges*, 29(2), 2013, pp. 151-153.
10. P.E. Hart, N.J. Nilsson and B. Raphael, "A formal basis for the heuristic determination of minimum cost paths". *IEEE Transactions on Systems Science and Cybernetics*, 4(2), 1968, pp. 100-107.
11. D. Harabor and A. Grastien, "Online graph pruning for pathfinding on grid maps". *Proceedings of the 25th AAAI Conference on Artificial Intelligence (AAAI-11)*, 2011, pp. 1114-1119.
12. A. Nash, K. Daniel, S. Koenig and A. Feiner, "Theta*: any-angle path planning on grids. In *Proceedings of the 22nd AAAI conference on Artificial intelligence (AAAI-2007)*, 2007, pp. 1177-1183.
13. K. Yakovlev, E. Baskin and I. Hramoin, "Grid-based angle-constrained path planning". *Proceedings of the 38th Annual German Conference on Artificial Intelligence (KI-15)*, (Dresden, Germany, 2015), pp. 208-221.

Development of the Insectoid Walking Robot with Inertial Navigation System

Vitaly Egunov, Andrey Kachalov, Michail Petrosyan, Pavel Tarasov, Elena Yankina
*Computers and Systems Department, VSTU, Leninaav, 28,
Volgograd, 400005, Russia*

*E-mail: vegunov@mail.ru, dmn.info@mail.ru, mih95@inbox.ru, tarasradio@mail.ru
www.vstu.ru*

Abstract

The article is devoted to the problem of controlling an insectoidwalking robot- hexapod. An inertial navigation system based on the accelerometer ADXL345 and the gyro ITG-3200 is used in the developed robot. The options for filtering data obtained from the inertial sensors and the methods of combining the accelerometer and gyroscope data to determine the roll and pitch are under consideration in the article. The original software has been designed to visualize the mobile robot position. For this purpose, the authors have developed a microcomputer program that transmits the calculated total deviations (roll and pitch) over a wireless Wi-Fi network to a personal computer which runs the developed program that process the data. The obtained data are processed and used to display an object implemented with the help of OpenGL library.

Keywords: accelerometer, gyroscope, inertial navigation, mobile robot - hexapod, discrete integration, complementary filter.

1. Introduction

Currently, research in robotics is extremely relevant. There is a huge number of robots that replace a human in high risk areas (whether it is a manufacturing workshop or technogenic catastrophe liquidation), deliver people from the necessity of doing monotonous work, make our life easier. More sophisticated models capable of analyzing information [1] and making decisions, recognizing objects and manipulating them appear all the time.

Walking robots are actively designed and researched[2,3]. This is due to the fact that walking structures have a number of advantages compared to classical wheeled and caterpillar vehicles, for example, when moving on the difficult geographic terrain surface,

such as debris, tough terrain, also inside buildings where it is necessary to move along narrow corridors, staircases and mines [4].

A team of authors have designed and made a walking robot-hexapod, which has been tested on being controlled by various approaches. The robot was developed on the basis of a single-board computer Raspberry Pi 3 Model B and the inertial sensor GY-85, which includes the accelerometer ADXL345 and the gyroscope ITG-3200. The designed 3D model of the robot prototype was printed with the 3D printer at the Computer and System Department, Volgograd State Technical University. The functioning robot prototype is shown in Figure 1.



Fig.1 Developed robot-hexapod

2. Robot Control

One variant of robot controlling is to process the inertial sensor data and then to generate control actions over servo drives. The interaction with the inertial sensor connected to the Raspberry Pi microcomputer occurs via the I2C interface. Before reading the data, the module is configured to the required operating mode by recording the initializing values to the registers of the module. After this, the data are periodically read from the accelerometer ADXL345 and the gyroscope ITG-3205. To remotely monitor the current state of the robot, the resulting platform deviations are transmitted via the wireless Wi-Fi network from Raspberry Pi to a personal computer where one can track the object deviations on the constructed 3D object (a cube with multi-colored faces) that is implemented using the OpenGL library in C++.

To determine the object tilt angles, one can use both the gyroscope and the accelerometer. In the case of the former, the tilt angle is determined by discrete integration of the rotation speed, which is determined by the gyroscope. However, this sensor has notable drawbacks which are zero drift and gradual error accumulation in calculating the angle. In the case of the accelerometer, its use is justified for determining the tilt angles of fixed objects. If some force acts on the object, one cannot determine the object orientation using the accelerometer only. I.e. it can be concluded that using the gyroscope or the accelerometer separately is not

enough to solve the task. In this project we have combined the both sensors readings using a complementary filter.

A personal computer program has been developed to visualize the object position using the OpenGL library. OpenGL is one of the most popular application software interfaces for developing applications in both 2D and 3D graphics. In the given program, this library is used to visualize the robot platform to vividly demonstrate the inertial navigation sensors functioning. The simulated platform is a parallelepiped with faces of different colors, which responds to sensor deviations (along the x and y axes). The values of the roll and pitch are displayed on the screen together with the data obtained as a result of processing the data from the accelerometer along the x and y axes, as well as the angular values of the gyroscope in three axes.

To display an object, the figure is drawn on the faces, and the color is specified with the `glColor3f(r, g, b)` function. The simulated platform rotation of is implemented using the function `glRotatef(Angle, Xtrue, Ytrue, Ztrue)` (Figure 2).

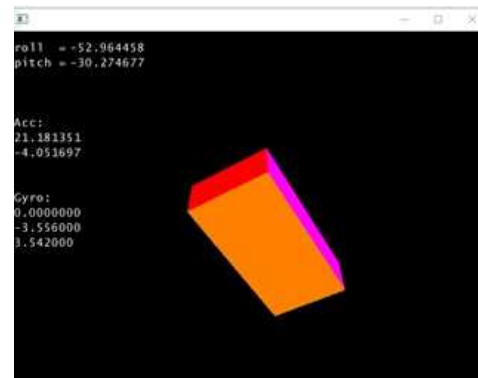


Fig.2 The program result on a personal computer

In addition to the drawn figure, the display shows a console window, in which the roll and pitch values are displayed for clarity, which in turn are written to the csv file and can be used for the further analysis. According to the obtained data, graphs are constructed (Fig. 3), the graphs illustrate the platform deviation along the corresponding axes. The charting program is written in Python using the Matplotlib data visualization library.

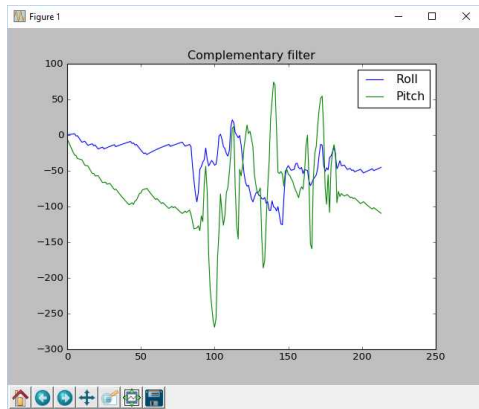


Fig. 3 – Graph obtained from the data file res.csv

In this project sockets were chosen as a means of networking between the PC and Raspberry Pi 3. And on the server side the program runs on the Raspbian OS, and the client uses Windows.

3. Alternative Robot Control using FRUND software

As an alternative approach to robot control, the Multibody Dynamics System FRUND was used, it allows to solve this problem and, on the basis of the walk generator, to obtain motions trajectories for robot engines. By far, robots such as the anthropomorphic robot [2, 5], the robot-hexapod [3] and other types of robots [6- 8] have been modeled using the FRUND system[6]. In this paper, we will consider the motion synthesis for controlling the robot-hexapod, the description of the software architecture for robot control. In general, the robot control diagram with the use of FRUND can be represented, as shown in Fig. 4.

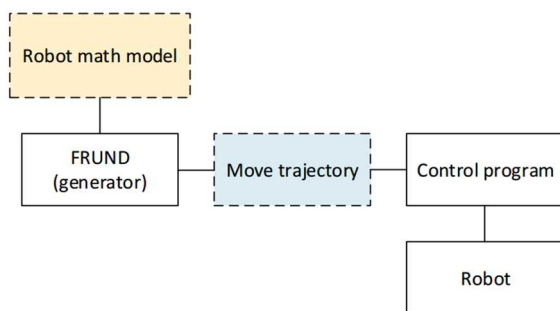


Fig. 4 Diagram of robot control with the use of FRUND.

Referring to the diagram, we can see that the input of the FRUND system receives the robot mathematical model (the structure of its links, nodes). The link system that determine the type of the robot movements is added to the mathematical model. Applied to the hexapod, it can be walking forward with a certain gait, turning left, etc. At the same time, a system of equations is formed, the result of which is a set of trajectories for each robot engine that can be used for direct control.

When forming motions (trajectories), the inverse dynamic problem method is used. It allows by setting the displacements of the robot finite nodes in time to receive the movements of all the other nodes. More information about this method application for controlling an android can be found in.

To control the robot-hexapod various types of gaits and motion directions that can be performed by the robot have been generated. The mediator between these files and the robot is the control system. Its structure is shown in modules in Fig. 5.

The purpose of the modules:

- Hexapod Instance encapsulates the work logic with the robot hardware, the input takes angles to control the drives;
- Hexapod provides methods for controlling drives, is used to perform robot configuration;
- Packet master implements generating packets methods for transmission to the robot; interface allows to specify angles for one drive;
- Serial Port Master implements transmitting packages to the robot via the Serial port;
- Storage stores the robot drives and system variables configuration;
- FRUND Generator implements reading the movements file and execution the movements with a given speed;
- Console Interface implements control from the console, allows running the program with the motion file parameter.

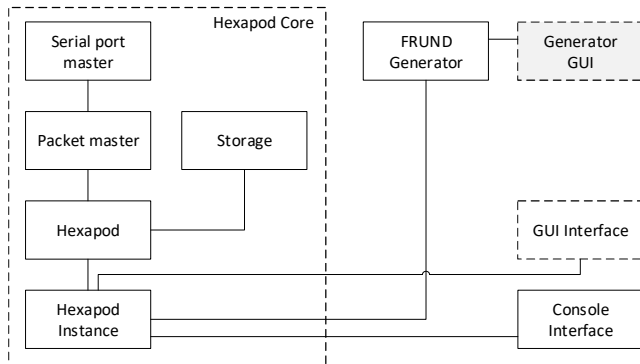


Fig. 5 – Software structure for robot control

Thus, to control the robot means to run the control program with a parameter (motion file), to search the port to which the robot is connected and, after connecting to the robot, to execute movements from the file. It is also possible to control via the graphical interface. In this case, the operator is able to change the engine settings and their layout.

The development of the control process involves changing the control scheme as follows:

- files generated by the FRUND system will be placed in a data storage device that will be installed in the robot;
- motion control of the robot will be done directly from the robot's board instead of files;
- a remote control will be connected to the robot board via a wireless channel, it will allow changing the movement type, direction and switching robot between manual and automatic control.

4. Conclusions

To sum up the following can be said:- the FRUND system allows to control various robots of complex structure;- in the simplest case, control can be done by writing a short interface program that converts the movement files into robot commands;- future tasks include the implementation of feedback systems to enhance adaptive control capabilities and the implementation of autonomous control.

Acknowledgements

Work is performed with the financial support of the Russian Foundation for Basic Research and the

Administration of Volgograd region (project #16-47-340385)

References

1. Robotic Complex Central Processing Node Performance Requirements Assessment / Egunov V.A., Kirnosenko S.I., Andreev A.E. // *World Applied Sciences Journal (WASJ)*. - 2013. - Vol. 24, Spec. Issue 24 : Information Technologies in Modern Industry, Education & Society. - C. 37-42.
2. Gabbasov, B., Danilov, I., Afanasyev, I., and Magid, E. (2015, December). Toward a human-like biped robot gait: Biomechanical analysis of human locomotion recorded by Kinect-based Motion Capture system. *In Mechatronics and its Applications (ISMA), 2015 10th International Symposium on (pp. 1-6)*. IEEE.
3. Zhu, Y., Guo, T., Liu, Q., Li, Q., Yan, R.A study of arbitrary gait pattern generation for turning of a bio-inspired hexapod robot. // *Robotics and Autonomous Systems*. – 2017. Vol. 97, c. 125-135.
4. Deng, H., Xin, G., Zhong, G., Mistry, M Gait and trajectory rolling planning and control of hexapod robots for disaster rescue applications // *Robotics and Autonomous Systems*. – 2017. Vol. 95, c. 13-24.
5. Yao, P., Li, T., Luo, M., Zhang, Q., Tan, Z. Mechanism Design of a Humanoid Robotic Torso Based on Bionic Optimization // *International Journal of Humanoid Robotics* - 2017. Vol. 14(4),1750010
6. Gorobtsov A. S. Synthesis of parameters of controlled motion of multi-link mechanical systems of arbitrary structure by the inverse problem method / A. S. Gorobtsov // *Mechatronics, Automation, Control*.– 2004. – №6. – pp. 43-50.
7. Synthesis of Control Algorithm and Computer Simulation of Robotic Manipulator-Tripod / Nesmianov I., Vorob'Eva N., Dyashkin-Titov V., Zhoga V., Skakunov V., Terekhov S., Egunov V., Al-Hadsha F.A.H. // *Creativity in Intelligent Technologies and Data Science. CIT&DS 2015 : First Conference (Volgograd, Russia, September 15-17, 2015) : Proceedings / ed. by A. Kravets, M. Shcherbakov, M. Kultsova, O. Shabalina. – [Switzerland] : Springer International Publishing, 2015. – P. 391-403. – (Ser. Communications in Computer and Information Science. Vol. 535)*.
8. Sun, T., Xiang, X., Su, W., Wu, H., Song, Y. A transformable wheel-legged mobile robot: Design, analysis and experiment // *Robotics and Autonomous Systems*. – 2017. Vol. 98, c. 30-41

Enhancing semi-dense monocular vSLAM used for multi-rotor UAV navigation in indoor environment by fusing IMU data

Andrey Bokovoy

Lab “Intelligent dynamic systems”, Federal Research Center “Computer Science and Control” of Russian Academy of Science, ul. Vavilova, 44/2, Moscow, Russia, 119333

Moscow, Russia

*Faculty of Science, Peoples’ Friendship University of Russia (RUDN University), ul. Miklukho-Maklaya, 6, Moscow, Russia, 117198
Moscow, Russia*

Konstantin Yakovlev

Lab “Intelligent dynamic systems”, Federal Research Center “Computer Science and Control” of Russian Academy of Science, ul. Vavilova, 44/2, Moscow, Russia, 119333

Moscow, Russia

*Faculty of Computer Science, Higher School of Economics, ul. Myasnitskaya, 20, Moscow, Russia, 101000
Moscow, Russia*

*E-mail: {bokovoy,yakovlev}@isa.ru, 1042160097@rudn.university, kyakovlev@hse.ru
eng.rudn.ru
www.hse.ru*

Abstract

We propose the enhancement of the modern vision-based monocular simultaneous localization and mapping (vSLAM) method, e.g. LSD-SLAM, used for compact multi-rotor UAV indoor navigation, by fusing inertial measurement unit (IMU) data with camera images. We suggest removing the cost-expensive loop-closure optimization algorithm from the vSLAM pipeline and replacing it with the computationally efficient flow estimation procedure based purely on IMU data. The input IMU flow is being processed by the Extended Kalman Filter (EKF) based techniques for localization purposes and used further in LSD-SLAM algorithm for UAV pose estimation. We evaluate the proposed algorithm using the modeled indoor environment originally used for RoboCup Rescue Simulation League 2013 competition and “hector_quadrotor” – commonly used in modelling simulated UAV model. Evidently, implementation of the suggested enhancement results in significant drop-down of the runtime and leads to obtaining maps and trajectories of higher accuracy.

Keywords: vision-based SLAM, IMU, monocular camera, navigation, UAV.

1. Introduction

Nowadays, the vision-based monocular simultaneous localization and mapping (vSLAM) methods and algorithms are widely used for semi-autonomous and autonomous navigation of micro unmanned aerial vehicles (UAV)^{1,2,3,4,5}. Considering the restrictions

associated with micro UAV, e.g. small size, low energy battery capacity, low wireless channel capacity, low performance of on-board computers a challenging task is to improve the performance of such methods time-wise while keeping the localization and mapping accuracy at the same or better level than in original methods.

© The 2018 International Conference on Artificial Life and Robotics (ICAROB2018), Feb. 1-4, B-Con Plaza, Beppu, Oita, Japan

One of the bottlenecks of the vSLAM methods is the loop-closure detection⁶. Loop-closure detection algorithms perform global map and trajectory optimization on the basis of comparison of previously received and current data^{7,8}, especially the data relative to the position the system has already been to. That mechanism provides more accurate trajectory estimation and mapping in a long run but takes a significant amount of time to proceed. The main question behind this paper is whether we can replace the loop-closure algorithm in modern vSLAM method with IMU data fusion while decreasing processing time and keeping the same or better map and trajectory accuracy.

The main motivation is to step towards using such a method on board of micro UAV operating in indoor, GPS-denied environments. We provide the experimental evaluation of IMU+vSLAM method in simulated environment.

2. Approach overview

We use LSD-SLAM⁹ as the core method for vision-based localization and mapping of micro UAV. We have chosen this method based on evaluations from Ref. 10, as the one that produces highly detailed dense map and accurate trajectory while processing video stream in real-time on modern PC. In order to replace the loop-closure procedure inside the LSD-SLAM method, we fuse the micro UAV IMU data with the position coordinates from received LSD-SLAM using Extended Kalman Filter (EKF)¹¹ techniques. This way trajectory and map is computed considering the fused position data and the loop-closure algorithm is no longer a part of LSD-SLAM processing pipeline.

3. Experimental evaluation

3.1. Algorithm implementation

We implemented our algorithm for widely used in robotics framework – Robot Operating System (ROS). The framework provides a modular structure for different components (nodes) and the communication mechanism (topics, services), that keeps all the inner algorithms independent and extendable. We modified LSD-SLAM open-source code, provided by its authors, to disable loop-closure algorithm and added some minor changes and statistics gathering.

3.2. Simulation

We use Gazebo for robot an environment simulation. For indoor flight simulation we choose quadcopter “hector_quadrotor”. This UAV model has a wide array of onboard sensors (including IMU, cameras, laser scanners and etc.) suitable for navigation tasks. IMU operates with 200Hz frequency while camera is able to produce a 640x480pix images with 30FPS. All the communication with quadcopter goes through ROS. The algorithm is in charge of mapping, localization and navigation processes. That way, we simulate the off-board computation scenario, when the heavy algorithms processed on control station while UAV’s fly controller only takes care of basic stabilization tasks, movement and sensor data output.

Indoor environment involved in the experiment is the model of National Institute of Standards and Technologies that was used during RoboCup Rescue Simulation League 2013 for Gazebo simulating environment (fig. 1). Overall square of the environment is 6 300m² consisting of multiple rooms and doors.

We used 10 different for the simulation. The trajectories’ length varied from 25m to 183m. There were 7 trajectories with loops and 3 without them. The UAV was expected to fly with 1m/s speed. The IMU

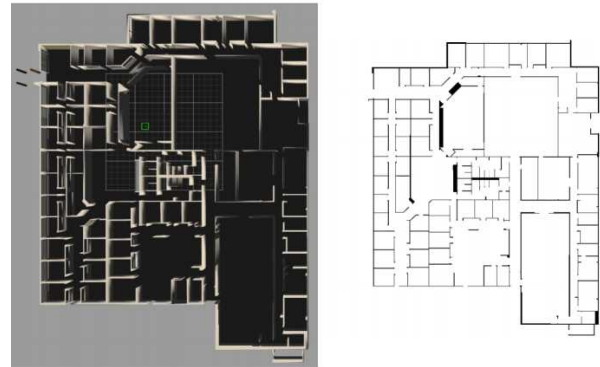


Fig. 1. The model of National Institute of Standards and Technologies for RoboCup Rescue Simulation League competition.

data flow is part of Gazebo UAV simulation model. For IMU and vSLAM position data fusion we use the “robot_pose_ekf” node. The main criterions for evaluation are processing speed, the accuracy of the estimated trajectory and the accuracy of the map, that is

measured by median deviation from ground-truth map over all the points of vSLAM’s output map.

4. Experimental results

Table 1 presents the results of the experiment. Original

Table 1. The experimental results.

Scenario	Length (m)	Loop-closures	Average processing time (sec)		Average deviation from ground-truth trajectory (m)		Average deviation from ground-truth map (m)	
			LSD-SLAM	IMU+LSD-SLAM	LSD-SLAM	IMU+LSD-SLAM	LSD-SLAM	IMU+LSD-SLAM
traj_1	25,3	-	0,189	0,137	0,23	0,24	0,35	0,34
traj_2	28,9	+	0,211	0,141	0,18	0,13	0,52	0,5
traj_3	39,2	+	0,231	0,156	0,33	0,34	0,57	0,51
traj_4	58,3	+	0,288	0,135	0,38	0,34	0,56	0,53
traj_5	59,2	+	0,29	0,143	0,41	0,37	0,62	0,57
traj_6	91,5	-	0,192	0,149	0,81	0,6	0,93	0,71
traj_7	97,2	+	0,291	0,147	0,69	0,63	0,85	0,77
traj_8	101	+	0,295	0,143	0,71	0,65	0,86	0,78
traj_9	110,2	-	0,185	0,159	0,73	0,66	1,12	0,89
traj_10	125,3	+	0,315	0,141	0,78	0,69	0,98	0,91

and modified (with IMU data fusion) LSD-SLAM algorithms are compared. The results are also presented as plots (fig.2, fig.3) for better visualization.

As shown on fig. 2, the original SLAM and IMU+SLAM processing times grow with the length of the trajectory (see table 1 for the lengths values). However, the original LSD-SLAM’s processing time on trajectories with loops is drastically higher, compared to non-loop scenarios. That is the result of loop-closure algorithm’s global map and trajectory optimization process. In non-loop scenarios (traj_1, traj_6, traj_9) IMU+LSD-SLAM’s processing time is slightly less than the LSD-SLAM’s one.

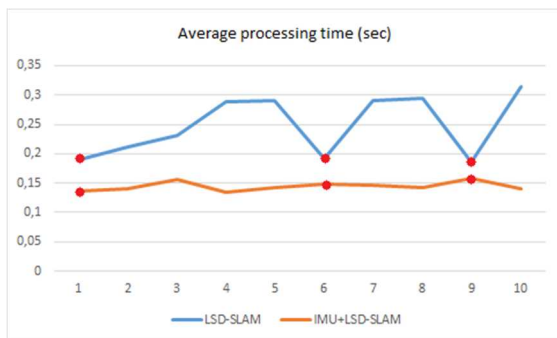


Fig. 2. The average processing time of LSD-SLAM and IMU+LSD-SLAM algorithms. Red dots represents speed of non-loop scenarios.

Fig. 3 shows the average deviation from ground-truth of trajectories built by original LSD-SLAM and IMI+LSD-SLAM algorithms.

As we can see, the trajectory accuracy of original algorithm is on pair with the presented method. The

only significant difference occurs with traj_6 scenario due to complex path that consists of sharp rotations of UAV. Original LSD-SLAM loses its tracking during such movements and it forces LSD-SLAM to reallocate the UAV’s position which leads to the reduced accuracy.

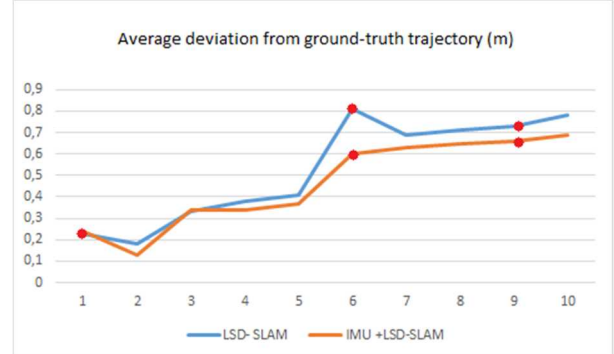


Fig. 3. The average deviation from ground-truth trajectory of LSD-SLAM and IMU-LSD-SLAM. Red dots represent the deviation of non-loop scenarios.

Fig. 4 shows the average deviation of map, compared to ground truth. This measurement represents the accuracy of the map built by LSD-SLAM and IMU+LSD-SLAM algorithms.

IMU+LSD-SLAM is on pair with original LSD-SLAM except the results of traj_6 and traj_9 scenarios. The traj_6 map accuracy is influenced by sharp UAV

maneuvering and traj_9 represents the accuracy loop-closure algorithm during long length flights.

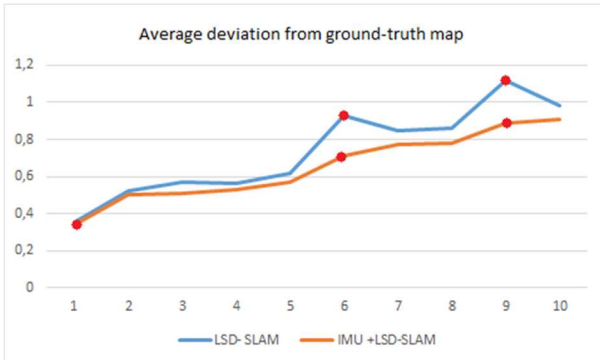


Fig. 4. The average deviation from ground-truth map of LSD-SLAM and IMU-LSD-SLAM. Red dots represent the deviation of non-loop scenarios.

5. Conclusion

We have proposed to enhance the original monocular LSD-SLAM method by removing time-consuming loop closure detection procedure and replacing it with the IMU fusion technique. Conducted experimental evaluation shows that such an enhancement leads to better runtimes (30% on average, reaching 44,5% for some scenarios), while improving the accuracy of the estimated map and trajectory (7% and 10% accuracy increase respectively compared to original LSD-SLAM algorithm).

In future we plan to use the proposed method for real-time micro UAV navigation in indoor, GPS-denied environments.

Acknowledgements

The research was partially supported by Russian Foundation for Basic Research (RFBR), projects №№ 15-07-07483, 17-29-07053.

References

- Blösch, Michael, Stephan Weiss, Davide Scaramuzza, and Roland Siegwart. Vision based MAV navigation in unknown and unstructured environments. In *Robotics and automation (ICRA), 2010 IEEE international conference on*, pp. 21-28
- Fraundorfer, Friedrich, Lionel Heng, Dominik Honegger, Gim Hee Lee, Lorenz Meier, Petri Tanskanen, and Marc Pollefeys. Vision-based autonomous mapping and exploration using a quadrotor MAV. In *Intelligent Robots*

© The 2018 International Conference on Artificial Life and Robotics (ICAROB2018), Feb. 1-4, B-Con Plaza, Beppu, Oita, Japan

- and Systems (IROS), 2012 IEEE/RSJ International Conference on, pp. 4557-4564. IEEE, 2012.
- Yang, Shaowu, Sebastian A. Scherer, and Andreas Zell. Robust onboard visual SLAM for autonomous MAVs. In *Intelligent Autonomous Systems 13*, pp. 361-373. Springer International Publishing, 2016
- Buyval A, Gavrilentov M. Vision-based pose estimation for indoor navigation of unmanned micro aerial vehicle based on the 3D model of environment. In *Mechanical Engineering, Automation and Control Systems (MEACS), 2015 International Conference on 2015 Dec 1* (pp. 1-4). IEEE.
- Yakovlev, K., Khithov, V., Loginov, M., Petrov, A. Distributed control and navigation system for quadrotor UAVs in GPS-denied environments. In: Filev D. et al. (eds) *Intelligent Systems'2014. Advances in Intelligent Systems and Computing*, vol 323. pp. 49-56. Springer, Cham
- Bokovoy A., Yakovlev K. Original Loop-closure Detection Algorithm for Monocular vSLAM. In *Analysis of Images, Social Networks and Texts, 2017 6th international conference, AIST 2017, Moscow, Russia, July 27-29*, p.202-213
- Angeli, A., Filliat, D., Doncieux, S. and Meyer, J.A., 2008. Fast and incremental method for loop-closure detection using bags of visual words. *IEEE Transactions on Robotics*, 24(5), pp.1027-1037.
- Vokhmintcev A., Yakovlev K. (2017) A Real-Time Algorithm for Mobile Robot Mapping Based on Rotation-Invariant Descriptors and Iterative Close Point Algorithm. In: Ignatov D. et al. (eds) *Analysis of Images, Social Networks and Texts. AIST 2016. Communications in Computer and Information Science*, vol 661. pp. 357-369.
- Engel J, Schöps T, Cremers D. LSD-SLAM: Large-scale direct monocular SLAM. In *European Conference on Computer Vision 2014 Sep 6* (pp. 834-849). Springer, Cham.
- Buyval, A., Afanasyev, I., & Magid, E. (2017, March). Comparative analysis of ROS-based Monocular SLAM methods for indoor navigation. In *Ninth International Conference on Machine Vision* (pp. 103411K-103411K). International Society for Optics and Photonics.
- Ljung L. Asymptotic behavior of the extended Kalman filter as a parameter estimator for linear systems. *IEEE Transactions on Automatic Control*. 1979 Feb;24(1):36-50.

Method of Finding of Android Program Motion for the ZMP Trajectory of a Certain Type

Alexander Gorobtsov

Higher Mathematics Department, VSTU, Lenina av, 28,
Volgograd, 400005, Russia

Pavel Tarasov, Andrey Skorikov, Alexey Markov, Andrey Andreev

Computers and Systems Department, VSTU, Lenina av, 28,
Volgograd, 400005, Russia

E-mail: vm@vstu.ru, markovalex95@gmail.com, scorpion_energy@mail.ru,
tarasradio@mail.ru, andan2005@yandex.ru,
www.vstu.ru

Abstract

We consider the problem of finding of the programmed motion of biped robot with a given ZMP trajectory. It is assumed that it provides a stable ZMP trajectory of the robot motion. The equations of the robot motion consist of the equations of the robot dynamics itself and the stability conditions equations, which include the coordinates of the ZMP trajectory. It is proposed to seek the solution of stability equations on a limited set of some concerted movements of the robot. Several types of such coordinated movements are considered. The application of this method for the android with a mass of 60 kg and height of 160 cm is described. The parallel algorithms of the computational aspect of the method is presented.

Keywords: biped robot, ZMP trajectory, programmed motion, MBS modeling.

1. Introduction

The control strategy of biped robots dynamic walking is based on the walking pattern generation, which considers the stable program zero moment point (ZMP) trajectory. One of the reasons of difference between the actual ZMP trajectory and the program ZMP trajectory is the imperfect dynamic model of the robot. There are many research works on the walking pattern generation of humanoid robots [1-4] derived from simple dynamic models of the robots. In this paper, a generator of program ZMP trajectory for biped humanoid robots using the multibody systems dynamic (MBS) methods is investigated.

©The 2018 International Conference on Artificial Life and Robotics (ICAROB2018), Feb. 1-4, B-Con Plaza, Beppu, Oita, Japan

2. Theoretical description

The dynamic model of the robot can be expressed in the form:

$$\begin{cases} \mathbf{M}\ddot{\mathbf{x}} - \mathbf{D}^T \mathbf{p} = \mathbf{f}(\dot{\mathbf{x}}, \mathbf{x}, t) + \mathbf{u}(t) \\ \mathbf{D}\dot{\mathbf{x}} = \mathbf{h}(\dot{\mathbf{x}}, \mathbf{x}) \end{cases} \quad (1)$$

In equations above \mathbf{x} is the state vector of dimension n , \mathbf{M} is an inertia matrix, $\mathbf{f}(\dot{\mathbf{x}}, \mathbf{x}, t)$ is the external forces vector, $\mathbf{u}(t)$ is a control forces vector, \mathbf{D} is the matrix of the variable coefficients of the constraints equations with the dimension $k \times n$, k is number of constraints equations, $\mathbf{h}(\dot{\mathbf{x}}, \mathbf{x})$ is right side constraints equations vector, \mathbf{p} is Lagrange multipliers vector.

Eq.(1) is the generalized equation of motion of any control mechanical system and well known in multibody dynamics [5]. Let control motion is the movement of some prescribed point of the system along program trajectories $\mathbf{w}(t)$, where $\mathbf{w}(t)$ is vector with the dimension m . Eq. (1) can be transformed by substituting control forces $\mathbf{u}(t)$ on constraints equation due to program trajectories $\mathbf{w}(t)$:

$$\begin{cases} \mathbf{M}\mathbf{x} - \mathbf{D}^T\mathbf{p} - \mathbf{D}_w^T\mathbf{p}_w = \mathbf{f}(\mathbf{x}, \dot{\mathbf{x}}, t) \\ \mathbf{D}\mathbf{x} = \mathbf{h}(\mathbf{x}, \dot{\mathbf{x}}) \\ \mathbf{D}_w\mathbf{x} = \mathbf{w}(t) \end{cases} \quad (2)$$

where \mathbf{D}_w is the matrix of the variable coefficients of constraints equations according to program trajectories $\mathbf{w}(t)$ with the dimension $k \times m$, $\ddot{\mathbf{w}}(t)$ is second derivation of a program trajectories, \mathbf{p}_w is the Lagrange multipliers vector due to $\mathbf{w}(t)$. Eq. (2) are equivalent to Eq. (1), but (2) haven't contain unknown control forces $\mathbf{u}(t)$. Hence numeric integration of (2) provides kinematics parameters of the program movement $\mathbf{x}^*(t)$ and can be used for walking pattern generation.

For control of walking robot based on the system (1) and equation (2) in the last equation of the system linkage (2) three types of equations must contain: the equations defining the motion of the body of the walking robot, the equations specifying the motion of the foot points of the walking propulsion and equations, ensuring the stability of the robot:

$$\begin{aligned} \mathbf{D}_{wb}\ddot{\mathbf{x}} &= \ddot{\mathbf{w}}_b \\ \mathbf{D}_{wf}\ddot{\mathbf{x}} &= \ddot{\mathbf{w}}_f \\ \mathbf{D}_{ws}\ddot{\mathbf{x}} &= \ddot{\mathbf{w}}_s \end{aligned} \quad (3)$$

The function \mathbf{W}_b sets the program motion of the points of the robot body, \mathbf{W}_f - the movement of the foot points of the walking propulsors, \mathbf{W}_s - the movement of some additional points in an additional links equations. Function \mathbf{W}_b contains six components and defines the spatial movement of the body.

The function \mathbf{W}_f sets the movement of the points of the stepping propulsor with regard to the given kinematic parameters of the characteristic points of the robot body, in particular, the points of touching of the walking motion the body. A function \mathbf{W}_s implicitly depends on \mathbf{W}_b that is necessary for the step planning parameters.

Additional links equations described by the last equation of system (3) can be divided into two groups - equations of the trajectory of the ZMP, which determines the stability of the robot and the equations of the coordinated mutual displacement of the links necessary for elimination of 2 extra degrees of freedom from the system.

The main role in ensuring the sustainability of robots the equations defining the trajectory of the ZMP in the plane of the supporting surface of the robot are playing. For the x coordinate of the ZMP equation has the form:

$$\sum_{i=1}^n ((\ddot{z}_i + g)m_i x_i - \ddot{x}_i m_i z_i + (\ddot{z}_i + g)m_i x_{zmp}) + \mathbf{K}_y = 0. \quad (4)$$



Fig. 1. Robot AR600 (<https://youtu.be/9BRt542QoSs>)

Where x_i, y_i, z_i are the coordinates in the respective directions of the mass center of the i -th body, m_i is the mass of the i-th body, \mathbf{K}_y is projection of kinetic moment on y axis, x_{zmp} is coordinate of the trajectory of the zero moment point.

The equation for the y coordinate of the ZMP is written similarly, from the condition of equality of moments regarding the x-axis.

Equations (4) are the equations which include both the coordinates of the bodies and their second derivatives. The direct inclusion of such link equations into system (2) using Lagrange multipliers is difficult.

To date for biped robots quite a large number of approximate methods for solving such a problem are developed. First, we can distinguish a group of methods, which neglect the members of the second derivatives, considering them to be small, which corresponds to the

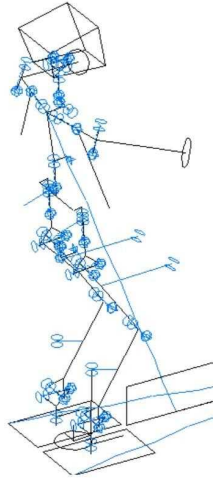


Fig. 2. Design scheme of the MBS model of AR600.

quasistatic regime of motion. In this case, equation (4) becomes the usual equation linking the coordinates of the bodies and their impact are taken into account by using Lagrange multipliers [6-9].

In our work we propose to look for a program motion of robot that meets the equations (4), as the sum of the movements of a certain type. The contribution of each movement is determined by a random multiplier that minimizes the residual error of equation (4).

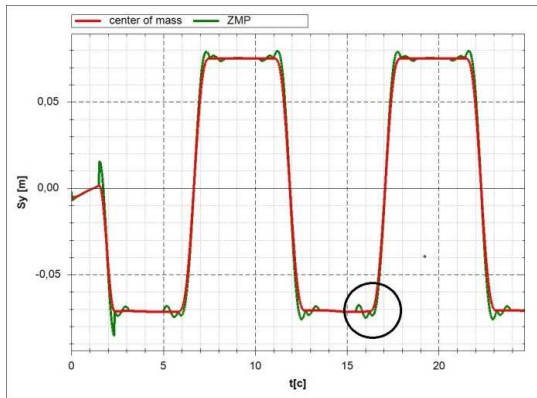


Fig. 3 The program trajectory of the center of mass and the ZMP along the y coordinate.

As the basic equations to ensure stability of the robot, are the equations of motion of the robot mass center, which are obtained from equations (4) with the exception of members from the second derivatives of the coordinates. These equations are linear with respect to the coordinates and have the form

©The 2018 International Conference on Artificial Life and Robotics (ICAROB2018),Feb. 1-4, B-Con Plaza, Beppu, Oita,Japan

$$\sum_{i=1}^n (m_i x_i + m_i x_{zmp}) = 0. \quad (4)$$

Equations of such type are matched with the equations of motion of a robot using Lagrange multipliers. In equation (5) there are time functions $x_{zmp}(t), y_{zmp}(t)$ that describe the desired ZMP trajectory. To adjust program motion, the additional link equations are proposed of the form :

$$\sum_{i=1}^n a_{ij} x_i + h_j \alpha_j(t), j = 1, m \quad (6)$$

Here a_{ij} are the coefficients of the auxiliary equations of links, h_j is a variable parameter of the j-th link equation, $\alpha_j(t)$ is some functions, m is the number of auxiliary equations. Equation (6) can have the physical meaning of the slope of the hull, a wave of the hands, etc.

3. Theoretical and experimental analysis

Theoretical and experimental studies were conducted on the robot AR600 (Fig. 1). This platform is used in various researches of robot's gait to date (e.g. [10]). The MBS model for this robot was elaborated, a design scheme of model is shown in Fig.2. Figure 3 shows the program functions that determine the trajectory of the ZMP and which are included in the equation (5). On the basis of the solution of the system of equations (3) program angle values of the actuators were found, which were implemented on the robot AR600 using PID controllers. In addition to the program functions of the movement of the robot mass center $y_{zmp}(t)$ Fig. 3 shows the y coordinate of the ZMP trajectory calculated by (4). As can be seen from Fig. 3, taking into account the accelerations in determining the trajectory of the ZMP, makes a significant disturbance – the area highlighted by a circle in Fig.3 – which increases with the growth of the speed of the robot, which leads to loss of stability.

To compensate the mismatch between program and actual trajectory of ZMP the motion of lifting of the robot mass center at the start and the end of the load transfer from one foot to the other was taken as equations (6):

$$\sum_{i=1}^n m_i z_i + h \alpha(t). \quad (7)$$

Where $h\alpha(t)$ - the empirical function shown in Fig. 4. The specified function is selected from the conditions for creating a stabilizing moment due to the inertial forces of vertical movement of the robot mass center. Fig. 5 shows the comparative trajectories of the ZMP in the lateral direction with regard to the equation (7). As it can be seen from the figure, equations of the type (6,7) allow you to change the trajectory of the ZMP in a fairly wide range.

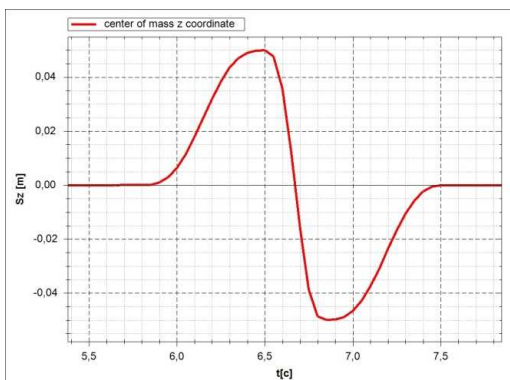


Fig. 4. Function $h\alpha(t)$.

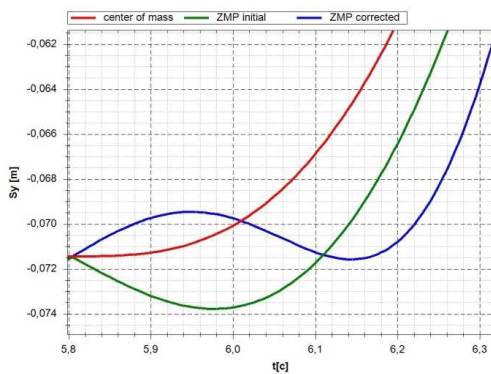


Fig. 5. Program ZMP trajectory without and with consideration of equation (7).

Equations included in (6) can be selected empirically or through formal procedures, for example, by solving the problem of parametric optimization for the set of parameters a_{ij} and criterion (4). This task requires significant computational costs and, therefore, can be resolved by using parallel computing, since it allows

independent calculation of the partial derivatives of the criterion function.

Acknowledgements

Work is performed with the financial support of the Russian Foundation for Basic Research and the Administration of Volgograd region (project #16-47-340385)

References

1. Jin'ichi Yamaguchi, Noboru Kinoshita, Atsuo Takanishi and Ichiro Kato. Development of a biped walking robot adapting to the human's living floor. *Proceedings of the 1996 IEEE International Conference on Robotics & Automation*, pages 232-239, Minneapolis, Minnesota, April, 1996.
2. Graham Mann, Stability Control in an Actively-Balanced Bipedal Robot. *School of Computer & Information Science*, Edith Cowan University.
3. Masato Yirose, Kenichi Ogawa. Honda Humanoids Robot Development. *Phil. Trans. R. Soc. A* 2007 365, 11-19.
4. Gabbasov, B., Danilov, I., Afanasyev, I., and Magid, E. (2015, December). Toward a human-like biped robot gait: Biomechanical analysis of human locomotion recorded by Kinect-based Motion Capture system. In *Mechatronics and its Applications (ISMA), 2015 10th International Symposium on (pp. 1-6)*. IEEE.
5. Shabana A.A. *Dynamics of Multibody Systems*/ A.A. Shabana//New York , NY, Cambridge University Press, 2005.
6. Jung-Yup Kim, Ill-Woo Park, Jun Ho-Oh. Experimental realization of dynamic walking of the biped humanoid robot KHR-2 using zero moment point feedback and inertial measurement. *Advanced Robotics, Vol. 20*. No. 6. pp. 707-736 (2006)
7. Kim J. H. and Oh J. H., Realization of dynamic walking for the humanoid robot platform KHR-1, *Advanced Robotics 18*, 749-768 (2004).
8. Kim, J. Y., Park, I. W. & Oh, J. H. J. Walking Control Algorithm of Biped Humanoid Robot on Uneven and Inclined Floor *Journal of Intelligent & Robotic Systems* (2007) 48: 457. DOI :10.1007/s10846-006-9107-8.
9. Ill-Woo Park, Jung-Yup Kim and Jun-Ho Oh. Online Walking Pattern Generation and Its Application to a Biped Humanoid Robot – KHR-3 (HUBO). *Advanced Robotics 22* (2008), p. 159-190
10. Magid, E., & Sagitov, A. (2017, June). Towards Robot Fall Detection and Management for Russian Humanoid AR-601. In *KES International Symposium on Agent and Multi-Agent Systems: Technologies and Applications* (pp. 200-209). Springer, Cham.

Path planning for Indoor Partially Unknown Environment Exploration and Mapping

Aufar Zakiev, Roman Lavrenov, Evgeni Magid

*Intelligent Robotic Systems Laboratory, Higher Institute for Information Technology and Information Systems (ITIS),
Kazan Federal University, 35 Kremlyovskaya street, Kazan, 420008, Russian Federation
<http://kpfu.ru/robolab.html>*

Vadim Indelman

*Autonomous Navigation and Perception Lab, Technion-Israel Institute of Technology, Haifa, Israel
E-mail: zaufar@it.kfu.ru, lavrenov@it.kfu.ru, magid@it.kfu.ru, vadim.indelman@technion.ac.il*

Abstract

This paper addresses a problem of partially unknown environment exploration and mapping. The proposed path planning algorithm provides global and local goals search taking into account limited sensing range and visibility constraints that arise from obstacles. Looking for local goals near a global path maximizes robot utility and helps avoiding returns to regions with low potential gain. All stages were tested in ROS/Gazebo simulations and results were compared with a naive algorithm that was proposed earlier.

Keywords: robotics, algorithm, modelling, mapping, ROS/Gazebo, indoor exploration, path planning

1. Introduction

Unknown environment automatic mapping is a fundamental task for all kinds of mobile robots. It is essential for every autonomous robotic system to perform mapping as precise as possible to make feasible further effective usage of a generated map in navigation procedures. A result of such mapping that is performed by one robot could be applied then for localization and path planning by other robots. However, previously these maps are often incomplete since every robot has its own operational limits (e.g., sensory limitations, time and power limitations) and robots that reuse such imperfect map are forced to operate in partially unknown environment, which constrains robot capabilities and may significantly decrease its effectiveness. Thus, it is important to have a good strategy to make possible efficient map update when its part is still undiscovered.

The problem of partially unknown or uncertain environment exploration¹ is discussed in research dedicated to single-robot exploration based on best exploring position search²; in terms of multi-robot exploration³ using greedy tactics⁴ or sophisticated

algorithms designed specially for indoor environment exploration⁵. However, these approaches are tested in simulations with synthetic input maps or used high-quality maps without artifacts that are impossible to avoid during a mapping process (e.g., impulse noises, incorrect sensory processing results, sensory limitations of real robotic system, etc.). In this paper, we propose a path planning method for an indoor partially known environment exploration and mapping. It was tested in simulations that were created using real sensory data. The algorithm performance was compared with previously proposed methods.

2. Partially unknown environments exploration challenges

A popular and effective way of mapping is using laser range finder (LRF) devices, which provide quite precise data about local landscape around a robot. The obtained data is represented in a form of height map images. Each pixel of the height map stores data about corresponding region of the environment. Pixels can have three possible values: black (usually interpreted as occupied region), white (obstacle-free) or gray (no occupancy data)⁶.



Fig. 1. A region of the original map with odometry caused artifact (obstacle-free space behind the wall).

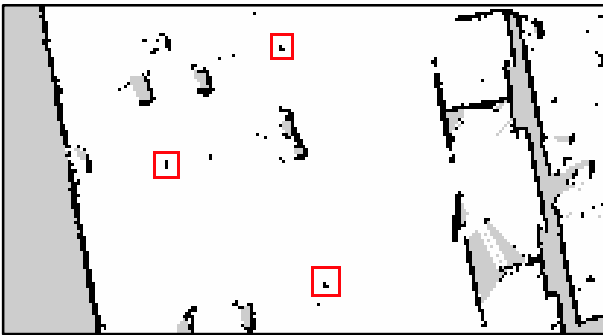


Fig. 2. A region of the original map with noisy regions (several examples of noise are encapsulated within red rectangles).

However, mapping algorithms during mapping procedures heavily rely on odometry data, which decrease map precision and cause various artifacts in the map (Fig. 1). Scanning device imperfection leads to eventual noises in sensory data (Fig. 2) or/and incomplete data (Fig. 3). Another problem is that a scanning LRF is constrained by obstacles (e.g. walls, doors, etc.) and this should be taken into account during path planning to unknown regions of the map. In addition, it is very important to use predictable forms and assumptions on indoor environments, e.g., they are structured and walls should surround every location (room, corridor, etc.).

3. Proposed approach

This section describes our algorithm, which is partially based on our previous research work. First, noise reduction within a map is performed using our modified median filter built-in map preparation tool⁷.



Fig. 3. A region of the original map with highlighted space between distinct laser rays.

Then, the robot takes the filtered map as an input and, assuming its initial position within the map, one of many localization techniques could be applied to determine robot location. For localization we had selected Adaptive Monte Carlo Localization⁸ (AMCL) method. Next, the robot preforms as follows:

1. Reachable information gain regions are marked.
2. A global goal is selected with a greedy approach based on information gain property of regions.
3. Local goals are selected taking into account LRF limitations and a path toward the global goal.
4. The robot sequentially travels through the local goals toward the global goal.
5. Return to step No.1 until reachable information gain regions are available within the map.

3.1. Reachable information gain regions marking

Reachable information gain regions are unknown map regions, which (possibly) could be explored by the robot (shown on Fig. 4). The definition of such regions is recursive:

- Every unknown cell of the map, which is adjacent to an obstacle-free cell, is included in reachable information gain region.
- Every unknown cell, which is adjacent to another reachable information gain cell is also included in reachable information gain region.
- Recursion depth is set in advance or controlled manually, and depends on map resolution. Using approximate wall thickness as a base depth value produces good results in practice.

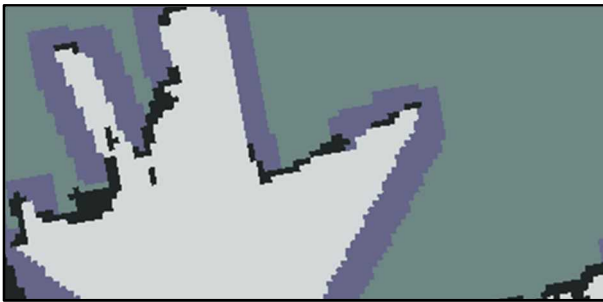


Fig. 4. A region of the original map with highlighted (in purple color) reachable information gain regions.

This method takes into account the structured pattern of an indoor environment to properly estimate the utility of each position on the map: the farther the robot moves from frontier cells, the more chances it has to find a particular obstacle, which limits information gain.



Fig. 5. A region of the original map. A preferred observing position by naive approach (left) and by the proposed approach (right). Circles and arrows show sensory radius of the robot.

3.2. Global goal selection

A global goal is computed with the following strategy: the global goal is an obstacle-free cell with maximum count of reachable information gain cells in the LRF-sensing radius. This is a greedy approach that was used in previous works⁴. Previous methods considered only frontier points as candidates for the global goal. Our approach uses a different strategy: the global goal could be any obstacle-free point within the map. This makes the global goal selection more optimal in cases when several information gain regions could be observed from a single point. Figure 6 illustrates advantages of this approach.

3.3. Local goals selection

Local goals are reachable information gain regions that are located within a predefined radius from a global path. Local goals allows the robot to explore small reachable regions while following the global path toward the global goal. Such algorithm prevents the robot from returning to the previously explored locations, thus providing a more efficient time and energy consumption. Figure 6 demonstrates an example of different behavior of the greedy approach (top image) and our algorithm (bottom image). The robot starts at red X-mark, but while with the greedy approach it begins from exploring a large unknown area (region 1) and then returns back to the small region (region 2), the exploring sequence of our algorithm is the opposite is, which saves time for passing the same region (region 1) twice.

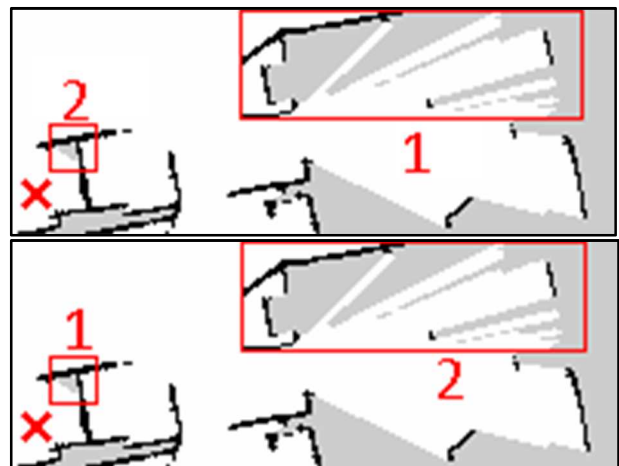


Fig. 6. The robot starts at red X-mark. Greedy approach exploring sequence (top) and our approach sequence (bottom).

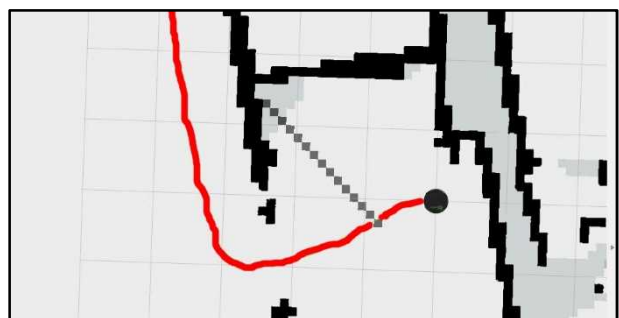


Fig. 7. Red spline represents the global path. The line starting on the global path is the LRF ray towards the local goal.

It is important to emphasize that local goals must be within the LRF line of sight, i.e., there should be no obstacles on the way of the LRF ray. This condition is verified by simulating LRF rays from a robot pose on the global path toward a region of interest: when the ray does not intersect any obstacle, it is possible to observe the region of interest from the pose. Bresenham's line algorithm⁹ is used to simulate such rays on occupancy grid (illustrated in Fig. 7). This algorithm allows to raster straight LRF rays and visualize them on occupancy grid.

4. Comparison with the greedy approach

To prove the efficiency of our approach, a comparison with the greedy method³ was performed. Both algorithms were simulated in ROS Gazebo environment and for the simulations we used a system with i7-4700HQ CPU, NVIDIA GeForce 770M GPU, and 24GB RAM.

The results are summarized in Table 1. Two approaches were tested for a simulated exploration task that was run for 3, 5, 15 and 20 minutes within the same map. The results demonstrated that the naive algorithm performs better and collects more data if the exploration time is limited; in such case it is more efficient to skip exploration of low information gains and to proceed directly toward high information gain regions exploration. However, when only low information gain regions remain, the naive method produces long distance paths with multiple returns. This way, as exploration time grows, our approach becomes more and more efficient.

Table 1. Map exploration percentage depending on the method and exploration time.

Approach	Simulation time in min.			
	3	5	15	20
Naive method	73%	77%	85%	88%
Proposed method	72%	73%	83%	95%

5. Conclusions and future work

Path planning for partially known environments is an important task in robotics. The results of previous explorations could be reused, and an efficient exploration algorithm saves time and energy consumption of a robot. In this paper we proposed an exploration algorithm that

shows better performance than a naive greedy approach for long-time exploration of indoor environments. As a part of future work, we plan to test the proposed algorithm within various environment in ROS Gazebo simulation¹⁰. The algorithm will be integrated into the control system of a real robot “Servosila Engineer” and tested in real-world exploration scenarios.

Acknowledgements

This work was partially supported by the Russian Foundation for Basic Research (RFBR) and Ministry of Science Technology & Space State of Israel (joint project ID 15-57-06010). Part of the work was performed according to the Russian Government Program of Competitive Growth of Kazan Federal University.

References

1. V. Pshikhopov, Path Planning for Vehicles Operating, *Uncertain 2D Environments* (Butterworth-Heinemann, 2017).
2. H. H. González-Banos and J. C. Latombe, Navigation strategies for exploring indoor environments, *The Int. J. of Robotics Research* (21.10-11.2002), pp. 829-848.
3. A. Andreychuk and K. Yakovlev, Applying MAPP Algorithm for Cooperative Path Finding in Urban Environments, *Int. Conf. on Interactive Collaborative Robotics* (Springer, Cham, 2017) 1-10.
4. R. Simmons, D. Apfelbaum, W. Burgard, D. Fox, M. Moors, S. Thrun and H. Younes, Coordination for multi-robot exploration and mapping, *17th National Conf. on Artificial Intelligence and 12th Conf. on Innovative Applications of Artificial Intelligence* (2000), pp. 852-858.
5. C. Stachniss, O. M. Mozos and W. Burgard, Efficient exploration of unknown indoor environments using a team of mobile robots, *Annals of Mathematics and Artificial Intelligence* (2008), pp. 205-227.
6. A. Elfes, Using occupancy grids for mobile robot perception and navigation, *Computer* (1989), pp. 46-57.
7. R. Lavrenov, A. Zakiev and E. Magid, Automatic mapping and filtering tool: From a sensor-based occupancy grid to a 3D Gazebo octomap, *Int. Conf. Mechanical, System and Control Engineering* (2017), pp. 190-195.
8. F. Dellaert, D. Fox, W. Burgard and S. Thrun, Monte carlo localization for mobile robots, *IEEE Int. Conf. Robotics and Automation* (1999), pp. 1322-1328.
9. J. E. Bresenham, Algorithm for computer control of a digital plotter, *IBM Systems journal*, (1965), pp. 25-30.
10. M. Sokolov, I. Afanasyev, R. Lavrenov, A. Sagitov, L. Sabirova and E. Magid. Modelling a crawler-type UGV for urban search and rescue in Gazebo environment, *Int. Conf. on Artificial Life and Robotics* (2017), pp.360-363.

Simulation of service robot swarm behavior

Alexei Lushnikov, Vlada Kugurakova, Arthur Nizamutdinov
*Higher School of ITIS, Kazan Federal University, Kremlyevskaya str., 18,
Kazan, Russia*

Timur Satdarov
KUKA Robotic,
Kazan, Russia

*E-mail: alexkenny@gmail.com, vlada.kugurakova@gmail.com,
yalopata@gmail.com, timur.satdarov@kuka.com
<http://kpfu.ru/eng/itis>*

Abstract

In this paper, we present an implementation 3D simulation of a swarm of intelligent service robots in Unity3D. Swarm's task and purpose is clean-up of an assigned area. We compared and analyzed different possible algorithms of such swarm's behavior. Implementation includes prevention of collision between robots themselves and humans that walk through their area of effect and can be expanded to any other obstacle, moving or stationary. The implementation is suitable for serving as a basis for future real-life construction of a service robot swarm.

Keywords: robotics, algorithm, modelling, service robot, swarm behavior, simulation, virtual experiments

1. Introduction

Systems of autonomous mobile robots are capable to solve a numerous class of civil and military tasks, including firefighting, rescue operations, agriculture and other tasks in different fields. Therefore, tasks of reconfiguration of robot swarms are topical, studied enough and using in practice. The used approaches are based on different principles and, accordingly, based on various mathematical methods. Application of multi-agent decentralized methods of interaction of robot groups allows creating robotic systems more flexible to reconfiguration, sustainable to counteraction and with low cost. Releasing a person from routine "dirty" work related to cleaning both streets and more complex surfaces (roofs, walls, windows) is one of the simplest

applications of using a swarm of autonomous robots, except for the transportation and storage of different items, which is already well considered in the literature and implemented in production. In this article, we are invited to review our simulation of the behavior of a swarm of intelligent service robots clearing the territory in an area.

2. Relevance

Modern methods described in the literature of implementing a robot swarm, offer systems, which include direct connection of robots or using a centralized system for coordination of robots. These systems are exposed to a hardware error and/or malicious attacks on a centralized system [1]. The

bioengineering approach suggests the application of parallel and distributed behavior of social insects. This, in particular, the development of collective memory for robots and zones covered by the test space, the self-organization of autonomous robots for continuous dynamic coverage of the test space [2] and the solution of other specific accompanying problems: unpredictable dynamics of the external environment, up to conscious counteraction [3]; errors in the algorithm of robots in connection with incompleteness and contradictions on the status of other participants and the external environment; obstacles of different shapes (convex, concave and curved) with varying velocities [4]; a lot of ways of development, achievement of goals, distribution of roles, structure of the collective; errors of communication between objects in the served territory, their interaction with each other; prevention of collision between robots themselves and humans that walk through their area of effect and can be expanded to any other obstacle, moving or stationary [5]; problems in the communication architecture, protocols, operating facilities; technical breaking [6] of the autonomous robot and ways of their elimination.

The rationale for using the bioinspired approach is given in our other work [7], which, however, has little correlation with the bioengineering approach proposed below when using heuristic swarm algorithms.

The following implementation is suitable for serving as a basis for future 3D modeling of a service robot and real-life construction of a service robot swarm.

3. Implementation algorithms

One of the problems for the realization of the idea of using a swarm of service robots capable of self-cleaning on the zoned territory is the “task of optimizing navigation and route”. To solve it, we can use various heuristic algorithms, because they provide acceptable results for a sufficient time frame. There are a lot of swarm algorithms: ant colony algorithm, bee colony algorithm; particle swarm method; firefly algorithm, gravity search algorithm water drops algorithm, etc.

3.1. The ant colony algorithm

One of the superior heuristic groups of algorithms is the ant colony (ACO) group of algorithms [8, 9]. These

algorithms are simulating the real ants behavior. This idea appeared during an observation how ants search the shortest way from anthill to a food source (Fig.6). For the first time, these algorithms have been applied in the combinatorial graph task, for the well-known traveling salesman problem [10]. The algorithm is based on the mechanism simulating the real ants' behavior, when they are looking for food. As in the classical ACO [11], this modification can be divided into conditional steps, such as: placement and initialization, movement of agents, pheromone update and breakpoint condition checking. The idea of the algorithm is to model the behavior of ants, their ability to find the shortest way from the colony to the food source in short-term, and adaptation to new changeable conditions and to find the new shortest way. They focus on the solution of various graph problems, which makes it reasonable to apply ACO to solve the optimization problems of the trajectory, in order to move robots in the environment with static obstacles. Some known applications of ACO [12] have shown competitive results.

Replacing ants with robotic cleaners we demonstrate a simulation of the algorithm. This method is far from an optimal method, and in the case of robots, the movement of a bunch of robots will block a movement of pedestrians.

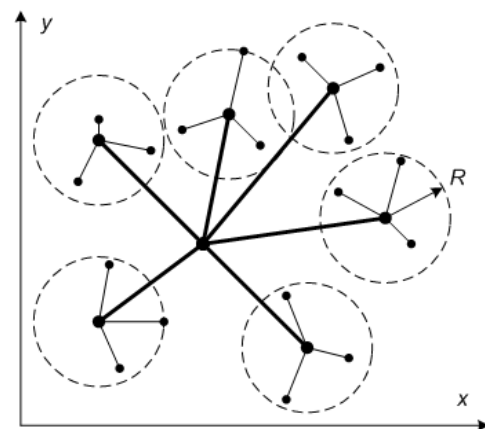


Fig.1, bee colony algorithm

3.2. Bee colony algorithms

Bees algorithm (BA) [13] and artificial bee colony (ABC) algorithm [14] are inspired by the foraging behavior of bees. In spite of both algorithms having

been developed for function optimization, there are several studies of bee colonies on solving discrete and combinatorial optimization problems, such as transportation problem, scheduling problems, data mining problems and resource allocation problem. An extensive literature survey and a classification of the algorithms on behavioral characteristics of the honey bees have been researched in [15].

The main idea of a bee colony in nature is an exploration of an area around a hive in order to search for nectar and its collection. According to the model developed by Tereshko [14], the collective intelligence of honey bee swarm contains three main components: “food” sources (with parameters: a proximity to the nest, a richness of energy and an ease of extracting this energy), “scout” bees and “forager” bees (also in a colony there are drones and uterus, but they do not collect nectar. Scout bees explore the space around and report about perspective places, in which the greatest amount of the nectar was found (bee dance – mechanism of sharing information in a hive) [14]. Then forager bees collect the nectar in these places and collect the information about amount of nectar in some neighborhood from the area indicated by the scout bees. Works of these types of bees in a hive provide an effective exploration of space around and collecting of nectar (Fig.1).

4. Implementation of simulation of service robots by bee colony algorithm

Simulation of the algorithm is created replacing bees with robotic cleaners:

1. Robots move, covering the whole selected surface area. Each robot searches garbage and collects it. If one of the robots finds more garbage, it saves this value as the personal best position of collecting. If the PBP of this robot essentially differs from the PBP of other robots, this position became global best position (GBP), and all robots aim to this point to collect garbage. The PBPs are not erased, and after collecting garbage robots return to their positions. If the robot does not find garbage during the N-time, it starts helping another robot with higher PBP.
2. One robot moves from a starting point searching garbage, and when it finds garbage, robot collects it. If it cannot do it, robot returns to the starting point,

informing other robots about its PBP, which go to the specified point to collect garbage.

5. Comparison of algorithms

Ant colony algorithm is difficult in implementation and unpractical: difficulty of the creation of visual and informative trail; implementation of movement by trail because of some problems; entanglement of trails and impossibility to determine a path of a robot. A bee colony algorithm is more flexible to sharing information between robots.



Fig. 2, a schematic plan of the robot work

6. Street cleaning plan

A schematic work plan for robots was drawn up during preparation for the implementation of 3D simulation (Fig. 2): robot’s storage location; the drain for snow; robots that clean the streets (they are numbered); information board with a description of the robot parameters.

Creating a scene. For a realistic and visual representation of the work of robots, the scene was created including a typical street attributes. The crossroad, the bus stop, a dozen trees and several houses were put on the stage as decorations. The working area of the robots is located between houses and the fence near the road.

Simulation of the robots work. Robots leave the box, in which they are stored and charged, and then move to their coverage areas. The first robot immediately begins cleaning the street, while the second, third and fourth occupy their position on the sidewalk, only after that they begin cleaning. For optimal coverage of the rectangular area, the robot moves in a zigzag, completely covering the area.

Precipitation, mud, garbage. Each cell of the robot’s advancement is a cell with garbage or precipitation, for

example freshly fallen snow. With the passage of time, the amount of snow in each cell increases uniformly. The robots collect snow during the passage of the cell. Snow accumulates inside robots. If on the road large accumulations of snow then the robot collecting it as much as possible, informs the target's coordinate to other robots and they stop their work and rush to a new target. The robot which collected the snow returns to the base for unloading. Also, a robot returns if has a critical battery charge level. The information board is located on the lower right corner of the simulation. It displays data of robots by their number. It displays the robot's number, the level of its charge, and the amount of snow that it has already collected. Also, it displays the temperature. If temperature is positive, then puddles are displayed instead of snow on the roads.

7. Conclusion

The result of the research is the 3D simulation of service robot swarm using of bee algorithm. The simulation demonstrated an opportunity for implementation of this robot system. Further implementation of robot swarm using this simulation is possible. Factors of the external environment and possible errors of robot algorithm should be taken into account in the implementation.

Acknowledgements

This work was funded by the subsidy allocated to the Kazan Federal University for the state assignment in the sphere of scientific activities.

References

1. T. Bontzorlos and G. C. Sirakoulis, Bioinspired algorithm for area surveillance using autonomous robots, in *Int J Parallel Emergent Distrib Syst.* 2017; 32(4). – pp 368-85.
2. A. Scheidler, D. Merkle and M. Middendorf, Swarm controlled emergence for ant clustering, in *Int J Intell Comp Cybern.* 6 (1), (2013). – pp. 62-82.
3. I. Afanasyev, A. Sagitov and E. Magid, ROS-based SLAM for a Gazebo-simulated mobile robot in image-based 3D model of indoor environment, in *International Conference on Advanced Concepts for Intelligent Vision Systems.* Springer, Cham. (2015, October). – pp. 273-283.
4. P. Raja and S. Pugazhenthii, Path Planning for Mobile Robots in Dynamic Environments using particle swarm optimization, in *IEEE International Conference on Advances in Recent Technologies in Communication and Computing, India,* (2009). – pp. 401-405.
5. R. Khusainov, I. Shimchik, I. Afanasyev and E. Magid, 3D modelling of biped robot locomotion with walking primitives approach in Simulink environment. In *Informatics in Control, in Automation and Robotics 12th International Conference, ICINCO 2015 Colmar, France,* July 21-23, 2015 Revised Selected Papers. Springer International Publishing. (2016). – pp. 287-304.
6. E. Magid, and T. Tsubouchi, Static balance for rescue robot navigation: Discretizing rotational motion within random step environment, in *International Conference on Simulation, Modeling, and Programming for Autonomous Robots.* Springer, Berlin, Heidelberg. (2010, November). – pp. 423-435.
7. V. Kugurakova, M. Talanov, and D. Ivanov, Neurobiological Plausibility as Part of Criteria for Highly Realistic Cognitive Architectures, in *Procedia Computer Science,* vol. 88, 2016, – pp. 217–223.
8. M. Dorigo and L. M. Gambardella, Ant colony system: a cooperative learning approach to the traveling salesman problem, in *IEEE Trans Evol Comput.* (1997).
9. M. Dorigo, G. Di Caro and L. M. Gambardella, Ant algorithms for discrete optimization, in *Artificial Life,* 1999.
10. A. A. Kazharov and V. M. Kureichik, Ant colony optimization algorithms for solving transportation problems, in *Journal of Computer and Systems Sciences International,* 49(1), (2010). – pp. 30-43.
11. R. A. Neydorf, R., O. T. Yarakhmedov, V. Polyakh, I. Chernogorov and D. Vucinic, Robot path planning based on ant colony optimization algorithm for environments with obstacles. vol. 72, (2018). – pp. 175-184.
12. M. D. Toksari, Ant colony optimization for finding the global minimum, in *Appl Math Comput.,* vol. 176(1), (2006). – pp. 308-316.
13. D. T. Pham, A. Ghanbarzadeh, E. Koç, S. Otri, S. Rahim and M. Zaidi, The bees algorithm—a novel tool for complex optimisation problems, in *Proceedings of Innovative Production Machines and Systems Virtual Conference* (2006), pp. 454-461.
14. D. Karaboga, *An Idea based on Honey Bee Swarm for Numerical Optimization, Technical Report-TR06,* Erciyes University, Engineering Faculty, Computer Engineering Department, (2005).
15. V. Tereshko, Reaction–diffusion model of a honeybee colony's foraging behavior, in M. Schoenauer (Ed.), in *Parallel Problem Solving from Nature VI,* Lecture Notes in Computer Science, 1917, Springer-Verlag, Berlin (2000), – pp. 807-816.

Smart Spline-Based Robot Navigation on Several Homotopies: Guaranteed Avoidance of Potential Function Local Minima

Roman Lavrenov

*Intelligent Robotic Systems Laboratory, Higher Institute for Information Technology and Information Systems (ITIS),
Kazan Federal University, 35 Kremlyovskaya street, Kazan, 420008, Russian Federation*

E-mail: lavrenov@it.kfu.ru

http://kpfu.ru/robofab.html

Abstract

Potential function based methods provide powerful solutions in tasks of local and global path planning. They are characterized implementation simplicity, but suffer from navigation function local minima. In this paper we propose a modification of our original spline-based planning algorithm. Voronoi-based approach provides a good initial path as first iteration. A new safety criterion is integrated into path planning to guarantee path safety. The modified algorithm was implemented in Matlab environment and demonstrated significant advantages over the original algorithm.

Keywords: robotics, algorithm, modelling, mobile robot, path planning, Voronoi graph, potential field, optimization criteria, virtual experiments.

1. Introduction

Path planning, which is a fundamental feature of a mobile vehicle autonomous navigation, is concerned with automatic planning of a collision-free path between initial and target configurations. The classical path planning problem (“piano movers problem”) is defined for complete a priori knowledge about environment. A robot is informed about its own shape, start and target position and orientation, and a set of obstacles in the environment. The robot searches for a continuous path from its initial position to the target position, while avoiding collisions with static obstacles along its way. The path should satisfy some particular criteria of its optimality.

One of the classical yet still popular approaches for dynamical solution of a collision avoidance problem is a potential field approach¹. This technique is based on an artificial potential field generated at a global or a local

level with an attractive pole in a role of a target and obstacles being represented with repulsive surfaces². Then a robot follows the potential gradient toward its minimum³. The major advantages of potential field methods are simplicity and a capability of applying them reactively for mobile and stationary obstacles negotiation. Its typical and significant drawbacks include path oscillations (for certain obstacle configurations) and existence of local minima that attract the robot and then keep it captured inside.

Previously⁴ we had proposed a path planning algorithm for a car-like mobile vehicle that could attain a target configuration from its initial configuration within a well-known environment providing a smooth obstacle free path. In order to improve the performance of the original algorithm, to add flexibility for path optimization and a possibility for further fast dynamic replanning, we integrate Voronoi Graph approach into our algorithm⁵. The new approach was tested in our previous work and

shown the results, which significantly overperformed the original algorithm.

2. Spline-based robot navigation with original potential field approach

The spline-based method, proposed by Magid et.al. about a decade ago⁴ navigates a car-like robot in a planar known environment populated with static obstacles. It considers an omnidirectional circle-shape robot that is reduced to a point in a 2D configuration space. Each obstacle is represented with a set of intersecting circles of different sizes. To provide a collision free path, a repulsive potential function has a high value inside an obstacle and on its boundary and a small value in free space. High potential function value in the obstacle’s center pushes all points of a path outside in order to minimize path cost during local optimization procedure. The path cost function sums up three components:

$$F(q) = \gamma_1 T(q) + \gamma_2 R(q) + \gamma_3 L(q) \quad (1)$$

Where $T(q)$ function takes into an account all N obstacles of the environment and their influence (as potential field) on the robot along the entire path. The example of influence of obstacles to potential field is demonstrated in Fig. 1. $R(q)$ is a function for smoothness property of the path. And $L(q)$ function accumulated path length.

The original algorithm of spline-based path planning works iteratively, beginning with start point S and target point T , and utilizes the environment obstacles as its input data. An initial path is suggested as a straight line between points S and T . Eq. (1) sets a current path cost, which is further optimized with Nelder-Mead Simplex Method⁶ in order to minimize the path cost and provide a next spline with +1 increase in its flexibility degree and complexity as well. A resulting better path serves as an initial guess for the next iteration.

The original method succeeds to provide a collision free smooth path for any complexity of the environment only if each obstacle is approximated with a single circle. However, when the obstacles are approximated with a number of intersecting circles, the intersections introduce local maxima of the global potential field. If an initial spline passes through intersection of several circles that form a single obstacle, the cost function $F(q)$ may succeed pushing the spline out of intersection area and

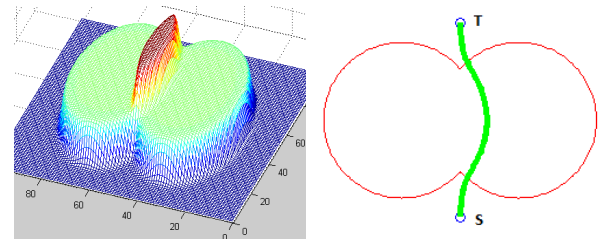


Fig. 1. A global potential field of the environment (left) and a final path between start (S) and target (T) positions that was suggested by the original algorithm.

then fail in escaping from a local minima at further iterations (Fig. 1, on the right).

3. Adding path safety parameter

We introduce an additional path quality evaluation criterion - average distance from obstacles. While navigating in obstacle populated environments, a robot should maximize its distance from the obstacles, and this feature is integrated into $T(q)$ component of our cost function. However, in some operations, there may be a requirement to stay at some defined distance from obstacle boundaries. This criterion may be required for the range-limited sensors of the robot. A distance of the robot from all obstacles of environment is calculated in each configuration $q(t)$ along the parametrically defined path as follows:

$$q(t) = \min_{\forall c \in C} \sqrt{(x(t) - x(c))^2 + (y(t) - y(c))^2} - r(c) \quad (2)$$

Here C is a set of all circular obstacles c with the center at $(x(c), y(c))$ and radius $r(c)$; further, these elementary circular obstacles may intersect to form compound obstacles. Average distance (α) is predefined. The effect of the average distance on the cost function Eq. (1) we can calculate with:

$$A(q) = \sum_{\forall t \in [0,1]} (\alpha - q(t))^2 \quad (3)$$

All four criteria are combined into the cost function:

$$F(q) = \gamma_1 T(q) + \gamma_2 R(q) + \gamma_3 L(q) + \gamma_4 A(q) \quad (4)$$

Figure 2 shows the result of path planning methods with and without the new criteria. In both cases, we searched a path from S to T . Blue points on the trajectory indicate control points for constructing a spline¹⁰. Thus, in the environment in Figure 2, the path was found in 4

iterations: top image shows a path without the new criteria, while a path with new criteria with parameters $\alpha=5$, $\gamma=1$ appears in the bottom. The algorithm with a new criterion builds a safer path. The red arrows in the figure indicate the places where the path became farther from the obstacles.

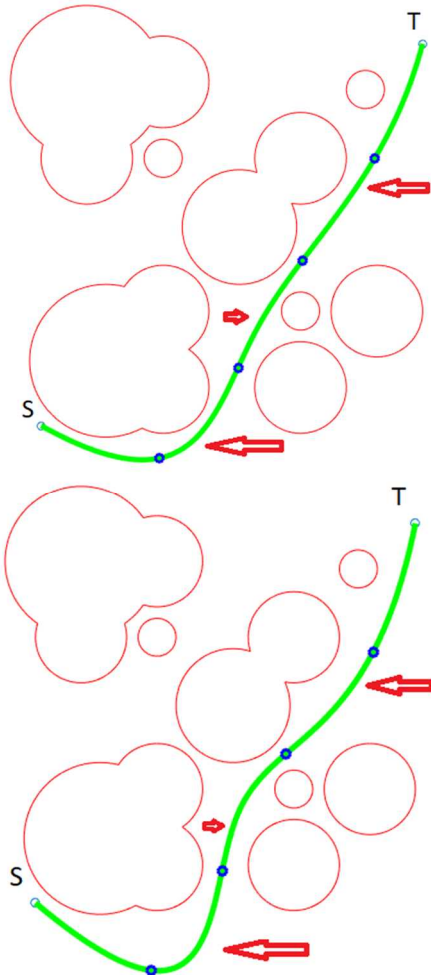


Fig. 2. Path calculated by the original algorithm without (top) and with the new criteria (bottom). The red arrows mark the points of interest where the new criteria influence is clearly visible.

Unfortunately, despite the use of a new criterion route optimization is performed only locally, the effect of the additional parameter is also local. The path remains in the same homotopy group even in the case when it is possible to bypass any obstacle from the other side.

4. Voronoi graph based solution

In order to provide a good initial spline that could be further improved locally with regard to user selection of the cost weights, we apply Voronoi graph approach⁷. With the three steps we prepare the environment by grouping circles into obstacles¹⁰: register circle obstacles to form a single compound obstacle, find outer and inner boundaries of each compound obstacle, and remove inner boundaries. For example, in Fig.3 (in the left image) the three inner obstacle boundaries will be removed.

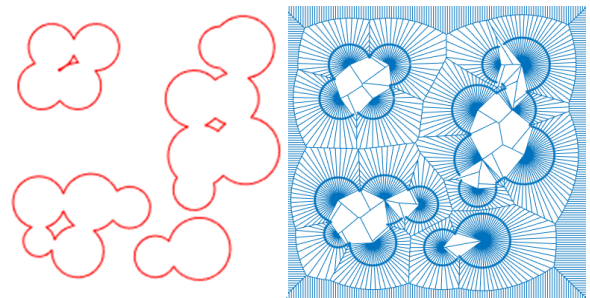


Fig. 3. Inner and outer boundaries of obstacles (left) and the process of Voronoi graph calculating (right).

Next, Voronoi graph is constructed based on a classical approach¹¹. Upon obtaining Voronoi graph VG, we connect start position S and target position T points to VG and apply Dijkstra algorithm⁸. For example in Fig. 4 you can see created Voronoi graph as tiny red lines and calculated path as fil red line. Any path (S, T) on Voronoi graph VG is guaranteed to be collision free and maximally safe with regard to distance from obstacle boundaries, and thus could provide a good initial spline for the original spline-based method⁴. A small set of special points is utilized to form via points for the initial spline¹⁰ (blue points in Fig. 4 and Fig.5).

5. Conclusions and future work

In this paper, we have presented a method for calculating a smooth and safe path for mobile robot in static planar environment. A significant modification of our original spline-based path planning algorithm for a car-like mobile vehicle navigation helps avoiding local minima problem and adds more flexibility for path optimization. We have integrated a Voronoi graph approach into the first iteration of spline optimization. Furthermore, Voronoi graph provides an opportunity to vary paths

from different homotopy classes with regard to dynamic changes in optimization function criteria as well as supports a fast dynamic replanning in a case when an initially off-line selected path becomes unavailable. The algorithm was implemented in Matlab environment and its results were compared with our original algorithm. The new approach requires less optimization iterations that the original algorithm due to a smart selection of an initial spline. While the original algorithm fails to find an existing path in complicated environments with multiple concave obstacles, its smart version was successful in all simulated tests. For example, original approach cannot find path in environment shown in Fig.5. Voronoi-based method find the path by 3 iteration.

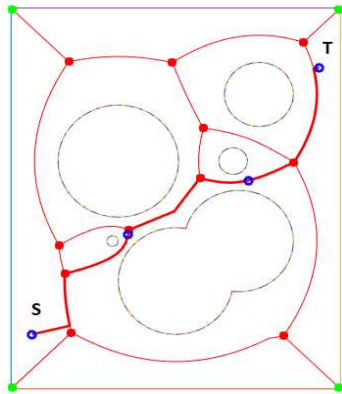


Fig. 4. Path within Voronoi graph.

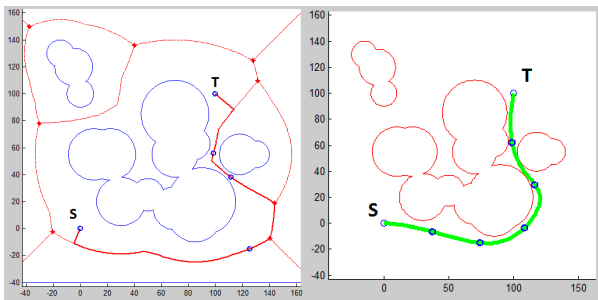


Fig. 5. Path on Voronoi graph (left) and resulting path after three iteration with the modified algorithm (right).

As our future work, we plan to integrate a number of additional parameters of 3D environments into a cost function. We also plan to create a C++ library of the method and further extend the proposed method for the navigation of a heterogeneous robotic team operating in an urban search and rescue scenario⁹.

⁹ © The 2018 International Conference on Artificial Life and Robotics (ICAROB2018), Feb. 1-4, B-Con Plaza, Beppu, Oita, Japan

Acknowledgements

This work was partially supported by the Russian Foundation for Basic Research (RFBR) and Ministry of Science Technology & Space State of Israel (joint project ID 15-57-06010). Part of the work was performed according to the Russian Government Program of Competitive Growth of Kazan Federal University.

References

1. S. Fleury, P. Soueres, J.-P. Laumond, and R. Chatila, Primitives for smoothing mobile robot trajectories. *IEEE transactions on robotics and automation*, **11**(3) (1995) 441-448.
2. O. Khatib and B. Siciliano, *Springer handbook of robotics*. (Springer, 2016).
3. E. Magid, T. Tsubouchi, E. Koyanagi, and T. Yoshida, Building a search tree for a pilot system of a rescue search robot in a discretized random step environment. *J. of Robotics and Mechatronics*, **23**(1) (2011) 567-581.
4. E. Magid, D. Keren, E. Rivlin, and I. Yavneh, Spline-based robot navigation. *IEEE/RSJ Int. Conf. on Intelligent Robots and Systems* (2006), pp. 2296-2301.
5. E. Magid, R. Lavrenov and I. Afanasyev, Voronoi-based trajectory optimization for UGV path planning. *Int. Conf. on Mechanical, System and Control Engineering* (2017), pp. 383-387.
6. J. C. Lagarias, J. A. Reeds, M. H. Wright and P. E. Wright, Convergence properties of the Nelder-Mead simplex method in low dimensions. *SIAM J. on optimization*, **9**(1) (1998) 112-147.
7. R. Lavrenov, F. Matsuno and E. Magid, Modified spline-based navigation: guaranteed safety for obstacle avoidance. *In: Ronzhin A., Rigoll G., Meshcheryakov R. (eds) Interactive Collaborative Robotics. Lecture Notes in Computer Science*, 10459 (Springer, Cham, 2017) 123-133.
8. H. M. Choset, *Principles of robot motion: theory, algorithms, and implementation* (MIT press, 2005).
9. E. Magid, R. Lavrenov, M. Svinin and A. Khasianov, Combining Voronoi graph and spline-based approaches for a mobile robot path planning. *In Lecture Notes in Electrical Engineering* (Springer International Publishing, 2018), in press.
10. E. W. Dijkstra, A note on two problems in connexion with graphs. *Numerische mathematik* **1**(1) 269-271.
11. A. Andreychuk and K. Yakovlev, Applying MAPP Algorithm for Cooperative Path Finding in Urban Environments. *In: Ronzhin A., Rigoll G., Meshcheryakov R. (eds) Interactive Collaborative Robotics. Lecture Notes in Computer Science*, 10459 (Springer, Cham, 2017) 1-10.

Virtual Experimental Stand for Automated Fiducial Marker Comparison in Gazebo Environment

Ksenia Shabalina¹, Artur Sagitov¹, Hongbing Li², Edgar A. Martinez-Garcia³, Evgeni Magid¹

¹*Intelligent Robotics Department, Higher School of Information Technology and Information Systems, Kazan Federal University, Kremlyovskaya str. 35, Kazan, Russian Federation*

²*Department of Instrument Science and Engineering, Shanghai Jiao Tong University, Shanghai, China*

³*Institute of Engineering and Technology, Universidad Autónoma de Ciudad Juárez, Chih., 32310, Mexico*

*E-mail: ks.shabalina@it.kfu.ru, sagitov@it.kfu.ru, lihongbing@sjtu.edu.cn, edmartin@uacj.mx, dr.e.magid@ieee.org
http://kpfu.ru/robofab.html*

Abstract

This paper presents experimental automated approach for comparing fiducial marker systems. Previously we compared ARTag, AprilTag, CALTag systems under three types of adverse conditions: systematic occlusion, arbitrary overlap with an object and marker rotation. In effort to improve statistical significance of our previous work with manual experiments, we faced a challenge of conducting over a thousand additional experiments. Using Gazebo environment we implemented virtual robot system that performs all necessary manipulations automatically. Further, we investigate adding Gaussian noise in order to make simulations more realistic.

Keywords: Robotics, fiducial marker system, recognition algorithms, experimental comparison, ROS, simulation.

1. Introduction

Fiducial marker systems (FMS) are systems of markers that are automatically detected by a camera with help of corresponding algorithms. FMS find their applications in various areas: physics, medicine, robotics, augmented reality, metrology etc. Taking in consideration only application in robotics, marker systems are used in robot navigation¹, localization² and mapping³, camera calibration⁴ and tasks that require camera pose estimation⁵. As our global goal is to calibrate Russian humanoid robot AR-601M mono camera and manipulators using FMS, we faced many FMS options. Each FMS has its strengths and drawbacks that are derived from the original area of its applications. Therefore, we need to compare markers in order to select a single suitable FMS from a large number of existing systems for our specific task. There are several marker performance criteria⁶. In our work, we are particularly interested in

marker occlusion resistance since the occlusion is a rather usual and unavoidable while working with humanoid robot manipulators. If the markers are located on the robot itself, they may become overlapped with varying intensities by other workspace objects (e.g. its own manipulators) and have some inclination angle with regard to a camera, which also affects its detectability⁶.

Previously, we conducted manual experiments^{7,8} to evaluate FMSs resistance to overlapping marker's area (systematic occlusion and arbitrary overlap with an object) and various rotations. Since it is time consuming to conduct such experiments with thousands of trials manually, we have decided to automate them and to start from experiments in ROS/Gazebo environment (Fig. 1).

This paper presents automated approach of conducting experiments with marker systems to evaluate occlusion resistance. Section 2 presents our related work of comparing FMS in presence of occlusions, in Section 3 we briefly overview ROS Gazebo environment and in

Section 4 we describe our simulated world in Gazebo and experiment setup. Section 5 shows the results of experiments and analyze of it. Finally, we conclude and plan our future work in Section 6.

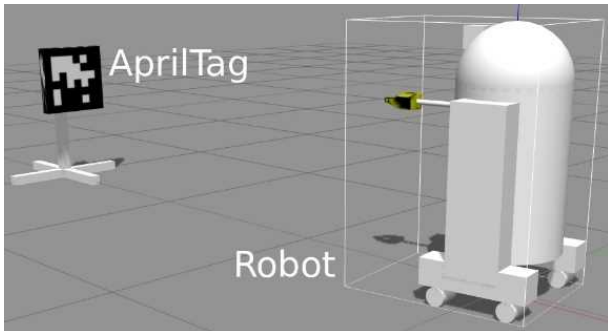


Fig. 1. Gazebo world environment: a tag holding automated stand (on the left) and a robot with a camera (on the right).

2. Related Work

During the selection of a most suitable FMS we have selected three systems most applicable in our field: ARTag^{5,6}, AprilTag³ and CALTag⁹. As mentioned above, initially we conducted all the experiments manually. Our experimental work consisted of two main parts: pilot experiments with web camera Genius FaceCam 1000X⁷ and experiments with AR-601M humanoid⁸ (Fig. 2). We outlined two experiment designs: simple and compound. First design (simple) consisted of systematic occlusion and arbitrary overlap with an object. The second design (compound) consisted of several types of occlusion: marker rotation, systematic occlusion, marker rotation with systematic occlusion and arbitrary overlap with an object. The examples of first set of experiments are showed in Fig.3. Figure 4 demonstrates the scheme of marker rotation during second design experiments. Figure 5 shows example of a marker rotation experiment. These two experimental designs initially were carried out using Genius FaceCam 1000X camera for investigating FMS's applicability using low-cost equipment. After initial experiments were completed, the same experiments were performed using humanoid robot AR-601M mono camera Basler acA640-90gc.

Analyzing the results of our experiments, we concluded that AprilTag and ARTag demonstrated high sensitivity to edge occlusions, while showing satisfactory results in the experiments with arbitrary overlap and achieved perfect score in the marker rotation tests.

© The 2018 International Conference on Artificial Life and Robotics (ICAROB2018), Feb. 1-4, Beppu International Convention Center, Oita, Japan

CALTag system on the other hand showed high resistant to all types of occlusion: edge occlusion, arbitrary overlap with an object and tag rotation.

3. ROS Gazebo Environment

Robot Operating System (ROS) is the most fast-growing and popular framework for programming robots that was initially developed by Willow Garage. The main idea of ROS framework is a collaborative construction of robotics software. Everyone can use and improve ROS packages - an atomic unit in ROS system that represents one or more functionalities or ways to solve particular problem - or create a new one.

Gazebo is a popular 3D simulator for simulation of different type of robots, helping with the creation of new robots and testing algorithms in rather realistic conditions. Gazebo includes physics simulation, robot and environment models, and custom plugins. We selected Gazebo for our virtual experiments due to its integration with ROS, accessible custom joint controllers and a convenient way to design a robot with urdf-files.



Fig. 2. AR-601M humanoid robot.

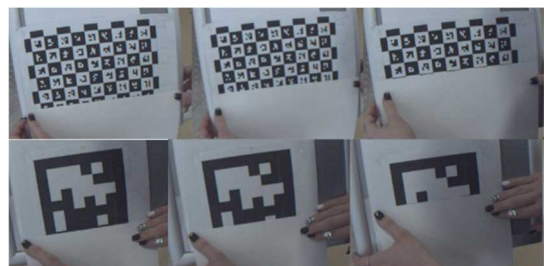


Fig. 3. Systematic occlusion experiments using AR-601M mono camera.

4. Experiment Setup

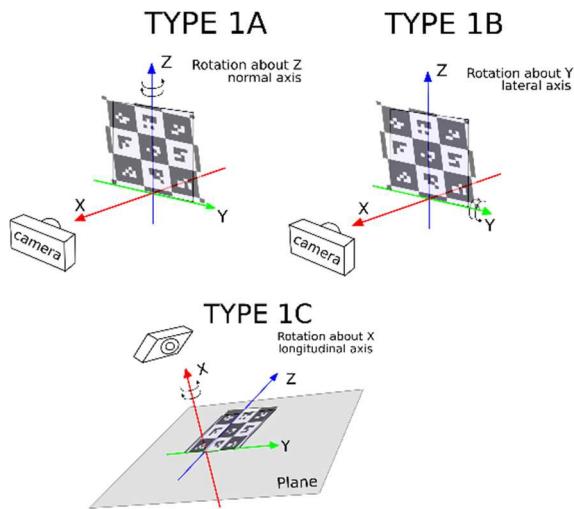


Fig. 4. Scheme of marker rotation experiments.

We targeted to automate execution of thousands of experiments with each of the FMS families to minimize time and effort that are required by real world experiments. For this purpose, we created a Gazebo world with two robots: R2D2-like robot (observer) and the tag-managing robot (performer). The performer robot is actually several interchangeable robot models designed for each type of experiments. In this Section we discuss the design and results of pilot virtual experiments with AprilTag markers rotation around Z axes. Those type of experiments are presented in the Fig. 4 as Type 1A.

The performer was implemented using `ros_control` package for its controllers. We tuned a PID controller and designed a procedure to perform rotation around Z axis by a given angle (from 0 degrees to 90 degrees) in both directions (implemented as `tag_rotation_node` node). Using already existing implementation of AprilTag in ROS (`apriltags_ros` by Mitchell Wills) we detected a tag in a set of camera frames while the performer rotated AprilTag publishing the results of the detection (ID of a tag and an angle of its rotation). As the performer rotated the tag, it published current angle of rotations. Thus, we could deduce, which angles resulted errors in detection or rotation estimation by comparing messages from aforementioned nodes. The comparison process was automated, as during launching virtual experimental stand we specified the tag family and ID, experiment type, number of repetitions, noise level and when experiments

were completed we received summary of experiments (number of errors in detection, rotation estimation etc.)

To make our experiments closer to real word conditions, we added Gaussian noise parameters for the camera of R2D2-like robot. We used three values for noise standard deviation (stddev) parameters: 0.009, 0.09 and 0.1. Figure 6 shows examples of camera view with varying levels of Gaussian noise. Image on the left represents stddev parameter of 0.009 and it is considered to be a common case for a real camera. In the central image the camera has 0.09 stddev, which represents moderate level of noise. Image on the right shows the camera with 0.1 stddev, representing high levels of noise, and its threshold value serves as a boundary condition of marker recognition possibility or failure.

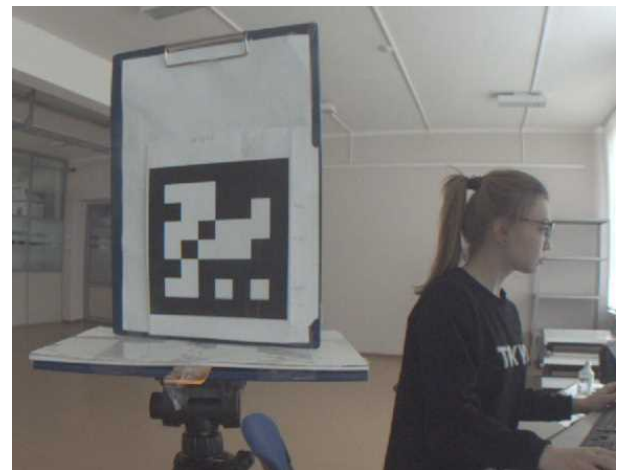


Fig. 5. Manual marker rotation experiments around Z-axis. Type 1A in scheme of rotation experiments.

5. Experimental Results

To test the virtual experimental stand we chose four randomly selected AprilTag type marker with the same IDs as in previous work⁷: ID 4, 6, 8, 9. The stand performed 3000 experiments for each marker with the results of experiments demonstrated in Table 1. Every marker could be successfully detected with up to 41 degrees of rotation with low noise and up to 25-38 degrees with high level of noise. This factors explain the low percentage of successful experiments in Table 1, because the rotation was performed up to 89 degrees. As was expected, with noise level increase the number of successfully detected and recognized markers decreased. Moreover, virtual experiments with noise also

demonstrated that some markers are significantly more successful than others (e.g., ID4), which emphasizes the necessity of various markers performance comparison.

Table 1. Detection rate (in percentage) during rotation of markers around Z-axis with varying camera noise levels.

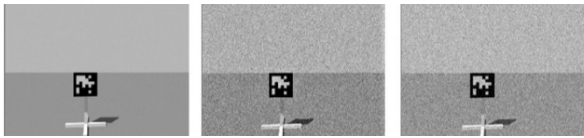


Fig. 6. Camera image with low (on the left), moderate (in the center) and high level of noise (on the right).

Tag ID	stddev		
	Low (0.009)	Moderate (0.09)	High (0.1)
4	60,8%	42,2%	30,2%
6	49,8%	35,4%	22,7%
8	40,9%	32,4%	25,3%
9	43,3%	20,8%	17,4%

6. Conclusions and Future Work

This paper presents experimental automated approach for comparing fiducial marker systems (FMS). Previously we compared ARTag, AprilTag, CALTag systems under three types of adverse conditions: systematic occlusion, arbitrary overlap with an object and marker rotation. In effort to improve statistical significance of our previous work with manual experiments, we faced a challenge of conducting over a thousand additional experiments, and pilot experiments of such automated approach were presented in this paper.

We constructed a world in Gazebo environment, which consisted of R2D2-like robot and AprilTag marker holding robot that rotates AprilTag for a given angle (from 0 degrees to 90 degrees) in both directions. We integrated it with AprilTag node tag detector in such way that we could detect the marker in each robot camera frame. To make simulated experiments close to real world conditions, we investigated three different Gaussian noise standard deviation values. Then we performed experiments applying different noise levels and analyzing AprilTag system recognition under rotation. The system detected tags with up to 40 degrees rotation with a low level of noise and up to 25-38 degrees with high. Virtual experiments with noise demonstrated

that some markers are significantly more successful than others, which emphasizes the comparison necessity.

As a part of our future work we plan to construct an automatic tool for marker rotation and test it with several FMSs. The most resistant for all types of occlusion marker system will be selected for further AR-601M camera and manipulator calibration.

Acknowledgements

This work was partially supported by the Russian Foundation for Basic Research and Ministry of Science Technology and Space State of Israel (project IDs 15-57-06010, 17-48-160879). Part of the work was performed according to the Russian Government Program of Competitive Growth of Kazan Federal University.

References

1. R. Kuriya, T. Tsujimura and K. Izumi, Augmented reality robot navigation using infrared marker, *Proc. 24th IEEE Int. Symposium on Robot and Human Interactive Communication* (2015), pp. 450-455.
2. V. Dhiman, J. Ryde and J. J. Corso, Mutual localization: Two camera relative 6-DOF pose estimation from reciprocal fiducial observation, *Proc. IEEE/RSJ Int. Conf. on Intelligent Robots and Systems* (2013), pp. 1347-1354.
3. E. Olson, AprilTag: A robust and flexible visual fiducial system, in *Proc. IEEE Int. Conf. on Robotics and Automation* (2011), pp. 3400-3407.
4. M. Fiala, Comparing ARTag and ARToolKit Plus Fiducial Marker Systems, *Proc. IEEE Int. Workshop on Haptic Audio Visual Environments and their Applications* (2005), pp. 148-153.
5. M. Hirzer, Marker Detection for Augmented Reality Applications, *Seminar/Project Image Analysis Graz* (2008), pp. 1-25.
6. M. Fiala, ARTag, a fiducial marker system using digital techniques, *Computer Vision and Pattern Recognition* (2005), vol.2, pp. 590-596.
7. A. Sagitov, K. Shabalina, R. Lavrenov and E. Magid. Comparing fiducial marker systems in the presence of occlusion, *Proc. Int. Conf. on Mechanical, System and Control Engineering* (2017), pp. 377-382.
8. K. Shabalina, A. Sagitov, L. Sabirova, H. Li, and E. Magid. ARTag, AprilTag and CALTag Fiducial Systems Comparison in a Presence of Partial Rotation: Manual and Automated Approaches, *Lecture Notes in Electrical Engineering* (Springer, in press).
9. B. Atcheson, F. Heide, W. Heidrich. CALTag: High Precision Fiducial Markers for Camera Calibration, Vision, Modeling, and Visualization Workshop (2010), vol.10, pp. 41-48.

An Automated Optical Inspection system for a tube inner circumference state identification

Chung-Wen Hung*, Jhen-Gu Jiang, Hsien-Huang P. Wu, Wei-Lung Mao

Department of Electrical Engineering, National Yunlin University of Science & Technology, 123 University Road,
Section 3, Douliou Yunlin 64002, Taiwan, R.O.C

E-mail: wenhung@yuntech.edu.tw
www.yuntech.edu.tw

Abstract

An automated optical inspection, AOI, system for a chopstick tube inner circumference state identification is proposed. This AOI system is installed after the material feed equipment to screen for cost reduction. The tube status identification is based on the proposed machine vision software, and implemented with EmguCV library. The algorithms of image processing are used to sort the material into five groups. In this paper, the algorithm will be detailed, and the experimental results will show the proposed AOI system is workable.

Keywords: Machine Vision, AOI, EmguCV, Tube inner circumference.

1. Introduction

As AOI technology advances, it is adopted in more and more production lines, but due to cost, not for traditional industry factories, such as chopstick factories. An expensive process for chopsticks is the chopstick defect detecting, and laborers check the good quality only in the final phase. However, most of the defective products are caused by the original flawed material. Only rely on the naked eye to determine the defects, it is too difficult and waste time. In the other hand, the optical detection methods will not damage the surface of the tube. An AOI system for chopstick material is proposed in this paper. Machine vision technology is used to screen out the tube for flaws before they are processed. In order to have the recovery of defective materials, the defects are sorted into four types: "Large", "Small", "Deformed" and "Empty".

In machine vision, the quality of object imaging can be a critical part. The complexity and accuracy of the algorithm are related to it. Therefore, the Charge-coupled Device, CCD, and

telecentric lens are used to enhance the accuracy of the machine vision system. In order to prevent the influence from the environment light, a stable light source is needed [1], and a circular light source is used to ensure uniform illumination of each tube. The proposed system is based on the machine vision software library, EmguCV[2], to quickly confirm a tube was imaged clearly and in compliance with the imaging requirements of the defect inspection.

2. Related researching

2.1. Region of Interest, ROI

The purpose of ROI is to separate the images captured by the CCD in a particular area by filters, binarization, image cuts, etc. Moreover, it is used to reduce the computational resources required in image processing [3], and it can also reduce the error in the operation of subsequent algorithms with the prior threshold design.

2.2. Edge detection

After the image filtering, grayscale, binarization, the black-and-white boundary point in the ROI will be detected and marked, and the marked line segment is the outline which is the peripheral line of the tube. In many algorithms, Canny detector[4] is more effective in the edge extraction, so in this paper, Canny detector is used to extract the edge of the tube.

2.3. Component Labeling

When edges or binarization of an image is detected, labeling is used to cluster the pixels connected to the same area into the same object. Its purpose is to isolate the noise in some images[5] or the non-interesting content that can not be completely removed in the previous step. These noise and non-interesting content can be ruled out by simple threshold judgment, and then the most complete image information for subsequent feature extraction is got.

3. The development library: EmguCV

There are many software packages developed for AOI, and they are also popular. Such as Halcon, an image processing software from Germany, claims the most effective computer vision software in Europe and Japan. However, due to cost issue, this paper developed the system based on open source libraries. EmguCV is an open source image processing development kit that includes the many relevant libraries required for many applications such as image processing, machine learning and computer vision. Users can choose according to their own needs different programming languages such as C #, VB, C++.and so on. EmguCV solved the lack of OpenCV Graphical User Interface, GUI, and is suitable for more application development.

4. Hardware specifications and configuration

Table 1 shows the specifications of the CCD and lens used in the system proposed this paper. The CCD with a telecentric lens can effectively reduce the image deformation which caused by the normal lens [1]. In order to average the light on each tube and minimize the shadow [6, 7], the light source used in this system is a circular parallel ring light. Figure 1 is the configuration for camera, lens, light and tubes used in this paper. The relative distance between the lens and the tube depends on the working distance of the lens itself.

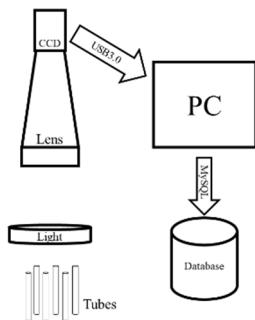


Figure.1 Schematic diagram of the AOI

© The 2018 International Conference on Artificial Life and Robotics (ICAROB2018), Feb. 1-4, B-Con Plaza, Beppu, Oita, Japan

Table 1. Specification of the CCD and lens

Camera	
Interface	USB 3.0
Sensor type	CMOS
Shutter	Rolling shutter
Resolution	3840 x 2748 Pixel
Lens	
Magnification	0.184
Working distance	132.9mm
Computer	
OS	Windows 7
CPU	I7-5500 x64
Development tools	Visual Studio 2017

5. Algorithm and flow chart

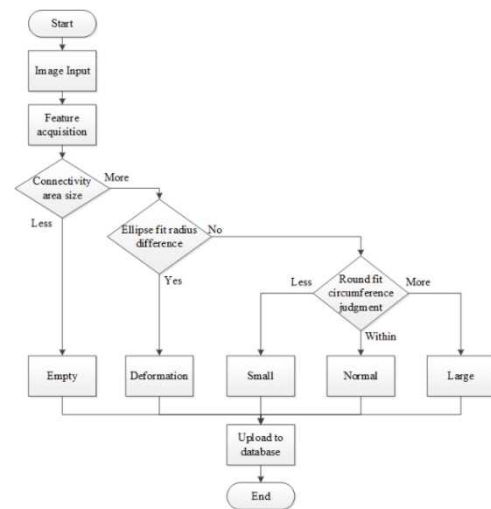


Figure.2 A flowchart of the system

The system flow chart is shown in Figure 2. The main purpose of the system is the inner circumference measurement of the chopstick tube. There is no any image filter adopted in the preprocessing stage in this proposed system. Because the maintenance of the image original information is most important, and filters may remove some critical information. The AOI system sorts the defect materials into five modes: one empty situation, and four defect types. The inspection algorithms are detailed in following:

5.1. Empty

By connecting the size of the region, the system could determine whether the tube on the fixture. If the connected region is bigger than the setting threshold, the system will indicate no tube on the fixture, otherwise. The threshold setting is based on analysis of the inner area of pre-shot photographs.

5.2. Deformation tube

The ellipse fitting algorithm is used to fit an under testing tube to the most suitable ellipse [8]. The difference between the two radii of the fitting ellipse is used to determine whether the tube has a deformation situation. When the difference is bigger than the setting threshold (about 8 pixels), the tube will be denoted as “deformation”.

5.3. Iron filing elimination algorithm

Except empty and deformation, iron filing effect has to be eliminated. The iron filings effect is caused in the process or factory environment, and these iron filings have significant influences on the accuracy in the precise identification. The iron filing elimination algorithm is proposed to eliminate this effect. The Inscribed and circumcircled circles are estimated [8]. When the circumference difference of the two circles is big, the circle fitting is used to estimate the tube inner circumference. Contrary in small difference, what means minor iron filing effect, the circumference is integrated from pixels directly.

6. Experimental results

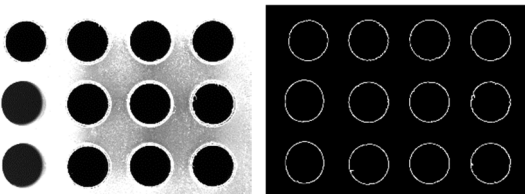


Figure.3 Edge detection

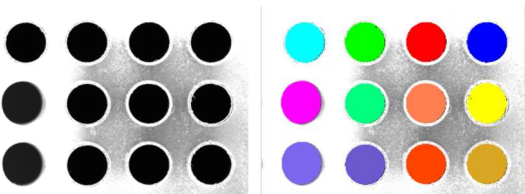


Figure.4 Connectivity region



Figure.5 Photo of the AOI system

6.1. Experimental hardware system

The block diagram and photo of the proposed system are shown in Figure 1 and 5. The results of the pre-processing are present in Figure 3 and Figure 4, what are Edge detection and connectivity region functions.

6.2. Circumference Threshold

The circumference threshold is a key parameter to sort the tube into “Normal”, “Large” and “Small” types when not empty and deformation. As Figure 6, the tubes of three types provided by the factory are measured, then threshold could be decided.

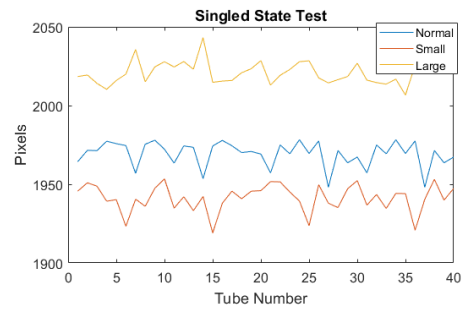


Figure.6 Single state comparison graph

6.3. Mix state test results

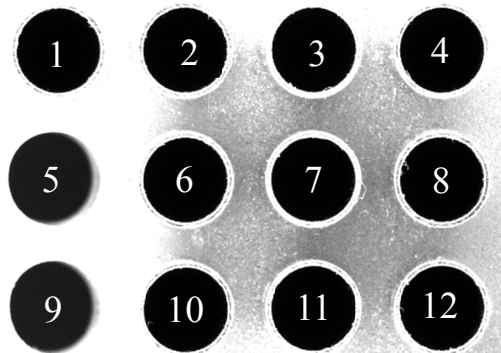


Figure.7 Serial Numbering

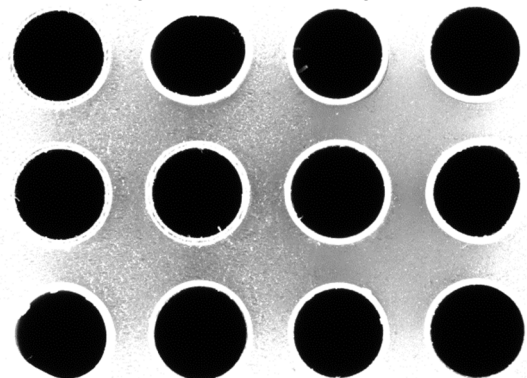


Figure.8 Mixed test 1

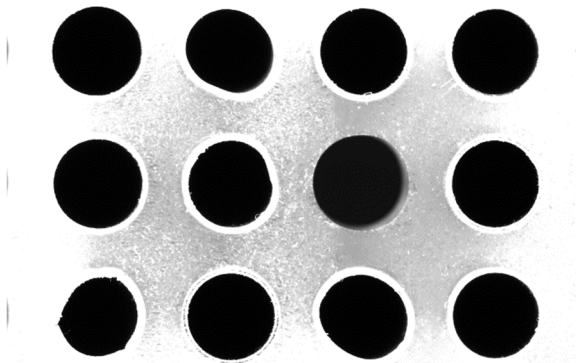


Figure.9 Mixed test 2

Table 2. Test Results 1

Serial Number	Real situation	Identify results
1	Normal	Normal
2	Deformed	Deformed
3	Small	Small
4	Small	Small
5	Normal	Normal
6	Normal	Normal
7	Large	Large
8	Deformed	Deformed
9	Deformed	Deformed
10	Large	Large
11	Small	Normal
12	Large	Large

Table 3. Test Results 2

Serial Number	Real situation	Identify results
1	Large	Large
2	Deformed	Deformed
3	Normal	Normal
4	Small	Normal
5	Large	Large
6	Deformed	Deformed
7	Empty	Empty
8	Normal	Normal
9	Deformed	Deformed
10	Normal	Normal
11	Deformed	Deformed
12	Small	Small

Figure 7 shows the serial number of tubes. The Figure 8 and 9 are the sampling photo, and the Tables 2 and 3 are the inspection results. There is only one error in every test, and the recognition rate of the algorithm reaches 91.67%.

7. Conclusion

An AOI system for a chopstick tube inner circumference state identification is proposed, in this paper. The system can effectively identify a variety of different types of the tube by comparing various parameters and threshold design. The experimental result indicates the 91.67% of the recognition rate, and the system can be used in automated production lines and effectively reduce the production loss.

Acknowledgment

This work is partially supported by the Ministry of Science and Technology, ROC, under contract No. MOST 106-2221-E-224-025, and 106-2218-E150-001.

References

1. H. Liao, Z. Chen and X. Zhang, "Calibration of Camera with Small FOV and DOF Telecentric Lens", *Proceeding of 2013 IEEE International Conference on Robotics and Biomimetics*, Shenzhen, China, 2013.
2. EmguCV.org Available at www.emgu.com/wiki fourth November 2017
3. W. C. Tham, S.I. Woolley, S. Cribbs and D. Anderson, "Diagnostically lossless compression of pipeline inspection data", *Proceedings of Data Compression Conference 2002*, Snowbird, UT, USA, 2002
4. J. Canny, "A computational approach to edge detection", *IEEE Transactions on Pattern Analysis and Machine Intelligence*. Vol. PAMI-8, Iss. 6, Nov. 1986
5. J. Song, Z. Zhao, Q. Zeng and Y. Wei, "An algorithm for eliminating the isolated regions based on connected area in image classification" *Proceeding of IGARSS 2004. 2004 IEEE International Geoscience and Remote Sensing Symposium, Anchorage, AK, USA, 2004*
6. K. W. Khawaja, A. A. Maciejewski, D. Tretter, and C. A. Bouman, "Camera and Light Placement for Automated Assembly Inspection" *Proceeding of Robotics and Automation, 1996. Proceedings of IEEE International Conference on Robotics and Automation*, Minneapolis, MN, USA, USA, 1996
7. Mónica Valenzuela-Delgado Wendy Flores-Fuentes, Miguel E. Bravo-Zanoguera, Alejandro S. Ortiz-Pérez, Daniel Hernandez-Balbuena, Moises Rivas-López, Oleg Sergiyenko, "Felix F. Gonzalez-Navarro, Machine vision system to measuring the velocity field in a fluid by Particle Image Velocimetry: Special Case of Magnetohydrodynamics" *2017 IEEE 26th International Symposium on Industrial Electronics (ISIE)*, Edinburgh, UK, 2017
8. Truc Le and Ye Duan, "CIRCLE DETECTION ON IMAGES BY LINE SEGMENT AND CIRCLE COMPLETENESS", *2016 IEEE International Conference on Image Processing*, Phoenix, AZ, USA, 2016

Implementation of the Mobile Based Robot Arm for Image Recognition

Ji-Hua Li

Graduate school Engineering Science and Technology, National Yunlin University of Science & Technology, 123 Sec. 3, University Road, Douliou, Yunlin 64002, Taiwan

Jr-Hung Guo

Department of Electrical Engineering, National Yunlin University of Science & Technology, 123 Sec. 3, University Road Douliou, Yunlin 64002, Taiwan

Kuo-Lan Su*

Department of Electrical Engineering, National Yunlin University of Science & Technology, 123 Sec. 3, University Road Douliou, Yunlin 64002, Taiwan

E-mail: tpemail77@yahoo.com.tw, g9710801@yuntech.edu.tw, sukl@yuntech.edu.tw

Abstract

The paper develops a mobile based robot arm using KNRm system. The platform of the mobile based robot arm is built as triangle style. The structure of the robot arm uses the Matrix elements that are manufactured by Barden-Powell International Company. The mobile based robot arm integrates some sensors, three DC servomotor motors, one RC servomotor, a controller, and an image recognition module. The mobile platform embeds a robot arm on the front side. The robot arm is one degree of freedom. The driver device of the robot arm is a RC servomotor. The cargo puts on the plank. The robot arm must rise up and put down the plank. In the experimental results, the mobile based robot arm can search and recognize the assigned plank using image binanzation method and Otsu algorithm by the image recognition system. Finally, the robot arm moves approach to the assigned color plank, and catches the plank moving to the assigned position, and puts down the plank.

Keywords: Mobile based robot arm, KNRm system, image binanzation method, Otsu algorithm.

1. Introduction

Autonomous mobile robot and robot arm is the popular subject in recent years. The disadvantage of autonomous mobile robot can not work with the human behavior in the dangerous environment and the robot arm has not the mobility function. It is a good solution to combine autonomous mobile robot and robot arm, and build up a mobile based robot arm. They have been implemented widely in many areas. Thus, how to plan the mobile robot efficiently to complete missions using the robot arm in the unknown and complexity environment, and how to control the robot arm to cooperate with the mobile robot are challenging tasks.

In the past literatures, many experts research on mobile robot. Peng et al. designed a where/track mobile platform to search and rescue in dangerous environment. The motion modes of the mobile platform can be

switched alternatively to adapt on different ground situations [1]. Bloesch et al. presented a state estimation approach for legged robots based on stochastic filtering, and designed an unscented Kalman filter and outliers rejection methodology based on a consistent formulation of the underlying tochastic model [2]. Su et al developed a mobile platform, based on KNR controller. The mobile robot embed a robot arm with four degrees of freedom, and used of light sensors and touch sensors for line tracking and detects the initial location [3].

The paper is organized as follows: Section II describes the system architecture of the mobile based robot arm, and explains the functions of the mobile robot. Section III using an example explains the motion planning method for the mobile robot. Section IV presents the experimental results for the mobile based robot arm to catch and put down the plank using the

© The 2018 International Conference on Artificial Life and Robotics (ICAROB2018), Feb. 1-4, B-Con Plaza, Beppu, Oita, Japan

image recognition system. Section VI presents the brief concluding remarks.

2. Mobile Based Robot Arm

The mobile robot uses omi-direction wheels to be controlled by three DC servomotors. The prototype of the mobile robot is shown in the Fig. 1. The direction angle of each servomotor is 120 degree for each other. The axis location of the mobile robot is defined shown in Fig. 2. The moving direction describes as following:

1. If the mobile robot moves along the Y axis, then

$$-V_1 = V_2, \quad V_3 = 0 \quad (1)$$

2. If the mobile robot moves along the X axis, then

$$-V_1 = -V_2 = 2V_3 \quad (2)$$

3. If the mobile robot rotates along the clockwise direction, then

$$V_1 = V_2 = V_3 \quad (3)$$

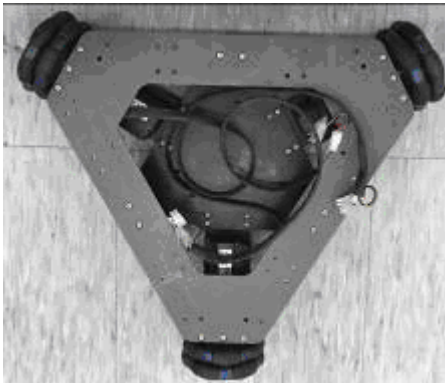


Figure 1. The prototype of the mobile robot

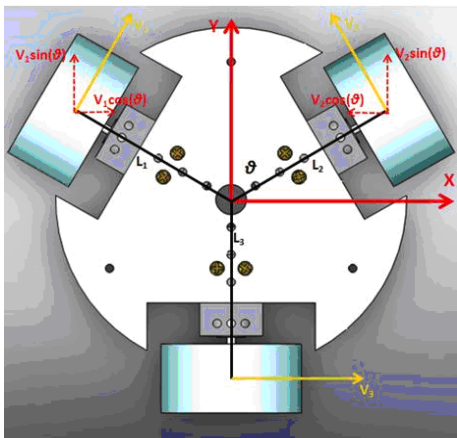


Figure 2. The axis definition of the mobile robot

The KNRm system controls each DC servomotor to execute the rotation range and movement displacement according to the feedback signal of the encoder sensor. The control core of the KNRm system uses PID control law and trapezoidal acceleration and deceleration algorithm to control each DC servomotor, and tune the mobile robot to follow the programmed trajectories. The mobile robot uses three spring elements to decrease vibration and increase moving stability of the robot arm. The robot arm can catch the assigned plank very easily. Three spring elements are fixed on the driver axis.

The robot arm fixes on the front side of the mobile platform to be driven by one RC servomotor as shown in Fig. 3. The structure of the robot arm is built using Matrix elements. The image system is embedded on the top of the gripper to recognize position and color of the box, and searches the assigned box on the competition playground. Then the mobile robot moves to the box, and catches the plank on the box using the robot arm, and moves the plank to put down on another box.

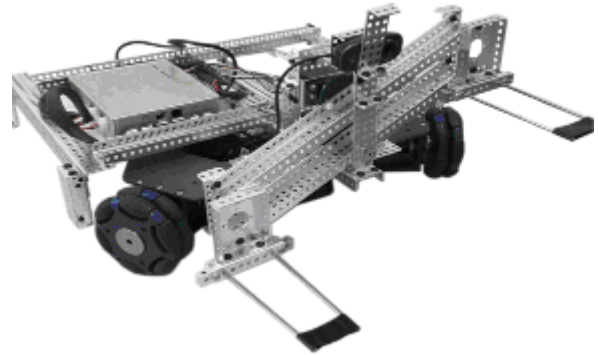


Figure 3. The prototype of the mobile based robot arm

3. Motion Analysis

We explain the motion scenarios of the mobile robot moving on the competition playground (length 4m and width 2m). The start position “S” is assigned on the left side of the competition playground. The size is length 60cm and width 60cm respectively shown in Fig. 4. The “B” is the target position. The mobile robot must catch the assigned plank moving to the “B”.

For a example, we describe the motion scenario for the mobile based robot arm to finish the assigned task. First, the mobile robot stays at the start position shown in Fig. 5(a), and moves to the assigned box shown in Fig. 5(b). The position of the box can be measured

before the competition. The mobile robot records the axis values (X and Y) of each box, and programs the motion trajectory moving to the assigned box according to shape and color of the box. Then the robot arm of the mobile robot catches the object that is located on the top of the box shown in Fig. 5(d), and moves to the centre position of the competition playground. The mobile robot puts down the object in the area shown in Fig. 5(e). Finally, the mobile robot must finish the task in the limitation time, and moves to the start position to stop shown in Fig. 5(f).

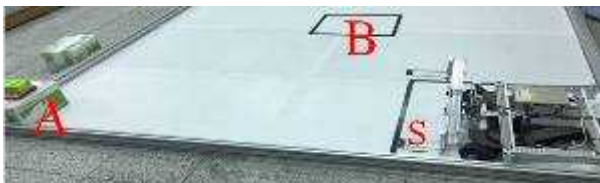
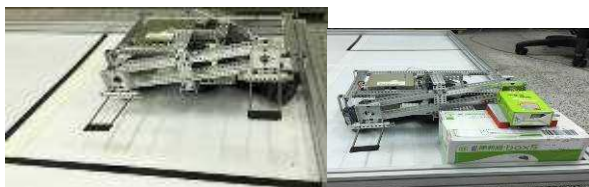
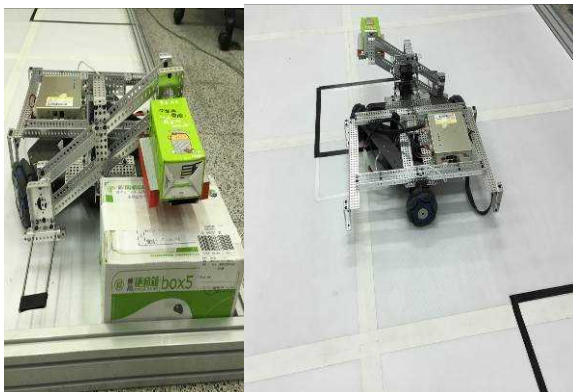


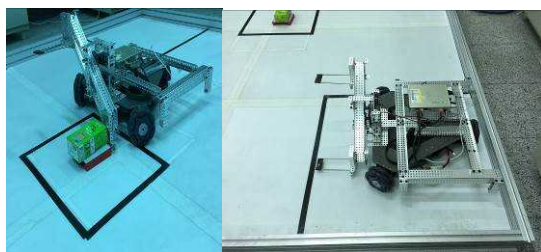
Figure 4. Competition playground and start position



(a) (b)



(c) (d)



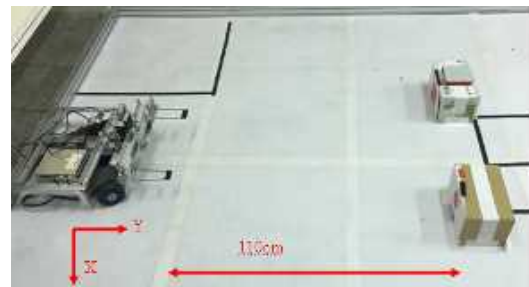
(e) (f)

Figure 5. Motion processing of the mobile robot

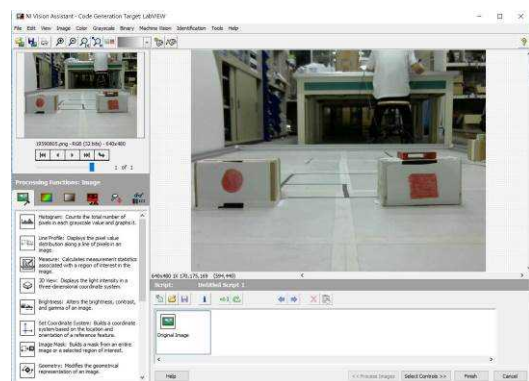
4. Experimental Results

We implement the experimental result on the competition playground using the mobile based robot arm. First, the mobile robot searches the positions of all boxes using the image system to focus on the assigned color and shape mark. The image system can set the parameters using the vision acquisition module and vision assistant module of the LabView software. We put two boxes on the competition playground, and use various graph on the front side of each box shown in Fig 6(a). One is rectangle; the other is circle. The vision system of the mobile robot catches the graph in the centre of each frame, and computes the average value of the measured signals using add array element function.

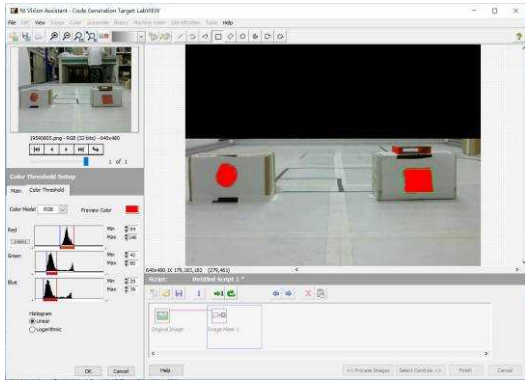
The pre-processing of the vision system uses LabView Software. The processing of image recognition includes four steps, such as open objects, remove small objects, convex hull and particle analysis. The vision system can recognize shape and color of the assigned mark for all boxes shown in Fig.6(b), and compute and remove small objects of the assigned mark shown in Fig. 6(c). Then the vision system finishes convex null and particle analysis for the mark of the box shown in Fig. 6(d) and (e).



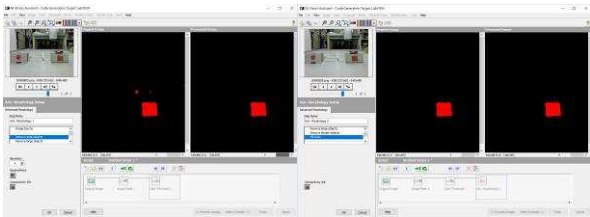
(a)



(b)

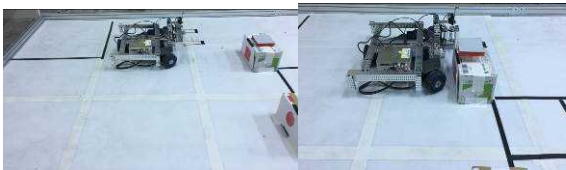


(c)



(d)

(e)



(f)

(g)



(h)

Figure 6. Experimental results

Finally we implement the experimental scenario using the developed mobile based robot arm. The mobile robot can search and move to the position of the assigned box using the vision system show in Fig. 6(f). The control box of the KNRm system uses LabView software to recognize shape and color of the mark to be right. The mobile robot tunes the direction of the robot arm to catch the image of the mark in the centre of the

flame. Then the mobile robot moves to the assigned box, and controls the gripper of the robot arm to catch the assigned color plank show in Fig. 6(g). Finally, the mobile robot moves to the target position “B” to put down the plank, and moves to the start position to stop shown in Fig. 6(h).

5. Conclusion

We designed a mobile robot with a robot arm using KNRm system, and used the Matrix elements to construct the robot arm. The main core of the KNRm system programs trapezoidal acceleration and deceleration algorithm and Proportional-Integral-Derivative (PID) algorithm to control each DC servomotor of the mobile robot, and used image binarization method and Otsu algorithm to classify color and shape of the mark through image recognition system. The mark was located on the front side of the box. In the experimental results, the mobile robot can search and move to the plank, and catch the assigned plank moving to the target position to put down the plank.

Acknowledgements

This work was supported by the Ministry of Science and Technology in Taiwan, (MOST 106-2221-E-224-019).

References

1. A. Peng, Y. Zhou, J. Hu and Y. Ou, “Mechanical design for wheel/track transform mobile platform-search and rescue robot,” *IEEE International Conference on Robotics and Biomimetics*. P.1787, 2014
2. M. Bloesch, C. Gehring, P. Fankhauser, M. Hutter, M. A. Hoepflinger and R. Siegwart, State Estimation for Legged Robots on Unstable and Slippery Terrain, *IEEE/RSJ International Conference on Intelligent Robots and Systems*, pp.6058-6064, 2013.
3. J. H. Guo, K. H. Hsia, K. L. Su and J. T. Wang, Development of the Mobile Robot With a Robot Arm, *International Conference on Industrial Technology(ICIT)*, Taipei, Taiwan, March 14-17, pp.1648-1653, 2016.

Reinforced Quantum-behaved Particle Swarm Optimization Based Neural Networks for Image Inspection

Li-Chun Lai

Computer and Intelligent Robot Program for Bachelor Degree, National Pingtung University

Chia-Nan Ko

Department of Automation Engineering, Nan Kai University of Technology

t105@nkut.edu.tw

Abstract

The paper combines the niche particle concept and quantum-behaved particle swarm optimization (QPSO) method with chaotic mutation to train neural networks for image inspection. When constructing the reinforced quantum-behaved particle swarm (RQPSO) to train neural networks (RQPSONNs) for image inspection, first, image clustering is adopted to capture feasible information. Then the database of image can be built. In this research, the use of support vector regression (SVR) method determines the initial architecture of the neural networks. After initialization, the neural network architecture can be optimized by RQPSO. Then the optimal neural networks can perform image inspection. In this paper, the program of RQPSONNs for image inspection will be built. The values of root mean square error (RMSE) and peak signal to noise ratio (PSNR) are calculated to evaluate the efficiency of the RQPSONNs. Moreover, the experiment results will verify the usability of the proposed RQPSONNs for inspecting image. This research can be used in industrial automation to improve product quality and production efficiency.

Keywords: Quantum-behaved particle swarm optimization, Niche particle, Support vector regression, Image inspection

1. Introduction

The application of image inspection is quite extensive including medical science, machine vision, and predicting analysis of patterns in smart automation production fields.¹⁻⁵ The input images are first filtered by a high-pass filter, which is used to remove direct current and enhance high-frequency components. And then the filtered input images, which are overlapped rather than displaced from each other in the plane, serve as the input images.⁶ Neural networks have the capacities of learning, adaption, and nonlinear mapping of images.⁷

The PSO algorithm possesses the ability of high convergent speed, easily falling in some local optima is its fatal defect. Many researchers have presented revised PSO algorithms and obtained good results.⁸ Another improvement on traditional PSO algorithm is quantum-behaved particle swarm optimization (QPSO).⁹ However, in QPSO, particles fall into local optimal state in multimode optimization problems and cannot find any

better state.¹⁰⁻¹² To overcome the premature phenomenon in QPSO, a modified quantum-behaved particle swarm optimization (MQPSO) is proposed to identify nonlinear systems.¹³ Authors proposed niche particle swarm optimization (NPSO) for image segmentation.¹⁴ In NPSO algorithms, particles changing the place of the course to center the appropriate position (niche) of the particle will be absorbed. Then, particles amalgamate the small appropriate position (small niche) to become a large appropriate position (big niche).¹⁵

This paper combines the niche particle concept, quantum-behaved particle swarm optimization (QPSO) method with chaotic mutation to train neural networks for image inspection. When constructing the reinforced quantum-behaved particle swarm (RQPSO) to train neural networks (RQPSONNs) for image inspection.

2. Modified Quantum Particle Swarm Optimization

From the view of classical dynamics, to avoid explosion and guarantee convergence, particles must be bounded and fly in an attractive potential field. Clerc and Kennedy⁸ have proved that if these coefficients are properly defined, the particle's position p_i will converge to the center of potential field, $pf^c = [pf_1^c, pf_2^c, \dots, pf_n^c]$, and is defined as:

$$pf_i^c = \frac{(c_1 \cdot r_1 \cdot p_i^l + c_2 \cdot r_2 \cdot p^g)}{(c_1 \cdot r_1 + c_2 \cdot r_2)}, i = 1, 2, \dots, n. \quad (1)$$

where p_i^l and p^g are the best position of the i th particle and the global best position; c_1 and c_2 are cognitive and social constriction coefficients, respectively; r_1 and r_2 are random numbers between 0 and 1.

Inspired by the behavior that particles move in a bounded state and preserve the global search ability, Sun et al.¹² proposed the QPSO algorithm. In the QPSO model, the solution of time-independent Schrödinger equation for this system in one dimensional space can be expressed as:¹⁰

$$p_i = pf_i^c \pm \frac{L}{2} \cdot \ln\left(\frac{1}{\lambda}\right), \quad (2)$$

where λ is a random number uniformly distributed on $[0, 1]$ and L is the characteristic length of delta potential well (called "Creativity" of particles) which specifies the search scope of a particle. The mainstream thought point and can be expressed as the following forms:¹²

$$mbest = \left[\sum_{i=1}^n \frac{P_{i,1}}{n}, \sum_{i=1}^n \frac{P_{i,2}}{n}, \dots, \sum_{i=1}^n \frac{P_{i,n}}{n} \right], i = 1, 2, \dots, n, \quad (3)$$

$$L = 2 \cdot \beta |mbest - p_i|, \quad (4)$$

The creative coefficient β with adaptive annealing learning mechanism according to the change rate of optimal estimation has the form:

$$\beta = \beta_{\max} - \Delta\beta \cdot (\Delta fit)^{\gamma}, \quad (5)$$

$$\Delta fit = |p^g - p_i^l|, \quad (6)$$

where $\Delta\beta$ is step length of β , Δfit is the change rate of optimal estimation so far. The mechanism of adaptive annealing learning can overcome the stagnation problem to accelerate the convergent speed.

3. Reinforced Quantum-Behaved Particle Swarm Optimization Neural Networks

3.1. Radial basis function neural networks

One can use a neural network to estimate the input-output relation of a dynamic system. In this paper, radial basis function neural networks (RBFNNs) are adopted because they have a simple structure, as shown in Figure 1. When the Gaussian function is chosen as the radial basis function, RBFNNs can be expressed in the form

$$\hat{y}_j(t+1) = \sum_{i=1}^L G_i w_{ij} = \sum_{i=1}^L w_{ij} \exp\left(-\frac{\|\hat{\mathbf{x}} - \mathbf{m}_i\|^2}{2\sigma_i^2}\right) \quad (7)$$

where $\hat{\mathbf{x}}(t) = [\hat{x}_1(t), \hat{x}_2(t), \dots, \hat{x}_m(t)]^T$ is the input vector; $\hat{\mathbf{y}}(t) = [\hat{y}_1(t), \hat{y}_2(t), \dots, \hat{y}_m(t)]^T$ is the output vector; w_{ij} is the synaptic weight; G_i is the Gaussian function; \mathbf{m}_i and σ_i are the center and width of G_i respectively; and L is the number of the Gaussian functions, which is also equal to the number of hidden layer nodes.

Given a set of training input-output pairs $(\mathbf{x}^{(k)}, \mathbf{y}^{(k)})$, $k = 1, 2, \dots, N$, the optimization problem of RBFNNs is to determine the values of w_{ij} , \mathbf{m}_i , and σ_i to minimize the index

$$J = \sum_{k=1}^N \|\mathbf{y}^{(k)} - \hat{\mathbf{y}}^{(k)}\|^2, \quad (8)$$

where $\hat{\mathbf{y}}^{(k)}$ is the corresponding output of RBFNNs when the input $\hat{\mathbf{x}}$ to the network is equal to $\mathbf{x}^{(k)}$

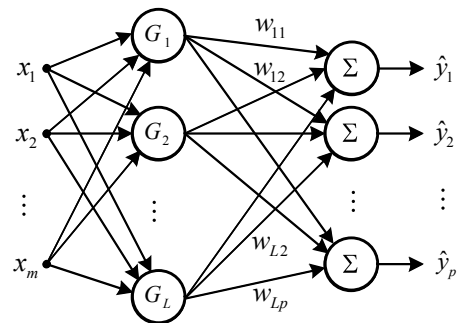


Fig. 1. The structure of RBFNNs.

3.2. Niche evolution

The appropriate position evolves (niche evolution) can solve the multimodal function optimization problems effectively.¹⁶ Adopt the structure of appropriate position and search some local extreme values synchronously and avoid early convergence. It is difficult to determine the appropriate radius (niche radius) σ_{share} . Define the niche radius as follows:¹⁷

$$\sigma_{share} = \sigma_0 r e^{\left(-\lambda \frac{d_{avg}}{R}\right)} \quad (9)$$

$$r = \max_{1 \leq i \leq N} \{u_i - v_i\} \quad (10)$$

$$d_{avg} = \frac{2}{N(N-1)} \sum_{i=1}^{N-1} \sum_{j=i+1}^N d(\varphi_i, \varphi_j) \quad (11)$$

$$R = \sqrt{\sum_{i=1}^N (u_i - v_i)^2} \quad (12)$$

where λ is an adjusting parameter, R is norm of $[u, v]$, σ_0 is the relative parameter of σ_{share} . d_{avg} is the average distance of particles.

3.3. Chaotic mutation

The Chaos phenomenon in nonlinear science means a kind of definite but unpredictable motion state. It has already been applied to optimizing stochastic optimization problems efficiently. This study adopts chaotic mutation operation to avoid falling into some local extreme value. The logistic equation of Chaos iterating is expressed as follows:¹⁶

$$\eta_j^{k+1} = \mu \eta_j^k (1 - \eta_j^k) \quad k = 1, 2, \dots \quad (13)$$

4. Simulation Results

In this paper, a work piece for image inspection is performed by the proposed RQPSONNs. The experiment results will verify the usability of the proposed RQPSONNs for inspecting image shown as Figure 2.



Fig. 2. (a) work piece on the conveyor belt (b) work piece finished inspection.

5. Conclusions

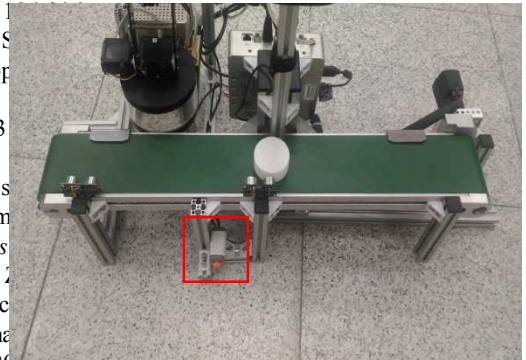
In the study, RQPSONNs combining the niche particle concept, quantum-behaved particle swarm optimization (QPSO) method with chaotic mutation to train neural networks is proposed to solve image inspection. Moreover, the experiment results will verify the usability of the proposed RQPSONNs for inspecting image.

Acknowledgements

This work was supported in part by the Ministry of Science and Technology, R.O.C., under grants MOST 106-2221-E-252-001.

References

1. L. M. Chen, Z. Chen, and A. S. Feng, Image analysis algorithm and verification for on-line molecular sieve size and shape inspection, *Advanced Powder Technology* 25(2) (2014) 508-513.
2. G. B. Massoud, R. R. Denis, and D. Carl, Multivariate image analysis for inspection of multilayer films, *Polymer Testing* 40 (2014) 1-10.
3. J. H. Chen, M. C. S. Self-organizing map of image processing model in *Construction* 73 (2015) 1-10.
4. J. Liu, Z. Tang, Application of self-organizing structures to automatic image inspection in *Journal of Process Control* 25 (2015) 1-10.
5. Y. G. Cen, R. Z. Zou, and Z. Wei, Defect detection on the low-rank matrix in *Part C* (2015) 1200-1215.
6. X. P. Deng and D. M. Zhao, High-pass filtering and frequency spectrum correlation for larger size image recognition, *Optik* 123 (2012) 924-927.
7. P. Banumathi, Artificial neural network techniques used for identifying defects in woven fabric images, *International Journal of Latest Trends in Engineering and Technology* 3(3) (2014) 248-252.
8. A. Ratnaweera, S. K. Halgamuge, and H. C. Watson, Self-organizing hierarchical particle swarm optimizer with time-varying acceleration coefficients, *IEEE Transactions on Evolutionary Computation* 8 (2004) 240-255.
9. M. Clerc and J. Kennedy, The particle swarm: explosion, stability, and convergence in a multidimensional complex space, *IEEE Transactions on Evolutionary Computation* 1 (2002) 68-73.
10. Y. Fang, Y. D. Zhao, M. Ke, X. Zhao, H. H. Lu, and K. P. Wong, Quantum-inspired particle swarm optimization for power system operations considering wind power



- uncertainty and carbon tax in australia, *IEEE Transactions on Industrial Informatics*. 8(4) (2012) 880-888.
11. S. L. Ho, S. Y. Yang, G. Z. Ni, and J. Huang, A quantum-based particle swarm optimization algorithm applied to inverse problems, *IEEE Transactions on Magnetics* 49(5) (2013) 2069-2072.
 12. J. Sun, W. Fang, X. Wu, V. Palade, and W. Xu, Quantum-behaved particle swarm optimization: analysis of individual particle behavior and parameter selection, *Evolutionary Computation* 20(3) (2012) 349-393.
 13. C. N. Ko, Y. M. Jau and J. T. Jeng, Parameter Estimation of Chaotic Dynamical Systems Using Quantum-behaved Particle Swarm Optimization Based on Hybrid Evolution, *Journal of Information Science and Engineering* 31(2) (2015) 675-689.
 14. M. M. Bai, H. Sun, and L. Y. Wu, Method for image segmentation based on niche particle swarm optimization, *Computer Engineering and Applications* 46(3) (2010) 183-185.
 15. G. J. Cheng, Y. An, Z. Wang, and K. Zhu, Oil well placement optimization using niche particle swarm optimization, in *Proceedings of 2012 Eighth International Conference on Computational Intelligence and Security (CIS)*, pp. 61-64.
 16. H. Li, Y. Zhang, A. Wang, Medical Image Registration Based on JS Measure and Niche Chaotic Mutation Quantum-Behaved Particle Swarm Optimization, in *Proceedings of 2010 6th International Conference on Wirelless Communications Networking and Mobile Computing*, pp.23-25.
 17. O. L. Zhao, The research of the niche particle swarm optimization based on self-adaptive radius technology, in *Proceeding of 2009 Asia Pacific Conference on Information Processing*, pp. 97-100.

Development of IoT Module with Backup and Data-security Functions

Jr-Hung Guo*

Department of Electrical Engineering, National Yunlin University of Science & Technology, Taiwan

Kuo-Hsien Hsia†

Department of Electrical Engineering, Far East University, Taiwan

Kuo-Lan Su*

Department of Electrical Engineering, National Yunlin University of Science & Technology, Taiwan

E-mail: g9710801@yuntech.edu.tw, khhsia@mail.feu.edu.tw, sukl@yuntech.edu.tw

Abstract

Internet of Things (IoT) is one of the most popular research topics. There have been many studies and products about this topic. However, there is few researches about the correctness of data and the mutual support of modules. In this paper, we developed an IoT module with multi-sensor and communication interface. It debugs and confirms the data from multiple modules and sensors using the fusion and the redundant algorithms. It can also sustain or replace a possibly fail IoT module via multiple communication interface. The dynamic security key technology is used to ensure the security of data transmission. Hence the IoT system can be more stable and more secure.

Keywords: Internet of Thing (IOT), data fusion, data redundant, dynamic security key.

1. Introduction

Internet of things (IoT), in the past decade, is a very hot research topic. Many consumer and industrial products have already used the IoT technology. However, the security issue of IoT devices has only been taken seriously for the past two years. It is mainly due to less computation power or memory of the microprocessor used in IoT devices. In previous studies, Wurm et al used both commercial and industrial IoT devices as examples from which the security of hardware, software, and networks are analyzed and backdoors are identified [1]. Those security vulnerabilities are a common problem for most devices. Security solutions and mitigation methods

were discussed to help IoT manufacturers secure their products. Sivanathan et al undertook a deeper exploration of network-level security solutions for IoT, by comparing flow-based monitoring with packet-based monitoring approaches [2]. They showed that flow-based monitoring can achieve most of the security benefits of packet-based monitoring, and at dramatically reduced processing costs. Premnath et al showed that a small size of key reduce the cryptographic computational processing requirements quite drastically for IoT nodes [3]. It estimates the cost of breaking public key crypto systems when the adversary is limited by the available resources (i.e., dollar cost) and time (i.e., number of days). It also presents the trade-off between the processing loads for an IoT node versus the

desired time span of privacy protection. Kuusijärvi et al discussed the security challenges of IoT devices at that time and proposed a solution to secure these devices via a trusted Network Edge Device [4]. The major benefit of this approach is that the system can protect the IoT devices with user-defined policies. Additional benefit is the possibility to manage the countermeasures of multiple IoT devices/gateways at once, via a shared interface, thus largely avoiding the per-device maintenance operations. Sadeghi et al gave an introduction to industrial IoT systems, the related security and privacy challenges, and an outlook on possible solutions towards a holistic security framework for industrial IoT systems [5]. From previous researches we know that the security of IoT devices is very important. Therefore, in this paper, we will develop a dynamic data encryption method for IoT module of low-order microprocessors, so that most IoT devices can communicate securely.

2. System Architecture

In this paper, we use 8051 series microprocessor-based IoT module used to develop communication data encryption, and use redundant algorithms and data fusion algorithms to confirm the accuracy of the data detected by multiple modules/sensors with wrong data isolation. The block diagram of this module is shown in Figure 1. The IoT module has UART (Universal Asynchronous Receiver/Transmitter), WIFI, Ethernet and 433/868/915 MHz tri-band multi-channel RF communication module. It can use three kinds of communication interfaces at the same time. So it can be used in different applications because of the powerful communication function. In this IoT module, we designed a communication protocol, as shown in Table 1, to ensure the efficiency/accuracy of data communication. We use the State byte to transmit the index value of the initial dynamic password. Its structure is shown in Table 2. This protocol and the dynamic security key method can ensure the secure communications.

3. Dynamic Security Key Method

In each IoT module will default to 64 ~ 128byte length of the initial security key Table, the structure shown in Table 3.

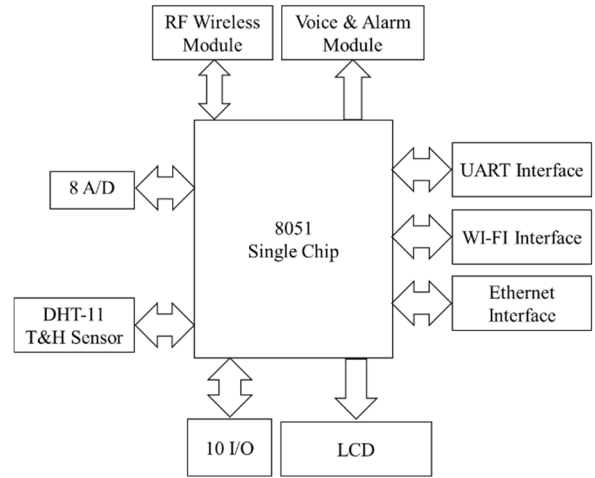


Fig. 1. IOT module Architecture.

At the first communication of the modules, the sender must first randomly generate the address of the Initial Security Key Table. This address is generated by the program counter in the 8051, or similar register or random numbers in other chips. According to the length of ID, this address will be taken an AND operation with 01111111 or 00111111, and the result will be sent to the

Table 1. Communication Protocol.

Byte 0	Byte 1	Byte 2	Byte 3	Byte 4
35H	ID	Sensor Kind	Module	State
4N(N=1~16)				Checksum
Data/Parameter				SUM(all byte)

Table 2. State Byte Structure.

bit 7	bit 6	bit 5	bit 4	bit 3	bit 2	bit 1	bit 0
0	Sensor disable	Electricity low	Deciding factor	Sensor status			
1	Initial password section						

Bit7=0 Sensor status and deciding factor.

Bit7=1 Initial password section.

Table 3. Initial Security Key Table (Example).

01	02	03	04	05	06	07	08
09	0A	0B	0C	0D	0E	0F	10
11	12	13	14	15	16	17	18
19	1A	1B	1C	1D	1E	1F	20
21	22	23	24	25	26	27	28
29	2A	2B	2C	2D	2E	2F	30
31	32	33	34	35	36	37	38
39	3A	3B	3C	3D	3E	3F	40

receiver via State byte of the communication packet. After the confirmation of the correctness by the receiver, a new password generated by PC (Program Counter) and DTPR (Data Pointer Register) will be sent back to the sender as the password for sending the next data verification. The receiver will store these data including sensor kind, module and 4-byte password. Each module can store up to 64 groups (because both the sender and receiver have to store), and overwrite if full. Therefore, if the previously communicated module password is overwritten, the receiver will request the sender to regenerate the encryption key again according to the way of the first communication. The Initial Security Key Table can be regenerated from time to time by the central monitoring system. The dynamic security key process is shown in Figure 2.

Next, we use the actual examples to illustrate the process of generating and using the entire security key. Taking Table 1 as an example, if the PC register is 01D1H, it is obtained after AND with 00000000 00111111.

$$\begin{array}{r}
 00000001\ 11010001 \\
 \text{AND) } 00000000\ 00111111 \\
 \hline
 00000000\ 00001011 = 11\text{H}
 \end{array}
 \tag{1}$$

At this point the sender will send 11H to the receiver, the receiver will get from the address 11H 4 Byte password 11H 12H 13H 14H. Then combine the values of PC and DPTR two registers to get 4 Byte data and XOR with 11H 12H 13H 14H. If PC = 0824H, DPTR = 238AH, the following way to generate encrypted security key.

$$\begin{array}{r}
 08\ 24\ 23\ 8A \\
 \text{XOR) } 11\ 12\ 13\ 14 \\
 \hline
 19\ 36\ 30\ 9E
 \end{array}
 \tag{2}$$

Then the encrypted security key, back to the sender. After the sender receives this set of security keys, it will from the generated initial segment 11H obtain the decryption key 11H, 12H, 13H, 14H, and then use this set of keys to solve the real security key.

$$\begin{array}{r}
 19\ 36\ 30\ 9E \\
 \text{XOR) } 11\ 12\ 13\ 14 \\
 \hline
 08\ 24\ 23\ 8A
 \end{array}
 \tag{3}$$

The result of the solution will be 11H 12H 13H 14H, the resulting security key 08H 24H 23H 8AH XOR again. Then compare the received data is 19H 36H 30H 9EH, if the same to confirm that this group of security key decoding is correct. Then use 4 byte to do data

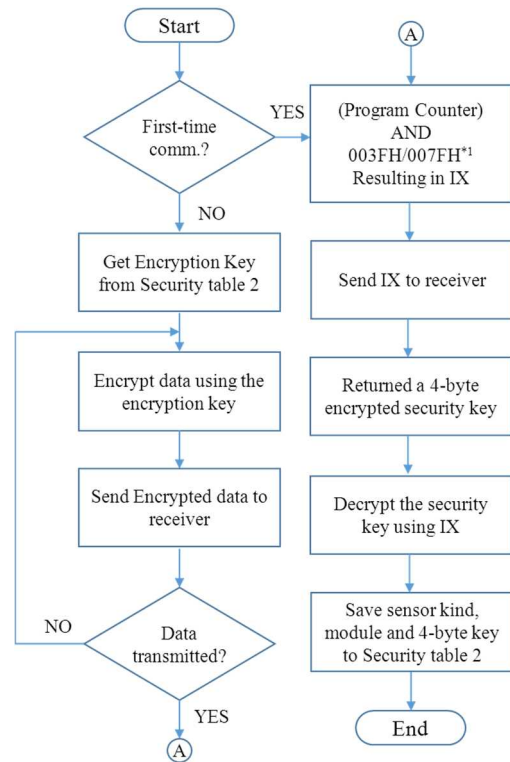


Fig. 2. Dynamic Security Data Transmission Flow Chart.

transmission encryption. The sender in the data transfer is completed, will re-use the value of PC and DPTR to obtain a new 4 Byte security key. And then sent to the receiver. So every communication security key will be different. And because PC, DPTR two register values are unpredictable, so we can achieve a very good data security key.

4. Algorithm

To analyze each sensor more accurately and reduce the misjudgment rate, we used the adaptive fusion method in the monitoring system. This algorithm is very suitable for digital detection signals, and the module sensor data after redundant algorithm processing are all digital. We can analyze the data using the adaptive fusion method.

(A) Redundant management algorithm

In each IoT module, we use redundant management method to calculate exact sensor values, and isolate the faulty measurement values. The redundant measurement values l of the observed system are described as following. For the i_{th} measurement value m_i and boundary error b_i , we can compute the indicator function $I_i(k)$, and

find the power estimated value $\hat{x}(k)$ of each power detection unit at a given sample time k .

$$\hat{x}(k) = \frac{\sum_{i=1}^l m_i(k) I_i(k)}{\sum_{i=1}^l I_i(k)} \quad (4)$$

$$I_i(k) = \sum_{j=1, j \neq i}^l f \left[\left| m_i(k) - m_j(k) \right| \leq (b_i(k) + b_j(k)) \right] \quad (5)$$

$i = 1, 2, \dots, j-1, j, j+1, \dots, j$

$$f[*] = \begin{cases} 1, & \text{if } * \text{ is true} \\ 0, & \text{if } * \text{ is false} \end{cases} \quad (6)$$

(B) Adaptive Fusion Method

Consider a binary hypothesizing-and-testing system with n area detecting point, in which each detecting point employs a predetermined decision rule. The two hypotheses are H_0 and H_1 , where H_0 means that the event does not occur, and H_1 means that the event occurs. They have a priori probabilities $P_0 = P(H_0)$ and $P_1 = P(H_1)$, respectively. The system structure is shown in Fig. 3. Finally we can get the amended rule, detailed derivation can refer the last two references [6,7]. Define the initial weight value as:

$$\hat{w}_0 = \log \frac{P_1}{P_0} \quad (7)$$

Then we define the following parameters:

- u_i : results of individual modules or sensors detect events,
- m : number of points that the event occurs
- n : number of points that the event does not occur
- m_{1i} : number of points that $u_i = +1$ and H_1
- m_{0i} : number of points that $u_i = 0$ and H_0
- n_{1i} : number of points that $u_i = +1$ and H_0
- n_{0i} : number of points that $u_i = 0$ and H_1

Because Adaptive Fusion Method is a digital type of assessment method, so we can get the following evaluation equation.

(1) If the module/sensor signal is reliable, then the weight change is (set $\Delta m_{1i} = 1, \Delta m_{0i} = 1$):

$$\Delta \hat{w}_i \approx \begin{cases} \frac{1}{m_{1i}} \Delta m_{1i} = \frac{1}{m_{1i}} \text{ if } u_i = +1 \text{ and } H_1 \\ \frac{1}{m_{0i}} \Delta m_{0i} = \frac{1}{m_{0i}} \text{ if } u_i = 0 \text{ and } H_0 \end{cases} \quad (8)$$

(2) If the module/sensor signal is not reliable, then the weight change is (set $\Delta n_{1i} = 1, \Delta n_{0i} = 1$):

$$\Delta \hat{w}_i \approx \begin{cases} -\frac{1}{n_{1i}} \Delta n_{1i} = -\frac{1}{n_{1i}} e^{\hat{w}_i + \hat{w}_0} \cdot \Delta n_{1i} = -\frac{1}{m_{1i}} e^{\hat{w}_i + \hat{w}_0} \text{ if } u_i = +1 \text{ and } H_0 \\ -\frac{1}{n_{0i}} \Delta n_{0i} = -\frac{1}{n_{0i}} e^{\hat{w}_i + \hat{w}_0} \cdot \Delta n_{0i} = -\frac{1}{m_{0i}} e^{\hat{w}_i + \hat{w}_0} \text{ if } u_i = 0 \text{ and } H_1 \end{cases} \quad (9)$$

Finally, we can get the adaptive fusion rule of each sensor weight as:

$$\hat{w}_i^+ = \hat{w}_i^- + \Delta \hat{w}_i \quad (10)$$

where \hat{w}_i^+ and \hat{w}_i^- represent the weight after and before each updating. And the criteria that \hat{w}_i^+ reach stable can be set by the monitoring system.

5. Experimental Results

We use MCS-51 series of single-chip microprocessor to develop dynamic security key technology and the redundant method and adaptive fusion method to isolate the problematic sensors or IoT modules. The module could have communication interfaces of Ethernet, WiFi, RF and others. This IoT module is a modular design. Up to 3 communication interfaces can be installed on demand at a time to ensure successful communication. When there is a problem with the data in the IoT module, the monitoring system will isolate the problematic IoT module data. IoT module communication interface and group status are shown in Figure 3.

Figures 4(a) & (b) show the two IoT modules that the actual IoT module uses dynamic security key to connect successfully. Figure 4(c) shows the real picture of the dynamic security key in the monitoring system. In this screen we can see the status of each IoT module connection and dynamic security key. And in this screen can also be updated IoT module default dynamic security key table. Figure 4(d) shows the monitoring screen of the IoT module A/D and I/O status.

6. Conclusion Tables

We used the dynamic security key technology and redundant methods, and adaptive fusion method on the IoT module of 8051 single-chip main controller. Because the 8051 single-chip is a lower-order microprocessor, it is difficult to use complex encryption techniques. We use PC and DPTR registers of 8051 single-chip microprocessor to generate the index of the dynamic security key table. Then the dynamic security key will be re-obtained in every communication. This method makes the encryption key unpredictable, and can ensure data communications security without heavy loading of a

single chip microprocessor. Practical test has confirmed the effectiveness of this method. In addition, we also use redundant methods and adaptive fusion methods on IoT modules to identify and isolate IoT module data. The effectiveness of this method has also been verified by actual test. The method developed in this paper can also easily be transferred to other single-chip microprocessors. In the future, we will continue to increase the complexity of the dynamic security key for more secure communications. And we will also continue to strengthen IoT module data confirmation and backup mechanism, IoT system can be more stable for more applications.

References

1. J. Wurm, K. Hoang, O. Arias, A.R. Sadeghi and Y. Jin, Security analysis on consumer and industrial iot devices, *2016 21st Asia and South Pacific Design Automation Conference (ASP-DAC)*, IEEE (2016) 519-524.
2. A. Sivanathan, D. Sherratt, H.H. Gharakheili, V. Sivaraman and A. Vishwanath, Low-cost flow-based security solutions for smart-home IoT devices, *2016 IEEE International Conference on Advanced Networks and Telecommunications Systems (ANTS)* (2016) 1-6.
3. S.N. Premnath and Z.J. Haas, Security and privacy in the internet-of-things under time-and-budget-limited adversary model, *IEEE Wireless Communications Letters* 4(3) (2015) 277-280.
4. J. Kuusijärvi, R. Savola, P. Savolainen and A. Evesti, Mitigating IoT security threats with a trusted Network element, *2016 11th International Conference for Internet Technology and Secured Transactions (ICITST)*, IEEE (2016) 260-265.
5. A.R. Sadeghi, C. Wachsmann and M. Waidner, Security and privacy challenges in industrial internet of things, Design Automation Conference (DAC), in: *Proceedings of the 52nd ACM/EDAC/IEEE Design Automation Conference (DAC'15)*, IEEE, (2015) 1-6.
6. N. Ansari, J.G. Chen and Y.Z. Zhang, Adaptive decision fusion for unequiprobable sources, *IEE Proceedings-Radar, Sonar and Navigation* 144(3) (1997) 105-111.
7. N. Ansari, E.S.H. Hou, B.O. Zhu and J.G. Chen, Adaptive fusion by reinforcement learning for distributed detection systems, *IEEE Transactions on Aerospace and Electronic Systems* 32(2) (1996) 524-531.

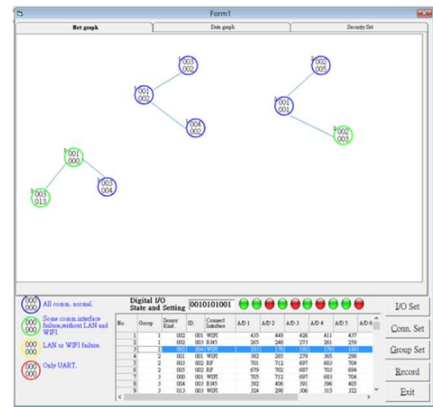


Fig. 3. IOT Module communication interface, and group status.

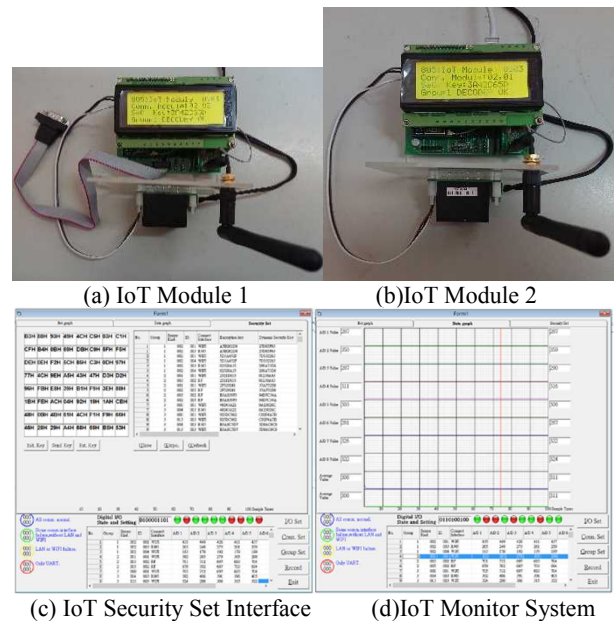


Fig. 4. IoT Conn. States and User Interface.

Development of Auto-Stacking Warehouse Truck

Kuo-Hsien Hsia*, Ming-Guang Wu, Jun-Nong Lin, Hong-Jie Zhong, and Zh-Yao Zhuang

Department of Electrical Engineering, Far-East University, Taiwan

Tainan, 74448, Taiwan (R.O.C.)

E-mail: khhsia@mail.feu.edu.tw

www.feu.edu.tw

Abstract

Warehouse automation is a very important issue for the promotion of traditional industries. For the production of larger and stackable products, it is usually necessary to operate the stacker for the stacking and storage of the products. The general autonomous warehouse-truck does not have the ability of stacking objects. In this paper, we develop a prototype of auto-stacking warehouse-truck that can work without direct operation by a skill person. Just commanded with an RFID card, the stacker truck can move under the prior-planned route, and pick and deliver the product from the designated storage area or deliver and put the product to the designated storage area in the warehouse. It can significantly reduce the manpower requirements of the skilled-person of forklift technician and improve the safety of the warehousing area.

Keywords: Warehouse automation, Stacking truck, Autonomous warehouse truck, RFID.

1. Introduction

The industrial automation has been developed for more than 60 years. It includes manufacturing automation, warehouse automation, and logistics automation. No matter in which one of these automations, robots always play an extremely important and crucial role in the industrial automation. For the manufacturing industry, object movement is always inevitable in the process of purchasing of raw materials or components, loading of materials, packing of finished products, import of goods and the shipment of goods. A conveyor belt is usually used for delivering these components, semi-finished products and finished product in the production line. However, after the product is completed and packaged, it is necessary to carry the manpower to carry and stack products when entering the warehouse or when shipping from the warehouse.

Although the automation of manufacturing processes and the automation of manufacturing industries have been able to evolve to unmanned factories, it is usually still necessary to manually drive the stacker from factory to warehouse, from warehouse to delivery, to inbound and outbound delivery of the warehouse, etc. to carry out stacking and picking operations. To drive a stacker requires professional training. In Taiwan, a technician license (Technician for fork lift operation) with the Ministry of Labor is required to qualify for driving a stacker. In addition, where people work, they must also cooperate with lighting, air circulation, and various conditions of work safety. Therefore, if it is not necessary to work with manpower, then the cost of lighting and air conditioning can be saved and the space can be used more effectively. Hence many researchers have invested in storage automation research. Many logistics providers

also include warehouse automation as one of the most important work items available today.

Giordano et. al considered a matrix-based discrete event control approach for a warehouse [1]. Xie et al use RFID (radio frequency identifier) and wireless sensor network in managing a warehouse [2]. In [3], Adinandra et al said that autonomous mobile robots (AMR) have emerged as a means of transportation system in warehouses. Wang et al proposed a positioning system composed of an RFID reader equipped with forklift and terrestrial channels embedded RFID tags to improve warehouse management efficiency [4]. Amazon makes extensive use of robots for product collation and warehouse management and had 45,000 robots across 20 fulfillment centers in the early 2017 [5].

In this paper, we will develop a small warehouse truck with the function of auto-stacking. Here “auto-stacking” means the goods can be stored in stack manner with detection of numbers of stacked goods and it will alarm when the storage area is full.

2. System Architecture

In the case of a typical factory, when the goods are manufactured by the production line and packaged, they are usually manually moved to a van and then stacked by a technician of folk-lifter to the warehouse area. When there is a shipping requirement, the same way, they will be transported in the same way from the warehouse area to the shipping area for packing or into the container. Different products will be placed in different warehouses or different counter. We assume that on the product or its package, there is an RFID (radio frequency identifier) tag for identification. In addition, our scenario assumes that the warehouse is an unmanned environment and all orders are made in the shipping area or packing area. Because an unmanned storage environment does not need any lighting for vision and air-conditioning, it is energy-saving. It also can reduce the possibility of potential danger of injury caused by the devices movement or improper operation since no person is required to work in it. The flow of the goods with RFID tag is shown in Figure 1.

Thus the warehouse truck with the auto-stacking ability should be composed of three parts: the driver part to driving the motors of the truck and the mechanism of the folk-lift device, the control part to command the truck the destination and route, and the sensor part including RFID

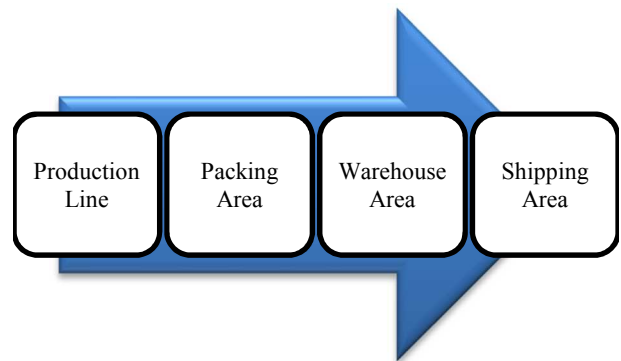


Fig. 1. Flow of goods with RFID tag.

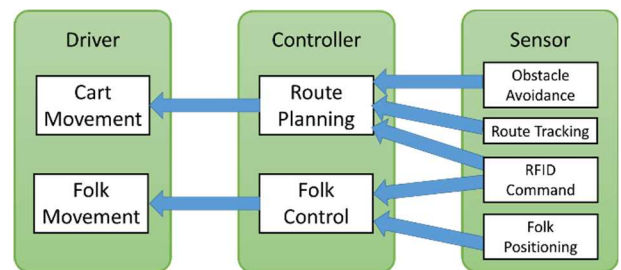


Fig. 2. System architecture of the auto-stacking warehouse truck.

reader for commanding, sensors for obstacle avoidance and tracking the route, and sensors for the folk of the truck. The system architecture of the auto-stacking warehouse truck is shown in Figure 2.

3. Simulation

The scenery of our simulation includes a shipping area (also the packing area) and two warehouse area. The warehouse truck will be commanded to take the goods from factory packing area to the correct location of the warehouse and to leave the goods in the correct storage counter or to take the correct good from the storage counter of the warehouse to the shipping area. The goods can be stacked in the designated warehouse. For simplicity, the warehouse truck moves under the guide of a marked curve on the floor. To distinguish different warehouse, we marked a colored tag on the track. The whole simulation scenery is shown in Figure 3.

Our experimental truck is based on aluminum extruded material as a skeleton. A microchip 16-Bits MCU is used as the kernel and an Arduino chip is supplemented to control the truck. An infrared trace sensor is used to

detect the route planned in advance, so that the truck can follow the route. A color sensor is used to read different storage areas. Truck moving and the fork moving up and down is driven by a 12VDC deceleration motor. The fork stretching is driven by a 5VDC stepper motor. Figure 4 shows our experimental auto-stacking warehouse truck. The truck is initially in the packing area. We use an RFID card to command the truck to pick up the goods and take it to the designated storage counter. The goods will be stored in a stacked manner.

There are two function buttons and an emergency stop switch on the truck, with the green button for picking goods up from the warehouse area to the shipping area, and the yellow one for delivery goods to the warehouse area for stack. The different warehouses are distinguished by two RFID cards. There is a stacking limitation in each warehouse area. The truck can move under the command of pushed button and the read RFID message. Once the destination warehouse is full of goods and a goods is planned to be stacked into, the warning light will be bright. The alert can be released by changing the command mode. In our simulation, the goods can be smoothly transported from the packing area to the storage area for stacking, or picked up from the storage area and transported to the shipping area. Figure 5 shows the scenario that a goods is in transportation to the warehouse area A.

4. Discussion and Conclusion

In this paper, we have made a brief discussion of the advantages of an unmanned warehouse. In order to improve the space efficiency of the limited storage area, stacked storage of goods is a good idea. In order to realize such a warehouse concept, we designed a simulated warehouse truck with function of auto-stacking. It can move on the specified route and store the goods in a stacked way to the designated area. When the stack area is full, it can alert the operator to change his instructions. This idea can be realized in a real warehouse area with cubic packed goods such as televisions, refrigerators, or air conditioners.

References

1. V. Giordano, J.B. Zhang, D. Naso and F. Lewis, Integrated supervisory and operational control of a warehouse with a

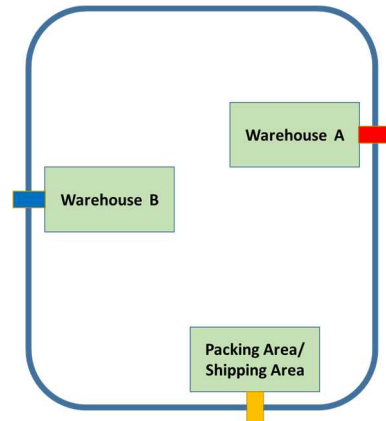


Fig. 3. Simulation Scenery.



Fig. 4. Our experimental auto-stacking warehouse truck.



Fig. 5. A snap of the warehouse truck working.

matrix-based approach, *IEEE Trans. Automation Sci. and Engr.* 5(1) (2008) 53 – 70

2. Z. Xie, W. He, L. Lv and J. He, The implement of warehouse management system based on RFID and wireless sensor network, *IET Int'l Conf. on Wireless Sensor Network 2010* (2010) 98-103.

3. S. Adinandra, J. Caarls, D. Kostić, J. Verriet and H. Nijmeijer, Flexible transportation in warehouses, in: *Automation in Warehouse Development* (Springer, London, 2012).
4. H. Wang, T. Cheng, and Z.A. Wu, Research on positioning algorithm of forklift-mounted RFID reader, *Sensors & Transducers* **174**(7) (2014)164.
5. S. Shead, Amazon now has 45,000 robots in its warehouses, *Business Insider, UK*, Jan. 2017. Available at: <http://uk.businessinsider.com/amazons-robot-army-has-grown-by-50-2017-1>

Development of Four-axis SCARA Robotic Arm Built on Automation Control System

Jr-Hung Guo

*Department of Electrical Engineering, National Yunlin University of Science & Technology, 123 Sec. 3, University Road
Douliou, Yunlin 64002, Taiwan*

Kuang-Wei Chuang

*Department of Electrical Engineering, National Yunlin University of Science & Technology, 123 Sec. 3, University Road
Douliou, Yunlin 64002, Taiwan*

Kuo-Lan Su*

*Department of Electrical Engineering, National Yunlin University of Science & Technology, 123 Sec. 3, University Road
Douliou, Yunlin 64002, Taiwan*

E-mail: tpemail77@yahoo.com.tw, g9710801@yuntech.edu.tw, sukl@yuntech.edu.tw

Abstract

The paper presents a integral design method to integrate “DFM” (Design for Manufacturing) and “DFV” (Design for Verification), and completes the production system from simulation to actual verification using the SCARA robot arm. In the aspect of kinematics of horizontal joint, the 2D model is established by mathematical derivation and the analysis of the robot arm characteristics using “Jacobian” kinematic, and integrates into the verification design. The electromechanical integration of the proposed system includes a SCARA robot arm, automatic control components, sensors; electrical elements, pneumatic circuit design and software programming for implement. Then user can lead the robotic arm to run the coordinates and movement path with proper accuracy, efficiency and reliability. The program language of the SCARA uses “DRL” (DELTA Robot Language) that is developed by DELTA Company. This research also proposes a design method using automatic palletizing simulate layout for the SCARA robot arm, and verifies the precious positioning of the SCARA robot arm.

Keywords: DFM, DFV, SCARA robot arm, DRL

1. Introduction

A robot arm is a mechanical device that is driven by some electronic motors or pneumatic actuators. A well-trained robot arm can be instead of laborers to complete assigned tasks automatically. The purpose of the paper is to implement a four-degree-of-freedom SCARA robot arm, and finishes the assigned tasks. In the control aspect, a PLC-based (ASDA-MS system) controller is used to control the SCARA robot arm.

There are some researches regarding the robot arm in recent years. For example, Su et al. designed a seven-joint robot arm using PC-based controller. The robot arm can catch the pencil to write the assigned words on the platform, and plotted the house outlook, and built a church using some wooden blocks [1]. Sim et al.

presented a binocular stereo vision to decide the desired location of the SCARA robot arm [2]. Cao et al. designed a 5-DOF SCARA robot arm for welding, and built the model and the kinematic equations using D-H method [3].

The paper is organized as follows: Section II describes the system architecture of the SCARA robot arm, and explains the functions of the PLC-based controller (ASDA-SM). Section III describes the specifications and operation range of the SCARA robot arm. Section IV presents simulation result and experimental scenario for the SCARA robot arm to catch a pen to verify the working precision. Section VI presents the brief concluding remarks.

2. System Architecture

© The 2018 International Conference on Artificial Life and Robotics (ICAROB2018), Feb. 1-4, B-Con Plaza, Beppu, Oita, Japan

The system architecture of the SCARA robot arm system is shown in Fig. 1. The implementation system contains a PC-based computer, a PLC-based controller (ASDA-SM), four AC servomotors, a solenoid and a gripper and a human machine interface (HMI). We use a ASDA-SM controller, a ball spline, four AC servomotors, a solenoid and a gripper to integrate the SCARA robot arm. The solenoid drives the gripper can catch the assigned object.

The core of the program language is DRAS. The DRAS is developed by the DELTA Company, and is match with the national standard communication protocol (IEC61131-3), and integrates the PLC control system, and parameter setting of each servo-controller (ASDA-MS), and the driver software of the HMI. The function of DRAS can communicates with the PC system via Modbus interface, and processes the vision signals through Emgu system using Visual Studio C # language.

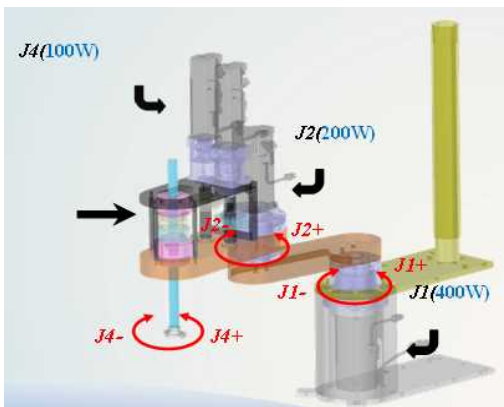


Figure 1. The SCARA robot arm

The prototype of the controller (ASDA-SM) shows in the Fig. 2. We explain each function of the controller. The controller can use MODBUS, RS485 or RS232 interface to connect with the computer. “A” part is the communication port with the HMI device. The controller can use EtherNet, USB1, USB2 or DMCNET interface to connect with the computer in the “B”. “C” part is the standard AC power input (R,S,T). “D” part is the DC power input (24V) and enable of the servomotor. “E” part is output terminal with digital signals. “F” part is enable the DC power input (24V). “G” part connects to the ground to protect the controller. Four AC servomotors will connect with the part “H” of the controller. The limit positions of each servomotor connect with the part “I”, and decide the moveable

range of each joint. “J” part is the digital signals with 24 points for users. “K” part connect with the encoder of each servomotor as feedback signal and measure the real-time rotation angle.

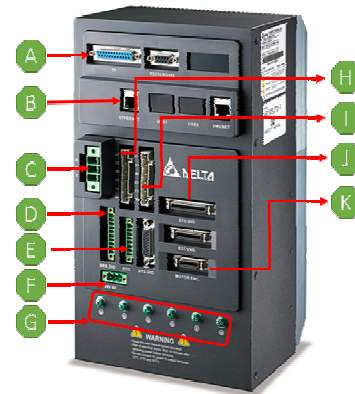


Figure 2. PLC-based controller (ASDA-SM)

3. SCARA Robot Arm

The SCARA robot arm has four DOFs, (Degree of Freedom) to be shown in Fig. 3. The first and second joints rotate along the Z axis. The rotation radius of two joints is the same to be 205mm. the rotation angle of the first joint is $\pm 130^\circ$, and the second joint is $\pm 150^\circ$. The movement displacement of the third joint is 150mm. the rotation angle of the fourth joint is $\pm 180^\circ$. The specifications of the SCARA robot arm are shown in the table1. The prototype of the SCARA robot arm is shown in Fig. 3. The operation range of the robot arm is shown in Fig. 4. User can program various working space of the robot arm using the simulation software.

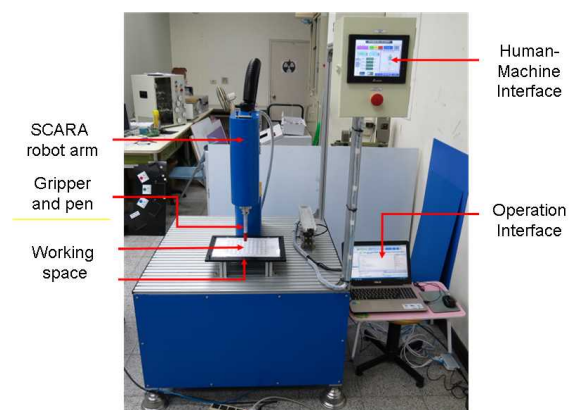


Figure 3. Prototype of the SCARA robot arm

In the assigned task, the SCARA robot arm can complete various assigned tasks such as coming and going on two points or many points. In the first task, we will test the moving precision and positioning precious for the SCARA robot arm to be right. Then user can use the robot arm to work in automation field.

Table 1. Specifications of the SCARA robot arm

Axes number		4
Degree of freedom		4 Dof*
Length(Join 1+Join 2)		410mm(205mm+ 205mm)
Loading	Nor.	1 kg
	Max.	3 kg
Operation range	J1	$\pm 130^\circ$
	J2	$\pm 150^\circ$
	J3	150mm
	J4	$\pm 180^\circ$
Precision	J1+J2	$\pm 0.01\text{mm}$
	J3	$\pm 0.01\text{mm}$
	J4	$\pm 0.01^\circ$
Radius of ball spline		16 ψ
Weight		About 18 kg

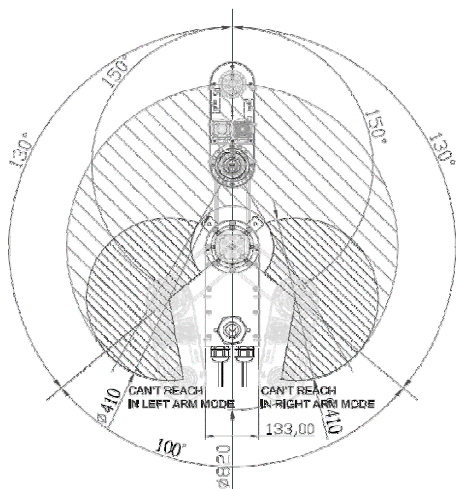


Figure 4. Operation range of the SCARA robot arm

4. Experimental Results

We implement the operation precision of the SCARA robot arm. In the experiment, the robot arm catches a pen to touch on eighty positions with concentric circles, and see the offset distance from the centre point. The maximum radius of each concentric circle is 5mm. the

distance of each concentric circle is 20mm shown in Fig. 7. The operation processing of the robot arm is from top to bottom, and touches each point is from left to right. First we can make the simulation method to verify the robot arm to do the assigned task. The simulation results are shown in Fig. 5. The robot arm runs the processing from the first point that locates on the upper left corner of the working space. We can see the robot arm touch the tenth point shown in Fig. 5(a). Then the robot arm touch the twenty point, the thirty point,, the seventy point and the eighty point shown in Fig. 5(b)-(h).

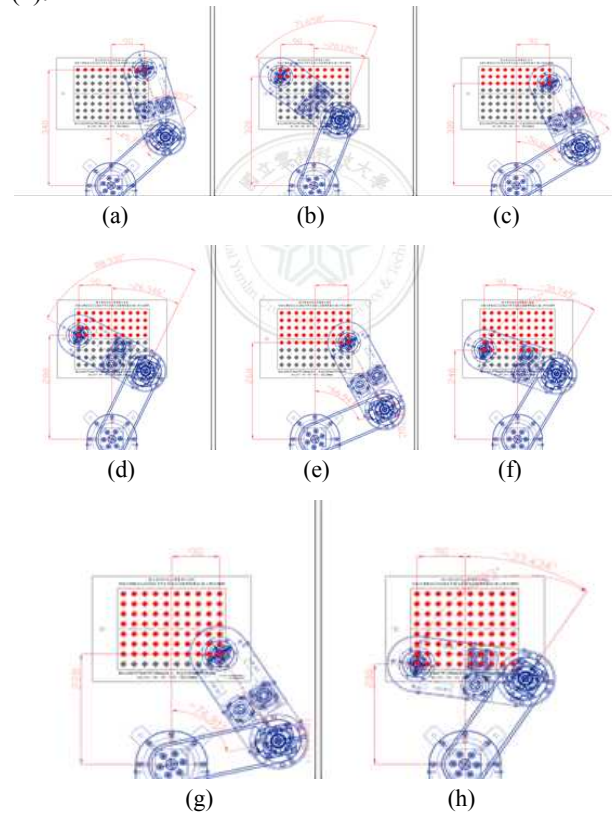


Figure 5. Simulation results of the SCARA robot arm

In the experimental scenario, the SCARA robot arm catches a pen to touch eighty points with concentric circles. The working space and the relation distance of each working position are shown in Fig. 6. The SCARA robot arm must control the pen moving to known position of each point, and falls down to touch the assigned point. The robot arm touches the first point shown in Fig. 6(a). Then the pen of the robot must rise up and move to the next point to do the same processing. The robot arm touches the tenth point, the fifty point

and the eighty point shown in Fig. 6(b)-(d). Finally we can see the experimental result show in Fig. 7. The robot arm can control the pen to touch the centre position of each concentric circle.

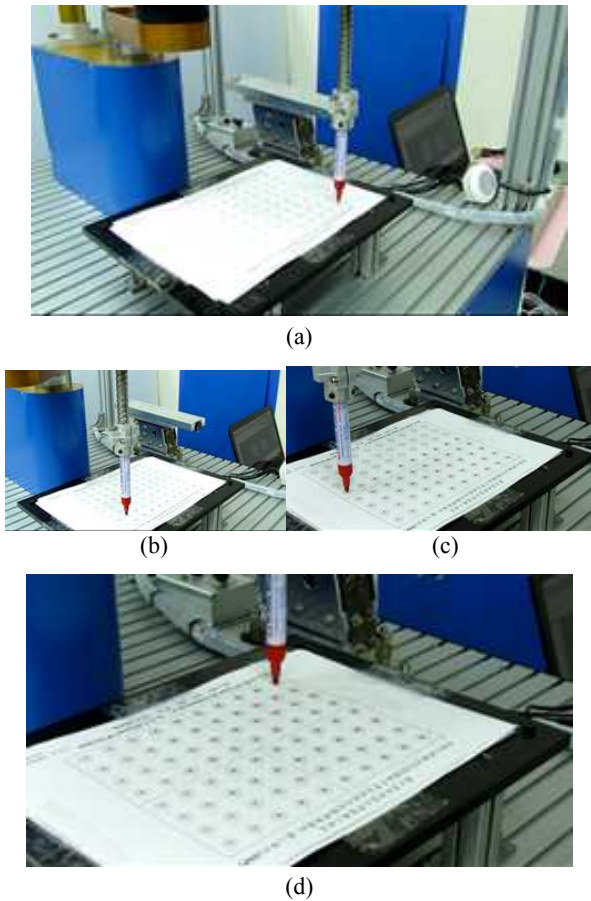


Figure 6. Working process of the SCARA robot arm

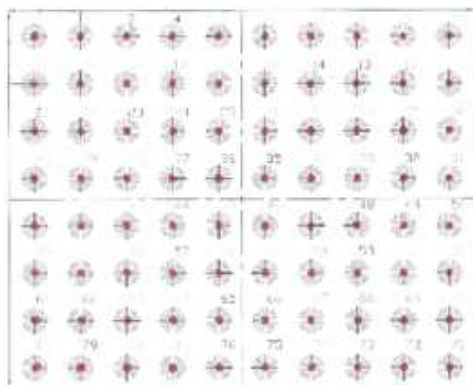


Figure 7. Experimental result of the SCARA robot arm

5. Conclusion

The papers implemented the working precision for a four joints SCARA robot arm, and controlled the robot arm using PLC based system. The PLC based control system is ASDA-MS that is produced by DELTA Company in Taiwan. We calculated motion displacement and rotation angle of each joint according to the known position of each concentric circle. In the experimental results, the SCARA robot arm used the simulation method to verify the control processing to be right. Then the robot arm catch the pen to test the positioning precious to be nice, and finished to touch eighty points on the working space.

Acknowledgements

This work was supported by the Ministry of Science and Technology in Taiwan, (MOST 106-2221-E-224-019).

References

1. S. T. Su and K. L. Su: Development of the Motion Control for a Robot Arm, *International Journal of Research and Surveys* (ICIC Express Letter, Part B: Applications), Vol. 7, No. 3(2016), pp.717-724.
2. H. S. Sim, Y. M Koo, S. H. Jeong, D. K. Ahn and B. N. Cha: A study on visual feedback control of SCARA robot arm, *International Conference on Control, Automation and System* (2015), pp.1268-1270.
3. K. L. Su, B. Y. Li and C. H. Chang : Vision Based Multi-pattern Formation Exchange of Mobile Robots, *International Symposium on Robotics* (2012), pp.196-200.
4. K. L. Su, B. Y. Li and C. H. Chang : Vision Based Multi-pattern Formation Exchange of Mobile Robots, *International Symposium on Robotics* (2012), pp.196-200.

Novel Detection Scheme for Stolen Password File

I-Hsien Liu

Department of Electrical Engineering, National Cheng Kung University, Tainan City, 70101, Taiwan

Chia-Hsiu Chen

Institute of Computer and Communication Engineering, National Cheng Kung University, Tainan City, 70101, Taiwan

Jung-Shian Li

Department of Electrical Engineering, National Cheng Kung University, Tainan City, 70101, Taiwan

E-mail: ihliu@cans.ee.ncku.edu.tw, chchen@cans.ee.ncku.edu.tw, jsli@mail.ncku.edu.tw

www.cans.ee.ncku.edu.tw

Abstract

The use of traditional password is the most common and important authentication credential for today's online society. How to avoid password cracking and detect the event of stolen password file has become an important information security issues. Accordingly, our research improves the Honeyword system proposing a new password storage mapping method. If the password file is stolen, an attacker could not know any user's correct password. We apply to Open LDAP Server to prove its feasibility.

Keywords: System Security, Password Security, Honeyword System, Open LDAP.

1. Introduction

Over the past decades, with the popularity of personal computers and mobile devices, the convenience of the Internet, and the development of social networks, more and more people rely on the Internet to deal with or share things on life, such as online payment, online shopping, etc. The school also provides a variety of online services, such as course enrollment system, online courses, etc., to provide teachers and students more convenient campus life. All of the above are need to use the user authentication to achieve identity confirmation in order to use the appropriate application.

Password, still the most important credential for today's account certification. Therefore, it plays a very important role in human life. The evolution of the password so far has developed a variety of forms to achieve certification. For example, fingerprints, sound waves, retina and so on. However, the traditional digital password authentication credential is still widely accepted by the public, but in the

past few decades, the content of this certification mechanism hasn't been much change.

In recent years, information security issues have gradually been taken seriously, system security has become one of the considerations in the use of services by users. In particular, the password is the first line of defense, but the file leaks are endless. These common password leak events, causing the user's personal information to be stolen. Not only the occurrence of identity theft, but also cause serious property damage. According to Gemalto's 2016 report [1], the most serious is the account access, followed by identity theft.

2. Background and Related work

2.1. Open LDAP

Open LDAP is an open source implementation of the Lightweight Directory Access Protocol (LDAP). LDAP is a subset of the X.500 directory standard protocol and is a cross-platform standard transport protocol. It is not only available on demand, but also simpler than the

X.500 and supports TCP / IP. It not only retains the advantages of the X.500 directory, but also reduces the overall cost of management, so that the system access to directory services can be more convenient.

The LDAP data model is stored in a tree-like structure, providing faster search efficiency. Ldap has many advantages, such as the user can communicate with each other through a common protocol, so that the host can exchange the data between different protocols or non-uniform data format. In addition, the manager can classify the data in the directory and control the user's access rights, so that they can provide security to protect personal data [2].

OpenLDAP stores the password in the userPassword attribute, and provides a variety of password encryption options, such as: SSHA, CRYPT, MD5, SHA, etc., so that password storage is more secure. During the authentication process, slapd in OpenLDAP will look for the password stored in the list until it matches the password provided by the user, or until all the values in the userPassword are searched, and then given the user related access rights according to the result based on the query.

2.2. Honeyword System

The concept of Honeyword was first introduced by Juels and Rivest [3]. Their main concept was to design a defense mechanism to detect whether a password file was leaked. In the paper, the author assumes that the attacker can obtain the password file and the ability to convert the password into plaintext. The principle of Honeyword is to store the user's real password with the (k-1) fake password generated by the Honeyword generator, so the password file is stored in a format with a user with multiple possible passwords. As a result, even if the password file leaked, the attacker cannot know which one is the user's real password. If he wants to log in as a fake identity, there is a great possibility of entering a fake password, so the system will find the password file may be compromised. At this point, the system can trigger the alarm based on the safety policy set by the administrator, and notifying the administrator to make the corresponding deal. The password file structure is shown in Figure 1.

The principle of Honeyword is as follows: when a new user registers, he will submit a set of account u_i and password p_i to the system, then the Honeyword generator

User Name	Password List
u_1	$H(W_{1,1}), H(W_{1,2}), H(W_{1,3}) \dots, H(W_{1,k})$
u_2	$H(W_{2,1}), H(W_{2,2}), H(W_{2,3}) \dots, H(W_{2,k})$
u_3	$H(W_{3,1}), H(W_{3,2}), H(W_{3,3}) \dots, H(W_{3,k})$
...	...
u_i	$H(W_{i,1}), H(W_{i,2}), H(W_{i,3}) \dots, H(W_{i,k})$

Fig. 1. The password file structure

Gen (k) will produce a set of fake passwords $W_i = (w_{i,1}, w_{i,2}, \dots, w_{i,k})$, which contains the correct password for the new user w_i , $c_i = p_i$. And further for security reasons, the index table c will be stored on a third-party server, independent of the login server. The encrypted password list will be stored as $H_i = (v_{i,1}, v_{i,2}, \dots, v_{i,k})$, where j -th will be the real user's password w_i , j .

In the Honeyword system, a very important part is Honeyword generator. In [3] this paper, the author describes the three ways to generate the password, respectively, as follows:

2.2.1. Chaffing by tweaking

A way to replace a selected character position, which must be replaced by the same type of character, such as letter-to-letter, symbol-to-symbol, digit-to-digit, and so on. One of the common practices is "chaffing-by-tail-tweaking", which is a way to change the last few digits to generate Honeywords. For example: password123, if you choose to change the last two digits and generate three Honeywords, the Honeyword generator may generate a password list of $W = \{\text{password135}, \text{password148}, \text{password123}, \text{password107}\}$.

2.2.2. Chaffing-with-a-password-model

This method is using the same syntax module to do the replacement, that is, the group as a unit, such as: letter group, digital group. To the above example: password123, will be divided into $W8 | D3$, that is, 8 letters 3 digital form. Assuming that you want to generate two Honeywords, it is possible to generate a password list of $W = \{\text{chaffing345}, \text{keyboard987}, \text{password123}\}$.

This will be more effective than "Chaffing by tweaking" because it makes Honeyword more realistic and closer to the real password, so that the attacker cannot tell the difference between the real password and Honeywords, increase the possibility of entering the fake password.

2.2.3. Chaffing with "tough nuts"

This kind of Honeyword is a way to confuse the attacker, this password will increase the length of the characters or the complexity of characters composition, it can improve the difficulty of password cracking, thereby increasing the attacker's attack time.

There is also a way that Honeyword is produced in a mixed way, such as "chaffing-by- tweaking-digits" with "chaffing-with-a-password-model". In this way, you can first generate a group of models, and then generate b passwords by replacing digits, so that will form $k = a \times b$ passwords. The strength of this approach will be stronger than using only one way to generate Honeywords, improving the security of the system. Another important security device in the paper is a third-party security server, where the author will set the honeychecker to store the user and its index value. It is independent of the login server and is used to confirm the index value of the user's password.

3. Mapping-password System

With the importance of identity authentication to modern networks, the security and reliability of cryptographic authentication is becoming increasingly important. However, the user and the password they use are still the weakest part of the security mechanism since the appearance of password authentication [4]. Therefore, in order to enhance the security of certification, we propose a mapping-password system in accordance with the concept of Honeyword system [3]. We put the user's password in the system in random order, so that the user password of the mapping account is not the original user set on the surface. This not only retains the detection mechanism of the password file leakage, but also reduces the system storage cost.

When a real user wants to use the system service, they will establish their own account, provide their own user name and password to the system. The system will be based on this name and password to verify the login, and

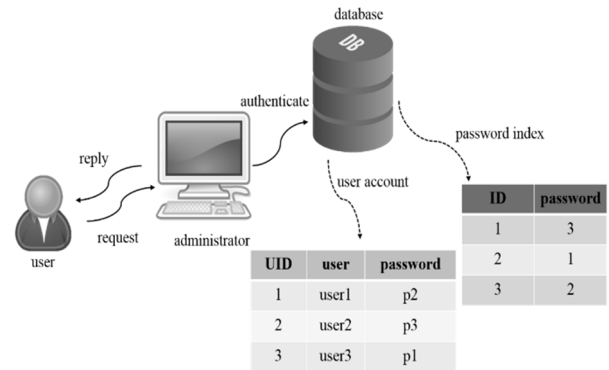


Fig. 2. System Architecture

then respond the privilege to the login. As described in Introduction, it is possible to know that an attacker can steal a user's password in different ways, such as sniffing, sending malware, and so on at different layers in the network architecture, and then they can crack the password by brute force, dictionary attack and different password crack tool. So in this case, we assume that the attacker:

- Has the ability to obtain the real user-related account password file in the system, and
- Has the ability to get the password in plain text and wants to log in the system.

Our system architecture is mainly composed of three parts, including the user, administrator and database, the system architecture is shown in Figure 2.

The manager section mainly manages the registration of the user and the login authentication, and makes appropriate processing when the login abnormal. In order to make the password authentication system more secure, the administrator needs to limit the password setting according to the management policy, for example, the minimum characters of the password length, the minimum types of the password characters and so on. The last is the database, which mainly contains two tables. A data table to store the user's account, the hash function after the password, another data table is the password checklist, store the user ID and user's true password index.

In order to verify the feasibility of this certification mechanism, we put this design running on the existing OpenLDAP version as our server. We chose Open LDAP because it is an open source directory server, not only based on the X.500 standard, but also support TCP / IP,

Table 1. System Comparison.

	Traditional	Honeyword	Mapping-password
<i>Storage Method</i>	one to one	one to multiple	one to one
<i>Storage Costs</i>	$h(p) \times N$	$(t \times h(p) + c + n_L) \times N$	$(h(p) + 2 \times c) \times N$
<i>Probability of Attack Success</i>	100%	$1/t$	$1/N$
<i>Detection Rate</i>	0%	$(t-1)/t \%$	100%

and simplifies the implementation method. Whether in companies or schools it is widely used, so it is important to improve the security of OpenLDAP. Then we choose MySQL as our database, which is because although MySQL is a related database, but it is open source, and the algorithm is efficient and reliable.

4. Performance Evaluation

We compare the differences between the traditional system, the Honeyword system, and the system we proposed. As you can see in Table 1, our passwords are stored in the same way as traditional systems, and the Honeyword system stores multiple passwords for a single user. While our system requires additional ID and index values compared to traditional system storage costs, but we reduce the cost of storing additional t passwords for each user compared to the Honeyword system, greatly reducing the system's storage cost.

In the probability of attack success part, assuming that the attacker has obtained the password file, and successfully cracked into a plaintext password, then the probability of attack success is 100% in the traditional system. That is because in the traditional way of password storage, the username maps the real user password. Honeyword system is based on the number of fake passwords and the flatness of fake passwords to determine the probability of attack success. The more the fake password, the smaller the probability that each user will be successfully attacked, but the extra storage will be required. As for our system, as the number of people rise, the probability of attack success will become smaller, and do not need to spend additional storage cost.

5. Conclusion

The user is not easy to remember too complex password, and will use the same password in different accounts, resulting in the password is still easy to be cracked. We refer to the idea of Honeyword system [3], propose a mapping-password system to improve it. According to the experimental results, we can see that there is no obvious performance ratio between the original system and our system, so it will not bring too much overhead to the system. We believe that our proposed system will be able to effectively improve the security of password authentication, and can detect the account leak event, effectively prevent the attacker intrusion, so that the leak event is no longer belatedly discovered.

Acknowledgements

This work was supported by the MOST (Ministry of Science and Technology) under contracts numbers MOST 106-3114-E-006-003- and MOST MOST 106-2221-E-006-033 -.

References

1. Gemalto, *2016 Mining for Database Gold - Findings from the 2016 Breach Level Index*, (Gemalto, 2016).
2. The OpenLDAP Foundation, *OpenLDAP Software 2.4 Administrator's Guide*, (The OpenLDAP Project, 2017).
3. A. Juels and R. L. Rivest, Honeywords: Making password-cracking detectable, in *Proc. 2013 ACM SIGSAC* (Berlin, Germany, 2013), pp. 145–160.
4. L. Tam, M. Glassman and M. Vandenwauver, The psychology of password management: a tradeoff between security and convenience, *Behaviour & Information Technology*, 29(3) (2010) 233-244.

Honeypot System of SCADA Security Survey

Kuan-Chu Lu

*Department of Electrical Engineering, Institute of Computer and Communication Engineering,
National Cheng Kung University, Tainan*

I-Hsien Liu

*Department of Electrical Engineering, Institute of Computer and Communication Engineering,
National Cheng Kung University, Tainan*

Jung-Shian Li

*Department of Electrical Engineering, Institute of Computer and Communication Engineering,
National Cheng Kung University, Tainan*

E-mail: kclu@cans.ee.ncku.edu.tw, ihliu@cans.ee.ncku.edu.tw, jsli@mail.ncku.edu.tw

Abstract

Now the infrastructure employs SCADA system for monitoring, such as nuclear power plants, water conservancy bureau, manufacturing, and logistics industry. With the rapid development of the internet, IOT (internet of things) turns every massive infrastructure from a concealed network to an open access network for convenience. Consequently, the system faces attack threats never occurred before. That is the reason why we need to build a safe and protected scheme for prevented the external attack and have to avoid SCADA system crashed. For protecting the important assets, we should understand the tools can preserve system safety to prevent the attackers invading the SCADA system. This study surveys defensive mechanisms of varying SCADA system and proposed an effective defensive structure to protect the SCADA system.

Keywords: Infrastructure security; SCADA; Industrial control Security; Network Security; IOT; Honeyd.

1. Introduction

With the rising of critical infrastructure and the thriving Internet, all the energy production and distribution (such as nuclear power plants, gas pipelines, and power grids as well) to utilities (such as water, wastewater processing, water transport, transportation, and manufacturing) rely on Industrial Control Systems, ICS. And the Supervisory Control and Data Acquisition, SCADA, system (for remote control, remote monitoring, and data collection as well) is a special type of industrial control system. Its main orientation is for the wide area of industrial system [1]. The above data processing and communication

capabilities are all developed through the development of network infrastructure and information technology.

In other words, the convenience and rapid popularity of the Internet which makes the critical infrastructure and users' key information rely on computers and networks working properly. But, also be accompanied by multi-types network security threats and the challenge of how to protect. In addition, hacker attacks have been on the rise in recent years. In 2014, a report from Industrial Control Systems Cyber Emergency Response Team, ICS-CERT pointed out that a total of 257 attacks had been conducted on key infrastructure, such as energy facilities, key manufacturing facilities, water resources

© The 2018 International Conference on Artificial Life and Robotics (ICAROB2018), Feb. 1-4, B-Con Plaza, Beppu, Oita, Japan

facilities, transportation facilities, information technology systems, nuclear power plant equipment, communications equipment, and government departments in United States in 2013. Among them, energy facilities, key manufacturing equipment, water, transportation, science and technology and power plants are account for a relatively high proportion. Obviously, the hackers attacked mainly the targets these critical infrastructures [2].

At present, enterprises and government units usually carried out the real-time monitoring and defense against the complicated and changeable network attacks to resist the invasion of attackers. Information security departments mostly use information security equipment such as Intrusion Detection System, IDS, or Intrusion Prevention System, IPS, to resist potential threats. However, this usually detects only the loopholes in the malware attacks on computers and devices. But as malware attacks evolve in an endless stream, they will be compromised by malicious software programs [3].

The new technologies are needed to identify the malware- style attacks and at the same time to achieve the effect of being able to deceive the attacker. In other words, its purpose is to entice an attacker's invasion, expose the location of the vulnerability and monitor the attacker's location which can help the information security managers fix quickly and learn about attacking styles. And the honeypot technology can achieve these requirements [4] [5]. An outstanding honeypot design must have the professional ability and good technical capacity, this has made honeypot design a challenge for the most experienced information security software architects [3]. Therefore, this article will introduce the SCADA first, following by what is honeypot, the evolution of honeypot, and industrial system honeypot etc. Then, put forward how to install the honeypot on the SCADA system structure, to introduce to the install process. Finally, to discuss how to prevent and ensure the system has a stable and secure environment.

2. Literature Review

This section will explore the SCADA's basic equipment and structure, meanwhile to describe what is meant by honeypot, honeynet origin, the evolution of honeypot, honeynet industrial system, the formation of industrial system honeypot etc.

2.1. Introduction of SCADA

Supervisory Control and Data Acquisition, SCADA, is a monitoring and data collection system. It is a structure system dominated by information network technology in Industrial Control Systems, ICS. The SCADA is mainly composed of Human Machine Interface (HMI), Engineering Workstations, LAN, database system, router device, Programmable Logic Controller (PLC), Intelligent Electronic Device, IED, a set of remote terminal devices. As shown on Figure 1 [6].

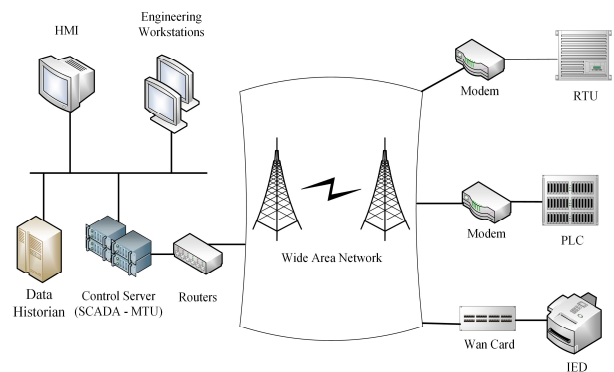


Fig. 1. Basic SCADA System Structure Diagram [6].

2.2. The Evolution of Honeypot

Honeypot hardware was quite expensive before 2006. Numerous researches, including honeynet project, needed to have the study topics and find workable cases [7], plus with the issues such as honeypot deployment and maintenance cost, leading to the restricted development. However, virtualization technology had been gradually popularized from 2006 to 2008. This allowed the virtual machine to act as a honeypot and collect detailed data on network-threat attacks with low cost and convenience, however, honeypot technology was unable to be transferred to industrial control systems. Therefore, there will be another dedicated honeypot on the industrial control system. The following will introduce the industrial control system honeypot and honeynet.

2.2.1. Industrial System Honeypot

Honeyd could not be built into the industrial control system environment because it needed to have a

dedicated honeypot software to build and run [8], for example, conpot and gaspot are all honeypots specially used for industrial control systems. The main reason is that the communication protocol on the two trapping systems is Modbus rather than TCP / IP. In addition, the test environment is usually a more special environment, such as power companies, water companies, oil farms, transport industries, factories, etc. It needs to be adjusted and set up according to different communication protocols in different fields, and different with the traditional honeypot structure.

2.2.2. Honeyd

Honeyd is an ideal framework developed by Niels Provos [9], a free software provided by GNU. Users do not need to deploy dozens of expensive devices. Users can set up and run multiple virtual machines on their own computer network. In other words, users can configure multiple virtual machines, while simulating a variety of different types of server which allow users to simulate the unlimited numbers of computer environments. Mainly for the security software to avoid network virus intrusion, including the famous Code Red, Slammer and Blaster worms.

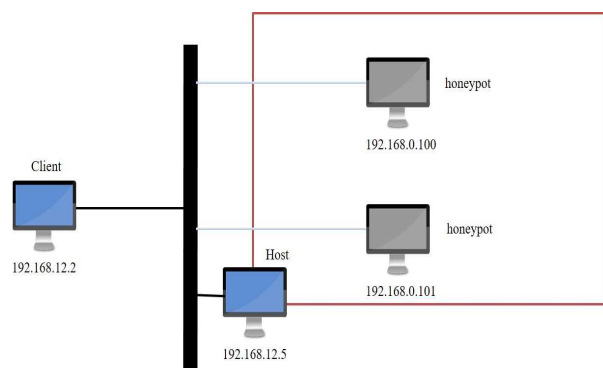


Fig. 2. Basic Honeyd Structure Diagram. [10]

3. SCADA System Security

In recent years, the critical infrastructure in many countries has been threatened by anonymous organizations. As the times change, the SCADA system has evolved into an open system from a previously closed system, also it can be applied to the network to manipulate other machinery and equipment, and collect

data, with a huge amount of information and the ability to influence national power causing as the target by cyber hackers, terrorist organizations and the competition among countries. Therefore, this section will explore the SCADA system on the security protection to understand that the system has suffered serious incursions which may threaten the livelihood of the people and the national information security, also to provide the safety information to the relevant researchers. And put forward a honeynet structure diagram to prevent SCADA system from being attacked.

3.1. SCADA System Defense Method

It is urgently needed to prevent cyber attacks through taking steps to strengthen its defense because the enterprise network may attack the SCADA network. Most of the security measures could not defend against network attacks. Network attacks from the SCADA agreement into the SCADA system [11] because the limited computing power of current features of SCADA, resulting in low data rates and difficulty in applying the existing cryptographic techniques [12]. The National Institute of Standards and Technology and European Network and Information Security Agency developed especially network security standards for SCADA system to prevent hackers attack and control the disaster.

3.2. SCADA System Honeyd Structure

This study relied on the basic SCADA structure as shown in Figure 3. Because many network attacks will enter the central control of the SCADA system via the TCP / IP network to achieve the control system or implant the virus code for the purpose. Therefore, it needs to set up the fake environment in honeypot interface of TCP / IP which would let the attackers mistakenly think they have entered the control system which could protect the defense system itself. Furthermore, it can also collect the attackers' attack paths and ways to achieve part of the outer network defense effect of SCADA system. In the industrial system, the industrial system honeypot could be set up in the industrial control system environment to prevent attackers to skip TCP / IP and attack the system directly, and simulate the environment of industrial control equipment, so that attackers could not identify the authenticity of the system to achieve the purpose of defense systems and data protection.

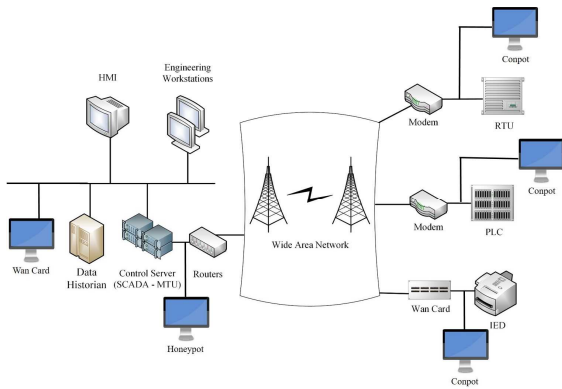


Fig. 3. Basic Honeypot Structure.

4. Conclusion

Basically, SCADA systems could be used in critical infrastructure systems such as power generation, water conservancy, and transportation. Therefore, a good structure and strategies to protect the system's network security from threats and attacks is needed. The system will be broken by new threats from the tremendous changes of cyber attacks if the security technologies adopted not mature enough. Therefore, this study proposed a framework of using the honeypot for defense plan approach. The main effect is to simulate the simulation to deceive the enemy, in addition, the system could also collect the attack paths and attack ways to understand the loopholes of system and safety.

In other words, system developers need to follow the plan-do-check-act procedure. First, to consider which network vulnerabilities are the easiest to compromise when coming the cyber attacks and use the attacker's thinking view to take protective measures and plan the system security guidelines to resist threat attacks, then, to choose the information security defense which is very important to the system developer who is not only familiar with the strategy of defense security, but need to understand the system threats that may pose an attack, so as to be able to protect the security of SCADA system.

Acknowledgements

This research plan of MOST106-3114-E-006-003- and MOST106-2221-E-041-003-could not be completed without the financial support of Ministry of Science and Technology, Taiwan, R.O.C.

References

1. Serbanescu, A. V., Obermeier, S., & Yu, D. Y. (2015). A flexible architecture for industrial control system honeypots. In *e-Business and Telecommunications (ICETE), International Joint Conference*, 4, 16-26.
2. ICS-CERT, (2014). ICS-CERT Year in Review. [online]. Available: https://ics-cert.us-cert.gov/sites/default/files/Annual_Reports/Year_in_Review_FY2014_Final.pdf. [Access date: 18 Aug. 2017]
3. Ahmed, H. M., Hassan, N. F., & Fahad, A. A. (2017). Designing a smartphone honeypot system using performance counters. *Karbala International Journal of Modern Science*, 3(1), 46-52.
4. Ahmed, H. M., Hassan, N. F., & Fahad, A. A. (2013). A Survey on Smart Phone Honeypot. *International Journal of Computers & Technology*, 11(4), 2476-2480.
5. Assmaa, A. F., Hanaa, M. A., & Nidaa, F. H. (2014). Design requirements of a smart phone honeypot system. *International Journal of Computer Application*, 6(4), 97-104.
6. Stouffer, K., Falco, J., & Scarfone, K. (2011). Guide to industrial control systems (ICS) security. *NIST special publication*, 800(82), 16.
7. Spitzner, L. (2003). The honeynet project: Trapping the hackers. *IEEE Security & Privacy*, 99(2), 15-23.
8. Winn, M., Rice, M., Dunlap, S., Lopez, J., & Mullins, B. (2015). Constructing cost-effective and targetable industrial control system honeypots for production networks. *International Journal of Critical Infrastructure Protection*, 10, 47-58.
9. Provos, N. (2004). A Virtual Honeypot Framework. In *USENIX Security Symposium*, 173, 1-14.
10. Openstuff Wiki, (2013). HowtoHoneypot. [online]. Available: <http://stankiewicz.free.fr/Wikka/wikka.php?wakka=HowtoHoneypot>. [Access date: 2 Nov. 2017]
11. Fovino, I. N., Carcano, A., Masera, M., & Trombetta, A. (2009). An experimental investigation of malware attacks on SCADA systems. *International Journal of Critical Infrastructure Protection*, 2(4), 139-145.
12. Ijure, V. M., Laughter, S. A., & Williams, R. D. (2006). Security issues in SCADA networks. *Computers & Security*, 25(7), 498-506.

An EtherCAT battery test system

Chung-Wen Hung*, Bo-Min Wang, Wen-Ting Hsu, Jhen-Gu Jiang

Department of Electrical Engineering, National Yunlin University of Science & Technology, 123 University Road,
Section 3, Douliou Yunlin 64002, Taiwan, R.O.C

E-mail: wenhung@yuntech.edu.tw

Abstract

A battery test system is a key equipment to ensure lifetime of batteries and portable device performance. On the other hand, because the real time requirement of the in industry 4.0, EtherCAT (EtherNet Control Automation Technology) communication is considered a standard interface of industry 4.0. The EtherCAT interface is based on Ethernet hardware, and with the advantages such as larger transmission bandwidth, shorter update time and minimization on synchronization time jitter. In order to upgrade battery test system competitiveness in the future, this paper proposed an EtherCAT interface for an original battery test system. The TwinCAT (The Windows Control and Automation Technology) environment Developed by Beckhoff is adopted to be the EtherCAT interface Master, and Renesas EC-1 evaluation board is used as EtherCAT interface slave controller. The commands are sent to the battery test module through the RS485 interface from the EC-1 evaluation board. Finally, C# software is proposed to provide friendly GUI interface for user.

Keywords: Battery test system, EtherCAT, TwinCAT, Renesas EC-1

1. Introduction

Due to global warming and Energy shortage, renewable energy is becoming increasingly important. A battery test system is a key equipment to ensure lifetime of batteries and renewable device performance. On the other hand, because of the real time requirement of the in industry 4.0, EtherCAT communication is considered a standard interface of industry 4.0. The EtherCAT interface is based on the Ethernet hardware, and with the advantages such as larger transmission bandwidth, shorter update time, and minimization on synchronization time jitter. New automation equipment is asked to build in the EtherCAT communication interface. In order to upgrade battery test system, this paper proposed an EtherCAT interface for a traditional battery test system. The TwinCAT environment developed by Beckhoff is adopted to be the EtherCAT system Master, and Renesas EC-1 evaluation board is used as EtherCAT interface

slave controller. The commands are sent to the battery test module through the RS485 interface from the EC-1 evaluation board. Finally, C# software is coded to provide friendly GUI interface for user. Market is a lack of battery test equipment with EtherCAT communication interface. This paper can help Battery package manufacturers to establish new automation production line based on Industry 4.0 standard. The system architecture and software will be detailed, and experimental results will be present to show system workable.

2. Related Research

2.1. EtherCAT and CoE

There are some studies discussed about the advantages of EtherCAT. EtherCAT is proposed to be a new industrial communication protocol in these years. Compared to other industrial communication protocol like Modbus,

CAN, and Profibus, EtherCAT is more reliable and more immediate. EtherCAT upgrade a level for network performance by DMA technology of reading network data, all data are processed by hardware [1]. For example, EtherCAT master captures input/output signal, slave connect up to ten devices, but the EtherCAT system delay less than a millisecond [2]. In EtherCAT, the CoE(CANopen over EtherCAT) protocol is used to transport PDO(Process Data Object) defined in CANopen. CANopen has been already used widely in many field, including process data(CiA401), motor control(CiA402), and other applications (CiA4XX). EtherCAT follows CANopen protocol and keeps its advantages. [3] verified feasibility of CoE. A successful CoE case, a TwinCAT-based servo motor control system, was discussed in [4].

2.2. Battery test system

A battery test system is used to charge or discharge the batteries, and measure the parameters of a battery, including voltage, current, temperature, and electricity. A study proposed A battery automatic measurement system which is based on personal computer to measure various parameters and to build battery model automatically [5]. In recent years, there are some studies focused on the resolution of the low voltage measurement for lithium battery. [6] tested the different lithium-ion capacitor batteries made by three different manufacturers, after charging and discharging more than 10,000 times at different voltages and temperatures, then evaluate their life and performance compared by recording lithium-ion battery capacity. The above battery test system research can be used as a reference system.

3. System Architecture and Specification

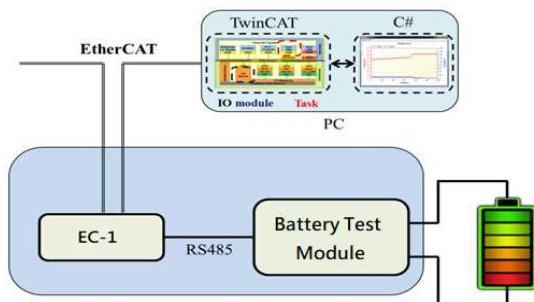


Fig. 1. EtherCAT battery test system architecture

Fig. 1 is the TwinCAT-based EtherCAT battery test system architecture proposed in this paper. EtherCAT interface and system software is designed for a mature battery test module. The commands are sent to the battery test system through the RS485 interface from the EC-1 evaluation board. EC-1 is EtherCAT communication interface and used to exchange the system information with EtherCAT Master, TwinCAT. Finally, C# GUI software is coded to monitor and control the battery test system.

Table 1. EtherCAT Specification

EtherCAT Master	
Platform	Windows 7 PC
EtherNet Adapter	Intel I350-T2
Master Software	TwinCAT
GUI Software	C#
EtherCAT Slave	
Slave Hardware	Renesas EC-1

Table 1 is the specification of the proposed EtherCAT system and environment. Master is a Windows PC with Intel dual port EtherNet adapter I350-T2. TwinCAT is adopted as EtherCAT master, and it provides a bridge to C# which provides a GUI interface. Slave communication is performed by a Renesas EC-1 board. EC-1 builds in an ESC (EtherCAT Slave Controller), it is used to decode and encode EtherCAT packets from master.

4. Software and Hardware Environment

4.1. C#

C# is a multi-paradigm programming language encompassing strong typing, imperative, declarative, functional, generic, object-oriented, and component-oriented programming disciplines. The battery test software proposed in this paper is coding in C#. The proposed C# program also can control EtherCAT devices via TwinCAT environment.

4.2. TwinCAT

TwinCAT is an automated software framework developed by Beckhoff. And it runs on Visual Studio in the Windows PC. TwinCAT is adopted to be the EtherCAT interface Master in the system proposed in this paper.

4.3. EC-1

EC-1 is the EtherCAT slave communication board developed by Renesas, there is an ESC on the board. EC-1's development environment is recommended IAR Embedded Workbench what is provided by IAR System.

5. Interface Implementation

5.1. EtherCAT master

In this paper, TwinCAT is used to control the EtherCAT system. And the describe file .xml for the battery test system is necessary. Fig. 2 shows the operation interface of the TwinCAT program. The right portion indicates connected Slave objects, and the left screen shows the accessing results with the selected object.

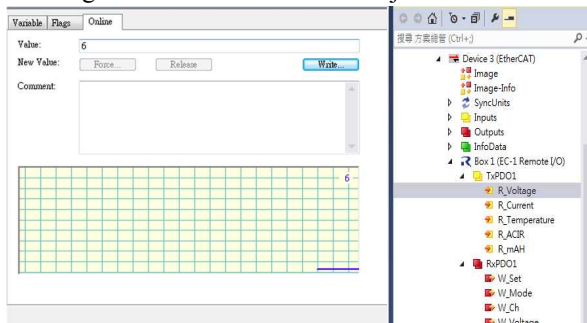


Fig. 2. TwinCAT

5.2. EtherCAT slave

The EC-1 firmware proposed in this paper performs communication interface between the battery test system hardware and TwinCAT. The firmware includes the EtherCAT data link layer and the Cia401 PDO object dictionary function. Finally, the testing commands are sent to the battery test module through the RS485 interface from the EC-1 evaluation board.

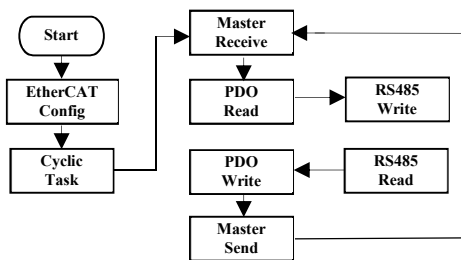


Fig. 3. EC-1 firmware flow chart

Fig. 3 presents the flowchart of the proposed firmware. The left half of the flowchart is the initializations of EtherCAT Slave address and PDO object. After the configuration, the right half of the flowchart is a cyclic task including EtherCAT PDO Read / Write and RS485 communication.

5.3. GUI battery control software

The GUI application software is coded under the Microsoft Visual Studio C# development environment. It has powerful compilation capabilities such as C / C++. In addition, it is also object-oriented and has a rich library of components that speed up application development.

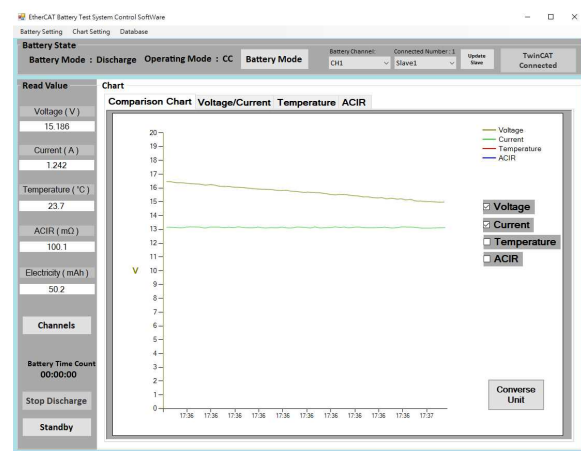


Fig. 4. GUI battery control software

The proposed software shown in Fig. 4 provides a user-friendly human-machine interface. The battery control software communicates with TwinCAT. The battery control software can read battery parameters via TwinCAT, it also sends charging or discharging commands by TwinCAT. Moreover, the control program also has battery protection settings, battery condition setting, curve data display, and Excel data table functions.

6. Experimental Results

The experimental results are presented in this section. After the TwinCAT system opening, and the EC-1 and battery testing module are turned on, the proposed GUI software can be used to control the battery test module. The GUI software includes the TwinCAT connection function, and it also can be used to set module in the standby mode, charging mode or discharging mode. The mode changes from standby mode to charging mode as shown in Fig. 5. The battery charging mode is CC-CV, which indicate constant current and constant voltage,

respectively. The battery charging runs in CC mode until the battery voltage is charged to the target value, then in CV mode.

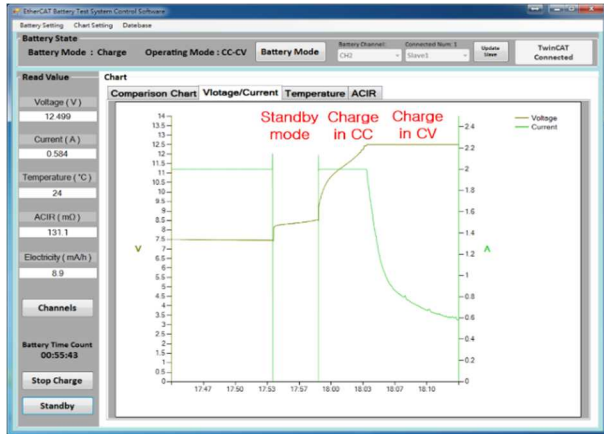


Fig. 5. Battery start to charge

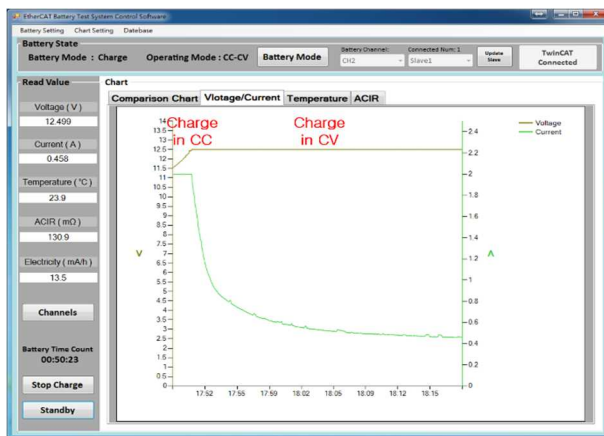


Fig. 6. Battery charging in CC-CV mode



Fig. 7. Battery discharging in CC mode

Fig. 6 shows the operating mode is from CC to CV and the battery current decreases and tends to be constant. The system is set to discharge mode, as shown in Fig. 7, and the battery runs in CC mode. In CC discharge mode, the battery current is fixed, and the battery voltage decreases and the slop tends to be constant. The above results show that the EtherCAT battery test system works precisely and correctly.

7. Conclusion

The EtherCAT communication interface is proposed in this paper, the ESC firmware for EC-1 and .xml file in TwinCAT master for the battery test system are developed. Also, the application C# program is provided. The battery system is built in the EtherCAT interface, and it will have the EtherCAT advantages, like as great reduction of the synchronization time between battery channels and flexible topology. Moreover, the integrity and richness of the proposed C# control program help users to use this battery test system easily. The experimental results show the proposed system workable.

Acknowledgment

This work is partially supported by the Ministry of Science and Technology, ROC, under contract No. MOST 106-2221-E-224-025, and 105-2622-E-224-017 - CC3.

References

1. EtherCAT Technology Group, "Ethernet & Fieldbus : Beckhoff Real-time Ethernet : Ultra High Speed I/O", EtherCAT Technology Group, Jul 01, 2005
2. J. Qi and L. Wang, "Networked Motion Control System Design Based on EtherCAT", Intelligent Computation Technology and Automation, 2009.ICICTA '09. Second International Conference on, Changsha, Hunan, Oct. 2009, pp. 77-79
3. Yongming Chen, Hua Chen, Mingzhong Zhang and Yin Li, "The relevant research of CoE protocol in EtherCAT Industrial Ethernet," Intelligent Computing and Intelligent Systems, 2010 IEEE International Conference on, Xiamen, Oct. 2010, pp. 67-70
4. Z. Chang-Cheng, X. Jian-Ming, J. Yao, M. Jie and X. Lin-Tao, "Design of servo drive slaves based on EtherCAT," The 27th Chinese Control and Decision Conference, Qingdao, May 2015, pp.5999-6004
5. B. Schweighofer, K. M. Raab and G. Bresseur, "Modeling of high power automotive batteries by the use of an automated test system," in IEEE Transactions on Instrumentation and Measurement, vol. 52, no. 4, Aug. 2003, pp. 1087-1091

6. M. Uno and A. Kukita, "Cycle Life Evaluation Based on Accelerated Aging Testing for Lithium-Ion Capacitors as Alternative to Rechargeable Batteries," in IEEE Transactions on Industrial Electronics, vol.63, no. 3, March 2016, pp. 1607-1617

Surface defect detection for tube object based on automated optical Inspection

Hsien-Huang Wu, Chang-Jhu He

Department of Electrical Engineering, National Yunlin University of Science and Technology
Douliou, Yunlin, Taiwan R.O.C.

E-mail: wuhp@yuntech.edu.tw, m10412067@yuntech.edu.tw

<http://el404.ee.yuntech.edu.tw/>

Abstract

Extrusion tube is a very popular product in the plastic industry produced by an extruder machine, for example, tubes used in washer machine or in reverse osmosis (RO) water purification system. To guarantee the quality of the tube produced for medical use, a surface defect detection system is needed. In this paper, we use a single camera combined with a telecentric lens and properly designed mirror set to achieve the complete coverage of the object surface for full defect detection. Based on the properly designed image acquisition equipment and image analysis techniques, the final system for extrusion tube defect detection can successfully detect defects of black spots, bumps, injury, etc., with a defect detection rate of about 95%, and the detection speed is up to 1578 mm/s. This speed of detection makes the detection system can be deployed on the production line without interfering the operation of the tube machinery.

Keywords: Automatic Optical Inspection, Extrusion Molding Tube, Defect Detection, Light Path

1. Introduction

With the gradual mature of industrial technology, the traditional human control has been slowly transformed into industrial automation. To achieve industrial automation, vision is an indispensable technique and therefore automatic optical inspection (AOI) technology has gaining popularity in the traditional industry. With the progress of science and technology, the required precision and accuracy for product quality are getting higher and higher, so the use of AOI to improve the traditional manpower, has become increasingly important. With the advent of Industry 4.0, combined with the reduced cost of the camera and faster processing efficiency of the compute, the machine vision used in AOI has also been paid more and more attention. In the image recognition, applications are divided into four major categories: detection, measurement, identification and positioning. Automated detection with high efficiency, high stability, high reliability and so on, has definitely became the industry's trend.

The tubular imperfections dealt with in this article also appeared in a number of other applications, such as cylindrical surface inspection using Line-Scan cameras for surface scanning.¹⁻³ Paper⁴ proposed a precision grinding inspection system of metal surfaces for the

prototype cylindrical roller. Several research has been conducted for non-flat surface, for example, flaw detection on the surface of the steel^{5,6} where precision is higher than 95%; evaluation of the cone of the trajectory for a bullet^{7,8} and real-time defect detection for high-reflection surface⁹ which use mirror for inspection of specular reflection surface. Another system similar to that of ours is the inspection of medical glass tube¹⁰, which uses three 8k Line-Scan cameras to capture 360-degree image for surface defect detection. All the above systems were developed for not flat surface, and it shows that defect detection for a tubular object¹¹⁻¹⁴ need to use a 360-degree system to capture the image¹⁵⁻¹⁸. This is also true for the extrusion tube that was investigated in this paper.

2. Hardware architecture

This section will provide a detailed description of the defect detection system for the extrusion tube, such as the camera, the lens and the light source, and the 360 degree imaging system. Our goal is being able to acquire images for a full coverage of the tube using only one single camera and proper mirror design. Using the principle of straight line and reflection of light, we can obtain four sides of the object by the use of six mirrors. This design

is based on OPTO 360 degree optical System¹⁹ and was modified to be used in a continuous object. The rule of design is that all four optical (or light) paths of view need to have the same length, as is illustrated in Fig. 1 as path L1 (blue), path L2 (light pink), path (green) L3, and path L4 (red).

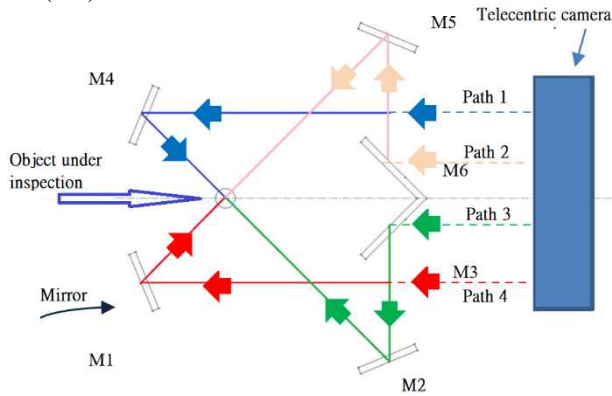


Fig.1. 6M4V Optical path design

According to the above rule that each light path would be the same and the symbols used in Fig. 1, we have $L1=L2=L3=L4$.

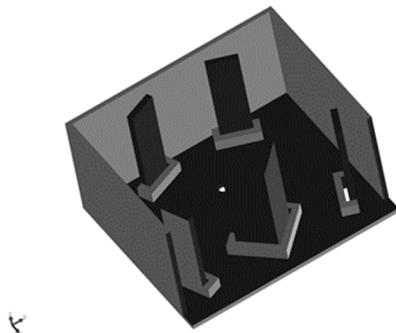


Fig. 2. Design of 4 view image acquisition system

The equipment implemented is shown in Fig. 2 for 4-view acquisition based on six mirrors and one single camera.

3. Software architecture

As shown in Fig. 3, the software system will load the configuration file at the beginning of the execution process. The settings of the parameter include the median filter mask size, the background threshold value, the size range of the defect, and the repeated area of the test object. The camera is then initialized to wait for the user to press

the start button for starting the defect detection process.



Fig. 3. Main processing procedure

The image processing flow of the system is illustrated in Fig. 4. It first extracts four ROI's (Region of Interest) which contain the region of the tube. Then a median filter is applied to remove the candidate defect. Finally, we take an absolute value difference (AbsDiff) between the original image and the median filtered image and the defect area will show up. One example of this processing is shown in Fig. 5.

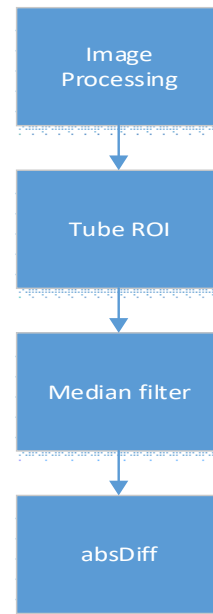


Fig. 4. Flow of image processing

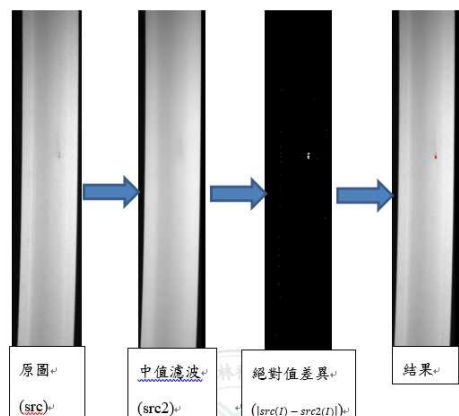


Fig. 5 One example of defect detection process

6. Experimental results

The image acquisition device implemented by using 3D printer is shown in Fig. 6, where six mirrors were used for four views, and therefore, a 6M4V system. The images taken with this 6M4V device and the results of defect detection are illustrated in Fig. 7.

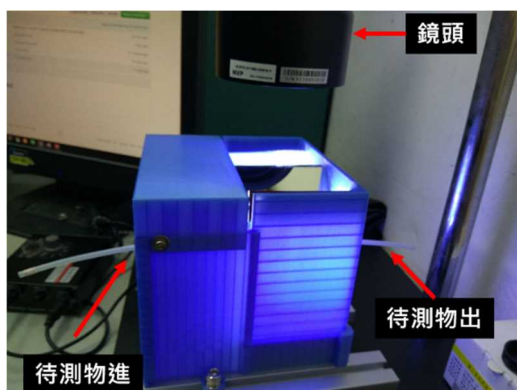


Fig. 6. 6M4V actual shooting architecture

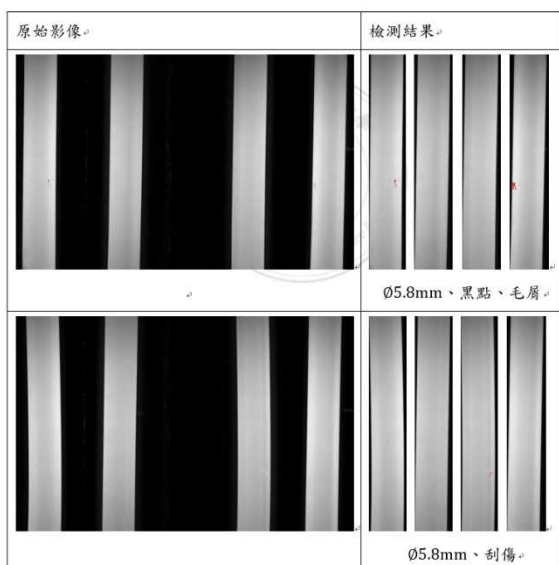


Fig. 7. Results obtained by using 6M4V

5. Conclusions

In this paper, a successful design of the mirror to achieve a single camera for panoramic ring shot has been obtained. It can successfully detect the black spots, pits, crush and other defects for the extrusion tube. This AOI technology has proven to achieve automated testing, reduce labor costs, and improve efficiency and quality. The current speed of detection is 1578 mm/s which can meet the production rate of a extruder machine for medical extrusion tube.

Acknowledgements

The authors wish to express their appreciation for the financial support of the Ministry of Science and Technology under project MOST 106-2221-E-224-018-. The extrusion tubes used in the experiments were kindly supplied by Everplast Machinery Co., Ltd., Taiwan. Their generous support is greatly appreciated.

References

1. Y. N. K. Y. H. MORIKAWA, "Image Processing System for Visual Inspection of Cylindrical Parts."
2. Y.-C. Chiou and W.-C. Li, "Flaw detection of cylindrical surfaces in PU-packing by using machine vision technique," *Measurement*, vol. 42, pp. 989-1000, 2009.
3. M. Ali, M. Mailah, S. Kazi, and H. Tang, "Defects detection of cylindrical object's surface using vision system," in *Proceeding of The 10th WSEAS International Conference on Computational Intelligence, Man-Machine Systems and Cybernetics (CIMMACS'11)*, Jakarta, 2011, pp. 1-3.
4. F. Pernkopf and P. O'Leary, "Visual inspection of machined metallic high-precision surfaces," *EURASIP Journal on Applied Signal Processing*, vol. 2002, pp. 667-678, 2002.
5. W.-b. Li, C.-h. Lu, and J.-c. Zhang, "A local annular contrast based real-time inspection algorithm for steel bar surface defects," *Applied Surface Science*, vol. 258, pp. 6080-6086, 2012.
6. J. P. Yun, S. Choi, B. Seo, and S. W. Kim, "Real-time vision-based defect inspection for high-speed steel products," *Optical Engineering*, vol. 47, pp. 077204-077204-8, 2008.
7. A. Zographos, M. Robinson, J. Evans, and C. Smith, "Ballistics identification using line-scan imaging techniques," in *Security Technology, 1997. Proceedings. The Institute of Electrical and Electronics Engineers 31st Annual 1997 International Carnahan Conference on*, 1997, pp. 82-87.
8. D. Li, "Ballistics projectile image analysis for firearm identification," *IEEE Transactions on image processing*, vol. 15, pp. 2857-2865, 2006.
9. G. Rosati, G. Boschetti, A. Biondi, and A. Rossi, "Real-time defect detection on highly reflective curved surfaces," *Optics and Lasers in Engineering*, vol. 47, pp. 379-384, 2009.
10. P. Foglia, C. A. Prete, and M. Zanda, "An inspection system for pharmaceutical glass tubes," *WSEAS Trans. Syst*, 2015.
11. C. C. Lam and J. G. Kemper, "Ultrasonic detection of flaws in tubular members," ed: Google Patents, 2003.

12. C. C. Lam, J. G. Kemper, and A. Manocchio, "Flaw detection in tubular members," ed: Google Patents, 2004.
13. B. I. Cantor, J. H. Flora, and P. J. Latimer, "Apparatus and method of discriminating flaw depths in the inspection of tubular products," ed: Google Patents, 1992.
14. J. S. Cruickshank, "Method and apparatus for the inspection of tubular members," ed: Google Patents, 1989.
15. J. A. Beckstead and S. R. Nordhauser, "360 degree/forward view integral imaging system," ed: Google Patents, 2000.
16. Y. Yagi and M. Yachida, "Omnidirectional visual sensor having a plurality of mirrors with surfaces of revolution," ed: Google Patents, 2000.
17. E. Driscoll Jr, H. Morrow, A. J. Steinhauer, and W. C. Lomax, "Panoramic camera," ed: Google Patents, 2002.
18. S. G. Wu and Y. S. Kuo, "360-degree panoramic cylindrical object imaging mirror design method, mirror and imaging device," ed: Google Patents, 2014 (in Chinese).
19. OPTO, "OPTO 360° Optical System."

Client Searching Privacy Protection in Encrypted Database

I-Hsien Liu

Department of Electrical Engineering, National Cheng Kung University, Tainan City, 70101, Taiwan

Chuan-Gang Liu

Department of Applied Informatics and Multimedia, Chia-Nan University of Pharmacy and Science, Tainan City, 71710, Taiwan

Cheng-Jui Chang

Institute of Computer and Communication Engineering, National Cheng Kung University, Tainan City, 70101, Taiwan

Jung-Shian Li

*Department of Electrical Engineering, National Cheng Kung University, Tainan City, 70101, Taiwan
E-mail: ihliu@cans.ee.ncku.edu.tw, chgliu@mail.cnu.edu.tw, cjchang@cans.ee.ncku.edu.tw, jsli@mail.ncku.edu.tw
www.cans.ee.ncku.edu.tw*

Abstract

In recent years, Cloud Storage Providers (CSP) works hard to successfully achieve cheap cloud storage. To prevent losing important data in their own device, some of the people backup their data to the cloud. It becomes much more important for securing the data stored in the cloud. SEDS (Searchable Encryption Support Dynamic), provides multi-keyword based searchable encryption method for the semi-trusted cloud simulations.

Keywords: Multi-keyword Search, Searchable Encryption, Privacy Preserving.

1. Introduction

Cloud service provider (CSP) started providing cloud storage to general user. CSP like Dropbox providing free storage space for users. User get used to upload their personal file to the cloud such as photos, videos, medical records, business documents, and so on. But, the hijacking event on CSP never stops. Yahoo [1], one of the leader on search engine, Verizon tried to lower the deal with Yahoo after the huge amount client account stolen.

From SC Media [2], hacker can monitor 58.8 million data by the unsecured database in the cloud. Furthermore, some of the open source database becomes their next target. Data storing in the cloud can not only rely on the CSP privacy policy, but also control the authorization of sharing data by the data owner which is the risen of Searchable Encryption. Data owner can encrypt the file

in their own way and share the secret key to the user who is authorized by the owner.

2. Background and Related work

2.1. Searchable Encryption

The evolution of Searchable Encryption could learn from the growth of search engine. The pioneer announces the Searchable Encryption and provide single keyword search [3] [4]. But user type in keyword may not be that exactly, fuzzy keyword search helps the system to solve this situation [5] [6].

2.2. Dummy Keyword

By generating multi-keyword index to provide much more accuracy of search result and data presentation, N. Cao [7] announce the first multi-keyword and ranked

search function. Definite dummy keyword to secure searching process.

2.3. Synonym Keyword

Sometimes the user types in not the exactly keyword but the synonym keyword, adding semantic database becomes another trend of Searchable Encryption. Z. Fu [8] adds a synonym list, mapping synonym keywords to the correct keyword in the metadata. To improve the efficiency of searching, clustering the data by using k-Nearest Neighbor. But in text mining, synonym keywords in a 100% mapping policy isn't the real correlation of keyword relationship. Another scheme [9] sets a semantic database in a private cloud, user send the keywords to the private cloud to transfer the exactly keyword and create the search trapdoor. While protecting the trapdoor, apply a special encrypt type named one-to-many order preserving encryption (OM-OPE), same plain-text can be encrypted to m kinds of ciphertext. It's a great secure method but the time of encryption is another problem.

2.4. Dynamic Update

While the data upload to the cloud server, data owner may insert or delete data often. The dynamic scheme in Searchable Encryption becomes a serious problem. S. Kamara [10] announces a keyword-based Red Black tree to support dynamic scheme. Define the amount of keywords are fixed, but using symmetric type of encryption couldn't prevent some cloud threat model. Z. Xia [11] constructs a binary search index, putting some fake nodes for dynamic insert in order to prevent re-construct tree.

Binary tree is not able to afford the huge amount of data. B tree indexing in hard disk storage releases storage space and accelerates the speed of searching in the index, G.Graefe [12] introduces some B tree dynamic scheme. M. Ondrejčka [13] keeps the rules of B tree, putting the data in the leaf node, comparing data at each level of the tree.

3. Searchable Encryption Support Dynamic Scheme

3.1. System Architecture

In our research, we set the three different entities show in Figure 1: Data Owner, Data User, Cloud Storage Server.

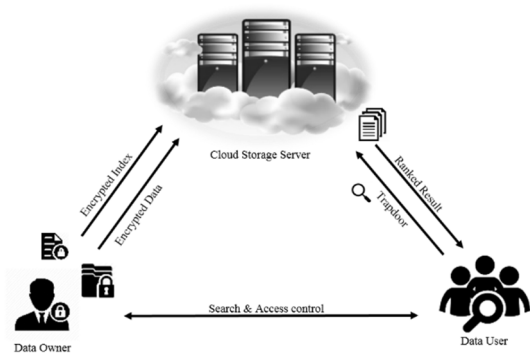


Fig. 1. System Architecture

3.1.1 Data Owner

After the data preprocessing mentioned before, Data Owner builds a metadata to map the keywords in vector type data. Then constructs a searchable tree index I from the data vectors. Encrypting the source data collection F to encrypted collection C before upload to the cloud server. Data Owner sends the metadata and the secret key to the data user in a safe tunnel, the authorization process and the encrypt type of data are not considered in our research.

3.1.2 Data User

The authorized Data User types in the interesting keywords than create the trapdoor TD according to the metadata Data Owner shared. Data User chooses the amount of data k , and send the trapdoor TD to the cloud with the coefficient k .

3.1.3 Cloud Storage Server

Cloud Storage Server stores the encrypted data collection C and the searchable tree index I . While receiving the trapdoor TD from the user, Cloud Storage Server executes the special search algorithm to search the relevance files than response the user top k ranked file. Besides, in dynamic scheme, Cloud Storage Server received the update package P from the owner, Cloud Storage Server updates the encrypted data collection C and index I according to the attribute of the package P .

3.2. Data Pre-Processing

While extracting keywords from documents, finding the keyword representing the data is the main goal in text mining. Before calculating TF-IDF of the keywords, stripping punctuation from text file, removing the stop

words, and stemming to the original file helps to count the correct word existing term frequency.

3.3. Threat Model

The semi-trust cloud server we considered is named as Honest and Curious server. We could comprehend the meaning from the words Honest and Curious. The server will honestly execute the process we set, but the server is also curious during the execution in order to find some specific information.

3.3.1 Known Ciphertext Model

The cloud server only has the encrypted data collection C and the searchable tree index I . The server tries to decrypt the encrypted data collection by the well-known attack model Ciphertext-only attack(COA). [14]

3.3.2 Known Background Model

The cloud server with more intelligence and curious about the process the user search processes, monitoring the relation between trapdoor and search result. Using the result to find the rules of trapdoor generation. Furthermore, the server may compare two similar trapdoor to figure out the difference of search result corresponding to the difference keyword. Than using the relationship to help decrypting the data collection C . [15]

3.4. Design goal

While supporting multi-keyword ranked search, adding dynamic scheme is the trend of Searchable Encryption. We construct the index by B tree to accelerate the search efficiency in the padding search request step. The disadvantage of B tree is that we construct the index is slower, but we have close efficiency in dynamic scheme.

4. Performance Evaluation

The source data we take are the 315 IEEE 2014 INFOCOM papers. By extracting the top relevance keyword for each file, picking the top 3 to 10 $TF \times IDF$ value as the keyword represent the file. In the metadata, we padding 0 value in the data vector until the keyword dimension reach the common multiple of 500.

Comparing our scheme SESD efficiency with the binary tree structure EDMRS & BDMRS [18]. Than we set the attribute of B tree as 4 which means the father node contain 4 child nodes. And the total leaf node are 1024, this makes B tree and the binary tree in perfect(both full

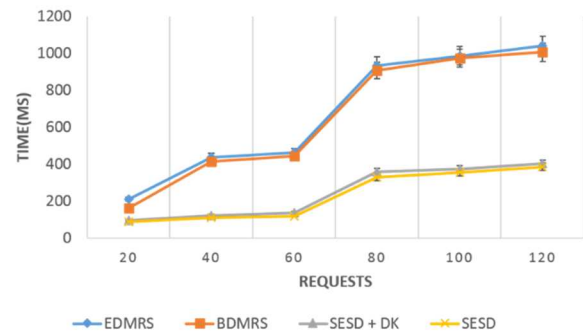


Fig. 2. Tree Searching Efficiency in difference search require k

and balanced). In the evaluation section, the dummy keyword length we added is 10.

In the first step, we compare the performance of tree construction. The disadvantage of B tree structure is the more using comparison operator in tree construction which retard the performance. In tree search step, the most time we spend is the multiplier in finding the most relevance path.

To compare the search performance between B tree and binary tree, we restrict two different condition. The first condition, we evaluate the keyword dimension 3500 index with different search request number k as the Figure 6. Searching in B tree spend half time of binary tree. In other condition, we restrict the search request number k as 40, than evaluate the search process in different keyword dimension index. As the Figure 2, the performance is great because we spend half time of binary tree.

5. Conclusion

In our research, we choose the B tree structure to enhance the search process. By changing the structure, the efficiency of dynamic scheme is close to the binary tree. Also, in dynamic scheme we add a new parameter to find out the real path of target file and update the tree according to the path stack. The extra cost we spend is the more time in tree construction. But in cloud computing, the action of dynamic and searching process are much more importance while the tree is large enough. And in data privacy, to prevent the less keyword in query is the trend of user behavior, we add more random feature to flatten the trapdoor generation.

In future works, adding the search result verification in the data user side is the trend. Because the trusted of the

user to the search engine may cause the user search only once for the file interested, and the less search result user view. Trying to rearrange the search result in the data user side can reach the reliability from the user.

Acknowledgements

This work was supported by the MOST (Ministry of Science and Technology) under contracts numbers MOST 106-3114-E-006-003- and MOST MOST 106-2221-E-006-033 -.

References

1. T. Spangler, *Verizon Hacks \$350 Million From Yahoo Deal After Massive Data Breaches*, (Variety, 2017).
2. B. Barth, *Unsecured database lets hacker expose 58 million plus records from data management firm*, (SCMedia, 2016).
3. D. X. Song, D. Wagner and A. Perrig, Practical Techniques for Searches on Encrypted Data, in *Proc. 2000 IEEE Symposium on Security and Privacy*, (Washington, DC, USA, 2000), pp.44-55.
4. R. Curtmola, J. Garay, S. Kamara and R. Ostrovsky, Searchable symmetric encryption: improved definitions and efficient constructions, in *Proc. the 13th ACM conference on Computer and Communications Security*, (Alexandria, Virginia, USA, 2006), pp. 79-88.
5. C. Wang, K. Ren, S. Yu and K. M. R. Urs, Achieving usable and privacy-assured similarity search over outsourced cloud data, in *Proc. IEEE INFOCOM 2012*, (Orlando, FL, USA, 2012), pp. 451-459.
6. B. Wang, S. Yu, W. Lou and Y. T. Hou, "Privacy-preserving multi-keyword fuzzy search over encrypted data in the cloud, in *Proc. IEEE INFOCOM 2014*, (Toronto, Canada, 2014), pp. 2112-2120.
7. N. Cao, C. Wang, M. Li, K. Ren and W. Lou, Privacy-preserving multi-keyword ranked search over encrypted cloud data, *IEEE Transactions on Parallel and Distributed Systems*, 25(1) (2014) 222-223.
8. Z. Fu, S. Xingming, N. Linge and L. Zhou, Achieving effective cloud search services : multi-keyword ranked search over encrypted cloud data supporting synonym query, *IEEE Transactions on Consumer Electronics*, 60(1) (2014) 164-172.
9. Z. Xia, Y. Zhu, X. Sun and L. Chen, Secure semantic expansion based search over encrypted cloud data supporting similarity ranking, *Journal of Cloud Computing*, 3(8) (2014) 1-11.
10. S. Kamara and C. Papamanthou, Parallel and Dynamic Searchable Symmetric Encryption, in *Proc. International Conference on Financial Cryptography and Data Security 2013*, (Okinawa, Japan, 2013), pp. 258-274.
11. Z. Xia, X. Wang, X. Sun and Q. Wang, A Secure and Dynamic Multi-Keyword Ranked Search Scheme over Encrypted Cloud Data, *IEEE Transactions on Parallel and Distributed Systems*, 27(2) (2016) 340-352.
12. G. Graefe and H. Kuno, Modern B-tree techniques, in *Proc. ICDE 27th*, (Hannover, Germany, 2011), pp. 1370-1373.
13. M. Ondrejčka and J. Pokorný, Extending Fagin's Algorithm for More Users Based on Multidimensional B-Tree, in *Proc. of East European Conference on Advances in Databases and Information Systems '08*, (Pori, Finland, 2008), pp.199-214.
14. TutorialsPoint, *Attacks On Cryptosystems*, (TutorialsPoint, 2017)
15. W. Sun, B. Wang, N. Cao, M. Li, W. Lou, Y. T. Hou and H. Li, Privacy-preserving multi-keyword text search in the cloud supporting similarity-based ranking, in *Proc. 8th ACM SIGSAC*, (Hangzhou, China, 2013), pp. 71-82.

Study of real-time biomimetic CPG on FPGA: behavior and evolution

Timothée Levi^{*1}, Yanchen Guo¹, Kazuyuki Aihara¹, Takashi Kohno¹
IIS, The University of Tokyo, 4-6-1 Komaba, Meguro-ku
Tokyo, 153-8505, Japan¹

E-mail: levi@sat.t.u-tokyo.ac.jp, guoyanchen@sat.t.u-tokyo.ac.jp, aihara@sat.t.u-tokyo.ac.jp, kohno@sat.t.u-tokyo.ac.jp

Abstract

Locomotion is one of the most basic abilities in animals. Neurobiologists have established that locomotion results from the activity of half-center oscillators that provides alternation of bursts. Central Pattern Generators (CPGs) are neural networks capable of producing rhythmic patterned outputs without rhythmic sensory or central input. We propose a network of several biomimetic CPGs using biomimetic neuron model and synaptic plasticity. This network is implemented on a FPGA (Field Programmable Gate Array). The network implementation architecture operates on a single computation core and in real-time. The real-time implementation of this CPGs network is validated by comparing it with biological data of leech heartbeat neural network. From these biomimetic CPGs, we use them for robotic applications and also for biomedical research to restore lost synaptic connections.

Keywords: Biomimetic neural network, CPG, FPGA, Silicon neuron

1. Introduction

Locomotion in robotic and neuroscience field is highly important, and its complexity depends on the degree of fitting the nature. The locomotion is based on the activity of half-center oscillators. The first half-center oscillator was proposed by Brown¹ in 1914. These oscillators which mimic the rhythmic movements are programmed by central pattern-generating (CPG) networks consisting of neural oscillators². These CPGs provides alternating burst without rhythmic sensory or central input³. Usually, in robotic field, the CPGs are made using simple neuron-models, and are not in biological time scale (accelerated time). These two specifications do not able bio-hybrid experiments between biological cells and artificial cells. Therefore, we could say that these CPGs are bio-inspired and not biomimetic. A bio-inspired system is inspired by nature for conducting engineering

task (neural network for image processing, data mining, etc.). A biomimetic system mimics the nature for simulating the living behavior and/or replaces it (rebuilding the living part). Biomimetic system can perform bio-hybrid experiments. While multi-legged robots need CPG to move or coordinate their movements, researchers implement an Amari-Hopfield CPG⁴ or basic CPGs like Van der Pol⁵, modeled as non-linear oscillators. Those models provide sinusoidal oscillations that are not biomimetic.

To be closer to the nature, we developed biomimetic CPGs. These CPGs will mimic the animal locomotion like swimming in xenopus, salamander⁶, and lamprey⁷, as well as leech heartbeat system^{8,9}. This article is decomposed into three parts: description and results of the biomimetic network of CPGs, applications on robotic field and biomedical neuroscience research.

2. Biomimetic CPGs

We propose a network of hundreds biomimetic CPGs using biomimetic neuron, synapse and short-term plasticity models. For instance the salamander locomotion needs 40 CPGs⁶.

2.1. Model of the Leech Heartbeat system

Our CPG is based on the Leech heartbeat neural network system⁹. The simplest biomimetic CPG is the one responsible for the leech heartbeat (Figure 1). This CPG consists of two neurons, connected to each other via inhibitory synapses. As this is the most basic network, it is ideal for achieving a better understanding of various phenomena that control its activity. This pair of neurons, also known as an elementary oscillator, is also the smallest network capable of generating oscillations under normal conditions. We add two excitatory neurons connected with excitatory synapses for detecting burst activity of the elementary oscillator.

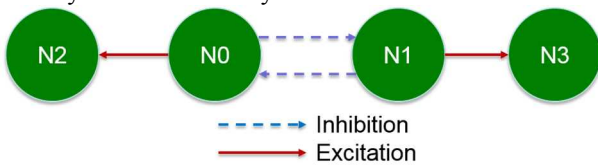


Fig. 1. A diagram of the CPG in the leech heartbeat system, composed of one elemental oscillator (N0 and N1). Synapses between N0-N1 couple are inhibitory. N2 and N3 are burst-detector neurons. They are spiking just one time when a burst occurs in their connected neuron. N2-N3 are respectively connected to N0-N1 by excitatory synapses.

2.2. Neuron, synapse and short-term plasticity model

The biomimetic CPG that we designed is presented in details in^{10,11}. No CPGs network and no real-time period modifications were possible in¹⁰.

The neuron model choice is very important, because we have to choose between the biological plausibility and the cost computation. The choice of model was based on two criteria: the family of neurons able to be reproduced and the number of equations. These criteria were used to compare several models, from the simple one: the Leaky Integrate and Fire model (LIF)¹² to the most complex one: the Hodgkin-Huxley model (HH)¹³.

In the article by Hill⁹, HH model is used to reproduce the leech heartbeat system. Nevertheless, the HH model

requires a large number of parameters and the LIF model is too simple for reproducing the neural network behavior in Hill⁹.

The Izhikevich model (IZH)¹⁴ represents a good trade-off as it is based on two equations and is capable of reproducing many different families of neurons by changing four parameters. Furthermore, this model is resource-frugal, a key advantage when the aim is to design a large CPG network embedded in the same board. As we chose the neuron model, we have to choose carefully the synapse model. This model should be biomimetic with few resources. In case of excitatory (inhibitory) synapse, a positive contribution (negative contribution) is added to the postsynaptic neuron when the presynaptic neuron spikes. Furthermore, we add the short-term plasticity described by Izhikevich¹⁵ that is different from Spike-Timing Dependent Plasticity (STDP) and that manages the depression or the facilitation of the synaptic strength. This synaptic plasticity is similar to the one described in Hill⁹.

2.3. Design of real-time system

This network is implemented in a digital platform: Xilinx Kintex-7 FPGA (Field Programmable Gate Array). The network implementation architecture operates on a single computation core. This digital system works in real-time, requires few resources and is low power consumption. It is essential in robotic applications. The implementation of one CPG is validated by comparing it with biological data of leech heartbeat neural network¹⁰. These CPGs could reproduce biological activity of CPG neural networks not only in terms of period but also in terms of variation of duty cycle and bursting period.

This implementation is low resources. Table 1 presents the used resources for 128 CPGs in Xilinx Kintex-7 FPGA family. Using full resources, we can implement 984 CPGs. For instance, salamander locomotion needs 40 CPGs.

Table 1. Utilization of the resources for the implementation of 128 CPGs

Kintex-7	Utilization	Available	Percentage
LUT	26795	203800	13,1
FF	9479	407600	2,3
BRAM	43	445	9,6
DSP	40	840	4,7

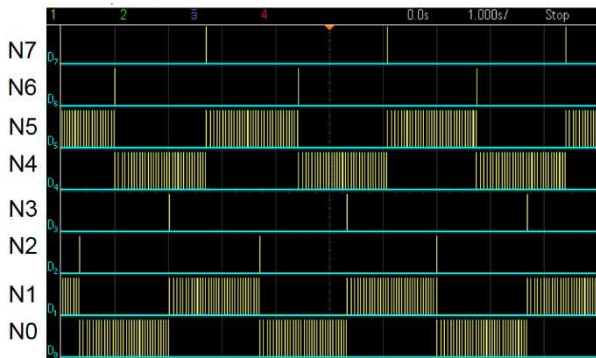


Fig. 2. Two real-time CPGs (N0-N1 and N4-N5) with their burst-detection neurons (N2-N3 and N6-N7). Time axis is one second by division.

Figure 2 describes the FPGA implementation results for two CPGs (N0-N1 and N4-N5) with their two burst-detector neurons (N2-N3 and N6-N7).

The real-time behavior of CPG system is mandatory as we can use for robotic applications (section 3), bio-hybrid experiments but also to simulate different topologies and lost connections as it can exist in the nature (section 4). Using software, simulation time is too long as neuron model and synaptic plasticity use complex non-linear differential equations. Thanks to this real-time system, we can simulate several topologies of CPG network and then find some treatment protocol when neuronal connections are lost.

3. Robotic applications

Usually simple CPGs are often used for robotic application but biomimetic CPGs are rarely used. Nevertheless some few works^{6,16-20} developed biomimetic motion for robotics. To demonstrate the feasibility of using our biomimetic CPGs. We create forward locomotion for artificial salamander with different periods and different phases between CPGs. We reproduce the forward locomotion explained in¹⁶ using a loop of seven CPGs (from CPG0 to CPG6) with crossed inhibition connections between them. Figure 3 describes two different forward locomotions with different periods. We can modify the period in real-time by tuning the weight of the crossed synaptic connections between the CPGs. We also investigated a master CPG which controls the activity of seven CPGs with excitatory connections between the master CPG and CPG0. Thanks to this master CPG, we can directly choose the frequency and phases between CPGs using just two parameters (period

of the master CPG and value of the excitatory synapse weight).

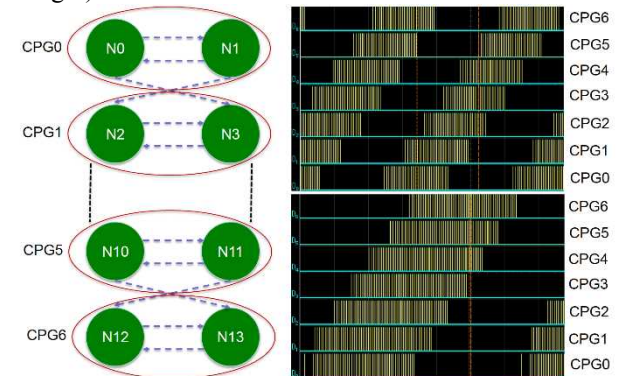


Fig. 3. Forward locomotion with two examples of speed using a chain of 7 CPGs. Time axis is one second by division. Signal are the left neuron (N0, N2, N4, N6, N8, N10 and N12) of each CPG.

4. Biomedical applications

How to restore locomotion activity when some connections are lost? We simulated several cases. Here, we present one study where one CPG does not work anymore as the inhibition connection between N6 and N7 is lost. In that case, N7 is always firing and N6 is always inhibited as Figure 4 (top) describes it.

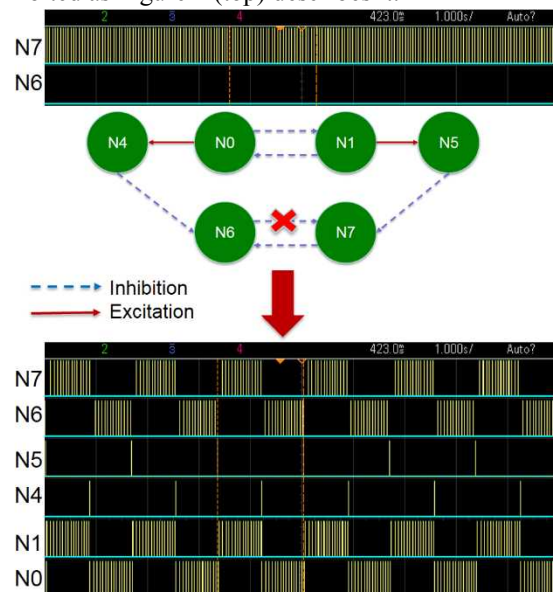


Fig. 4. Reconstruction of a lost synaptic connection. The couple N6-N7 recovers its CPG activity. Time axis is one second by division.

This result shows that thanks to new synaptic connections from other CPG, we can restore a lost activity (figure 4 bottom). As our biomimetic CPGs can be connected to living neurons, this research can be extent to bio-hybrid experiments and uses these biomimetic CPGs as neuroprostheses during spinal cord lesion.

5. Conclusion

This article demonstrates a real-time network of biomimetic CPGs. This system can be used in robotic applications for smoother and closer behavior to biological animals. It can also be used for bio-hybrid robotic (living part and artificial part) as it was demonstrated that this system can be connected to biological neurons^{21,22}. Another advantage is that real-time systems can simulate several topology of CPGs and simulate different hypothesis and protocol treatment for biomedical applications like spinal cord injury²³.

6. Acknowledgements

Authors thank Social Cooperation Program for Brain-Morphic AI to Resolve Social Issues, IIS, UTokyo.

7. References

1. T. Brown, On the nature of the fundamental activity of the nervous centres; together with an analysis of the conditioning of rhythmic activity in progression and a theory of the evolution of function in the nervous system. *Journal of Physiology*, 48, 18-46, 1914
2. E. Marder and D. Bucher, Central pattern generators and the control of rhythmic movements. *Current Biology* 11, 986-996, 2001
3. S. Hooper, Central Pattern Generators, *Current Biology*, 10, 176-177, 2000
4. S. Amari, Characteristic of the random nets of analog neuron-like elements, *IEEE Trans. on System, Man and Cybernetics*, 2, 643-657, 1972
5. B. Van Der Pol, The heartbeat considered as a relaxation oscillation, and an electrical model of the heart. *Philosophical Magazine*, 6, 763-775, 1928
6. A. Ijspeert, A. Crespi, D. Ryczko, J. Cabelguen, From swimming to walking with a salamander robot driven by a spinal cord model. *Science*, 315, 1416-1420, 2007
7. AH. Cohen, GB. Ermentrout, T. Kiemel, N. Kopel, KA. Sigvardt, TL. Williams, Modelling of intersegmental coordination in the lamprey central pattern generator for locomotion. *Trends in Neuroscience*. 15, 434-438, 1992
8. GS. Cymbalyuk, Q. Gaudry, MA. Masino, R.L. Calabrese, Bursting in Leech Heart Interneurons: Cell-Autonomous and Network-Based Mechanisms. *J. Neuroscience*, 22, 10580-10592, 2002
9. AA. Hill, J. Lu, MA. Masino, OH Olsen, RL Calabrese, A model of a segmental oscillator in the leech heartbeat neuronal network, *J Comput Neurosci.*, 10, 281-302, 2001
10. M. Ambroise, T. Levi, S. Joucla, B. Yvert, S. Saïghi, Real-time biomimetic Central Pattern Generators in an FPGA for hybrid experiments. *Frontiers in Neuroscience*, 7, 215, 2013
11. M. Ambroise, T. Levi, Y. Bornat, S. Saïghi, Biorealistic spiking neural network on FPGA, *47th Annual Conference on Information Sciences and Systems CISS*, 1-6, 2013
12. G. Indiveri, Synaptic plasticity and spike-based computation in VLSI networks of integrate-and-fire neurons. *Neural Information Processing, Letters and Reviews*, 11, 135-146, 2007
13. AL. Hodgkin, AF. Huxley, A quantitative description of membrane current and its applications to conduction and excitation in nerve, *The Journal of Physiology*, 117, 500-544, 1952
14. E.M. Izhikevich, Simple model of spiking neurons. *IEEE Transactions on Neural Networks*, 14, 1569- 1572, 2003
15. E.M. Izhikevich and G. Edelman, Large-scale model of mammalian thalamocortical systems, *Proceedings of the National Academy of Sciences of the United States of America*, 105, 3593-3598, 2008
16. T. Matsuo, T. Yokoyama, D. Ueno, K. Ishii, Biomimetic Motion Control System Based on a CPG for an Amphibious Multi-Link Mobile Robot, *Journal of Bionic Engineering*, 91-97, 2008
17. J.H. Barron-Zambrano and C. Torres-Huitzil, FPGA implementation of a configurable neuromorphic CPG-based locomotion controller, *Neural Netw.*45, 50-61, 2013.
18. C. Li, R. Lowe, T. Ziemke, Humanoids Learning to Walk : a Natural CPG-Actor-Critic Architecture, *Frontiers in Neurorobotics*, 7:5, 2013
19. E. Donati, F. Corradi, C. Stefanini, G. Indiveri, A spiking implementation of the lamprey's Central Pattern Generator in neuromorphic VLSI, *IEEE BioCAS 2014*, 2014
20. C. Qi, W. Jiang, S. Yang, Y. Qin, B. Deng, W. Xile, A real-time FPGA implementation of a biologically inspired central pattern generator network, *Neurocomputing*, 244, 63-80, 2017
21. S. Joucla, M. Ambroise, T. Levi, T. Lafon, P. Chauvet, S. Saïghi, Y. Bornat, N. Lewis, S. Renaud, B. Yvert,, Generation of locomotor-like activity in the isolated rat spinal cord using intraspinal electrical microstimulation driven by a digital neuromorphic CPG, *Frontiers in neuroscience*, 10, 2016
22. T. Levi et al., Biomimetic neural network for modifying biological dynamics during hybrid experiments, *Journal on Artificial Life and Robotics*, May 2017
23. M. Capogrosso et al., A brain-spine interface alleviating gait deficits after spinal cord injury in primates, *Nature*, 539, 284-288, November 2016

A Metaheuristic Approach for Parameter Fitting in Digital Spiking Silicon Neuron Model

Takuya Nanami

*The University of Tokyo, Institute of industrial Science
Tokyo, Japan*

Filippo Grassia

*LTI Lab., University of Picardie Jules Verne
Saint-Quentin, France*

Takashi Kohno

*The University of Tokyo, Institute of industrial Science
Tokyo, Japan*

nanami@sat.t.u-tokyo.ac.jp, filippo.grassia@u-picardie.fr, kohno@sat.t.u-tokyo.ac.jp

Abstract

DSSN model is a qualitative neuronal model designed for efficient implementation in digital arithmetic circuit. In our previous studies, we developed automatic parameter fitting method using the differential evolution algorithm for regular and fast spiking neuron classes. In this work, we extended the method to cover low-threshold spiking and intrinsically bursting. We optimized parameters of the DSSN model in order to reproduce the reference ionic-conductance model.

Keywords: Spiking neuron model, Low-threshold spiking, Intrinsically bursting, Differential evolution, FPGA

1. Introduction

The silicon neuronal network is composed of analog and (or) digital circuits that solve the differential equations of neuronal and synaptic models. Different kinds of neuronal models have been used in silicon neuronal networks because of the trade-off between reproducibility of neuronal activities and computational efficiency. For example, Merolla *et al.*¹ constructed a digital silicon neuronal network comprising 1 million spiking neurons and 256 million synapses. They adopted Leaky integrate-and-fire (LIF) model that is one of the most commonly used and simple neuron models. Thomas *et al.*² implemented 1024-spiking neurons of Izhikevich (IZH) model³ on a field-programmable gate array (FPGA). Those LIF, expanded LIF, and IZH models are categorized as integrate-and-fire (I&F) based model

which approximates a spiking process by the resetting of the state variables. The I&F-based models can be implemented resource-efficiently, but are capable of reduced reproducibility of complex neuronal activities. For example, these models assume that the amplitude of spikes is fixed, whereas the spike intensity is nonuniform in the nervous system.⁴

We have been studying qualitative neuronal models for digital as well as analog circuit implementation that satisfy both the reproducibility of neuronal activities and low computational cost.^{5, 6, 7, 8} The core idea of our qualitative-modeling-based approach is to reproduce the core mathematical structures that a wide variety of neuronal activities. In our previous studies,^{9, 10} we extended the DSSN models⁷ to support various neuronal classes; regular spiking (RS), fast spiking (FS), intrinsically bursting (IB), low-threshold spiking (LTS),

elliptic bursting (EB), and parabolic bursting (PB). We also studied an automatic parameter fitting method using the differential evolution (DE) algorithm¹¹ for the RS and FS classes.¹²

In this work, we developed the method for the low-threshold spiking and intrinsically bursting classes. Parameters were optimized to reproduce waveforms of the ionic-conductance models in Ref. 13 and reduce the circuit resource requirements for implementation.

The remainder of this paper is organized as follows. Section 2 introduces our neuron model, the DE algorithm, and details of our parameter optimization procedure. The result is shown in Section 3. Section 4 summarizes this work and suggests ideas for the future.

2. Method

2.1. Digital Spiking Silicon Neuron model

The 4-variable DSSN model is a qualitative neuron model that can simulate various neuronal classes (RS, FS, IB, LTS, EB, and PB) by Euler's method with fixed point operation. Its equations are given by

$$\frac{dv}{dt} = \frac{\Phi(u)}{\tau} (f(v) - n - q + I_0 + I_{stim}), \quad (1)$$

$$\frac{dn}{dt} = \frac{1}{\tau} (g(v) - n), \quad (2)$$

$$\frac{dq}{dt} = \frac{\varepsilon}{\tau} (h(v) - q), \quad (3)$$

$$\frac{du}{dt} = \frac{\varepsilon_u}{\tau} (v - v_u - \alpha_u u), \quad (4)$$

$$\Phi(u) = \begin{cases} \Phi_0 & (u < r_{u0}) \\ \Phi_1 & (r_{u0} < u < r_{u1}) \\ \Phi_2 & (r_{u1} < u), \end{cases} \quad (5)$$

$$f(v) \equiv \begin{cases} a_{fn}(v - b_{fn})^2 + c_{fn} & (v < 0) \\ a_{fp}(v - b_{fp})^2 + c_{fp} & (v \geq 0), \end{cases} \quad (6)$$

$$g(v) \equiv \begin{cases} a_{gn}(v - b_{gn})^2 + c_{gn} & (v < r_g) \\ a_{gp}(v - b_{gp})^2 + c_{gp} & (v \geq r_g), \end{cases} \quad (7)$$

$$h(v) \equiv \begin{cases} a_{hn}(v - b_{hn})^2 + c_{hn} & (v < r_h) \\ a_{hp}(v - b_{hp})^2 + c_{hp} & (v \geq r_h), \end{cases} \quad (8)$$

where v corresponds to the membrane potential. Variables n and q are the fast and slow variables which abstractly describe the activity of the fast and slow ion channels, respectively. Variable u is the slowest variable that modifies the structure of the fast subsystem comprising v and n , and used in only the IB mode. In the RS, FS, and LTS modes, u is fixed. Parameter I_0 is a

constant and I_{stim} represents the input stimulus. Parameters $\Phi_0, \Phi_1, \Phi_2, \varepsilon, \varepsilon_u$, and τ control the time constants of the variables. Parameters, $r_g, r_h, v_u, \alpha_u, a_x, b_x$, and c_x , where x is fn, fp, gn, gp, hn , or hp , are constants that adjust the shape of the v -, n -, q - and u -nullclines. Parameters r_{u0} and r_{u1} are used to select Φ depending on u . All of the variables and constants in this qualitative model are purely with no physical unit. Cubic shaped v -nullcline is a key to replicate the spiking dynamics. Because multipliers are resource-consuming in a digital arithmetic circuit, the DSSN model adopts a piecewise quadratic function for the v -nullcline so that its numerical integration step requires only one multiplication between variables.

2.2. Differential evolution algorithm

The DE algorithm¹¹ is a popular heuristic method to solve optimization problems using a real number function. It is one of the population-based optimization algorithms in which a number of parameter sets are converged to quasi-optimal solutions with which the DSSN model reproduces the target waveform. The initial random parameter sets have to be selected carefully so that the behavior of the DSSN model does not diverge. Detailed explanation is written in the previous study.¹²

2.3. Parameter optimization procedure

The LTS class neurons are found in the thalamus. It has the spike-frequency adaptation as with the RS class, and has the rebound bursting; neurons in the LTS class generate a burst firing just after the termination of a sufficiently strong and long hyperpolarizing stimulus. The IB class is a well-known bursting neuron class in the cortex. Neurons in the IB class generate a burst firing immediately at the onset of a sufficiently strong stimulus, then continue spiking until its termination.

The DSSN model has 28 parameters, and exploring their spanning space is not realistic for the computers with average power. To avoid this problem, we divided the state variables of the DSSN model into two groups based on their time scale, and tuned each group in sequence. In our previous study,¹² the RS and FS classes were characterized as the degree of spike-frequency adaptation, and we just optimized parameters of fast state variables in order to reproduce the saddle-

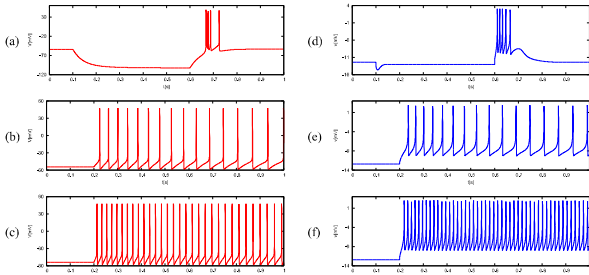


Fig. 1. Waveforms of the ionic-conductance model (red) and the DSSN model (blue) of the LTS class in response to an inhibitory (top) and weak excitatory (middle) and strong excitatory (bottom) step stimulus input.

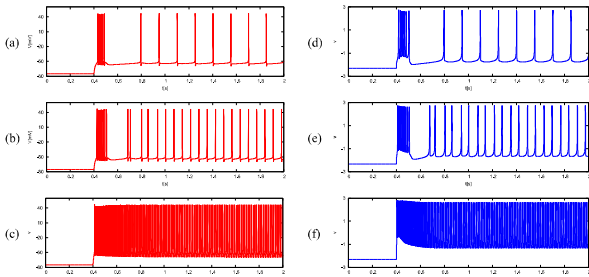


Fig. 2. Waveforms of the ionic-conductance model (red) and the DSSN model (blue) of the IB class in response to a weak (top) and middle (middle) and strong (bottom) excitatory step stimulus input.

node on invariant circle bifurcation. However, LTS and IB classes have more complex structure in their fast subsystem. For the LTS class, we firstly explored the parameter group responsible for the dynamics of the fast state variables v and n so that the fast subsystem of our model is consistent with that of the ionic conductance model of the LTS class. Then, the parameters related to the slow state variable q were determined so that the dynamical behavior of the whole ionic conductance model of the LTS class is reproduced. For the IB class, we firstly fitted the parameters responsible for the dynamics of the state variables v , n , and q so that the dynamical behavior of the corresponding subsystem in the ionic conductance model of the IB class is reproduced. Then, the parameters related to the remaining variable u were determined so that the dynamical behavior of the whole ionic conductance model of the IB class is reproduced.

In the DSSN model's circuit implementation, multiplication between a coefficient and a state variable was realized by shifters and adders, and we needed a larger number of adders and shifters as the number of digits with value 1 in the fixed point representation of the

coefficient increases. Parameters were optimized for not only reproducing waveforms of the ionic-conductance model but also reducing the circuit size. We defined the cost function as follows,

$$f_1(x) = f_{w1}(x) + k_{b1}f_{b1}(x), \quad (9)$$

where $f_{w1}(x)$ is the function that calculates cost from the waveforms of the ionic conductance model and the DSSN model with parameter vector x , based on the difference of spike timing as well as the mean square error of the state variable corresponding the membrane potential. In this function, minimum and maximum values of waveforms are normalized to 0 and 1 for comparison. Function f_{b1} is a number of digits with value 1 in the binary fixed-point expression of the coefficients in x . Constant k_{b1} is to balance these two cost functions. Parameters responsible for the dynamics of the fast variables were determined to minimize the cost function f_1 using the DE algorithm.

3. Result

We found two parameter sets with which the DSSN model reproduces the activities of the ionic-conductance models for LTS and IB classes (Fig. 1). We evaluated the similarity of the spiking patterns between the ionic-conductance model and the DSSN model by calculating some statistics while changing the stimulus intensity (Fig. 3). For the LTS class, we used C_V and L_V ¹⁴ and these are explained in our previous study.¹² Our fitted model's $C_V - L_V$ characteristics are not completely the same as that of the reference model, but share the trend that C_V and L_V decreases as the stimulus intensity increases. For the IB class, we measured the number of spikes in the bursting duration and average firing rate after the bursting. With both models, the number of spikes in the bursting duration increases linearly as the average firing rate increases, although the exact value does not coincide completely. The similarity of these characteristics will be further estimated based on the requirements specified by the circuits' applications.

The results in Figs. 1 and 2 were obtained by numerical integration with fixed-point operation and the Euler's method ($dt = 2^{-13}$ s). The same results are expected to be observed in the following FPGA implementation, because this condition is the same as our VHDL codes. We compiled the DSSN models for Xilinx XC7VX690T using Xilinx Vivado Design Suite.

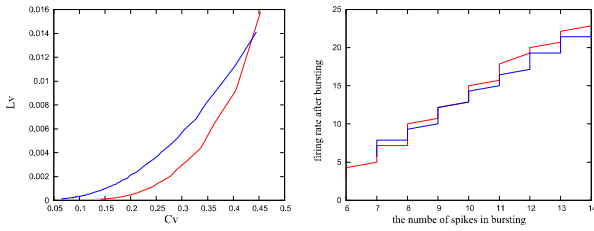


Fig. 3. Statistical properties of the ionic-conductance model (red) and the DSSN model (blue). In the LTS mode (left), the x-axis and y-axis are C_v and L_v . In the IB mode (right), x-axis corresponds to the number of spikes in the bursting and y-axis corresponds firing rate after the bursting.

Table 1 : Device Utilization.

	LTS	IB	LTS(hand-fitted)	IB(hand-fitted)
FF	120	136	122	140
LUTs	938	1265	1264	1639
DSPs	1	1	1	1

Device utilization is listed in Table 1. In the column labeled LTS (hand-fitted) and IB (hand-fitted), the resource usage for LTS and IB settings in Ref. 9 is shown. The requirement for LUTs was reduced without any loss of the reproducibility of the neuronal activities.

4. Conclusion

In this work, we extended the parameter optimization method for the DSSN model in the LTS and IB class modes. These classes have complex mathematical structures of the fast subsystem, thus we carefully designed our fitting procedure in order to reproduce important structures in these classes. We could find parameter sets with which the DSSN model reproduces the characteristics activities of LTS and IB classes using average-power PC (a Xeon E5-2667 CPU with a NVIDIA P100 GPU). Cost functions f_{bx} were introduced to reduce the necessary circuit size. In our future work, we will apply our silicon neuronal networks to the spike pattern recognition.¹⁵

Acknowledgement

This work was partially supported by JSPS SAKURA Program and JST PRESTO and CREST

References

1. P. A. Merolla, J. V Arthur, R. Alvarez-Icaza, A. S. Cassidy, J. Sawada, F. Akopyan, B. L. Jackson, N. Imam, C. Guo, Y. Nakamura, B. Brezzo, I. Vo, S. K. Esser, R. Appuswamy, B. Taba, A. Amir, M. D. Flickner, W. P. Risk, R. Manohar, and D. S. Modha, "A million spiking-neuron integrated circuit with a scalable communication network and interface", *Science*, Vol. 345, pp. 668–673, 2014
2. D. B. Thomas and W. Luk, "FPGA accelerated simulation of biologically plausible spiking neural networks," *Proc. - IEEE Symp. F. Program. Cust. Comput. Mach. FCCM 2009*, pp. 45–52, 2009.
3. E. M. Izhikevich, "Which model to use for cortical spiking neurons ?", *IEEE Trans. Neural Netw.* vol. 15, pp. 1063–1070, 2004
4. H. Alle and J. R. P. Geiger, "Combined analog and action potential coding in hippocampal mossy fibers", *Science*, vol. 311, pp. 1290–1293, 2006
5. T. Kohno and K. Aihara "A three-variable ultralow-power analog silicon neuron circuit" *2016 International Symposium on Nonlinear Theory and Its Applications*, Japan, November 27th–30th, pp. 190–193, 2016
6. T. Kohno, M. Sekikawa, J. Li, T. Nanami, and K. Aihara, "Qualitative-Modeling-Based Silicon Neurons and Their Networks," *Frontiers in Neuroscience*, Vol. 10, No.273, pp. 1–16, Jun., 2016.
7. T. Kohno and K. Aihara. Digital spiking silicon neuron: Concept and behaviors in gj-coupled network. *Proceedings of International Symposium on Artificial Life and Robotics 2007*, 2007.
8. J. Li, Y. Katori, and T. Kohno, "An FPGA-based silicon neuronal network with selectable excitability silicon neurons," *Frontiers in Neuroscience*, Vol. 6, pp. 1–13, Dec., 2012.
9. T. Nanami and T. Kohno. "Simple cortical and thalamic neuron models for digital arithmetic circuit implementation", *Frontiers in Neuroscience*, Vol. 10, No.181, pp. 1–12, 2016
10. T. Nanami, K. Aihara, and T. Kohno, "Elliptic and parabolic bursting in a digital silicon neuron model", *2016 International Symposium on Nonlinear Theory and Its Applications*, Japan, November 27th–30th, 2016
11. R. Storn, K. Price, "A Simple and Efficient Heuristic for global Optimization over Continuous Spaces", *Journal of Global Optimization*, Vol. 11, pp. 341–359, 1997.
12. T. Nanami, F. Grassia, and T. Kohno, "A parameter optimization method for Digital Spiking Silicon Neuron model", *Journal of Robotics, Networking and Artificial Life*, Vol. 4, pp. 97–101, 2017.
13. M. Pospischil, M. Toledo-Rodriguez, C. Monier, Z. Piwkowska, T. Bal, Y. Fregnac, H. Markram, and A. Destexhe. "Minimal Hodgkin-Huxley type models for different classes of cortical and thalamic neurons". *Biological Cybernetics*, Vol. 99, pp. 427–441, 2008.
14. S. Shinomoto, K. Shima, and J. Tanji, "Differences in spiking patterns among cortical neurons.," *Neural Comput.*, vol. 15, no. 12, pp. 2823–2842, 2003.
15. T. Masquelier, R. Guyonneau, and S. J. Thorpe, "Competitive STDP-based spike pattern learning.," *Neural Comput.*, vol. 21, pp. 1259–1276, 2009.

Real-time Digital Implementation of HH neural network on FPGA: cortical neuron simulation

Farad Khoystate¹, Sylvain Saïghi¹, Timothee Levi^{1,2}

¹IMS Lab, University of Bordeaux, France

²IIS, The University of Tokyo, Japan

farad.khoystate@u-bordeaux.fr, sylvain.saighi@u-bordeaux.fr, levi@sat.t.u-tokyo.ac.jp

Abstract

Research on neurological disorder led to an alternative treatment using biomimetic and real-time hardware as neuroprosthesis. These devices must follow several requirements such as the connection between cells and machine or the neurons activities, the bio-hybrids experiments. Furthermore, timing and shape of the action potential (AP) must reproduce the same dynamics of a real nerve impulse. The system must be real time, biomimetic and tunable. Thus, a Field Programmable Gate Array (FPGA) has been chosen to carry the implementation of cortical neurons. The Hodgkin-Huxley (HH) model is the most plausible and realistic one. A model including Fast Spiking (FS), Regular Spiking (RS) and Low-Threshold Spiking (LTS) neurons has been implemented in a Field Programmable Gate Array (FPGA) as a neural network. Some digital methods were used like the CORDIC algorithm or Euler method to solve exponential and differential equations. Here a pipelined implementation of a cortical neural network which contains 150 neurons is presented. This should allow future studies of neurological effect on cells and neurons replacement.

Keywords: Silicon neuron, Hodgkin-Huxley, FPGA, neurological diseases, CORDIC

1. Introduction

The brain's complexity raises different purposes going from image recognition to the study of neurons dynamics using mathematical model and computational tools. Also, the augmentation of neurological diseases affecting people around the world brings scientists to think about different treatments using technology. Consequently, research on neuroprosthesis has been increased and should be used as a treatment or as a device allowing studying and characterizing cells dynamics. Such devices require studying the way in which cells and machine interact, and, the intrinsic spontaneous activity of neural network. Neural model should be also adapted

to the recorded electrical activity in order to reproduces the same dynamics and functions as the brain.

Neurological illness affects cognitive and motor capabilities aiming the Central Nerve System (CNS) which contains more complex cells like cortical neurons. Several cells exist and have different firing behavior. Fast Spiking (FS), Regular Spiking (RS), Intrinsically Bursting (IB) and Low Threshold Spiking (LTS) are studied in this paper. RS, FS, LTS and IB are the main cortical neurons¹⁵.

Implementations of a biodetailed and biorealistic model into an embedded system have been a topic of research for years. To fulfil these conditions, the bursting dynamic of neurons and the shape of the

action potential (AP) must be taken into account. Different models have been compared² such as the Leaky integrate and fire³, Izhikevich³ and Hodgkin-Huxley (HH) model. It has been shown that the HH model, especially the multicompartmental one⁴, is the most realistic and the best choice.

Designs of biomimetic analog chips for robotics or biomedical applications allow multiple advantages like low consumption, a fast process and the use of small devices⁵⁻⁶. However, these technologies are difficult to create, to tune and are expensive. Whereas, the increasing numbers of digital platforms like Field Programmable Gate Array (FPGA) show that they are powerful, fast, tunable and cheaper. Some implementations of neural network have been done in a FPGA⁷⁻⁸ but few used the HH model⁹⁻¹⁰ and among these last none of them aimed bio-hybrid experiments¹¹⁻¹².

In this paper we present the implementation of a neural network of cortical neurons using Hodgkin-Huxley equation in a FPGA dedicated for the neurological diseases study.

2. Materials and methods

2.1 Equations

The first plausible equation which reproduces the shape of the Action Potential (AP) was proposed by Hodgkin-Huxley¹³. In order to reproduce the shape and the bursting dynamics of a cortical neuron model has been used¹⁴. The equations are able to simulate Fast Spiking (FS), Regular Spiking (RS), Intrinsically Bursting (IB) and Low Threshold Spiking (LTS) neurons. The dynamics bursting of these cells have been described and localized¹⁵.

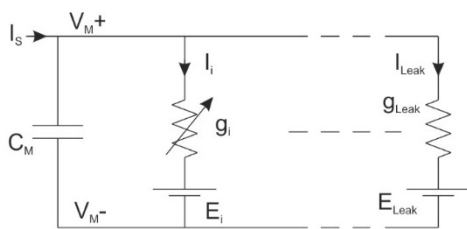


Fig. 1. Equivalent Electrical circuit of the membrane according Hodgkin-Huxley

$$C_m \frac{dV_m}{dt} = I_{stim} - \sum I_i \quad (1)$$

Where V_m is the membrane potential, C_m is the membrane capacitance; I_i is the different ionic currents and I_{stim} is the stimulation current. The current is representing by the following equation:

$$I_i = g_i \cdot m^p \cdot h^q \cdot (V_m - E_i) \quad (2)$$

Where g_i is the maximum conductance; m and h are gating variables for activation and inactivation. E_i is the ion-specific reversal potential and p and q are integers.

According to Hodgkin and Huxley¹³, the values of the activation and deactivation parameters are updated by the equation (3).

$$\frac{dx}{dt} = \frac{x_{\infty}(V) - x}{\tau_x(V)} \quad (3)$$

Where $x \in \{m, n, h, p, q, r, s\}$ and $\tau_x(V)$ and $x_{\infty}(V)$ are obtained by (4) and (5).

$$\tau_x(V) = \frac{1}{\alpha_x(V) + \beta_x(V)} \quad (4)$$

$$x_{\infty}(V) = \frac{\alpha_x(V)}{\alpha_x(V) + \beta_x(V)} \quad (5)$$

Where α and β are exponential-based equations. The chosen equations¹¹ include five ionic currents which are sodium, potassium, leakage, slow potassium (for spike-frequency adaptation) and calcium.

2.2 Implementation

There are requirements concerning the electrical system for bio-hybrid platforms and neurological diseases study. The device must be real-time, tunable, light in resources and containing a large number of neurons. The FPGA (Field Programmable Gate Array) is the best component including flexibility, speed and stability.

FPGA platform with a Kintex-7 FPGA “xc7k325tffg900” family has been used. A Digital to Analog Converter (DAC) is used to output the signals. The DAC has a 12bits precision and a 2.5V reference voltage. The frequency of the system is 200MHz.

Several methods have been used to store values and perform complex operations such as exponential, differential equation resolution and multiplication. All operations are fully pipelined. Fixed point numbers of 39 bits have been used with 20bits for the decimal part and 18bits for the integer part. The last bit is for the sign. The choice of the length has been set for an optimal concession between precision and material cost. Xilinx 7 series of FPGA include “Digital Signal Process” (DSP) used to do multiplications which have been chosen for the implementation. One of the most used operators in the HH equations is the exponential. The implemented method is the Coordinate Rotation

Digital Computer (CORDIC) algorithm¹⁶¹⁵ for his low material cost, speed and precision. It allows the computation of sinh and cosh functions and indirectly the exponential by the addition of the two hyperbolic functions. The Euler method is used for the resolution of the differential equation (6) as it is a good accuracy and low cost of implementation.

$$f(t + dt) = f(t) + dt \cdot f'(t) \quad (6a)$$

$$f_{i+1} = f_i + dt \cdot f'_i \quad (6b)$$

Where the chosen value of the time step dt is $10\mu s$. The time step determines the precision of the result. The smaller the value, the more accurate is the result. However, it implies a limited number of neuron computations between the moment t and $t+dt$. Changing dt apply a difference of amplitude and frequency on the spike trains. Then, $10\mu s$ is the best compromise for accuracy and calculation time.

The implementation structure (fig. 2) has different parts. The HH module computing all equations¹¹ is piloted by a controller unit which calculates the time step, the period to enable reading and writing into the Random Access Memory (RAM) and the neuron index. This module also pilots the Neuron Type unit, allowing to choose the parameters according to the neuron types (FS, RS, IB or LTS). The RAM stores the values of the membrane potential and the gating variables. Previous Values of these are used to perform the Euler method.

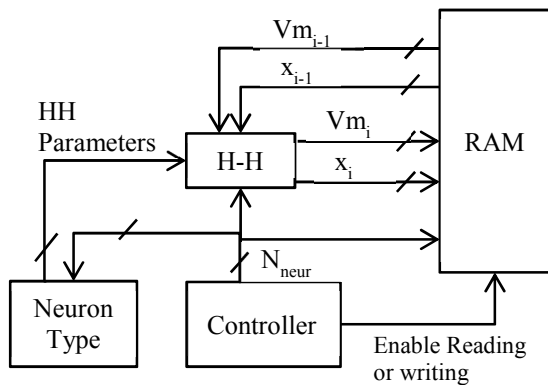


Fig. 2. Implementation structure of the neural network; $V_{m_{i-1}}$ and x_{i-1} respectively represents the previous values of the membrane voltage and the gating variables; N_{neuron} is the index of the neuron and HHparameters contain the values of conductance, neuron size, reversal potential, and membrane capacitance for FS, RS, IB and LTS neurons.

3 Results

Data was captured from an oscilloscope and imported on Matlab for the comparison (fig. 3). Dynamics, amplitude and frequency are similar between software simulations and the FPGA's output for all cortical neurons. 150 neurons are computed in real-time. All type of cortical cells can be selected. Ressources taken by the FPGA is shown on (Table 1.). Use of Look Up Table (LUT) has been increased from¹⁷. It can be explained by the utilization of the CORDIC algorithm which reduces the use of DSP but increases the use of memory. Also, more current, gating variables, parameters and features have been added. Furthermore, the pipeline architecture and the different parallel computations need shift registers for synchronization.

Simulations were done using NEURONS software then implementing on Matlab. The implemented model was compared with biological data.

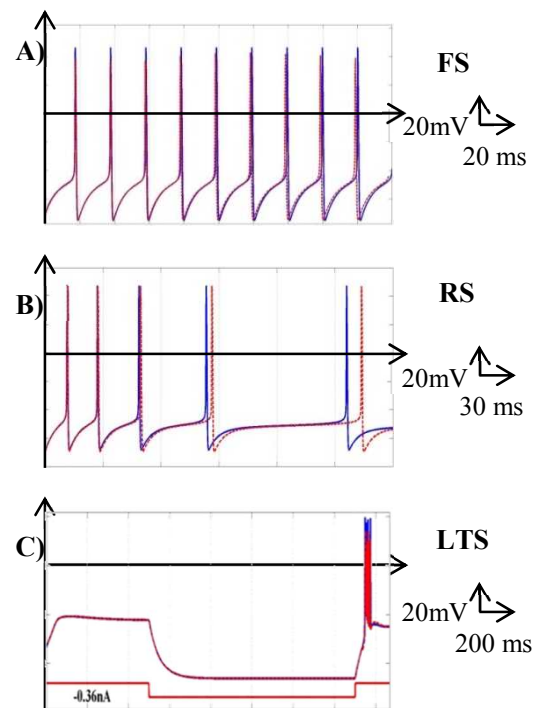


Fig. 3. Comparison of signals from matlab (blue lines) and from DAC Output (red dotted lines); A) FS Neurons with a stimulation current of 0.5 nA; B) RS neuron with a stimulation current of 0.75 nA; C) LTS Neuron with a Stimulation current of -0.36nA;

Table 1. Device resources for the kintex 7 FPGA representing the number of Look Up Table (LUT), Flip Flop (FF) and DSP used.

	Used	Utilization (%)
LUT	169003	82.93
LUTRAM	3141	4.91
FF	65059	15.96
DSP	332	39.52

4 Conclusions

Cortical Neurons have been implemented using Hodgkin-Huxley model in FPGA. The output is performed in real-time and can be used for bio-hybrid experiments. The implementation was validated by a comparison with software simulations and FPGA outputs. More than 150 neurons can be implemented including synapses. In the future, networks of the Hodgkin-Huxley multicompartmental model will be implemented.

The objective of this work can be split up in two goals. First, the study of neurological diseases can be done using this platform. The bio-hybrid experiments for communication between machines and cells are a step towards the implementation of a “diseases neurons” and the observation of their effect on a biological culture. Second, the long term objectives could be summarize by the development of neuro-prostheses which could replace affected neurons or restore the lost communication between different neural networks¹⁸.

References

- Brette R. (2015), What is the Most Realistic Single-compartment Model of Spike Initiation?, PLOS Computational Biology
- Indiveri G (2007), Synaptic plasticity and spike-based computation in VLSI networks of integrate-and-fire neurons. Neural Information Processing, Letters and Reviews 11:135-146
- Izhikevich, E.M. (2003), Simple model of spiking neurons, IEEE Transactions on Neural Networks, vol.14, no.6, 1569-1572
- Davison A, Feng J, Brown D (2000), A reduced compartmental model of the mitral cell for use in network models of the olfactory bulb, Brain Research Bulletin, 51:5, 393-399
- Levi T, Lewis N, Tomas J, Saïghi S, Renaud S, Bornat Y, Alvado L (2008), Neuromimetic Integrated Circuits, VLSI Circuits for Biomedical Applications, Iniewski Editor
- Indiveri G. et al. (2001), Neuromorphic silicon neuron circuits, Frontiers in Neuroscience, 5:73
- Ambroise M, Levi T, Joucla S, Yvert B, Saïghi S. (2013), Real-time biomimetic Central Pattern Generators into FPGA for hybrid experiments, Frontiers in Neuroscience, 7: 215
- Grassia F., Levi T., Kohno T., Saïghi S. (2014), Silicon neuron: digital hardware implementation of the quartic model, Journal of Artificial Life and Robotics, 19:215-219
- Bonabi Y, Asgharian H., Safari S. and Ahmadabadi M. (2014), FPGA implementation of a biological neural network based on the Hodgkin-Huxley neuron model, Frontiers in Neuroscience, 8:379
- Lu M, Wang J-L, Wen J, Dong X-W (2016), Implementation of Hodgkin-Huxley neuron model in FPGAs, Asia-Pacific International Symposium on Electromagnetic Compatibility, 1:1115-1117
- S. Joucla, M. Ambroise, T. Levi, T. Lafon, P. Chauvet, S. Saïghi, Y. Bornat, N. Lewis, S. Renaud, B. Yvert., Generation of locomotor-like activity in the isolated rat spinal cord using intraspinal electrical microstimulation driven by a digital neuromorphic CPG, *Frontiers in neuroscience*, 10, 2016
- T. Levi et al., Biomimetic neural network for modifying biological dynamics during hybrid experiments, *Journal on Artificial Life and Robotics*, May 2017
- Hodgkin AL, Huxley AF (1952), A quantitative description of membrane current and its applications to conduction and excitation in nerve, The Journal of Physiology, 117:500-544
- Pospischil M, Toledo-Rodriguez M, Monier C, Piwkowska Z, Bal T, Frégnac Y, Markram H, Destexhe A (2008), Minimal Hodgkin-Huxley type models for different classes of cortical and thalamic neurons, Biological Cybernetics, 99:427-441
- Connors B. W, Gutnick M. J (1990), Intrinsic firing patterns of diverse neocortical neurons, Trends Neurosciences 13:99-104
- Andraka R (1998), A survey of CORDIC algorithms for FPGA based computers, Proc. ACM/SIGDA Conf., p191-200
- Levi T., Khoiratee F., Saïghi S., Ikeuchi Y. (2017), Digital implementation of Hodgkin-Huxley neuron model for neurological diseases studies, Artificial Life and Robotics
- P. Bonifazi et al., In vitro large-scale experimental and theoretical studies for the realization of bi-directional brain-prostheses. *Frontiers in Neural Circuits*, 7:40, March 2013

Finding appropriate parameter voltages for driving a low-power analog silicon neuron circuit

Atsuya Tange

*Department of Electrical Engineering and Information Systems, The University of Tokyo, 4-6-1 Komaba,
Meguro-ku, Tokyo, 153-8505, Japan*

Takashi Kohno

*Institute of Industrial Science, The University of Tokyo, 4-6-1 Komaba,
Meguro-ku, Tokyo, 153-8505, Japan
E-mail: tange@sat.t.u-tokyo.ac.jp, kohno@sat.t.u-tokyo.ac.jp
www.u-tokyo.ac.jp*

Abstract

This research focuses on a silicon neuron circuit designed utilizing a qualitative neuronal modeling approach. In this circuit, temperature, fabrication mismatch, and secondary effects of transistors cause the difference between the intended characteristics and those in the implemented circuits. Therefore, we have to tune the bias voltages for each neuron instance to realize the desired dynamical behavior after circuit implementation. We constructed an algorithm to automatically find appropriate values for the bias voltages.

Keywords: neuromorphic hardware, neuromorphic chip, silicon neurons, analog VLSI

1. Introduction

Silicon neuron is electronic circuit that mimics electrophysiological behavior of neurons. It is supposed to be used as the basic elements of silicon neural networks, whose aim is to simulate the behavior of the nervous system in real-time or faster. They can be used not only as the high-speed brain simulators for neuroscientific researches but also as a basic technology for the next generation low-power intelligent computing systems. In addition, they can be used to construct bio-silico hybrid systems in connection with neurons, which can be an ideal technology for neuroprosthetic devices.

In this research, we focus on an analog silicon neuron circuit designed by using the techniques of qualitative neuronal modeling whose power consumption is as low as about 3 nW.¹ This circuit is composed of metal-oxide-semiconductor field-effect transistors (MOSFETs) in their subthreshold region for low-power consumption. By

utilizing the qualitative modeling techniques, the model of this circuit was designed so that it can reproduce the dynamical structures in the excitable nerve membrane. The parameter tuning procedure is supported by the feedback amplifiers integrated in the silicon neuron circuit.

The characteristics of this circuit are influenced by temperature, transistors' fabrication mismatch, and their secondary effects (short channel effect, etc). They make the expected circuit characteristics in designing stage and actual behavior of the individual circuit inconsistent. Therefore, it is required to adjust bias voltages of transistors in silicon neuron circuit to get the desired dynamical behavior.

The procedure to do it by hand has been established³, but it is not realistic to execute the procedure for each silicon neuron circuit when we build the large-scale silicon neuronal networks comparable to the human brain which contains about 100 billion neurons.

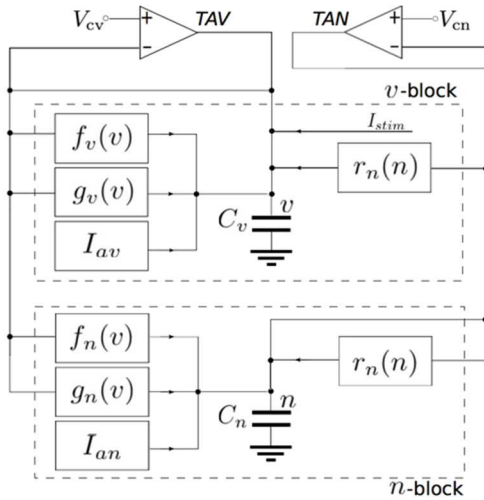


Fig. 1. Block diagram of our qualitative-modeling-based low power silicon neuron circuit

To solve this issue, a system to fit characteristics of silicon neuron automatically is essential. In this work, the same metaheuristic algorithm used in the previous similar works^{2, 3, 4}, the Differential Evolution (DE) method⁵, is used to find proper bias voltages. The DE method performed better in terms of convergence speed and simulation time, compared to other popular metaheuristic algorithms, such as Genetic Algorithm and Simulated Annealing.³ All the results in this work was obtained by circuit simulation using ngspice.

Our silicon neuron model is explained in the next section and our parameter fitting algorithm is in section 3. The results and discussion are in section 4 and 5, respectively.

2. A low-power analog silicon neuron model

Our silicon neuron circuit is composed of two blocks, the v - and n -blocks (Figure 1). Each block's dynamics is represented as below.

$$C_v \frac{dv}{dt} = f_v(v) - g_v(v) + I_{av} - r_n(n) + I_{stim}, \quad (1)$$

$$C_n \frac{dn}{dt} = f_n(v) - g_n(v) + I_{an} - r_n(n), \quad (2)$$

where v and n represents the membrane potential and the dynamics of ionic channels, respectively.

For each function, $f(x)$ ($x = v, n$) is an ideal I-V characteristics of a differential pair circuit, $g(x)$ and $r(n)$ are ideal I-V characteristics of a cascoded transistor circuit with source degeneration with a detached bulk voltage. Both of them are in sigmoidal shape and the latter has

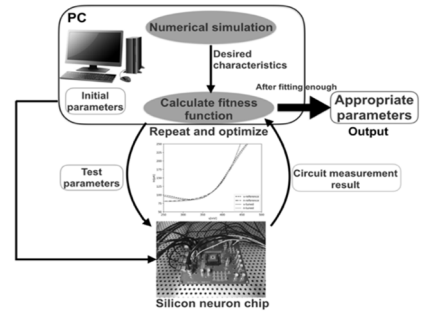


Fig. 2. Automatic bias voltages tuning system for silicon neuron

shallower gradient than the former. They are combined to construct the mathematical structures in the neurons. I_{ax} and I_{stim} are constant current and input stimulus, respectively. They are generated by transconductance amplifiers.

There are nine bias voltages to tune this circuit, one of which is related to the time constant of n and the others affect the shape of the sigmoidal curves.

Our circuit can reproduce Class1 and 2 neurons in the Hodgkin's classification⁶, by reconstructing specific dynamical structures for each class. In this work, we concentrated on the Class1 neuron mode of our circuit.

To estimate the dynamical structures in our circuit, the transconductance amplifiers (TAV and TAN in Figure 1) are used to draw the nullcline of each variable. The nullclines are drawn by measuring the current I_v , the output current of TAV, and I_n , the output current of $r_n(n)$, while sweeping V_{CV} in DC analysis. Their equations are represented as below.

$$I_v = f_v(v) - g_v(v) + I_{av} + I_{stim} \quad (3)$$

$$I_n = f_n(v) - g_n(v) + I_{an} \quad (4)$$

3. Automatic parameter voltages fitting algorithm

Figure 2 illustrates the block diagram of our automatic parameter fitting system. Here, we use circuit simulation instead of actual circuit measurement because this work focuses on the efficient verification of our fitting algorithm in this system. It finds the appropriate parameter values by optimizing the difference between the reference data and the simulation result.

This optimization is done by using the DE method which searches for the best-fitted parameter vector by repeating the mutation, crossover, and selection of parameter vectors for a number of generations. The

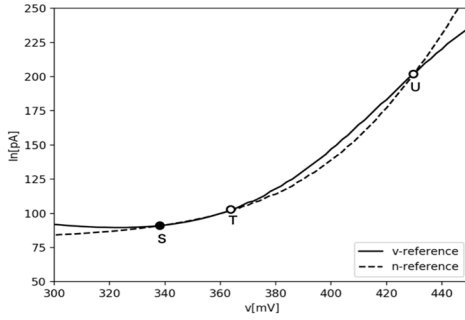


Fig. 3. Nullclines in the Class1 neuron mode

automatic parameter fitting algorithm we suggest is composed of the 2 steps explained below.

3.1. Step1: Fitting nullclines

At first, we fit the shape of the v - and n -nullclines to a given reference nullclines. Figure 3 shows the nullclines in the Class1 neuron mode without stimulus. The two nullclines intersect each other at three points, “S”, “T”, and “U”. They represent a stable node, a saddle point, and an unstable node, respectively. Point “S” corresponds to the resting state and “T” is responsible for the threshold phenomena of neuronal spike generation.

The fitness function for the DE method is calculated by summing the difference between the nullclines obtained in the simulation and the reference nullclines. The fitness function is written as follows:

$$F_1 = \frac{1}{N} \sum_{i=1}^N (s_i(x) - r_{i,x})^2, \quad (5)$$

$$i = 1, 2 \dots N, N = 75, x = v, n,$$

where $s_i(x)$ and $r_{i,x}$ represent the coordinate of a point on the nullclines in simulation result and the reference nullclines, respectively. i is index of each point and x represents v or n . The voltage range of the nullclines is limited to between 300 and 450 mV. This range covers the three intersections of the nullclines in the Class1 neuron mode. Four parameters, fx_Vb , fx_Vdlt , gx_Vm , lax_Vin ($x=v, n$) are tuned for each nullcline. Parameter rn_Vm is fixed at a random value in this step.

Initial vectors are generated in the range between -100mV and +100mV compared to the values used for generating the reference data. The DE method’s optimization step was repeated for 400 generations and 40 vectors were contained in each generation.

3.2. Step2: Fitting neuron characteristics

The nullcline fitting procedure in Step1 was not sufficient

© The 2018 International Conference on Artificial Life and Robotics (ICAROB2018), Feb. 1-4, B-Con Plaza, Beppu, Oita, Japan

to produce the desired behavior similar to the reference model, because our circuit’s dynamical properties are sensitive to the shape of the nullclines and rn_Vm cannot be fitted in Step1. In this step, we fit the dynamical behavior in response to stimulus using the DE method. Threshold current, spike width in response to pulse stimulus, and spike frequency in response to sustained stimulus are used for fitness function.

The definition of the threshold current is the minimum amplitude of the pulse stimulus that makes the membrane voltage exceed 400mV. The spike width is defined as time width when the membrane voltage at the middle of the spike amplitude.

Our silicon neuron circuit is equipped with transconductance amplifiers for generating current stimulus. Pulse stimulus with 500 μ s time width was generated by applying a pulse voltage to the transconductance amplifier. We applied pulse stimulus with a variety of amplitude by increasing the pulse voltage by 7mV step for 20 pulses. The threshold current and the spike width were measured with the firstly observed spike in this sequence.

For the spike frequency, two amplitudes of sustained stimulus, 10pA and 15pA, were applied for 300ms using the transconductance amplifier.

All of the 9 parameters are tuned in this step. The initial parameter value was distributed in the range within the value obtained by Step1 ± 2 mV except for rn_Vm . For rn_Vm , an initial value was found by sweeping until spikes are generated in response to both pulse and sustained stimulus with the other parameters’ value obtained by Step1. The range for this sweeping was between the reference model’s parameter value (435 mV) -6mV to +12mV.

In this step, the fitness function is calculated as follows:

$$F_2 = |(\mathbf{a} - \mathbf{b})\mathbf{W}|,$$

where

$$\mathbf{a} = \begin{bmatrix} I_{thr_{try}} \\ t_{sw_{try}} \\ f_{10pA_{try}} \\ f_{15pA_{try}} \end{bmatrix}, \quad \mathbf{b} = \begin{bmatrix} I_{thr_{ref}} \\ t_{sw_{ref}} \\ f_{10pA_{ref}} \\ f_{15pA_{ref}} \end{bmatrix}, \quad (6)$$

$$\mathbf{W} = \begin{bmatrix} 1 \\ I_{thr_{ref}}/t_{sw_{ref}} \\ I_{thr_{ref}}/f_{10pA_{ref}} \\ I_{thr_{ref}}/f_{15pA_{ref}} \end{bmatrix}.$$

\mathbf{a} is obtained by each transient simulation result and \mathbf{b} is obtained by the reference model. Elements of weight

Table 1. Comparison of silicon neuron characteristics

	Reference	Tuned	Error (%)
I_{th} [pA]	262.1	259.6	-0.953
t_{sw} [ms]	18.0	17.4	-3.30
f_{10pA} [Hz]	29.9	30.8	+3.01
f_{15pA} [Hz]	42.9	43.5	+1.40

vector, \mathbf{W} , are calculated by dividing $I_{thr_{ref}}$ by elements of \mathbf{b} , respectively.

In this step, the DE method's step was repeated for 200 generations and 45 vectors were contained in each generation.

4. Results

Table 1 shows the characteristic of our silicon neuron circuit with the parameters obtained by our fitting algorithm. For all the criteria, the error is less than 4%.

Figure 4 shows the reference transient data and simulation results of the fitted circuit. The amplitude of spikes seems to be well fitted.

The reference data was generated by using ngspice simulation. Thus the ideal fitting result is identical to the parameter set used for the reference data generation, with which the error is zero. But as shown in Table 1, our algorithm could not find the original parameter set but found a local optimum point.

5. Discussion

In this research, we proposed an algorithm to find proper parameter values to obtain the desired dynamical properties for individual silicon neuron circuit instance. This algorithm will be crucial for operation of large-scale silicon neuron networks. The error for the criteria in the fitting procedure was less than 4%. From the viewpoint of engineering application, defining the maximum acceptable error is a difficult problem, because it depends on specific applications but they are not established yet. From the viewpoint of neuromimetics, this error is acceptable when our algorithm is used to tune a number of silicon neuron instances to Class 1, because there is a wide distribution (far larger than 4%) of dynamical properties in the same class of neuronal cells.

We will also try to apply this algorithm in fitting Class 2 neuron. In addition, our algorithm will be improved to be applicable to the three variable ultralow-power silicon neuron circuit.⁷ This circuit can realize a wide variety of

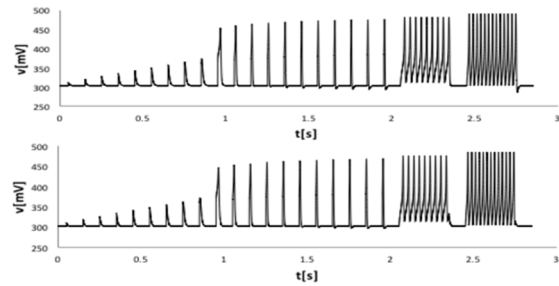


Fig. 4. Transient data of the reference (top) and the simulation results of the tuned circuit (bottom)

neuronal classes such as the regular spiking, the square-wave bursting, and the elliptic bursting.

In the future, we will apply this algorithm to a real circuit.

Acknowledgement

This study was partially supported by JST PRESTO and CREST and JSPS-MAEDI SAKURA Program.

References

1. T. Kohno and K. Aihara, "A qualitative-modeling-based low-power silicon nerve membrane," *2014 21st IEEE Int. Conf. Electron. Circuits Syst. ICECS 2014*, pp. 199–202, 2015.
2. L. Buhry, F. Grassia, A. Giremus, E. Grivel, S. Renaud, and S. Saighi, "Automated parameter estimation of the Hodgkin-Huxley model using the differential evolution algorithm: application to neuromimetic analog integrated circuits," *Neural Comput*, vol. 23, no. 10, pp. 2599–2625, 2011.
3. L. Buhry, S. Saighi, A. Giremus, E. Grivel, and S. Renaud, "Parameter estimation of the Hodgkin-Huxley model using metaheuristics: Application to neuromimetic analog integrated circuits," *2008 IEEE-BIOCAS Biomed. Circuits Syst. Conf. BIOCAS 2008*, pp. 173–176, 2008.
4. E. Green, "A Multistage Heuristic Tuning Algorithm for an Analog Silicon Neuron Circuit," no. *Icarob*, pp. 4–6, 2017.
5. R. Storn and K. Price, "Differential Evolution – A Simple and Efficient Heuristic for global Optimization over Continuous Spaces," *J. Glob. Optim.*, vol. 11, no. 4, pp. 341–359, 1997.
6. A. L. Hodgkin, "The local electric changes associated with repetitive action in a non-medullated axon," *The Journal of Physiology*, vol. 107, no. 2, pp. 165–181, Mar. 1948.
7. T. Kohno and K. Aihara, "A three-variable ultralow-power analog silicon neuron circuit," no. 1, pp. 1–4.

A low power silicon synapse with tunable reversal potential.

Ashish Gautam

*Graduate School of Engineering, The University of Tokyo, 4-6-1 Komaba, Meguro-ku,
Tokyo, 153-8505, Japan*

Takashi Kohno

*Institute of Industrial Science, The University of Tokyo, 4-6-1 Komaba, Meguro-ku,
Tokyo, 153-8505, Japan*

*E-mail: asgautam@sat.t.u-tokto.ac.jp, kohno@sat.t.u-tokyo.ac.jp
www.u-tokyo.ac.jp*

Abstract

Synapses are a building block of signal processing and computation in neuronal cell's networks. We present concept and simulation results of a pseudo five-bit, low power silicon synapse circuit capable of emulating both excitatory (NMDA/AMPA type) and inhibitory (GABA type) responses. The post synaptic current generated in this circuit is proportional to the difference between the post synaptic membrane potential and a tunable synaptic reversal potential.

Keywords: Synapse, neuromorphic, reversal potential, synaptic weights.

1. Introduction

Research interest in the field of neuromorphic engineering has grown significantly in the last decade. The driving force behind the research is an attempt to arrive at a novel computing architecture which surpasses the limitations of the currently prevalent von-Neumann architecture by taking advantage of a highly parallelized network structure of localized memory and processing units to emulate the information processing in neuronal cell's networks. Neuronal and synaptic circuits that emulate the dynamics of neuronal cells and synapses form the building blocks of this nascent computing architecture. Over the years a wide variety of neuronal and synaptic circuits with a varied degree of detail have been proposed. Earlier models¹ simplified

post-synaptic currents as pulses and others replicated the exponentially rising and decaying characteristic of these currents. Recently proposed models² focused on reducing the hardware footprint by sharing of synaptic circuits having a single synapse circuit emulate multiple synapses. These circuits are compact and power-efficient but do not reproduce the synaptic reversal potential which is thought to be playing an important role in the information processing. In addition, their static power consumption was not evaluated even though it has a large impact on the power consumption of large-scale networks.

We propose a low-power synaptic circuit with synaptic reversal potential that has pseudo five-bit of synaptic weights, implementing a familiar kinetic model of synaptic conductance. Our design places its emphasis on ultra-low power consumption and the exponential

©The 2018 International Conference on Artificial Life and Robotics (ICAROB2018), Feb. 1-4, B-Con Plaza, Beppu, Oita, Japan

profile of synaptic current emulating the currents mediated by various neurotransmitters (AMPA, NMDA, GABA_A, and GABA_B) in the brain. In addition, the synaptic current in our circuit is proportional to the difference between the membrane potential and the synaptic reversal potential.

2. Synaptic Model

It was shown that the kinetic models of the chemical synapses which describe the neurotransmitter kinetics can describe and reproduce the synaptic activities precisely³. Following the analysis discussed in Ref.3, the post-synaptic current in our circuit is given by the simplest version of the kinetic models.

$$I_{\text{syn}}(t) = g_{\text{syn}} * r(t) * (V_{\text{syn}}(t) - E_{\text{syn}}), \quad (1)$$

where r represents the fraction of bound post-synaptic receptors, g_{syn} is the maximal value of synaptic conductance, V_{syn} is the post-synaptic potential and E_{syn} is the synaptic reversal potential.

3. Proposed Synaptic Circuit

3.1. Description and analysis

The schematic diagram of the proposed synaptic circuit is shown in Fig. 1. It consists of three major blocks, the input stage (devices M1 to M10), the integrator (C_{syn} , M11, and M12) and the transconductance amplifier (M13 to M19). The input stage is functionally similar to log domain integrator synapse circuit proposed by Merolla et al.⁴ with roles of PMOS and NMOS interchanged. The PMOS transistor M1 acts as a switch, transistor M2 and the inverter I0 together provide the necessary charge to be injected during the rising and falling phase of the input pulse so as to avoid the distortion of the current waveform at the switching points of the input pulse due to the effect parasitic capacitors inherent in the Metal-Oxide-Semiconductor Field-Effect Transistor (MOSFET) device. Transistors M3, M5, M7, and M9 act as switches and determine the state of corresponding branches shown in the figure. These branches are for implementing synaptic weights discussed later. For the present discussion, we assume only the branch consisting M3 is turned ON leaving M5, M7, and M9 in the OFF state. An input pulse at the gate of transistor M1 pulls the drain terminal of NMOS M4

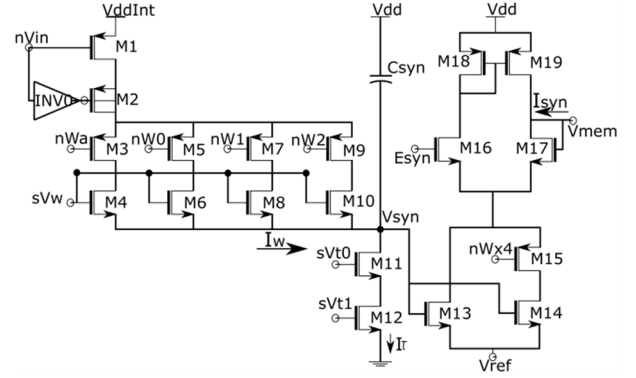


Figure. 1: Schematic diagram of the proposed synaptic circuit. Dimensions of the transistors: $M4=0.3758*(w/l)$, $M6=w/l$, $M8= 2*(w/l)$ and $M10=4*(w/l)$. Nets sVt0 and sVt1 are shorted and connected to a common node V_t . Tail transistor M14 is three times wider than M13.

to V_{dInt} and current that flows through the device is given by (ignoring the short channel effect)

$$I_w = I_{w0} e^{\frac{(k*sV_w - V_{\text{syn}})}{U_T}}, \quad (2)$$

where I_{w0} represents the leakage current, sV_w is the voltage applied to the gate of M4 and V_{syn} represents the source voltage of the transistor M4. This current is then integrated by the RC network formed by capacitor C_{syn} and the NMOS transistors M11 and M12 (as their gates are shorted they act as a single transistor). During the charging phase, these transistors are not in saturation as V_{syn} is initially 0. When the input pulse turns off, the gate of the transistor M1 goes high, the current I_w shuts off and the capacitor begins to discharge linearly through the transistors M11-M12. When these transistors are saturated the current I_τ is given by

$$I_\tau = I_{\tau0} e^{\frac{(kV_\tau)}{U_T}}, \quad (3)$$

where $I_{\tau0}$ represents the leakage current, V_τ controls the time constant of the synaptic circuit. Voltage V_{syn} is fed into the tail transistor of the transconductance amplifier (M13 and M14), which generates a current proportional to the difference of the voltage applied at the inputs of the differential pair ($E_{\text{syn}} - V_{\text{mem}}$). The generated current I_{syn} is given by

$$I_{\text{syn}} = I_o e^{\frac{(kV_{\text{syn}} - sV_{\text{ref}})}{U_T} * \tanh\left(\frac{k}{2U_T}(E_{\text{syn}} - V_{\text{mem}})\right)}. \quad (4)$$

The source of the tail transistors is connected to V_{ref} , which minimizes the leakage current when V_{syn} is set to zero during the inactive state of the synapse

circuit and turns off the tail transistor as soon as possible during the discharging phase when the transistors M11-M12 come out of saturation. By differentiating Eq. (4) we get

$$\frac{dI_{syn}}{dt} = I_{syn} * \frac{k}{U_T} * \frac{dV_{syn}}{dt}, \quad (5)$$

and the dynamics of the node V_{syn} is given by

$$C_{syn} * \frac{dV_{syn}}{dt} = (I_w - I_\tau), \quad (6)$$

combining Eq. (5) and Eq. (6), we get

$$\frac{C_{syn}}{I_\tau} * \frac{U_T}{k} * \frac{dI_{syn}}{dt} + I_{syn} = \frac{I_{syn} * I_w}{I_\tau}. \quad (7)$$

In the log domain integrator synapse described in Ref. 4, the right-hand side of Eq. (7) comes out to be a constant due to the inverse relation between I_w and I_{syn} . This is not exactly true in our circuit due to the body effect of the NMOS transistor M4, but to avoid complexity in our analysis we neglect the body effect and approximate the dynamics of our circuit as that of the log domain integrator. By this Eq. (7) reduces to the equation of a first order low pass filter and its response to a spike arriving at t_i^- and ending at t_i^+ during the charging phase is given by

$$I_{syn}(t) = I_{const} \left(1 - \exp\left(-\frac{t-t_i^-}{\tau}\right) \right), \quad (8)$$

and during the discharge phase

$$I_{syn}(t) = I_{syn}^+ \exp\left(-\frac{t-t_i^+}{\tau}\right), \quad (9)$$

where I_{const} is the constant term on the right-hand side of Eq. (9), I_{syn}^+ is the initial condition at t_i^+ and τ is the time constant given by

$$\tau = \frac{C_{syn} * U_T}{k * I_\tau}. \quad (10)$$

During the discharge phase, a small current flows out of the V_{syn} node back into the synaptic input stage due to the parasitic capacitance of the NMOS transistors M4, M6, M8, and M10 which is comparable to I_τ for higher values of time constant (100ms to 200ms), and in this range to calculate the time constant this additional current flowing out of the V_{syn} node must be added to I_τ in Eq. (10).

3.2 Pseudo five-bit synaptic weights.

Wang et al. proposed a programmable five-bit synaptic weight circuit⁵, where the weights are set by an on-chip

©The 2018 International Conference on Artificial Life and Robotics (ICAROB2018), Feb. 1-4, B-Con Plaza, Beppu, Oita, Japan

DAC. Because the number of synaptic circuits in silicon neuronal networks is very large, their footprint size has to be minimized. We propose a more compact circuit whose resolution is almost five-bit. In Fig.1 the four branches consisting of transistors M3 to M10, with the NMOS transistors sized appropriately provide 4 bit of synaptic weight. The fifth bit is represented by node nWx4 which when active turns ON the switch M15 and incorporates transistor M14 along with M13 as the tail device thus providing four times increase in the magnitude of synaptic current. Table 1 below lists down the synaptic weights given by the five-bit input, nWa, nW0, nW1, nW2, and nWx4. We call it pseudo five-bit as the total number of weight values we get are 27 instead of 32. In our circuit, instead of using 32 transistors to realize full five-bit, we used seven full-sized transistors for M6, M8 and M10 and one half size transistor for M4. This shrinks not only the footprint of these transistors but also that of M2 by reducing the charge injection phenomenon.

Table 1. Pseudo five-bit synaptic weights.

nW2	nW1	nW0	nWa	nWx4	Weight Value
0	0	0	0	0	0
0	0	0	1	0	1
⋮	⋮	⋮	⋮	⋮	⋮
1	1	1	1	0	15
0	1	0	1	1	16
0	1	1	0	1	17
⋮	⋮	⋮	⋮	⋮	⋮
1	1	1	1	1	26

4. Simulation Results

We designed our synaptic circuit to be connected to the silicon neuron circuit in Ref. 6. The scale of synaptic current in our circuit was designed so as to interact with this silicon neuron circuit, whose membrane capacitance is about 900fF. Since the membrane capacitance of the neuronal cells is about several hundreds of picofarads and the scale of synaptic currents is about several hundreds of picoamperes, the synaptic current scale of our silicon synapse circuit is set to about 10pA. This range is far smaller than that in other silicon synapse circuits in Ref.2 and Ref.5. The static power consumption of our circuit was less than 2pW. To

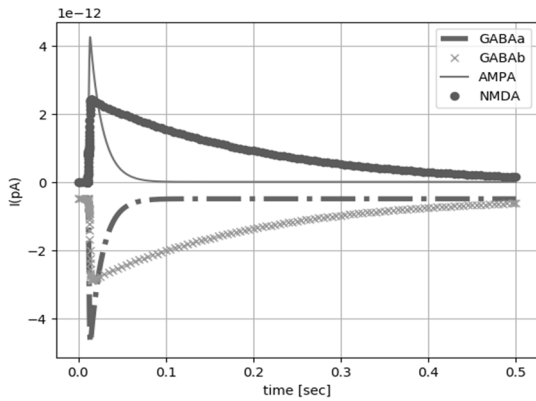


Figure 2: Synaptic currents emulating the response of (a) AMPA (b) NMDA (c) GABAA (d) GABAB neurotransmitters. sV/w was set to 80mV for NMDA and GABA_b mode and to 110mV for AMPA and GABA_a mode.

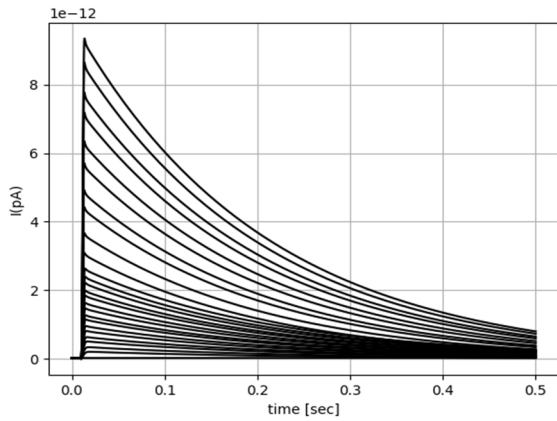


Figure 3: Synaptic current output over the dynamic range of the synaptic weights.

process an input spike the dynamic energy consumption was calculated to be about 500fJ. This value was arrived at by subtracting the value of static energy dissipated from the total energy consumed to process an input spike, with the circuit configured to peak current value of 3pA and time constant of 200ms. For the maximum current of 10pA and maximum time constant of 200ms, this value was calculated to be about 1.5pJ. Figure 2 shows the waveform of the synaptic currents emulating the response of various neurotransmitters and Fig. 3 shows the plot of synaptic currents over the dynamic range of synaptic weights described in Table 1. These results were obtained by circuit simulation using Spectre. All the traces are in typical shape of the synaptic current waveforms. The offset observed in the

inhibitory setting (GABA_a and GABA_b in Fig. 2) will be compensated by silicon neuron circuit’s parameters.

5. Conclusion

We designed a silicon synapse circuit for a low power silicon neuron circuit using Taiwan Semiconductor Manufacturing Company (TSMC) 250nm CMOS process and presented the simulation results. Our circuit is designed to consume lower power compared to 2.8pJ⁷ which implements a DPI synapse discussed in Ref.2. We were unable to find static power consumption value for previously described synaptic circuits in Ref.2 and Ref.5. The area occupied by a single synapse is 26.02x140.2 μm^2 . In our future work, we plan to reduce the area of synaptic circuits by significantly reducing the size of the integrator stage and sharing one transconductance amplifier with many input stages, as well as improve the bit resolution of the synapse circuit.

6. Acknowledgements

This study was supported by JST PRESTO and CREST, and VDEC, The University of Tokyo in collaboration with Cadence Design Systems, Inc.

References

1. Mead, C. (1989). *Analog VLSI and neural systems*. Reading, MA: Addison-Wesley.
2. Bartolozzi, C; Indiveri, G (2007). Synaptic dynamics in analog VLSI. *Neural Computation*, 19(10):2581-2603.
3. Destexhe, et.al. (1998). *Kinetic models of synaptic transmission*. In *Methods in neuronal modelling, from ions to networks* (pp. 1–25). Cambridge, MA: MIT Press.
4. Merolla P and Boahen K. 2004. A recurrent model of orientation maps with simple and complex cells. In: *Advances in Neural Information Processing Systems 16 (NIPS)* MIT Press, Cambridge, MA. pp. 995-1002.
5. Wang, Y., & Liu, S. (n.d.). Programmable synaptic weights for an aVLSI network of spiking neurons. *2006 IEEE International Symposium on Circuits & Systems*. doi:10.1109/iscas.2006.1693637.
6. Kohno, T., & Aihara, K. (n.d.). A three variable ultralow-power analog silicon neuron circuit. *NOLTA 2016* (Yugawara, Japan, November 27-30, 2016).
7. Giacomo Indiveri, Federico Corradi, and Ning Qiao. Neuromorphic architectures for spiking deep neural networks. In *IEEE International Electron Devices Meeting (IEDM)*, 2015.

New methodology of neural network reconstruction for "in vitro" culture on MultiElectrode Array (MEA)

Timothee Leleu

*Institute of Industrial Science, University of Tokyo, Japan
E-mail: timothee@sat.t.u-tokyo.ac.jp*

Timothee Levi

Institute of Industrial Science, University of Tokyo, Japan

Takashi Kohno

Institute of Industrial Science, University of Tokyo, Japan

Kazuyuki Aihara

Institute of Industrial Science, University of Tokyo, Japan

Abstract

Techniques for inferring the network structure are generally based on cross-correlations and result in ambiguous reconstruction. Recently, we have proposed a method for which there is one-to-one correspondence between statistical properties of packets of spikes (or avalanches) and the network structure. This method utilizes higher order statistics of spike trains. We show using numerical simulations of biologically realistic neuron models that the proposed method is general, and is well-fitted for the analysis of cultured neuronal networks coupled to microelectrode arrays.

Keywords: Network structure reconstruction, packets of spikes, neuronal avalanches, cultured neuronal networks.

1. Introduction

The realization of neural prostheses that could help millions of people affected with motor and cognitive disabilities requires engineering the interface between neuronal cell assemblies and the non-organic machine¹. The proper simulation of neuronal activity that can reproduce biologically realistic properties of neurons is necessary for achieving this task. First, the electrophysiological patterns should be simulated accurately and efficiently in terms of computational resources². Second, it is necessary to reconstruct the neural network structure, such as micro-connectivity and the strength of synaptic connections between pairs of neurons. This requires developing efficient techniques for inferring the network structure from recorded activity.

From viewpoint of time series analysis, the task of reconstructing the network structure requires solving the network reconstruction inverse problem using the experimental data. This is a very difficult problem and it is well-known that classical reconstruction methods, such as pairwise correlations³, cannot be used to reconstruction unambiguously the network structure⁴. Indeed, cross-correlation techniques are not adapted for determining the directionality of connections⁵ and cannot distinguish between the effects resulting from connections between pairs of neurons and the ones resulting from a shared input to these neurons⁴. In the following, we describe a method that allows utilizing the higher order statistics of spike trains in order to reconstruct the network structure unambiguously⁶. Higher order correlations in neuronal activity, called

neuronal avalanche, occur when the brain is operating near a critical state⁷. These neuronal avalanches occur both “in vitro”^{7,8} and “in vivo”⁹, but can be identified more clearly “in vitro” experiments which have comparatively lower noise levels due to smaller synaptic density and better controlled experimental environment. In particular, we show using numerical simulations of Izhikevich spiking neurons² that the proposed method allows for accurate reconstruction compared to classical network reconstruction methods¹⁰.

2. Proposed method

The proposed methodology for reconstructing the network structure consists in the following steps (see Fig. 1): (1) the pre-processing of the raw data and binning of spiking activity (2) the detection of spike packets or neuronal avalanches, (3) inferring the network structure using the statistical properties of neuronal avalanches. We note $\Omega = \{\omega_{ij}\}_{ij}$ the matrix of the inferred network structure with ω_{ij} the inferred strength of synaptic connection from neuron j to i . Note that the proposed method is limited to the reconstruction of excitatory connections for the sake of simplicity. Moreover, we focus on the analysis of biological data recorded from cultured neural networks coupled to microelectrode arrays.

2.1. Pre-processing of raw data

First, spikes are detected from the recorded biological data. Bandwidth reduction for selective band amplification and noise reduction is applied. Next, a

discrimination threshold is computed. Lastly, neurobiological spike signals are extracted using, for example, the wavelet transform.

2.2. Detection of neuronal avalanches

The second step consists in the time-binning of the spiking activity. The detected spike train can be discretized in time by considering the binary matrix A such that $A(n, j) = 1$ if a spike triggered by the neuron j has been detected during the time-bin n , and $A(n, j) = 0$ otherwise. We define a neuronal avalanche as a packet of spikes, indexed by p and starting at the time-bin n_p , as the spiking activity in subsequent time-bins that is preceded and succeeded by two empty time-bins indexed by n_{p-1} and $n_{p+\Delta n_p}$, respectively, where Δn_p is the duration of the packet p . The spiking activity during a packet, noted A_p , is given as follows¹⁰:

$$A_p = \{A(n, i)\}_{n \in \{n_p, \dots, p+\Delta n_p-1\}}, \quad (1)$$

where $A(n_p, j) = 1$ with j the index of the neuron that has triggered the packet p , $A(n_{p-1}, i) = 0$, and $A(n_{p+\Delta n_p}, i) = 0, \forall i$. The spiking activity during a packet can be further summarized by summing the matrix A_p with respect to the time-bins, i.e., by considering the vector $L_j^{(p)}$ defined as follows:

$$L_j^{(p)} = \{L_{ij}^{(p)}\}_i, \quad (2)$$

with $L_{ij}^{(p)} = \sum_{n=n_p}^{p+\Delta n_p-1} A(n, i)$. Lastly, the averaged composition of packets, noted m_{ij} , can be calculated by distinguishing the packets as a function of the neurons j that have triggered them as follows:

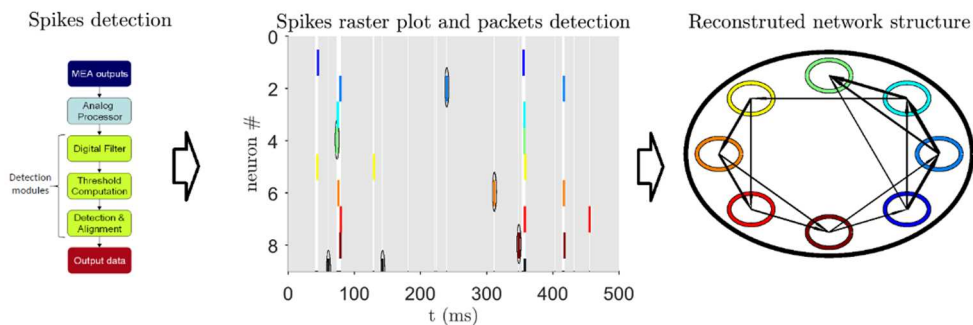


Fig. 1. Schema illustrating the proposed method with (from left to right): pre-processing of raw data, detection of neuronal avalanches, and application of the inversion formula.

$$m_{ij} = \frac{1}{N_j} \sum_p L_{ij}^{(p)}, \quad (3)$$

where N_j is the number of packets that start from the neuron j .

2.3. Inversion formula

The network structure can then be inferred from the averaged composition matrix of packets $M = \{m_{ij}\}_{ij}$ using the following formula, called inversion formula^{6,11}:

$$\Omega \propto I - M^{-1}, \quad (4)$$

where I is the identity matrix of size and M is invertible. Note that eq. (4) can be rewritten as follows using the Neumann series:

$$M \propto \sum_{k=0}^{\infty} \Omega^k. \quad (5)$$

The proposed method for the reconstruction of network structure from the analysis of neuronal avalanches is illustrated in Fig. 1.

3. Evaluation of reconstruction accuracy

In order to test the proposed method, we simulate the activity of neuronal networks using the Izhikevich model², which reproduces numerous electrophysiological features of cortical neurons. The parameter values chosen for the numerical simulations of excitatory and inhibitory neurons correspond to regular spiking (RS) and fast spiking (FS) neurons, respectively. Then, the accuracy of the network reconstruction methods are measured using the Pearson correlation κ between inferred weights and the ones used for the numerical simulations of the Izhikevich model. The

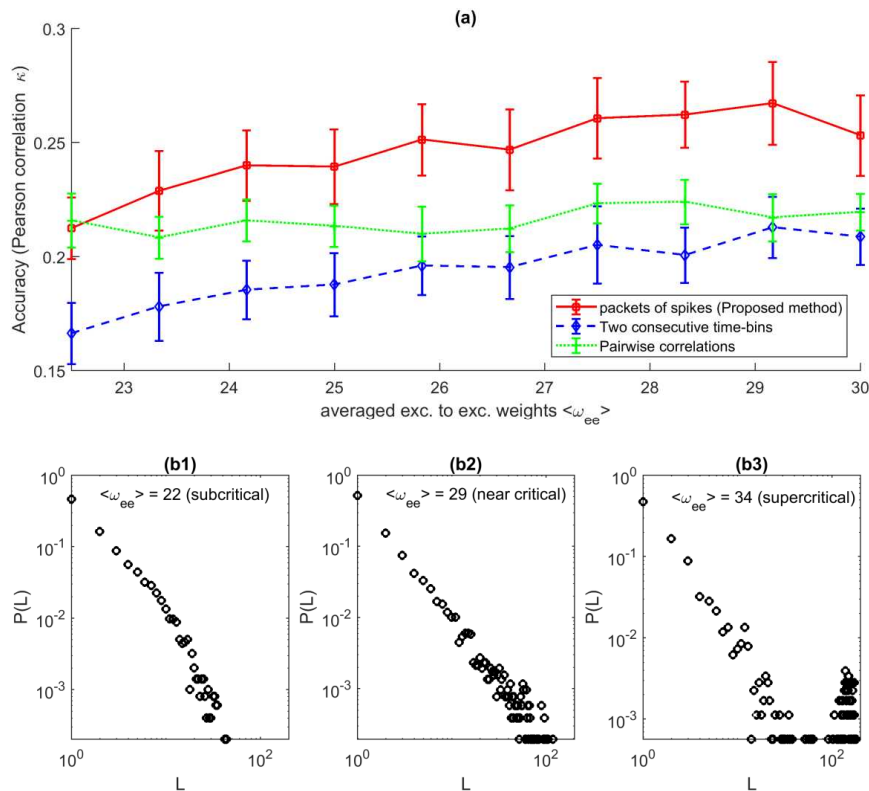


Fig. 2. (a) Accuracy of the network reconstruction measured by the Pearson κ correlation between inferred and true weights vs. averaged strength of excitatory to excitatory connections $\langle \omega_{ee} \rangle$. (b1), (b2), and (b3) show the distribution $P(L)$ of avalanche sizes L in the subcritical, near critical, and supercritical regimes, respectively. In simulations of the Izhikevich model, synaptic noise is modeled by white noise with mean -2 (-2) and standard deviation 5 (6.25) for excitatory (inhibitory) neurons. The proportion of inhibitory neurons and sparsity of connections are 0.1 and 0.2, respectively.

accuracy of the proposed method is compared to the classical method based on pairwise correlations that is described in Appendix A. Lastly, we keep a fix fraction of weights to be non-zero in all cases in order to avoid larger reconstruction errors solely because a greater number of inferred weights are non-zero. This fraction is given by the sparsity of the original network structure.

3.1. Reconstruction at the critical regime

Fig. 2 (a) shows that the proposed method performs better than the ones using the pairwise correlations and two consecutive time-bins, notably near the critical regime. The two consecutive time-bins method utilizes only the two first time-bins of each packet in order to reconstruct the network structure. The distribution $P(L)$ of the avalanche sizes L is shown in Fig. 2 (b1), (b2), and (b3) when the averaged recurrent excitatory connection strength used in numerical simulation, noted $\langle \omega_{ee} \rangle$, is small (subcritical regime), intermediate (near critical regime), and large (supercritical regime), respectively. Smaller and very larger packets do not contain much information about the network structure. In particular, larger packets become identical because the whole network becomes active. It has been suggested that the critical regime is the one at which neuronal networks operate⁷⁻⁹. Thus, these results suggest that the proposed method is well-fitted for the analysis of biological data.

Acknowledgements

This research was supported by ImPACT Program of Council for Science, Technology and Innovation (Cabinet Office, Government of Japan). Authors thank the Social Cooperation Program for Brain-Morphic AI to Resolve Social Issues, IIS, UTokyo.

Appendix A. Pairwise correlation method

The network structure is classically reconstructed using correlation c_{ij} of spiking activity within packets between neurons i and j as follows:

$$c_{ij} = \frac{\langle \delta r_i \delta r_j \rangle}{\sqrt{\langle \delta r_i^2 \rangle \langle \delta r_j^2 \rangle}}, \quad (\text{A.1})$$

where $\langle \rangle$ represent time averages; r_i , the instantaneous firing rate obtained by smoothing the spike train over a

window at proximity of the time t ; and δr_i , the variation of firing rate given as $\delta r_i(t) = r_i(t) - \langle r_i \rangle$.

References

1. P. Bonifazi, F. Difato, P. Massobrio, G.L. Breschi, V. Pasquale, T. Levi, M. Goldin, Y. Bornat, M. Tedesco, M. Bisio, R. Galron, S. Kanner, J. Tessadori, S. Taverna, and M. Chiappalone, In vitro large-scale experimental and theoretical studies for the realization of bi-directional brain-prostheses, *Frontiers in Neural Circuits*. **7**(2013) 40.
2. E.M. Izhikevich, Simple model of spiking neurons, *IEEE Transactions on neural networks*. **14**(6) (2003) 1569–1572.
3. V.M. Eguiluz, D.R. Chialvo, G.A. Cecchi, M. Baliki, and A.V. Apkarian, Scale-free brain functional networks, *Physical review letters*. **94**(1) (2005) 018102.
4. D.H. Perkel, G.L. Gerstein, and G.P. Moore, Neuronal spike trains and stochastic point processes: II simultaneous spike trains, *Biophysical journal*. **7**(4) (1967) 419–440.
5. T. Schreiber, Measuring information transfer, *Physical review letters*. **85**(2) (2000) 461.
6. T. Leleu and K. Aihara, Unambiguous reconstruction of network structure using avalanche dynamics, *Physical Review E*. **91**(2) (2015) 022804.
7. J.M. Beggs and D. Plenz, Neuronal avalanches in neocortical circuits, *Journal of neuroscience*. **23**(35) (2003) 11167–11177.
8. N. Friedman, S. Ito, B. Brinkman, M. Shimono, R. DeVille, K.A. Dahmen, J.M. Beggs, and T.C. Butler, Universal critical dynamics in high resolution neuronal avalanche data, *Physical review letters*. **108** (20) (2012) 208102.
9. E.D. Gireesh, and D. Plenz, Neuronal avalanches organize as nested theta-and beta/gamma-oscillations during development of cortical layer 2/3, *PNAS*. **105** (21) (2008) 7576–7581.
10. T. Leleu, T. Levi, T. Kohno, and K. Aihara, Network structure reconstruction using packets of spikes in cultured neuronal networks coupled to microelectrode arrays, *NOLTA journal*, in revision.

Technique of Recovery Process and Application of AI in Error Recovery Using Task Stratification and Error Classification

Akira Nakamura, Kazuyuki Nagata

Intelligent Systems Research Institute

National Institute of Advanced Industrial Science and Technology (AIST)

Central 2, 1-1-1 Umezono, Tsukuba, Ibaraki, 305-8568 Japan

Kensuke Harada

Robotic Manipulation Research Group

Systems Innovation Department

Graduate School of Engineering Science, Osaka University

1-3 Machikaneyama, Toyonaka 560-8531, Japan

Natsuki Yamanobe

Intelligent Systems Research Institute

National Institute of Advanced Industrial Science and Technology (AIST)

Central 2, 1-1-1 Umezono, Tsukuba, Ibaraki, 305-8568 Japan

E-mail: a-nakamura@aist.go.jp, k-nagata@aist.go.jp,

harada@sys.es.osaka-u.ac.jp, n-yamanobe@aist.go.jp

www.aist.go.jp

Abstract

We have proposed an error recovery method using the concepts of task stratification and error classification. In this paper, the recovery process after the judgment of error is described in detail. In particular, we explain how to change the parameters of planning, modeling, and sensing when error recovery is performed. Furthermore, we apply artificial intelligence (AI) techniques, such as deep learning, to error recovery.

Keywords: error recovery, task stratification, error classification, manipulation, artificial intelligence

1. Introduction

Error recovery is an important research topic in robotic manipulation tasks in industrial production, plant maintenance, and housework. However, systematical methods of error recovery have not yet been developed. We propose error recovery using the concepts of task stratification and error classification. In the proposed method, the judgment of error is performed in the processes of the practice of a system. In this paper, the recovery process after the judgment of error is described in detail. In particular, we explain how to change the

parameters of planning, modeling, and sensing when error recovery is performed. This contributes to systematic error recovery.

Performing extensive error recovery leads to the accumulation of data about the recovery method. Furthermore, we apply artificial intelligence (AI) techniques, such as deep learning, to error recovery.

The rest of the paper is organized as follows: The concept of error recovery is described in Section 2. We modify the process of error recovery based on the size of error. The recovery processes in the case of a small error and a large error are explained in Sections 3 and 4,

© The 2018 International Conference on Artificial Life and Robotics (ICAROB2018), Feb. 1-4, B-Con Plaza, Beppu, Oita, Japan

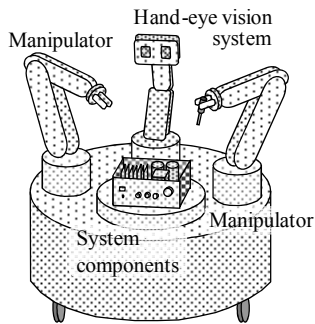


Fig. 1 Manufacturing and maintenance robot for audio-visual system components

respectively. We describe the usefulness of applying AI to error recovery in Section 5.

2. Concept of error recovery

This section describes the proposed error recovery method. The target task is the manipulation of a robot in an industrial factory and a power generation plant (Fig. 1). Concrete instances are assembly, disassembly, part replacement, and maintenance. In recent years, the role of robots in human life and industrial facilities has increased, and robotic manipulation during domestic tasks such as cleaning, washing and cooking is also a target of our error recovery system (Fig. 2).

2.1. Manipulation skill

First, we explain a fundamental unit and the composition of the manipulation task. Manipulation is considered based on a movement unit as a "skill".

We analyzed human motions in tasks such as disassembly and reassembly and found that the movements consisted of several significant motion primitives. We refer to such motion primitives as "skills" [1], [2]. We considered three fundamental skills, i.e., move-to-touch, rotate-to-level, and rotate-to-insert, all of which play an important part in such tasks. A specific task is composed of sequences of skill primitives. Moreover, several skills can be defined based on the modified versions of these three fundamental skills [3].

In addition, composite tasks can be stratified, and a higher task possesses a lower task as a subtask; this is described later.

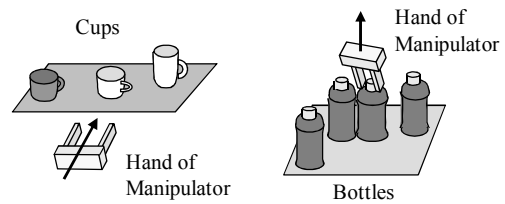


Fig. 2 Manipulators of robots working in daily life

2.2. Proposed error recovery method

Even though extensive research has been performed on techniques to recover an error that occurs in a manipulation system [4]–[6], systematization of error recovery has not yet been achieved. Most of these techniques are applied for the recovery of a small error that occurs in the trajectory of a manipulation robot. There are a few studies on recovery planning for a large error, which causes failure of achievement of an ordered task.

The proposed error recovery technique uses task stratification and error classification, which we proposed in Reference [7]. First, the cause of an error is estimated when it occurs. Next, the appropriate correction for the candidate of the cause is performed on a system. The manipulation returns to the previous step, and the task is re-executed successively (Fig. 3). The possibility of error occurrence would be small as the system is corrected.

If an error is small, the process returns to the lowest layer of a task hierarchy (Fig. 4). On the contrary, if an error is large, the process moves to a high-ranking layer of the hierarchy, and it is re-executed from the previous step (Fig. 4). Fig. 3 shows process flow for the former case, in which stratification is not considered, and the flow of the latter case is provided in Reference [8].

In Reference [7], we proposed error recovery using a backward correction process, which returns to the previous step. However, if an error is small, we perform error recovery using a forward correction process, in which an easy modification that shifts a trajectory is added to the system without returning to the previous step. In other words, in Reference [8], we propose an error recovery method in which it is possible to select a backward correction process or a forward correction process (Fig. 5).

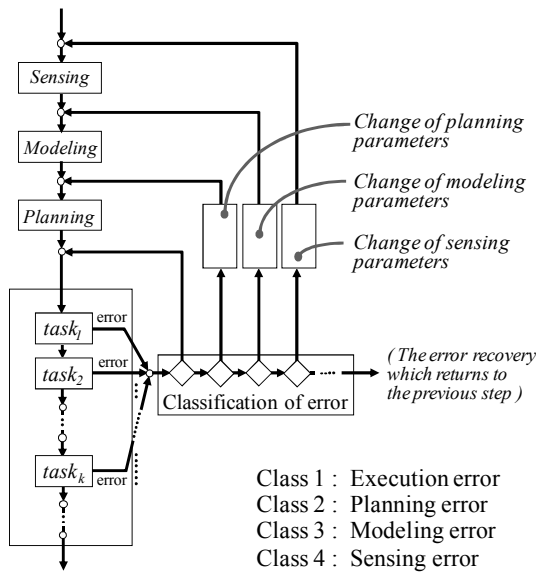


Fig. 3 Fundamental process flow with error recovery

3. Recovery process in the case of a small error

This section describes the error recovery technique for the case of a small error. In particular, the correction of an error is described in detail.

3.1. Conventional methods of controlling error

Conventional control methods have been used to correct a minute error in a trajectory. Techniques that use adaptive control, such as model reference adaptive control (MRAC) and self-tuning adaptive control, are the most popular. In such methods, the error in a trajectory can be minimized using a special control law while operating it. Therefore, it is a kind of error recovery using a forward correction process.

3.2. Concept of proposed error recovery method

We proposed an error recovery method using task stratification and error classification in Reference [7] (Fig. 3, Fig. 4). In this method, a system is revised based on the estimated cause of error, and the process is returned to the previous step and re-executed. In other words, the method can be interpreted as recovery through a backward correction process. We considered the following four kinds of errors: (Class 1) execution error,

(Class 2) planning error, (Class 3) modeling error, and (Class 4) sensing error [7]. The process of handling an error is explained in detail. However, as a process is repeated without making modifications in (Class 1) execution error (Fig. 3), we consider the remaining three kinds of errors in this study.

3.2.1. (Class 2) Planning error

Planning error occurs in cases where the equations used to express a manipulation system do not express an actual system and the parameters used in planning are incorrect (Fig. 3). It includes the following corrections:

- Correction of the parameters of the equations used to express a manipulation system.
- Change in the initial condition for re-executing. For example, revision of the position and orientation of fingers.
- Change in the boundary condition and the threshold in the control process.
- Change in size, the direction of power, and the torque

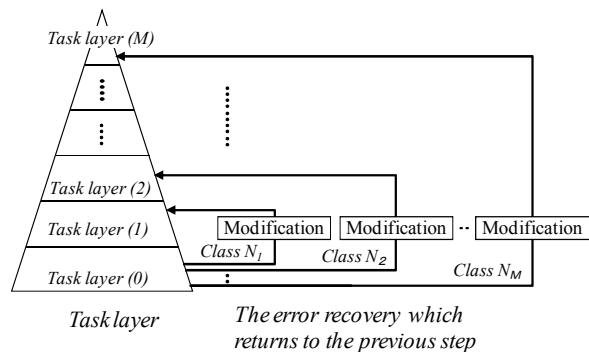


Fig. 4 The expression of task stratification and the process flow of the error recovery

to be provided.

- Change in the planning technique to be used.

3.2.2. (Class 3) Modeling error

Modeling error occurs when a geometry model in software does not express the actual geometry accurately. A concrete correction (Fig. 3) includes the following: First, a change point about a single object is recorded.

- Change in position and orientation.
- Change in size.

- Change in shape.

- Change in various parameters of the sensing

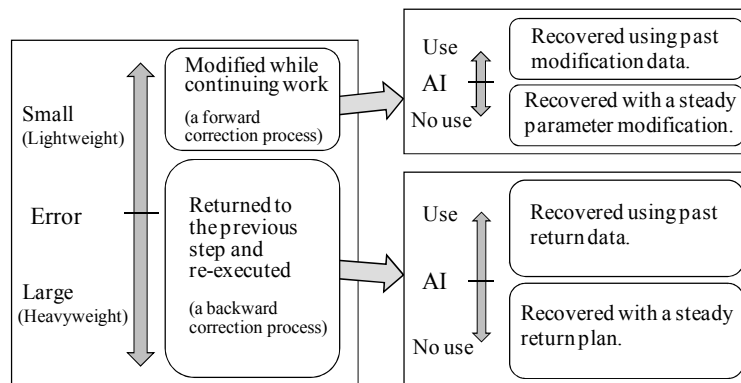


Fig. 5 Table about the error recovery technique

The models of all objects in a working environment are considered as targets for these corrections. However, in several cases, the corrections are performed only for objects directly related to work. For example, in work involving touching an object grasped in two fingers against a face of a board, the grasped objects, two fingers, and the face of the board are considered as the subjects of geometric models.

Next, it is important to be accurately model the relation between the objects. The following aspects should be considered for correctly modeling the relation between the two fingers and the grasped object when the task of touching the grasped object is performed:

- It is important that the location of the face touching the object is expressed correctly with respect to position and orientation. It is corrected if necessary.
- When the grasped object moves because of slipping, it is important to express it using a correction.

For example, the grasped object may slip between the two fingers owing to collision. Similarly, it is important to express the relations between multiple objects accurately.

3.2.3. (Class 4) Sensing error

Sensing error is caused by inaccurate sensing and insufficient calibration. If an error occurs during working practice, and its cause is judged to be a sensing error, the practice task is stopped and modification is performed (Fig. 3). A concrete correction includes the following:

equipment.

- Change in the calibration parameters of the equations used to express the relation between a manipulator and a vision system.

We consider a correction process for the above-mentioned error. It is desirable to know the ranges of the values of the parameters to be revised beforehand. The value of a parameter is changed such that possibility of error occurrence decreases, and re-execution is performed. The values of parameters should be changed as strategically as possible. In addition, it is necessary to identify the interaction between parameters. If other parameters depend on a parameter, then it is necessary to change the values of these dependent parameters.

4. Recovery process in the case of a large error

In this section, we explain the process of error recovery by returning to a higher layer, as shown in Fig. 4. In Reference [7], we considered the repair task of audio-visual system components as an example and explained the stratification of the task in detail.

In the case of a large error, it is frequently necessary to return to the previous step. When practice fails completely, the process may have to return to the starting point, i.e., the highest layer. The working environment may change significantly because of failure. For example, multiple objects may move, fall, and break in the working environment because of failure of practice. In such a case, the contents of the re-execution task may have to be changed significantly or entirely. Even when not

returning to the highest layer, it is better to reconsider a re-execution task in a few cases.

Plural passes may occur in a re-execution task. In such a case, it is suitable to select a pass based on an evaluation standard to be established. There are various evaluation standards; however, considering that an error has caused the re-execution, a method of selecting a pass that ensures the achievement of the final goal of the task is the most desirable.

5. Possibility of the application of AI

In recent years, it has been shown that using AI techniques, such as deep learning, is effective for solving problems in several fields. In addition, the use of AI is efficient for error recovery.

When an error is small, it is easy to apply AI for parameter correction (Fig. 5). It is easy to estimate which parameter should be changed and how much it should be corrected because there is a large amount of past data. When an error is large, the use of AI contributes equally to error recovery (Fig. 5). It is easy to estimate the higher layer to which a pass should be returned as there is a large amount of accumulated data.

It is effective to use AI in the following processes in our error recovery technique:

- Estimation of the cause of error.
- Parameter correction (which parameter should be changed and how much)
- Selection of a point in a higher layer to return to (i.e., return to which step)
- Determination of the contents of a pass for re-execution (by what kind of task)

Applying AI is effective for error recovery. However, as abundant data are necessary, it is required that there is much outbreak of the error, and demand contradicts ideal performance in a sense. When there are only a few errors, there is less experience; thus, it is important to plan and perform recovery steadily, and not to the extent to which AI can be used for recovery.

6. Conclusion

Theoretical systematization of error recovery has not yet been developed. We proposed error recovery using task stratification and error classification. In this paper, we described the recovery process carried out after the

judgment of error in detail. In particular, we explained how to change the parameters that express various conditions in planning, modeling, and sensing errors when recovery is performed. Then, we changed the process of error recovery based on the size of an error. The technique was derived based on task stratification. If an error is large, the recovery process may move to a higher layer. This implies returning to the previous step. Our recovery method can be applied to various sizes of errors. We explained the possibility of applying AI techniques, such as deep learning, to error recovery. Abundant available data on error recovery contribute to the usefulness of AI. Future studies will include the application of our method to an actual system. Moreover, in error recovery using AI, we will study a technique of modifying system parameters in the case of a small error and a method of constructing the re-execution task in the case of a large error.

References

1. T. Hasegawa, T. Suehiro and K. Takase, A model-based manipulation system with skill-based execution, *IEEE Trans. Robot. Autom.*, 8(5) (1992) 535-544.
2. A. Nakamura, T. Ogasawara, T. Suehiro and H. Tsukune, Skill-based backprojection for fine motion planning, in *Proc. IEEE/RSJ Int. Conf. on Intell. Robots Syst.*, (Osaka, Japan, 1996), 2, 526-533.
3. A. Nakamura, T. Ogasawara, K. Kitagaki and T. Suehiro, Using robust and simplified geometric models in skillbased manipulation, in *Proc. IEEE/RSJ Int. Conf. on Intell. Robots Syst.*, (Hawaii, USA, 2001), 1, 138-145.
4. B. R. Donald, Planning multi-step error detection and recovery strategies, *Int. J. Robot. Res.*, 9(1) (1990) 3-60.
5. E. Z. Evans and C. S. George Lee, Automatic generation of error recovery knowledge through learned reactivity, in *Proc. IEEE Int. Conf. Robot. Autom.*, (San Diego, USA, 1994), 2915-2920.
6. C. M. Baydar and K. Saitou, Off-Line error prediction, diagnosis and error recovery using virtual assembly systems, in *Proc. IEEE Int. Conf. Robot. Autom.*, (Seoul, Korea, 2001), 818-823.
7. A. Nakamura and T. Kotoku, Systematization of error recovery in skill-based manipulation, *Artificial Life and Robotics*, Springer, 14(2) (2009) 203-208.
8. A. Nakamura, K. Nagata, K. Harada, N. Yamanobe, T. Tsuji, T. Foissotte and Y. Kawai, Error recovery using task stratification and error classification for manipulation robots in various fields, in *Proc IEEE/RSJ Int. Conf. on Intell. Robots Syst.*, (Tokyo, Japan, 2013), 3535-3542.

Motion selection for 3D robotic snap assembly

Peihao Shi, Kensuke Harada, Weiwei Wan, Ixchel G. Ramirez

*Department of Systems Innovation, Osaka University, 1-3 Machikaneyama-cho
Toyonaka, Osaka, Japan.*

Juan Rojas

*School of Mechanical and Electrical Engineering, GDUT, 100 Waihuanxi Lu, Gongxue 2, 105
Guangdong University of Technology, Guanzhou, Guangdong, China*

Hiromu Onda

*AIST, 1-1-1 Umezono
Tsukuba, Ibaraki, Japan*

Abstract

In this paper, we aim to provide an assembly method for a snap joints assembly task. We create a 3D cellphone model and use ADAMS simulation environment to analyze the relative motion between screen and backer part. We focus on two points in this research. 1) Two kinds of relative motion between the screen and backer parts, i.e., the rotation-based and the translation-based methods, are compared, and 2) difference between assembly and disassembly is analyzed. By using the maximum elastic energy in an assembly process, we show that 1) the rotation-based assembly motion has better robustness than the translation-based assembly motion in cellphone assembly tasks when we set the same initial position error, and 2) The rotation-based assembly method is more effective for snap joint disassembly.

Keywords: Robotic Assembly, Snap joints, Strain Energy.

1. Introduction

Snap joints connection is one of the typical examples of plastic parts assemblage. As the widely application and mass-production of plastic parts, snap joints assembly is becoming more and more popular in assemble method of Industrial products. In snap joint assembly, the connection between two parts is built by elastic deformation of snap joints. [1] Fig.1 shows an example of the snap assembly task. Because of the elastic deformation of the snap joints, it becomes relatively hard for an industry robot to finish snap joints assembly task. As for the research on robotic snap joints assembly. Rojas et al. have proposed a force control method [5] and identification of assembly state [6-8] for the snap assembly problem.

In this paper we aim to provide a better assembly method for a cellphone snap joints assembly task. We create a 3D model of a cellphone, and use ADAMS

simulation environment to analyze the assembly process of the cellphone. Using the Maximum Elastic Energy (MEE) as an index for evaluating the quality of a snap joints assembly tasks, we compare two kinds of assembly methods, i.e., rotation-based and translation-based methods. We also compare the difference of MEE in assembly and disassembly when we choose different assembly method. By using the maximum elastic energy in an assembly process, we show that 1) the rotation-based assembly motion has better robustness than the translation-based assembly motion in cellphone assembly tasks when we set the same initial position error, and 2) the rotation-based assembly method is more effective for disassembly tasks.

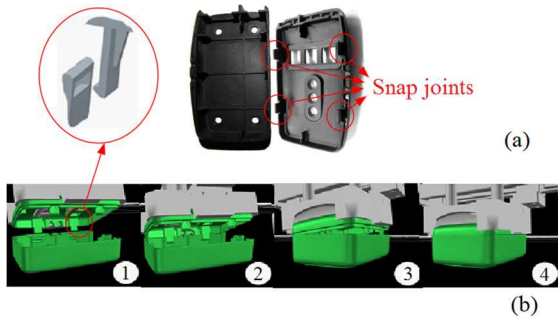


Fig.1 Snap assembly task

2. Approach and Definitions

We create a 3D model of a cellphone used in a physics simulation environment where the screen part contains four snap joints as shown in Fig. 2. We simulate the assembly process by using the predefined relative motion between two parts. Throughout a physics simulation of a snap joint assembly, we consider obtaining the function curve of strain energy and obtaining the MEE from the strain energy curve.

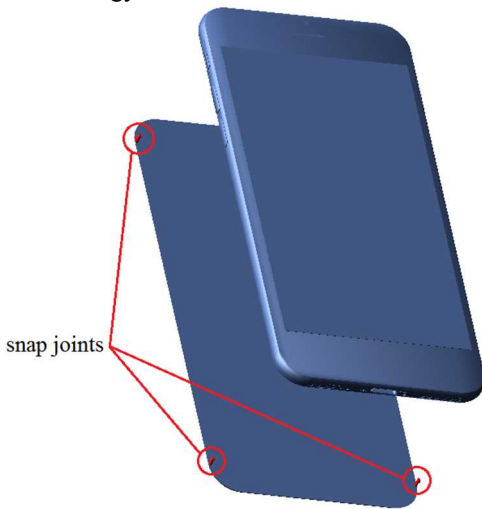


Fig.2 3D cellphone model.

We consider $E_i(s)$ as the total elastic energy in the assembly process. Let s be the functions of a scalar, $0 \leq s \leq 1$, and s changes from 0 to 1 as the part is being assembled. The maximum elastic energy (MEE) U_i is being defined for snap assembly/disassembly task of Part i . [9]

$$U_i = \max_{0 \leq s \leq 1} E_i \quad (1)$$

By compare the MEE of different assembly methods, we can choose the better assembly method which the MEE is smaller.

3. Experiment and Analysis.

In this section, we set two kinds of relative motions where one is translational assembly and the other is rotational assembly. These two motions are representative human assembly motion. The rotation based relative motion is shown in Fig. 3 where the snap on one side of the screen part first contact the backer part, then the screen part is rotated until the snap joints on another side comes into contact with the backer part, finally the screen part translates until it completely fits into the backer part. On the other hand, translation based relative motion is shown in Fig. 4 where the screen part simply translates to fit into the backer part. We compute and compare the MEE of rotation-based/translation-based relative motion. And the better assembly method is be defined as the one bring smaller MEE in assembly process.

3.1 Initial Position Errors.

In robotic assembly tasks. Influence of initial position errors can be used as a criterion of robustness of assembly. In our experiment, we set the initial position errors of screen part to 0mm, 1mm, 2mm to compare the rotation-based and translation-based assembly motion.

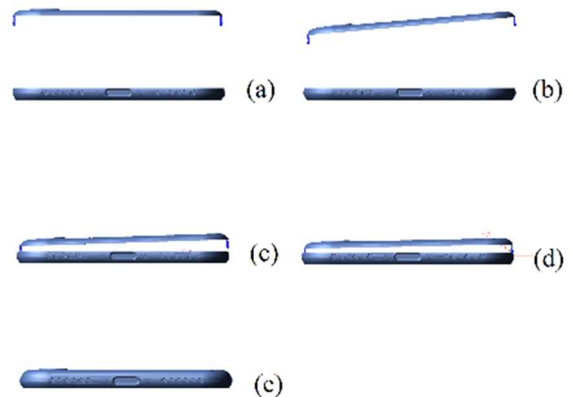


Fig.3 Rotation-based relative motion.

Fig. 5 and Fig 6 shows the simulation results when we set the initial position errors to 0mm. The result

shown the MEE of translation based-motion (1.19J) is bigger than the MEE of the rotation-based motion (0.94J).

Fig. 7 and Fig. 8 shows the simulation result when we set the initial position errors to 1mm. The result shown the strain energy of translation based-motion (2.17J) is bigger than the rotation-based motion (1.12J).

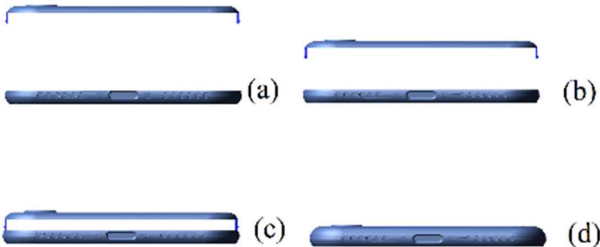


Fig.4 Translation-based relative motion.

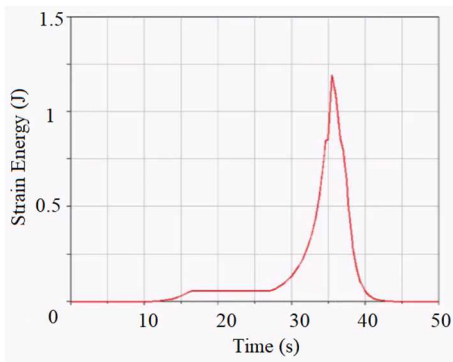


Fig. 5 Stain energy of 0mm position error in translation-based assembly

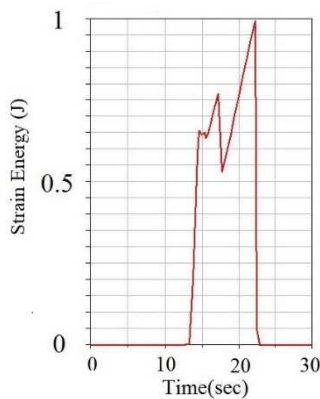


Fig. 6 Stain energy of 0mm position error in rotation-based assembly

Fig. 9 and Fig. 10 shows the simulation result when we set the initial position errors to 1mm. The result

shown the strain energy of translation based-motion (3.51J) is bigger than the rotation-based motion (1.13J).

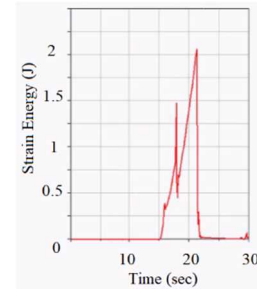


Fig. 7 Stain energy of 1mm position error in translation-based assembly

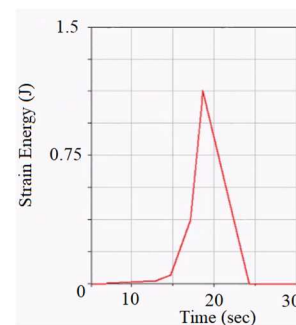


Fig. 8 Stain energy of 1mm position error in rotation-based assembly

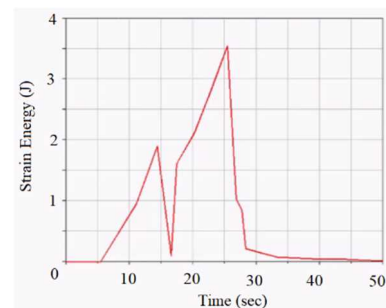


Fig. 9 Stain energy of 2mm position error in translation-based assembly

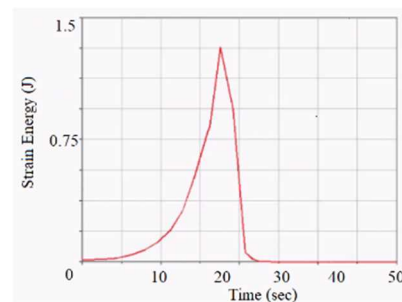


Fig. 10 Stain energy of 2mm position error in rotation-based assembly

The simulation result shown a conclusion: when we set the same initial position errors, the MEE in rotation-based assembly process is smaller than translation-based assembly process. And proved rotation-based assembly method has better robustness than translation-based assembly method.

3.2 difference of assembly and disassembly.

As the second point, we analyze the difference of assembly and disassembly in two kind of assembly methods. The MEE is different in assembly and disassembly when we use translation-based assembly method. Fig. 11 shows the MEE in assembly/disassembly process based on translation-based relative motion. The MEE in assembly process is 1.19J, it is smaller than the MEE in disassembly process (1.52J). Nevertheless, Fig. 12 shows the MEE in assembly/disassembly process when we use rotation-based assembly method, the MEE is almost same in assembly and disassembly process (0.94J).

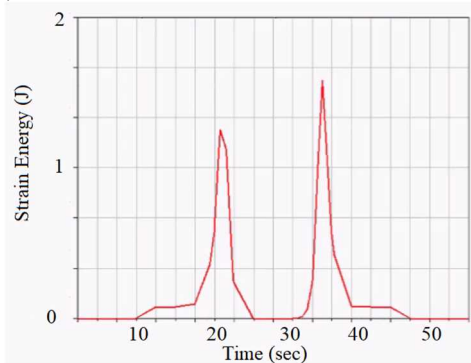


Fig. 11 Stain energy of assembly/disassembly process in translation-based assembly

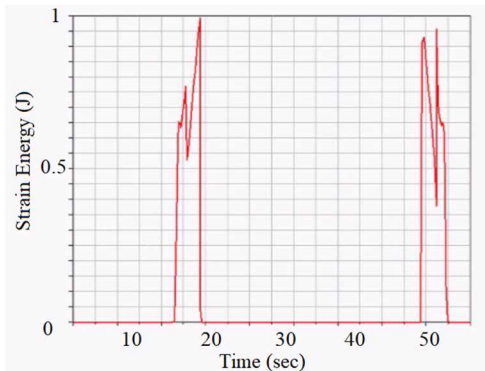


Fig. 12 Stain energy of assembly/disassembly process in rotation-based assembly

The simulation result shown that the rotation based assembly method is more effective when we disassembly the cellphone screen part.

Conclusions.

This paper analyzes the 3D cellphone snap joints assembly task. We compare two kinds of assembly method from the following points. First is the initial position errors of screen part. Second is difference between assembly and disassembly.

Based on the simulation result. We can draw the following conclusions: the rotation-based assembly method has better robustness than translation-based assembly method when we set same initial position error. The rotation-based assembly method is more effective when we disassembly the cellphone screen part.

References

1. P. Shi, K. Harada et al., *Extended Directional Blocking Graph (EDBG) for Snap Joint Assembly*. (The 34-th Annual Conference of the RSJ, 2016)
2. Randall H. Wilson and Jean-Claude Latombe, *Geometric reasoning about mechanical assembly*, (Artificial Intelligence, 71, pp.371-396, 1994.)
3. [3] H. Chang and T.-Y. Li, *Assembly Maintainability Study with Motion Planning*, (Proc. of IEEE Int. Conf. on Robotics and Automation, 1995.)
4. D. Koditscheck, *An Approach to Autonomous Robot Assembly*, (Robotica, vol. 12, no. 2, pp. 137-155, 1994.)
5. J. Rojas, K. Harada et al., *A Constraint-Based Motion Control Strategy for Cantilever Snap Assemblies*, Proceedings of 2012 IEEE International Conference on Mechatronics and Automation, 2012, pp.1815-1821.
6. J. Rojas, K. Harada et al., *A Relative-Change-Based Hierarchical Taxonomy for Cantilever-Snap Assembly Verification*, IEEE/RSJ International Conference on Intelligent Robots and Systems, 2012, pp.356-363.
7. J. Rojas, K. Harada et al., *Early Failure Characterization of Cantilever Snap Assemblies using the PA-RCBHT*, IEEE International Conference on Robotics & Automation (ICRA), 2014, pp.3370-3377.
8. J. Rojas, K. Harada et al., *Strategies, Controllers, and Coordination: Bi-Manual Snap Assembly Automation*, International Conference on Robotics and Biomimetics, 2014, pp.1266-1271.
9. P. Shi, K. Harada et al., *Initial Motion Analysis for Robotic Snap Assembly*. (The 35-th Annual Conference of the RSJ, 2017)

Control Performance Assessment Method as Assessment of Programming Learning Achievement

Yoshihiro Ohnishi

*Faculty of Education, Ehime University, 3, Bunkyocho
Matsuyama, Ehime 790-8577, JAPAN
E-mail: ohnishi@ehime-u.ac.jp,
www. ehime-u.ac.jp*

Abstract

It is an important problem how to estimate the learning achievement of the programming learning. However, the quantitative evaluation method according to the learning achievement is difficult. On the other hand, "work" of a control program influences the control performance of the plant by petrochemical industry, and to have an influence on the operation cost, Improvement of a program and am planning for productivity improvement are suggested by evaluating the control performance quantitatively. This research considers the using control performance assessment method for the achievement value of the programming learning.

Keywords: programming learning, control performance assessment, minimum variance, learning achievement

1. Introduction

It is an important problem how to estimate the learning achievement of the programming learning. However, the quantitative evaluation method according to the learning achievement is difficult. On the other hand, "work" of a control program influences the control performance of the plant by petrochemical industry, and to have an influence on the operation cost, Improvement of a program and am planning for productivity improvement are suggested by evaluating the control performance quantitatively. The idea of control performance assessment is becoming important in the process control area[Huang and Shah, 1999], [Jelali, 2006],[Jelali, 2013]. This research considers the using control performance assessment method for the achievement value of the programming learning.

2. Control performance assessment

The judgement of whether a controller is showing the desirable performance has been formed out of the subjectivity of the expert operator familiar with a plant concerned in the past. There is an index of rise time, the overshoot amount and an attenuation vibration characteristic as the quantitative control performance index of the controller. However, these index can be obtained in the transient state which is at the time of a set value change. The controlled value of the process control system represented by the petrochemical plants can give the reference value as the constant value to the temperature, the pressure and the flow rate. In this case, the steady state control performance which is the minimizing the control error variance is more important

than the target value tracking performance or the disturbance reply. For example, in the system of temperature control to keep the constant value of temperature as shown in Fig.1, it is required to keep the temperature higher than some point. It's necessary to set the high reference value to keep the minimum temperature before the adjustment indicated on figure 1 left side. It's possible to reduce the output variance after the adjustment indicated on figure 1 right side, and even if the target value lower than the before adjustment, it's possible to keep the minimum temperature. The energy the adjustment back requires more than this case and before an adjustment can be done small. Thus it's sometimes tied with efficiency of the energy to disperse a control error small.

These ways have the method based on the benchmark of the minimum variance control [Harris, 1989], the method to consider a fluctuation of the manipulated value as well as output error [Grimble, 2002], the method to express the control performance to compare with data in the past in a plant concerned, and the way to limit the structure of the controller for example the a model based predictive control or PID control and express the control performance in the structure.

This research defines the good program makes the good control which realize the small output variance.

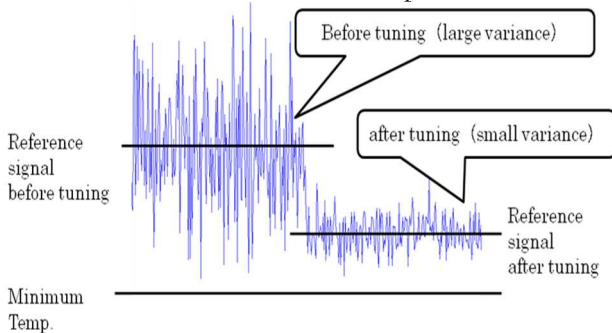


Fig. 1 The example of the temperature control systems.

3. MV-index

This section introduces the calculation of MV-index which is proposed by Desborough and Harris [Desborough and Harris, 1991].

The generalized controlled object described as following

equation.

$$y(t) = z^{-d} G_p(z^{-1})u(t) + G_n(z^{-1})\xi(t) \quad (1)$$

Where $y(t)$ and d system output and minimum estimate value of dead time, respectively. $u(t)$ is control input, and $\xi(t)$ is probability noise including such as observation noise. In addition, when information about dead time can't obtain nothing, d is set as 1. Feedback control law is given as following equation for Eq.(1).

$$u(t) = G_c(z^{-1})e(t) \quad (2)$$

Where, $e(t)$ means the control error signal which is defined as:

$$e(t) := r(t) - y(t) \quad (3)$$

From substituting (1)(1) into (3):

$$e(t) = \frac{r(t) - G_n(z^{-1})\xi(t)}{1 + z^{-d} G_p(z^{-1})G_c(z^{-1})} \quad (4)$$

Here, by considering the steady state, control error signal can obtain as following equation.

$$e(t) = \frac{-G_n(z^{-1})\xi(t)}{1 + z^{-d} G_p(z^{-1})G_c(z^{-1})} \quad (5)$$

where, the noise transfer function $G_n(z^{-1})$ can be divided the term about the dead time before and the term about the dead time after by the following Diophantine equation:

$$G_n(z^{-1}) = G_{n1}(z^{-1}) + z^{-d} G_{n2}(z^{-1}) \quad (6)$$

where, $G_{n1}(z^{-1})$ is polynomial given by following equation.

$$G_{n1}(z^{-1}) = n_0 + n_1 z^{-1} + \dots + n_{d-1} z^{-d+1} \quad (7)$$

From eqns.(5) and (6)

$$e(t) = -\{ G_{n1}(z^{-1}) + z^{-d} G_{n2}(z^{-1}) \} \xi(t) \quad (8)$$

Where $G_d(z^{-1})$ is defined as following equation:

$$G_d(z^{-1}) := \frac{G_{n2}(z^{-1}) - G_{n1}(z^{-1})G_p(z^{-1})G_c(z^{-1})}{1 + z^{-d} G_p(z^{-1})G_c(z^{-1})} \quad (9)$$

And, eqn.(8) is expressed as following equation including

$$\begin{aligned} e(t) &= -\left\{ \underbrace{n_0 \xi(t) + \dots + n_{d-1} \xi(t-d+1)}_{b(t)} \right. \\ &\quad \left. + \underbrace{d_0 \xi(t-d) + d_1 \xi(t-d-1) + \dots}_{w(t-d)} \right\} \\ &= -\{b(t) + w(t-d)\} \end{aligned} \quad (10)$$

Here, $b(t)$ isn't associated with control input and if $w(t-d)$ is possible to be 0 by control input, let $b(t)$

minimum variance output.

Here, σ_e^2 shows actual variance of control error and σ_{MV}^2 shows achievable minimum variance of control error at this system.

Furthermore, minimum-variance control performance assessment index η is shown by following equation:

$$\eta = \frac{\sigma_{MV}^2}{\sigma_e^2} \tag{11}$$

The range is $0 \leq \eta \leq 1$ because $\sigma_e^2 \geq \sigma_{MV}^2$. The large value of MV-index η means that good control performance.

MV-index can be calculated by eqn.(19). However, the numerator of eqn.(11) cannot be calculated directly. This term is obtained as following procedure⁽³⁾.

The following equation can be derived by multiplying z^{-d} for both sides of eqn.(10)

$$e(t-d) = -\{G_{n1}(z^{-1}) + z^{-d}G_d(z^{-1})\}\xi(t-d) \tag{12}$$

$\xi(t-d)$ can be express from eqn.(12).

$$\xi(t-d) = -\frac{e(t-d)}{G_{n1}(z^{-1}) + z^{-d}G_d(z^{-1})} \tag{13}$$

The following equation can be derived by eqn.(8) and eqn.(14).

$$e(t) = -G_{n1}(z^{-1})\xi(t) - \frac{G_d(z^{-1})}{G_{n1}(z^{-1}) + z^{-d}G_d(z^{-1})}e(t-d) \tag{14}$$

Here, the following equation is also obtained because the first term of eqn.(14) is same as b(t) of eqn.(11),

Since the coefficient of the second term of eqn. (15) can

$$e(t) = -b(t) - \frac{G_d(z^{-1})}{G_{n1}(z^{-1}) + z^{-d}G_d(z^{-1})}e(t-d) \tag{15}$$

be expressed as the finite transfer function, (15) can be expressed as the following AR model:

$$e(t) = -b(t) - \sum_{i=0}^p \alpha_i e(t-d-i) \tag{16}$$

The order p must be enough larger than the order of the controlled object. The relations of eqn.(16) are composed by the following matrix equation of the form

$$\mathbf{e} = \mathbf{X}\boldsymbol{\kappa} + \mathbf{b} \tag{17}$$

where, \mathbf{e} and \mathbf{X} are constructed by previous signals. And, $\boldsymbol{\kappa}$ and \mathbf{b} are the autoregressive parameter vector and modeling error vector, respectively.

These are expressed as

$$\mathbf{e} = [e(n), e(n-1), \dots, e(d+p)]^T \tag{18}$$

$$\mathbf{X} = \begin{bmatrix} e(n-d) & \dots & e(n-d-p+1) \\ e(n-d-1) & \dots & e(n-d-p) \\ \vdots & \ddots & \vdots \\ e(p) & \dots & e(1) \end{bmatrix} \tag{19}$$

$$\boldsymbol{\kappa} = [-\alpha_1, -\alpha_2, \dots, -\alpha_p]^T \tag{20}$$

$$\mathbf{b} = [b(n), b(n-1), \dots, b(d+p)]^T \tag{21}$$

where, n is the sample length.

The parameters of eqn.(20) can be obtained by:

$$\hat{\boldsymbol{\kappa}} = (\mathbf{X}^T \mathbf{X})^{-1} \mathbf{X}^T \mathbf{e} \tag{22}$$

Therefore, the minimum variance can be obtained by

$$\sigma_{MV}^2 = (\mathbf{e} - \mathbf{X}\hat{\boldsymbol{\kappa}})^T (\mathbf{e} - \mathbf{X}\hat{\boldsymbol{\kappa}}) \tag{23}$$

4. Simulation Example

This section demonstrates the effectiveness of the proposed scheme by a simulation example. The following equations are used as the controlled object:

$$G(s) = \frac{0.5}{20s+1} e^{-Ls} \tag{24}$$

These models are discredited by 1.0[s] sampling interval.

The following equations are obtained.

$$y(t) = 0.951y(t-1) + 0.0243u(t-3) + \xi(t) \tag{25}$$

Where, the mean value of ξ is 0, $\xi\sigma = 0.05^2$. The manipulate value u is limited as $0 < u < 100$.

First, the ON-OFF control expressed as the following rule was employed for the controlled object (25)

$$\text{If}(y(t) < 30) \text{ then } u(t)=100 \text{ else } u(t)=0.0 \tag{26}$$

This method is an example algorithm which is used by beginner. This algorithm is Conditional branch type which is studied on technology class in Junior high school.

Fig 2 is the control result by using the ON-OFF control. And MV-index is 0.0208 which calculated on $200 \leq t \leq 1200$.

Next, the following PID control method is employed.

$$u(t) = k_p \{e(t) + \frac{e(t)}{\Delta T_i} + T_D \Delta e(t)\} \tag{27}$$

Where, k_p is proportional gain, T_I is the reset time, T_D is the derivative time. Each value was set as $k_p = 7.7$, $T_I = 17$, $T_D = 0.9$, respectively. Fig.3 shows the control result by this PID control method. And MV-index is 0.2585 which is calculated on $200 \leq t \leq 1200$.

From the result of Fig.2, the input value is very oscillatory. The variance of the output value becomes large by the oscillatory input. From Fig.3, the variance of the output signal become small by the PID control. The MV-index can be the good metric to evaluate the programing performance.

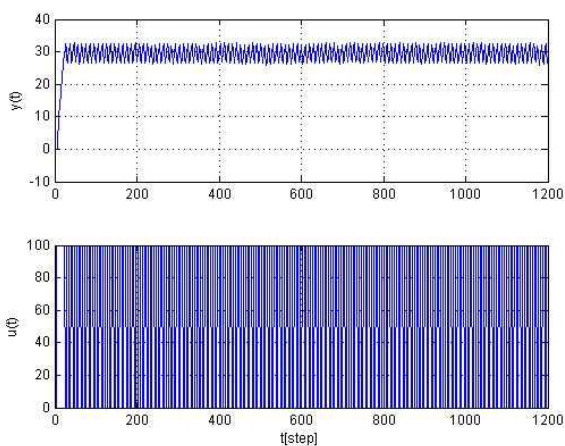


Fig. 2 The result of the ON-OFF control.

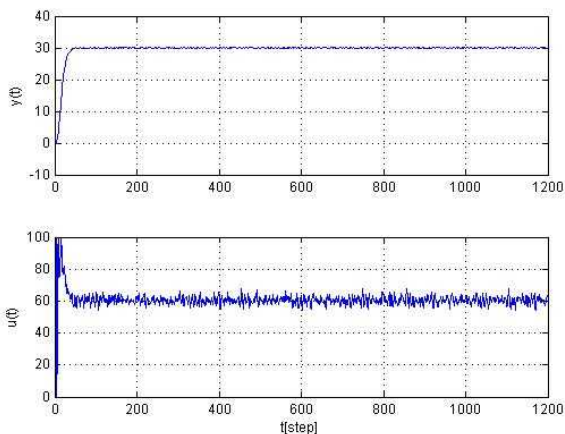


Fig. 3 The result of the PID control.

5. Conclusions

This paper considers the using control performance assessment method for the achievement of the

programming learning. In this paper, a method based on the controller performance assessment was proposed. The effectiveness of the proposed method was evaluated by the simulation example.

References

1. B. Huang and S. L. Shah: *Performance Assessment of Control Loops: Theory and Applications*, Springer, London (1999)
2. M. Jelali : An overview of control performance assessment technology and industrial applications, *Control Engineering Practice*, Vol.14, pp. 441-466 (2006)
3. M. Jelali : *Control Performance Management in Industrial Automation* ,Springer, London (2013)
4. T. J. Harris: Assessment of Closed Loop Performance, *Canadian Journal of Chemical Engineering*, Vol.67, pp. 856-861 (1989)
5. M. J. Grimble: Controller performance benchmarking and tuning using generalized minimum variance control. *Automatica*, Vol. 38, pp.2111-2119 (2002)
6. L. Desborough and T. J. Harris: Performance assessment measures for univariate feedback control, *The Canadian Journal of Chemical Engineering*, Vol 70, pp.1186-1197 (1992)

Practice of Control Education by Experiment using Robot

Shinichi Imai

*Graduate school, Tokyo Gakugei University,
4-1-1 Nukuikita-machi, Koganei-shi, Tokyo, Japan*

Matsui Hideto

*Graduate school, Tokyo Gakugei University,
4-1-1 Nukuikita-machi, Koganei-shi, Tokyo, Japan*

Akira Yamada

*Graduate school, Tokyo Gakugei University,
4-1-1 Nukuikita-machi, Koganei-shi, Tokyo, Japan*

*E-mail: shimai@u-gakugei.ac.jp, b122810x@st.u-gakugei.ac.jp, le@u-gakugei.ac.jp
<http://www.u-gakugei.ac.jp/>*

Abstract

In this paper, for students who attend lectures in control engineering, there are not many students whose understanding is insufficient. The reason why understanding is insufficient is to use many formulas. For that reason, various studies have been conducted on control education. Therefore, in this research, propose a control education method using a robot so that interests and interests are given to students, practice lessons and verify its effectiveness.

Keywords: Control education, robot, Feedback control, Practical education

1. Introduction

Today in sophisticated industrial society, globalization of society advances, rapid progress of science and technology and remarkable change of industrial structure are progressing. In recent years, with the development of computer technology, computerized control is used in various fields. Therefore, the importance of control engineering in the industrial world in Japan is increasing, and training of teachers who can instruct control education is necessary. In control technology as well, control technology is used for nearly all devices such as air conditioners, electric pots, automobiles, etc. from familiar objects to robots, aircraft and spacecraft. In addition, classes of "measurement and control" are being implemented in the teaching of junior high school

technology from 2012. Therefore, many reports are reported that aim to enhance control education^{1,2}.

However, although control engineering is a mathematical content and contents of learning that is difficult for beginners to understand, it is a practical university that is useful only when control theory expressed by mathematical expression is used, and it is a smooth bridge between schooling and practicality. Experiments are essential academics. In learning control engineering, many universities and colleges have conducted methods to learn how to use control theory and learn effectiveness by simulation on a computer, but do not realize what the learned contents are used for. Current situation is that students' interests and interests are not good. Also, in the "Industry" of "High School Study Guidelines"³ each subject which is mainly established in

the Department of Specialization ", there is an item " Electron Measurement Control "within the subject, and outline of electronic measurement control, sequence Control, feedback control, and learning the basics of computer control are included. From this, it is indispensable to handle feedback control and sequence control in industrial high school.

Therefore, in order to make students interested / interested, it is thought that it is desirable to learn through experiments, not only at the school. However, the experimental apparatus related to control has many large-scaled apparatuses and the price is very expensive and it is difficult to conduct experiments with a small number of people.

The purpose of this research is to develop controlled educational materials which can learn each operation of manual control, automatic control, PID control experientially using a robot.

2. Content on measurement and control described in the guidelines for teaching high school

In the case of teaching the lesson of control, it is more desirable to acquire expert knowledge related to the guidance contents as well as knowledge on the guidance contents as well as to achieve smoother and more advanced instruction. Therefore, it is necessary to construct a lesson curriculum for students of teacher training college based on the guidelines for teaching. In the commentary on teaching guidelines for high school educational guidelines in industrial edition, contents related to control and items to be handled are clearly stated in the 24th electronics measurement control and others as follows.

- (1) Outline of electronic measurement control
- (2) Sequence control
- (3) Feedback control
- (4) Basics of computerized control

In addition, it is described that the above contents comprehensively understand measurement technology, automatic control technology and computer technology. Sequence control aims to handle the fundamentals of sequence control, equipment of sequence control, use of basic circuits and programmable controllers, and to

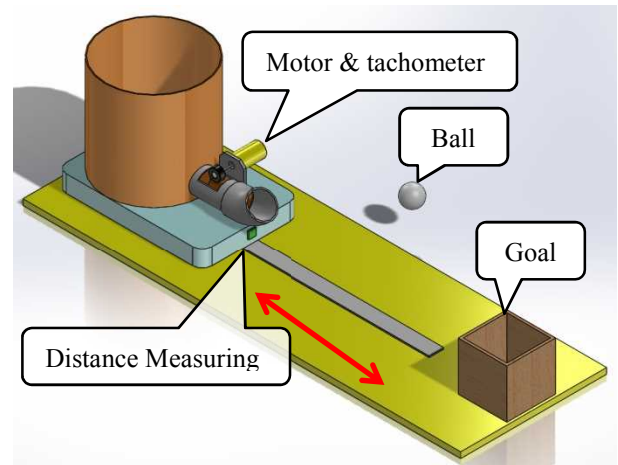


Fig.1 Control teaching materials robot

acquire knowledge and techniques concerning sequence control. Typical equipment such as switches, relays, and timers used for sequence control, types and uses of sensors that detect physical quantities of light, temperature, force, and logic elements are taken up. Also learn about features, functions, characteristics, symbol symbols and make them available for actual use. Feedback control aims to handle the basics of feedback control, control characteristics and utilization of feedback control, and to acquire knowledge and techniques related to feedback control. Here, it is described that typical feedback control examples such as process control, servo control and the like are taken up, understanding of the outline thereof is made and it is made available for practical use.

3. Educational robot teaching materials

Fig.1 shows the overall image of the educational robot teaching material. The robot can blow ping-pong balls. The robot is composed of a motor for flying ping - pong balls, a tachometer capable of detecting the speed of the motor, and distance measuring (GP2Y0E03) for determining the distance to ping pong balls. This robot can control the number of revolutions of the motor according to the distance of distance measuring, and can go to the goal with the ping-pong ball.

3.1 Precautions for production

In making a robot, cautioned is as follows.

- (1) The operation of control can be visually recognized
- (2) Produce at low price.

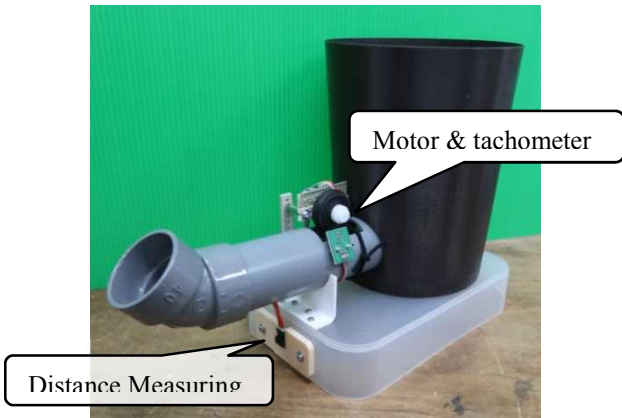


Fig.2 robot

It is possible to actually observe how the control input computed based on the theory is added to the controlled object or the behavior of the controlled object. Also, by listening to the operation sound of the device, touching the switch or the button, you can feel the operation of the device. Furthermore, since teaching materials break down when used, it is intended to facilitate the exchange of parts. Fig.2 shows the actual appearance of the robot. Parts of this robot are purchased at a 100 yen shop. The parts cost is about 5000 yen per one.

3.2 Hardware

Hardware is shown in Fig.3 and the circuit diagram of the robot is shown. The computer uses Arduino Uno Rev3 (Next, Arduino). Using this computer, calculate the input to the motor from commands from the operation unit and information from the sensor. Connect Arduino and personal computer (PC). The PC displays the results of input and output and various gains. In addition, as shown in Fig.4, a volume is attached to the circuit board, so that it is possible to adjust each gain. Next, there is a switch that switches between manual control and automatic control.

3.3 Software

Arduino converts the input analog voltage to a numeric value (integer) from 0 to 1023 in Arduino by 10 bit resolution. The output voltage is controlled by PWM control. The output can change the duty ratio by specifying one numerical value (integer) of 0 to 255 with 8 bit resolution. When the numerical value is 0, the duty ratio is 0%, in the case of the numerical value 128 it is 50%, in the case of the numerical value 255 it is 100%. From the voltage output by the tachometer, the rotation speed of the rotor is calculated from the following formula.

$$e = \frac{5.0}{1024} e_i \quad (1)$$

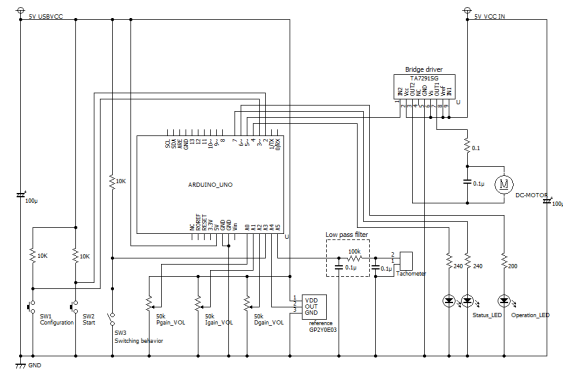


Fig.3 circuit

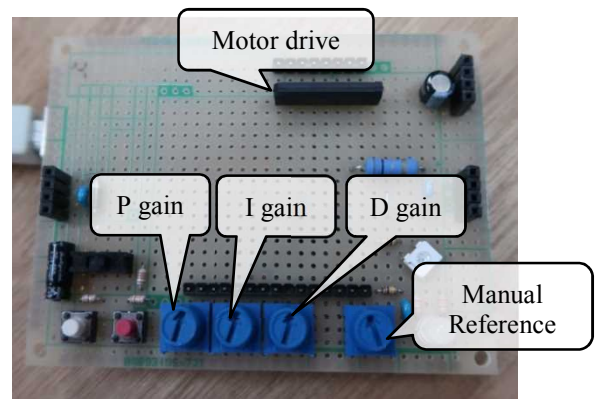


Fig.4 Operation

$e[V]$ is the output voltage of the sensor, and e_i is a numerical value from 0 to 1023. Skip the ping-pong balls from the motor to the goal and measure the output voltage of the tachometer 10 times when the position of the robot is blown at 10 cm intervals. The relationship between the voltage and the position of the tachometer is found by the least squares method.

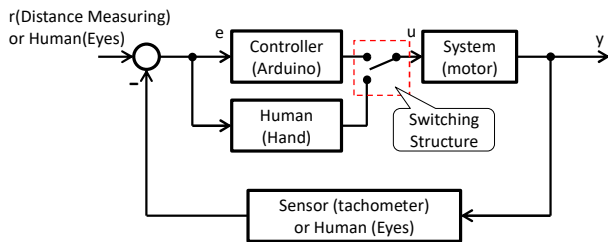
4. Experience contents

Practice hands-on training using a robot. Specific contents of education in experiential experiments are as follows.

- Difference between manual control and automatic control
- Difference between ON-OFF control and PID control
- How to adjust the PID gain of automatic control

Consider the block diagram as shown in Fig.5. However, $r(t)$ is the target value, $y(t)$ is the output, and $e(t)$ is the deviation ($=r(t)-e(t)$) between the target value $r(t)$ and the output value $y(t)$. $u(t)$ is the input (manipulated variable).

Fig.5 Block diagram



4.1 ON-OFF control

Learn that accurate control cannot be done in the sense that it uses a simple ON-OFF control to make it perfectly match the target value. We teach that control result not only output, but also important to observe input. The ON-OFF control is expressed by the following equation.

$$u(t) = \begin{cases} u_c, & e(t) > 0 \\ 0, & e(t) \leq 0 \end{cases} \quad (2)$$

where, u_c is a constant value.

4.2 P control

Design a proportional controller and give an appropriate proportional gain K_p to observe the output. P control is expressed by the following equation.

$$u(t) = K_p e(t) \quad (3)$$

In the case of stable control, steady state deviation occurs and learns that it becomes unstable when K_p increases.

4.3 PI control

In consideration of the problem in the proportional controller, an integral controller is introduced in addition to the proportional controller. The PI control is expressed by the following equation.

$$u(t) = K_p e(t) + K_I \int_0^t e(\tau) d\tau \quad (4)$$

where, K_I is the integral gain. In this case, unlike the P control, learn that the steady-state error can be made zero.

4.4 PID control

Learn about PID control with proportional controller, integral controller plus differential controller. PID control is expressed by the following equation.

$$u(t) = K_p e(t) + K_I \int_0^t e(\tau) d\tau + K_D \frac{de(t)}{dt} \quad (5)$$

where, K_D is the differential gain. Understanding of PID control is deepened by finding the optimum gain while trying trial and error on the three gains. Fig.5 and Fig.6 show the robot output results.

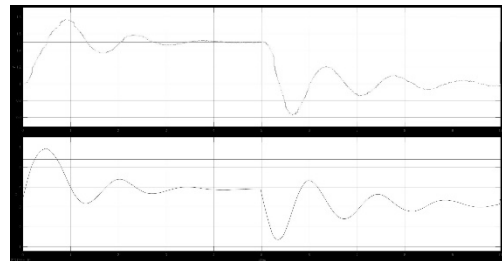


Fig.5 Gain unadjusted result

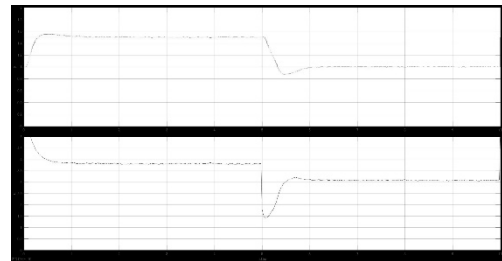


Fig.6 Gain adjusted result

As shown in Fig.5, since the gain is not appropriately adjusted, it can be seen that it is an oscillatory response. Fig.6 shows that the response is improved because the gain can be adjusted. The results of the questionnaire on class practice will be reported on the day of presentation due to space limitations.

5. Conclusion

In this paper, we developed teaching materials that can realize the usefulness of measurement and control. As a result, manual control and automatic control of the motor could be performed. For future plans, we would like to set issues such as equipment troubles and difficulty level setting in practice and want to improve.

References

1. K.Asato, K.Teruya, T.Nagado and S.Tamaki, Development of Magnetic Levitation System for Science and Technology Education: Magnetic Levitation Control by Using a Hall Element Displacement Sensor with Neural Network, *IEEJ journal paper(D)*, 136(10)(2016) 744-752
2. T. Asai, K. Osuka, M. Ishikawa and M. Inoue, A Motivational Lecture Using an Experimental Control System to Get Personal Experience and Its Effectiveness *Transactions of the Society of Instrument and Control Engineers*, 48(10) (2012) 622-631.
3. Ministry of Education, Culture, Sports, Science and Technology: *High School Study Guidelines Explained* (Industrial Edition), Jikkyo Shuppan Co., Ltd., (2010)

Development of Support Teaching Material for Nurturing Cooperativity through Playing

Kazuo Kawada

*Department of Technology and Information Education, Hiroshima University,
1-1-1 Kagamiyama, Higashi-Hiroshima, Hiroshima 739-8524, Japan
E-mail: kawada@hiroshima-u.ac.jp*

Teruyuki Tamai

*Matsuyama Municipal Kamogawa Junior High School,
2-7-19 Kamogawa, Matsuyama, Ehime 791-8004, Japan
E-mail: tama.wr@gmail.com*

Abstract

We have been conducted educational activities utilizing robots corresponding to each stage from kindergartens to junior high schools. In this study, we propose and verify an educational material that supports collaborative operating by experiences related to people and things. Specifically, three children have a joystick for operating a robot. The robot does not move unless you manipulate the joystick at the same time. I developed the supporting teaching material that nurture cooperativeness through play.

Keywords: Cooperation, Teaching Material, Operation, Evaluation

1. Introduction

Recently, in Japan, it is a problem that coordination through desirable group activities is not acquired by change of social situation. Specific problems include the following:

1. Unable to build a good human relationship with others.
2. Unable to work for a group.
3. Unable to solve problems with other people by discussing them.

Also, it is pointed out that there are Japanese children who can not successfully adapt to groups in kindergartens and elementary schools connection.

On the other hand, in November 2014, Japanese minister of education, culture, sports, science and technology consulted Central education council in relation to an emphasis on the quality and quantity of knowledge, emphasis on the quality and deepening of learning, learning subjectively and collaboratively learning to find

and solve problems, and shows how to improve teaching methods for them. For this reason, there are many researches on learning methods^{2,3,4} in educational subjects. However, research that nurtures cooperativeness which is important for character education using a robot is a little.

Therefore, in this study, we proposed and developed cooperative teaching material and evaluate cooperativeness. Specifically, we gave children joysticks to operate a carrier, and made the mechanism that the carrier did not move unless it was operated at the same time.

2. Proposed Teaching Material

The proposed teaching material is shown in Fig.1 with the concept as follows.

- 3 people cooperate in maneuvering
- Remote control type (joystick type)
- Data recording (using a data logger)

Figure 2 shows the system configuration of this teaching material. The joystick states (0V or 5V) of 3 people are sent to a micro-controller⁴. Then, the states of each joystick are stored in the data logger by the micro-controller or the data is transferred to the tablet PC by Bluetooth.

The algorithm for operation of this teaching material is adapted to adjust the speed of the crawlers of a carrier by the following equations.

$$Speed_{Right} = \frac{Speed_{MAX} \cdot MD_R}{3} \quad (1)$$

$$MD_R = JS_{1R} + JS_{2R} + JS_{3R} \quad (2)$$

$$Speed_{Left} = \frac{Speed_{MAX} \cdot MD_L}{3} \quad (3)$$

$$MD_L = JS_{1L} + JS_{2L} + JS_{3L} \quad (4)$$

where $Speed_{Right}$ ($Speed_{Left}$) is the speed of the right crawler (the left crawler) of the vehicle and $Speed_{MAX}$ is the maximum speed of the crawler. Further, JS_{1R} (JS_{1L}), JS_{2R} (JS_{2L}) and JS_{3R} (JS_{3L}) denote signals on the right side (the left side) of the joysticks of the operator A, the operator B and the operator C, respectively. The left and right sides of joysticks are set to 0 when not moving, 1 when moving to the forward side, and -1 when moving to the backward side. MD_R (MD_L) denotes the sum of JS_{1R} , JS_{2R} and JS_{3R} (the sum of JS_{1L} , JS_{2L} and JS_{3L}), and the signal of a majority decision is output as shown in Fig.3. With these signals of majority decision, the carrier can not move unless the operator cooperatively operates.

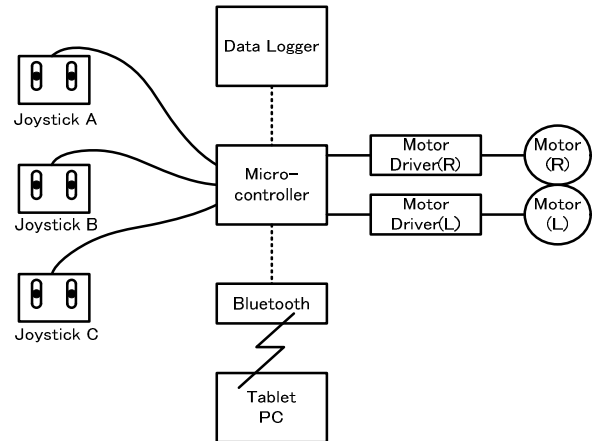


Fig.2 Schematic figure of prototype equipment.

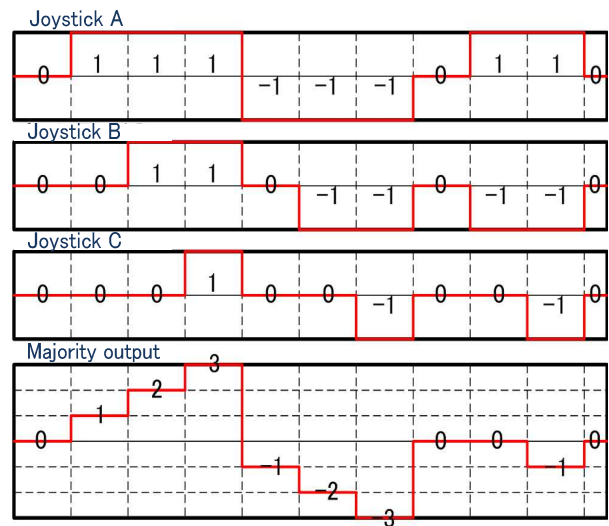


Fig.3 Majority decision.

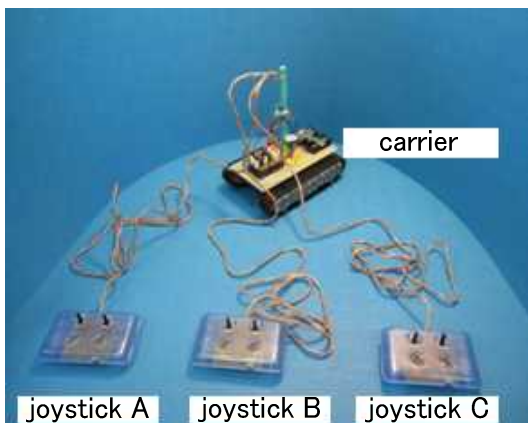


Fig.1 Proposed teaching material.

3. Curriculum for Nurturing cooperation

The curriculum for nurturing cooperativity using suggested teachings is explained. Since it is supposed to practice in elementary school classes as shown in Table 1, it is a curriculum conducted in 90 minutes class (45 minutes × 2 times).

The first 10 minutes explain the objectives of lesson. The next 20 minutes explain the rescue activities using proposed teaching material, rescue field (Fig.4) and rescue dummy (Fig.5). At this time, students are instructed that the operated carrier goes to the dummy place quickly for rescue. And, the students with joysticks

rescue the dummy without talking for 15 minutes. For next 15 minutes, the students freely rescue dummies with talking. For another 20 minutes, the students rescue the dummy according to instructions of the leader. Finally, the importance of cooperativeness is summarized.

Table1 Curriculum.

Time	Contents
10[min]	Learning about cooperativeness
20[min]	Learning about rescue activities
15[min]	Rescue activities without talking
15[min]	Rescue activities with talking
20[min]	Rescue activities by a leader's direction
10[min]	Summarize the lesson

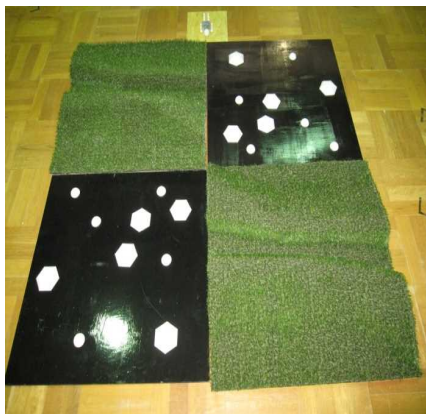


Fig.4 Rescue Field.



Fig.5 Rescue dummy.

4. Experiments and Results

We verified the effectiveness of teaching material. Subjects are three students of an elementary school. Experiments were conducted in the following 2 cases.

Case 1: Three students operate the carrier without talking

Case 2: Students operate carrier according to instructions from a leader (selected from 3 children)

© The 2018 International Conference on Artificial Life and Robotics (ICAROB2018), Feb. 1-4, B-Con Plaza, Beppu, Oita, Japan

Figs 4 and 5 show the behavior of joystick operation by the students in Case 1. If the operations of three students match, the values of MD_R and MD_L appear at -3 or 0 or 3. It is clear that the students are not cooperating, because there are many times that are numerical values other than -3 or 0 or 3.

Figs 6 and 7 show the behavior of joystick operation by the students in Case 2. Since the operations of three students are almost in agreement, the numerical values of MD_R and MD_L appear in -3 or 0 or 3. For these reasons, it is clear that cooperative operations are possible by instructions from the leader. Moreover, when cooperative operations were possible, it proved that the joystick operation of three students synchronized.

5. Conclusions

In this paper, we proposed the teaching material to support cooperative development by direct experiences. The experimental results by using proposed teaching material show that when students cooperatively are able to operate, it proved that the joystick operations synchronized. In the future, we plan to further develop the teaching material and curriculum for nurturing cooperativeness.

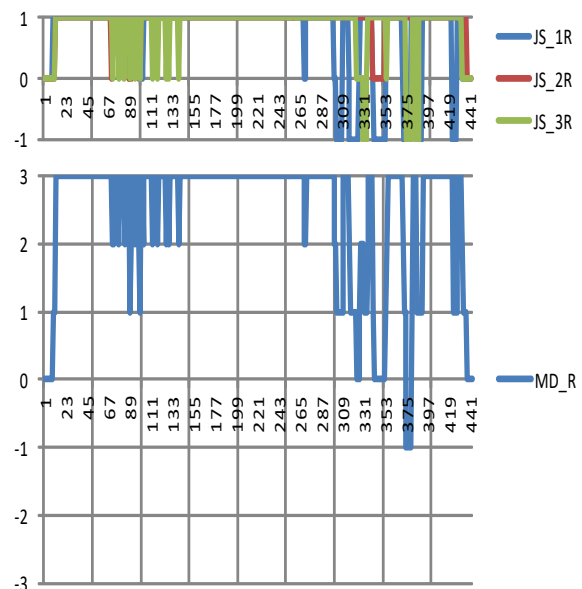


Fig.4 Behaviors of the right joystick operation in case 1.

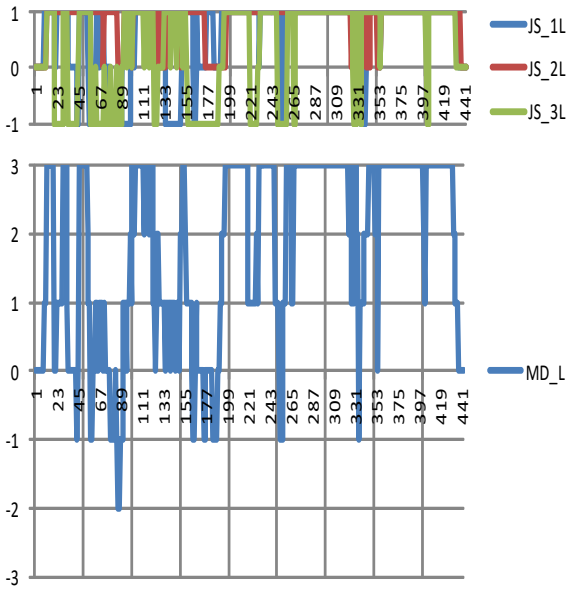


Fig.5 Behaviors of the left joystick operation in case 1.

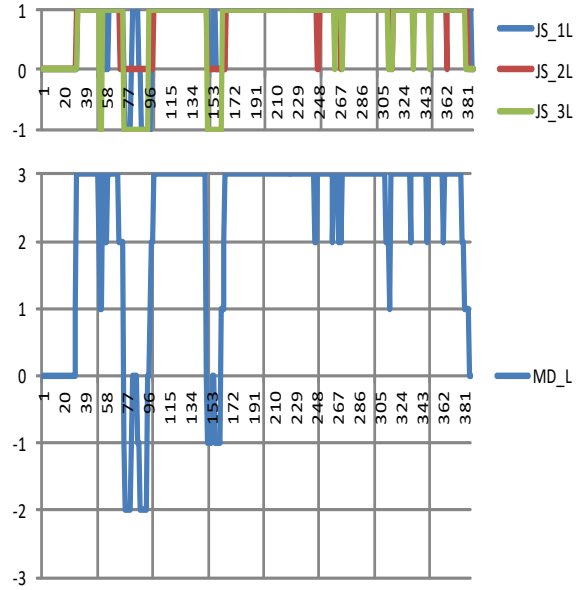


Fig.7 Behaviors of the left joystick operation in case 2.

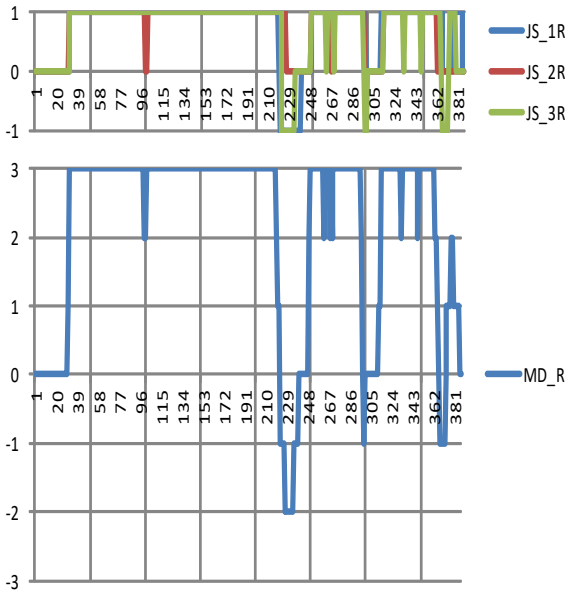


Fig.6 Behaviors of the right joystick operation in case 2.

References

1. A. Omae, A Study on the Significance and Problems in the Cooperation between Preschool Programs and Eleme, *Institute for Culture and Human Research*, 15 (Kyoto Bunkyo University, 2015) pp.15-32. (in Japanese)
2. T. Minoshima, T. Kiminoka, M. Nagamatsu, K. Kawada, N. Yoshida, and T. Yamamoto, Towards the implementation of social development in early school education by using robotics, *The Annals of Education Research*, 40 (Hiroshima University, 2012) pp.285-288. (in Japanese).
3. K. Kawada, M. Nagamatsu, and T. Yamamoto, An Approach to Rescue Robot Workshops for Kindergarten and Primary School Children, *J. Robotics and Mechatronics*, 25(3) (Fuji Technology Press, 2013), pp.521-528.
4. T. Yamashiro, K. Kawada, M. Nagamatsu, and T. Yamamoto, A Practice of ‘Monozukuri’ Education Featuring “Rescue Robots Production” in an Elementary School, *Trans. on JSME*, 77(776) (2011), pp.1465-1476, (in Japanese).
5. M. Banzi, and M. Shiloh, *Getting Started with Arduino*, 3rd Edition, (Maker Media, 2014).

On methods for teaching in training for keeping tempo constant in music*

Hideyuki Tanaka †

Graduate School of Education, Hiroshima University,
Kagamiyama 1-1-1, Higashi-hiroshima, Hiroshima, 739-8524, Japan

Keita Ueda‡

Department of Education, Hiroshima University,
Kagamiyama 1-1-1, Higashi-hiroshima, Hiroshima 739-8524, Japan

E-mail: tanakalpha@hiroshima-u.ac.jp †

Abstract

Ability of keeping rhythm is one of important factors in playing music. In this paper, the authors carry out experiments of training for keeping steady tempo in music. They compare the effects of visual and verbal feedbacks for informing the performance. Participants include experts and non-experts.

Keywords: Rhythm in music, ability of keeping steady tempo, visual feedback, verbal feedback

1. Introduction

In music, rhythm is one of the important factors, and keeping steady tempo is the basis for playing music. Rhythm indeed plays a fundamental role in music, and there is no music without rhythm¹. Music is an art based on a time factor, and rhythm forms a basic element in music rather than melodies and harmonies².

Though rhythm is one of the most important factors, it is not necessarily easy even for music teachers to give instructions of rhythms to students in public schools. In Ref. 3, researchers stated that capabilities of students for tapping rhythms depend on their interests in music, and that the gap between students being good at or bad at tapping rhythm is getting wider. They moreover reported that there are many students who cannot correctly tap the rhythm in singing difficult songs in junior high and high school, and they further informed that there are music

teachers who are worrying about not knowing systematic methods for teaching rhythms.

There have been researches^{4,5} of objectively evaluating the performance of the rhythm in music. In Ref. 4, effects of a feedback of information of music play⁴ has been studied, and the performance of playing the musical instrument has been visualized and used for feedbacks⁵. Several researches have focused on the position of striking the drum pad^{6,7,8}. However, researches on feedbacks for keeping tempo have not been done enough. Though Ref. 7 has given players feedbacks by graphs, languages, and numerical values, and it has not been clarified which feedback is effective.

In this research, we carry out experiments of training for keeping steady tempo in music. We compare the effects of visual and verbal feedbacks and analyze the results dividing participants into groups of experts and non-experts.

2. Experimental setup and feedbacks

2.1. Experimental setup

We show a schematic picture of the experimental setup in Fig. 1. The participants tap the rhythm, beating the drum pad and holding a stick by their dominant hand. The microphone captures the sound of the beat and send the signal to the laptop PC of the windows OS. The PC analyzes the signal and obtain the time of the impacts by removing reverberation and provides information for the visual and verbal feedbacks. In an offline setup, the visual feedback or the verbal feedback is given by the display or by the language.

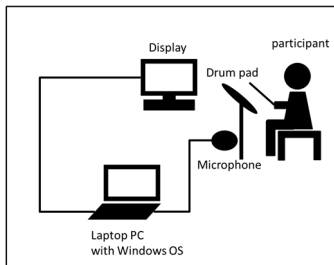


Fig. 1: A schematic picture of the experimental setup.

We assign the speed of the beat as 60 beats per minutes, and the participants try to keep the designated tempo in two minutes. Before the experiments, we ask the participants to maintain the tempo as close to the designated one as possible. We then carry out 10 times of trials for each participants and give a visual or verbal feedback after each trial in an offline setting.

2.2. Visual feedback for informing performance

Fig. 2 shows a graph used for visually informing the periods between impacts.

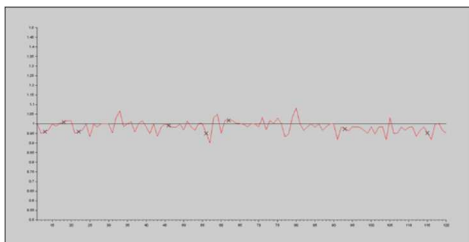


Fig. 2: The graph showing the tempo and time. The horizontal and vertical axes respectively express time and the periods between impacts. The red line shows the result of the performance, where black crosses are estimated from

interpolation because of missing data. The constant line 1 is the designated period; the participants tap the rhythm better, if all the periods are close to the designated one.

We inform participants how to read the graph and they can visually understand how s/he tapped the rhythm after the experiment.

2.3. Verbal feedback for informing performance

In order to obtain objective data, we give a feedback based on numerical values calculated by the laptop computer. To this end, we define evaluation criteria to automatically judge the tendency of the beats by the computer. Dividing the experiment into the first half and the second half, we measure the periods and analyze whether s/he keeps the steady rhythm and taps the rhythm in a designated tempo. We moreover observe average tempos of the first half and the second half and compute the difference between them.

Let $y(k)$ be the k -th period, where $k = 1, 2, 3, \dots, N$. The number N_p of the first half data is given by $N_p = N/2$ for even number N or $N_p = (N + 1)/2$ for odd number N , and the number N_f of the second half is $N_f = N - N_p$. To judge whether the rhythm is steady, we define the following criteria respectively for the first half and the second half:

$$H_p = \max_{k=1,2,\dots,N_p} (|e(k)|) - \min_{k=1,2,\dots,N_p} (|e(k)|),$$

$$H_f = \max_{k=N_p+1,\dots,N} (|e(k)|) - \min_{k=N_p+1,\dots,N} (|e(k)|),$$

where $e(k)$ is the error between the designated period r and the k -th period $y(k)$:

$$e(k) = r - y(k).$$

The root mean squares (RMS) of errors between the designated period and $y(k)$ for the first and second half are respectively defined as

$$P_p = \sum_{k=1}^{N_p} (e(k))^2, \quad P_f = \sum_{k=N_p+1}^N (e(k))^2.$$

The average periods of the first and the second half are respectively given by

$$M_p = \frac{1}{N_p} \sum_{k=1}^{N_p} y(k), \quad M_f = \frac{1}{N_f} \sum_{k=N_p+1}^N y(k),$$

and the absolute value of the difference between them by

$$M_c = |M_d|,$$

where M_d is defined as

$$M_d = M_p - M_f.$$

We moreover compute the mean μ and the variance σ^2 of the data $y(k)$ as follows:

$$\mu = \frac{1}{N} \sum_{k=1}^N y(k), \quad \sigma^2 = \frac{1}{N} \sum_{k=1}^N (y(k) - \mu)^2.$$

We give the verbal feedbacks to the participants for the first and second half as follows:

- **Good in the first (or second) half:** Tapping the rhythm in the designated tempo, if $H_p < 0.15$ and $P_p < 0.1$ hold (or if $H_f < 0.15$ and $P_f < 0.1$ hold).
- **Fairly good in the first (or second) half:** Tapping the steady rhythm in the designated tempo but not keeping it in the designated tempo, if $H_p < 0.15$ holds (or if $H_f < 0.15$ holds).
- **Not good in the first (or second) half:** Tapping the rhythm not in the designated tempo, if $H_p > 0.15$ holds (or if $H_f > 0.15$ holds).

Concerning the average speeds for the first and second half, we moreover give the following feedbacks:

- **Slow in the first (or second) half:** The beat is slower than the designated tempo, if $M_p < 1.05$ holds (or if $M_f < 1.05$ holds).
- **Fast in the first (or second) half:** The beat is faster than the designated tempo, if $M_p > 1.05$ holds (or if $M_f > 1.05$ holds).

Comparing the speeds of the first and second half, we further give the following feedbacks:

- **Getting slower:** The tempo of the second half is slower than the first one, if $M_d < 0$ and $M_c > 0.05$.
- **Getting faster:** The tempo of the second half is faster than the first one, if $M_d > 0$ and $M_c > 0.05$.

2.4. Experiments

The number of participants is 45, including 27 persons who have enough experiences of playing music and 18 persons who have not. We divide them into the experienced and non-experienced, by asking them whether they have experiences of playing the instruments not in elementary, junior high or high schools. We moreover divide them 3 groups of giving a visual feedback (9 from 27 experienced and 6 from 18 non-experienced, a verbal feedback (9 from 27 experienced, 6 from non-experienced), and no-feedback (9 from 27 experienced, 6 from 18 non-experienced).

The participant first listen to the signal of 60 BPM (beat per minute) for the reference, where they can choose just

listening to the signal or beating the drum pad according to the signal. They then try to maintain the tempo in 120 seconds. After the trial, we give a visual or verbal feedback to the participants in the groups of under feedbacks. We carry out 10 trials and give them 5-minutes rests after the 4th and 7th trials, by taking physical and mental fatigues of participants into account.

3. Results of experiments

We first compare the abilities of experienced and non-experienced participants of tapping the rhythm as the designated tempo, focusing on the evaluation values P_p and P_f . The results indicated that the error of experienced participants between the designated tempo and the tapped rhythm is smaller than that of non-experienced participants in all the groups of the visual, verbal and no feedbacks.

We next compare the effects of visual, verbal, and no feedbacks. Figs. 3 and 4 show the RMS P_p and P_f of the error $e(k)$ respectively for experienced and non-experienced participants. These figures show that the participants under the visual or verbal feedback (F.B.) can maintain the error smaller than those under no feedback. The verbal feedback is more effective than the visual one for the performance of the experienced participants.

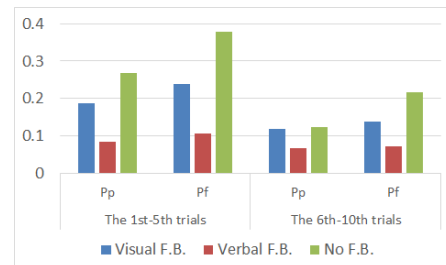


Fig. 3: The RMS P_p and P_f of experienced participants.

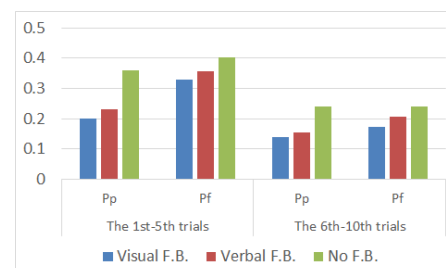


Fig. 4: RMS P_p and P_f of non-experienced participants.

We further compare the effects of visual, verbal, and no feedbacks by using the variance σ^2 . Figs. 5 and 6 show σ^2 of experts and non-experts, respectively.

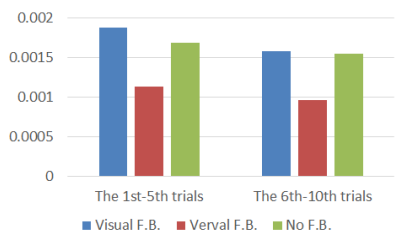


Fig. 5: Variances σ^2 of experienced participants.

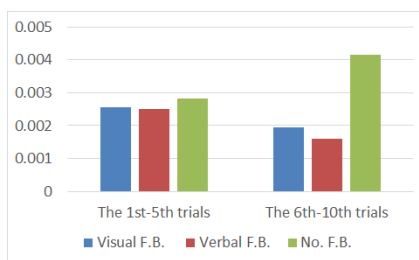


Fig. 6: Variances σ^2 of non-experienced participants.

We see from Figs 3. and 5 that experienced participants can suppress RMS of the error $e(k)$ using visual feedbacks, but not the variance σ^2 . The result implies that they can recognize the error in average (in the sense of RMS) and that they can accelerate or decelerate by looking at the graph, if they beat fast or slow respectively. However, the result indicates that they cannot properly control the variance of periods, by looking at the graph. On the other hand, the verbal feedback, often used for music plays, gives better results than the visual one.

Regarding the variance in the group of the visual feedback, we have obtained information through questionnaire, by asking how they thought of the feedback between trials; they answered: “To achieve better performance, I don't worry about the details.”, “I tapped the rhythm without thinking too much.”, and “I just cared the intervals of the reference signals between trials.” Several experienced participants thus considered that tapping the rhythm subconsciously leads to better performances.

Summarizing the above results, the visual feedback by the graph possibly provides too much information for the experienced participants to maintain the variance of the rhythm, whereas the verbal feedback does appropriate information to them. Experienced participants are thus

confused by the difference between their own feeling of rhythm and the feedback indicated by the graph. Ref. 9 indeed mentions that there are people who have their own feeling of rhythms. For further researches, it should be noted that the visual feedback may improve results if we simplify the graph.

4. Conclusions

We have carried out experiments of training for keeping steady tempo in music. We compared the effects of visual and verbal feedbacks for informing and improving their performance. The obtained results indicated that the visual feedback by a graph seems to give too much information to the experienced participants, and the information possibly disturbed expert participants in maintaining the steady tempo, because they have their own feeling of rhythms.

References

1. Y. Akutagawa, *Basics of music (in Japanese)* (Iwanami Shoten Publishers, 1971).
2. T. Umemoto, *Music psychology (in Japanese)* (Seishin Shobo, Publishers, 1986).
3. N. Mizuno, H. Ando, and M. Yoshida, Developmental musical beat stability of children (in Japanese), in bulletin of Gifu Women's University (2015), pp. 53–61.
4. T. Yonekawa and A. Nishikata, Rhythm pattern accuracy diagnosis system capable of objective evaluation and commentary feedback, *IEICE Transactions on Information and System*, **E86-D**(1) (2003), 71-78.
5. Y. Nishii and I. Kurimoto, Development for Detected system of error in the sense of hearing (in Japanese), *IPSI SIG Technical Reports*, **93**(32) (1993), 17-23.
6. Y. Tsuji and A. Nishikata, Improvement of beginners' drumming play by expert's teaching for drumming form, in Proc. of the 2004 IEICE General Conference, (2004), p157.
7. Y. Tsuji and A. Nishikata, Analysis of drumming play based on parallel measurement of rhythm and drumming form (in Japanese), *The transactions of the Institute of Electronics, Information and Communication Engineers*. **D-I, J88-D-I**(1) (2005), pp.99-107.
8. Y. Tsuji and A. Nishikata, Development and evaluation of drum learning support system based on rhythm and drumming form, (in Japanese), *The transactions of the Institute of Electronics, Information and Communication Engineers*, **D-I, J88-D-I**(2) (2005), pp.508-516.
9. U. Ichikawa, *This is the point for improving in playing the drum (in Japanese)*, Ongaku no tomo sha, Corp. Publishers, (1988).

Reinforcement Learning as a Theoretical Framework for Education*

Masayasu Nagamatsu[†], Yuki Moriguchi

Faculty of Education, Hiroshima University, 1-1-1 Kagamiyama
Higashihiroshima, Japan[‡]

E-mail: nagamatu@hiroshima-u.ac.jp, m176972@hiroshima-u.ac.jp
www.hiroshima-u.ac.jp

Abstract

Reinforcement Learning as a computational model of human learning, has recently become the subject of intensive investigation (Barto, A.G., 2005; Vigortio, C.M., 2010). Recent findings include: neural signature of hierarchical reinforcement learning, and multiple roles of reward signals in the human brain. These findings not only provide further theoretical evidences that complementary for traditional statistical inference in educational research, but also provide framework for model based design of educational processes. Types of evidence for education, and its relation to recent findings of human reinforcement learnings are discussed.

Keywords: reinforcement learning, reward signal, dopamine, intrinsic motivation, evidence, educational research.

1. Introduction

Researchers in many field have been attracted^{1,2} to the study of reinforcement learning because of its simplicity and high flexibility of adapting to new environment. The model has been successfully applied to the learning of artificial^{3,4} and natural^{5,6} systems, or both⁷. But when we try to model the learning process of humans, a problem arise. Bananas, juice can be good rewards for mammals such as monkeys. But for humans, these tangible rewards are relatively cheap to the human value systems, and might bring negative side effects⁸⁻¹¹ to the long time behavior.

Recent studies have focused on these higher order processing of reward, enabling us to model the key components of experiential learning for human. Some

researchers suggest¹² that these topics are “ripe for attack by young synthesizers and theoreticians”. The purpose of this study is to summarise these findings relating to human experiential learning and aiming to serve them as theoretical evidence for educational research.

2. Educational practice and neural science : a bridge (still) too far?

In 1997, a paper titled “Education and the brain: a bridge too far” has been published and repeatedly cited since then. The author of the paper suggested the possible bridges are; (1) a bridge between educational practice and cognitive psychology. This seems well established. (2) a second bridge between cognitive psychology and brain science. This model is feasible

*

‡

© The 2015 International Conference on Artificial Life and Robotics (ICAROB 2015), Jan. 10-12, Oita, Japan

because cognitive science has brought insight into the process of knowledge acquisition.

The remaining missing link is related to motivation, or emotional aspects, because motivations are not the main issue of cognitive science. For this reason, these approaches are sometimes called “cold” approaches¹³⁻¹⁴. Things are drastically changing by two reasons. First, computational method such as reinforcement learning and deep learning, both of them are biologically inspired or having some biological counterpart.

2.1. Conjoint reward processing

According to the comprehensive review by Schultz (Ref.15, p.889), reward processings are done by two functionally different components. The first part is related to explicit reward signal. Second part is related to conjoint reward signal, and processed largely at cortex (dorsolateral prefrontal cortex and parietal association cortex). Such conjoint reward signal is a key to understand human reward processing. Educational research such as Refs. 13-14 shows that reward orientation and motivational beliefs plays important role in educational practices.

2.2. Subjective reward perception

Schultz(Ref.15) also explained about subjective reward perception¹⁶. “Neuronal reward responses may depend on the subjective perception of reward-predicting stimuli.” The fact that reward depends on individual perception is big empirical finding. Ref. 17 Shows top 20 principles for enhancing teaching / learning. The first principle is as follows.

Principle 1: Students’ Beliefs or Perceptions about Intelligence and Ability Affect Their Cognitive Functioning and Learning Student knowledge about intelligence itself can vary and affect how students process.

This implies that how students perceive their achievement is subjective, therefore depend on individual difference of perception.

In the study of teacher education, similar problem of perception plays essential role. Refs. 18-19 shows that teacher’s beliefs about student motivation difficult to alter.

Beliefs, by contrast, are relatively static (at least in terms of their core applications —see the discussion of 'unboundedness' below). When beliefs change, it is more likely to be a matter of a conversion or gestalt shift than the result of argumentation or a marshalling of evidence. (Ref.18)

This observation is not only suggestive for teacher education, but also suggestive for modeling human reward processing.

For example, a teacher may believe that students who fail are simply lazy; another teacher may believe that learning math is a function of drilling. (Ref. 19)

Such perception difficult to alter, because these perception is not a result of conscious processing, but rather acquired from teacher’s experience.

3. Type of evidences in educational practice

In educational studies, the types of evidence has long been the matter of debate. One of the core issue is related to quantitative vs. qualitative evidence. The above findings strongly indicate that even the quantitative evidence deeply rely on subjective perception of teachers and students. Recent studies in the processing of reward will afford the

4. Future directions ?

Recent advances in the study of reward processing has enabled us to model the key issues in educational practice, likewise the empirical finding about the studies of student belief and teacher belief shows that these processings will play key roles in educational practice.

References

1. M Schlüter, A Baeza, G Dressler, K Frank, *et al.* A framework for mapping and comparing behavioural theories in models of social-ecological systems *Ecological Economics*, 131 (2017) 21–35.
2. Giuseppe Carleo and Matthias Troyer Solving the quantum many-body problem with artificial neural networks, *Science* 355, 602–606 (2017)
3. Jürgen Schmidhuber: Deep learning in neural networks: An overview, *Neural Networks* 61 (2015) 85–117

4. Busoniu, Lucian, Babuska, Robert, De Schutter, Bart: A comprehensive survey of multiagent reinforcement learning, *IEEE Transactions on Systems Man and Cybernetics Part C-Applications and Reviews*, 38(2)156-172
5. Gershman, S.J.; Daw, N.D. Reinforcement Learning and Episodic Memory in Humans and Animals: An Integrative Framework, *Annual Review of Psychology* 68, 101-128(2017)
6. Sonuga-Barke, E.J.S., *et al.* Annual Research Review: Transdiagnostic neuroscience of child and adolescent mental disorders - differentiating decision making in attention-deficit/hyperactivity disorder, conduct disorder, depression, and anxiety, *Journal of Child Psychology and Psychiatry* 57(3) 321-349 (2016)
7. Todd M. Gureckis and Bradley C. Love: Computational Reinforcement Learning, In *Oxford handbook of computational and mathematical psychology*, pp.99-117, Oxford University Press(2015)
8. Lepper, M.R., Henderlong, J, and Gingras, I. (1999) Understanding the effects of extrinsic rewards on intrinsic motivation - Uses and abuses of meta-analysis: Comment on Deci, Koestner, and Ryan (1999), *Psychological Bulletin* 125(6) 669-976.
9. Eisenberger, R. and Cameron, J. (1996) Detrimental effects of reward - Reality or myth?, *American Psychologist* 51(11) 1153-1166.
10. R Eisenberger, J Cameron (1998) Reward, Intrinsic Interest, and Creativity: New Findings, *American Psychologist* 53(6) 676-679.
11. Schmid, B & Adams, J (2008) Motivation in Project Management: The Project Manager's Perspective, *Project Management Journal* 39(2) 60-71.
12. Montague, PR., Hyman,SE; Cohen,JD.(2004) Computational roles for dopamine in behaviour, *Nature* 431, 760-767
13. Pintrich, P.R, Marx,R.W., Boyle, R.A.(1993) Beyond Cold Conceptual Change: The Role of Mol Beliefs and Classroom Contextual Factors in the Process of Conceptual Change, *Review of Educational Research*, 63(2),167-199.
14. Wolters, C.A, YU, S.L, and Pintrich,P.R(1999)The Relation Between Goal Orientation and Student's Motivational Beliefs and Self-regulated Learning, *Learning and Individual Differences*, 8(3),211-238.
15. Schultz, W.(2015) Neuronal Reward and Decision Signals: From Theories to Data, *Physiological Review*, 853-951.
16. De Lafuente O, Romo, R.(2011) Dopamine neurons code subjective sensory experience and uncertainty of perceptual decisions, *Proc. Natl Acad Sci USA* 49 19767-19771.
17. Lucariello, J.M., *et al.*(2016) Science Supports Education: The Behavioral Research Base for Psychology's Top 20 Principles for Enhancing Teaching and Learning, *Mind, Brain and Education* 10(1) 55-67.
18. Pajares, M. F. (1992) Teachers' beliefs and educational research: Cleaning up a messy construct, *Review of Educational Research* 62, 307-332.
19. Nespor, J.(1987) The role of beliefs in the practice of teaching, *Journal of Curriculum Studies* 19, 317-328.

Negative Test Case Generation from an Extended Place/Transition Net-Based Mutants

Tomohiko Takagi

*Faculty of Engineering, Kagawa University
2217-20 Hayashi-cho, Takamatsu-shi, Kagawa 761-0396, Japan*

Tetsuro Katayama

*Institute of Education and Research for Engineering, University of Miyazaki
1-1 Gakuen-kibanadai nishi, Miyazaki-shi, Miyazaki 889-2192, Japan
E-mail: takagi@eng.kagawa-u.ac.jp, kat@cs.miyazaki-u.ac.jp*

Abstract

In negative testing, the large state space and feasibility problems cause the difficulty of generating negative test cases from EPN (Extended Place/transition Net)-based mutants. This paper shows the overview of EPN-based mutants, and the details of our negative test case generation technique. In the technique using ACO (Ant Colony Optimization), ants heuristically search better paths (i.e., negative test cases) to find foods (i.e., intended failures) on a field (i.e., an EPN-based mutant).

Keywords: Software Testing, Negative Testing, Model-Based Testing, Test Case Generation

1. Introduction

EPN (Extended Place/transition Net)-based mutants are formal behavioral models of software that contain intended failures.¹ In negative testing, well-selected EPN-based mutants are used to generate negative test cases to confirm that software does not include serious or possible failures. However, the large state space and feasibility problems on EPNs cause the difficulty of generating the negative test cases from EPN-based mutants.

The aim of this research is to construct a technique in which effective negative test cases to reach intended failures are generated from EPN-based mutants. In this technique using ACO (Ant Colony Optimization), ants heuristically search better paths (that is, negative test cases) to find foods (that is, intended failures) on a field (that is, an EPN-based mutant). This paper shows the overview of EPN-based mutants in section 2, the details of our negative test case generation technique in section

3, discussion in section 4, and, conclusion and future work in section 5.

2. Overview of EPN-Based Mutants

This section shows the overview of EPN-based mutants.

An EPN is a PN (Place/transition Net) that is extended by VDM++ (one of specification description languages that are used in VDM)² in order to formally define actions and guards on transitions, and it is suitable to represent the essential behavior of complex software. A simple example of an EPN is given in Fig. 1. This example has three places (p_1 , p_2 , and p_3) and four transitions (t_1 , t_2 , t_3 , and t_4), and some transitions have guards and actions. For example, t_3 has " $v \geq p$ " as a guard and " $v := v - p$;" as an action. v is an instance variable of nat type that was initialized to 0, and p is an input parameter (an argument) of nat type for t_3 . When p_2 contains one or more tokens and also the guard of t_3 is satisfied, the firing of t_3 can be done with the execution of its action. Thus guards cause the feasibility problem

when specific transitions need to be selected to construct good test cases. Additionally, a state is expressed as a set of a marking (an array of the number of tokens on places) and values of instance variables, and therefore the introduction of instance variables accelerates the large state space problem.

EPN-based mutants (hereinafter, referred to as mutant models) are EPNs that contain intended failures of software, and they can be constructed by applying one or more existing mutation operators to an EPN that represents the expected behavior of software (hereinafter, referred to as an original model). Fig. 2 shows a simple example of a mutant model that was constructed by an arc insertion operator.

3. Negative Test Case Generation Technique

A negative test case in this study is a sequence of successive markings and transitions that starts from an initial marking and ends with an occurrence of an intended failure. It can be created based on a mutant model that were discussed in the previous section. For example, the mutant model shown in Fig. 2 can produce a negative test case " $\{[0,2,0], v=0\} \rightarrow t_1(2) \rightarrow \{[1,1,0], v=2\} \rightarrow t_3(1) \rightarrow \{[1,1,1], v=1\}$ ". The last marking of this example negative test case originally should be $[1,0,1]$, and it succeeds in reaching the intended failure. Effective negative test cases are created as shorter sequences to reach intended failures, so as to be able to be executed by test engineers within a limited period of time. However, the large state space and feasibility problems that were discussed in the previous section cause the difficulty of constructing such negative test cases.

In this section, we propose an effective negative test case generation technique using ACO. ACO is one of meta-heuristic algorithms, and it is suitable to solve complex and time-consuming problems. In this technique, ants heuristically search better paths (that is, shorter negative test cases) to find foods (that is, intended failures) on a field (that is, a mutant model).

This technique consists of the following six steps.

- (i) a ants are created (a is a natural number), and they are placed onto an initial marking of a mutant model. Each ant remembers the initial values of instance variables of the mutant model.

For example, when the mutant model shown in Fig. 2 is given to this technique, ants are placed onto $[0,2,0]$, and they remember " $v=0$ ".

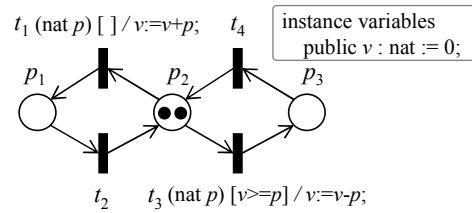


Fig. 1. Simple example of an EPN.

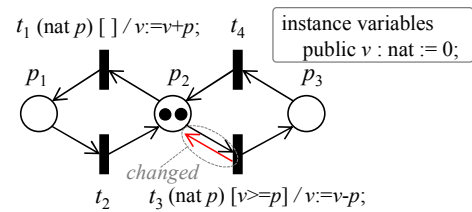


Fig. 2. Simple example of EPN-based mutants.

- (ii) Each ant starts searching a path as follows. First, an ant finds all feasible transitions on its current state (that is, a marking that the ant currently stays on, and values of instance variables that the ant remembers). If the ants find a new 3-tuple (*from-marking, transition, to-marking*), the pheromone value of the 3-tuple is initialized to an initial pheromone value τ_0 (τ_0 is 0 or a positive real number). The ant then selects a feasible transition at random in proportion to the pheromone values of all feasible 3-tuples, and goes to a next marking. If the selected transition has actions, the ant executes the actions and updates the values of instance variables that the ant remembers. For example, in Fig. 2, an ant on the state $\{[1,1,0], v=2\}$ finds feasible transitions t_1, t_2 and t_3 . When the pheromone values of the 3-tuples ($[1,1,0], t_1, [2,0,0]$), ($[1,1,0], t_2, [0,2,0]$) and ($[1,1,0], t_3, [1,1,1]$) are τ_1, τ_2 and τ_3 , respectively, the probabilities of selecting t_1, t_2 and t_3 are $\tau_1/(\tau_1+\tau_2+\tau_3), \tau_2/(\tau_1+\tau_2+\tau_3)$ and $\tau_3/(\tau_1+\tau_2+\tau_3)$, respectively. The ant repeats the above-mentioned selection of a transition, until an intended failure has appeared or the length of a path from the initial marking (that is, the number of transitions that the ant has selected) has reached l (l is a natural number) or the ant has reached a final marking (the definition of a final marking is optional). In this technique, an intended

failure appears if there are differences on markings, values of instance variables, and feasible transitions between the mutant model and its original model.

- (iii) If there are ants that have succeeded in reaching an intended failure (hereinafter, referred to as effective ants), an ant that has found the shortest path among the effective ants (hereinafter, referred to as an iteration-best ant) is found. If the path of the iteration-best ant is shorter than the path of a best-so-far ant (that is, an effective ant that has found the shortest path through all the previous iterations in this technique), the iteration-best ant becomes a new best-so-far ant, and it is kept as a candidate solution.
- (iv) If the number of iterations of this technique reaches i (i is a natural number), the path of the best-so-far ant is determined as a final solution (that is, the best negative test case on the mutant model), but if a best-so-far ant does not exist (that is, if there are no effective ants through all iterations), it is concluded that the mutant model cannot produce a negative test case.
- (v) The pheromone values of all 3-tuples that have been found are updated by the following equation.

$$\tau_t(x+1) = (1 - \rho) \cdot \tau_t(x) + \sum_{k=1}^a \Delta \tau_t^k \quad (1)$$

In Eq. (1), $\tau_t(x)$ expresses a pheromone value of a 3-tuple t in x th iteration. ρ is a positive real number that is less than 1.0, and it means an evaporation rate of pheromone. $\Delta \tau_t^k$ expresses a pheromone value that an ant k adds onto a 3-tuple t , and it is given by the following equation.

$$\Delta \tau_t^k = \begin{cases} \frac{1}{L_k}, & \text{if the ant } k \text{ is effective and } t \in P_k \\ 0, & \text{otherwise} \end{cases} \quad (2)$$

In Eq. (2), P_k is a path that has been found by an ant k , and L_k is the length of P_k (that is, the number of transitions of P_k).

- (vi) All the ants are removed from the markings of the mutant model, and this technique returns to step (i).

This technique has five parameters (a , τ_0 , l , i , and ρ) to adjust its performance. There are no parameter values that are appropriate for all software development projects, and therefore test engineers need to determine them by using a trial-and-error method.

4. Discussion

We developed a prototype of a tool that supports this technique, and applied it to examples on a trial basis. In

this section, we discuss the effectiveness of this technique based on its experimental results.

The examples are based on an EPN of an electronic money charging system that was introduced to discuss a positive testing technique in Ref. 3. That is, four mutant models were manually constructed by applying four kinds of mutation operators to the EPN. The mutation operators used in this experiment were two kinds of model-based mutation operators (arc insertion and arc omission) and two kinds of code-based mutation operators (numeric constant replacement and inequality sign replacement), and they were applied to different transitions of the EPN.

Subsequently, we applied the prototype of the tool to each mutant model, and successfully got a short negative test case from each mutant model. The processing time per one mutant model was about 80 seconds. The environment of this experiment was a laptop computer with i7-4650U processor (1.70 GHz, up to 3.30 GHz) and 8 GB RAM. The parameter values of this technique is $a=2$, $\tau_0=0.1$, $l=20$, $i=50$, and $\rho=0.03$.

The processing time will be acceptable to most of test engineers. However, the performance of this technique depends on the structure of a mutant model, characteristics of an intended failure, and parameter values of this technique. Thus further experiments are expected in future study. Test engineers need to determine the parameter values for this technique by using a trial-and-error method, but it may not be easy. Additionally, the quality of negative test cases depends also on the quality of mutant models, which should be discussed in another study.

5. Conclusion and Future Work

In this paper, we proposed a new technique to generate an effective negative test case from an EPN-based mutant.

The negative test case generation from an EPN-based mutant is a complex problem, since guards and instance variables in an EPN-based mutant cause the feasibility problem and the large state space problem, respectively. Therefore, ACO that is one of meta-heuristic algorithms was introduced into this technique. In this technique, ants heuristically search better paths (that is, shorter negative test cases) to find foods (that is, intended failures) on a field (that is, an EPN-based mutant). We developed a prototype of a tool that supports this technique, and applied it to examples on a trial basis. We found that short

negative test cases could be generated within a reasonable time. However, the performance of this technique depends on several conditions, and further experiments are expected in future study. Also, it may not be easy for test engineers to determine the parameter values for this technique.

There is still room to improve the performance of this technique. For example, we plan to add a pheromone value to each sequence of successive 3-tuples, in order to enable ants to search paths effectively. Subsequently, we will apply the improved technique to non-trivial examples in order to evaluate its effectiveness.

Acknowledgements

This work was supported by JSPS KAKENHI Grant Number 26730038.

References

1. T. Takagi, S. Morimoto and T. Katayama, Development of a Tool for Extended Place/Transition Net-Based Mutation Testing and Its Application Example, *Journal of Robotics, Networking and Artificial Life (JRNAL)*, Vol.4, No.2 (Sept. 2017), pp.168-174.
2. J. Fitzgerald, P.G. Larsen, P. Mukherjee, N. Plat and M. Verhoef, *Validated Designs for Object-Oriented Systems*, (Springer-Verlag London, 2005).
3. T. Takagi, A. Akagi and T. Katayama, Heuristic Test Case Generation Technique Using Extended Place/Transition Nets, *Applied Computing and Information Technology, Studies in Computational Intelligence*, Vol.727 (2017), pp.103-115.

Development of a Mutant Generation Tool Using a Genetic Algorithm for Extended Place/Transition Nets

Tomohiko Takagi

*Faculty of Engineering, Kagawa University
2217-20 Hayashi-cho, Takamatsu-shi, Kagawa 761-0396, Japan*

Shogo Morimoto

*Graduate School of Engineering, Kagawa University
2217-20 Hayashi-cho, Takamatsu-shi, Kagawa 761-0396, Japan
E-mail: takagi@eng.kagawa-u.ac.jp, s17g483@stu.kagawa-u.ac.jp*

Abstract

In EPN (Extended Place/transition Net)-based mutation testing, mutant EPNs need to be created by inserting intended failures into an original EPN, and we develop a tool using a genetic algorithm to generate better mutant EPNs. In the algorithm, a set of mutant EPNs corresponds to a chromosome, and the fitness of each chromosome is evaluated based on an original EPN weighted by metrics. This paper shows the algorithm, the functions of the tool, and the discussion about its effectiveness.

Keywords: Software Testing, Mutation Testing, Model-Based Testing, Mutant Generation

1. Introduction

An EPN (Extended Place/transition Net) is a place/transition net that includes actions and guards written in a specification description language of VDM (Vienna Development Method),¹ and it is used as a formal model to represent the relatively detailed behavior of software. When model-based mutation testing² is performed based on the EPN, failures are intentionally inserted into an original EPN (EPN that represents the expected behavior of software) in order to create mutant EPNs, and then a test suite (a set of test cases) to be evaluate is executed on the mutant EPNs.³⁻⁵ The ratio of killed mutant EPNs (mutant EPNs whose failures were detected by the test suite) to all of the created mutant EPNs is called a mutation score, and it gives test engineers a measurement of the quality of the test suite. A large number of higher-quality mutant EPNs are needed to expect the higher degree of accuracy for a mutation score.

In our previous study⁵, we developed a tool to construct an original EPN, construct mutant EPNs, execute a test suite, calculate a mutation score, and so on. However, the systematic techniques to generate higher-quality mutant EPNs had not been established, and the tool provides only the way to generate mutant EPNs at random by use of model-based mutation operators and the way to construct mutant EPNs by manual application of model-based or code-based mutation operators.

To address this problem, we construct an algorithm to generate better mutant EPNs, and develop a tool to execute the algorithm. In this algorithm using a GA (Genetic Algorithm), a set of mutant EPNs corresponds to a chromosome (an individual), and the fitness of each chromosome is evaluated based on an original EPN weighted by metrics. Test engineers can select suitable metrics for the evaluation, that is, can define the meaning of "quality of mutant EPNs".

© The 2018 International Conference on Artificial Life and Robotics (ICAROB2018), Feb. 1-4, B-Con Plaza, Beppu, Oita, Japan

The rest of this paper is organized as follows. In section 2, we propose an algorithm to generate better mutant EPNs. Section 3 shows the functions of the tool in which the proposed algorithm has been implemented. Section 4 gives the discussion about the effectiveness of the tool, and finally section 5 shows a conclusion and future work.

2. Mutant EPN Generation Algorithm

In this section, we propose an algorithm to generate better mutant EPNs.

2.1. Overview of the way to address problems

A mutant EPN is an EPN that includes an intentional failure, and it is created by applying one or more mutation operators to an original EPN that test engineers had constructed based on specifications of SUT (Software Under Test). The mutation operators can be broadly classified into model-based ones³ and code-based ones. The combination of the mutation operators and the parts of the original EPN to be mutated brings astronomical numbers of possible mutant EPNs, and therefore they should be selected based on quality. However, it is not obvious (a) how to evaluate the quality of mutant EPNs, and (b) how to apply mutation operators in order to generate high-quality mutant EPNs.

In this study, we introduce weights⁴ into an original EPN in order to address (a). The weights are values between 0.0 and 1.0 that represent fault-proneness and the impact on software reliability. They are calculated based on metrics relating to usage distribution, complexity, and test execution history, and then are given to each transition of an original EPN. It is assumed that a good mutant EPN includes an intentional failure relating to a highly-weighted transition, and therefore the quality of mutant EPNs can be evaluated based on the weights.

The weights are calculated by the following steps.

- (i) Test engineers select metrics suitable for SUT, and then gather materials for evaluation of the metrics.
- (ii) Test engineers define the relationships between the original EPN and the materials.
- (iii) The metrics are evaluated based on the materials.
- (iv) According to the results of (ii), the results of (iii) are given to each transition of the original EPN, and then they are converted to values between 0.0 and 1.0.

A simple example of an original EPN with weights is shown in Fig. 1. It consists of three places (p_1 , p_2 , and p_3),

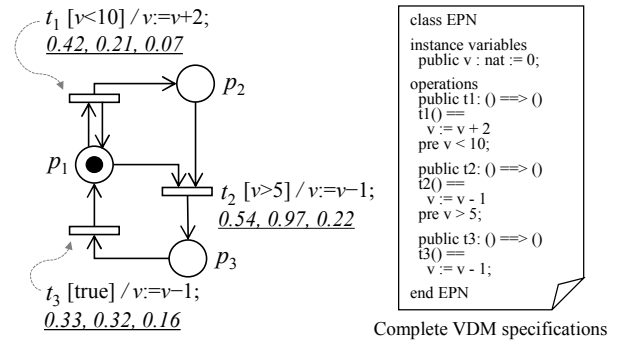


Fig. 1. Example of an original EPN with weights.

three transitions (t_1 , t_2 , and t_3), and eight arcs. There is a token on p_1 . Each transition has a guard, an action, and three weights. For example, t_1 has " $v < 10$ " as a guard, " $v := v + 2$," as an action, and "0.42, 0.21, 0.07" as weights.

Also, we introduce a GA into our mutant EPN generation algorithm in order to address (b). The GA is a well-known metaheuristic approach that imitates natural selection, and it is suitable to solve a problem in which it is difficult to formulate equations and get a best solution within reasonable time and cost. In our algorithm, a set of mutant EPNs corresponds to a chromosome, and the fitness of each chromosome is evaluated based on an original EPN weighted by metrics. Chromosomes with higher fitness tend to remain in next generation (and thus tend to take part in producing offspring). Finally a chromosome with highest fitness is selected as a solution. The details of our algorithm is shown in the next section.

2.2. Algorithm

The mutant EPN generation algorithm consists of the following six steps.

- (i) An initial population is generated for the first generation. The population consists of N_c ($N_c \geq 2$) chromosomes, and a chromosome consists of N_g ($N_g \geq 2$) genes. A chromosome represents a set of mutant EPNs (that is, a candidate solution). N_g is the number of genes, that is, the number of mutant EPNs that test engineers need for the evaluation of a mutation score. Each gene is generated by applying a mutation operator to an original EPN. A mutation operator to be used is randomly selected based on a uniform distribution, and a part of the original EPN to be mutated is randomly selected according to a distribution of weights.

- (ii) In order to generate new chromosomes (that is, offspring), mutation and crossover is applied to the existing chromosomes (that is, parents) in the population of current generation. In mutation, chromosomes are randomly selected with a mutation probability p_m ($0.0 \leq p_m \leq 1.0$), and a gene that is randomly selected in the selected chromosome is replaced with a new gene that is generated by the same way as (i). In crossover, chromosomes are randomly selected with a crossover probability p_c ($0.0 \leq p_c \leq 1.0$) in order to make pairs, and then genes between randomly selected cut positions are exchanged in a copy of each pair. Finally, new chromosomes are added to the population of current generation.
- (iii) Fitness of each chromosome in the population of current generation is evaluated by the following equation.

$$fitness(c) = \sum_{i=1}^M imp_i \cdot eval_i(c) \quad (1)$$

In Eq. (1), c is a chromosome to be evaluated, M ($M \geq 1$) is the number of kinds of metrics that test engineers introduced to calculate weights, imp_i expresses the degree of importance of i th metrics, and satisfies the following.

$$\begin{cases} \sum_{i=1}^M imp_i = 1.0 \\ 0.0 \leq imp_i \leq 1.0, \quad (i=1, 2, \dots, M) \end{cases} \quad (2)$$

$eval_i(c)$ in Eq. (1) expresses the result of evaluating i th metrics in c , and it is defined as follows.

$$eval_i(c) = \frac{\sum_{j=1}^T \{weight_{i,j} \cdot (1 - 2^{-num(c,j)})\}}{\sum_{j=1}^T weight_{i,j}} \quad (3)$$

In Eq. (3), T is the number of transitions of the original EPN, $weight_{i,j}$ is a value of a weight given by i th metrics on j th transition, and $num(c, j)$ expresses the number of genes of c in which j th transition and/or its ingoing/outgoing arc(s) are mutated.

- (iv) If the number of alternation of generations reaches G ($G \geq 1$), a chromosome with the highest fitness through all generations is selected as a final solution, and this algorithm is terminated.
- (v) N_c chromosomes that the initial population of next generation consists of are selected from the population of current generation. To be precise, two chromosomes are randomly selected based on a uniform distribution from the population of current

generation, and their fitness are compared. Then one with higher fitness is selected and is moved to the population of next generation, and another is returned to the population of current generation. These are repeatedly performed until the number of the population of next generation reaches N_c .

- (vi) Generation is changed, and then this algorithm returns to (ii).

3. Functions of a Mutant EPN Generation Tool

This section shows the functions of our tool in which the proposed algorithm has been implemented.

The tool includes (a) a function to construct an original EPN, (b) a function to generate mutant EPNs, (c) a function to execute a test suite on mutant EPNs and calculate its mutation score. (a) and (c) had already been implemented and discussed in our previous study,⁵ and therefore we concentrate on the implementation of (b) in this study. (b) includes two new sub-functions, that is, a sub-function to calculate weights based on metrics, and a sub-function to generate better mutant EPNs by a GA-based algorithm.

3.1. Weight calculation sub-function

As already discussed in section 2.1, we introduce weights into an original EPN, and our tool provides a sub-function to calculate weights based on metrics. Fig. 2 shows a screen shot of our tool (a main window) that is executing the sub-function. Its GUI (Graphical User Interface) consists of (A) a pane to start calculation and output the results, (B) a pane to select materials for the evaluation of metrics, and (C) a pane to show an original EPN with weights.

A user of our tool, that is, a test engineer first selects materials by using (B). (B) consists of three tab pages that specialize in materials relating to usage distribution, complexity, and test execution history, respectively. For example, in Fig. 2, an access log file of Apache is selected in order to evaluate usage distribution of a Web application to be tested. Keywords of actions that appear in the selected access log file are automatically extracted based on a specified log format, and a test engineer defines the relationship between the actions and the transitions of an original EPN.

After selecting materials, a test engineer pushes a button to start calculation on (A), and then confirms its results on (C). In Fig. 2, weights based on usage

distribution and complexity are displayed in blue and red characters, respectively. The former is the ratio of the frequency of executing each transition, and the latter was given by $1.0 - MI/100$, where MI means a maintainability index. If there are no problems on the results, a test engineer pushes an output button on (A) in order to generate an xml file of an original EPN with weights.

3.2. Mutant EPN generation sub-function

Our tool also provides a sub-function to generate better mutant EPNs by the GA-based algorithm that was discussed in section 2.2. After completing the calculation of weights, a test engineer specifies the parameter values for the algorithm on a dialog box of our tool, and our tool starts mutant EPN generation. Fig. 3 shows a screen shot of our tool (a sub-window) that gives the results of mutant EPN generation to a test engineer. Its GUI consists of (A) a pane to show the lists of all genes of all chromosomes in all generation, and (B) a pane to show a mutant EPN.

On (A), a test engineer selects an arbitrary generation from the upper left list, and all chromosomes with fitness in the selected generation are shown in the lower left list. Additionally, a test engineer selects an arbitrary chromosome from the list, and all genes of the selected chromosome are shown in the right list. If a test engineer selects an arbitrary gene in the list, a mutant EPN that corresponds to the selected gene is shown in (B). A mutated part in the mutant EPN is highlighted in order that a test engineer can easily understand it.

After the sub-window that shows the results of mutant EPN generation is closed by a test engineer, our tool shows only a final solution (that is, a chromosome with the highest fitness through all generations) on its main window shown in Fig. 4. Our tool allows a test engineer to modify the final solution, if needed. The modification function was already discussed in our previous study.⁵

4. Discussion

This section gives the discussion about the effectiveness of our tool shown in the previous section.

In this study, we applied our tool to an original EPN of an OFMS (Online File Management System) that was discussed in Ref. 5. The environment to run our tool was

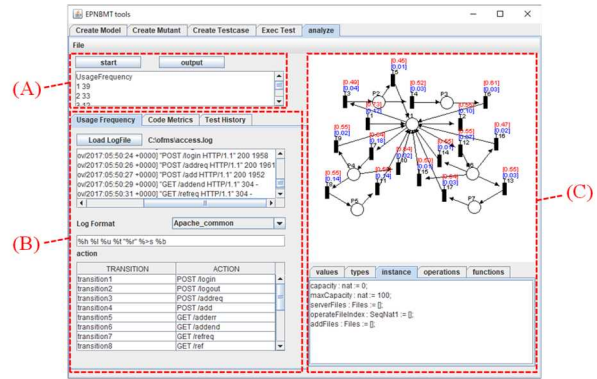


Fig. 2. Screen shot of the tool in calculating weights based on metrics.

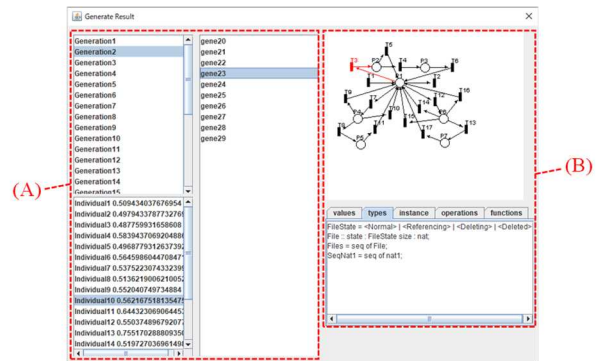


Fig. 3. Screen shot of the tool that shows the results of mutant EPN generation by the GA-based algorithm.

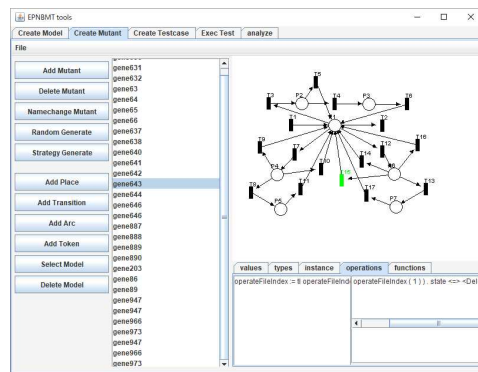


Fig. 4. Screen shot of the tool that shows a final solution.

a personal computer with i5-6500T processor (2.50 GHz, up to 3.10 GHz) and 4 GB RAM.

First, we developed a prototype of the OFMS based on the original EPN. The size of the prototype is about 830 lines of JavaScript code. We then selected two metrics in order to calculate weights for transitions of the original EPN. One is RFT (the Ratio of the Frequency of executing each Transition), and another is MI (Maintainability Index). RFT relates to usage distribution, and an access log file of Apache was gathered as its material. MI relates to complexity, and an output file from an existing source code analysis tool was gathered as its material. We opened the materials on our tool, and determined the setting to execute automatic weight calculation. The effort of these manual operations on our tool was about 10 minutes. We then started the automatic weight calculation by our tool, and successfully got the original EPN with weights. The processing time for the calculation was about 6.5 seconds. The effort and the time seem to be acceptable for most of test engineers.

Subsequently, we generated mutant EPNs based on the original EPN with weights, by using our tool. The parameter setting for the mutant EPN generation algorithm was $N_c=30$, $N_g=30$, $p_m=0.5$, $p_c=1.0$, $G=30$, $imp_1=0.5$, and $imp_2=0.5$ (imp_1 and imp_2 are the degree of importance of RFT and MI, respectively). Our tool executed the algorithm, and successfully outputted 30 mutant EPNs as a final solution. The processing time for the algorithm was about 2.1 seconds, and it seems to be acceptable for most of test engineers. The average quality (that is, average fitness) of candidate solutions in the first generation is about 0.65, and the quality of the final solution is about 0.97. The improvement of about 0.32 was achieved through the alternation of generations by the GA-based algorithm, and therefore our tool seems to be effective, at least in this case. We reviewed the outputted mutant EPNs, and found that:

- mutation operators were intensively applied to highly weighted transitions and their related elements (that is, parts that correspond to frequently used and/or complex functions of the prototype),
- but some mutant EPNs included non-effective intended failures that would not be important or would not be made in actual development, and also, there were equivalent mutant EPNs.

An additional algorithm to select appropriate mutation operators based on the structure of an original EPN, and an additional algorithm to detect equivalent mutant EPNs need to be developed in order to make more improvements of the effectiveness.

© The 2018 International Conference on Artificial Life and Robotics (ICAROB2018), Feb. 1-4, B-Con Plaza, Beppu, Oita, Japan

5. Conclusion and Future Work

In order to improve EPN-based mutation testing, we introduced weights into an original EPN to evaluate the quality of mutant EPNs, and then we proposed a GA-based algorithm to generate high-quality mutant EPNs within reasonable time and cost. Moreover, we have developed a tool including the functions to calculate weights based on metrics and to execute the GA-based algorithm. The results of applying the tool to a non-trivial example indicated its effectiveness, and the room for further improvements.

Our future work includes the development of additional algorithms to select appropriate mutation operators based on the structure of an original EPN, and also to detect equivalent mutant EPNs.

Acknowledgements

This work was supported by JSPS KAKENHI Grant Number 26730038.

References

1. J. Fitzgerald, P.G. Larsen, P. Mukherjee, N. Plat and M. Verhoef, *Validated Designs for Object-Oriented Systems*, (Springer-Verlag London, 2005).
2. F. Belli, C.J. Budnik and E. Wong, Basic Operations for Generating Behavioral Mutants, in *Proc. of 2nd Workshop on Mutation Analysis in conjunction with ISSRE'06* (Nov. 2006), pp.9.
3. T. Takagi, R. Takata, Z. Furukawa, F. Belli and M. Beyazit, Metrics for Model-Based Mutation Testing Based on Place/Transition Nets, in *Proc. of Joint Conf. of 21st Int. Workshop on Software Measurement and 6th Int. Conf. on Software Process and Product Measurement (IWSM-MENSURA)* (Nov. 2011), pp.7-10.
4. T. Takagi and T. Teramoto, Extended Mutation Score Based on Weighted Place/Transition Nets to Evaluate Test Suites, in *Proc. of 15th Int. Conf. on Computer and Information Science (ICIS)* (June 2016), pp.959-961.
5. T. Takagi, S. Morimoto and T. Katayama, Development of a Tool for Extended Place/Transition Net-Based Mutation Testing and Its Application Example, *Journal of Robotics, Networking and Artificial Life (JRNAL)*, Vol.4, No.2 (Sept. 2017), pp.168-174.

Implementation of RETUSS to Ensure Traceability between Class Diagram in UML and Java Source Code in Real Time

Keisuke Mori*, Tetsuro Katayama*, Yoshihiro Kita†,
Hisaki Yamaba*, Kentaro Aburada*, and Naonobu Okazaki*

*University of Miyazaki, 1-1 Gakuen-kibanadai nishi, Miyazaki, 889-2192, Japan

†Tokyo University of Technology, 1404-1 Katakura, Hachioji, 192-0914, Japan

E-mail: mori@earth.cs.miyazaki-u.ac.jp, kat@cs.miyazaki-u.ac.jp, kitayshr@stf.teu.ac.jp,
yamaba@cs.miyazaki-u.ac.jp, aburada@cs.miyazaki-u.ac.jp, oka@cs.miyazaki-u.ac.jp

Abstract

Ensuring of the traceability of deliverables is one of effective methods to secure the quality of software. It can verify that the requirements are reflected in the programs. But it has two problems: taking much labor and time, and causing mistakes by human handling. This paper has implemented RETUSS (Real-time Ensure Traceability between UML and Source-code System) in order to solve the above two problems. RETUSS can ensure traceability between Class diagram in UML and Java source code in real time.

Keywords: Software Quality, Traceability, UML, Java

1. Introduction

It's increasing the importance of software in society, and it's becoming more important to secure the quality of software. Ensuring of the traceability of deliverables is one of effective methods to secure the quality of software¹. It can verify that the requirements are reflected in the programs, specify the scope of the impact due to the modification in the requirements, and remove the gap between the documents and the source code. But it has the following two problems:

- Taking much labor and time to modify similarly other related deliverables by modifying some in a deliverable
- Having a risk that you cannot ensure traceability because of causing mistakes to ensure traceability by human handling

This paper has implemented RETUSS (Real-time Ensure Traceability between UML and Source-code System) in order to solve the above two problems.

© The 2018 International Conference on Artificial Life and Robotics (ICAROB2018), Feb. 1-4, B-Con Plaza, Beppu, Oita, Japan

RETUSS can ensure traceability between Class diagram in UML and Java source code in real time.

UML² (Unified Modeling Language) is a visual language for expressing the design and pattern of software. It is used for requirement specification and system design documents³. RETUSS targets Class diagram, which is an important diagram expressing the static structure of the system in UML. It also targets source codes in Java language.

2. RETUSS

Figure 1 shows an overview of RETUSS implemented in this paper. RETUSS has the following five areas:

- Menu Bar
- File List Area
- Drawing Item Selection Area
- UML Description Area
- Source Code Description Area

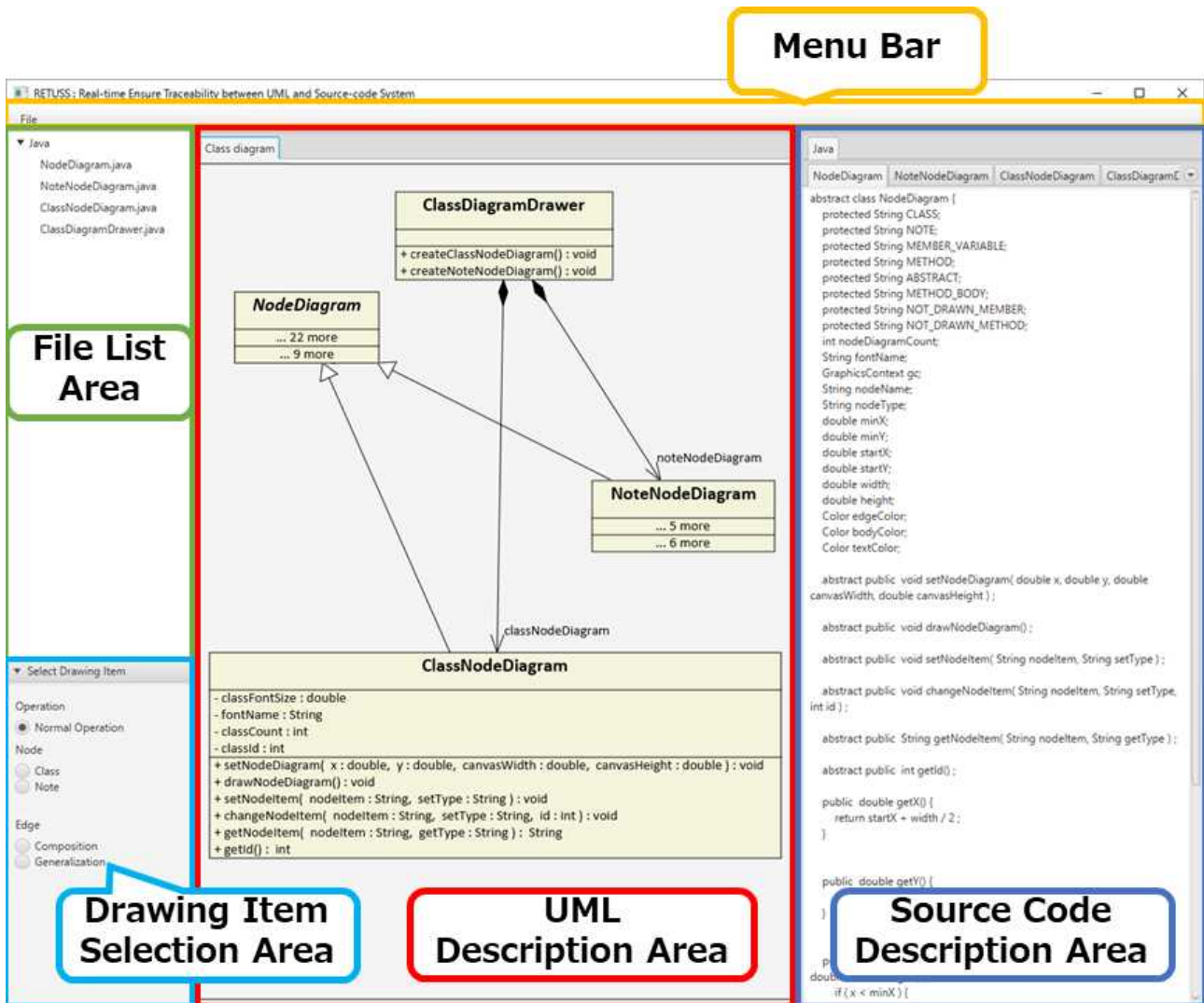


Fig. 1. Overview of RETUSS

In addition, RETUSS has the following three functions:

- Open java a file
- Description of Class diagram
- Description of Java source code

A user can describe Class diagrams in the UML Description Area in the "Description of Class diagram" function. Items and functions that can be described are as follows:

- Description of Classes and Notes
- Moving Classes and Notes

- Modifying Class name and Note content
- Deleting Classes and Notes
- Adding Attributes and Operations in Class
- Modifying the Attributes and Operations in Class
- Deleting Attributes and Operations in Class
- Hiding Attributes and Operations in Class
- Description of Composition and Generalization between Classes

A user can describe Java source code in the Source Code Description Area in the "Description of Java source code" function. When the user describes Java source code, RETUSS draws Class diagram corresponding to source code's contents in UML Description Area. RETUSS

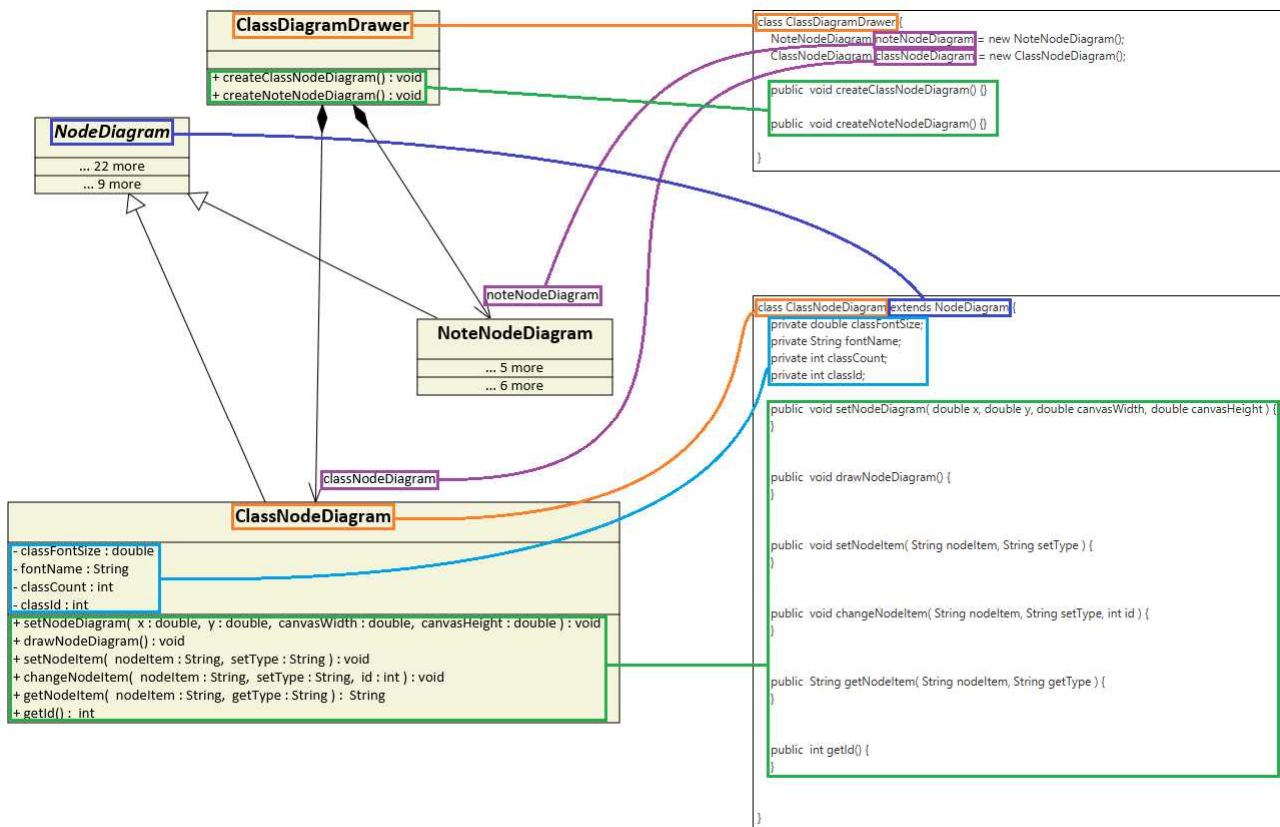


Fig. 2. The correspondence between the Class diagram and Java source code in executing the application example

draws multiple Classes corresponding to Java source code in the Source Code Description Area. Because one tab corresponds to one Class, a user draws Class of the corresponding the Java source code in the text area of each tab.

3. Application Example

As an application example, a part of Class diagram showing the structure of RETUSS itself is adopted to verify that the functions of it are operated correctly. Figure 1 shows a screenshot of RETUSS in executing the application example, and Figure 2 shows the correspondence between the Class diagram and Java source code at this time.

By looking at the ClassNodeDiagram class of the Class diagram and the Java source code in Fig. 2, the Class name, the Class name of the Generalization destination, the Attributes and Operations in the Class diagram correspond to the class name, the class name of the inherited destination, the field and the method in the

Java source code, respectively. Similarly, by looking at the ClassDiagramDrawer class, the Class name, the Related end name of the Composition destination, Operation in the Class diagram correspond to the class name, field, and method in the Java source code, respectively.

Hence, it is clear that RETUSS can ensure traceability between Class diagram in UML and Java source code.

4. Evaluation of Usefulness

To consider RETUSS usefulness, we experiment with experimental participants. As an experimental method, the experimental participants modify Class diagrams and Java source code the ensured traceability. Specifically, the experimental participants modify Class diagram and the Java source code to ensure traceability for requirements change when the Class diagram and Java source code already exist. As a modification method, two cases are prepared: case A using RETUSS, and case B

Table 1. The time required by three experimental participants to ensure traceability in each case (seconds).

Trials count	Case A	Case B
One	113	292
Two	76	148
Three	129	229
Average	106	223

without using. For each case, we measure and compare the time required for the experimental participants to ensure traceability between the modified Class diagram and Java source code.

Table 1 shows the time required by three experimental participants to ensure traceability in each case.

The average time required for modifying in case A using RETUSS was 106 seconds. On the other hand, the average time required for modifying in case B without using RETUSS was 223 seconds. Case A could be reduced by 52.7% compared to case B.

Further, in case B without using RETUSS, some mistakes were caused because of ensuring traceability by human handling. During the modification, for example, mismatch between Visibility of Class and access modifiers of Java source code, and deletion of curly braces of a method body of Java source code. On the other hand, the above mentioned errors did not occur in case A using RETUSS, because it can ensure traceability automatically.

Hence, it's possible to reduce labor and time and eliminate causing for human handling to ensure traceability by using RETUSS.

5. Related Research

EA⁴ (Enterprise Architect) and Astah⁵ are modeling tools that describe UML. Both EA and Astah can generate source code from UML and UML from source code automatically. EA and Astah can ensure traceability of source code are language such as Java, C# and C++.

EA, Astah and RETUSS support the design phase and maintenance phase of software development in using UML. EA and Astah can generate skeleton Java source code from Class diagram and Class diagrams from implemented Java source code in methods automatically. But EA and Astah cannot ensure traceability between Class diagrams and Java source code in real time. On the

other hand, RETUSS can ensure traceability between Class diagrams and Java source code in real time.

Therefore, RETUSS takes less time to modify similarly other related deliverables by modifying some in a deliverable, compared to the other two tools.

6. Conclusion

In this paper, we have implemented RETUSS, that ensures traceability between UML and source code in real time with the aim of solving two problems in ensuring traceability.

We applied RETUSS to a part of Class diagram of the structure of itself, and our tool ensured traceability between Class diagram in UML and Java source code. Finally, as a result of experiments with the experimental participants, the time could be reduced by 52.47% to ensure traceability between the Class diagram and the Java source code, and elimination causing for human handling by using RETUSS. Therefore, RETUSS can solve two problems in ensuring traceability.

Consequently, RETUSS is expected to support to secure the quality of software.

Future works are as follows:

- Correspond to the same Attribute and same Operation
- Correspond to incompatible syntax in Java source code
- Extension of Class diagram description function

References

1. SQuBOK Sakutei Bukai, *Guide to the Software Quality Body of Knowledge*, 2nd edn. Ohmsha, 2014 (in Japanese).
2. *Welcome To UML Web Site!*, <http://www.uml.org/>, (accessed December 7).
3. Dan Pilone, Neil Pitman, *UML 2.0 in a Nutshell*. O'Reilly Media, 2009.
4. *UML tools for software development and modelling - Enterprise Architect UML modeling tool*, <https://www.sparxsystems.com/>, (accessed December 7).
5. *Astah - Software Design Tools for Agile teams with UML, ER Diagram, Flowchart, Mindmap and More | Astah.net*, <http://astah.net/>, (accessed December 7).

Prototype of a Tool to Defect Specific Comments

Satoshi Tanoue*, Tetsuro Katayama* Yoshihiro Kita†,
Hisaki Yamaba*, Kentaro Aburada*, and Naonobu Okazaki*

*University of Miyazaki, Japan, †Tokyo University of Technology, Japan
tanoue@earth.cs.miyazaki-u.ac.jp, kat@cs.miyazaki-u.ac.jp, kitayshr@stf.teu.ac.jp,
yamaba@cs.miyazaki-u.ac.jp, aburada@cs.miyazaki-u.ac.jp, oka@cs.miyazaki-u.ac.jp

Abstract

This paper has developed a prototype of a tool to detect specific comments. With the prototype, you can use regular expressions, describe patterns of detected strings in a configuration file, and then detect specific comments. The prototype was applied to projects with 5,000 LOC (Lines of Code) or more. As a result, the recall rate achieved 100% and the precision rate achieved 80%. Reducing improper comments and comments detected by the prototype which express tasks remaining in the source code can improve understandability of the source code.

Keywords: comments, static analyze, maintenance, understandability.

1. Introduction

Comments can be described in a natural language without affecting the behavior of software. Therefore, using comments can describe contents that cannot be expressed by source code. For example, TODO comments can add tasks that exist in the source code as comments. By describing them appropriately, they give effective information to programmers. Therefore, comments indicating tasks remaining in the source code, such as TODO comments, need to be detected as necessary to check that issues remain in the source code.

On the other hand, there are problematic comments if they exist in the source code, such as repair history comments. The repair history comments have a problem that it is difficult to confirm that the maintenance is done, and the number of codes that need to be read increases. In this paper, such problematic comments are called improper comments.

Although improper comments and comments indicating tasks remaining in source code such as TODO comments can be found visually, it cannot be checked sufficiently due to lack of human resources or

development delay. Since, supporting the detection by tools is required.

Therefore, this paper implements a prototype of a tool to detect specific comments which users choose to improve the quality of the source code.

The prototype can describe the pattern of the detected character string in the configuration file by using the regular expression. The configuration file is described in XML (Extensible Markup Language) format¹. The prototype detects comments matching the pattern of the character string described in the configuration file. It described once can be reused in other projects. As for a comment to be detected newly, it can be flexibly coped with by adding the pattern of the detected character string to the configuration file. By using this prototype, it is possible to detect specific comments which users choose.

2. The Implemented Prototype

The implemented prototype has been developed in Java language. It runs on any OS if it can be installed Java virtual machine. An overview of the prototype in this research is shown in Fig 1. The developed prototype

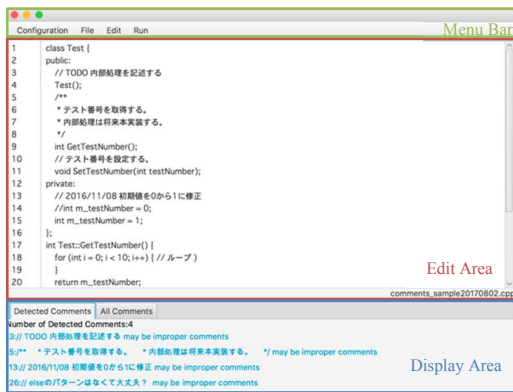


Fig. 1. Overview of the prototype

consists of a Menu Bar, an Edit Area, and a Display Area. The user can utilize the function of the prototype by selecting a menu item from the menu bar.

The function of the prototype is shown below.

- Changing Character Code
- Open File
- Save File
- Analyze Comments
- Analyze Comments of Multiple Files
- Clear Edit Area
- Clear Display Area
- Function to Support Description of Regular Expressions

2.1. Analyze comments

Comments correspond to line comments (//) and block comments (/ * * /). In case of programming languages in which the notation of line comments (//) and block comments (/ * * /), you can analyze comments. "Analyze Comments" first extracts all comments existing in the source code. Next, it matches based on the pattern of the detected character string described in a configuration file.

When the description content of the comments is matched in the pattern of the detected character string, it is detected. Finally, it is necessary to visually determine whether or not the detected comments are a detection target comment.

2.2. A configuration file

An example of the configuration file is shown in Fig 2. In the configuration file, it is possible to describe the pattern of the detected character string with the regular expression that can be accepted by Java language.

```
<?xml version="1.0" encoding="UTF-8" ?>
<comments>
  <comment type="TODO Comments">
    <RegExp>TODO</RegExp>
    <RegExp>(?)future</RegExp>
  </comment>
  <comment type="Anbiguous Comments">
    <RegExp>>?</RegExp>
    <RegExp>>maybe</RegExp>
  </comment>
</comments>
```

Fig. 2 An example of the configuration file

Table 1. Details of project A

LOC	Comments	Comments to be detect
6854	1990	24

3. Implements

The "Analyze Comments" function of the implemented prototype consists of extraction comments and pattern matching.

3.1. Extract comments

JavaCC (Java Compiler Compiler) ² is adopted to extract comments. JavaCC is often used as a parser generator that can use Java language. The grammar of JavaCC is similar to EBNF (Extended Backus Naur Form)³.

By using this parser generator JavaCC, the prototype generates a parser to extract comments from the source code and extracts all comments in the source code.

3.2. Pattern matching

To do pattern matching, the prototype obtains the contents from the configuration file. The configuration file is described in XML format. To extract the pattern of the detected character string from the configuration file, the prototype uses the DocumentBuilderFactory class which is a Java XML parser. It determines whether the comments obtained by the method of section 3.1 matches the character string detection pattern, and displays comments matched with the pattern on the "Detected Comments" tab.

4. Evaluation of the Prototype

We applied the implemented prototype to two projects A and B with LOC (Lines of Code) of 5000 lines or more

Table 2. Results of the application to project A.

Executions	Comments to be detect	Detected comments	Detected comments to be detected	Precision (%)	Recall (%)
1	24	32	21	65.6	87.5
2	24	30	24	80.0	100
3	24	28	23	82.1	95.8

Table 3. Details of project B

LOC	Comments	Comments to be detect
9394	1584	24

developed by SKYCOM Corporation, and examined the precision and recall rate. The calculation formula of the precision rate is as follows.

$$\frac{\text{Number of Detected Comments to be detect}}{\text{Number of Detected Comments}}$$

The calculation formula of the recall rate is as follows.

$$\frac{\text{Number of Detected Comments to be detect}}{\text{Number of Comments to be detect}}$$

As an evaluation method, the total number of comments and comments to be detected is visually checked, and the precision rate and the recall rate are calculated from both the result confirmed visually and the analysis results by using the prototype. Comments to be detected were defined by employees in SCYCOM Corporation. Many comments on this evaluation were written in Japanese.

First, the prototype is applied to project A for adjustment of a configuration file. Details of project A are shown in Table 1. The results are shown in the Table 2. In the first application of the project A, because the pattern of the detected character string described in the configuration file is insufficient, the recall rate was 87.5%, the precision rate was 67.5%, both of which were not satisfactory values. Therefore, a keyword indicating that it was ambiguous which was not described in the configuration file such as ambiguous Japanese words meaning "probably" or "maybe" were added as a pattern of the detected character string. As a result, at the second time, the recall rate can be 100%.

On the other hand, the precision rate was 80%. We examined the cause of lowering the precision rate, and found that there are many false detections on comments explaining the processing itself.

Therefore, as a third time, in order to check how much the character string detection of the comments explaining

the processing itself affects the recall rate, the pattern of detected the character string of the comments explaining the processing itself was deleted from the configuration file. This project includes one comment explaining the process itself. As a result, it became impossible to detect the comment, the precision rate increased to 82.1%, but the recall rate fell to 95.8%.

Even in other projects, in order to confirm that the same configuration file can be used, the configuration file used in project A was applied to project B. Details of project B are shown in Table 3. The result of applying to project B is shown in Table 4. In the first execution, the recall rate was 100% and the precision rate was as high as 92.3%. In project B, the recall rate became 100% because there were no comments explaining the processing itself. It was confirmed that the configuration file adjusted to obtain good results can be used as it is for other projects.

5. Discussion

In this section, we consider related researches and comparison with grep command.

5.1. Related research

Technical debt is a metaphor coined to express non-optimal solutions that are taken in a software project to achieve some short-term goals⁴. Technical debt can be deliberately or inadvertently incurred⁵. One example of the deliberate technical debt is self-admitted technical debt. It can be found from source code comments. In previous studies, the detection of self-admitted technical debt was heavily dependent on visual observation⁶.

Maldonado and et al. proposed a method to automatically detect self-admitted technical debt using natural language processing technology⁷. In Maldonado's method, the recall rate cannot achieve 100%. This means that there is a leak in the comments to be detected. Although the detected comments are different from our method, it is difficult to make the recall rate 100% since Maldonado's method uses machine learning. In the prototype, the recall rate can be surely made 100% by preparing the detected character string pattern.

Table 4. Results of the application to project B.

Executions	Comments to be detect	Detected comments	Detected comments to be detect	Precision (%)	Recall (%)
1	24	26	24	92.3	100

5.2. Comparison with grep command

Even if you use grep command⁸ or the text search function of a text editor, you can do the same thing as the prototype. So, we actually quantitatively evaluated how much difference is made with grep command. We prepare the same pattern as the detected character string described in the configuration file adjusted, and apply grep command using the pattern of this detected character string. As a result, recall rate is 76.7% and precision rate is 100% in project A, precision rate is 40.0% and recall rate is 100% in project B.

In the evaluation experiment of grep command, the pattern "?" of the detected character string matched "?" of the ternary operator existing in the source code.

In this prototype, since all comments are first extracted and then pattern matching is performed, the pattern of the detected character string does not match the ternary operators in the source code. Therefore, the precision rate can be higher than grep command.

6. Conclusion

In this paper, we have developed the prototype of a tool to detect specific comments which users choose in order to improve the quality of the source code. With the prototype, you can use regular expressions and describe patterns of detected strings in the configuration file. Thus, it is possible to detect a specific comment which users choose. Even when another comment to be newly detected appears, it can flexibly cope with by adding the pattern of the detected strings to the configuration file.

The implemented prototype was applied to projects with LOC (Lines of Code) of 5000 lines or more, and examined the precision and recall rate. As a result, by adjusting the pattern of detected strings, the recall rate achieved 100% and the precision rate achieved 80%. Moreover, the configuration file which was determined once can be applied as it is to other projects. That is, it can be confirmed that it can be reused. By using the prototype, it is possible to detect comments showing user's tasks

remaining in the source code and improper comments existing in the source code. Reducing their comments of the source code can reduce the problems existing in the source code and improve understandability of the source code.

The future issues are shown below.

- Improvement of precision
- Detection of only the comment explaining the processing itself
- Detection of unmaintained comments undocumented comments

Acknowledgements

I would like to thank S. Kai and Y. Uehara of SKYCOM Corporation for cooperating in evaluating the prototype.

References

1. W3C: Extensible Markup Language (XML) 1.0 (Fifth Edition), *W3C* (online), <https://www.w3.org/TR/2008/REC-xml-20081126/> (accessed 2017-7-29).
2. JavaCC: The Java Parser Generator, *JavaCC* (online), <https://javacc.org> (accessed 2017-7-29).
3. for Standardization, I. O.: Information technology – Syntactic metalanguage – Extended BNF, *Technical Report ISO 14977:1966(E)*, International Organization for Standardization (1995).
4. Cunningham, W.: The WyCash Portfolio Management System, *SIGPLAN OOPS Mess.*, Vol. 4, No. 2, pp. 29–30 (online), DOI: 10.1145/157710.157715 (1992).
5. Fowler, M.: Technical debt quadrant, Martin Fowler (online), <https://martinfowler.com/bliki/TechnicalDebtQuadrant.html> (accessed 2017-7-29).
6. Potdar, A. and Shihab, E.: An exploratory study on self-admitted technical debt, *2014 IEEE International Conference on Software Maintenance and Evolution*, pp. 91–100 (online), DOI: 10.1109/ICSME.2014.31 (2014).
7. Maldonado, E., Shihab, E. and Tsantalis, N.: Using Natural Language Processing to Automatically Detect Self-Admitted Technical Debt, *IEEE Transactions on Software Engineering*, (online), DOI: 10.1109/TSE.2017.2654244 (2017).
8. Foundation, F. S.: GNU Grep 3.0, Free Software Foundation (online), <https://www.gnu.org/software/grep/manual/grep.html> (accessed 2017-7-29).

A Recipe Decision Support System with Recognition Ability Recording Function Using Knowledge Information and Agent

Keita Saito, Taro Asada, Yasunari Yoshitomi, Ryota Kato, Masayoshi Tabuse

Graduate School of Life and Environmental Sciences, Kyoto Prefectural University,

1-5 Nakaragi-cho, Shimogamo, Sakyo-ku, Kyoto 606-8522, Japan

E-mail: {yoshitomi, tabuse}@kpu.ac.jp, {t_asada, r_kato}@mei.kpu.ac.jp}

http://www2.kpu.ac.jp/ningen/infsys/English_index.html

Abstract

Herein, we report on the development of a recipe recommender system with a recognition ability recording function based on collaborative filtering and impression words, and which uses MikuMikuDanceAgent (MMDAgent) as a human interface. Our previously proposed system has been modified to facilitate recording the recognition ability of the user. In this process, the agent poses questions to the user at appropriate times during interactions in order to determine if there is any noticeable deterioration in his/her recognition ability.

Keywords: Recipe recommendation, Collaborative filtering, Impression word, MMDAgent, Elderly persons

1. Introduction

When caring for elderly persons, it is well known that if dementia can be identified in its early stages, appropriate treatment can be initiated to improve symptoms and/or delay progression. Since declining memory acuity is one of the initial symptoms of dementia, this study reports on the development and evaluation of a new system that can help quantify a subject's memory and is based on our previously reported recipe recommender system¹. In the current study, we have adopted MikuMikuDanceAgent (MMDAgent)² which is a toolkit for building voice interaction systems, as a human user interface (UI).

2. Recipe recommendation method using collaborative filtering

The recipe recommendation method¹ proposed in our current study is based on collaborative filtering, which,

in turn, is based on our previously reported music recommendation method³. That method for recipe recommendation will be explained briefly below.

We began by preparing a database composed of recipes that had been already been subjectively scored at three-levels with "1" being the most appealing to "-1" being the least appealing. We then transformed the subjective scores of "-1" to "0". Those values ("0" or "1") are expressed as "evaluation scores" below.

3. Recipe recommendation method using impression words

Our recipe recommendation method also uses impression words¹. In this study, 10 impression words pairs (see Table 1) extracted from "Sizzle Word Report 2014"⁴ were used. This method is also based on our previously reported music_recommendation method³.

Table 1. Impression word pairs¹.

Good flavor — Refreshing flavor
Mellow — Spicy
Sweet — Gentle
Addicted — not Addicted
Rich — Crispy
Juicy — Scratchy
Warm — Cool
Melty — Chewy
Seasonal Limited — not Seasonal Limited
Authentic — not Authentic

Each of the recipes prepared in advance was assigned one of seven score levels ranging from “-3” to “+3” by the participating test subjects who used the selected impression word pairs to make their evaluations. We then transformed these subjective scores to a three-level scale (“-3” to “-2” as “-1”, “-1” to “+1” as “0” and “+2” to “+3” as “+1”). These values are expressed as “impression evaluation scores” below.

More specifically, when a recipe that has not been recommended to a user has the same values (except for a “0”) as that for at least one recommended recipe that has a high user evaluation based on the three-level score for at least five impression words, that recipe is treated as having a positive evaluation by the user. In contrast, when a recipe that has not been recommended to the user has the same scores (disregarding the “0”) as that for another recipe that has just been recommended to the user, even though it has a negative user evaluation based on the three-level score for at least seven impression words, that recipe is treated as having a negative evaluation by the user.

4. Recipe recommendation using the collaborative filtering and impression words

Fig. 1 shows a flowchart of the proposed system, which combines collaborative filtering and impression words based on the authors’ recipe recommendation method¹. First, the system recommends recipes stored in the database to the user. Both the recommendation process using collaborative filtering and that using impression words are terminated when the number of recommended recipes reaches the pre-set upper limit (K). In our proposed system, the recommendation process using collaborative filtering is terminated when there no users in the user reference list that show the same exact evaluation for the recommended recipe as have the users up to that point. The recommendation process then continues by identifying the most similar recipe, from the viewpoints of three-level scores (disregarding “0”)

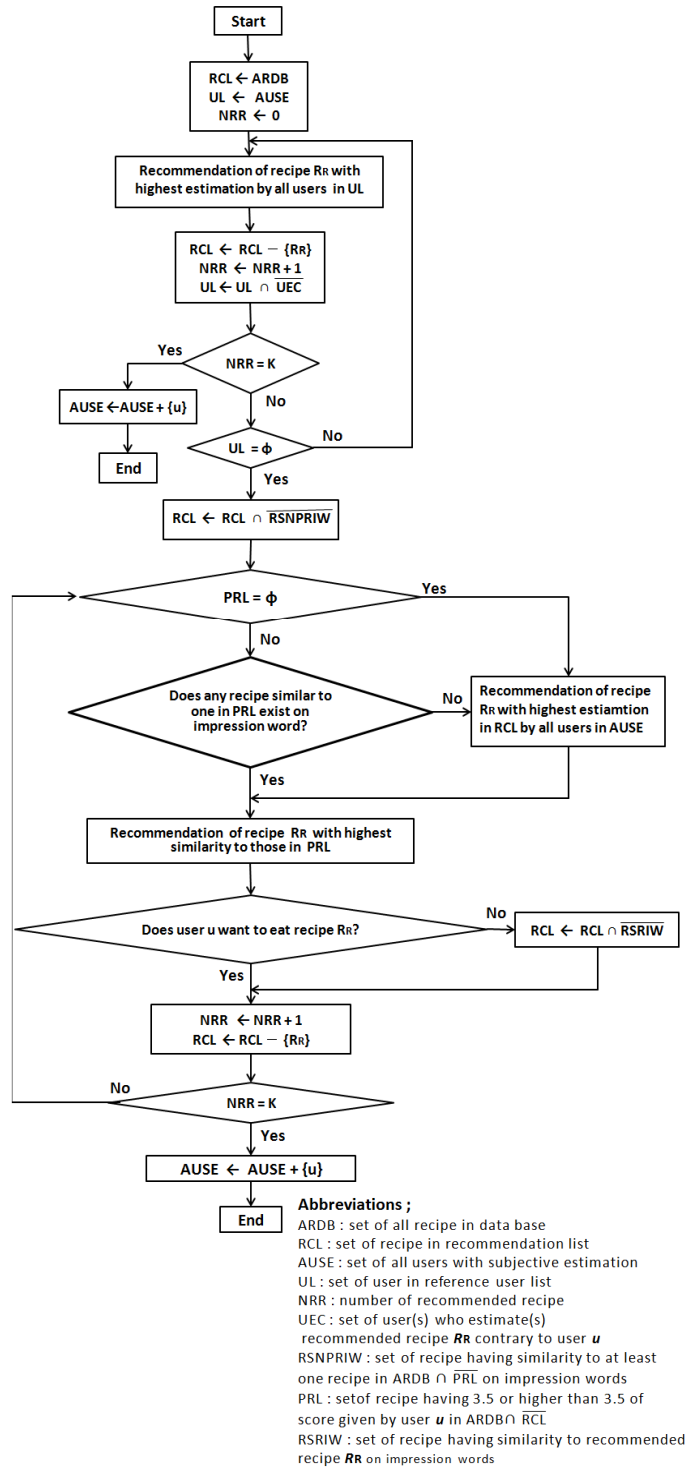


Fig. 1. Recipe recommendation using collaborative filtering and impression words.

based on impression words, to that successfully recommended among recipes not yet recommended.

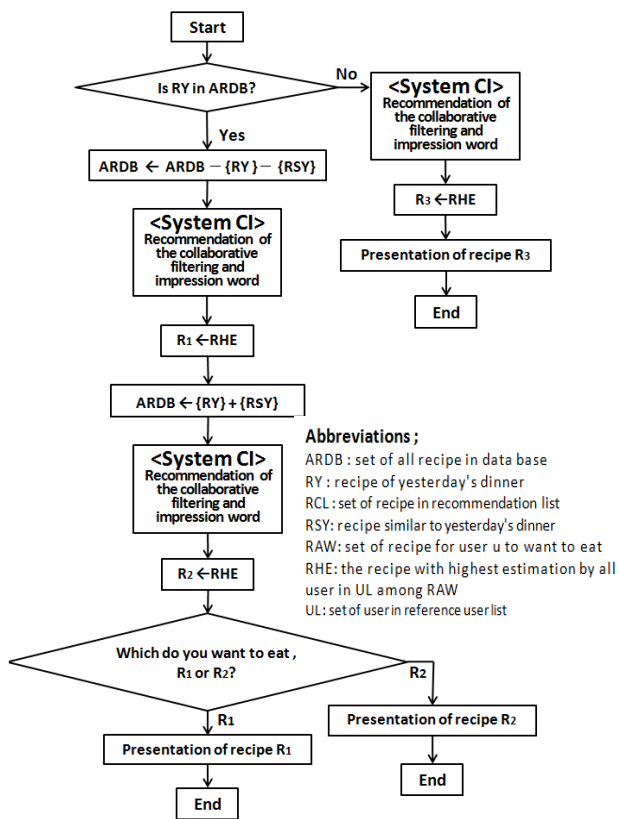


Fig. 2. Recipe recommendation considering yesterday's dinner.

Just before concluding the recommendation process, the user database is updated with subjective evaluations of the recipe by adding the viewpoints of those users recommending the recipe. In addition, the proposed system ultimately narrows down the recipe choices using methods that consider yesterday's recipe.

First, recipes in groups that are similar to the recipe that user selected the day before are recommended. Next, recipes in groups that differ from previous day's selection are also recommended. As in the impression word recommendation, judgments regarding a recipe whose impressions are similar to yesterday's dinner recipe are based whether the "impression evaluation score" coincides with five or more of the impression 10-item word pairs. Fig. 2 shows a recipe recommendation flowchart that considers yesterday's dinner.

5. Proposed system

In this section, we propose a system that records the user's recognition function while recommending recipes. To check the user's recognition capabilities, we use two question types.

One requests answers to three simple questions after displaying a sentence that has been excerpted from junior or senior high school home economics textbooks. The other asks the user to recall some recipes recommended via the method discussed in Section 4.

We designed our proposed system based on the assumption that it would be used by elderly persons. Accordingly, the input method was changed from "input by voice recognition" to "input by computer mouse" because of concerns that the speech recognition accuracy of elderly persons could deteriorate.

6. Performance evaluations

6.1. Conditions

From a total of 49 recipes that exclude side dishes, soups, and arranged dishes, main course dishes that one or more user had designated as "I have never tried" were extracted from the 293 entries in the "Rakuten recipes"⁵ category for use in our evaluation. The impression words selected were four pairs of "taste expression", four pairs of "texture expression", and two pairs of "situation expression" extracted from the "Sizzle Word Report 2014"⁴. Synonyms and antonyms were verified using the Weblio dictionary⁶. Similar expressions in the "expression" rankings were grouped together and chosen via the following procedure¹:

- Step 1:** The top 10 words satisfying the condition that their antonyms are within the top 25 words are chosen in each ranking.
- Step 2:** The words that ranked within the top 10 and their antonyms within the same ranking are chosen.
- Step 3:** The words ranked within the top 10 are chosen under the restriction that their antonyms are out of ranking.
- Step 4:** Processing repeats for words ranking below the top 10.

In this report, we changed the scoring method used for collaborative filtering evaluation scores from "recipe preference"¹ to "whether I want to eat" based on the idea that "the recommendation accuracy" would be improved due to the enhanced fitting of the question and the database.

Next, the proposed system recommended recipes to five new participating users who were not among the 14 users who entered evaluations into the database. K was set to 15, and experiments were conducted under the following two conditions:

Recommendation accuracy = Number of recipes to which the user replied, “I want to try” divided by the number of recommended recipes.

Final recommendation accuracy = Number of users that recommended the recipe that the user most wants to try divided by the number of users.

For the questions, we selected two sentences from Ref. 7 and three from Ref. 8.

The proposed system evaluates the user’s state as being in one of four conditions according to the cognitive function score, which is based on a scale from 0 to 20 points. If the score is 14 points or more, a judgement of “No problem” is issued; if the score is from 10 points to 13 points, a judgement of “slightly deteriorated cognitive function” is tendered; if the score is from six to nine points, the system determines that “there is a decrease in cognitive function”; for five point scores or less, the system decides that there is a “possibility that the cognitive function may have been greatly deteriorated”. Scoring itself is based on the cognitive function test⁹.

Our experiment was performed on a Dell Optiplex 780 personal computer (PC) equipped with an Intel Core 2 Duo E8400 3.00GHz central processing unit (CPU) and 4.0 GB of random access memory (RAM). The Microsoft Windows 7 Professional operating system (OS) was installed on the PC and Microsoft Visual C++ 2010 were used as the development languages.

6.2. Results and discussions

Fig. 3 shows the recommendation accuracy of five new users. The mean value of the proposed system’s recommendation accuracy was 77.3%, while that of the random recommendation was 43.7%. The value of the final recommendation accuracy of the proposed system was 40.0%.

As a result of experiments involving five users without memory abnormalities, we found that the average score of cognitive function was 18.0. In our future work, it will be necessary to conduct experiments involving elderly test subjects and then evaluate the results obtained. In addition, since it is possible that healthy persons will become irritated if repeatedly asked questions aimed at gauging their memory abilities while researching recipes, it will be necessary to think about ways to measure memory more naturally during user-agent interactions. Furthermore, since dementia negatively impacts computational power and language

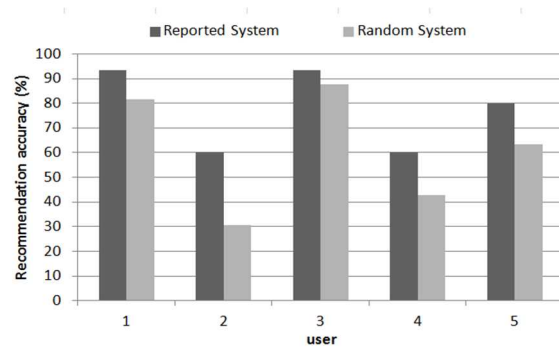


Fig. 3. Accuracy recommendations of five new users.

ability in addition to memory, we would like to develop a system that can measure those abilities as well.

7. Conclusion

In this paper, we proposed a recipe recommendation system that combines collaborative filtering and impression words. Our proposed system is equipped with a function for checking the memory condition of a user using a recommendation system outlined in our previously study¹. The tests conducted to date indicate that our proposed system is more effective than random recommendations, and that it is capable of providing an accurate evaluation of a user’s recognition ability.

Acknowledgements

We would like to thank the subjects for their cooperation in the experiments.

References

1. K. Saito, T. Asada, Y. Yoshitomi, R. Kato, and M. Tabuse, A recipe decision support system using knowledge information and agent, *J. Robotics, Networking and Artif. Life* to appear.
2. MMDAgent. <http://www.mmdagent.jp/> Accessed 25 July 2016.
3. S. Yoshizaki, Y. Yoshitomi, C. Koro, T. Asada T, Music recommendation hybrid system for improving recognition ability using collaborative filtering and impression words. *J. Artif. Life and Robotics* **18**(1-2) (2013) 109-116.
4. Sizzle Word Report2014. <http://www.bmft.jp/pdf/services/kotoba14.pdf/> Accessed 25 July 2016.
5. Rakuten recipe. <http://recipe.rakuten.co.jp/category/> Accessed 17 December 2017.
6. Weblio dictionary. <http://thesaurus.weblio.jp/> Accessed 25 July 2016.
7. Y. Niida and K.,Kusuda, *Home economics textbook for elementary school* (in Japanese), (Yama-kei Publishers, Tokyo, 2008).
8. M. Miyamoto etc. (eds.), *Home basis - future by partnership* (in Japanese), (Jikkyo Shuppan, Tokyo, 2012).
9. Dementia Net. <https://info.ninchisho.net/check/ch20/> Accessed 20 December 2017.

A System for Analyzing Facial Expression and Verbal Response of a Person while Answering Interview Questions by Agent

Taro Asada¹, Daichi Kogi², Ryoichi Shimada³, Yasunari Yoshitomi¹, Masayoshi Tabuse¹
*1: Graduate School of Life and Environmental Sciences, Kyoto Prefectural University,
1-5 Nakaragi-cho, Shimogamo, Sakyo-ku, Kyoto 606-8522, Japan
E-mail: {yoshitomi, tabuse}@kpu.ac.jp, t_asada@mei.kpu.ac.jp}
http://www2.kpu.ac.jp/ningen/infsys/English_index.html
2: S.Ten Nines Kyoto Co.,Ltd.
13-1 Shinmei-cho, Nishikyogoku, Ukyo-ku, Kyoto 615-0864, Japan
3: JFE Systems, Inc.
4-1-3 Taihei, Sumida-ku, Tokyo 130-0012, Japan*

Abstract

We have developed a system for analyzing the facial expressions of a person obtained while answering interview questions posed by an agent. The image signal input from a video camera that is collected while the subject is answering questions is analyzed by our real-time system. Additionally, the fundamental frequencies and the time-to-utterance of the answerer just after a question is terminated are measured in order to help estimate the interviewee's mental state at the time the answer is given.

Keywords: Facial expression analysis, Movement analysis, Mouth area, Interview on video, MMDAgent.

1. Introduction

In Japan, society is aging at an unprecedentedly rapid pace, the average age of the population has been increasing, and these trends are expected to continue. Simultaneously, the number of elderly people with dementia and/or depression living in underpopulated areas is increasing very rapidly. However, since there is a gap between the number of patients and the number of available healthcare professionals, it is difficult to provide adequate psychological assessments and support for all patients.

To improve the quality of life (QOL) of elderly people living in care facilities or in their homes, we previously developed a method for analyzing the facial expressions of a person who is having a conversation with another person on a videophone.^{1,2} However, it was acknowledged that facial expression intensities could be

affected by (1) the conversation topic, (2) the conversation partner, and (3) the facial expression of the partner. Accordingly, in order to fix all of (1), (2), and (3), we previously developed a system for analyzing the facial expressions of a person while answering the interview questions on video.³

In the present study, in order to improve system convenience, such as by allowing easy changes to the interview questions, we developed a system capable of analyzing the facial expressions of a person in real-time while he or she is answering interview questions posed by an agent. In this system, the moving image in our method is captured by a webcam and analyzed in real-time via Open Source Computer Vision Library (OpenCV) image-processing software⁴ along with a previously proposed feature parameter (facial expression intensity)¹ that is based on the mouth area that we

focused on in that research. Additionally, in our new system, the time-to-utterance of the answerer just after an interview question and the fundamental frequencies of his or her voice are measured to provide clues regarding his or her mental state.

2. Proposed System and Method

2.1. System overview and method outline

We constructed two modules for use in our proposed system, which is based on our previously reported research.⁵ The first is a module for showing an interview by an agent on the computer screen for the answerer, and the second is a module for real-time facial expression analysis of the moving imagery captured in real-time by a webcam. The frames of the moving images are then changed from RGB image data into YCbCr image data, after which the Y component obtained from each frame in the dynamic image is used to analyze the facial expressions.

The proposed method consists of: (1) extracting the mouth area, (2) measuring the facial expression intensities, (3) selecting the reference frame, (4) measuring the time-to-utterance of the answerer just after an interview question, (5) calculating the feature parameters for the facial expression strength, and (6) measuring the fundamental frequencies for voices of the answerer using a conventional method. In the following subsections, (2) and (3) are explained in detail. For details on (1), and the judgment of utterance mentioned in (4), see Refs. 1 and 2. For details on (5), see Ref. 1.

2.2. Measurement of facial expression intensity

For the Y component of the selected frame, the feature vector for the facial expression was extracted for the mouth area. The extraction is performed by using a two-dimensional discrete cosine transform (2D-DCT) for each 8×8 pixel section. In order to minimize the influence of facial expression intensity due to the jaw and/or neck line(s), the bottom left and right areas of the mouth areas are excluded.⁸

To measure the feature parameters of the facial expressions, we selected low-frequency components from the 2D-DCT coefficients for use as the facial expression feature vector elements. However, the direct current component was not included. In total, 15 feature vector elements were obtained. The facial expression intensity is defined as the norm of the difference vector,

which is a vector of the difference between the feature vector for the expressionless face and that for an observed expression. The facial expression intensity candidate, which is defined as the norm of the difference vector between two feature vectors, was used for selecting the reference frame.²

2.3. Reference frame selection and error reduction processing

The reference frame selection method used is based on our reported research.⁶ In this process, the first 20 continuous frames of mouth area data that are successfully extracted after the webcam recording begins are treated as reference frame candidates. Then, beginning with the first reference frame candidate, the facial expression intensity of all candidate frames is measured, and the sum of all facial expression intensities is calculated. The candidate frame with the minimum value is selected as the reference frame. In this method, by applying the minimum value filter to the measured facial expression intensity of the last three frames, the influence of mouth area extraction error induced by OpenCV is reduced.

3. Simulated interview using MMDAgent

The interview video was made from a video recording of a scene in which a psychiatrist interviewed a subject.³ Although a video on which an actual psychiatrist is displayed would be ideal, it is impractical to create new videos whenever it becomes necessary to update questions and/or make intonation changes. Accordingly, in this research, we used MikuMikuDanceAgent (MMDAgent),⁷ which is a freeware animation program that allows users to create and animate movies, to create an agent.

To produce the agent's voice, we used the speech synthesis function setting built into MMDAgent.⁷ Agent motions during the interview included "nodding" and "blinking" movements that were designed to mimic the actual mannerisms of the psychiatrist who was recorded on the interview video used in the previously reported study³.

4. Experiments

4.1. Conditions

The agent interview was created while referring to a scene in which a psychiatrist interviewed a subject. In

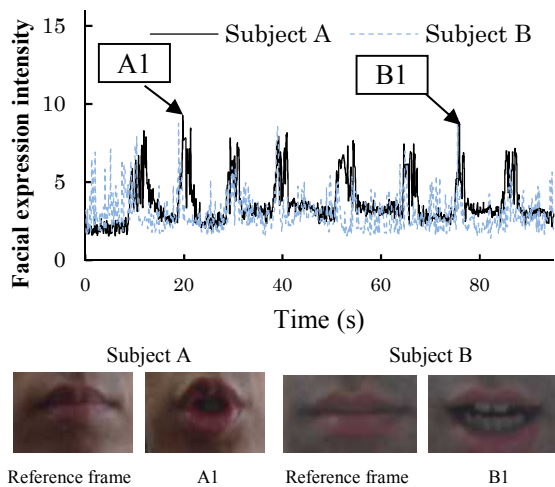


Fig. 1. Changes in facial expression intensity of mouth area for Subjects A and B (upper graph). Reference frame and mouth area images are shown during Experiment 1 (A1 and B1), as indicated on the graph (lower images).

that interview, the agent asked the subject eight fundamental questions generally used to ascertain the condition a patient with potential depression. A preliminary experiment was then conducted to decide the appropriate interval time between questions.

In this study, we used a Dell XPS 9350 personal computer (PC) equipped with an Intel Core i7-6560U 2.2GHz central processing unit (CPU) and 8.0 GB of random access memory (RAM) for a computational environment. The Microsoft Windows 7 Professional operating system (OS) was installed on the PC and Microsoft Visual C++ 2008 Express Edition was used as the development language.

Five males (Subject A in his 30s, Subjects B, C, D, and E in their 20s) participated in the experiments. Each of the subjects was interviewed by the agent for about 95 seconds. As an initial experimental condition after the start of the interview, the subjects were instructed to maintain a neutral facial expression without speaking for about five seconds. Then, in the first three experiments, Subjects A and B were requested to intentionally respond with expressions of three types of emotions (Experiment 1, relaxed; Experiment 2, excited; and Experiment 3, depressed). In Experiment 4, subjects C, D, and E were requested to respond naturally to the same interview as that used in Experiments 1 and 2.

The visual of mouth area and audio information of the subjects in the experiments were saved as BMP and

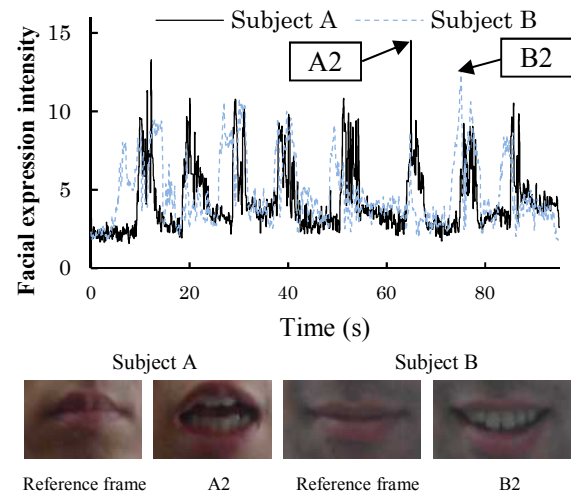


Fig. 2. Changes in facial expression intensity of mouth area for Subjects A and B (upper graph). Reference frame and mouth area images are shown during Experiment 2 (A2 and B2), as indicated on the graph (lower images).

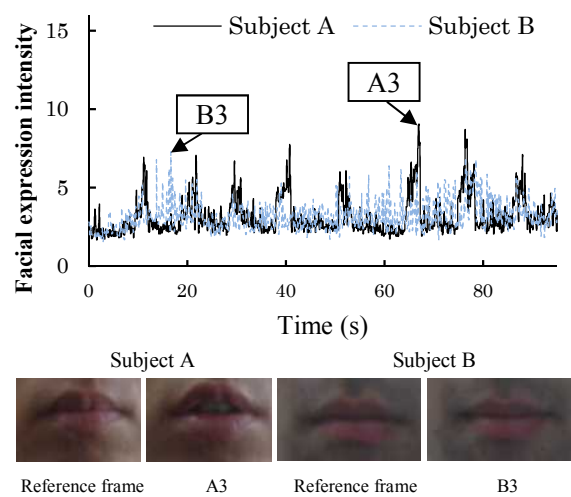


Fig. 3. Changes in facial expression intensity of mouth area for Subjects A and B (upper graph). Reference frame and mouth area images are shown during Experiment 3 (A3 and B3), as indicated on the graph (lower images).

WAV files. The BMP files were used for measuring the feature parameters of the facial expressions, while the WAV files were used for measuring the time-to-utterance of the subject just after an interview question was given and the fundamental frequencies of the subject.

4.2. Results and discussion

The facial expression intensity for the mouth area became high every time during the response to a question (Figs. 1-3). Note that the feature parameters for facial

expressions for the mouth area tended to be greater in Experiment 2 than in both Experiments 1 and 3 (Table 1). In addition, the average of the fundamental frequencies of the voice of the subjects was greater in Experiment 2 than in both Experiments 1 and 3 (Table 2). The order of increasing time-to-utterance of the answerer just after an interview question was terminated was Experiments 2, 1, and 3 (Table 3).

The time-to-utterance of the answerer just after an interview question for Subjects C, D, and E in Experiment 4 was longer than that for Subjects A and B in Experiments 1, 2, and 3 (Table 3).

Based on these results, we conclude that it is possible to use our interview by agent system for medical examinations (Tables 1-3).

Table 1. Feature parameters for facial expressions.

Exp.	1(relaxed)	2(excited)	3(depressed)	4(naturally)
Subject A	3.5	4.1	3.1	
Subject B	2.9	4.8	3.1	
Subject C				4.0
Subject D				4.0
Subject E				2.1

Table 2. Average of fundamental frequencies of subject voices in Experiments 1-4.

Exp.	1(relaxed)	2(excited)	3(depressed)	4(naturally)
Subject A	137.9	157.9	106.9	
Subject B	110.7	145.4	103.7	
Subject C				102.3
Subject D				143.6
Subject E				132.1

(Hz)

Table 3. Time-to-utterance of the answerer just after an interview question was terminated.

Subject	A		B		C		D		E	
Exp.	1	2	3	1	2	3	4	4	4	4
Q.1	1.2	1	1.6	0.9	1	0.9	1.1	2.1	2.4	
Q.2	1.3	0.7	1.7	0.4	0.7	1.1	3.3	1.3	1.2	
Q.3	1.4	0.7	1	1.1	0.3	0.7	1.3	0.9	0.5	
Q.4	1.3	1	1.7	0.9	0.5	1	0.9	1.3	0.9	
Q.5	1	0.7	1	0.5	1.4	1.2	2.7	1	1	
Q.6	1	0.6	1.2	0.5	0.3	1.1	0.8	1.4	1.3	
Q.7	1	1	1.3	0.8	0.8	0.7	1.9	2.4	1.6	
Q.8	1.6	0.6	1	0.9	0.6	0.5	1.6	1.5	2.2	
Ave.	1.2	0.8	1.3	0.8	0.7	0.9	1.7	1.5	1.4	

(s)

5. Conclusion

Herein, we reported on the development of a system for analyzing the facial expressions of a person while he or she is answering interview questions posed by an agent. Moreover, the time-to-utterance of the answerer just after an interview question and the fundamental

frequencies of his or her voice were measured in order to help analyze his or her mental state. It is believed that this system could prove useful in the treatment of persons suffering from psychiatric ailments such as depressive disorder and dementia.

Acknowledgements

The authors would like to thank Professor J. Narumoto of Kyoto Prefectural University of Medicine for his valuable support and helpful advice in the course of this research. We would like to thank the students of the Graduate School of Kyoto Prefectural University for their assistance in our experiments. This research was partially supported by the Center of Innovation Science and Technology based Radical innovation and Entrepreneurship Program (COI STREAM) of the Ministry of Education, Culture, Sports, Science, and Technology of Japan.

References

1. T. Asada, Y. Yoshitomi, R. Kato, M. Tabuse, and J. Narumoto, Quantitative evaluation of facial expressions and movements of persons while using video phone, *J. Robotics, Networking and Artif. Life* **2**(2) (2015) 111-114.
2. T. Asada, Y. Yoshitomi, R. Kato, M. Tabuse, and J. Narumoto, A system for facial expression analysis of a person while using video phone, *J. Robotics, Networking and Artif. Life* **3**(1) (2016) 37-40.
3. T. Asada, Y. Yoshitomi, and M. Tabuse, A system for analyzing facial expression and verbal response of a person while answering interview questions on video, *J. Robotics, Networking and Artif. Life* **4**(2) (2017) 114-117.
4. Open CV. <http://opencv.org/> Accessed 7 December 2017.
5. T. Asada, D. Kogi, R. Shimada, Y. Yoshitomi, and M. Tabuse, A system for facial expression analysis of a person while answering interview questions by agent (in Japanese), in *Proc. of Human Interface Symposium 2017* (Osaka, Japan, 2017), pp.533-536.
6. R. Shimada, T. Asada, Y. Yoshitomi, and M. Tabuse, Real-time system for horizontal asymmetry analysis on facial expression and its visualization, *J. Robotics, Networking and Artif. Life* to appear.
7. MMDAgent. <http://www.mmdagent.jp/> Accessed 25 July 2016.
8. Y. Yoshitomi, T. Asada, K. Mori, R. Shimada, Y. Yano, M. Tabuse, Facial expression analysis and its visualization while writing messages, in *Proc. of Int. Conf. on Artif. Life and Robotics* (Beppu, Oita, Japan, 2018), in press.

Facial Expression Analysis and its Visualization While Writing Messages

Yasunari Yoshitomi¹, Taro Asada¹, Kenta Mori², Ryoichi Shimada³, Yuiko Yano¹, Masayoshi Tabuse¹

1: Graduate School of Life and Environmental Sciences, Kyoto Prefectural University,

1-5 Nakaragi-cho, Shimogamo, Sakyo-ku, Kyoto 606-8522, Japan

E-mail: {yoshitomi, tabuse}@kpu.ac.jp, t_asada@mei.kpu.ac.jp}

http://www2.kpu.ac.jp/ningen/infsys/English_index.html

2: Neyagawa City Hall

1-1 Honmachi, Neyagawa, Osaka Prefecture 572-8555, Japan

3: JFE Systems, Inc.

4-1-3 Olinas Tower 17F, 4-1-3 Taihei, Sumida-ku, Tokyo 130-0012, Japan

Abstract

We have developed a real-time system for expressing emotion as a pictograph selected according to the facial expression while writing a message. The image signal is analyzed by our real-time system using image processing software (OpenCV) and a previously proposed feature parameter. We applied the system to post a message and a pictograph expressing the facial expression while writing the message on an SNS. The experimental results suggest that our system can be useful for expressing emotions while writing messages.

Keywords: Facial expression analysis, Real-time system, Mouth area, Visualization, Writing messages, OpenCV.

1. Introduction

Social network services (SNSs) have become very popular worldwide as communication tools on the Internet. For example, Twitter, one of the most popular SNSs, has 328 million users active monthly.¹ We can post a message, a static image, or a moving image on Twitter. However, we cannot post information on Twitter about our real emotions while writing a message.

One of our current studies is aimed at expressing the real emotions of persons writing messages for posting on an SNS site by analyzing their facial expressions and visualizing them as pictographs. In this paper, we propose a real-time system for analyzing a facial expression while writing a message, visualizing the facial expression as a

pictograph, and posting the pictograph on Twitter together with the message. The moving image in our method is captured by a webcam and analyzed in real-time via Open Source Computer Vision (OpenCV) image-processing software² by using a previously proposed feature parameter (facial expression intensity)³ that is based on the mouth area. The visualization method proposed in this paper is based on a previously reported method.⁴

2. Proposed System and Method

2.1. System overview and outline of the method

In this system (see Fig. 1), a webcam moving image captured in real-time is analyzed via the following process.



Fig. 1. Display of the proposed system at startup.

The proposed method consists of (1) extracting the mouth area, (2) calculating the facial expression feature vectors, (3) determining the facial expression intensity and calculating its average value while writing a message, (4) and posting the message and an automatically selected pictograph for the message on Twitter. The details of these steps are explained in the following subsections.

2.2. Mouth area extraction

First, moving image data are changed from RGB to YCbCr image data, after which the face area is extracted from the YCbCr image as a rectangular shape, and the lower 40% portion of the face area is standardized. Next, the mouth area is extracted from that portion. The mouth area was selected for facial expression analysis because it is where the differences between neutral and smiling facial expressions appear most distinctly.

2.3. Facial expression intensity measurement

For the Y component of the selected frame, the facial expression feature vector is extracted for the mouth area using a two-dimensional discrete cosine transform (2D-DCT) for each 8×8-pixel section. In this study, two 8×8-pixel sections at each of the left and right lower corners (see Fig. 2) are not included for this measurement, because these sections might cause errors due to the appearance of the jaw and/or neck line(s) there. To measure the feature parameters of the facial expressions, we select low-frequency components from the 2D-DCT coefficients as the facial expression feature vector elements; however, the direct current component is not included. In total, 15 feature vector elements are obtained. The facial expression intensity is defined as the norm difference between the facial expression feature vectors of the reference and target frames. In this

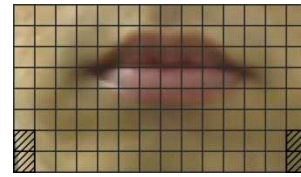


Fig. 2. Mouth area. The four 8×8-pixel sections excluded from the measurement in mouth area appear as cross-hatched squares.

study, the first 20 continuous frames of mouth area data successfully extracted after the webcam recording begins are treated as reference frame candidates. The reference frame selection method is explained in detail in Reference 5.

2.4. Posting a message and an automatically selected pictograph for the message on Twitter

Facial expression intensity is measured using our previously discussed method⁴, in which a straight line is drawn on a graph image prepared using OpenCV. A pictograph is automatically selected by comparing the average value of facial expression intensity and a threshold decided experimentally beforehand, and then the message and the selected pictograph are posted on Twitter when the user presses a button. In this system, two pictographs, expressing neutral and smiling facial expressions, are used (see Fig. 3).

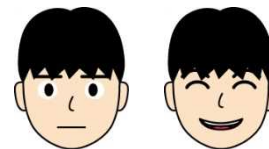


Fig. 3. Two pictographs expressing a neutral (left) or smiling (right) facial expression.

3. Experiment

3.1. Conditions

The experiment was performed on a Dell XPS 9350 PC equipped with an Intel Core i7-6560U 2.2 GHz central processing units (CPUs) and 8.0 GB of random access memory (RAM). The Microsoft Windows 7 Professional operating system (OS) was installed on the PC and Microsoft Visual C++ 2008 and 2013 Express Editions were used as the development language.

CoreTweet⁶, as a library, and the Twitter API were used to post a message and pictograph on Twitter.

Seven males (subjects A to D in their 20s, subjects E and F in their 30s, and subject G in his 50s) participated in the experiments.

We first performed experiments with six males (all except subject G) under the two conditions listed below. As an initial condition in the experiment, the subjects were instructed to maintain a neutral facial expression and face forward without speaking for about five seconds just after the start of the experiment. After the initial state of a neutral facial expression was terminated, the subjects were requested to intentionally respond with one of two types of facial expressions (Experiment 1, neutral; Experiment 2, big smile) and write a message, 'このぬいぐるみかわいくない' (in Japanese), which means, 'This stuffed toy is pretty, isn't it?' Experiments 1 and 2 were performed three times for each subject. In each experiment, facial expression intensity measurements were performed for each subject during writing a message for 40 seconds and then the average facial expression intensity for that message was calculated. In order to distinguish between the neutral and smiling facial expressions on the basis of average facial expression intensity for a message, a threshold was set as the average of the maximum among neutral expressions and minimum among smiling expressions of the six subjects.

Two additional experiments (Experiments 3 and 4) were next performed with only subject A. The same initial conditions were used in these experiments as in Experiments 1 and 2. After the initial state of a neutral facial expression was terminated, the subject was requested to intentionally respond with two types of emotions (Experiment 3, neutral; Experiment 4, smiling) and write a message, '明日は情報伝達システム学サブゼミに参加します。時間は5時限目、場所は先生の部屋です。' (in Japanese), which means, 'I will attend the discussion section held at the professor's room of the information communication system lab. in fifth period tomorrow.' Fig. 4 shows snap-shots of Experiments 3 and 4, which were extracted from the captured moving images of those experiments. In each experiment, facial expression intensity measurement was performed for 30 seconds and then the average facial expression intensity for that message was calculated, after which both the message and the

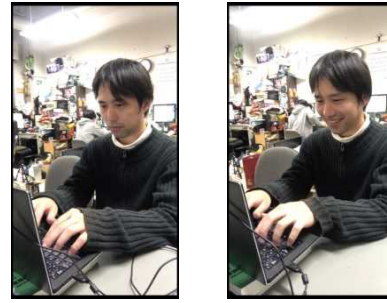


Fig. 4. Snap-shots of subject A in Experiment 3 (neutral; left) and Experiment 4 (smiling; right).



Fig. 5. Messages and pictographs posted on Twitter in Experiment 3 (neutral; upper) and Experiment 4 (smiling; lower).

pictograph expressing the facial expression while writing the message were posted on Twitter. Then, subjects B, C, D, and G participated in two questionnaire surveys comprising questions asking them to assign one of four adjectives (neutral, happy, sad, or angry) to (a) each of the captured moving images, and (b) for each of the messages accompanied by pictographs (see Fig. 5) in Experiments 3 and 4.

3.2. Results and discussion

The ranges of average values of facial expression intensities in Experiments 1 (neutral) and 2 (big smile) were 2.13 to 3.70 and 3.50 to 15.61, respectively. Therefore, the threshold for distinguishing between the two types of facial expressions was determined as 3.60. Thus, in the proposed system, a facial expression having an average facial expression intensity under 3.60 is judged to be a neutral facial expression, whereas one 3.60 or higher is judged to be a smiling expression.

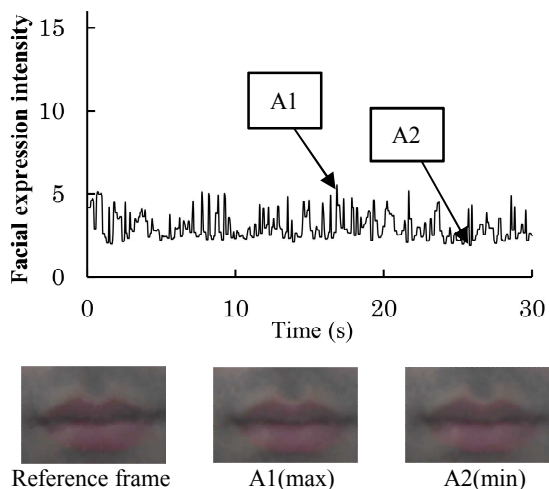


Fig. 6. Changes in facial expression intensity of mouth area for subject A (upper graph). Mouth images are shown for two moments during Experiment 3 (neutral) (A1 (maximum of facial expression intensity) and A2 (minimum of facial expression intensity)), as indicated on the graph (lower images), along with that of reference frame.

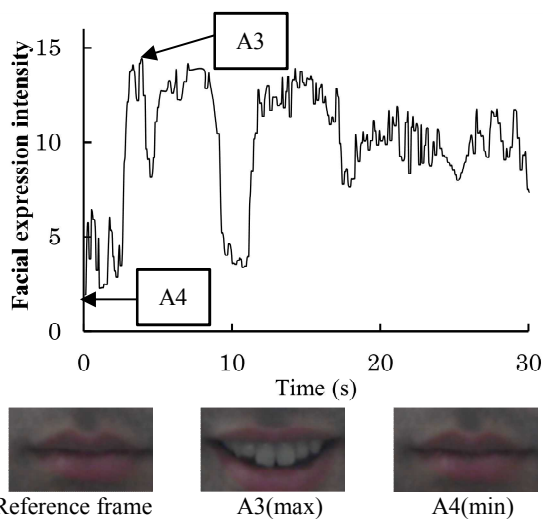


Fig. 7. Changes in facial expression intensity of mouth area for subject A (upper graph). Mouth images are shown for two moments during Experiment 4 (smile) (A3 (maximum of facial expression intensity) and A4 (minimum of facial expression intensity)), as indicated on the graph (lower images), along with that of reference frame.

As shown in Figs. 6 and 7, our proposed system was able to distinguish between the two types of facial expressions, neutral and smiling. The average facial expression intensities for the two types were 2.94 and 9.60, respectively, in Experiments 3 and 4, respectively.

The former value is under 3.60 and the latter is above 3.60, resulting in our proposed system selecting the neutral pictograph (Fig. 5, upper) in Experiment 3 and the smiling pictograph (Fig. 5, lower) in Experiment 4 for posting on Twitter. The results of the questionnaire surveys show that our proposed system distinguished correctly between the two types (neutral and smiling) of facial expressions for the subject, and that the pictographs selected by the system correctly reflected the facial expressions while writing messages for the subject.

Note, in the case of subject F, for a typical example, the effect of exclusion of the four 8×8-pixel sections from the measurement in mouth area (see Fig. 2) was estimated to be about 22% in terms of difference in facial expression intensity.

4. Conclusion

We have developed a real-time system for expressing emotion as a pictograph selected according to the facial expression while writing a message. We applied the system to the posting on Twitter of both a message and a pictograph. The experimental results suggest that our system can be useful for expressing emotions during writing messages.

Acknowledgements

We would like to thank the subjects for their cooperation in the experiments.

References

1. http://files.shareholder.com/downloads/AMDA-2F526X/5451637324x0x951000/718EA233-DF7E-4ECB-AC2B-BFAB3F067C72/Q217_Shareholder_Letter.pdf Accessed 13 December 2017.
2. Open CV. <http://opencv.org/> Accessed 13 December 2017.
3. T. Asada, Y. Yoshitomi, R. Kato, M. Tabuse, and J. Narumoto, Quantitative evaluation of facial expressions and movements of persons while using video phone, *J. Robotics, Networking and Artif. Life* **2**(2) (2015) 111-114.
4. T. Asada, K. Mori, R. Shimada, Y. Yoshitomi, and M. Tabuse, Facial expression analysis in real time while writing messages (in Japanese), in *Proc. of Human Interface Symposium 2017* (Osaka, Japan, 2017), pp. 469-472.
5. R. Shimada, T. Asada, Y. Yoshitomi, and M. Tabuse, Real-time system for horizontal asymmetry analysis on facial expression and its visualization, in *Proc. of Int. Conf. on Artif. Life and Robotics* (Oita, Japan, 2017), pp. 120-123.
6. CoreTweet. <https://github.com/CoreTweet/> Accessed 20 December 2017.

Recognition of Finger Spelling from Color Images Using Deep Learning

Yusuke Yamaguchi, Masayoshi Tabuse

Graduate School of Life and Environmental Sciences, Kyoto Prefectural University,
1-5 Nakaragi-cho, Shimogamo, Sakyo-ku, Kyoto 606-8522, Japan
E-mail: y_yamaguchi@mei.kpu.ac.jp, tabuse@kpu.ac.jp

Abstract

We have developed a system to recognize finger spelling in Japanese sign language using deep neural networks. As deep neural networks, we adopt Faster R-CNN. By defining an output class for each finger letter and learning the object detection network, it is possible to output where the finger letter exists in the input image. This method does not require depth cameras, magnetic sensors, or other special equipment when used. Furthermore, this does not require preprocessing that extracts the hand region using human skin colored regions and color gloves used in other methods using color images. We synthesized a training data set by processing images taken with Kinect. As the test data, we input images of performing finger letters into the trained network and check the score of the output area and class.

Keywords: Recognition of Finger Spelling, Deep Learning, Faster R-CNN, Color Image.

1. Introduction

Many deaf and hard of hearing people in Japan usually use Japanese Sign Language (JSL). On the other hand, most hearing people use spoken language, and many of them do not know sign language. In order to break down barriers between them, development of a sign language interpretation system is urgent. Finger spelling is a visual language that represents characters using hand shapes, and is used mainly to express words of proper nouns or that is not defined as sign language.

The method of acquiring finger spelling features is roughly divided into "contact type" and "non-contact type" depending on the sensor to be used. In the "contact type" method, equipment such as a data globe [1] or a color globe [2] is attached to the user. These sensors take time and effort to attach, and there is also a risk of affecting sign language operations. "Non-contact type" has burden on the user less than "contact type". Especially a single color camera is the most plain and popular sensor. In the method using only a single RGB

image, it is necessary to devise a method for extracting a hand region. A method of extracting a hand region from a color image using human skin colored regions [3] or a special background [4] has been proposed. These methods require restrictions on the use situation.

This paper deals with 41 kinds of finger spelling, without movement, recognition using Faster R-CNN as an approach to these challenges. We trained the network using the data generated based on the image captured by Kinect, and in the experiment we recognized the video of the sign language teaching material video.

2. Faster R-CNN

Faster R-CNN [5], which is an object detection network, is a method that speeds up R-CNN [6] and Fast R-CNN [7].

2.1. R-CNN, Fast R-CNN

Fast R-CNN is a method that reduces the number of times of convolution processing with the highest calculation

cost in R-CNN. Like the R-CNN, region proposal is acquired by the selective search. Then, the entire image is convoluted, and a feature map of the object proposed region is extracted from the convolutional feature map. The extracted feature map is pooled by the Region Of Interest (ROI), and is input to fully connected layer (hereinafter referred to as subnets). ROI pooling pools the feature map of any size into regions partitioned into the set grid sizes, so that feature maps of arbitrary sizes can be obtained.

In this method, since it is unnecessary to pass each region proposal to the CNN, it is possible to perform object detection approximately 100 times faster than R-CNN. However, the processing cost of selective search used in the pre-processing of Fast R-CNN is a bottleneck.

2.2. Faster R-CNN

Faster R-CNN is a network that performs "region proposal" with Region Proposal Network (RPN), which was done by selective search of Fast R-CNN. Faster R-CNN has the structure shown in the Fig 1. In this method, it is possible to detect the region proposals and determine the object class of the region at the same time, and it is possible to detect objects faster than Fast R-CNN.

As with Fast R-CNN, convolution is performed on the input image to obtain a feature map. RPN raster-scans a detection window (called an anchor) against a feature map to detect an object. The anchor is a method of applying k detection windows around the region of interest and raster scanning. The area designated by the anchor is input to the RPN, and the score of the objectness and the rectangular area on the input image are outputted. The area designated by the anchor is also input to the subnet of Fast R-CNN, and object recognition is performed when it is judged as an object by RPN.

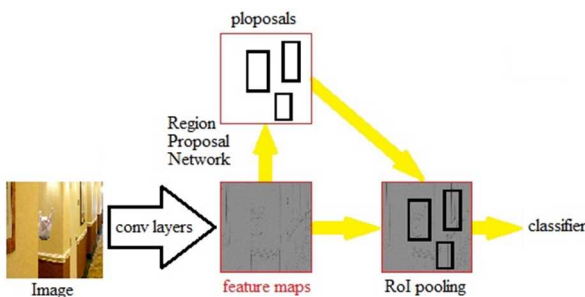


Fig. 1. The overview of Faster R-CNN.

These processes of Faster R-CNN can be trained end-to-end as a single network.

3. Experiments

First, we trained Faster R-CNN using the finger spelling movement data set. After that, we input the finger spelling image into the trained network and confirmed whether the output was correct or incorrect. If a class of output having maximum score is the same class as the input image and the output area indicates the part of the hand performing the finger spelling on the image, let the output be correct.

3.1. Network details

In this experiment, we used Faster R-CNN connected to the fifth convolution layer of VGG-16. The learning parameters are as shown in the table 1. We used approximate joint training [5] to train Faster R-CNN.

3.2. Experiments data

Deep neural network like Faster R-CNN requires a large amount of various types of training data. However, there are no popular data sets for training and recognizing sign language and finger spelling.

Therefore, we created training data based on images taken with finger spelling movements. We prepared training data by processing a small number of original images and generating large amounts of various variation data. For recognition experiments, images are used as learning materials for sign language and finger spelling.

Table 1. Learning parameters.

Parameters	setting
base learning rate (lr)	0.001
Schedule of learning rate (lr_policy)	Step
gamma	0.1
anchor	9
average loss	100
momentum of SGD	0.9
weight decay	0.0005

3.2.1. Training-validation data

We used Microsoft's motion sensor Kinect v2 to capture images. Kinect is a multi-sensor device that can handle

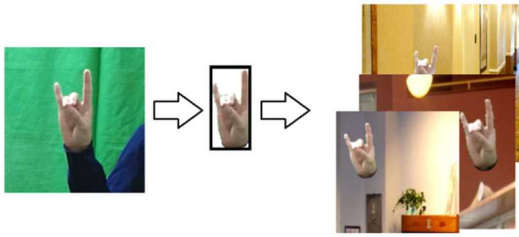


Fig. 2. The flow to generate some training-validation data from a finger spelling image captured by Kinect with SUN397 dataset.

color camera, depth camera, audio, etc., and can detect 25 joints of a person [8]. When capturing finger spelling movements, the subject stands facing forward with respect to Kinect. When acquiring images, we use blue or green clothing and background which is complementary color of human skin color.

We trimmed the hand image from the color image, centered on the coordinates of the hand obtained by Kinect, erased the green and blue parts, and made a hand-only image. Images with only the tip from the wrist were deformed with the following random parameters and arranged at random coordinates of the background image. At this time, we randomly selected one image from SUN397 which is the image data set for scene recognition as the background image and used it. In order to increase the dispersion of the learning data, image processing was randomly executed according to the following list. The number shown in parentheses is the probability of execution.

- rotation in the range of -10 degrees to +10 degrees(1),
- extend the height and width from 1.0 times to 1.2 times(1),
- contrast emphasis(1/3) or reduction(1/3),
- Gamma correction in the range of 0.75 to 1.5(1),
- Blur in kernel size 1 to 5(1/2),
- Gaussian noise with mean 0 and sigma 15(1/3),
- salt-and-pepper noise for 0.4% of pixels in equal ratio(1/4).

Based on samples from each subject, we generated roughly 500 pairs of training data for each finger spelling and summed up to generate 66,281 data. 80% of the generated data was used as training data and the remaining 20% was used as validation data.

We captured sample images from three subjects who do not know sign language. Before experiments, the

subjects sufficiently confirmed how to operate the finger spelling described in the textbook [9].

3.2.2. Recognition data

Since there is no general evaluation data, we use images of commercial teaching materials [9] shown in Fig. 3 as data for evaluation. The resolution of this movie is 720×480. This movie reproduces mirrored images for right-handed people and small mirrored images for left-handed people at the same time. In this experiment, training was carried out only with the movement by the right hand, so only the output to the lower right area was recorded.

4. Results and discussion

The left axis in Fig. 4 shows the mean Average Precision (mAP) for each 10000 iterations using test data. mAP becomes flat after 60,000 times.

Even when the recognition score of the lower limit was set to 0.8, 0.5 and 0.2, the recognition rate after 140,000 times was 64.4%, 76.1% and 78.8% respectively.

33 classes are recognized correctly for almost all frames, and 8 classes are misrecognized for all frames. We divided the 8 classes that failed to recognize into 3 groups that seemed to be similar misrecognition causes as shown in the table 2. In group 1, finger shapes are similar. Since Kinect needs to use about 2 meters away to detect joints of a person, acquired images are low resolution. Therefore, it is insufficient to train the complex feature of finger spelling. Group 2 has a shape that the fingers protrude forward, and it seems that training data could not correspond to them because the appearance changes greatly as the viewpoint changes a little. We would like to respond by brushing up to flexible learning data that can correspond to this. In Group 3, the

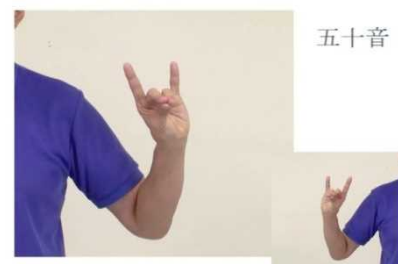


Fig. 3. One of frames of video used for recognition.

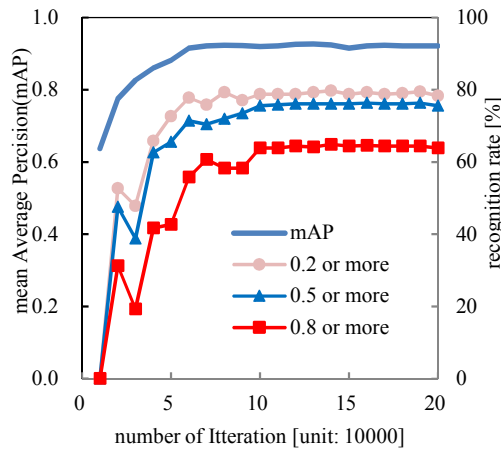


Fig. 4. The right axis shows recognition rate by minimum score to allow output and the left axis shows mean average precision for each iteration.

erroneously recognized area outputted contained arms as shown in Fig. 5. It seems that the convolution feature including the arm resembled that class. In order to deal with this, it is necessary to consider a learning method considering the arm. In addition, it is necessary to experiment the image other than the moving image used in the experiment and confirm the usefulness of this method. In the sign language recognition system, it is also necessary to have a system capable of recognizing

Table 2. Class group that was misrecognized due to close cause.

group	input	output
group 1	chi'	to', 'ra'
	hi'	u', 'ra'
	ra'	u'
	ru'	ka'
group 2	so'	ha'
	tsu'	u', 'me', 'wa'
group 3	na'	fu', 'su'
	ma'	ne'

finger spelling with movement.

5. Conclusion

We trained Faster R-CNN and conducted an experiment to recognize JSL fingers without movement from a single color image. In the experiment using the video of

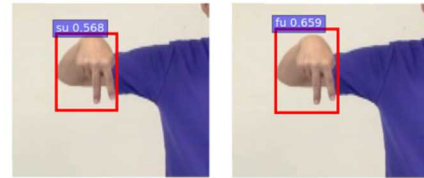


Fig. 5. Finger spelling 'na' overlaps the arm like 'su' and 'fu'.

teaching material of finger spelling, recognition rate of 78.8% was obtained.

6. Reference

1. T. Yamane, T. Funatomi, M. Iiyama, M. Minoh, Estimation of Rigid Transformation of Finger Segments from Data Glove, *IEICE Technical report*, Vol.111, No.353, pp.77-82, 2011.
2. M. Osato, M. Suzuki, A. ITO, S. Makino, Feature Value Combination for Finger Character Recognition Using a Color Glove, *IEICE Technical report*, Vol.105, No.375 pp.93-105, 2011.
3. K. Miura, Y. Chang, N. Mukai, Recognition of Fingerspelling in Japanese Sign Language based on Nail Detection and Wrist Position, *ITE Technical Report*, Vol. 37, No. 17, pp. 199-202, 2013.
4. K. Hirose, Recognition of Japanese Manual Alphabet Using Thinning Image, *CVIM*, Vol. 93, No. 66, pp.1-6, 1993.
5. S. Ren, K. He, R. Girshick, J. Sun, Faster R-CNN: Towards Real-Time Object Detection with Region Proposal Networks, *NIPS* 2015.
6. R. Girshick, J. Dnahun, T. Darrell, J. Malik, Rich feature hierarchies for accurate object detection and semantic segmentation, *CVPR* 2014.
7. R. Girshick, Fast R-CNN, *ICCV* 2015.
8. J. Shotton, A. Fitzgibbon, A. Blake, A. Kipman, M. Finocchio, B. Moore, and T. Sharp, Real-Time Human Pose Recognition in Parts from a Single Depth Image, *CVPR* 2011.
9. K. Matsumoto, Introduction to sign language understood from zero with DVD (in Japanese), *Shufunotomo Co., Ltd.*, Chiyoda-ku, Tokyo, 2011.

Recognition of Texting While Walking Using Convolutional Neural Networks

Junpei Miyachi, Masayoshi Tabuse

Graduate School of Life and Environmental Sciences, Kyoto Prefectural University,
1-5 Shimogamohangi-cho, Sakyo-ku, Kyoto 606-8522, Japan
E-mail: j_miyachi@mei.kpu.ac.jp, tabuse@kpu.ac.jp

Abstract

In recent years, texting while walking has become a problem with the spread of smartphones. Pedestrians who operate a smartphone while walking decrease attention to their surrounding environment. The purpose of this study is to detect the pedestrians using surveillance camera for the support of accident preventions in railways. We propose the method of texting while walking recognition using convolutional neural networks. We show the classification results of a pedestrian who is texting while walking.

Keywords: Texting while walking, Pose estimation, CNN.

1. Introduction

The life of people becomes more convenient by smartphone in recent year. However, the number of people who operate a smartphone while walking is increasing. Texting while walking is one of dangerous acts because the pedestrian decreases attention to their surrounding environment. It is the cause of falling from station's platform or bumping into someone in public areas such as railway stations. A monitoring system is one of measures for the support of accident preventions. Therefore, detecting pedestrians who operate a smartphone using a surveillance camera is required.

Pedestrians which are texting while walking have the similar features of posture. They tend to bring their arm up to chest level and walk with their head down. In order to recognize the posture, we employ convolutional neural networks (CNN) that is one of deep learning, which has improved results in various fields in recent years. It is expected to obtain effective features for recognition by learning. In this paper, we propose the method of the texting while walking recognition using CNN. Although deep learning generally requires a large quantity of training data for adequate learn, it is a burden to collect

the data. Therefore, we generate training data from a small amount of sample. We verify the effectiveness of the recognition method using this dataset.

2. Related works

2.1. Studies on recognition of texting while walking

Some studies on recognition of texting while walking are reported. Minamoto *et al.* [1] proposed a detect method of texting while walking using HOG features for guide dog robot. The robot recognizes the pedestrian facing his front to it. Shinmura *et al.* [2] recognized a pedestrian which are texting while walking using HOG features and SVM classifier for a vehicle-mounted camera. They targeted a pedestrian facing his front, left and right side to the camera. Pedestrians turning to each direction are mixed at a platform of a railway station. Regarding the accidents in a station, it may occur in any direction on the platform. Therefore, recognition of texting while walking is required regardless of the pedestrian direction.

2.2. Convolutional neural networks

CNN is widely used in computer vision since ImageNet Large Scale Visual Recognition Challenge in 2012 (ILSVRC2012). The conventional method combined hand-crafted features and statistical analysis. In contrast, CNN can learn the feature value for recognition. It composes of convolution, pooling and fully connected layers.

2.2.1. Convolution layer

In a convolution layer, it conducts sum-of-product operation pixel value z_{ijm} of an input image and a weight filter h_{pqkm} . The sum-of-product operation is expressed using the following equation:

$$z_{ijm} = f \left(\sum_{k=0}^{K-1} \sum_{p=0}^{H-1} \sum_{q=0}^{H-1} z_{i+p,j+q,k}^{(l-1)} h_{pqkm} + b_m \right), \quad (1)$$

where K denotes a number of channel, b_m denotes a bias in filter m . The output is a value which activation function f is applied. It plays a role of feature extraction in each position on the image.

2.2.2. Pooling layer

In a pooling layer, values of obtained feature maps are integrated in a local area. It plays a role of immutable output for local translation. In this study, we adopt max pooling which selects a max value in the area. The pixel value z_{ijk} obtained by max pooling is expressed using the following equation:

$$z_{ijk} = \max_{(p,q) \in P_{ij}} z_{pqk}, \quad (2)$$

where P_{ij} denotes a set of pixel, which takes a square domain centering the pixel (i, j) on an input image.

2.2.3. Fully connected layer

Fully connected layer is a layer that all nodes is connected with next layer's them. It integrates information of the former layer and calculate the output. The calculation is expressed using the following equation:

$$z_j = f \left(\sum_{i=1}^l w_{ji} x_i + b_j \right), \quad (3)$$

where w_{ji} denotes a weight of the edge.

3. Recognition method of texting while walking

We constitute a network as a classifier of normal walking and texting while walking. The CNN learning uses generated images for training data.

3.1. Training data generation

A large number of training data are needed for deep learning. Therefore, we generate training data from a small amount of samples by combining a human image with a background image. Moreover, we apply transformation processing such as rotation, scaling and gamma correction to the synthetic image. The transformation parameters are randomly assigned. Generating procedures of training data are as below.

- (i) Rotation and scaling processing are applied for human images in a random order.
- (ii) The human region of the image is cut out.
- (iii) The human region and a randomized position of a background image are combined.
- (iv) Gamma correction is performed to the synthetic image.

3.2. Recognizing texting while walking using CNN

Classified pedestrian images are obtained by performing



Fig. 1. A human image for cutting out the human region (left), background image (center), and generated image for training data (right).

human detection to images including human. The image is input to CNN.

The CNN structure used in this study is based on Alexnet [3]. Alexnet consists of 5 convolutional layers, 3 pooling layers and 3 fully connected layers, which is applied to various works as high performance and versatility. It is shown in Fig. 2. In the input layer, input image is resized to 227×227 , and it is input to CNN. We use ReLU function for the activation function in all convolutional layers and two fully connected layers. In output layer, the number of units in output layer is 2 to classify into normal walking and texting while walking. The softmax function is used for the activation function, and class probability is output. The classified result selects the best probability class.

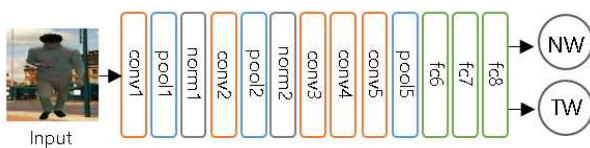


Fig. 2. The CNN structure used in this study. “conv”, “pool”, “norm” and “fc” denote convolutional, pooling, normalization and fully connected layer, respectively. “NW” and “TW” denote normal walking and texting while walking, respectively.

4. Experiments

We performed an experiment of recognizing a pedestrian which is texting while walking using CNN.

4.1. Conditions

4.1.1. Datasets

We collected pedestrian images taken with camera for datasets used in experiments. We prepared the pedestrian images for 11 pedestrians, which are both the state of texting while walking and normal walking. The number of pedestrian images are 10 images for 2 types (texting while walking or normal walking) and 4 direction (front, left, right, back), respectively. Therefore, there are 880 pedestrian images in total. For background images, we used SUN397 dataset in SUN database which is used for scene recognition. There are 458 images in “street” category in the dataset. We randomly selected 100 images for background images.

According to section 3.1, we generated learning samples. The number of learning samples is 88,000 images in total (880 pedestrian images \times 100 background images). The 10 people images (= 80,000 images) of them are for learning data, while 1 person

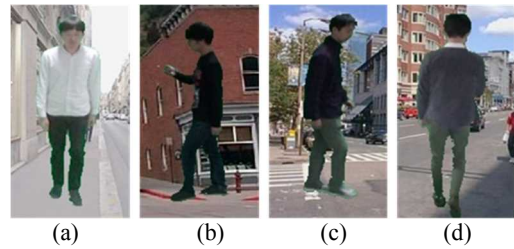


Fig. 3. Example of training data. (a)front normal walking, (b) left texting while walking, (c)right normal walking, and (d)back texting while walking.

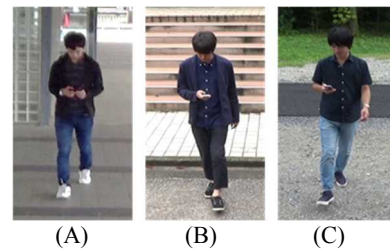


Fig. 4. Example of test samples of each subjects. Let A, B and C be them, respectively.

images (= 8,000 images) are for validation data. Fig. 3 shows example of training samples. For test data, we took videos for 3 subjects, 100 images for each type were randomly selected from among images obtained by performing human detection (Implementation: OpenCV) to the videos. The number of test samples is 2,400 images (2 types \times 4 directions \times 100 images \times 3 subjects) in total. Example of test samples is shown in Fig. 4.

4.1.2. Training setting

Hyperparameters are used in learning using CNN. In this experiment, mini batch learning to shorten learning time is performed, let 200 the number of mini batch, hence epoch number is 100. Let 0.0002 be the initial value of learning rate, 0.1 times the rate every 10 epochs. Learning times is set to 40,000 that is 100 epochs.

4.1.3. Developing environment

The experiment was performed in the following computational environment: the OS was Ubuntu 14.04 LTS; the CPU was Intel(R) Core(TM) i7-6700 CPU 4.00GHz; the GPU was Geforce GTX 1080; the development language was python 2.7.6 and C++. Caffe which is framework for deep learning was used for learning of CNN.

4.2. Method

We classified human images for test data using CNN. To evaluate the effectiveness of the recognition method, we also experimented using HOG features and SVM classifier (HOG+SVM), which is one of the conventional method. F-measure which is calculated from precision and recall was adopted for performance indicator, and we compared two methods.

4.3. Results and discussion

Table 1 and Table 2 show results of classification using HOG+SVM and CNN, respectively. In comparison with overall average of each method, CNN obtained higher results than HOG+SVM. It was verified that CNN have the high performance for recognizing texting while walking. In regard to the average of each direction, front direction was the best result in all direction. On the other hand, left and back direction was relatively low results. In back direction, a pedestrian's right arm hid with his body. In left direction, because human images prepared in this experiment had a smartphone in right hand, the similar situation occurs. Subject C's result was different from subject A and B. The cause may be that subject C was wearing short sleeves. Since used dataset have no images such as a pedestrian wears short sleeves, it is assumed that appearance of skin part of arms have an influence on recognition accuracy. High values was obtained from subject A in each direction. This seems that he placed his left hand on the smartphone.

Table 1. The classification result using HOG + SVM.

F-measure				
Direction	A	B	C	Ave.
Front	0.802	0.882	0.639	0.779
Left	0.355	0.510	0.628	0.508
Right	0.577	0.698	0.964	0.764
Back	0.790	0.713	0.317	0.632
Overall	0.669	0.718	0.663	0.684

Table 2. The classification result using CNN

F-measure				
Direction	A	B	C	Ave.
Front	0.985	0.985	0.853	0.938
Left	0.914	0.645	0.623	0.739
Right	0.890	0.919	0.930	0.914
Back	0.934	0.772	0.338	0.718
Overall	0.932	0.844	0.724	0.836

5. Conclusion

We proposed the recognition method of texting while walking. In this method, we apply pedestrian images obtained by performing human detection to input, and it is classified into normal walking and texting while walking using CNN. In this experiment, dataset including training images which is generated human images was used for training. As a result, average F-measure was 0.836, and it exceeded the conventional method. Therefore, the present study has demonstrated that the proposed method is effective for recognizing pedestrians which is texting while walking.

As an area of future work, we intend to put emphasis on features of the upper half of the body because the information of a pedestrian texting while walking is summarized for the part such as hand position and facial direction. In addition, we will recognize other dangerous acts in platform.

References

1. H. Minamoto and M. Sano, Recognize Careless Behavior of Walker –Detect Texting While Walking–, *The 6th IEEEJ SIG on Visual and Hearing Impaired Support* (2015).
2. F. Shinmura, Y. Kawanishi, D. Deguchi, I. Ide, H. Murase and H. Fujiyoshi, Pedestrian's Inattention Estimation based Recognition of Texting While Walking from In-Vehicle Camera Images, *IEICE Technical Report* (2015), pp. 83–88.
3. A. Krizhevsky, I. Sutskever and G. E. Hinton, ImageNet Classification with Deep Convolutional Neural Networks, *Advances in Neural Information Process. Systems 25* (2012), pp. 1097–1105.

A Study on the Lumbar Burden Evaluation of Work using One Smartphone

Mizuki Maiguma[†], Hiroki Tamura[‡], Koichi Tanno
Faculty of Engineering, University of Miyazaki,
1-1, Gakuen-kibanadai-nishi, Miyazaki-shi, Japan

**Department of Environmental Robotics, Faculty of Engineering, University of Miyazaki,
1-1, Gakuen-kibanadai-nishi, Miyazaki-shi, Japan
E-mail: hi13041@student.miyazaki-u.ac.jp[†], htamura@cc.miyazaki-u.ac.jp[‡]*

Abstract

In this paper, we propose the human lumbar burden evaluation method and state estimation system using a smartphone and its application on agricultural work. The proposed system consists of two functions, 1) "State estimation" has a function of estimating posture (Stand up, Sit down, Crouch, Walk, etc.) of the subject. 2) "Lumbar burden estimation" has a function to estimate the angle of the waist from the angle of the subject's upper body and calculate the lumbar burden in combination with other parameters. The aim of this paper is to get the data of the subject's work status in the agricultural field in a simple manner and quasi-real time and help improve the agricultural work efficiency by constructing the agricultural work burden evaluation system were using a smartphone. In this paper, we show on the experimental results of two functions and the evaluation of the actual agricultural work.

Keywords: smartphone, lumbar burden, gyro sensor, state estimation, acceleration sensor, JACK

1. Introduction

In recent years, agricultural workers in Japan have decreased and aging rapidly so it is necessary to review the physical environment of agricultural work. One solution to reduce this problem, technological developments has been made to reduce the burden of agricultural workers and automation various agricultural machinery. On the other hand, it is difficult to quantitatively compare how much newly developed agricultural machinery reduces the burden of conventional agricultural work. Therefore, in this paper, we are focusing on lumbar burden to evaluate burden reductions by introducing agricultural machinery by IT and aiming to build a work burden evaluation system.

To construct the system, we used a smartphone equipped with various sensors such as acceleration sensor, gyro sensor, and so on [1]. This paper examines whether the proposed system can be realized with one

smartphone, unlike previous research that used two smartphones.

2. Previous Research

Our previous research, one smartphone (iPhone4s, iOS 7.0) equipped with RFID compatible RW module jacket installed in the breast pocket and one in the front pocket of the pants. The work burden evaluation carried out with two smartphones. To evaluate the lumbar burden, the pressure of lumbar intervertebral disc calculated from the waist angle and knee flexion angle. At this time, the waist angle can estimate from the device inclination angle (upper body angle) of the smartphone attached to the breast pocket and the device inclination angle (thigh inclination angle) of the smartphone attached to the front pocket of the pants. The upper body angle is α , the waist angle is β , and the thigh inclination angle is γ , which is shown in Fig.1. The waist angle was calculated Eq. (1).

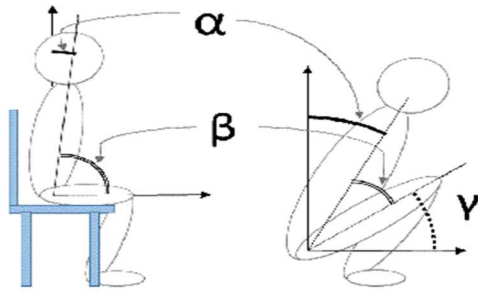


Fig.1 three angles used for calculation of lumbar burden

$$\beta = 180 - (\alpha + \gamma) \quad (1)$$

The knee flexion angle can calculate from the thigh inclination angle. The tilt angle of the device calculated from the gravity acceleration that obtained from the acceleration sensor and it means the tilt angle of the device against the direction of the center of gravity of the body. The device inclination angle (slope angle θ) showed in Fig. 2 and its calculation formula is shown in the Eq. (2). In addition, grav-Y and grav-Z are defined the gravitational acceleration of the Y-axis and the Z-axis. The unit is degree.

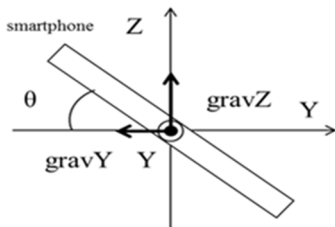


Fig.2 Tilt angle of the device in the direction of gravity

$$\text{Slope angle } \theta = \arctan \left(\frac{\text{gravZ}}{\text{gravY}} \right) \times \pi / 180 \quad (2)$$

The estimation formula used for calculating the lumbar burden based on the estimation formula used in "MIYADAI Pro" developed by Professor Mitarai of Miyazaki University. We substitute the calculated waist angle and knee flexion angle into this lumbar burden estimation formula to calculate the lumbar intervertebral disk pressing force. In our research, burden evaluation carried out using the same estimation formula.

3. Proposed method

In this chapter, we describe the method of estimating the loads that can be determined by the state and the estimated lumbar burden using a smartphone.

3.2 Algorithm for state determination

The flowchart of the smartphone that attached on the breast pocket can be seen in the Fig. 3.

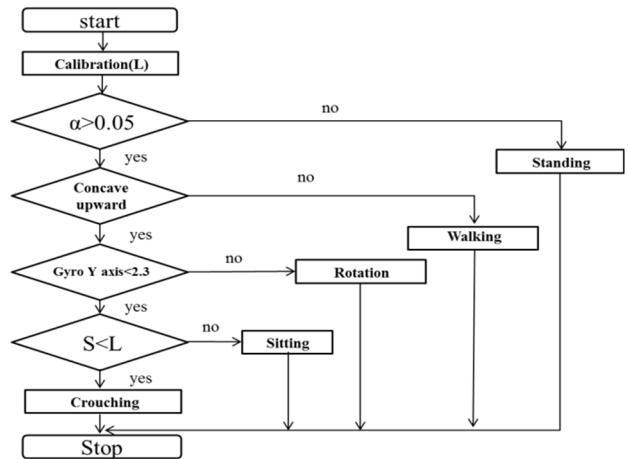


Fig.3 Algorithm flowchart

Subject attaches the smartphone to the breast pocket, and resting for a few seconds in a standing state. The criterion value L [deg] of the subject's state is determined after performing calibration. The α is defined the moving average of the vector composite value of acceleration x, y, z given by the user with 20 data. It assume that the case where α exceeds the threshold value 0.05 is in operation. The operation is a state that waiting for determination of walking, rotation, crouching, and sitting. When gyro sensor Y axis exceeds 0.06 [radian/10msec], the state turns to the rotation. In addition, when the angle of the device is below a certain value during the operation. this means in a crouching or sitting state. When it is judged that the tilt angle of the device is stabilizes after the smartphone goes down has been measured, the case where the tilt angle S [deg] of the device is equal or more than -15 [deg] of the judgment value it is assumed to be sitting, the exception is crouching.

3.3 on tantization of thigh inclination angle

In this section, we describe methods to stabilize the angle of the thighs. The waist angle is calculated using the slope angle of the device obtained from the attached smartphone and the slope of the thigh. Since the mounting position is set in the breast pocket of the subject, it is impossible to detect the thigh inclination angle. Hence, it is necessary to make the constant thigh inclination angle when it is determined operation. Nevertheless since the way of walking and crouching is different depends on the person, it is impossible to determine obviously the inclination angle of the thigh. Therefore, prior to conducting the experiment, the thigh inclination angle in the walking, rotation, and crouching is confirmed beforehand and used as the input information.

4. Verification experiment

In this chapter, we describe the two methods. There are the experiments verification, the performance verification of the state determination and accuracy verification of the compression force of the lumbar intervertebral disc.

4.1 Performance experiment of state determination

In this section, we describe the experimental method of the performance verification of the state determination to estimate lumbar burden. The state determination is necessary for estimating lumbar burden is performed using the thigh inclination angle in each state measured on each subject. This experiment was conducted 3 times on 8 subjects. Subjects work in the order of standing, walking (6 steps), rotation (6 times), stumbling (1 time), sitting (1 time). The interval between each motion is 3 seconds. The motion at that time was recorded with a video camera, and the motion in the movie was taken as a true value. The analysis method compares the state determination (smartphone value) determined by the application installed in the smartphone with the true value, and calculates the identification rate when the determination is made. The calculation method of the identification rate is shown in Eq. (3).

$$\text{Identification rate (\%)} = \frac{\text{smartphone value(s)}}{\text{true value(s)}} \times 100 \quad (3)$$

4.2 Verification experiment of estimation accuracy of lumbar intervertebral pressure force

Experimental tools are one smartphone, a mowing machine (5.5kg), and an automatic mowing machine (80.0kg). Automatic mowing machine operates by the remote controller (0.5kg). The method is to wear a smartphone in the breast pocket of the subject and get them to do farm work freely. We record that motion with a video camera and confirm the moving state from this video data. In this experiment, the burden analysis software JACK 6.1 version (JACK) was use for comparison. JACK is the software that can create virtual human on the desktop manually, allocate work to that virtual human, and can analyze its dynamic burden. We create a digital human model with the agricultural attitude, the load of the subject in the movie taken during the experiment, and calculate the lumbar burden. The calculated value taken is a true value.

5. Result

In this chapter, we describe the result verification method. There are the experiments verification, the performance verification of the state determination and accuracy verification of the compression force of the lumbar intervertebral disc.

5.1 The result of experiment performance experiment of state determination

In this section, we describe the experimental results of the performance verification of state determination. Table 1 indicates the action (Action) actually performed by the subject, the motion estimation (Estimation) by the proposed method, and its identification rate.

Table1. Distinguish rate of state determination

		ACTION					
		standing	Walking	Rotation	Crouching	Sitting	
Estimation[%]	standing	100	14.9	0	2.8	29.5	
	Walking	0	61.2	0	0	0	
	Rotation	0	0	86.3	0	5.6	
	Crouching	0	0	0	85.3	4.5	
	Sitting	0	0	8.4	0	26.9	
	else	0	31.3	13.3	16.1	40.7	
Total							71.9

From the Table 1 we can see that the overall identification rate was 71.9 %. The identification rate of walking and sitting state judgment was bad, and the

identification rate of the rotation and crouching judgment was good.

5.2 The result of verification experiment of estimation accuracy of lumbar intervertebral pressing force

In this section, we describe the experimental result of the verification accuracy estimation of the lumbar intervertebral disc pressing force. The lumbar burden estimation result during using mowing machine indicated in the fig.4. The vertical axis represents the lumbar burden (N), and the horizontal axis represents time (min).

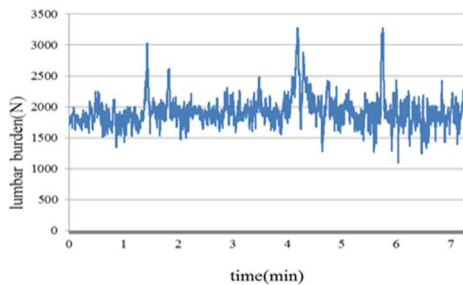


Fig.4 lumbar burden estimation graph

From the results in Fig.4, the maximum value was 3278 N, the minimum value was 749 N, and the average value was 1704 N. During using the automatic mowing machine, the maximum value was 2820 N, the minimum value was 484 N, and the average value was 882 N.

5.2.1 Comparison with JACK

In comparison with the JACK, JACK measurement used the Fig.5 as a digital human model.



Fig.5a automatic mowing machine



Fig.5b mowing machine

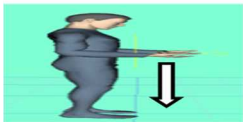


Fig.5c automatic mowing machine (JACK)



Fig.5d mowing machine (JACK)

Fig. 5a indicates that the image which using the remote controller and Fig. 5b shows that the image which using the mowing machine. In addition, a digital human model created with the model shown in Fig. 5a and Fig. 5b as a model, and shown in Figs. 5c and 5d. The arrow in the image represents the direction of the force. At the time of remote control operation, 0.5 kg force applied to the hand in the direction of gravity, and it is necessary to distribute the weight of 5.5 kg during mowing operation. Therefore, we are applying 4 kg to the shoulder and 1.5 kg to the arm. The momentary lumbar burden calculated under the above conditions, and the result showed in table 2.

Table.2 comparison the result of smartphone and JACK

	Smartphone(N)	JACK(N)	Error(N)
Remote controller	529	526	23
Mowing machine	1202	779	423

Although the error between smartphone measurement result and the JACK measurement result which using the remote controller was small, the error in the result of the mowing machine was large.

6. conclusion

In this paper, we have estimated the lumbar burden in agricultural work using one smartphone. Based on the result, the error between the smartphone value and Jack value using remote controller was small, and using Mowing machine was large. The reason for this result is measuring lumbar intervertebral pressing force when the subject lifts an object in the direction of gravity as the proposed method. However, in the experiment of this time, it considered that the method of calculating the lumbar burden is different in the action of pulling the object and the operation using the mowing machine.

7. Reference

[1] Hamano Masafumi, Arai Ismail "Proposal of Authentication Method for Smartphone Using Accelerometer and Gyro Sensor" *Research Report Ubiquitous Computing System (UBI)* ,17 ,March 2014

A Study on High Accuracy Stride Estimation on Smartphone Combining Acceleration Sensor and Gyro Sensor

Shunta Nonaka †, Hiroki Tamura ‡, Koichi Tanno

Faculty of Engineering, University of Miyazaki,

1-1, Gakuen-kibanadai-nishi, Miyazaki-shi, Japan

E-mail: hi14028@student.miyazaki-u.ac.jp †, htamura@cc.miyazaki-u.ac.jp ‡

Abstract

The stride is an important parameter in human motion analysis and has been extensively studied by many researchers. This paper focuses on smartphones that are popular in the world, regardless of the measurement environment. In previous research, the stride estimation using the acceleration sensor or the gyro sensor mounted on the smartphone had been studied. However, the stride estimation accuracy has an error rate of about over 10 %. In this paper, we propose a highly accurate stride estimation method using stride correction parameter obtained from cross section movement in addition to conventional sagittal surface stride using acceleration sensor and gyro sensor mounted on a smartphone. Based on the testing results, the error rate of our proposed method with the stride estimated by the Kinect sensor (RGB-D sensor) as the true value was about 6%. It makes possible to estimate the stride with high accuracy.

Keywords: Locomotive Syndrome, Acceleration sensor, Gyro Sensor, Stride Estimation Method, Smartphone

1. Introduction

The Japanese Orthopedic Association proposed the concept of Locomotive Syndrome (Locomo) in 2007 [1]. Locomo is a state that the movement function is deteriorating due to the failure of the exerciser. Therefore, the author's group has been developing a system to estimate locomo from walking motion using the kinect sensor as a safer and less burdensome locomotive method for locomotion [2]. However, there are about 47 million people currently including the reserve army of the locomo population in Japan. The simple locomo evaluation system is necessary to evaluate the number of people's motor functions that is about half of the Japanese population.

In this paper, we examine the evaluation of walking motor function using the smartphone. The smartphone is one of the daily sensors. A wearable device such as a smartphone using an acceleration sensor and/or gyro sensor has weak accuracy in a specific environment compared with a motion capture system using the kinect sensor. Therefore, in this paper, we propose the highly accurate stride estimation method to apply the locomo

estimation. We aim to build a system using smartphones that have accuracy like kinect sensors.

2. Previous Research 1

In the previous research, a gyro sensor of a smartphone is mounted on the thigh. The hip joint angle calculated from the integrated value of the angular velocity. The angular velocity calculated by using the X-axis of the gyro sensor. Assuming that the angular velocity of X-axis is " g_x " and the time when the hip joint angle becomes maximally is " θ_{max} ", the hip joint angle used for stride estimation is expressed by Eq. (1). The integration interval was determined by the slope of the device calculated by the arc tangent of the gravitational acceleration of the Y-axis and the Z-axis. When issuing in front of the right foot, the inclination of the device is from time to maximize " t_0 " (right foot rearmost) to the minimum to become time " t_1 " (landing in front right most). Further, if the length of the foot is " L_{leg} " and the stride is " L ", the calculation formula of the stride is expressed as Eq. (2).

© The 2018 International Conference on Artificial Life and Robotics (ICAROB 2018), Feb. 1-4, B-Con Plaza, Beppu, Oita, Japan

$$\theta_{max} = \int_{t_0}^{t_1} g_x(t) dt \quad (1)$$

$$L = L_{leg} |\theta_{max}| \quad (2)$$

3. Proposal method

The method we propose aims to estimate steps with high precision. Therefore, the calculation of the conventional sagittal plane method is added by the method for the stride correction parameters obtained from the cross section movement. To improve the length of the step obtained from the sagittal plane, pelvic rotation motion is measured with a gyro sensor to the hip joint. It is because the smartphone is fixed to the thigh. In Fig.1, L_1 and L_3 , we can see that the stride lengths obtained by the acceleration sensor, and L_2 is a correction amount that takes into consideration the rotation of the lumbar region obtained by the gyro sensor. First, the formula for obtaining the stride length using L_1 and L_3 is shown in Eq. (3). When the difference between the direction of gravity and the angle of the thigh inclination is θ_1 and θ_2 , then L_1 and L_3 are given by Eq. (3).

$$L_1 + L_3 = L_{leg} (\sin \theta_1 + \sin \theta_2) \quad (3)$$

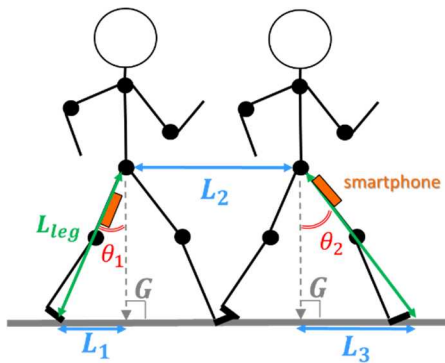


Fig.1. One stride image.

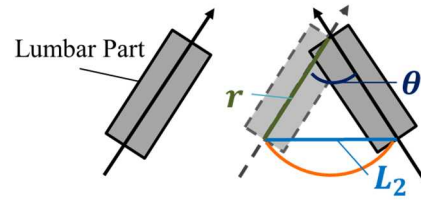


Fig.2. Correction amount by rotation of waist.

Then, L_2 is obtained using Eq. (4). The r is representing the width of the waist.

$$L_2 = 2r \sin\left(\frac{\theta}{2}\right) \quad (4)$$

$$\theta = \left| \int_{t_0}^{t_1} g_y(t) dt \right| \quad (5)$$

In Fig.2, “ θ ” is representing an angle due to the rotation in the transverse plane, and it can be calculated using Eq. (5). The rotation of the cross section is expressed by a value “ g_y ” of Y-axis gyro sensor. The integration interval can be determined by the values that form the Y-axis and Z-axis of the acceleration sensor. It is from the moment t_0 at which the foot is pulling the most backward until the moment t_1 when the foot is stepped forward and landed, or from the moment of landing to the moment when the foot reaches the back. After calculating the rotation angle, the distance calculated from the rotation of the lumbar region can be calculated by using the expression for obtaining the string of the circle. Therefore, if the desired stride is L , the stride is estimated by Eq. (6). We call the proposed method 1 about the stride length of Eq. (6).

$$L = L_1 + L_3 + L_2 \quad (6)$$

4. How to judge walking

To build a system that calculates the stride from walking motion, it is necessary to estimate the state that a person is walking. Therefore, in this section, we describe the walking judgment method of a person. To determine the walking state, the trend of the smartphone is calculated from the value of the accelerated sensor

used. In this research, we installed the smartphone to the thigh as in Fig.3.

The tilt of the device can be used directly to track the movement of the thighs. It is possible to capture the periodic movements of the thigh that is walking. The smartphone iPhone 4S (iOS 7.0) used for this research has a function capable of detecting gravitational acceleration. The inclination angle (rad) of the device can be calculated from the detectable gravitational acceleration on the Y axis and the Z axis by Eq. (7).



Fig.3. Position to install smartphone.

$$\theta_1, \theta_2 = \arctan\left(\frac{\text{gravity } Z}{\text{gravity } Y}\right) \quad (7)$$

The example waveform when a person walking can be seen in Fig. 4.

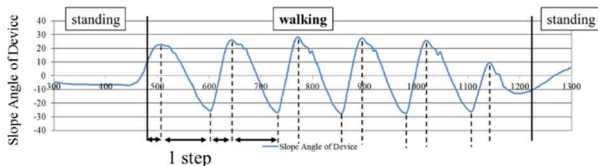


Fig. 4. Device tilt during walking.

The periodic waveform indicates walking is occurring, but it may not be determined that the subject is walking. It is because there are individual differences such as forward inclination and backward inclination in the posture. When the inclination angle of the device is within ± 10 (degree), it is judged that the subject is standing. Fig.4 "walking" showed that a positive value represents a state when the foot is stepping forward and a negative value represents a state when the foot is pulled backward. Therefore, in this paper, from the positive peak to the positive peak or from the negative

peak to the negative peak is taken as the stride length (1 step).

5. Method of judging landing

The Y-axis value and the Z-axis acceleration sensor are used to determine the landing (hereinafter "acceleration YZ"). The YZ acceleration value is not the acceleration of gravity used in the determination of the subject acceleration produced by the subject. As shown in Fig.3, when the smartphone is installed on the thighs, the magnitude of the acceleration YZ represents the acceleration in the sagittal plane. Fig. 5 shows that the slope of the smartphone and YZ acceleration during walking.

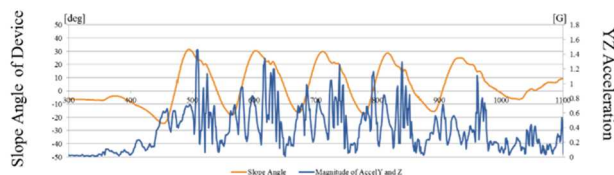


Fig.5. Changes in the magnitude of YZ acceleration

Fig. 5 shows that it is quite difficult to find features when landing. However, by disassembling into each quadrant as shown in Fig.6, the feature amount at landing can be measured. Fig. 7 shows that the waveform of YZ acceleration when Fig.5 is divided into four quadrants.

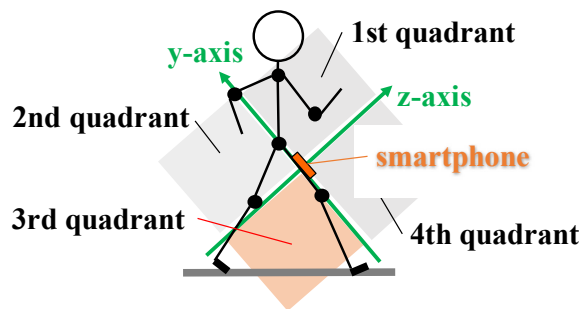


Fig.6. Device axis and quadrant as seen from sagittal plane

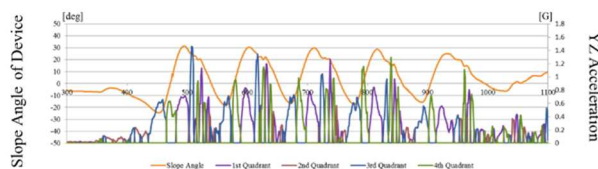


Fig.7. Quadrant decomposition of the magnitude of YZ acceleration

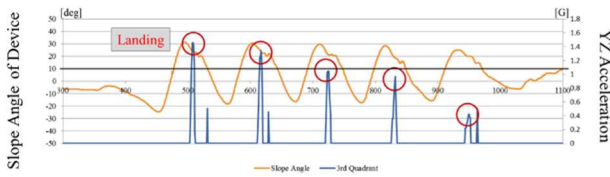


Fig.8. YZ acceleration in the third quadrant only

In order to see what type of YZ acceleration is occurring in what kind of motion, it can compare the tilt of the device tracking the movement of the foot with the YZ acceleration in Fig.7. First, when the inclination of the device is near from the peak of the downward convex, it means YZ acceleration enters the third quadrant. When the tilt of the device is negative, the foot is in the state of being pulled to the back most, and that state can be said to capture the acceleration of the kicking leg. Next, the YZ acceleration takes the fourth quadrant. It means that the fourth quadrant is oriented mainly in the direction of walking, which shows that it captures the movement in the process of stepping forward. Next, take the first quadrant. It can be seen in Fig.7 that the first quadrant means upward when steps are taken. It means that the force in the direction of walking weakened. Then, after the first quadrant, move the foot in the third quadrant direction representing the lower part of the thigh. This means the moment of landing. After the third quadrant, which means landing, the waveform is slightly disturbed, but the device vibrates after landing.

Therefore, the landing assessment is performed using the first peak of the third quadrant that occurs temporarily because the slope of the device is 10 (degree) or more (shown in Fig. 8). The value of 10 (degree) is to prevent peak misrecognition.

6. Experimental Results

In this section, we show the result of stride estimation. We experimented with simultaneous measurements between kinect and smartphone sensors. The number of subjects is 54 (Men: 12, Women: 42) at the age of 20 to 60. The proposed method 2 is a hybrid with the previous research 1 and proposed method 1. This is based on the results calculated from preliminary experiments, when the waist rotation amount exceeds 12 cm, the stride had a tendency to decrease error.

Fig. 9 can be seen that the proposed method 1 is better than in previous studies 1 and 2. From this fact, it is assumed that the method of combining the sagittal and transverse fields more accurately captures motion rather

than a method that only focuses on the sagittal plane.

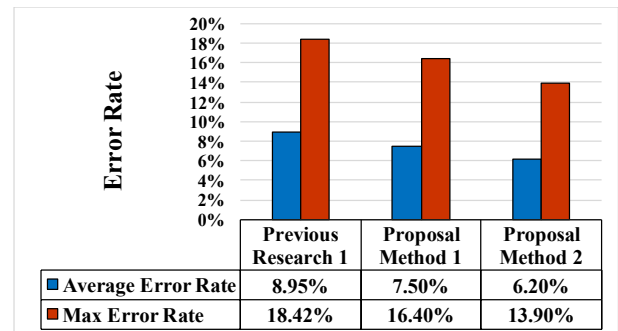


Fig. 9. Estimation accuracy of each strides estimation method.

7. Conclusions

In this paper, the movement of the sagittal during walking motion that focuses on the movement of the cross-section, a method for estimating the step with high accuracy studied.

The results of proposed method 1 have the improvement rate of about 1.5% as an average error rate and the improvement rate of about 2.0% as a maximum error rate from previous research 1. The stride estimation method of proposed method 1 is more significant than the previous research.

Furthermore, the results of proposed method 2 have the improvement rate of about 2.8% as an average error rate and the improvement rate of about 4.5% as a maximum error rate from previous research 1.

By classifying walking based on the amount of rotation of the lumbar region, it was possible to estimate according to individual differences, and improvement of versatility was confirmed. From these results, the error rate of our proposed method 2 with the stride estimated by Kinect sensor (RGB-D sensor) as the true value was about 6.2%, making it possible to estimate the stride with high accuracy.

8. References

- [1] New concept "Locomo (exerciser syndrome)" The Japanese Orthopedic Association <https://www.joa.or.jp/jp/public/locomo/> (accessed 2017-12-7)
- [2] Kouta Momose, etc., "Basic study on evaluation method for patient with locomotive syndrome using a RGB-D sensor", *IEICE Technical Rep.*, vol.113, no. 486, NLP2013-182, pp. 103-106, March, 2014, (Japanese)

Development of Multi-Sensory Smart Objects Tracking Module for Mobile Robot Platforms

B.A.D.J.C.K. Basnayake, Y.W.R. Amarasinghe

*Department of Mechanical Engineering, University of Moratuwa,
Katubedda, 10400, Sri Lanka*

E-mail: janakabasnayake@gmail.com, ranamajp@gmail.com

www.mrt.ac.lk

Abstract

This paper presents a development of a Multi-Sensory Smart Objects Tracking Module (MSSOTM) using a MEMS-based IR thermal array sensor combined with ultrasonic and laser-based distance measuring system. The system consists of two-axis motorized rotatable sensor platform and controlled by a DSP based centralized controller. Further, MSSOTM is capable of identifying, localizing and sorting of stationary and moving objects as well. The implemented system was tested and validated using Robotino® mobile robot platform.

Keywords: IR thermal imaging, obstacle detection and segmentation, laser range finder, mobile robots

1. Introduction

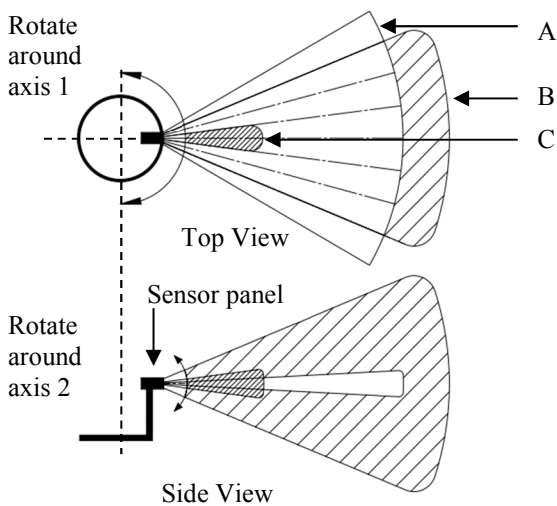
In mobile robot systems, the ability to navigate in its environment is important. Often, the surrounding environment is dynamic and unknown, so obstacle detection and mapping are essential for mobile robot platforms which are operating in a dynamic environment. Ultrasonic, laser and IR technologies based non-contact obstacle identification system and distance measurement systems were used for robotics navigation systems. Dirk Bank introduced a novel ultrasonic sensing system for autonomous mobile systems using a wide-angled ultrasonic transducers array¹. His proposed system was capable to obtain substantial information about the objects in the environment. Hyunwoong Park et al. has presented a novel rotating IR range sensor system for a mobile robot platforms². Radially mounted rotatable IR range sensors used to detect objects and map the environment. Some other researchers have proposed Laser Detection and Ranging (LADAR) sensors for tracking obstacles^{3,4,5}. Different types of LADARs which have been used for develop obstacle detectors are comparatively precise than the ultrasonic sensors. But they are not capable of tracking live objects.

According to the literature, most of the researchers focusing on develop obstacle identifications and environment mapping systems for mobile robot navigations⁶. Objects separation such as live objects (humans, animals etc.) and positioning are difficult compared with stationary obstacles identification, because of their behaviors. But it is important for robotic platforms which operate in living premises in order to perform collision-free navigation and localization features. This research presents the development of MSSOTM which capable of detecting, localizing and separating of movable and stationary living object in a certain range. At the present stage, the system has developed to identify the live objects and control a mobile robotic platform to follow the target. Developed system will use in navigation, human following and obstacles avoiding applications in mobile robot systems.

2. Proposed System and Working Principle of MSSOTM

The proposed system mainly consists of none contact Micro-Electro-Mechanical-Systems (MEMS) - based IR thermal array sensor and range finding sensors which are

mounted on a two axis rotatable platform as shown in Fig. 1. Non-contact thermal array sensor used to identify the heated objects (live objects) and their directions by analyzing the thermal profile of the surfaces in within the sensor Field of View (FoV). This will generate important information about the presence of live objects to the mobile robot. Distances to the objects are another parameter essential to the mobile robot to maintain collision free proper navigation in the action. Therefore range finding sensors are included in the system which is based on ultrasonic long distance ranging sensor and short distance laser-ranging sensor mounted on the same platform. Independently controllable two axes rotatable platform provides facility to orient sensors to required directions and it is facilitated to expand sensing coverage of the system. Combining these two sensory systems, the system can provide accurate directional and distance information about the presence of the objects and obstacles as well. The designed system has a Digital Signal Processor (DSP) as the central controller and a wireless communication link to communicate with a computer. And also it has an analog and digital input-output module which can be used for interface with a mobile robot platform as shown in Fig. 2.



A – Detection range of IR thermal sensor
 B – Detection range of ultrasonic ranging sensor
 C – Detection range of Laser ranging sensor

Fig. 1. Layout of installation arrangement and detection ranges of sensors.

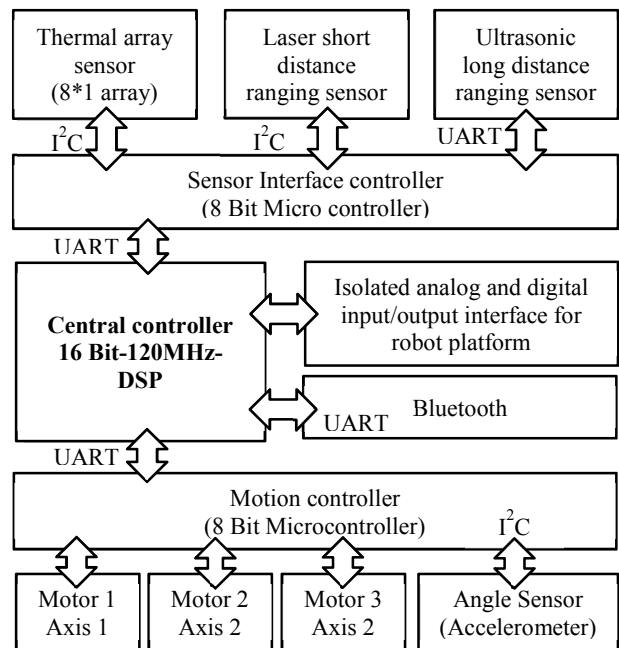


Fig. 2. Block diagram of developed MSSOTM

2.1. Development of IR thermal image based live objects identification system

Since infrared radiation is emitted by all objects with a temperature above absolute zero according to the black body radiation law, thermal imaging makes it possible to see detect heat objects with or without visible illumination. When viewed through a thermal detector, warm objects stand out well against cooler backgrounds.

2.1.1. MEMS IR thermal sensor

MEMS IR thermal array sensors are precise tiny non-contact sensors which can be used to measure the surface temperatures of the objects in different application areas. This system is based on eight by one pixel array sensor (Omron D6T) which is having four frames per second data acquisition speed and 62.8°, six degree FoV along the X and Y directions respectively. Measurement range of the selected sensor is five to 50 °C and its detecting range is up to six meters. The sensor has provided eight temperature values related to the array positions and one for the sensor body temperature through an I2C serial bus.

2.1.2. Live object detecting algorithm

The function of the detecting algorithm compares the surface temperatures captured by the thermal sensor with a reference temperature⁷. The reference temperature is a dynamic value which is related to the ambient temperature at any location. The thermal sensor has

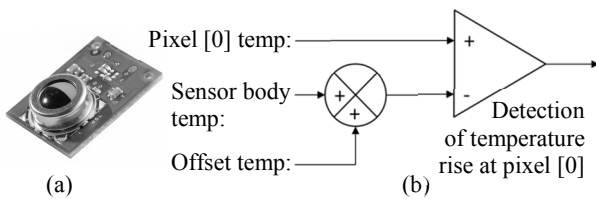


Fig. 3. (a) Omron D6T IR Thermal array sensor (b) Block diagram of heat object detecting algorithm

features to measure the inside temperature of the sensor body. The system is taking this sensor body temperature as ambient temperature and modifies it by adding some offset value to generate reference temperature to the comparators. If the surface temperature at any pixel element is greater than the reference temperature value, then it is identified as a live object presence in a specific direction as shown in Fig. 3. While scanning the environment for objects, after detecting the temperature rise occurred in the environment by any of sensor pixel, sensor platform will rotate around the axis 1 and take the detected direction to the middle of thermal sensor FoV. At this time distance measuring sensors are also in the same direction with the thermal sensor around the axis 1. While measuring surface temperature by thermal sensor rotating around axis 2, distance measurement sensors also take the distance to the heated object by rotating in the same axis. This is done by two axes rotatable platform with independently rotatable two platforms around the axis 2. After measuring distance profile and thermal profile in the same direction as shown in Fig. 4. This information is fed to the sorting algorithm running on the DSP in order to clarify the detected heated object as a human, animal or other object presence on the premises.

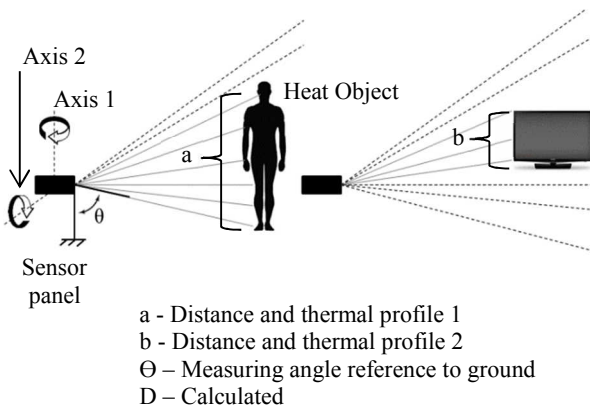


Fig. 4. Operation of measuring system and measuring parameters

2.2. Ultrasonic and laser combined distance measurement system

The distance measurement system is developed using two types of range sensors for long distance and short distance measurement. Long distance range sensor is based on the integrated ultrasonic probe (URM07) which is having inbuilt temperature compensation. The sensor is working up to 100 mm to 5000 mm of range with 60° of detecting angle. It has one centimeter of resolution and one percent of accuracy. The sensor can be read through a digital serial interface. VL53L0X is precise Time-of-Flight (ToF) based laser-ranging sensor which is having two-meter detecting range and one millimeter of resolution with a narrow detecting angle compared to the ultrasonic range sensor. The importance of using LADAR is, it is provision to take precise measurements on near objects and identify the motions as well.

2.3. Two-axis rotatable sensor platform with self-tilt compensation

Two-axis rotatable platform is developed to position sensors to required angles and directions. Both axes are driven by stepper motors with optical reference limit switches. For the 2nd axis, two individual motors are used to rotate two individual platforms. One is used for the IR thermal sensor and the other one is for distance measuring sensors. While it's operating, the central controller can change the angles of the individual platforms mounted on 2nd axis reference to the ground, which is done by using accelerometer-based feedback control system developed on the motion controller.

3. Testing and Validation of MSSOTM

The developed MSSOTM as shown in Fig. 5. was tested and validated using Robotino® robot platform.

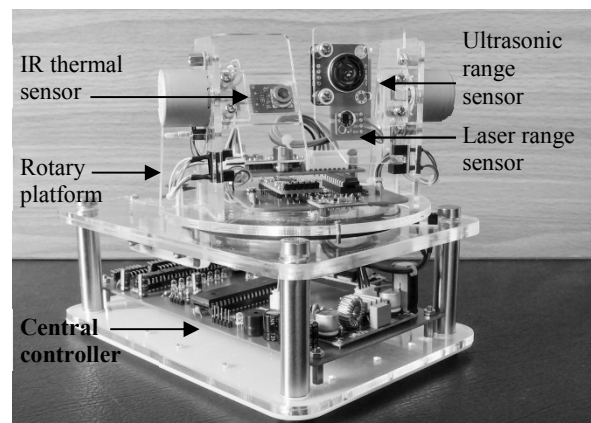


Fig. 5. Developed prototype of MSSOTM

Robotino® is a flexible mobile robot platform for research and education manufactured by Festo. Robotino® has inbuilt radially arrange IR ranging sensor array which can be used for obstacle identification and it has a tactile bumper sensor attached to the bottom edge of the chassis which can be used for the safety. And also it has the facility to connect external devices through the inbuilt input/output (I/O) interface.

3.1. Testing on developed experimental setup using Robotino®

In this experiment, developed MSSOTM was programmed to human following application and control commands are taken from the device interface. The prototype was mounted on the Robotino® and connects the I/O lines as shown in Fig. 6. Robotino has programmed using Robotino® View to read the defined I/Os and perform the given actions. The deferent objects with various shapes and dimensions such as chairs, walls, and computers as the stationary objects and a person as a live object were scanned by MSSOTM. According to objects locations, MSSOTM was generated moving commands to the Robotino® for follow the person avoiding the other objects as considering the obstacles as shown in Fig.7.

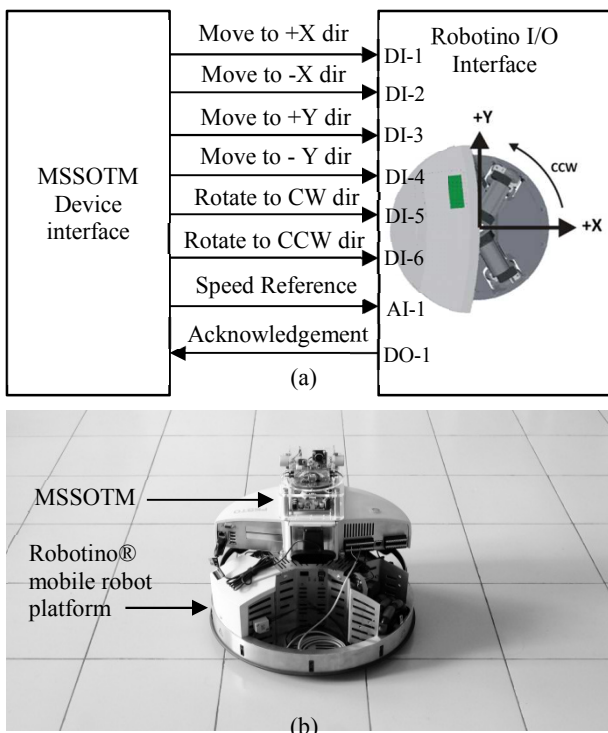


Fig. 6.(a) Layout of the prototype interface with Robotino® (b) Experiment setup

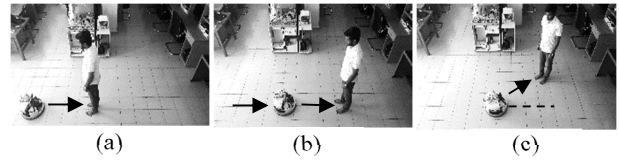


Fig. 7. (a) Identify a person from the front direction of robot platform. (b) Identify the motion of the person and move the robot along the +X direction to follow the person (c) Identify a person from a different angle and change the moving direction of the robot.

4. Conclusion

In this research, a multi-sensory smart obstacles identification system was proposed as an external sensor module for mobile robot platforms. The prototype of the proposed design was developed and tested with Robotino® mobile robot platform. Future work of this research includes improvement on control and identification algorithms for working in the real environment with enhanced performance.

References

1. D. Bank, A novel ultrasonic sensing system for autonomous mobile systems, *IEEE Sensors Journal* 2 (6) (2002) 597-606.
2. H. Park, S. Baek, S. Lee, IR sensor array for a mobile robot, in: *Proceedings, 2005 IEEE/ASME International Conference on Advanced Intelligent Mechatronics*, 2005, pp. 928
3. M. Kise, Q. Zhang, N. Noguchi, AN OBSTACLE IDENTIFICATION ALGORITHM FOR A LASER RANGE FINDER BASED OBSTACLE DETECTOR, *Transactions of the ASAE* 48 (3) (2005) 1269-1278.
4. H. Kim, M. Miwa, J. Shim, An obstacle avoidance system of an unmanned aerial vehicle using a laser range finder, *Journal of the Korean Society of Marine Engineering* 37 (7) (2013) 737-742.
5. T. T. Hoang, D. T. Hiep, P. M. Duong, N. T. T. Van, B. G. Duong, T. Q. Vinh, Proposal of algorithms for navigation and obstacles avoidance of autonomous mobile robot, in: *2013 IEEE 8th Conference on Industrial Electronics and Applications (ICIEA)*, 2013, pp. 1308-1313.
6. T.-J. Lee, D.-H. Yi, D.-I. Cho, A Monocular Vision Sensor-Based Obstacle Detection Algorithm for Autonomous Robots, *Sensors* 16 (3) (2016) 311
7. Basnayake, B. A. D. J. C. K., Amarasinghe, Y. W. R., Attalage, R. A., & Jayasekara, A. G. B. P. Occupancy identification based energy efficient Illuminance controller with improved visual comfort in buildings. In *Engineering Research Conference (MERCon)*, 2017 Moratuwa (pp. 304-309). IEEE.

Design and Development of a Conductive Polymer Based 3D - Printed Tactile Sensor with Square Type Spring Structure

W.H.P. Sampath, A.H.T.E. De Silva, T.A.U. Roshan, Y.W.R. Amarasinghe

Department of Mechanical Engineering, University of Moratuwa.

Katubedda, 10400, Sri Lanka

E-mail: peshan@ieee.org, ahteranga@gmail.com, tauroshan@gmail.com, ranamajp@gmail.com

www.mrt.ac.lk

Abstract

In this research, a novel tactile sensor (with 50mm×50mm×56mm dimensions) has been developed using a silicone rubber based conductive polymer sensing element array incorporated to a novel 3D printed square type spring structure. Initial characterisation has been completed for the sensor. The structure stated in this paper has been designed for force scaling purpose and it's numerically analysed prior to the fabrication to avoid any mechanical failures and ABS Plus and Polylactic acid were used in the 3D printing fabrication.

Keywords: Square type spring structures, Conductive Polymers, 3D Printing,

1. Introduction

Tactile sensors are being used to capture physical world data through tactile parameters with the assistance of different sensing principles. The advancement in the fields of robotics and automation requires further attention in the development of tactile sensors. Human skin plays a vital point as a tactile sensor¹ as it allows to sense number of tactile parameters simultaneously while conductive polymer based piezoresistive tactile sensors allows the researchers to gain the flexible quality which is prevailed in human skin. However, prevailing tactile sensors are yet to identify more than two parameters simultaneously.

In this research, design, development and testing of a novel tactile sensor with the dimensions of 50mm×50mm×56mm based on a 2×2 conductive polymer based sensing element array incorporated to a square type spring structure. 3D printing technology is utilized to fabricate this spring structure. Sensing element described under this research is highly customizable in

the performance and the base material is a Silicone Rubber which has enhancements by silica and carbon black, with Silane as the coupling agent³.

The spring structure stated in this paper has been designed for force scaling purpose and numerically analyzed using COMSOL Multiphysics prior to the fabrication. Circuitry for embedded electrodes was also developed in this research with a wireless communication between the sensor assembly and the developed user interface which allows to use the sensor as a plug and play device

2. Proposed design and working principle

When considering force sensors, it's essential to define a working range and controlling the working range can be done by overseeing the deflection applied to the sensing element³. With the introduction of an external square

type spring structure (described under Fig. 1) to sensing elements, working range can be easily altered.

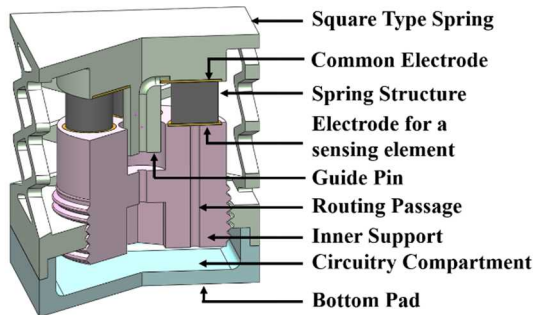


Fig. 2. Quarter sectional view of the proposed design

The spring structure is designed to facilitate a 2x2 array of sensing elements and designed for three separate parts. Furthermore, the proposed sensing structure considered following design features.

- 3 Degrees of Freedom due to the inclusion of 2x2 sensor array.
- The initial compression for sensing elements to initiate conductive paths, screw thread type mechanical fastening between the spring and inner support is used.
- An overload protection to the sensor structure is given by the horizontal and vertical clearance between guide pin and the inner support.
- Structure facilitates electrodes, routing for wires and a compartment for internal circuitry.

3. Design and Simulation of square type spring structure

3.1. Development of square type spring structure

A two-layered saw tooth shape (Fig. 2(a)) is featured in a single square type spring and a fillet radius of R (shown in Fig. 3(b)) is introduced to enhance the mechanical strength of the structure.

3.2. Structural analysis and design constraints of square type spring structure

A Finite Element Analysis (FEA) was performed using COMSOL Multiphysics for the simplified structure shown in Fig. 3(a) by compressing the combination of spring structure and sensing elements (simulated as a virtual spring), along the centre axis by 2 mm prescribed displacement. Maximal deformation of the sensing

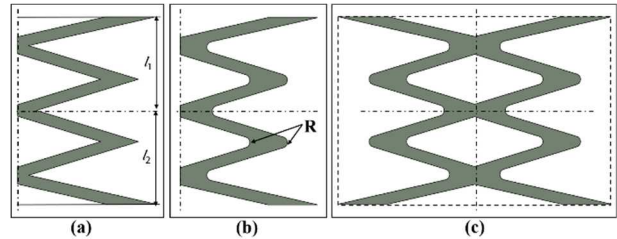


Fig. 1. Square type spring structure (a) A two-layered saw tooth shape is used (b) Fillet is to enhance the mechanical strength (c) Single spring

element during the load testing is obtained as 2mm for the expansion of its range. ABS Plus which has maximum tensile strength of 3.6×10^7 N/m² is used with the 3D printing fabrication and it's analysed as a maximum von-Misses stress of 2.79×10^7 N/m² (Fig. 3(b)) in the simplified assembly.

Considering a series and parallel spring system (shown

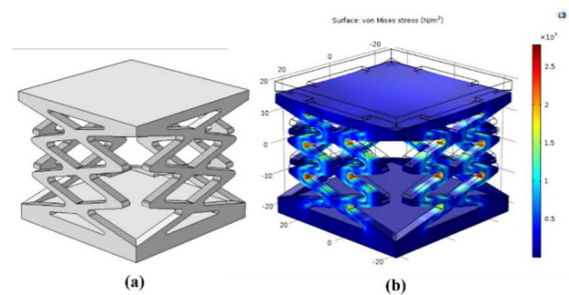


Fig. 3. Structural Analysis (a) Simplified model of the spring structure (b) Structural analysis carried out using COMSOL Multiphysics.

in Fig. 4), an analytical model for total stiffness - K (Equation 1) also derived for the stiffness of the sensor and the stiffness of the pill and structure under a force component was calculated as 20270 N/m and 16258 N/m

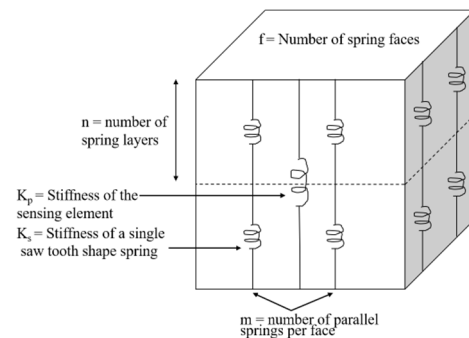


Fig. 4. Simplified to a series and parallel spring system respectively. The clearance between the guide pin and inner support also derived using Fig. 5. for a tilt angle of

θ for a force applied on the top surface which reached the maximum allowable deflection of the guided pin.

$$K = \left(\frac{K_s}{n} \times m \right) \times f + K_p \quad (1)$$

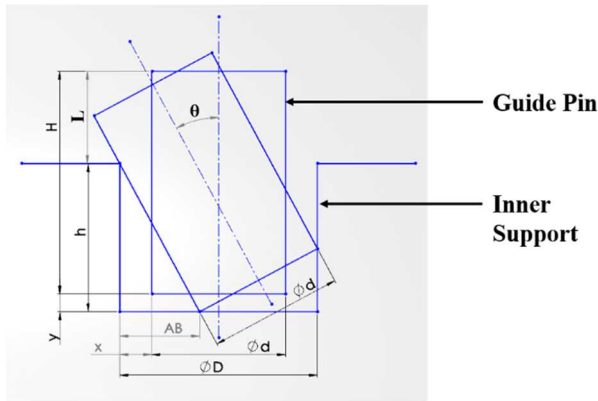


Fig. 5. Clearance decided as a overload protection to the structure

Consider distance AB,

$$h = (D - d \cos \theta) / \tan \theta \quad (2)$$

Vertical clearance y is given,

$$y = L - H + (D - d \cos \theta) / \tan \theta \quad (3)$$

Horizontal clearance x is given,

$$x = (D - d) / 2 \quad (4)$$

4. Fabrication of the Tactile sensor

Fabrication of the tactile sensor was carried out under two stages. First, the fabrication of sensing element and then the sensing structure.

4.1. Fabrication of conductive polymer based sensing elements

Conductive polymer based sensing element used under this research is mainly based on Room Temperature Vulcanization (RTV) Silicone Rubber. For the enrichment of the performance of the polymer, inclusion of Nano-materials such as Super conductive carbon black - KETJENBLACK EC-600JD and Nano Silica (SiO₂) is carried out and Si-69 Silane Coupling agent added to the mixer as a bonding element.

A mechanical moulding method is used to develop the sensing element while the mould described under Fig. 6(a) is designed into three layers to ease the removal process of sensing element from the mould.

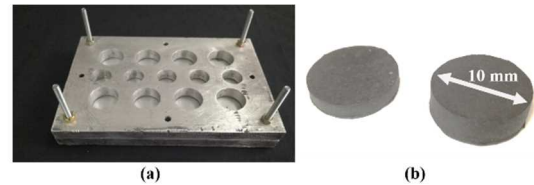


Fig. 6. Sensing element fabrication (a) Three-layer mould used for the fabrication (b) Fabricated sensing pills

The mould is capable of developing sensing elements with different geometries and with different thickness ranges (Fig. 6(b)) in one batch of production. A key feature of this production process is sensing elements can be developed according to the required geometry and size with different performance levels.

4.2. Fabrication of sensing structure

Three parts shown under Fig. 6 is fabricated using 3D printing technology as it eases the fabrication process of complex geometries. Square type spring structure (Fig.

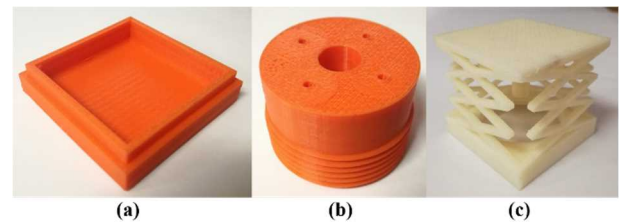


Fig. 7. 3D Printed sensor parts (a) Bottom pad (b) Inner support (c) Square type spring structure

7(c)) is made from ABS Plus with 100% infill ratio while PLA with 75% infill ratio is used for remaining two parts.

5. Assembling, Packaging and Testing

5.1. Assembling and packaging

Fabricated sensing structure and sensing elements have been packaged as shown in Fig. 8 using embedded full electrodes configuration with a common electrode at the top, to the structure.

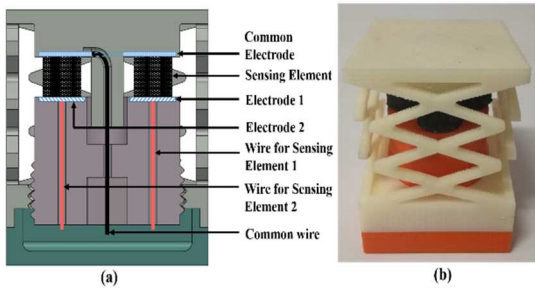


Fig. 8. Packaged sensor (a) Electrode configuration of the sensor (b) Packaged sensor

5.2. Testing and characterisation

Sensing elements are tested for its characterisation using a static load test. The basic characteristics such as conductivity, force range, hysteresis and non-linearity were found out with an apparatus shown in Fig. 8 and Fig. 9 shows the hysteresis curve for a sensing element.

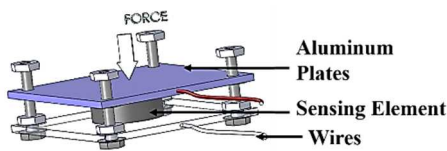


Fig. 8. Testing apparatus

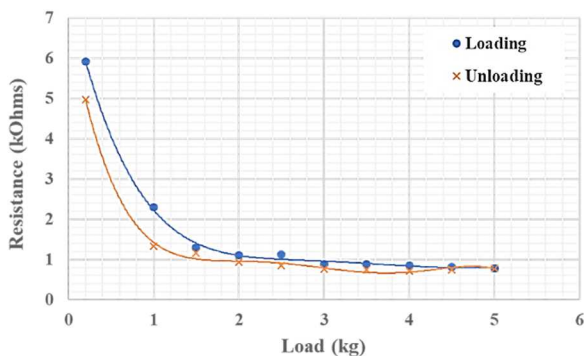


Fig. 9. Resistance change in a sensing elements vs applied load plot

5.3. Characterisation of Sensor

Assembled sensor is checked with static load test. Output obtained from a single sensing element under an axial loading condition is shown under Fig. 10.

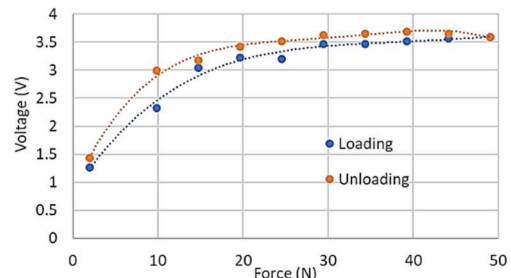


Fig. 10. Output of a sensing element vs axially applied force before the signal conditioning

5.4. Signal Conditioning, Data Acquisition and Communication

Signal conditioning is carried out to convert the non-linear sensor output data to a linear combination with use of ATmega328 development board based signal conditioning circuitry (Fig. 11). Bluetooth uses to communicate with the GUI available at the users' device.

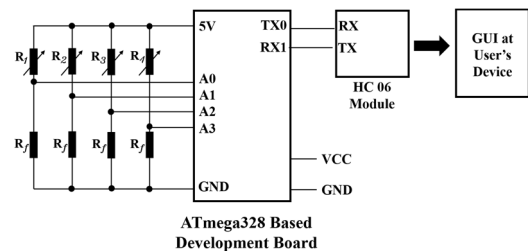


Fig. 11. Data acquisition, signal conditioning and communication

6. Conclusion

This square type spring structure minimized deflection of the sensing element while it allows the expansion to the operation range. This sensor designed to overcome the inherent issues in conductive polymer based sensing elements using an internal signal conditioning circuitry.

References

1. T. D. I. Udayanga et al, "Development of a quantum tunnelling composite based 1-dof tactile sensor, *International Journal of Advanced Information Science and Technology (IJAIST)*.
2. M. Tiwana et al, "A review of tactile sensing technologies with applications in biomedical engineering", *Sensors and Actuators A: Physical*, vol. 179, pp. 17-31, 2012.
3. A H.T.E. De Silva et al, Design and development of a novel 3d printed 1-dof tactile sensors with conductive polymer based sensing element, in: *SENSORS, 2016 IEEE*

Design and Development of a Shape Memory Alloy Spring Actuated Gripper for Minimally Invasive Surgeries

T.A.U. Roshan, Y.W.R. Amarasinghe

*Department of Mechanical Engineering, University of Moratuwa.
Katubedda, 10400, Sri Lanka*

N.W.N. Dayananda

*Department of Electronic and Telecommunication Engineering, University of Moratuwa.
Katubedda, 10400, Sri Lanka*

*E-mail: tauroshan@gmail.com, ranamajp@gmail.com, nuwan@uom.lk
www.mrt.ac.lk*

Abstract

A Shape Memory Alloy based Spring Actuated Gripper (SMASAG) has been designed and developed for Minimally Invasive Surgeries. Further, the research is consist of design and development of an SMA spring and actuator force characterization by a developed testing apparatus. The gripping motion is achieved by a compact mechanism.

Keywords: shape memory alloy, minimally invasive surgeries, gripper, 3D printing.

1. Introduction

Minimally Invasive Surgery (MIS) is an emerging and highly favorable surgery procedure for similar open surgeries. It has been developing since the late 80s and widely accepted due to several advantages over conventional surgeries.¹ The equipment used to perform these MIS are ranging from simple tools to high-end remote-controlled devices with the observation of the surgical field through a scope.² The surgical manipulations are performed in a confined space and the miniaturization of actuators in such tools is a requirement. There are several types of actuators which give advantages as well as disadvantages over miniaturization.³ From those, Shape Memory Alloy (SMA) can be taken as a possible actuation material.⁴ The best known SMA for biomedical applications is called NiTiNOL. These NiTiNOL alloys possess several advantages.⁵ which are most important in actuator designs for MIS tools. Over the years several research groups have developed gripper

prototypes which are driven by SMA actuators⁶ with different techniques. According to the literature in most cases, activation method was direct heating (Joule heating) of SMA material. In this research, the SMA material was activated by a fluid flow which was under controlled temperature and flow rate corresponding to the activation requirements. Also designed a compact mechanism for transferring the force generated by the actuator to the gripping jaws with analyzing the Kinematics. Because it is very much important in these type of tools in order to enhance the performance. Further 3D printing was used to develop the prototype for validation.

2. Design of SMASAG and Working Principle

2.1. Working principle of SMASAG

The proposed gripper composed of several components and the functionality and the importance of each and every component is described as follow,

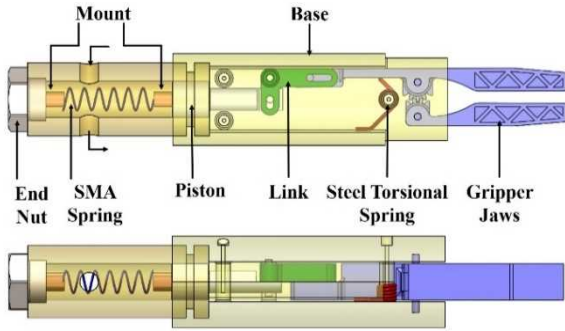


Fig. 1. Proposed gripper assembly

The gripper is actuated by a Linear actuator structure and that is designed as a Piston/Cylinder assembly. It has an End Nut which facilitates easy disassembly. Both End Nut and the Piston have Mounts where the SMA spring is attached inside the cylinder. There are openings in the Cylinder body to pass water for heat and cool SMA Spring actuator. The stroke length of the actuator was limited to five millimeters.

The linear motion of the piston is converted to an angular motion by a Link which is hinged to the Base structure and consists of two slots that limit the motion of two Pins connected to the Piston and the Driver Jaw. The slots are designed in a manner where there are no sudden lockups occur with pins.

The rotational motion of the Link is transferred to the Driver jaw by the reaction force between the pin-slot joint and makes the Jaw to rotate around a hinge on the Base. In order to achieve compactness, the Gripper pair was connected via a Sector Gear pair. The main two actuation elements can be considered as the SMA spring and the steel torsion spring which are supporting for the opening and closing of gripper jaws respectively. The development and the characterization of SMA spring and the torsion spring is elaborated in the following subsections.

2.2. Design of SMASAG

The design of SMASAG is followed by the designing of actuator supporting structure or the outer packaging of the actuator, SMA based spring and the torsional spring.

2.2.1. Design of outer packaging of the actuator

The outer packaging or the structure of the actuator consists of a Cylinder which has an outer diameter of 20 mm, a bore of 10 mm and it is 50 mm in length. Also, the Piston has a diameter which is matched to the cylinder

bore providing the smooth movement with the prevention of leakages and it is 33.7 mm in length. The End Nut facilitates the final assembly of the actuator and has 15 mm across flats and threaded to the Cylinder by an M12 standard thread. There are two mounts for SMA spring attachment and both of them are threaded to the End Nut and the Piston by M6 standard thread.

2.2.2. Design of SMA spring

The design of the SMA spring is related to the SMA shape setting operation and there, a fixture is designed to constrain the spring shape.

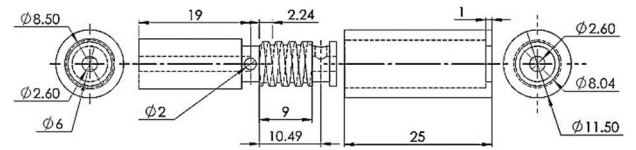


Fig. 2. SMA shape setting fixture design

According to the design dimensions in Fig. 2. (in millimeters) of this fixture, the SMA spring has four turns with two point two four pitch and the spring diameter is eight millimeters.

2.2.3. Design of torsion spring

This provides the closing action of the Gripper Jaws. Choosing a High spring constant may cause excessive forces on the object and partial opening of gripper jaws. Low spring constant may cause partial gripping. Following equations will facilitate to design the torsional spring with correct spring constant.

$$R_{LJ} = \left(\frac{r_A}{r_G} \right) F_{SMA} \cos \beta \quad (1)$$

$$L_{ix} = L_{i0} - D_T \theta \quad (2)$$

$$C^2 = L_{i0}^2 + L_{ix}^2 - 2L_{i0}L_{ix} \cos \theta \quad (3)$$

$$L_{Cx} = L_{C0} + C \quad (4)$$

$$F_{JS} = R_{LJ} \frac{L_H \cos(\alpha + \beta) + F_G L_G}{L_{Cx}} \quad (5)$$

$$N_E = \frac{L_{i0} + L_{20}}{3\pi D_T} \quad (6)$$

$$N_A = N_B + N_E \quad (7)$$

$$k_{per\ turn} = \frac{d_T^4}{10.8 D_T N_A} \quad (8)$$

$$F_{SJ} = \frac{d_T^4}{10.8 D_T N_A} \frac{\theta}{2\pi} \quad (9)$$

$$F_{SJ} = F_{JS} \quad (10)$$

Here N_A , N_B and N_E are the Actual, Body and Effective turns of the torsional spring.

Fig. 3. Presents the parameters used in the above equations. Eq. (1) to Eq. (5) can be used to calculate the force exerted on the torsional spring due to the actuation force by the SMA spring and Eq. (6) to Eq. (10) related to the calculation of a number of turns of the torsion spring.

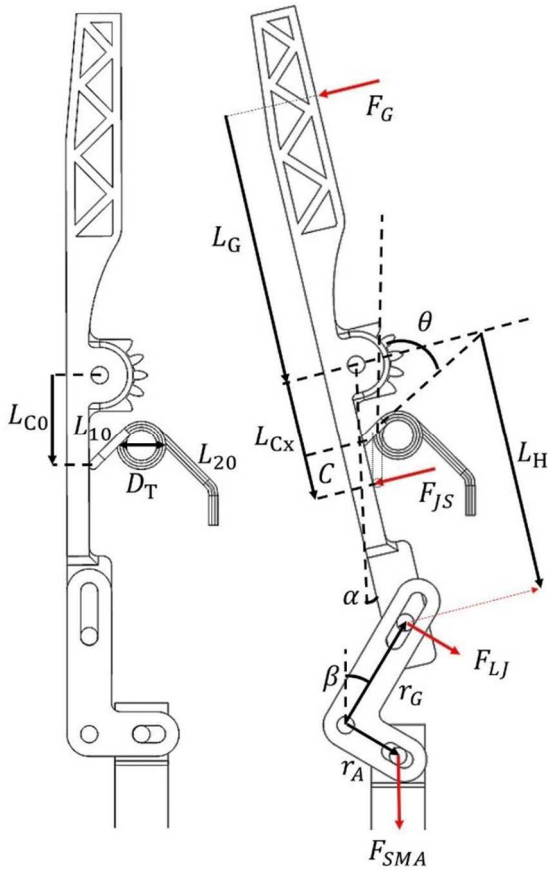


Fig. 3. Free body diagram and calculation parameters

3. Fabrication of SMASAG and Force Characterization of SMA Actuator

3.1. Fabrication of SMA actuator

The SMA material which was used to fabricate the spring was a commercially available material called NiTiNOL which is composed of Ni - 55%; H - 0.001%; O - 0.05%; N - 0.001%; C - 0.05%; Ti - Balance. The obtained NiTiNOL material was in the form of straight wires with different diameters and transformation temperatures. So a

Fixture need to be used in order to get them in the correct Spring shape while shape setting at high temperature.



Fig. 4. Fabricated fixture

As the NiTiNOL wire tend to regain its trained shape while increasing the temperature above Autunitic final temperature, it is very much important to use fixtures (Fig. 4.) when inducing newly defined shape into the material. So the fixture was placed in a Muffle furnace for temperatures and aging times indicated in Table 1. and water quenched to get the final spring shape.(Fig. 5.)

Table 1. NiTiNOL wire shape setting details

Wire Diameter (mm)	Shape Setting Temperature ($^{\circ}\text{C}$)	Aging Time (mins)	Transformation Temperature ($^{\circ}\text{C}$)
1.0	500	25	60 ± 5
1.0	500	30	80 ± 5



Fig. 5. Shape set NiTiNOL spring

3.2. Fabrication of outer packaging and the Gripper

The fabricated SMASAG is depicted in Fig. 6. The Base structure and the Gripper jaws were made out of ABS Plus material with the use of 3D printing technology.



Fig. 6. Fabricated SMASAG

3.3. Force characterization of SMA spring

After shape setting the NiTiNOL wire into a spring shape, it is important to have an understanding of the amount of force that can be exerted through it on the mechanism. So an apparatus was developed to measure the force that can be achieved when springs are constrained to recover to their initial shape.

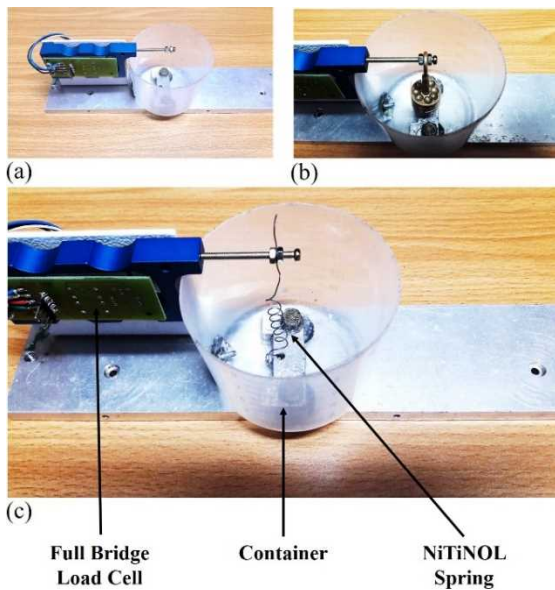


Fig. 7. (a) Force measuring apparatus (b) Calibrating by known weights (c) NiTiNOL spring attachment

The apparatus shown in Fig. 7 (a). consists of a Full bridge load cell and a container which was used to immerse the Spring in water while one end connecting to the base of the container rigidly and the other end connecting to the load cell attachment. In the first place load cell was calibrated by known weights as in Fig. 7 (b). and after that NiTiNOL spring was attached to measure the force as in Fig. 7 (c). Finally, the container was filled with water and gradually increased the temperature by a heater.

The Full bridge load cell was connected to a 24-bit load cell amplifier (HX711). And the HX711 was connected to a microcontroller (ATmega 2560) based development board in order to acquire data. After obtaining raw data values from the amplifier, the development board was sending those raw data to a computer via serial communication and all the data processing tasks were conducted from a LabVIEW generated program. Also, a Graphical User Interface (GUI) was developed to plot and display data.

Simultaneously the temperature of the water was measured through a four and half true RMS Digital Multimeter which is compatible with thermocouple probes. Those obtained values were plotted and Fig.8 shows the variation of force with the temperature for

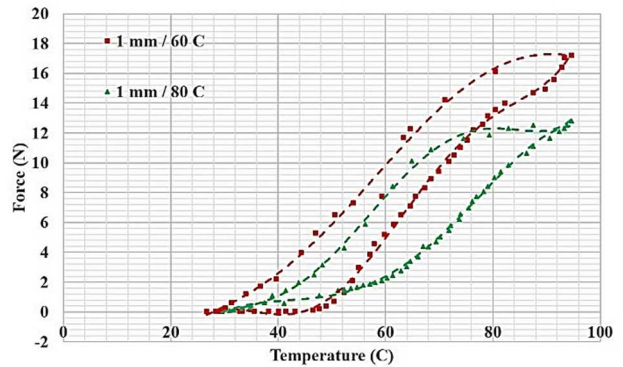


Fig. 8. Force measurement using the apparatus NiTiNOL springs which has same coil and wire diameter with different transformation temperatures.(Table 1.)

Conclusion

In this work, an SMA spring actuator based gripper was designed and fabricated. The work carried out to achieve that task includes, force characterization of a NiTiNOL spring. The results show that, as the transformation temperature reduces with same wire diameter, the required force could be achieved quickly as all the springs were tested under same conditions. Future works include testing and Gripper force analysis of the SMASAG.

References

1. C. Song, "History and Current Situation of Shape Memory Alloys Devices for Minimally Invasive Surgery," *Open Med. Devices J.*, vol. 2, pp. 24–31, 2010.
2. R. H. Petersen, "Video-assisted thoracoscopic thymectomy using 5-mm ports and carbon dioxide insufflation," *Ann. Cardiothorac. Surg.*, vol. 5, no. 1, pp. 51–55, Jan. 2016.
3. J. Mohd Jani, M. Leary, A. Subic, and M. A. Gibson, "A review of shape memory alloy research, applications and opportunities," *Mater. Des. 1980-2015*, vol. 56, pp. 1078–1113, Apr. 2014.
4. D. Mantovani, "Shape memory alloys: Properties and biomedical applications," *JOM*, vol. 52, no. 10, pp. 36–44, Oct. 2000.
5. D. Stockel and A. Melzer, "The Use of NiTi Alloys for Surgical Instruments," *Conflu. Med.*, 1995.
6. Shaoze Yan, Xiajie Liu, Feng Xu, and Jinhui Wang, "A Gripper Actuated by a Pair of Differential SMA Springs," *J. Intell. Mater. Syst. Struct.*, vol. 18, no. 5, pp. 459–466, May 2007.

Design and Development of Quantum Tunneling Composite based Tactile Sensors

T.D.I. Udayanga, D.A.M.R. Fernando, H.L.P.L. Chaturanga, B.A.D.J.C.K. Basnayake and Y.W.R. Amarasinghe

Department of Mechanical Engineering, University of Moratuwa

Katubadda, Sri Lanka.

t.i.udayanga@ieee.org

www.mrt.ac.lk

Abstract

Tactile sensor is a device which acquire information about physical entities such as pressure, force, texture, etc., with the aid of physical touch and convert them in to useful electrical signals. With the advancements of robotics and mechatronics, currently, there is a great demand for tactile sensors so as to use them in various applications to acquire tactile data. In this study, a miniaturized novel enclosed tactile sensor was designed and developed using Quantum Tunneling Composite (QTCTM), which is a conductive polymer composite, as the sensing element. An enclosed novel structure was proposed so that the sensing element and spring will be omitted from the environmental effects. Proposed sensor structure was analysed and manufactured. Experiments were carried out and results shows that the sensitivity of this developed tactile sensor to be 0.02 V/N and repeatability of ± 3 N.

Keywords: Sensors, Tactile Sensing, Quantum Tunneling Composite, FEA.

1. Introduction

Tactile sensors is a device which uses tactile sensing to acquire data from the physical environment. Tactile Sensing is measuring tactile parameters such as temperature, vibration, texture, shape, force, pressure with the aid of physical touch. Tactile parameters may often include, temperature, vibration, softness, texture, shape, composition shear and normal force.^{1, 2} Even though tactile sensing came to the attention of researchers in the 1970s, tactile sensors haven't been developed much comparing with the non-contact sensors.^{3, 4} But with the advancements of robotics and automation, currently, there is a need of tactile feedback systems with optimum performance.⁵ Application areas of tactile sensing has been expanded as new fields of applications has emerged recently regarding tactile sensing. Robotics,⁶ medical,^{7,8} entertainment and communication⁹ are some of these identified application areas of tactile sensors. Over the past decades, many sensing principles

are identified which can be incorporated with tactile sensors such as Piezoresistive,^{10, 11} Piezoelectric^{12, 13}, Optical,¹⁴ Capacitive,^{15,16} Conductive Polymer/Composite.^{17,18} Each of these sensing principles have their own advantages and disadvantages.^{1, 19} Hence, use of them in applications should be considered according to the performance required.

At the early stage of this research, as published in Ref. 20, a tactile sensor was developed. But further in to the research identified issues associated with that design such as poor maintenance of geometrical and dimensional tolerances, low dimensional accuracy and precision associated with the manufacturing technique. Due to these manufacturing errors, alignment Problems Occurred during assembling stage and offsetting errors occurred while transferring force to sensing element. Also due to the insufficient physical contact between electrode and the sensing element, noise was added to the output signal and it might has been one of a cause for the hysteresis error of the developed sensor.²⁰ So in this

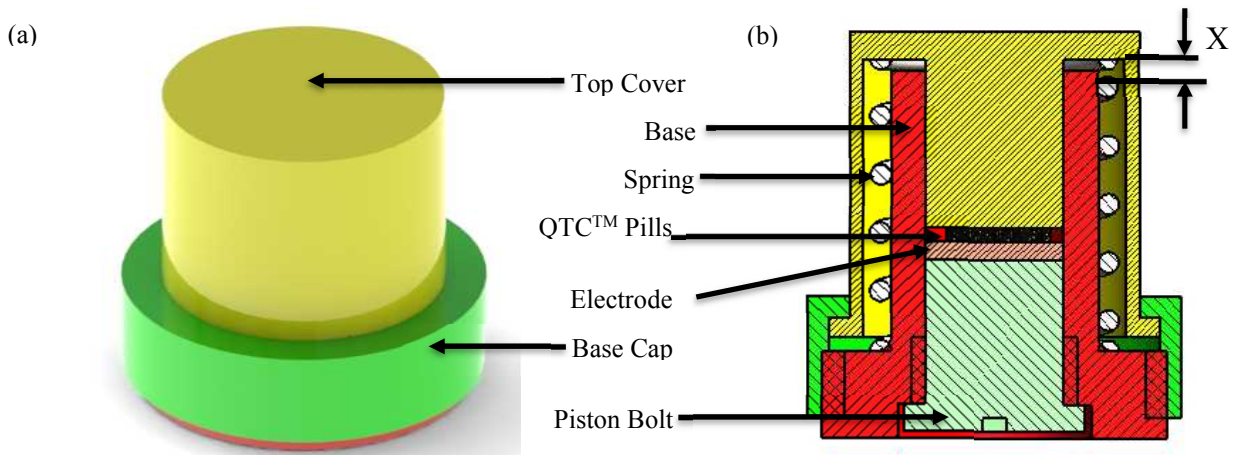


Fig. 1. Proposed Conceptual Of the Novel Enclosed Tactile Sensor; (a) Isometric View , (b) Sectional Front Elevation

paper a novel enclosed design was discussed, which was designed to overcome the issues identified, to add overload protection characteristics and to minimize the environmental effect to the sensing element.

Following chapters will discuss about the structural design of the proposed sensor, sensing principle and Finite Element Analysis of structure and experiments and results conducted regarding the developed sensor.

2. Proposed Structural Design

Conceptual Design and the components of the designed novel enclosed sensor structure is shown in Fig. 1. In this sensor structure, force is applied to the top cover and then it is transferred to the sensing element while scaling down the force through the spring. In this design, space between the top cover and the base (dimension X as shown in Fig. 1) is controlled such that it will provide an overload protection to the sensing element. Overload condition can be set by adjusting the piston bolt and the base cap in the structure. This will affect the force range of the sensor, as this controls the allowable maximum displacement for the QTC™ pill. Hence, with this newly added feature now force range of the sensor can be adjusted suitable to the application not only by changing the spring used in the structure but also by adjusting the piston bolt and the base cap of the structure.

Another advantage of this structure is that the sensing elements (QTC™ pills) are not open to the environment as they are enclosed in the structure. This will ensure that the environmental conditions such as dust, humidity will not affect the performance of the sensing element.

3. Analysis and Simulation of Proposed Structure

To validate the proposed sensor structure, Finite Element Analysis (FEA) was performed solely for validating the proposed sensor structure and to verify whether it follows the proposed working principle at development of 1-DOF Tactile Sensor.²⁰ Analysis was performed using COMSOL Multiphysics software, which is a FEA software.

Fig. 2 shows the results of the FEA analysis for sensor structure. According to the results shown in Fig. 2. (c), proposed structure with sensing element shows a linear relationship between the force applied and the structural displacement. This validate that the proposed structure is working on the working principle described at Ref. 20.

4. Fabrication of Enclosed Tactile Sensor

When fabricating electrode as discussed in Ref. 20, one of the major issue identified was create the physical contact between the sensing element and the electrode. Since the solution from previous stage of sensor development is not an optimum, it is required to find the best method to create an optimum physical contact. From the literature, it was found that vacuum depositing Aluminium on both surfaces will give the optimum results.²¹ Since vacuum depositing facilities are not available in Sri Lanka, next optimum available solution, which is to use silver paste to create the physical contact between electrode and sensing element is used when developing sensing element configuration.

Using CNC machining techniques each structural components were fabricated, as such machining techniques ensures high dimensional precision and accuracy. After fabricating each and every structural

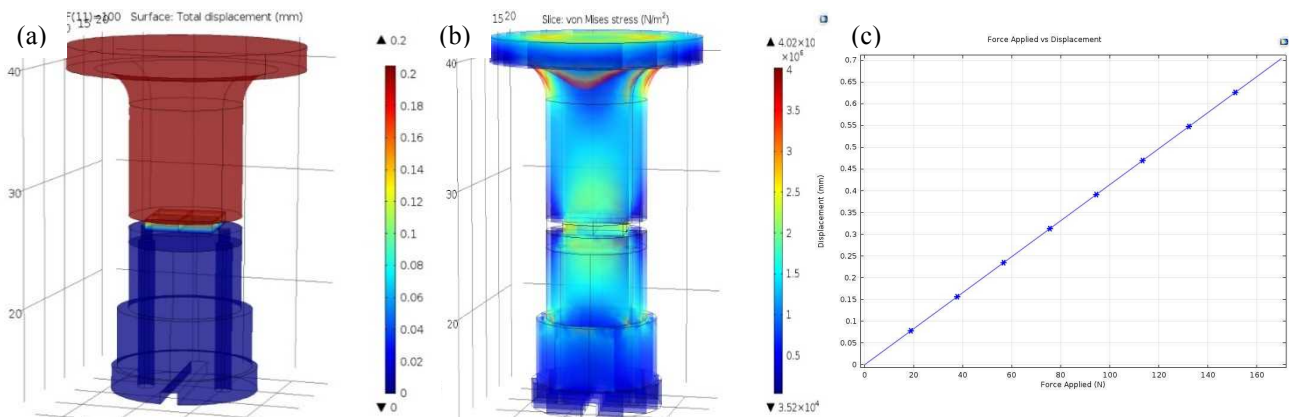


Fig. 2. Results of the FEA performed for the Proposed Structure; (a) Total Deformation Variation, (b) Equivalent Stress Variation, (c) Force vs Deformation Plot

components, they were assembled together with electrode configuration. Fig. 3 shows the fabricated structural components and assembled and finalized novel enclosed 1-DOF tactile sensor.

5. Experiment and Results

Experiments were carried out to find the relationship between the developed sensor output and input, to find the sensitivity of the sensor, to find the sensor range, to find the resolution of the sensor and the repeatability of the sensor. The experiment was designed using Universal Tensile Testing Machine. Purpose of using this machine to conduct experiment for the sensor is to deliver a gradually increasing and decreasing force to the sensor Fig. 4 shows the results of these experiments carried out using the above developed experimental setup. Table 2 shows the sensor characteristics values calculated from the experimental results.

Table 2. Sensor Characteristics Values Calculated for Developed sensor

Sensor Characteristics	Value
Sensor Range	0 – 170 N
Sensitivity	0.2209 V/N
Resolution	0.5 N
Repeatability	± 3 N

6. Conclusion and Discussion

In these results Fig. 4. (a) shows the relationship between sensor input and the sensor output with standard deviation at each data point. Also Fig. 4. (b) shows the repeatability analysis for the developed sensor. According to these results, it can be seen that the hysteresis error of the developed sensor was increased comparing with the experimental results of Ref. 20. Reasons behind this phenomena may be due to errors cause by the universal tensile testing machine and errors present in the QTC™ material use for the experiment.

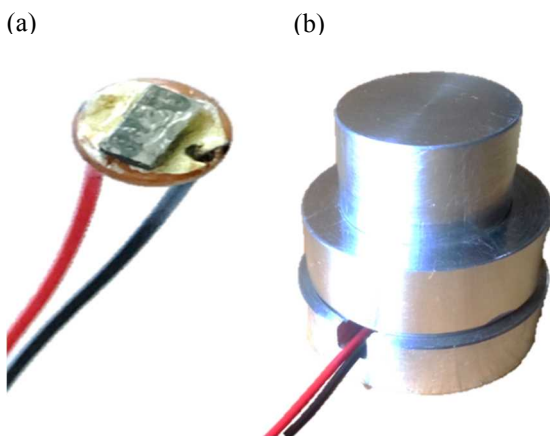


Fig. 3. (a) Fabricated Sensing Configuration, (b) Fabricated Enclosed Sensor

References

1. M. I. Tiwana, S. J. Redmond, and N. H. Lovell, “A review of tactile sensing technologies with applications in biomedical engineering,” *Sens. Actuators Phys.*, vol. 179, pp. 17–31, Jun. 2012.
2. H. I. Jaafar, “Current Trend of Tactile Sensor in Advanced Applications,” *Sens. Transducers*, vol. 143, no. 8, pp. 32–43, Aug. 2012.
3. M. H. Lee and H. R. Nicholls, “Review Article Tactile sensing for mechatronics—a state of the art survey,” *Mechatronics*, vol. 9, no. 1, pp. 1–31, Feb. 1999.
4. M. H. Lee, “Tactile Sensing: New Directions, New Challenges,” *Int. J. Robot. Res.*, vol. 19, no. 7, pp. 636–643, Jul. 2000.

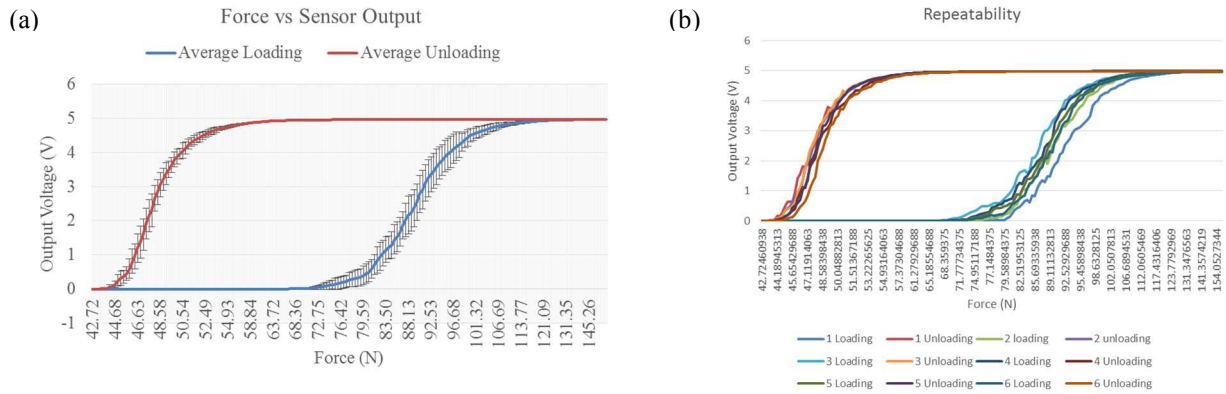


Fig. 4. Experiment Results; (a) Force vs Sensor Output, (b) Repeatability Analysis for the Developed Sensor

5. P. Estevez, J. M. Bank, M. Porta, J. Wei, P. M. Sarro, M. Tichem, and U. Staufer, "6 DOF force and torque sensor for micro-manipulation applications," *Sens. Actuators Phys.*, vol. 186, pp. 86–93, Oct. 2012.
6. H. Yousef, M. Boukallel, and K. Althoefer, "Tactile sensing for dexterous in-hand manipulation in robotics—A review," *Sens. Actuators Phys.*, vol. 167, no. 2, pp. 171–187, Jun. 2011.
7. A. Sarvazyan and V. Egorov, "Mechanical Imaging – a Technology for 3-D Visualization and Characterization of Soft Tissue Abnormalities. A Review," *Curr. Med. Imaging Rev.*, vol. 8, no. 1, pp. 64–73, Feb. 2012.
8. A. Hamed, S. C. Tang, H. Ren, A. Squires, C. Payne, K. Masamune, G. Tang, J. Mohammadpour, and Z. T. H. Tse, "Advances in Haptics, Tactile Sensing, and Manipulation for Robot-Assisted Minimally Invasive Surgery, Noninvasive Surgery, and Diagnosis," *J. Robot.*, vol. 2012, p. e412816, Dec. 2012.
9. "iPod," Apple. [Online]. Available: <http://www.apple.com/ipod/>. [Accessed: 18-Apr-2016].
10. P. Estevez, J. M. Bank, M. Porta, J. Wei, P. M. Sarro, M. Tichem, and U. Staufer, "6 DOF force and torque sensor for micro-manipulation applications," *Sens. Actuators Phys.*, vol. 186, pp. 86–93, Oct. 2012.
11. B. A. D. J. C. K. Basnayake, Y. W. R. Amarasinghe, R. A. Attalage, T. D. I. Udayanga, and A. G. B. P. Jayasekara, "Artificial intelligence based smart building automation controller for energy efficiency improvements in existing building," *International Journal of Advanced Automation Science and Technology*, vol. 40, no. 40, 2015.
12. Javad Dargahi, Mojtaba Kahrizi, Nakka Purushotham Rao, and Saeed Sokhanvar, "Design and microfabrication of a hybrid piezoelectric - capacitive tactile sensor," *Sens. Rev.*, vol. 26, no. 3, pp. 186–192, Jul. 2006.
13. J. Brugger, D. Briand, T. Polster, and M. Hoffmann, "Aluminum nitride based 3D, piezoelectric, tactile sensor," *Procedia Chem.*, vol. 1, no. 1, pp. 144–147, Sep. 2009.
14. M. Ohka, H. Kobayashi, and Y. Mitsuya, "Sensing characteristics of an optical three-axis tactile sensor mounted on a multi-fingered robotic hand," in *2005 IEEE/RSJ International Conference on Intelligent Robots and Systems*, 2005, pp. 493–498.
15. H.-K. Lee, S.-I. Chang, and E. Yoon, "A Flexible Polymer Tactile Sensor: Fabrication and Modular Expandability for Large Area Deployment," *J. Microelectromechanical Syst.*, vol. 15, no. 6, pp. 1681–1686, Dec. 2006.
16. H. B. Muhammad, C. M. Oddo, L. Beccai, C. Recchiuto, C. J. Anthony, M. J. Adams, M. C. Carrozza, D. W. L. Hukins, and M. C. L. Ward, "Development of a bioinspired MEMS based capacitive tactile sensor for a robotic finger," *Sens. Actuators Phys.*, vol. 165, no. 2, pp. 221–229, Feb. 2011.
17. S. Nambiar and J. T. W. Yeow, "Conductive polymer-based sensors for biomedical applications," *Biosens. Bioelectron.*, vol. 26, no. 5, pp. 1825–1832, Jan. 2011.
18. Y. W. R. Amarasinghe, A. L. Kulasekera, and T. G. P. Priyadarshana, "Design and simulation of 1-DOF tactile sensor for gripping force measurement," in *2013 IEEE 8th International Conference on Industrial and Information Systems*, 2013, pp. 399–402.
19. M. R. Cutkosky, R. D. Howe, and W. R. Provancher, "Force and Tactile Sensors," in *Springer Handbook of Robotics*, B. S. Prof and O. K. Prof, Eds. Springer Berlin Heidelberg, 2008, pp. 455–476.
20. T.D.I. Udayanga, D.A.M.R. Fernando, H.L.P.L. Chaturanga, Y.W.R. Amarasinghe and D.V. Dao, 2015. "Development of a Quantum Tunneling Composite based 1-DOF Tactile Sensor," *International Journal of Advanced Information Science and Technology*, vol. 40, no. 40, 2015.
21. M. Ohmukai, Y. Kami, and R. Matsuura, "Electrode for Force Sensor of Conductive Rubber," *J. Sens. Technol.*, vol. 2, no. 3, pp. 127–131, 2012.

Analog Circuit Design of a Novel 4D Chaotic System

Dechu Tan, Hong Niu

College of Electronic Information and Automation, Tianjin University of Science & Technology
80 Mailbox, Tianjin University of Science & Technology, No. 1038 Dagu Nanlu, Hexi District,

Tianjin, 300222, China
E-mail: spots@163.com
www.tust.edu.cn

Abstract

In this paper, a novel four-dimensional (4D) autonomous chaotic system is reviewed, and its corresponding new analog circuit is presented based on the modified module-based approach to chaotic circuit design. The chaotic phase portraits of the new circuit are given to illustrate the good qualitative agreement between the numerical simulation and the experimental realization.

Keywords: novel 4D chaotic system, analog circuit design, modified module-based approach, experimental realization

1. Introduction

Circuit design of chaotic system has been an important field in the study of chaos. Many methods have been proposed.¹⁻³ The modified module-based approach is one of the common methods for analog circuit design of chaotic system.⁴ This method does not need to convert the differential equations of the chaotic system to the integral ones, and the value of each element is determined by comparing the coefficients of the equations of the system with those of the equations of the circuit correspondingly. The advantages of the method are high accuracy of the simulation and experimental results, but less number of elements. In this paper, the analog circuit of the 4D chaotic system proposed in Ref. 5 is designed via the modified module-based approach.

The rest of this paper is organized as follows. In Section 2, the model of the novel 4D chaotic system and its numerical simulation phase portraits are reviewed. In Section 3, the analog circuit of the system is constructed based on the modified module-based approach. In

Section 4, the phase portraits of the experimental circuit are given. The conclusions are drawn in Section 5.

2. Review of the Novel 4D Chaotic System

The novel 4D chaotic system has been discussed in Ref. 5. It is formulated as

$$\begin{aligned}\dot{x} &= a(y - x), \\ \dot{y} &= c(x + y) + z - xw, \\ \dot{z} &= mx - y - hz, \\ \dot{w} &= xy - bw,\end{aligned}\tag{1}$$

where $x, y, z, w \in \mathbb{R}$ are state variables, and $a = 25$, $b = 3$, $c = 18$, $m = 19$ and $h = 14$.

The Lyapunov exponents of the system (1) respectively are

$$\lambda_1 = 2.6686 > 0, \lambda_2 = 0.0003 \approx 0,$$

$$\lambda_3 = -11.7885 < 0, \lambda_4 = -14.8804 < 0,$$

when the initial values are $(x_0, y_0, z_0, w_0) = (1, 1, 1, 1)$. It indicates that the system (1) is chaotic. The phase portraits of the system (1) are shown in Fig. 1(a)-(f).

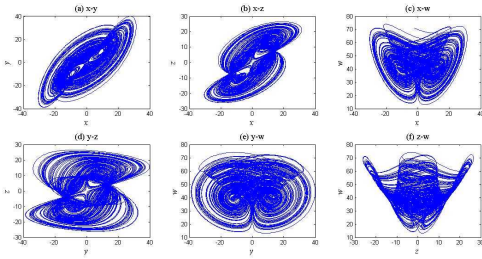


Fig. 1. Phase portraits of the novel 4D chaotic system: (a) x-y (b) x-z (c) x-w (d) y-z (e) y-w (f) z-w

3. Analog Circuit Design of the Novel 4D Chaotic System

The analog circuit of the system (1) is constructed based on the modified module-based approach to chaotic circuit design, which consists of scale transformation of variables, time scale transformation, normalization for equations, circuit module design and determination of parameters.^{3,4}

3.1. Scale Transformation of Variables

The active analog elements used in this paper are TL082CP and AD734AN, whose supply voltages are $\pm 15V$, so that the output saturation voltage is $13.5V$. From the numerical simulation results shown in Fig. 1, it can be found that the maximum absolute values of the variables are all greater than the output saturation voltage. It means that the distortion will occur when observing the phase portraits of the design circuit, and even the elements could be destroyed. Therefore, the scale transformation of variables should be performed.

Let $x = 10\tilde{x}$, $y = 10\tilde{y}$, $z = 10\tilde{z}$ and $w = 10\tilde{w}$, then the system (1) is represented as

$$\begin{aligned} \frac{dx}{d\tau} &= -ax + ay, \\ \frac{dy}{d\tau} &= cx + cy + z - 10xw, \\ \frac{dz}{d\tau} &= mx - y - hz, \\ \frac{dw}{d\tau} &= 10xy - bw, \end{aligned} \quad (2)$$

where \tilde{x} , \tilde{y} , \tilde{z} and \tilde{w} are still denoted as x , y , z and w for convenience.

3.2. Time Scale Transformation

Let $\tau = \tau_0 t$, where $\tau_0 = 100$, and substitute it into Eq. (2). Then,

$$\begin{aligned} \frac{dx}{dt} &= -a\tau_0 x + a\tau_0 y, \\ \frac{dy}{dt} &= c\tau_0 x + c\tau_0 y + \tau_0 z - 10\tau_0 xw, \\ \frac{dz}{dt} &= m\tau_0 x - \tau_0 y - h\tau_0 z, \\ \frac{dw}{dt} &= 10\tau_0 xy - b\tau_0 w. \end{aligned} \quad (3)$$

3.3. Normalization for Equations

Consider that the signals are all put into the negative inputs of the operational amplifiers, then Eq. (3) should be normalized to

$$\begin{aligned} \frac{dx}{dt} &= -a\tau_0 x - a\tau_0 (-y), \\ \frac{dy}{dt} &= -c\tau_0 (-x) - c\tau_0 (-y) - \tau_0 (-z) - 10\tau_0 xw, \\ \frac{dz}{dt} &= -m\tau_0 (-x) - \tau_0 y - h\tau_0 z, \\ \frac{dw}{dt} &= -10\tau_0 (-x)y - b\tau_0 w, \end{aligned} \quad (4)$$

to make the equations of the system consistent with those of the circuit.

3.4. Circuit Module Design

The circuit schematic diagram of the novel 4D chaotic system is designed based on Eq. (4), as shown in Fig. 2. The equations of the circuit can be described as

$$\begin{aligned} \frac{dx}{dt} &= -\frac{1}{R_1 C_1} x - \frac{1}{R_2 C_1} (-y), \\ \frac{dy}{dt} &= -\frac{1}{R_3 C_2} (-x) - \frac{1}{R_4 C_2} (-y) - \frac{1}{R_5 C_2} (-z) \\ &\quad - \frac{1}{10R_6 C_2} xw, \\ \frac{dz}{dt} &= -\frac{1}{R_7 C_3} (-x) - \frac{1}{R_8 C_3} y - \frac{1}{R_9 C_3} z, \\ \frac{dw}{dt} &= -\frac{1}{10R_{10} C_4} (-x)y - \frac{1}{R_{11} C_4} w. \end{aligned} \quad (5)$$

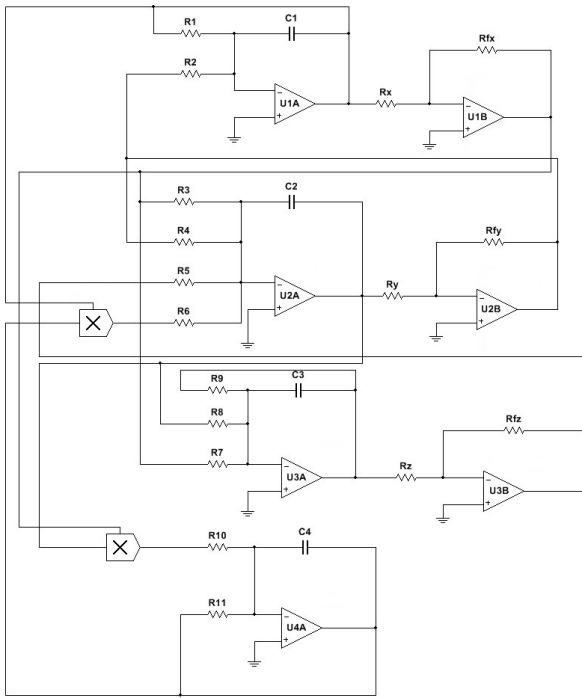


Fig. 2. Circuit schematic diagram of the novel 4D chaotic system

3.5. Determination of Parameters

Comparing the corresponding coefficients of Eq. (5) and Eq. (4) yields

$$R_1 = R_2 = \frac{1}{a\tau_0 C_1} = 40k\Omega,$$

$$R_3 = R_4 = \frac{1}{c\tau_0 C_2} = 55.5k\Omega,$$

$$R_5 = R_8 = \frac{1}{\tau_0 C_2} = 1M\Omega,$$

$$R_6 = R_{10} = \frac{1}{100\tau_0 C_2} = 10k\Omega,$$

$$R_7 = \frac{1}{m\tau_0 C_3} = 52.6k\Omega,$$

$$R_9 = \frac{1}{h\tau_0 C_3} = 71.4k\Omega,$$

$$R_{11} = \frac{1}{b\tau_0 C_4} = 333.3k\Omega,$$

where $C_1 = C_2 = C_3 = C_4 = 10$ nF.

4. Experimental Circuit of the Novel 4D Chaotic System

4.1. Experimental Circuit

Substitute the TL082CP operational amplifiers and the AD734AN analog multipliers into the circuit schematic diagram shown in Fig. 2. The experimental circuit of the novel 4D chaotic system is presented in Fig. 3. The parameters of the elements have been marked in the figure.

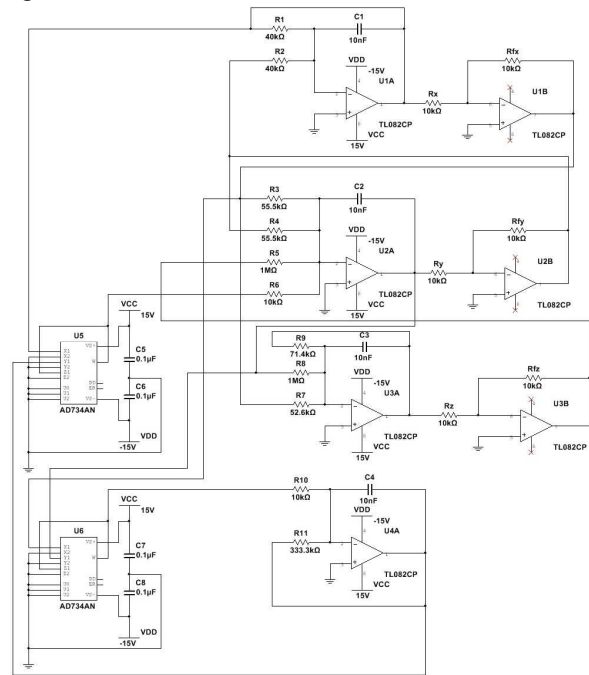


Fig. 3. Experimental circuit of the novel 4D chaotic system

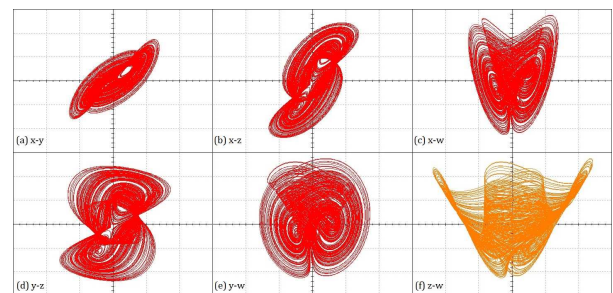


Fig. 4. Phase portraits of the experimental circuit: (a) x-y (b) x-z (c) x-w (d) y-z (e) y-w (f) z-w

4.2. Experimental Results

The phase portraits of the experimental circuit are drawn via Multisim, as shown in Fig. 4(a)-(f). The

scales of x , y , z and w are 2 V/Div, 2 V/Div, 1 V/Div and 1 V/Div, respectively. By comparing the phase portraits in Fig. 4(a)-(f) with those in Fig. 1(a)-(f) correspondingly, it can be confirmed that there is a good qualitative agreement between the numerical simulation and the experimental realization. It demonstrates that the experimental circuit of the novel 4D chaotic system is correct.

5. Conclusions

In this paper, the analog circuit of the novel 4D chaotic system is designed via the modified module-based approach. The experimental results obtained by Multisim demonstrate the feasibility of the design circuit. Furthermore, the actual hardware circuit of the novel 4D chaotic system is being implemented. The study in this paper has some engineering significance.

References

1. R. Kiliç, A comparative study on realization of Chua's circuit: Hybrid realizations of Chua's circuit combining the circuit topologies proposed for Chua's diode and inductor elements, *International Journal of Bifurcation and Chaos* 13(6) (2003) 1475–1493.
2. Z. Xu, C. Liu and T. Yang, Study on a new chaotic system with analysis and circuit experiment, *Acta Physica Sinica* 59(1) (2010) 131–139.
3. S. Yu, *Chaotic Systems and Chaotic Circuits: Principle, Design and Its Application in Communications* (XiDian University Publishing House, Xi'an, 2011).
4. H. Niu, Stability control and circuit implementation of a novel 3D chaotic system with variable coefficient, *Dynamical Systems and Control* 5(1) (2016) 31–40.
5. H. Niu, Analysis and control of a novel 4D chaotic system, in *Proceedings of the 2017 International Conference on Artificial Life and Robotics*, eds. M. Sugisaka, Y. Jia, T. Ito and J. Lee (Miyazaki, Japan, 2017), pp. 165–168.

A method of end-to-end self-understanding of Chinese paper-dictionaries

Zhijian Lv¹, Yizhun Peng²

¹Beijing Institute of Science and Technology Information (BISTI), China;

²College of Electronic Information and Automation,
Tianjin University of Science and Technology, China

E-mail: *luzj@bjstinfo.ac.cn

Abstract

This paper introduces a method of end-to-end self-understanding of Chinese paper-dictionaries. In this method, a page of Chinese paper-dictionaries is scanned into an electronic image. And then the electronic image is preprocessed, including un-distortion, side scrapping, binarization, and so on. Finally, using an end-to end deep learning method, the pre-processed electronic image is intelligently segmented, text recognized, and context understood. Our method has been applied to self-understand a serial of Chinese paper-dictionaries, which have more than 13000 pages and 2.1 millions of entries. And its correct rate of self-understanding of Chinese phrases is more than 99.5%. Its performance has proved it's availability.

Keywords: end-to-end self-understanding, image-segmentation,

1. Introduction

Convolutional networks (Convnets) have made progresses in recognition, including whole-image classification [9, 14, 15] and local tasks with structured output, including bounding box object detection [13, 5, 8], part and keypoint prediction [16, 10], local correspondence [10, 3], and semantic segmentation [11, 1, 2, 12, 7, 6, 4].

Semantic segmentation faces an inherent tension between semantics and location: global information resolves what while local information resolves where. Deep feature hierarchies encode location and semantics in a nonlinear local-to-global pyramid. J. Long et al [18]proposed a fully convolutional network (FCN) trained end-to-end, pixels-to-pixels on semantic segmentation[17] and defined skip architecture to take advantage of this feature spectrum that combines deep, coarse, semantic information and shallow, fine, appearance information. The approach does not make use of pre- and post-processing complications, including superpixels [2, 7], proposals [7, 6], or post-hoc refinement by random fields or local classifiers[2, 7].

The model transfers recent success in classification[9, 14, 15] to dense prediction by reinterpreting classification nets as fully convolutional and fine-tuning from their learned representations.

In the next section, we review related works on FCN for semantic segmentation, and then introduce the FCN to self-understand a serial of Chinese paper-dictionaries. The following section demonstrate its performance. Finally, we conclude our method of self-understand Chinese Dictionaries using FCN.

2. FCNs and its corresponding architectures for semantic segmentation

2.1. Fully convolutional networks

Convnets is defined as follows:

$$y_{ij} = f_{ks}(\{x_{si+\delta i, sj+\delta j}\}, 0 \leq \delta i, \delta j \leq k) \quad (1)$$

, where x_{ij} for the data vector at location (i, j) in a particular layer; and y_{ij} for the following layer; k is called the kernel size; s is the stride or subsampling factor; and f_{ks} determines the layer type, such as a matrix multiplication for convolution or average pooling, a

spatial max for max pooling, or an elementwise nonlinearity for an activation function, and so on for other types of layers.

These basic components (convolution, pooling, and activation functions) of convnets operate on local input regions, and depend only on relative spatial coordinates. Each layer of data in a convnet is a three-dimensional array of size $h \times w \times d$, where h and w are spatial dimensions, and d is the feature or channel dimension. The first layer is the image, with pixel size $h \times w$, and d color channels. Locations in higher layers correspond to the locations in the image they are path-connected to, which are called their receptive fields.

This functional form is maintained under composition, with kernel size and stride obeying the transformation rule

$$f_{k's'} \circ g_{k's'} = (f \circ g)_{k'+(k-1)s', s's'} \quad (2)$$

While a general deep net computes a general nonlinear function, a net with only layers of this form computes a nonlinear filter, called a deep filter or fully convolutional network. An FCN naturally operates on an input of any size, and produces an output of corresponding spatial dimensions.

A real-valued loss function composed with an FCN defines a task. If the loss function is a sum over the spatial dimensions of the final layer, $l(x; \theta) = \sum_{ij} l'(x_{ij}, \theta)$, its gradient will be a sum over the gradients of each of its spatial components. Thus stochastic gradient descent on computed on whole images will be the same as stochastic gradient descent on l' , taking all of the final layer receptive fields as a minibatch. When these receptive fields overlap significantly, both feedforward computation and backpropagation are much more efficient when computed layer-by-layer over an entire image instead of independently patch-by-patch.

2.2. Segmentation Architecture of FCNs

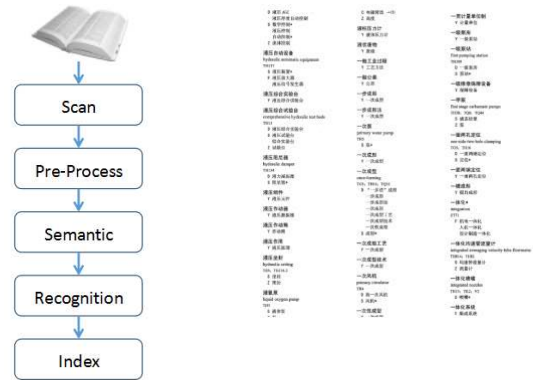
ILSVRC classifiers are cast into FCNs and augmented for dense prediction with in-network upsampling and a pixelwise loss. Segmentation is trained by fine-tuning and skips between layers to fuse coarse, semantic and local, appearance information are add into FCNs. And then a skip architecture is learned end-to-end to refine the semantics and spatial precision of the output. a per-pixel multinomial logistic loss and validate with the standard metric of mean pixel

intersection over union, with the mean taken over all classes, including background are introduced into training. The training ignores pixels that are masked out (as ambiguous or difficult) in the ground truth.

3. Self-understanding of Chinese dictionaries

Information technologies (abbr. IT) have applied into our lives. In IT systems, entries, usually captured from paper based dictionaries, are basic elements and used for text processing. However, It is a hard work that billions of entries are captured from paper-based dictionaries. And then many manual works have done in these field. There are still so many paper-based dictionaries to be processed.

Convnets are driving advances in semantic segmentation and object recognition. So FCNs are introduced to transfer paper-based dictionaries into electronic dictionaries for various kinds of applications. Firstly these dictionaries are scanned into electronic images. And then these image are pre-processed, semantic segmented, recognized with an OCR engine, finally indexed, as shows in Fig1-A.



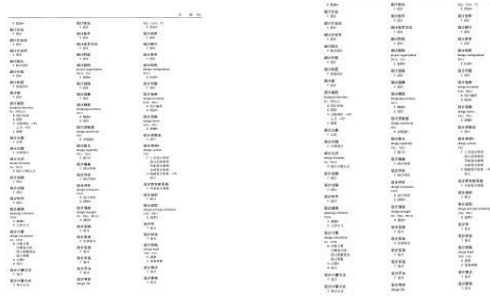
A: The workflow of self-understanding of a paper-based dictionary with a scanner. B an electronic image

Fig 1. The workflow of self-understanding of a paper-base dictionaries and an example of its electronic images .

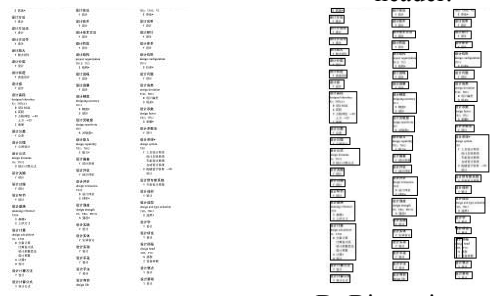
3.1. Pre-processing

An standard processed image is very important for FCNs, which are used for segmentation and recognition.

An image, captured from a page of a paper-based dictionary with a scanner, is pre-processed before it is segmented and recognized. These pre-processes include removal of header and footer, distortion, and binary.



A: The original image. B: removal of edges including footer and header.



C: a transformed image D: Binary image and primary contours

Fig.2 Performance of pre-processing of a captured image

3.2. Contour templates of entries

In Chinese dictionaries, entries are classified into different types and nested in other entries. Some entries have child entries. And child entries have their own child entries.

Contour templates of entries are introduced into the semantic segmentation. Before segmentation is done, an entry contour template set is built according to the entry types, such as follows in Fig 3.



Fig 3. Contour templates of entries

© The 2018 International Conference on Artificial Life and Robotics (ICAROB2018), Feb. 1-4, B-Con Plaza, Beppu, Oita, Japan

3.3. Semantic segmented using FCNs

According to the FCNs provided by J. Long et al, each net is decapitated by discarding the final classifier layer, and convert all fully connected layers to convolutions. a 1×1 convolution with channel dimension 21 is appended to predict scores for each of the PASCAL classes (including background) at each of the coarse output locations, followed by a (backward) convolution layer to bilinearly upsample the coarse outputs to pixelwise outputs.

In our FCNs, the perimeter of the contour of an entry are appended into loss functions.

4. Experiments

We selected a serial of paper-base Chinese dictionaries, which have more than 13,000 papers and 2.1 millions of entries. In our method, a page of Chinese paper-dictionaries is scanned into an electronic image. And then the electronic image is preprocessed, including un-distortion, side scrapping, binarization, and so on. Finally, using an end-to end deep learning method, the pre-processed electronic image is intelligently segmented, text recognized, and context understood.

In the procedure of scanning, about 1000 pages were manually adjusted. In pre-processing. In addition, pre-processing is vital to the final recognition performance.

And its correct rate of self-understanding of Chinese phrases is more than 99.5%. Its performance has proved it's availability.

5. conclusion

This paper apply FCNs into self-understanding of Chinese paper-dictionaries. The procedure includes scanning, pre-processing, semantic segmentation, and OCR recognition. Its performance has proved it's availability.

But this method will be improved in the following fields, including pre-processing, loss function of FCNs, and contour templates.

Acknowledgements

The research is partly supported by Information Production Line Construction (Phase I), Beijing Municipal Financial Grant: Information Production Line Construction (Phase I)(PXM2017_178214_000005), Special Grant for Reform and Development of BISTI (2017).

References

1. D. C. Cireşan, A. Giusti, L. M. Gambardella, and J. Schmidhuber. Deep neural networks segment neuronal membranes in electron microscopy images. In NIPS, pages 2852–2860, 2012. 1, 2, 4, 7
2. C. Farabet, C. Couprie, L. Najman, and Y. LeCun. Learning hierarchical features for scene labeling. *Pattern Analysis and Machine Intelligence, IEEE Transactions on*, 2013. 1, 2, 4, 7, 8
3. P. Fischer, A. Dosovitskiy, and T. Brox. Descriptor matching with convolutional neural networks: a comparison to SIFT. CoRR, abs/1405.5769, 2014. 1
4. Y. Ganin and V. Lempitsky. N4-fields: Neural network nearest neighbor fields for image transforms. In ACCV, 2014. 1, 2, 7
5. R. Girshick, J. Donahue, T. Darrell, and J. Malik. Rich feature hierarchies for accurate object detection and semantic segmentation. In *Computer Vision and Pattern Recognition*, 2014. 1, 2, 7
6. S. Gupta, R. Girshick, P. Arbelaez, and J. Malik. Learning rich features from RGB-D images for object detection and segmentation. In ECCV. Springer, 2014. 1, 2, 8
7. B. Hariharan, P. Arbelaez, R. Girshick, and J. Malik. Simultaneous detection and segmentation. In *European Conference on Computer Vision (ECCV)*, 2014. 1, 2, 4, 5, 7, 8
8. K. He, X. Zhang, S. Ren, and J. Sun. Spatial pyramid pooling in deep convolutional networks for visual recognition. In ECCV, 2014. 1, 2
9. A. Krizhevsky, I. Sutskever, and G. E. Hinton. Imagenet classification with deep convolutional neural networks. In NIPS, 2012. 1, 2, 3, 5
10. J. Long, N. Zhang, and T. Darrell. Do convnets learn correspondence. In NIPS, 2014. 1
11. F. Ning, D. Delhomme, Y. LeCun, F. Piano, L. Bottou, and P. E. Barbano. Toward automatic phenotyping of developing embryos from videos. *Image Processing, IEEE Transactions on*, 14(9):1360–1371, 2005. 1, 2, 4, 7
12. P. H. Pinheiro and R. Collobert. Recurrent convolutional neural networks for scene labeling. In ICML, 2014. 1, 2, 4, 7, 8
13. P. Sermanet, D. Eigen, X. Zhang, M. Mathieu, R. Fergus, and Y. LeCun. Overfeat: Integrated recognition, localization and detection using convolutional networks. In ICLR, 2014. 1, 2, 4
14. K. Simonyan and A. Zisserman. Very deep convolutional networks for large-scale image recognition. CoRR, abs/1409.1556, 2014. 1, 2, 3, 5
15. C. Szegedy, W. Liu, Y. Jia, P. Sermanet, S. Reed, D. Anguelov, D. Erhan, V. Vanhoucke, and A. Rabinovich. Going deeper with convolutions. CoRR, abs/1409.4842, 2014. 1, 2, 3, 5
16. N. Zhang, J. Donahue, R. Girshick, and T. Darrell. Partbased r-cnns for fine-grained category detection. In *Computer Vision—ECCV 2014*, pages 834–849. Springer, 2014. 1
17. J. Long, E. Shelhamer, T. Darrell. The IEEE Conference on Computer Vision and Pattern Recognition (CVPR), 2015, pp. 3431-3440.

A Multi-robot Rescuing System

Huailin Zhao¹, Zheng Wu², Xiaoxing Wang³

^{1,2,3}*School of Electrical and Electronic Engineering,
Shanghai Institute of Technology, Shanghai 201418, China
E-mail: 964003999@qq.com*

Abstract

The study subject is a multi-agent system consisting of a few mobile robots. In the system, each robot collaborates with the other ones, and they all work together to complete the disaster rescuing tasks such as the fire fighting. The multi-agent system control theory is applied in the system, where each mobile robot is an independent intelligent individual. The robots communicate wirelessly among them. Even though there is trouble with the individual robots, the others will collaborate among them in time and adjust their control policy to ensure the system itself working normally and complete the disaster rescuing task. In the system, an upper computer is designed for supervising, human-machine interfacing and being the transferring station of the data exchange. The experiment shows that the multi-robot distributed control system based on WIFI, GPS and INS information is able to achieve the consistent action such as rescue gathering.

Keywords: multi-agent system, cooperative control, WIFI communication.

1. Introduction

With the development of the robot and artificial intelligence, the intelligent robot technology has gradually become an important strategy in the high-tech field¹. Its application has covered many aspects, including service robots in daily life, exploring robots used in the ocean or space, the rescuing robot used in this research, and so on². Compared to the single robot with limited performance and high cost, the multi-robot cooperation system can meet different occasions, improve work efficiency, and reduce cost. The other robots in the multi-robot system can change their control strategy autonomously in case that there is trouble with a small amount of robots³. This project uses smart vehicles as the robots. In the collaboration system, the smart vehicles exchange their motion information such as speed, position, and the moving direction by wireless communication, make judgment and control decision independently, collaborate actively, so as to improve the system efficiency⁴.

2. System overview

The multi-vehicle system applies the distributed control theory that every smart vehicle is an integrated individual and can carry out information processing and decision-making on its own⁵. The redundancy and scalability of the system is significantly increased, relative to the centralized top-down control one. Even some individual smart vehicles become invalid, the rest adjust their control strategies timely by active collaboration to avoid paralysis of the whole system⁶.

2.1 Design of the smart vehicle hardware

The whole system is made up of two smart vehicles temporarily that will be extended to three smart vehicles

or more in the future. In the rescue collaboration, each smart vehicle needs to know the motion information of itself and the others in time, so it needs to configure GPS navigation module, inertial navigation module and WiFi communication module⁷.

The project temporarily uses an upper computer as the communication interface between the two smart vehicles, and is used to assist system monitoring at the same time.

Each smart vehicle uses the microcontroller STM32 as the control core, which is the 32-bit of 64kb or 128kb memory microprocessor based on ARM core, with good performance and cheap price. The GPS navigation module selects ATK-NEO-6M, the inertial navigation module MPU6050, and the WiFi module ATK-ESP8266, which are produced by the company ALIENTEK. The three modules communicate with STM32 separately.

The STM32 has 4 serial ports, with 4 USART data registers and 8 pairs of pins for the chip. In this project, serial port 1 connects to the WiFi module, serial port 2 to the inertial navigation module, and serial port 3 to the GPS navigation module.

The specific hardware structure is shown in Figure 1.

Figure 2 shows the serial communication pin relationship of the controller STM32 which uses 4 pins including PA9, PA10, PB10 and PC11.

2.2 Design of the smart vehicle software

The collaboration algorithms and the related data are completed in the main loop. And the data with the wireless module, GPS navigation module, inertial navigation are completed by the serial interrupt programs. Figure 3 shows the flow chart of the smart vehicle software.

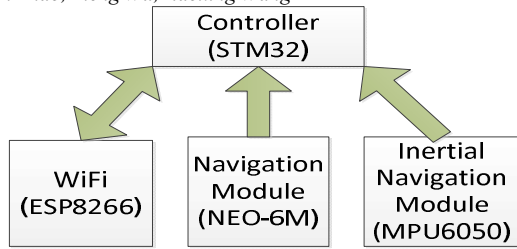


Fig. 1. Hardware structure of the smart vehicle

Serial Port	RXD	TXD
1	PA10	PA9
2	PA3	PA2
3	PB11	PB10
4	PC11	PC10

Fig. 2. Pin connection of the controller

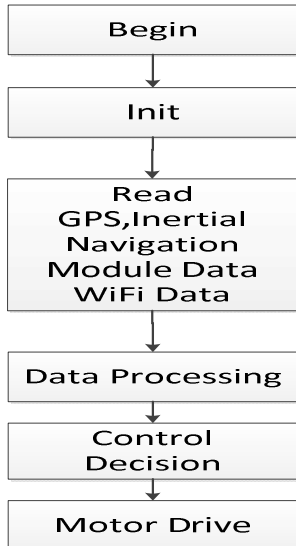


Fig. 3. Flow diagram of the smart vehicle

3 Design of the communication program

ATK-ESP8266 is the high-performance UART - WiFi module made by the company ALIENTEK, it is the core unit of ESP8266 module made by the company AI - THINKER. The module certified by FCC and CE meets the European and American standard⁸.

The WiFi module supports the communication modes including AP, STA, AP+STA. And it supports any IP node as a server or client. This project uses the PC as AP and the server, and the smart vehicles as STA and the client. The server supports multiple connections and the client supports passing through. In other words, the client is set to pass through and connected to the server. Therefore the STM32(client) can directly

communicate with the upper computer⁹. Figure 4 shows the diagram of the system communication.

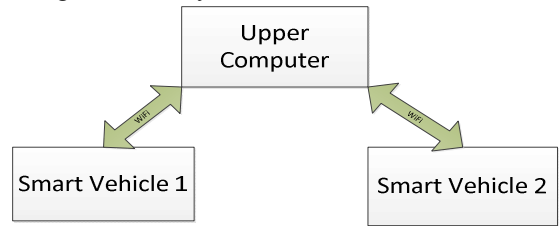


Fig. 4. Diagram of the system communication

3.1 Design of the WiFi communication protocol

First, the AT instruction is sent to the WiFi module by a serial helper to carry on the configuration of the layer aggregation module. The configuration contents are saved to the flash of the module so that the configuration can be the default later. The communication protocol is very important for this kind of data volume, multi-point communication system. The communication protocol is as follows:

- Check whether the data is correct by agreement.
- Determine the data source, such as vehicle No.1 or vehicle No.2.

The agreement applied in this project includes the following items:

- The general agreement: frame end with '\r\n'.
- The STM32 sends the GPS address to the upper computer, and the data starts with alphbat 'R', longitude, latitude, and ends with '\r\n'.
- From the upper computer to the STM32, the GPS data is sent three times. The data format is as follows: latitude 1, longitude 1: latitude 2, longitude 2: latitude 3, longitude 3. A comma is used to separate the latitude and the longitude. And a colon is used to seprate each group of the data.

3.2 Data formation

Because there is no pass through mode on the service , there must be an AT instruction before the upper computer sends the data. Command: AT+CIPSEND= channel number, character length '\r\n'. In other words, the number of data characters sent by the upper computer must be fixed¹⁰.

3.3 Data receiving and processing

Regardless of that the upper or lower computer is receiving data, the frame tail should be judged.

Starting from the upper computer, the protocol format of the STM32 is R, latitude, longitude, because the upper computer does not exist pass through, the module will add a message, so the actual effect received is +IPD: channel number: character length: R,latitude, longitude '\r\n'.

For example:
 AT+CIPMUX=1
 OK
 AT+CIPSERVER=1,5000
 OK
 0,CONNECT
 +IPD,0,1:1

+IPD	Channel number	Characters long	R	latitude	longitude	\r	\n
------	----------------	-----------------	---	----------	-----------	----	----

Table 1. Data receiving format

The key to the recognition is that +IPD can be represented by the smart vehicle. The channel number can identify the data from that vehicle, and the R represents the beginning of the data, and finally the latitude and longitude are separated by a comma.

4. Design of the navigation module

GPS is based on satellite positioning and time transfer, and GPS positioning function is widely used in modern measurement and modern construction.

4.1 Introduction to the NMEA-30183 protocol

NMEA-30183 is the standard format developed by the national Marine electronics association used of electronic equipment in the sea. It has become a unified RTCM standard protocol for GPS navigation devices.

This project uses \$GPRMC standard location information.

The basic format of the \$GPRMC is as follows:

\$GPRMC,(1),(2),(3),(4),(5),(6),(7),(8),(9),(10),(11),(12)*hh(CR)(LF)

Among them:

- (1) UTC time, HHMMSS(hour,minutes,second)
- (2) Positioning status, A= valid location, V= invalid location
- (3) Latitude ddmm.mmmmm
- (4) Latitude hemisphere N (northern hemisphere) or S (southern hemisphere)
- (5) Longitude ddmm.mmmmm
- (6) Longitude hemisphere E (east longitude) or W (west longitude)
- (7) The rate of the ground
- (8) The moving direction of the ground
- (9) UTC date ddmmyy
- (10)Magnetic declination
- (11)Direction of magnetic deflection, E (east) or W (west)
- (12)Mode indication (A = autonomic positioning, D= difference, E= estimation, N= data invalid)

The GPS module used in this experiment can be accurate to 5 decimal places. The accuracy of STM is accurate to meters. The conversion process is listed below:

On the longitude line, the latitude is one degree difference, the the actual distance is about 111 kilometers; On the latitude line, the longitude is one

degree difference, the actual distance is $111 * \cos\theta$ kilometers. θ refers to the Shanghai is located in east longitude $120^{\circ} 51' - 122^{\circ} 12'$, north latitude $30^{\circ} 40' - 31^{\circ} 53'$.The decimal is the latitude 120.85-122.02, longitude 30.67-31.8. The units are degrees, which are the integer parts that the GPS module reads, which means you can also read the decimal point five places on this basis.

Accuracy is:

$$\begin{aligned} \text{latitude} &: \Delta S_{\text{min}} = 111\text{km} * 10^{-5} = 1.1\text{m} \\ \text{longitude} &: \Delta S_{\text{min}} = 111\text{km} * \cos \text{latitude} * 10^{-5} \end{aligned} \quad (1)$$

In fact, the accuracy of the module fluctuates within a certain range, and the measured accuracy is about 3-5 meters.

4.2 Design of the data processing and filtering program with the GPS module

The reading of the whole data is interrupted by USART serial port. After I receive my cache, according to NMEA 0183 to judge strings on the cache. judging the USART3_RX_BUF[t] received a 'G' and 'C' in the interrupt, if it is, then received a string "\$GPRMC", then enter the Data_change () function to determine character and the last to turn a string into a U32.

The Data_change() is function that according to the postion of the comma to judge what data and the length of the string. For example, the data after the third comma representation of latitude, and the data between third and fourth comma is the length of the latitude data string. In the process need to put the string into digital quantity.

Due to the precision of the GPS module, the GPS data will jump in a small range , so after successfully stored data, the data of the STM32 will average filtering. Data will be received into a length of 5 array DataN [I], after average filtering through the sum divided by five.

Code:

```
((DataN[0]+DataN[1])/2+(DataN[2]+DataN[3])/2+DataN[4])/3
```

Here is not divided by five directly. This is to prevent overflow.

4.3 Design of the data processing and filtering program with the inertial navigation module

Due to the accuracy and response speed of the GPS, can't timely feedback direction, so the introduction of inertial navigation module MPU6050 compensation. MPU6050 is the 6 axis accelerometer gyroscope. three axis acceleration, three axis gyroscope. STM32 reads MPU6050 measurement data. MPU6050 module with kalman filtering, therefore, STM32 reads the data has been through filtering processing.

5 Motion control and collaboration algorithm

STM32 direct output PWM wave and can adjust the pulse width, so as to control servo motor rotating speed and direction. Motor servo system can realize high precision control, make sure that motion state of the motor can be timely follow the specified input values change. Servo motor receives many pulse, will turn the corresponding angle, so as to realize position control.

5.1 Structure of the control system

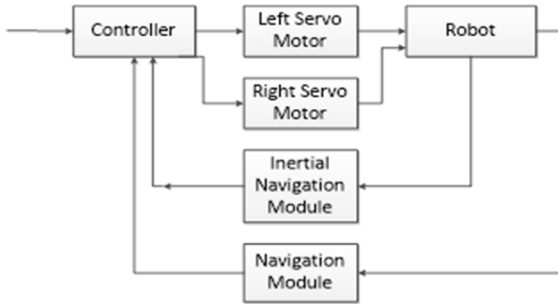


Fig. 5. Servo motor control system

The whole movement control structure as shown in the figure 5. With double closed-loop control, the right motor control direction and location at the same time, the left motor control position. Inner ring MPU6050 inertial navigation module corrects the angle, The current value of the GPS plus angle offset of MPU6050 to measure minus GPS target direction as input values . The right motor only responsible for the control direction. But due to the left motor movement, right motor must have the output to a stable direction¹¹.

As the direction control make PI, continuous correction of the course of the deviation, call function math.h () and the inverse trigonometric function atan (), with latitude divided by precision to calculate the declination, the same method of calculating the heading angle, and the heading angle plus MPU6050 as the offset, finally, the offset minus the heading angle¹². Parameter tuning using the first P after I method. Due to the relationship between motor speed and GPS sampling speed, the pure proportional link of the outer ring has little effect on the system. The inner parameters have larger impact. First through the test to get the appropriate Kp then add Ki¹³.

$$\frac{MV}{200} = Kp \frac{angle}{1000} + Ki \sum \frac{angle}{32767} \quad (2)$$

$$angle = \text{atan}(\text{latitude}/\text{longitude})$$

The above formula, MV is output, angle is deviation of angle, 32767 is the length of the short. To cooperate with MPU6050 output and use range¹⁴.

5.2 Collaborative algorithm

Assuming the car is S1 away from the target location and the distance between the two cars is S2, In order to

prevent the two cars from colliding with each other, we need a safe distance. Taking into account the accuracy of the GPS module, the safety distance is set to 2.5 meters. In the process of gathering two cars, S1 and S2 will be smaller and smaller, when the distance of S2 is less than or equal to 2.5, the number two car will take the position of number one car as the setting value¹⁵.

6 Experimental tests and conclusions

6.1 Kp setting

Let's set Kp firstly. We do this way: changing the car's orientation and then let it move self-driven. The software Tracker is used to track its tracking. The waveform is shown in Fig.6.

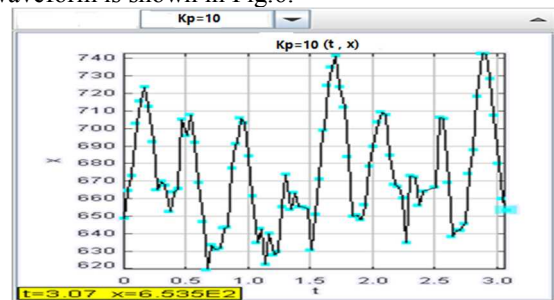


Fig. 6. Stability curve with Kp = 10

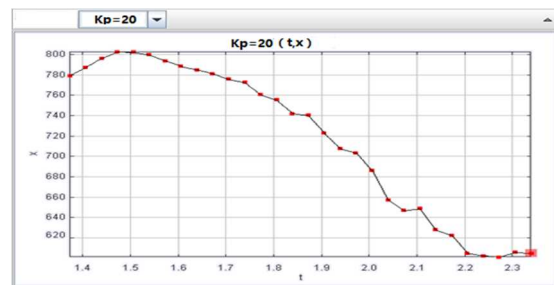


Fig. 7. Stability curve with Kp = 20

Comparing with Figure 6 and Figure 7, the system is stable when Kp = 20. Therefore, we set Kp=20.

6.2 Ki setting

Now Let's set Ki. Too large integration may result in poor stability. Figure 8 shows that with Ki=5.

Figure 9 shows that with Ki=2. Compared to Figure 8, the system is more stable. Therefore we simply set Ki=2.

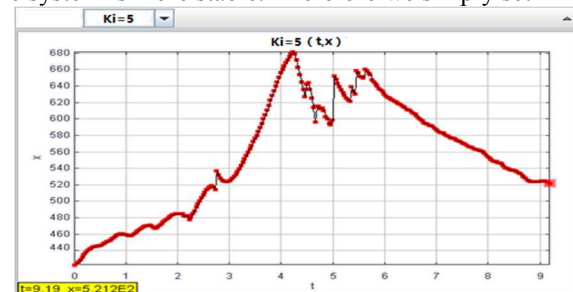


Fig. 8. Stability curve with Ki = 5

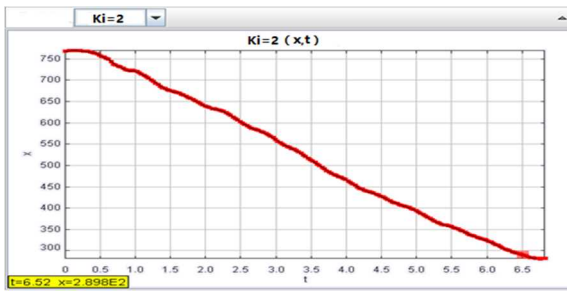


Fig. 9. Stability curve with $K_i = 2$

6.3 Collaborative experiment

In the end, the two vehicles can communicate with each other, keeping the distance of 70 cm in motion. Normally, two vehicles stay within 2m.



Fig. 10. Collaborative experimental

6.4 Conclusion

The robot rescue system, consisting of two smart vehicles, is able to realize the inner communication between the two vehicles and coordinate movement. The two vehicles don't collide with each other during the following-up movement. The next step is to achieve collaboration among three smart vehicles or more. And the whole system will remove the upper computer to achieve direct communication among the smart vehicles.

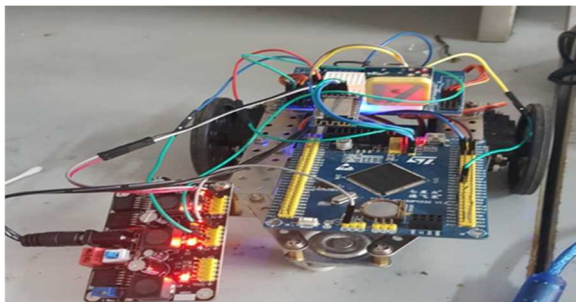


Fig. 11. Smart vehicle

References:

1. Weston J Wratkils C. Multi-class Support Vector Machines. Royal Holloway College, 1998 : 726. 732
2. Yawei Hou, Huailin Zhao. Handwritten Digit Recognition Based on Improved BP Neural Network.

- The 13th Chinese Intelligent Systems Conference (CISC2017, Oct. 14-15, Mudanjiang, China).
3. Huailin Zhao, Yawei Hou, Shifang Xu, Congdao Han, Masanori Sugisaka. Research on a Method of Character Recognition for Self-learning Errors. The 2017 International Conference on Artificial Life and Robotics (ICAROB 2017), Jan.19-22, Miyazaki, Japan, p190-193.
4. Krebel U Pairwise classification and support Vector machines. Cambridge MA : MIT Press, 1999 : 255 ~256
5. Huailin Zhao, Shunzhou Wang, Shifang Xu, Yani Zhang, Masanori Sugisaka, A Method of Detecting Abnormal Crowd Behavior Events Applied in Patrol Robot. Journal of Robotics, Networking and Artificial Life. Vol. 4(1), 2017, p77-80.
6. Huailin Zhao, Yangguang Guo, Masanori Sugisaka, Design of the Multi-Car Collaboration System, the 2017 International Conference on Artificial Life and Robotics (ICAROB 2017), Jan. 19-22, Miyazaki, Japan, p186-190.
7. Qiwen Zheng, Zhongyu Shen. Research on collaborative control system of multi-smart car based on wireless communication network. Nanjing normal university, 2012
8. Huailin Zhao, Xuyao Hao, Albert Wang, Chao Li, Design and implementation of an intelligent cooking robot based on Internet of things. Lecture Notes in Electrical Engineering. Vol.338, 2015, p423-430.
9. Huailin Zhao, Masanori Sugisaka, "Simulation study of CMAC control for the robot joint actuated by McKibben muscles", Applied Mathematics and Computation (ISSN0096-3003), Vol.203, 2008, p457-462.
10. Wang zhiwen, guo ge. 2003. Mobile robot navigation technology and prospect [J]. Robot. 25(5):470-474.
11. Shunzhou Wang, Huailin Zhao, Weiren Wang, Huijun Di, Xueming Shu. Improving Deep Crowd Density Estimation via Pre-Classification of Density. The 24th International Conference on Neural Information Processing (ICONIP2017, Nov.14-18, 2017, Guangzhou, China).
12. Yawei Hou, Huailin Zhao. Handwritten Digit Recognition Based on Depth Neural Network. 2017 International Conference on Intelligent Information and BioMedical Science (ICIIBMS2017, Nov.24-26, 2017, Okinawa, Japan).
13. Haitao Ou, WeiDong Zhang, Wenyan Zhang, etc., based on the intelligent traffic control system of multi-agent technology. Electronic journal, 2000(12) : 52.55
14. Huailin Zhao, Bei Wang, "Configuration of the Mckibben Muscles and Action Intention Detection for an Artificial Assistant Suit", International Journal of Advanced Robotic Systems (ISSN 1729-8806), Vol. 9, 2012, p1-7.
15. Huailin Zhao, Wei Ren, Consensus Problem of Distributed Multi-agent Systems, Proceedings of the 2015 International Conference on Artificial Life and Robotics (ICAROB 2015), Japan, p201-206.

Dynamic Analysis and FPGA implementation of A Novel Hyper-Chaotic System with One Equilibrium Point

Shanfeng Wang, Hongyan Jia, Zhiqiang Guo

Department of Automation, Tianjin University of Science and Technology,
1038 Daguanlu Road, Hexi District, Tianjin 300222, PR China

E-mail: jiahy@tust.edu.cn

www.tust.edu.cn

Abstract

In recent decades, the study on the chaotic system and hyper-chaotic system attracts more and more interest with developing of non-linear subjects. This paper firstly presents dynamic numerical analysis of a novel hyper-chaotic system with one equilibrium, which includes, bifurcation diagram, Lyapunov exponent and so on. Then, based on the method of converting continuous-time differential equation to discrete-time differential equation, FPGA (Field Programmable Gate Array) implementation for the novel hyper-chaotic system is finished, and the results from FPGA implementation are consistent with those from numerical analysis. The work in this paper may provide a method for the application of the hyper-chaotic system.

Key words: Hyper-chaotic system; one equilibrium; dynamic characteristics; FPGA

1. Introduction

Since Lorenz chaotic system is found in 1963^[1], Chaos research becomes gradually a hot topic. Especially, in recent decades, with developing of science and technology, many new chaotic systems are presented, including Chen system^[2], Liu system^[3], and so on^[4-6]. On the other hand, some hyper-chaotic systems also are generated on the basis of the chaotic systems, such as Lorenz hyper-chaos^[7, 8], four-dimensional non-autonomous hyper-chaos^[9], and so on^[10, 11].

At the same time, circuit implementation of chaotic systems attracts more and more interest, such as chaotic systems control circuit, chaotic synchronization circuit^[12], chaotic generation circuit^[8, 11], and chaotic digital circuit^[13-15], etc. Particularly, because the hyper-chaotic systems have unpredictability more than chaotic system, the application of hyper-chaotic system has become a hot topic. So, it is necessary for application of chaotic system to design chaotic circuit.

In this paper, a novel one equilibrium hyper-chaotic system based on Lü chaotic system is presented. Although this hyper-chaotic system has one equilibrium, it has complex dynamic character. Therefore, the chaotic characteristics is analyzed, including bifurcation diagram, Lyapunov exponent diagram and so on. On the basis of numerical analysis, the FPGA implementation of the novel hyper-chaotic system will be introduced. According to the result of experiment, it may provide a method for the application of the hyper-chaotic system.

2. The hyper-chaotic system

A novel hyper-chaotic system with only one equilibrium point is introduced by ref[16], which is described by (1):

$$\begin{cases} \dot{x} = a(y - x) \\ \dot{y} = -xz + cy - w \\ \dot{z} = xy - bz \\ \dot{w} = ky \end{cases} \quad (1)$$

Where x, y, z, u is status variable, and a, b, c is parametric variable of the system. The new system shows chaotic dynamic characteristics, when the initial value is $(1, 1, 1, 1)$ and $a = 36, b = 3, c = 20, k = 10$, and the hyper-chaotic attractors of the system (1) are shown in Fig. 1,

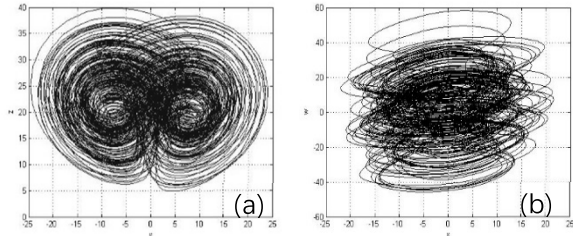


Fig. 1. Phase portraits of hyper-chaotic system (1):
(a) $y-z$ plane; (b) $x-w$ plane

3. The dynamic character of the novel hyper-chaotic system

Now, when parameters a, b, k is fixed as $a = 36, b = 3, k = 10$, the dynamic behaviors of novel hyper-chaotic system (1) are discussed with variety of parameter c .

3.1 bifurcation diagram

Bifurcation diagram can describe the property of system with variety of parameter. The bifurcation diagram of system (1) is shown in Fig. 2.

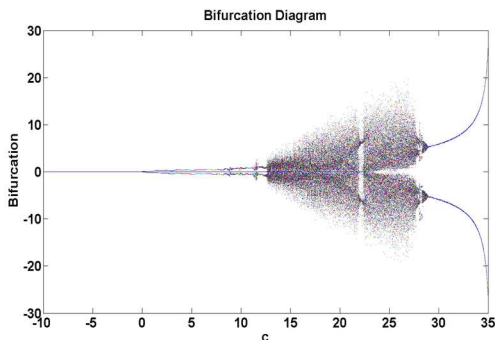


Fig. 2. Bifurcation diagram of system (1)

Generally, according to the bifurcation theory, the system (1) has no chaotic attractor, when bifurcation diagram is one line; the system (1) is periodic, when points is several lines in bifurcation diagram; the system (1) will show

chaotic character, when points are dense in bifurcation diagram. Obviously, when $c < 0$, chaos is not discovered in this new system; when $0 < c < 13, c = 22$ or $28 < c$, the system shows periodicity or cycle; and when $13 < c < 22$ or $22 < c < 28$, the system shows chaos.

Next, to further explain the character of system (1), the Lyapunov exponent is presented in this paper.

3.2 Lyapunov exponent

Lyapunov exponent can describe the characteristics of chaotic motion. Because the fourth Lyapunov exponent (LE4) is always negative value on region of $-10 < c < 35$, the three Lyapunov exponents (LE1, LE2, LE3) are provided. The Lyapunov exponent of system (1) is shown in Fig. 3.

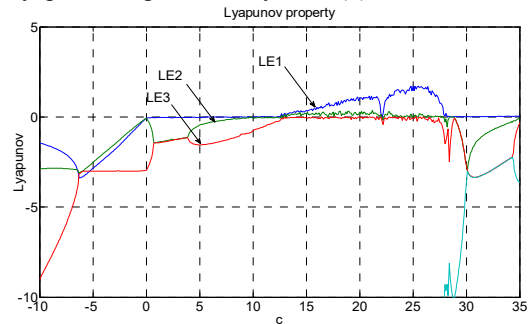
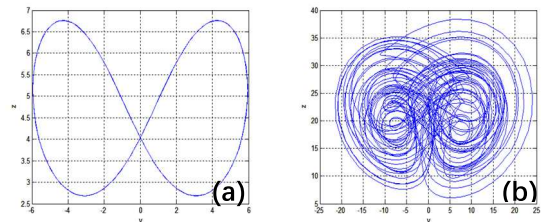


Fig. 3. Lyapunov exponent of system (1)

According to Lyapunov exponent theorem, the system shows chaotic dynamics, when it only includes a positive Lyapunov exponent. Therefore, from the Fig. 3, chaos can be not discovered in system (1), when parameter $c < 0$; the system (1) shows quasi periodicity or cycle, when parameter $0 < c < 13, c = 22$ or $28 < c$; the system (1) shows chaos, when parameter $13 < c < 22$ or $22 < c < 28$. the chaotic behavior of system (1) can be proved from Lyapunov exponents and bifurcation diagram. Similarly, the phenomenon can also be described by phase trajectory, as shown in Fig. 4.



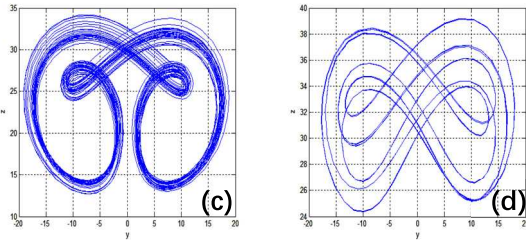


Fig. 4. The phase trajectory of y-z phase plane (a) $c = 5$; (b) $c = 15$; (c) $c = 22$; (d) $c = 28$

4. FPGA implementation of hyper-chaotic system

At present, some analog circuits of chaotic system are introduced^[9, 16]. However, some disadvantages are discovered in the implementation of analog circuit. Therefore, implementation of digital circuit attracts more and more interest. In this paper, the method of digital circuit is introduced.

4.1 Bilinear Transformation Method

The method of converting a continuous-time integer order integral operator to discrete-time differential equations is called IIM (Impulse Invariance Method). According to this method, the step is as follows.

The continuous-time integer order operator is described, as follows:

$$H(s) = \frac{1}{s} \tag{2}$$

The discrete-time integral operator is obtained by using IIM. As follows:

$$H(z) = T \frac{z}{z-1} \tag{3}$$

Where T is sample frequency.

According to discrete-time transfer function(3), the model of integer order integral operator is found by using DSP Builder Library on Matlab/Simulink platform^[14]. As follows:

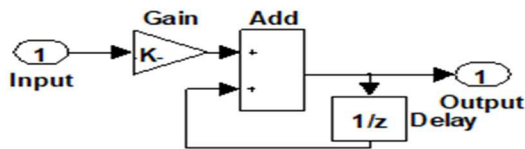


Fig. 5. The model of integer order integral operator

4.2 FPGA implementation

As compared with other processors, FPGA is a dedicated hardware in processing logic. And the working way of FPGA is parallel compute, which using hardware description language to achieve the design of systems^[13, 15]. FPGA is a better tool to show chaotic or hyper-chaotic attractor^[14]. The process of FPGA implementation is shown in Fig. 6. The experiment results are obtained, as showed in Fig 6. The results are in agreement with the results of the numerical analysis, which physically proves the system (1)

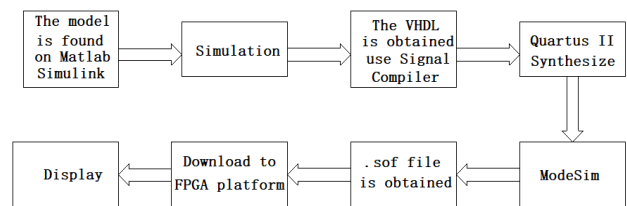


Fig. 6. The process of FPGA implementation

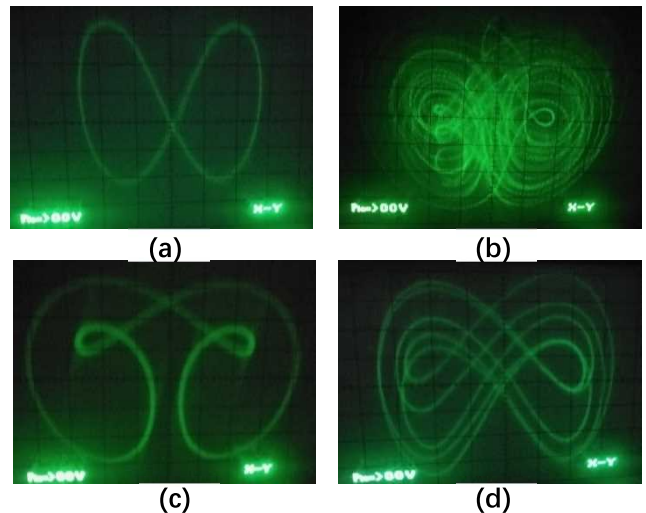


Fig. 7.The results of FPGA implementation y-z phase plane: (a) $c = 5$; (b) $c = 15$; (c) $c = 22$; (d) $c = 28$;

5. Conclusion

In this paper. Firstly, a hyper-chaotic system with only one equilibrium point is introduced. Secondly, the dynamic characteristics of the hyper-chaotic system is discussed, including bifurcation diagram, Lyapunov exponents diagram and phase trajectory diagram. Thirdly, the method of

FPGA implementation is presented, and the experimental results is obtained in FPGA hardware platform. Finally, it can be concluded that the hyper-chaotic system with only one equilibrium can show chaos dynamic, and the FPGA implementation provides a method for the application of the hyper-chaotic system.

Acknowledgements

The research is partly supported by the Research Fund for the National Natural Science Foundation of China (Grant No.61573199). It is also supported by the Young Scientists Fund of the National Natural Science Foundation of China (Grant No.11202148).

References

- 1 Edward N. Lorenz. Deterministic Nonperiodic Flow [J]. *Journal of Atmospheric Sciences*, 1963, 20(2): 130-41.
- 2 Guanrong. Chen, T. Ueta. Yet another chaotic attractor [J]. *Int J Bifurcat Chaos*, 1999, 9(7): 1465-6.
- 3 Chongxin Liu, Tao Liu, Ling Liu, et al. A new chaotic attractor [J]. *Chaos Solitons & Fractals*, 2004, 22(5): 1031-8.
- 4 Jinhu Lu, Guanrong Chen. A new chaotic attractor coined [J]. *Int J Bifurcat Chaos*, 2002, 12(3): 659-61.
- 5 Leon O Chua, Motomasa Komuro, Takashi Matsumoto. The double scroll family [J]. *IEEE Transactions on Circuits & Systems*, 1986, 33(11): 1072-118.
- 6 Sundarapandian Vaidyanathan. *Adaptive Controller and Synchronizer Design for the Qi-Chen Chaotic System* [M]. Springer Berlin Heidelberg, 2012.
- 7 Yuxia Li, Wallace KS Tang, Guanrong Chen. Generating hyperchaos via state feedback control [J]. *Int J Bifurcat Chaos*, 2005, 15(10): 3367-75.
- 8 Yuxia Li, Guanrong Chen, W. K. S. Tang. Controlling a unified chaotic system to hyperchaotic [J]. *IEEE Transactions on Circuits & Systems II Express Briefs*, 2005, 52(4): 204-7.
- 9 Shijian Cang, Guoyuan Qi, Zengqiang Chen. A four-wing hyper-chaotic attractor and transient chaos generated from a new 4-D quadratic autonomous system [J]. *Nonlinear Dynamics*, 2010, 59(3): 515-27.
- 10 Cheng Hsien Chen, Long Jye Sheu, Hsien Keng Chen, et al. A new hyper-chaotic system and its synchronization [J]. *Nonlinear Analysis Real World Applications*, 2009, 10(4): 2088-96.
- 11 ShiJian Cang, ZengQiang Chen, ZhuZhi Yuan. Analysis and circuit implementation of a new four-dimensional non-autonomous hyper-chaotic system [J]. 2008,
- 12 G. Grassi, S. Mascolo. Design of nonlinear observers for hyperchaos synchronization using a scalar signal; proceedings of the IEEE International Symposium on Circuits and Systems, F, 2002 [C].
- 13 M. F. Tolba, A. M. Abdelaty, N. S. Soliman, et al. FPGA implementation of two fractional order chaotic systems [J]. *Aeu-Int J Electron C*, 2017, 78(162-72).
- 14 Guangyi Wang, Xulei Bao, ZhongLin Wang. Design and FPGA Implementation of a new hyperchaotic system [J]. *Chinese Physics B*, 2008, 17(10): 3596-602.
- 15 Roger Woods, John Mcallister, Richard Turner, et al. *FPGA-based Implementation of Signal Processing Systems* [J]. Wiley Publishing, 2008, 15(15): 153-68.
- 16 HongYan Jia, ZengQiang Chen, ZhuZhi Yuan. A novel one equilibrium hyper-chaotic system generated upon Lü attractor [J]. *Chinese physics B*, 2010, 19(2): 020507.

Analysis and Circuit Implementation for a New Fractional-Order Chaotic System

Zhiqiang Guo, Hongyan Jia, Shanfeng Wang

¹ College of Electronic Information and Automation,
Tianjin University of Science and Technology, China;

E-mail: jiahy@tust.edu.cn

Abstract

This paper firstly recommends a new fractional-order chaotic system, only including six terms and three multipliers, which is different from the Lorenz and other existing fractional-order systems. Then the phase trajectory diagrams, Lyapunov exponents diagrams and bifurcation diagrams will be showed to investigate the different dynamical characteristics based on this chaotic system. At last, an analog circuit is designed to implement the system, further verify the effectiveness in practical application.

Keywords: fractional-order chaotic system, Lyapunov exponents, bifurcation, circuit implementation

1. Introduction

Chaos is a special form of motion of nonlinear dynamical systems, which has been widely studied in the past few decades¹⁻³. Since the chaos phenomenon has been found in large number of fractional-order systems, the dynamic characteristics of the fractional system have begun to attract more and more interest. At present, some fractional-order chaotic systems have been proposed and researched, such as the fractional-order Lorenz system⁴, the fractional-order Chen system⁵, the fractional-order Lü system⁶, and the fractional-order Qi system⁷.

Now, fractional-order chaotic systems have been investigated in some factors, such as dynamic characteristics⁸⁻⁹, circuit implementation¹⁰⁻¹¹, synchronization¹²⁻¹³, and secure communication¹⁴ of the chaotic system. Furthermore, the fractional-order systems are more complex to be implemented by analog circuits than integer-order systems. Therefore, in order to investigate the fractional-order systems and apply them in some practical engineering, it is very necessary and meaningful to design hardware circuits to implement them.

This paper based on a new fractional-order chaotic system, firstly discusses and analyzes the basic dynamic

characteristics. And the phase trajectory diagrams, Lyapunov exponents diagrams and bifurcation diagrams are showed to verify them. At last, an analog circuit is designed to implement this fractional-order chaotic system, and the results of circuit implementation and numeral simulation are similar. Thus, this new fractional-order chaotic system can be applied in the project.

2. A new fractional-order chaotic system

Recently, a new chaotic system is investigated¹⁵, and the basic dynamic characteristics have been showed, such as phase trajectory, Lyapunov exponents, bifurcation, etc. The dynamic equation of the new chaotic system is

$$\begin{cases} \dot{x} = -ax + byz \\ \dot{y} = cy - dxz \\ \dot{z} = -kz + mxy \end{cases} \quad (1)$$

Where, a , b , c , d , k and m are the system parameters, and when $a = 4$, $b = 3$, $c = 1$, $d = 7$, $k = 1$, $m = 2$, the system is chaotic. The system (1) can be translated into fractional-order form as:

$$(2) \quad \begin{cases} \frac{dx^\alpha}{dt} = -ax + byz \\ \frac{dy^\beta}{dt} = cy - dxz \\ \frac{dz^\gamma}{dt} = -kz + mxy \end{cases}$$

Where, a, b, c, d, k and m are the system parameters, x, y, z are state variables, and $\alpha = \beta = \gamma = 0.9$ is fractional order. In order to analyze the different states of the chaotic system, the Lyapunov exponents and bifurcation diagrams are firstly given to investigated them. When fixing the system parameters $a = 5, b = 3, d = 5, k = 1, m = 2$, selecting $c \in [0, 6]$, and setting the initial value of the system to $(1, 1, 1)$, the Lyapunov exponent diagrams and bifurcation diagram of this system are showed in Fig.1 and Fig.2, respectively. Obviously, when selecting $c \in [1.4, 4]$, the system shows chaos. Particularly, when $a = 5, b = 3, d = 5, k = 1, m = 2$, and fixing $c = 3$, the chaotic phase trajectory diagrams are given in Fig.3.

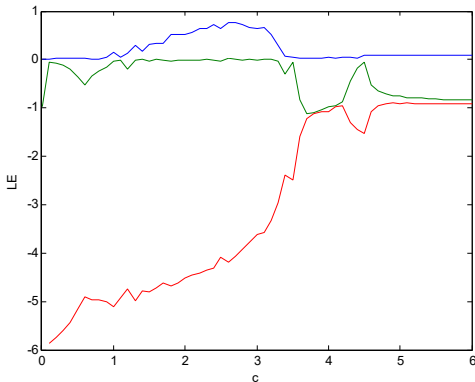


Fig.1. Lyapunov exponents diagram when $a = 5, b = 3, d = 5, k = 1, m = 2$, varying c .

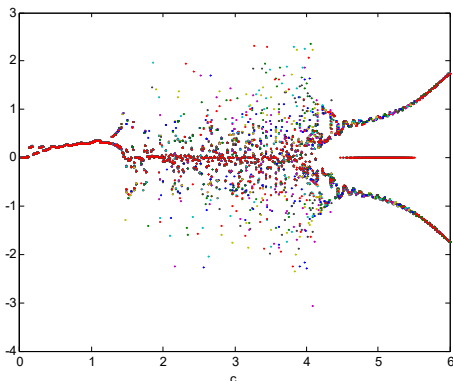


Fig.2. Bifurcation diagram when $a = 5, b = 3, d = 5, k = 1, m = 2$, varying c .

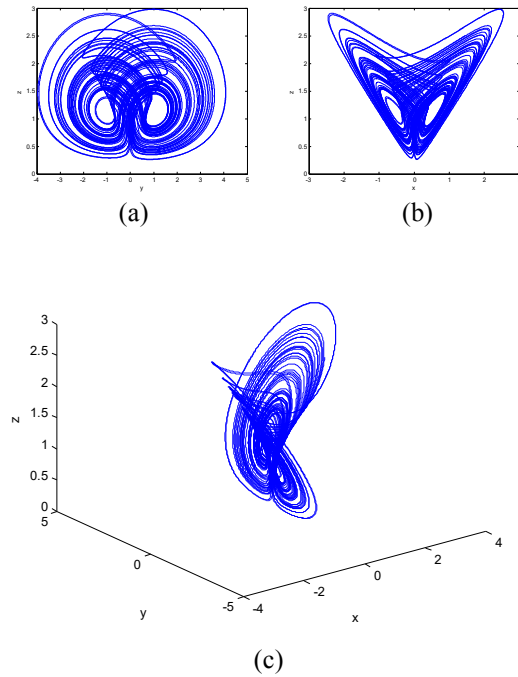
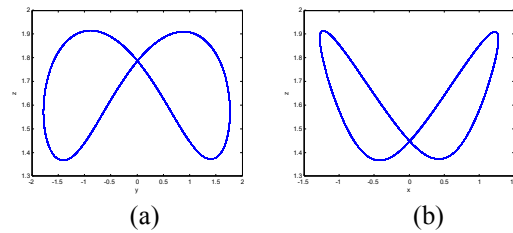


Fig.3. Chaotic phase trajectory diagrams, when $a = 5, b = 3, c = 3, d = 5, k = 1, m = 2$: (a) $y - z$ plane; (b) $x - z$ plane; (c) $x - y - z$ plane.

Furthermore, it can be seen that the fractional-order system shows period state, when $a = 5, b = 3, d = 5, k = 1, m = 2$, and selecting $c \in [4, 6]$, from Fig.1 and Fig.2. Particularly when fixing $c = 5$, the period phase trajectory diagrams are showed in Fig.4.



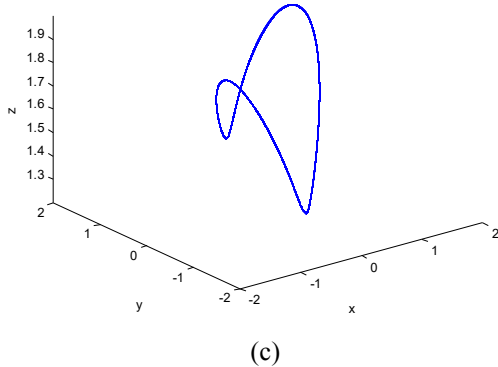


Fig.4. Period phase trajectory diagrams, when $a = 5$, $b = 3$, $c = 5$, $d = 5$, $k = 1$, $m = 2$: (a) $y - z$ plane; (b) $x - z$ plane; (c) $x - y - z$ plane.

3. Circuit implementation

The method of approximation conversion from time domain to frequency domain is adopted to design a circuit for the novel system (2). Based on Bode diagrams, the approximation of $1/s^{0.9}$ with discrepancy 2dB is described as follows:

$$\frac{1}{s^{0.9}} \approx \frac{2.2675(s+1.292)(s+215.4)}{(s+0.01292)(s+215.4)(s+359.4)} \quad (3)$$

There, the unit circuits can be used to achieve the $1/s^{0.9}$ unit, as shown in Fig.5.

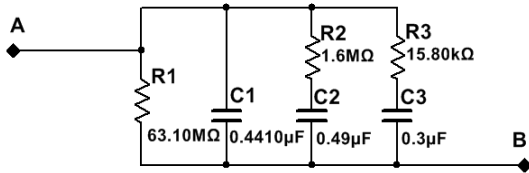


Fig.5. Circuit unit of the $1/s^{0.9}$

Then, an analog circuit is designed to implement this fractional-order system by the circuit unit of the $1/s^{0.9}$, which is showed in Fig.6.

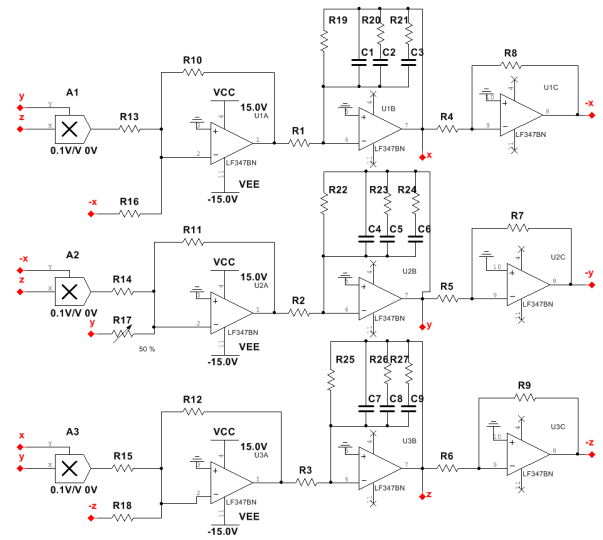
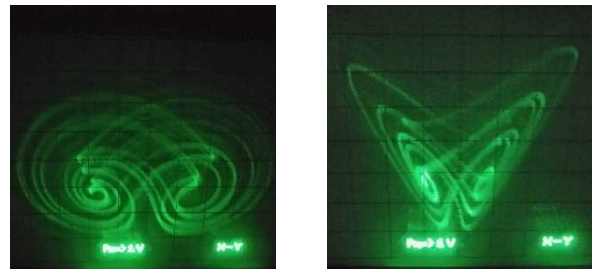


Fig.6. Analog circuit of system (2)

Where the electronic components mainly include resistors, capacitors, the amplifier LF347BN and the analog multiplier AD633 (output gain is 0.1). Parameters of the analog circuit for the system are $R_1 = R_2 = R_3 = R_4 = R_5 = R_6 = R_7 = R_8 = R_9 = R_{10} = R_{11} = R_{12} = 10K\Omega$, $R_{13} = 3.33K\Omega$, $R_{14} = 3.33K\Omega$, $R_{15} = 5K\Omega$, $R_{16} = 20K\Omega$, $R_{18} = 100K\Omega$, $R_{19} = R_{22} = R_{25} = 63.10M\Omega$, $R_{20} = R_{23} = R_{26} = 1.6M$, $R_{21} = R_{24} = R_{27} = 15.8K\Omega$, $C_1 = C_4 = C_7 = 0.4410\mu F$, $C_2 = C_5 = C_8 = 0.49\mu F$, $C_3 = C_6 = C_9 = 0.3\mu F$, and the R_{17} is variable resistor. When $R_{17} = 33.33K\Omega$, the system (1) shows chaos, and the results of circuit implementation are showed in Fig.7. If changing $R_{17} = 20K\Omega$, corresponding system shows period state, the results are showed in Fig.8. The results of numerical simulation and circuit implementation are similar, Comparing Fig.1, Fig.2 with Fig.7, Fig.8, respectively. Thus, this new fractional-order chaotic system can be implemented.



(a) (b)

Fig.7. The results of circuit implementation, when $a = 5$, $b = 3$, $c = 3$, $d = 5$, $k = 1$, $m = 2$: (a) $y - z$ plane, (b) $x - z$ plane.

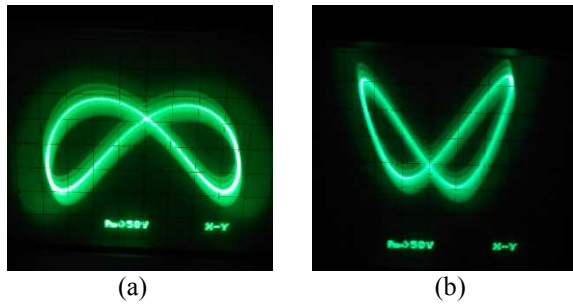


Fig.8. The results of circuit implementation, when $a = 5$, $b = 3$, $c = 5$, $d = 5$, $k = 1$, $m = 2$: (a) $y - z$ plane, (b) $x - z$ plane.

4. Testing and conclusion

In this paper, a new fractional-order chaotic system is investigated. By the numerical simulation, phase orbits diagrams, the Lyapunov exponents diagrams, and bifurcation diagrams of the proposed system are also given to verify its dynamic characteristic. At last, an analog circuit is designed to implement this system, and some circuit results observed by the oscilloscope are given to show chaos and period can be generated in the new fractional-order system from the viewpoint of physics.

Acknowledgements

The research is partly supported by the Research Fund for the National Natural Science Foundation of China (Grant No.61573199). It is also supported by the Young Scientists Fund of the National Natural Science Foundation of China (Grant No.11202148).

References

1. Shihua Li, Haixing Cai, Research on circuitry realization and synchronization of Chen chaotic systems, *Acta Phys. Sin.*, 53(2004), 1687-1693.
2. Chunguang Li, Guanrong Chen: Chaos in the fractional order Chen system and its control. *Chaos, Solitons and Fractals* Vol. 22 (2004), p. 549
3. Guanrong Chen, Ueta T, Another chaotic attractor, *Int. J. Bifurc. Chaos*, 9(1999), 1465-1466.
4. Yongguang Yu, Hanxiong Li, Sha Wang, and Junzhi Yu, Dynamic analysis of a fractional-order Lorenz chaotic system. *Chaos, Solitons and Fractals* Vol. 42 (2009), p. 1181.
5. Changpin Li, Guojun Peng, Chaos in Chen's system with a fractional order. *Chaos, Solitons and Fractals* Vol. 22 (2004), p. 443
6. Junguo Lu, Chaotic dynamics of the fractional-order Lü system and its synchronization. *Physics Letters A* Vol. 354 (2006), p. 305
7. Yanling Guo, Guoyuan Qi, Topological horseshoe in a fractional-order Qi four-wing chaotic system. *Journal of Applied Analysis and Computation* Vol. 5(2015), p. 168
8. Junguo Lu, Guanrong Chen, A note on the fractional-order Chen system. *Chaos, Solitons and Fractals* Vol. 27 (2006), p. 685
9. Yongguang Yu, Hanxiong Li, Sha Wang, and Junzhi Yu, Dynamic analysis of a fractional-order Lorenz chaotic system. *Chaos, Solitons and Fractals* Vol. 42 (2009), p. 1181.
10. Hongyan Jia, Qinghe Wang, Qian Tao, Wei Xue, Analysis and Circuit Implementation for the Fractional-order Chen System. *Chaotic Modeling and Simulation* 2016; 3: 299-308.
11. Hongyan Jia, Qian Tao, Zengqiang Chen, Analysis and circuit design of a fractional-order Lorenz system with different fractional orders, *Systems Science & Control Engineering: An Open Access Journal* 2014; 2: 745-750.
12. Cang Shijian, Chen Zengqiang, et al., Projective synchronization of fractional-order memristive systems with different structures based on active control method. *International Journal of Sensor Networks* 2013; 14: 102-108.
13. Weihua Deng, Changping Li, Chaos synchronization of the fractional Lü system, *Physica A*, 353(2005), 61-72.
14. Hongyan Jia, Qinghe Wang. Synchronization of two four-wing fractional-order chaotic system and its applications in secure communication, *Atlantis Press* 2016; 60: 1005.
15. P. Gholamin, A.H. Refahi Sheikhani. A new three-dimensional chaotic system: Dynamical properties and simulation, *Chinese Journal of Physics*, 55 (2017): 1300-1309.

Application of a Conservation Chaotic System in Image Encryption

Shilong Liu, Mei Zhang, Wei Xue*

*College of Electronic Information and Automation,
Tianjin University of Science and Technology, China;*

*E-mail: * xuwei@tust.edu.cn
771398586@qq.com
www.tust.edu.cn*

Abstract

In this paper, the dynamic behaviors of a conservative system are analyzed based on its phase trajectory, Poincaré map, Lyapunov spectrum. On this basis, the conservative system is applied to digital image encryption and the security performance of the algorithm is analyzed and verified. The conservative system also has the characteristics of pseudo randomness and similar noise, whose safety is high, and is not easy to be cracked. Therefore, the conservative system has a quite high research value and application prospect.

Keywords: Conservative; Chaotic system; Numerical simulation; Algorithm; Image encryption.

1. Introduction

In 1954, Kolmogorov, the former Soviet Union master of probability, delivered the famous paper "Hamiltonian function with minor changes in conditions of periodic motion to maintain", which lays the foundation for the conservative system to produce chaos theory. In 1963, Lorenz E N, an American meteorologist, discovered the first chaotic attractor-Lorenz attractor in dissipative systems and then delivered a paper "Deterministic Nonperiodic Flow"¹, which reveals a series of basic properties of chaotic motion, such as deterministic aperiodicity, extreme sensitivity to initial values, long-term behavior unpredictability, and so on. His research opened a new door for the development of chaos and greatly inspired the enthusiasm of scholars for the study of chaos at home and abroad. Subsequently, many new systems have been proposed to promote the rapid development of chaotic dynamics theory, such as Chen system², Lü system³, Liu system⁴, Qi system⁵, and so on. The chaotic signal based on the conservative system

has potential application value in image encryption and secure communication⁶.

With the rapid development of 4G network and period of big data, a variety of image information spread rapidly on the network. However, these information are faced with the threat of stealing and destruction. How to transmit information safely and effectively becomes the focus of attention. Due to high initial sensitivity, unpredictability and similarity of the broadband power spectral density and other prominent features, the chaotic signal has natural concealment. Even if two identical chaotic systems with a very small difference in initial conditions, their movement orbit will soon become irrelevant. In early 1990, Matthews⁷ first applied the chaotic system to the image encryption algorithm. In the early stage, the low-dimensional chaotic system is applied to image encryption. Although the low-dimensional chaotic system was designed easily, the random sequence acquired was fast.⁸ However, low complexity and low security is easy to be captured by reconstructing the attractor's embedded delay to decipher

the information.⁹ The conservative chaotic system has the characteristics of pseudo-randomness, similar to noise.¹⁰ More importantly, there is no obvious chaotic attractor in the conservative system. Different initial values can lead to different kinetics, which makes conservative chaos for image encryption with obvious advantages.¹¹ Image encryption based on chaotic system processes digital image that makes the cipher-text image disorder, covers the plaintext information and achieves the effect of image encryption.¹² In this paper, the application of the conservative chaotic system proposed in literature 13 has been studied in image encryption.

2. Numerical analysis of a conservative chaotic system

In the literature 13, a new four-dimensional autonomous dynamical conservative chaotic system is constructed. The system contains four quadratic terms. The sum of the quadratic term and the primary term coefficients is also 0. The mathematical model as follows:

$$\begin{cases} \frac{dx}{dt} = ayw \\ \frac{dy}{dt} = xz \\ \frac{dz}{dt} = -xy + bw \\ \frac{dw}{dt} = -axy - bz \end{cases} \quad (1)$$

On evaluating the dissipativity of the new system, it is found that the divergence flow of (1) is conservative if and only if $\nabla V = 0$.

$$\nabla V = \frac{\partial \dot{x}}{\partial x} + \frac{\partial \dot{y}}{\partial y} + \frac{\partial \dot{z}}{\partial z} + \frac{\partial \dot{w}}{\partial w} = 0 \quad (2)$$

Calculation manifests that the theoretical value of ∇V is 0. Hence the system is conservative.

When the system parameters are taken $a = 10, b = 5$, and system initial value is $(1, -1, 1, -1)$, the conservative system phase trajectory show in Fig.1:

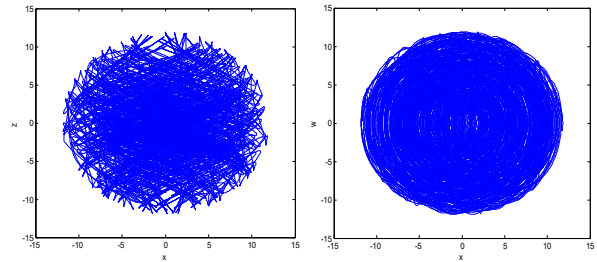


Fig.1 Phase portraits of system (1)

Fig.2 is the Poincaré map of the system (1) with the above parameters at $z=1$ and $y=1$. It can be seen that the x-y cross section and z-w cross section generate a dense and fractal point set. The system is chaotic.

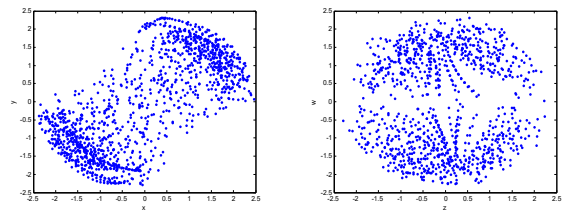


Fig.2 Poincaré map

The Lyapunov exponent can display motion characteristics of the system. Its positive and negative values and size in one direction, denotes the degree of divergence or convergence of the adjacent orbits in the attractors for a long time.¹⁴ In order to describe the overall effect of nonlinear dynamics, the Lyapunov exponent is obtained by averaging the stretching or compressing rate of each point of the motion track after a long time. The Lyapunov exponent of the system is shown in Fig.3. When $b=5.3$, there are $L_1=1.7075, L_2=0.0975, L_3=-0.0781$ and $L_4=-1.7375$, respectively. The results show that the exponential value are approximately symmetric with the X-axis, and the system (1) is conservative.

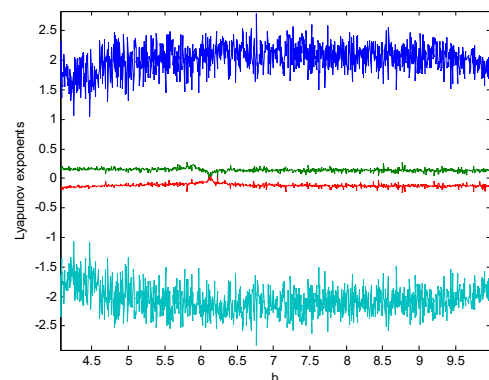


Fig.3 Lyapunov exponent spectrum of system (1)

3. Research on encryption algorithm based on conservation chaotic system

3.1. Encryption process

Color images are made up of red, green, and blue, while they are stored in the form of matrix in the computer. The image is encrypted by using the space-based scrambling diffusion algorithm. Firstly, three primary colors are separated from the color image. We can get three primary color matrixes I_{R1} , I_{G1} , I_{B1} . Secondly, the key, which is composed of system parameters and initial values, is inserted into the chaotic system to generate chaotic sequence. The three primary color matrixes I_{R2} , I_{G2} , I_{B2} are obtained by XOR encryption operation with I_{R1} , I_{G1} , I_{B1} trichromatic matrixes and chaotic sequences. Finally, the encrypted image is synthesized by the encrypted three primary color matrix. The original image encryption results are shown in Fig.4:



Fig.4 Encryption results of the original image

3.2. Decryption process

The process of decrypting a ciphertext image is the inverse of the encryption. First of all, the encrypted three primary color matrixes I_{R2} , I_{G2} , I_{B2} are separated from the ciphertext image. The key is inserted into the chaotic sequence generated by the chaotic system. According to the sequence matrix, the image is performed by XOR inverse operation. Then the sequence generated by the chaotic sequence is used to scramble the pixel position of the three primary color matrix after XOR decryption. Finally, the original image is synthesized by the three primary color matrix. Decryption results are shown in Fig.5.



Fig.5 Decryption results of the original image

4. Algorithm security performance analysis

4.1. Histogram analysis

The grayscale histogram describes the number of pixels in each gray scale. The G component before and after encryption are shown in Fig.6. It can be seen from the diagram that the distribution of the pixels on each gray level fluctuates greatly before encryption. Because the difference of points is large, the distribution of image information is obvious. After encryption, the distribution of each grayscale pixel points is more uniform and less fluctuant. It can effectively covers the distribution rule of pixels in the original image. Meanwhile, it also can resist the attack of statistical analysis and enhance the security of image information.

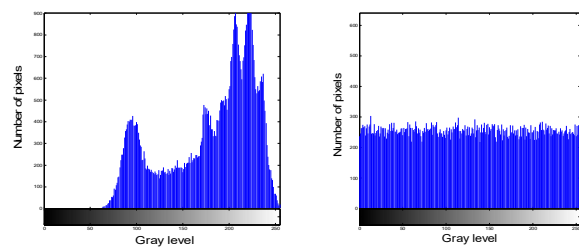


Fig.6 Histograms before and after image encryption

4.2. Adjacent pixel correlation analysis

Tab.1 shows the correlation coefficients of the image pixel in various directions. From the original image and encrypted image, the pixels of one row and one column are taken to calculate the correlation coefficient of adjacent pixels. The correlation coefficients of the adjacent pixels in the horizontal and vertical directions are shown in Tab.1:

Tab.1 The correlation of adjacent pixels

Different images	Different directions	
	Horizontal direction	Vertical direction
The original image R pixel matrix	0.97757	0.9555
Encrypted image R pixel matrix	0.0042708	0.001601
The original image G pixel matrix	0.97161	0.94387
Encrypted image G pixel matrix	0.00021523	0.0022991
The original image B pixel matrix	0.95435	0.92538

Encrypted image	0.00039443	0.003629
B pixel matrix		

It is easy to see that the correlation coefficient of the adjacent pixels in original image approaches 1. The coefficient indicates a high correlation between an adjacent pixel and the other. The correlation coefficient of the encrypted image is close to 0, and the adjacent pixel points are basically irrelevant. Therefore, the algorithm has good security for statistical analysis.

4.3. Key sensitivity test

The system parameter $a=10$, $b=5$, and the initial value are set to $(1, -1, 1, -1)$. In this condition, we encrypt the image. When you enter the correct key, the image can be accurately decrypted. If we change the initial value as $y_0 = -1.000000001$, other initial values and parameter values are unchanged, the image decryption fail. As shown in the Fig.7, it can be seen that extremely small key changes cannot successfully decrypt the image, which indicates the high sensitivity to the key in this system.

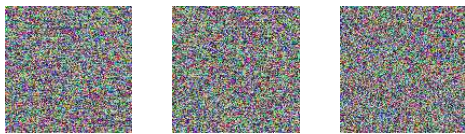


Fig.7 Decryption result of the wrong key

5. Conclusion

In this paper, the chaotic characteristics of a conservative chaotic system are analyzed by plotting the phase trajectories, Lyapunov exponential graph and Poincaré cross section map. According to the chaotic sequence generated by the system (1), the digital image is encrypted and decrypted by pixel scrambling. The application of image encryption in image encryption is studied. Finally, the security performance of the image before and after encryption are analyzed, such as the histogram, the correlation of neighboring pixels and the key sensitivity. The results show that the encryption algorithm based on this system has a good security, reliability and application value.

Acknowledgements

The research is partly supported by the Research Fund for the National Natural Science Foundation of China (Grant

No.61573199). It is also supported by the Young Scientists Fund of the National Natural Science Foundation of China (Grant No.11202148).

References

1. Lorenz E N. Deterministic non-periodic motion [J]. *Atoms Sci.* 1963, 20(2): 130-141.
2. Chen G R, Ueta T. Yet another chaotic attractor [J]. *International Journal of Bifurcation and Chaos.* 1999, 9(7): 1465-1466.
3. Lü J H, Chen G R. A new chaotic attractor coined [J]. *International Journal of Bifurcation and Chaos.* 2002, 12(3): 659-661.
4. Liu C X, Liu L, Liu T et al. A new butterfly-shaped attractor of Lorenz-like system [J]. *Chaos, Solitons and Fractal.* 2006, 28(5): 1196-1203.
5. Qi G Y, Chen G R, van Wyk M A, et al. A four-wing chaotic attractor generated from a new 3-D quadratic autonomous system [J]. *Chaos, Solitons and Fractals.* 2006, 28(5): 1196-1203.
6. CANG Shijian, WU Aiguo, WANG Zhonglin, XUE Wei. Chaotic Behavior of a Generalized Hamiltonian System and Its Circuit Implementation [J]. *Complex Systems and Complexity Science.* 2017, 14 (1) :103-110
7. Matthews. On the Derivation of a "Chaotic" encryption algorithm [J]. *Cryptologia.* 1989, 13(1): 29-42.
8. Huang L L, Xin F, Wang L Y. Circuit implementation and control of a new fractional-order hyper-chaotic system[J]. *Acta Physica Sinica.* 2011, 60(1): 010505-1-010505-9.
9. Grigorenko I, Grigorenko E. Chaotic dynamics of the fractional Lorenz system [J]. *Physical Review Letters.* 2003, 91(3): 034101-1-034101-4.
10. Q. Zhang, H. Zhang, Z. Li, One-way Hash function construction based on conservative chaotic system, in: *Information Assurance and Security*, 2009
11. Shijian Cang, Aiguo Wu, Ruiye Zhang, Nose-Hoover-like system: Theoretical analysis and numerical demonstrations, *Preprint submitted to Applied Mathematical Modelling*, 2017
12. Wang Q Y, Zhou S B. Image encryption algorithm based on fractional-order Chen chaotic system [J]. *Journal of Computer Applications.* 2013, 33(4): 1043-1406.
13. Cang Shijian, Wu Aiguo, Wang Zenghui. Four-dimensional autonomous dynamical systems with conservative flows: two-case study [J]. *Nonlinear Dynamics.* 2017, 89:4
14. XUE Wei, XIAO Hui, Xu Jinkang, JIA Hongyan. A fractional-order hyper-chaotic system and its application in image encryption [J]. *Journal of Tianjin University of Science & Technology.* 2015(5): 67-71

Study on Plant Disease Detection Based on Near Field Acoustic Holography

Xiuqing Wang*, Jiangfan Wang, Jimin Zhao, Qing Liu, Qi Chen

College of Electronic Information and Automation,
Tianjin University of Science and Technology, China

E-mail: *lwqly@163.com
www.tust.edu.cn

Abstract

In the process of crop cultivation, pests and diseases have the most obvious impact on crop growth, yield and quality. In order to quickly and effectively prevent pests and diseases, real-time understanding of crop growth, in order to reasonably accurately and accurately spraying pesticides based on disease information is particularly important. The key to implementing precision spraying is accurate positioning of crop diseases. In this paper, the main stem of plant is taken as the research object. Through the acquisition of acoustic emission signal, the acoustic field model of disease stress is established based on near-field acoustic holography, and the sound field of three-dimensional space is reconstructed by algorithm to analyze the sound field of the sound source. Identify the plant's sound source signals, locate the sound source location, make an effective judgment of the plant damage status, determine the disease situation, and establish the optimal control strategy.

Keywords: Disease detection, Near-field acoustic holography, Statistical best, Distribution source boundary point method

1. Introduction

Although China is a big agricultural country, the quality of grain is declining year by year. The main reason is that crop diseases are more serious and the technology for detecting plant diseases is not advanced enough. In order to effectively and accurately spray pesticides on plants, we need to develop a new method that can break the previous constraint of detecting plant diseases.

The study found that the acoustic emission signals produced by crops under certain conditions are one of the important sensitive information for understanding their growth status and disease status. Through acoustic holography [1-3], the study of acoustic emission signals can identify the source of acoustic emission and locate the plant disease defect site in the early stage without obvious symptoms, and can spray pesticides precisely and efficiently, effectively manage disasters and increase economic benefits.

2. Statistics optimal cylindrical near-field acoustic holography

2.1 Fundamental

Taking into account the stem of the plant as a cylinder, the use of cylindrical measurement can obtain more and more accurate sound field information to improve the reconstruction accuracy, it uses the cylindrical surface as a holographic reconstruction. From the wave equation, the Helmholtz equation can be obtained for a steady-state sound field that does not depend on time variables.

$$\nabla^2 p(x, y, z) + k^2 p(x, y, z) = 0 \quad (1)$$

Where ∇^2 is the Laplace operator, $p(x, y, z)$ is the complex sound pressure at the space point, $p(x, y, z)$ is a function of Cartesian coordinates x, y, z ; $k = \omega / c = 2\pi / \lambda$ is the acoustic wave number; c is the acoustic velocity; λ is the acoustic wavelength.

If the integral operation is regarded as a summation operation, $r=a$ is equivalent to the minimum cylinder

radius surrounding the sound source, the holographic cylinder radius $r=r_h$, and the position relationship between the reconstructed cylinder radii $r=r_s$ and $r=a$ are shown in Fig.1.

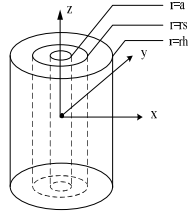


Fig.1. Cylindrical acoustic holographic simulation model

According to the above formula and the relationship between the holographic surface and the reconstructed surface and the smallest cylinder, the relationship between the two-dimensional Fourier transform of the sound pressure on the reconstructed cylinder and the holographic cylinder can be obtained as

$$p(r_s) \approx \sum_{n=1}^N C_n(r_s) p(r_{h_n}) = p^T c(r_s) = p^T (A^+ A + \varphi^2 I)^{-1} A^+ b \quad (2)$$

Equation (2) is NAH reconstruction formula based on the statistical optimal cylinder [4-6].

2.2 Numerical simulation

Simulation process is as follows:

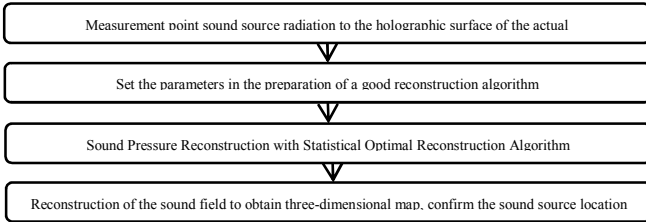


Fig.2. acoustic holographic algorithm flow chart

The experiment uses R15a acoustic emission sensor to measure, the resonant frequency of 150 kHz, the operating frequency range of 50 ~ 200 kHz, so choose 50 ~ 200 kHz as the simulation frequency range. By continuously modifying experimental parameters such as holographic cross-section radius and holographic cylindrical height, measuring point spacing and reconstructing cross-section radius, the parameter range to achieve the best simulation results is explored to realize sound source reconstruction.

Assuming that the acoustic emission signal is at the center of the plant axis, the acoustic field generated is assumed to be independent of the corner of the cylinder and changes only as the z-coordinate changes to reveal the cylinder surface. The raised position is the AE signal source position.

2.2.1 Single source simulation and analysis

The main variables affecting reconstruction accuracy are: reconstruction radius r_s , holographic measurement radius r_h , measurement height L , Holographic measurement point $M*N$, where M is the number of measurement points in the circumferential direction and N is the number of measurement points in the axial direction. This topic select the sound source frequency of 60 kHz simulation experiments, modify the relevant experimental parameters to find the best recognition effect. Without changing the number of holographic points, the number of holographic points selected is $9 * 9$. The radius of reconstructed radius, the radius and height of the holographic measurement surface, the distance between the reconstructed surface and the holographic surface are continuously adjusted, and the influence on the reconstruction effect is observed.

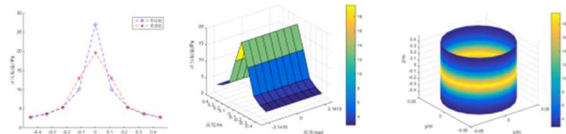


Fig.3. Reconstructed sound pressure map for $r_s = 0.045$ m, $r_h = 0.05$ m, $L = 0.9$ m

It can be seen from Fig.3 that the amplitude of the sound pressure of the sound source is conspicuous, and the reconstruction sound pressure of each measuring point is close to the corresponding theoretical sound pressure, which can realize sound source recognition.

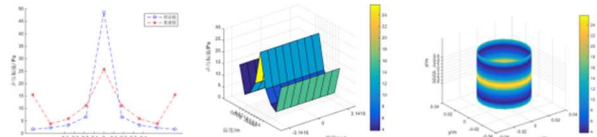


Fig.4. Reconstructed sound pressure diagram for $r_s = 0.025$ m, $r_h = 0.08$ m, $L = 1.45$ m

As can be seen from the experimental simulations in Fig.3, Fig.4 and more, several changes to the holographic measuring radius and height of the plant lead to the following conclusion:

- The maximum radius of the experimental subject (main stem of the plant) is 0.1 m and the maximum height is 1.5 m. When the change of the holographic cylinder radius exceeds 0.1m and the cylinder height exceeds 1.5 m, the adjustment of other parameters cannot achieve the expected reconstruction effect and the sound source cannot be identified.
- The reconstructed result is better when the ratio of reconstructed radius to holographic radius is greater than or equal to 0.4, which can accurately identify the sound source position. As the distance between the holographic surface and the reconstructed surface decreases, the reconstruction error decreases and the position of the sound source becomes more

and more prominent.

- Under the same parameter configuration, the reconstruction accuracy will decrease with the increase of the sound source frequency. Although the reconstruction results deviate from the theoretical results, the overall trend is unchanged and the sound source localization can still be achieved.
- The parameters of holographic measurement points, the height of holographic measurement surface, the radius of reconstruction surface and the radius of holographic surface are mutually influential. The accuracy of obtaining sound pressure information will increase with the height of holographic cylinder and the number of measurement points but the measurement points and cylinder height is too large or too small, will have an impact on the reconstruction results.

2.2.2 Multiple source simulation and analysis

Due to the special physiological characteristics of plants, acoustic emission signals do not occur singly. Therefore, noise sources with multiple frequencies should be simulated. In order to eliminate the influence of ambient noise on the reconstructed results, filtering needs to be performed. In this study, the windowing function of simultaneous filtering in the axial and circumferential directions proposed by Chen et al.

Based on the single-source simulation in this experiment, this section introduces noise at multi-source frequency $f_1=80\text{kHz}$, $f_2=100\text{kHz}$, $f_3=120\text{kHz}$ when $r_h=0.05\text{m}$, $r_s=0.045\text{m}$, the measurement point is 9×9 , and the height of measurement surface is 0.9m . The signal to noise ratio is 35 dB , and the introduction of the window function to filter noise.

Specific simulation results shown in Fig.5, Fig.6.

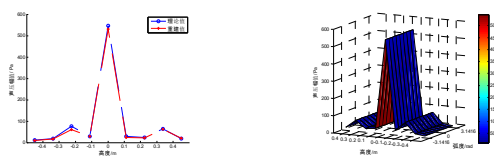


Fig.5. Reconstructed sound pressure map of filtered Three sound sources when $\alpha = 0.2$, $k_c = 17$

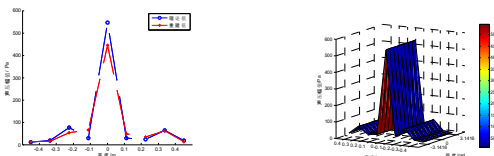


Fig.6. Reconstructed sound pressure map of filtered Three sound sources when $\alpha = 0.2$, $k_c = 20$

As can be seen from Figure 2-6 and Figure 2-7, although the filtered reconstruction value and the theoretical value may have errors, the location of the

sound source can still be judged.

In summary, the sound pressure information is acquired through the R15 acoustic emission sensor array, and the distribution of acoustic emission source locations under different disease levels can be obtained through the reconstruction algorithm. The localization of a sound source containing random noise can be achieved by adding a window function to perform spatial wave number domain filtering.

3. Distribution of source boundary point method

3.1. Fundamental

According to the consolidation deduction of the known formula, the sound pressure value on the reconstruction surface is obtained by singular value decomposition and generalized inverse transformation of the transfer matrix G_p , and the specific reconstruction formula is as follows:

$$p_c = G_p^+ p_q = V_p \sum p^{-1} U_p^H p_q \quad (3)$$

In the formula, the superscript "+" represents the generalized inverse; p_q is the M-order acoustic pressure vector on the holographic surface; and p_c is the reconstructed surface acoustic pressure.

3.2. Numerical simulation

3.2.1 Single source simulation and analysis

According to the size of the general plant radius, the radius of the holographic cylindrical surface is selected to be 0.01m , the radius of the reconstructed spherical surface is 0.009m , and the sound source is located in different positions for $f = 60\text{kHz}$. $f = 60\text{ kHz}$, assuming the sound source is located $d=0.006\text{m}$ from the center of the sphere (at the origin) in the direction of the 7th node.

Respectively $h=0.001\text{m}$; $h=0.003\text{m}$; $h=0.005\text{m}$; $h=0.007\text{m}$; compare the reconstructed value with the theoretical value, the result is shown in Fig.7.

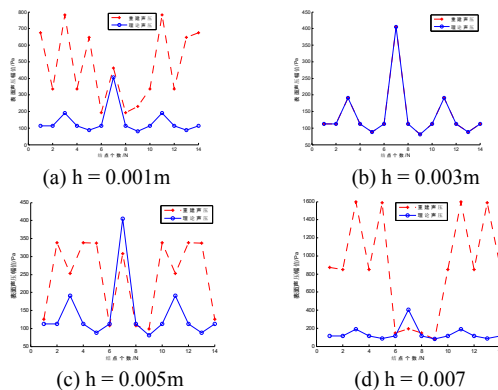


Fig.7. Comparison of reconstructed and theoretical values

It can be seen from the simulation diagrams (a), (b), (c) and (d) that when $f = 60$ kHz, the sound source is assumed to be located $d=0.006$ m from the center of the sphere in the direction of the 7th node with an interval of 0.002m from 0.001m to 0.008m, the final $h=0.003$ m, the reconstruction accuracy is high, the reconstructed value is consistent with the theoretical value, the other values of the reconstruction error is larger.

3.2.2 Dual sound source simulation and analysis

Since acoustic emission signals do not necessarily occur uniquely, different frequency sources can be represented by multiple frequency signals, each of which represents the signal after each acoustic emission signal passes through a narrow-band filter. According to the experimental results of single-source simulation parameters selection, $f_1 = 100$ kHz and $f_2 = 150$ kHz multi-source reconstruction, the reconstruction results in Fig.8.

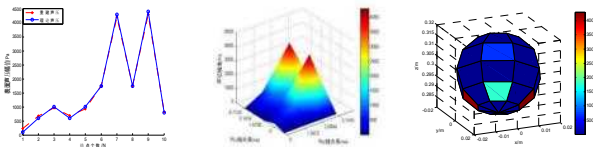


Fig.8. Reconstructed sound pressure diagram for Two-source (100,150 kHz)

4. Conclusion

In this paper, for the characteristics of plant disease stress, near-field acoustic holography is applied to the detection of plant diseases. The main stem of plant is taken as the research object. Based on the acoustic emission signal acquisition and near-field acoustic holography, the optimal cylindrical near-field acoustic holography and distributed source boundary point method were used to reconstruct the acoustic field information of the sound source surface so as to identify and locate the location of the acoustic emission source and determine the plant stress state. Through research, timely detection and identification of diseases, so as to establish the optimal prevention and control strategies to improve the control effect and reduce the cost of prevention and treatment.

The statistical optimal cylindrical near-field acoustic holography technology can accurately identify the position of the sound source, eliminate the window effect and winding error, and improve the reconstruction accuracy. However, this method can only be applied to the conformal surface, which is unavoidable limitations.

© The 2018 International Conference on Artificial Life and Robotics (ICAROB2018), Feb. 1-4, B-Con Plaza, Beppu, Oita, Japan

However, in this method, the measuring range of the main stem of the plant is larger than that of other methods, which makes it easier for us to study the disease situation of more plants.

Distribution of source boundary point method can avoid the problems of interpolation, numerical quadrature and singular integral in the algorithm. The reconstruction result is highly sensitive to introducing noise and can be regularized by singular value truncation filtering. The method can realize the reconstruction of any shape of the sound source, but also can make the holographic surface have more choices. The advantage is that high precision, fast, widely used.

Acknowledgements

The research is partly supported by the Research Fund for Tianjin Applied Basic and Advanced Technology Research Program (14JCZDJC39000) .

References

1. Haibin Zhang. Non - conformal surface near - field acoustical holographic theory and experimental study on steady circumstance sound field [D]. Shanghai: Shanghai Jiao Tong University, 2008. (in Chinese)
2. Yongbin Zhang. Near - field acoustic holography based on equivalent source method and particle velocity measurement [D]. Hefei: Hefei University of Technology, 2010. (in Chinese)
3. Jinquan Zhang. Noise source identification and sound field visualization based on beam forming technology [D]. Hefei: Hefei University of Technology, 2010. (in Chinese)
4. Williams E G . Regularization methods for near-field acoustical holography[J]. Journal of the Acoustical Society of America, 2001, 110(4):1 976~1 988.
5. Williams E G, Houston B H , Herdic P C, et al. Fast Fourier transform and singular value decomposition formulations for patch near-field acoustical holography[J]. Journal of the Acoustical Society of America, 2003, 114(3):1 322 ~1 333.
6. Moohyung Lee, Stuart Bolton J. A one - step patch near - field acoustical holography procedure[J]. Journal of the Acoustical Society of America, 2007, 122(3): 1 662 ~1 670.

Simulation of Cell Dielectric Properties Based on COMSOL

Shudong Li, Xiaoyan Chen*, Fengze Han

College of Electronic Information and Automation,
Tianjin University of Science and Technology, China;

E-mail: * cxywxr@tust.edu.cn
www.tust.edu.cn

Abstract

The dielectric properties of cells can be observed by injecting a low amplitude current at different frequencies (1MHz~100MHz). The simulation research is taken on the software platform named COMSOL Multiphysics. The electric field and the cell model is created with prior information. By simulation, it's verified that at low frequencies, the region of interest (ROI) behaves the conductivity characteristic while the electrical signal cannot pass through the cell membrane due to its capacitor properties. With the excitation frequency increasing, the ROI behaves more permittivity characteristic that the current flowing through the cell membrane becomes more and the current density increases. The research of the cell dielectric properties provides an auxiliary method to diagnose the status of the cell.

Keywords: dielectric properties, cell model, excitation frequency, finite element method (FEM), auxiliary method

1. Introduction

1.1 Cell structure

From the biological point, cells are the smallest units that constitute the biological tissues. Most biological cells consist of cell fluid and membrane. The cell fluid can be divided into intracellular fluid and extracellular fluid as shown in Fig.1. Intracellular fluid can be regard as saline solution which consists of water mainly, inorganic salt and other metabolite. Extracellular fluid provides the living environment for cells with appropriate PH value, saline concentration and so on. Both of the two fluids have good electrical conductivity^[1].

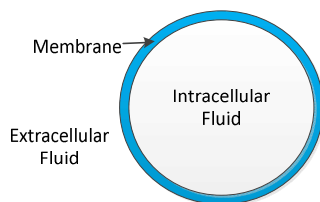


Fig.1. Simplified single cell structure model

The cell membranes are composed of insulating bilayer phospholipid and proteins. The membranes separate the intracellular and extracellular fluid. However, water and some micro-molecular proteins can exchange between intracellular and extracellular fluid through membranes. This is because membranes are permeable selective due to the structure of itself.

1.2 Cell dielectric properties

The specified cell structure determines its special electrical characteristics. When a direct current or a low frequency alternating current is applied to the cell, the current cannot flow into the cell because of the insulated membrane. This behavior is called low-frequency dielectric property. When the excitation frequency gradually increasing, the membrane becomes electrically invisible and the current can inject into the cell by passing through the membrane. This performance can be defined as high-frequency dielectric property^[2]. The current lines flow as shown in Fig.2.

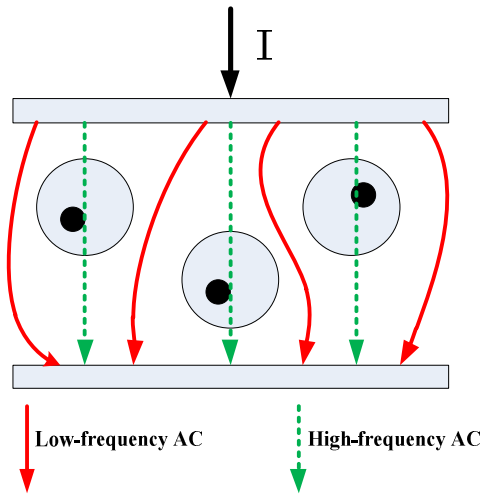


Fig.2. Current flows through the cell

According to the theory of cell dielectric properties, cell membrane has the characteristic of capacitance and the two cell fluids has the characteristic of resistance^[3]. The electrical characteristics of single cell can be equaled to an electrical circuit as shown in Fig.3(a), where the parameters represent different parts of the cell.

- R_m : equivalent resistance of membrane
- C_m : equivalent capacitance of membrane
- R_i : equivalent resistance of intracellular fluid
- C_i : equivalent capacitance of intracellular fluid
- R_e : equivalent resistance of extracellular fluid
- C_e : equivalent capacitance of extracellular fluid

While R_m , C_i and C_e are much larger than C_m , R_i and R_e , less current would go through them, so these can be neglected to achieve a simplified equivalent electrical model as shown in Fig.3(b).

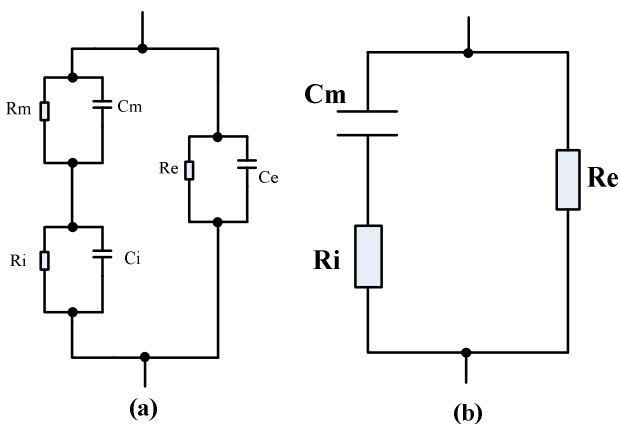


Fig.3(a). A equivalent circuit model of single cell
 (b). Simplified equivalent circuit model of single cell

1.3 Finite element method

The finite element method (FEM) was defined and published by Clough in 1960. With the development of computer, the numerical solution of differential equations has been developed and applied a lot. The main idea of FEM is to approach an entire continuous domain by finite discrete domains. The unknown function on the entire domain is represented by functions on each discrete domain approximately^[4]. A commercial software named COMSOL Multiphysics is a powerful solution engine.

2. Method

This section uses the software COMSOL Multiphysics to build the model of single cell. The geometric shape of model and the value of dielectric properties of cell are selected referring to blood cells^[5].

2.1. Single cell model

2.1.1 Modeling and parameter settings

The parameters of the single cell model is shown in Fig.4.

The meaning of the parameters is as follows:

- ϵ_e : permittivity of extracellular fluid
- σ_e : conductivity of extracellular fluid
- ϵ_i : permittivity of intracellular fluid
- σ_i : conductivity of intracellular fluid
- ϵ_m : permittivity of membrane
- σ_m : conductivity of membrane
- R: radius of single cell
- T_m : thickness of membrane

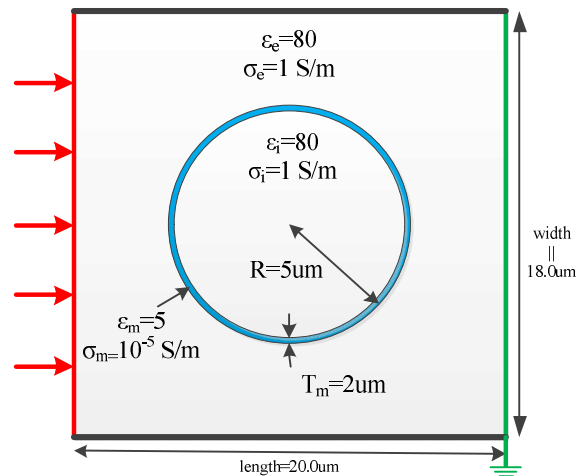


Fig.4. Geometric and electrical parameters of single cell model

As shown in Fig.4, the excitation current with current density of $1A/m^2$ enters the region of interest (ROI) from

the left boundary and flows out from the right boundary. The above and bottom boundaries are electrical insulation.

2.1.2 Meshing grid

Meshing is the process by which the active geometrical space (domain) of a model is sub-divided into a collection of sufficiently smaller spaces so that linear or higher order polynomial approximations can be used as a reasonable analog of the functional physical behavior being modeled, which is the core of finite element method.

The software COMSOL is used to generate the grid. If using coarse meshing method (CMM) to structure the grid, the accuracy of calculation results is not enough because of the less grids. But too refined meshing grid takes a lot of memory which leads to long time calculation. All things considered, this paper used standard meshing method (SMM) that the number of generated elements is between coarse meshing methods (CMM) and refine meshing method (RMM) to create the meshing grid as shown in Fig.5 and Fig.7.

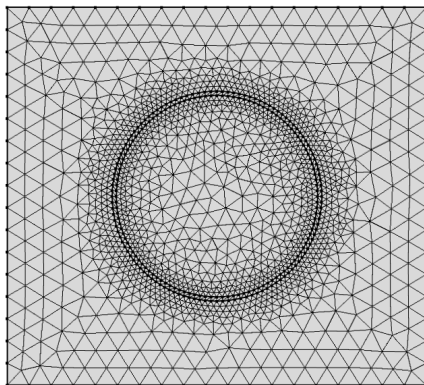


Fig.5. Meshing grid of single cell model (3014 elements)

2.2. Multi-cell model

Because of the special electrical properties of cell membranes, cells show different characteristics in the electric field with different frequencies and the changes of cell membrane's electrical properties lead to changes on physiological state of cells.

In order to observe the dielectric properties of cells under different physiological states, this paper established a multi-cell model based on the single cell model in section 2.1 as shown in Fig.6(a) and the meshing grid using SMM is shown in Fig.6(b).

And three simulation works were implemented to watch the influence on cells that caused by the changes on the membrane electrical parameters. Table.1 shows the parameters setting of three groups of experiments. The

parameters of two cell fluids and the four boundaries' electrical characteristics are the same with the single cell model in Fig.4.

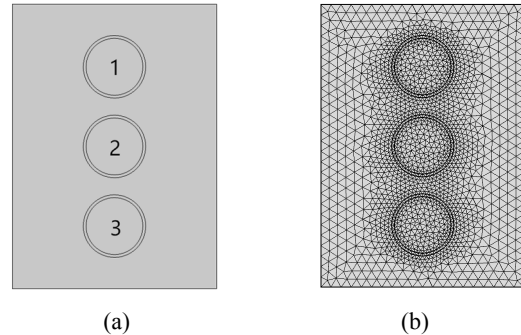


Fig.6(a). Geometric model of multi-cell
(b) Meshing grid of multi-cell model (2962 elements)

Table.1. Membrane electrical parameters of multi-cell model

	Group A		Group B		Group C	
	ϵ_m	σ_m (S/m)	ϵ_m	σ_m (S/m)	ϵ_m	σ_m (S/m)
1	5	10^{-2}	3	10^{-5}	3	10^{-8}
2		10^{-5}	5		5	10^{-5}
3		10^{-8}	7		7	10^{-2}

3. Simulation result

3.1. Single cell simulation result

The current density distribution at three typical different frequencies (1MHz, 50MHz and 100MHz separately) as shown in Fig.8. It can be observed that there is no current flowing through the cell model at 1MHz. It is because the membrane works as capacitance in parallel with a large resistance. The membrane has high insulation and low conductivity at low frequency. With the frequency gradually increasing, a part of current starts to pass through the membrane at frequency 50MHz.. It's apparent that the cell membrane becomes electrically invisible when the frequency reaches 100MHz .The current density in the whole domain is homogeneous.

3.2. Multi-cell simulation result

Table 2 shows the three sets of simulation results, in the same current field, the three cells with different membrane have respective frequency response. This because the membrane works as a capacitance in parallel with a large resistance, when setting different electrical parameters

(permittivity ϵ and conductivity σ) to the membrane, the value of the capacitance and the resistance changed. The simulation results proves that the change of cell's physiological status can affect its dielectric properties on account of changes on membrane.

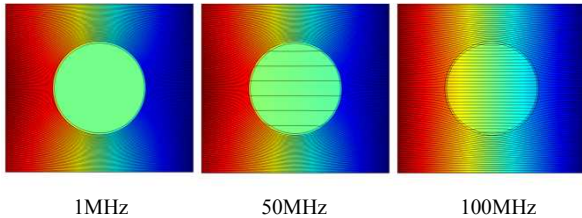


Fig.8.Current density distribution of single cell at different frequency

Table.2. Multi-cell model simulation results

Group A (changes on σ_m)			
Group B (changes on ϵ_m)			
Group C (changes on ϵ_m and σ_m)			

4. Discussion

The finite element method has been widely used in mechanics of biological tissue^[6]. But at the cell level, there are few papers that introduce the electromagnetic characteristics^[7].

This paper preliminarily build single cell model and multi-cell model from microcosmic view and conduct a tentative research at the dielectric properties of the biological cell with finite element method. Comparing with traditional method, this simulation method only needs to set geometric and electrical parameters without building a whole mathematical model. The simulation method based on COMSOL was proved to be successful and this paper provides an auxiliary method to diagnose the status of the cell.

5. Acknowledgements

The authors would like to thank the EIT research group from Tianjin University of Science and Technology. This paper was supported by a grant from the National Natural Science Foundation of China (Grant No.61301246) and a grant from the Science and Technology Project of Tianjin (12JCYBJC19300). It was also supported by the Reform in Education from Tianjin Municipal Education Commission of China (171005704B).

References

1. RJ Yerworth, RH Bayford, G Cusick, M Conway, DS Holder, Design and performance of the UCLH Mark 1b 64 channel electrical impedance tomography (EIT) system, optimized for imaging brain function, *Physiol Meas*, 2002,23: 149-158.
2. XY Chen, XQ Lv, Meng Du, Experimental verification of depolarization effects in bioelectrical impedance measurement, *Bio-Medical Materials and Engineering*, 2014,24: 3675-3683.
3. JR Wang, BY Sun, HX Wang, Qing Sun, Experimental Study of Dielectric Properties of Human Lung Tissue in Vitro, *Journal of Medical and Biological Engineering*, 2014, 34(6): 598-604.
4. Jiaming Jin, The finite element method in electromagnetics, John&Sons, 2014.
5. K Asami, Dielectric dispersion in biological cells of complex geometry simulated by the three-dimension finite difference method, *Journal of Physics D: Applied Physics*, 2006, 39(3): 492.
6. A Tchako, A M Sadeyh, Stress Changes in intervertebral discs of the lervical spine due to partial discectomies of and fusion, *Journal of Biomechanical Engineering*, 2009, 131(5):1-11.
7. C Ding, X Liu, P Shang, Progress of the technology and application of dielectric spectroscopy of cell suspensions, *Beijing Biomedical Engineering*, 2014, 33(1):94-99.

Research on the Method of Electrical Impedance Tomography Based on Conjugate Gradient Iterative Algorithm

Yuanli Yue ^{1*}, Xiaoyan Chen², Ze Liu¹, Fengzhi Dai ²

¹ College of Electronic Information Engineering,
Beijing Jiaotong University, China;

² College of Electronic Information and Automation,
Tianjin University of Science and Technology, China;
E-mail: * 17120205@bjtu.edu.cn
www.bjtu.edu.cn

Abstract

Electrical impedance tomography is a new technology of medical imaging, which can be used to detect the real time internal electrical impedance. This article is doing research on the method of electrical impedance tomography by conjugate gradient iterative algorithm. The finite element analysis software COMSOL is utilized to make a two-dimensional model about a circular field with 16 electrodes. The software MATLAB is used to finish the tomography reconstruction work by applying two different reconstruction algorithms. After tomography reconstruction, a variety of evaluation methods and numerical analysis is applied to estimate the reconstructed image quality, such as the correlation coefficient and the similarity relative error evaluation.

Keywords: EIT, conjugate gradient iterative algorithm, COMSOL, reconstruction, MATLAB

1. The introduction of EIT

Electrical impedance tomography (EIT) is a newly developed technique that can be used to detect internal images¹. It is used to detect electrical impedance of the biological tissues. The principle of EIT is based on the electrical characteristics of the medium inside the field. By injecting exciting current, the voltages on the boundary are measured. It can estimate the distribution of the conductivity changes². By detecting the collected voltage data, using an algorithm to reconstruct the distribution of the electrical conductivity inside the field. Because the conductivities of different human tissues are different, the conductivity of different regions located at same section is also different. The data measured by EIT system can directly reflect the distribution of conductivity and its variations³.

The conductivity of tissues and organs in human body is different, and the characteristic value of conductivity is

different when human body in different pathological states⁴. Based on this feature, EIT can analyze the abnormal electrical conductivity in the tissues or organs, and then determine the lesions of organs and tissues. For the existing medical imaging technology, such as Computed Tomography (CT), type-B ultrasonic, and nuclear magnetic resonance techniques. These diagnose methods use harmful X-rays and harmful radionuclides when performing body scans and tests, and have the disadvantage of high technical cost. On the contrary, EIT is non-toxic and harmless to human body⁵.

EIT has outstanding advantages, large technical potential and broad application prospects. The main advantages of EIT technology can be broadly described in the following aspects:

- Electrical impedance tomography equipment is small in size, simple in structure and easy to carry.

© The 2018 International Conference on Artificial Life and Robotics (ICAROB2018), Feb. 1-4, B-Con Plaza, Beppu, Oita, Japan

Electrical impedance tomography has the characteristics of portability and flexibility, and the equipment can be miniature the size of the whole system to a laptop size. Moreover, the operating system is in graphical visualization⁶. Because of the small size, the EIT equipment can be transported to the scene of the accident in time, saving time for first aid.

- The imaging speed is fast and in real-time

EIT has fast imaging speed, so it can be used as a real-time medical equipment for clinical monitoring and bedside monitoring. Other medical imaging techniques have hysteresis and their imaging speed is slower. At this stage, many researchers are studying electrical impedance tomography.

2. Research of the field

EIT has a broad application prospect and advantages. The researchers are mainly focus on the accuracy of reconstruction and the speed of reconstruction. While the research are still in the initial stage at China, and there is still a big gap between the research progresses. The researches in China mainly focus on the improvement of the algorithm. At present, the technology should be closely integrated with the clinical and practical. In the future, researcher need to develop high-quality algorithms and effective incentive model⁷.

At present, the development of EIT has some deficiencies compared with other technologies in image resolution and measurement accuracy. But it has its advantages, it can be designed according to the needs of its system. In real-time monitoring, it has great advantage. These advantages makes it becomes the main direction of current imaging technology. In addition to the application of medical imaging and clinical medicine, EIT can also be applied into industry to do industrial non-destructive testing, fluid detection, nondestructive testing and fault diagnosis. Up to now, EIT systems have been involved in the field of industrial testing and medical applications.

The research of EIT mainly include forward problem research, inverse problem research and hardware system design. There has include conjugate gradient iterative algorithm, sensitivity coefficient method, Newton-Raphson method, Landweber iterative method, Tikhonov regularization, equipotential back projection method⁸. It is a difficult problem to evaluate the effectiveness of EIT in the future, and that is an important subject to establish an

effective evaluation method of electrical impedance image in the future.

3. The principle of EIT

Principle of electrical impedance tomography is an extension of Ohm's law, setting the resistance of the object is R , the exciting current applied to the resistor R , and the measurement of surface resistance voltage R on target can be obtained the resistance value. After the weak excitation current is injected, the system can detect different current flows on the object with different resistances. Through the measurement of a large number of current data, the appropriate algorithm can be used to reconstruct the image of the resistance and conductivity of the target in different regions.

A certain number of electrodes are attached to the surface of the body, and the current is used as the excitation signal to the measured region or object. Measure the voltage on the surface of the object, select different excitation and measurement mode, and observe the conductivity of the measured area. The working system diagram is shown in the Fig.1:

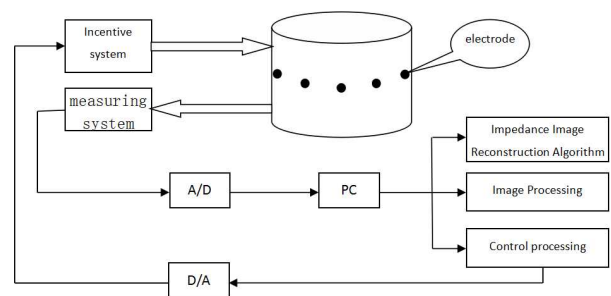


Fig.1. System work diagram of EIT

3.1. Forward problem

According to the electrical conductivity of the target, the excitation signal is applied to the boundary. By solving the Laplace equation, the node voltage in the region is obtained, and can get the electric potential distribution in the field. Then, the boundary voltage of the measured object is obtained, so that the electric field can be analyzed step by step, which is the forward problem of EIT.

The EIT forward problem is shown in the Fig.2:

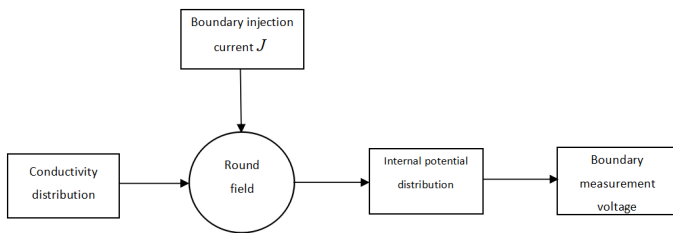


Fig.2. Solving the forward problem of EIT

The target of EIT is the electric field under the special boundary condition, and the electric field is described by a partial differential equation. In the process of solving the equation, the image object is equivalent to the resistance, so it can be converted to the process of solving the Maxwell equations. The excitation frequency used in the measurement is set from 10 to 100Hz, and the free charge movement and the dielectric constant in the target are ignored in the experiment. The Maxwell equations are obtained:

$$\begin{aligned} \nabla \cdot D &= \rho \\ \nabla \cdot B &= 0 \\ \nabla \cdot E &= -\frac{\partial B}{\partial t} \\ \nabla \times H &= j + \frac{\partial D}{\partial t} \end{aligned}$$

In the formula, H is the strength of the magnetic field, J is the current density, D is the potential shift, B is the magnetic induction, E is the field strength, ∇ is the Poisson operator)

The numerical method is mainly used in solving the EIT forward problem, the main methods are finite volume element method, boundary element method, and finite element method and so on.

3.2. Inverse problem

The inverse problem of EIT is the process of solving the illicit nonlinear inverse problem. The key technique lies in the reconstruction of the impedance image by giving the target boundary measurement and solving the electrical impedance distribution in the model. By applying a weak excitation signal to the measured object, the distribution of the object inside can be obtained, and can get the boundary voltage of the measured area. In essence, the solution of the inverse problem is the process of reconstructing the image, the reconstruction of the forward problem and the characteristic of the conductivity inside the object region can be obtained. Therefore the problem is known as the

inverse problem of EIT, also known as the inverse problem of EIT. The inverse problem process is divided into two kinds of imaging methods, dynamic imaging and static imaging. The solution of the inverse problem is that the voltage solved by the forward problem is the same as the actual measured potential difference within the specified deviation, and the reconstructed image solved by the inverse problem is the approximation of the real image. Finally only can get approximate solution, it is difficult to get an accurate solution. The EIT inverse problem is shown in the Fig.3.

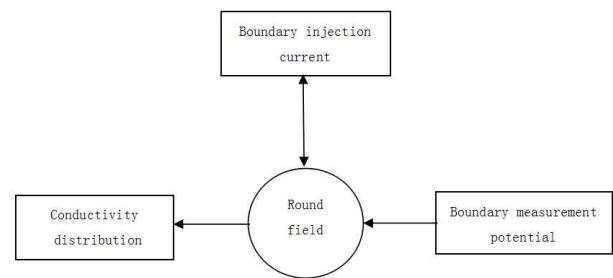


Fig.3. EIT inverse problem

The inverse problem of EIT is mainly based on the known conditions and other information to reverse the unknown parameter information in the target object, so as to reconstruct the more realistic image. In the process of studying the inverse problem, it is mainly to find the appropriate algorithm to improve the stability of the reconstruction operation to reduce the amount of reconstruction. In this paper, using the conjugate gradient iterative algorithm to reconstruction.

4. Introduction of Conjugate Gradient Iteration Algorithm

At present, the algorithm for the study of electrical impedance imaging technology has a certain foundation, there are many mature electrical impedance imaging algorithms. The focus for different algorithms is different. These algorithms have their own advantages and their shortcomings, select the algorithm according to the target needs, to estimate the effect of the image to choose. The method used in this paper is conjugate gradient algorithm⁹.

Conjugate gradient iteration is an iterative method for solving the numerical solution of sparse linear equations. It is an algorithm between Newton algorithm and gradient algorithm. Conjugate gradient iterative method is a more

effective method to solve the nonlinearity. The convergence speed is faster than the steepest descent method, and its jaggging phenomenon is overcome. The convergence is better than the Newton method and the computation is smaller. This algorithm is simple, easy to program, small storage space to make it an important way to solve the optimization problem¹⁰. This algorithm only needs to solve the first derivative, overcome the shortcomings of convergence, it has widely used.

The conjugate gradient iterative algorithm is a linear search based on n (n is the highest order of the equations) conjugate directions. Theoretically, the iterative number of steps is n, so that we can find the optimal solution. It applies to the coefficient matrix that is symmetric positive definite.

Suppose there is a linear system $Ax = b$, A is a $N \times N$ dimension symmetric positive definite coefficient matrix, $X \in R^{N \times 1}$, $b \in R^{N \times 1}$. In order to obtain the exact solution of $Ax = b$, we define the following function:

$$f(x) = \frac{1}{2} x^T Ax - b^T x$$

Then the gradient of $f(x)$ is $\nabla f = Ax - b$, or it can be expressed by the margin function $r = Ax - b$. When the gradient ∇f or margin function r is equal to 0, and the function $f(x)$ has a minimum value.

5. COMSOL software two-dimensional model and MATLAB simulation

EIT problem mainly refers to the process of electrical impedance tomography reconstruction. In this paper, the software COMSOL is used to simulate the Jacobi matrix, and reconstruct the conductivity distribution in the target field. Using COMSOL to model, building a uniform distribution of 16 around the electrode, the establishment of a circular area. This paper solve the forward problem of EIT accurately by COMSOL modeling to improve the quality of the image.

First, a two-dimensional model is created by COMSOL, circular field is plotted, and 16 electrodes are distributed around the circular field. The field conductivity is 0.037 s/m^2 , the conductivity of the target small circle is 0.138 s/m^2 , and the electrode is selected as the titanium electrode. The normal current density of the injected current is set to $+1 \text{ A/m}^2$ and -1 A/m^2 , and other electrodes are set to be electrically isolated. The ratio of the homogenous field to

the inhomogeneous field set to 1:10. In order to enhance the contrast, the homogenous field and the inhomogeneous field are established, which are shown in the Fig.4. Adjacent excitation measurement mode of operation to solve the problem. The conjugate gradient iterative algorithm is used to solve the inverse problem.

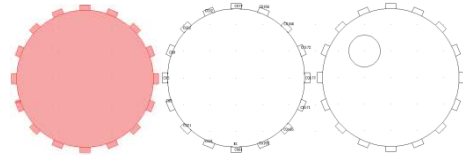
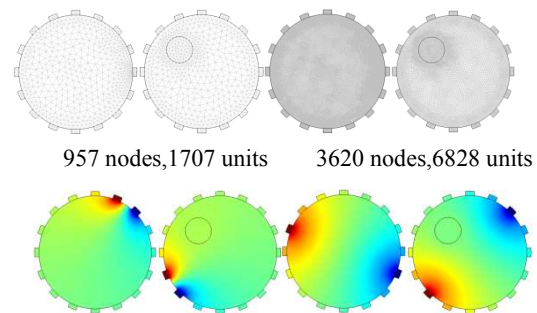


Fig.4. Two - dimensional model

The finite element analysis of the established two-dimensional model can be divided into general meshing grid and fine meshing grid. Split the target field into 957 nodes and 1707 units. Using relative excitation and adjacent modes, space-field and full-field simulation, the results shown in Figure 5.



Adjacent incentives relative incentives

Fig.5. Different pattern of division and incentive mode

In the forward problem, the sensitivity matrix and the reference potential vector are generated. Then change the number of different iterations, imaging in MATLAB. The number of iterations from 10 times to 90 times were imaging, to see their imaging results. The result is shown in the Fig.6.

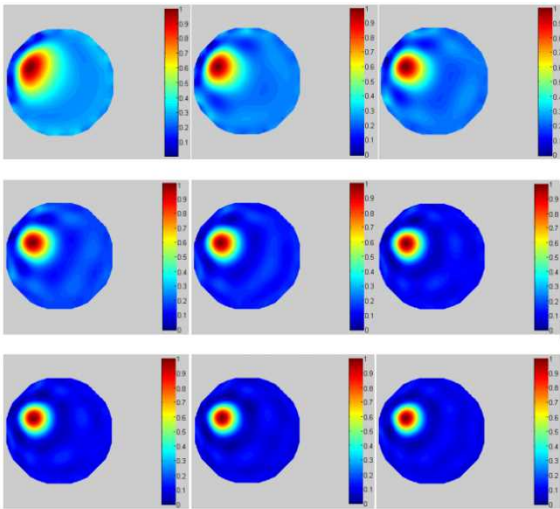


Fig.6. The images reconstructed by different iterations

6. Reconstruction of image quality evaluation indicators and analysis

For the reconstruction images of MATLAB, evaluate the quality of their imaging results and images, the general evaluation of electrical impedance tomography indicators are similarity, the maximum correlation coefficient and the relative error. Using different metrics to evaluate the quality of reconstruction.

6.1. Similarity

The structural similarity index refers to an evaluation index that can be used to compare the similarity of two different images. The range of similarity values ranges is -1 to +1. In the evaluation of the reconstruction, if the two images are exactly same, the similarity value is 1. For the reconstruction, the more the value of the similarity is closer to 1, the better the quality of the reconstruction is, and the better the reconstructed image is consistent with the original model.

Comparing and analyzing the similarity values obtained with different iterations is shown in Table 1-1. Increasing the number of iterations to reconstruct the image accuracy is getting better.

Table 1-1 SSIM and the number of iterations

iterations	100	300	500	700
SSIM	0.2450	0.3034	0.3380	0.3388

6.2. Relative error

The relative error is used to describe the reconstructed image quality. The relative error is the deviation between the actual image and the reconstructed image. Generally speaking, when the value of the relative error is smaller, the quality of the reconstructed image is better, the larger the relative error value indicates that the reconstructed effect of the image is poor. The relative error can be expressed by:

$$E_R = \frac{\|\sigma^* - \sigma\|}{\|\sigma^*\|}$$

σ^* is the true conductivity of the original image; σ is the conductivity of the reconstructed image.

According to the results obtained in the image reconstruction under MATLAB, the relative error a numerical image is shown in the Fig.7.

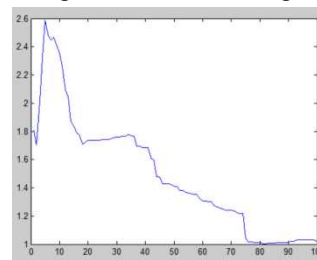


Fig.7. Relative error after 100 iterations

By comparing the number of iterations, the number of iterations is 75, the relative error is the smallest.

6.3. Correlation coefficient

The correlation coefficient is the evaluation index proposed by the application mathematician Karl Pearson, and it is mainly used to illustrate the degree of correlation between two variables. The correlation coefficient is calculated based on the difference between the two variables and their average. The results of the two deviations is defined to describe the correlation between the two variables.

Compare the data of the largest correlation coefficient, the result is shown in Fig. 8.It can be concluded that the correlation coefficient is close to 1 as the number of iterations increases.

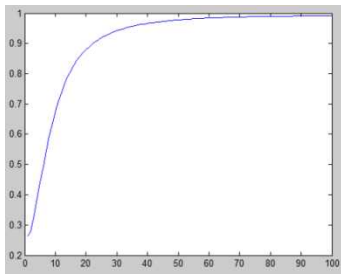


Fig.8. The correlation coefficient at 100 iterations

7. Conclusion

Through the analysis of the effect of imaging and evaluation of three indicators. It can be found that by increasing the number of iterations within a certain range to improve the quality and speed of imaging, can improve the resolution. The correlation coefficient is increasing infinitely close to 1, the relative error a is getting smaller and smaller, the value of similarity is getting bigger, which indicates that the image quality of the image is getting higher and higher. Finally, it can be seen in 75 times near the best imaging results.

The shape of the circular field under 75 iterations tends to be smooth, the contour is gradually clear, the artifacts are gradually reduced, and the imaging effect becomes better, which indicates that the quality of image reconstruction is getting higher. As the number of iterations continues to increase, the imaging effect does not change significantly.

The wide application of EIT in medicine, can be used to see the body of the internal tomography. The shortcoming of this paper is that only one imaging algorithm is used to image, and then the algorithm can be improved and improved, and the method of combining the various algorithms is used to study the electrical impedance imaging technology.

8. Acknowledgements

The authors would like to thank the EIT research group from Tianjin University of Science and Technology. This

paper was supported by a grant from the National Natural Science Foundation of China (Grant No.61301246) and a grant from the Science and Technology Project of Tianjin (12JCYBJC19300). It was also supported by the Reform in Education from Tianjin Municipal Education Commission of China (171005704B).

References

1. Ying Qian, New Advances in Medical Ultrasound Equipment, *Medical equipment information*, 2002(11): 25-27.
2. Yan Wang, Study on Performance and Evaluation Method of Electrical Impedance Tomography System. *Beijing: China Union Medical College*, 2009.
3. Yongbo He, Tao Song, Huixian Wang. Magnetic resonance electrical impedance tomography. *Beijing Biomedical Engineering*, 2006.2: 99-102.
4. Tang Mingxin, Dong Xiuzhen, Electrical impedance tomography reconstruction impedance tomography, *Proceedings of a meeting on electrical impedance tomography*, Copenhagen, 1990, 5:212-216.
5. Shujun Chen. Image Reconstruction Algorithm and Implementation of Electrical Impedance Tomography. Nanjing: *Nanjing University of Science and Technology*, 2008.
6. S. M. Huang, A. Plaskowski, Tomography imaging using two-component flow using capacitance sensors. *J. Phys. E*, 1989, 22(3): 173-177.
7. Lian Gong, Ping Huang, Yin Liu. An Effective Image Reconstruction Algorithm for Electrical Impedance Imaging. *China Electromechanical Society of Electromagnetic Field Theory and Application Symposium*, 1987.
8. Xiuzhen Dong, Mingxin Qin, Mengxing Tang. A Practical Dynamic Electrical Impedance Tomography Algorithm. *Chinese Journal of Biomedical Engineering*, 2000, 19 (3): 348-352.
9. Seo J K, Kwon O, Ammari H, et al. A mathematical model for breast cancer lesion estimation: Electrical impedance technique using TS2000 commercial system. *IEEE. Trans BME*, 2004: 76-79.
10. Ruigang Liu, Xiuzhen Dong, Feng Fu. An Image Postprocessing Algorithm for Electrical Impedance Tomography, *Medical and health equipment*, 2006(08): 1898-1906.

Research on Acoustic Emission Wireless Sensing System

Xiuqing Wang ^{1*}, Qing Liu ¹, Yang Li ², Jimin Zhao ¹, Jiangfan Wang ¹

¹ College of Electronic Information and Automation,
Tianjin University of Science and Technology, China;

² TEXAS A and M University, U.S.A
E-mail: * lwxqly@163.com
www.tust.edu.cn

Abstract

Piezoelectric ceramic acoustic emission sensor and fiber Bragg grating acoustic emission sensor are used to build two kind of acoustic emission wireless sensing systems. The acoustic emission signal source is simulated by breaking the automatic pencil lead core. The acoustic emission signal is monitored by the acoustic emission sensor, and the characteristics of acoustic emission signal are extracted and uploaded to the host computer platform through wireless sensor network. A comparative experiment of piezoelectric ceramic acoustic emission sensing system and fiber Bragg grating acoustic emission sensing system is carried out.

Keywords: acoustic emission, piezoelectric ceramic sensor, fiber Bragg grating sensor, wireless sensor network

1. Introduction

Acoustic emission testing is an important nondestructive testing technology, which has been widely used in many fields, such as petroleum, electric power, railway, etc. Because wired routing is too cumbersome and not suitable for remote and harsh environment applications, wireless sensor networks are widely used in industrial, agricultural and other fields of automatic monitoring. This paper builds acoustic emission wireless sensing system combined wireless sensor network technology for monitoring of the acoustic emission signal. Besides, through the contrast experiment of piezoelectric ceramics acoustic emission sensing system and fiber Bragg grating acoustic emission sensing system, it can be seen the unique advantages of the latter.

2. The Hardware Structure Design

The traditional acoustic emission system is mainly based on piezoelectric ceramic sensors, whose working principle is based on the piezoelectric effect of

piezoelectric materials. With the development of fiber Bragg grating technology, the advantages of fiber Bragg grating acoustic emission sensor have been explored and developed, and the sensor has been widely used in the field of acoustic emission detection¹. Acoustic emission signals are changeable and have a wide dynamic range and the signals are divided into burst and continuous acoustic emission signals². In this paper, acoustic emission signal source is simulated by breaking the automatic pencil lead core, which will produce burst acoustic emission signal. Considering the large amount of acoustic emission waveform data and the limited speed of wireless network transmission, the method of extracting the acoustic emission waveform characteristic parameters is adopted to realize real-time monitoring the acoustic emission signal through the wireless sensor network, which has been extensive applied in acoustic emission detection since 1950s. The characteristic values such as amplitude, rise time, descent time and duration are uploaded to the host

© The 2018 International Conference on Artificial Life and Robotics (ICAROB2018), Feb. 1-4, B-Con Plaza, Beppu, Oita, Japan

computer software through wireless sensor network to complete the subsequent processing.

2.1. Fiber Bragg grating acoustic emission wireless sensing system

The principle of fiber Bragg grating sensing detection is that the light propagating in the fiber core will scatter at each grating surface. If the Bragg condition is satisfied, the reflection of each grating plane will gradually accumulate, and finally a reflection peak will be formed in the direction. In this paper, an acoustic emission wireless sensing system based on fiber Bragg grating technology is presented, whose block diagram is shown in Fig.1.

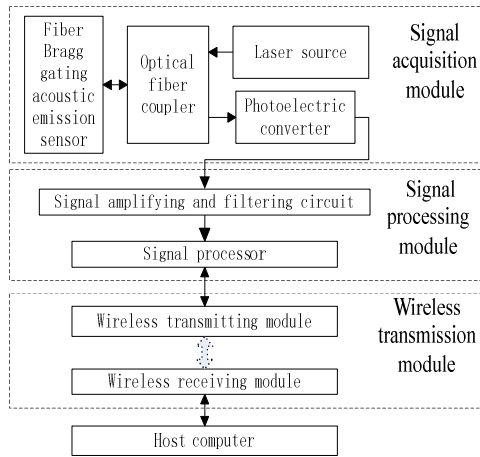


Fig.1. block diagram of fiber Bragg grating acoustic emission wireless sensing system

As shown in Fig.1, the sensing system is mainly composed of signal acquisition module, signal processing module, wireless transmission module and host computer. The signal acquisition module consists of a fiber Bragg grating acoustic emission sensor with a center wavelength of 1553 nm and some optical components. The sensor is fixed on the experimental wood plank, and the acoustic emission signal source is simulated by breaking the automatic pencil lead core. The optical components are narrow linewidth laser source, optical fiber coupler and high-speed photoelectric converter. A narrow linewidth laser emitted from laser source is incident to the fiber grating through an optical fiber coupler. It is reflected by the fiber grating and then incident to the high-speed photoelectric converter through the optical fiber coupler. The optical signal is converted into the electrical signal output by the photoelectric converter. The system

adopts the principle of intensity demodulation. In signal processing module the electrical signals produced by the photoelectric converter are amplified, filtered and extracted for characteristic values. Next, the processed results are transmitted to the host computer through the wireless network for display, analysis, storage and other operations. At the same time, the host computer can also issue commands to the system acquisition and processing module, such as starting or stopping collection, change the configuration parameters and so on.

2.2. Piezoelectric ceramic acoustic emission wireless sensing system

The structure of piezoelectric ceramic acoustic emission system is similar to that of the system based on fiber Bragg grating sensor on the whole, as shown in Fig.2. The center response frequency of the piezoelectric ceramic sensor is 151.37 kHz. The piezoelectric ceramic sensor transmits the acquired acoustic emission signal to the amplifying and filtering circuit, and then acquisition and processing circuit collects and processes the signal. The characteristic parameters are transmitted to the host computer software through the wireless network.

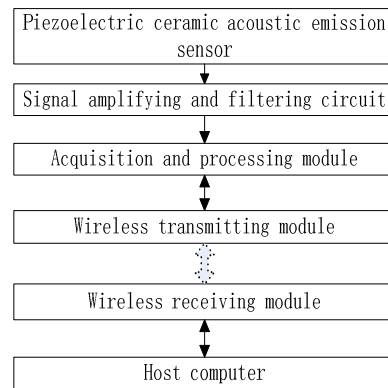


Fig.2. block diagram of piezoelectric ceramic acoustic emission sensing system

3. Contrast Experiment

Piezoelectric ceramic sensor is a traditional acoustic emission sensor, while fiber Bragg grating acoustic emission sensor is a novel one. In order to compare the differences between two acoustic emission sensing systems, this part makes a comparative experiment. As shown in Fig.3, a piezoelectric ceramic acoustic

emission sensor with center response frequency of 151.37 kHz and a fiber Bragg grating acoustic emission sensor with central wavelength of 1553 nm are fixed on the same wood plank. Before fixing, the plank should be polished, the surface of the contact of piezoelectric ceramic sensor should be coated with corresponding couplant and the fiber Bragg grating sensor should be glued to the plank, so that the two sensors can be fully contacted with the plank to reduce the error. The acoustic emission signal source is simulated by breaking the automatic pencil lead core at the same distance with the two sensors, and the acquisition results of the two systems are compared.

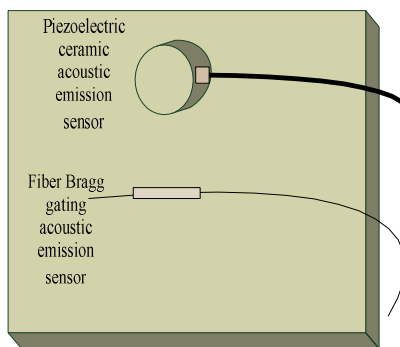


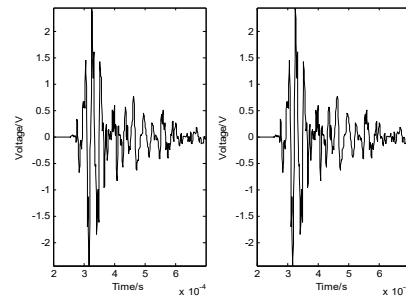
Fig.3. Schematic diagram of contrast experiment

The experimental results show that there are differences in the acoustic emission signal waveform between two sensing systems. Next, a typical acoustic emission event is introduced as an example. In this paper, breaking a lead core is temporarily defined as an acoustic emission event.

3.1. Time domain waveform of acoustic emission

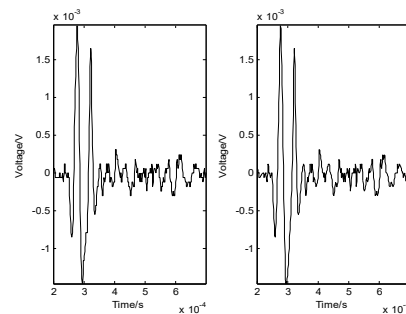
Fig.4 (a) and Fig.5 (a) are the waveforms in the time domain collected by processors of two systems when an acoustic emission event occurs. It can be seen that the waveform obtained by fiber Bragg grating system has fewer oscillations in the duration. It is pointed out that such difference is related to the inherent structural characteristics of the sensor itself³. The upper and lower surfaces of the piezoelectric ceramic sensor can cause the superposition of the acoustic emission signals, while the fiber Bragg grating acoustic emission sensor itself does not have such problem. Therefore, the waveform will not produce distortion, which is the advantage of the system based on fiber Bragg grating acoustic emission sensor than the other in principle.

© The 2018 International Conference on Artificial Life and Robotics (ICAROB2018), Feb. 1-4, B-Con Plaza, Beppu, Oita, Japan



(a) Original waveform (b) Recovered waveform

Fig.4. Time domain waveform detected by piezoelectric ceramic acoustic emission sensing system



(a) Original waveform (b) Recovered waveform

Fig.5. Time domain waveform detected by fiber Bragg grating acoustic emission sensing system

Because the waveform data of acoustic emission signal is very large, it will occupy a lot of memory space. A time-domain waveform storage method of acoustic emission signal is proposed. The feature points of the waveform are stored on the acquisition processor, and the software simulates the signal waveform by polynomial interpolation. Fig.4 (b) and Fig.5 (b) are recovered results. We can see that the method can successfully recover signal waveforms.

3.2. Estimation of power spectral density by Welch method

The power spectrum of the signal reflects many important features of the signal, and the extraction of the signal characteristics using the power spectrum is an important method of the signal processing field. This paper calls the PSD function of the Matlab signal processing toolbox, and estimates the Welch power spectral density of the two acoustic emission waveforms shown in Fig.4 (a) and Fig.5 (a). The result is shown in Fig.6. In order to facilitate the power spectral density analysis, some characteristic parameters of power

spectrum are defined in this paper. High energy frequency band is a frequency band with high density of relative power spectrum⁴, which is expressed in H. H of the piezoelectric ceramic system and the fiber Bragg grating system are respectively expressed as H1, H2. X represents the energy in a certain frequency band; N represents the total frequency band energy; R represents the energy ratio, that is $R=X/N$.

It can be starkly found that the power spectral density of piezoelectric ceramics system on the vertical axis is much larger than that of fiber Bragg grating system on the whole. This is due to the amplitude difference of acoustic emission signals collected by the two systems, and the amplitude of the time domain waveform collected by the piezoelectric ceramic system is larger than that of the fiber Bragg grating system.

From the view of Fig.6, H1 is mainly concentrated in the range of 0-200 kHz, while H2 is mainly concentrated in the range of 0-80 kHz. That is to say, in the frequency range of 80-200 kHz, R value of the piezoelectric ceramic system is larger than that of the fiber Bragg grating system. This phenomenon may be related to the characteristics of piezoelectric ceramic sensor, whose frequency response in the 80-200 kHz frequency range near its center response frequency is higher than that in the 0-80 kHz frequency range.

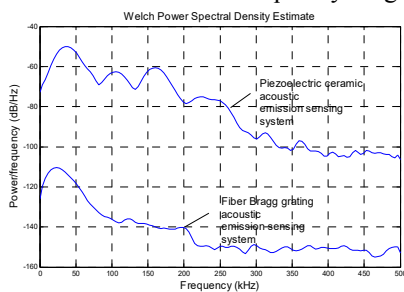


Fig.6. Welch power spectral density estimation of acoustic emission signals detected by two sensing systems

4. Conclusion

In this paper, two acoustic emission wireless sensing systems are built, one is based on Fiber Bragg grating sensor, and the other is based on piezoelectric ceramic sensor. With the signal produced by the breaking lead core as research object, contrast experiment is carried out, and differences of the two systems are found:

The acoustic emission signal collected by the fiber Bragg grating system has fewer oscillations than that of

the piezoelectric ceramic system. The reason may be that the upper and lower surfaces of the latter will superimpose the oscillations of acoustic emission signals. Compared with the other, the fiber grating acoustic emission sensor does not have the upper and lower surfaces, and can avoid the problem of the waveform distortion.

In the power spectral density estimation by Welch method, there is a difference in H between the two systems, the low frequency distribution is similar. This may be caused by the frequency response characteristics of the piezoelectric ceramic sensor whose response to different frequency signals is different. When the frequency of the detected signal is near its center response frequency, it can restrain the noise effectively, and has a good detection result. However, when the frequency of the detected signal is unknown, its frequency may not be near the central response frequency, the signal detected may bring errors.

From the above analysis, the fiber Bragg grating acoustic emission system is superior to the system based on piezoelectric ceramic sensor for monitoring acoustic emission signals. The causes of the differences in time domain waveform and power spectral density estimation by Welch method need further study.

Acknowledgements

This work is supported by Tianjin Research Program of Application Foundation and Advanced Technology (14JCZDJC39000) .

References

1. Faye Zhang, Mingshun Jiang, Qingmei Sui, Acoustic emission localization system based on FBG sensors and support vector machine. *Journal of Vibration, Measurement and Diagnosis*, 2017, 37 (1): P189 - P194.
2. Gongtian Shen, Rongsheng Geng, Shifeng Liu, Parameter analysis of acoustic emission signals. *Nondestructive Testing*, 2002, 24(2): P72- P77.
3. Ning Li, Peng Wei, Hong Mo, Bearing state monitoring using a novel fiber Bragg grating acoustic emission technique. *Journal of vibration and shock*, 2015, 34(3): P172- P177.
4. Jianwei Liu, *AE-infrared characteristics and damage evolution generated from rock under variable angle shear* (Jiangxi, Jiangxi University of Science and Technology, 2014)

ORiN PAC (PC-based Automation Controller) - Integrated Development Environment for Manufacturing System -

Toshihiro Inukai

DENSO WAVE INC., 1, Yoshiike, Kusagi, Agui-cho
Chita-gun, Aichi, 470-2297, Japan

E-mail: toshihiro.inukai@denso-wave.co.jp

Abstract

This paper introduces application examples of ORiN PAC (PC based control system utilizing ORiN as middleware). The manufacturing system is composed of huge kinds of devices, and it is necessary to make device programs for controlling these devices in cooperation. The mfg. system becomes increasingly complicated, and along with the increase in programming cost, the improvement of programming efficiency became a big issue. In this paper, we propose ORiN PAC as a solution to realize "one software architecture" applicable from small scale to large scale mfg. systems. This solution has been used in the real factories in the world (not just a demo), and it will be quite important also for realizing "Industrie 4.0" world.

Keywords: Industrie 4.0, Manufacturing System, Cyber Physical System, ORiN

1. Introduction

PC-based Automation becomes gradually popular in the industrial control field, with the spread of open standard industrial networks such as EtherCAT[1], POWERLINK[2] and PROFINET[3]. The background is as follows:

- (i) Increase of mfg. software development cost → Improve the efficiency by using IT tools
- (ii) Increase of difficulty to ensure mfg. software engineers → Use IT engineers of non-mfg. fields
- (iii) Increase of mfg. system complexity → Utilize open standard IT hardware and software

To cope with the situation, PAC (PC-based Automation Controller) is spreading recently, and it will be a key component of Industrie 4.0 world.

However most of mfg. software engineers hesitate to use PAC because it's too general. So they want a framework suitable for PAC (that is ORiN PAC).

The target field of this study is "low production volume (1 to below around 1000) and wide variety zone" of mfg. system in Figure 1. Because the productivity of this zone is basically low, and for "high production volume products", mfg. system should be optimized to minimize the direct cost.

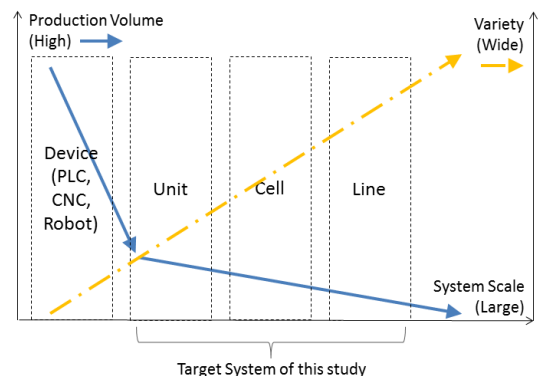


Fig. 1. Production volume and scale of mfg. system

2. Automation System Architecture

A main goal of Industrie 4.0 is flexibility. Many engineers have been trying to realize it with several architectures such as PLC-centric, Robot-centric and CNC-centric. However it is difficult to achieve the flexibility for them because of the complexity and the versatility of mfg. systems. Each device has own strategy, management and control parts in Figure 2. In this scenario, it is difficult to make the whole system optimized and flexible.

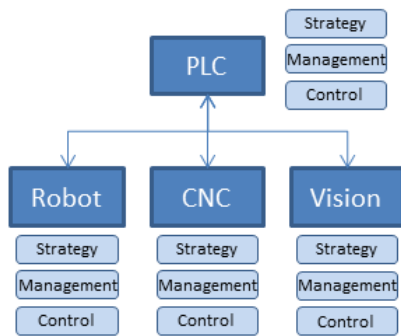


Fig. 2. Typical architecture of current mfg. system

To realize flexibility (reusability, changeability), separation of the three parts is required first. Also, simplification and encapsulation (i.e. object-oriented approach) are also required as shown in Figure 3.

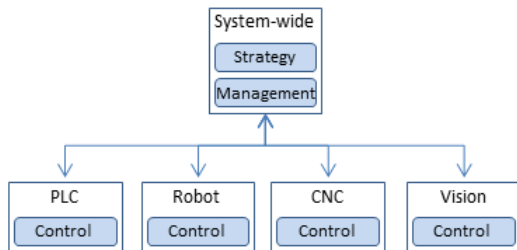


Fig. 3. Proposed architecture of mfg. system

On the other hand, that is a standard approach for IT world. Therefore several companies (e.g. Beckhoff Automation, B&R, Phoenix Contact ^{a)}) had already started PAC business. However, it's still difficult for mfg. system engineers to control the whole system that includes legacy devices and/or the other platform sub-systems.

^{a)} Phoenix Contact calls it "PLCnext" concept.

3. ORiN

To make PAC easy, a framework suitable for PAC is required. Therefore, Fraunhofer IESE (Germany) started a middleware project (BaSys 4.0[4]) in 2016.

Japan also started an "open standard middleware for automation" project (ORiN[5]) in 1999, and ORiN Forum[6] members have been maintaining and improving it continuously. ORiN is an acronym of "Open Resource interface for the Network", and the features are as follows.

- ORiN provides three standards: CAO (Controller Access Object), CRD (Controller Resource Definition) and CAP (Controller Access Protocol),
- CAO provides a standard program interface for both of device and application,
- CRD provides a standard data schema to describe the static information such as profiles of device,
- CAP provides a standard communication protocol to cooperate with remote CAO systems,
- These standards have a unified concept, but it can be used individually.

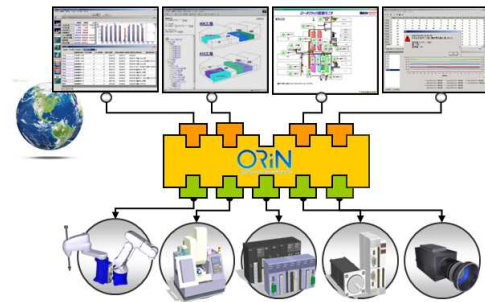


Fig. 4. ORiN architecture

4. ORiN PAC Application Examples

ORiN PAC is a "PC-based automation controller utilizing ORiN as middleware." In this section we show two examples.

All devices in Figure 5 are connected to ORiN PAC, and one Visual Basic program is controlling whole system. The programmer could make a program for FA devices as for PC devices (peripherals).

The next in Figure 6 is a multi-vender robot control system which was difficult to develop conventionally. Four different manufacture's robot (DENSO, Kawasaki YAMAHA, Yaskawa) were connected.

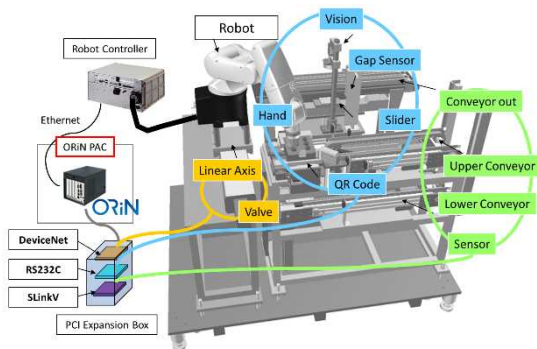


Fig. 5. Integrated cell control



Fig. 6. Multi-vender robot control

5. Realtime Extension Examples

ORiN is not a standard for realtime system. Therefore in the case realtime control is required, some kind of realtime extension should be combined with ORiN PAC. Figure. 7,8 and 9 show three realtime extension examples: for Robot (Fig. 7), for Automation (Fig. 8) and for Multi-purpose (Fig. 9). ORiN PAC provides gateway libraries (TwinCAT3 ADO provider and INtime NTX provider).

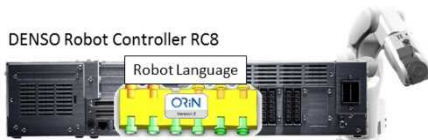


Fig. 7. ORiN Robot controller

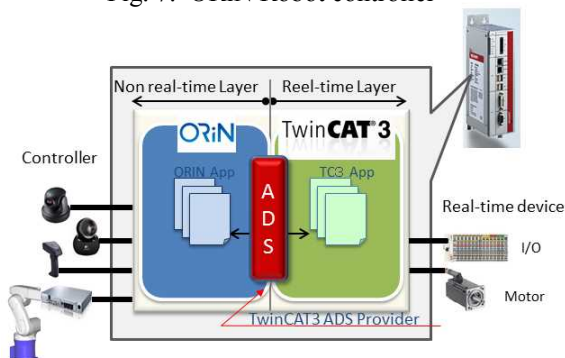


Fig. 8. ORiN Automation controller

© The 2018 International Conference on Artificial Life and Robotics (ICAROB2018), Feb. 1-4, B-Con Plaza, Beppu, Oita, Japan

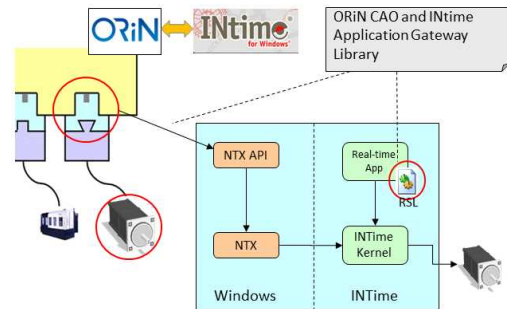


Fig. 9. ORiN Multi-purpose controller

6. ORiN PAC with OSS

The success of OSS (Open Source Software) in the office automation brought impact to the factory automation. ROS[7] is one of them, and it becomes popular in the lab. However it is still difficult to be used in an “industrial” solution because of the lack of the following issues: safety certification (e.g. ISO, UL), field network certification (e.g. EtherCAT, PROFINET), communication support for various automation devices (e.g. PLC, Robot) and various upper-level systems (e.g. SCADA, MES). OSS community is basically not interested in supporting those proprietary technologies.

By combining ORiN PAC with OSS, the applicable field is expanded. In the following examples, ORiN PAC provides ROS libraries (CAP-ROS node and ROSSerial-CAO gateway provider).



Fig. 10. Manipulator (above) and mobile robots (below) applications by ORiN and ROS

7. Additional Advantages

There are several additional advantages in ORiN PAC approach. In this section, we describe three examples.

7.1. Integrated Development Environment

Automation device vendors are basically providing a proprietary development tool. The mfg. programmers must learn how to use it, and that is one reason of poor productivity of mfg. software.

At four examples in Figure 5, 6, 8 and 9, the mfg. programmers can use Microsoft Visual Studio, as with IT software developers. Of course, software asset management tools such as Subversion and Git are very useful for them.

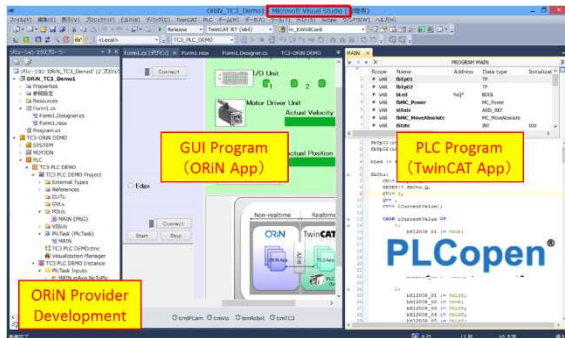


Fig. 11. Integrated development environment

7.2. Digital Twin

Digital Twin is one of key topics of Industrie 4.0. We thought that is a technology for high volume production products. But it is useful for the mfg. system which is typically low volume. For example, in case of the mfg. line design, the combination of real devices and virtual environment will yield quite big benefit to reduce the development cost [8].

7.3. Combination with ORiN IoT

CPS (Cyber Physical System) is also one of key topics of Industrie 4.0. A CPS provides connections to upper-level systems for strategic communication. ORiN IoT architecture shown in Figure 12 provides most of global standard communication ways for each IoT application platform. And ORiN PAC systems can be easily connected to ORiN IoT systems with CAP. This means that ORiN PAC doesn't need to have IoT specific functions.

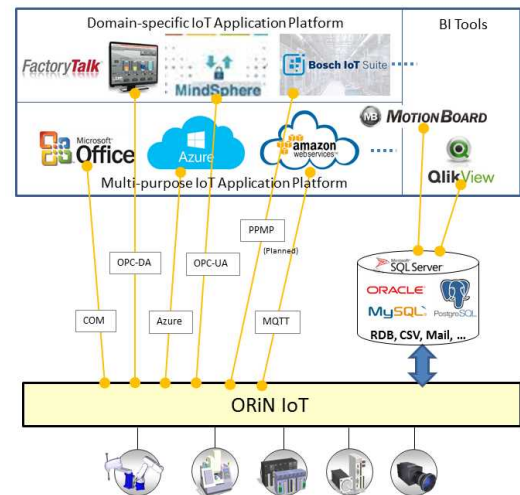


Fig. 12. ORiN IoT architecture

8. Conclusion

We proposed ORiN PAC architecture and its possibility in this paper. We hope this will be a hint for realizing a smart factory.

Acknowledgements

This work is supported by NEDO (New Energy and Industrial Technology Development Organization) and ORiN Forum members.

References

1. EtherCAT, <https://www.ethercat.org/>
2. POWERLINK, <http://www.ethernet-powerlink.org/>
3. PROFINET, <http://www.profinet.com/>
4. BaSys 4.0, <https://www.basys40.de/>
5. Makoto MIZUKAWA and Satoshi SAKAKIBARA, Implementation and applications of open data network interface ORiN, in *Proc. of the SICE Annual Conference*, pp. 1340–1343, 2004
6. ORiN, <http://www.ori.jp/>
7. ROS, <http://www.ros.org/>
8. Toshihiro INUKAI, Hironori HIBINO and Yoshiro FUKUDA, Simulation Environment Synchronizing Real Equipment for Manufacturing Cell, in *Journal of Advanced Mechanical Design, Systems, and Manufacturing*, Vol. 1, No. 2, 2007

Research on the Synchronization and Circuit Realization of a Four-Wing Chaotic System

Yiqiao Qin, Fengzhi Dai *, Yuxing Ouyang, Qijia Kang, Ce Bian, Baochang Wei, Runhua Mao, Shengbiao Chang

Tianjin University of Science and Technology,
1038 Daguanlu Road, Hexi District, Tianjin, 300222, China;
E-mail: * dai fz@tust.edu.cn
www.tust.edu.cn

Abstract

This paper introduces a three-dimensional four-wing chaotic system and the system is analyzed and circuit verified. The paper adopts two synchronous control strategies to control the three - dimensional four-wing chaotic system. One is the feedback synchronization controller based on the observer, and the other is the synchronization controller based on theory of stability. The feasibility of these two methods is proved by analyzing the numerical data and the circuit implementation. On this basis, we conducted signal encryption research. The results verify the feasibility of the synchronous design and encryption design.

Keywords: Chaos, Chaotic synchronization, Secure communication, Circuit realization

1. Introduction

The meaning of chaotic secure communication is that through a series of algebraic operations, the signal that needs to be transmitted can be superimposed on a chaotic signal which is generated by a chaotic system. Because of the pseudo randomness of the chaotic signal, the mixed signal will have no regularity, and be similar to the noise signal. The characteristic guarantees the security of the information that it is difficult for eavesdroppers to restore the original information even if they intercept the mixed signal. After receiving by legitimate people, the useful information can be distinguished from the mixed signal through the synchronization between systems of the sender and the recipient.

2. Analysis of four-wing chaotic systems

The mathematical expression of a 3D four-wing chaotic system is as Formula 1:

$$\begin{cases} \dot{x} = ax + ky - yz \\ \dot{y} = -by - z + xz \\ \dot{z} = -x - cz + xy \end{cases} \quad (1)$$

When the system variables are selected as $b=12$, $c=5$, and $k=1$, we get the bifurcation graphs as shown in Fig.1. The research of encryption and chaotic communication should be based on the chaotic state of the system, so the selected parameters are $a=5$, $b=12$, $c=5$, $k=1$.

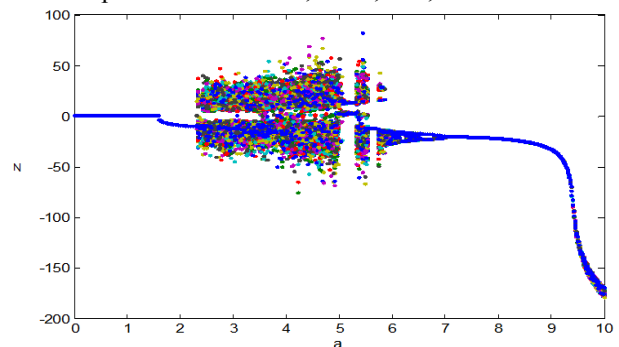


Fig.1. Bifurcation graphs of four-wing chaotic systems

When the parameters are $a=5$, $b=12$, $c=5$, and $k=1$, the x - y - z plane phase diagram, the x - y plane phase diagram

and the y-z plane phase diagram of the system are shown in the following Fig.2.

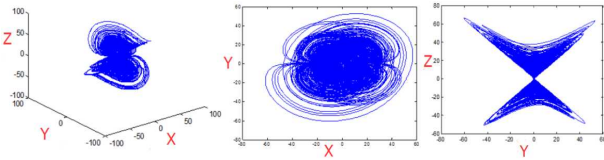


Fig.2. plane phase diagram

There are two kinds of synchronization control of chaotic systems proposed in this paper. The first is feedback synchronization controller based on the observer, and the second is the controller based on stability theory.

3. Design of synchronization system

3.1. The 1st method of synchronization control

When the parameter value is $(a, b, c, k) = (5, 12, 5, 1)$, the observer of drive system is Formula 2.

$$\begin{bmatrix} \dot{x}_1 \\ \dot{y}_1 \\ \dot{z}_1 \end{bmatrix} = \begin{bmatrix} 5 & 1 & 0 \\ 0 & -12 & -1 \\ -1 & 0 & -5 \end{bmatrix} \begin{bmatrix} x_1 \\ y_1 \\ z_1 \end{bmatrix} + \begin{bmatrix} -y_1 z_1 \\ x_1 z_1 \\ x_1 y_1 \end{bmatrix} + C \quad (2)$$

Set

$$D = \begin{bmatrix} 10 & 0 & 0 \\ 0 & 0 & 0 \\ 0 & 0 & 0 \end{bmatrix} \quad (3)$$

Because A-D matrix has only negative real parts, according to Routh criterion, it is a Hurwitz stable matrix.

According to formula 4, and corresponding to formula 2, the synchronization system can be get as Formula 5.

$$\frac{d_{x_2}}{d_t} = Ax_2 + BF(x_2) + C + s(x_1) - s(x_2) \quad (4)$$

$$\begin{cases} \dot{x}_2 = 10x_1 - 5x_2 + y_2 - y_1 z_1 \\ \dot{y}_2 = -12y_2 - z_2 - x_1 z_1 \\ \dot{z}_2 = -x_2 - 5z_2 + x_1 y_1 \end{cases} \quad (5)$$

The following is the simulation of this design. Set the time of simulation is $[0 - 5]$, the time step is 0.0001, X_0 is $(3, -6, 7)$, Y_0 is $(3, 0, 0)$. the result of the MATLAB simulation is shown in Fig.3. Through synchronous timing diagram, it can be observed that although the initial value is different, the drive system and the synchronization system have been fully synchronized as the time goes by.

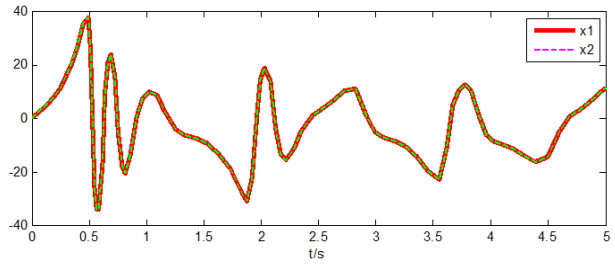


Fig.3. synchronization diagram of The first method

3.2. The 2nd method of synchronization control

The driving system for the four wing chaotic system is shown in Formula 2. Its response system is as Formula 6.

$$\begin{cases} \dot{x}_2 = 5x_2 + y_2 - y_2 z_2 + U_1 \\ \dot{y}_2 = -12y_2 - z_2 + x_2 z_2 + U_2 \\ \dot{z}_2 = -x_2 - 5z_2 + x_2 y_2 + U_3 \end{cases} \quad (6)$$

U_i ($i=1, 2, 3$) is the controller. The error variables between the response system and the drive system are as Formula 7.

$$e_1 = x_2 - x_1, e_2 = y_2 - y_1, e_3 = z_2 - z_1 \quad (7)$$

Construct Lyapunov exponent and its derivative can be obtained as Formula 8.

$$\dot{V} = \dot{e}_1 e_1 + \dot{e}_2 e_2 + \dot{e}_3 e_3 \quad (8)$$

When \dot{V} is always negative, through Lyapunov stability theory, the error system is globally asymptotically stable at the origin. In this case, the system as shown in Formula 2 is synchronized to the system as shown in Formula 6.

Through algebraic calculation, a proper controller can be constructed to synchronize the two systems completely. The controller in the system is selected as Formula 9. It is easy to prove that is always negative.

Through the Formula 9 and the Formula 6, the response system can be obtained as Formula 10.

$$\begin{cases} U_1 = -10e_1 - e_2 e_3 - e_2 \\ U_2 = 0 \\ U_3 = e_1 + e_2 - 2x_1 e_2 \end{cases} \quad (9)$$

$$\begin{cases} \dot{x}_2 = -5x_2 - 2y_2 z_2 + 10x_1 + y_1 + y_2 z_1 + y_1 z_2 + y_1 z_1 \\ \dot{y}_2 = -12y_2 - z_2 + x_2 z_2 \\ \dot{z}_2 = -5z_2 + y_2 - y_1 - x_1 + x_2 y_2 + 2x_1 y_1 - 2x_1 y_2 \end{cases} \quad (10)$$

Matlab simulation results are as Fig.4, and the related parameters are the same as those in the previous.

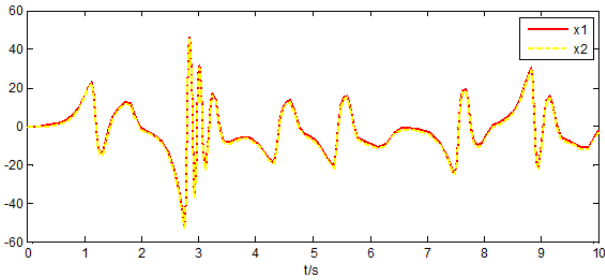


Fig.4. synchronization diagram of The second method

4. Circuit design of four wing chaotic system

The first synchronous control method mentioned above is feedback synchronization controller based on the observer.

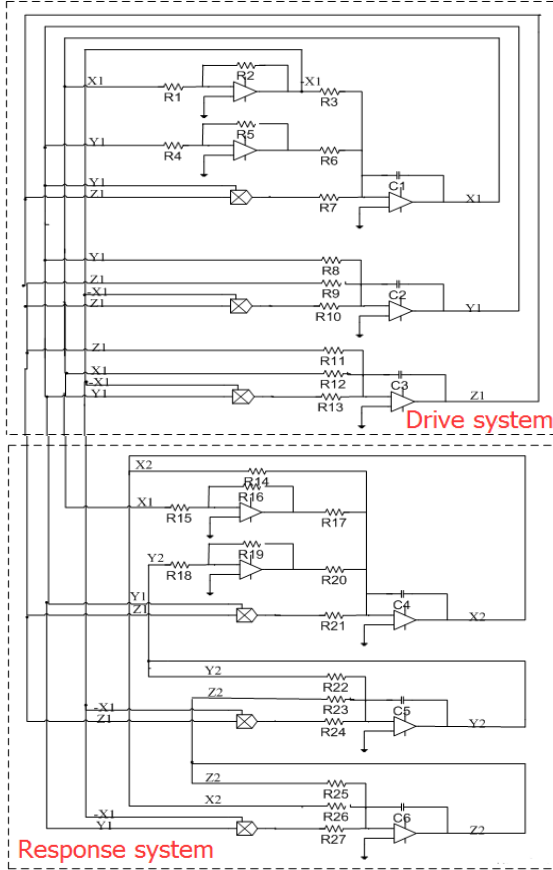


Fig.5. synchronization diagram of The second method

According to the response system shown in Formula 5 and the drive system and the Formula 2, the communication circuit is designed as shown in Fig.5. It is composed of operational amplifiers LF347, analog multipliers AD633, resistors and capacitors to perform additive, subtraction and multiplication operations.

The values of some basic components in this circuit are as follows:

- $R1=R2=R4=R5=R16=R18=R19=10k\Omega$,
- $R6=R9=R12=R20=R23=R26=1000k\Omega$,
- $R3=R11=R13=R14=R25=200k\Omega$,
- $R8=R22=83.3k\Omega$,
- $R7=R10=R17=R21=R24=R27=100k\Omega$,
- $C1=C2=C3=C4=C5=C6=10nF$.

The second synchronous control method mentioned above is the controller based on stability theory. According to the response system shown in formula 10 and the drive system and the formula 2, the communication circuit is designed as shown in Fig.6.

The values of some basic components in this circuit are as follows:

- $R14=R28=200k\Omega$,
- $R4=R28=200k\Omega$,
- $R18=R19=R23=R32=100k\Omega$,
- $R15=R20=R21=R22=R26=R27=100k\Omega$,
- $R7=R17=R33=R34=50k\Omega$,
- $R16=R25=R29=R30=R31=1000k\Omega$,
- $R24=83.3k\Omega$,
- $C1=C2=C3=C4=C5=C6=10nF$.

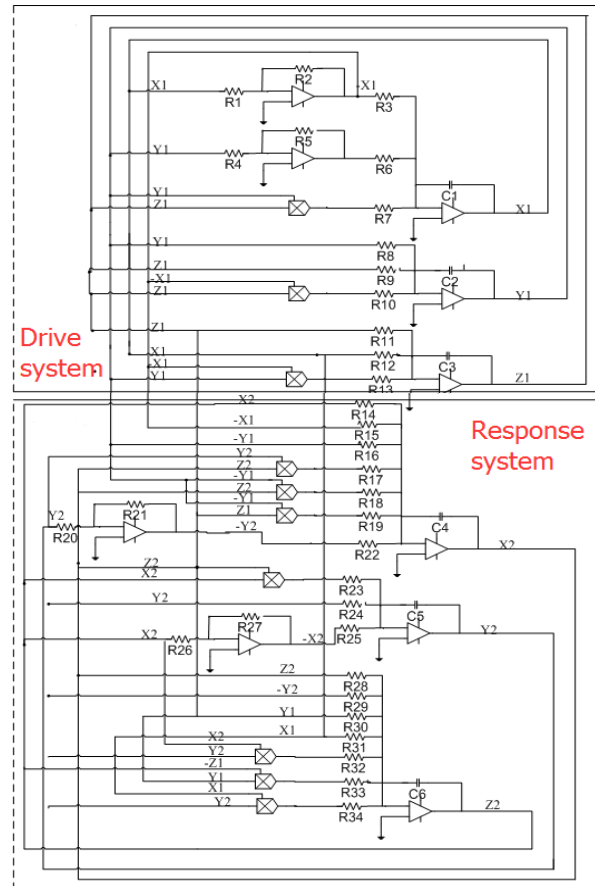


Fig.6. synchronization diagram of The second method

5. Testing and conclusion

We set the original sine signal as S1, the decrypted signal as S2, the mixed signal as H, the signal produced by the drive system as X1, and the signal error as deviation. The initial value X0 is (3, -6, 7), Y0 is (3, 0, 0), and the simulation time is (0s - 5s).

The simulation result of feedback synchronization controller based on the observer is shown as Fig.7.

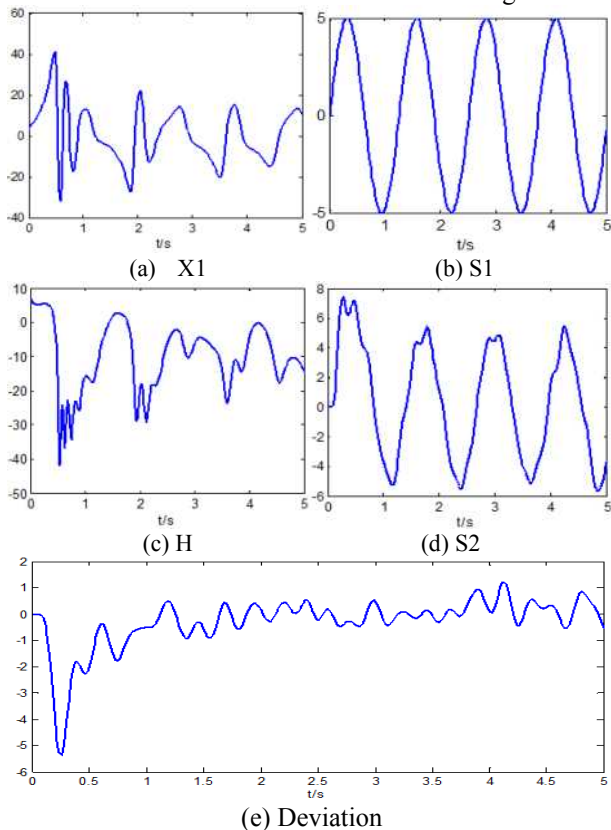


Fig.7. simulation result of The first method

The simulation result of the controller based on stability theory is shown as Fig.8.

We set the original sine signal as S1, the decrypted signal as S2, the mixed signal as H, the signal produced by the drive system as X1, and the signal error as E. The initial value X0 is (3, -6, 7), Y0 is (3, 0, 0), and the simulation time is (0s - 10s).

Acknowledgements

The research is partly supported by the Research Fund for the Reform in Education from Tianjin Municipal Education Commission of China (171005704B), and the Science & Technology Fund Planning Project of Tianjin Higher Schools (20140710-1400020005).

© The 2018 International Conference on Artificial Life and Robotics (ICAROB2018), Feb. 1-4, B-Con Plaza, Beppu, Oita, Japan

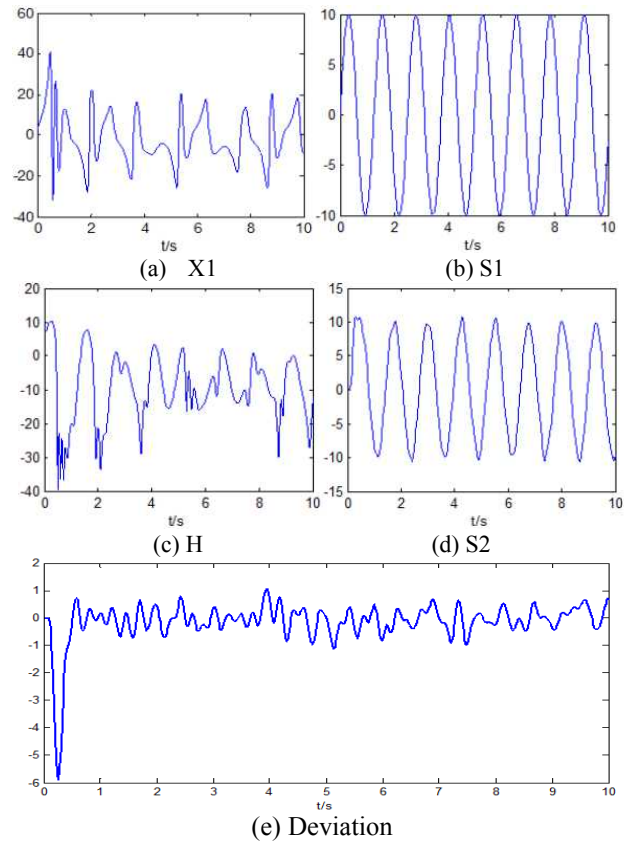


Fig.8. simulation result of The second method

References

1. Shu-Yi S, Fu-Hong M, Xue-Hong W, et al. Implementation of a new chaotic system based on field programmable gate array, *Acta Physica Sinica*, 63 (6) (2014) 60501-60502.
2. Yang-Zheng L, Chang-Sheng L, Xin-Chao L. A new smooth quadratic chaotic system and its digital signal processing implementation, *Physics*, (6) (2011) 60507.
3. Bao B, Xu J. Generalized Projective Synchronization for Multi-wing Chaotic Attractors, *ICECE*, (2010) 5234-5237.
4. Y Lin, C Wang, HE Haizhen, LL Zhou, A novel four-wing non-equilibrium chaotic system and its circuit implementation, *Pramana*, 86(4) (2016) 801-807.
5. K Guo, *Chaos synchronization and its application in secure communication* (Xi'an, Xi'an Technological University, 2013)
6. FF Li, *Research on chaotic synchronization control and Application* (Nanjing, Nanjing University of Aeronautics and Astronautics, 2007)
7. X G Liu, W Yang, W Liu, Y Dai, Designing S-boxes based on 3-D four-wing autonomous chaotic system, *Nonlinear Dynamics*, 84 (4) (2015) 1867-1877.

Design of Control System for Reboiling Part of Distillation Process

Lingran An¹, Fengzhi Dai^{1*}, Yujie Yan¹, Yuxing Ouyang¹, Zhongyong Ye¹, Xia Jin¹, Baochang We¹, Hongwei Jiao²

¹ College of Electronic Information and Automation,

Tianjin University of Science and Technology, China;

² Tianjin Technology School of Printing and Decoration, China

E-mail: * dai fz@tust.edu.cn

www.tust.edu.cn

Abstract

This paper selects the control system for re-boiling part of distillation process for major research. The control scheme is determined according to the influence of the relevant parameters on the distillation process. The hardware part uses the Siemens S7-200 series PLC as the main control machine. The lower position machine uses STEP 7-Micro / WIN programming software, and writes the control program through the ladder diagram. It combines the PID algorithm and single closed-loop control to complete the field data collection and processing and communication with the host computer. The host computer uses the configuration king named kingview6.55 monitoring system software to complete the automatic control system monitoring.

Keywords: Distillation Column, Reboiler, Control System, PLC

1. Introduction

In the distillation process, the reboiler not only affects the vapor phase load of the distillation column system, but also has a direct effect on the temperature of the kettle and the product quality of the tower kettle. Therefore, the proper choice of reboiler control scheme can play an important role in the overall energy consumption, stability and safety of the distillation process.

Some researchers have attempted to use intelligent control methods such as the neural network and fuzzy control for the distillation column in order to solve the problem of the time denaturation and the coupling of variables in the distillation control system¹. Some researchers also analyzed the advanced control algorithm of the distillation column theoretically, and proposed a multivariable dynamic decoupling control algorithm combined with the predictive PI algorithm to propose a dual control scheme for the stripping section².

Classic distillation column reboiler control methods are steam and condensate, they have their own advantages and disadvantages. The researchers optimized it to form a cascade circuit with the temperature of the kettle, thus improving the regulation efficiency and increasing the stability of the control system³. In view of the problems such as the delay of the sensitive plate temperature and poor operability during the reboiler control, the researcher reformed the reboiler control system based on the existing control and solved the problem of equipment operation stability⁴.

2. Overall scheme design

The process piping and control flow diagram of the reboiler part are shown in Fig.1. A portion of the liquid at the bottom of the column is heated by reboiler E102 and then returned to the column to maintain the continuous distillation process. The other part is controlled by the regulating valve VA120, as a product

of the bottom of the column. The liquid level of the reboiler is controlled by LIC101. The reboiling part uses the electric heating rod to heat the liquid, and the heating power is controlled by the TIC101. The cooling water starts from the cooling water pump P102, passes through the valve VA109, then flows through the rotor flowmeter F101, then enters the top condenser E101, then passes through the kettle cooler E103, then enters the cooling tower T102, finally returns to the cooling water tank V103.

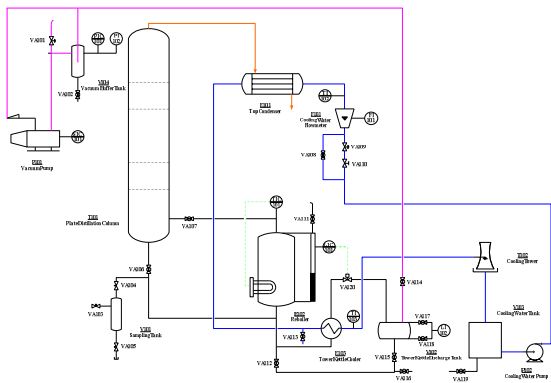


Fig.1 The process piping and control flow diagram of the reboiler part

2.1. Determination of detection scheme

First, determine the detection points of the control system as follows:

- FI101: Detect the cooling water flow flowing into the tower top condenser E101 in the cooling water circulation system.
- LI102: Detect the liquid level of the tower kettle discharge tank V102.
- TIC101: Detect the vapor phase temperature of the reboiler E102.
- TI102: Detect the temperature of the cooling water inlet.
- TI103: Detect the temperature of the cooling water outlet.
- LIC101: Detect the liquid level of the reboiler E102.

Then, we select the measuring instruments according to the detection point:

- The detection point FI101 selects the glass rotor flowmeter, for the On-site display of the cooling water flow.

- The detection point LI102 is the on-site display parameter, so the glass tube liquid level meter is selected.
- The detection point LIC101 needs electric remote transmission, so the remote transmission magnetic flap level gauge is selected.
- The three temperature detection points TIC101, TI102 and TI103 choose the Pt100 temperature sensor.

2.2. Determination of control scheme

First of all, determine the control points of the control system as follows:

- LIC101: Control the liquid level of the reboiler E102 by controlling the opening degree of the regulating valve VA120.
- TIC101: Control the vapor phase temperature of the reboiler E102 by controlling the heating power of the heating rod.

Then we complete the selection of actuators according to the selected control points:

- The control point LIC101 needs to control the opening degree of the regulating valve through the analog output of the PLC, so the electric proportional regulating valve is selected.
- The actuator of the control point TIC101 selects the solid-state voltage regulator.

The control scheme chooses the single closed loop control system, and the control algorithm of the regulator adopts PID operation adjustment. The control block diagrams of LIC101 and TIC101 are as follows:

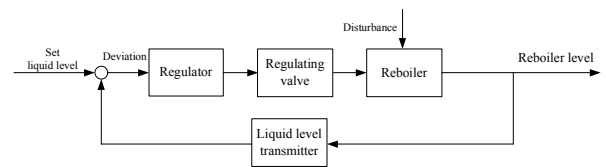


Fig.2. The control block diagram of liquid level of the reboiler

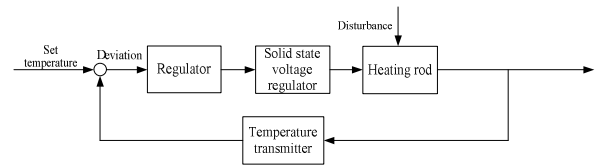


Fig.3. The control block diagram of vapor phase temperature of the reboiler

3. System circuit module design

The input and output points of this control system include: 2 digital input points (start and stop switches), 1 digital output point (LED indicator), 4 analog input points (cooling water inlet / outlet temperature, reboiler level and reboiler temperature), 2 analog output points (solid-state voltage regulator and control valve opening degree). Therefore, the CPU222 module is selected, which has 8 native digital inputs and 6 native digital outputs, allowing up to 2 I / O expansion modules. One EM231 analog expansion input modules and an EM232 analog expansion output modules are selected as required. The hardware wiring diagram is shown in Fig.4.

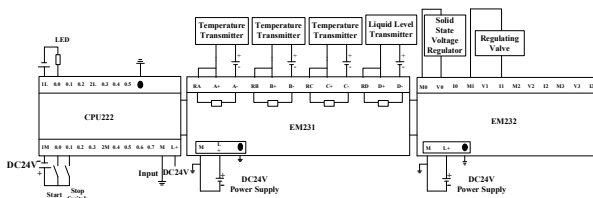


Fig.4. The hardware wiring diagram

4. Programming software design

The control layer of the control system of reboiling part of distillation process is the PLC system. It is used to receive on-site data and control the site equipment according to the pre-designed control strategies, while send the on-site data and equipment state to the PC machine⁵. This design selects the S7-200 series PLC as the controller, and the programming software uses the STEP 7-Micro/WIN software of the German SIEMENS company S7-200 series PLC.

4.1. The main program design

The control layer of the control system of reboiling part of distillation process is the PLC system. It is used to receive on-site data and control the site equipment according to the pre-designed control strategies, while send the on-site data and equipment state to the PC machine⁵. This design selects the S7-200 series PLC as the controller, and the programming software uses the STEP 7-Micro/WIN software of the German SIEMENS company S7-200 series PLC.

The PLC program is designed in a structured way. The main program completes all functions of the system, and calls each module in turn according to the system requirements and subroutine functions. The first scan

cycle of the PLC work needs to initialize the system, and the subsequent system programs are periodically invoked by a timer. When the timing time arrives, it reads the field detection data and calls the data conversion and scaling conversion subroutines to process and store the collected data. A part of the data is compared with the set value to calculate the deviation, for the PID instruction wizard to perform the operation. Finally, the control output conversion subroutine is called, which transforms the data after the PID operation and then outputs it to the actuator.

4.2. PID operation subroutine design

In STEP7-Micro/WIN V4.0, we can use the wizard to generate a PID instruction or program, and then call it in the main program. After completing the configuration of the PID loop through the wizard, the specified PID regulation subroutine PIDx_INIT and interrupt program PID_EXE will be automatically generated. The PIDx_INIT instruction performs the PID function based on the inputs and outputs we have previously set in the PID wizard, and it can be invoked every time the scan is performed. In this design, the vapor phase temperature control system of the reboiler and the liquid level control system of the reboiler adopt PID wizard to generate the instructions⁶.

5. Monitoring software design

This design adopts kingview6.55 monitoring system software. Generally, such a system can be divided into three layers: control layer, monitoring layer and management layer. The monitoring layer is connected to the lower connection control layer and the upper connection management layer. It not only realizes the real-time monitoring and control of the site, but also completes the important function of uploading and release, configuration development in the automatic control system. The configuration software also provides visual monitoring images for the participants, which is helpful for the real-time monitoring of the test subjects.

PLC and PC are connected by PC-PPI cable hardware, and the monitoring software of PC is communicated with PLC through PPI⁷. First of all, we complete the definition of the external equipment and the communication between the Kingview6.55 and the external equipment in the software. Secondly, we define the variables in the control system. Finally, we design the configuration screen, which are: reboiler operation monitor main interface, production report and data curve.

6. Summary and prospect

This design adopts DCS control system based on programmable controller Siemens S7-200. Its contents mainly include the overall scheme design of the reboiler part of the distillation process control system and the design of hardware and software.

This paper focuses on the design of the reboiler control system in the distillation process. However, the complete distillation process also includes the feed part and the reflux part, and this design is not combined with the two links. Therefore, the small S7-200 series PLC selected in the implementation of the hardware can not satisfy the whole complete distillation control. In the overall control, a medium or large PLC can be selected to achieve complete control.

Because the control points selected in this design are only to control a link, the selection of software and algorithms is relatively simple. The algorithms of complete distillation control is relatively complex, and the nonlinear control technology can be applied to the distillation column. In addition, adaptive control algorithms, predictive control algorithms, inference control algorithms and robust control algorithms can be developed. It is also possible to consider intelligent control methods such as neural network and fuzzy control for distillation tower.

Acknowledgements

The research is partly supported by the Research Fund for the Reform in Education from Tianjin Municipal Education Commission of China (171005704B).

References

1. Jiangpeng Wang, *Simulation study on temperature control of rectification tower based on fuzzy decoupling*, (Yunnan, Kunming University of Technology, 2015)
2. Yanming Zhou, *Theoretical analysis and design of advanced control algorithm of rectification tower*, (Shanghai, Donghua University, 2014)
3. Jun Shen, Analysis and optimization of typical temperature control scheme for rectification tower reboiler, *Chemical and pharmaceutical engineering*, 2015, 6: P1-P5.
4. Zhongwu Zhu, Dabo Jiang, The process and piping design of two reboiler and distillation column, *Fertilizer design*, 2016, 3: P15-P18.
5. Liguó Wen, *The design of the control of distillation column based on PLC*, (Heilongjiang, Northeast Petroleum University, 2013)
6. Xueyong Shi, Realization of PID control in the liquid level of distillation tower kettle, *Science and Technology Economic Guide*, 2017, 3: P72.
7. Yahui Mu, The practical technology of Kingview software, *Yellow River Water Conservancy Press*, 2012: P34-P35.

Research on intelligent control system based on machine vision

Ce Bian¹, Fengzhi Dai^{1*}, Meili Li², Yuxing Ouyang¹, Yiqiao Qin¹, Runhua Mao¹, Baochang Wei¹, Shengbiao Chang¹

¹ College of Electronic Information and Automation, Tianjin University of Science and Technology, 1038 Daguananlu Road, Hexi District, Tianjin, 300222, China;

² China University of Petroleum-Beijing, China

E-mail: * dai fz@tust.edu.cn
www.tust.edu.cn

Abstract

Machine vision is widely used in today's factories. This paper studies the motion control system based on machine vision. In the past, it is difficult for machine vision to extract valid information from the lens which has plenty of complex shapes, transparent and reflective elements in the electronic industry. This paper studies precise motion control based on machine vision.

Keywords: machine vision, motion control system, image process, servo motor, precision

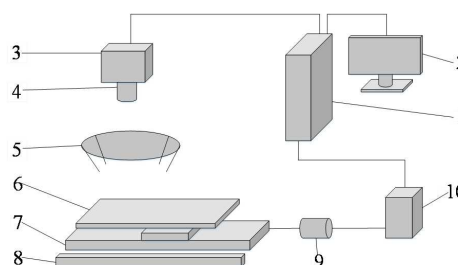
1. Introduction

In LED industry, the lens is transparent and has a complex shape. It is necessary to determine the outline and attitude of the lens when acquiring image information. The first thing is to collect the outline of lens. Image edge belongs to high-frequency signal. It can produce great influence when the edge and the shape capturing part of irregular shape of lens.

2. The main hardware analysis

Machine and computer vision usually refer to the digital processing of the image by the computer, thus to analyze the pixels in the picture. The application of machine vision in the industry field totally is different from ordinary computer vision. Machine vision system can adapt to the most of the industrial environment.

Machine vision system is an integrated system that includes the digital image processing, industrial control, LED lighting, optical imaging, sensors, analog and digital video, computer hardware and software, human-machine interface, as shown in Fig.1.



1: industrial computer, 2: monitor, 3: industrial camera, 4: lens, 5: LED light source, 6: PCB, 7: mobile platform, 8: raster ruler, 9: servo motor, 10: motor drive.

Fig.1 Hardware design of machine vision

2.1. Components of Machine Vision

1. Lighting mode. LED, as a new kind of green light source, is applied to the machine vision system with luminous stability and can be controlled by manual and programming adjustment.

2. The Image sensor. CCD and CMOS sensor are used to convert image information into digital information by

using photodiode. They transfer digital signal in a different way. Through the transferring way of CCD sensor, each pixel data was transmitted to the next pixel line by line. Through the amplifier amplify the date then output at the end; CMOS sensors are not suitable for long-distance data transmission. Each signal can transmits data through an amplifier and A/D conversion circuit when period) collected by each pixel in a circuit similar way.

3. Image storage. The period time that the camera taking photos is small relative to the data processing time which is less than 40 milliseconds. Unprocessed information deposit onto a buffer zone, and then by way of first in first out for processing.

4. The image collection card can collect standard or non-standard GRB signals that simulate black and white component. The card support camera which scans each line one by one or scans each line the GRB component separately.

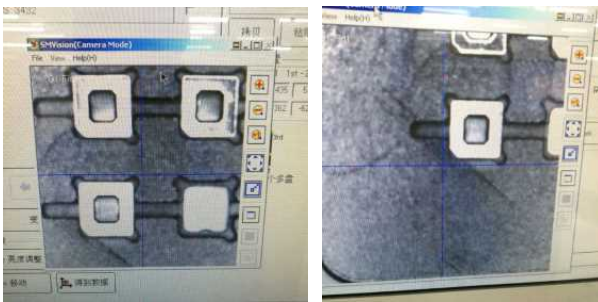


Fig.2 Lens image

5. Image pre-processing. The image information processing in the machine vision system is to highlight the needed elements in the image instead of considering the image quality. So it is unnecessary to be similar to the original image after in a pre-processing of images.

Image processing means to separate the objects from the background. Firstly, we need to identify the edges. Edge is a collection of pixels that have a step change in the adjoined pixel. The edge is usually determined by the sudden change of the gray level. Commonly there are three edges, the stepped edge, the roof edge and the linear edge. To get the information of the image, the smoothness image is mainly to deal with the noise in the pixel and reduce the noise to improve the image quality. The smoothing treatment is handled primarily by a

low-pass filter which blocking the high-frequency noise signal and leaving the low-frequency useful signal.

2.2. Motion control system

The XY mobile platform discussed in this article is that motion control card sends pulses separately to two servo motors control each axial movement. It's going to be the direction of the vector X and Y. After superimposed motion trajectory, the motion control system cannot control the head of trajectory. In order to control the head of the trajectory, interpolation is an excellent solution to this problem. There are four types of interpolation, comparison method, numerical integral method, time division method and the spline interpolation method. This paper studies the point-by-point comparison interpolation method. It means starting from the origin point. System compares the given trajectory at every feed step. Through the result of deviation, it will judge the axis feed for the next step.

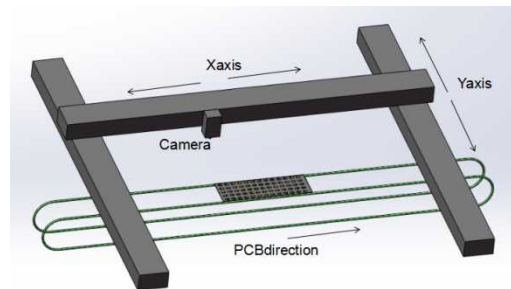


Fig.3 The structure of SMT

1. Stepping motor is an actuator that converts electrical pulse into angular displacement, and controls pulse number and pulse frequency. The permanent magnet is the rotor of the servo motor. The driver adjusts the rotation speed and angle according to the comparison between feedback value of encoder and the target value.
2. The servo motor is controlled by encoder feedback when stepping motor work speed pulse and direction pulse are required.
3. The step motor controls the angle of rotation by controlling the number of pulses. One pulse corresponds to one step angle. The servo motor controls the rotation angle by controlling the length of pulse time.

4. Stepping motor occurs low-frequency vibration at low speed.
5. The output torque of stepping motor decreases with the increase of speed and decreases sharply at high speed. The servo motor will be running smoothly at low speed.
6. Stepping motor cannot be overloaded. Ac servo motor is the constant torque output, and the torque will work in a constant way when running at the rated speed. Ac servo motor has strong overload capacity.
7. The stepping motor from the stationary acceleration to the working moving speed needs 200 ~ 400ms. The ac servo system accelerates from rest to its rated speed only a few ms.

3. The algorithm

3.1. Algorithm analysis

There are a lot of information that is not necessary in the images. So it is essential to separate the useful information.

There are three kinds of image segmentation. The edge segmentation is to use the sharp change of pixel gray degree to separate the helpful information. Region-dependent segmentation is to select several primary pixel points and then extend them to make judgments. Threshold segmentation is a traditional segmentation method. The central principle is to select the appropriate threshold for segmentation.

This article explains the method to delete the useless information in the image after segmentation, as shown in the following figures Fig.4 to Fig.7.



Fig.4 Ideal image information



Fig.5 Decision of Lens direction

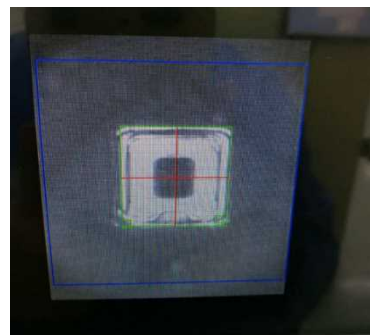


Fig.6 Decision of Lens edge

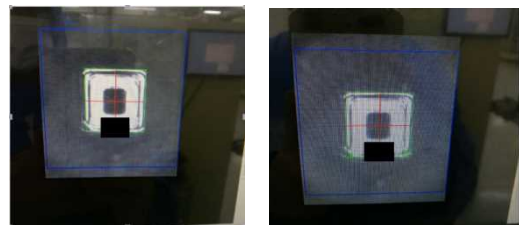


Fig.7 Lens image after removing the superfluous

3.2. Coordinate conversion

This study selects traditional camera calibration method. There are four coordinate systems that will be used in the process of camera calibration. They are the world coordinate system, camera coordinate system, image physical coordinate system and image pixel coordinate system, as shown in Fig.8.

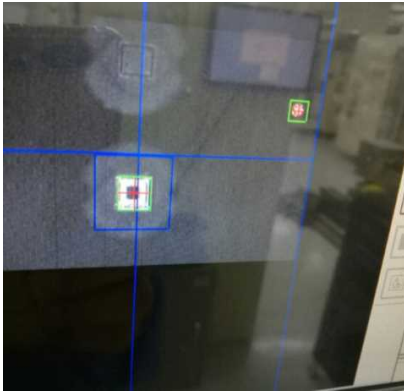


Fig.8 Four coordinates relative to the position

4. Conclusion

This article uses SMT in the electronics as research object to analyze the intelligent control system based on machine vision. The visual system analyzes the image by collecting different images information. The control system drives the actuating parts to obtain optimal closed-loop precise control. The most useful information collection and the precision of the motion control directly affect the performance of SMT machine. The moving control system selects performs component according to the comparison between stepping motor and servo motor.

The paper presents the following points:

- (1) Image segmentation is used to remove the complex interference information.
- (2) Double processing of image acquisition information is used to get the accurate component coordinates.

- (3) The semi-closed loop control system adds the feedback to realize the precise closed-loop control.

Acknowledgements

The research is partly supported by the Research Fund for the Reform in Education from Tianjin Municipal Education Commission of China (171005704B).

References

1. Zhi-Yuan Zhang. Research on robot motion control based on machine vision. *North China Electric Power University*, 2014.
2. Niblett Timothy J, Church Richard L. The Shortest Covering Path Problem. *International Regional Science Review*, 391, 2016.
3. S.Y.Chen, Han-Tang Tong, Carlo Cattani. Markov Models for Image Labeling. *Mathematical Problems in Engineering*, 2012: 163-170, 2012.
4. Ting-Ting Ding, Zhou Fang, Bo Liu, Junan Zhang. Fast calibration and error analysis based on machine vision detection. *Manufacturing automation*, 2014.
5. Lei-Hong Li, Qun Guan, Kai-Heng Hu, Yu Yang. The development of camera calibration system based on OpenCV in vc (VC) ++ environment. *Computer applications and software*, 6: 19-21+31, 2011.
6. Li-Tao Wang, Chun-Xiao Zhuang, Qiu-Cheng Wang. Digital image geometry transformation based on VC programming. *Science and technology innovation and application*, (17): 53-53, 2015.
7. Zheng Zhang, Chao Zhang, Shuxia Zhang, Hailing Han. Digital image processing and machine vision--Visual C++ and Matlab realization. *The people's mail and telecommunications press*, 2014.
8. Chang-Hao Dong. Study on interactive PCB image segmentation based on graph theory. *The PLA Information Engineering University*, 6: 22, 2013.

Development of NC Power Based on Buck Circuit

Yuxing Ouyang, Fengzhi Dai*, Runhua Mao, Ce Bian, Baochang Wei, Yiqiao Qin, Shengbiao Chang, Qijia Kang

*College of Electronic Information and Automation, Tianjin University of Science and Technology,
1038 Daguananlu Road, Hexi District, Tianjin, 300222, China*

*E-mail: * dai fz@tust.edu.cn*

www.tust.edu.cn

Abstract

This paper develops a kind of power-supply module which uses digital control and buck circuit. The module can convert 220v alternating current into 0-30V direct current. In the aspect of circuit design, it is mainly AC-DC, DC-DC conversion circuit and SCM minimum system circuit. In the aspect of control circuit, for feedback signal of current sensor, the power-supply module can obtain average value by multiple means and remove the mutation value.

Keywords: Buck circuit, SCM, AC-DC conversion circuit, DC-DC conversion circuit

1. Introduction

With the development of power electronic technology and digital control technology, more and more devices combine these two technologies. This paper develops a power module which combines MCU with Buck circuit to enhance the digital control of the power supply module to a certain extent to make up for the lack of traditional power supply module¹.

At present, the traditional power conversion circuit uses TL494 as the PWM signal generator and the MOS tube as the switch element. The voltage regulation is realized by building analog circuits and adjusting the resistance of sliding rheostat or potentiometer to change the duty ratio of PWM.

A closed-loop system can also be formed by building an analog circuit, but this closed-loop system has a simple structure and low anti-interference ability. The most important thing is that this conversion method which based on analog circuits has its own insurmountable shortcomings, such as the inability to display parameters such as voltage and current in real time and the disadvantage of not being able to adjust in real time. Moreover, the conventional power conversion

circuit has a complicated structure, low stability, easy to generate errors, and consumes a certain amount of energy because it needs to withstand a large amount of resistance.

The main circuit of the NC power based on Buck circuit is divided into the following three modules: The first module is AC-DC conversion circuit. Its function is to convert the 220V AC to the 30V DC through a transformer, a bridge rectifier module and filter capacitor; the second module is the DC-DC conversion circuit. Its function is to convert the 30V DC to the 0-30V DC through the Buck circuit; the third module is the microcontroller control circuit, its main function is to protect the special requirements of constant voltage or constant current, through reading the current sensor feedback signal and adjust the PWM duty cycle to change the voltage output².

This paper is organized as follows. Section 2 describes the hardware circuit design, and Section 3 introduces the control strategies. The main circuit simulation is implemented in Section 4, and the conclusions are presented in Section 5.

2. The hardware circuit design

The basic circuit of the system is divided into step-down rectifier filter circuit, Buck circuit, measurement circuit, SCM supply circuit, 430F149 minimum system circuit, LCD liquid crystal display circuit and independent key circuit. The step-down rectifier filter circuit is discussed in Section 2-1. Section 2-2 describes the Buck circuit. Section 2-3 introduces the 430F149 minimum system circuit³.

2-1. The step-down rectifier filter circuit

This circuit includes the transformer, full-bridge rectifier and filter capacitor. The role of the transformer is to convert 220V AC to 30V AC. After the rectification action of the full bridge rectifier module, the alternating current is converted to direct current, but the waveform of the direct current is unstable. Using the filter capacitor can make the DC waveform more stable⁴. The step-down rectifier filter circuit is shown in Fig.1.

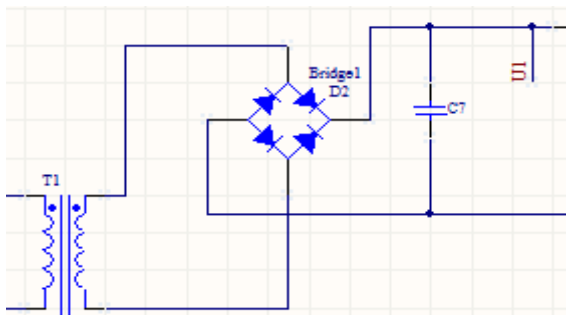


Fig.1 The step-down rectifier filter circuit

2-2. The Buck circuit

Buck circuit is mainly composed of the MOS tube IRF540, inductor, capacitor and freewheeling diode. MOS tube IRF540 mainly used in the circuit as a high-power switching components, is the core of the DC-DC circuit. The diode protects the entire circuit by preventing the reverse flow of current. Inductance and capacitance form a low-pass filter, making the circuit output current waveform smoother. The buck circuit is shown in Fig.2.

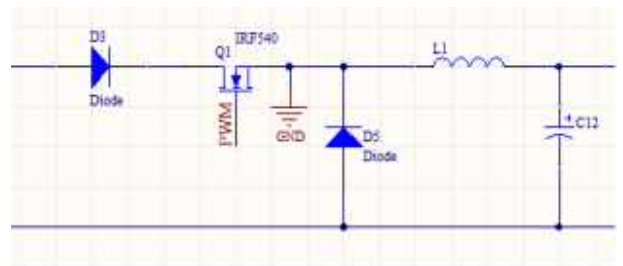


Fig.2 The buck circuit

2-3. The circuit of the system

Other circuits are related to the control chip. 430F149 microcontroller peripheral circuits include reset circuit, crystal oscillator circuit and power supply circuit. Power supply circuit mainly uses the LM7805 regulator module and LM117 regulator module. This part of the circuit can be about 30V DC voltage into 3.3V DC voltage, so as to provide a stable microcontroller voltage. The circuit of the system is shown in Fig.3.

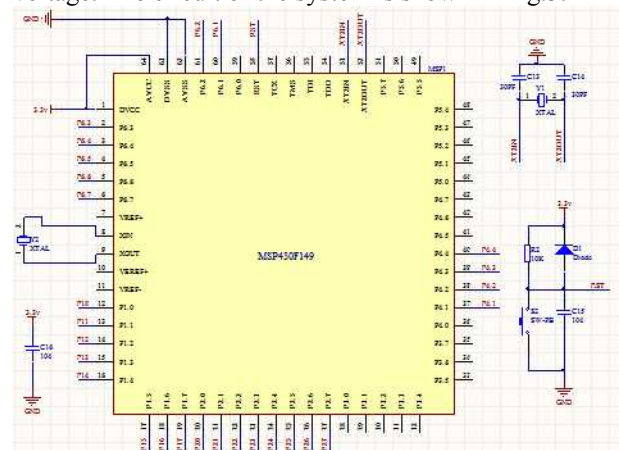


Fig.3. The circuit of the system

3. The control strategies

Good hardware circuits and powerful control ICs play a crucial role in NC power, but control strategies are also an integral part of maintaining the proper operation of a device⁵. For the NC power developed in this paper, the control strategy is mainly used in the chips on the ACS712 current sensor module feedback signal processing. The system can be based on the signal to adjust the PWM signal output. However, due to the sensor itself may be some problems, we can improve the situation to some extent through data processing. The PWM signal output must also have a certain control

strategy, in order to improve the voltage conversion capability of the entire system⁶.

Because the ACS712 current sensor feedback is an analog signal, when subjected to external interference may be abrupt changes in value, making the measurement error. The control strategy adopts the method of filtering the mutation value and obtaining the average value. We remove each group of five data with larger absolute deviation value and retain the five data with smaller absolute deviation value. A total of 25 sets of data for the five groups, we again average these 25 data, the average as the true value of the feedback signal.

After obtaining the feedback value of the data processing, we use the difference between the feedback value and the set value to adjust the duty cycle of the PWM. Because the load will have a certain voltage and current limit, so we adjust the PWM duty cycle, the step value should not be too large, to prevent overshoot. However, if the step value is too small will affect the adjustment time, making the adjustment time increases, which will not be conducive to real-time response of the entire system. Therefore, we set the threshold method to adjust the PWM duty cycle. When the difference between the actual feedback value and the set value is larger, we adopt a larger step value to adjust the duty cycle of the PWM, and when the actual feedback value approaches the set value, reduce the step value.

Through this strategy, the voltage conversion ability of the entire system can be well improved, and the real-time response of the whole system is good.

4. The main circuit simulation

The maximum input voltage of LM78XX series voltage regulation module is 36V, so the voltage after the filter module of variable voltage rectifier must be reduced below 36V. Buck circuit which capacitance and inductance parameters will directly affect the time that system circuit to reach steady-state. So, we need to go through a software simulation to find one or more sets of optimization data. Section 4-1 introduce the AC-DC conversion simulation circuit. Section 4-2 introduce the buck circuit simulation.

4-1 The AC-DC conversion simulation circuit

In the AC-DC conversion simulation circuit, we set three measurement points, namely the input voltage U_i , transformer output voltage U_{1i} and rectified output voltage U_1 . We use voltmeters and oscilloscopes as measurement tools. The oscilloscope detects the waveform of the final output voltage U_2 and the time it takes for the voltage to reach steady-state time. The simulation result of AC-DC circuit is shown in Tab.1.

Tab.1 The simulation result of AC-DC circuit

U_i (V)	n1:n2	U_{1i} (V)	U_1 (V)	C(μ F)	T(ms)	W
220	7:1	31.149	42.357	500	4.924	S
220	8:1	27.492	36.768	500	4.924	S
220	9:1	24.437	32.688	500	4.924	S
220	10:1	21.993	29.234	500	4.924	S

(Note: C: Filter capacitor, T: steady-state time, W: Waveform, S: stable.)

If we hope that the final output voltage of the overall circuit U_2 range between 0-30V, then its AC-DC circuit part of the output voltage values U_1 which after rectification must be above 30V. Taking into account the MOS tube IRF540 protection and as much as possible to reduce the heating power, AC-DC circuit output voltage values should be as close to 30V. According to the above two points, when we select the transformer turns ratio is 9: 1 turns the circuit can make the output voltage value U_1 is 32.688V.

4-2 The buck circuit simulation

Buck circuit as the core circuit of the NC power supply studied in this paper will directly affect the efficiency of the entire system, so the parameters of each component is particularly important⁷. We through the circuit simulation to determine the Buck circuit capacitance, inductance parameters. Select the optimal parameters to keep the output waveform stable, reducing the time it takes for the Buck circuit to reach steady state.

From the experimental data in Tab.2 we can know that actual simulation values and theoretical values are different. Experimental data show that when we select the capacitance and inductance of the larger values, the longer the time required to reach steady state, but the waveform is relatively smooth. When the selected capacitance and inductance is small, although the

steady-state time is shorter, but the waveform is unstable. So, we choose the capacitance and inductance parameters should choose the middle value, so we choose 470uF and 100mH.

Tab.2 The simulation result of Buck circuit

U1(V)	D	TV(V)	SV(V)	L ₁ (mH)	C ₂ (uF)	S(ms)
32.688	20%	6.538	5.915	100	470	203.4
32.688	40%	13.075	12.590	100	470	247.6
32.688	60%	19.613	19.388	100	470	255.2
32.688	80%	26.240	25.981	100	470	272.1
32.688	90%	29.412	29.285	100	470	250.5
32.688	90%	29.412	29.149	1000	470	397.4
32.688	90%	29.412	29.275	10	470	101.7
32.688	90%	29.412	29.275	100	47	68.7
32.688	90%	29.412	29.338	100	4700	799.9

(Note: D: Duty cycle, TV: Output theoretical value, SV: Output simulation value, S: Steady-state time)

From the circuit simulation results we can see that we can determine the transformer turns ratio of 9: 1, and in the Buck circuit, the specific value of the capacitor is 470uF and the inductor value is 100mH.

5. Conclusion

Developed in this paper based on Buck circuit NC power supply, which can output any value between 0-30V stable voltage, but also real-time display current and voltage values and other parameters. The device can not only be used as a constant current source to a certain extent, but also can freely switch between a constant current source and a constant voltage source.

We are free to set the working hours of the equipment programmatically and enable the equipment to automatically calculate and display the voltage, current and consumed energy values across the load and enable the automatic alarm function when these values reach the limit. At the same time, we incorporated data

processing and control strategies to ensure the stability of the equipment and formed a closed-loop control system. In the whole system, the analog circuit part is responsible for the voltage conversion, the digital control part is responsible for the regulation of the system, and the two parts work independently and complement each other, so that the power supply module is intelligentized and the device can be more safely and steadily for the load Power supply⁸.

Acknowledgements

The research is partly supported by the Research Fund for the Reform in Education from Tianjin Municipal Education Commission of China (171005704B).

References

1. Chun-Wei Feng, Wei-Feng Min, Juan Lei. Design of a High-precision Numerical Control LED Constant Current Driver. *Electronics World*, 14(14): 113-114, 2017.
2. Yin-qiao Li, Yu-Ling Liu, Xue-Feng Liu, Shan Huang. Design of NC DC power supply based on MSP430. *Computer Measurement and Control*, 24(12): 231-233+236, 2016.
3. Zhen-Feng Xiao, Rong-Xiang Yuan, Xiang-Tian Deng, Xiao-Lei Liu. Remote Intelligent Fault Monitor Based on MSP430F169. *Electric Power Automation Equipment*, 33(01): 160-164, 2013.
4. Zheng-Sen Jiang. Homemade Raiders of Precision CNC Power Supply. *Journal of Radio*, (9): 58-63, 2012.
5. Xiu-Hua Wang. NC Constant Current Source Based on Integrated Switching Regulator Chip. *Power Technology*, 5: 738-739, 2012.
6. Tian-Chen Huang, Song Jia, Jian-Hua Yu. Design and Realization of High Precision NC DC Current Source. *Instrumentation Technology and Sensor*, (6): 27-29, 2013.
7. Zhong-Hua Yun, Huan-huan Yin, Yong-Feng Li. Simulation and Research of DC Buck Chopper in Multisim. *Application Engineering of Computer Engineering*, (16): 216-218, 2015.
8. Zhao-Lin Huang, Wen-Tong Wu, Xiao-Jun Jing, et al. Design of precision numerical control direct current power supply. *Control Automation*, 8(8): 134-137, 2011.

Simulation of PID Temperature Control System Based on Neural Network

Yujie Yan, Fengzhi Dai *, Lingran An, Yuxing Ouyang, Zhongyong Ye, Xia Jin, Ce Bian

*College of Electronic Information and Automation,
Tianjin University of Science and Technology, China*

*E-mail: * daifz@tust.edu.cn
www.tust.edu.cn*

Abstract

The system designed in this paper is a combination of neural network and PID control. BP neural network has a great advantage in solving the control of nonlinear and uncertain systems. It can use the steepest descent learning method to adjust the threshold and weight values by back propagation. The ultimate goal is to adjust the PID controller adjustable parameters by the neural network learning algorithm. Using MATLAB software to simulate, the results show that the system has a strong following performance and a high anti-interference ability. Experiments show that the PID temperature control system based on neural network has some practicality.

Keywords: neural network, PID control, MATLAB, temperature

1. Introduction

Control theory has undergone several stages of development and made historic contributions to aerospace, military and industry. However, both the classical control theory and the modern control theory rely too much on the mathematical model, which limits these applications greatly¹.

Main plant temperature control system is a typical large delay, nonlinear and time-varying system. If we use a conventional PID controller, we will not achieve the desired control effect. The work of this paper is to select the most widely used BP neural network algorithm and to control the main steam temperature of the power plant by combining the control strategy of three-layer BP neural network with PID classic incremental numerical control algorithm. Because the main steam temperature of the power plant is a time-varying uncertain object, it has different mathematical models under different load values. Basing on the data of the literature, we conducted simulations under different loads. In addition to verifying

the following performance of the neural network PID control system, it also increases the test of anti-jamming capability. It is another practical attempt and exploration to combine the traditional PID control and neural network control to achieve the main steam temperature control².

2. PID temperature control system based on BP neural network

BP neural network is a kind of multi-layer feed-forward network. It follows the error backwards and can learn a lot of input and output information. To minimize the error of network, It use the steepest descent learning method to adjust the threshold and weight values by back propagation.

2.1. PID control system based on neural network

In the actual control system, the PID controller still occupy more than 90%. In this paper, the design of the control system, which has not only the advantages of classical PID controller, but also the advantages of neural

network control³. As long as the input-output error of the system is not 0, the system continuously adjusts the neural network weights to obtained optimal PID controller parameters. PID control system based on neural network shown in Fig.1.

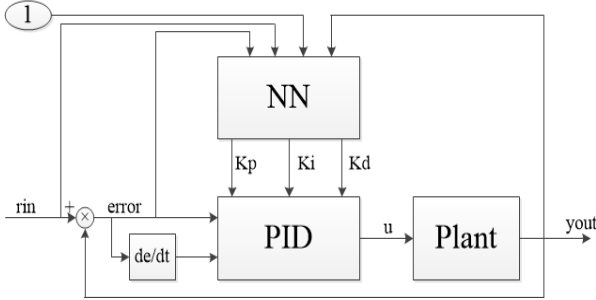


Fig.1 PID control system based on neural network

2.2. Algorithm of PID control system based on BP neural network

Use incremental PID control algorithm, the expression is:

$$u(k) = u(k - 1) + k_p (e(k) - e(k - 1)) + k_i e(k) + k_d (e(k) - 2e(k - 1) + e(k - 2)) \tag{1}$$

Because the kp, ki, kd are adjustable coefficients, the above formula can be expressed as:

$$u(k) = f[u(k - 1), k_p, k_i, k_d, e(k), e(k - 1), e(k - 2)] \tag{2}$$

Among them, f(*) is a nonlinear function trained by neural network. This design chooses 4-5-3 BP neural network structure. Because the three coefficients must be positive, the activation function of the neurons in the output layer is a non-negative⁴. The formula is as follows:

$$g(x) = \frac{1}{2} (1 + \tanh(x)) = \frac{e^x}{e^x + e^{-x}} \tag{3}$$

The activation function of hidden layer neurons is:

$$f(x) = \tanh(x) = \frac{e^x + e^{-x}}{e^x - e^{-x}} \tag{4}$$

Select the performance index function E(k), our goal is to minimize E (k):

$$E(k) = \frac{1}{2} (rin(k) - yout(k))^2 \tag{5}$$

Use the gradient descent method to correct neural network weight coefficient:

$$\Delta w_{ii}^{(3)}(k) = -\eta \frac{\partial E(k)}{\partial w_{ii}^{(3)}} + \alpha \Delta w_{ii}^{(3)}(k - 1) \tag{6}$$

In the formula α is the inertia coefficient and η is the learning rate. The above formula adds the inertia term to make the system converge quickly. Through calculation and simplification, get the output layer weight calculation formula⁵:

$$\Delta w_{ii}^{(3)}(k) = \eta \delta_i^{(3)} o_i^{(2)}(k) + \alpha \Delta w_{ii}^{(3)}(k - 1) \tag{7}$$

The same can be introduced hidden layer weight value formula:

$$\Delta w_{ii}^{(2)}(k) = \eta \sigma_i^{(2)} o_j^{(1)}(k) + \alpha \Delta w_{ii}^{(2)}(k - 1) \tag{8}$$

Summarize the algorithm steps are as follows:

- Determine the structure of BP neural network, that is, determine the number of input layer, output layer and hidden layer node. Give the initial value and the learning efficiency of each layer's weight coefficient.
- Give the input rin (k) and output yout (k) of the system and calculate the error error (k).
- Calculate the input and output of neurons in each layer of neural network, and the output of output layer is the three adjustable parameters of PID controller.
- Calculate the PID controller output u (k).
- Learning through neural networks, online adjustment of the weighted coefficient, to achieve adaptive control of PID parameters.
- Set k = k + 1, return to the first step.

3. Application of neural PID control system for main steam temperature system in power plant

Thermal power plant power supply system by the boiler, steam turbine generator and other equipment. There are many factors that determine the stability and efficiency of the thermal power plant, and the main steam temperature of the boiler is the most important factor that affects the stability and accuracy of the power plant.

3.1. Main steam temperature control characteristics

It is usually required that the main steam temperature be controlled as accurately as possible rather than within a certain safety margin. In fact there is a saying that about every 5 degrees lower thermal efficiency decreased by 1%. If the steam temperature is too high, the steam pipe will react at high temperature and even rupture. If the steam temperature is too low, the humidity will increase and affecting the safe operation of the system. Moreover, long-term operation of the unit in the inappropriate temperature range will greatly reduce the service life⁶.

3.2. Main steam temperature control model and method in power plant

Main steam temperature control of power plants has three basic disturbances. The amount of water to be reduced is often used as an adjustment signal, and the system structure under this adjustment signal is relatively simple and easy to control. Although the load disturbance can also affect the main steam temperature, it is an external disturbance. Control system under smoke disturbance boiler structure is too complicated for practical application. After the water temperature changes have a disturbance, the temperature released by the superheater is greatly reduced. However, the desuperheater outlet temperature adjustment is faster, with outstanding advancement, this section we call the lead zone. Therefore, the main steam temperature control system commonly used in power plants is a PID cascade control system.

Neural network-based power plant main steam temperature control scheme, is to combine the neural network with the traditional PID controller to make up for the artificial tuning PID parameters inaccuracy. The block diagram of main steam temperature control system of power plant controlled by neural network is shown in Fig.2.

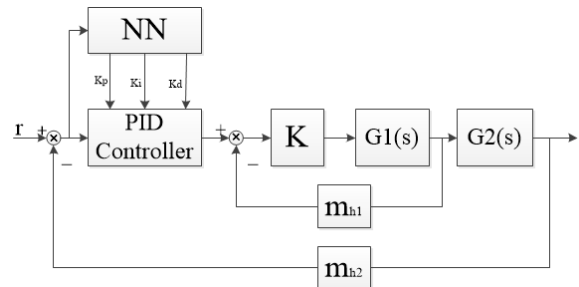


Fig.2 Power plant main steam temperature control system

The role of the main circuit of the control system is to maintain the steam temperature given by the superheater, the role of the secondary circuit is to eliminate the interference. R in the above picture is the input of the system steam temperature, m_{h1} , m_{h2} are the temperature transmitter transfer function. $G1(s)$ is the transfer function of the lead-in area of the control system, $G2(s)$ is the transfer function of the inert zone of the control system, and K is the transfer function of the actuator.

3.3 Simulation of main steam temperature control based on neural network.

The main steam temperature control of thermal power plants varies dynamically under each load. According to the literature, the transfer function of the inert region can be approximated as e^{-10s} . When the system load is 100%, the transfer function of the lead zone is⁷:

$$G1(s) = \frac{0.815}{(1+18s)^2} \quad (9)$$

Carry on MATLAB simulation under this load, the result is as follows:

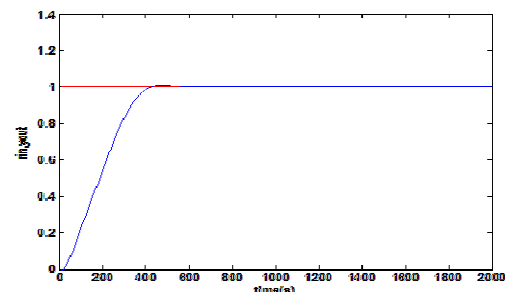


Fig.3 100% step load response curve

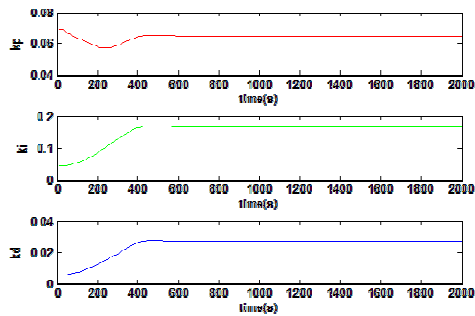


Fig.4 Parameter curve

Due to space limitations, this article will not repeat the simulation results under other loads. In fact, under different loads, the simulation results show that the system follows well. Especially when the system is running at full capacity, it can perfectly determine the three adjustable parameters of the PID to achieve the best control effect.

A good control system needs to achieve stable, fast, accurate control effect. Due to the interference of main steam temperature control system in thermal power plants, the anti-interference ability of the system should also be improved in practical application. In the simulation can add a 0.1 interference to simulate the actual power plant interference signal. Although there are some disturbances in the disturbance, the system quickly returned to normal. The result is as follows:

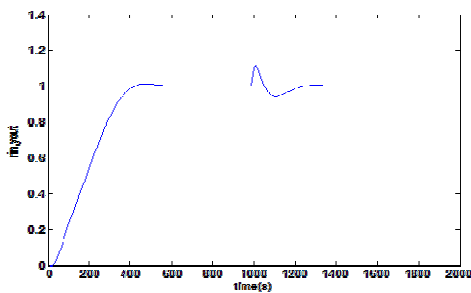


Fig.5 Step response curve plus interference

In addition, it is found in the other load simulations that there is fluctuation in the front of the curve, and the overshooting is relatively large. According to experience,

at this time it is best to reduce the learning rate and reduce the set initial value. The design of this simulation also verified, although only reduce the learning efficiency, the adjustment time and overshoot are smaller, greatly improving the control effect. All the simulation results show that this design has a good anti-interference effect in addition to good follow-up performance.

4. Conclusion

At present, the use of neural network PID control system is widely used in industry, agriculture and other fields. This control system also controls the drying of the barley malt, the raw material for beer. In addition can also be used in car medical thermostat control system. After we continue to explore, in the future neural network control must have a greater application prospects.

Acknowledgements

The research is partly supported by the Research Fund for the Reform in Education from Tianjin Municipal Education Commission of China (171005704B).

References

1. Peng Ge, PID algorithm based on neural network in the furnace temperature control application. Northeastern University, 2005: 10-15.
2. Weiguang Zhao, Ying Yang, Improved algorithm of PID controller in cascade control system of power plant main stream temperature. *Power System Engineering*, 2008, 24(6): 61-63.
3. Lei Ouyang, Based on self-tuning PID controller temperature control system. Anhui: Anhui University of Science, 2009: 5-8.
4. Linfang Sun, Mengmeng Shao, Xuying Liu, Superheated steam temperature modeling based on improving BP algorithm. *Techniques of Automation and Applications*, 2010, 29(4):1-3.
5. Chunxia Dong, Neural network fuzzy PID control in the furnace temperature control application. Hebei: Hebei University of Technology, 2004: 8-12.
6. Wei Qin, Based on the AM2301 temperature and humidity meter design, *Hunan Agricultural Machinery*, 2012, 9: P59 - P60.
7. Zhi Wei, Dongjie Gao, The control of main steam temperature for supercritical once-through boilers. *Control Systems*, 2008,24 (4): 17-18.

Design and research on real-time material management system based on production process

Baochang Wei, Fengzhi Dai *, Yuxing Ouyang, Haifang Man, Yiqiao Qin, Runhua Mao, Ce Bian

*College of Electronic Information and Automation,
Tianjin University of Science and Technology, China*

*E-mail: * dai fz@tust.edu.cn*

www.tust.edu.cn

Abstract

The paper primarily introduces the real-time material management system in the course of machinery production. This system is developed and designed using C# language and SQL2008 database, using C/S and B/S mixed mode, the C# language-related programming skill and database information together, through the C/S and B/S architecture for network communication, the database Server-related production material information sharing management system feedback to the specific user, thus enhancing the production efficiency.

Keywords: database, C# language, ASP.NET, module design, real-time material system.

1. Introduction

With the rapid development of science and technology, the automation level of enterprise production is higher and higher. For corporations, Production management is the main part of its development. An efficient production management system plays a key role in the continuous development of enterprises and the improvement of their overall competitiveness.

In the whole enterprise production, the use of material amount is an indispensable part of production management, because in most industry production cost, material cost accounts for a large proportion. Therefore, to achieve efficient management of materials can save a lot of cost for enterprise production. In addition, the degree of information sharing has become an important symbol of the level of enterprise modernization. The standardized design of the database is considered as one of the effective links to solve the problem of enterprise data management [1]. Through the data visualization analysis to achieve the collection and sharing of information in the production management stage, Enterprises can more effectively arrange material inventory, improve the utilization of

production machines, reduce inventory losses, improve staff efficiency and customer service levels.

In this paper, based on computer communication technology, we create material production information system, establish database and data communication system. This system is developed using C # language and SQL2008 design database, SQL Server 2008 database management system for data storage and management, performs data warehouse functions [2]. C # programming, combined with ASP.NET technology, the system has a safe and reliable performance [3]. Network communication is carried out through C/S and B/S architecture, and the information of production materials related to the database is shared to the user to realize real-time monitoring of the target in the production process. The company realizes production process automation through network technology, computer technology and database technology.

2. System overall functional framework design

The producer needs to know and monitor the production status in real time, and can master the whole production process without going to the

production site. In addition, enterprises hope that through the information management system accurate and timely control of production operations, in order to be able to quickly and accurately refueling work to achieve the full range of product production control. Prior to this project, we reviewed the relevant materials and visited the actual operation of the machinery in the workshop and the actual use of the materials. The Production site is shown in Fig.1.

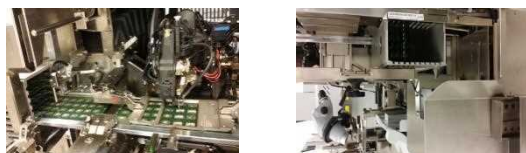


Fig.1. production site

2.1 The overall system design goals

To build a software system, the overall framework model of the software system (blueprint) is first planned [4]. The main objective of this project is to design a production material real-time management communication system. System users are divided into two categories, one is the operation workers, They mainly operate the production process in real time; The other group is the production manager, which is mainly responsible for looking at the overall production situation and determining the specific production requirements of the product. The system development process includes the development of the mobile front desk and the computer PC terminal and the design of the background database. Among them, the worker through the mobile terminal for inquiries, Production manager through the PC side to view. Then, according to the actual demand design and development of the foreground procedure, the relevant functions of the production schedule information in the production process are realized. System function module connection diagram is shown in Fig 2.

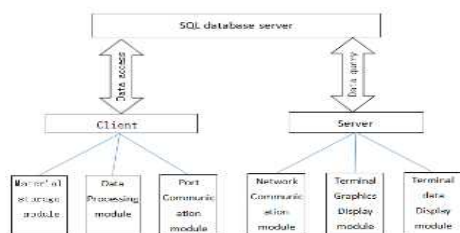


Fig.2. System function module connection diagram

2.2 System demand analysis

The system is mainly used for information interaction between production speed and material management in workshop production. In order to ensure the security of information, it works mainly within the company's internal local area network. System requirements in the PC terminal and mobile terminal devices on the display, according to the display function to design a different interface. Describe the main functions of each module and to achieve. The system should realize the information sharing in the company's production process.

2.3 Overall design planning

After the system function analysis, it can be divided into three modules: Background database server system module, User front desk device system module, User mobile Android device system module. Project overall module diagram is shown in Fig 3.

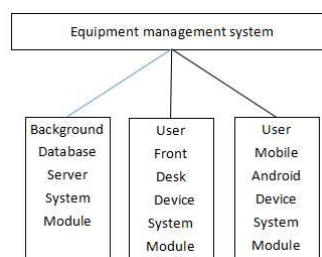


Fig 3. Project overall module diagram

2.3.1 Background database server system module design

The module is mainly to store some data in the production process, such as production materials information. According to the actual situation of production, the background database server system module can divide itself into several sub-modules: Production information module and equipment management module

- Production information module

The function of this module is mainly to provide the user with some information in the production process, including production equipment list, production record, production material situation, production machine and material inquiry and so on.

- Equipment management module

The module is controlled by the database administrator, according to the operation status, set the product, input the material information, and modify the production speed.

2.3.2 User front desk device system module design

The module is used to view production information. The manager needs to check the overall demand of the production workshop through the computer, Do not need to go to the scene to be able to know the production workshop need material situation, facilitate timely and accurate delivery. After the material is delivered, the worker will log on the PC side, feed the data back to the database, and update the relevant display information.

2.3.3 User mobile Android device system module design

The module mainly provides production information for production operators, the mobile terminal window is developed using jQuery Mobile, Through the AJAX technology to receive the return data and analysis. Loading the terminal APP into the phone allows the operator to easily query the real-time production status.

3. Design and Implementation of Database Management System

Based on the comprehensive consideration of material production information data volume, operation platform support degree, software development cost and other aspects, the system background database is developed using Microsoft SQL Server 2008 relational database. The following are the main steps in database design:

A: According to the actual production requirement design database to store data, carry on the overall frame design, grouping.

B: According to the data packet design to create the form.

C: Set the properties of the data in the table

D: Determine the relationship between tables and optimize the data structure.

Generally speaking, the design database system mainly includes data demand analysis, conceptual model design, logical structure design. As a database application management system, all production data involved in the production process should be stored in the database system.

3.1 data demand analysis

Through the analysis of system function requirements, need to establish a database server system that can store the front-end client display

information, including product number, production schedule, running machine code, the required materials. Through the software development, based on the working conditions of the production workshop, the real-time information of machinery production is precisely understood, and the information is summarized into the database server

3.2 Database Conceptual Structure Design

Currently widely used and can effectively represent the data conceptual model is the entity-contact diagram, it is also called E-R chart. E-R chart reflects the relationship between entity type and attribute. The entity and properties of the database system design are shown in the Fig 4, where the rectangle represents the entity set and the ellipse represents the properties of the entity.

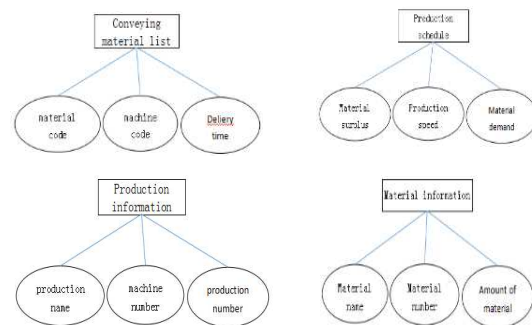


Fig 4 entity and properties of the database system design

3.3 Database logical structure design

The logical structural design of data is to transform the data conceptual model into a concrete data model supported by DBMS on the computer. According to the analysis of data needs, we can get the relevant entities that are available for production and determine the relationship between the entities.

4. System implementation and testing

In the first half of the article, the system is analyzed and the overall framework is designed, and the design of each functional module and the creation of database are realized. This section will implement the design of the corresponding interface based on the previous analysis.

4.1 System background database administrator interface implementation

This interface is used by database administrators to modify the data in the update production. The database administrator is required to log in to determine the identity before entering the system, after logging is eligible to modify and query the data and other operations. Database administrator login interface is shown in Fig 5.



Fig 5. Database administrator login interface

4.1.1 Mobile terminal information display interface

The interface displays the real-time production status of the machine in the production workshop, including the machine code of each machine, production status, and material consumption (expressed as a percentage of the material). For ease of differentiation, the production status of each machine is represented by rectangles, the whole rectangle represents the total amount of materials (background set to yellow), and the consumption of materials is expressed in red. Information display interface is shown in Fig 6.

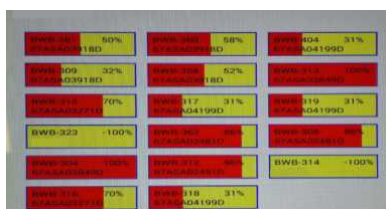


Fig 6. Information display interface

4.1.2 Prepare material information display interface

The interface is distributed on the lower left of the mobile information display interface, and the real-time data status of the parts of the machine is displayed in the same interface for the production personnel to view. Prepare material information display interface is shown in Fig 7.

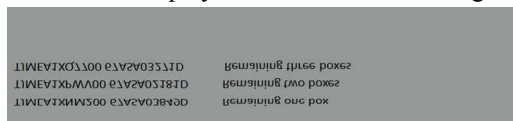


Fig 7. Information display interface

4.2 Background database login module test

System can distinguish between different users, according to the user's login information to determine whether to allow access to the system, when the user name and password exist an incorrect, the user cannot enter, to prevent non-professionals from making arbitrary changes to the database. Randomly selected multiple user names and passwords for testing, and found that only the user name and password match to enter the system, achieving the desired results.

5. Conclusion

Through continuous analysis and improvement, the overall functional framework of the system was established, and an effective database management display system for enterprises was implemented. Through the system module test, all achieved the expected effect, satisfied the enterprise to realize the various functional requirements.

Acknowledges

Thanks to Tianjin University of Science and Technology, it provides me with a good learning environment so that I can devote myself to studying. Thanks to my graduate tutor, he helped me a lot in study and life.

References

1. Jun Chen, Research on Data Standards and Database Design of Urban Rail Network. Guangzhou: South China University of Technology, 2015:27-32.
2. Fuqiang Luo, Visual C#. NET program design tutorial. Beijing: people's post and telecommunications press, 2012.
3. Jinjin Zhu, Tuhao Shen, Kejin Bao, The realization of Ethernet communication between computer and PLC industry based on net
4. Zhang F, Cui Y. Design of distributed warehouse management system based on CSLA.NET // Pacific-Asia Conference on Circuits.2010:292-295.
5. Lijuan Liu, The application of interaction design in man-machine interface design. *Electronic Technology and Software Engineering*, 2015(6):76-76.

Stability Control of Inverted Pendulum Based on Multi-loop PID

Zhongyong Ye ¹, Fengzhi Dai ^{1*}, Yuxing Ouyang ¹, Yujie Yan ¹, Xia Jin ¹, Lingran An ¹, Hongwei Jiao ²

¹ College of Electronic Information and Automation,
Tianjin University of Science and Technology, China

² Tianjin Technology School of Printing and Decoration, China

E-mail: * dai fz@tust.edu.cn
www.tust.edu.cn

Abstract

The traditional PID control can be very good for the stability of the pendulum angle control, but for the location control of car that loads the pendulum, it can do nothing. That is, the car will go along the rail without restrictions on the movement. The car and inverted pendulum system is a single-input multiple output instability system, so the multi-loop PID controller is designed based on the output feedback that is particularly important. Simulation shows the feasibility of using the multi-loop PID control, indicating that improved PID control is entirely feasible.

Keywords: Inverted pendulum, Multi-loop PID control, Output feedback, Simulink

1. Introduction

Inverted pendulum as a typical instability, a serious non-linear system, used to test the control methods of instability, nonlinear and rapid control. Using different control methods to control different types of inverted pendulum has attracted the attention of many scientists all over the world and has become one of the most challenging topics.

Inverted pendulum system has two balance points: the stability of the suspended state equilibrium point and the inverted state of the unstable equilibrium point. Control of inverted pendulum includes pendulum control and stability control. Pendulum will swing from the stable equilibrium point to the unstable equilibrium point, and the stable control will be inverted the pendulum system stabilized near the unstable equilibrium point.

Now there have been many papers published about the pendulum and stability control, and these results adopt different control ideas for swinging and stabilization and implement these two processes with unified control theory.

2. Mathematical Modeling

An inverted pendulum system consists of an inverted pendulum shown in the Fig.1, and the car along the rail movement. The inverted pendulum is fixed on the car.

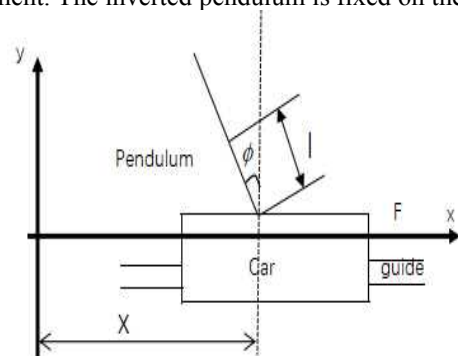


Fig.1 Model of Inverted pendulum system

2.1 Parameters

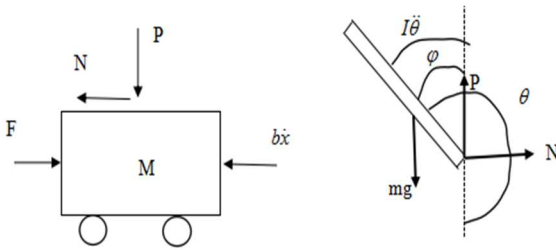
- M Car quality

- m Pendulum quality
- b Car friction coefficient
- l Pendulum rotation axis to The length of the rod center of mass
- J Pendulum inertia
- F The force added to the car
- x Car displacement
- θ The angle between the pendulum and the vertical downward direction
- ϕ The angle between the pendulum and the vertical upward direction

2.2 Mathematical modeling

Fig.2 is the system of car and pendulum force analysis. Among them, N and P are the horizontal and vertical components of the interaction force between the car and pendulum.

In the actual inverted pendulum system, the positive and negative directions of detecting and executing the device have been completely determined. Therefore, the definition of the variable direction is as shown in Fig.2, and the directions of the figure are all positive vectors.



(a) Car force analysis (b) Swing rod force

Fig.2 Force analysis of trolley and pendulum in the system

Assume $X = \{x, \dot{x}, \phi, \dot{\phi}\}$, $u = \ddot{x}$, we can get the car acceleration as the input inverted pendulum system state space expression:

$$\begin{bmatrix} \dot{x} \\ \ddot{x} \\ \dot{\phi} \\ \ddot{\phi} \end{bmatrix} = \begin{bmatrix} 0 & 1 & 0 & 0 \\ 0 & 0 & 0 & 0 \\ 0 & 0 & 0 & 1 \\ 0 & 0 & \frac{3g}{4l} & 0 \end{bmatrix} \begin{bmatrix} x \\ \dot{x} \\ \phi \\ \dot{\phi} \end{bmatrix} + \begin{bmatrix} 0 \\ 1 \\ 0 \\ \frac{3}{4l} \end{bmatrix} u \quad (1)$$

$$y = \begin{bmatrix} x \\ \dot{x} \\ \phi \\ \dot{\phi} \end{bmatrix} = \begin{bmatrix} 1 & 0 & 0 & 0 \\ 0 & 0 & 1 & 0 \end{bmatrix} \begin{bmatrix} x \\ \dot{x} \\ \phi \\ \dot{\phi} \end{bmatrix} + \begin{bmatrix} 0 \\ 0 \end{bmatrix} u \quad (2)$$

3. PID controller design

3.1 Inverted double loop PID controller design

In the traditional PID controller design, the control can well control the stability of the pendulum angle to the limitations of the traditional PID. However, the position of the car cannot be well controlled. That is to say, the car will move along the unrestricted movement of the guide rail.

Therefore, it is particularly important to design a double-loop PID controller based on the inverted pendulum system with output feedback. By modeling the pendulum angle and car acceleration, the pendulum displacement and car acceleration transfer functions are:

$$\frac{\Phi(s)}{V(s)} = \frac{ml}{(I + ml^2)s^2 - mgl} \quad (3)$$

$$G_2(S) = \frac{X(S)}{V(S)} = \frac{1}{S^2} \quad (4)$$

The double loop PID controller is actually a kind of feedback correction idea. Under the condition that the open-loop value of the local feedback loop is far greater than 1, the characteristics of the local feedback loop mainly depend on the feedback device, and irrespective of the enclosed part, proper selection of the form and parameters of the feedback correction device can make the performance of the corrected system that meets the requirements of a given indicator.

However, it should be pointed out that when designing the feedback correction system, the stability of the inner loop needs to be taken into consideration and the choice of the feedback correction parameters should be made improper so that the inner loop loses its stability. Therefore, it is difficult for the entire system to work stably and reliably and not convenient for the system to be open loop debugging.

Therefore, the feedback loop formed within the system, the best is stable. Still with the car's acceleration as input

to the pendulum angle and the car's displacement as the output, the resulting dual loop PID correction control system block diagram shown in Fig.3.

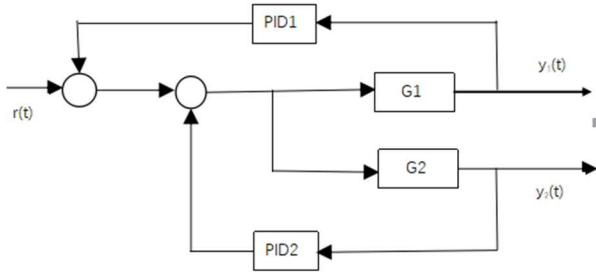


Fig.3 Dual loop PID control system structure

Substituting the system parameters into G1 (S) and G2 (S) gives the transfer function:

Transfer function of pendulum angle and car acceleration

$$G_1(S) = \frac{\Phi(s)}{V(s)} = \frac{0.02725}{0.0102125s^2 - 1.26705} \quad (5)$$

Transfer function of car position and car acceleration

$$G_2(S) = \frac{X(S)}{V(S)} = \frac{1}{S^2} \quad (6)$$

3.2 Double-loop inverted pendulum simulation

This paper considers the pendulum angle as the outer loop, and the car displacement as the inner loop. The outer loop control object (transfer function Eq.(3)) and the inner loop control object (transfer function Eq.(4)) into the control system that is shown in Fig.3. Then we can get the Simulink simulation shown in Fig.4.

The simulated curves are shown in Fig.5 and Fig.6 respectively. The simulation results show that the dual-loop PID control scheme can achieve the double stability of the car position and pendulum angle well and achieve the desired control purpose and requirements. Moreover, during debugging, we found that this system has low sensitivity to the change of PID parameters. When the specified parameters change within a certain range, the controller can effectively control the inverted pendulum and make it run stably.

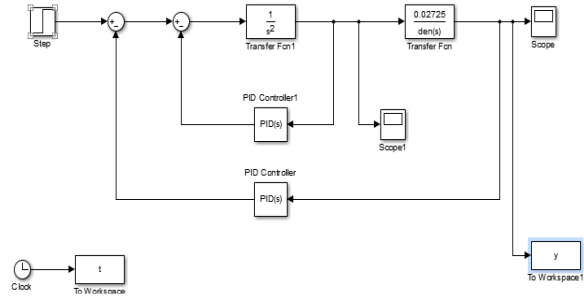


Fig.4 Double loop PID control system model diagram

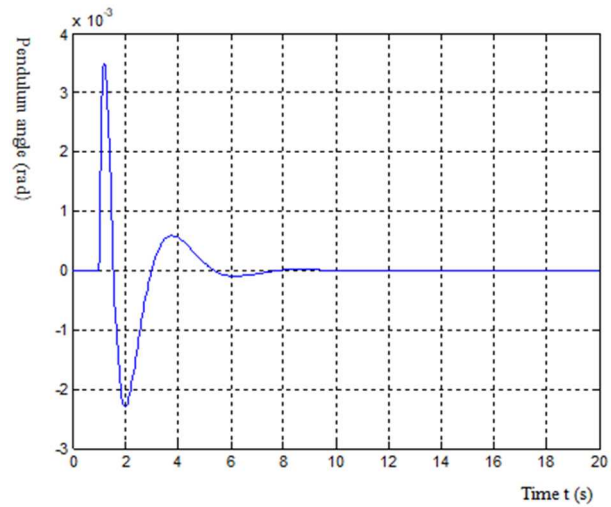


Fig.5 Two-loop control system pendulum angle simulation curve

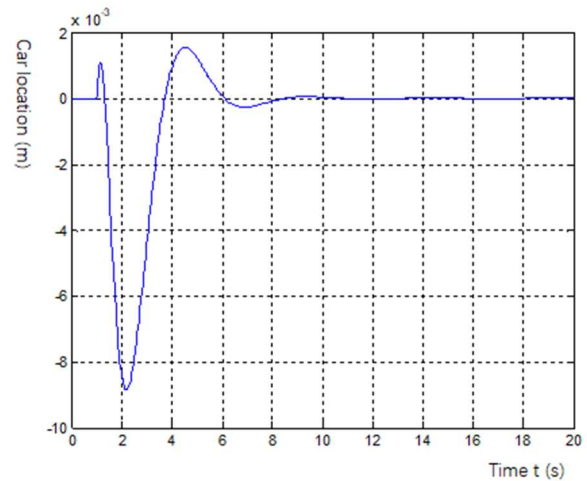


Fig.6 Double loop control system car position simulation curve

4. Summary

The inverted pendulum control has the importance of engineering to verify many control laws. Of course, the project most commonly used the PID control law that is simple and reliable, low cost, with more important practical. The PID control law is also based on the idea of feedback, which means that the feedback control occupies a fundamental role in the entire automatic control theory.

In this paper, the first level inverted pendulum is using the conventional PID control. But we found that one PID control can only control one variable, and an inverted pendulum is a typical single-input dual-output nonlinear system. The traditional PID cannot do both the amount of control, so we use the dual-loop PID control, and it is sure enough that the simulation shows that the dual-loop PID controller is feasible, and can meet our requirements for the PID controller, thus to solve the shortcomings of the traditional PID.

Acknowledgements

The research is partly supported by the Research Fund for the Reform in Education from Tianjin Municipal Education Commission of China (171005704B). And at this point, I would first like to thank to my tutor, Dr. Fengzhi Dai. From the beginning of the paper to the final draft, I have always received the meticulous guidance and help from Dr. Dai. His pragmatic and rigorous scholarship and work style deeply infected me, so I benefit greatly! During the research, I consulted a large number of papers

about inverted pendulum, mastered a certain theoretical knowledge, completed the design of the inverted pendulum controller, exercised my own ability to analyze and solve problems, and laid the foundation for future work solid foundation.

References

1. Yixiao YIN, *Study on Linear Inverted Pendulum System*. Shandong, Shandong Agricultural University, 2015.
2. Hailong Liu, *Design and Research of Inverted Pendulum Experiment System*. Dalian, Dalian University of Technology, 2006.
3. Li D Y. The cloud control of triple inverted pendulum and its dynamic balance mode. *Engineering Science*, 1999, 1(1):41-46.
4. Wang P H, Li X B, Fu F Q, Wang Q. The full process variable structure control of 3-stage system. *Machinery Design & Manufacture*, 2009, 7(1):127 - 129.
5. Yude Wang, PID Parameter Adjustment Simulation Study. *Electric Automation*, 2011, Vol.33, No.6: 1-6.
6. Lin Li, Double Circuit PID Control of Inverted Pendulum. *Journal of University of Shanghai for Science and Technology*, 2012. Vol 32: 75-76.
7. Li Z S. *Artificial Intelligence: Retrospection and Expectation*. Beijing: Science Press, 2006:174-207.
8. Li Z S, Wang Y X, Tan Z, Wen Y L. The swing-up and handstand control and its implementation of cat double pendulum. *Proc of the 5th world congress on intelligent control and automation, Hangzhou: IEEE, 2004: 2360-2364.*

Design of Intelligent Saving Robot Based on Six-legged Robot

Xinyu Zhang, Xiaokun lin, Feng Dai *

*College of Electronic Information and Automation,
Tianjin University of Science and Technology, China*

*E-mail: * dai fz@tust.edu.cn
www.tust.edu.cn*

Abstract

In recent years, along with the humanity to have high mobility in the complex environment, and high reliability and easy to expand increasingly urgent demand for mobile platform, also the multi legged robot research and algorithm improvement of gait, scientists have considered the research to the application of biped multi legged robot. The motion of the biped robot is confined to the plane, unable to overcome many mountain disaster or rough terrain. Therefore, a rescue robot based on six legged robots is considered. This robot can use mobile phone app to switch robot mode or remote control robot through Bluetooth or wireless mode. And it can be controlled by switch between the automatic and manual mode, and the robot can realize obstacle jumping through sensors to identify the types of obstacles. The robot is loaded with an electronic compass, a camera and a gyroscope, which can intelligently record the path of travel and automatically return to its starting position along the path.

Keywords: Six-legged Robot, Saving robot, Remote Control

1. Introduction

Nowadays, the research on the six legged robot is popular in the world. In addition to the industrial six legged robot is indirectly applied to sorting, most of the six legged robots are only used for entertainment and teaching. Six legged robot with wheeled and tracked robot while showing great advantages in the common way, but in some practical engineering applications, such as disaster relief and rescue, have not appeared the figure of six legged robot. Our most common dance robots are written only through the upper computer, into the action group, and then perform the action group to complete the various dance movements. This robot can only be used for teaching and entertainment, and cannot be applied to practical engineering applications. The robot is in the original dance of the six legged robot based on transformation and special rational design of it and add it to the main control chip, the dance of the six legged

robot's mechanical flexibility and a variety of sensors, programming algorithm, which completely turned into intelligent robots, autonomous unmanned control through complex the environment and a variety of additional high-end convenient features to make it more effective to complete the task. Its purpose is to make foot robot can be applied to practical engineering applications, so that it can accomplish rescue, disaster relief and other high-risk work, so as to solve the traditional obstacles such as robots, traffic difficulties and other issues. Through innovation, robots can serve human beings more effectively.

2. The hardware structure design

To better fit the look of the six legged robot, we placed the relevant sensors and hardware modules on a previously designed 15*15 PCB. Multiple modules

contact each other and perform their duties. At the same time, we have set aside some blank modules on the basis of independent design, which is convenient for later modification and replacement. Taking into account the limited space inside the robot and the central area, we take the upper and lower double layer design to provide a good environment for the operation of the LCD and GPS modules. The design of the structure is shown in Fig.1.

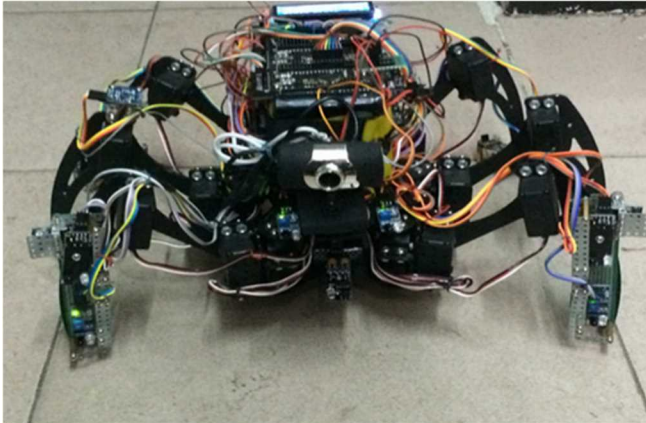


Fig.1 The design of the structure

2.1. Servo control panel

The robot has 18 digital servos, so we have to design a 32-way steering engine panel. The steering engine control panel uses the ATmega16 as the main control. The ATmega16 AVR kernel has a rich instruction set and 32 general-purpose working registers. All registers are directly connected to the arithmetic logic unit (ALU), so that one instruction can access two separate registers simultaneously in one clock cycle. This architecture greatly improves code efficiency and has a data throughput rate of up to 10 times higher than the average CISC microcontroller.

ATmega16 has the following features: 16K bytes of in system programmable (Flash has the ability to read and write at the same time, namely RWW), 512 byte EEPROM and 1K byte SRAM, 32 common I/O port line, 32 general-purpose working registers, JTAG interface for boundary scan, supports on-chip debugging and programming, compared with three the flexible mode of timer / counter (T/C), internal / external interrupt chip, programmable serial USART, serial interface with initial condition detector, 8 Road 10 with selectable differential input stage programmable gain (TQFP package) ADC has an on-chip oscillator Programmable Watchdog Timer, a the SPI serial port, and the six can be selected by the software power saving mode.

2.2. Main control chip

STC12C5A60S2/AD/PWM series microcontroller is a single clock / machine cycle macro crystal technology production (1T) chip is a high speed, low power consumption, strong anti-jamming and a new generation of 8051 single-chip instruction code is fully compatible with the traditional 8051, but the speed is 8-12 times faster. Internal integrated MAX810 dedicated reset circuit, 2 way PWM, 8 way high-speed 10 bit A/D conversion (250K/S), for motor control, strong interference occasions. STC12C5A60S2 has several important characteristics:

- chip integrates 1280 bytes RAM.
- each I/O port drive capacity can reach 20mA, but the whole chip should not exceed 120ma.
- has the EEPROM function.
- There is an independent baud rate generator A/D conversion, 10 bit precision ADC, a total of 8 channels, the conversion speed of up to 250K/S (250 thousand times per second)
- The robot uses independent STC12c5a60s2 microcontrollers, each of which is responsible for the operation of each function of the robot.

The main control chip is shown in Fig.2.



Fig.2. STC12C5A60S2

2.3. L3G4200D three axis digital gyroscope sensor

Simultaneously determine the position of 6 directions, move track, accelerate. A single axis can only measure two directions, that is, a system requires three gyroscopes, and one of the 3 axes can replace the three single axis ones. 3 axis small size, light weight, simple structure, good reliability, is the basic component of the development of laser gyro. The biggest function of the three axis gyroscope is to measure angular velocity to distinguish the motion state of the object, so it is also called motion sensor. Digital three axis gyroscope can support ISP communication and IIC communication. This robot takes IIC communication. And the L3G4200D three axis gyroscope digital characteristics that we found in practical applications to a certain angle gyroscope from a horizontal position, the detected module tilt angle

and then to send to the microcontroller module the current location for the starting position, the robot to step provides a convenient. The L3G4200D is shown in Fig.3.



Fig.3. L3G4200D

2.4. GY-271 three axis digital electronic compass

HMC5883L uses anisotropic magnetoresistive (AMR) technology, which has the advantage of being unmatched by other magnetic sensor technologies. The anisotropic sensor has characteristics of high sensitivity and high precision linear axis. Solid phase structure for the orthogonal axis line sensor with low sensitivity can be used to measure the size and direction of the earth's magnetic field, the measurement range from 8 to milli Gauss (Gauss). Honeywell's magnetic sensor is the most sensitive and reliable sensor in the low magnetic field sensor industry. The GY-271 three axis digital electronic compass is shown in Fig.4.

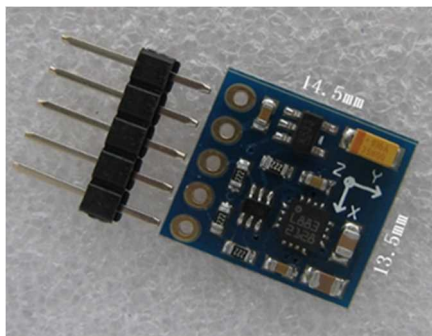


Fig.4. GY-271 three axis digital electronic compass

2.5. HD camera and wireless Bluetooth module

In order to make the robot better with the mobile phone and other mobile terminal communication, we adopt

Bluetooth wireless Wi-Fi and 720P HD camera for image acquisition and transmission, the remote control method is more stable than ordinary safe and reliable.

The HD camera and wireless Bluetooth module is shown in Fig.5.



Fig.5. HD camera and wireless Bluetooth module

2.6. Steering engine

The servos are 18 1501 digital servos. Six legged robots with 3 legs each. 1501 metal gear torque, fast speed, low noise, virtual and dead are very small, only need to send a signal to the locking angle, with high control precision, good linearity, in strict accordance with the control protocol, the output angle accurately and fast response and other advantages. At the same time programmable features also make the digital steering gear in dealing with jitter, and offside to more convenient and accurate, slow and more gentle, more smooth, more effective for the motor to provide the torque needed to start. When using servo controller, PC slider index 500~2500 (0.5ms~2.5ms), corresponding to the 1501 digital servo 0~180. The steering engine is shown in Fig.6.



Fig.6. Steering engine

3. System circuit module design

The basic modules of the system include power module, obstacle passing module and route memory module. Through the cooperation of three modules, the basic functions of transmission, obstacle avoidance and route feedback are completed.

3.1. power module design

In order to provide energy effectively, the 5V DC power supply is adopted, and the DC-DC exchange module is shown in Fig.7.

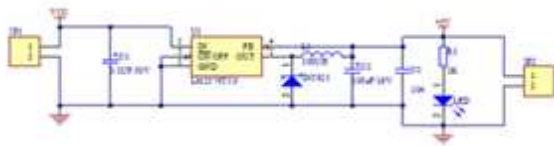


Fig.7. power module design

3.2. Robot obstacle passing module (sensor distribution design)

In order to exercise effective and efficient real-time control and monitoring of the robot, selects the best multiple sensor mounting points, the perfect realization of the linkage and communication module, and ensure the smooth motion. The sensor distribution design is shown in Fig.8.

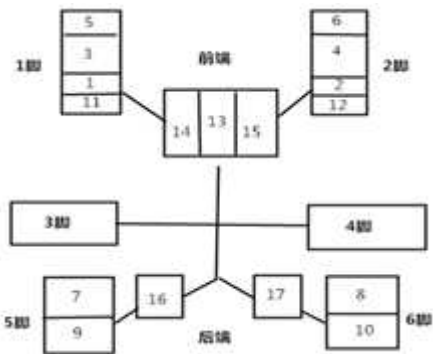


Fig.8. sensor distribution design

3.3. Robot route memory module (electronic compass and gyroscope application design)

In order to accurately measure the route and facilitate the distance when moving, the application of electronic compass and gyroscope is introduced. According to the electronic compass readings, according to a rough

estimate of the robot landmark location, although the GPS module including the design of hardware, but the signal is often terrain and object occlusion, leading to the accuracy greatly reduced the effectiveness of GPS signal under complex terrain condition is only 60%. And, in still conditions, the GPS cannot give the heading information. In order to make up for this deficiency, the method of combining electronic compass and GPS for directional navigation is adopted. It can effectively compensate the GPS signal, and ensure that the navigation directional information 100% is effective, even after the GPS signal is lost, the lock can also work normally, and the "lost star" is not lost".

L3G4200D three axis digital gyroscope and master chip communication mode is IIC communication. In any leg of six legged robot gyroscopes in robot leg and lower leg corresponding tilt direction axis has two times the number of changes per two times the number of changes is counted as one step. Then, the robot moves through the main control of the digital gyroscope repeatedly two digital changes step. The combined measurement by directional and pedometer can estimate distance, and the central chip data exchange through WIFI and Bluetooth transmission, real-time display of the completion schedule and tasks can be mobile terminal.

4. Introduction of functional module

In the course of development, the robot has applied some basic scientific principles, and through scientific calculation and adjustment, the machine has been running smoothly and accurately in the plan.

4.1. Robot gait principle

The gait of the six legged walking robot is varied, in which the triangle gait is the typical gait of the six legged walking robot. "Six feet" insects usually do not walk six feet at the same time while walking, but instead divide three pairs of feet into two groups, alternating with a triangular support structure.

At present, most of the six legged robot adopts the structure of insects, 6 legs distributed on both sides of the body, front and rear foot and the right side of the body on the left side of the foot as a group, before and after the left foot and right midfoot for another group, were composed of two triangular bracket, rely on the leg before and after the implementation of paddling support and swing, this is a typical triangle gait, as shown in figure. In the diagram, the robot hip moves horizontally and vertically. At this point, B, D, F feet swing feet, A, C, and E feet do not move, just support the body forward.

Because the body gravity center is low, not coordinated Z movement, easy stability, so this walking program can be widely used. The Sketch map of triangle gait is shown in Fig.9.

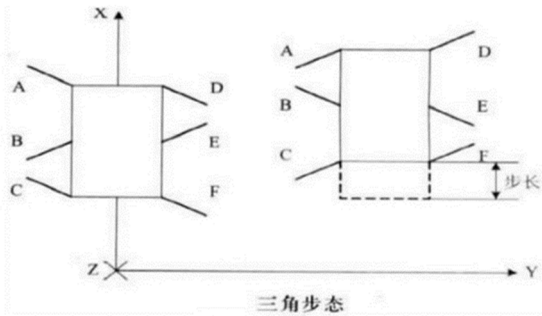


Fig.9. Sketch map of triangle gait

4.2. Azimuth calculation of electronic compass

When the 3 axis magnetometer work can read XYZ three axis magnetic field intensity, and cannot directly used for numerical calculation of azimuth angle, because the readings may be some other devices layout containing magnetic materials, the formation of hard iron drift coordinates, as shown in the following figures. The Azimuth calculation of electronic compass is shown in Fig.10 and Fig.11.

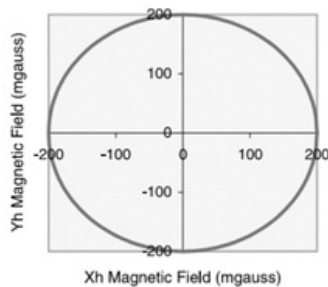


Fig.10. Xh-Yh Figure

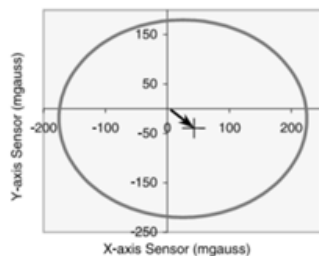


Fig.11. X-Y Figure

The XYZ value used for azimuth calculation must remove the drift value so that the center of the circle returns to the origin. The specific method is: the level of uniform rotation, XY axis rotation data collection equipment, 90 degrees (at the level of Z axis Z axis) uniform rotation to collect data, the data is read into the shaft of the maximum value and minimum value by 2, you get a offset value of each axis.

$$X_{offset} = (X_{max} + X_{min}) / 2$$

$$Y_{offset} = (Y_{max} + Y_{min}) / 2$$

$$Z_{offset} = (Z_{max} + Z_{min}) / 2$$

Then, the naked values of each axis read by the magnetometer subtract the offset value calculated previously, and the Heading values used for angle calculation can be obtained

If only horizontal measurements are used, azimuth = arctan(YH/XH). If our device is not in a horizontal position at the time of measurement, the azimuth of the compass will deviate when the above formula is applied, and then the acceleration sensor will be used to compensate the tilt angle of the magnetometer. As shown.

To compensate for the inclination of the electronic compass, the roll angle (theta) Roll and pitch angle (Pitch) must be calculated first. Enter the following formula and calculate the Heading value.

$$X_h = X * \cos(\varphi) + Y * \sin(\theta) * \sin(\varphi) - Z * \cos(\theta) * \sin(\varphi)$$

$$Y_h = Y * \cos(\theta) + Z * \sin(\theta)$$

Considering the 4 quadrants of the angle, the formula of the heading angle can be changed into the following formula.

$$\text{for}(X_h < 0) = 180 - [\arctan(Y_h/X_h) * 180/\pi]$$

$$\text{for}(X_h > 0, Y_h < 0) = -[\arctan(Y_h/X_h) * 180/\pi]$$

$$\text{for}(X_h > 0, Y_h > 0) = 360 - \arctan(Y_h/X_h) * 180/\pi$$

$$\text{for}(X_h = 0, Y_h < 0) = 90$$

$$\text{for}(X_h = 0, Y_h > 0) = 270$$

5. Testing and conclusion

The robot can achieve the following main functions in the actual test: the robot can pass all kinds of obstacles, such as self-climbing, stiles, obstacle avoidance, obstacle etc. We can switch to the man-machine control mode, and the operator can use the mobile phone APP to control the robot wirelessly.

The robot also has a one-button automatic return function, and the controller automatically returns to the point of departure by simply pressing the automatic return key. In the design process, the test was moved outdoors, in the natural environment as the experimental site, the environment obstacle robot testing in the outdoor space of this complex capacity, if the robot should be applied to the engineering practice, the robot should be able to adapt to the requirements of the design environment.

The actual error under the design of subtle errors and hardware, the robot automatically return to the starting point of the position deviation distance error is sometimes not the expected range, and the distance coefficient of nonlinear proportional distance error with the robot walking in the actual test for an average of 0.0112. The deflection error is within the range of 4 to 20 degrees.

Acknowledgements

The research is partly supported by the Research Fund for the Reform in Education from Tianjin Municipal Education Commission of China (171005704B).

References

1. Yusuke OTA, Yoshihiko INAGAKI, Kan YONEDA, et al. *Research on a Six—Legged Walking Robot with Parallel Mechanism*. Proceedings of the 1998 IEEE/RSJ Intl. Conference on Intelligent Robots and Systems, Victoria.
2. Bares J E. Whittaker W I. Configuration of autonomous walkers for extreme
3. Xu Xiaoyun, Yan Guozheng, Ding Guoqing. Research on micro six legged bionic robot and its triangle gait. *Optics and precision engineering*, 2002, 8(10): 392-393.
4. Fu Li, Liu Weiguo, Iran, multiple servo control with PwM microcontroller wave generating method, *micro motor*, 2006, 34(2).
5. Hu Xia. Research on Key Technologies of six legged walking robot. Hangzhou: Zhejiang University, 2008)
6. ray Jingtao, peak, Cui Ying. The research status and Prospect of multi legged walking robot. Beijing: Journal of mechanical design, 2006.
7. Zhang Haitao. Energy analysis of walking machines under horizontal static stability. Calculation of joint drive power. *Journal of Tianjin University of Science and Technology*, 2001 (2):13.15.
8. Gan Jianguo, Zhu Wei, the stem. *Six legged walking machine with guiding gait research of Robot*, 1996, 16 (4):235.

Research on multi-object recognition algorithm based on video

Yong Hou¹, Runhua Mao¹, Yan Yu¹, Yuxing Ouyang¹, Ce Bian¹, Binhu Song¹, Baochang Wei¹,
Yiqiao Qin¹, Shengbiao Chang¹, Fengzhi Dai^{1*}, Hongwei Jiao²

¹ College of Electronic Information and Automation,
Tianjin University of Science and Technology, China;

² Tianjin Technology School of Printing and Decoration, China
E-mail: * daifz@tust.edu.cn
www.tust.edu.cn

Abstract

This paper mainly studies and improves the detection and tracking algorithm of the robot fish video and presents a background extraction method based on HSV color space. This method is more efficient than the background extraction method of RGB color space, which improves the recognition, anti-jamming ability and robustness. Through the experiment, it has a strong adaptability to external influences such as background water surface fluctuation, reflective, light change shadow.

Key words: Robotic fish, tracking recognition, machine vision, color space

1. Introduction

The current tracking algorithm of moving objects¹ improve the matching degree of the object and the correctness of the matching by optimizing the characteristics of the tracked object, and predicts the possible occurrence of the object at the next moment or determine the object's search direction by the manner of effective narrowing the object search range. Meanwhile, in order to get a better prospect, this paper presents color-space model based on HSV². After remodeling the original color-space, we remove the main light interference in the image and the shadow interference of the robotic fish effectively, which makes the segmentation and recognition of multiple robotic fish³ more accurate. So the improvement of this algorithm makes the original matching tracking algorithm more robust.

2. Object Recognition

RGB channel modeling is used in the experimental platform. The background mainly

color is blue, so adjusting the coefficients to 1: 2: 7 according to the Lagrange multiplier algorithm makes a better distinction between foreground and background.

First take the static background without fish, save as a static background image. Then make arithmetic of subtraction on the background. In order to eliminate the influence of reflections and shadows, use the edge average method to set threshold and median filtering to filter out these interference points. Then used the template matching algorithm to match the previously designed oval template with the extracted fish. And then fuzzy positioning⁴ of the fish in the water within the camera's video recording range by using the basic means of human's eyes' recognition. The robotic fish's position in the water is transmitted to the computer by the operator using the mouse frame selection method. To identify the scope of this fuzzy framework for the recognition of the position and attitude of the robotic fish in the water⁵.

In order to make the matching more robust, the template matching algorithm uses a double template, the foreground template matches the white part, and the background part matches the

black background part, so that our matching algorithm is faster and more robust⁶.

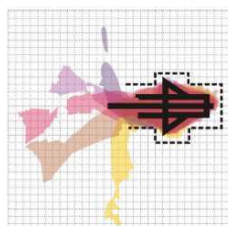


Fig.1 Double layer formwork

But in the actual competitions, it was found that imperfect pool modeling, changing competition environment, reflection of the pool, and some environmental factors seriously affected the players' play⁷. Therefore, it is necessary to improve the large platform algorithm.

The influence of robot fish pool modeling has the following points:

- The influence of the light in the pool, such as uneven lighting, the pool edge blocking the light, resulting in the background of the previous collection is invalid;
- The shadow of the fish has an influence on the fish's marking;
- Irregular reflection caused by water sloshing, serious distortion of color caused by the collection of many irregular reflective areas;
- Not suitable for color fish.

3. Algorithm improvement

3.1 Algorithm Introduction

In order to recognize the color of fish, and to better filter out the light and fish shadows⁸, this paper presents a better classification algorithm based on the color feature of HSV feature space.

Compared with the RGB channel, HSV is closer to human perception of color. The color property H can reflect the variety of the color more accurately, and the sensitivity of the change of the environment is relatively low, so it is very suitable for the image processing.

First we need to analyze how these different colors of fish, pool, and back light are distributed in the HSV space so that they can be classified later to realize the concept of program algorithm as follows:

First we manually select 20*20 pixels range area as the analysis object;

Then load our selected image, select the area as far as the robot fish or to be separated from the center of the object;

Put all of these points in the HSV three-dimensional space, and then draw these 20*20 points in the 3 dimensional diagram.

These values are collected and arranged, and the actual color is distributed as table 1.

Table 1 spatial numerical distribution of HSV

	Black	Gray	White	Red	Orange
H (min)	0	0	0	0	11
H (max)	180	180	180	11	25
S (min)	0	0	0	43	43
S (max)	255	43	30	255	255
V (min)	0	46	221	46	46
V (max)	46	220	255	255	255

Continuous table 1 spatial numerical distribution of HSV

	Yellow	Green	Cyan	Blue	Purple
H (min)	26	35	78	100	125
H (max)	34	77	99	124	155
S (min)	43	43	43	43	34
S (max)	255	255	255	255	255
V (min)	46	46	46	46	46
V (max)	255	255	255	255	255

Data analysis:

As the laboratory pool is glass, the reflection is more serious than the competition pool. Under sunshine, the pool color is distributed between cyan and blue. We adjust the full range of color to 0, also is black background.

There is also a problem to be solved, part of the red distribution in the 0-10 and 156-180, which will affect our identification of red Koi fish, make part of the fish's foreground show black and some show white. We need to adjust this part of the red but show the black to highlight range, while the black fish's foreground needs other ways to handle it.

3.2 Improvement of experimental parameters

We have adjusted the desired part of the color to the highlighted, and then adjusted the chromaticity of the background and the illuminated part to zero. We can see the effect as follows: we still cannot see the black fish (left one).

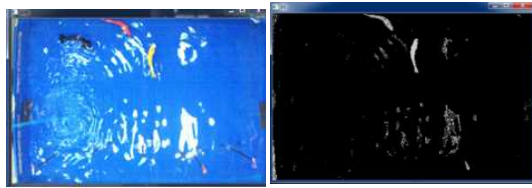


Fig.2 Parameter adjustment of H channel
V S R B color channel (top right of S)

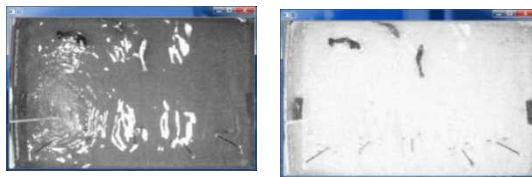
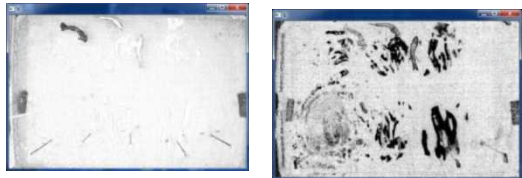


Fig.3 Other color channel testing (V S R B channels
respectively)

In Fig.3, we can find that the B and V channels in these figures can be used because black fish can be clearly extracted without introducing other effects such as lighting, pool background, etc.

3.3 Algorithm experiment and improvement

At this time, we tried to merge these channels with the reclassified H channels⁹, and came to the following results:

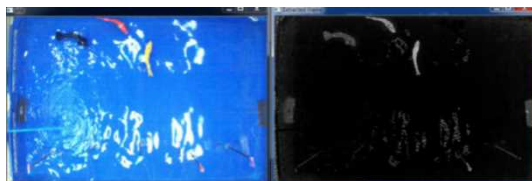


Fig.4 Dual channel fusion

We can see the black fish again, but there are some watery impurities. Here, the median filter is used to filter the image.

4. Testing and conclusion

4.1 Test under different circumstances

Compared to the previous foreground extraction method, the present method is simpler, the complexity of the algorithm is low. It is not necessary to collect the background, just open the camera to go to select the fish for the game,

© The 2018 International Conference on Artificial Life and Robotics (ICAROB2018), Feb. 1-4, B-Con Plaza, Beppu, Oita, Japan

and the operation is convenient. In addition, solve all the problems caused by the previous environment, so it will be integrated into the global machine fish platform to further test results in various universities.



Fig.5 Pool test of Guangxi University of Science and
Technology

From the test results of Guangxi science and Technology University, we can see even if the human eye cannot see the yellow fish, the computer can also identify part of the fish body.

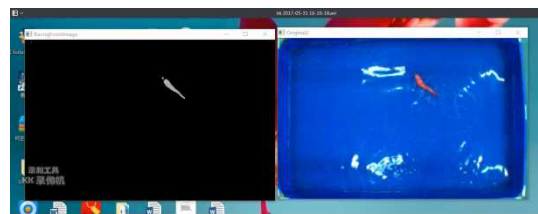


Fig.6 Pool test of China University of Geosciences

It can be seen that the fish and the ball in the pool are well separated.

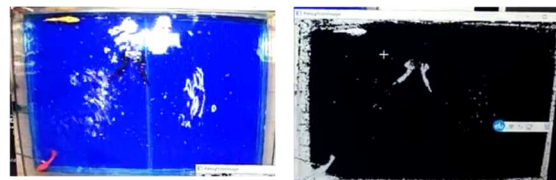


Fig.7 Glass pool test results of Peking University

It can be seen from pool video in different environment that the red fish and yellow fish are extracted and the light part turned black.



Fig.8 Pool test results of Beijing University of
Technology

It can be seen that there are many impurities in the pool, the reflection light is very serious, the whole pool's pixel value fluctuates violently, but the method can still extract the fish effectively.

4.2 Different light interference test

Highlights test:

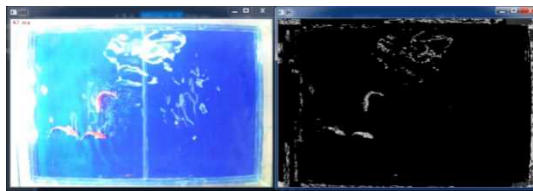


Fig.9 Pool test results (highlights) of Peking University

We experimented with maximizing light disturbances, partially whitening the fish, and manipulating the video without changing any parameters. We can see that this method is still effective and can extract the outline of the fish.

Lack of light test:

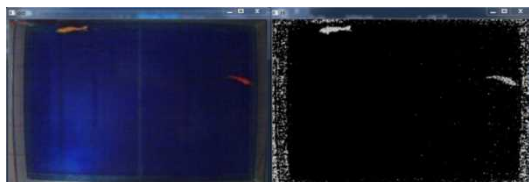


Fig.10 Pool test results (lack of light) of Peking University

It can be seen that the fish can be extracted without any indoor light source.

Above, this algorithm has been proved to be effective and can completely replace the previous foreground extraction algorithm.

5. Conclusion

The main light interference in the image and the shadows interference of the robot fish is effectively removed after the original color space re-modeled, it make segmentation of the robot fish more accurate. Due to the improvement of the algorithm, the original matching tracking algorithm is more robust. The deficiency is that this method only suitable for background pure environment. Collision with

the robotic fish cannot make a good distinction, the follow-up test will further study to solve this problem.

Acknowledgements

The research is partly supported by the Research Fund for the Reform in Education from Tianjin Municipal Education Commission of China (171005704B).

References

1. Chang Xiangkui The research on Tracking Algorithms of Video Moving Objects. Henan University. 2007
2. Zhang Jun, Dai Ke-xue, Li Guo-hui. HSV color-space and codebook model based moving objects detection, 2008,(03):423-427.
3. Wang Yaowei, Ji Zhijian, Zhai Haichuan. A survey on motion control of the biomimetic robotic fish. *CAAI Transactions on Intelligent Systems*, 2014, 9(3) : 276-284.
4. Tang Yufeng. Research and realization of the multi-target tracking system for robotic fish based on global vision. East China Jiaotong University. 2013.6
5. Ding Guangshuai, Lei Yunhong. Algorithm for Localization of Underwater Robot Based on Regional Treatment in Machine Vision. *Ordnance Industry Automation*. 2010, 29(11):74-78.
6. Jia Guimin, Wang Xiangjun, Zhang Shihai. Target Tracking Algorithm Based on Adaptive Template Update in Complex Background. *Acta Optica Sinica*. 2009.3.
7. Xu Yuru. Difficulties and Development Trend of Intelligent Water Robot Technology. China Automation Conference and the summit of the two integration. 2009.
8. Zhao Xuechun, Qi Feihu. Automatic Recognition of Vehicle License Based on Color Segmentation. *Journal of Shanghai Jiaotong University*. 1998.10.
9. Song Xiaowei. Color Information Fusion for Visual Object Tracking. Xidian University. 2009.1.

Reinventing the Flavor Wheel

Hiroki Fukushima

Kyushu Women's University, 1-1 Jiyugaoka, Yahata-nishi-ku
Kitakyushu City, 805-006, Japan

Abstract

In this paper, the author proposes a new type of flavor wheels. The tasting words of former flavor wheels are arranged based on the taxonomical classification of the objects. In this study, the author proposes the new structure of flavor wheels: a) arrange tasting words based on the co-occurrence relationships, and b) not a hierarchical structure, but the network structure.

Keywords: flavor wheel, taste, odor, sake, luxury grocery items

1. Introduction

1.1. General Flavor Wheels

A flavor wheel, or a fragrance circle is a chart that is used in the domain of evaluating alcohol drinks or other luxury grocery items. There are various patterns of flavor wheels in the various domain, such as wine, coffee, whiskey, beer, and so on. The flavor wheel for chocolate shown in Figure. 1 is a typical example of flavor wheels, that has the hierarchical structure of the expression words.

As for Japanese sake, a flavor wheel based on the classifications of scientific flavor components was presented recently (Utsunomiya, 2012) (Figure. 2).

1.2. Drawbacks of the Traditional Flavor Wheels

The author points out mainly two drawbacks of ordinal flavor wheel: a) the lack of the relationships among the words and genres. And b) the hierarchical structure does not reflect the cognitive process of our representation of the tastes.

This study aims to overcome these two drawbacks and propose a new type of flavor wheel.

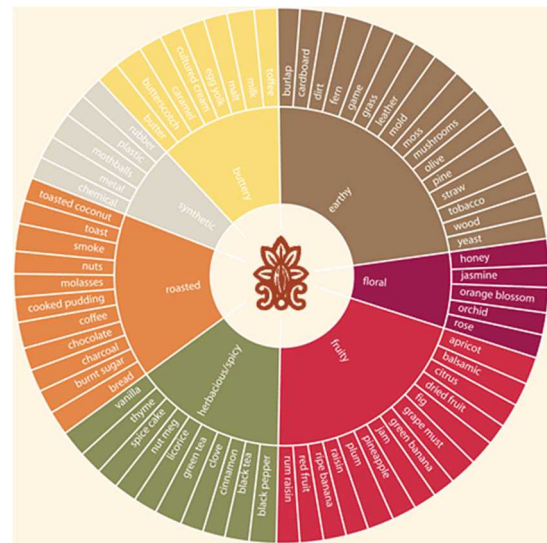


Figure. 1

An example of a general form of flavor wheels. This wheel is made by Chocopolis – a famous chocolate company in Seattle. Various expression-words for flavors in chocolate is arranged in the outer circle, and abstract genres are set as the inner circle.

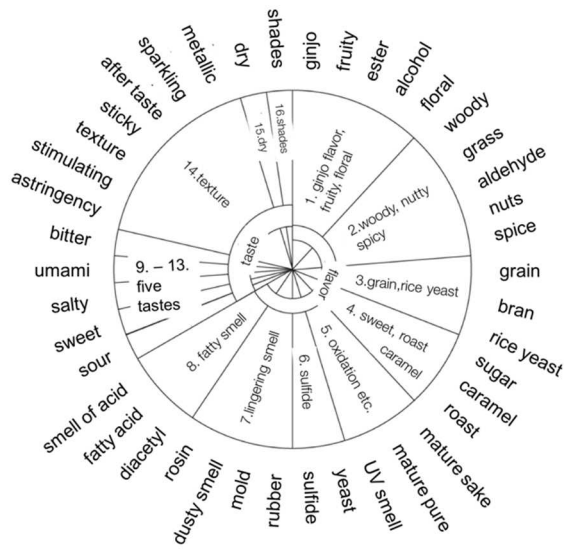


Figure. 2
A flavor wheel for sake, presented by Utsunomiya (2012). Translated by the author from Japanese to English for this paper.

1.3. Reinventing the Flavor Wheels

In order to overcome the drawbacks of the traditional flavor wheels, the author proposes a new format of the flavor wheel, applying natural language processing technologies.

The features of the new format are: a) arrange tasting words based on the co-occurrence relationships, and b) not a hierarchical structure, but the network structure.

2. Method

2.1. Corpus

In this study, the author used Sake Corpus: the corpus of Japanese sake tasting expressions. The corpus is based on books and magazines written entirely in Japanese, and Table 1 summarizes the details of each. Note that paragraphs refer to the different sake brand descriptions. The size of the Sake Corpus was 120,789 words.

The corpus is based on the (a) sake-reviewing books and magazines sold in Japan, and (b) the tasting comments and expressions provided given by 6 tasters including the author.

Table 1. Details of Sake Corpus

	Details
Tokens	120,789
Types	6,018
Sentences	5,582
Paragraphs (brands of sake)	2,388
Average Frequency	10.50
Standard Deviation	(64.55)

2.2. Selecting Basic Tasting Words

From the nouns in the corpus, the author picked up the basic tasting words. The conditions of the selection are: a) name of concrete foods (or objects) for expressing the tastes; b) the frequency is over three.

Under these conditions, following words are selected as the tasting words of sake: *white cedar, plum, caramel, cacao, chocolate, liche, grape fruit, lactate, raw cream, yoghurt, raisin, muscat grape, banana, vanilla, melon, grape, apple, peach, strawberry, pear, flower, nectar, truffle, cheese, cream, plum, maple syrup, candy, mineral, nut, Yubari king melon, hazelnut, almond, milk, cashew, walnut, butter, kaki (persimmon*

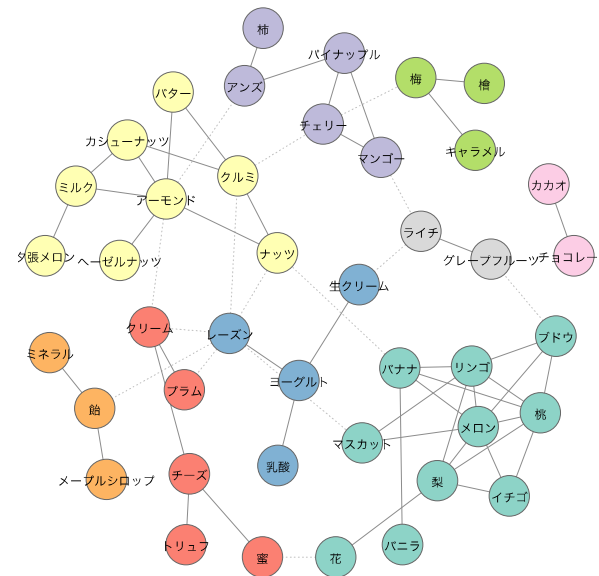


Figure. 3
The co-occurrence network of the basic tasting words in the sake corpus.

fruit), apricot, pineapple, mango, and cherry.

2.3. Analyzing Co-occurrence networks

Co-occurrence networks are generally used to provide a graphic visualization of potential relationships between people, organizations, concepts or other entities represented within written material. The generation and visualization of co-occurrence networks have become practical with the advent of electronically stored text amenable to text mining.

In this study, in order to determine the order and arrangement of the tasting words on the flavor wheel, the author uses the strength of co-occurrence relationships among the tasting words.

Based on the Jaccard index, the author made the co-occurrence network. Note that the Jaccard index is the correlation index in the corpus content words.

For drawing the co-occurrence networks and calculating the Jaccard index, the author used KH Coder (Higuchi, 2004) as a coding tool.

2.4. Arranging the Basic Tasting Words

In this section, the author presents the new type of flavor wheel with the basic tasting words and the co-occurrence network.

Clusters

In the former style of the flavor wheels, the clusters of the expression words are determined based on the hierarchical structure of scientific features or the taxonomical classifications.

In this study, the author tries to generate the new style of flavor wheel, in which the words and the clusters are arranged based on the relationships of co-occurrence networks.

Thus, in the new flavor wheel, the cluster reflects not the taxonomical classifications, but the relationships of the words in the reviewing sentence. This means that this study stresses the importance of human expressions rather than scientific measurement.

The composition of the word clusters may differ from our knowledge: the *cream* and *raw cream* are set in a separate category, on the other hand, *ume-plum* and *caramel* are set in the same category. These categorizations would never occur as long as we accept the taxonomical classifications. However, in the real context of the tasting reviews, *ume-plum*, and the

caramel is used for the same sake in order to express the complex flavor of sake.

The Structure: Inner Circle and Outer Circle

In the new flavor wheel, the tasting words are arranged on the double layer. The words of the inner circle are prototype members of the category. And the words of outer circle are peripheral members of the category.

The prototype member is determined based on the numbers of the links each word has in the co-occurrence network. More links a word has, more typical the word would be in the category.

3. Result

As a result, the author produced the reinvented Flavor Wheel for sake, as shown in Figure. 4.

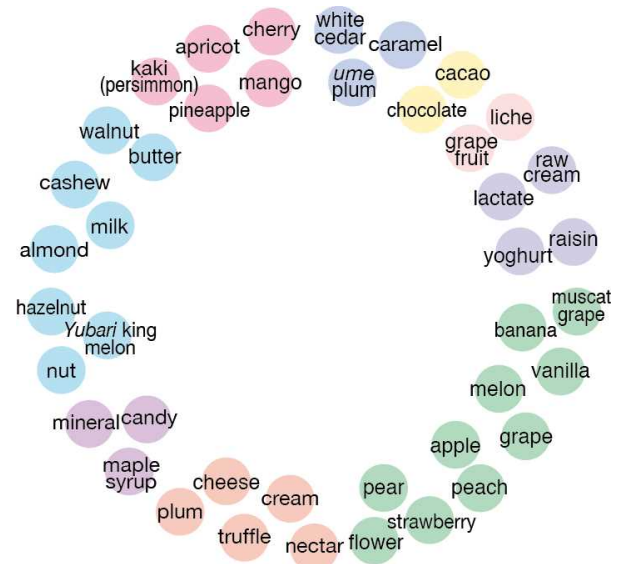


Figure. 4

Newly reinvented Flavor Wheel of Sake. This flavor wheel is based on the sake tasting expression corpus (120,000 words in Japanese). The category (cluster) and the arrangement of the words are determined by co-occurrence relationships (Jaccard index). Inner words are prototype members of the category, and the outer words are peripheral members of the category.

Categories

The flavor wheel consists of nine clusters, but it would be almost nonsense to give an abstract name to each category. The category is the “result” of the expressions, and only we have to do is not naming it but considering the hidden relationships and guessing why the two words are arranged side by side on the base of our sense of taste.

The Composition of the Categories

As same as the distance and connections of the words, the composition of the nine categories reflects the distance of the usage tendency (co-occurrence frequency).

4. Discussions

Our sensory domain of taste or odor is not the carbon copy of the sensor machine. And the taxonomical classifications and the perceptual category of taste do not share the same structure.

The taxonomical classifications and the category of the natural language have the hierarchical structure. This would be because the natural language is a vision and auditory-dominant system (Fukushima, Imai, & Tanaka, 2017).

The author has argued that the cognitive system of the taste is not the hierarchical process from basic level to upper/lower level, but the gradational categorization on the plain surface (Fukushima, 2018). The nouns of the natural languages have the hierarchical concept structure. On the other hand, verbs, adjectives, and adverbs have the gradational category (Tanaka & Fukaya, 1998). Thus, the author presumes that the category of the sensory domain of taste is the adjective category. From this viewpoint, the supporting tools for expressing the sense of taste should be focused on adjectives rather than nouns. The future development of the flavor wheel would be the reflection of the co-occurrence relationships between the tasting words and adjectives.

Reference

1. Fukushima, H. (2018). A Phenomenological Model for Generating the Tasting Description of Japanese Sake. In T. Ogata (Ed.), *Content Generation Through Narrative Communication and Simulation*. IGI Global.
2. Fukushima, H., Imai, M., & Tanaka, S. (2017). The Usage Mechanism of Japanese Ideophones in the Description of Taste: Morphological and co-occurrence analysis of the description of wines and sakes. *International Journal of Computational Linguistics Research*, 8(3).
3. Higuchi, K. (2004). Quantitative Analysis of Textual Data : Differentiation and Coordination of Two Approaches. *Sociological Theory and Methods*, 19(1), 101–115. <http://doi.org/10.11218/ojjams.19.101>
4. Tanaka, S., & Fukaya, M. (1998). <Imizukeron> no Tenkai (*The Evolvement of the <Sense-Making Theory>*). Kinokuniya.
5. Utsunomiya, H. (2012). Flavor Wheel. *Kagaku To Seibutsu (Chemistry and Biology)*, 50(12), 897–903.

Acquiring Short Scripts and Setting a Case Frame in Each Acquired Script: Toward Random Story Generation

Jumpei Ono

*Graduate School of Software and Information Science, Iwate Prefectural University
Takizawa, Iwate, 020-0693, Japan*

Takashi Ogata

*Faculty of Software and Information Science, Iwate Prefectural University
Takizawa, Iwate, 020-0693, Japan
E-mail: g236m001@s.iwate-pu.ac.jp, t-ogata@iwate-pu.ac.jp*

Abstract

The integrated narrative generation system, that the authors have developed, generates a story to translate the story into the surface representation. In the story generation process, the INGS uses narrative knowledge that was automatically acquired from existing narrative works. This paper presents a method to acquire short scripts, which are a kind of narrative knowledge, from existing works in Aozora Bunko for the story generation. This paper presents a mechanism to generate random story-like event sequences by using 23,751,142 bi-gram scripts acquired based on the method proposed below. The authors aim to use the scripts generated by the method as a first set to be revised through the next learning process.

Keywords: Case frame, Integrated narrative generation system, Knowledge acquisition, Random story generation, Script, Verb concept.

1. Introduction

The integrated narrative generation system (INGS)¹ is a system that generates a narrative automatically. The system not only generates a story but translates the story into the surface representation. In story generation, the INGS uses knowledge about story structure and dictionaries² that systematically store nouns, verbs, and so on. The authors call story content knowledge, which is stored knowledge bases of the INGS. The dictionaries are called conceptual dictionaries. A variety of generated stories depend on the scale of the knowledge base. If the knowledge base is small scale, story generation by the INGS fails frequently. However, expanding the knowledge base in manually has limitations. Therefore, the authors have attempted to acquire knowledge

automatically.³ This paper details the attempt to acquire short scripts based on bigrams acquired from existing narrative works for story generation.

A script that Schank has mentioned involves knowledge about human actions in a particular situation.⁴ For example, a restaurant script describes the procedure procedures for ordering and eating dinner at a restaurant. We attempt to not only acquire Schank's scripts but to also acquire the temporal sequences of events.

The INGS consists of one part mechanisms and one part knowledge. Knowledge refers to dictionaries for concepts and language notation¹, and to knowledge bases that build partial structures of a story (e.g., the narrative content knowledge base). By using this knowledge, the mechanisms generate various aspects in a narrative, such

© The 2018 International Conference on Artificial Life and Robotics (ICAROB2018), Feb. 1-4, B-Con Plaza, Beppu, Oita, Japan

as a story, discourse, and surface representation (i.e., sentences, music, or images).

2. A Method for Story Generation in the INGS

Fig.1 shows a story structure that is generated in the INGS. The structure has a hierarchical structure that consists of states, events, and relations. A state describes static information regarding characters, things, locations, and times in a story. An event describes dynamic information that represents the difference between two states. A relation links several events by some relationship such as Causal relationship.

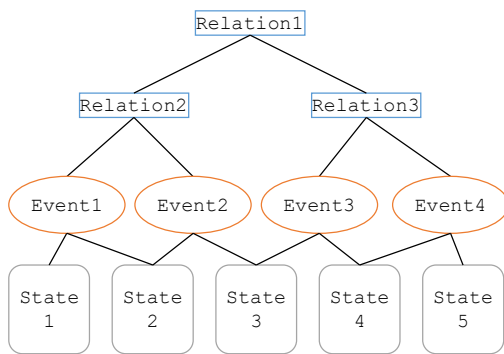


Fig. 1. An example of a story structure.

Story generation in the INGS is the expansion and transformation of a story structure using story techniques. A story technique is a formal procedure for expanding the structure of a story and draws on a knowledge base that corresponds to the particular technique. Fig. 2 shows an example of using a story technique; the technique selects applicable knowledge and expands the structure of the story by using that knowledge.

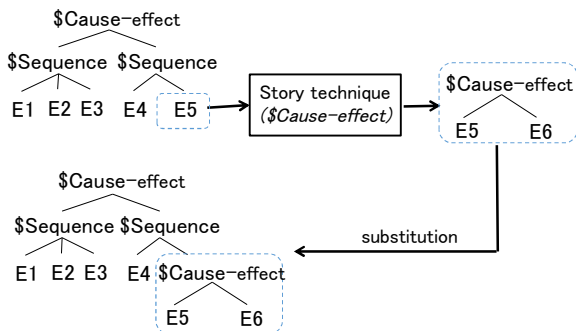


Fig. 2. A method for expanding a story structure (Fig. 8 in Ref. 1).

Fig. 3 shows an example of automatically-acquired knowledge. This knowledge is applied to an event that includes “eat,” and the story technique adds an event that includes “drink” to the structure of the story. (&v age1) or (&v obj1) are variables described by the cases. These variables denote the position or location where the generated character, thing, or location is inserted based on the restrictions. Cases that have the same variables also have the same character, thing, or location.

```
(script (食べる 2[eat] (食べる 2[eat] 飲む 2[drink]))
  ((event 食べる 2[eat] (agent (&v age1))
    (counter-agent (&v age2)))
  (1 (event 食べる 2[eat] (agent (&v age1)) (counter-agent (&v age2))))
  (2 (event 飲む 2[drink] (agent (&v age1)) (object (&v obj1))))))
```

Fig. 3. Example of a short script.

Potential selection points in story generation involve mainly the “application point of the story technique,” “applying a story technique,” and “using knowledge.” The “application point of story technique” and “applying a story technique” steps can be controlled based on a parameter that is inputted into the INGS. For example, if “parameter length” is increased, a story technique is selected that increases the number of events within the story.

3. Acquiring Short Scripts from Existing Works

The mechanism for acquiring short scripts has three steps: acquiring bigrams, making short scripts, and setting a case frame. This section explains each of the three steps.

3.1. Acquiring bigrams from existing text

Bigrams that consist of two verbs are acquired by applying morphological analysis to existing text. The acquired bigram is called a verb bigram. For example, verb bigrams are acquired as shown in Fig. 4. The procedure for acquiring bigrams is as follows:

- (i) Morphological analysis: The mechanism analyzes a text using a morphological analyzer.
- (ii) Extracting verbs from results: The mechanism extracts verbs from the results of morphological analysis.

- (iii) Making bigrams: The mechanism creates pairs of verbs in the order of the results of extraction. For example, if the result of extraction is (A B C), then the mechanism combines two pairs of verbs (A B) and (B C). $N - 1$ verb bigrams are created from N verbs.
- (iv) Removing a part of the bigram: The mechanism removes bigrams that include verbs that are not stored in the conceptual dictionary, because the INGS cannot use such bigrams in story generation.

<p><Target text> 男がウィスキーを運ぶと、女はパスタを食べていた。 彼はウィスキーを机に置き、椅子に座った。 [When a man carried whisky, a woman was eating pasta. He puts the whisky on the table and sits down on the chair.]</p>
<p><Acquired bi-grams> (運ぶ 食べる) (食べる 置く) (置く 座る) [(carry eat) (eat put) (put sit)]</p>

Fig. 4. Example of acquired bigrams.

3.2. Making short scripts

The acquired verb bigrams are made into short scripts. This step connects the verb concepts to verbs that are included in verb bigrams. Verb concepts are assigned a number in the INGS because the INGS provides the plural of the verb. For example, the verb concept “食べる 1” has a meaning like “earn,” while the verb concept “食べる 2” has a meaning like “eat.”

Short scripts ($X_n Y_k$) were created from verb bigram ($X Y$) ($X_n Y_k$) consists of verb concepts X_n and Y_k ; ($X Y$) consists of verb X and verb Y). In this case, verb X has i kinds of meaning, verb Y_k has j kinds of meaning, and the number of short scripts is equal to i multiplied by j . In making short scripts, we need to consider the meaning of a verb. However, in this paper, the authors created all patterns of ($X_n Y_k$) with the procedure shown in Fig. 5.

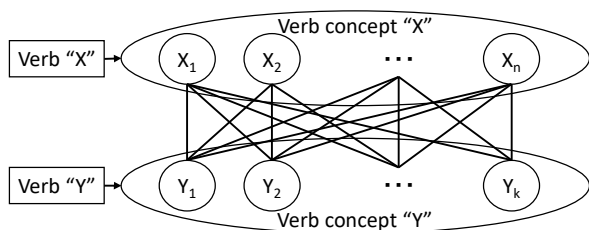


Fig. 5. An image of making short scripts by a bigram.

3.3. Setting a case frame

By setting a case frame in a short script, the INGS can generate a story using the short script. Fig. 6 shows the procedure for setting the case frame in short scripts ($X_n Y_k$). A case frame consists of cases that require a verb. For example, a verb concept has a description as seen in Fig. 7. Here, the elements of the “case-frame” are the case frame. A case frame has restrictions based on the noun conceptual dictionary. The restrictions define the probability of cases that are included in a verb concept.

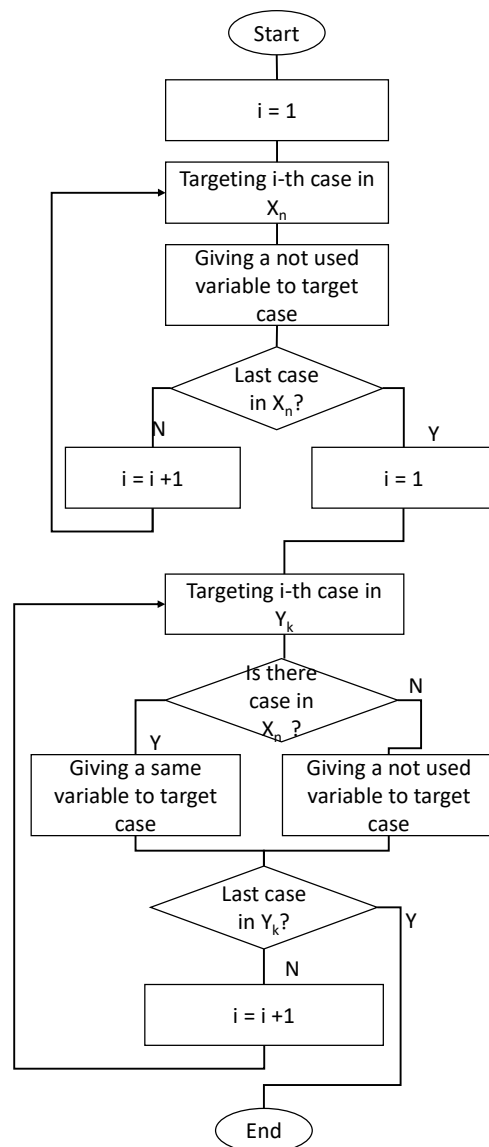


Fig. 6. A flowchart for setting a case frame.

```

((name 食べる 2[eat])
(sentence-pattern "N1 が N2 を 食べる"["N1 eat N2"]))
(case-cons-set
((case-frame
((agent N1) (counter-agent N2) (location N3) (object nil) (instrument nil) (from
nil) (to nil) (adverb nil) (possessive nil) (situation nil) (purpose nil)
(experiencer nil) (source nil) (idiom nil) (information nil) (as nil)))
(constraint
((人[human] -死人[corpse] -人間<人称> [human<person>]-準人間[semi-human])
(鯨[whale] 馬[horse] 牛[cattle] 豚[hog] 山羊[goat] 羊[lamb] 鹿[deer] 猪[wild boar]
兎[rabbit] 家禽[poultry] 猟鳥[game bird] 魚[fish] たこ・いか・えび・かに
[octopus/squid/shrimp/crab])
(場所[location] -交通路[traffic route] -公共施設{その他}[public building{etcetera}]
-地域 [local] -崖 [cliff] 山{部分}[mountain{parts}] 平地 [flatland] 岸
[bank])))
((case-frame
((agent N1) (counter-agent nil) (location N3) (object N2) (instrument nil) (from
nil) (to nil) (adverb nil) (possessive nil) (situation nil) (purpose nil)
(experiencer nil) (source nil) (idiom nil) (information nil) (as nil)))
(constraint
((人[human] -死人[corpse] -人間<人称> [human<person>]-準人間[semi-human])
(食料[food] -調味料[flavoring] -飲物・たばこ[drink/cigarette] -汁[soup])
(場所[location] -交通路[traffic route] -公共施設{その他}[public building{etcetera}]
-地域 [local] -崖 [cliff] 山{部分}[mountain{parts}] 平地 [flatland] 岸
[bank])))
(is-a (v 身体動作[physical action])))

```

Fig. 7. Example of a verb concept.

4. Result

Please provide a shortened running head (not more than four words, each starting with a Capital) for the title of your paper. This will appear with page numbers on the top right-hand side of your paper on odd pages. In this paper, the authors acquired short scripts from 13,331 works in the Aozora Bunko.⁵ The acquisition mechanism used MeCab in the morphological analysis. We acquired short scripts from each work. In analyzing each work, we did not consider structures such as paragraphs in each work. Table. 1 shows the number of acquired verb bigrams and short scripts. (MeCab was downloaded from “<http://taku910.github.io/mecab/>”)

Table 1. Amount of Short scripts.

Type	Amount
Verb bigram	552,773
Short script	23,751,142

5. Using Short Scripts for Story Generation

The INGS uses a technique that allows the generated story to converge on one result based on several parameters that are set beforehand. Specifically, the INGS performs story generation by using selection rules at several points of the generation process. The authors have adopted random generation in order to gradually change a narrative. A summary regarding random narrative generation is presented in Ref. 6. In this section, a generated story is presented.

Currently, parameters have not been applied by the authors in order to evaluate whether acquired knowledge alone suffices for random story generation. This method accomplishes generation by applying various story techniques that INGS has available, and uses scripts that were acquired automatically which are stored hierarchically, based on verbs. When the INGS selects an event that randomly, and if the event can be expanded by any story technique, the INGS selects a story technique

in those story techniques randomly. However, if the event cannot be expanded by any story technique, the INGS then selects another event randomly. Fig. 8 shows how a generated story is transformed into a natural language sentence by a sentence generation mechanism in the INGS. Although the authors have experience with the topic of random generation, previous attempts to generate a story through random methods failed owing to the lack of a knowledge base.

若主人は溝で酩酊しました。若主人は溝で肅清の夢を見ました。特急が溝で滑りました。若主人は溝でわれに帰りました。引力がトレーシングペーパーより起こりました。若主人は特急をトレーシングペーパーと反対にしました。若主人はトレーシングペーパーで地政学へ駄目を押しました。若主人はトレーシングペーパーでカメレオンを抜きました。若主人は派出所で酩酊しました。若主人は派出所で派出所を放浪しました。若主人は派出所で酩酊しました。若主人は派出所で酩酊しました。若主人は派出所で酩酊しました。若主人は派出所で寝ました。若主人は上で上を放浪しました。若主人は上で専攻に音を上げました。若主人は上でカメレオンを捕獲しました。審理に上で競争力がありました。カメレオンは上で稲刈りに干渉しました。若主人に上でカメレオンは居ました。審理は上で審理との矛盾がありました。若主人は上で審理を発音しました。若主人は上で働きました。若主人は鉄塔で働きました。若主人は鉄塔で働きました。若主人は鉄塔で働きました。若主人は鉄塔で居残り手当を得ました。若主人は溝で働きました。若主人は溝で働きました。若主人は溝で居残り手当を得ました。若主人は縄暖簾でビアを飲みました。[A young host is extremely drunk in a ditch. The young host dream of liquidation in the ditch. A super - express slips by a ditch. The young host comes to the young host' self in a ditch. A tracing paper is generated by attraction. The young host reverses the super - express against a ditch. The young host makes sure of the tracing paper. The young host passes a Chamaeleon. The young host is extremely drunk in a police box. The young host wanders in a police box. The young host is extremely drunk in the police box. The young host is extremely drunk in the police box. The young host goes to bed in the police box. The young host wanders through the upper part. The young host is at the young host's wits' end for a special study. The young host catches the Chamaeleon. A judge is competitive. The Chamaeleon interferes in the upper part. The young host has the Chamaeleon. The judge contradicts the judge. The young host pronounces the judge. The young host works in the upper part. The young host works in a pylon. The young host works in the pylon. The young host works in the pylon. The young host work s in the ditch. The young host works in the ditch. The young host earns in the ditch. The young host drinks a beer.]

Fig. 8. Generated sentence using a story structure

© The 2018 International Conference on Artificial Life and Robotics (ICAROB2018), Feb. 1-4, B-Con Plaza, Beppu, Oita, Japan

6. Conclusion

This paper showed short script acquisition from existing works. The authors acquired 23,751,142 short scripts from existing works that were stored the Aozora Bunko. The acquired short scripts were used for story generation in the INGS. In future works, the authors will acquire longer scripts. In addition, they will attempt to acquire scripts semantically, because the results in this paper did not consider the semantic structure of a story.

The authors' goal is the random generation of a story. We presented story generation by using knowledge, which was obtained automatically. Based on the discussion above, a method to change narratives and to set parameters for a narrative generation was presented.

For future research, the aim is to increase automation by using learning mechanisms. For example, we propose a generation strategy composed of a preliminary story generation, a valuation of the story, and elements conjecture where operating parameters are not input manually, and instead are selected automatically. Through the learning operations at some selection points, generation results improve using a bottom-up process. A second option would be the construction of a system although maintaining the consistency of a story in a narrative generation process is very difficult, and maintaining consistency would be our goal.

References

1. T. Ogata, Computational and Cognitive Approaches to Narratology from the Perspective of Narrative Generation, in T. Ogata & T. Akimoto (eds.), *Computational and Cognitive Approaches to Narratology* (IGI Global, Pennsylvania, 2016), pp. 1-74.
2. T. Ogata, Building Conceptual Dictionaries for an Integrated Narrative Generation System, *Journal of Robotics, Networking and Artificial Life*, (2015), pp. 270-284. doi:10.2991/jrnal.2015.1.4.6
3. T. Arai and T. Ogata, Acquiring and Using Event Sequences Based on Verbs from Novels, *Proc. of The 31st Annual Conference of the Japanese Society for Artificial Intelligence*, (2017), 1D2-OS-29a-5in2.
4. R. C. Schank, *Tell Me a Story: A New Look at Real and Artificial Memory* (John Brockman Associates, 1990).
5. Aozora Bunko, <http://www.aozora.gr.jp>, 1998. (Last access date, Dec. 2016)
6. T. Ogata, T. Arai and J. Ono, Random Narrative Generation in an Integrated Narrative Generation System, in *Proc. of Forum on Information Technology*, (2016), pp. 133-134.

A Method of *Naimaze* of Narratives Based on *Kabuki* Analyses and Propp's Move Techniques for an Automated Narrative Generation System

Takashi Ogata

Department of Software Informatics, Iwate Prefectural University
Takizawa, Iwate, 020-0693, Japan

E-mail: t-ogata@iwate-pu.ac.jp

Abstract

Naimaze in *kabuki* has been known as a narrative creation method, or a group of techniques that combines components in existing *kabuki* works or in the narratives from other genres for making a new work. Various elements, such as stories, plots, characters, and places, can be used as components in *naimaze*. The author aims to use the *naimaze* method in automated narrative generation systems that we have been developing, namely the Integrated Narrative Generation System (INGS) and the *Geino* Information System (GIS). In this paper, the author first presents an approach to design the narrative techniques of *naimaze* in the INGS (and GIS) by applying the method for combining “moves” as explained in V. Propp’s narratological study, “morphology of the folktale.” A move by Propp means a narrative macro level unit, or a kind of sequence that is composed of several “functions;” and he showed various ways to combine several moves to construct an entire narrative structure. The next section discusses the many possibilities of *naimaze* techniques and the implementation of experimental programs based on various *kabuki* analyses; and the utilization of the Propp’s move method as a preliminary attempt for *naimaze* techniques in the INGS and GIS. This paper also outlines the direction of future research for designing and implementing an organized *naimaze* technique group.

Keywords: Kabuki, *Naimaze*, Multiple narrative structures, Integrated narrative generation system, *Geino* information system.

1. Introduction

The author has been studying *kabuki*^{1,2,3,4,5} in order to introduce the acquired narrative knowledge and a wide range of techniques into two types of mutually related narrative generation systems, called the Integrated Narrative Generation System (INGS)^{6,7} and the *Geino* Information System (GIS).⁸ In particular, the author has been studying *kabuki* from the viewpoint of multiple narrative structures or the multiple narrative structure model.^{6,7} The generation process of a narrative work and the repetitive production process of several narrative works can be considered from the viewpoint of

generation and production through multiple narrative structures. For example, a narrative’s generation flow comprises the multiple structures of a story at a semantic level and a plot at a constructive level.

The author considers a *kabuki* narrative as a particularly rich object for the multiple narrative structures model. In the first step of studying *kabuki* as a means of narrative generation and production, the author has analyzed the multiplicity of *kabuki* with regard to the following fifteen kinds of elements shown in Fig. 1. This figure also shows the overview of the relationship between the INGS and GIS. For instance, the element of a “person” in *kabuki* can be divided into

the following three aspects: the real “person” who lives in the actual world; the “person” as an actor who has a history of performing roles; and the “person” of the *kabuki* character that appears on stage. Each person has their own history or story.

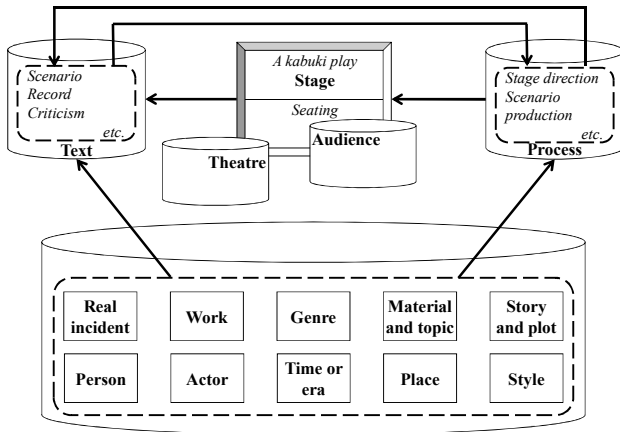


Fig. 1. Multiple narrative structures of *kabuki* and INGS and GIS. [Source: Ogata (2016).⁸]

Naimaze in *kabuki* has been known as a narrative creation method or a group of techniques that combines components in existing *kabuki* works or in the narratives from other genres for making a new work. Various elements, such as stories, plots, characters, and places, can be used as components in *naimaze*. The author aims to use the *naimaze* method in the INGS and GIS. In this paper, after the author describes our previous studies in *kabuki* narrative generation as background information, the author presents an approach for designing the narrative techniques of *naimaze* for the INGS (and GIS) by applying the method for combining “moves” as explained in V. Propp’s narratological study, “morphology of the folktale.”⁹ A move by Propp means a narrative macro level unit, or a kind of sequence that is composed of several “functions;” and he showed various ways to combine several moves to construct an entire narrative structure. The next section displays many possibilities of *naimaze* techniques and the implementation of experimental programs based on various *kabuki* analyses; and the Propp’s move method is utilized as a preliminary attempt for *naimaze* techniques in the INGS and GIS. This paper, further, shows the direction that will be taken by future research when designing and implementing an organized *naimaze* technique group in these systems based on our future *kabuki* studies.

2. Background

Previous *kabuki* studies by the author include the following topics:

- (1) Preliminary and comprehensive considerations regarding *kabuki* and narrative generation
- (2) An entire framework of the multiple narrative structures of *kabuki*
- (3) Studying and considering several topics, including “person,” “story,” and “*tsukushi*,” in the multiple narrative structures of *kabuki*.
- (4) Introducing knowledge acquired from research, analyses, and considerations of *kabuki* into our narrative generation systems (INGS and GIS).

In (1),^{10,11,12} the author has studied the history and characteristics of *kabuki* and considered the narrative methods or techniques for connecting them to our narrative generation research.

In the next point (2),^{13,14,15,16} the author has presented an entire framework of the multiple narrative structures of *kabuki* that comprise the multiple structures among the components, the multiple structures in each component, and the multiple structures for synthesizing their multiplicities, in order to understand and deal with a whole system of *kabuki* from the viewpoint of the multiple narrative structures model of *kabuki*.

The objectives of (3) include deeper analysis and study of each component of the above-mentioned multiple narrative structures and an in-depth consideration of the multiple connections or relationships of these *kabuki* components. In particular, the author has considered through investigations regarding “person”¹⁷ and “story”.¹⁸ However, *tsukushi* or *zukunftshi*¹⁹ is not included in the current list of the multiple narrative structures (Fig. 1). By the term *tsukushi* (or *zukunftshi*), the author means a thorough, or often exhaustive, description of a group of objects, including places such as mountains and cities, objects such as fish and foods. *Naimaze* descriptions frequently appear in Japanese classical literature, such as novels, stories, and long poems; and *geino* works, such as dances, *ningyo joruri* works, and *kabuki* works. Gunji²⁰ regarded *basho zukushi* (the *tsukushi* of places), such as *michiyuki* (a symbolic travel scene), as a type of *kabuki* esthetics that is propagated through the Japanese literary and *geino* traditions. Gunji discussed *basho zukushi* in *kabuki* from the viewpoint of unique arrangements between spatial and temporal aspects in a narrative, different from the *emakimono* style in which the temporal aspect is superior. The author understands

zukushi or tsukushi as an important element in the multiple narrative structures of kabuki. On the other hand, it is located in a meta-level element that crosses fifteen kinds of elements shown in Fig. 1.

The final point (4) aims to introduce knowledge acquired from research, analyses, and considerations of kabuki into our narrative generation systems (INGS and GIS).¹⁸ One of the objectives of the study of kabuki's narrative generation by the author is to comprehensively and precisely describe a "kabuki narrative generation system model." According to this macro objective, one of the present goals is to introduce the acquired kabuki narrative knowledge, methods, and techniques into mutually related systems, the INGS and GIS.

3. Naimaze: The Usage of Propp's Move Method for Mixing Narratives

The author presents a method for simulating naimaze in kabuki based on our previous paper²¹ related to Propp's folktale theory.⁹ Propp presented a method of combining stories using several patterns of combining "moves." In Propp's narratological theory, the most basic narrative units for folktale-like stories are thirty-one kinds of "functions." A move is composed of the selective sequence of functions and many actual folktales are combinations of several moves. Table 1 shows examples of the combination patterns of moves as proposed by Propp. The author's idea is to implement the naimaze in kabuki by using Propp's move method.

Table 1. Move combination patterns [Source: Ogata & Hosaka (2004)²¹.]

1	<p>"One move directly follows another move."</p>
2	<p>"A new move begins before the termination of the first one."</p>
3	<p>"An episode may also be interrupted in its turn, and in this case fairly complicated schemes may result."</p>
4	<p>"A tale may begin with two villainies at once, of which the first one may be liquidated completely"</p>

© The 2017 International Conference on Artificial Life and Robotics (ICAROB 2017), Jan. 19-22, Seagaia Convention Center, Miyazaki, Japan

	before the other is."
5	<p>"Two moves may have a common ending."</p>
6	<p>"Sometimes a tale contains two seekers."</p>

The following descriptions provide the explanations and texts for three types of examples of naimaze using Propp's method. These examples are not the results of automatic generation, but human attempts:

- **[Example 1: Narukami + Sanmai no Ofuda]** The first example shows that a folktale story, *Sanmai no Ofuda*²² is based on the story of a kabuki work, *Narukami*²³ using the method 1 in Table 1. In particular, *Sanmai no Ofuda* (second part) is connected to *Narukami* (first part) and the main characters in *Sanmai no Ofuda* are changed to the characters in *Narukami*.
- **[Example 2: Kanjinchō in Sanmai no Ofuda]** The second is an example in which, using method 2 in Table 1, the story of *Kanjinchō*²⁴ is inserted into the first move by the story of *Sanmai no Ofuda*, and the main characters in *Kanjinchō*, Benkei and Minamoto no Yoshitsune, appear.
- **[Example 3: Characters in Sukeroku → Characters of Gogo no Eiko]** The final example deals with the naimaze of characters only. This example does not use the Propp's method. In particular, in the story of *Sukeroku*²⁵ of kabuki, the characters are replaced by the main characters in *Gogo no Eiko*²⁶ by Yukio Mishima, the chief, Fusako, Ryūji, Noboru, and Yoriko.

[Example 1] *The rain has stopped falling and the whole country is suffering from a drought. This is because Narukami Shonin (a priest) holds a grudge against the Emperor for not keeping his promise, and has caged the dragon god of rain behind a waterfall. A beautiful young woman appears, heading for Shonin's hermit cave in the northern mountain. She says that she wants to wash the clothes of her dead husband in which her feelings for him linger, but because there is no water, she has come to the waterfall to find the water to wash the clothes. To say farewell to her husband, the woman crosses the river toward Shonin, and lifts up the hem of her skirt to reveal her white legs, and without thinking,*

Shonin bends forward toward her. To the suspicious Narukami Shonin, the woman turns and says that she wants to become a nun and his disciple. Shonin sends out his two disciples, Hakuunbô (the white cloud bonze) and Kokuunbô (the black cloud bonze) to bring her nun garments, and then the woman suddenly becomes sick. The surprised Shonin attends to her, and while doing so he touches her breast. He has never touched a woman before and he is gradually unable to control his desire due to the softness of her skin. Seizing her chance, the woman brings out to drinking cups and gets Shonin drunk, and in his drunkenness he reveals that he keeps the dragon god imprisoned behind a sacred rope across the waterfall. As Shonin sleeps drunkenly, the woman creeps away and cuts the rope and releases the dragon god, and immediately it begins to rain heavily. The woman was in fact Kumonotaema Hime (Princess), the most beautiful woman at the court, sent by the Emperor to break the power of Narukami. When he revives and becomes aware of what happened, his hair stands on end and he becomes enraged, he turns into flames, he fights and knocks down the disciples who attempt to stop him, and he chases after the princess. The princess, who can see Narukami chasing after her, throws down the second paper charm and says a curse, "Make a big river appear behind me," and sure enough, a big river appears. But Narukami uses his magic powers to swallow the water in the river. Next, the princess uses her final charm and says the curse, "Make a sea of fire appear" and a sea of fire appears. But Narukami uses the water he has swallowed to put out the sea of fire. The princess hurries back to the temple and seeks the help of the priest, who makes her promise to train more seriously after that, and hides her in a large pot. The priest begins baking rice cakes in the hearth. Then Narukami enters the temple and demands that the priest give him the princess. The priest says that before that, let's see which one of us is the best at changing shapes. He asks "Can you make yourself as big as a mountain?" "Yes I can" replies Narukami, and makes himself as big as a mountain. The priest then asks, "Can you make yourself as small as bean?" "I can do that too" Narukami replies, and makes himself as small as a bean. The priest picks up Narukami, who is now the size of a bean, stuffs him in the rice cake he is baking, and eats him.

[Example 2] Once upon a time there was a temple in a village, in which lived a young monk and a Buddhist priest. One day the young monk said to the priest that he wanted to go to the mountain to collect chestnuts. The priest takes out three charm cards and gives them to the

young monk. The young monk goes to the mountain and becomes so absorbed in collecting chestnuts that he is still on the mountain when the sun goes down. Then, an old woman appears and invites the young monk to stay at her home. But during the night, the boy wakes up and sees the woman in her true form of a mountain witch, sharpening a knife in the kitchen preparing to eat him. The young monk says "I want to use the toilet," so the mountain witch thinks about it, and ties him up with a rope and takes him to the toilet. The young monk attaches one of the paper charms to a pillar in the toilet, and says "Pretend to be me and answer the witch," and he flees out of the window. The witch asks "Are you finished?" and the paper charm replies in the voice of the young monk, "Just a little longer." The witch then asks again, "Are you finished?" and the paper charm again replies in the voice of the young monk, "Just a little longer." Finally the witch cannot stand it any longer and breaks down the door of the toilet, to find that the young monk has disappeared without a trace and there is only the torn paper charm. Realizing she had been tricked, the witch chases after the young monk. The young monk, who can see the witch chasing after him, throws down the second paper charm and says a curse, "Make a big river appear behind me," and sure enough, a big river appears. But the witch uses her magic powers to swallow the water in the river. Next, the young monk uses his final charm and says the curse, "Make a sea of fire appear" and a sea of fire appears. But the witch uses the water she has swallowed to put out the sea of fire. The young monk hurries back to the temple and seeks the help of the priest. The young monk and his party are trying to pass, with the priest taking the lead, wearing the disguises of yamabushi mountain priests. The priest says that they are travelling to seek donations for the rebuilding of the destroyed Todaiji Temple. However, already the information has been delivered to the barrier keeper, Saemon Togashi, that the young monk and his party are travelling disguised as mountain priests, and he gives the strict order that no mountain priests are to be allowed to pass. Indignant at this, the priest and his friends chant an esoteric Buddhist prayer to Togashi, to attempt to clear his suspicion. This impresses Togashi and is reminded of the previous words of the priest, and he orders him to read the kanjincho (a subscription list of people who have donated). The priest pulls out a blank scroll that he happens to have and spontaneously begins to read it, pretending it is the kanjincho. But Togashi is still suspicious, and asks him difficult question about the life of a yamabushi disciple and about esoteric prayers, but the priest answers without hesitating. Togashi lets them

pass, but still has strong doubts about one of the lower-ranked men in the group, who is actually the young monk. The priest beats his master the young monk with his pilgrim's staff, which clears him of suspicion. The young monk, who had escaped from danger, compliments the priest for his quick thinking, but the priest bursts into tears and apologizes to his master for the rude way he had to save his life. Responding to this, the young monk gently takes the priest by the hand and has him think of the story of the battle in which they pursued Taira together. Then Togashi appears and apologizes for his previous rudeness and offers them sake to drink. The priest drinks the sake and performs a dance. The young monk and his party escape while the priest dances. The priest puts on his *oi* (a wooden box carried on one's back to store items for a pilgrimage) takes his leave of Togashi, and hurries after his master. Then the mountain witch enters the temple and demands that the priest give her the young monk. The priest says that before that, let's see which one of us is the best at changing shapes. He asks "Can you make yourself as big as a mountain?" "Yes I can" replies the witch, and makes herself as big as a mountain. The priest then asks, "Can you make yourself as small as bean?" "I can do that too" the witch replies, and makes herself as small as a bean. The priest picks up the witch, who is now the size of a bean, stuffs her in the rice cake he is baking, and eats her.

[Example 3] *Soga no Goro, who appears as a guest named Hanakawado Sukeroku, goes to Yoshiwara (the entertainment district) to search for Genji's treasured sword "Tomokiramaru." In Yoshiwara, which is a place where various men gather, he intentionally tries to start fights with men so that they will draw their swords, revealing if they have the sword he is searching for. Agemaki is a courtesan who is frequented by Sukeroku, and the magnificently bearded Ikyuu also appears with Agemaki. Sukeroku thinks that Ikyuu might have Tomokiramaru and tries to get him to draw his sword, but he is unable to. Sukeroku's older brother, Soga no Juro, then appears as a seller of white sake, and on hearing the opinion of his younger brother, he himself starts trying to pick fights. Soon Agemaki returns to the stage accompanied by a samurai. Sukeroku tries to pick a fight with the samurai, but surprisingly that samurai is his mother, Manko, in disguise, who has come because she is worried about the two brothers. Manko dresses Sukeroku in an easily breakable paper kimono and warns him against a fierce fight, and they return to Juro. Ikyuu once again appears on the stage. Ikyuu sees that Sukeroku is actually Soga no Goro, draws*

Tomokiramaru and tries to persuade him to betray Genji. Sukeroku of course does not agree to this, cuts-down Ikyuu, retrieves Tomokiramaru, and leaves Yoshiwara.

4. Future Research Directions

In the future, the author will design and implement the *naimaze* techniques for narrative generation in the INGS and GIS in accordance with the following directions:

- **Positioning of *naimaze* in the multiple narrative structures model of *kabuki*:** *Naimaze* is made to correspond to the positioning of the meta-level concept for fifteen topics of the multiple narrative structures. *Naimaze* is not an element that is included in the topics and is regarded as a kind of narrative technique that, so to speak, utilizes several elements in the topics in the meta-level and traverse. For example, although applying a *naimaze* method or technique to a story or plot is the most general usage, *naimaze* is also related to the element of a "character" as in a "person." In particular, though it is a possibility of *naimaze* to mix "stories" or "plots" of two or more narratives, the usage of the *naimaze* of "stories" or "plots" is related to the *naimaze* of "characters" of different works. Similarly, introducing "characters" from different existing works into a new work enables the associative relationship of the new work to past works.
- **Narrative elements that enable diverse *naimazes*:** The most basic mechanism of *naimaze* is related to, or needs, the consideration of the following aspects: (1) object, (2) basic method or technique, and (3) strategic method or technique. The first necessary step for implementing *naimaze* techniques is to make these issues clear at the macro design level. Regarding (1) "object," in the elements of the multiple narrative structures of *kabuki* shown in Fig. 1; "real incident," "work," "material and topic," "story and plot," "person," "time or era," and "place" can be considered the objects of *naimaze* in the ordinary sense. Furthermore, as a possibility, "text," "genre," "actor," and "style" may also become the objects. Regarding (2), "basic method or technique" comprises a group of formal methods or techniques for conducting the *naimaze* of each object. Further, there are *naimaze* methods or techniques for simultaneously processing several objects. At the most formal level, namely methods or techniques in the program's implementation

level here, functions called narrative techniques, which expand or transform a story structure or narrative discourse structure generated by the INGS, can also be utilized for *naimaze*. This means that *naimaze*'s techniques can also be located as a group of narrative techniques in the INGS. Additionally, concrete knowledge of *kabuki* and the other narratives is required for designing and implementing *naimaze* methods or techniques. This kind of knowledge, namely, *kabuki*-oriented knowledge, can be stored in the GIS as a part of the author's framework of narrative generation. *Naimaze*'s methods and techniques can be designed and implemented through mutually related narrative generation systems, the INGS and GIS. Finally, (3) "strategic method" means a kind of control mechanism that enables the effective use of *naimaze*. In addition to an ordinary plan in which previously defined strategic control methods are used for *naimaze* generation, another idea of the author concerning this problem is to prepare a different control method that executes random narrative generation, *naimaze* in this case, and incrementally narrows down the range of generated narratives through repetition and storage of the evaluation of the results and process²⁷.

5. Conclusion

The author has been conducting a synthetic study of narrative generation systems based on mutually relating two systems, the INGS and GIS. *Naimaze* methods or techniques of *kabuki* dealt with in this paper will be introduced into these narrative generation systems in the future. In this paper, the author proposed several basic methods of *naimaze* using our previous research based on the move connection theory by Propp. Next, the author listed several future issues for introducing *naimaze* as a group of narrative techniques into the INGS and GIS. These issues, at the same time, can be designed and implemented on the basis of the author's research results and ideas shown in this paper, including the multiple narrative structures of *kabuki* and the narrative generation through random generation and continuous evaluation.

Acknowledgements

This work is supported by the Support Center for Advanced Telecommunications Technologies Research Grant (2015-2017) and Kayamori Foundation of

Information Science Advancement Research Grant (2017).

References

1. S. L. Leiter, *Historical Dictionary of Japanese Traditional Theatre, 2nd Edition*. (Rowman & Littlefield, Lanham/Boulder/NY/London, UK, 2014).
2. T. Imao, *Henshin no Shisō [The Theory of Metamorphosis]*. (Hōsei University Press, Tokyo, Japan, 1970).
3. T. Kawatake, *Kabuki: Baroque Fusion of the Arts*, trans. Connel Hoff, F. and J. (The International House of Japan, Tokyo, Japan, 2003).
4. T. Watanabe, *Kabuki - Kajo Naru Kigo no Mori [Kabuki: The Forest of Excessive Signs]* (Shinyosha, Tokyo, Japan, 1989).
5. T. Watanabe, *Kabuki - Kata no Shinzui [Kabuki: The Essence of Kata]* (Kadokawa-Gakugei-Shuppan, Tokyo, Japan, 2013).
6. T. Ogata, Computational and Cognitive Approaches to Narratology from the Perspective of Narrative Generation, in T. Ogata & T. Akimoto (eds.), *Computational and Cognitive Approaches to Narratology* (Information Science Reference (IGI Global), Hershey, PA, USA, 2016), pp. 1-74.
7. T. Ogata & S. Asakawa, Aspects of Content Generation Through Narrative Communication and Simulation. in T. Ogata & S. Asakawa (eds.), *Content Generation Through Narrative Communication and Simulation* (Information Science Reference (IGI Global), Hershey, PA, USA, in press-b).
8. T. Ogata, *Kabuki* as Multiple Narrative Structures. in T. Ogata & T. Akimoto (eds.), *Computational and Cognitive Approaches to Narratology* (Information Science Reference (IGI Global), Hershey, PA, US A, 2016), pp. 391-422.
9. V. Y. Propp, (1968). *Morphology of the Folktale*, trans. L. Scott. (University of Texas Press, Austin, TX, USA, 1968). (Original work published 1928).
10. T. Ogata, A Preliminary Consideration of the Multiple Narrative Structures of *Kabuki*. in *Proc. of the 49th Special Interest Group on Language Sense Processing Engineering in Japanese Society for Artificial Intelligence*, (2015), pp. 59-64.
11. T. Ogata, Towards *Kabuki* (1): From Narratives of Arbitrariness and Edition to Narratives of Multiplicity and Existence. in T. Ogata, Y. Kawamura, & A. Kanai, in *Artificial Narratology: Artificial Intelligence/Cognition/Social Process and*

- Narrative Generation* (Hakutoshobo, Tokyo, Japan, in press-b).
12. T. Ogata & J. Ono, Distribution of Contents and Media in Narratives: A Preliminary Consideration of Games, *Kabuki*, and *The Tale of Genji*. in *Proc. of the 50th Special Interest Group on Language Sense Processing Engineering in Japanese Society for Artificial Intelligence*, (2015), pp. 97-115.
 13. T. Ogata, (2017). Analyzing Multiple Narrative Structures of *Kabuki* Based on the Frameworks of Narrative Generation Systems, in *Proc. of the 2017 International Conference on Artificial Life and Robotics*, (2017), pp. 629-634.
 14. T. Ogata, On Narrative Multiplicity of *Kabuki* and the Other Narratives. in *Proc. of the 53th Special Interest Group on Language Sense Processing Engineering in Japanese Society for Artificial Intelligence*, (2017b), pp. 19-29.
 15. T. Ogata, The Multiple Narrative Structures of *Kabuki* and *Geino* Information System. in *Proc. of the 31th Annual Conference of the Japanese Society for Artificial Intelligence*, (2017c), 1D2-OS-29a-4.
 16. T. Ogata, Towards *Kabuki* (2): Aspects of Multiple Narrative Structures. in T. Ogata, Y. Kawamura, & A. Kanai, (eds.), *Informational Narratology: Artificial Intelligence, Cognition and Social Process, and Narrative Generation* (Hakutoshobo, Tokyo, Japan, in press-b).
 17. T. Ogata, The Multiple Narrative Structures of “Person” in *Kabuki*. in *Proc. of the 52th Special Interest Group on Language Sense Processing Engineering in Japanese Society for Artificial Intelligence*, (2017a), pp. 113-118.
 18. T. Ogata, An Integrated Approach to Narrative Generation: From Mishima and *Kabuki* to Narrative Generation Systems. in T. Ogata & S. Asakawa (eds.), *Content Generation Through Narrative Communication and Simulation*, (Information Science Reference (IGI Global), Hershey, PA, USA, in press-a).
 19. T. Ogata, T. (2016c). Narrative Generation of “Zukushi”: Towards Its Systematization Through Surveying *Kabuki* and Developing a Proper Noun Conceptual Dictionary in INGS. in *Proc. of the 30th Annual Conference of the Japanese Society for Artificial Intelligence*, (2016c), 1K5-OS-06b-2.
 20. M. Gunji, *Kabuki no Bigaku [Aesthetics of Kabuki]*. (Engeki Shuppansha, Tokyo, 1963).
 21. T. Ogata, & Y. Hosaka, Transformation of Story in the Story Generation System Based on Narratology, in *Proc. of the 9th International Symposium on Artificial Life and Robotics Vol.2*, (2004), pp. 593-596.
 22. *Sanmai no Ofuda - Wikipedia [The Three Charms: Wikipedia]*. (n.d.). Retrieved from the Japanese Wikipedia:
<https://ja.wikipedia.org/wiki/%E4%B8%89%E6%9E%9A%E3%81%AE%E3%81%8A%E6%9C%AD>
 23. Japan Actors’ Association, & The Organization for the Preservation of *Kabuki* (2017). *Narukami - Kabuki Enmoku An’nai [Narukami: Kabuki Play Guide]*. Retrieved October 20, 2017, from <http://enmokudb.kabuki.ne.jp/repertoire/502>
 24. *Kanjinchō - Wikipedia [The Subscription List: Wikipedia]*. (n.d.). Retrieved from the Japanese Wikipedia:
<https://ja.wikipedia.org/wiki/%E5%8B%A7%E9%80%B2%E5%B8%B3>
 25. *Sukeroku - Wikipedia [Sukeroku: Wikipedia]*. (n.d.). Retrieved from the Japanese Wikipedia:
<https://ja.wikipedia.org/wiki/%E5%8A%A9%E5%85%AD>
 26. Y. Mishima, *Gogo no Eikō* (Kōdansha, Tokyo, Japan, 1963). (trans. S. Mitchell, *The Sailor Who Fell from Grace with the Sea* (Knopf, NY, USA, 1965).
 27. T. Ogata, T. Arai, & J. Ono, Random Narrative Generation Using an Integrated Narrative Generation System. in *Proc. of the 15th Information Science and Technology Forum*, (2016), pp. 133-134.

Narratology goes to Creativity ---Cognitive Content Generation

Akinori Abe*

*Division of Behavioral Science, Faculty of Letters, Chiba University, 1-33 Yayoicho, Inageku,
Chiba, 263-8522, Japan[†]*

Dwango Artificial Intelligence Laboratory, Tokyo, Japan

E-mail: ave@ultimaVI.arc.net.my

Abstract

In the previous studies, I discussed the creativity in IMDJ (Innovators Marketplace on Data Jacket). The Innovation Game seems a game where a new production will be obtained during the combination of various techniques, materials and previous products. Accordingly I discussed IMDJ performance from the perspective of abduction. In addition, more important matter is the effect of communication among participants which is plays a significant role in creativity. That is, for creativity, important matters are "action of a novel relational product" and "the role of interaction and collaboration with other individuals." Then I discussed the role of comfortable communication (narratology) by robots in the creative situation as well as usual situation. In this paper, I will discuss the role of narratology which is based on the cognitive content generation in the creative task.

Keywords: creative task, Innovators Marketplace on Data Jacket, interaction, narratology, cognitive content generation

1. Introduction

In this paper, I will discuss the role of narratology or story telling in the creative tasks (contents generation). Narratology was regarded as a concept in story telling or generation. For instance, literary works generation can be achieved by the concept of narratology [1,2]. Previously I discussed the possibility of the literary works generation by computer [1]. Also Rolf Jensen showed the importance of story in selling products [3]. These can be regarded as creative tasks and by the story or narrative, the creativity enhanced in several situations. Thus story or narratology is very important in creativity. For the conversation activation with a robot, Yamaguchi, Neguri and Otake showed very interesting results [4]. They

analyzed the conversation data by the frequency of evoked laughter in each topic and in all participants. The reproduced stories presented by the robot created more laughter than the original stories presented by human. They concluded that the robot successfully enlivened group conversation through evoking laughter. The frequency of laughter will not be connected with the creativity. However this result show the possibility of the introducing of a proper robot for the activation of the general meeting/conversation which will cause us to the better creativity. Therefore, in this paper, I also discuss this type of conversation with a robot. Of course the conversation can be discussed in the context of narratology or story telling.

2. Computational literature generation

Usually several techniques are used in the computational literary works generation. In fact, one of the special feature can be used in the computational literary works generation is the “intertextuality” proposed by J. Kristiva [5]. Kristiva defined **intertextuality** as follows:

The word's status is thus defined horizontally (the word in the text belongs to both writing subject and addressee) as well as vertically (the word in the text is oriented towards an anterior or synchronic literary corpus)... each word (text) is an intersection of words (texts) where at least one other word (text) can be read... any text is constructed as a mosaic of quotations; any text is the absorption and transformation of another.

This is a very promising feature. Because computers are good at such as cutting, searching, selecting, and combination of small materials.

3. The role of narratology in creativity

Several applications and activities of narratology and story telling are shown in [6]. In fact narratology and story telling are for literary works. However, recently they have been applied to medical interview and therapies. As shown in the facts in product selling and advertisements, by the story an additional value can be added to the products. During the dinner in the Restaurant Story in London, we can enjoy the story as well as the taste of the food. The story might be regarded as an atmosphere, but it can also be regarded as an additional value. We can say more that without story no product can have value inside. Thus story or narratology is very important in creativity. By the story or narratology, the creativity will be enhanced in several situations.

4. Abduction as story generator

4.1. Computational abduction

Peirce defined abduction from a philosophical point of view as the operation of adopting an explanatory hypothesis [7]. For the computational abduction, several systems have been proposed. One of them is Theorist [8]. Theorist is considered as a computational hypothetical reasoning system. A hypothetical reasoning which is an explanatory reasoning generates (collects, selects) a consistent hypothesis set from hypothesis candidates to explain the given observation. The generated hypothesis set can be regarded as an answer (solution) which can explain the observation.

4.2. Computational literary work generation

For the computational literary works generation, I adopted the concept of “intertextuality.” Its feature of text as a mosaic of quotations construction and absorption and transformation of another text is easily achieved by abduction. That is, a randomized generation is quite easy¹ but not so interesting. A logical generation can be achieved by abduction. For instance, if the final goal or result is known, for the explanation of the final goal or result, several quotations which can be regarded as hypotheses are abduced. I applied abduction to a simple discourse generation which dealing with humour [9]. In this framework, the structure of the previous conversation is referred to to generate a new conversation. In addition, a humorous conversation is generated by AAR [10] (the extension of Theorist). This type of application was developed for the activation of conversation. This procedure can be applied to the normal conversation as well. Of course an additional emotion can be added to the conversation by this method. In addition, the above application is based on situational inference change. A suitable situation change can lead our thinking in the better direction. Accordingly, if we use this type of situation change not only for making joke but also for giving a certain stimulation, innovative activities can be encouraged.

5. Emotional robot

In [11], we discussed what type of communication tool can encourage user's communication and make users feel enjoyable and comfortable. We conducted experiments by using the following six types of bots:

1. standard (adjustment) type: many responses (aizuchi) and introductions to the conversation.
2. conversation introduction type: many introductions to the conversation are given.
3. response type: many responses are given.
4. non-sympathy type: blame and non-sympathy words are given.
5. puppet type: imagine the feature of the puppet and speak according to it.
6. humour type: more playful, and no context is considered.

For the type-2 robot (conversation introduction type) and the type-6 robot (humour type), an evaluation as enjoyable is high. On the other hand, for the type-3 robot (response type) and type-4 robot (non-sympathy type), an evaluation as boredom is high. From the results, type-2 and type-6 robots will activate and enhance the

communication and creativity. Communication and creativity might have a strong relationships.

6. IMDJ procedure

Innovation Marketplace on Data Jacket (IMDJ) is called as Innovation Game. The Innovation Game seems a game where a new production will be obtained during the combination of various techniques, materials and previous products. To summarize the game, when a requirement is given, a proposal will be generated accordingly. Even if the proper techniques are not on the game board, techniques which were used in the previous game can be searched and used. In this sense, the strategy used in this game can be regarded as abduction. Here, I will show the brief strategy of the Innovation Game. In the Innovation Game participants do their best to explain the certain requirement by generating or collecting a set of hypothesis (in this case, a set of techniques) in the current environment. Many creative activities can be performed as a case of abduction. This type of inference strategy can be considered as abduction. Of course, if the current environment changes, the inference strategy has the characteristic of non-monotonic reasoning. A strategy “generating or collecting a set of hypothesis (in this case, a set of techniques) to explain a certain requirement.” can be formalized as hypothetical reasoning. For the formalization, please see [12]. When we make an inference in IMDJ, we basically search or generate techniques by abduction and combine the consistent techniques to produce our proposal that can satisfy the requirements. This type of inference can be regarded as a creative inference. In addition, when we cannot find proper techniques to satisfy the requirements, we perform an analogical mapping from techniques in other context to those in the current context. Then we can generate a proper hypothesis set (techniques) to create proposal as a combination of consistent techniques.

7. The role of narratology in IMDJ

7.1. Creativity

In [13], I defined creativity as follows:

Creative means novel and creative work comes from nothing or from something relative but whose relation to the work was hidden. Actually, for creativity, a sort of intuition or special sense will be necessary. An intuition or special sense will emerge with some stimulus like information (background knowledge). In emergence, knowledge will work as a catalyst.

For the creativity, the importance of “action of a novel relational product” and “the role of interaction and

collaboration with other individuals” are pointed out. These types of creativity can be achieved by a simple abduction. Accordingly, the abductive process shown in the above can include creativity. However, for the more attractive creativity, a “storytelling” will be necessary. In addition, the value of products will depend on the story they tell. Thus narratology is also the important factor for creativity. It is pointed out that “creative individuals are often thought of working in isolation, the role of interaction and collaboration with other individuals is also critical.” During collaboration, it is more necessary to consider the existence of a storyteller. Abduction can have a role of the collaboration between participants and storytellers. Thus by abduction a certain story can be generated as well as a combination of several techniques to explain a requirement.

7.2. The narratology in IMDJ

An abductive procedure will be performed in the product generation (creativity) in IMDJ. Where the possible products can be generated as explaining the requirement. In the above, I show the effect of the communication robots in conversations. According to my definition, for the creativity, a sort of intuition or special sense will be necessary. An intuition or special sense will emerge with some stimulus such as information (background knowledge). In emergence, knowledge will function as a catalyst. The catalyst can be obtained during conversation or listening to the story told by the other participants. That is, the effect of communication among participants is plays a significant role in creativity. A communication among users is very important to reorganize or improve their thinking. In addition, sometimes even a new idea might appear. This type of communication can be discussed from the perspective of narratology or story telling. As discussed in the previous section, narratology is a very important concept in valuable activities as well as literary works generation. It is necessary to consider the effect of narratology even during a technical discussion. For instance, for a technical discussion, there should be a certain story. Moderators or communication robots (if applicable) should produce a certain story during the discussion. If they can properly generate or add a story to the technical discussion, participants can produce the better products.

8. Conclusions

In this paper, I mainly discuss the effect of narratology or story telling in several situations including IMDJ. Recently, it has been discussed the importance of narratology or story telling in several applications such as an advertisement and intellectual tasks. In [12], I discussed and formalized the role of abduction in the

product generation. Abduction can also has the role of the collaboration between participants and storytellers. Thus by abduction a certain story can be generated as well as a combination of several techniques to explain a requirement. For the better product generation in IMDJ the importance of narratology or story telling should be considered.

References.

1. Abe A., The possibility of the Generation of Literary Works by Computer. In (Ogata T. and Akiomoto T. eds.), *Computational and Cognitive Approaches to Narratology*, (2016) pp. 75-89.
2. Ogata T., Computational and Cognitive Approaches to Narratology from the Perspective of Narrative Generation in Computational and Cognitive Approaches to Narratology (Ogata T. and Akiomoto T. eds.), (2016) pp. 1-74.
3. Jensen R., *The Dream Society: How the Coming Shift from Information to Imagination Will Transform Your Business*. Mcgraw Hill (1999)
4. Yamaguchi K., Nergui M., and Otake M., A Robot Presenting Reproduced Stories among Older Adults in Group Conversation. *Applied Mechanics and Materials* (HJ. Patthi Bin Hussain, Zhu Yuesheng, Murthy Rallapalli and Jamaluddin Mahmud eds.), Volumes 541–542 (2014) pp. 1120-1126.
5. Kristeva J., *Desire in Language: A Semiotic Approach to Literature and Art*. Columbia University Press (1980).
6. Abe A.: Narratology and Creativity, In *Content Generation through Narrative Communication and Simulation* (Ogata T. and Asakawa S. eds.) (2018). to appear
7. Peirce C. S., Abduction and Induction, chap. 11, *Philosophical Writings of Peirce*, Dover (1955)
8. Poole D., Goebel R., and Aleliunas R., Theorist: A Logical Reasoning System for Defaults and Diagnosis, in *The Knowledge Frontier: Essays in the Representation of Knowledge* (Cercone N.J., McCalla G. Eds.), (1987) p. 331-352, Springer-Verlag
9. Abe A., Applications of Abduction, *Proc. of ECAI98 Workshop on Abduction and Induction in AI*, pp. 12-19 (1998)
10. Abe A., Abductive Analogical Reasoning, *Systems and Computers in Japan*, 31(1), (2000) pp. 11-19.
11. Abe A. and Hayashi M., On communication via bots for the computational therapy, *Proc. of Int'l Workshop on Language Sense on Computer in IJCAI2016* (2016) pp. 61-66.
12. Abe A., The Role of Abduction in IMDJ, *Proc. of IJCAI2015 International Workshop on Chance Discovery, Data Synthesis and Data Market*, (2015) pp. 59--64
13. Abe, A., User's interests change as Chance Discovery, *Proc. of KES2002* (2002), pp. 1291-1295.

A Framework for *Haiku* Generation from a Narrative

Takuya Ito

*Faculty of Software and Information Science, Iwate Prefectural University,
Sugo 152-52, Takizawa, Iwate, Japan**

Takashi Ogata

*Faculty of Software and Information Science, Iwate Prefectural University,
Sugo 152-52, Takizawa, Iwate, Japan
E-mail: g031n019@s.iwate-pu.ac.jp*

Abstract

The primary goal of the authors' research related to the generation of narratives and *haikus* is to complete a mutual transformation mechanism between a narrative and a *haiku*. In this work, the authors propose a framework for transforming a narrative into *haiku*-like sentences. The paper shows a basic method of generating *haiku*-like sentences from a fragmented narrative by selecting, arranging, and modifying the elements in the narrative. The authors have been developing an Integrated Narrative Generation System (INGS) that automatically generates narratives. The authors aim to introduce the developed *haiku*-relating mechanism into the INGS in the future.

Keywords: Artificial intelligence, Narrative generation, Haiku, Haiku-like sentence, Haiku generation.

1. Introduction

The authors have earlier presented a method for generating a narrative from a *haiku*.¹ By analyzing the relationships between a *haiku* and the interpreted sentences of a *haiku*, these relationships can be used to obtain new interpreted sentences. Conversely, Nitta² proposed methods to generate a *haiku* from a narrative. This method establishes a meta-sentence and core sentences about the narrative.

The primary goal of the authors' research related to the generation of narratives and *haikus* is to complete a mutual transformation mechanism between a narrative and a *haiku*³, a kind of a catchphrase about the narrative. The authors aim to generate a narrative from a *haiku* or a catchphrase, as well as a *haiku* or a catchphrase from a narrative. A *haiku* is the shortest form of poetry in the world and expresses a scene or feeling using only seventeen syllables. The authors consider that a *haiku* can function as a kind of catchphrase for representing the essence or theme of a narrative. In addition, the authors

have developed an Integrated Narrative Generation System (INGS)⁴ that automatically generates narratives. The authors also aim to use a *haiku*-generation mechanism in the INGS. Based on the above background and purposes, the authors have conducted studies related to the generation of *haikus* or *haiku*-like sentences and narratives. In earlier studies, the authors have presented the following methods for *haiku* generation: a method using the transition patterns of word categories in *haikus*⁵, a method based on appearance frequency and co-occurrence of concepts and words in *haikus*⁶, and a method using deep learning for the transition patterns of words and characters in *haikus*⁷.

This paper deals with *haiku* generation from a narrative. The next section proposes a framework to generate a *haiku* from a narrative. In section 3, the authors demonstrate *haiku* generation using the proposed framework.

2. A Haiku Generation Framework from a Narrative

A *haiku* is composed of three parts with five syllables, seven syllables, and five syllables. To develop a framework for generating a *haiku* or a *haiku*-like sentence from a narrative, the authors focus on the factors of “selection,” “arrangement,” and “modification” of the elements of a narrative. Because *haikus* generated by the proposed mechanism do not include *kigos* words (describing seasons) that are, traditionally, necessary elements in most *haikus*, the authors call a *haiku* generated by the mechanism a “*haiku*-like sentence.” Based on these factors, the authors present the following algorithm to generate a *haiku*-like sentence from a narrative.

- (i) Selecting a format for a *haiku*-like sentence. For generating a *haiku* according to various methods, the system preliminarily prepares several formats and selects one of the formats that suits the purpose.
- (ii) Extracting one or more sentences in a narrative, which is the input information in this system, according to the condition of the selected method. These conditions are shown in the examples in the next section.
- (iii) Extracting one or more elements from the sentences extracted in (ii) and substituting the extracted elements in the sentence format selected in (i).
- (iv) Adjusting the above information according to the standard *haiku* form of three parts of five, seven, and five syllables. If necessary, the system adds one or more *kirejis* to the selected elements in the *haiku* to be generated. (*Kireji* is a category of words used to regulate the sounds of a *haiku* and especially indicates emotional emphasis in the psychological aspect of linguistic rhetoric.)

In the above algorithm, step (i) corresponds to the “arrangement” of narrative information. Steps (ii) and (iii) correspond to the “selection.” Step (iv) corresponds to “modification.”

3. Generation Processes of a Haiku-like Sentence from a Narrative

The authors present the following three types of methods of *haiku*-like sentence generation from a narrative using the above general framework. A story shown in Fig. 1 was used as the input narrative for all the methods.

父が家屋で狼に困る。 [A father is embarrassed a wolf in his house.] 息子のアランが家屋で父を励ます。 [His son, Alain encourages his father in his house.] 父が「アランが外出する」ことを禁止する。 [The father forbids Alain from going out.] アランが家屋で泥を洗う。 [Alain washes off mud in his house.] アランが牧場で衣服を乾かす。 [Alain dries clothes in a stock farm.] 狼が牧場で羊を襲う。 [The wolf attacks sheep in a stock farm.] アランが狼を待ち構える。 [Alain waits for the wolf.] アランが狼を襲う。 [Alain attacks the wolf.] アランが狼を殴る。 [Alain hits the wolf.] 狼が逃げる。 [The wolf escapes.] アランが狼を逃がす。 [Alain misses the wolf.] 父がアランを称える。 [The father praises Alain.]

Fig. 1. An input narrative.

3.1. A haiku-like sentence that summarizes a character's action

This method is expected to generate a *haiku*-like sentence that expresses an overview or summary of a character's action in the narrative. It selects two sentences in the narrative that includes a character as a designated agent to generate a *haiku*-like sentence using the elements in the selected sentences. The process is explained as follows.

- (i) **Selecting a format of *haiku*-like sentence:** In this example, the system selects a format, “S V1+O1 V2.” In this format, S means a designated character (or agent) in the narrative. V1 corresponds to a verb in the selected first sentence and O1 is the object of V1. V2 corresponds to a verb in the second sentence that was selected.
- (ii) **Extracting two sentences that have a designated character in the narrative:** For example, according to a character, “wolf,” “The wolf attacks sheep in a stock farm.” and “The wolf escapes.” are extracted.
- (iii) **Extracting the agent, verb, and object cases from the sentences selected in (ii) and substituting them with each element in the format type selected in (i):** A character or agent “the wolf,” which is included in the sentences selected in (ii), is substituted with S in the format selected in (i). Then, a verb, “attacks,” which was extracted from the first sentence selected in (ii), is substituted with V1. Furthermore, “sheep” is substituted with O1 and “escapes” is substituted with V2. At last, “狼 (the

wolf), 襲う (attacks), 羊を (sheep), 逃げる (escapes)” are acquired.

- (iv) **Adjusting syllable number in each part according to a haiku format:** For “狼 (Ookami)” that has four syllables, a one-syllable *kireji*, “や (ya),” is added. Similarly, “襲う羊 (Osou hitsuji)” that has six syllables is extended with a one-syllable *kireji*, “や (ya).” Further, as “逃げる (Nigeru)” has three syllables, a two-syllable *kireji*, “かな (kana),” is added. Finally, the following *haiku*-like sentence is created.

Ookami ya / Osou Hitsuji ya / Nigeru kana

狼や 襲う羊や 逃げるかな

[The Wolf / Attacks Sheep / (Who) Escapes.]

3.2. A haiku-like sentence that expresses a scene in which a character appears

In the next method, the authors expect to generate a *haiku*-like sentence that describes a scene in a narrative. This method extracts a sentence that has the character as a designated agent. Further, it selects the sentence before or after and generates a *haiku*-like sentence using the elements of the selected sentences. The detailed algorithm is described here.

- (i) **Selecting a format of haiku-like sentence:** In this example, the system selects a format, “S1 S2+V1 V2.” S1 is a designated character (or agent) in the narrative. S2 is a character who appears in a sentence before or after the sentence containing S1, and V1 is a verb showing the action of S2. V2 is a verb that shows S1’s action.
- (ii) **Extracting a sentence that has a designated character in the narrative and selecting a sentence that is located before or after of the selected sentence:** When “the wolf” is selected as a character or agent and a sentence, “the wolf escapes.” is extracted, the system extracts sentences, “Alain hits the wolf.” and “Alain misses the wolf.” In this example, the former is selected.
- (iii) **Extracting the agent, verb, and object cases from the sentences selected in (ii) and substituting them with each element in the format type selected in (i):** A character or agent, “the wolf,” which is included in the sentences selected in (ii), is substituted with S1 in the format selected in (i). Then, the character or agent, “Alain,” which is extracted from the second sentence selected in (ii), is substituted with S2. Moreover, “hits” is substituted

with V1 and “escapes” is substituted with V2. Thus, “狼 (the wolf), アラン (Alain), 殴る (hits), 逃げる (escape)” are acquired.

- (iv) **Adjusting syllable number in each part according to a haiku format:** As “狼 (Ookami)” has four syllables, it is extended using a one-syllable *kireji*, “や (ya).” Similarly, the one-syllable *kireji*, “や (ya)” is added to “アラン殴る (Alain Naguru)” that has six syllables. For “逃げる (Nigeru)” that has three syllables, a two-syllable *kireji*, “かな (kana),” is added. Finally, the following *haiku*-like sentence is created.

Ookami ya / Alain Naguru ya / Nigeru kana

狼や アラン殴るや 逃げるかな

[The Wolf / (Who is) Hit by Alain / Escapes.]

3.3. A haiku-like sentence that focuses on a location

This method enables to generate a *haiku*-like sentence that focuses on a location in a narrative according to the following process.

- (i) **Selecting a format of haiku-like sentence:** The system selects a format, “S1+V1 S2+V2 L.” S1 corresponds to a character (or agent) in the first sentence selected and V1 is a verb that shows S1’s action. S2 is a character in the second sentence and V2 is a verb that shows the action by S2. L is a word representing a location or place.
- (ii) **Extracting sentences that have a word representing a location or place and selecting two sentences from them:** When “his house” is defined, the system extracts the sentences containing “his house.” The sentences “A father is embarrassed a wolf in his house.,” “His son, Alain encourages his father in his house.,” and “Alain washes off mud in his house.” are extracted. In this example, “A father is embarrassed a wolf in his house.” and “Alain washes off mud in his house.” are selected.
- (iii) **Extracting the agent, verb, and object cases and a word representing a designated location from the sentences selected in (ii) and substituting them with each element of the format type selected in (i):** An agent, “A father,” which is included in the sentences selected in (ii), is substituted with S1 in the format selected in (i). Then, a verb unit, “is embarrassed,” which is extracted from the first sentence selected in (ii), is substituted with V1. Furthermore, “Alain” is substituted with S2 and

“washes off” is substituted with V2. “his house” is substituted with L. As a result, “父 (A father), 困る (is embarrassed), アラン (Alain), 洗う (washes off), 家屋 (his house)” are acquired.

- (iv) **Adjusting syllable number in each part according to a haiku format:** For “アラン洗う (Alain Arau)” that has six syllables, an one-syllable *kireji*, “や (ya)” is added. Moreover, “家屋 (Kaoku)” is extended by a two-syllable *kireji*, “かな (kana).” Finally, the following *haiku*-like sentence is created.

Chichi Komaru / Alain Arau ya / Kaoku kana
 父 困る アラン 洗う や 家屋 かな
 [A Father is Embarrassed / Alain Washes / at His House.]

4. Future Works

A short-term plan is to evaluate the generated *haiku*-like sentences or the processes according to specific goals. These goals are related to “what in a narrative must be represented through a *haiku* or *haiku*-like sentence?”

One of the macro goals is, as described in the first section in this paper, to design and implement a mutual transformation mechanism between narrative and *haiku*. Fig. 2 shows the overview. This mechanism also enables us to use one or more *haiku* or *haiku*-like sentences as the input information to the INGS system. Furthermore, in the relationships with advertising application systems that the authors have been developing⁸, such a circulative mechanism could contribute to the implementation of a new advertising method in which both long narrative explanations and short *haiku*-like representations can mutually be generated for a product or brand.

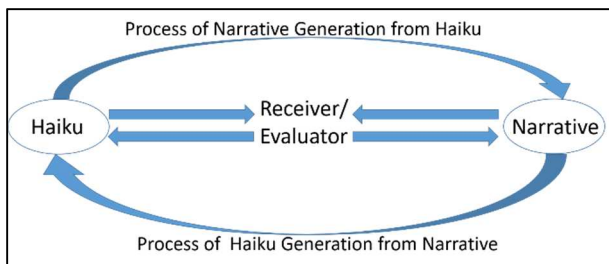


Fig. 2. An entire image of mutual transformation between narrative and *haiku*.

5. Conclusion

The authors presented a framework to generate a *haiku*-like sentence in which one or more designated elements

are extracted from a narrative used as the input and these elements are arranged and modified according to the *haiku* form. Three types of methods were shown according to the framework in this paper. Future work will include various topics, including evaluating the generated *haiku*-like sentences, completing the development of a mutual transformation mechanism between narrative and *haiku*, and applying the results to various applications such as advertising narrative generation.

References

1. T. Ito, T. Arai, and T. Ogata, Narrative Generation from Semantic Networks of *Haiku*, in *Proc. of the 31st Annual Conference of the Japanese Society for Artificial Intelligence*, (Nagoya, Japan, 2017), 1D3-OS-29b-1in2.
2. Y. Nitta, Interpretation and Generation of *Haiku* by Regular Expression, *IEICE Technical Report*, **115**(69) (2015) 31-36.
3. T. Ito, and T. Ogata, On *Haiku*/Narrative Generation, in *Proc. of the 56th Special Interest Group on Language Sense Processing Engineering*, (Morioka, Japan, 2017), pp. 35-37.
4. T. Ogata, Computational and Cognitive Approaches to Narratology from the Perspective of Narrative Generation, in T. Ogata and T. Akimoto (eds.), *Computational and Cognitive Approaches to Narratology* (IGI Global, PA, USA, 2016), pp. 1-74.
5. T. Ito, T. Ogata, Analysis of Transition of Part of Speech in Haikus: Toward Using in Haiku Generation, in *proc. of the 34th Annual Meeting of the Japanese Cognitive Science Society*, (Kanazawa, Japan, 2017), P2-48.
6. T. Ito, T. Ogata, Haiku Generation Using Appearance Frequency and Co-occurrence of Concepts and Words, in *Proc. of the 11th International Conference on Cognitive Science*, (Taipei, Taiwan, 2017), Presentation Number: 121.03.
7. K. Igarashi, T. Ito, and T. Ogata, Haiku Generation Using Deep Learning Based on Words and Characters, in *Proc. of the 56th Special Interest Group on Language Sense Processing Engineering*, (Morioka, Japan, 2017), pp. 33-34.
8. Y. Zhang, J. Ono, and T. Ogata, Single Event and Scenario Generation Based on Advertising Rhetorical Techniques Using the Conceptual Dictionary in Narrative Generation System, in *Proc. of the 4th IEEE International Conference on Digital Game and Intelligent Toy Enhanced Learning*, (Takamatsu, Japan, 2012), pp. 162-164.

Cognitive Content Generation for Healthy Ageing

Yuki Hayashi

*Graduate School of Science and Engineering, Chiba University, 1-33 Yayoi-cho, Inage-ku, Chiba-shi
Chiba, 261-0004, Japan**
E-mail: yu@chiba-u.jp

Akinori Abe

*Faculty of Letters, Chiba University, 1-33 Yayoi-cho, Inage-ku, Chiba-shi
Chiba, 261-0004, Japan / DWANGO Artificial Intelligence Laboratory, Tokyo, Japan †*
E-mail: ave@ultimaVI.arc.net.my

Abstract

From the viewpoint of preventing dementia, balanced meal, moderate exercise, intellectual activities and social interaction are important. We considered shopping activities were proper to encourage those factors because the activities were intellectual in human daily activities. In this paper, we are going to construct Shopping Game and discuss how to evaluate the activities in the game from the viewpoint of preventing dementia. In addition, we will discuss content generation in Shopping Game.

Keywords: Prevention of dementia, Shopping activities, Shopping Game, Content generation.

1. Introduction

Dementia is a general term for a decline in mental ability enough to interfere with daily life. Alzheimer's is the most common type of dementia. Otake pointed out balanced meal, moderate exercise, intellectual activities and social interaction were important from the viewpoint of preventing dementia¹.

We considered shopping activities were proper to encourage those factors because the activities were intellectual in human daily activities. Shopping activities are one of the daily activities and people should do that usually by themselves. Some people visit a real grocery store and the others use online store or delivery service (e.g. COOP). In addition, convenient stores are visited not only by the young and also by the elderly in Japan, so

shopping activities are one of the essential daily activities for many people. Therefore, in the situation of shopping activities, we thought we could activate intellectual activities to prevent dementia. In addition, we have to take psychological stress into consideration. One of the solutions is gamification. Gamification is a method which applies some ingredients or ideas in the field of game to the other field⁴. For example, gamification is used for rehabilitation or learning support.

In this paper, we construct Shopping Game and discuss how to evaluate the activities in the game from the viewpoint of preventing dementia. In addition, we will discuss content generation in Shopping Game.

2. Method - Shopping Game

In many researches about consumer behavior³, they usually observe consumers in a real grocery shop. However, this way of observation may be difficult for observers and for participants. Abe said that “The way of observation in my research requires lots of time and labor, so it is difficult to collect lots of shopping activities data.³”. Accordingly, we developed Shopping Game.

In this game, user can move a character and walk around virtual store (Fig. 1). Upper part means a basket which the character has and lower part means a floor in the virtual store. If user wants a particular item, he/she can drag the picture of item from floor to basket. On the other hand, if user stops purchasing an item, he/she can drag the picture of item from basket to floor. There are many areas in the store, for example, vegetables, bakery or snacks. When a character approaches a certain area, user can see information on each item, which information fundamentally consists of name, amount and price.



Fig. 1. The structure of Shopping Game

Participants were 34 people, and 12 of them were house-workers, 11 were boarders and 11 were home-students. They can play the game depending on their purposes. They often told us some comments. So we recorded their activities and utterances.

3. Results

As shown in Fig. 2, participant (A) has a stickle preference to a specific item (milk-X). You can see that the specific item activated utterances. In addition, a

choice of milk was caused by a choice of meat. This participant showed her ability of budget management

[In front of beverage area] I see ... oh, I want milk-X. milk ... My family like milk-X. We will not purchase the others. I know milk-X is more expensive than the others, but milk-Y is not better than milk-X ... meat ... [She gave up to purchase beef at meat area previously] I chose pork and saved my money. So I can spend my money on milk!

Fig. 2. The utterances of participant (A)

Participant (B) was house-worker and (C) was her daughter (Fig. 3). They discuss which vegetables are good for *yakisoba*. In this case, they could not find a noodle for *yakisoba* in the end, so they planned to purchase a noodle at the other shop.

B: What's best for our lunch? ... ok, let's cook *yakisoba*. First, I need green peppers ...
 C: Why?? [She dislikes green pepper]
 B: I also need a cabbage.
 C: How about carrots?
 B: Carrots remain in a refrigerator.
 B: oh ... where is noodle [for *yakisoba*]?? This shop doesn't have one??
 B: Now, let's drop in at Shop-P in our way to home. [She said to her daughter] Just remember it!
 C: Shop-P?
 B: Yes, I don't want to change my plan [to cook *yakisoba*]. If I do so, I should return all these vegetables to vegetable area. It's troublesome!!

Fig. 3. The utterances of Participant (B) and (C)

When our participants play the game, they showed some types of utterances / conversation. We summarized intellectual activities of our participants into Table. 1. This game will be used as the following purposes. To prevent dementia, cognitive functions would be trained. In the future, evaluation of cognitive functions would be also added. The game would be useful to activate a communication. Otake said “The shortage of social communication is one of the main factor of dementia²”. So we plan to make a situation where some users can simultaneously play the game to communicate with each other.

Table. 1. A list of units observed in shopping activities.

Class	Symbol	Activity
<i>Notice</i>	n_1	To simply notice an item
	n_2	To discovery an item which a shopper wanted
	n_c	To notice a item which a shopper has already noticed
<i>Result</i>	r_{+1}	To put an item into a shopping cart
	r_0	Not to put an item into a shopping cart
	r_{-1}	To move an item from a shopping cart to a selling zone
<i>Search</i>	s_1	To search some items in a store
	s_2	To search some items in a selling zone
	s_3	To notice or discover a selling zone
	s_4	To arrive at a selling zone
	s_5	To move toward a checkout counter
<i>Knowledge</i>	k_1	Price or market price of an item
	k_2	Producing area of an item
	k_3	The best season for an item
	k_4	Freshness of an item
	k_5	Use of an item
	k_6	Characteristics of an item
	k_7	Family's preferences
	k_8	Arrangement in a store
	k_9	Stock in a store
	k_{10}	Evaluation on a store
<i>Planning</i>	p_1	To check a shopping cart
	p_2	To check route during shopping activities
	p_3	To check a shopper's plan
	p_4	To consider a shopper's plan
	p_5	To adjust balance of items
	p_6	To manage a shopper's budget
	p_7	To recall stock in a shopper's house
	p_8	To predict stock in a shopper's house
<i>Idea</i>	i_1	To compare items
	i_2	To combine items
	i_3	To use an item as other purpose
	i_4	To substitute an item for other item

4. Discussion - Shopping Game with content generation

In the future, Shopping Game has to change its contents automatically depending on its user. Some functions will be added to the Shopping Game. From the viewpoint of cognitive training, out of stock and change of price are needed. In addition, it is good for user to be sometimes shown some special items with discount or with best season. Furthermore, other shoppers would influence on user so some virtual shoppers which move automatically are needed in the virtual store.

Recently, healthy ageing has been an important concept to decrease risk of disease, care independence or any other troubles. For example, WHO has recommended healthy lifestyle to younger and middle-aged people. In addition, a concept "ME-BYO" which was originally

generated in oriental medicine has been accepted around the world. This concept means inarticulate zone between health and disease and encourages healthy life style. So preventing dementia is the problem not only for the elderly but also for the young or middle-aged people. We have to enhance our game taking diversity of users into account.

5. Conclusions

In this paper, we proposed Shopping Game for healthy ageing. It played a role of cognitive training for users and it activated their utterances / conversations. In the future, we consider it will be also used for evaluation of cognitive functions so we have to make a criteria for users' performance.

References

1. M. Otake, Coimagination method for nursing care, *Chuohoki Publishing CO.,Ltd.*, (2011).
2. M. Otake, Conversation Support Robot for Promoting Cognitive Activity of Older Adults, *Journal of the Japanese Society for Artificial Intelligence*. **29**(6) (2014) 591-598.
3. S. Abe, Shopping Activities and Information Processing-a trial of protocol analysis-, *Yokohama management study*. **4**(2) (1984) 33-48.
4. S. Deterding, M. Sicart, L. Nacke, K. Ohara, D. Dixon, Gamification. using game-design elements in non-gaming contexts. *CHI'11 Extended Abstracts on Human Factors in Computing Systems*. (2011) 2425-2428.

The Influence of Story Writing Worksheets on Art Appreciation

Kotone Tadaki

*Graduate School of Humanities and Public Affairs, Chiba University
1-33 Yayoi-cho, Inage-ku, Chiba 263-8522, Japan*

Akinori Abe

*Graduate School of Humanities and Public Affairs, Chiba University
1-33 Yayoi-cho, Inage-ku, Chiba 263-8522, Japan
E-mail: kotonetadaki@yahoo.co.jp*

Abstract

In Japan, many art museums prepare various types of worksheets for visitors. Usually, these worksheets include some kinds of guides to make visitors to understand and appreciate the artwork more. One typical approach is encouraging to create a story about the artwork. In this paper, we conducted the experiment by using the worksheet to determine the influence of this kind of worksheets while appreciating abstract paintings.

Keywords: art appreciation, story, worksheet, education

1. Introduction

1.1. Background

For museum educator and teachers, the very simple question “How do we appreciate the artworks?” has been a major challenge for years. J.A. Schmidt et al (1989) described novice strategies for understanding paintings by using verbal protocol. Novice can be defined as people who have never thought about visual analysis for art. This research was aiming to build a computer-based education program for the student. J.A. Schmidt et al (1989) suggested that it is possible that art instructor or educator’s teaching strategies did not fit novice strategies. Novice frequently uses the semantic features or contents (e.g. theme and symbolism) than formal elements (e.g. lines, shapes and colour) which instructor usually uses when teaching them to understand the artwork. However, when novice watching the abstract paintings, the strategy changes. Novice frequently uses the formal element than semantic features.

T. Okada and J. Inoue (1991) suggested the difference between two novice strategies is caused by a lack of specific forms in abstract paintings. From this point of view, they conducted the experiment using a survey to determine whether differences in evaluation and impression exist between abstract paintings and representational paintings. The research question was “will people use different strategies to evaluate the painting for each abstract painting and representational painting?”. From their result, they conclude that the artistic evaluation for abstract paintings is highly affected by the tenderness and the taste and the artistic evaluation for representational paintings is highly affected by the strangeness and the impact.

These two papers can be one possible answer for D. O’hare (1976) which showed un-trained subject (novice) prefer representational paintings than abstract paintings. K. Ishibashi and T. Okada (2010) tried to overcome this situation by making novices copying and creating the artwork. K. Ishibashi and T. Okada (2010) pointed out that representational paintings are easy to understand for a novice because when they appreciate representational

paintings they have more background knowledge available to use. These background knowledges were made up in education usually in school. K. Ishibashi and T. Okada (2010) call this phenomenon the reality constraint (写実的制約: translated by Y. Tanaka and S. Matsumoto (2013)). According to K. Ishibashi and T. Okada (2010)'s experiment, copying can relax the reality constraint because by copying the painting, novice gets the artist's point of view.

Y. Tanaka and S. Matsumoto (2013) also suggested the possible solution to relax the reality constraint. Y. Tanaka and S. Matsumoto (2013) used a commentary to relax the constraint instead of making novices to copy the painting. The word "commentary" in this research means a short text to explain the artwork which is usually displayed with artworks in museums. They made two types of commentaries which were object commentary and formal commentary. The object commentary provides information about the object drawn on the specific painting. The formal commentary provided information about style, colour, technique and various technical aspects of the artwork. When they compare the survey (free description) between two conditions, reading the commentary with technical information (formal commentary condition) relaxed the reality constraint. When reading a formal commentary, novice tried to think deeply beyond what was drawn on the painting. Also, the description of the painting was more diverse in formal commentary condition.

Two possible solutions to relax the reality constraint was suggested. K. Ishibashi and T. Okada (2010)'s idea can be used for developing an effective educational program on museums. Y. Tanaka and S. Matsumoto (2013)'s idea may possibly develop the quality of commentary.

1.2. Research Aim

We will conduct the experiment to determine whether the story making experience using worksheets relax the reality constraint or not.

As T. Okada and J. Inoue (1991) suggested, abstract paintings lack the forms. Both of two experiments (K. Ishibashi and T. Okada (2010), Y. Tanaka and S. Matsumoto (2013)) tried to relax the constraint by obtaining the artist's point of view not by filling the lack of forms.

In this paper, we aimed to overcome the lack of forms in abstract paintings by creating imaginary forms. When creating a story, a writer needs the character and situation.

Therefore, if they need to write a story about the abstract painting, they possibly create characters and situation from the painting. Once they find the characters or an emotion expressed in the paintings, we can say they made an imaginary outline of the painting to form a character or emotion.

Our research questions are (1) are elements of the artwork do they used to create a story? (2) If (1) was true, will story creating worksheet helped to image a form on the painting? and (3) how story creating worksheet changes the attitude to the painting?

We should note that the experiment in this paper was conducted in Japanese. All stimuli used in the experiment was written in Japanese. Therefore, although procedures and results of this paper may improve art museums in Japan, it might not fit non-Japanese museums.

2. Worksheets

When we visit a museum and trying to understand the displayed item such as the Old Master's painting, bones of dinosaurs or ancient accessories, we first look for some information to help us. Usually, they are installing a small piece of paper called "caption" ("commentary" on Y. Tanaka and S. Matsumoto (2013)) next to the item. Visitors can use captions to obtain information by reading a few sentences written in the caption.

However, the information which can installed as captions is very limited. For example, by using captions, museum staffs can inform the exact name of the artwork but cannot inform how curators understand and appreciate the artwork.

To overcome this weakness of captions, museums providing many types of tools. One of the typical examples of the tools is the worksheet.

In this research, we focused on worksheets. Worksheets are the easiest tool to install among educational programs and captions. Since worksheets are the easiest to install, the content included on the worksheet is flexible. The equipment we need to create the worksheets is only a printer and papers. Some museum such as The Metropolitan Museum of Art¹, Guggenheim Museum² and Yokohama Museum of Art ("The Elegant Other: Cross-cultural Encounters in Fashion and Art" Exhibition)³ distributed their worksheets (called "family guide" in The Metropolitan Museum of Art, "family

¹ The Metropolitan Museum of Art. (2018, December 8). Retrieved from <https://www.metmuseum.org/learn/kids-and-families/family-guides>

² The Solomon R. Guggenheim Foundation. (2018, December 8). Retrieved from <https://www.guggenheim.org/for-families>

³ Yokohama Museum of Art. (2017, November 30). Retrieved from <http://yokohama.art.museum/education/school/worksheet.html> (in Japanese)

© The 2018 International Conference on Artificial Life and Robotics (ICAROB2018), Feb. 1-4, B-Con Plaza, Beppu, Oita, Japan

activity guide” in Guggenheim Museum) on their website. These uploaded worksheets are available for print and visitors themselves, visitors’ parent or teacher can print the worksheet before visiting the exhibition. If the museum thought their target visitors have enough ability to use online resources, the equipment they need is only a computer.

In this section, we will introduce three worksheets with story creating activity used at museums in Japan.

1.1.2. Example1: Main building Tour Guide (Tokyo National Museum)

There are two floors called the Japan gallery in Tokyo National Museum’s main building. The Japan gallery is the largest permanent collection exhibition in Tokyo National Museum showing the Japanese history from Yayoi period to Meiji period (about B.C.300-A.D.1850). We can guess that this worksheet was made for school visitors or elementally school students since there are boxes to write the school name and grade on the handout. This handout was made of two completely separable pages. Since there are two floors in Tokyo National Museum, each page represents each floor. Both of handouts include the map on the front page and worksheet on the back.



Fig. 1 Tour guide of Tokyo National Museum

The worksheet about the first floor includes Karuta (traditional playing card) style worksheet. Karuta is a traditional card game in Japan. One player will read up the rhyme written on Yomihuda (cards with short sentences) and the others will touch the corresponding Ehuda (cards with pictures which show the situation written in corresponding Yomihuda). On the worksheet, there is empty frame of Yomihuda and Ehuda and visitors

can make their own Karuta by filling their own rhyme and pictures. Creating sets of sentences and pictures are a similar process with creating a story and adding the illustration to the story. Therefore, we can regard this Karuta style worksheet as a story creating worksheet.

The second worksheet is a blank newspaper style worksheet. By using this worksheet, visitors can tell about the favourite item they found in Tokyo National Museum. When visitors filling this worksheet, they are asked to research or image about the history of a specific item. The worksheet can be separated into four small part. In each part, visitors asked to fill the blank box. The first part (Fig.1 left page’s top-right) is asking the information about Tokyo National Museum. The second part (Fig.1 left page’s top-left) is about the impression of the favourite item and history of the item. The Third part (Fig.1 left page’s middle) is to list up the three favourite things about the item. The Fourth part (Fig.1 left page’s bottom) is to sketch the item.

The first worksheet encourages to create a story about what was expressed on the item or the artwork. The second worksheet encourages to create a story about the object’s history.

1.1.3. Example2: Family Guide “Shall We Dance?” (The Metropolitan Museum of Art)

This worksheet is one of 18 worksheets uploaded on The Metropolitan Museum of Art’s website⁴. The worksheet is about three artworks related to dancing. Each page includes a detailed commentary and fun fact. One of these three artworks is a stained-glass window. For this stained-glass window, the worksheet instructed to create own story. The worksheet also suggested to eight sentences which can be used to create story such as “Once upon a time there was a young girl and boy. Their names were...and...”, “They went to a costume party to celebrate the...” or “The party was held at...”.

1.1.4. Example3: MOMAT Collection Children’s Self Guide (The National Museum of Modern Art, Tokyo)

The National Museum of Modern Art, Tokyo prepared a set of worksheets for their permanent exhibition. This set of worksheets contains six pages and each page contains activity for one painting. Therefore, by using this

⁴ The Metropolitan Museum of Art. (2018, December 8). Retrieved from <https://www.metmuseum.org/learn/kids-and-families/family-guides>
© The 2018 International Conference on Artificial Life and Robotics (ICAROB2018), Feb. 1-4, B-Con Plaza, Beppu, Oita, Japan

worksheet, visitors can think deeply about every six artworks.

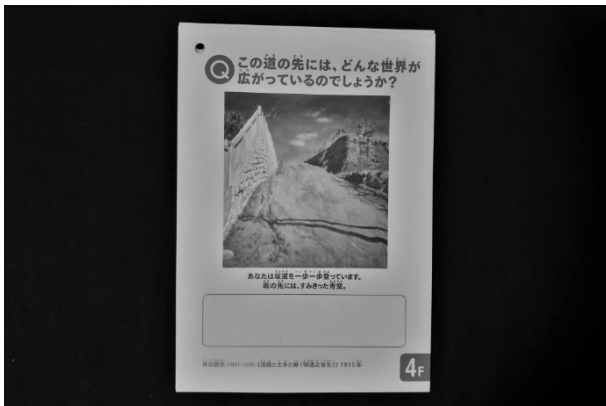


Fig. 2 MOMAT Collection Children's Self Guide

One page about Ryusei Kishida's artwork includes the question encouraging to create a story. On the painting, there is a brown coloured road crossing the square canvas bottom to up. The question on the worksheet is "If you walk up this road, what will you see?" and "You are climbing up the hill road step by step. You can see blue sky in front of you." There is a blank box to write an answer at the bottom of the page.

3. Experiment

Our research questions are listed below.

- (1) Are elements of the artwork do they used to create a story?
- (2) If (1) was true, will story creating worksheet helped to image a form on the painting?
- (3) How story creating worksheet changes the attitude to the painting?

Since this experiment will be conducted on 23rd December 2017, we could not report the result on this paper. Results will be presented at the conference.

3.1. Participants

Participants will be a group of university student including both of undergraduate and graduate. All of the participant do not have an art major which means we can regard them as novices.

3.2. Stimuli

We used 18 artworks as stimuli. six of them are representational paintings and others are abstract paintings. Every artwork will be displayed with simple caption and label. All participants will answer the worksheet and questionnaire during appreciating the artwork.

3.3. Conditions

We will have three conditions for each participant (within-subject factor). The participant will see six abstract paintings without creating a story (abstract condition), six representational paintings without creating a story (representational condition) and six abstract paintings using a worksheet to create a story (story condition). All participants will follow this order. If the story creating worksheet helped to image a form on the painting, the result of story condition will be similar to representational condition and differ from the result of abstract condition.

References

1. J. A. Schmidt, J. P. McLaughlin and P. Leighton, Novice Strategies for Understanding Paintings, *Applied Cognitive Psychology*. **3**(1) (1989) 65-72.
2. T. Okada and J. Inoue, A psychological analysis about the elements of artistic evaluation on viewing paintings, *The educational sciences Journal of the Yokohama National University*. **31** (1991) 45-66.
3. D. O'hare, Individual differences in perceived similarity and preference for visual art: A multidimensional scaling analysis, *Perception & Psychophysics*. **20**(6) (1976), 445-452
4. K. Ishibashi and T. Okada, Facilitating Creative Drawing by Copying Art Works by Others, *Cognitive studies: bulletin of the Japanese Cognitive Science Society*. **17**(1) (2010), 196-223.
5. Y. Tanaka and S. Matsumoto, *Cognitive Constraints and its Relaxation in Appreciation of Painting*, *Cognitive studies*. **20**(1) (2013), 130-151.

Rolling Bearings Fault Diagnosis Method Using EMD Decomposition and Probabilistic Neural Network

Caixia Gao*, Tong Wu, Ziyi Fu

School of Electrical Engineering and Automation, Henan Polytechnic University
Jiaozuo 454000, China

E-mail: gcx81@126.com, 249419152@qq.com, Fuzy@hpu.edu.cn
<http://www.hpu.edu.cn/www/index.html>

Abstract

Aiming at the problem that the vibration signal of the early fault is weak. A fault diagnosis method of rolling bearing combined with empirical mode decomposition (EMD), principal component analysis (PCA) and probabilistic neural network (PNN) is proposed, in which the energy, kurtosis and skewness of first few IMFs are extracted as fault feature, the dimension of feature set is reduced by PCA, the new set is put into the PNN to identify fault recognition. The simulation shows that this method has higher fault diagnosis accuracy.

Keywords: Rolling bearing, fault recognition, empirical modal decomposition, principal component analysis, probabilistic neural network.

1. Introduction

Rolling bearings are common and vulnerable parts in rotating machinery. According to statistics, 30% of the rotating machinery faults are caused by the bearing failure, so the condition of the rolling bearing is closely related to the operation of the machinery, and it is of great importance to detect and diagnose the fault of rolling bearings.¹

At present, there are many scholars studying the fault diagnosis of rolling bearings. The Ref.1 uses a method of combining EMD decomposition with singular value difference spectrum. The Ref.2 uses the fast independent component analysis to extract the fault feature, but it does not extract the fault information in depth, and the Ref. 3 uses the wavelet packet de-noising method combined with LMD to extract fault information. In Ref.4, discrete wavelet transform is

proposed to extract the feature, but the adaptability of wavelet analysis is not as strong as EMD and EEMD when dealing with non-stationary signals. It can be seen from the above bibliographies that how to better distill the fault features from non-stationary and noisy bearing signal is the key to fault diagnosis of rolling bearings.

In the operation of rotating machinery, the vibration signal usually has non-stationary and nonlinearity characteristics, so it is difficult to obtain good effect in feature extraction by using traditional Fourier transform as the theoretical basis. And the collected signal is accompanied by a certain degree of noise. Therefore, the EMD is used to deal with the vibration signal, and then the energy, kurtosis and skewness are calculated for each IMF component to form feature set. After that, use the principal component analysis to remove the redundant information effectively and reduce the dimension of the feature set on the basis of preserving

*Corresponding author: Caixia Gao (1981-), female, associate professor, master tutor, fault diagnosis research. Tel (Tel.): 0391-3987580. E-mail: gcx81@126.com.

© The 2018 International Conference on Artificial Life and Robotics (ICAROB2018), Feb. 1-4, B-Con Plaza, Beppu, Oita, Japan

the integrity of the main features of the feature set. Finally, the feature set of the reduced dimension is put into the PNN, and the state classification of the rolling bearing can be got.

2. Fault Feature Extraction Based on EMD

EMD is a self-adapting time-frequency analysis method, which is different from the wavelet analysis in that is that there is no basis function system, that is, when analyzing the series, the original sequence is divided into a limited number of intrinsic functions rather than with certain basis functions, and each component shows uniqueness and reflects the information at each unique time scale in the signal. The decomposed signal is a stationary signal. In essence, EMD is a method to turn non-stationary signals into stationary ones. The main calculation procession sees Ref.1. Use EMD to decompose the bearing signal, taking a number of high-frequency components and abandoning the last several IMF components which are generally low-frequency noise-based.¹

The method of extracting characteristic parameters of signals with multiple characteristic parameters is improved on the basis of intrinsic mode energy method. As a single energy method is the overall energy calculation for each component of IMF, it may lose some useful fault information for the extracted feature signal. Therefore, this paper adds two feature quantities, namely, the kurtosis and skewness of the signal.⁵

The kurtosis index is a dimensionless parameter which bears no relationship to the speed, size and load of the bearing and is particularly sensitive to the impulse signal, so it is quite suitable for pitting damage fault of the surface. Generally the normal bearing kurtosis index is close to 3.

The skewness index reflects the asymmetry of the vibration signal, indicating the degree of deviation of the center of the signal probability density function from the standard normal distribution and reflecting the asymmetry of the signal amplitude distribution compared with its ideal mean. Except the machinery with quick-return characteristics, if there is friction or collision in a certain direction, it will cause the asymmetry of the vibration waveform so that the degree of bias index increases.

They are calculated as follows:

$$\begin{aligned}
 \text{Energy : } E &= \sum_{i=1}^n X_i^2 & (1) \\
 \text{Kurtosis : } K &= \frac{1}{n-1} \sum_{i=1}^n (X_i - \bar{X})^4 / \sigma^4 & (2) \\
 \text{Skewness : } K &= \frac{1}{n-1} \sum_{i=1}^n (X_i - \bar{X})^3 / \sigma^3 & (3)
 \end{aligned}$$

The flow chart of multi-feature extraction is shown in Fig1.

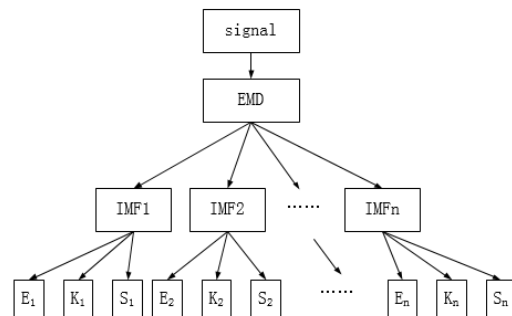


Fig.1. The flow chart 1 of multi-feature extraction.

If taking the first n IMF components after EEMD decomposition, then the number of dimension of the final extraction of the feature set is 3n.

3. Principal Component Analysis of Fault Feature

In the process of modern production industry, generally a lot of process variables will be collected to detect and control the process. Principal component analysis is a commonly used analytical method in multivariate statistical analysis, and there's a fundamental difference between this method and the mentioned Fourier system based method or other time-domain and frequency-domain analysis methods. It is characterized by the simultaneous processing of multiple dimension variables data from which finds the hidden statistical information characteristics and can eliminate the correlation between different dimensions well, so that a number of related variables can be turned into a few independent variables, that is, a new feature set of less dimensions rather than the original feature set reflects most of the information that should be originally available. And the principal component analysis can

eliminate the noise and redundancy in the fault data and improve the accuracy. The main calculation procession sees Ref. 6.

4. Probabilistic neural network

PNN was first proposed by Dr. Specht, and it can get the Bayesian optimal results when used for pattern classification. It has the following advantages: ① Easy for training with fast convergence; ② strong fault-tolerant characteristics; ③ network nodes are up to the number of training samples and the number of patterns to decide.

The structure of the PNN network is divided into four layers, namely the input layer, hidden layer, sum of layers and the output layer. The raw data is processed as a PNN diagnostic model after a series of previous processing. The main calculation procession sees Ref. 7.

5. The classification of rolling bearing fault

5.1. Description of the experiment

In order to verify the effectiveness of the diagnostic method in this paper, the data is taken from the Department of Electrical Engineering and Computer Science, Case Western Reserve University, USA.⁸

The analyzed data is obtained with the motor in 2 horsepower, and there are the inner ring fault data, outer ring fault data, rolling element failure data, and normal bearing data. The above four kinds of data form the original data of this experiment. Select 1024 data as a group from the original data and 40 groups for each state from the above four states, totally 160 groups of data, of which 10 groups randomly selected for each state as the training group and the remaining 30 groups as the test group.

5.2. Feature extraction and principal component analysis

In this experiment, EMD is used to decompose the above-mentioned vibration signals, and then each IMF component is calculated for the energy, kurtosis and skewness. Next, PCA method is used to reduce the dimension, and finally input into PNN for state classification. The classification flow chart is as follows.

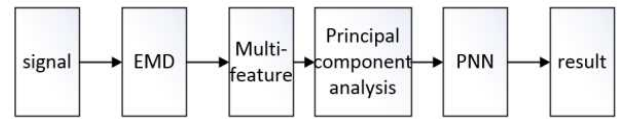


Fig.2. Troubleshooting flowchart.

After EMD decomposition of the fault data, a limited number of IMF components and the last residual amount are generated. Their frequencies are arranged from high to low, so the low-frequency components are generally discarded. The first five components are taken here.

Five IMF components are obtained after EMD for each group of data, forming five-dimensional data, and then calculate each IMF component for the energy, kurtosis, and skewness, getting 15-dimensional data to form a multi-feature data set.

Then, the principal component analysis is performed on the multi feature data sets, and the following principal component analysis table 1 is obtained

Tab.1. Part of the main component contribution table.

Main component number	Contribution rate %	Cumulative contribution rate %
1	47.5	47.5
2	24.5	72.0
3	7.6	79.6
4	4.8	84.4
5	4.5	88.9
6	3.9	92.8
7	3	95.8

In general, the cumulative contribution rate of the main component analysis up to 85% can keep most of the original signal information.⁶As can be seen from the above table, starting from the 7th main element, the cumulative contribution rate reaches 95.8%, meeting the requirement of dimensionality reduction for the original data set.

5.3. Pattern recognition based on PNN

This paper is based on the EMD intrinsic mode energy method to improve. First, the energy of the first 5 IMF is calculated and then input into PNN, and the diagnostic accuracy is 85.33%; and then adds the other two features to form a 15-dimensional feature set, enter the PNN, the diagnostic accuracy is 91%. It can be

concluded that after adding two features, PNN will increase the diagnostic accuracy.

Finally, the data analyzed by the principal component analysis are input to the PNN in turn for pattern recognition.

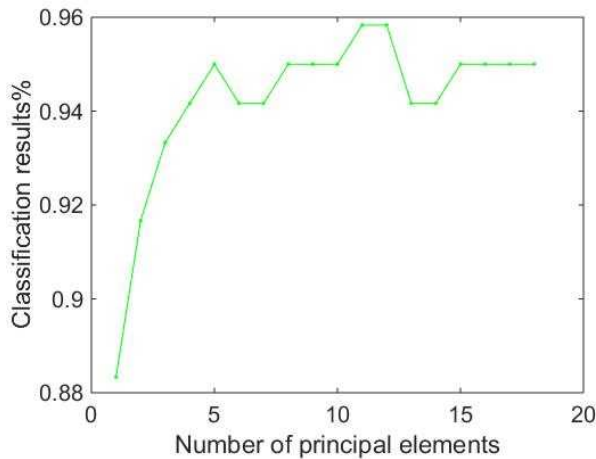


Fig.3. The number of different principal components to diagnose the correct rate.

As can be seen from the figure above, when the number of principal components reaches five, the correctness rate reaches 95%, and the cumulative contribution rate at this time is 88.9%. Then as the number of principal components increases, the cumulative contribution rate increases. The correct rate of accuracy fluctuates about 95%. Therefore, taking five main elements is the final solution, which can ensure the accuracy and efficiency. The comparison of the three methods is shown in Table 2.

Tab.2. Comparison of three methods for correct diagnosis.

Method	Energy method	Multi - feature method	Multi - feature PCA
Accuracy	85.33%	91%	95%

It can be seen that the accuracy of the energy method is low, and the accuracy is improved effectively when two features are added. It is thus obvious that the kurtosis and skewness of vibration signal can be used to make up the deficiency of energy feature in fault information completeness. Finally, on the basis of multi-feature method, the PCA is processed to further

improve the fault diagnosis accuracy, which proves that PCA can effectively remove the noise and redundancy in the vibration signal.

6. Conclusion

(i) The feature set of the principal component analysis has higher accuracy rate than that of the feature set without main component analysis, which indicates that the principal component analysis can eliminate the redundancy and noise in the information to a certain extent.

(ii) When the principal component analysis is used to reduce the dimensionality of the data, the higher the contribution rate is, the higher the accuracy is, but it remains within a certain range after reaching a certain limit.

Acknowledgements

Fund Project: National Key Research and Development Program (2016YFC0600906)

References

1. C. Zhang, J. J. Chen and Y. L. Xu, A bearing fault diagnosis method based on EMD and difference spectrum theory of singular value, *J. Vib. Eng.* **24**(5) (2011) 540-545.
2. Q. Yang, L. Wang and Y. C. Liu. FICA-IPNN ensemble fault diagnosis approach of rolling bearing, *J. Electric Machines and Contr.* **18**(3) (2014) 74-78.
3. W. Sun, B. S. Xiong and J. P. Huang. Fault diagnosis of a rolling bearing using Wavelet packet de-noising and LMD, *Vib. Shock.* **31**(18) (2012) 153-156.
4. J. Chebil, M. Rairi and N. Bushikhah. Signal analysis of vibration measurements for condition monitoring of bearings, *Australian J. Basic and Applied Sci.* **5**(1) (2011) 70-78.
5. F. J. Pei, K. L. Bi and M. R. Lv. Fault diagnosis of roller bearings based on characteristic parameters and probabilistic neural network, *China Mechanical Eng.* **25**(15) (2014) 2055-2058.
6. Q. Q. Liang, H. Han and X. Y. Cui. Fault diagnosis for refrigeration system based on PCA-PNN, *J. Chem. Ind.* **67**(3) (2016) 1023-1031.
7. L. X. Yang and Y. L. Zhu. High voltage circuit breaker fault diagnosis of probabilistic neural network, *Power Syst. Prot. Contr.* **45**(10) (2015) 63-67.
8. K. A. Loparo . *Bearings Vibration Data set*, (Case Western Reserve University, Cleveland, Ohio, USA, 2003

Detection of Dangerous Driving Behavior via Fuzzy Inference System

Shangzheng Liu*, Qinghui Zhu

*School of Electric and Electrical Engineering, Nanyang Institute of Technology, 80 Changjiang Road
Nanyang, 473004, Henan, P.R.China*

Fuzhong Wang

*School of Electrical Engineering and Automation, Henan Polytechnic University, 2001 Century Avenue
Jiaozuo, 454003, Henan, P.R.China
www.nyist.edu.cn, www.hpu.edu.cn*

Abstract

Aiming at identifying fatigue driving, a new detection scheme for the analysis of fatigue driving was proposed in this paper. On the basis of a comprehensive analysis of the factors that influenced fatigue driving, the proposed system uses driver's eye's closure time, the beat frequency of sight line, pupil diameter size as 3 indices. The proposed system is evaluated, and the results indicate that it is a feasible method for the evaluation on fatigue driving.

Keywords: fatigue driving, fuzzy inference system, fatigue detection, eye movement.

1. Introduction

Driving safety is influenced by two key factors: 1) the mental states of the driver 2) the external environment. Various psychological conditions, e.g., fatigue, distraction and motion sickness can affect driving safety.

Fatigue driving has a close relation with traffic accidents such as collision, personal injury and so on. Investigations show that up to 37% of all vehicle fatalities involve a fatigue driving or drowsy driving in the United States¹. In Europe, drowsy driving contributes to one fourth to one third of road accidents². Some researchers found that fatigue driving has been estimated to be involved in 2% to 23% of all crashes^{3,4}.

The degradation in driving performance because of fatigue accounts for a small, but significant, percent of highway accidents⁵. The growing number of accidents

caused by fatigue driving has been becoming a serious societal problem in recent years. Therefore, it is of great significance to detect fatigue driving and to develop an efficient intervention for driving mental fatigue not only to reduce the social cost of traffic safety but to improve the health of drivers and passengers.

Fatigue driving detection measures include subjective evaluation method and objective evaluation method. The objective method can be categorized into: 1) evaluation of biomedical signals, including pulse rate, EEG, changes of head position, eye-closure rate, and eyelid movement; 2) evaluation of driver-vehicle data, including steering angle, throttle/brake input, and speed. The major drawback of the techniques based on biomedical signals is that they require directly placing sensors on the subject's body.

* Corresponding author

© The 2018 International Conference on Artificial Life and Robotics (ICAROB2018), Feb. 1-4, B-Con Plaza, Beppu, Oita, Japan

2. Fatigue Driving Detection Method

2.1. Percentage of eyelid closure

The time of eye closure/opening is a good indicator of fatigue. PERCLOS (Percentage of Eyelid Closure Over the Pupil Over Time) is defined as percentage of eyes closing time over a particular time. Studies show that it is a good indicator of fatigue. Figure (1) shows the PERCLOS principle, it is calculated as following formula:

$$p = \frac{t_3 - t_2}{t_4 - t_1} \times 100\% \quad (1)$$

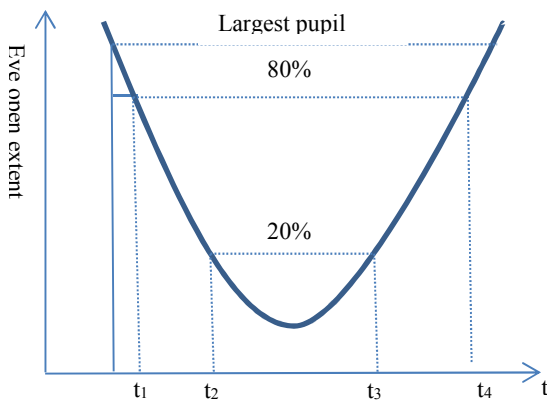


Fig.1. PERCLOS Principle

The p_s is the value of PERCLOS. T_1 is the time needed that eyes closed totally to 80%. T_2 is the time that eyes closed from 80% to 20%. T_3 is the time from 20% closed to 20% open, t_4 is the time needed from 20% open to 80%.

In specific tests there are three measurements: P70, P80 and EYEMEA(EM). P70 is the time eyelid closure over pupil more than 70%. P80 is the time eyelid closure over pupil more than 80%. EM is the mean square value of the percentage of eye closure speed. The study shows that P80 can reflect the degree of fatigue well, so that P80 can be used as a determine indicator in the evaluation of fatigue driving.

2.2. Pupil diameter

When people are in fatigue and non-fatigue state, the difference in pupil is obvious. While a person is fatigue, the pupil diameter reduces significantly, and it is

relatively steady while a person is in sober state. Therefore, through changes of pupil, the driver fatigue can be effectively identified.

2.3. Percentage of saccade

Humans don't look at a scene in fixed steadiness; instead, the eyes move around, locating interesting parts of the scene. When scanning immediate surrounding, human eyes make jerky saccadic movements and stop several times, moving quickly between each stop. Saccades to an unexpected stimulus normally take about 200 milliseconds (ms) to initiate, and then last from about 20–200(ms). When human is fatigue, the number of eye jump declines.

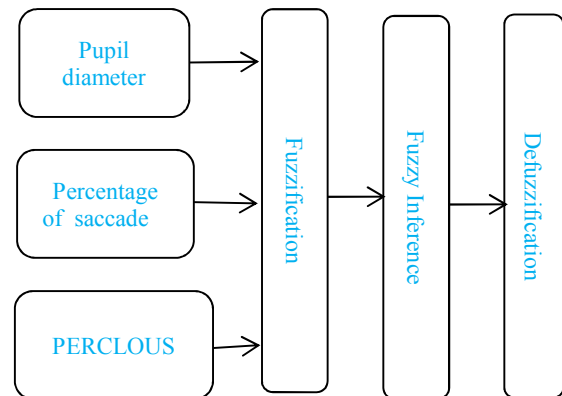


Fig.2. Fuzzy Inference Model

3. Fuzzy Fatigue Driving Detection Model

Obviously, alert state and sleep are crisp. But fatigue is vague. Therefore, fuzzy inference system is used to identify fatigue driving. The fuzzy inference model of fatigue driving detection is shown in Fig. 2. The inputs are the PERCLOS, percentage of saccade and the size of pupil diameter. The output is the membership of fatigue.

3.1. Fuzzification

The universe of PERCLOS is [0%, 100%]. For convenience, multiplying scaling factor 100, the universe is mapped to [0,100]. Pupil Diameter is changed from 10 to 50(pixels), the corresponding scaling factor is 2. Percentage of saccade varies from 0 to 0.005(1/ms), the scaling factor is 20000. The membership of PERCLOS, pupil diameter and percentage of saccade are showed in Fig.3, Fig.4 and

Fig.5 respectively. The linguistic variables for inputs output are F (Fatigue), D (Distraction) and N (Normal).

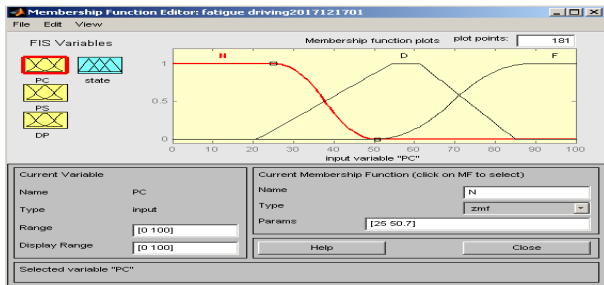


Fig.3. Membership function of PERCLOS

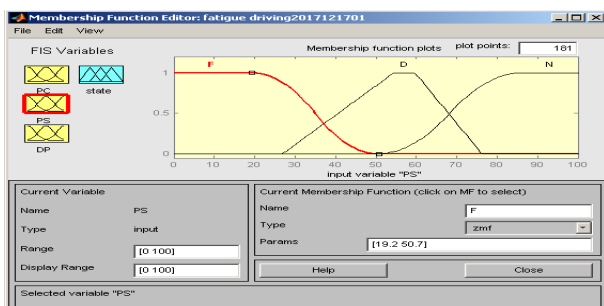


Fig.4. Membership Function of Percentage Saccades

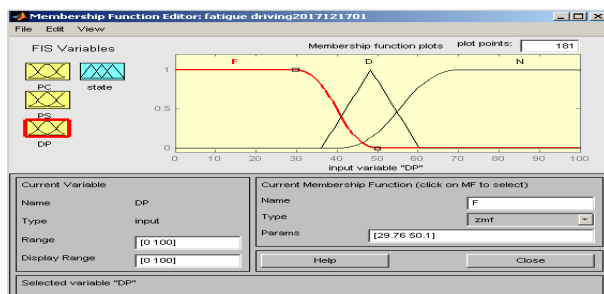


Fig.5. Membership Function of Pupil Diameter

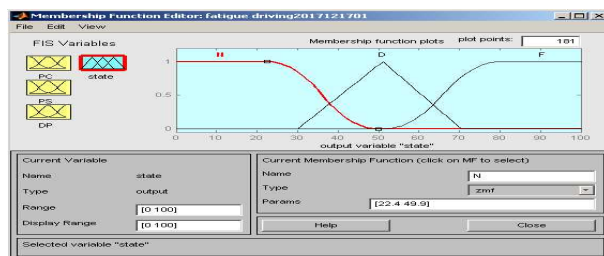


Fig.6 Membership of output

3.2. Rules

The model has 3 inputs. Therefore, we have 27 fuzzy rules. The rule is as follow:

IF PERCLOS is N, Percentage of saccade is N and pupil diameter is N, then status is N. The rules are shown in Table 1.

Table 1. Rule table for fatigue detection

PERCLOS	pupil	saccade		
		N	D	F
N	N	N	N	N
	D	N	N	D
	F	N	D	F
D	N	N	N	D
	D	N	D	D
	F	D	D	F
F	D	D	D	F
	F	F	F	F

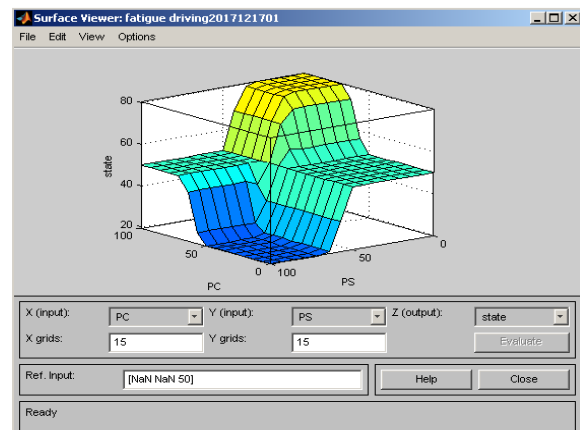


Fig.7. Surface of FIS

3.3. Defuzzification

Defuzzification operates on the implied fuzzy sets produced by the inference mechanism and combines their effects to provide the “most certain” output. We consider “center of gravity” (COG) defuzzification method for combining the recommendations represented by the implied fuzzy sets from all the rules.

4. Case Analysis

In order to verify the practicality and accuracy of the proposed model in fatigue driving, this paper takes some simulation in MATLAB. The GUI of experiment

results is shown in Fig.7. 7 samples are examined⁶. The results are shown in Table 2.

Table 2. Testing results

Data	FIS output	Evaluation of state
PERCLOS 42		
1 Percentage of saccade 38 Pupil diameter size 27	32.7	N
PERCLOS 51		
2 Percentage of saccade 36 Pupil diameter size 28	50	D
PERCLOS 63		
3 Percentage of saccade 32 Pupil diameter size 25	71.4	F
PERCLOS 72		
4 Percentage of saccade 16 Pupil diameter size 21	80.4	F
PERCLOS 63		
5 Percentage of saccade 28 Pupil diameter size 25	71.4	F
PERCLOS 85		
6 Percentage of saccade 19 Pupil diameter size 21	80.4	F
PERCLOS 38		
7 Percentage of saccade 39 Pupil diameter size 41	30	N

The results of test show that the system output agrees with the expected. Therefore, the evaluation value of the FIS can approximately be regarded as the value of fatigue driving state. The result shows that using fuzzy inference model to detect fatigue driving is feasible.

5. Conclusions

Nowadays, with the sharp increasing of vehicles, to improve overall safety is becoming more important. In this paper, we present a fuzzy inference system for estimating fatigue driving. The results show that the proposed system can accurately identify the driver's fatigue and distraction.

Acknowledgements

This paper was supported by key technology R & D program of Henan (Project No.122102210243) and Basic and frontier projects of Henan (Project No.162300410194).

References

1. H. Summala, and T. Mikkola, Fatal accidents among car and truck drivers, *Human Factors*, **36**(2) (1994) 315–326.
2. M. Dangelmaier, D. Spath, A. Bekiaris, and C. Marberger, Effective warning of a drowsy driver - the AWAKE experience, *In Proc. 10th Int. Conf. Human-Computer Interaction, Theory and Practice(Part II)*, eds. J.A. Jacko and C. Stephanidis (Grete, Greece, 2003), pp. 43-47.
3. C. Craye and A. Rashwan et al, A multi-modal driver fatigue and distraction assessment, *Int. J. ITS Res.* **14**(2) (2016) 173-194.
4. J. D. Lal, and A. Craig, A critical review of the psychophysiology of driver fatigue, *Biol. Psychol.*, **55**(3) (2001) 173-194.
5. X. Gao and Y. Zhang et al, Evaluating driving fatigue detection algorithms using eye tracking glasses, *in 7th Annu. Int. IEEE EMBS Conf. Neural Eng.* (Montpellier, France, 2015), pp.767–770.
6. Liu Qing and Li Zhi-feng, Evaluation studies on ship driving fatigue based on BP artificial neural network, *in Proc. 8th Int. Conf. Nat. Comput.* (Chongqing, China, 2012), pp.217–221.

Feature points designing and matching for the target spacecraft in the final approaching phase of rendezvous and docking

Wenjing Pei, Yingmin Jia*

*The Seventh Research Division and the Center for Information and Control
School of Automation Science and Electrical Engineering, Beihang University (BUAA), 37 Xueyuan Road, Haidian
District
Beijing, 100191, China
E-mail: wenjingpei@buaa.edu.cn; ymjia@buaa.edu.cn
www.buaa.edu.cn*

Abstract

In this paper, the images are acquired by CCD, the noise in which is removed by Gaussian Filter. Canny Edge Detection is used to extract the edges of the target spacecraft, and Progressive Probabilistic Hough Transform (PPHT) is applied to detect the lines. After that, feature points are designed on two solar panels. Thus 48 feature points can be obtained. Feature points matches by Scale-invariant feature transform (SIFT). Experimental results show that our method has better running speed and accuracy.

Keywords: Lines detection, feature points designing and matching, Space-craft rendezvous and docking, the target spacecraft, solar panels

1. Introduction

Spacecraft rendezvous and docking is a very complex and challenging proceeding. It involves the vision measurement of the chaser spacecraft to the target spacecraft. The relative velocity, location and attitude between two space-crafts must be measured accurately and rapidly, which will directly determine the success or failure of rendezvous and docking, especially in the final approaching phase.

As a result of the weak light in space, images acquired are easier to underexpose. Furthermore, spatial images often inevitably mix with different levels of noise and distortion. In this way, it is necessary to smooth the obtained images¹. The main purpose of images smoothing is to eliminate the noise and

preserving the images feature. It depends on whether or not the image features are extracted accurately.

Edges often carry a lot of important information of the images. Nowadays, many edge detection methods have been proposed²⁻³. Classical edge detection techniques include Sobel Operator⁴, Laplacian Operator, and so on⁴⁻⁵. Canny Operator was put forward in 1986 by John F. Canny⁶. Moreover, setting proper upper and lower threshold, we can extract all possible edges. Thus, the contours of the target space-craft are got.

Numerous methods for lines detection have been proposed⁷⁻⁸. Traditional lines detection methods include Hough Transform, improved Hough Transform and LSD (Line Segment Detector)⁹. However, there are little studies for vision systems of space-craft rendezvous and docking.

*Corresponding author

© The 2018 International Conference on Artificial Life and Robotics (ICAROB2018), Feb. 1-4, B-Con Plaza, Beppu, Oita, Japan

In this paper, we propose an algorithm for space images to detect the lines, design and match feature points for images. It will directly affect further extraction of motion information.

2. Methodology

There are two solar panels and the fore-end cabin in the target spacecraft model, which correspond to the lines and characteristic circle, as shown in Fig. 1.

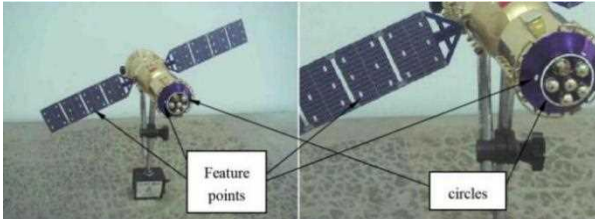


Fig.1. the surface of target spacecraft model

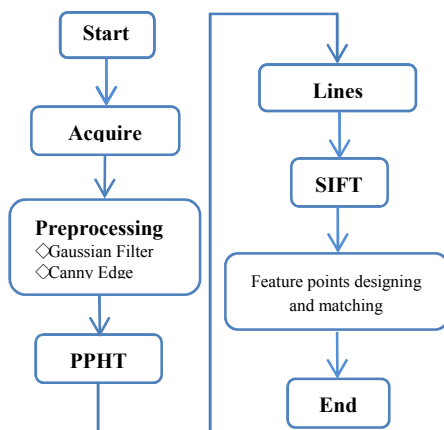


Fig.2. the overall process of feature extraction

Fig.2 shows the overall process of the proposed method for feature extraction. Using CCD imaging sensor acquired space images. After that, the detection process starts with preprocessing the images. First, the images are grayed and denoised by Gaussian Filter. Then Canny Edge Detector is applied for obtaining all possible edges of the target spacecraft. Second, PPHT is utilized to detect the lines. Select all of the correct lines and compare it with other detection method. Finally, SIFT is used to feature points designing and matching and 48 feature points are obtained. The detail process is as follows.

2.1. Image preprocessing

Images preprocessing mainly consists of two steps: images denoising by Gaussian Filter and Canny Edge Detector. It is necessary for the obtained images to reduce noise. Gaussian Filter can remove most of the noise, while Canny Edge Detector can extract the edges by setting upper threshold and lower threshold.

2.1.1. Gaussian Filter

Gaussian Filter is a low-pass filter and can attenuate high frequency signals. Furthermore, Gaussian Filter is a linear filtering method, which can smooth out the noise by a Gaussian function. It has been widely used in the field of image processing.

One-dimensional Gaussian function can be expressed as:

$$G(x, y) = \frac{1}{\sqrt{2\pi}\sigma} \exp(-x^2 / 2\sigma^2) \quad (1)$$

Similarly, two-dimensional Gaussian function can be expressed as:

$$G(x, y) = \frac{1}{\sqrt{2\pi}\sigma} \exp(-(x^2 + y^2) / 2\sigma^2) \quad (2)$$

Here, x, y are represented the distance from the origin to the horizontal and vertical axis respectively; σ^2 is the variance of the Gaussian distribution. The value of each pixel is as a weighted average in this pixel's neighborhood. It will result in some blur, so it can preserve edges and boundaries of objects better than other methods.

2.1.2. Canny Edge Detection

Canny Edge Detection can extract all possible edges by setting upper threshold ($T1$) and lower threshold ($T2$); The detail description see in ⁶.

2.2. Lines detection

PPHT is a modified method on the basis of Hough Transform (HT). It has obvious advantages, which doesn't accumulate all possible points but only a part of them are accumulated. In this way, it can reduce the computed quantity greatly and shorten calculating time. Parametric equations of lines are defined (3), where (ρ, θ) is the parameter space in the pixel space. Their relationship is as shown in Fig. 3.

$$\rho = x \cos \theta + y \sin \theta$$

(3)

Fig.3. relationship (x, y) and (ρ, θ)

The detail proceedings are as follows:

- ① Select a new point randomly as voting accumulator (ρ, θ) , then remove this pixel from the input image.
- ② If the highest peak, that is (ρ, θ) is greater than T3 (a predefined threshold), go to ③. If not, go to ①.
- ③ Find all lines and select the longest segment that can be denoted from starting point P0 to ending point P1.
- ④ All the points of the longest line are removed from the input image.
- ⑤ Remove all points of the selected lines in ③(P0-P1) from the accumulator, which means they do not need voting process.
- ⑥ If the segment is longer than a predefined minimum length, then take P0-P1 as one of the output results directly.
- ⑦ Go to ①.

2.3. Feature point designing and matching

In this paper, we design 48 feature points on two solar panels of the target spacecraft. There are 24 feature points on the left solar panel and the right solar panel respectively. They consist of three groups with 8 feature points which are almost on the same line.

Then, they are both numbered from 0 to 7 symmetrically, as shown in Fig.4.

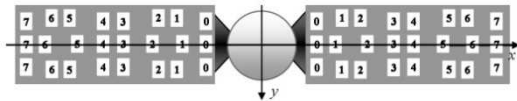


Fig.4. Feature points designing

Feature point matching means finding out the relationship between feature points adjacent images. SIFT algorithm is used to match images. Firstly, feature points on the left solar panel and the right solar panel are matched by SIFT algorithm with adjacent frame respectively. Then, the obtained images merged with the

original image. Finally, feature points are matched. The details are as follows.

The two-dimensional image is represented as $I(x, y)$ and its scale space at different scales is $L(x, y, \sigma)$, Where

$$L(x, y, \sigma) = G(x, y, \sigma) \otimes I(x, y) \quad (4)$$

Difference of Gaussian (DOG) Pyramid is used to detect the extreme, the details is as follows:

$$\begin{aligned} D(x, y, \sigma) &= (G(x, y, k\sigma) - G(x, y, \sigma)) \otimes I(x, y) \\ &= L(x, y, k\sigma) - L(x, y, \sigma) \end{aligned} \quad (5, 6)$$

$$G(x, y, \sigma) = \frac{1}{2\pi\sigma^2} e^{-(x^2+y^2)/2\sigma^2}$$

Here, $G(x, y, \sigma)$ is Gaussian convolution kernel; (x, y) is coordinates of pixels and σ^2 is the variance of Gaussian normal distribution. One point is a feature point, if it is the extreme point. The gradient magnitude and orientation are assigned as $m(x, y)$ and $\theta(x, y)$:

$$\begin{aligned} m(x, y) &= \sqrt{(L(x+1, y) - L(x-1, y))^2 + (L(x, y+1) - L(x, y-1))^2} \\ \theta(x, y) &= \arctan \frac{L(x, y+1) - L(x, y-1)}{L(x+1, y) - L(x-1, y)} \end{aligned} \quad (7, 8)$$

The same parts of the two images have the same eigenvectors, so their distance is the nearest. Let $a = (a_1, a_2, \dots, a_n), b = (b_1, b_2, \dots, b_n)$ are two eigenvectors, U_{ab} is denoted as the distance between a and b.

$$\begin{aligned} U_{MIN} / U_1 &< R, 0 < R \leq 1 \\ U_{ab} &= \left(\sum_{i=1}^n (a_i^2 + b_i^2) \right)^{1/2} \end{aligned} \quad (9, 10)$$

U_{MIN} is the nearest distance, and U_1 is the next nearest distance. R is matching threshold. If $U_{MIN} / U_1 < R$, we can think it is right matching and vice versa.

3. Experimental Results

In this experimental, we use Shenzhou-7 spacecraft model as the target spacecraft. Vision system consists of two CCD cameras and a computer, which is used as chasing spacecraft. The ratio of the target spacecraft to the original size is 1:40. Figure 5 displays two original images.

Fig.6. shows the results of Canny Edge Detection. In this processing, the original image is grayed and smoothed by Gaussian Filter first. Fig.7. shows the results of detection of lines with PPHT which represent

two solar panels. This method can improve running speed greatly. The comparison table is as follows:

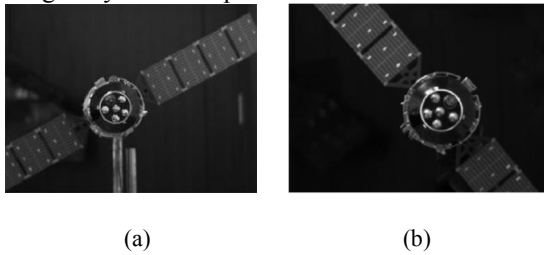


Fig.5. the original image

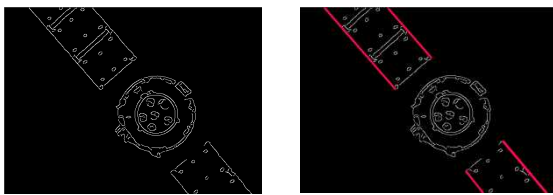


Fig.6. Canny Edge Detector Fig.7. the lines detection

Gaussian Filter just needs 67.23ms, while it takes 154.17ms with no Filter. It shows that using Gaussian Filter can improve running speed greatly. Besides, we use Visual C++ and OpenCV programming to realize the lines detection.

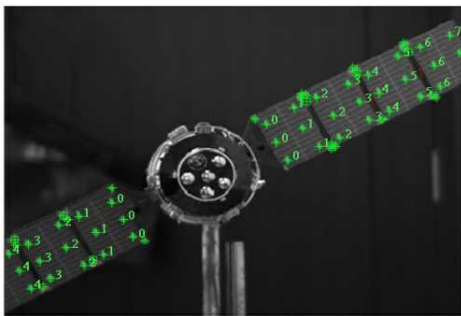


Fig.8. Feature points matching

Fig. 8 shows that SIFT algorithm is used to adjacent images. Feature points matching are implemented on the left solar panel and the right solar panel respectively. Then add them to the original image.

4. Conclusion

In the final approaching phase of spacecraft rendezvous and docking, features extraction accurately and fast directly determine whether the whole proceeding is successful or fail. In this paper, the algorithm of lines is proposed. After smoothing images by Gaussian Filter,

we utilize Canny Edge Detection to obtain the possible edges of the target spacecraft. Then PPHT is used to complete the lines detection. Finally, feature points designing and matching are implemented on the left and the right solar panel respectively. In this way, 48 feature points are obtained on two solar panels. In the future, we will continue to improve matching algorithm. Besides, we will study to feature points designing and matching on the fore-end cabin in the target spacecraft.

5. Acknowledgements

This work was supported by the NSFC (61327807, 61521091, 61520106010, 61134005), and the National Basic Research Program of China (973 Program: 2012CB821200, 2012CB821201).

6. References

1. D. T. Kuan, A. A Sawchuk, T. C. Strand, Adaptive noise smoothing filter for images with signal-dependent noise, *IEEE Trans. Pattern Anal. & Machine Intelligence*, **PAMI-7**(2) (2009) 165-177.
2. M. C. Shin, D. B. Goldgof, K. W. Bowyer and S. Nikiforou, Comparison of edge detection algorithms using a structure from motion task, *IEEE Trans. Syst. Man & Cybernetics Part B: Cybernetics*, **31**(4) (2001) 589-601.
3. D. Demigny, On optimal linear filtering for edge detection, *IEEE Trans. Image Process.*, **11**(7) (2002) 728-737.
4. W. Gao, X. Zhang and L. Yang, An improved sobel edge detection, *IEEE Int. Conf. Comput. Sci. Inf. Technol.* (Chengdu, China, 2010), pp. 67-71.
5. S. Tai and S. Yang, A fast method for image noise estimation using laplacian operator and adaptive edge detection, *IEEE Int. Symp. on Commun., Contr. Signal Process.*, (Malta, 2008), pp. 1077-1081.
6. P. Bao, L. Zhang and X. Wu, Canny edge detection enhancement by scale multiplication, *IEEE Trans. Pattern Anal. Machine Intelligence*, **27**(9) (2005) 1485-1490.
7. H. Ye, G. Shang, A new method based on hough transform for quick line and circle detection, *Int. Conf. Biomed. Eng. Informatics*, (Shenyang, China, 2015), pp. 52-56.
8. R. Grompone, J. Jakubowicz, J. Morel and Gregory Randall, LSD: a fast line segment detector with a false detection control, *IEEE Trans. Pattern Anal. Machine Intelligence*, **32**(4) (2010) 722-732.
9. K. Murakami and T. Naruse, High speed line detection by hough transform in local area, *Conf. Pattern Recognit.*, (Barcelona, Spain, 2000), pp. 467-470.

Construction and Visualization of Atmospheric Corrosion Level Map

Dongmei Fu*, Gaoyuan Wang, Tao Yang, Chao Wu, Mengchen Cui

School of Automation and Electrical Engineering, University of Science and Technology Beijing, 30 Xueyuan Road
Haidian District, Beijing, China
E-mail: fdm_ustb@ustb.edu.cn
www.ustb.edu.cn

Abstract

To solve the problem of how to construct the Chinese atmospheric corrosion level map of carbon steel based on the atmospheric environment and ISO 9223-2012 standard has a major practical value. Specific to the uneven distribution of data samples, this paper proposes an improved inverse distance weighted method based on density to realize the data interpolation. On the basis of interpolation, the paper constructs the carbon steel atmospheric corrosion level map of China.

Keywords: atmospheric corrosion; corrosion map; inverse distance weighted.

1. Introduction

Atmospheric corrosion is the interaction result of metallic materials with their surrounding atmospheric environment. There are two factors affecting atmospheric corrosion¹: one is the metal itself, the other is the atmospheric environment. When the material is determined, the atmospheric corrosion is only related to the atmospheric environment. According to ISO9223-2012 standard², these factors are the time of wetness, sulfur dioxide concentration and chloride ion concentration.

As metal materials will corrode in the atmosphere, it is of great significance to obtain the corrosion level map and the corrosion rate map, which accord with the practical geographical distribution, for materials selections and anti-corrosion³. Through the atmospheric corrosion map, the corrosive state of various regions can be easily checked and an intuitive understanding of the atmospheric corrosivity distribution is provided, making the materials development and anti-corrosion measures

practical. Fathoni U, et al.⁴ plotted the atmospheric corrosion map of Malaysia based on 10-year historical data using inverse distance weighted interpolation. Ivan Cole et al.⁵ plotted nearly 2000 data samples of the exposed materials using inverse distance weighted interpolation Vietnam atmospheric corrosion map; Chico B et al.⁶ adopted the carbon steel, zinc and other metal materials corrosion rate data and used the method of spatial interpolation to depict the atmospheric corrosion map of Spanish. Around 1990s, the Institute of metal corrosion and protection, Chinese Academy of Sciences used spatial interpolation to plot the atmospheric corrosion maps of Shenyang City⁷ and Hainan Province⁸. Tidblad J et al.⁹ established the corrosion rate prediction models of carbon steel and zinc and further plotted the atmospheric corrosion maps of the future European. Carbon steel is the most commonly used metal material for industrial and agricultural production and people's life, but so far, there's not any carbon steel atmospheric corrosion map

*Corresponding author.

© The 2018 International Conference on Artificial Life and Robotics (ICAROB2018), Feb. 1-4, B-Con Plaza, Beppu, Oita, Japan

of China being constructed based on ISO9223-2012 standard.

In order to construct the carbon steel atmospheric corrosion maps according to ISO9223-2012 standard, the problem to be firstly solved is to procure the values of time of wetness, sulfur dioxide concentration, chloride ion concentration of any sites in the map. However, the places for continuous monitoring these data are very limited; therefore, the data interpolation is necessarily needed. This paper used the inverse distance weighted method and the density-based improved inverse distance weighted method to calculate the data interpolation respectively. Upon the basis of interpolation, the carbon steel atmospheric corrosion level map of China is to be constructed.

2. Inverse Distance Weighted Method and Improvement

The inverse distance weighted interpolation states that as to getting the values of unknown points, those known points which are closest to the unknown ones contribute most while the contribution is inversely proportional to the distance¹⁰, as the following formula shows:

$$z_0 = \frac{\sum_{j=1}^n \frac{z_j}{d_j^p}}{\sum_{j=1}^n \frac{1}{d_j^p}} \quad (1)$$

where z_0 is the interpolation value of the unknown point, z_j is the value of the j^{th} known point, d_j is the distance from the unknown point to the j^{th} known point, and p is the power of that distance.

Inverse distance weighted interpolation is one of the mostly used methods with simplicity and easily understandability. However, there is one obvious problem in Eq. (1): when the data density is seriously uneven, the interpolation result will greatly weaken the global distance factor but tend to adopt the data locally with higher density. In view of this, this paper proposes the following improved algorithm:

- Local domain for any point $A(x,y)$
Set S is the local area, and N is the number of points within local domain. Define that the local domain for the point $A(x,y)$ is a circle with radius $R = \sqrt{S/N}$.

- Data density ρ
Specific to the point $A(x,y)$ with its local domain, the data density is defined to be $\rho=S/N$. Setting a threshold t , high density domain \emptyset^+ has $\rho \geq t$ while low density domain \emptyset^- has $\rho < t$.
- Interpolation for the point $A(x,y)$
As for any point $A(x,y)$ to be interpolated, when $A(x,y) \in \emptyset^-$, taking the average value of all the points in domain \emptyset^+ as one known data with location to be the central point in the domain. According to Eq.(1) to calculate the final interpolation result. When $A(x,y) \in \emptyset^+$, the result can be obtained directly by Eq.(1).

3. Atmospheric Corrosion Level Map of China Based on ISO9223-2012

The figure 1 below is the flow chart of the map construction.

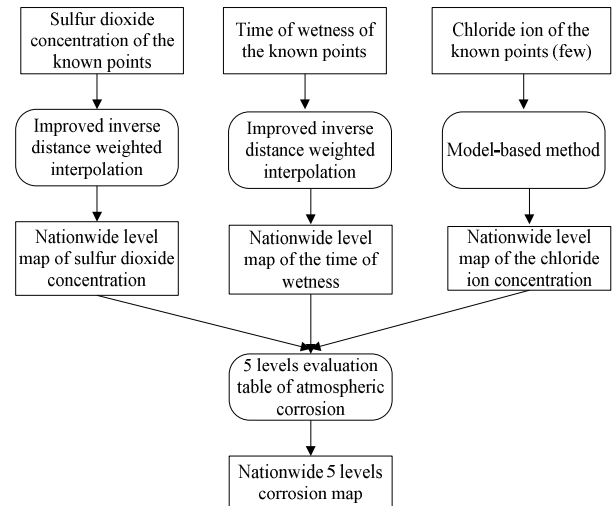
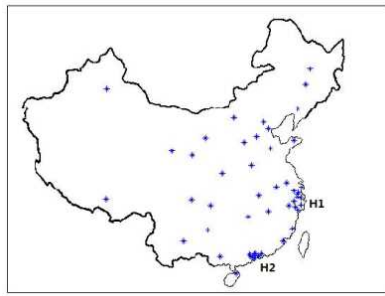
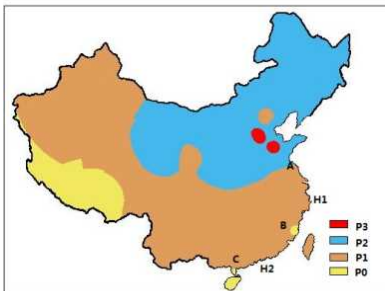


Fig. 1. Process of corrosion level map construction

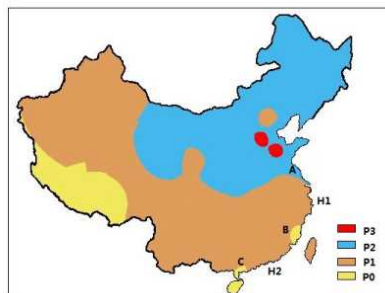
The sulfur dioxide concentration data come from China Statistical Yearbook and there are statistical data of totally 49 major cities in China. The distribution of those cities is shown in Figure 2(a). Using inverse distance weighted interpolation method results in Figure 2(b), and using density-based improved inverse distance weighted interpolation method results in Figure 2(c) (with parameter $R = 4, t = 5$, and the calculation afterwards takes the same parameters.)



(a). SO₂ sampling distribution map



(b). SO₂ level map(original)



(c). SO₂ level map(improved)

Fig. 2. SO₂ sampling and level map of China

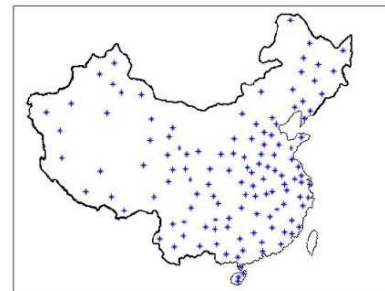
Figure 3 (a) shows the distribution of time of wetness in 135 major cities nationwide. It is obvious to see that the data points of time of wetness are densely distributed and relatively even compared with the distribution of sulfur dioxide concentration.

There is no significant difference between Fig.3(b) and Fig.3(c) because the distribution of data points for time of wetness is much more uniform.

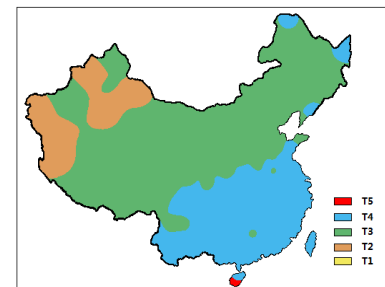
The Chloride ions in the atmosphere mainly come from the ocean. The distribution of chloride ion concentration is directly related to the distance away from the sea. Chloride ion concentration reaches the

© The 2018 International Conference on Artificial Life and Robotics (ICAROB2018), Feb. 1-4, B-Con Plaza, Beppu, Oita, Japan

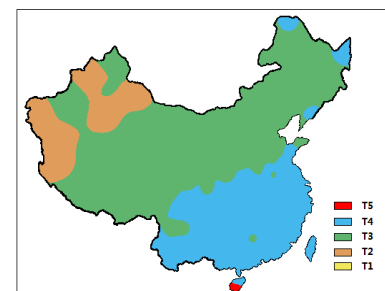
highest in the coastal areas and gradually degrades along with the distance from the coast to the interior land. Further, in a very short distance, the chloride ion concentration decreased rapidly while then the decline rate slowed. The resulting national chloride concentration level map is shown in Figure 4.



(a). Time of wetness distribution



(b). Time of wetness level map(original)



(c). level map(improved)

Fig. 3. Time of wetness sampling and level map of China

According to ISO9223-2012 standard and the flow chart of Fig.1, it is ready to get a map of atmospheric corrosion level map of carbon steel in China, as shown in Fig.5 and Fig.6.

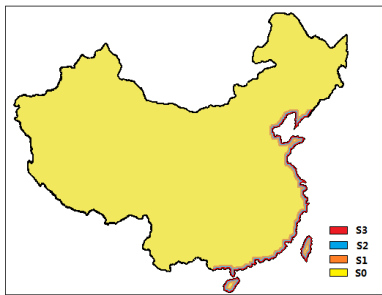


Fig. 4. Cl⁻ concentration level map

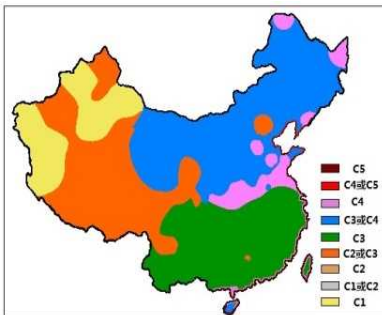


Fig. 5. Corrosion map(original)



Fig. 6. Corrosion map(improved)

4. Conclusions

In this paper, an improved inverse distance weighted interpolation method based on density is proposed. According to ISO9223-2012 standard, the paper constructed the carbon steel corrosion level map based on original inverse distance weighted interpolation method and the improved one. In view of the representation of the corrosion map, there is no major impact on most areas; however, in the local view, the

central domain of the map is kind of sparse without improvement, while the eastern and southern domains tend to severe. The reasons are that the data points in the eastern domain are relatively denser with high sampling. Though in the central and western domain, data points increased, but except for high sampling in Urumqi, Xinjiang province, the other areas still have low density.

Acknowledgements

This work was supported by National Material Environment Corrosion Field Scientific Observation and Research Platform.

References

1. M. Dai and Z. Liu, Analysis of the conjunction between environmental factors and atmospheric corrosion of carbon steel, *Corros. Prot.* **21**(4) (2015) 147–148.
2. ISO 9223-2012, *Corrosion of metals and alloys - Corrosivity of atmospheres - Classification, determination and estimation* (Avenue Marnix 17, B-1000 Brussels, 2012).
3. X. Li, D. Zhang, Z. Liu, et al, Share corrosion data, *Nature* **527**(7579) (2015) 441–442.
4. U. Fathoni, C. M. Zakaria, C. O. Rohayu, Development of corrosion risk map for Peninsular Malaysia using climatic and air pollution data, in *IOP Conf. Ser.: Earth Environ. Sci.*, (Mashhad, I. R. Iran, 2013), pp. 2088–2092.
5. C. Ivan, H. N. Viet, Steel corrosion map of Vietnam, *Tạp chí khoa học và Công Nghệ* **48**(6) (2014) 109–115.
6. B. Chico, D. L. Fuente, et al, Corrosivity maps of Spain for zinc in rural atmospheres, *Revista De Metalurgia* **46**(6) (2010) 485–492.
7. Z. Wang, H. Chen, An investigation on atmospheric corrosiveness in Hainan province, *J. Chin. Soc. Corros. Prot.* **16**(03) (1996) 225–229.
8. H. Chen, G. Yu, et al, Atmospheric corrosion map development in Shenyang, *Corros. Sci. Prot. Technol.* **4**(3) (1992) 195–201.
9. J. Tidblad, Atmospheric corrosion of metals in 2010-2039 and 2070-2099, *Atmos. Environ.* **55** (2012) 1–6.
10. F. W. Chen, C. W. Liu, Estimation of the spatial rainfall distribution using inverse distance weighting (IDW) in the middle of Taiwan, *Paddy Water Environ.* **10**(3) (2012) 209–222.

Multiple-Model Adaptive Estimation With A New Weighting Algorithm

Weicun Zhang*, Sufang Wang, Yuzhen Zhang

School of Automation and Electrical Engineering, University of Science and Technology Beijing, 30 Xueyuan Road
Haidian District, Beijing, China

E-mail: weicunzhang@ustb.edu.cn, zhangyz_ustb@163.com
www.ustb.edu.cn

Abstract

This paper presents a new scheme of weighted multiple-model adaptive estimation for a discrete-time stochastic dynamic system with large parameters uncertainty, in which the classical weighting algorithm is replaced by a new weighting algorithm to reduce the calculation burden and to relax the convergence conditions.

Keywords: multiple model adaptive estimation; weighting algorithm.

1. Introduction

There are many approaches to address the modeling uncertainty and nonlinearity problems in state estimation, filtering, and control. Among others, the multiple model adaptive estimation (MMAE) or multiple model adaptive control (MMAC) schemes have received much attention. The use of multiple models for adaptive estimation originated from Magill¹. Later on, Lainiotis², Athans et al.^{3,4}, Anderson and Moore⁵, and Li and Bar-Shalom⁶ studied MMAE/MMAC for different purposes.

In recent years from late 1990's, MMAC is a research focus in adaptive control area⁷⁻¹⁸. In parallel, there are also more and more studies conducted in MMAE¹⁹⁻²¹.

There are mainly three tasks (or steps) to complete an MMAE system in design stage, Task 1: to construct a 'local' model set to cover the parameters uncertainty or nonlinearity of the system as described in (1); Task 2: to design a 'local' Kalman filter (KF) set according to the 'local' model set, in which each 'local' KF is designed for each 'local' model; Task 3: to devise a weighting

algorithm to generate weights for each 'local' KF. After that, each 'local' KF generates its own state estimate and a corresponding output error (residual) to feed the weighting algorithm. The 'global' MMAE state estimate is then a weighted summation of each 'local' KF's estimate. Figure 1, which was borrowed from reference 20, depicts the logic structure of an MMAE system.

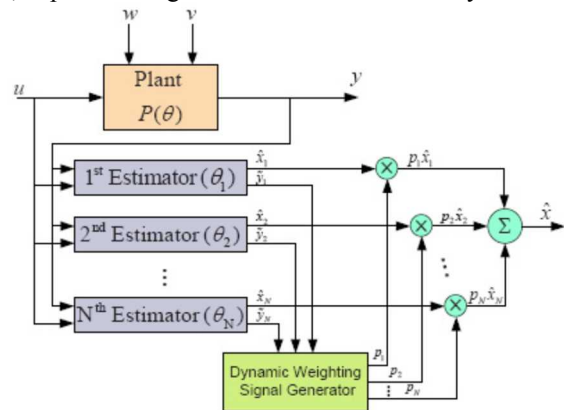


Fig. 1. The block diagram of an MMAE²⁰

In this paper, a new weighting algorithm adapted from reference 17 is adopted with two purposes, one is

*Corresponding author.

to simplify the classical weighting algorithm that depends on dynamic hypothesis test concept and Bayesian formula^{1, 9}; the other is to relax the convergence condition of the classical weighting algorithm.

The reminder of the paper is organized as follows. Section 2 give a brief description of an MMAE system; Section 3 presents the weighting algorithm; Section 4 is the main result about the convergence of the state estimation; Section 5 includes two cases of simulations; Finally, some conclusions will be drawn in Section 6.

2. The Multiple-Model Adaptive Estimator

Consider a discrete-time system described by the following state-space equation

$$\begin{aligned} x(k+1) &= A(k, \mathcal{G})x(k) + B(k, \mathcal{G})u(k) + v(k) \\ y(k) &= C(k, \mathcal{G})x(k) + \omega(k) \end{aligned} \quad (1)$$

$x(k) \in \mathbb{R}^n$ is the state of the system, $u(k) \in \mathbb{R}^m$ the control input, $y(k) \in \mathbb{R}^q$ the system output, $\omega(k) \in \mathbb{R}^r$ an measurement noise that cannot be measured with uncertain variance $R = \{R_1, \dots, R_N\}$, and $v(k) \in \mathbb{R}^p$ system noise that cannot be measured with uncertain variance $Q = \{Q_1, \dots, Q_N\}$. The matrices $A(k, \mathcal{G})$, $B(k, \mathcal{G})$, and $C(k, \mathcal{G})$ are assumed piecewise continuous, uniformly bounded in time, and contain unknown constant parameters denoted by vector $\mathcal{G} \in \mathbb{R}^l$. The initial condition $x(0)$ of (1) is assumed deterministic but unknown. Consider a finite set of candidate parameter values $\Theta := \mathcal{G}_1, \mathcal{G}_2, \dots, \mathcal{G}_N$ indexed by $i \in 1, \dots, N$.

The MMAE can be described as follows:

$$\hat{x}(k) = \sum_{i=1}^N p_i(k) \hat{x}_i(k) \quad (2)$$

where $\hat{x}(k)$ is the estimate of the state $x(k)$ at time k , and $p_i(k); i = 1, \dots, N$ are time-varying weights generated by the weighting algorithm, which will be given in the next section. In (2), each "local" state estimate $\hat{x}_i(k), i = 1, \dots, N$ is generated by a corresponding 'local' KF, which is described as follows.

$$\begin{aligned} \hat{x}_i(k | k-1) &= A_i \hat{x}(k-1) + B_i u(k-1) \\ P_i(k | k-1) &= A_i P_i(k-1) A_i^T + Q_i \\ K_i(k) &= P_i(k | k-1) C_i^T (C_i P_i(k | k-1) C_i^T + R_i)^{-1} \\ \hat{x}_i(k | k) &= \hat{x}_i(k | k-1) + K_i(k) (y(k) - C_i \hat{x}_i(k | k-1)) \\ P(k) &= (I - K_i(k) C_i) P(k | k-1) \end{aligned} \quad (3)$$

where $A_i := A(k, \mathcal{G}_i)$, $B_i := B(k, \mathcal{G}_i)$, $C_i := C(k, \mathcal{G}_i)$, $\hat{x}_i(k | k)$ is the $\hat{x}_i(k)$ in equation (2).

We expect that if the j^{th} model M_j in the model set is (or close to) the real plant model, then the corresponding j^{th} KF will generate the correct state estimation $\hat{x}_j(k)$. In addition, if the j^{th} weight $p_j(k)$ converge to 1, and others to 0. Then the state estimates of the MMAE will converge to $\hat{x}_j(k)$.

Thus the key point for an MMAE system is to construct an effective weighting algorithm as well as an appropriate model set to include the real model or the closest model to the plant. The weighting algorithm will be described in the next section.

3. Weighting Algorithm

We adopt a novel weighting algorithm which was put forward in reference 17 for MMAC systems, to replace the classical weighting algorithm based on dynamic hypothesis test and Bayesian formula^{1, 9}.

$$l_i(0) = \frac{1}{N}; p_i(0) = l_i(0) \quad (4)$$

$$l'_i(k) = 1 + \frac{1}{k} \sum_{p=1}^k \|e_i(p)\|^2 \quad (5)$$

$$l_{min}(k) = \min_i l'_i(k) \quad (6)$$

$$l_i(k) = l_i(k-1) \frac{l_{min}(k)}{l'_i(k)} \quad (7)$$

$$p_i(k) = \frac{l_i(k)}{\sum_{i=1}^N l_i(k)} \quad (8)$$

where $\|\cdot\|$ denotes the Euclidean norm.

According to reference 17, we have the following convergence result of weighting algorithm (4) - (8).

Theorem 1. *If $M_j \in \mathcal{M}$ is the model closest to the true plant in the following sense with probability one*

$$\left\{ \begin{array}{l} \sum_{r=1}^k \|e_j(r)\|^2 < \sum_{r=1}^k \|e_i(r)\|^2, \forall k \geq 1 \\ \frac{1}{k} \sum_{r=1}^k \|e_j(r)\|^2 \rightarrow S_j \\ \frac{1}{k} \sum_{r=1}^k \|e_i(r)\|^2 \rightarrow S_i \\ S_j < S_i, i \neq j \end{array} \right. \quad (9) \quad \hat{x}(k) \rightarrow \hat{x}_j(k) \quad (13)$$

where S_j is a constant, S_i may be constant or infinity. Then the weighting algorithm (4)-(8) leads to

$$p_j(k) \rightarrow 1; p_i(k) \rightarrow 0, i = 1, \dots, N, i \neq j \quad (10)$$

To adapt the above-mentioned weighting algorithm to MMAE problem, we need only to redefine the error signal as estimation error or residual of each 'local' KF, i.e.,

$$e_i(k) = y(k) - y_i(k) = y(k) - C_i \hat{x}_i(k) \quad (11)$$

It is worth pointing out that the convergence condition for the weighting algorithm (4)-(8) is fewer than that for the classical weighting algorithm. To be specific, the convergence condition (9) means the discriminability of $e_i(k)$, while the convergence conditions for classical weighting algorithm include ergodic, stationary, and discriminability of $e_i(k)$, for more details please be referred to reference 9.

4. Main Results

In this section, the convergence analysis of MMAE systems is conducted. The results are delivered in the following theorems.

If model set M includes the only real model of system (1), we have the following result.

Theorem 2. If $M_j \in M$ is the only real model of system (1) in the following sense with probability one

$$\left\{ \begin{array}{l} \sum_{r=1}^k \|e_j(r)\|^2 < \sum_{r=1}^k \|e_i(r)\|^2, \forall k \geq 1 \\ \frac{1}{k} \sum_{r=1}^k \|e_j(r)\|^2 \rightarrow S_j \\ \frac{1}{k} \sum_{r=1}^k \|e_i(r)\|^2 \rightarrow S_i \\ S_j < S_i, i \neq j \end{array} \right. \quad (12)$$

where S_j is a constant, S_i may be a constant or infinity.

Then the state estimates of MMAE will converge to the optimal estimates given by the j^{th} KF corresponding to M_j , i.e.,

Proof. According to Theorem 1, condition (12) leads to

$$p_j(k) \rightarrow 1; p_i(k) \rightarrow 0, i = 1, \dots, N, i \neq j \quad (14)$$

Then we have

$$\hat{x}(k) = \sum_{i=1}^N p_i(k) \hat{x}_i(k) \rightarrow \hat{x}_j(k) \quad (15)$$

Further, by Lemma 2 in reference 17 we know that the variance of state estimation error will converge to its minimum value, i.e.,

$$E[\hat{x}(k) - x(k)]^T [\hat{x}(k) - x(k)] \rightarrow E v^T(k) v(k) = Q \quad (16)$$

That completes the proof. \square

If the real model of system (1) is not included in model set M , but there is a closest model to system (1), we have the following result.

Theorem 3. If M_j is the model closest to the true plant in the following sense with probability one

$$\left\{ \begin{array}{l} \sum_{r=1}^k \|e_j(r)\|^2 < \sum_{r=1}^k \|e_i(r)\|^2, \forall k \geq 1 \\ \frac{1}{k} \sum_{r=1}^k \|e_j(r)\|^2 \rightarrow S_j \\ \frac{1}{k} \sum_{r=1}^k \|e_i(r)\|^2 \rightarrow S_i \\ S_j < S_i, i \neq j \end{array} \right. \quad (17)$$

where S_j is a constant, S_i may be a constant or infinity.

Then the state estimates of MMAE will converge to the estimates given by the j^{th} KF corresponding to M_j , i.e.,

$$\hat{x}(k) \rightarrow \hat{x}_j(k) \quad (18)$$

Proof. According to Theorem 1, condition (17) leads to

$$p_j(k) \rightarrow 1; p_i(k) \rightarrow 0, i = 1, \dots, N, i \neq j \quad (19)$$

Then we have

$$\hat{x}(k) = \sum_{i=1}^N p_i(k) \hat{x}_i(k) \rightarrow \hat{x}_j(k) \quad (20)$$

That completes the proof. \square

To get sharper convergence rate, we make two modifications in weighting algorithm (4) - (8), i.e., we adopt the following equations to replace equation (5), and equation (7), respectively.

$$l'_i(k) = 0.001 + \frac{1}{k} \sum_{p=1}^k \|e_i(p)\|^2 \quad (21)$$

$$l_i(k) = l_i(k-1) \left\{ \frac{l_{\min}(k)}{l_i(k)} \right\}^2 \quad (22)$$

5. Conclusions

A new MMAE scheme is proposed with an improved weighting algorithm which was borrowed from MMAC systems. Both theoretical analysis and simulation results verified the effectiveness of the proposed MMAE scheme. The future work will be focused on improving further the algorithm to get more rapid convergence rate; adapting the weighting algorithm for state estimation of time-varying and non-linear systems.

Acknowledgements

This work was supported by National Key Technologies Research and Development Program of China (No. 2013BAB02B07) and National Science Foundation of China (No. 61520106010).

References

1. D. T. Magill, Optimal adaptive estimation of sampled stochastic processes, *IEEE Trans. on Automat. Contr.* **10** (1965) 434–439.
2. D. G. Lainiotis, Partitioning: A unifying framework for adaptive systems I: Estimation II: Control, *IEEE Trans. Automat. Contr.* **64** (1976) 1182–1198.
3. M. Athans, et. al, The stochastic control of the F-8c aircraft using a multiple model adaptive control (mmac) method part I: Equilibrium flight, *IEEE Trans. Automat. Contr.* **22** (1977) 768–780.
4. M. Athans (eds.), *Investigation of The Multiple Method Adaptive Control (MMAC) Method For Flight Control Systems* (Technical Report NASA-CR-2916, NASA Technical Reports, 1979).
5. B. D. O. Anderson and J. B. Moore, *Optimal Filtering* (Prentice Hall, New Jersey, USA, 1979).
6. X. R. Li and Y. Bar-Shalom, Multiple-model estimation with variable structure, *IEEE Trans. Automat. Contr.* **41** (1996) 478–493.
7. B. D. O. Anderson, et. al, Multiple model adaptive control: Part I: Finite controller coverings, *Int. J. Robust Nonlinear Contr.* **10** (2000) 909–929.
8. M. Athans, S. Fekri and A. Pascoal, Issues on robust adaptive feedback control, in *Preprints 16th IFAC World Congress* (Plenum, Prague, Czech Republic, July 2005), pp. 9–39.
9. S. Fekri, M. Athans and A. Pascoal, Issues, progress and new results in robust adaptive control, *Int. J. Adapt. Contr. Signal Process.* **20**(10) (2006) 519–579.
10. S. Fekri, M. Athans and A. Pascoal, Robust multiple model adaptive control (RMMAC): A case study, *Int. J. Adapt. Contr. Signal Process.* **21**(1) (2007) 1–30.
11. J. Hespanha, D. Liberzon, A. S. Morse, et. al, Multiple model adaptive control: Part II: Switching, *Int. J. Robust Nonlinear Contr.* **11** (2001) 479–496.
12. A. S. Morse, Supervisory control of families of linear set-point controllers - Part I: Exact matching, *IEEE Trans. Automat. Contr.* **41** (1996) 1413–1431.
13. A. S. Morse, Supervisory control of families of linear set-point controllers - Part II: Robustness, *IEEE Trans. Automat. Contr.* **42** (1997) 1500–1515.
14. K. S. Narendra and J. Balakrishnan, Adaptive control using multiple models, *IEEE Trans. Automat. Contr.* **42** (1997) 171–187.
15. K. S. Narendra and O. A. Driollet, Stochastic adaptive control using multiple models for improved performance in the presence of random disturbances, *Int. J. Adapt. Contr. Signal Process.* **15** (2001) 287–317.
16. G. J. Schiller and P. S. Maybeck, Control of a large space structure using MMAE/MMAC techniques, *IEEE Trans. Aerosp. Electron. Syst.* **33** (1997) 1122–1131.
17. W. Zhang, Stable weighted multiple model adaptive control: discrete-time stochastic plant, *Int. J. Adapt. Contr. and Signal Process.* **27**(7) (2013) 562–581.
18. M. Huang, X. Wang and Z. Wang, Multiple model self-tuning control for a class of nonlinear systems, *Int. J. Contr.* **88**(10) (2015) 1984–1994.
19. A. P. Aguiar, M. Athans and A. Pascoal, Convergence properties of a continuous-time multiple-model adaptive estimator. In *Proc. of ECC'07-European Contr. Conf.*, eds. S. G. Tzafestas, E. E. Camacho and P. G. Groumpos (Kos, Greece, July, 2007), pp. 1530–1536.
20. A. Pedro Aguiar, V. Hassani, A. Pascoal and M. Athans, Identification and convergence analysis of a class of continuous-time multiple-model adaptive estimators, In *Preprints 16th IFAC World Congress* (Plenum, Seoul, South Korea, July 2008), pp. 8605–8610.
21. J. Bernat and S. Stepien, Multi-modelling as new estimation schema for high-gain observers, *Int. J. Control.* **88**(6) (2015) 1209–1222.

Revisit Constrained Control of Chaos

Yunzhong Song[†], Ziyi Fu, Fuzhong Wang

College of Electrical Engineering and Automation, Henan Polytechnic University, 2001 Century Avenue, Jiaozuo
454003, P.R.China

E-mail: songhpu@126.com, fuzy@hpu.edu.cn, wangfzh@hpu.edu.cn
www.hpu.edu.cn

Abstract

Only two conditions were considered in Physics Letters A296 (2002) 87, and thereafter a special problem was investigated in Physics Letters A359 (2006) 624. In this paper, a soft control scheme dominated and featured just by one single flexible factor is suggested to improve the already existing results.

Keywords: chaos control, soft control, flexible factor, Lorenz system

1. Introduction

An additive, scalar, and inequality constrained control method has been introduced to the well known chaotic system Lorenz system by Tian, Tade, and Levy¹. The resulting control law is bang-bang one and can stabilize the unstable equilibria, where two cases such that control action added at the first and second equations of the Lorenz system are reported. Some special phenomena like difficulty in stabilizing equilibria induced by control action added on the third equation of the Lorenz system, is touched upon and overcome by the combination of a logic cell and the switching control law which appeared in Song, Zhao and Qi². In this paper, we will consider to use a soft control law which is chattering free in steering the chaotic Lorenz system to its desired unstable equilibria.

The motivation to come to this paper lies in the two following reasons. The first one is from the incompleteness of the policy itself. It is well known that the strict bang-bang control action can bring the disruptive damage to the actuator, especially for its mechanical parts. To overcome that limitation, the improved version of the control policy should be introduced in. And the second one is from the system point. The newly proposed policy is made possible, and the alignment among the different suggestions should be joined in. From the original idea to the transient process proceeding strategies, and including the newly coming ones here, should be encapsulated together, so as to facilitate their future employment.

2. Control of Lorenz System with Soft Technology

This part will start with the retrospect of the optimal control of chaos system, which will be covered by

[†] Corresponding author

© The 2018 International Conference on Artificial Life and Robotics (ICAROB2018), Feb. 1-4, B-Con Plaza, Beppu, Oita, Japan

subsection 2.1, then the main results will be followed at 2.2, after that some comments will be provided to clarify the idea further in 2.3.

2.1. Problem formulation

For Lorenz system

$$\begin{aligned} \dot{x}_1 &= f_1(x_1, x_2, x_3) = -\sigma(x_1 - x_2), \\ \dot{x}_2 &= f_2(x_1, x_2, x_3) = rx_1 - x_2 - x_1x_3, \\ \dot{x}_3 &= f_3(x_1, x_2, x_3) = x_1x_2 - bx_3. \end{aligned} \tag{1}$$

Parameters like $\sigma = 10, r = 28$, and $b = 8/3$ are taken, which results in chaotic motion. And the corresponding three system equilibria are

$$\begin{aligned} x_e^{(1)} &= [0, 0, 0]^T, \\ x_e^{(2,3)} &= [\pm\sqrt{b(r-1)}, \pm\sqrt{b(r-1)}, r-1]^T = [\pm 6\sqrt{2}, \pm 6\sqrt{2}, 27]^T. \end{aligned}$$

All of them are unstable. The control purpose is to stabilize $x_e^{(2)}$ or $x_e^{(3)}$. Now we recall control on the third equation of Lorenz system. Using an additive and constrained control like references [1-3], we have $\lambda_3 = 0$ and $\dot{\lambda}_3 = 0$. Suppose $[\lambda_1, \lambda_2]^T$ has non-zero solution, the following switching surface can be gotten.

$$S(x) = f_1 \frac{\partial f_2}{\partial x_3} - f_2 \frac{\partial f_1}{\partial x_3} = \sigma x_1^2 - \sigma x_1 x_2 = 10x_1^2 - 10x_1 x_2 = 0. \tag{2}$$

It can be easily checked that both $x_e^{(2)}$ or $x_e^{(3)}$ are on this surface. So the two possible bang-bang control laws are

$$u_+ = -M \operatorname{sgn}[S(x)], u_- = M \operatorname{sgn}[S(x)] \tag{3}$$

Where $M=3$. According to the already existing conclusions derived by references [2-3], when u_+ successfully stabilizes $x_e^{(3)}$, u_- fails in stabilizing $x_e^{(2)}$. In virtue of the ergodic characteristic of the chaotic system, the control action u_- can be improved as

$$u_- = \begin{cases} -M \operatorname{sgn}[S(x)], & |x_1 - c| \leq \beta, \\ 0, & |x_1 - c| > \beta. \end{cases} \tag{4}$$

where x_1 is the first state coordinate of the chaos system, $c=8$ is around $x_{e1}^{(2)}$, $x_{e1}^{(2)}$ is the first coordinate of $x_e^{(2)}$. Constant c can also be chosen as $x_{e1}^{(2)}$ itself, $\beta = 1$. From the known results, we can find that the control action for stabilizing both $x_e^{(3)}$ and $x_e^{(2)}$ switches frequently between $+M$ and $-M$. And that will become

worsen when they approach their steady states so nearby, this phenomena is not permitted in many situations.

2.2. The main results

In order to get rid of chattering in control action, we suggest the following control action

$$u = -M[S(x)]^\alpha \tag{5}$$

where $1 > \alpha > 0$, α is named as flexible factor. Control action as Eq.(5) can be named as soft control, this will be explained later. It is more interesting that when α changes from a smaller positive value to a relatively bigger positive value, u transfers from u_+ to u_- , naturally and simultaneously (according to Ref. [1-3], control action renders $x_e^{(3)}$ stabilization is named as u_+ , and vice versa). Some typical values of α is listed as Tab.1.

Table 1. Flexible factor values and the corresponding control actions.

α	u
1/9	u_+
1/5	u_+
1/4	u_+
1/3	u_+
3/7	u_+
4/9	u_-
1/2	u_-
4/5	u_-

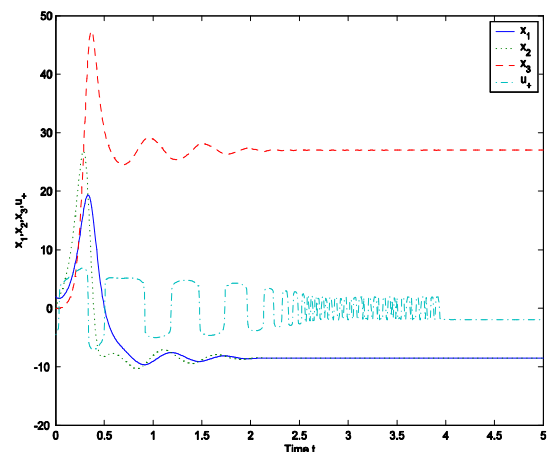


Fig.1 Control results of u_+ in (5) with $M=3, \alpha = 1/9$.

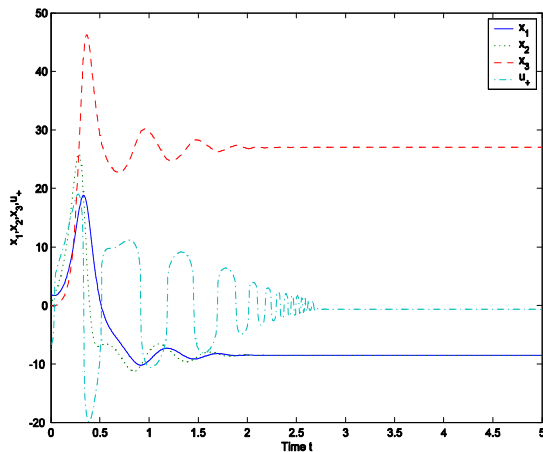


Fig.2 Control results of u_+ in (5) with $M=3$, $\alpha =1/4$.

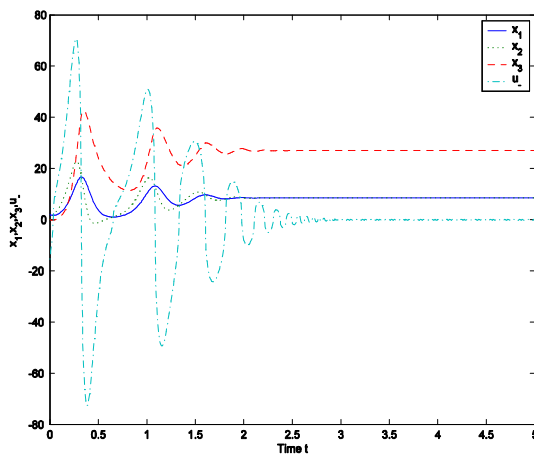


Fig.3 Control results of u_- in (5) with $M=3$, $\alpha =4/9$.

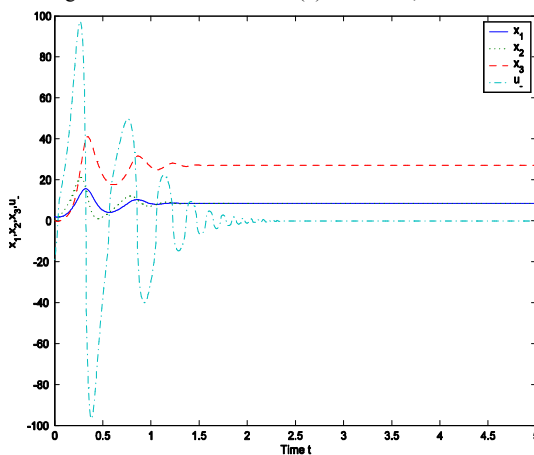


Fig.4 Control results of u_- in (5) with $M=3$, $\alpha =1/2$.

The control results about α selected as $1/9$, $1/4$ and $4/9$, $1/2$, are demonstrated as Fig.1, Fig.2, Fig.3, and Fig.4, respectively. And the listed values of α like $3/7$ and $4/5$ in Tab.1, their counterparts results are omitted here. Please notice that control actions are impelled to zero in very short time, compared to their bang-bang counterparts.

Where, among Fig.1 and Fig.2, the control actions are corresponding to u_+ , while among Fig.3 and Fig.4, the control actions are correlated with u_- (Please refer to Tab.1). Since control action ceases at last, we coin soft control to declare its peculiarity.

2.3. Some comments

To be specific, the soft control introduced with the flexible positive factor, which is constrained among 0 and 1, enables the possibility of chattering reduction and smoothly switching between the two different control directions, simultaneously. And besides that, the starting point of control is set free from the neighbouring target points, and this will reduce the burden of the unnecessary barrier, which is expressed via constraints of inequality. And even more, prospective control strategy for chaos systems can be enriched according to the unification of the ideas covered by the series papers as [1-3] and this one. The initiation began at the switching surface and the optimal control policy, and followed by full states targeting through the introduction of constrained inequality. And the stay to go trick came as the third one. To drive the idea further, in the present paper, our aim is try to move the control action from the positive ones to the negative ones seamlessly, and to facilitate the potentially application of the optimal control strategy. Of course, the mild cost must be paid to turn the flexible factor from one into another.

3. Conclusion

In conclusion, with flexible factor joined in, a soft control law, not only chattering has been shut down greatly but also the adjustment of control action becomes easily, is realized to stabilize the unstable equilibria of Lorenz system.

Chaos system is just one kind of complex systems, and it is far from the toughest one. Examples like high performance expected vehicle control, which was pioneered in Jia⁴ and the customarily designed manner

of regulation in Jia⁵, can be the solid instantiations of this. As to the massive volume and large scale complex systems, not only the plant itself, but also the surrounded hostile environment factors, will impede the successful manipulation of them. It is so hard for us to spell out some adversary factors of the harsh environments. They can be the time varying delays, incomplete noisy uncertain and unreliable information, augmented annoying disturbances, and multi-inputs multi-outputs. And these make adaptive schemes become the first candidate, please referring to Jia⁶. For the single large quantity system, which was just come into our view in recently years, philosophy of regulation has been varied sharply. The main stream has been shifted from hardware to software, and contemporarily, the new trend occurs, i.e. from both of them to the wetware, that pushes strongly in learning from the organized behavior of group habited living beings and our mankind society system. Without any doubt, this can be said as a large jump in regulation in complex systems deployment. This can be easily seen in Song, Fu and Wang⁷, Song⁸ as well as Meng and Jia⁹. So, the soft strategy demonstrated here deserves its further exploration in the near future, to the plant we face, the task we try to overcome, the unpleasant disturbance we must cope with, all of these must be set via balanced negotiation, co-operation.

Acknowledgements

This work is partially supported by NSFC Grant (61340041 and 61374079) and the Project-sponsored by SRF for ROCS, SEM to Yunzhong Song.

References

1. Y. Tian, M. Tade and D. Levy, Constrained control of chaos, *PLA*, **296** (2002) 87-90.
2. Y. Song, G. Zhao and D. Qi, Some comments on constrained control of chaos, *PLA*, **359** (2006) 624-626.
3. Y. Song, Z. Fu and F. Wang, Targeting chaos system via minimum principle Control, *JRNAL*, **3-4** (2017) 249-252
4. Y. Jia, Robust control with decoupling performance for steering and traction of 4WS vehicles under velocity-varying motion, *IEEE. T. Contr. Syst. T*, **8**(2000) 554-569.
5. Y. Jia, Alternative proofs for improved LMI representations for the analysis and the design of continuous-time systems with polytopic type uncertainty: a predictive approach, *IEEE Trans. Autom. Contr.l*, **48**(2003) 1413-1416.
6. Y. Jia, General solution to diagonal model matching control of multi-output-delay systems and its applications in adaptive scheme, *Prog Nat Sci*, **19**(2009) 79-90.
7. Y. Song, Ziyi Fu, Fuzhong Wang, Socialized multi-agent system rendezvous via networks of networks, *JRNAL*, **3** (2016) 136-139.
8. Y. Song, Consensus of agents with mixed linear discrete dynamics, *IJCAS*, **14** (2016) 1139-1143.
9. D. Meng, Yingmin Jia, Robust consensus algorithms for multiscale coordination control of multivehicle systems with disturbances, *IEEE Trans. Ind. Electron.*, **63** (2016) 1107-1119.

Research on Filtering for Random Data Packet Dropouts and Delays in Wireless Sensor Networks

Sumin Han*, Fuzhong Wang

School of Electrical Engineering and Automation, Henan Polytechnic University, Jiaozuo 454000 P.R.China

hansumin@hpu.edu.cn; wangfzh@hpu.edu.cn

www.henan polytechnic university.edu

Abstract

A wireless transmission data model is proposed to solve uncertain packet losses and delays in the wireless sensor network. It constructs a transmission output by the Bernoulli distribution sequence to express the random packet dropouts and delays. Based on the minimum variance estimation, the optimal fusion filter and covariance matrix is derived. The effectiveness of the system is verified by a simulation example. It is indicated that the higher the packet loss probability is, the lower the estimation accuracy is.

Keywords: Fusion filter, packet dropouts, delays, wireless transmission.

1. Introduction

Data losses, delays and bandwidth constraints have become a common problem in the fields of unreliable wireless communications. Especially in wireless sensor networks, since data from the measurement node to the network is confronted with the conditions such as node saturation, network congestion, stochastic delays, packet losses or random noise measurements and transmission errors, they will ultimately lead to the packet losses and delays of data transmission problem¹. Therefore, the research of distribution filter and fusion filter for this problem is widely concerned.

In recent years, lots of results are reported frequently. About data dropouts, delays and random measurement errors in the wireless sensor networks. Generally, two main aspects are concerned: one is the modeling of stochastic system; the other is the design of the filter. There are two main approaches about modeling random systems: Markov chains and Bernoulli sequences. Many papers²⁻⁵ have been

published analyzing random time delays of the wireless transmission system with the related Markov chain model. However, the approach is limited not to be applied in more fields for the system's complexity and switching difficulty. Moreover, it requires stable states and constant Kalman gain, which is very difficult to meet.

The literatures⁶⁻¹⁰ are aimed to express the system model in the relevant forms of Bernoulli random sequence, and to study the random data drop and delay problems of linear or nonlinear systems with complex derivation.

In this paper, a transmission delay model based on Bernoulli distribution sequence is proposed to consider the random two-step error that can occur in linear time-varying systems. For simplifying the complex formula derivation and calculation, it is assumed that one step variance error matrixes are orthogonal with each other. The last section demonstrates the simulation of the optimal fusion Kalman filter.

* Corresponding author

© The 2018 International Conference on Artificial Life and Robotics (ICAROB2018), Feb. 1-4, B-Con Plaza, Beppu, Oita, Japan

2. Problem Formulation

Consider the following linear time-varying stochastic sensor systems with stochastic uncertainties of white noises, the system model is:

$$\begin{cases} x(k+1) = \phi(k)x(k) + w(k) \\ y(k) = H(k)x(k) + v(k) \end{cases} \quad (1)$$

where $x(k) \in \mathfrak{R}^n$ is the state vector, and $y(k) \in \mathfrak{R}^m$ is the measured output for m sensors. $w(k)$, $v(k)$ are mutually uncorrected gauss white noises. For system (1), we make the following assumptions.

$$\begin{aligned} E[w(k)] &= 0, E[v(k)] = 0 \\ E[w(k)w^T(j)] &= R\delta_{kj}, \\ E[v(k)v^T(j)] &= Q\delta_{kj}, E[w(k)v^T(j)] = 0 \end{aligned}$$

In order to avoid network congestion, we assume that the packets from the sensor end will be sent only once in each moment. When the data is delayed, it is possible that the adjacent two measurement data arrives at the local processor at the same time. Namely, if the local processor doesn't receive a packet at k moment, the packet at $k-1$ or $k-2$ moment will be received at this moment. Certainly, it means that the packets will be delayed or delayed. The data received by the local processor is referred as transmission output through the wireless transmission, expressed by the following model:

$$\begin{aligned} z(k) &= \gamma_0(k)y(k) + (1 - \gamma_0(k))\gamma_1(k) \times \\ & y(k-1) + (1 - \gamma_0(k))(1 - \gamma_1(k))y(k-2) \end{aligned} \quad (2)$$

where $\gamma_i(k) \in \mathfrak{R}^m$ are mutually uncorrected random variables obeying Bernoulli distributions with the probabilities $Pr[\gamma_i(k) = 1] = \bar{\gamma}_i$, $Pr[\gamma_i(k) = 0] = 1 - \bar{\gamma}_i$, $0 \leq \bar{\gamma}_i \leq 1, i=0,1$. Formula (2) can be explained as follows. The measured value $y(k)$ arrives the local processor with a certain probability $\bar{\gamma}_i$. If $\gamma_0(k) = 0, \gamma_1(k)=1$, the local process receives the last one-step data $y(k-1)$. If $\gamma_0(k) = 0, \gamma_1(k)=0$, the local process receives the last two-step data $y(k-2)$. In this way, the random transmission errors can be simply revealed. For the existence of a lifetime of network nodes, the data will naturally disappear after a period of time with the energy exhausted. Hence, the transmission model in this paper mainly considers two step delays.

3. Optimal Filter

Based on the transmitted outputs $z(1), z(2) \dots z(k-1)$, our aim is to design the optimal filter based on the minimum variance estimation. The optimal state is

$$\hat{x}(k+1|k+1) = \hat{x}(k+1|k) + K(k+1)\tilde{z}(k+1) \quad (3)$$

By minimizing the covariance error matrix $P(k+1|k+1)$, the optimal filter and the Kalman gain can be derived, where

$$P(k+1|k+1) = E\{[x(k+1) - \hat{x}(k+1|k+1)] \times [x(k+1) - \hat{x}(k+1|k+1)]^T\}$$

The innovation is

$$\tilde{z}(k+1) = z(k+1) - \hat{z}(k+1|k) \quad (4)$$

where

$$\begin{aligned} \hat{z}(k+1|k) &= \gamma_0(k+1)H(k)\hat{x}(k+1|k) + \\ & (1 - \gamma_0(k+1))\gamma_1(k+1)H(k)\hat{x}(k|k-1) + \\ & (1 - \gamma_0(k+1))(1 - \gamma_1(k+1)) \times \\ & H(k)\hat{x}(k-1|k-2) \end{aligned} \quad (5)$$

According to the recursive projection theorem and the orthogonality of the innovation sequences, the basic equations of the optimal filter is derived by the minimum variance.

$$K(k+1) = pP(k+1|k)H^T(k) \times [A(k) + B(k) + C(k) + S_1 + S_2 + S_3]^{-1} \quad (6)$$

with

$$\begin{aligned} A(k) &= p^2H(k)P(k+1|k)H^T(k) \\ B(k) &= p^2(1-p)^2H(k)P(k|k-1)H^T(k) \\ C(k) &= (1-p)^4H(k) \times \\ & P(k-1|k-2)H^T(k) \\ S_1 &= p^2R \\ S_2 &= p^2(1-p)^2R \\ S_3 &= (1-p)^4R \end{aligned}$$

where $\bar{\gamma}_i = p, i = 0,1$.

Covariance matrix can be renewed :

$$\begin{aligned} P(k+1|k+1) &= \\ & [I - \gamma_0(k+1)K(k+1)H(k)]P(k+1|k) \times \\ & [I - \gamma_0(k+1)K(k+1)H(k)]^T + K(k+1) \\ & \times [B(k) + C(k) + S_1 + S_2 + S_3]K(k+1)^T \end{aligned} \quad (7)$$

Considering two-step packet losses or delays, Kalman gain and covariance matrix will be updated only by attaining the last two steps' states. So, only the initial values of three points are known, iteration will start. As (5) and (8) shows, the initial values of optimal states $\hat{x}(2|2)$, $\hat{x}(1|1)$, $\hat{x}(0|0)$ and of the covariance matrix $P(2|2)$, $P(1|1)$, $P(0|0)$ must be given.

4. Simulation Example

Consider the discrete linear system including one sensor node. The corresponding time varying discrete-time model is given as follows:

$$\begin{cases} x(k+1) = \begin{bmatrix} 0.724 & -0.7788 \\ 0.2\sin\frac{k\pi}{50} & 0 \end{bmatrix} x(k) + w(k) \\ y(k) = [1 \quad 1]x(k) + v(k) \end{cases}$$

For formula (2), $\gamma_i(k)$ is obeyed Bernoulli distribution with the probability of p .

$$Q = \begin{bmatrix} 1.044 & 0 \\ 0 & 0.9392 \end{bmatrix} \quad R=0.2847$$

$$\hat{x}(0|0) = \hat{x}(1|1) = \hat{x}(2|2) = 0,$$

$$P(0|0) = P(1|1) = P(2|2) = 0.11,$$

where I is the unit matrix

Base on the initial values, iteration will begin at the node $k=2$. The main operations of each iteration are generalized as follows:

- 1) Compute prediction state $\hat{x}(k+1|k)$;
- 2) Compute the transmission out prediction state $\hat{z}(k+1|k)$
- 3) Compute one step prediction covariance matrix $P(k+1|k)$;
- 4) Compute the filter gain $K(k+1)$ by (6);
- 5) Compute the optimal state $\hat{x}(k+1|k+1)$;
- 6) Compute covariance matrix $P(k+1|k+1)$.

When $p=0.8$, we obtain the predicted values by the model shown in Fig. 1. Fig.1 demonstrates that the values of the two states by the fusion filtering and true values. Fig.2 gives the estimation errors of the system by the optimal fusion. It is illustrated the estimation errors can be quickly stable.

As mentioned above, p is the probability of Bernoulli sequence, which indicates the data arrival probability, so it will influence the estimation accuracy of the model to a certain extent. In this paper, the accuracy of the model is analyzed as shown in Fig. 2.

The following points can be seen from Fig. 1 and Fig. 2:

- 1) When the data arrival probability p is more than 0.8, the state estimation of this filter is in line with the real value;
- 2) The model and the corresponding filter has good characteristics of dynamics and stability.
- 3) With the increase of the data arrival probability p , the estimation error has been improved

According to the above analysis, it can be seen that the data arrival probability p reflects the degree of random packet dropouts and delays. The larger p is, the less the degree of the packets and delays happens. When p is relative small, the prediction accuracy is low, which indicates the measurement error is relative large.

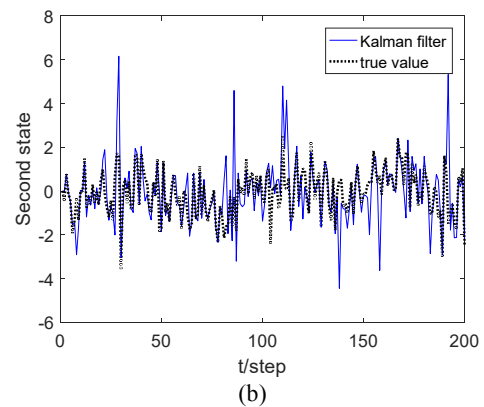
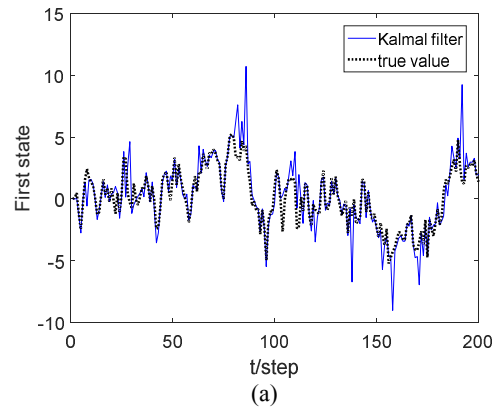


Fig.1 Fusion filter

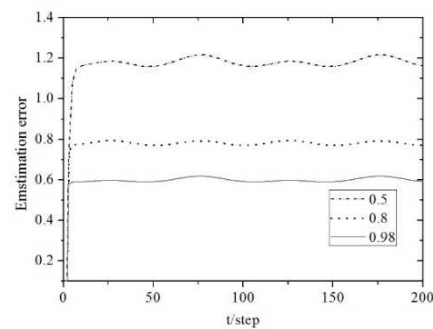


Fig.2 The covariance error of the first estimated value when data arrival probability $p=0.5,0.8,0.98$

5. Conclusion

The paper describes the transmission output model using a Bernoulli sequence with the random packet dropouts and delays in a wireless network. We derive the optimal filter and covariance error matrix based on the minimum variance criterion. From the discussion and simulation results, some conclusions can be reached.

Firstly, the model and the corresponding filter have a valuable performance for the random packet dropouts and delays in the wireless network. Secondly, the packet probability p is an important parameter influencing the estimation accuracy. It is main challenge in the future research because the smaller p needs a higher accuracy.

Acknowledgements

This work was supported by National Key Research and Development Program (2016YFC0600906).

References

1. I. F. Akyildiz, W. Su, Y. Sankarasubramaniam, et al. Wireless sensor networks: a survey, *Computer Networks*, **38**(4) (2002) 393-422.
2. O. Costa. Stationary filter for linear minimum mean square error estimator of discrete-time Markovian jump systems, *IEEE Trans. Autom. Contr.*, **47**(8) (2002) 1351-1356.
3. S. Smith, P. Seiler. Estimation with lossy measurements: Jump estimators for jump systems. *IEEE Transactions on Automatic Control*. **48**(12) (2003) 2163-2171.
4. B. Yin, G. Yin. Stability of Markov modulated discrete-time systems with delays, *Automatica*, **39**(8) (2008) 1339-1351.
5. X. M. Zhang, Q. L. Han. Network-based H_∞ filtering using a logic jumping-like trigger, *Automatica*. **49**(5) (2013) 1428-1435.
6. M. Moayedi, Y. K. Foo, Y. C. Soh. Adaptive Kalman filtering in networked systems with random sensor delays, multiple packet dropouts and missing measurements, in *Proc. 48th IEEE Con. on. IEEE*, (China, Shanghai, 2009), pp.2058-2063.
7. B. Chen, W. A. Zhang, L. Yu. Distributed fusion estimation with missing measurements, random transmission delays and packet dropouts, *IEEE Trans. Autom. Contr.*, **59**(7) (2014) 1961-1967.
8. J. Ma, S. Sun. Optimal linear estimators for systems with random sensor delays, multiple packet dropouts and uncertain observations, *IEEE Sensors J.*, **59**(11) (2011) 5181-5192.
9. J. Ma, S. Sun. Linear estimators for networked systems with one-step random delay and multiple packet dropouts based on prediction compensation, *IET Signal Processing*, **11**(2) (2017) 197-204.
10. H. Rezaei, R. E. Mahboobi, M. Farsi. Robust filtering for uncertain networked systems with randomly delayed and lost measurements, *IET Signal Processing*, **9**(4) (2015) 320-327.

Optimal Hohmann-Type Impulsive Ellipse-to-Ellipse Coplanar Rendezvous

Xiwen Tian, Yingmin Jia*

*The Seventh Research Division and the Center for Information and Control, School of Automation Science and Electrical Engineering, Beihang University (BUAA), 37 Xueyuan Road, Haidian District
Beijing, 100191, China*

*E-mail: tianxiwen123@163.com; ymjia@buaa.edu.cn
www.buaa.edu.cn*

Abstract

This paper devotes to the problem of ellipse-to-ellipse coplanar rendezvous, where the solution and distribution of Hohmann-type optimal impulsive rendezvous are investigated. The analytical relation between the initial states and rendezvous time are derived for Hohmann-type, and the optimal impulse amplitudes are given thereupon. The distribution boundary of Hohmann-type model is obtained according to the Hohmann transfer and Hohmann with coasts. Simulations are demonstrated to analyze the influences of the solution and distribution.

Keywords: Optimal impulsive rendezvous, Hohmann-type rendezvous, ellipse-to-ellipse, optimal distribution.

1. Introduction

Optimal impulsive rendezvous is aimed at obtaining minimum-fuel guidance strategy for spacecraft rendezvous, which has attracted considerable attention. Despite that Lawden's necessary conditions¹ for optimal impulsive trajectories and Lion's improving methods² for non-optimal trajectories have provided some guidelines to solve the optimal problem where the initial states and rendezvous time are specified, the distributions of optimal models cannot be obtained clearly in these way. So far, only Prussing's theory³ of optimal impulsive rendezvous on close circular orbits is complete in its theoretical system, which derives the solutions and distributions of optimal impulsive models by solving the primer vector equations and boundary value problem. A reference frame in mean velocity orbit was built by Frank⁴, and showed better performance in describing the impulse locations and magnitudes than the mean radius orbit in Prussing's results. Xie⁵ focused

on the selection of reference frame for optimal impulsive rendezvous, and investigated the effect on the classification, distribution and guidance precision. For the case of elliptic orbit rendezvous, Wang⁶ used the state transition matrix given by Yamanaka⁷ to calculate the optimal solution of four-impulse model, but the analytical solution and the distribution are difficult to be achieved. Chen^{8,9} studied the ellipse-to-circle coplanar rendezvous based on his results on the dynamical equations for elliptic orbit rendezvous in low eccentricity, and provided the solutions and distributions of all types optimal models. Motivated by which, our previous work¹⁰ considered the ellipse-to-ellipse coplanar rendezvous and obtained the analytical solution and distribution of four-impulse model. In this paper, we will further investigate the Hohmann-type model for optimal impulsive ellipse-to-ellipse coplanar rendezvous.

* Corresponding author

© The 2018 International Conference on Artificial Life and Robotics (ICAROB2018), Feb. 1-4, B-Con Plaza, Beppu, Oita, Japan

2. Dynamics Description

The relative motion between two spacecrafts in elliptic orbits was derived in our previous work¹⁰, which is still used in this paper and given as follow:

$$\begin{cases} \delta\dot{r} = 3\delta r + 2\delta\theta \\ \delta\ddot{\theta} = -2\delta\dot{r} \end{cases} \quad (1)$$

The initial and terminal states of system (1) are

$$\begin{aligned} x_0 &= [x_{01}, x_{02}, x_{03}, x_{04}]^T \\ x_F &= [0, 0, 0, 0]^T \end{aligned} \quad (2)$$

where

$$\begin{aligned} x_{01} &= k_c (1 + e_c \cos f_c)^{-1} - k_t (1 + e_t \cos f_t)^{-1} \\ x_{02} &= \beta \\ x_{03} &= k_c^{\frac{1}{2}} e_c \sin f_c - k_t^{\frac{1}{2}} e_t \sin f_t \\ x_{04} &= k_c^{\frac{3}{2}} (1 + e_c \cos f_c)^2 - k_t^{\frac{3}{2}} (1 + e_t \cos f_t)^2 \end{aligned} \quad (3)$$

β is the difference of phase angle between two spacecrafts; e_c, e_t and f_c, f_t are their eccentricities and true anomalies, respectively.

The states at phase angle τ was also deduced[10]:

$$x(\tau) = \begin{bmatrix} 2d_4 - d_3 \cos(\tau + \varphi) \\ \beta - 3d_4\tau + 2d_3 \sin(\tau + \varphi) - 2d_3 \sin \varphi \\ d_3 \sin(\tau + \varphi) \\ -3d_4 + 2d_3 \cos(\tau + \varphi) \end{bmatrix} \quad (4)$$

where

$$\begin{aligned} d_1 &= x_{03}, d_2 = 3x_{01} + 2x_{04} \\ d_3 &= \sqrt{d_1^2 + d_2^2}, d_4 = 2x_{01} + x_{04}, \varphi = \arcsin\left(\frac{d_1}{d_3}\right) \end{aligned} \quad (5)$$

3. Optimal Hohmann-Type Rendezvous

The solution to primer vector equations corresponding to system (1) can be given in the following form:

$$\begin{aligned} \lambda_1 &= A \cos \tau + B \sin \tau + 2C \\ \lambda_2 &= 2B \cos \tau - 2A \sin \tau - 3C\tau + D \end{aligned} \quad (6)$$

Hohmann-type model is a special case of optimal two-impulse rendezvous, where the coefficients of (6) are

$$A = B = C = 0, D = \pm 1 \quad (7)$$

then $\lambda_1 = 0, |\lambda_2| = 1$. It can be verified that the necessary conditions of optimal impulsive rendezvous are satisfied for any phase angle τ .

3.1. Solution of Hohmann transfer

The impulse direction can be obtained from the solution (6), while the impulse time and magnitudes needed be calculated according to the following boundary value problem:

$$\begin{bmatrix} 2(1-C_\tau) & 0 \\ 4S_\tau - 3\tau_F & 0 \\ 2S_\tau & 0 \\ -3 + 4C_\tau & 1 \end{bmatrix} \begin{bmatrix} \Delta V_1 \\ \Delta V_2 \end{bmatrix} = x(\tau_F) \quad (8)$$

where $S_\tau = \sin \tau, C_\tau = \cos \tau$, ΔV_1 and ΔV_2 are the magnitudes of two impulse, and τ_F is the rendezvous time. From (4) and (8), we have

$$\begin{aligned} \Delta V_1 &= -\frac{d_3 \sin(\tau_F + \varphi)}{2S_\tau} \\ \Delta V_2 &= \frac{-2d_4 + d_3 \cos(\tau_F + \varphi)}{2(1-C_\tau)} \end{aligned} \quad (9)$$

then

$$d_3 (\sin(\tau_F + \varphi) - \sin \varphi) = 2d_4 \sin \tau_F \quad (10)$$

Substituting (5) into (10), it can be obtained that

$$\sqrt{x_{01}^2 + d_1^2} \sin(\tau_F + \theta) = -d_1 \quad (11)$$

where

$$\cos \theta = \frac{x_{01}}{\sqrt{x_{01}^2 + d_1^2}}, \sin \theta = -\frac{d_1}{\sqrt{x_{01}^2 + d_1^2}} \quad (12)$$

On the other hand, from the second row of (8), it has

$$\Delta V_1 = \frac{-\beta + 3d_4\tau - 2d_3 \sin(\tau_F + \varphi) + 2d_3 \sin \varphi}{(4S_\tau - 3\tau_F)} \quad (13)$$

Combining (5), (9) and (13), it has

$$-\frac{3\tau_F (x_{01} C_\tau + d_1 S_\tau)}{2(1-C_\tau)} + 2d_1 = f_c - f_t \quad (14)$$

The appropriate initial states and rendezvous time which satisfy the necessary conditions of Hohmann transfer can be obtained by solving (11) and (14) together, and then, the second impulse ΔV_2 can be obtained as

$$\Delta V_2 = -d_4 + \frac{d_3 \sin(\tau_F + \varphi)}{2S_\tau} \quad (15)$$

3.2. Distribution of Hohmann-type model

The distribution of optimal Hohmann-type rendezvous is to illustrate the existence of feasible solution. To investigate the distribution, rendezvous time is chosen as the X-coordinate and the special phase angle defined below as Y-coordinate:

$$\delta\theta_F = -\beta + 1.5d_4\tau_F - d_3 \sin(\tau_F + \varphi) + d_3 \sin \varphi \quad (16)$$

Let τ_{Fh} be rendezvous time solved by (11) and (14), and $\delta\theta_{Fh}$ is the corresponding special phase angle. If $\tau_F = \tau_{Fh}$ and $\delta\theta_F = \delta\theta_{Fh}$, then it is just the Hohmann transfer. The two impulses are implemented at $\tau_1 = 0$ and $\tau_2 = \tau_F$. However, when the real rendezvous time is longer than τ_{Fh} , the coasts are needed to save the fuel.

If $\tau_F > \tau_{Fh}$ and $\delta\theta_F = \delta\theta_{Fh}$, it is a Hohmann model with terminal coast. The two impulses are implemented at $\tau_1 = 0$ and $\tau_2 = \tau_{Fh}$, and the residual time $\tau_F - \tau_{Fh}$ is for terminal coast. The special phase angle $\delta\theta_F$ and rendezvous time τ_F should satisfy the following relation

$$\begin{aligned} \delta\theta_F &= \delta\theta_{Fh} + 1.5d_4(\tau_F - \tau_{Fh}) \\ &+ d_3 \sin(\tau_{Fh} + \varphi) - d_3 \sin(\tau_F + \varphi) \end{aligned} \quad (17)$$

$$\tau_{Fh} = \tau_2 - \tau_1, \tau_F \in [\tau_{Fh}, +\infty)$$

If $\tau_F > \tau_{Fh}$ and the special phase angle $\delta\theta_F$ satisfies

$$\begin{aligned} \delta\theta_F &= \delta\theta_{Fh} - 1.5d_4(\tau_F - \tau_{Fh}) \\ &+ d_3 \sin(\tau_F - \tau_{Fh} + \varphi) - d_3 \sin \varphi \end{aligned} \quad (18)$$

$$\tau_{Fh} = \tau_2 - \tau_1, \tau_F \in [\tau_{Fh}, +\infty)$$

then, after the initial coast for time $\tau_F - \tau_{Fh}$, the special phase angle will become exactly $\delta\theta_{Fh}$. This case is a Hohmann model with initial coast, and the impulses are implemented at $\tau_1 = \tau_F - \tau_{Fh}$ and $\tau_2 = \tau_F$.

Let

$$\begin{aligned} \delta\theta_{Fh1} &= \delta\theta_{Fh} + 1.5d_4(\tau_F - \tau_{Fh}) \\ &+ d_3 \sin(\tau_{Fh} + \varphi) - d_3 \sin(\tau_F + \varphi) \end{aligned} \quad (19)$$

$$\delta\theta_{Fh2} = \delta\theta_{Fh} - 1.5d_4(\tau_F - \tau_{Fh})$$

$$+ d_3 \sin(\tau_F - \tau_{Fh} + \varphi) - d_3 \sin \varphi$$

If $\tau_F > \tau_{Fh}$ and $\delta\theta_{Fh1} < \delta\theta_F < \delta\theta_{Fh2}$, then there exists a Hohmann model with both initial coast and terminal coast. As shown in Fig.1., this case is illustrated in the middle of the curves expressed by (17) and (18), that is the shadow part. Denote $(\tau_{F0}, \delta\theta_{F0})$ as the intersection point of the curves determined by (16) and (18), then the two impulses are implemented at $\tau_1 = \tau_{F0} - \tau_{Fh}$ and $\tau_2 = \tau_{F0}$. The initial and terminal coast last for time $\tau_{F0} - \tau_{Fh}$ and $\tau_F - \tau_{F0}$, respectively.

From the above, the optimal Hohmann-type impulsive rendezvous has four models, all of whose impulse magnitudes are determined by (9) and (15), and impulse direction is along the tangential direction.

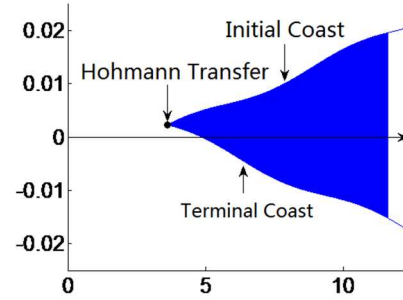


Fig. 1. Distribution of Hohmann-type model.

4. Simulations

In this section, simulation examples are presented to show the guidance performance and distribution of Hohmann-type impulsive rendezvous.

4.1. Hohmann ellipse-to-ellipse rendezvous

It is assumed the semi-major axis and eccentricities of the target orbit and chaser orbit are initially $a_t = 6730$ (km), $a_c = 6750$ (km), $e_t = 0.0005$ and $e_c = 0.0004$, respectively. Let τ_F and β (rad) be the appropriate rendezvous time and initial difference of phase angle, respectively, which satisfy (11) and (14). And denote R_r (m) as the optimal radius of reference frame, R (m) as the initial relative distance, Δa (m), Δe and $\Delta\theta$ (rad) as the guidance errors.

Table 1. Results of Hohmann impulsive rendezvous

	1	2	3	4
f_c	30°	150°	210°	330°
τ_F	3.62	3.44	2.80	2.68
β	7.12e-03	9.68e-03	6.04e-03	3.46e-03
R_r	6.70e+06	7.92e+06	7.81e+06	6.71e+06
R	4.99e+04	7.05e+04	4.83e+04	2.71e+04
Δa	6.80e+01	3.38e+04	3.09e+04	2.49e+01
Δe	3.38e-05	4.51e-03	4.22e-03	8.92e-06
$\Delta\theta$	5.82e-06	2.87e-04	3.50e-05	3.80e-06
ΔR	1.29e+02	5.14e+03	5.71e+02	5.08e+01

Simulation results of Hohmann transfer for ellipse-to-ellipse rendezvous are demonstrated in Table 1, which shows that: (1) with different true anomalies, even if the other initial states are the same, the

rendezvous time and initial difference of phase angle which satisfy (11) and (14) varies much; (2) the optimal radius of reference frame also changes with the true anomaly; (3) the guidance precision is high when the chaser initially stays around the perigee.

4.2. Distribution of Hohmann-type model

To investigate the distribution of Hohmann-type ellipse-to-ellipse rendezvous, we take rendezvous time τ_F as the X-coordinate and $\delta\theta_F/d_4$ as Y-coordinate. Fig.2 shows the distribution of Hohmann-type model with different true anomalies and eccentricities.

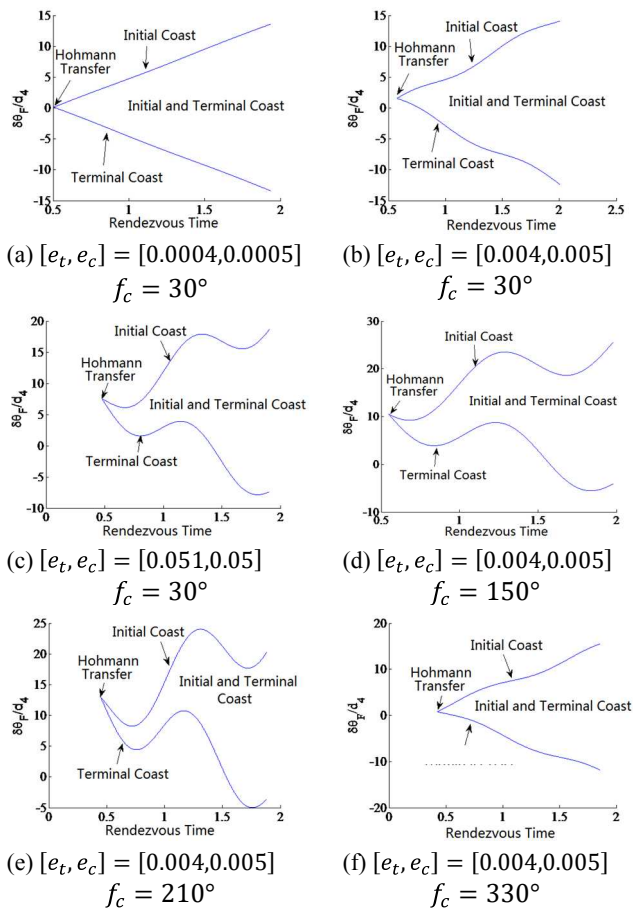


Fig. 2. Distribution of Hohmann-type model.

5. Conclusion

This paper extends our previous work¹⁰ to the Hohmann-type optimal impulsive rendezvous. By

defining the special phase angle, we derived the analytical solution for Hohmann transfer, and obtained that the optimal Hohmann-type impulsive rendezvous has four models, i.e. Hohmann transfer, Hohmann with initial coast, Hohmann with terminal coast and Hohmann with both coasts. In further research, we will integrate all optimal models in one map, including four-impulse, three-impulse, three-impulse with coasts, two-impulse, two-impulse with coasts, and Hohmann-type.

Acknowledgements

This work was supported by NSFC (61327807, 61521091, 61520106010, 61134005) and the National Basic Research Program of China (973 Program: 2012CB821200, 2012CB821201)

References

1. D. F. Lawden, *Optimal Trajectories for Space Navigation* (London: Butterworths, 1963).
2. P.M. Lion and M. Handelsman, Primer vector on fixed-time impulsive trajectories, *AIAA J.*, **6**(1) (1968) 127-132.
3. J. E. Prussing, *Optimal Multi-Impulse Orbital rendezvous*, Sc.D. Thesis. (Cambridge: Dept. of Aeronautics and Astronautics, Massachusetts Institute of Technology, 1967).
4. C. L. Frank and L. D. Plexico, Improved solution of optimal impulsive fixed-time rendezvous. *J. Spacecraft and Rockets*, **19**(6) (1982) 521-528
5. Y. C. Xie, C. Q. Chen, H. Zhang and J. Hu, Selection of reference systems for optimal impulsive rendezvous between two near circular orbits (in Chinese), *Chinese Space Sci. Technol.*, **28**(2) (2008) 8-14.
6. J. X. Wang, H. X. Baoyin, J. F. Li and F. C. Sun, Optimal four-impulse rendezvous between coplanar elliptical orbits. *Phys. Mech. Astron.*, **54**(4) (2011) 792-802.
7. K. Yamanaka and F. Ankersen, New state transition matrix for relative motion on an arbitrary elliptical orbit, *J. Guid. Contr. Dynam.*, **25**(1) (2002) 60-66.
8. C. Q. Chen and Y. C. Xie, Dynamical equations for a kind of elliptic orbit rendezvous (in Chinese), *Aerospace Contr.*, **26**(5) (2008) 12-17.
9. C. Q. Chen and Y. C. Xie, Optimal impulsive ellipse-to-circle coplanar rendezvous, *Sci. in China Series E: Tech. Sci.*, **52**(5) (2009) 1435-1445.
10. X. W. Tian, Y. M. Jia and C. Q. Chen, Optimal four-impulse ellipse-to-ellipse coplanar rendezvous, *Contr. Conf. IEEE*, (2016) 5498-5503.

Research on SVG Control Method Under Unbalanced Conditions

Zheng Zheng, Yousong Zhou*, Guopeng Zhang

School of Electrical Engineering and Automation, Henan Polytechnic University
Jiaozuo, 454000, China

E-mail: zhengzh@hpu.edu.cn, z2410767638@163.com, hpoyz@163.com

http://www.hpu.edu.cn/www/index.html

Abstract

In order to reduce the complexity of traditional methods, a PCI (Proportional Complex Integral) controller is adopted to control SVG under unbalance-grid condition, which has better performance than PI controller to eliminate steady-state error to compensate nonlinear loads. Based on the $\alpha\beta$ frame, the proposed control scheme considerably reduces total algorithm complexity. The current control loop is designed based on mathematical modeling under unbalanced conditions. Simulation and experimental results are provided to validate the correctness of the proposed methods.

Keywords: SVG; complex filter; steady-state error; proportional complex integral control;

1. Introduction

In recent years, the research of SVG (Static Var Generator) mainly focuses on both the rapid and accurate detection of reactive current and the simplification of reactive power control methods^{1,2}. Proportional resonance control method used in paper³⁻⁴ can be realized the non-static input current. The method has high requirements for the accuracy of the hardware and parameters of the device, which is difficult to achieve the ideal state. Non-beat control method and predictive control method are used in paper⁵⁻⁷. The precise model designs of these control methods has some difficulties, which easily lead to the instability of the system.

This paper presents PCI control method based on $\alpha\beta$ stationary reference frame. The control method not only effectively eliminates the steady-state error of AC current, but also improves the compensation performance of the equipment.

2. Control Method

The main circuit structure of SVG of the voltage source is shown in Fig.1. Three-phase power grid phase voltage is expressed as e_a, e_b and e_c ; Three-phase load side current is represented by i_{la}, i_{lb} and i_{lc} ; The DC side voltage of the SVG is expressed as u_{dc} .

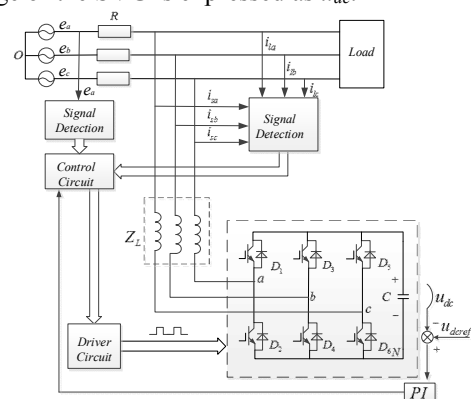


Fig.1. Main circuit topology of SVG

*Corresponding author

2.1. Positive and negative component separation method based on complex filter

A method, used complex filters to the separation for positive and negative sequence components of the grid current, which is proposed in this paper. The principle block diagram is shown in Fig. 2. In figure, ω_c is the cut-off frequency of the filter.

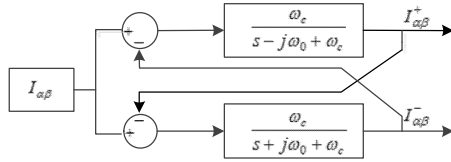


Fig. 2.Current Positive and Negative Sequence Component Separation Calculation

From Fig. 2, $I_{\alpha\beta}^+(s)$ and $|F(s)|$ are satisfied with

$$I_{\alpha\beta}^+(s) = \frac{\omega_c(s + j\omega_o)}{s^2 + 2\omega_c s + \omega_o^2} I_{\alpha\beta}(s) = F(s)I_{\alpha\beta}(s) \quad (1)$$

$$|F(s)| = \frac{|\omega_c(\omega + \omega_o)|}{\sqrt{(\omega_c^2 - \omega^2)^2 + 4\omega_c^2\omega^2}} \quad (2)$$

By Clarke transformation, we can obtain

$$\begin{bmatrix} I_\alpha \\ I_\beta \end{bmatrix} = \frac{2}{3} \begin{bmatrix} 1 & -\frac{1}{2} & \frac{1}{2} \\ 0 & \frac{\sqrt{3}}{2} & -\frac{\sqrt{3}}{2} \end{bmatrix} \begin{bmatrix} I_a \\ I_b \\ I_c \end{bmatrix} = \begin{bmatrix} I_\alpha^+ + I_\alpha^- \\ I_\beta^+ + I_\beta^- \end{bmatrix} \quad (3)$$

A specific block diagram is obtained, as shown in Fig. 3.

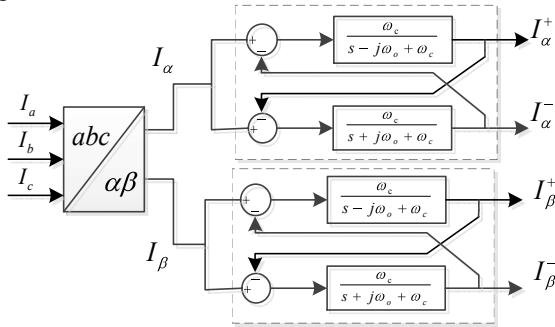


Fig.3. Three-phase Unbalanced Current Positive and Negative Sequence Component Separation Calculation

2.2. PCI control method

The traditional proportional complex integral control method is based on α - β stationary reference frame, as shown in Fig. 4. When the current is controlled in a three-phase coordinate system, the amount of control

calculation is increased due to complexity of the coordinate transformation. In this paper, according to the equivalent transformation of variables, proportional complex integral control method which can be directly applied to three-phase coordinate system is designed.

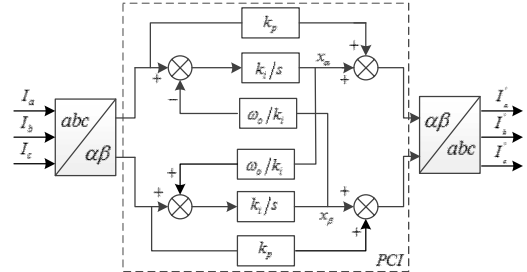


Fig.4. PCI Control Based on Coordinate System

The phase of the three phase coordinate system varies by 120°, we can obtain

$$\begin{cases} -j\sqrt{3}x_a = x_b - x_c \\ -j\sqrt{3}x_b = x_c - x_a \\ -j\sqrt{3}x_c = x_a - x_b \end{cases} \quad (4)$$

The control block diagram of the three phase coordinate system is obtained by (4), as shown in Fig. 5.

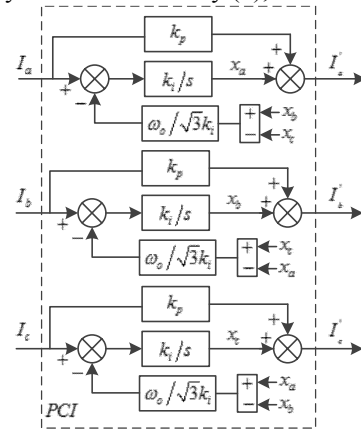


Fig. 5.PCI Control Based on Three-phase Coordinate System

3. Analysis of simulation result

The relevant system parameters are shown in Table 1.

Table 1.Parametric results figure

Parameter	Value	Parameter	Value
Grid Line Voltage	400V	DC side voltage	700V
Grid Frequency	50Hz	DC bus capacitor	6μF
Grid Reactance	5mH	The rated Capacity	200kVar

In the system, the bandwidth is usually selected to be 10 times higher than the base wave frequency, and also less than 1/5 of the switching frequency, so the range of bandwidth f_b is 500 to 2000. The transfer function of the closed loop of the system is obtained as:

$$T(s) = \frac{I_o(s)}{I_r(s)} = \frac{K(k_p s + k_i - j\omega_o k_p)}{Ls^2 + (Kk_p + R - j\omega_o L)S + Kk_i - j\omega_o(Kk_p + R)} \quad (5)$$

$$|T(s)| = \frac{K\sqrt{k_p^2(\omega - \omega_o)^2 + k_i^2}}{\sqrt{(L\omega\omega_o - L\omega^2 + Kk_i)^2 + (Kk_p + R)^2(\omega - \omega_o)^2}} \quad (6)$$

$$\angle T(s) = \arctan\left(\frac{k_p(\omega - \omega_o)}{k_i}\right) - \arctan\left(\frac{(Kk_p + R)(\omega - \omega_o)}{L\omega\omega_o - L\omega^2 + Kk_i}\right) \quad (7)$$

When only k_p is considered, the closed loop amplitude frequency features are

$$|T(s)| = \frac{Kk_p}{\sqrt{(L\omega)^2 + (Kk_p + R)^2}} \quad (8)$$

Where $f_b=650\text{Hz}$, $\omega_b=4100\text{rad/s}$, (8) give rises to $k_p=0.1$. Under the requirements of the system bandwidth, the design make $f_b=690\text{Hz}$, $\omega_b=4330\text{rad/s}$, (6) give rises to $k_p=20$. Under the condition of unbalanced working conditions, the control strategy diagram of the static reactive power generator is shown in Fig. 6.



Fig. 6. The Model of SVG Based on Complex Filter and PCI Control

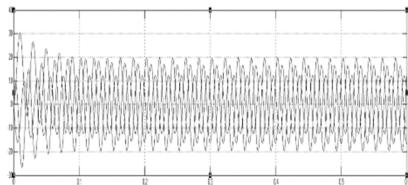


Fig.7. (a) Load side three phase current waveform diagram

According to above model, Matlab software is used to simulate. It is a three-phase current on the load side in Fig. 7. Fig.8 shows PI control and PCI control steady

- state error comparison of the output current waveform of SVG. When the system is controlled with PCI control after 0.5s, the SVG output current is close to the command current, and the error is controlled to 0.1 A. So the PCI control has a good effect in the steady state error control.

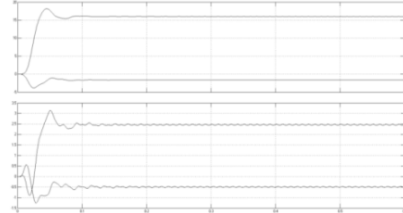


Fig.7. (b) Load side three phase current positive and negative sequence component

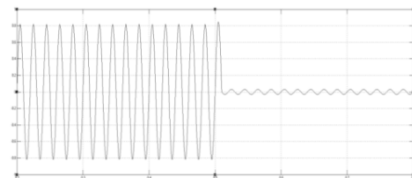


Fig. 8. PI control and PCI control steady-state error comparison

4. The Experimental Test

In this paper, RT-LAB semi-physical platform is verified to the proposed strategy, as shown in Fig. 9. The SVG control circuit is based on the core of DSP28335, and the main part of the circuit is realized by the RT-LAB platform. For the system, the input grid phase voltage is 311V, the DC voltage is 700V, and the pure resistance load resistance is 100 Ω.

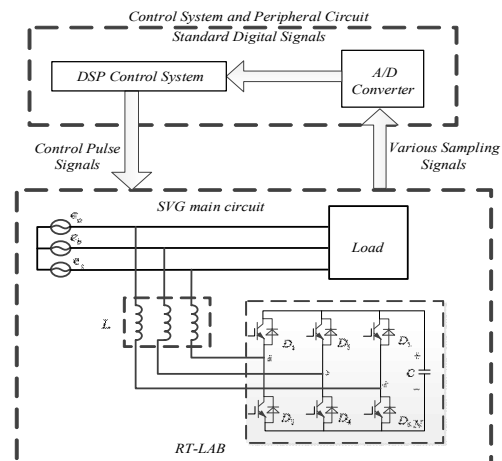


Fig.9. Schematic diagram of the experimental system

In order to avoid the disturbance caused by the start of the equipment, the equipment is cut off after the normal running time of 1s, and the experimental waveforms of this system are shown in Fig. 10, Fig. 11 and Fig. 12.

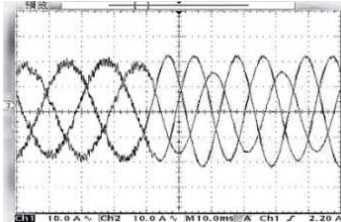


Fig. 10. Three - phase current waveform on grid side

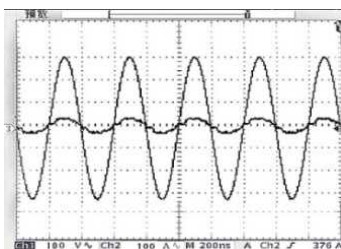


Fig. 11. Grid side a phase voltage current waveform

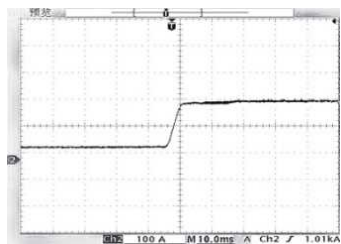


Fig. 12. Side of the three - phase current imbalance waveform

Fig.10 shows that three-phase current state can achieve the balance when the device is in normal operation; while the device is disconnected, the state becomes unbalanced. As shown in Fig.11, after A Phase is compensated, the phase of the voltage and current is the same, which achieve a better compensation effect. From Fig.12, it can be seen that unbalancedness degree is reduced from 0.28 to 0.06 for the three phase current of the load, which achieve the state's demand for unbalancedness degree.

The experimental results show that the SVG control method based on complex filter and PCI control method

can realize real-time compensation for reactive and negative sequence components under unbalanced conditions.

5. Conclusion

Under unbalanced condition, the PCI controller is studied using in SVG to compensate nonlinear loads. Compared with traditional control method, the proposed scheme can considerably reduces total algorithm complexity. The current control loop is designed based on the mathematical modeling under unbalanced input conditions, and parameters of PCI controller is designed. An experimental platform is built based on DSP 28335 and RT-Lab. Simulation and experimental results are given to demonstrate the effectiveness of the proposed control scheme.

Acknowledgements

Fund projects: National Natural Science Foundation (U1504518).

References

1. Y. Liu and C. Shao, Reconstruction strategies for phase currents in three phase voltage source PWM inverters, *J. Inf. Contr.* **36**(4) (2007)506-513.
2. Y.N.Yu, R.F. Yang, et al. Attractive beat control of cascaded H-bridge SVG, *J. Trans. China Electrotechnical Soc.* **01**(25) (2017) 50-58.
3. L. Ma, X.M. Jin, et al. Analysis of three-phase grid-connected inverter proportional resonant control and grid voltage feed-forward, *J. Trans. China Electrotechnical Soc.* **08**(27) (2012) 56-62.
4. S.Bhowmik, R.Spee, J.Enslin. Performance optimization for doubly-fed wind power generation systems. *J. IEEE Trans. Ind. Appl.* (1999) 2387-2394.
5. X.G. Zhang, R.Wang and D.G. XU. A dead-beat control strategy for circulating-current in parallel connection systems of three-phase PWM converters, *J. Proceedings of the CSEE*, **02**(33) (2013) 31-37.
6. Z.J.Fang, S.X. Duan, et al. Formation mechanism and suppression strategy of prediction control error applied in a battery energy storage inverter, *J. Proc. CSEE*, **10**(30) (2013) 1-9.
7. W. Chen and J. Wu. Adaptive control of ASVG by using diagonal recurrent neural network, *J. Proc. CSU-EPSSA*, (1999) 33-37.

Dynamics Analysis of Payload On-orbit Catapult Separation Based on ADAMS

Yi Li, Yingmin Jia*, Jianheng Ling

*The Seventh Research Division and the Center for Information and Control
School of Automation Science and Electrical Engineering
Beihang University (BUAA), 37 Xueyuan Road, Haidian District
Beijing, 100191, China
E-mail: liyi309@163.com; ymjia@buaa.edu.cn; lingjianheng1987@163.com
www.buaa.edu.cn*

Abstract

In this paper, a catapult separation device equipped with guide mechanism is considered, and the corresponding dynamic model is described firstly. Then, employing the dynamic simulation software ADAMS, the virtual prototype model of the separation device is established, and the whole process of on-orbit separation is simulated. Finally, the structure parameters of the guide mechanism such as the number of roller group or distance between groups are studied. The simulation results could provide references for the optimization of the separation device.

Keywords: Guide mechanism, catapult separation, virtual prototype, angular velocity.

1. Introduction

On-orbit separation refers that satellite platform separates payload with a separation device, and the payload enters its preset orbit successfully¹. The common schemes for on-orbit separation include pyrotechnic separation, electromagnetic separation and catapult separation. Pyrotechnic separation has security problem since the separation process with explosive material would produce large impact and interference on onboard devices; electromagnetic separation requires more power consumption, meanwhile, it's easily influenced by external magnetic field; however, catapult separation has the following advantage: simple structure, less power consumption and easy to control, therefore, the catapult separation is chosen in this paper.

Due to the deviations of compressing spring parameters, machining errors or external disturbances, the mass center of the payload is not on the resultant

force in the process of catapult separation. The additional torque introduced by the eccentric separation would affect the attitude or even cause tumbling of the payload, so it is very important to study the separation dynamics of eccentric payload. Jeyakumar² established the dynamic equations for the satellite separation system using the helical compression spring mechanism. In Jiang's research³, characteristics of the constrained and centroid biased on-orbit satellite separation were analyzed, and then the dynamic model of the separating motion was formulated. Based on multi-body dynamic theory, Shen⁴ built the eccentric separation model, and simulated the dynamic during the separation by ADAMS software. Zhang⁵ built virtual prototype model of separation mechanism to simulate the whole process of payload on-orbit launch, and analyzed the stability of on-orbit launch considering the influence of separation mechanism error. Shu⁶ focused on the multi-body dynamics during separation/release, and established the

* Corresponding author

© The 2018 International Conference on Artificial Life and Robotics (ICAROB2018), Feb. 1-4, B-Con Plaza, Beppu, Oita, Japan

simulation model based on ADAMS. The above researches stressed on dynamics analysis of tube-shape eccentric sub-satellite separation, and analyzed the influences of separation mechanism parameters on satellite platform by employing MATLAB or ADAMS platform. On basis of the previous studies, in this paper, a new type of catapult separation device equipped with guide mechanism is presented, and the influences of the guide mechanism's parameters on the payload attitude are analyzed in ADAMS/View.

2. Problem Formulation

2.1. Description of catapult separation device

As shown in Fig. 1, the catapult separation device includes driving motors, differential gear mechanism, four compression springs, the guide mechanism, a car used for loading the payload, and so on, the guide mechanism consisting of rollers plays a crucial role in restraining angular velocity of the payload. According to the general design scheme, the whole separation process can be divided into three phases:

- (i) the payload moves together with the car, in other words, they maintain relative static,
- (ii) the car collides with the buffers in the end of whole distance, the payload moves along the guide mechanism under the effect of inertial force, and the payload is still not out of the car in this phase,
- (iii) the payload is completely out of the guide mechanism's constraints, that means the car and the payload move respectively.

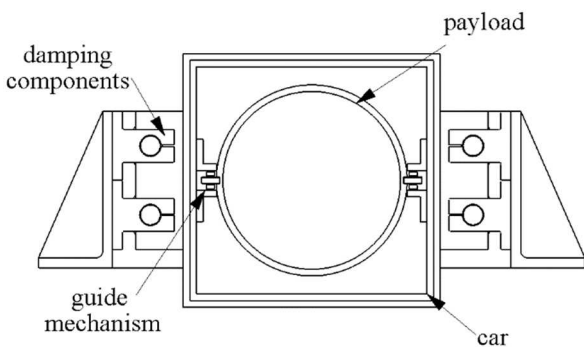


Fig. 1. Schematic drawing of the catapult separation device

2.2. Dynamics description

During the process of catapult separation, the separation impulse is provided by release of the energy stored in the compressing springs. Based on the structure of the separation device, the force of the payload include spring force and the contact force produced by the rollers. By means of multi-body dynamics theory, the force and the moment of payload are analyzed and calculated as follows:

$$F = \sum_{i=1}^n F_{li} + \sum_{i=1}^n F_{ri} + \sum_{j=1}^k F_{sj}, \quad (1)$$

$$M = R_b^r \left(\sum_{i=1}^n r_{li} \times F_{li} + \sum_{i=1}^n r_{ri} \times F_{ri} + \sum_{j=1}^k r_{sj} \times F_{sj} \right). \quad (2)$$

where F_{li} , F_{ri} are the contact forces of the i th group of the rollers, and F_{sj} is the spring force of the j th spring. R_b^r is transformation matrix, from inertia reference coordinate system to the payload coordinate system. r_{li} , r_{ri} and r_{sj} are the position vectors mapped in inertia reference coordinate system.

Based on Hertz contact theory, the nonlinear spring damping contact model is adopted to model the contact force which can be expressed as

$$F_{li} = \begin{bmatrix} F_{Ni} \\ F_{si} \end{bmatrix} = \begin{bmatrix} -F_0 + (K\delta_{li} - C\delta_{li}\dot{\delta}_{li}) \\ -\mu F_{Ni} \end{bmatrix}, \quad (3)$$

where F_{Ni} represents the normal pressure, F_{si} represents the friction force. F_0 is the preload, C and K represent the damping factor and equivalent system stiffness, respectively, δ_{li} denotes the normal deformation and μ satisfies

$$\mu = \begin{cases} -\text{sign}(v) \cdot \mu_f, & |v| > v_f \\ -\text{step}(|v|, v_f, \mu_f, v_s, \mu_s) \cdot \text{sign}(v), & v_s < |v| \leq v_f \\ \text{step}(v, -v_s, \mu_s, v_s, -\mu_s), & |v| \leq v_s \end{cases} \quad (4)$$

where μ_f states the dynamic frictional coefficient, and μ_s represents the static frictional coefficient. v is the velocity of the payload, v_f denotes the dynamic slip velocity while v_s denotes the static slip velocity.

3. Virtual Prototype Modeling

Using the ADAMS software, the virtual prototype model including the satellite platform, the payload and the catapult separation device is established as shown in Fig. 2. In general, there is a constraint relationship known as joint between two components, this model has three kinds: Fixed joint, Revolute joint, and Translational joint.

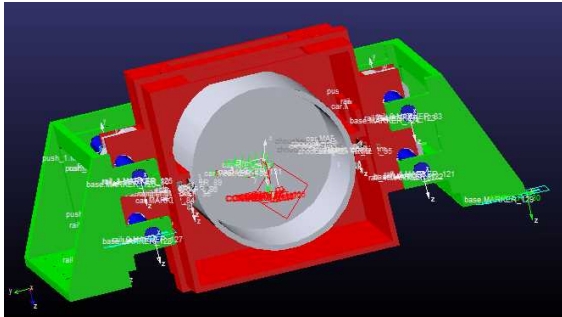


Fig. 2. Virtual prototype model of separation system

Then, we should define force, torque, and contact for the virtual prototype model. The defined contacts are demonstrated in Table 1, calculating for which there are two methods: restitution method and impact method. According to the dynamics analysis in chapter 2, we adopt the impact method in this model.

Table 1. Contacts of the model

Schedule	Rigid 1	Rigid 2
Contact 1	car	payload
Contact 2	car	buffer
Contact 3	roller_11	payload
Contact 4	roller_12	payload
Contact 5	roller_21	payload
Contact 6	roller_22	payload

4. Simulation

The payload’s angular velocity is the main target of measuring the stability of on-orbit catapult separation. Many factors influence the separation angular velocity, including various structure parameters of the device and the motion of the satellite platform. Here, the structure parameters of the guide mechanism are discussed. By

analyzing the influence rules of the parameters under different conditions, we can optimize and redesign the guide mechanism.

We assume that the initial angular velocity of the satellite platform is zero, and the orbit motion of the payload is neglected in the process. The mass of the platform is $M = 500kg$, the mass of the payload is $m = 5kg$; the stiffness coefficients of four compression springs are set as $k_1 = 2.43N/mm$, $k_2 = 2.46N/mm$, $k_3 = 2.47N/mm$, $k_4 = 2.48N/mm$ respectively; the spring stroke length is $\Delta x = 90mm$ (the velocity of the car will be $4m/s$), the gravity is neglected; and the simulation time is $0.1s$, the step is 200, the lock is released at $t = 0.034s$, otherwise.

The guide mechanism primitively has two groups of rollers, and now we add one group of rollers between the two groups on the premise of little change of the separation velocity as shown in Fig. 3, the distance between the added group and the first group is set as $l = 75mm$.

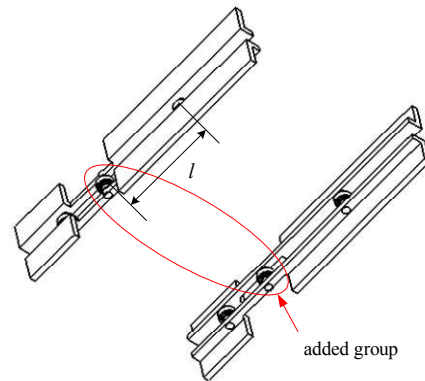


Fig. 3. Installation of the groups of rollers

Fig. 4 shows the final roll angular velocity (rotation about x axis) decreases from $0.849^\circ/s$ to $0.553^\circ/s$, the yaw angular velocity (rotation about y axis) decreases from $1.063^\circ/s$ to $0.870^\circ/s$, and the pitch angular velocity (rotation about z axis) decreases from $0.594^\circ/s$ to $0.4^\circ/s$ after adding one group of rollers. So adding groups of rollers on the premise of little change of the separation velocity could restrain the separation angular velocity.

Considering the guide mechanism has three groups of rollers, we try to adjust the distance between the middle group and the first group, that is, the distance is implemented at $l_1 = 50mm$, $l_2 = 35mm$, respectively. The simulation results are illustrated in Fig. 5.

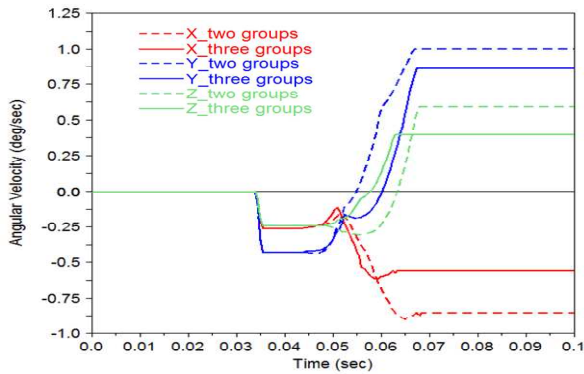


Fig. 4. The angular velocity after adding one group of rollers

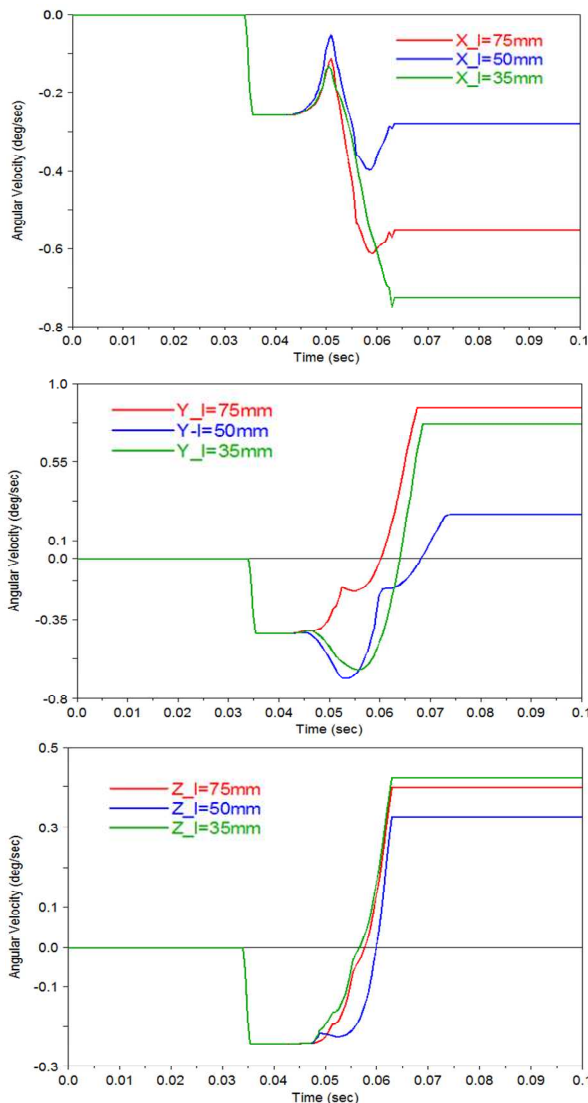


Fig. 5. The angular velocity with different distances

When the distance decreases to 50 mm, the angular velocities including roll, yaw and pitch decrease as well (the roll angular velocity decreases to 0.280°/s, the yaw angular velocity decreases to 0.353°/s and the roll angular velocity decreases to 0.327°/s); however, if the distance continues to decrease to 35 mm, the angular velocities will increase instead.

5. Conclusion

In this paper, a new type of catapult separation device equipped with guide mechanism is considered; using the ADAMS software, the virtual prototype model is established. The simulation results show that adding one group of rollers and adjusting it to the center of the other two groups could restrain the angular velocity effectively.

Acknowledgements

This work was supported by the National Basic Research Program of China (973 Program: 2012CB821200, 2012CB821201), the NSFC (61327807, 61520106010, 61134005, 61521091).

References

1. J. P. Yuan, et al. *Spacecraft Counter Orbit Dynamics* (China Astronautic Publishing House, 2014).
2. Jeyakumar. D, B. N. Rao. Dynamics of satellite separation system, *J. Sound Vib.*, **297**(1) (2006) 444-455.
3. C. Jiang, Z. K. Wang, L. Fan, et al. Dynamics analysis of the constrained and centroid biased on-orbit satellite separation (in Chinese), *Flight Dyn.*, **28**(1) (2010) 76-79.
4. X. F. Shen, Y. Z. Xiao, et al. Dynamic simulation of eccentric sub-satellite based on Monte Carlo method (in Chinese), *Aerospace Shanghai*, **31**(1) (2014) 12-17.
5. L. Zhang, Y. Liao and G. Tang. Dynamic simulation of payload on-orbit launch (in Chinese), *J. Projectiles Rockets Missiles Guid.*, **28**(4) (2008) 186-189.
6. Y. Shu and Z. Li. Dynamics simulation of on-orbit release and separation of payload (in Chinese), *Spacecraft Environment Eng.*, **29**(1) (2012) 18-22.
7. Nohmi M, Tanikawa J and Hosoda T. Simulation analysis of a tethered space robot for space experiment on sounding rocket by JAXA/ISAS, in Proc. *Int. Conf. Mechatronics and Automation. IEEE*, (China, Xi'an, 2010) 264-269.
8. Nenchev D N, Nohmi M and Uchiyama M. Tethered robot casting using a spacecraft-mounted manipulator, *J. Guid. Contr. Dyn.*, **24**(4) (2001) 827-833.

A Land Testbed for Experimental Research on Autonomous Ship Navigation

Keisuke Watanabe

*Department of Navigation and Ocean Engineering, Tokai University, 3-20-1 Orido Shimizu-ku
Shizuoka, Shizuoka, 424-8610, Japan**

Kazumasa Harada

*Department of Navigation and Ocean Engineering, Tokai University, 3-20-1 Orido Shimizu-ku
Shizuoka, Shizuoka, 424-8610, Japan†*

Koshi Utsunomiya

*Department of Navigation and Ocean Engineering, Tokai University, 3-20-1 Orido Shimizu-ku
Shizuoka, Shizuoka, 424-8610, Japan
E-mail: keisuke@tsc.u-tokai.ac.jp
www.u-tokai.ac.jp*

Abstract

In the development of automated ship technology, experimental system is essential. The main navigation system is supposed to consist of GPS, AIS (Automatic Identification System), RADAR and cameras. In this paper, we introduce the setup of our land based test robot which simulates several essential functions needed for experiments of our research. In our land test robot, 2 ultrasound distance sensors are used as a model of GPS, which determine the coordinate of the test robot measuring the distances from 2 walls. A swinging ultrasound ranging sensor with a servo motor is used to simulate the RADAR. A xbee wireless communication module simulates the AIS. The camera is used for image processing to determine the control algorithm to avoid the collision from other moving obstacles. In this paper, we describe our test robot's system assembly and several experiments to confirm functions of our concepts for our future experimental research on autonomous ship navigation.

Keywords: autonomous ship navigation, land based test robot, unmanned vehicle control

1. Introduction

The unmanned vehicle technology has been investigated intensively for these years from a car to an aircraft and the development of unmanned ship is also being investigated by major shipping companies from the view point of being able to use them on commercial base. Although there are many aspects to be investigated for the development of unmanned ship technology,

autonomous navigation technology is one of the most important key aspects. The research on automated ship navigation and control is not so new^{1,2}, which were investigated intensively during 1980s in accordance with the advancement of modern control theories as well as the navigation tools like GPS etc.

Unmanned and autonomous navigation have to be elevating to a new level of research these days. At present, there published many papers related to the autonomous

navigation^{3,4}, most of them are based on the computer simulations or commercial simulators. In these simulations, taking into account all uncertainties which occur during the maneuvering of the ship is almost impossible.

The importance of experimental research on this field becomes more important than before because the uncertain incidents like malfunction of sensor or dynamics modeling errors are possible to cause major fatal accidents such as ship collision. So we need an experimental system which can simulate various real situations on the sea. In the near future, we will develop a tank test system using plural ship models.

As the cost of tank tests is not negligible, we developed a land robot whose systems are the same components with the tank test system as the first step of our research. In this paper, we introduce the concept of our test system and the modules we developed. We also explain the collision avoidance experiment which is introduced to check the assembled modules.

2. Components of the land robot system

The essential navigation systems are GPS, AIS, RADAR, and cameras. Every ship has GPSs to measure their global position. AIS is used to send the ship status to other ships. The ship status includes the position of the ship, velocity vector, ship name, ship size, ship’s country etc. On the sea, we can check the AIS information on the monitor of RADAR. RADAR is used to detect obstacles or ships around us to avoid collision. We use not only RADAR but also AIS information to avoid collision. If a ship is entering our possible collision zone, we communicate each other and one of us must change the speed and course. The velocity vector of AIS is very important information to calculate the relative position between ships in the near sea area.

To emulate these systems, we set up the modules as shown in Table 1 and Fig.1. We will explain each module.

2.1. Ultrasound coordinate detection module

In our land or tank experiments, we cannot use GPS because the experiments are in the room. So we decided to use ultrasound ranging sensors to detect the distance from 2 walls to calculate the coordinate in the test field.

Table 1. Correspondence of ship and land test robot modules

Real ship	Test robot
RADAR	Ultrasound ranging sensor With a servo motor
XBee	Wireless communication for AIS emulation
GPS	2 ultrasound ranging sensors
Camera	USB Camera

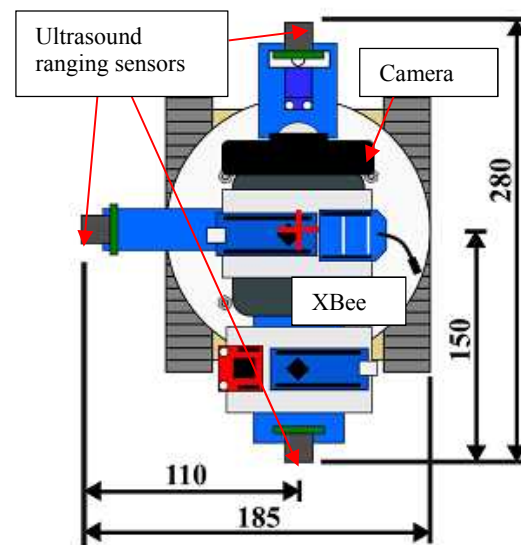


Fig. 1. Schematic view of the land test robot

2.2. Ultrasound collision avoidance module

This module emulates the RADAR of a ship. An ultrasound ranging sensor is attached to the front of the robot with a servo motor. By swinging it with a servo, we emulated a kind of front RADAR. Fig.2 shows a calibration result to verify this function. In Fig.2, upper image shows 2 obstacles, which are recognized successfully as shown in the lower graph.

2.3. Xbee module

AIS (Automatic Identification System) is very important for autonomous navigation algorithm. We implemented Xbee Series1 wireless serial communication module to emulate the AIS. A robot can broadcast its position and velocity to other robots as well as it can receive these information from others.

2.4. Camera image processing module

In the manned ship, the watch is very important. As for the unmanned ship, the image processing module will be used as the watch. We implemented a USB camera and are developing the collision avoidance program using OpenCV.

3. Experiments of the total system

The total system architecture is shown in Fig.3. The hardware modules are controlled by Arduinos. The main computer of the robot is a Raspberry Pi and the robot can be controlled or monitored through Wi-Fi from outside PC which emulates the computer of the control room where all the ships are monitored in land.

3.1. The mission of experiment

To develop the program which integrates each module, we made the mission of experiment as shown in Fig.4.

At first, the robot moves forward using its camera and ultrasound ranging RADAR. If the robot finds an obstacle by this RADAR and the distance from the obstacle becomes less than 10cm, the control mode changes to camera sensing mode. In the camera sensing mode, the camera image is processed to find a red object whose area is greater than a specific threshold value. If a red obstacle is confirmed, then the robot moves backward and turns 90 degrees left to avoid the collision to the obstacle. Then it keeps moving forward until it finds a wall and stops if the distance to the wall becomes 10cm.

3.2. The actuators

We will change the platform from this land based robot to a ship model in the near future. In this research, we hired crawlers as the actuator of the robot, considering its slow response in changing its heading angle. Usually, a ship's yaw motion response is not quick. That's why we didn't hire normal wheels.

3.3. The experimental result

The experimental field is as shown in Fig.5. The field is covered by 4 walls whose side length is around 1m, and the coordinate of the robot is measured by using 2 ultrasound ranging sonars which are attached to the left direction and the backward direction.

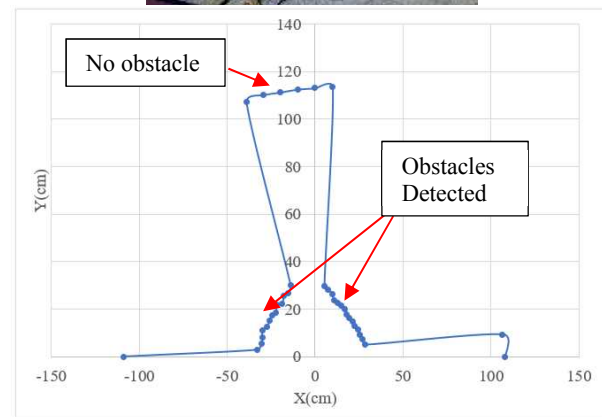


Fig. 2. RADAR emulated by a front ultrasound ranging sensor

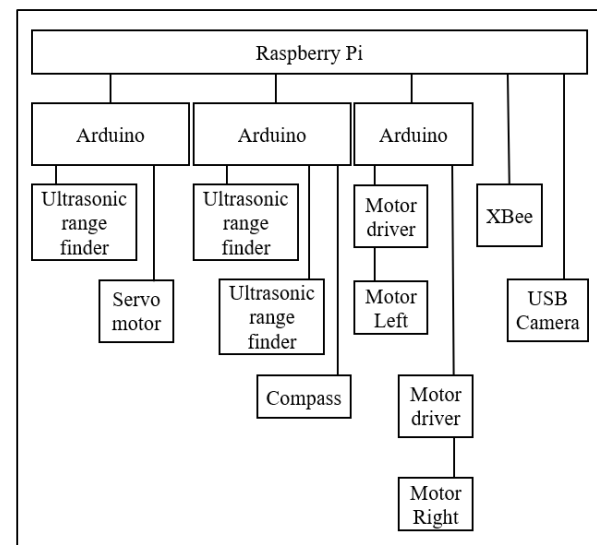


Fig. 3. The architecture of the robot

All the data were successfully transmitted from the robot to the monitoring PC by a Xbee module which emulates the AIS. We can also monitor the inner state of the robot and communicate through Wi-Fi connection.

Fig.6 shows the coordinate of the robot. The start point was around (87, 17). Then it moves parallel to the

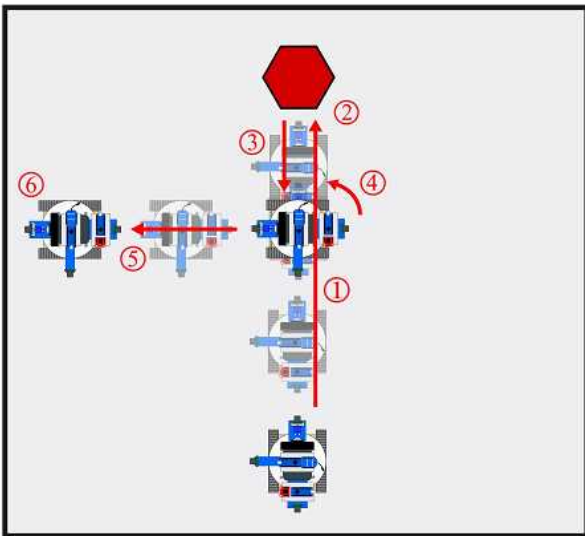


Fig. 4. Mission in experiment

Y-axis and found the red obstacle at around (80, 60). So it stopped and turned left then moved along parallel to the X-axis until it stopped around (12, 45), where the front sensor detected the wall to stop from 10cm distance.

4. Summary and future work

In this study, we developed a land robot which is supposed to emulate a ship model for our experimental research on autonomous ship navigation technology.

The essential navigation modules are GPS, AIS, RADAR and cameras. We emulated these modules by applying ultrasound ranging sensors, Xbee module, and USB cameras.

To confirm whether our system can work as we intended, we experimented the obstacle detection and avoidance test. The robot moves forward with measuring its coordinate and finding obstacles by the RADAR. When the robot finds an obstacle in front of it, then the image processing module is activated and if it finds a red obstacle, it turns 90 degrees left to avoid collision. Xbee module data communication as AIS emulation also succeeded. Although we still have several subjects to be improved, from the experimental result, all the modules we implemented functioned well as we intended.

We will fabricate more robots to develop the software for autonomous navigation algorithm. After brushing up the algorithm, we will transplant the system on several ship models to experiment in the tank.

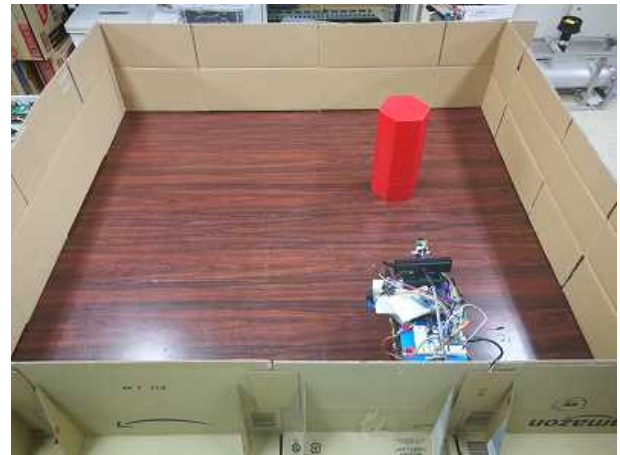


Fig. 5. The experimental field and the robot

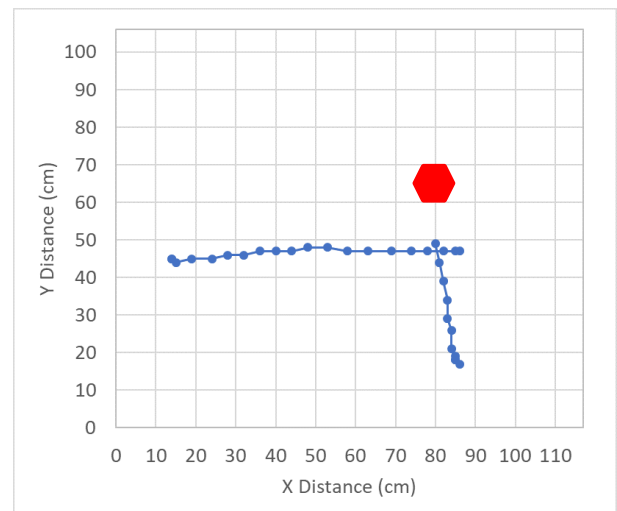


Fig. 6. The coordinate result of the experiment

References

1. K. Hasegawa, A. Kouzuki et al., Ship Auto-navigation Fuzzy Expert System (SAFES), *Proc. of the Society of Naval Architecture Japan*, vol.166 (1989), pp.445-452.
2. T. Koyama and K. Shimizu, Fundamentals of Automatic Harbour Maneuvering, *7th SCSS*, vol 3 (1984), pp.123-145.
3. Lloyds Register, *Cyber-enabled ships: Deploying information and communications technology in shipping – Lloyds Register's approach to assurance*. (2016).
4. Kongsberg, Automated Ships Ltd. and KONGSBERG to build first unmanned and fully-automated vessel for offshore operations. (2016) [Online]
5. Levander, O., Autonomous Ships on the High Seas. *IEEE Spectrum* (2017), Issue February.

Seafloor Image Color Enhancement Method based on Retinex model and Experiment Report in the undersea environment

Jonghyun Ahn

*Dept. of Human Intelligence Systems, Kyushu Institute of Technology
2-4 Hibikino, Wakamatsu, Kitakyushu, Fukuoka, Japan
E-mail: ahn@brain.kyutech.ac.jp*

Shinsuke Yasukawa

*Institute of Industrial Science, University of Tokyo
4-6-1 Komaba Meguro, Tokyo, Japan
E-mail: yskw@iis.u-tokyo.ac.jp*

Yuya Nishida

*Dept. of Human Intelligence Systems, Kyushu Institute of Technology
2-4 Hibikino, Wakamatsu, Kitakyushu, Fukuoka, Japan
E-mail: ynishida@lsse.kyutech.ac.jp*

Takashi Sonoda

*Dept. of Human Intelligence Systems, Kyushu Institute of Technology
2-4 Hibikino, Wakamatsu, Kitakyushu, Fukuoka, Japan
E-mail: t-sonoda@brain.kyutech.ac.jp*

Keisuke Watanabe

*Dept. of Navigation and Ocean Engineering, Tokai University
3-20-1 Orido Shimizu, Shizuoka, Shizuoka, Japan
E-mail: keisukejapan@gmail.com*

Kazuo Ishii

*Dept. of Human Intelligence Systems, Kyushu Institute of Technology
2-4 Hibikino, Wakamatsu, Kitakyushu, Fukuoka, Japan
E-mail: ishii@brain.kyutech.ac.jp*

Abstract

Underwater imaging is an important part to seafloor observation by underwater robot. Underwater robots provide many images, which contain seafloor environment, and these images contribute to various fields such as marine biology, marine geology and fishery science. However, underwater images has different properties, such as uneven illumination and light attenuation, compared to images which taken in air, and these properties impede image checking by researchers. In this paper we propose an image enhancement based on scale-gain Retinex, and the proposed method is experimented on the Suruga-bay in Japan.

Keywords: underwater imaging, underwater robot vision, seafloor image enhancement, seafloor observation

1. Introduction

Underwater Robotics is one of the solutions for observation sea environment. Recently, various underwater robots are developed to explore sea, and underwater robots provide seafloor images to researchers [1-3]. The obtained images by underwater

robots contribute to various fields such as marine biology, marine geology and fishery science. However, seafloor images have low visibility because of the light attenuation. The obtained images by underwater robots have properties such as uneven illumination and attenuated color by the light attenuation. These problems are shown in Fig.1.

© The 2018 International Conference on Artificial Life and Robotics (ICAROB2018), Feb. 1-4, B-Con Plaza, Beppu, Oita, Japan

Obtained image is taken by underwater robot: TUNA-SAND, and the many red snow crabs are contained in images. However, main colors of images are blue and green because red light is highly attenuated; left side of image looks dark because of light source in the intensity of image. These problems show attenuated color and uneven illumination, and these low visibility images are difficult to check whole area of seafloor images.

In this paper, we propose a seafloor image enhancement method, which can improve visibility of images, and the proposed method is experimented on Suruga-bay (Depth: 33m).

2. Proposed Image Enhancement Method

The proposed image enhancement method using Retinex theory [4,5]. The Retinex theory is a famous method to improve images against uneven illumination. In the Retinex theory, one image comprises reflectance factor and illumination factor. The equation of relation between reflectance factor and illumination factor is;

$$I_\lambda(x, y) = R_\lambda(x, y) \cdot L_\lambda(x, y), \quad (1)$$

where I denotes an image, λ is color space such as red space, green space and blue space in RGB color space, x, y are coordinates in image, R is reflectance factor and L is illumination factor from light source. R is the factor related real color, which is uninfluenced by illumination, of object. The illumination factor is estimated by Gaussian filter and the equation is;

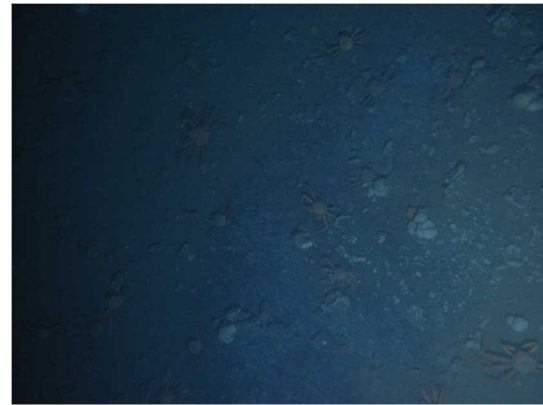
$$L_\lambda(x, y) = K \cdot \exp\left(\frac{-(x^2+y^2)}{\sigma^2}\right) * I_\lambda(x, y), \quad (2)$$

K is a normalization factor and σ is the standard deviation of the distribution. I and the estimated illumination log-transform, and estimated illumination is subtracted I .

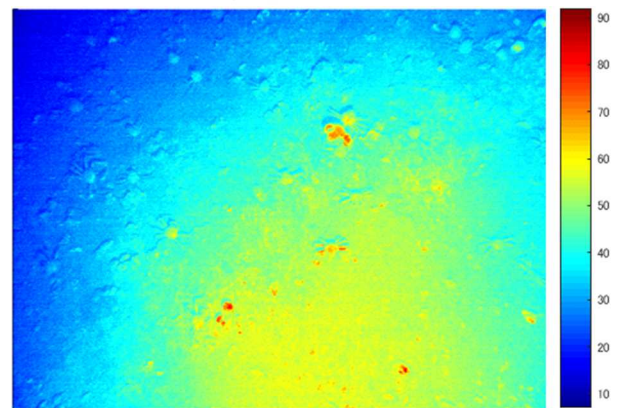
$$O_\lambda(x, y) = \alpha\{\log I_\lambda(x, y) - \log L_\lambda(x, y)\} + \beta. \quad (3)$$

O is Retinex output and α is scaling gain and β is offset parameter.

Recently, underwater image enhancement methods using Retinex are presented [6]. These methods show highly enhanced visibility of seafloor images. However, Retinex theory is not considered light attenuation in underwater environment, therefore the colors is not exactly same. Therefore, the underwater image enhancement method based on Retinex is necessary to



Obtained image by Underwater robot



Intensity of image

Fig.1. Example of underwater imaging problems by robot

restore color. But the each color intensity is normalized in processed image by Retinex, therefore it is difficult to restore color.

The proposed image enhancement method scale-gain Retinex, which presented by Kotera [7], is used. The scale-gain Retinex maintains the color factor in images, and only uneven illumination is improved. The estimated illumination in scale-gain Retinex is;

$$L(x, y) = K \cdot \exp\left(\frac{-(x^2+y^2)}{\sigma^2}\right) * Y(x, y), \quad (4)$$

Where Y is luminance of I . The scale-gain Retinex is don't use log-transform and it is;

$$O_\lambda(x, y) = A \frac{I_\lambda(x, y)}{L(x, y)}. \quad (5)$$

A is scaling gain.

As the process results of Retinex and scale-gain Retinex is shown in Fig.2.

The both images show even illumination compared to raw image in Fig.1. Processed image by Retinex show normalized RGB color (used parameter $\sigma:64$, $\alpha:256$, $\beta:128$); processed image by scale-gain Retinex show maintained RGB balance (used parameter $\sigma:64$, $A:80$). The proposed method combines the scale-gain Retinex with color attenuation model in water. In the proposed method scaling gain is;

$$P_{\lambda}(x, y) = \frac{A \cdot I_{\lambda}(x, y)}{\exp(-a_{\lambda} \cdot d) \cdot L(x, y) \cdot C_{\lambda}} \quad (6)$$

Where P is proposed method output, C is camera gain parameter of each color, a is attenuation constant and d is distance between seafloor and camera.

The proposed method based on the Beer-Lambert law [8] which attenuation model. The process result P is



Processed image by Retinex



Processed image by linear Retinex

Fig.2. Process results by Retinex and scale-gain Retinex

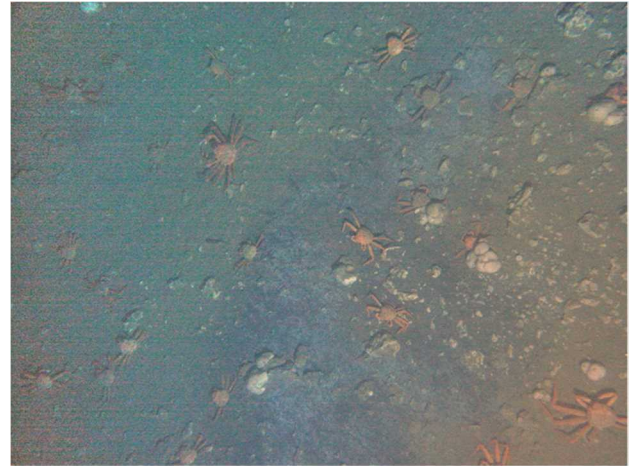


Fig.3. Process results by proposed image enhancement

shown in Fig.3.

We can check natural color in image in the Fig.3 compared to Fig.2, and even illumination.

3. Experiment in Suruga-bay

The sea experiment presents to check proposed image enhancement method. The concept of experiment is shown in Fig.4.

In the experiment, we sink the camera system which contains one camera and 2 light sources (LED array, 40W) and then the operator check the seafloor image via the cable on real-time. The experiment equipment, which contain camera and light, bring back seafloor sand to compare seafloor color values of photographed image and color value of sand in air condition.

The detail of system is shown in Fig.5. For the communication between ship and camera system, Power Line communication (PLC) is used, and LED1, 2 controlled by CPU via Arduino.

The photographed image, the sand image, which brings from seafloor, in air condition and processed result by proposed method are shown in Fig.6.

As the results, the averages each color value of sand image in air are red 47, green 49 and blue 44; the averages each color value of processed image by proposed method are red 70, green 67, and blue 68. The processed value show more high RGB values, but RGB balance show similar values compared to seafloor image.

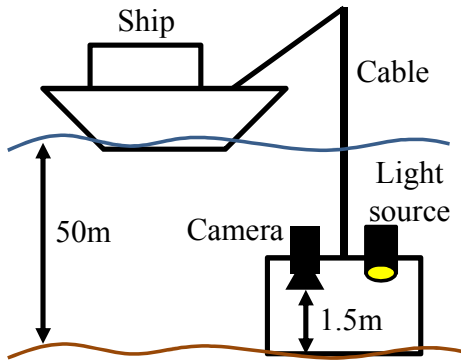


Fig.4. Concept of sea experiment

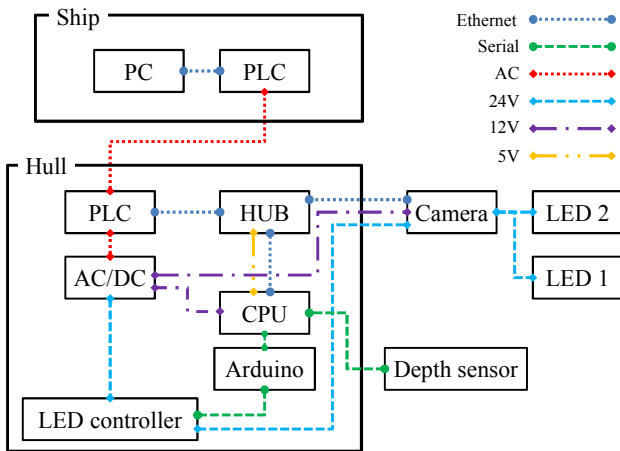


Fig.5. System of the experiment equipment

4. Conclusion

In this paper, we proposed image enhancement method using scale-gain Retinex and light attenuation model. As the result of experiment, we get similar RGB balance values; this result show possibility of color restoration of seafloor image. As the future work, we will apply proposed method to various colors image, and it is making easy to evaluation of color restoration.

References

1. T. Ura, "Observation of Deep Seafloor by Autonomous Underwater Vehicle." *Indian Journal of Geo-Marine Sciences*, vol.42, pp.1028-1033, 2013.
2. T. Nakatani, et al. "AUV TUNA-SAND and its Exploration of hydrothermal vents at Kagoshima Bay." *Oceans 2008-MTS/IEEE Kobe*, 2008.
3. K. Ishii, et al. "A New Tool to Access Deep-Sea Floor "Sampling-AUV".", *International Conference on Artificial Life and Robotics 2017*, pp.301-303, 2017.

© The 2018 International Conference on Artificial Life and Robotics (ICAROB2018), Feb. 1-4, B-Con Plaza, Beppu, Oita, Japan

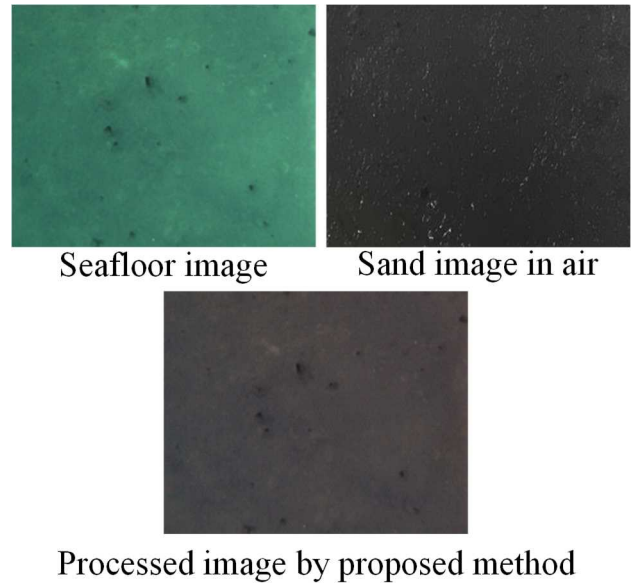


Fig.6. Process results by proposed image enhancement

4. E. H. Land, J. J. McCann. "Lightness and retinex theory," *Journal of the Optical Society of America*, Vol. 61, pp.1-11, 1971.
5. Z. Rahman, D. J. Jobson, G. A. Woodell, "Retinex processing for automatic image enhancement," *Electronic Imaging 2002, International Society for Optics and Photonics*, pp.390-401, 2002.
6. J. Ahn, et al. "Enhancement of deep-sea floor images obtained by an underwater vehicle and its evaluation by crab recognition." *Journal of Marine Science and Technology*, vol.22, pp1-13, 2017
7. H. Kotera and M. Fujita, "Appearance improvement of color image by adaptive scale-gain Retinex model," *10th Color Imaging Conference*, pp.166-171, 2002.
8. H.R. Gordon, "Can the lambert-beer law be applied to the diffuse attenuation coefficient of ocean water?," *Limnology and Oceanography*, vol. 34, no. 8, pp. 1389-1409,1989.

Simulation of Horizontal Vibration Suppression of a Suspended Structure for Seabed Mining

Keisuke Watanabe

*Department of Navigation and Ocean Engineering, Tokai University, 3-20-1 Orido Shimizu-ku
Shizuoka, Shizuoka, 424-8610, Japan*

Kazuo Ishii

*Department of Intelligence Systems, Kyushu Institute of Technology, 2-4 Hibikino, Wakamatsu-ku
Kitakyushu, Fukuoka, 808-0196, Japan
E-mail: keisuke@tsc.u-tokai.ac.jp, ishii@brain.kyutech.ac.jp
www.u-tokai.ac.jp*

Abstract

In a project of subsea mining in the near future, many work class robots such as crawlers, drilling machines, or ore collectors will be installed on the seabed. These robots are heavy but they must be landed on the seabed very softly to avoid impact damage from the seabed. So the installation method is very important and effective installation method should be investigated. In this paper, we examined vibration motion of a suspended heavy machine by a crane vessel through dynamics modeling and simulation in the horizontal plane. Descending speed of the machine affects the amplitude of the vibration, that is, if the descending speed is higher, larger amplitude will be observed. To suppress this vibration, we examined a velocity feedback control by attaching a thruster to the machine. From simulation results, we found horizontal vibration will be effectively suppressed by using simple feedback control.

Keywords: subsea mining, installation of subsea machines, control of suspended structure

1. Introduction

The mineral resource on or under the seabed has been told it will improve Japanese self-sufficiency of mineral resource. However, there had been no project realized due to two reasons. One reason is a technical issue that there hasn't been mature technology to develop the underwater deposit. The other reason is the project hasn't been profitable because subsea mining needs much more amount of investment than the land based project. Only recently these situations are changing better because many subsea oil production projects made technologies advanced and cheaper. So the subsea mining project will be possible to realize in the near future. As the offshore oil development has been flourished for these 20 years, the subsea production system have been fully matured

through the experience of many ultradeep projects worldwide. For example, Subsea production system (SPS), also named as 'subsea tie-back' (SSTB) or subsea, consists of subsea wells, subsea processing facilities, subsea flowlines, subsea controls, and surface Host, has capability to produce oil & gas without an offshore structure straightly up the subsea wells. A typical Subsea production system is shown as following Fig.1.

Subsea processing facilities, including manifolds, metering, separators, boosters, and subsea pumps e.g. extend the capabilities of subsea system, allows deeper water exploration, more wells producing and longer distance tie-back.

Subsea flowlines and risers, to transport the production flow to downstream process facility like surface host platforms, could be rigid pipes or flexible pipes. The water depth of the development becomes

© The 2018 International Conference on Artificial Life and Robotics (ICAROB2018), Feb. 1-4, B-Con Plaza, Beppu, Oita, Japan

deeper, and in some field like offshore Brazil pre-salt, the target water depth is generally more than 2000m.

In these projects, as the oil price were high, they can invest much money. But in the subsea mining project, we can't expect such investment as oil/gas development, so we need to investigate how we can minimize the total project cost more strictly than the oil/gas field^{1,2}.

In this research, we considered a possibility of using active control technique for deep water installation using a crane vessel³. The module or structure consists of a pendulum system whose arm length is becoming longer as the suspended structure is going down to the sea bed. An initial offset angle from the vertical axis will cause a vibration motion whose horizontal amplitude develops according to time during installation. Two dimensional equation of motion is derived and several simulation results will be shown for the cases of both free suspended situation and actively controlled situation. The control algorithm is LQR and a ROV is assumed attached to the structure as an actuator to suppress the vibratory motion to install the structure on the desired target point on the sea bed.

2. Derivation of the equation of motion

The coordinate system is shown in Fig.2. The module structure is supposed to be suspended from a crane on the vessel. The offset angle from the vertical axis is a parameter of the nonlinear pendulum motion of the structure.

It is assumed that the crane cable is paid out from the initial length l_0 [m] with the velocity of v [m/s]. The initial length corresponds to the height from the initial submerged point of the structure to the suspended point of the top of the crane arm. In this research, the force displacement excitation on the top of the crane arm due to wave induced motion of the vessel was not taken into consideration, the excitation is assumed forced oscillation by harmonic vibration of the angle of the cable.

The Lagrangian is, using the cable length $l(t)$,

$$L = T - U = \frac{1}{2}m(\dot{l}^2 + l^2\dot{\theta}^2) + mgl \cos \theta \quad (1)$$

Considering the added mass and fluid resistance force, the equation of motion of the pendulum system is,

$$(1 + C_m)m l^2 \ddot{\theta} + \left(2mlv + \frac{1}{2}\rho C_d A l\right)\dot{\theta} + mgl \sin \theta = f \quad (2)$$

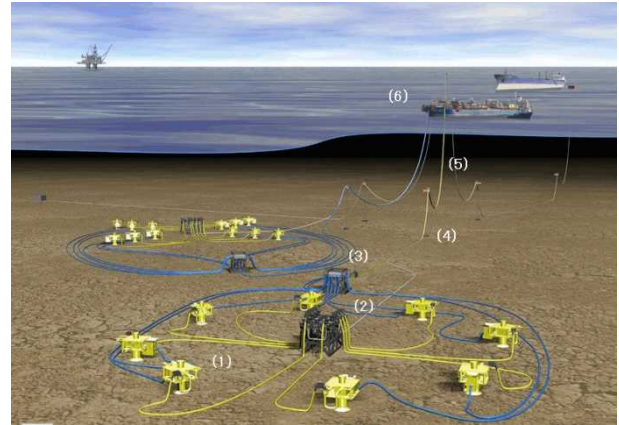


Fig. 1. Schematic View of Subsea Production System. (1) Subsea wellhead & trees, (2) Subsea manifold, (3) Subsea umbilical termination units, (4) Subsea flowlines, (5) Umbilicals & Risers, (6) HOST

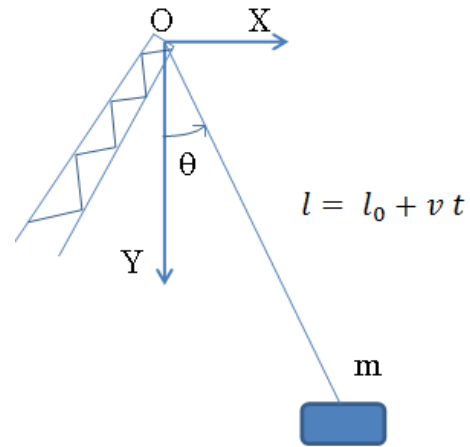


Fig. 2. Coordinate System of the Suspended Structure.

, where, f is the control force.

3. Simulation for free suspended situtaion

The analytical solution of the next free oscillatory motion becomes Bessel function in accordance with a parameter $l\theta$.

$$(1 + C_m)m l^2 \ddot{\theta} + \left(2mlv + \frac{1}{2}\rho C_d A l\right)\dot{\theta} + mgl \sin \theta = 0 \quad (3)$$

We made a simulation program using MATLAB with coding 4th order Runge-Kutta ODE solver which can be considered the effect of feedback force.

The simulation is using next parameters. The structure size is 5m wide 5m long 4m height. The mass is assumed 50tf. The water depth is assumed as 2500m. The initial offset angle is 20 deg. The paid out rate of the cable are 2 cases, which is 1m/s and 0.5 m/s. Added mass coefficient is assumed 1.0, whereas drag force coefficient is assumed as 3.0.

The simulation result of the paid out rate of the cable is 1.0m/s is shown in Fig.3. The horizontal displacement which means the fluctuation from the desired installation point is shown in Fig.4. As Fig.3 shows, the offset angle is decreasing according to time, which is due to damping effect of fluid resistance force. However, as the crane cable length is increasing, the horizontal offset from the desired point is developing. We assumed the drag coefficient higher assuming that some damping device is attached to the structure. But from the result shown in Fig.4, it seems very difficult to reduce the offset vibration amplitude only using passive fluid damping force.

To see the effect of cable paid out rate, we examined another simulation where the cable rate is 0.5m/s. If the paid out rate is slower, we can expect the offset becomes slower, whereas installation time becomes longer, which will cause higher operational cost.

Fig.5 shows the offset angle fluctuation when the cable speed is 0.5m/s. Compared to the result of $v=1.0\text{m/s}$, this result shows if the cable paid out rate is smaller, then the fluctuation amplitude is possible to be suppressed. Thus if we need to put the descending speed higher to reduce the installation time, it might be possible that the suspended structure's oscillatory motion becomes larger, which will cause degradation of installation accuracy.

As Fig.5 shows, if the descending velocity is set to lower, the horizontal displacement amplitude is still around 40m due to very long cable length.

Fig.6 shows the amplitude comparison between different cable paid out rate and the time taken from sea surface to sea bed. There is a trade-off relation between the installation speed and the natural offset amplitude around the desired installation point. These results show some new technique are to be deployed for more cost effective and precise, safer installation.

4. Simulation of LQR controlled installation

We considered LQR optimal control algorithm in this research. Because the EOM is non-linear, linearized EOM is used as a nominal model for control gain computation.

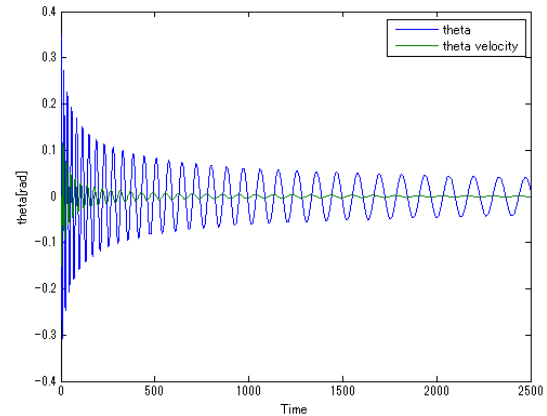


Fig. 3. Angle and Angular Velocity of the Pendulum Motion $v=1\text{m/s}$.

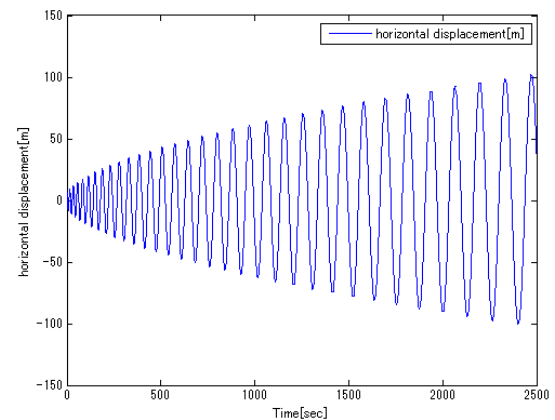


Fig. 4. Horizontal Amplitude when $v=1\text{m/s}$

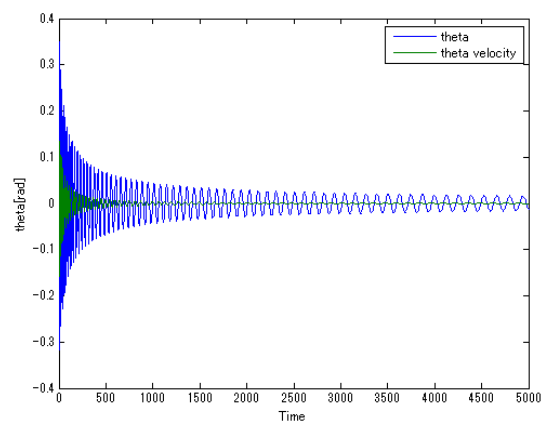


Fig. 5. Angle and Angular Velocity of the Pendulum Motion $v=0.5\text{m/s}$.

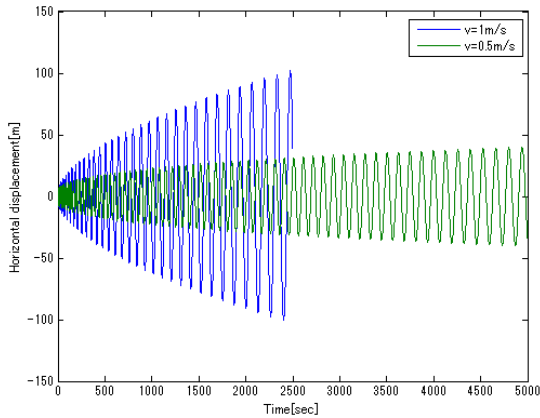


Fig. 6. Comparison of Horizontal Displacement

The cable length is time variant, however, in the nominal model for controller design, we fixed the cable length 1000m as the representative value for linearization. The simulation is done by using non-linear EOM, where the control force is calculated using the linearized LQR model. As the typical ROV thrust force is less than 7000N, the feedback gain is adjusted the maximum thrust force becomes less than 7000N.

Fig.7 shows the controlled horizontal displacement when the descending speed is 1m/s. These results indicate that the control feedback works very well to suppress the self-vibration of the structure. The offset from the the desired installation point is only 6m around, which means the very precise installation of the structure on the sea bed can be achievable. Fig.8 shows the control force result. The control force is less than 7000N and seems feasible using existing ROV as an actuator.

5. Summary

We investigated the possibility of applying active control to installation of subsea modules supposing subsea mining project in the near future. The suspended structure consists of a pendulum system with a crane vessel whose oscillation amplitude is affected by the descending speed of the structure. From our two dimensional simulation, we found if the descending speed is faster, then the oscillatory motion near the seabed becomes worse. However, if we deploy a ROV as an actuator for actively controlled installation, it is possible to suppress the oscillatory motion effectively.

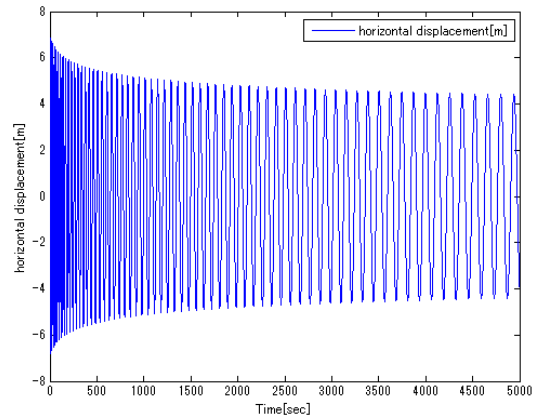


Fig. 7. Horizontal displacement in controlled case

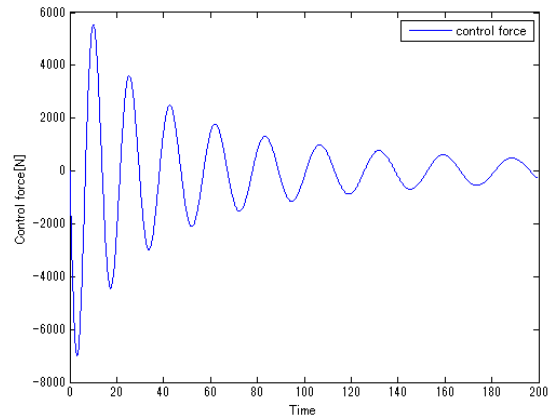


Fig. 8. Control force estimation

References

1. Watanabe Y., Watanabe K, et al., “A Self-Walking Vertical Mining System Concept Using DTH for Seafloor Mining and Its Preliminary Design”, OTC-27003-MS, *Offshore Technology Conference* (2016)
2. Watanabe K., Watanabe Y, et al. “A Self-Walking Vertical Mining System Concept Using DTH”, OTC-25825-MS, *Offshore Technology Conference* (2015)
3. Watanabe K., “A Possibility of Active Controlled Installation for Deep Water Subsea Production Modules”, *IEEE, ICETET2012*,(2012)

Analysis of Team Relationship using Self-Organizing Map for University Volleyball Players

Yasunori Takemura

*Nishinippon Institute of Technology, 1-11 Aratsu Kanda
Miyako, Fukuoka 800-0344, Japan**

Kazuya Oda

*Kyushu Institute of Technology, 2-4 Hibikino Wakamatsu
Kitakyushu, Fukuoka 808-0896, Japan*

Michiyoshi Ono

*Nishinippon Institute of Technology, 1-11 Aratsu Kanda
Miyako, Fukuoka 800-0344, Japan†*

E-mail: takemura@nishitech.ac.jp, oda-kazuya@edu.brain.kyutech.ac.jp, s148414@nishitech.ac.jp

Abstract

In Japan, sports efforts are actively being carried out to host the 2020 Olympic games. Especially in the field of sports science, researches on ergonomics, development of sports equipment and pattern recognition technology using artificial intelligence are actively researched. In previous research, we developed a clustering algorithm for positioning adaptation and relationships in team sports using Self-Organizing Maps in university rugby players. However, I have not yet confirmed whether the developed algorithm can be applied to other team sports. For this reason, we applied the same algorithm to an university volleyball player. Then, as an algorithm, we verify whether it can be generally used for team sports.

Keywords: Self-Organizing Maps, pattern recognize, sports science

Introduction

In Japan, sports efforts are actively being carried out to host the 2020 Olympic Games. Especially in the field of sports science, researches on ergonomics, development of sports equipment and pattern recognition technology using artificial intelligence are actively researched. The budget of Japanese sports in 2016 is 32.4 billion yen, and considering that the budget for 10 years ago was 19 billion yen, it is doubling momentum.

By the way, victory or defeat in team sports depends on each player's individual technique, physical strength, and

psychological condition. Similarly, it can be said that the suitability of an individual to a certain position in the team affects the team's performance [13].

In previous research, Barry and Cureton [1], Nicks and Fleishman [2], Larson [3], McCloy and Young [4] and others clustered physical features and conducted factor analysis in investigating sports performance. In Japan, Tokunaga studied the diagnosis criteria for athletic adaptation (i.e., suitability) in sports [5]. These works showed that physical features are one of the strongest factors determining athletic adaptation. However, Matsuda [6] showed that an athlete, no matter how good

his/her physical features, is not athletically suited to team sports without having good motivation in terms of setting goals and training. That is to say, for an individual or team to be successful, a player needs to have both good physical features (e.g., techniques, balance, height, and weight) and good psychological features. For example, Saijo [7] presented the psychological features of Japanese and New Zealand rugby players.

In this way, the suitability of a player in a certain position and the relationships between different positions in team sports are related to physical and psychological features. As it stands now, a coach or selector decides the player suitability and relationships between positions him/herself. However, does it follow that good decisions are made? Previous research has not clarified athlete adaptation to positions and relationships between positions considering both physical and psychological features[8].

In the present study, we develop a clustering algorithm for positioning adaptation and relationships in team sports. We consider the two main types of features, which are physical and psychological features, and introduce the concept of using an algorithm to cluster player features in team sports. In previous works, we developed clustering algorithm using SOM for team relationship map [8,9]. Previous work is adapted in university rugby players. However, I have not yet confirmed whether the developed algorithm can be applied to another team sports. For this reason, we applied the same algorithm to our volleyball players. Then, as an algorithm, we verify whether it can be generally used for team sports.

Research plan and method

Selection of sport

We apply a team-sport clustering algorithm to volleyball. Volleyball is selected because a volleyball team is one of the most necessary cooperative works and interaction between a player and teammates.

The text is to be typeset in 10 pt Times Roman, single spaced with interline spacing of 13 pt. Text area (excluding running title) is 6.75 inches across and 8.8 inches deep. Final pagination and insertion of running titles will be done by the publisher, so make sure that no page numbers are given in your paper and only the running titles provided in this template (authors' names and paper title) are used.

Describe the physical data and analysis using statistics

Physical data of members of the N university volleyball team were recorded in 2016 December. The N university volleyball team comprised 22 students. There were 3 RTs, 6 LTs, 7 CNTs, 2 STs and 4 LBRs. Physical features recorded were height [cm], weight [kg], grasping power (left hand, right hand) [kg], ante flexion [cm], toe touch [cm], jumping side to side [times], standing long jump [cm], 9 meters dash (3 round trips) [seconds], vertical jumping [cm], and back muscle strength [kg]. The data set thus had 11 physical dimensions. Data showing statistically characteristic results could be shown below. It shows the adaptation result of the position derived from the data.

Figure 1 shows the height data. The horizontal axis denotes individual positions. The vertical axis shows the height [cm].

As you can see from the Fig.1, LT, RT and CNT show that players with relatively high stature are selected, and ST and LBR can be said that it is not necessary to be a player with a high height. This shows that the height of LT, RT and CNT is required as an attack such as attack.

Figure 2 shows the result of jumping side to side. The vertical axis shows the how many times they can do [times]. The horizontal axis denotes individual positions. As you can see from the Fig.2,

It shows that only CNT shows a large value. In other words, it can be seen by looking at this figure that the reflexes are necessary for the CNT position. In this way, the suitability of the position can be understood by analyzing several items statistically, but in many items there is not a big difference, it is impossible to decide suitability of the position unconditionally. Also, since the number of population is different as statistical data, it is difficult to find the suitability of the position only by comparing statistical data unconditionally.

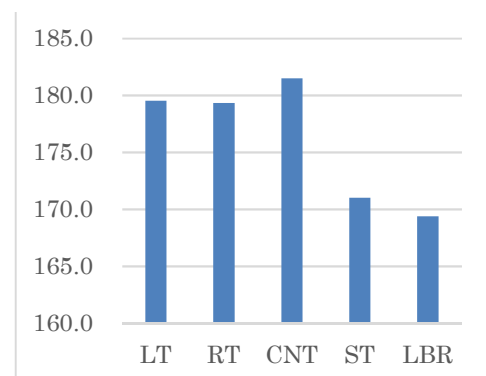


Fig.1 Heights of volleyball players (N university 2016 data)

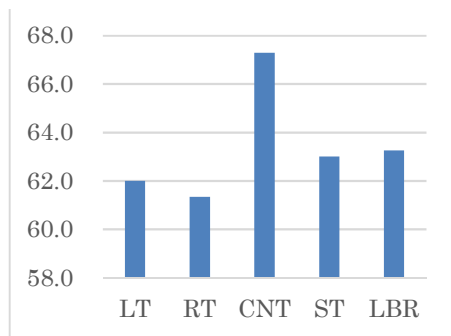


Fig.2 Jumping side-to-side result of volleyball players (N university 2016 data)

Describe the psychological data and analysis using statistics

Psychological data of members of N university volleyball club were recorded in 2016 December. The N volleyball club in 2017 comprised 22 students (There are same members as physical data).

Psychological features measured were those of the Diagnostic Inventory of Psychological Competitive Ability for Athletes (DIPCA.3) [8]. DIPCA.3 measures 12 types of psychological ability in a 48-item questionnaire. DIPCA.3 is often used before mental training, because it reveals athletic strengths and weaknesses. The DIPCA.3 check sheet consists of 48 questions that measure psychological ability and four questions that measure reliability. These questions have already been analyzed by good-poor analysis (G-P analysis), and the answers provide 12 criteria relating to five factors. The factors are motivation in sport, mental stability and concentration, confidence, operation capability and cooperativeness. Additionally, we measure the reliability of the answers by comparing answers to similar questions. To examine these factors in detail, 12 criteria are described. Motivation in sport consists of four criteria: endurance, fighting spirit, self-realization motivation and motivation to win. Mental stability and concentration consist of three criteria: the ability to relax, capacity to concentrate and self-control. Confidence consists of two criteria: determination and confidence. Operation capability consists of two criteria: predictive capability and judgment. Cooperativeness has only one criterion, which is simply described as cooperativeness. DIPCA.3 provides a total score (ability). Each criterion is scored, and the score of each factor is the sum of scores for the related criteria. The total score is calculated by summing the score for each factor. Table I gives the total scores, which are classified into five levels. A classification of 1 indicates a very low overall mental ability and a classification of 5 indicates a very high ability. Each mass describes the total score. The

methodology of DIPCA.3 is such that each person answers the 52 questions on a scale of 1 to 5 (1: I don't think so, 2: I rarely think so, 3: I sometimes think so, 4: I often think so, 5: I always think so) within 10 to 15 minutes.

Figure 3 shows the evaluation result of DIPCA.3. The horizontal axis denotes each evaluation criteria. The vertical axis shows evaluation value. Each evaluation maximum value is 20 [point]. The color bars describe the each position (LT, RT, CNT, ST, and LBR).

Comparing the psychological feature quantities, we can see that there is little difference between the positions. On the whole, however, RT knows that athletes with very psychological characteristics are selected. Moreover, as a whole, the ability as fighting spirit, self-realization and motivation to win is high in the team as a whole. Meanwhile, items such as confidence, deamination, endurance, and judgment need to be lowered in capability as whole team members.

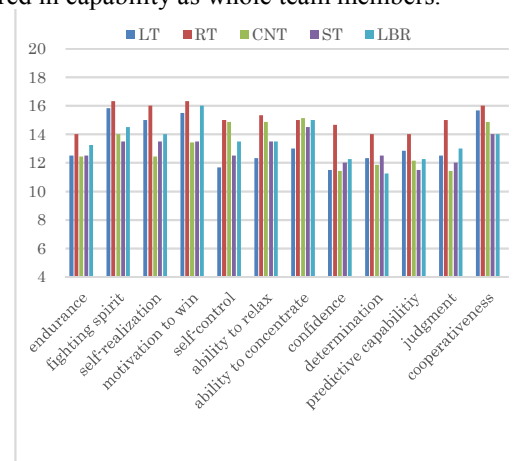


Fig.3 Psychological Result using DIPCA.3 (N university 2017)

Experimental Result

To evaluate the performance of the SOM algorithm, individually, at first, only x input data sets (only physical data sets) are used same as previous works[8]. Figure 4 shows the feature maps used for the 2017 physical data sets. Each lattice cell describes a unit. If a unit is the BMU for a data set, it is labeled as such as 1 line: number of player and 2nd line: position). The color of the lattice indicates the Euclidian distance to the neighboring unit (only fig.4) and figs.5 and 6 are described vector values. For example, blue indicates that the neighboring unit is nearby; red indicates that it is far away (Figs.5 and 6 are high score), and green indicates that it is at mid-distance (Figs. 5 and 6 are low score).

Fig.4 shows the feature map of physical data. For example, on the left side of the feature map, attack role people is gathered. On the other hand, right side is

gathered to defensive position people and ST position. Figure 5 shows the same feature maps, however, the color label describe about the height. Looking at this figure, high-height (red labeled) players are gathered on the left side, and players with relatively low height are gathered on the right side. That is, the same result as statistical data can be obtained also in the feature map using SOM. Next, Fig. 9 shows the results of coloring the results of jumps side to side. The jumps side to side does not have a relatively large difference. However, it turns out that the CNT person shows a relatively high numerical value (green). In this way, similar results to statistics can be found in SOM feature map. However, the suitability of the position within the team was not able to obtain distinctive results even if examining other items.

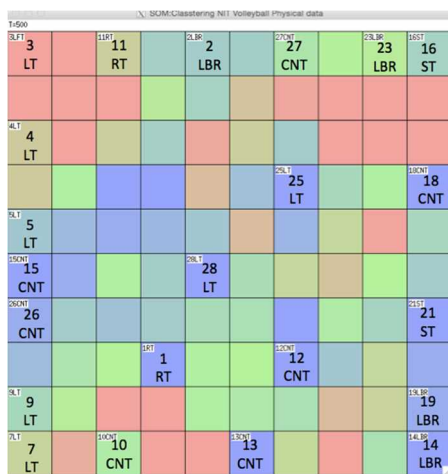


Fig.4 the feature maps which is inputted physical data sets

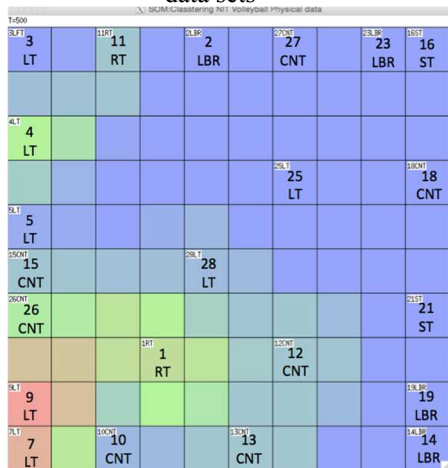


Fig.5 the feature maps of physical data sets which is colored by height data

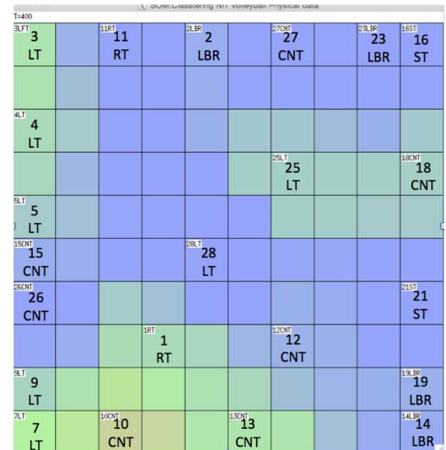


Fig.5 the feature maps of physical data sets which is colored by jump side to side

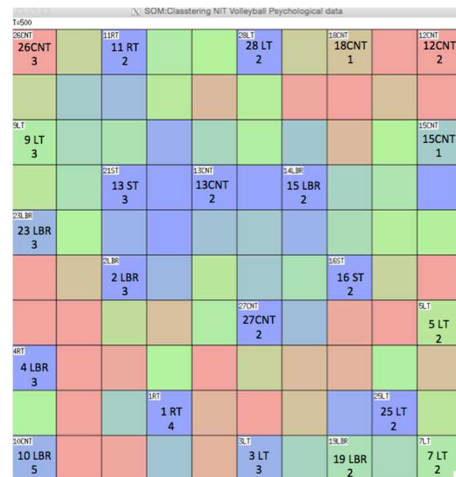


Fig.6 the feature map of psychological data sets result

Second, we input y data (psychology data sets). Figure 6 shows the feature map which is inputted psychological data sets. Each lattice cell describes a unit. If a unit is the BMU for a data set, it is labeled as such as 1st line: number of player and position and 2nd line: total score evaluation (1: low level to 5: high level using DIPCA.3 statistics result). In this figure, right up side is gathered to low-level players. On the other hand, left bottom side is gathered to high-level people. Therefore, players in the upper right corner of the map are mentally immature players and need mental training. On the contrary, many of the players belonging to the lower left are elected regular members, and the director also knows that they consider mental reach. In addition, because mental elements are still being analyzed, we will explain the details in the conference.

CONCLUSIONS

In this paper, we adopt team relationship clustering algorithm using SOM for volleyball team players. In previous works, we adopt team relationship clustering algorithm using SOM for university rugby players [13,14]. However, I have not yet confirmed whether the developed algorithm can be applied to another team sports. For this reason, we applied the same algorithm to our volleyball players.

In previous research [8,9], We succeeded in electing the position of the rugby players using the physical data sets. From the psychological data sets, we were able to find out what kind of people the regular members are. In addition, if two data groups are used comprehensively, the suitability of positioning and the selection of regular members were possible. In this paper, we confirmed whether we can obtain the same knowledge as statistical data by using physical data group according to the method. We also examined whether statistically similar results can be obtained for psychological data group as well. In the future, we need to analyze the suitability of the position and the relationship with the company. We also plan to analyze integrated physical data group and psychological data group.

In addition, as a future task, it is necessary to consider a method for general use because there is a difference in results, compared with the result of the clustering in the rugby player performed in the preceding research [13,14] and the result of the volleyball player.

Acknowledgement

This work was supported by a Grant-in-Aid for Young Scientists (B) 15K21570 from JSPS KAKENHI.

References

1. Barry, A.J. and T.K. Cureton, "Factor Analysis of Physique and Performance", *Res. Quart.*, 23-3:100 ~ 108, 1961
2. Nick, D.C. and E.A. Fleishman, "What Do Physical Adaptation Test Measure?," *A Review of Factor Analysis Studies, Educational and Psychological Measurement*, 22-1:77-95, 1962
3. Larson, L. A., "A Factor Analysis of Motor Ability Variables and Tests for College Men," *Res. Quart.*, 12: 499-517, 1941
4. Mcloy, C.H. and R.D. Young, " *Test and Measurement in Health and Physical Education*", New York, Applenton-Century-Crofts, Inc., pp.51-65, 1954
5. Tokunaga, "Factor Analysis about sports adaptation", *Japan Journal of Physical Education, Health and Sport Sciences*, Vol.22-2, pp.71-80,1977
7. Matsuda, R.N. Singer, " *Motor learning and human performance*", ISBN978-4-469-26119-6, Taishukan-shoren, 1986, In Japanese
8. O.Saijo, K.Suda, et., al., "On the Psychological Aptitude of Rugby Foot Ball Players –From Comparison New Zealand University Selected Team with Nippon College of Physical Education Team –", *Journal of Nippon College of Physical Education*, Vol22-2, pp.135-138, 1993
9. Y.Takemura, M.Yokoyama, S.Omori, R.Shimosaka, "Evaluation and Analysis of Relationship between Roles and Individual's Role Adaptation in Team Sports using SOM ~1st Report Data Analysis and Introduction of Theory", In: Cho Y., Matson E. (eds) *Soft Computing in Artificial Intelligence. Advances in Intelligent Systems and Computing*, vol 270. Springer, Cham
10. Y.Takemura, "Development of SOM algorithm for Relationship between Roles and Individual's Role in Rugby ~2nd Report : University Rugby teams analysis using physical data and Psychological data", *International conference on Artificial life and Robotics (ICAROB2017)*, pp.412-415, Miyazaki, 2017

© The 2018 International Conference on Artificial Life and Robotics (ICAROB2018), Feb. 1-4, B-Con Plaza, Beppu, Oita, Japan

Optimization for Line of Cars Manufacturing Plant using Constrained Genetic Algorithm using Constrained Genetic Algorithm

Keiji Kamei*

*Department of Production Systems, Nishinippon Institute of Technology, 1-11 Aratsu
Kanda, Miyakogun, Fukuoka 800-0394, Japan†*

Takafumi Arai

*Nissan Motor Kyushu Co. Ltd., 1-3 Shinhama-cho
Kanda, Miyakogun, Fukuoka 800-0395, Japan
E-mail: kamei@nishitech.ac.jp
www.nishitech.ac.jp/~kamei/*

Abstract

Recently, improvement of production efficiency on cars manufacturers is required. However, that improvements under existing circumstances are depending on experience and intuition by workers. We propose to objectively and efficiently improve a production line based on a GA. The difficulty of applying a GA is the number of racks and boxes is predetermined, and so we apply constrained GA. The results of simulation for virtual production line show that our proposal succeeded in reducing about 10 seconds per car compared with random positioning.

Keywords: Constrained Genetic Algorithm, Plant Optimization, Industrial Application, Car manufacturing

1. Introduction

Recently, improvement of production efficiency on cars manufacturers is required owing to increasing of demands in developing countries¹. On the other hand, that improvements under existing circumstances are depending on experience and intuition by workers at a production line. To overcome this situation, we propose to objectively and efficiently improve a production line without depending on experience and intuition. The production line of candidate for optimization is “Picking up assemblies” area, so that our aim is to optimize the positions of racks and boxes for assemblies. The difficulty of optimization of “Picking up assemblies”

area is that the number of racks to put assembly boxes and that boxes is predetermined.

Our optimization problem is similar to several path planning problems such as “Traveling Salesman Problem (TSP),” “Minimum Spanning Tree problem(MST).” Workers pick up assemblies while they goes back and forth between racks and an AGV. Accordingly, our optimization problem becomes synonymous with minimization of total length of moving path of a worker. The difference between path planning problems and our problem is that positions of waypoints for path planning problems are fixed; on the other hand, our problem changes positions of waypoints that are racks and boxes.

Since the number of racks and boxes is predetermined as mentioned, our approach has to put

*In 2007 he obtained his PhD at the Department of Brain Science and Engineering, Kyushu Institute of Technology. From April, 2007 to March, 2014, he was a lecturer. Since April, 2014, he has been an associate professor, Nishinippon Institute of Technology.

predetermined number of racks and boxes into a production line. For this, there is also a problem of “Knapsack Problem(KP)” in our optimization problem. It can be said that our optimization problem combines TSP, MST and KP for the reasons stated above.

To overcome difficulties, we propose to apply a Genetic Algorithm(GA)² to optimization for positions of racks and boxes. A GA is suitable for global search in a high dimensional space because a GA has also the ability of probabilistic random search based on genetic operations in addition to local search. A GA has many individuals(populations), and an individual has a chromosome that cords the parameters for optimization. Optimization processes are on the basis of genetic operations, i. e., selection, crossover and mutation. A process of crossover and mutation does not be constrained because parameters for optimization in a chromosome are independent in each; therefore, generated parameters of optimization are able to take all values within a set condition. By contrast, parameters of optimization in our problem are dependent on each other because the number of racks to put assembly boxes and that boxes is predetermined. Consequently, we are not able to apply a conventional GA to optimization. For this, we apply a “constrained GA” to optimization for positions of racks and boxes in a production line.

The details of our constrained GA are below. Gene loci correspond to racks and boxes positions in a constrained GA. Selection process in genetic operations is same way as a conventional GA. In crossover process, loss or duplication of some racks and boxes will occur. The way of adjustment of the number of racks is that all of duplicative racks are deleted then missing racks are randomly inserted to those positions. Mutation process for racks is executed after the adjustment of crossover process. Mutation process in a constrained GA changes gene loci in order to meet the conditions for the number of racks. Crossover and mutation process for positions of boxes in racks is executed after crossover and mutation process for racks. Crossover process for boxes is executed on the same stage each other, e.g., boxes in top stage of a rack are changed with boxes in top stage of another rack. In mutation process, genes for boxes are mutated randomly as same as a conventional GA in first. Following that, excess boxes are randomly chosen, then those boxes are deleted. Subsequently, shortfall in boxes are inserted randomly to meet the conditions for the

number of boxes. From a constrained GA in above, our proposal is able to meet the conditions for our optimization problem.

The results of simulation for virtual production line show that our proposal succeeded in reducing about 10 seconds per car compared with random positioning.

2. Virtual Environment of Production Line

We construct a virtual environment of production line to validate the effectiveness of our proposal. Table 1 shows the conditions for virtual environment, and Table 2 shows the number of assembly boxes for each car.

Table 1. Conditions of virtual environment. Length unit is millimeter.

Kinds of Rack(Length)	3(1000, 1500, 2000)
Stages in a Rack	3(Top, Middle, Bottom)
Kinds of Assembly Boxes	3
Length of a Line	15000
Distance of AGV and Racks	1500
Moving Speed of AGV	200[mm/s]
Walking Speed of a Worker	2000[mm/s]
Number of racks	1000×3, 1500×4, 2000×3
Types of Cars(Car names)	4(Car1, Car2, Car3, Car4)
Mixing Rate of Cars in Productions	Car1:0.5, Car2:0.25, Car3:0.15, Car4:0.1

Table 2. Number of assembly boxes for each car. “300”, “600” and “1000” correspond to width of assembly boxes. Width unit is millimeter.

	Width of assembly boxes		
	300	600	1000
Car1	15	4	2
Car2	15	3	1
Car3	10	3	1
Car4	10	0	1
Shared	30	5	5

A worker in virtual environment picks up the all of assemblies which correspond to a designated car in the Table 2. Besides, 20 shared assemblies are randomly designated from the all of shared assemblies.

The Fig. 1 shows the bird’ s-eye view of an example of virtual production line. The condition in that figure is initial state of picking up assemblies.

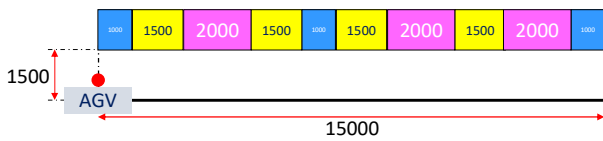


Fig. 1. Bird's eye view of an example of virtual production line. Values are distance and size of rack. Unit is millimeter. The red circle indicates a worker. The blue, yellow and magenta squares correspond to 1000, 1500 and 2000 size of racks, respectively.

A worker goes back and forth between racks and an AGV. An AGV moves at a constant speed on a lane. Consequently, it is safe to say that this optimization problem is same as minimization of the moving distance of a worker.

3. Optimization Problem

From the above section, our optimization problem is similar to several path planning problems such as "Traveling Salesman Problem (TSP)," "Minimum Spanning Tree problem(MST)." Our optimization problem becomes synonymous with minimization of total length of moving distance of a worker. The difference between path planning problems and our problem is that positions of waypoints for path planning problems are fixed; on the other hand, our problem changes positions of waypoints that are racks and boxes in order to minimize length of moving distance.

In addition, since the number of racks and boxes is predetermined as mentioned in the table 1 and 2, our approach has to put predetermined number of racks and boxes into a production line. For this, there is also a problem of "Knapsack Problem(KP)" in our optimization problem. It can be said that our optimization problem combines TSP, MST and KP for the reasons stated above.

4. Genetic Algorithm and Constrained

To overcome difficulties mentioned in the section 3, we propose to apply a GA to optimization for positions of racks and boxes. We explain the details of a conventional GA, and of a constrained GA to solve our problem.

4.1. Genetic Algorithm

A Genetic Algorithm(GA) is suitable for global search in a high dimensional space because a GA has also the ability of probabilistic random search based on genetic operations in addition to local search. A GA has many

© The 2018 International Conference on Artificial Life and Robotics (ICAROB2018), Feb. 1-4, B-Con Plaza, Beppu, Oita, Japan

individuals(populations), and an individual has a chromosome that cords the parameters for optimization. Optimization processes are on the basis of genetic operations, i. e., selection, crossover and mutation.

In a conventional GA, a process of crossover and mutation does not be constrained because parameters for optimization in a chromosome are independent in each; therefore, generated parameters of optimization are able to take all values within a set condition. On the other hand, parameters of optimization in our problem are dependent on each other because the number of racks to put assembly boxes and of that boxes is predetermined. Consequently, we are not able to apply a conventional GA to optimization. For this, we apply a "constrained GA" to optimization for positions of racks and boxes in a production line as mentioned in the next section.

4.2. Constrained Genetic Algorithm

We explain the details of a "constrained Genetic Algorithm" in this section. Gene loci correspond to racks and to boxes positions in a constrained GA. Selection process in genetic operations is same way as a conventional GA. In crossover process, loss or duplication of some racks and boxes will occur. The way of adjustment of the number of racks is that all of duplicative racks are deleted then missing racks are randomly inserted to those positions. The Fig. 3 illustrates an example of the way of adjustment.

	Racks									
	1000	1000	1000	1500	1500	1500	1500	2000	2000	2000
P1	9	4	2	5	7	6	8	1	0	3
P2	5	3	9	6	0	8	2	7	1	4
C1	9	3	2	5	0	6	8	1	0	3
C2	5	4	9	6	7	8	2	7	1	4

(a)

	Racks									
	1000	1000	1000	1500	1500	1500	1500	2000	2000	2000
P1	9	4	2	5	7	6	8	1	0	3
P2	5	3	9	6	0	8	2	7	1	4
C1	9	4	2	5	0	6	8	1	7	3
C2	5	0	9	6	7	8	2	3	1	4

(b)

Fig. 3. An example of crossover process for racks. P1, P2, C1 and C2 correspond to parent 1, 2 and child 1, 2, respectively. (a)Duplication and loss. (b)After adjustment.

Mutation process for racks is executed after the adjustment of crossover process. Mutation process in a conventional GA changes genes; by contrast, that process in a constrained GA changes gene loci in order to meet the conditions for the number of racks. The Fig. 4 illustrates an example of mutation for racks.

		Racks									
		1000	1000	1000	1500	1500	1500	2000	2000	2000	
Before	C1	9	4	2	5	0	6	8	1	7	3
	C2	5	0	9	6	7	8	2	3	1	4
After	C1	9	4	1	5	0	6	8	2	7	3
	C2	5	0	9	6	4	8	2	3	1	7

Fig. 4. An example of mutation process for racks. C1 and C2 correspond to child 1 and 2, respectively. Colored cells represent the mutated positions.

Crossover and mutation process for positions of assembly boxes in racks is executed after crossover and mutation process for racks. Crossover process for boxes is executed on the same stage each other, e.g., boxes in top stage of a rack are changed with boxes in top stage of another rack. In mutation process, genes for boxes are mutated randomly as same way as a conventional GA. Following those processes, the adjustment process in order to meet conditions is proceeded. Firstly, excess boxes that do not meet conditions in Table 2 are randomly chosen, then those boxes are deleted. Subsequently, shortfall in boxes are inserted randomly to meet the conditions for the number of boxes. If a box may not be able to insert to anywhere, that individual is deleted and an individual is newly generated.

From a constrained GA in above, our proposal is able to meet the conditions for our optimization problem.

5. Experiments

In this section, we validate the effectiveness of a constrained GA for optimization of a production line. The parameters for a constrained GA are shown in Table 3. The fitness function is as the Eq. (1).

Table 3. The parameters for a constrained GA.

	Case 1	Case 2
Num. of Individuals	4000	
Num. of Generations	50000	
Prob. of Crossover(Racks)	0.08	0.07
Prob. of Mutation(Racks)	0.02	0.025
Prob. of Crossover(Boxes)	0.08	0.07
Prob. of Mutation(Boxes)	0.02	0.025
Num. of Evaluation Cars	500	

$$f_i = \sum_{j=1}^{N_E} t_j / N_E \quad (1)$$

where i is individual number, t_j is total time of picking up of all of assemblies for car j , N_E is the number of evaluation cars for an individual.

Fig. 5 shows the changes in the fitness value of the best individual.

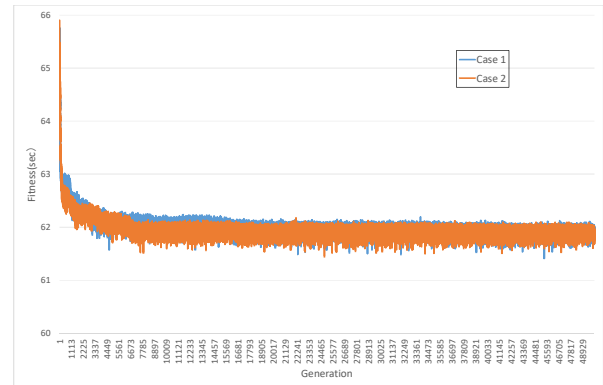


Fig. 5. Optimization results. “Blue line” shows “Case 1” and “Orange line” shows “Case 2” in Table 3.

Positions for racks and assembly boxes are randomly determined in the first generation; therefore, the maximum time for picking up in the first generation is about 70.9 second and the minimum is about 65.3 second. In contrast with the first generation, the time for picking up assemblies from the optimized positions in last generation is about 61.7 second from Fig. 5. For this, our proposal achieved to reduce about 10 seconds per car compared with random positioning.

6. Conclusions

We propose to optimize a production line of cars manufacturing plant by GA in this paper. The difficulties of our aim are that parameters of optimization in our problem are dependent on each other because the number of racks to put assembly boxes and that boxes is predetermined. Consequently, we are not able to apply conventional GA to optimization. For this, we apply a “constrained GA” to optimization for positions of racks and boxes in a production line.

From the results of experiment, our proposal achieved to reduce about 10 seconds per car compared with random positioning.

References

1. K. Kamei et. Al., *Development of the Recognition Method for Black Objects under Black Background Color* (SISA2017, Fukuoka, 2017), pp.352–357.
2. R. Pfeifer and C. Scheier, *Understanding Intelligence*, (MIT Press, Cambridge, 1999).

Slip Model of Ball Driven by Two Rollers

Kenji Kimura, Shota Chikushi, Kazuo Ishii

*Department of Human Intelligence Systems
Kyushu Institute of Technology
2-4 Hibikino, Wakamatsu-ku, Kitakyushu, Fukuoka, 808-0196 Japan
E-mail: kimura_kenji@edu.brain.kyutech.ac.jp,*

Abstract

Spherical wheel motion driven by rollers attract attention due to the possibility of uneven surface. RoboCup is a platform designed to promote the research fields such as Artificial Intelligent (AI) and robotics, and one of examples is the ball dribbling mechanism of RoboCup Middle size league robot, and this mechanism controls the ball with two driving rollers. As the result of the survey at the 2017 World Cup, all teams in the world have determined the roller arrangement heuristically, and no mathematical consideration has been made. In this study, we propose a model considering slip, discuss the relationship between slip ratio and robot speed using evaluation function, and verify the model by experiment.

Keywords: Spherical wheel motion, the ball dribbling mechanism, slip ratio,

1. Introduction

In recent years, development of a transmission mechanism of an actuator in locomotion and driving using a sphere has been actively conducted. At first, M.K. West proposes a holonomic mobile robot combining multiple spherical wheels like the Omni wheel[1], this has unconstrained in the direction orthogonal to the propulsion force. Omni-Ball wheels developed by Tadaguma solve the design restrictions of the above-mentioned spherical wheels[2]. The omni-directional locomotion function is realized by the passive rotation of the pair of hemispheres, and shows a capability to overcome a step difference higher than that of an omni-rollers. As a mobile robot that drives and moves monocytes. A ball balanced robot of Kumagai is mentioned[3], and by rotating the omni rollers independently by equally arranging the three omni rollers in an equilateral triangle shape, rotation of the sphere in an arbitrary direction is realized. Wada proposed two spherical power transmission which is a rotation pair of spherical bodies driven by two rollers[4], the upper spherical body is driven by two rollers, the lower sphere transmits power, the caster's, it is proposed an active caster that realizes steering and driving, and by driving the wheel shaft and the steering shaft, it is possible to move in all directions. In the RoboCup Middle Sized

League soccer robot, in recent years, a ball handling mechanism for further controlling the rotation of the ball is mounted. In the ball handling mechanism, two driving rollers are symmetrically arranged on the upper hemisphere. Tech United Turtles uses general rollers[5], CAMBADA uses omni rollers[6]. These roller placement problems rely on a lot of experimental data for these control. And all teams in the world have determined the roller arrangement heuristically, and no mathematical consideration has been made. Kimura introduced the mathematical non slip model[7], and discuss about non slip condition and the relationship between angular velocity vector and movement angle of the sphere is clearly in arbitrary two rollers arrangement. Chikushi experiments on non slip kinematic in two rollers symmetric arrangement using prototype[8].

In this research, we propose a kinematics slip model that takes slippage into account, clarify the relationship between the roller speed loss ratio and robot speed loss ratio depend on the arrangement of roller the world team, seeking accurate robot speed, Evaluate the placement.

2. Kinematics of Sphere by Rollers

2.1. The Existence of the Angular Velocity Vector of the Sphere

$\Sigma - xyz$, is fixed in the center of a sphere of radius r ,

© The 2018 International Conference on Artificial Life and Robotics (ICAROB2018), Feb. 1-4, B-Con Plaza, Beppu, Oita, Japan

as shown in Fig.1. \mathbf{P}_i indicates a position vector of the i^{th} wheel from the with respect to the \mathbf{O} . Center of the rollers and \mathbf{P}_i , \mathbf{O} are on the same straight line. And when represented by using polar coordinate $(\theta_{1,i}, \theta_{2,i})$, \mathbf{P}_i is denoted as follow

$$\mathbf{P}_i = r[\cos\theta_{1,i} \cos \theta_{2,i}, \sin \theta_{1,i} \cos \theta_{2,i}, \sin \theta_{2,i}]^T \quad (1)$$

let $\boldsymbol{\omega}$ be the angular velocity vector of the sphere of \mathbf{O} as the starting point \mathbf{O} , let \mathbf{n}_i be a unit vector along the roller axis as the starting point \mathbf{P}_i . The admissible angular velocity that satisfies the non slip condition is involved in the linear subspace $\text{span}\{\mathbf{P}_i, \mathbf{n}_i\}$ (spanned by the $\mathbf{P}_i, \mathbf{n}_i$ denoted). $\boldsymbol{\omega} \in \text{span}\{\mathbf{P}_i, \mathbf{n}_i\}$, if the peripheral roller speed v_i is given. the inverse kinematics is given by

$$\boldsymbol{\omega} \cdot \mathbf{n}_i = -(v_i/r) \quad (2)$$

As shown in Fig.1(a), the end-point set of $\boldsymbol{\omega}$ with respect to input v_i lies on a straight line $l_i(v_i)$ parallel to \mathbf{P}_i and distance v_i/r . $\boldsymbol{\omega}$ is not uniquely determined. As shown in Fig.1(a), the case of using two rollers ($i = 1$: left side, $i = 2$: right side), $l_1(v_1), l_2(v_2)$ has an intersection point. Therefore, $\boldsymbol{\omega}$ is uniquely determined.

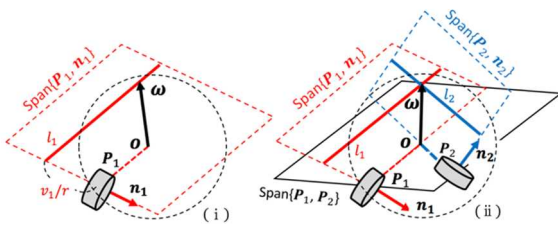


Fig. 1. (i) $l_i(v_i)$ is the end-point set of $\boldsymbol{\omega}$ ($\boldsymbol{\omega}$ is not uniquely determine) (ii) $\boldsymbol{\omega}$ is uniquely determined as an intersection point.

2.2. Slip Model of sphere driven by two rollers

In general, roller arrangement exists such that $l_1(v_1), l_2(v_2)$ have no intersection, as shown in Fig.2. α_i ($|\alpha_i| \leq \pi/2$) denotes the angle between $\text{span}\{\mathbf{P}_1, \mathbf{P}_2\}$ and \mathbf{n}_i , d_i denotes distance between $\text{span}\{\mathbf{P}_1, \mathbf{P}_2\}$ and $l_i(v_i)$, let $\hat{l}_i(v_i)$ be the orthogonal projection of $l_i(v_i)$ with respect to $\text{span}\{\mathbf{P}_1, \mathbf{P}_2\}$, the distance between \mathbf{P}_i and $\hat{l}_i(v_i)$ is $(v_i/r) \cos \theta_i$, therefore d_i is given by,

$$d_i = (v_i/r) \sin \theta_i \quad (3)$$

It is assumed that it is the optimum point of the end point of $\boldsymbol{\omega}$. Consider the center of the smallest radius sphere touching $l_1(v_1), l_2(v_2)$. The orthogonal projections component of $\boldsymbol{\omega}$ with respect to

$\text{span}\{\mathbf{P}_1, \mathbf{P}_2\}$, is expressed as intersection point of $\hat{l}_1(v_1), \hat{l}_2(v_2)$

$$\frac{1}{\sqrt{r^4 - (\mathbf{P}_1 \cdot \mathbf{P}_2)^2}} [(v_2 \cos \alpha_2) \mathbf{P}_1 - (v_1 \cos \alpha_1) \mathbf{P}_2] \quad (4)$$

The orthogonal projection component of $\boldsymbol{\omega}$ with respect to $\mathbf{P}_1 \times \mathbf{P}_2$, is given by

$$\frac{d_1 + d_2}{2} \frac{\mathbf{P}_1 \times \mathbf{P}_2}{\|\mathbf{P}_1 \times \mathbf{P}_2\|} \quad (5)$$

Using (1) (3) (4), slip-kinematics is given by

$$\boldsymbol{\omega} = \frac{1}{\sqrt{r^4 - (\mathbf{P}_1 \cdot \mathbf{P}_2)^2}} [(v_2 \cos \alpha_2) \mathbf{P}_1 - (v_1 \cos \alpha_1) \mathbf{P}_2] + \frac{v_1 \sin \alpha_1 + v_2 \sin \alpha_2}{2r} \frac{\mathbf{P}_1 \times \mathbf{P}_2}{\|\mathbf{P}_1 \times \mathbf{P}_2\|} \quad (6)$$

And, the sphere rolling velocity on the horizontal (robot speed) denote \mathbf{V} , using ω_x, ω_y (components of $\boldsymbol{\omega}$), $\|\mathbf{V}\|$ is given by

$$\|\mathbf{V}\| = r \sqrt{\omega_x^2 + \omega_y^2} \quad (7)$$

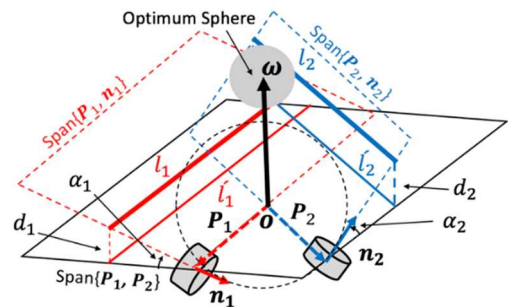


Fig. 2. when $l_1(v_1), l_2(v_2)$ has no intersection, $\boldsymbol{\omega}$ is defined the center of the smallest radius sphere touching $l_1(v_1), l_2(v_2)$.

2.3. Roller speed loss ratio and evaluation function

if $\boldsymbol{\omega} \notin \text{span}\{\mathbf{P}_i, \mathbf{n}_i\}$, the sphere slips with respect to rollers at \mathbf{P}_i . Using v_i and, the sphere rolling speed $-r(\boldsymbol{\omega} \cdot \mathbf{n}_i)$, roller speed loss ratio λ_i is defined as follows

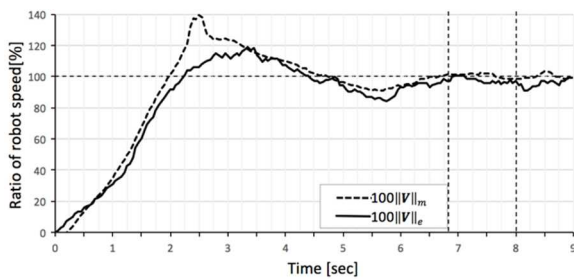
$$\lambda_i = 100 \left(1 - \frac{-r(\boldsymbol{\omega} \cdot \mathbf{n}_i)}{v_i} \right) \quad (8)$$

λ_i is function depend on α_1, α_2 , in particular, if $\boldsymbol{\omega} \in \text{span}\{\mathbf{P}_i, \mathbf{n}_i\}$, then $\lambda_i = 0$ [%] and, if $\mathbf{n}_i \perp \boldsymbol{\omega}$ ($\boldsymbol{\omega} \notin \text{span}\{\mathbf{P}_i, \mathbf{n}_i\}$), then $\lambda_i = 100$ [%]. The evaluation function is defined as follow

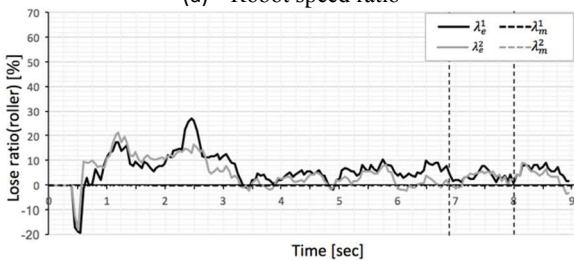
$$\lambda = (\lambda_1 + \lambda_2)/2 \tag{9}$$

3. Experiment

We experiment to estimated Robot speed and roller speed loss ratio. an experiment was conducted to measure Fixed parameters are given by $v_1, v_2 = 0.75[m/s]$, $\theta_{1,1} = 215, \theta_{1,2} = 275, \theta_{1,2} = \theta_{2,2} = 60[deg]$, and variable α ($\alpha_1 = \alpha, \alpha_2 = -\alpha$; two rollers are placed in symmetry) is each of case $\alpha = 0, 10, 20, 30 [deg]$, The target values are shown in Table 1. As a result, experimental value $100\|V\|_e, \lambda_1^e, \lambda_2^e$ (estimated value from the motor using (7) (8)) is closed to theoretical value $100\|V\|_m, \lambda_1^m, \lambda_2^m$, As shown in Fig. 4-7, The mean errors are showed in Table2, therefore these values extremely small and the validity of the slip model was proved.

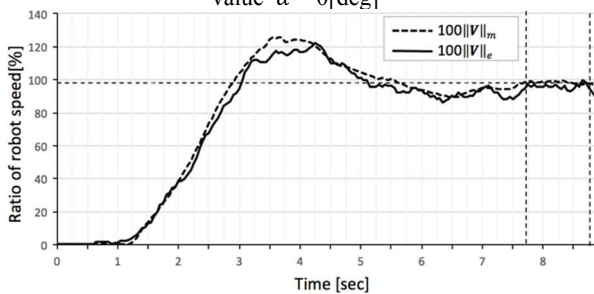


(a) Robot speed ratio

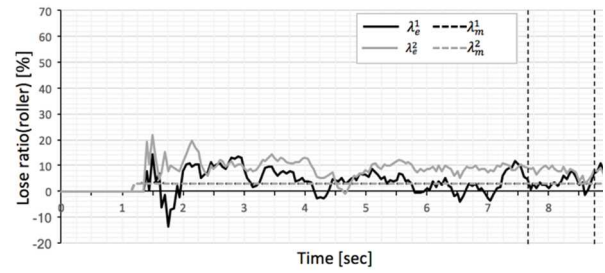


(b) Roller speed loss ratio

Fig. 4. Comparison theoretical value and experimental value $\alpha = 0[deg]$

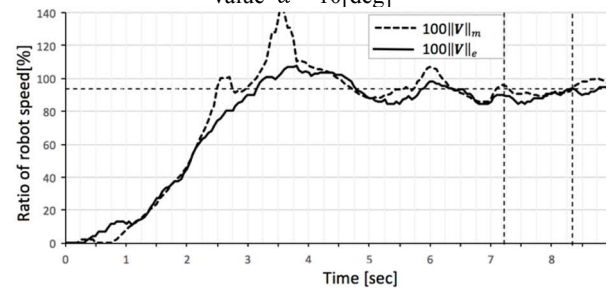


(a) Robot speed ratio

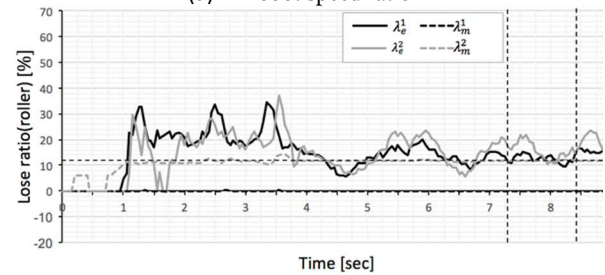


(b) Roller speed loss ratio

Fig. 5. Comparison theoretical value and experimental value $\alpha = 10[deg]$

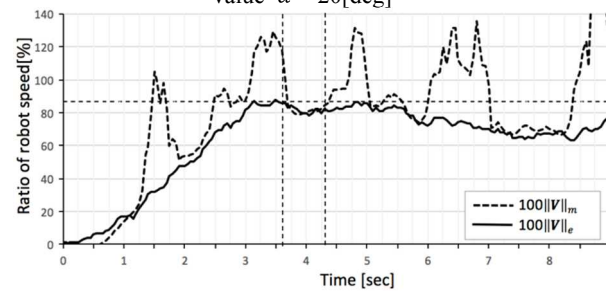


(a) Robot speed ratio

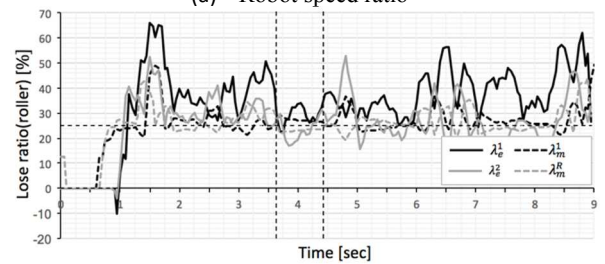


(b) Roller speed loss ratio

Fig. 6. Comparison theoretical value and experimental value $\alpha = 20[deg]$



(a) Robot speed ratio



(b) Roller speed loss ratio

Fig. 7. Comparison theoretical value and experimental value $\alpha = 30[\text{deg}]$

Table1. Theoretical value

α_i [deg]	0	10	20	30
$\lambda, \lambda_1, \lambda_2$ [%]	0	3	12	25
$100\ V\ $ [%]	100	98.5	93.5	84

Table2. Experimental value (average error)

interval [sec]	7.05~8	7.75~8.7	7.8~8.35	3.6~4.3
α_i [deg]	0	10	20	30
$100(\ V_m\ - \ V_e\)$ [%]	3.7	1.5	2.1	7.1
$\lambda_1^e - \lambda_1^m$ [%]	3.8	1.9	3.5	3.4
$\lambda_2^e - \lambda_2^m$ [%]	3.4	5.8	1.6	3.5

4. Consider of world teams

According to survey of the 2017 World Cup, world Roller arrangement angles are close to $\alpha = 0, 10, 20, 30$ [deg]. The horizontal axis shows the roller speed loss ratio, the vertical axis shows the robot speed loss ratio, as shown in Fig.8. four white mark is $(\lambda^e, 100(1 - \|V_e\|))$, these are on the evaluation curve, and four black mark $(\lambda, 100(1 - \|V\|))$, these are close to the evaluation and upper part curve, therefore, the validity of evaluation curve was proved. Moreover, RV-infinity ($\alpha=0$), Tech-U, Falcons ($\alpha_i=10$), The robot speed loss ratio is within 5[%], H-Musashi, NuBot ($\alpha=20$) is 9[%], Water ($\alpha=30$) is 18[%]. Therefore, if $\alpha = 0 \sim 10$ [deg], it is optimal roller arrangement to be possible in efficient motion.

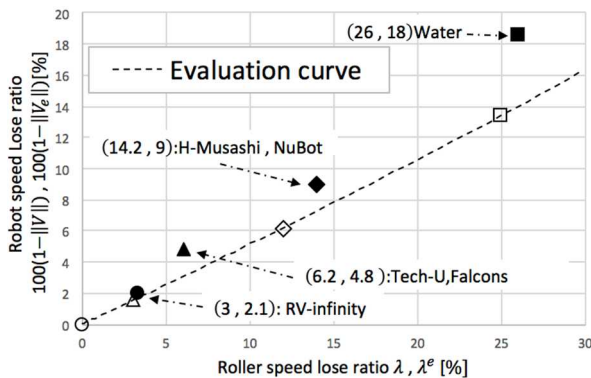


Fig.8 Relationship between evaluation value and experimental value in world teams

5. Conclusion

In this study, we proposed a kinematic model of spheres by roller driving considering slippage. Experiments measured the roller speed loss ratio in surge motion and the speed of advance of the robot and verified the accuracy of kinematic. We also clarified the relationship between the roller speed loss ratio and the robot speed loss ratio and discussed the speed loss ratio of the robot in the rollers arrangement of the world team, and clarified optimal arrangement of the ball dribbling mechanism. As a future task, we would like to consider the robot speed loss ratio in the all directions.

References

1. M. West and H. Asada. Design of a holonomic omnidirectional vehicle. *In Proceedings of the 1992 IEEE International Conference on Robotics and Automation*, Vol.(1992),pp.97-103,
2. Berengeres. Development of holonomic omnidirectional vehicle with “omni-ball”: spherical wheels. *In Proceedings of the 2007 IEEE/RAS-EMBS International Conference Robots and systems*, (2007), pp.33-39,
3. M. Kumagai, T. Ochiai: “Development of a robot balanced on a ball – Application of passive motion to transport”, *Proc. ICRA IEEE(2009)*, pp.4106-4111
4. M. Wada, Y. Inoue and T. HIRAMA, ”Kinematics and Mechanical Design of an Active-caster with a Ball Transmission” *The Robotics Society of Japan*, vol.31, No.6,(2013),pp.591-598,
5. Rob. Hoogendijk: “*Design of a Ball Handling Mechanism for Robocup*” Bachelor End Project, department Mechanical Engineering, Technische Universiteit Eindhoven
6. B. Cunha, A.J.R. Neves, P. Dias: “CAMBADA'2015: Team Description Paper” *RoboCup2015Hefei*
7. K. Kimura, K. Ishii, Y. Takemura, M. Yamamoto, “Mathematical Modeling and motion analysis of the wheel based ball retaining mechanism”, *SCIS & ISIS (2016)*, pp.4106-4111,
8. S.Chikushi, T. Weerakoon, T. Sonoda, K. Ishii, “Kinematics of Two-Roller-Driven Ball for RoboCup Soccer Robot”, *Journal of Robotics, Networking and Artificial Life*, Vol.4, No.3(2017), pp.248-253,

Strategy Analysis of Multi-Agent Games Using Self-Organizing Map

Moeko Tominaga

*Graduate School of Life Science Systems Engineering, Kyushu Institute of Technology
2-4 Hibikino, Wakamatsu-ku, Kitakyushu, Fukuoka, 808-0196, Japan
E-mail: tominaga-moeko@edu.brain.kyutech.ac.jp*

Yasunori Takemura

*Faculty of Engineering, NishiNippon Institute of Technology
1-11, Aratsu, Kanda-town, Miyako-gun, Fukuoka, 800-0397, Japan
E-mail: takemura@nishitech.ac.jp*

Kazuo Ishii

*Dept. of Human Intelligent Systems, Kyushu Institute of Technology
2-4 Hibikino, Wakamatsu-ku, Kitakyushu, Fukuoka, Japan
E-mail: ishii@brain.kyutech.ac.jp*

Abstract

As technology develops, realization of a symbiotic society between human beings and robots sharing their environment has become one of most important subjects. For example, soccer is a multi-agent game that require strategies such as each members' position and defense. The behavior of a player changes depending on the game situation such as winning or losing, score gap, remaining time. The players may play offensive when their team is losing, or be defensive when their team is winning with minimum score difference. In this paper, human soccer game is observed and analyzed to determine how the state vector of each players affect team behavior. The team strategy is analyzed based on parameters such as the positions, the number players, score, time and actions of soccer robots using Self-Organizing Map(SOM)

Keywords: Strategy, Self-Organizing Map, team behavior, SOM.

1. Introduction

Recently, social implementation of robot is highly expected as a solution to many social problems such as ensuring safety of a sustainable society, respond to rapid population decrease and aging population, establishing industrial base including the primary industry. In order to properly implement the robot society, it is necessary to return and present the research outcome to our society in a manner that is easy to understand while avoiding

deviation between social expectation and direction of research and development. Therefore, it is essential discuss how to achieve the coexistence with robots and what of the symbiotic society should be.

1.1. Cooperative Behavior

A cooperative behavior can be generated when multiple autonomous agents perform a single large task while interacting to each other. Multi-agent system (MAS) has

© The 2018 International Conference on Artificial Life and Robotics (ICAROB2018), Feb. 1-4, B-Con Plaza, Beppu, Oita, Japan

been conducted by many researchers in recent years as a solution to solve difficult problems that are challenging when using one agent. As test bed of MAS, RoboCup encourages the cooperation of multiple agents using method of learning such as reinforcement learning and neural network. Sandholm and Crites¹ shows that application of reinforcement learning in the Iterated Prisoner's Dilemma require sufficient measurement data and action for successful learning. In addition, Arai² compares the tracking problem in a lattice environment with Q-learning and Profit Sharing properly and concludes that Profit Sharing is suitable for learning in a multi agent environment. However, these studies have not yet considered application toward robots that operate in a real environment.

1.2. Robot Learning

In robot learning, information of the environment and prerequisite knowledge of robot itself are not primarily required. However, since learning requires a large number of trials, securing the robot's stable state and its action space is crucial in order to reduce the time cost and enable learning that fits the intention of the user. In a real robot, the configuration of state space containing the sufficient information to perform a task depends on the behavioral capacity of the robot. Likewise, the action space also depends on the perception ability. In response to this problem, Asada³ proposed a method of constructing the state space with recursive segmenting initial state vector. However, the behavior and state space composition method is based on the robot's experience which may raise concerns if the experience is biased, the behavior may be considered as strange habits like in

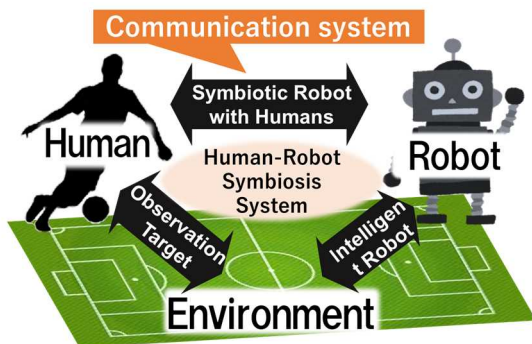


Fig.1. Human-Robot Symbiosis System

human beings, alternatively not leading to proper behavior selection.

1.3. Human-Robot Cooperation

As mentioned in the previously, various discussions have been made in acquiring cooperative behaviors among multiple real robots. However, when looking at the symbiotic society between humans and robots, we question the fact that the observation target for learning so far is a robot. In fact, even without the interface problem, it is not easy to communicate between humans and robots using the current multi agent system. This research consider cooperative behaviors between humans and apply it to robot. (see Fig.1) In learning of a real robot, experience bias and selection of input vector elements from state space in environment recognition is considered using neural network. In this paper, position in human cooperative behavior is analyzed using Self-Organizing Maps. Futsal is used as an object of observation of humans' cooperative behavior since the game's objectives is also cooperation of multiple agents in dynamic environment which includes all multi-objective/multiple constraint problems and real-time planning / reasoning is required.

2. Setting Observation Elements in Situation Analysis

In observing the human futsal match, firstly, we set as an object the elements which can be easily observed. As target, in addition to the coordinates and the speed of the athlete and the ball, the elapsed time of the game and the goal difference are considered. In this case, as the observation method, since the method of photographing the entire game field using the monocular camera was selected, the state space is established based on various

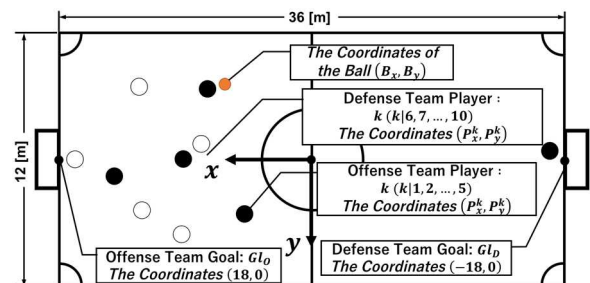


Fig.2. The Observation Environment of the Game

coordinate data in the field. Human futsal games were played on 5 vs 5 players familiar with team play and the coordinates of all players and balls were observed. (see Fig.2) Also, the observation vector \bar{A} is expressed by the Eq. (1).

$$\bar{A} = [\overline{p^{k=1}}, \overline{p^{k=2}}, \dots, \overline{p^{k=10}}, \bar{B}] \quad (1)$$

The player position coordinate P^k and the ball position coordinate B in the field are shown in the Eq. (2) and (3).

$$\overline{P^k} = [P_x^k, P_y^k] \quad (2)$$

$$\bar{B} = [B_x, B_y] \quad (3)$$

k is an ID for identifying the player. We observed a game consisting of a team of $k = 1, 2, 3, 4, 5$ players and a team consisting of $k = 6, 7, 8, 9, 10$ players. Incidentally, $k = 6, 10$ is the goalkeeper of both teams.

3. Self-Organizing Maps

Self-Organizing Maps is unsupervised learning, and it is known as competitive learning similar to information processing by the neural circuit of life. Competitive learning is an important concept in hierarchical neural networks. Each input neuron (input vector \bar{v}_i) in the input layer (input space V) is connected to all output layer neurons, and the coupling weight $\overline{w_{ij}}$ is given to the coupling. (see Fig.3) The algorithm of SOM⁴ consists of two hierarchies, a competitive hierarchy and a cooperative hierarchy. For the input, the best matching neuron is selected, and the load of that neuron and its immediate neuron is changed. With this structure,

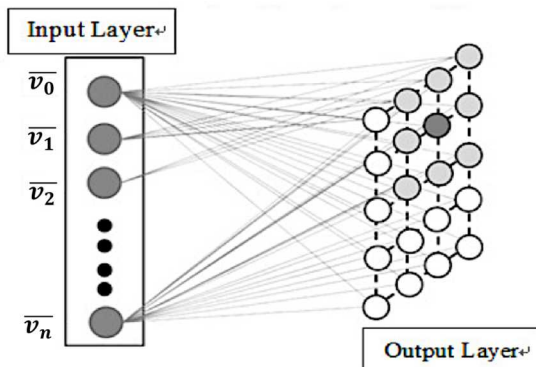


Fig.3. Overview of SOM algorithm

multidimensional input vectors can be reduced dimension in the output layer, and input vectors with similar features are placed closer to each other. As an application example of SOM, there is visualization that easily expresses complex data in two dimensions, etc. As with the clustering technology, creation of abstraction is possible. Since excellent interpolation performance is maintained, generalization of learning data is possible, and highly valid output is expected for unknown input data.

3.1. Algorithm

In this research, we used Batch type SOM which load taking into consideration all inputs generated after the competition phase of all input vectors, instead of incremental learning which load updating each time a new input vector is input. By using this method, it becomes unnecessary to consider the influence on the output by the input order of input vectors. The definition of batch type SOM in this research is shown in the following Eq. (4) to Eq. (5). Where i is the input vector ID and j is the ID of each neuron in the output layer.

1. Competitive phase

Selection of the best matching neuron i^* for each input vector \bar{v}_i .

$$i^* = \arg \min \|\overline{w_{ij}} - \bar{v}_i\| \quad (4)$$

2. Coordination phase

Updating the load of each neuron.

$$\overline{w_{ij}}(t+1) = \overline{w_{ij}}(t) + \frac{j}{M} \cdot \Delta \overline{w_{ij}} \quad (5)$$

Incidentally, the increase / decrease value $\Delta \omega_{ij}$ of the coupling load is expressed by the following equation (6).

$$\Delta \overline{w_{ij}}(t+1) = \Delta \overline{w_{ij}}(t) + \Lambda(i, i^*, \sigma_\Lambda) \cdot (\bar{v}_j^i - \overline{w_{ij}}) \quad (6)$$

In the second item on the right side, the combination of the minimum Euclidean distance rule and the neighborhood function is applied as a load update rule.

4. Experiment

Experiments were conducted with the parameters shown in Table 1

Table. 1: Parameters setting SOM

Learning time	t	10
Map size		30×30

4.1. Input Vector

The input vector is expressed by the following Eq. (7), except for the goalkeeper of the same team, the player coordinates are $k = 1, 2, 3, 4$ when $i = 1 - 428$ In the case of $i = 429 - 856$, $k = 6, 7, 8, 9$ are used, and the number of input vectors is $M = 856$. In this time, 6 challenges from set play to shoot were used as input data.

$$\bar{v}_i = [\bar{P}^k, \bar{B}] \quad (7)$$

4.2. Experimental Result

The outputted feature map is shown in Fig.4. The color gradation represents the Euclidean distance from the weight of the peripheral unit. Also, after learning, observe the unit selected by input vector again. From the set play to the shoot, the try who never took the ball to the opposing team is shown on the left figure, and the tried thing is shown on the right figure. It is color-coded by team. Referring to Fig. 4, it can be seen that the selected unit is inside the red unit in the left figure,

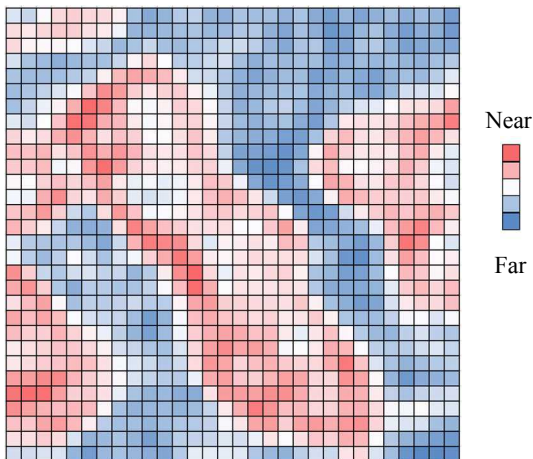


Fig.4. The feature map expressed by the gradation display after learning the coordinates of the athlete and the ball as the input vector

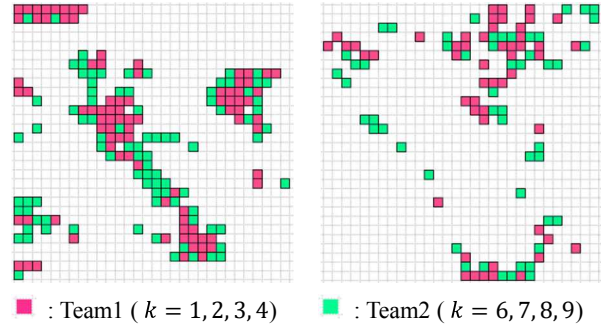


Fig.5. The unit selected by input data after learning (Left figure: the try who never took the ball to the opposing team / Right figure: the try which the ball has been taken is shown on the right figure)

outside the red unit in the right figure. As a result, we can clearly distinguish on SOM when one team consistently ran from monopolizing the ball, from the set play to the shoot, and when it was not possible.

5. Conclusion

In this research, the team strategy is analyzed based on parameters such as the positions of human player, time and actions using Self-Organizing Map (SOM). We developed the SOM map from the position of each player and ball on the field. As a result of experiments, it was found that discrimination is possible on the feature map when the pass turn was successful or failed. In the future, I would like to also examine the change in player's positioning when the pass turn fails.

References

1. T. W. Sandholm, R. H. Crites: On Multiagent Q- learning in a Semi-Competitive Domain, *Workshop Notes of Adaptation and Learning in Multiagent Systems Workshop, IJCAI-95*, 1995.
2. S. Arai, K. Miyazaki, S. Kobayashi: Methodology in Multi-Agent Reinforcement Learning : Approaches by Q- Learning and Profit Sharing, *Journal of Japanese Society for Artificial Intelligence*, 13(4), pp.609-618, 1998.
3. Y. Takahashi, M. Asada: Behavior Acquisition by Multi-Layered Reinforcement Learning , *Journal of the Robotics Society of Japan*, vol. 18, No.7, pp.1040-1046, 2000.
4. Kohonen. T, *Self-Organizing Maps*, Springer Japan
5. Van Hulle, Marc M: *Faithful representations and topographic maps from distortion-to information-based self-organization*, Kaibundo Publishing Co., Ltd., p9-92, 2001.

Recognition of Tomato Fruit Regardless of Maturity by Machine Learning Using Infrared Image and Specular Reflection

Takuya Fujinaga

*Dept. of Human Intelligence System, Kyushu Institute of Technology
2-4 Hibikino, Wakamatsu-ku, Kitakyushu, Fukuoka, 808-0196, Japan
E-mail: fujinaga-takuya@edu.brain.kyutech.ac.jp*

Shinsuke Yasukawa

*Center for Integrated Underwater Observation Technology,
Institute of Industrial Science, The University of Tokyo
4-6-1 Komaba, Meguro-ku, Tokyo 153-8505 JAPAN
E-mail: yskw@iis.u-tokyo.ac.jp*

Binghe Li

*Dept. of Human Intelligence System, Kyushu Institute of Technology,
2-4 Hibikino, Wakamatsu-ku, Kitakyushu, Fukuoka, 808-0196, Japan
E-mail: li-binghe@edu.brain.kyutech.ac.jp*

Kazuo Ishii

*Dept. of Human Intelligence System, Kyushu Institute of Technology,
2-4 Hibikino, Wakamatsu-ku, Kitakyushu, Fukuoka, 808-0196, Japan
E-mail: ishii@brain.kyutech.ac.jp*

Abstract

This paper presents a tomato fruit recognition method using plant characteristics of tomato and infrared images. Labor shortage and aging are problems in Japanese agriculture field. We aim to realize automatic harvesting and production management system of tomato. For that, it is necessary to detect the position and maturity of tomato fruit. Tomato fruit shows high reflectance against infrared light. The specular reflection part of the tomato fruit in the infrared image is used as training data. The Tomato harvesting robot can focus only on tomato fruit in the harvestable range by using infrared image. We use the images acquired at the actual tomato greenhouse to evaluate this proposed method. As a result of machine learning, *Precision* is 0.940, *Recall* is 0.808, and *F-measure* is 0.868.

Keywords: Tomato Harvesting Robot, Infrared Image, Specular Reflection, Machine Learning

1. Introduction

Stable production of crops by farmers is very important not only for our lives but also for natural environment conservation. However, problems such as aging, decrease of workers, shortage of successor are

becoming obvious in the agricultural field. Under such circumstances, attempt of smart-agriculture is being conducted. The smart-agriculture is to positively introduce ICT (Information and Communication Technology), IoT (Internet of Things) and etc. to improve work efficiency.

In tomato cultivation, there are a high technology greenhouse where temperature, humidity, carbon dioxide concentration and culture liquid are controlled and high wire cultivation is introduced for efficiency of harvesting work. Furthermore, the automation of harvesting and management in greenhouses by robot is expected as a next-generation technology to reduce the burden on workers.

Fruit detection technology using image information is necessary to predict fruit yield [1] and automatically harvest fruit [2, 3]. As a detection method of tomato fruit, study using optical properties of tomato has been done [4-7]. Since these require additional illumination and special sensors, the system is generally expensive. Study on fruit recognition by machine learning has also been actively done [1, 8-11]. Although there are attempts to predict the yield of tomatoes from RGB images, it is necessary to method of detecting only mature tomato fruit [9] or device such as acquiring image by illuminating light during the night [11].

We aim to introduce the robot can not only harvests tomato fruit but also monitors tomato growth state [12, 13] in the large-scale greenhouse. In particular, we focus on research and development of management system in tomato greenhouse. We proposed a generation method of a tomato growth state map using infrared image [12]. This map is used not only for planning the harvesting operation of the robot but also for grasping the state of the tomato fruit. We also proposed a tomato fruit detection method of template matching based using infrared images and specular reflection [13].

Although the infrared image is used in our proposed methods, it is easier to introduce the system because it adopts the sensor that can be used more easily than the method using other special sensors. The outline of robot, system and sensor are described in Chapter 2.

In this paper, we propose a tomato fruit detection method with specular reflection part of tomato fruit on infrared image as training data. Training results are evaluated by images acquired by robot in the real large-scale greenhouse.

2. Tomato automatic harvesting and production management system

2.1. Cultivation environment and robot

Describe the environment of the large-scale tomato

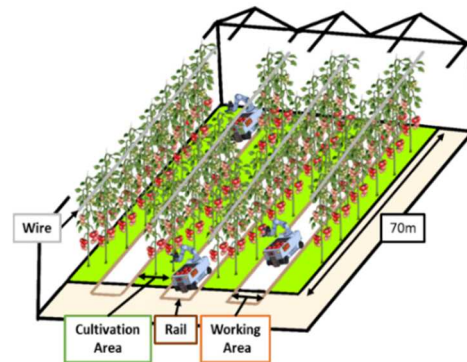


Fig.1 Tomato cultivation environment.

Tomato is cultivated in Cultivation Area. Laborers harvest and manage tomatoes on Rail in Working Area.



Fig.2 Overview of tomato harvesting robot.

Tomato harvesting robot consists of manipulator, end-effector, camera, computer and mobile mechanism.

greenhouse which we assume introduction of robots. As an example, there is Hibikinada greenhouse in Kitakyushu. This greenhouse area is about 8.5 ha. The outline of the cultivation environment in Hibikinada greenhouse is shown in Fig.1. As shown in Fig. 1, the tomatoes are arranged at a predetermined interval in the cultivation area. Length of this area is about 70 m, and there are hundreds of this area in greenhouse. There is the working area between this cultivation areas, and laborers move within this working area to harvest and manage (pruning, pest control) tomatoes. In order to control greenhouse temperature, the pipe through which warm water flows is installed on the working area. This pipe also has role as a rail for cart which is move way to decrease burden of workers.

We develop and research robot that can move on this rail as the first step to realize tomato automatic harvesting and production management system. The overview of tomato harvesting robot is shown in Fig.2. This robot

consists of a manipulator and an end-effector for harvesting tomato fruit, a camera for acquiring the image in the greenhouse, a computer for controlling the robot, and a moving mechanism for moving on the rail.

2.2. 2. *Tomato automatic harvesting*

Describe the movement of robot until automatic harvesting of tomato fruit. It is assumed that multiple robots are installed in the greenhouse as shown in Fig.1. The cultivation places are divided to section according to the type of tomato, and the robots harvest and monitor in place predetermined.

The robot decides the target cultivation area, moves to the working area, and moves on the rail. When the robot moves on the rail, images of the greenhouse are acquired in order to grasp growth state of tomato fruits. At this time, the position where image is acquired is measured from the encoder mounted on the moving mechanism and is saved. When the robot moves to the end of the rail, the tomato growth state map of the cultivation area is generated on the spot. Harvestable tomato fruits are detected from the map, and the robot harvests the tomato fruit.

2.3. *Production management system*

Fig. 3 is the image inside the greenhouse captured by the robot moving on the rail as shown in Fig. 1. Not only the tomato fruits in the front row but also the tomato fruits in the back row are confirmed. However, since the movable range of the manipulator is in the range up to the target cultivation area (the front row), it is not possible to harvest the tomatoes of behind (the back row).

Therefore, it is important to measure the 3-dimensional position of tomato fruit. So far, a method of get the 3-dimensional position of tomato fruit by the stereo vision system [6] or the 3-dimensional visual sensor using two wavelengths [7] is proposed. However, as mentioned in Chapter 1, these methods require illumination and special sensors.

In our system, Time of Flight (ToF)-based Kinect (Kinect v2) which can obtain three images multi-modal (Infrared image, RGB image, depth image) at a low price is used. The robot can ignore the tomatoes (fruits, stems, leaves) and the background in the back row by using the infrared image, and can focus on only the tomato fruits in the front row.



Fig.3 Image acquired in the tomato greenhouse. Tomato fruit within and outside the harvestable range are confused.

Not only can be light the processing of the robot in the sensing stage but also the greenhouse administrator who confirms the tomato growth state map can focus on only the front row, leading to the prevention of double confirmation of the tomato in the back row.

In addition, we aim to detect tomato fruits from this tomato growth state map and predict the yield and harvest time of the tomato fruit. Prediction of yield and harvest time leads to shortening of working hours, stabilization of market, and continuation of agricultural management.

As a previous step for that, it is necessary to detect the position of tomato fruit. In this paper, we propose a method which recognize tomato fruit regardless of maturity by applying tomato fruit detection method of template matching base using infrared image and specular reflection [13].

Using an infrared image not only removes tomatoes and background in the back row but also can apply the plant characteristics of tomato. The plant characteristics of tomato is described in Chapter 3.

3. *Machine learning using infrared and specular reflection*

3.1. *Specular reflection of tomato on infrared image*

It is possible to select parts fruit and other than fruit using spectral reflection characteristics of plants [14]. Tomato has high reflectance for fruit, stem and leaf against the wavelength band of near infrared light (around 800 nm). Regardless of maturity, the reflectance of tomato fruit is high in this wavelength band, and further it is possible to judge maturity (ripe fruit or unripe fruit) of the fruit.

In this paper, infrared image is used to detect tomato fruit regardless of maturity. For acquiring infrared image,

Kinect v2 is used, and this wavelength band of the near infrared light is 830 nm, which is considered to be a wavelength band effective for detecting tomato fruit.

On the infrared image, the tomato fruit shows the concentric circle with center is strong response and around is weak response. In the greenhouse, response intensity varies at the time of acquiring image due to the influence of sunlight and shadows of stem and leaf. Therefore, in previous study [13], the gradient orientation of the specular reflection part is used so that it does not depend on the response intensity. In this paper, we report tomato fruit recognition method by machine learning, using specular reflection part of tomato fruit as training data.

Here, specular reflection is generally the reflection of perfect light by a mirror, water surface, or the like. The specular reflection of tomato fruit described in this paper means reflection of infrared light from tomato fruit and stem and leaf with high reflectance when infrared light is projected on tomato.

3.2. Recognition method of tomato fruits using Support Vector Machine

In order not to depend on environment light, HOG features [15] of specular reflection part is used as training data. HOG features is a histogram of the gradient direction of the brightness, and it is known that it is robust to variation of illumination. Also, even when images of different resolutions are targeted for HOG features, they can be compared by resizing to the same resolution, so that a reduction in calculation amount can be expected.

For the training data and the test data, as shown in Fig. 1, the image acquired by the robot moved in the greenhouse is used.

As the training data, use the image of 21 * 21 pixel centered on the pixel with the highest response intensity of specular reflection part of tomato fruit. 21 * 21 pixel is almost of the same the size of the target tomato fruit in the image acquired from the camera position mounted on the robot.

The specular reflection part of tomato fruit is positive data, stem and leaf, planter is negative data. Support Vector Machine [16] which is one of pattern recognition models is used to classify training data.

For the test data, use an infrared image of 424 * 512 pixels focusing only on the tomatoes in the front row by removing the tomatoes in the back row and background.

In order to search the position of tomato fruit, a sliding window method is adopted, which extracts a candidate region while moving a constant small region for each constant pixel in the image. In the sliding window method, even one fruit may be recognized more than once. Therefore, the position of the tomato fruit is obtained using the Mean Shift method [17] that detects the maximum value of the density of the pixel group recognized multiple times.

4. Recognition result of tomato fruit regardless of maturity

4.1. Outline of training data and test data

Evaluate the proposed method using 70 images acquired at Hibikinada greenhouse. 40 images as training data and 30 images as test data. The illuminance in the greenhouse is 2800 to 9660 lx when acquiring the image.

The training data are classified as shown in Table 1. Here, two training data sets are prepared in order to evaluate the recognition accuracy due to the characteristic bias of the specular reflection part of the tomato fruit. Each training data set is selected by 20 different images from 40 acquired images, and positive data and negative data of 21 * 21 pixels are made. Sample images of positive data and negative data are shown in Fig.4. Fig. 4 (a) is positive data, which is a specular reflection part of tomato fruit on the infrared image. Fig.4 (b) and (c) are negative data, Fig.4 (b) shows a part where the stems are densely packed, and Fig. 4 (c) shows a part of stems and leaves. The time of the classifier is about 6.6 seconds in the training data set 1 and about 5.7 seconds in the training data set 2.

In this report, only tomato fruit that can be visually confirmed specular reflection part is subject of recognition. As mentioned in Section 3.1, specular reflection part of tomato fruit shows the concentric circle with center is strong response and around is weak response, so it can be visually confirmed. On the 30 test data, there are 604 tomato fruits, among which 480 tomato fruits can be confirmed specular reflection.

Table1 Outline of training data.

	Positive	Negative
Training data set 1	224	1184
Training data set 2	246	1030

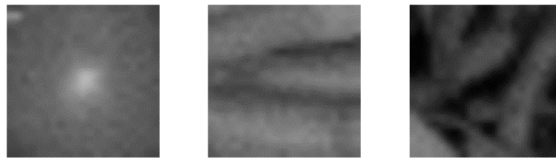


Fig.4 Sample image of positive and negative data.
(a) is positive data. (b) and (c) is negative data.

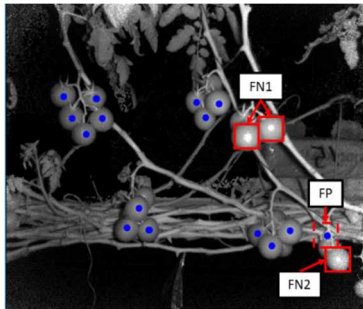


Fig.5 Recognition result.

Points is recognition result, solid line frame is False Negative, broken line frame is False Positive.

4.2. Result

For evaluation of recognition, evaluation index of *Precision*, *Recall*, *F-measure* is used. Equations (1), (2) and (3) show the calculation method for each evaluation index. True Positive (TP) is judged to be correct positive, False Positive (FP) judged as positive by mistake, False Negative (FN) judged erroneously negative.

Since only tomato fruit is targeted for recognition, True Negative judged to be correct negative not subject of evaluation.

$$Precision = \frac{TP}{TP + FP} \quad (1)$$

$$Recall = \frac{TP}{TP + FN} \quad (2)$$

$$F - measure = \frac{2 * Recall * Precision}{Recall + Precision} \quad (3)$$

An example of the recognition result of tomato fruit is shown in Fig.5. In Fig.5, points are the recognition position of the tomato fruit, the solid line frames are False Negative, and the broken line frame is False Positive. Table 2 shows the results of each evaluation index in each training data set.

Table2 Result of evaluation index.

	Precision	Recall	F-measure
Training data set 1	0.959	0.779	0.860
Training data set 2	0.922	0.835	0.877

5. Discussion

The *Precision* of training data set 1 is 0.959, and the *Precision* of training data set 2 is 0.922. The *Precision* is the evaluation index that the result is also positive, predicted as positive. Since the *Precision* exceeds 90% in both training data sets, the misrecognition is less than 10% of the total. This method for recognition of tomato fruit is likely to be effective.

As an example of incorrect recognition, there is FP in Fig. 5. As tomato not only fruit but also stem and leaf have specular reflection. Depending on how the stem and leaf are attached, it is thought that the misrecognition is done because there may be a case where the response is similar to that of tomato fruit.

Regarding the *Recall*, among the 480 tomato fruits, 374 (0.779) in the training data set 1 and 401 (0.835) in the training data set 2. Even though the specular reflection part can be confirmed in the tomato fruit by visually, approximately 20% of the tomato fruits are not recognized.

Examples which are not recognized as tomato fruit include FN1 and FN2 in Fig. 5. In FN1, due to the influence of the sunlight, it fades out and it is not recognized as specular reflection part. In FN 2, it slightly has specular reflection. However, the response of specular reflection part is not concentric circle, so it is not recognized as tomato fruit.

In the infrared image acquired by Kinect v2, there is a tendency that the accuracy of the edge portion of the image deteriorates. In Kinect v2, infrared light is projected, and it measures the time until reflected light returns to the device. Since the distance to the object is longer at the end part of the image than in the center of the image, the light attenuates due to the influence of environment light. Therefore, it is thought that accuracy drops.

We plan to apply this method to mosaic images. In the proposed method [12], mosaic image is generated from images acquired at regular intervals. However, we think that this problem can be solved by devising the generation of the mosaic image. In the case that tomato fruit dense in the center of the image, reducing the overlapping area at the time generation of mosaic image. We also consider a solution that infrared light is projected from the back of Kinect v2 and images are always acquired under the same illumination condition.

Tomato fruit which specular reflection cannot be confirmed is excluded, which is about 21% of the total. In this case, the bunches are dense and the fruits are overlapped with each other or the tomato fruits are hidden by stems and leaves. We consider two possible ways to deal with this problem.

First, similarly to the problem at the time of acquiring the infrared image described above, devising the generation of the mosaic image. Track the tomato fruit from the acquired video and cut out the image when specular reflection part can confirm. When generating the mosaic image, change the combine position between images.

The second is to use the method [18] to estimate the shape of the tomato based on the geometric and physical inference of the tomato. It is possible to grasp the tomato fruit which cannot be confirmed from the image by considering that tomato maintains stable state as a tomato bunch with the interaction force or gravity of the individual fruits of tomato.

6. Conclusion

In this paper, as a previous step of the tomato growth state map, the method of recognizing tomato fruits is proposed. By using the specular reflection part of the tomato fruit on infrared image as training data, *Precision* is about 0.940. The effectiveness of tomato fruit recognition method using tomato plant characteristics is shown. Since it is confirmed that the illuminance in the greenhouse is effective at 2800 to 9660 lx, we evaluate this method by changing the weather and illumination conditions in the future.

We decide the maturity of tomato fruit by comparing the position of tomato fruit on the infrared image and the RGB image. Furthermore, the proposed method is applied to the mosaic image which is the basic image of the tomato growth state map, and not only the position of the tomato fruit but also the maturity information is added. We aim to realize automatic harvesting of tomato fruit and tomato production control system that can predict the yield and harvest time of tomato fruit.

References

1. Bargouti, S., & Underwood, J. P. (2017). Image segmentation for fruit detection and yield estimation in apple orchards. *Journal of Field Robotics*, 1039-1060.
2. Lili, W., Bo, Z., Jinwei, F., Xiaoan, H., Shu, W., Yashuo, L., Qianbinb, Z., & Chongfeng, W. (2017). Development of a tomato harvesting robot used in greenhouse. *International Journal of Agricultural and Biological Engineering*, 10(4), 140-149.
3. Yaguchi, H., Nagahama, K., Hasegawa, T., & Inaba, M. (2016, October). Development of an autonomous tomato harvesting robot with rotational plucking gripper. In *Intelligent Robots and Systems (IROS), 2016 IEEE/RSJ International Conference on* (pp. 652-657). *IEEE*.
4. Kondo, N., Yamamoto, K., Shimizu, H., Yata, K., Kurita, M., Shigi, T., Monta, M., & Nishizu, T. (2009). A machine vision system for tomato cluster harvesting robot. *Engineering in Agriculture, Environment and Food*, 2(2), 60-65.
5. Hatou, K., Hashimoto, Y. (2002). Recognition system for tomato fruits based on the wire size reduction. *Environmental Control in Biology*. 40(1), 75-80.
6. Ota, T., Yamashita, T., Hayashi, S., & Komeda, T. (2010). Development of tomato harvesting robot with a vision system using specular reflection (Part 1) – Selection of Hand-Approach Direction by Image Processing-. *Agricultural Machine and Food Engineers*, 72(6), 587-594.
7. Fujiura, T., Nakao, S., Kondo, N., Dohi, M., & Yamashita A (1995). Dichromatic 3-D vision sensor for the agricultural robot. *Agricultural Technology Management*, 2(1), 59-64.
8. Sa, I., Ge, Z., Dayoub, F., Upcroft, B., Perez, T., & McCool, C. (2016). DeepFruits: A fruit detection system using deep neural networks. *Sensors*, 2016, 16, 1222.
9. Rahnemoonfar, M., Sheppard, C. (2017). Deep Count: Fruit Counting Based on Deep Simulated Learning. *Sensors*, 2017, 17, 905.
10. Arefi, A., & Motlagh, A. M. (2013). Development of an expert system based on wavelet transform and artificial neural networks for the ripe tomato harvesting robot. *Australian Journal of Crop Science*, 7(5), 699.
11. Yamamoto, K., Guo, W., Yoshioka, Y., & Ninomiya, S. (2014). On plant detection of intact tomato fruits using image analysis and machine learning methods. *Sensors*, 14(7), 12191-12206.
12. Fujinaga, T., Yasukawa, S., Li, B., & Ishii, K. (2017, September). Generation of mosaic image in tomato greenhouse using infrared image. *Smart Info-Media System in Asia*. 15-20.
13. Yasukawa, S., Li, B., Sonoda, T., & Ishii K. (2017, January). Development of a tomato harvesting robot. *The 2017 International Conference on Artificial Life and Robotics (ICAROB 2017)*, 408-411.
14. Kondo, N. (1988), Selection of suitable wavelength bands for discrimination between part body their spectral reflection. *Agricultural Technology Management*, 24(4), 175-183.
15. Dalal, N., & Triggs, B. (2005). Histograms of oriented gradients for human detection. *Computer Vision and Pattern Recognition*. 1(1), 886-893
16. Cortes, C., & Vapnik, V. (1995). Support-vector networks. *Journal of Machine learning*, 20, 273-297.
17. Comaniciu, D., & Meer, P. (2002). Mean shift: a robust approach to ward feature space analysis. *IEEE Transaction on Pattern Analysis and Machine Intelligence*, 24(5), 603-619.
18. Chen, X., Chaudhary, K., Tanaka, Y., Nagahama, K., Yaguchi, H., Okada, K., & Inaba, M. (2015, September). Reasoning-based vision recognition for agricultural humanoid robot toward tomato harvesting. In *Intelligent Robots and Systems (IROS), 2015 IEEE/RSJ International Conference on* (pp. 6487-6494). *IEEE*.

Comparative Study of Sequential Processing Terrain Referenced Navigation

Hyun Cheol Jeon

Department of Mechanical & Aerospace Engineering/ASRI, Seoul National University, 1 Gwanak-ro, Gwanak-gu, Seoul, 08826, South Korea

Chan Gook Park

Department of Mechanical & Aerospace Engineering/ASRI, Seoul National University, 1 Gwanak-ro, Gwanak-gu, Seoul, 08826, South Korea

E-mail: smartjhc@snu.ac.kr, chanpark@snu.ac.kr

Abstract

This study performs comparative analysis of sequential processing terrain referenced navigation (TRN) by applying various filtering techniques. TRN that prevents divergence of inertial navigation system using terrain information is an alternative to GNSS. In this paper, we consider extended Kalman filter (EKF) and point mass filter (PMF) which are widely used in the TRN. The EKF estimates state variables by linearizing a nonlinear models but it has risk of divergence due to linearization errors. On the other hands, the PMF estimates the state variables robustly but it has a disadvantage of high computational load. Through this study, the advantages and disadvantages of the TRN when applying the EKF and PMF are compared and analyzed.

Keywords: INS, Terrain Referenced Navigation, Sequential processing, nonlinear filtering, EKF, PMF,

1. Introduction

As a traditional method for estimating the position of vehicle, inertial navigation system (INS) has been used. However, since errors are accumulated in the process of integrating acceleration and angular velocity, the position of the vehicle calculated by the INS diverges over time. To overcome this shortcomings of the INS, INS/GNSS integrated navigation system that combining the INS and global navigation satellite system (GNSS) has been widely used. Although this system can provide the position information of the vehicle with a bounded error and a fast update rate, the GNSS is vulnerable to external signal disturbances such as jamming and spoofing. Therefore, terrain referenced navigation (TRN) has been developed which is robust to the external signal disturbance and can perform accurate navigation for a long time.

The TRN estimates the position of the vehicle by comparing the measured terrain elevation with digital elevation map (DEM) values of the flying area. Generally, a barometric altimeter and a radar altimeter are used for measuring terrain information, and the TRN algorithms are divided into two ways, depending on how the measurements are processed; batch processing and sequential processing TRN [1-3]. Batch processing TRN performs a position fix by matching a measured profile consisting of terrain elevation measurements collected along the trajectory of the vehicle with candidate profiles composed of DEM values. On the other hand, sequential processing TRN performs position correction every time a measurement is input by using a filtering technique such as extended Kalman filter (EKF) or point mass filter (PMF) as shown in Fig. 1.

© The 2018 International Conference on Artificial Life and Robotics (ICAROB2018), Feb. 1-4, B-Con Plaza, Beppu, Oita, Japan

EKF is a nonlinear filtering method of estimating the error states by linearizing the nonlinear system and measurement models [4]. It is relatively simple and has a small amount of computation, but it has a disadvantage in that it can be degraded or diverge when the nonlinearity is large or the initial position error is large. The PMF is a representative numerical Bayesian filtering technique that expresses probability distributions by dividing the state space into grids at regular intervals and estimates the states using this probability distribution [5]. Since the PMF uses the models as it is, it has an advantage that the state variable can be estimated effectively even for nonlinear and non-Gaussian noise models. However, because the amount of computation increases exponentially with the number of state variables, it is impossible for the PMF to estimate many state variables.

In this study, these two nonlinear filtering techniques are applied to the TRN and the results are compared in terms of computational complexity and performance. It is shown that which filter should be applied to the sequential processing TRN depending on whether a number of state variables are estimated inaccurately or a small number of state variables are estimated accurately.

2. EKF based TRN

The EKF is a nonlinear filtering technique that applies a standard Kalman filter to the error states by linearizing the nonlinear system and measurement models. Because the computational load of the EKF is smaller than that of other nonlinear filters, it is possible for the EKF to estimate many state variables such as position, velocity and attitude of the vehicle using the navigation equation as a system model. The following is a general nonlinear system and measurement model. The following is general nonlinear system and measurement model.

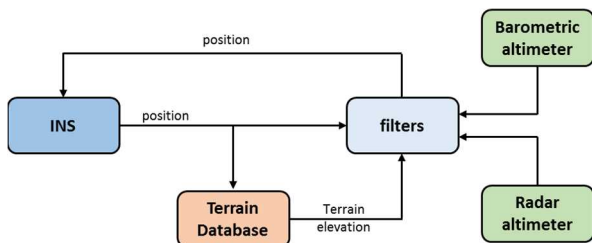


Fig. 1. Block diagram of the sequential processing TRN

$$\begin{aligned} \mathbf{x}_k &= f_{k-1}(\mathbf{x}_{k-1}) + \mathbf{w}_{k-1} \\ \mathbf{y}_k &= h_k(\mathbf{x}_k) + \mathbf{v}_k \end{aligned} \quad (1)$$

where f_{k-1}, h_{k-1} represent nonlinear system and measurement model, respectively. w_{k-1}, v_{k-1} represent system and measurement noise, respectively.

In the EKF based TRN, f_{k-1} represents navigation equation and h_{k-1} represents the vertical distance between the vehicle and the surface measured by the radar altimeter. The linearization of (1) is expressed as,

$$\begin{aligned} \delta \mathbf{x}_k &= \frac{\partial f_{k-1}}{\partial \mathbf{x}_{k-1}} \delta \mathbf{x}_{k-1} + \mathbf{w}_{k-1} \\ \delta y_k &= \frac{\partial h_k}{\partial \mathbf{x}_k} \delta \mathbf{x}_k + v_k \end{aligned} \quad (2)$$

where $\delta \mathbf{x}_k$ expresses the error states.

The measurement residual δy_k represents the difference between the actual radar altimeter measurement and the estimated radar altimeter measurement at the estimated vehicle position, which can be expressed as

$$\begin{aligned} \delta y_k &= \begin{bmatrix} -\frac{\partial h_{DEM}^{terrain}}{\partial L} & -\frac{\partial h_{DEM}^{terrain}}{\partial l} & 1 \end{bmatrix} \begin{bmatrix} \delta L \\ \delta l \\ \delta h \end{bmatrix} + v_k \\ &= \mathbf{H}_k \delta \mathbf{x}_k + v_k \quad v_k \sim N(0, R_{radar} + R_{DEM}) \end{aligned} \quad (3)$$

where, $\partial h_{DEM}^{terrain} / \partial L, \partial h_{DEM}^{terrain} / \partial l$ represent a latitudinal direction and a longitudinal direction slope, respectively. $\delta L, \delta l, \delta h$ represent latitude, longitude and altitude, respectively.

It is possible to estimate the position of the vehicle by applying the following Kalman filter to the linearized model like (2), (3).

$$\begin{aligned} \mathbf{P}_k^- &= \mathbf{F}_k \mathbf{P}_{k-1}^+ \mathbf{F}_k^T + \mathbf{Q}_k \\ \mathbf{K}_k &= \mathbf{P}_k^- \mathbf{H}_k^T (\mathbf{H}_k \mathbf{P}_k^- \mathbf{H}_k^T + R_k)^{-1} \\ \mathbf{P}_k^+ &= (\mathbf{I} - \mathbf{K}_k \mathbf{H}_k) \mathbf{P}_k^- \\ \delta \mathbf{x}_k^+ &= \mathbf{K}_k \delta y_k \end{aligned} \quad (4)$$

3. PMF based TRN

The PMF is a numerical solution of the following Bayesian filtering technique, which makes it possible to obtain robust and accurate estimation results for nonlinear and non-Gaussian problems.

$$\begin{aligned} p(x_k | Y_{k-1}) &= \int p(x_k | x_{k-1}) p(x_{k-1} | Y_{k-1}) dx_{k-1} \\ p(x_k | Y_k) &= \frac{p(y_k | x_k) p(x_k | Y_{k-1})}{\int p(y_k | x_k) p(x_k | Y_{k-1}) dx_k} \end{aligned} \quad (5)$$

However, in the process of performing the prediction, it is necessary to consider the relation with all propagated points in order to calculate the prior probability or the weight at one redesigned grid point as shown in (6). Therefore, in general, a large amount of computation corresponding to $O(N^2)$, where N is the total number of grid points.

$$p(x_k^i | Y_{k-1}) = \sum_{j=1}^N p(x_k^i | x_{k-1}^j) p(x_{k-1}^j | Y_{k-1}) \tag{6}$$

$$p(x_k^i | Y_k) \propto p(y_k | x_k^i) p(x_k^i | Y_{k-1})$$

Therefore, the PMF based TRN generally uses the linear system and nonlinear measurement model like (7), which estimates latitude L_k and longitude l_k and uses terrain elevation z_k as a measurement. In particular, in the case of TRN using the linear system model, it is possible to calculate the prior distribution using the kernel, so it is possible to greatly reduce the calculation amount of the PMF [6].

$$\begin{aligned} \xi_k &= \xi_{k-1} + \Delta \xi_{k-1} + \mathbf{w}_{k-1} \\ z_k &= g_k(\xi_k) + v_k \end{aligned} \tag{7}$$

where $\xi_k = [L_k \ l_k]^T$ and $\Delta \xi_{k-1}$ represents travel distance calculated by the INS. g_k represents terrain elevation.

Unlike the EKF based TRN, the PMF based TRN does not estimate altitude, so it use terrain elevation as a measurement, not a vertical range. Therefore, a barometric altimeter measurement $h_{k,baro}$ and a radar altimeter measurement $h_{k,radar}$ are used to measure terrain elevation.

$$\begin{aligned} z_k &= h_{k,baro} - h_{k,radar} \\ h_{k,baro} &= h_{true} + v_{k,baro} \\ h_{k,radar} &= h_{true} - h_{terrain} + v_{k,radar} \end{aligned} \tag{8}$$

Assuming that all measurement errors follow the Gaussian distribution, z_k is compared with the DEM value at the grid point $z_{DEM}(\xi_k^i)$, and the likelihood value is calculated as follows.

$$\begin{aligned} \delta z(\xi_k^i) &= z_k - z_{DEM}(\xi_k^i) \\ p(z_k | \xi_k^i) &= N(\delta z(\xi_k^i); 0, R_{radar} + R_{baro} + R_{DEM}) \end{aligned} \tag{9}$$

where ξ_k^i represents arbitrary redesigned grid point. $R_{radar}, R_{baro}, R_{DEM}$ represent measurement error variances, respectively.

The posterior distribution is calculated based on (6) using the calculated prior and likelihood. Estimation of

the state variables is computed through the weighted sum of each grid point and its corresponding probability

$$\hat{\mathbf{x}}_{k+1} = \sum_{i=1}^N \xi_{k+1}^i \omega_{k+1}^i \tag{10}$$

4. Simulation Results

To compare the performance of EKF based TRN and PMF based TRN, the TRN simulation was performed under the following conditions. It is assumed that the vehicle flies toward north at constant altitude with constant velocity as shown in Table 1. The INS was performed to simulate the movement of the vehicle, and a navigation grade IMU was applied. It was assumed that a barometric altimeter and a radar altimeter were used as the sensor for measuring the terrain information, and the SRTM 3arcsec is used as DEM. All measured noise is assumed to follow the Gaussian distribution, and its 1 sigma values are shown in the Table 2. To compare the simulation results, each algorithm was performed 30 times with Monte Carlo simulation, and the result was expressed as root mean square error (RMSE) as shown in Fig. 2.

As mentioned above, the PMF uses a nonlinear model without any assumptions such as linearization, so it can be seen that the estimation results are more accurate than that of the EKF. In addition, since the PMF does not estimate the altitude, it is necessary to use a barometric altimeter, so the inaccuracy of the measurement is greater than that of the EKF. However, better results are obtained due to the use of a more accurate model. The calculation time was 11.09 seconds for the EKF based TRN and 19.34 seconds for the PMF based TRN for one run. This is not a big difference because the PMF uses the kernel to calculate prior distribution. If the PMF is performed with iterative operation, much more computation time is required. Moreover, the EKF estimates 15 state variables, whereas the PMF estimates only 2 state variables. Thus, the EKF is much less computationally intensive for the same number of state variables.

Table 1. Trajectory conditions

Parameters	Values
Latitude	35.2° - 35.75°
Longitude	127.75°
Velocity	240m/s
Altitude	2000m

Table 2. Sensor conditions

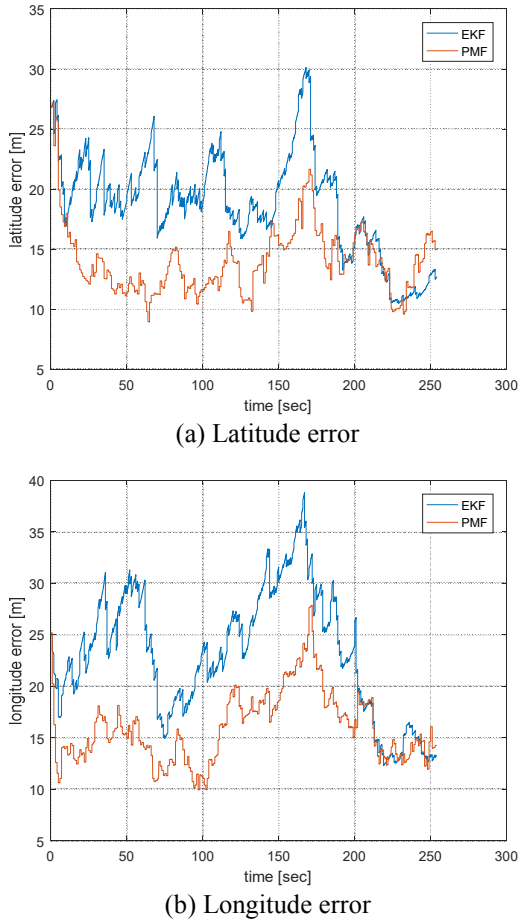


Fig. 2. RMSE results of the sequential processing TRN

Sensor	Error (1σ)
Baro altimeter	5m
Radar altimeter	15m
DEM	5m

5. Conclusions

In this paper, sequential processing TRN using various nonlinear filtering algorithm is studied. Since the TRN uses nonlinear terrain measurement, it is necessary to apply a nonlinear filter. Two nonlinear filters are applied to the TRN and the results of simulation are compared. The simulation results shows the characteristics of the two filtering techniques. Although both filters robustly estimate the vehicle position in the simulated area, the PMF using more inaccurate

measurements has obtained much more accurate estimates than that of the EKF. It is because the PMF uses a nonlinear model without any assumptions such as linearization. On the other hand, it can be seen that the computational load of the PMF that estimates only two state variables is larger than that of the EKF which estimates 15 state variables, and it is found that the PMF requires much more computational load in estimating the same number of state variables. By this research, it can be shown that which filter should be applied to the sequential processing TRN depending on whether a number of state variables are estimated with relatively degraded accuracy or a small number of state variables are estimated with relatively accurate performance.

Acknowledgements

This work has been supported by the Ministry of Science, ICT & Future Planning of Republic of Korea under Space Core Technology Development Program (Project number NRF-2013M1A3A3A02042468).

References

1. L. Zhao, N. Gao, B. Huang, Q. Wang and J. Zhou, A Novel Terrain-Aided Navigation Algorithm Combined with the TERCOM Algorithm and Particle Filter, *IEEE SENS J.*, 15(2) (2015), 1124-1131.
2. P. J. Nordlund and F. Gustafsson, Marginalized Particle Filter for Accurate and Reliable Terrain-Aided Navigation, *IEEE Trans. Aerosp. Electron. Syst.*, 45(4) (2009), 1385-1399.
3. N. Bergman, Recursive Bayesian estimation: Navigation and tracking applications, *Ph.D. dissertation, Linköping Studies in Science and Technology*, 1999.
4. D. Simon, *Optimal State Estimation: Kalman, H infinity, and nonlinear approaches* (Hoboken, NJ, John Wiley & Sons Inc., 2006)
5. M. Šimandl, J. Královec and T. Söderström, Advanced point-mass method for nonlinear state estimation, *Automatica*, 42(7) (2006), 1133-1145.
6. T. Furukawa, B. Lavis and H. F. Durrant-Whyte, Parallel grid-based recursive Bayesian estimation using GPU for real-time autonomous navigation, in *2010 IEEE International Conference on Robotics and Automation*, (Anchorage, AK, 2010), pp. 316-321.

Road Marking Map Matching for Road Vehicle Localization

Kyu Won Kim

Department of Electronic Engineering, Konkuk University, 120 Neungdong-ro, Gwangjin-gu, Seoul, 05029, South Korea

Gyu In Jee

Department of Electronic Engineering, Konkuk University, 120 Neungdong-ro, Gwangjin-gu, Seoul, 05029, South Korea

E-mail: kkw1125@konkuk.ac.kr, gjjee@konkuk.ac.kr

Abstract

In this paper, we propose map matching algorithm using road marking intensity map made of 3D LIDAR. The road marking is very useful in terms of availability because it is existed anywhere on the vehicle. The map matching algorithm is used phase correlation using FFT to enable very fast matching. In addition, the road marking map is generated by binarizing the intensity. As a result, a large-scale global map can be stored with a small capacity. Also, LIDAR scan data was accumulated for generating a high precise density local map. Accumulated local map can be supported sufficient information, especially longitudinal information. Therefore, it can be more robust and precise vehicle localization.

Keywords: autonomous vehicle, 3D LIDAR, binary road marking map, map matching.

1. Introduction

Recently, localization is becoming an issue of autonomous vehicle research. Generally, GPS is used as a sensor for localization. However, GPS has large error in urban area. To solve this problem, error correction using map is used. And the position of the vehicle is estimated by correcting the error by matching the data obtained through the map and the sensor. In general, maps are used for location estimation by storing road environments such as lanes [1], traffic lights [2], and curbs [3]. Among them, the road marking map using the reflectivity of LIDAR is highly available because it uses the road markings existing everywhere on the road.

In this paper, we propose a method of generating a map using the reflectance of road marking and matching the position with the 3D LIDAR scan data. First, the map

information of the global map is binarized to generate 2D binary road map for map matching. As a result, a large global map was created with a small capacity. Map matching algorithm using FFT-based phase correlation was performed to enable real-time matching. In order to derive a robust matching performance, sensor data obtained from 3D LIDAR is accumulated to generate a precise local map. Through this, we supplemented the relatively weak longitudinal information and derived road marking information that can be matched even in the rush hour.

2. 2D Binary Road Marking Map Generation

First of all, we generate Global road marking map. Map must be Accurate and precise for accurate location estimation for accurate localization. Therefore, the initial trajectory was generated using the expensive GPS-RTK

(Real Time Kinematic) / INS for precise map generation. However, when the map is generated using the basic SLAM [4], the road marking in the map is not consistent. To solve this problem, we performed trajectory optimization using Graph SLAM [5] to generate precise and accurate map trajectories. Based on the generated map trajectory, the map data was generated by accumulating the intensity data scanned with 3D LIDAR. At this time, the reflectivity information was calculated by averaging each grid in the map.

However, in order to calculate the reflectivity average, it is necessary to put the average and the number of scans each grid. In such a case, the map capacity increases exponentially when generating a wide range of global map. In order to prevent this, the average of the reflectance in the map is binarized. Also, we applied the Otsu Threshold method to generate threshold. Fig. 1 shows the result of generating the road markings with intensity and binary maps. The road markings are clearly extracted. And, Table 1 shows the capacity of each map, the map resolution is 0.1m. The intensity map shows 121 MB of storage capacity by storing the average and the number of scan. On the other hand, capacity of binary map is greatly reduced. And if you make a binary map

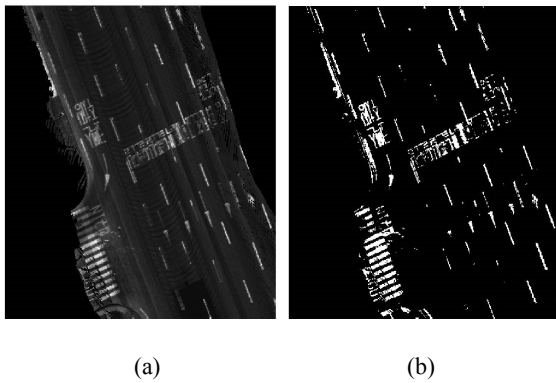


Fig. 1. Road Marking Map Generation Result.

(a) Intensity Map (b) Binary Map

Table 1. Capacity of Map

Map area (1.4km x 2km)	Intensity Map	Binary Map	Binary Map (Sparse Matrix)
Capacity	121MB	2.04MB	449KB

with sparse matrix, you can remove the place where 0 is included. So, the capacity will be further reduced.

3. Precise Local Map Generation

The localization using the map is performed by matching the global map and the local map obtained through LIDAR. Also, we have accumulated the LIDAR data [6] according to the progress of the vehicle and we use this to create a precise local map. A precise local map compensates for insufficient longitudinal information because it uses accumulated data according to the traveling direction of the vehicle. Fig. 2 shows how LIDAR data scanned from the road marking accumulates as the vehicle travels. As shown in figure, the previously scanned data is pushed backward as the vehicle moves and you can see the accumulation of the current scanned data. Also, it fills in the empty space between the layers as the data accumulates. So, the problem of reducing the density of the road marking is solved. Fig. 3 shows the process of generating a precise local map. As the accumulation progresses, it can be seen that the road marking information increases so as to clearly distinguish the road surface display in the longitudinal direction.

4. Map Matching Algorithm

4.1. FFT-based Phase Correlation

Localization of the vehicle is performed by matching a precise local map with the global map. The map matching method is based on FFT-based phase correlation. The FFT-based phase correlation equation is as follow.

$$corr(m, z) = F^{-1} \left\{ \frac{M(f)Z^*(f)}{|M(f)Z^*(f)|} \right\}$$

$$M(f) : F\{m(t)\} \quad Z(f) : F\{z(t)\} \quad (1)$$

Fig. 4 shows the FFT-based correlation results. (a) is a cross correlation result, and (b) is a phase correlation result. As shown in this figure, it can be seen that the (b) Correlation Peak is sharper than (a). However, even if phase correlation is used, noise is generated. And if Peak is 2 or more, wrong matching result can be obtained. To solve this problem, we applied a Gaussian filter based on the previously estimated position. As a result, noise is removed and only Peak results near the estimated location can be used, even if peaks occur at other locations. The Gaussian filter equation is as follow.

$$\begin{aligned}
 P_{peak} &= \max(corr) \\
 [x_{peak} \ y_{peak}] &= \text{find}(corr = P_{peak}) \\
 [x_{mean} \ y_{mean}] &= [E[x_{peak(t-k : t)}] \ E[y_{peak(t-k : t)}]] \\
 P_{gauss} &= \exp\left(\frac{(x - x_{mean})^2 + (y - y_{mean})^2}{-2\delta^2}\right) \\
 P_w &= corr \times P_{gauss}
 \end{aligned} \tag{2}$$

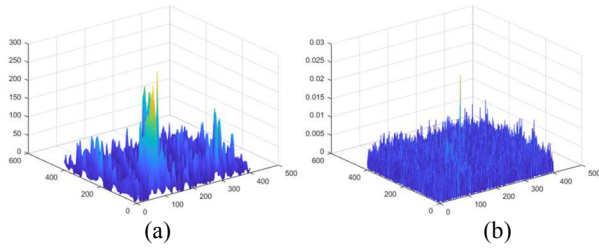


Fig. 4. FFT-based Correlation Result.

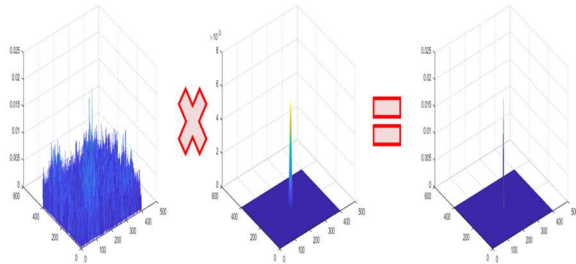


Fig. 5. Example of Gaussian Filter application result.

Fig. 5 shows an example of Gaussian filter application result. As shown in this figure, the noise except Peak is disappeared. Also, peaks at other positions are removed, and a sharp peak can be extracted based on the estimated position.

4.2. Matching Confidence Judgement

In the case of the localization using the map, if the matching is wrong, a large error may occur. Especially, in the case of autonomous vehicles, wrong positioning results can lead to serious accidents. Therefore, if the matching result is wrong, it should be detected and the wrong matching result should not be used. In this study, two parameters were generated to determine the reliability of the matching result. One is the PL (Protection Level), and the other is a PSR (Peak to Sidelobe Ratio) that determines the sharpness of the correlation. Equation of PL is as follow.

$$\begin{aligned}
 [\Delta x \ \Delta y] &= [(x_t - x_{t-1}) \ (y_t - y_{t-1})] \\
 c &= \text{cov}([\Delta x \ \Delta y]) \\
 \sigma_{pos} &= \max(\text{eigenvalue}(c)) \\
 K &= \text{Rayleigh}^{-1}(1 - P_{md}) \\
 P_{md} &: \text{probability of false matching} \\
 PL &= K \times \sigma_{pos}
 \end{aligned} \tag{3}$$

In addition, matching reliability can be judged through peak sharpness. Because it means that the matching result is certain. Therefore, we used the PSR to determine the sharpness of the peak. PSR is the ratio between the peak and the noise around peak. The larger the PSR value, the sharper the peak. The equation for obtaining PSR is as follow.

$$PSR = \frac{\text{peak} - \text{mean}(\text{sidelobe})}{\text{std}(\text{sidelobe})} \tag{4}$$

When the PL and PSR are obtained described above, the reliability of the matching result is determined based on the two parameters. Matching result is more reliable when PL is lower and PSR is higher. Fig. 6 shows an example of threshold setting

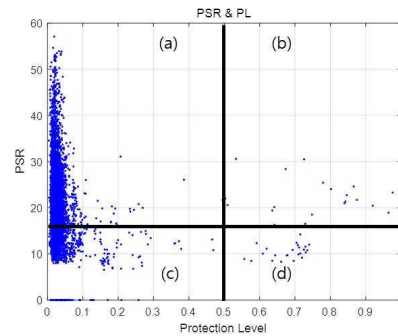


Fig. 6. Example of PL & PSR Threshold.

of PL and PSR. The results in (a) of Fig. 6 show high matching reliability. Therefore, this study used map matching results in (a) range, and if the results of other ranges were derived, Dead Recoking was performed through LIDAR Odometry using ICP until reliable results were obtained.



Fig. 7. Experimental Area.

5. Experimental Result

In order to verify the localization performance using the map matching algorithm proposed in this paper, we performed experiments in the urban area where the GPS error is large as shown in Fig. 7. And, we used the data of the rush hour time to estimate localization performance when there are many nearby vehicles. Also, 3D LIDAR used in the experiment was Velodyne HDL-32E. The reference trajectory used for the error analysis is based on the vehicle trajectory optimized through Graph SLAM in Section 2.

Fig. 8 shows the position error. As shown in Table 2, the GPS / DR RMS error occurs more than 6m, while the RMS error is less than 15cm in both lateral and longitudinal when using the map matching algorithm. Therefore, we confirmed that the map matching algorithm of this study has very precise and reliable positioning result.

6. Conclusion

In this paper, we propose a map matching algorithm using binary road marking map. And, we used a binary road marking map to store map information on a wide area in a small capacity. In addition, a precise local map is generated to supplement the lacking longitudinal road marking information, and matching is possible even when there are many obstacles such as a vehicle. And we applied the map matching algorithm using FFT -based Phase Correlation to improve the processing time and to obtain accurate and reliable localization result using the reliability determination algorithm.

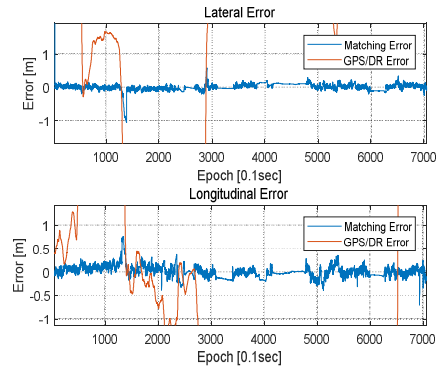


Fig. 8. Position Error.

Table 2. RMS Position Error

RMS Error[m]	Lateral	Longitudinal
GPS/DR	6.79	6.28
Map Matching	0.149	0.146

References

1. D. Kim, T. Jung, and K.-S. Yi, "Lane map-based vehicle localization for robust lateral control of an automated vehicle," *Journal of Institute of Control, Robotics and Systems (in Korean)*, vol. 21, no. 2, pp. 108-114, 2015.
2. J. Levinson, J. Askeland, J. Dolson, and S. Thrun, "Traffic light mapping, localization, and state detection for autonomous vehicles," *Proc. of Robotics and Automation (ICRA), 2011 IEEE International Conference on. IEEE*, May 2011.
3. A. Y. Hata, F. S. Osorio, and D. F. Wolf, "Robust curb detection and vehicle localization in urban environments," *2014 IEEE Intelligent Vehicles Symposium Proceedings. IEEE*, 2014.
4. C.-C. Wang and C. Thorpe, "Simultaneous localization and mapping with detection and tracking of moving objects," *Robotics and Automation, 2002. Proceedings. ICRA'02. IEEE International Conference on*, vol. 3. IEEE, 2002.
5. Thrun, Sebastian, and Michael Montemerlo. "The graph SLAM algorithm with applications to large-scale mapping of urban structures," *The International Journal of Robotics Research*, 25.5-6, pp. 403-429, 2006.
6. Z. J. Chong, B. Qin, T. Bandyopadhyay, M. H. Ang, E. Frazzoli, and D. Rus, "Synthetic 2d lidar for precise vehicle localization in 3d urban environment," *Proc. of Robotics and Automation (ICRA), 2013 IEEE International Conference on. IEEE*, 2013.

Control System Design of Directionally Maneuvering Multicopter with Constant Yaw Rate

Jaehyu Bae, Dong-Gyun Kim, Byoungjin Lee and Sangkyung Sung

Department of Aerospace Information Engineering/Konkuk University, 120 Neungdong-ro, Gwangjin-gu, Seoul, 05029, Korea

Joon Goo Park

School of Electronics Engineering/Kyungpook National University, 80 Daehakro. Bukgu. Daegu. 41566. Korea

E-mail: schumir@konkuk.ac.kr, sksung@konkuk.ac.kr

Abstract

This paper presents the controller design, implementation and flight test results of a multicopter system for achieving vertical axis rotating motion and a separated maneuvering in horizontal axis, simultaneously. For this, formulation for position and velocity control of the multicopter is designed and the trajectory guidance method is exploited. Especially, the quaternion - based motions and thrust control equations are newly derived, which can generate an independent differential thrust in the horizontal axis while maintaining a constant vertical axis rotation. In order to verify the performance of the designed controller, the algorithm is implemented in an onboard flight control computer. Flight test results demonstrate trajectory errors within 2m during cyclic motion.

Keywords: Multicopter, Rotating Motion, Separated Maneuvering, Differential Thrust, Flight Test,

1. Introduction

Multicopter is a type of unmanned aerial vehicle capable of vertical takeoff and landing. It is simpler in structure than a helicopter, which is the same vertical takeoff and landing aircraft, and is easily used by individuals, contributing to the private use of drones. Recently, small drones with the shape of a multicopter have been developed and their utilization is getting higher. Small Multicopter is used for leisure sports, spraying of pesticides, delivery service, and is often used to acquire information about the environment such as aerial photographing and 3D spatial information acquisition. [2]

On the other hand, the multicopter type gas has a symmetrical structure about the front, rear, left and right reference axes in terms of shape and kinetic model.

Therefore, it is not necessary to fix the head of the gas depending on the shape of the gas, and the instantaneous horizontal posture change can be used even when an arbitrary start is required.

Also, when using the sensor to acquire the information of the surrounding environment by using these characteristics, it is possible to obtain more information by rotating the sensor only by the operation of the gas separated from the horizontal maneuver without adding an actuator such as a gimbal for rotating the sensor can do.

In this paper, we propose the automatic flight control experiment including the cyclic heading maneuver using the Hexacopter. Section 2 introduces the dynamic model of Hexacopter which is used as a platform, and Section 3 explains the principle of the design of quaternion-based

© The 2018 International Conference on Artificial Life and Robotics (ICAROB2018), Feb. 1-4, B-Con Plaza, Beppu, Oita, Japan

horizontal start separation cyclic heading controller and the rotation maneuver. Section 4 introduces vehicle and flight experimental results, and conclusions are made in Section 5.

2. Multicopter Dynamics Modeling

The multicopter system representatively considered in this paper is hexacopter, while it can be extended to other symmetric multicopter system model. The dynamics of the hexacopter are derived by the Moment Equation, Total Thrust Equation and Energy Equation. Figure 1 shows the defined hexacopter model. [5]

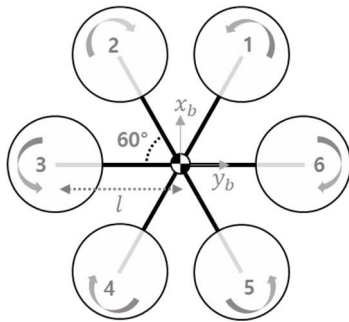


Figure 1 Hexacopter System Model.

Each rotor was ordered in the counterclockwise direction to the front right by 1 and the distance from the center of gravity to the center of each rotor was defined. Moment Equation can be used as the moment of rotation of each rotor by the thrust of the rotors.

$$\bar{M}_{con} = \begin{bmatrix} M_x \\ M_y \\ M_z \end{bmatrix} = \begin{bmatrix} l \cdot \left\{ \left(\frac{T_2}{2} + T_3 + T_4 \right) - \left(\frac{T_1}{2} + \frac{T_5}{2} + T_6 \right) \right\} \\ \frac{\sqrt{3}}{2} \cdot l \cdot (T_1 + T_2 - T_4 - T_5) \\ \kappa \cdot (T_1 - T_2 + T_3 - T_4 + T_5 - T_6) \end{bmatrix} \quad (1)$$

\bar{M}_{con} is the moment that should be generated for the control target, which is derived from the attitude controller in Section 3I. T_i is the thrust generated by each rotor, and the subscript is the number of the rotor defined

in the figure. And κ is a constant due to the relationship between the thrust and the rotation moment of the rotor. The sum of the thrusts generated by each rotor by the total thrust equations is equal to the magnitude of the total force, as shown below.

$$\|\bar{F}_{con}\| = \sum_{i=1}^6 T_i \quad (2)$$

Formulated as the total thrust equation in (2), the force to be generated for the trajectory control is derived from the position / velocity controller in Section III. And energy equation is derived to efficiently distribute the total amount of thrust to be generated to each rotor.

$$E = \sum_{i=1}^6 T_i^2, \min(E) \text{ condition} \quad (3)$$

The energy is assumed to be the sum of the squares of the thrusts of each rotor and is used under the condition that energy is minimum. The thrust to be generated in each rotor to satisfy all three conditions; that is moment, total thrust, and energy equation is Eq. (4). [3]

$$\begin{aligned} T_1 &= -\frac{M_x}{6 \cdot l} + \frac{M_y}{2\sqrt{3} \cdot l} + \frac{M_z}{6 \cdot \kappa} + \frac{\|\bar{F}_{con}\|}{6} \\ T_2 &= +\frac{M_x}{6 \cdot l} + \frac{M_y}{2\sqrt{3} \cdot l} - \frac{M_z}{6 \cdot \kappa} + \frac{\|\bar{F}_{con}\|}{6} \\ T_3 &= +\frac{M_x}{3 \cdot l} + \frac{M_z}{6 \cdot \kappa} + \frac{\|\bar{F}_{con}\|}{6} \\ T_4 &= +\frac{M_x}{6 \cdot l} - \frac{M_y}{2\sqrt{3} \cdot l} - \frac{M_z}{6 \cdot \kappa} + \frac{\|\bar{F}_{con}\|}{6} \\ T_5 &= -\frac{M_x}{6 \cdot l} - \frac{M_y}{2\sqrt{3} \cdot l} + \frac{M_z}{6 \cdot \kappa} + \frac{\|\bar{F}_{con}\|}{6} \\ T_6 &= -\frac{M_x}{3 \cdot l} - \frac{M_z}{6 \cdot \kappa} + \frac{\|\bar{F}_{con}\|}{6} \end{aligned} \quad (4)$$

3. Control System Design for Maneuvering

The controller generates the control moment via the position and velocity controller and the attitude controller based on the information provided in the guidance and navigation. To generate the control moment, we calculate the thrust to be generated in each rotor by Hexacopter dynamics in Section 2.

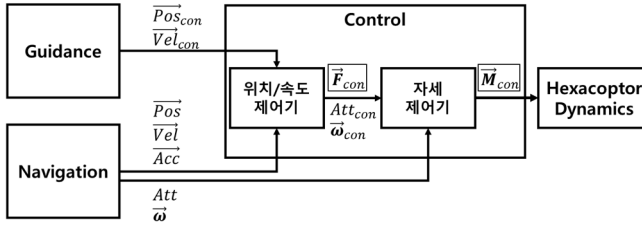


Figure 2 Control System Structure.

The position and velocity controller is the process of generating the force that the hexacopter must take through the position and speed control, Eq. (5) is the equation.

$$\begin{aligned} \vec{F}_{con} = & K_{P,Pos} \cdot (\overline{Pos}_{con} - \overline{Pos}) + K_{I,Pos} \cdot \int (\overline{Pos}_{con} - \overline{Pos}) dt \\ & + C_{drag} \cdot \|\vec{Vel}_{con}\| \cdot \vec{Vel}_{con} \\ & + K_{P,Vel} \cdot (\|\vec{Vel}_{con}\| \cdot \vec{Vel}_{con} - \|\vec{Vel}\| \cdot \vec{Vel}) \\ & + K_{D,Vel} \cdot (\vec{0}_{3 \times 1} - \overline{Acc}) \\ & + m \cdot \vec{g} \end{aligned} \quad (5)$$

The position control system takes a general formulation of PI control. PI control is performed on the difference between the control input value generated by the guidance and the actual position of the vehicle provided by the navigation. $K_{P,Pos}$ is the proportional control gain for the position, and $K_{I,Pos}$ is the integral control gain.

The velocity control requires a force proportional to the square of the speed. C_{drag} is a drag coefficient and is a coefficient by aerodynamic force, which is multiplied by the square of the velocity magnitude such that the vehicle can actually actuated. $K_{P,Vel}$ is the proportional control gain for the velocity, and $K_{D,Vel}$ is designed to react to sudden disturbances by multiplying the acceleration by the differential control gain for the velocity. And $m \cdot \vec{g}$ is the vertical drag of gravity.

For designing the attitude controller, it is proposed a new function for deriving the required control force, as in (6). The output of the function q is the quaternion of rotating vectors between \vec{a} and \vec{b} 's rotating in. [1] With this equation, the objective attitude quaternion for vehicle to have the desired \vec{F}_{con} is computed as (6)

$$\begin{aligned} \vec{a}_n &= \frac{\vec{a}}{\|\vec{a}\|}, \vec{b}_n = \frac{\vec{b}}{\|\vec{b}\|} \\ \vec{c}_n &= \frac{\vec{a}_n + \vec{b}_n}{\|\vec{a}_n + \vec{b}_n\|} \\ q &= [\vec{a}_n \cdot \vec{c}_n, \vec{a}_n \times \vec{c}_n]^T \end{aligned} \quad (6)$$

$$q_{con} = f_{inner_qua} \left(\begin{bmatrix} 0 \\ 0 \\ -1 \end{bmatrix}, \vec{F}_{con} \right) \quad (7)$$

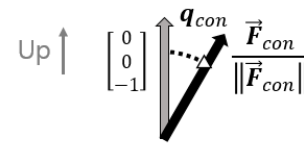


Figure 3 Attitude Quaternion for Generating Control Force.

For the ease of attitude regulation, perturbation quaternion q_δ is computed as (8), which in fact is differential quaternion between the Z axis direction vector of the q -reference body and the Z axis direction vector of the q_{con} -reference body.

q_δ is the magnitude of the attitude to be controlled and required to be converted into the Euler angle. Finally the moment \vec{M}_{con} is generated by the PD controller implementation.

$$\vec{M}_{con} = K_{P,Att} \cdot f_{qua2euler}(q_\delta) + K_{D,Att} \cdot (\vec{0}_{3 \times 1} - \vec{\omega}_b) \quad (8)$$

where $\vec{\omega}_b$ is the body rate obtained by gyroscope

For generating constant rotating system, rate controller is the Z-axis is designed.

$$M_{con,z} = K_{P,Att} \cdot f_{qua2euler}(q_\delta)_z + K_{D,Att} \cdot (r_{con} - r) \quad (9)$$

where r_{con} is the target rate in the rotation axis.

When the constant angular velocity of a vehicle produces a constant moment, the moment magnitude of the horizontal axis of the body takes a sinusoidal waveform, and the output of the motor is also sinusoidal. Figure 4 shows the moment of the rotating Hexacopter while generating the moment, and Eq. (10) shows the moment equation at that time.

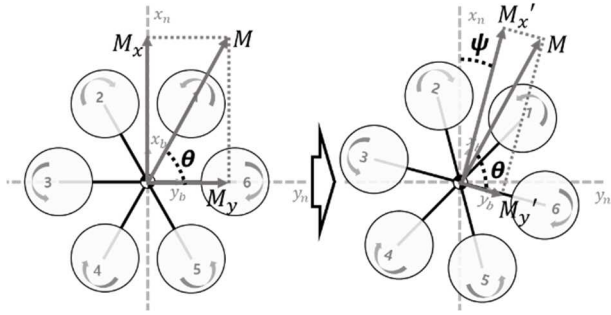


Figure 4 Moment via Vehicle Rotation.

$$\begin{aligned} M_x' &= M_x \cos \psi + M_y \sin \theta \\ M_y' &= -M_x \sin \psi + M_y \cos \theta \end{aligned} \quad (10)$$

It can be observed that the formula for the moment changes in sinusoidal form by (10). Consequently, the general thrust equation of hexacopter is obtained by

$$\begin{aligned} T &= A \cdot M_x + B \cdot M_y + C \cdot M_z \\ T' &= (A \cos \psi - B \sin \psi) \cdot M_x + (A \sin \psi + B \cos \psi) \cdot M_y \\ &\quad + C \cdot M_z' \end{aligned} \quad (11)$$

4. Experimental Results

Figure 5 shows the hexacopter system used in the experiment. Onboard FCS system is implemented for realizing the directional maneuvering under fixed rotating motion.



Figure 5 Hexacopter For Flight Demonstration.

A simple trajectory consisting of straight lines is used for flight test. Figure 6 and 7 shows the rotating angle of the vehicle and the control input at the motor while directional maneuvering. A constant rate of about 45deg/sec is achieved for rotating motion. For horizontal

maneuvering, a sinusoidal PWM input is generated, which is contaminated by external disturbance such as side wind effect.

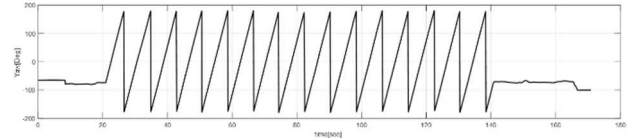


Figure 63 Rotation Angle (Yaw) .

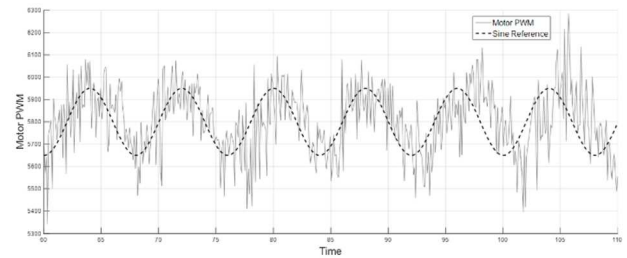


Figure 7 Motor control Input.

5. Conclusions

In this paper, a control system design of directionally maneuvering is presented with a constant rate motion. Experimental demonstration is presented for its verification.

Acknowledgements

This work was supported by the Ministry of Science, ICT & Future Planning of Republic of Korea (NRF-2016M1B3A1A01937380 and 2016R1A2B4010719).

References

1. B. J. Lee, "Design and Performance Analysis of an Attitude Reference System using GPS/INS Velocity Differential Vectors", Ph.D. Dissertation Dept. of Aerospace Information Engineering Konkuk University, 2017.
2. D. G. Kim, B. J. Lee, Y. J. Lee, and S. Sung, "Flight Control Test of Quadrotor-Plane with Hybrid Flight Mode of VTOL and Fast Maneuverability." *Journal of Institute of Control, Robotics and Systems*, 22.9, pp. 759-765, Sep. 2016.
3. T. S. Jin, "Dynamic Model and P-PD Control based Flight Performance Evaluation for Hexa-Rotor Type UAV." *The transactions of The Korean Institute of Electrical Engineers*, 64.7, pp. 1074-1080, Jul. 2015.

Automatic recognition of benthic species using image processing

Yuki Soejima, Yuya Nishida, Takashi Sonoda and Kazuo Ishii

*Department of Human Intelligence Systems
Kyushu Institute of Technology
2-4 Hibikino, Wakamatsu-ku, Kitakyushu, Fukuoka, 808-0196 Japan
E-mail: ishii@brain.kyutech.ac.jp,*

Abstract

For sustainable use of fisheries resources, it is important to estimate the amount of resources such as TAC (Total Allowable Catch), TAE (Total Allowable Effort) and their investigations have been conducted by bottomed net fishing, however, the method suffers environmental damages. The survey method for wider area that does not affect the ecosystem is needed. Recently, research using an autonomous underwater robot (AUV) is introduced as a new survey method as the solution. We also introduced an AUV for the survey of fish and crabs in the Sea of Okhotsk. The number of marine lives is measured manually, and the technique of automatic measurement of the number is needed for the observation. In this research, we propose an automatic marine life recognition method from seafloor images.

Keywords: Recognition, Benthic species, Underwater image processing

1. Introduction

Fishery resources that exist in the deep sea have been attracting attention, and many marine technologies have been developed to acquire resources. Among them, TAC (Total Allowable Catch) and TAE (Total Allowable Effort) are listed from the Fisheries Agency, and there is a trend to make it possible to use finite marine biological resources for a long time. Aquatic biological resources become sustainable resources that will not be depleted by continuing fishing at an appropriate catch. There is a possibility of depletion if catch of fish keeps in free competition. Therefore, it is necessary to manage resource amount to some extent.

In recent years, surveys using autonomous underwater robots (AUV) are proceeding, and among them, fishery resources can be observed in local waters. However, since the image captured by AUV is observed by a human being and the number of organisms is measured, a technique for automatically measuring the number of organisms in an image becomes necessary. In this study, we propose a pretreatment detection method to recognize benthos organisms from deep sea bottom images.

2. Recognition of benthic species

Images of the ocean floor surface photographed in the deep sea may be recognized as different organisms even if they are the same organism because the manner in which light is reflected in the image is different. Therefore, as a preprocessing of object recognition processing, a detection method was examined to generate an object divided object.

In the object detection method, object candidate detection (shown in Fig. 1, an algorithm is shown) for detecting objects with high attention by saliencies, object extraction for dividing living organisms and the seabed surface from the detected object candidates (an algorithm is shown in Fig. 2), As shown in FIG.

In the object candidate detection processing, a color correction image (showing the original image and the color correction image in Fig.3) is input, a saliency map is generated from the Fourier transform, and the object candidate area is generated from the binarization of the saliency map. The values of the sagitti within the candidate area are summed up, and the average value of the pixels is taken as the attention degree of the candidate area. We will detect candidates with high degree of attention (Figure 4 shows attention degree and candidate

area). In the next extraction processing, since the space of the detected candidate image is perceived at the color distance, it is converted into the Lab color space which is a psychological space which makes the color change uniform. Reduce color resolution by color reduction processing, and generate cluster mask for each color system. As assumptions to determine the number of clusters, we assume that "There are up to two kinds of interested organisms and other organisms at the same time in the overlooked candidate image, and the ocean floor surface is visible". The result of extracting the object is shown in Fig.5.



Fig.1 Flow of image processing



Fig.2 Flow of object extraction

3. Recognition Experiments

We verify the recognition rate by the object extracted data using object detection method of this research. For the experiment method, prepare 30 seabed surface images as original images. Input the seabed surface image and perform color correction processing. Those with high degree of attention were detected from the color corrected image and the feature vectors generated from the database by the BoK method were compared with the feature vectors of the teacher data by the histogram intersection method. As a result of recognition, the detection rate of the object candidate was 90%, the extraction rate of the object was 89%, and the recognition rate of the object was 67%. Table 1 shows experimental results.



Fig.3 Deep sea image using color correction.



Fig.4 Object candidate detection processing

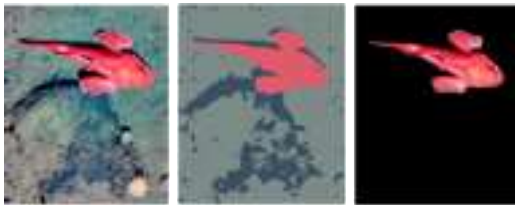


Fig.5 Object extraction processing

Table 1 Results of Recongition

	Num of Objects	Num Of Detection	Num. Of Candidate	Num Of Recognition	Succ ess rate [%]
Kichiji	15	15	15	10	67
Shrimp	15	14	11	7	64
Crab	10	7	6	4	67

4. Conclusion

With the detection method of this research, object extraction processing using color information in the

seafloor surface image became possible, so extraction of feature amount such as the seabed surface etc. appearing in other than object is reduced, only the feature amount of the living thing is extracted and object recognition Accuracy improved. Although the recognition rate is about 70%, it is about 55% in terms of overall processing accuracy. Because there are misrecognition of small objects and small shrimps and small shrimps in a situation where the target organisms are overlooked, it is necessary to utilize the morphological features of each kind of organism for classification.

References

1. Y. Junku, T. Ura and G. Bekey, *Underwater robots*, Springer Science & Business Media, 2012.
2. L. L. Whitcomb, "Underwater robotics: Out of the research laboratory and into the field," *ICRA'00. IEEE International Conference on*. Vol. 1., 2000.
3. Y. Nishida, T. Ura, T. Sakamaki, J. Kojima, Y. Ito and K. Kim, "Hovering Type AUV "Tuna-Sand" and Its Surveys on Smith Caldera in Izu-Ogasawara Ocean Area," *2013 OCEANS-San Diego*. IEEE, 2013.
4. T. Maki, Y. Sato, T. Matsuda, R. T. Shiroku and T. Sakamaki, "AUV Tri-TON 2: An intelligent platform for detailed survey of hydrothermal vent fields," *IEEE/OES Autonomous Underwater Vehicles (AUV)*, 2014.
5. Y. Nishida, K. Nagahashi, T. Sato, A. Bodenmann, B. Thornton, A. Asada and T. Ura, "Development of an autonomous underwater vehicle for survey of cobalt-rich manganese crust," *OCEANS 2015-MTS/IEEE Washington*, 2015.
6. T. Ura, "Observation of Deep Seafloor by Autonomous Underwater Vehicle," *IJMS*, 42(8), 1028-1033, 2013.
7. M. Bewley, B. Douillard, N. Nourani-Vatani, A. Friedman, O. Pizarro and S. Williams, "Automated species detection: An experimental approach to kelp detection from sea-," *Australasian Conference on Robotics and Automation*, 2012.
8. M. Boudhane and B. Nsiri, "Underwater image processing method for fish localization and detection in submarine environment," *Journal of Visual Communication and Image Representation*, 2016.
9. E. O. Hulburt, "Optics of Distilled and Natural Water," *Journal of the Optical Society of America* Vol. 35, Issue 11, pp. 698-705, 1945.
10. T. Nakatani, T. Ura, Y. Ito, J. Kojima, K. Tamura, T. Sakamaki and Y. Nose, "AUV" TUNA-SAND" and its Exploration of hydrothermal vents at Kagoshima Bay," *OCEANS 2008-MTS/IEEE Kobe Techno-Ocean*, 2008.
11. R. Szeliski, *Computer Vision: Algorithms and Applications*, Springer-Verlag London, 2010.

Koji Masuda, Yuya Nishida, Takashi Sonoda, Kazuo Ishii

12. B. L. McGlamery, "A computer model for underwater camera systems," *Ocean Optics VI. International Society for Optics and Photonics*, 1980.
13. J. S. Jaffe, "Computer modeling and the design of optimal underwater imaging systems," *IEEE Journal of Oceanic Engineering*, 1990.

AUV Homing Using Acoustic Chirp Signal

Koji Masuda, Yuya Nishida, Takashi Sonoda, Kazuo Ishii

*Department of Human Intelligence Systems
Kyushu Institute of Technology
2-4 Hibikino, Wakamatsu-ku, Kitakyushu, Fukuoka, 808-0196 Japan
E-mail: ishii@brain.kyutech.ac.jp,*

Abstract

For autonomous underwater vehicle (AUV), high autonomy is required in order to accomplish mission such as inspection, observation, manipulation under extreme environments, deep-ocean. One of necessary function for AUV is acoustic navigation. In this paper, we conducted homing experiments using a small AUV and acoustic pinger with chirp signal. The chirp signal has the feature that the frequency of signal change gradually, so that the signal is suitable to calculate the correlation between the time difference between hydrophones. The homing experiments are carried out and evaluated through tank tests.

Keywords: AUV, homing control, chirp signal

1. Introduction

In recent years, observation with underwater robots have been carried out. However, deep sea is dangerous environment for human beings due to high pressure, darkness and low temperature. Therefore, the exploration activity of underwater environment with underwater vehicle is expected. Especially Autonomous Underwater Vehicle (AUV) has been attracting attention to work or research in the water on behalf of the human. In addition, there is a growing need for a wide range search such as biological ecology observation and maintenance of the underwater structure. AUVs can operate without an umbilical cable and can be utilized in various fields have been attracting attention [1]. On the other hand, AUV is restricted the activity time due to battery capacity. Thus, operation of charging station in water is required for a battery-driven AUV to conduct observations for extended durations [2]. Utilization of charging station in the water is required for long-term operation to solve this problem.

The navigation system of AUV is one of important things for utilizing charging station. Acoustic positioning system is used because it is difficult to use radio wave such as GPS in water. In this paper, we describe a navigation system to the station with acoustic positioning system. In this system, sound source pinger is mounted the station and AUV is one meter class. Therefore, we

developed a compact acoustic positioning system that mounting is possible to the AUV. It has three hydrophones and receives signal from pinger. Sound source detection is calculated by Cross Correlation Function and Super Short Base Line method. In addition, we introduce chirp signal as the sound source to develop a robust acoustic positioning system against noises. In the experiment of sound source detection with hydrophone array, we measured ± 90 [deg] of area in front. According to the experimental result, the detection accuracy of the developed system module is within 10 [deg] of average error and 5 [deg] of standard variation, and the present result suggested that sound source detection is feasible in this system.

The positioning of AUV is important. However, acoustic positioning system is used since GPS cannot be used underwater. It is grouped into three classes such as Long Base Line (LBL), Short Base Line (SBL) and Super Short Base Line (SSBL). LBL is extremely accuracy compared with other methods but this method requires some ultrasonic beacon at the bottom of sea and its calibration. SBL and SSBL requires only one beacon. SBL detects the position of sound source from time difference of arrival. SSBL does it from phase difference and receiver array of AUV become compact. Moreover, SBL and SSBL are suitable for AUV because these methods don't require the calibration [3, 4]. In this research, SSBL method is applied for AUV for ease of operation. This

paper describes a navigation system with acoustic positioning system for AUV.

2. Acoustic Positioning System

The block diagram of the acoustic positioning system is shown in Fig. 1. This system consists of three hydrophones, amplifier, bandpass filter and micro processing unit (MPU). The acoustic wave received by each hydrophones is converted into an electrical signal. The signals are performed amplification and noise removal by the signal processing circuit. MPU takes a sample the signals at 250 [kHz]. The sampling data is sent to AUV's single-board computer and phase difference is obtained by calculating following Cross Correlation Function (CCF).

$$R_{xy}(m) = \frac{1}{M} \sum_{n=1}^M x(n)y(n+m) \quad (1)$$

x is value of reference signal voltage. y is value of received signal voltage. The argument m is obtained as the phase difference when R_{xy} is maximum.

CCF show a strong correlation when the target signals include many frequency range. Therefore, chirp signal is used as sound source with robustness against noises in mind. The chirp signal has a pulse wave form whose carrier frequency changes linearly with time and it is possible to obtain many frequency range within a certain time [5]. The sweep frequency range of pinger is from 28.75 [kHz] to 21.25[kHz], the duration time is 1 [msec].

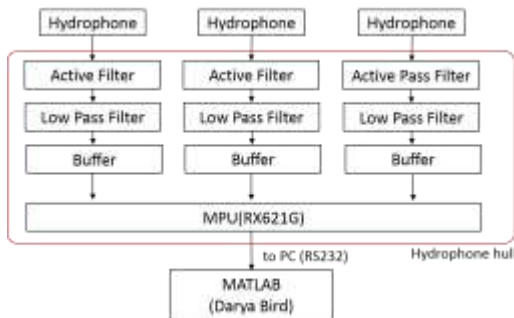


Fig. 1. Block diagram of acoustic positioning system.

3. Experiments

An experiment of sound source detection with developed acoustic positioning system module was carried out. Pinger and hydrophone array are set as

© The 2018 International Conference on Artificial Life and Robotics (ICAROB2018), Feb. 1-4, B-Con Plaza, Beppu, Oita, Japan

shown in Fig. 2. The experimental pool has a diameter of 6 [m], the distance between pinger and hydrophone array is r and the relative angle between pinger and hydrophone array is θ_{xy} . In this experiment, the measuring relative angle is set in total nine points from -90 [deg] to +90 [deg] in steps of 22.5 [deg]. Furthermore, the distance r is set in 2, 3 and 4 [m]. The number of samples of each angle are 15.

Figure 3-5 show the results of sound source detection. The Average in the figures shows average value of 15 data. In this figures, the maximum error at distance of 2, 3 and 4 [m] was 9.74, 7.67 and 6.56 [deg] and the distance between pinger and hydrophone array is closer, the detection accuracy is lower.

Figure 6 shows one of results of AUV homing experiments. Target position is about 10 [m] in front of AUV and the target depth is 3 [m]. AUV succeeded to reach the target using acoustic sensors.

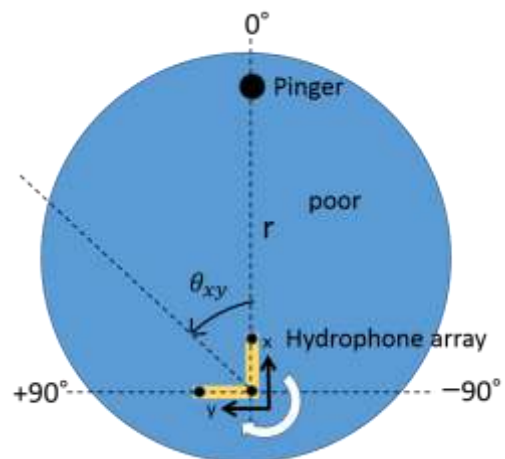


Fig. 2. Experimental environment.

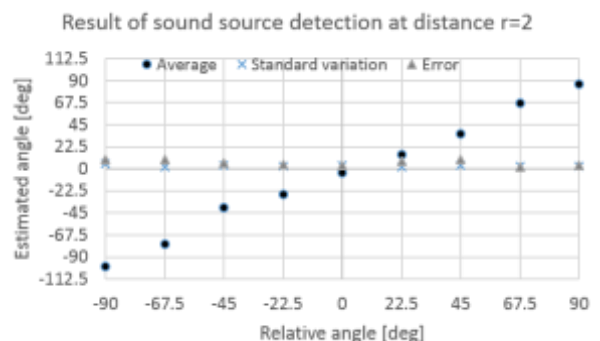


Fig. 3. Result of sound source detection at distance r=2[m].

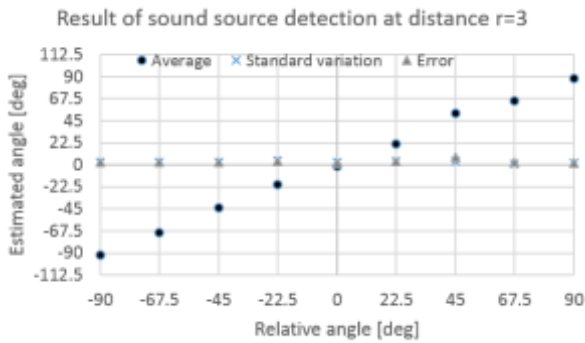


Fig. 4. Result of sound source detection at distance r=3[m].

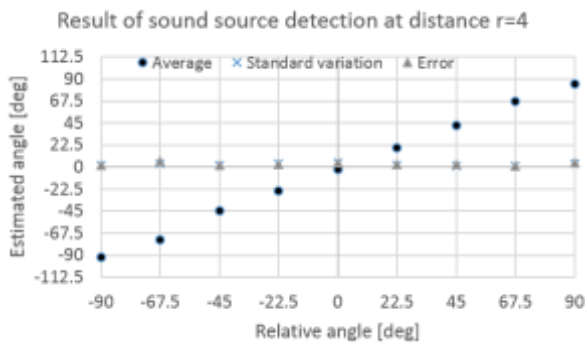


Fig. 5. Result of sound source detection at distance r=4[m].

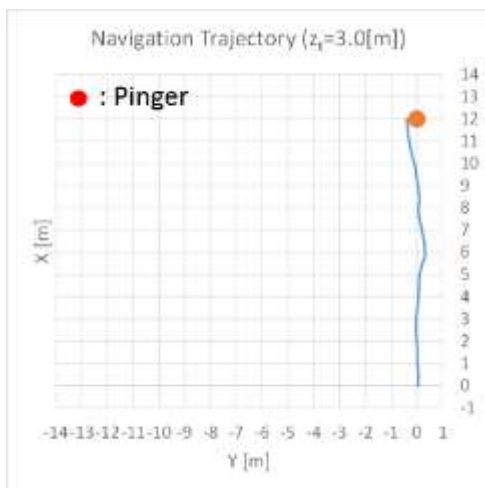


Fig.6 Experimental results of AUV homing.

4. Conclusion

The acoustic positioning system module mountable AUV was developed for navigation to charging station. The detection accuracy was verified in the experiment and the result suggest that it is available as navigation system. In the future, mounting the developed module on an AUV and implementation of motion for returning the station will be conducted.

References

1. H. Kondo, T. Maki, T. Ura, and T. Sakamaki, "AUV Navigation based on Multi-Sensor Fusion For Breakwater Observation," *ISARC2006 International Symposium on Automation and Robotics in Construction*, 2006.
2. J. Han, A. Asada, T. Ura, Y. Yamauchi, Y. Yagita, T. Maki, "Noncontact power supply for seafloor geodetic observing robot system," *J Mar Sci Technol*, pp183-189,2007.
3. Y. Eriguchi, I. Kazuo, K. Watanabe, "A Sound Source Localization System for Underwater Robots," *Proceedings of the 2008 JSME Conference on Robotics and Mechatronics*, Nagano, Japan, 2A1-A10, 2008.
4. Y. Watanabe, H. Ochi, T. Shimura, T. Hattori, "A Study on SSBL Underwater Positioning Using SS Communication," *Proceedings of Symposium on Ultrasonic Electronics*, Vol. 29, pp. 193-194, 2008.
5. I. Arai, Y. Tomizawa, M. HIROSE, "Pulse Compression Subsurface Radar," *IEICE Trans, Commun*, Vol. E83-B.No.9, 2000.